LANGMUIR Article
Cite This: Langmuir 2019, 35, 8709–8715 pubs.acs.org/Langmuir

Effect of Temperature on the Structure, Electrical Resistivity, and Charge Capacitance of Supported Lipid Bilayers

Shiju Abraham,[†] Tabea Heckenthaler,[†] Yakov Morgenstern,[†] and Yair Kaufman*[,†,‡]

[†]The Zuckerberg Institute for Water Research, The Jacob Blaustein Institutes for Desert Research, Ben-Gurion University of the Negev, Sde Boqer 8499000, Israel

[‡]Center for Bioengineering, University of California Santa Barbara, Santa Barbara, California 93106, United States

Supporting Information

ABSTRACT: Supported lipid bilayers with incorporated membrane proteins have promising potential for diverse applications, such as filtration processes, drug delivery, and biosensors. For these applications, the continuity (lack of defects), electrical resistivity, and charge capacitance of the lipid bilayers are crucial. Here, we highlight the effects of temperature changes and the rate of temperature changes on the vertical and lateral expansion and contraction of lipid bilayers, which in turn affect the lipid bilayer resistivity and capacitance. We focused on lipid bilayers that consist of 50 mol % dimyristoyl-*sn*-glycero-3-phosphocholine (zwitterionic lipid) and 50 mol % dimyristoyl-3-trimethylammonium-propane (positively charged lipid) lipids. This lipid mixture is known to self-assemble into a continuous lipid bilayer on silicon wafers. It is shown experimentally and explained theoretically that slow cooling (e.g., −0.4 °C min^{-1}) increases the resistivity significantly and reduces the capacitance of lipid bilayers, and these trends are reversed by heating. However, fast cooling (∼ −10 °C min^{-1} or faster) damages the membrane and reduces the resistivity and capacitance of lipid bilayers to practically zero. Importantly, the addition of 50 mol % cholesterol to lipid bilayers prevents the resistivity and capacitance reduction after fast cooling. It is argued that the ratio of lipid diffusion coefficient to thermal expansion/contraction rate (proportional to the heating/cooling rate) is the crucial parameter that determines the effects of temperature changes on lipids bilayers. A high ratio (fast lipid diffusion) increases the lipid bilayer resistivity and decreases the capacitance upon cooling and vice versa. Similar trends are expected for lipid membranes that consist of other lipids or lipidlike mixtures.

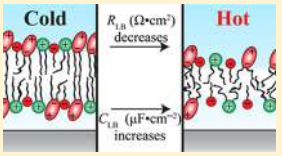

INTRODUCTION

Supported lipid bilayers with or without membrane proteins are often considered as simplified models of biological membranes; hence, they are frequently called biomimetic membranes. Since the lipid mixture and the type of membrane proteins that are incorporated in biomimetic membranes can be tuned, these biomimetic membranes are ideal for fundamental study of biological membranes, and they can potentially be used for diverse applications.[1−3] For instance, when aquaporins—membrane proteins that selectively transport water molecules through the lipid bilayer—are incorporated, the biomimetic membrane can potentially be used to purify water.[4−6] In other studies, different biosensing applications were demonstrated,[7−10] as well as drug-delivery applications.[11−13] For these applications, the main roles of lipid bilayers are (1) to serve as a suitable two-dimensional solvent for the membrane proteins; (2) to specifically adhere to certain cells (targets);[11] and finally, and maybe the most crucial role of lipid bilayers is (3) to prevent or slow down the transport of all ions and molecules through the membrane, thus exhibiting high resistivity and capacitance. Therefore, for the third role of lipid bilayers, their continuity (lack of holes and defects), resistivity, and capacitance are crucial.

There are many parameters that affect the continuity, resistivity, and capacitance of supported lipid bilayers, which were studied extensively before.[14−17] In addition, the effect of temperature on the average lipid area and the average lipid bilayer thickness,[18] as well as the phase changes that lipid bilayers undergo (e.g., liquid or gel-like), was also studied.[19−21] For instance, it was shown that the average lipid area of the dimyristoyl-*sn*-glycero-3-phosphocholine (DMPC) bilayer can contract by 3% as the temperature decreases from 36 to 30 °C.[18] Yet, to the best of our knowledge, the implications of temperature changes and the rate of temperature changes on the resistivity and capacitance were not explicitly studied.

Importantly, in some experiments or applications, temperature changes cannot be avoided and they are often overlooked. For instance, one often prepares vesicles or supported lipid bilayers and maintains them at a certain temperature, and then the vesicles or the supported lipid bilayers are transferred to a different solution of different temperature.

In this paper, we shed light on the effects of temperature changes on the continuity, resistivity, and capacitance of supported lipid bilayers. We focused on two lipid mixtures: a mixture that contains 50 mol % cholesterol and the other without cholesterol. Then, using electrochemical impedance spectroscopy (EIS) and fluorescence and atomic force microscopy (AFM), we studied the continuity, resistivity, and capacitance of the lipid bilayers at different temperatures

Received: March 11, 2019
Revised: June 3, 2019
Published: June 7, 2019

DOI: 10.1021/acs.langmuir.9b00726
Langmuir 2019, 35, 8709–8715

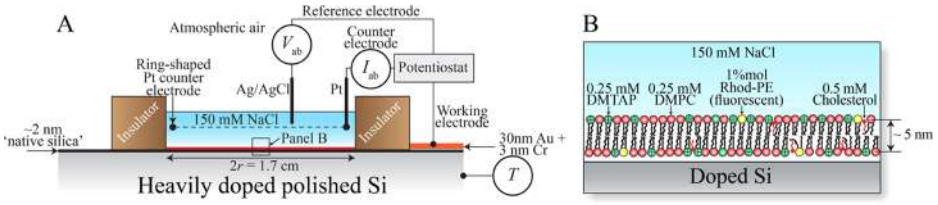

Figure 1. Schematic illustration of the experimental system. (A) Schematic illustration of the temperature-controlled electrochemical cell, which was used for electrochemical measurements, as well as for AFM and fluorescence imaging. (B) Schematic illustration of the lipid bilayer that was prepared on heavily doped silicon wafer (10^{20} P atoms cm^{-3}). Throughout the paper, two different lipid compositions were used, namely, 0.25 mM DMPC (zwitterion) + 0.25 mM DMTAP (positively charged) + 1 mol % Rhod-PE (fluorescent lipid) with or without 0.5 mM cholesterol.

and different cooling rates. Finally, we propose a qualitative model to describe the vertical and lateral reorganization of lipids in supported lipid bilayers that affect the resistivity and capacitance of supported lipid bilayers.

MATERIALS AND METHODS

Materials. Zwitterionic phospholipid, 1,2-dimyristoyl-*sn*-glycero-3-phosphocholine (DMPC); positively charged lipid, 1,2-dimyristoyl-3-trimethylammonium-propane (DMTAP); fluorescent lipid, 1,2-dimyristoyl-*sn*-glycero-3-phosphoethanolamine-*N*-(lissamine rhodamine B sulfonyl) (Rhod-PE); and cholesterol were purchased from Avanti Polar Lipids (Alabama). Chloroform (HPLC plus ≥ 99.9%) was purchased from Sigma-Aldrich. Other solvents and chemicals, such as ethanol, acetone, sodium chloride (NaCl), etc., were of analytical grade. Water used for cleaning and other solution preparation processes was taken from a Milli-Q gradient water purification system. The typical water resistivity was 18 MΩ cm.

Lipid Vesicle Mixtures. DMPC and DMTAP were dissolved in chloroform at a concentration of 3 mg mL^{-1}. These solutions were used as stock solutions. In addition, cholesterol (5 mg mL^{-1}) and Rhod-PE (0.2 mg mL^{-1}) were also dissolved in chloroform. The two different lipid mixtures that were used for this study, namely, 0.25 mM DMPC + 0.25 mM DMTAP + 1 mol % Rhod-PE with or without 0.5 mM cholesterol, were prepared by mixing the required concentration from the above stock solutions.

To prepare the vesicle solution for the AFM and electrochemical impedance spectroscopy measurements, initially, the particular lipid mixture was prepared in a clean glass vial using the lipid stock solution, which was left on a hot plate (55 °C) in a chemical hood for ∼1 h to completely evaporate the chloroform. A total lipid concentration of 0.5 mM was achieved by adding NaCl aqueous solution (150 mM, pH 7 ± 0.3, 1 mL) to the above dried lipid mixture. In addition to that, 1 mol % Rhod-PE was added to the two different lipid combinations as a fluorescent lipid to tag the lipid combination for fluorescence microscopy. In the second set of lipid mixture, cholesterol with a concentration of 0.5 mM was added to the lipid mixture, so the final mol ratio was 1:1:2: DMPC (zwitterionic)/DMTAP (positively charged)/cholesterol. Subsequently, the vesicle solution was ultrasonicated (2 min; 60 Hz) and heated (20 min; 55 °C) until a uniform vesicle solution was formed. These well-dispersed vesicles were then extruded through a track-etched polycarbonate membrane (pore size ∼100 nm, Avanti Polar lipids) ∼10 times at ∼55 °C to have a final homogeneous vesicle solution.

Self-Assembly of the Lipid Bilayers on Semiconductive Silicon Wafers. Initially, different single-side-polished, conductive silicon wafers (P-type; $N_A = 10^{20}$ P atoms cm^{-3}; thickness = 525 ± 25 μm; ⟨100⟩) with an electrical resistivity of 0.0008−0.001 Ω cm, purchased from Si-Mat Silicon Materials, Germany, were cut down to a smaller size (∼25 × 25 mm^2) to fit in the EC cell (Figure 1A). After cleaning the substrates with solvents (acetone, ethanol, and deionized water), N_2 gun, and UV−ozone (for 10 min), 3 nm chromium (Cr) followed by 30 nm gold (Au) were deposited on one of the edges (∼5 × 5 mm^2) using a thermal evaporation deposition technique (Vinci Technologies, France). This gold coating was done to achieve a better electronic contact with the electrochemical working electrode for impedance spectroscopy measurements. These substrates were cleaned again by the same process mentioned above prior to the vesicle fusion. Successively, the well-cleaned Si substrate was placed in the EC cell setup (inner substrate area of the EC cell is ∼2.27 cm^2, Figure 1A) and maintained at a constant temperature of 45 °C for the vesicle fusion. Furthermore, 400 μL of vesicle solution was uniformly poured on the Si substrate placed in the EC cell setup and thermally insulated for the next 30 min for the vesicle fusion and self-assembly of the lipid bilayer on the substrate. Then, the vesicles in the EC cell were rinsed with 150 mM NaCl aqueous solution at 45 °C to remove the excess vesicles that did not adsorb onto the Si surface. Then, the sample was kept at the same temperature or cooled down slowly at a rate of −0.4 °C min^{-1} or rapidly at a rate of <−10 °C min^{-1} depending on the different experimental conditions as elaborated in the text below.

Fluorescence Imaging. Different lipid compositions on the substrates were captured at different stages of the experiment using an epifluorescent microscope (Axio Zoom, V16, Zeiss, Germany). The epifluorescent microscope, which was coupled with the AFM, provided micrometer-resolved images of the surface. The homogeneity of the lipid assembly on the surface as well as the intensity variation with temperature change was continuously monitored employing this microscope. Finally, these fluorescent images were cropped and the intensity values were procured using Photoshop CC2018 (Adobe) software.

AFM Imaging and Force Spectroscopy. The atomic force microscopy (AFM) technique (JPK NanoWizard 4, JPK Instruments AG, Germany) was employed to acquire the surface topography at nanoscale resolution along with force spectroscopy to check the number and thickness of the lipid bilayers or the breakthrough force of the lipid bilayers. All of these measurements were done in NaCl (150 mM, pH 7 ± 0.3) aqueous solution at specific temperatures (45−24 °C) discussed in this study. Quantitative imaging mode was used to acquire the topography of the surfaces. V-shaped silicon tips (SNL-10 probes; Bruker) were used. The thermal noise method was employed to measure the spring constant of the cantilever, which was ∼0.30 N m^{-1}. During the force vs distance measurements, a constant velocity of 100 nm s^{-1} was applied for the approach and retraction of the piezoelectric actuator. JPK SPM-Data processing software was used to analyze all of the AFM data collected.

Electrochemical Impedance Spectroscopy. All of the electrochemical impedance spectroscopy (EIS) measurements were performed using a potentiostat (model: SP-300, Bio-Logic Science Instruments, France). As depicted in Figure 1, a three-electrode electrochemical system (EC cell) was used for the impedance and capacitance measurements. A silicon wafer, with the same specifications as mentioned in Materials section, was used as a working electrode. Ag/AgCl was used as a reference electrode, and a Pt ring (diameter ∼1.7 cm) was used as a counter electrode. Impedance spectra of the bare Si substrate were recorded as a control experiment prior to the actual impedance measurement of the samples. For the impedance and capacitance data processing, EC-Lab software was used, by fitting the equivalent circuits to the data.

DOI: 10.1021/acs.langmuir.9b00726
Langmuir 2019, 35, 8709−8715

RESULTS AND DISCUSSION

Effect of Temperature on Resistivity and Capacitance of Supported Lipid Bilayers. In this section, we discuss the effect of temperature on the lipid bilayer resistivity, R_{LB} (kΩ cm^2), and capacitance, C_{LB} (μF cm^{-2}), as measured by electrochemical impedance spectroscopy. All of the experiments were conducted in 150 mM NaCl, at pH 7 ± 0.3, aqueous solution. As depicted in Figure 2A, two lipid mixtures were studied: (1) 1:1:2 mol ratio of DMPC (zwitterionic)/DMTAP (positively charged)/cholesterol (i.e., 50 mol % cholesterol) or (2) 1:1:0 mol ratio (i.e., no cholesterol). Detailed description of the preparation of the supported lipid bilayers is provided in the Materials and Methods.

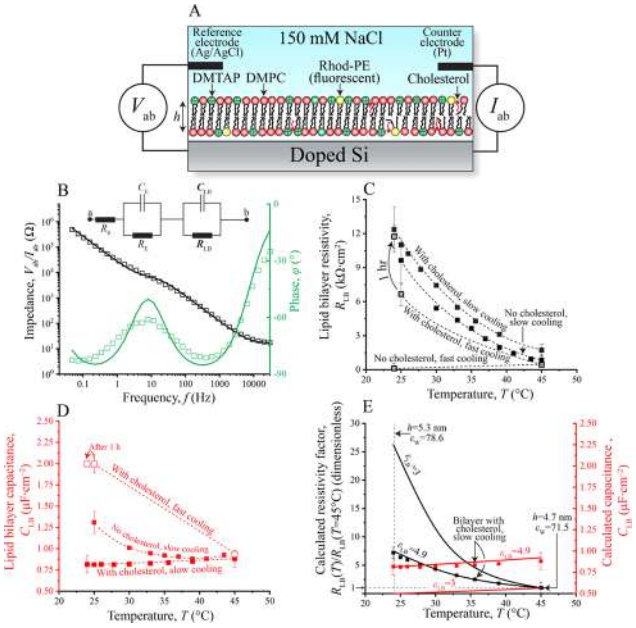

Figure 2. Measurements and calculation of the lipid bilayer resistivity, R_{LB}, and capacitance, C_{LB}, at different temperatures. (A) Schematic illustration of the experimental system. More details can be found in Figure 1. Each impedance vs frequency and phase shift vs frequency plot, $Z(f)$ ($Z = V_{ab}/I_{ab}$) and $\varphi(f)$ (Bode plot), was measured at constant temperature. (B) Example of a typical Bode plot that was measured at T = 33 °C during slow cooling of lipid bilayers with 50 mol % cholesterol. The empty squares are the measured data points, and the continuous curves are calculated Z and φ based on the equivalent electronic circuit (also shown in the panel) that was used to calculate R_{LB} and C_{LB}. Each data point in (C) and (D) is based on a Bode plot. (C) R_{LB} (T) for lipid bilayers with or without 50 mol % cholesterol, and the effect of slow (−0.4 °C min^{-1}) or fast cooling (<−10 °C min^{-1}). (D) C_{LB} (T) and the effect of cooling rate. The error bars represent the standard deviation of three independent experiments (different lipid bilayers). The dashed lines in (C) and (D) are guidelines (not models). (E) Continuous curves are the calculated R_{LB} and C_{LB} for different ϵ_{LB} values based on eqs 4 and 5. The data points correspond to lipid bilayers with 50 mol % cholesterol upon slow cooling, as shown in (C) and (D).

Figure 2B shows a typical Bode plot, $Z(f)$, which depicts the impedance of the supported lipid bilayer on the silicon wafer vs frequency at constant temperature, T. The equivalent electrical circuit in Figure 2B was fitted to each Bode plot to calculate R_{LB} and C_{LB} at each temperature. More details about electrochemical measurements of supported lipid bilayer resistivity and capacitance can be found elsewhere.[22,23] Finally, R_{LB} (T) and C_{LB} (T) are summarized in Figure 2C,D.

Figure 2C shows that upon slow cooling (−0.4 °C min^{-1}), R_{LB} increased for both lipid mixtures. However, when the lipid bilayers were cooled down rapidly (faster than −10 °C min^{-1}), R_{LB} reduced to zero and did not increase with time for the lipid bilayers without cholesterol. On the other hand, after rapid cooling of the lipid bilayers with cholesterol, R_{LB} increased with time, and it reached a similar value as measured after slow cooling. Importantly, for both lipid mixtures, the effect of temperature on R_{LB} was reversible, except for the case of lipid bilayers without cholesterol after rapid cooling. For that specific case, R_{LB} did not recover with time, not even after heating the sample back to 45 °C and cooling it slowly to 24 °C.

Figure 2D shows the effect of temperature on C_{LB}. In the case of the lipid bilayers with cholesterol, C_{LB} monotonically decreased as the lipid bilayers were cooled down slowly from 45 to 24 °C. On the other hand, for the lipid bilayers without cholesterol, C_{LB} initially decreased and then increased when the temperature went below ∼37 °C, which is the temperature of liquid-to-solid phase transition for the 1:1 mol ratio DMPC/DMTAP.[24]

Figure 2E depicts the calculated R_{LB} and C_{LB} at different temperatures. As elaborated in the Supporting Information, based on the Boltzmann distribution, R_{LB} is proportional to $\exp(\Delta E/kT)$, where k is the Boltzmann constant, T is the absolute temperature, and ΔE is the energy change as an ion is transferred from an aqueous environment to the center of the hydrophobic core of an uncharged lipid bilayer, which is given by[25]

$$E(T) = \frac{e^2}{8\pi\epsilon_0 a}\left(\frac{1}{\epsilon_{LB}} - \frac{1}{\epsilon_W}\right) - \frac{e^2}{4\pi\epsilon_0\epsilon_{LB}h}\ln\left(\frac{2\epsilon_W}{\epsilon_W + \epsilon_{LB}}\right) \quad (1)$$

where e is the charge of an electron; ϵ_0 is the vacuum permittivity; ϵ_{LB} and ϵ_W are the dielectric constants of the lipid bilayer and the water, respectively; a is the radius of an ion; and h is the thickness of the lipid bilayer. Note that the 1st term of eq 1 is the solvation energy (Born energy) of an ion that is transferred from ϵ_W to ϵ_{LB}, whereas the 2nd term is due to the presence of high dielectric constant in the vicinity of the ion when it is at the center of a thin infinite layer, such as a lipid bilayer.[26]

The effect of T on the dielectric constant of water can be approximated by[27]

$$\epsilon_W(T) = 87.740 - 0.4008T + 9.398 \times 10^{-4}\,T^2 - 1.410 \times 10^{-6}\,T^3 \ (T \text{ in } °C) \quad (2)$$

Assuming that the bilayers do not undergo phase transition, and based on previous X-ray studies,[18] the effect of T on the lipid bilayer thickness can be approximated by a linear correlation

$$h(T) = h_0 - a_T\Delta T \quad (3)$$

where h_0 is the thickness of the bilayer at a reference temperature and α_T is the vertical (height) thermal expansion/contraction coefficient, and it is assumed to be constant.

Unfortunately, the effect of temperature on ϵ_{LB} is not easy to predict even if the lipid bilayers do not undergo a phase transition. There are two contradicting trends that affect ϵ_{LB} as

DOI: 10.1021/acs.langmuir.9b00726
Langmuir 2019, 35, 8709−8715

the temperature changes. On one hand, as the lipid area decreases upon cooling, ϵ_{LB} is expected to decrease by pushing water molecules (high dielectric constant) out of the bilayer. On the other hand, in general, decrease in temperature increases the dielectric constant of organic molecules (see Figure 8.1 in ref 28). It is not clear which trend dominates the changes of ϵ_{LB}; therefore, as a first-order approximation, it was assumed that ϵ_{LB} remains roughly constant with T.

Considering eqs 1 to 3, the overall effect of temperature on R_{LB} can be approximated by

$$\frac{R_{LB}(T)}{R_{LB}(T_0)} = \frac{\exp\left(\frac{E(T)}{kT}\right)}{\exp\left(\frac{E(T_0)}{kT}\right)} \quad (4)$$

where R_{LB} (T_0) is the resistivity of the lipid bilayer at a reference temperature, T_0.

Finally, the capacitance per area (μF cm^{-2}) of the lipid bilayers is given by

$$C_{LB}(T) = \frac{\epsilon_0 \epsilon_{LB}}{h} \quad (5)$$

Figure 2E shows the calculated R_{LB} and C_{LB} based on eqs 4 and 5 for two different ϵ_{LB} values as indicated in the figure. For these calculations, it was assumed that a = 0.2 nm (roughly the size of Na^+ and Cl^-), $a_T \sim 0.03$ nm °C^{-1}, and h_0 = 4.7 nm at T_0 = 45 °C, where the values of a_T and h_0 were fitted to the data; yet, their values are within the range of previous publications.[18] Based on Figure 2E, it appears that changes in ϵ_W and h with temperature are enough to reproduce the measured changes in R_{LB} and C_{LB} upon slow cooling of the lipid bilayers with cholesterol. In addition, for ϵ_{LB} = 4.9, the absolute values of the calculated results commensurate with the measured results for the lipids bilayers with cholesterol upon slow cooling (data points in Figure 2E).

Importantly, based on Figure 2E, for the lipid bilayers without cholesterol or for fast cooling of both lipid mixtures, there is a discrepancy between the trend of the calculated C_{LB} and the measured values. According to eq 5, C_{LB} should monotonically decrease as the lipid bilayers are cooled, and the trend of the measured C_{LB} was not monotonic. It is most likely that this discrepancy was due to the phase transition that the studied lipid bilayers without cholesterol underwent at 36.7 °C, namely, from a liquid phase above 36.7 °C to a gel-like phase below 36.7 °C.[24] At a liquid-like phase, the hydrocarbon lipid tails are disordered, i.e., they are not stretched, which decreases the thickness of the lipid bilayers. On the other hand, in a gel-like phase, the hydrocarbon lipid tails are ordered (stretched), which increases the bilayer thickness. Thus, the phase transition imposes a thickness change, which is not considered in eq 3. In addition, thermal changes involve the reorganization of a large number of lipids. As elaborated in the next section, it is likely that during fast temperature changes, there is not enough time for the lipids to reach their optimal conformation.

Interestingly, however, it appears that ~10% changes in the lipid bilayer height, h (from 4.7 nm at 45 °C to 5.3 nm at 24 °C), together with the effect of temperature on the dielectric constant of water, ϵ_W, are enough to increase R_{LB} by a factor of 7. As demonstrated in Figure 2E, for lipid membranes, where ϵ_{LB} = 3, which can be the case of lipids with longer hydrophobic chains (e.g., 16 or 18 carbons), the effect of temperature on R_{LB} is expected to be significantly higher (factor of 30).

Effect of Temperature on the Areal Expansion and Contraction of Supported Lipid Bilayers. Other than the changes in the lipid bilayer height, h, as discussed in the previous section, the average area of a single lipid, A, also changes with temperature. For instance, based on X-ray studies,[18] A can contract by ~10% when lipid bilayers are cooled down from 45 to 24 °C. In this section, we discuss the lateral reorganization of supported lipid bilayers as the temperature changes, which can allow areal expansion and contraction without generating damages in the lipid bilayers.

Figure 3A,B shows AFM topography images of supported lipid bilayers without cholesterol at 45 and 25 °C, respectively,

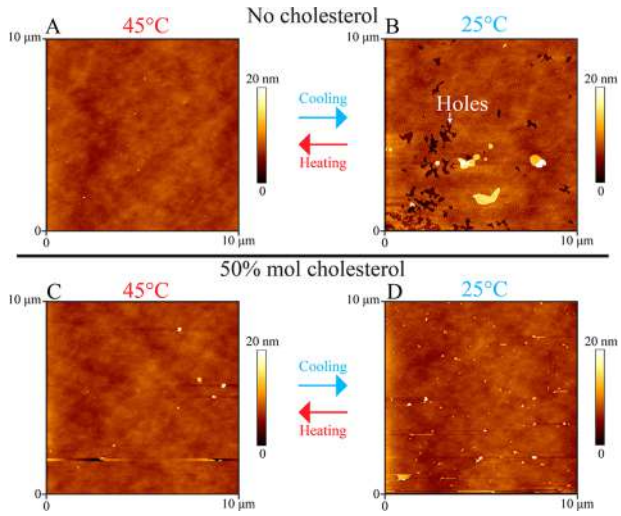

Figure 3. AFM topography images showing the effect of cooling on the continuity of the lipid bilayers. Lipid bilayer without cholesterol (A) at 45 °C and (B) at 25 °C. Lipid bilayer with 50 mol % cholesterol (C) at 45 °C and (D) at 25 °C. Holes formed in the bilayers without cholesterol regardless of the cooling rate, whereas no holes were detected in the bilayers with cholesterol. The phase transition for the DMPC/DMTAP mixture (50:50) takes place at 36.7 °C.[24] The addition of cholesterol prevents the phase transition at this temperature range.[30]

and Figure 3C,D shows the topography of lipid bilayers with cholesterol at the same temperatures. Evidently, the contraction of the lipid bilayer area during the cooling process generated holes in the lipid bilayers without cholesterol. The formation of holes in lipid bilayers at low temperatures was reported before.[29] On the other hand, in the case of the lipid bilayers with cholesterol, the lipid bilayers could contract and expand without generating defects/holes.

To shed light on how the lipid bilayers with the cholesterol can thermally expand and contract without generating holes, fluorescence images and AFM scans were acquired. Typical images of lipid bilayers with cholesterol at different temperatures are shown in Figure 4. Similar images of supported lipid bilayers without cholesterol are shown in Figure S1 (Supporting Information).

The fluorescence image in Figure 4A reveals three different levels of fluorescence, which can be interpreted as follows: (1) the homogeneous fluorescence throughout the image corresponds to the 1st lipid bilayer (see panel C) that covers the entire surface; (2) the brighter objects that are shown in the

DOI: 10.1021/acs.langmuir.9b00726
Langmuir 2019, 35, 8709−8715

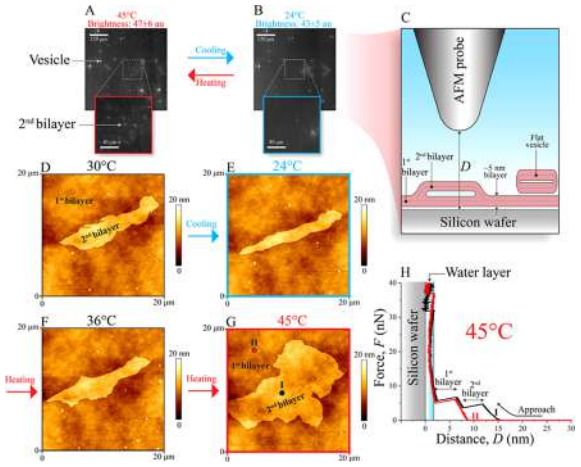

Figure 4. Fluorescence and AFM topography images of the lipid bilayer with 50 mol % cholesterol captured at different temperatures. Fluorescence image at (A) 45 °C and (B) 24 °C of the same area. The average fluorescence intensity was similar at different temperatures, but the heterogeneity (standard deviation) decreased as the sample lipid bilayer was cooled. The insets show that the bright objects, which were the 2nd lipid bilayer (see C), disappeared upon cooling and reappeared (sometimes at different locations) upon heating. AFM topography images showing that the 2nd lipid bilayer (D, E) contracted upon cooling and (F, G) expanded upon heating. (H) Force vs distance curves revealing the existence of the 1st and the 2nd lipid bilayers, as illustrated in (C).

inset correspond to a 2nd lipid bilayer that covers parts of the surface; and finally, (3) the brightest objects are intact vesicles that adsorbed onto the surface.

Figure 4B shows that the fluorescence of 2nd lipid bilayer faded out or completely disappeared as the temperature decreased from 45 °C (intensity was 47 ± 6 au) to 24 °C (43 ± 5 au). Note, however, that the average fluorescence intensity remained similar as the temperature decreased, i.e., the average lipid density per area, which included the 2nd lipid bilayers, remained the same. As will be discussed in the next section, the conservation of the average lipid density is crucial to maintain the continuity of lipid bilayers, as well as to increase R_{LB} and decrease C_{LB} as the temperature gradually decreases. We note that the fluorescence intensity of the 2nd lipid bilayer recovered when the temperature was increased back to 45 °C.

To shed light on how the average lipid density is conserved as the temperature changes, AFM images were acquired. Figure 4D shows a topography image of the 1st and the 2nd lipid bilayer at 30 °C. As the lipid bilayer was cooled down to 24 °C, the 2nd lipid bilayer contracted, as shown in Figure 4E, from ∼46 to ∼30 μm^2. This corresponds to 34% areal contraction, which is significantly more than the 3% areal contraction that is expected for this temperature change based on previous X-ray measurements.[18]

Then, when the lipid bilayer was heated to 36 °C and then to 45 °C, the 2nd lipid bilayer expanded significantly from ∼42 to ∼149 μm^2, as shown in Figure 4F,G. This is a 255% areal expansion. Finally, Figure 4H shows force vs distance curves as the AFM probe approached the silicon substrate. These force vs distance curves were acquired at the specific locations as indicted in Figure 4G. These force vs distance curves clearly show the probe's penetration into the 1st (red curve) and the 2nd lipid bilayer.

Importantly, based on the AFM and fluorescence images in Figure 4, it appears that the 2nd lipid bilayer contracted and expanded as the temperature decreased and increased significantly more than the expected thermal expansion at this range of temperature. In the next section, we propose a molecular mechanism that explains this large expansion and contraction of the 2nd lipid bilayer, as well as the lateral reorganization of the supported lipid bilayer as the temperature changes.

Qualitative Description of the Effect of Thermal Areal Contraction and Expansion on the Continuity of Supported Lipid Bilayers. Figure 5 illustrates a proposed a qualitative molecular mechanism by which the average lipid area, *A*, can contract or expand without generating holes in the lipid bilayer. According to this mechanism, during the first steps of the self-assembly of the supported lipid bilayer via the vesicle fusion mechanism (Figure 5A), vesicles adsorb onto the surface, flatten, rupture, and eventually form a lipid bilayer on the surface.[14,31] Importantly, some vesicles do not rupture during the self-assembly process; instead, they remain flattened on the surface. As shown in B, some of these flat vesicles can create a 2nd lipid bilayer that is fused to the 1st lipid bilayer. Other vesicles can flatten and remain separated from the 1st lipid bilayer.

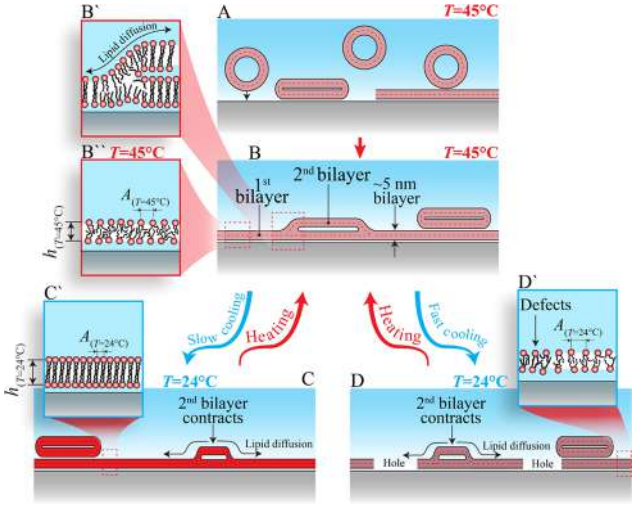

Figure 5. Proposed mechanism of the vertical and lateral changes that lipid bilayers undergo upon fast and slow temperature changes. (A) Vesicles initially can adhere to the surface, rupture, and form a continuous lipid bilayer on the surface. (B) Parts of the supported lipid membrane can consist of a 2nd lipid bilayer that is fused to the supported lipid bilayer (B′), flattened isolated vesicles (not illustrated), or several lipid bilayers (not illustrated). When the temperature decreases, the average area of a single lipid decreases, and thus the macroscopic lipid bilayer area contracts. (C, C′) If the rate of the lipid diffusion is faster than the rate of the bilayer area contraction (slow cooling), the lipids have time to reach the optimal area for the given temperature. (D) However, if the lipid diffusion rate is slower that the rate of the bilayer area contractions (fast cooling), defects (D′) and holes will form.

As the temperature decreases, the macroscopic area of the lipid bilayer contracts. As mentioned in the previous section, this areal contraction can be ∼10%, and it can generate holes in the lipid bilayers, thereby increasing the lipid bilayer energy by exposing the hydrophobic core to the aqueous solution. Alternatively, to compensate for the contracted area and avoid

DOI: 10.1021/acs.langmuir.9b00726
Langmuir 2019, 35, 8709−8715

increase in energy due to the holes, lipids can diffuse from the 2nd to the 1st lipid bilayer. If the contraction rate (proportional to the cooling rate) is slower than the diffusion rate, the lipids have enough time to reorganize and diffuse from the 2nd lipid bilayer to the 1st, thereby preventing the formation of defects and holes in the bilayer. This was the case for the lipid bilayers with cholesterol during the slow cooling process. The cholesterol prevented the lipid bilayer from transforming into a gel phase and thus the lipid diffusion remained relatively fast, even at 24 °C.

However, during fast cooling, the lipids do not have time to diffuse from the 2nd to the 1st lipid bilayer and defects and holes are expected to form. This was the case of the lipid bilayers without cholesterol. Below 36.7 °C, the specific lipid mixture transitions to a gel phase.[24] Typically, the diffusion coefficient of the lipid within lipid bilayers decreases by 2−3 orders of magnitude as the lipid bilayer transitions from a liquid (disordered) to a gel (ordered) phase.[30] The slow diffusion of the lipids in the gel phase slows down the reorganization of the lipids and thus defects and holes can form.

As discussed in the previous section, and according to the mechanism described in this section, the 2nd lipid bilayer is expected to expand and contract significantly more than 10%, since it needs to compensate for the areal changes of the 1st lipid bilayer as well.

CONCLUSIONS

Here, we studied the effects of temperature changes on lateral and vertical reorganization of lipids in supported lipid bilayers and the implications of this reorganization on the resistivity and capacitance of lipid bilayers. In our study, we focused on two lipid mixtures that consisted of DMPC and DMTAP with or without cholesterol. These lipid mixtures are known to form a continuous lipid bilayer on negatively charged smooth hydrophilic surfaces, such as silicon wafers, where the top layer is silica.[14]

In general, we found that the resistivity of lipid bilayers increases and the capacitance decreases as the temperature decreases. We theoretically reproduced these trends by considering the changes in the dielectric constant of water and changes in lipid bilayer thickness as temperature changes. However, experimentally, these trends only occur when the cooling rate is slower than the diffusion rate of the lipids in the lipid bilayer, which is −0.4 °C min^{-1} for the specific lipid mixture that was studied. On the other hand, for fast cooling, faster than −10 °C min^{-1}, or when the lipid bilayers undergo phase transition, from liquid to gel-like (diffusion coefficient decreases dramatically), the lipids do not have enough time to reorganize and defects in the lipid bilayer may form. These defects diminish the resistivity and capacitance of the supported lipid bilayers upon cooling. As demonstrated experimentally, one way to avoid damaging the lipid bilayer during temperature changes is by adding cholesterol to the lipid bilayers. Cholesterol prevents the phase transition of the lipid bilayer in the entire temperature range that was studied (24−45 °C).

We also found that the thermal lateral expansion and contraction of the lipid bilayer are compensated by diffusion of lipids from or to the 2nd lipid bilayer that forms during the self-assembly of the supported lipid bilayer. This 2nd lipid bilayer acts as a lipid reservoir that can supply or store lipids as the lipid density of the 1st ("main") lipid bilayer changes.

Finally, in general, at a certain temperature range, which may change from one lipid mixture to another, the thickness of lipid bilayers increases and the average area of a single lipid in lipid bilayers decreases as temperature decreases (illustrated in Figure 5B″,C′), and vice versa as temperature increases. Since these are the general trends, we expect our conclusions to be valid for lipid bilayers that consist of other lipids or lipidlike (e.g., block copolymers) molecules.

ASSOCIATED CONTENT

Supporting Information

The Supporting Information is available free of charge on the ACS Publications website at DOI: 10.1021/acs.langmuir.9b00726.

(1) Calculation of the effect of temperature on the lipid bilayer resistivity, and results showing (2) the effect of temperature on the topography of lipid bilayers without cholesterol (PDF)

AUTHOR INFORMATION

Corresponding Author

*E-mail: yairkauf@ucsb.edu.

ORCID

Yair Kaufman: 0000-0001-7771-8502

Notes

The authors declare no competing financial interest.

ACKNOWLEDGMENTS

Authors acknowledge Shlomo Kabalo from Alexandre Yersin Department of Solar Energy and Environmental Physics, Ben-Gurion University of the Negev for the thermal evaporation deposition of the metal layers. We also want to acknowledge Shaula C. Kaufman for the inspiring discussions. This work was supported by the Adelis foundation.

REFERENCES

(1) Sackmann, E. Supported Membranes: Scientific and Practical Applications. *Science* **1996**, *271*, 43−48.

(2) Castellana, E. T.; Cremer, P. S. Solid Supported Lipid Bilayers: From Biophysical Studies to Sensor Design. *Surf. Sci. Rep.* **2006**, *61*, 429−444.

(3) Richter, R. P.; Bérat, R.; Brisson, A. R. Formation of Solid-Supported Lipid Bilayers: an Integrated View. *Langmuir* **2006**, *22*, 3497−3505.

(4) Kumar, M.; Grzelakowski, M.; Zilles, J.; Clark, M.; Meier, W. Highly Permeable Polymeric Membranes Based on the Incorporation of the Functional Water Channel Protein Aquaporin Z. *Proc. Natl. Acad. Sci. U.S.A.* **2007**, *104*, 20719−20724.

(5) Kaufman, Y.; Berman, A.; Freger, V. Supported Lipid Bilayer Membranes for Water Purification by Reverse Osmosis. *Langmuir* **2010**, *26*, 7388−7395.

(6) Werber, J. R.; Osuji, C. O.; Elimelech, M. Materials for Next-Generation Desalination and Water Purification Membranes. *Nat. Rev. Mater.* **2016**, *1*, No. 16018.

(7) Limaj, O.; Etezadi, D.; Wittenberg, N. J.; Rodrigo, D.; Yoo, D.; Oh, S.-H.; Altug, H. Infrared Plasmonic Biosensor for Real-Time and Label-Free Monitoring of Lipid Membranes. *Nano Lett.* **2016**, *16*, 1502−1508.

(8) Cornell, B. A.; Braach-Maksvytis, V. L.; King, L. G.; Osman, P. D.; Raguse, B.; Wieczorek, L.; Pace, R. J. A Biosensor That Uses Ion-Channel Switches. *Nature* **1997**, *387*, 580−583.

(9) Nikoleli, G.-P.; Nikolelis, D. P.; Evtugyn, G.; Hianik, T. Advances in Lipid Film Based Biosensors. *TrAC, Trends Anal. Chem.* **2016**, *79*, 210−221.

DOI: 10.1021/acs.langmuir.9b00726
Langmuir 2019, 35, 8709−8715

(10) Zhang, Y.; Inal, S.; Hsia, C.-Y.; Ferro, M.; Ferro, M.; Daniel, S.; Owens, R. M. Supported Lipid Bilayer Assembly on PEDOT:PSS Films and Transistors. *Adv. Funct. Mater.* **2016**, *26*, 7304−7313.
(11) Butler, K. S.; Durfee, P. N.; Theron, C.; Ashley, C. E.; Carnes, E. C.; Brinker, C. J. Protocells: Modular Mesoporous Silica Nanoparticle-Supported Lipid Bilayers for Drug Delivery. *Small* **2016**, *12*, 2173−2185.
(12) Durfee, P. N.; Lin, Y.-S.; Dunphy, D. R.; Muñiz, A. J.; Butler, K. S.; Humphrey, K. R.; Lokke, A. J.; Agola, J. O.; Chou, S. S.; Chen, I.-M.; et al. Mesoporous Silica Nanoparticle-Supported Lipid Bilayers (Protocells) for Active Targeting and Delivery to Individual Leukemia Cells. *ACS Nano* **2016**, *10*, 8325−8345.
(13) Ashley, C. E.; Carnes, E. C.; Phillips, G. K.; Padilla, D.; Durfee, P. N.; Brown, P. A.; Hanna, T. N.; Liu, J.; Phillips, B.; Carter, M. B.; et al. The Targeted Delivery of Multicomponent Cargos to Cancer Cells by Nanoporous Particle-Supported Lipid Bilayers. *Nat. Mater.* **2011**, *10*, 389−397.
(14) Abraham, S.; Heckenthaler, T.; Bandyopadhyay, D.; Morgenstern, Y.; Kaufman, Y. Quantitative Description of the Vesicle Fusion Mechanism on Solid Surfaces and the Role of Cholesterol. *J. Phys. Chem. C* **2018**, *122*, 22985−22995.
(15) Garcia-Manyes, S.; Oncins, G.; Sanz, F. Effect of Ion-Binding and Chemical Phospholipid Structure on the Nanomechanics of Lipid Bilayers Studied by Force Spectroscopy. *Biophys J.* **2005**, *89*, 1812−1826.
(16) García-Sáez, A. J.; Chiantia, S.; Salgado, J.; Schwille, P. Pore Formation by a Bax-Derived Peptide: Effect on the Line Tension of the Membrane Probed by AFM. *Biophys. J.* **2007**, *93*, 103−112.
(17) Zhang, L.; Spurlin, T. A.; Gewirth, A. A.; Granick, S. Electrostatic Stitching in Gel-Phase Supported Phospholipid Bilayers. *J. Phys. Chem. B* **2006**, *110*, 33−35.
(18) Kučerka, N.; Liu, Y.; Chu, N.; Petrache, H. I.; Tristram-Nagle, S.; Nagle, J. F. Structure of Fully Hydrated Fluid Phase DMPC and DLPC Lipid Bilayers Using X-Ray Scattering From Oriented Multilamellar Arrays and From Unilamellar Vesicles. *Biophys. J.* **2005**, *88*, 2626−2637.
(19) Almeida, P. F. F.; Vaz, W. L. C.; Thompson, T. E. Lateral Diffusion in the Liquid Phases of Dimyristoylphosphatidylcholine/Cholesterol Lipid Bilayers: a Free Volume Analysis. *Biochemistry* **1992**, *31*, 6739−6747.
(20) Scomparin, C.; Lecuyer, S.; Ferreira, M.; Charitat, T.; Tinland, B. Diffusion in Supported Lipid Bilayers: Influence of Substrate and Preparation Technique on the Internal Dynamics. *Eur. Phys. J. E* **2009**, *28*, 211−220.
(21) Redondo-Morata, L.; Giannotti, M. I.; Sanz, F. Influence of Cholesterol on the Phase Transition of Lipid Bilayers: a Temperature-Controlled Force Spectroscopy Study. *Langmuir* **2012**, *28*, 12851−12860.
(22) Gritsch, S.; Nollert, P.; Jähnig, F.; Sackmann, E. Impedance Spectroscopy of Porin and Gramicidin Pores Reconstituted Into Supported Lipid Bilayers on Indium−Tin-Oxide Electrodes. *Langmuir* **1998**, *14*, 3118−3125.
(23) Purrucker, O.; Hillebrandt, H.; Adlkofer, K.; Tanaka, M. Deposition of Highly Resistive Lipid Bilayer on Silicon−Silicon Dioxide Electrode and Incorporation of Gramicidin Studied by Ac Impedance Spectroscopy. *Electrochim. Acta* **2001**, *47*, 791−798.
(24) Zantl, R.; Baicu, L.; Artzner, F.; Sprenger, I.; Rapp, G.; Rädler, J. O. Thermotropic Phase Behavior of Cationic Lipid−DNA Complexes Compared to Binary Lipid Mixtures. *J. Phys. Chem. B* **1999**, *103*, 10300−10310.
(25) Dilger, J. P.; McLaughlin, S. G.; McIntosh, T. J.; Simon, S. A. The Dielectric Constant of Phospholipid Bilayers and the Permeability of Membranes to Ions. *Science* **1979**, *206*, 1196−1198.
(26) Parsegian, A. Energy of an Ion Crossing a Low Dielectric Membrane: Solutions to Four Relevant Electrostatic Problems. *Nature* **1969**, *221*, 844−846.
(27) Malmberg, C. G.; Maryott, A. A. Dielectric Constant of Water From 00 to 1000 C. *J. Res. Natl. Bur. Stand.* **1956**, *56*, 1.
(28) Israelachvili, J. N. *Intermolecular and Surface Forces: Revised Third Edition*; Academic Press, 2011.
(29) Garcia-Manyes, S.; Oncins, G.; Sanz, F. Effect of Temperature on the Nanomechanics of Lipid Bilayers Studied by Force Spectroscopy. *Biophys. J.* **2005**, *89*, 4261−4274.
(30) Rubenstein, J. L.; Smith, B. A.; McConnell, H. M. Lateral Diffusion in Binary Mixtures of Cholesterol and Phosphatidylcholines. *Proc. Natl. Acad. Sci. U.S.A.* **1979**, *76*, 15−18.
(31) Johnson, J. M.; Ha, T.; Chu, S.; Boxer, S. G. Early Steps of Supported Bilayer Formation Probed by Single Vesicle Fluorescence Assays. *Biophys. J.* **2002**, *83*, 3371−3379.

DOI: 10.1021/acs.langmuir.9b00726
Langmuir 2019, 35, 8709−8715

Journal of Electroanalytical Chemistry 757 (2015) 65–72

Contents lists available at ScienceDirect

Journal of Electroanalytical Chemistry

journal homepage: www.elsevier.com/locate/jeac

Enhanced electrochemical biosensing efficiency of silica particles supported on partially reduced graphene oxide for sensitive detection of cholesterol

Shiju Abraham [a], Saurabh Srivastava [a], Vinod Kumar [b], Shobhit Pandey [c], Pankaj Kumar Rastogi [d], Narsingh R. Nirala [e], Sunayana Kashyap [e], Sunil K. Srivastava [f], Vidya Nand Singh [g], Vellaichamy Ganesan [d], Preeti S. Saxena [e], Anchal Srivastava [a,*]

[a] Department of Physics, Banaras Hindu University, Varanasi 221005, India
[b] Institute of Nanoscience & Technology, Mohali 160062, India
[c] Metallurgical Engineering Department, Indian Institute of Technology — (BHU), Varanasi, India
[d] Department of Chemistry, Banaras Hindu University, Varanasi 221005, India
[e] Department of Zoology, Banaras Hindu University, Varanasi 221005, India
[f] Department of Pure and Applied Physics, Guru Ghasidas University, Main Campus, Koni, Bilaspur 495009, India
[g] CSIR—National Physical Laboratory, New Delhi, India

ARTICLE INFO

Article history:
Received 22 April 2015
Received in revised form 8 September 2015
Accepted 11 September 2015
Available online 15 September 2015

Keywords:
Silica particles
Partially reduced graphene oxide, cholesterol sensing
Cyclic voltammetry
K_m value

ABSTRACT

The present work introduces partially reduced graphene oxide (pRGO)-silica (SiO_2) particles hybrid system (pRGOSHs) for sensitive and cost effective free cholesterol detection. Fabricated out of thin layers of pRGOSHs, these proposed ChOx/pRGOSHs/ITO based biosensors have a detection range of 2.6–15.5 mM with an appreciable detection limit of 1.3 mM and sensitivity of 11.1 μA/mM/cm^2. Low Michaelis–Menten constant (K_m) (4.9×10^{-4} mM) and high diffusivity constant (D) (3.2×10^{-10} cm^2/s) values clearly indicate enhanced immobilization of enzyme over the substrate. Additionally, electrochemical impedance studies indicate that the synergistic combination of SiO_2 and pRGO also results in much lower impedance values (40% and 18% decrease in comparison to SiO_2 and pRGO respectively) for an overall enhanced sensing performance. These results are further corroborated by the density functional theory based theoretical simulations indicating enhanced electron density (theoretically) in case of the proposed hybrid system. Finally, the present work also highlights the importance of Si–OH bonds formation in the proposed pRGOSHs composite system for attaining such enhanced biosensing ability.

1. Introduction

Cholesterol, a waxy steroid metabolite, is a direct indicator for hypertension, myocardial infarction and arteriosclerosis in human beings. Less than 200 mg dL^{-1} (5.17 mM) of cholesterol (serum part) in the human blood plasma is considered normal, however, higher levels of cholesterol leads to Hypercholesterolemia, a common issue owing to the present generation's eating habits [1]. Hypercholesterolemia leads to the nucleation of deadliest cardiovascular, coronary diseases and in extreme cases culminates into transient ischemic heart attacks [2]. Thus, close monitoring of cholesterol in food and blood using efficient, accurate and economic techniques has remained an active research area. Down this line chemical/colorimetric method, spectrophotometry, thin layer chromatography, gas–liquid chromatography, fluorimetric method, polarographic method and gas chromatography/mass spectrometry and electrochemical sensing have all been used for cholesterol detection [3]. Among these, electrochemical sensing route has gained much attention owing to its high portability, sensitivity, efficiency and accuracy. Thus constant efforts are being put in to find better materials for fabricating electrochemical electrodes which have better affinity towards bioanalytes and result in higher efficiency and improved response time [4].

Nanomaterials based electrochemical electrodes have shown tremendous potential with high sensitivity, selectivity and signal to noise ratio, owing to their high surface area and unique electro-chemical nature [5,6]. Among the various metallic and non-metallic nanomaterials employed for electrode fabrication, silica nanoparticles have gained much attention in recent past. With unique properties, such as porosity, large surface areas and pore volumes allowing better loading of reactive molecules per particle, good biocompatibility and low cytotoxicity; silica nanoparticles had already made their mark for therapeutic applications [7–9]. However, the potential of these economic mesoporous nanoparticles for sensing purposes was discovered once they were produced via the sol–gel technique [10], which showcased improved response time and detection limit [11–13]. However, these wormhole-like porous structured sol–gel synthesized silica nanoparticles are limited by low conductivity

* Corresponding author.
E-mail address: anchalbhu@gmail.com (A. Srivastava).

http://dx.doi.org/10.1016/j.jelechem.2015.09.016
1572-6657/

and diffusivity, a clear motivation for combining them with a conducting base material to form a composite material.

In the near past, graphene oxide (GO) based electrodes have also shown enhanced electrochemical activities for detection of various bioanalytes including DNA, enzyme and protein [14–16]. This is owing to GO's high 2-D surface area and abundant functional groups promoting enhanced immobilization of bioanalytes. Further, the electrochemical performance of GO has been seen to improve on synergistically combining with metal and metal oxide nanoparticles. By way of examples, Au/GO [17,18] combination for H_2O_2 and uric acid detection, GO/SiO_2 for urea detection [19], Pt/GO [20,21] for H_2O_2 sensing and catalytic reduction and Pd/GO [22,23] has been used for detecting chlorophenols, hydroquinone (HQ) and catechol (CC). Although appreciated for its sensing performance, especially its high loading capacity, the efficacy of GO composites is often questioned for its unbalanced conductivity. Completely reducing GO to form planar sp^2 hybridized reduced graphene oxide with good conductivity not only makes the material insoluble but also adversely effects the loading capacity due to complete loss in of functional groups. Therefore, the solution lies in partial restoration of the sp^2 hybridized network by mild reduction of GO thereby attaining conductivity, while simultaneously retaining some functional groups crucial for electrochemical sensing [24]. New to the biosensing domain, this balanced material known as partially reduced graphene oxides (pRGO), has proven its worth in the recent times [25,26].

Thus, with a better base material at hand (pRGO) having balanced conductivity and functional groups, and a clear motivation of combining SiO_2 nanoparticles (having enough hydroxyl functional group –OH) with a conducting material, the present work investigates the pRGO-silica nanoparticles composite as a sensing platform. The composite resolves the conductivity problems associated with SiO_2 nanoparticles, while uses their high porosity, biocompatibility and catalytic activity, by synergistically combining it with pRGO for enhanced biosensing performance. Further, these pRGO-silica nanoparticles composites are fabricated using a facile, fast and reproducible synthesis route, which is both economical, owing to easily available inexpensive silica, and ecological, owing to zero hazardous by products generation.

2. Experimental

2.1. Materials

Graphite flakes (NGS Naturgraphit GmbH, Germany), TEOS {Si$(OC_2H_5)_4$}, (Aldrich, purity ≥99% with trace metal basis), H_2SO_4, H_3PO_4, $KMnO_4$, H_2O_2, 1-ethyl-3-(−3-dimethylaminopropyl) carbodiimide hydrochloride (EDC), N-hydroxysuccinimide (NHS), hydrazine hydrate, ammonia solution, ethanol, etc. used were of analytical reagent grade. All the other chemicals employed for the fabrication of cholesterol biosensor, namely, cholesterol oxidase (ChOx), cholesterol, etc. were procured from Sigma-Aldrich.

2.2. Synthesis of GO and silica particles

Specifically, GO was prepared by the improved method proposed by Marcano et al. [27]. Briefly, a 9:1 combination of concentrated H_2SO_4/H_3PO_4 (240/26.7 mL) was added to 2 g of graphite flakes and 12 g of $KMnO_4$. The reaction mixture was then stirred for 12 h at a constant temperature of 50 °C. Finally this reaction was quenched by addition of ~270 mL of ice along with 2 mL of 30% H_2O_2. The as obtained yellowish slurry mixture was then shifted, centrifuged and filtered. The filtrate thus obtained was washed with 30% HCl and distilled water several times, until pH ~7 was achieved. At the end it was dried at 70 °C to procure the required solid GO.

The well-known Stober's method was employed for the production of uniform silica particles [28]. In short, in a round bottom flask, 75 mL of ethanol (98%) was taken and 7 mL of ammonia solution was added to it. The pH of the solution was adjusted ~12. This solution was then stirred for about 20 min. Under continuous stirring, the sol–gel reaction was initiated by adding 1.5 mL of TEOS to the above solution. The temperature was maintained at ~55 °C for 1 h and the stirring was continued for additional 3 h. The as obtained solution was then centrifuged at a speed of 3000 rpm for 15 min, followed by washing with ethanol and then drying in an oven at 80 °C. Finally, the white solid product obtained was used for further measurements.

2.3. Production of pRGO and SiO_2 decorated pRGO hybrid system (pRGOSHs)

100 mg of as-synthesized GO was well dispersed in 100 mL of distilled water (DW) by ultrasonication. This was done in order to restrict the GO sheets to single or few layers, with increased interlayer spacing. Further, pH of above dispersion was crucially adjusted to 10, by adding few drops of ammonia solution. To this dispersion, 300 μL of hydrazine hydrate (10 mg of silica particles dispersion was additionally added for the production of pRGOSHs) was added for the partial reduction while maintaining the temperature at 75 °C. Ultrasonication was done for an hour, followed by subsequent stirring for 3 h at 80 °C. The corollary was the partial reduction of GO to form pRGO (pRGOSHs). As the final step, this solution was washed several times and dried overnight at 70 °C.

2.4. Fabrication of pRGO and pRGOSHs thin film electrodes

The formation of both pRGO as well as pRGOSHs thin films over indium tin oxide (ITO) electrodes was achieved by electrophoretic deposition (EPD) technique {Fig. 3(a)}. In this, 10 mL colloidal solutions of pRGO and pRGOSHs (3 mg dL^{-1}) in acetonitrile were taken in two-electrode glass cell. A platinum foil of 1 × 2 cm was used as the counter electrode, while a well cleaned ITO-coated glass substrate of recorded sheet resistance of 30 Ω cm^{-1} was taken as the working electrode. These electrodes were positioned parallel to each other, separated by a distance of 1 cm. Film deposition over ITO-coated glass plate (0.25 cm^2) was accomplished by applying a DC voltage of 150 V for 45 s, in the case of pRGO and 50 V for 2 min, in the case of pRGOSHs. Further, about 10^{-5}–10^{-4} M of Mg$(NO_3)_2 \cdot 6H_2O$ was added as an electrolyte into the colloidal suspension, in order to create surface charge on both pRGO as well as pRGOSHs, which is essential for successful EPD. Finally, these electrodes were removed from the suspension, followed by thorough washing with deionized water and subsequent drying.

2.5. Solution preparation and fabrication of bioelectrodes

600 mg dL^{-1} (15.54 mM) of cholesterol stock solution was prepared in a heat bath maintained at 60 °C. Typically, cholesterol was dissolved in a flask (kept on heat bath) containing Triton X-100. This solution was further diluted with 0.02 M PBS solution (pH 7.0) for making different cholesterol concentrations (50 to 600 mg dL^{-1}). The EDC-NHS chemistry was applied on both pRGO and pRGOSHs electrodes to activate the COOH groups, prior to the immobilization of ChOx. For the immobilization of ChOx on pRGO/ITO and pRGOSHs/ITO electrodes, 5 μL of ChOx (1 mg dL^{-1}) (Cholesterol oxidase (EC1.1.3.6 ≥50 U mg^{-1})) was uniformly spread over these electrodes. After 4 h, the ChOx-pRGOSHs/ITO and ChOx-pRGO/ITO bioelectrodes were rinsed with PBS to remove any unbound ChOx and stored at 4°°C when not in use.

2.6. Characterization

pRGO, SiO_2 and pRGOSHs composites were characterized by X-ray diffraction (XRD) technique (Rigaku miniflex-II diffractometer at 30 kV, 15 mA). The wavelength of Cu-Kα1 radiation (λ = 1.5405 Å) was used for obtaining the XRD pattern. Surface morphology was investigated using scanning electron microscopy (SEM), employing JEOL — Model JSM6300F-SEM. Transmission electron microscopic (TEM) characterization was done using FEI Tecnai-G2 electron microscope. Further,

molecular structures of the materials were investigated using Fourier transform infrared (FT–IR) spectroscopy (Perkin Elmer Spectrum 65, FT–IR spectrometer). Additionally, UV–vis measurements were carried out with a Cary 5000 UV–vis absorption spectrometer from Varian, employing the double beam mode. Raman spectroscopic measurement was carried out using Horiba Raman System using 480 nm laser source. Electrochemical studies related to cholesterol detection and electrochemical impedance spectroscopy (EIS) experiments were performed with a CHI-660C workstation (CH instruments, USA). Cyclic voltammetry (CV) measurements were carried out using a three electrode cell (Fig. 3) with ChOx/pRGO/ITO and ChOx/pRGOSHs/ITO bioelectrodes as the working electrodes, platinum as the counter electrode, and Ag/AgCl electrode as a reference electrode in 50 mM phosphate buffer saline (PBS) of pH 7.0 containing 5 mM of $[Fe(CN)_6]^{3-/4-}$. EIS was analyzed between the frequency range 100 kHz to 1 Hz using 5 mV amplitude with an applied potential of 0.2 V.

3. Results and discussion

3.1. Structural studies

The XRD pattern of the as-synthesized samples, namely GO, pRGO, SiO_2 particles and pRGOSHs composites are presented in Fig. S1 (Supplementary material). GO shows a strong diffraction peak centered at ~11° (Fig. S1a), which corresponds to the (002) reflection plane and a d-spacing of ~8.0 Å. The turbostatic band of disordered carbon material can be noticed from the weak and broad band around 42° {(100) reflection}. The most prominent diffraction peak of pRGO (Fig. S1b) is observed at ~24. 5° (002), while the second strongest peak is observed around 11° (002), attesting the characteristic band of GO. The presence of prominent RGO peak and less intense GO peak confirms partial reduction of GO towards RGO. The interlayer spacing (d-spacing) is calculated as 3.6 Å for the 2θ value (24.5°). This value matches with the well-known XRD peak of RGO [29]. Silica particles show a broad strong peak at ~22.3° (Fig. S1c), owing to their well-known amorphous nature. Further in case of pRGOSHs (Fig. S1d), a strong peak centered at ~25.6° (corresponding to a ***d***-spacing of 3.4 Å) is observed. This broad peak is a collective spectral signature from both pRGO as well as SiO_2 particles. The peak around 10.2° is assigned to the (002) plane of GO in pRGOSHs.

SEM images of the pRGO, SiO_2 particles and pRGOSHs have been shown in Figs. 1(a) to (d). Fig. 1(a) reveals the formation of pRGO sheets with good uniformity, extending to several micrometers. Here the thickness is probably of typical molecular dimensions and the lateral dimensions are ranging from nanometers to several micrometers. Further, there are many wrinkles on the pRGO surfaces. The defects in the carbon lattice, due to the remnants of the epoxy reaction strings and other functional groups, provide an explanation for such wrinkles. Fig. 1(b) shows the micrograph of SiO_2 particles, uniformly distributed over a baronial range. This image reveals the formation of SiO_2 particles with very narrow size distribution of ~300 nm. The cross-sectional view of the pRGOSHs is shown in Fig. 1(c), which further clarifies the uniform loading of SiO_2 particles over all of the pRGO layers, including cavities and defects. The Fig. 1(d) shows clearer picture of distinct pRGO sheets, loaded with wrinkles and embellished with silica particles of narrow size distribution. Transmission electron microscopy (TEM) images further support the observation made through SEM and the SAED pattern of SiO_2 particles, confirming its amorphous characteristics (See Figure S2 in the supporting information).

Raman spectroscopy is a ubiquitously practiced technique for distinguishing between sp^2 and sp^3 hybridization in carbonaceous materials [30]. The two main characteristic Raman bands, observed in almost all carbon-based materials, are the G-band and the D-band. The Raman spectra of pRGO and pRGOSHs are shown in Fig. 2.

Here the pRGO sheets show prominent characteristic D band at 1356 and G band at 1584 cm^{-1}. Further the 2D band at 2695 cm^{-1} is also well resolved in the same spectrum. This observed 2D band, which is prominent in reduced form of graphene oxide, supports the partial reduction of GO to pRGO. In case of pRGOSHs, well resolved prominent

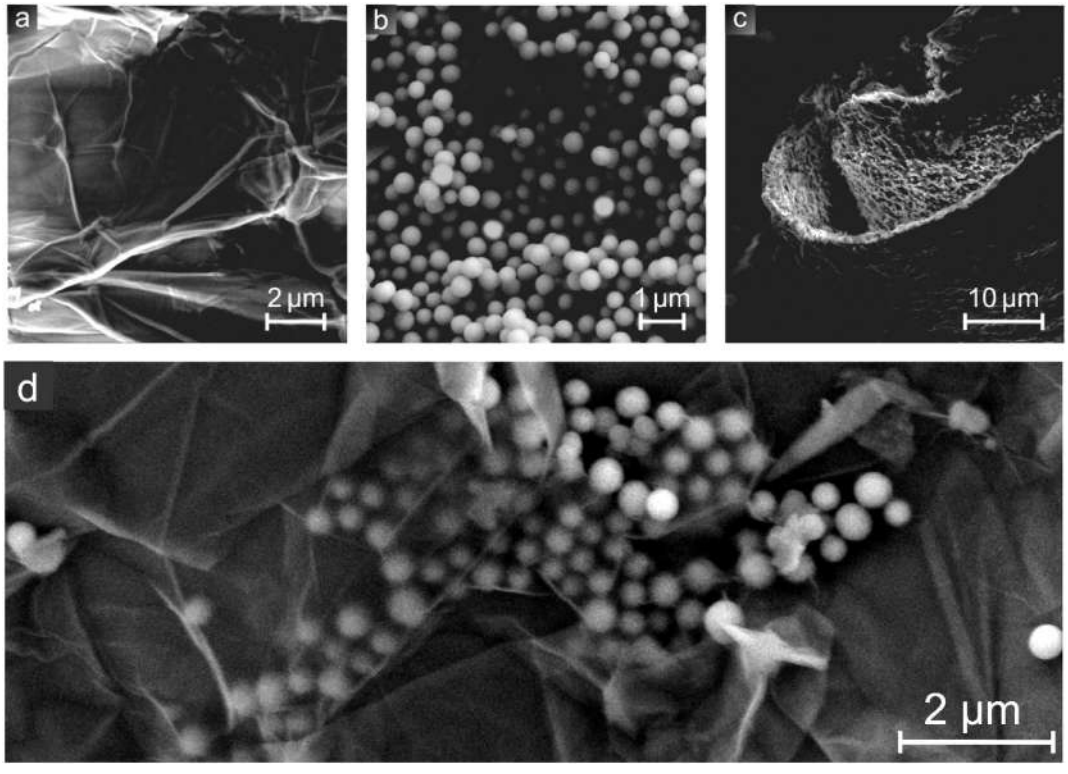

Fig. 1. SEM images of (a) pRGO nanosheets; (b) Silica particles with average size distribution of ~300 nm; (c) Cross-sectional view of pRGOSHs where silica particles are enveloped by pRGO sheets; (d) pRGOSHs in lateral dimension revealing good decoration of silica particles in between the sheets, opening up valuable space for enhanced immobilization of enzymes.

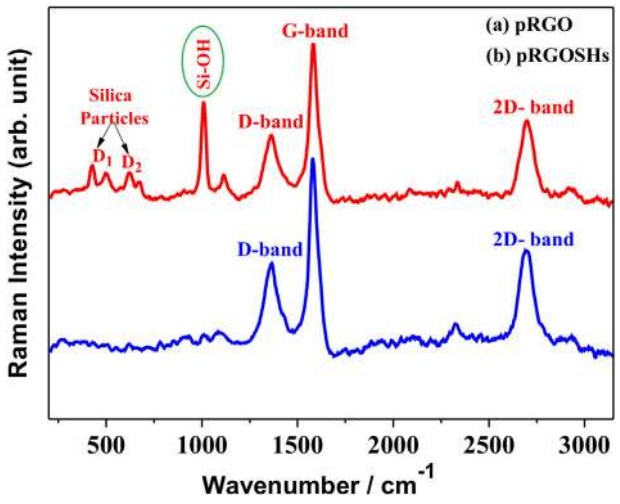

Fig. 2. Raman spectra of pRGO and pRGOSHs indicating prominent bands D, G and 2D. The Si–OH bond presence enabling the enhanced catalytic effect of SiO_2 particles is attested here.

Raman peak of both pRGO as well as of SiO_2 particles were obtained. Silica particle's characteristics are inferred from the bands around 495 and 620 cm^{-1}, which are referred to as D_1 and D_2, respectively. These are attributed to the symmetric oxygen ring breathing vibrations of regular four-membered (D_1) and three-membered (D_2) silica rings. Further, the Si–OH vibrations were observed at around 1000 cm^{-1} (Also discussed in FTIR spectrum, Supplementary material) which play a crucial role in empowering the SiO_2 particles for the enhanced biocompatibility and catalytic effect by providing links enabling enhanced charge transfer while maintaining better physical stability [31].

3.2. Electrochemical studies

Scheme 1 represents the electrochemical sensing set up used for cholesterol sensing. Part (a) and (b) denotes the EPD set up and thin film formation where as part (c) in the same figure shows the covalent immobilization of ChOx onto pRGOSHs/ITO via EDC–NHS coupling chemistry. Part (d) denotes the three electrode electrochemical cell, (e) is the electrochemical instrumentation part (f) represents the computer interface for the output signal.

3.2.1. Electrochemical characterization of electrodes

CV measurements have been carried out to characterize the electrochemical activities of the fabricated electrodes (pRGO, SiO_2 and pRGSHs). Fig. 3A represents cyclic voltammogram of pRGO/ITO, SiO_2/ITO and pRGOSHs/ITO electrodes, in PBS (pH ~ 7) containing 5 mM $[Fe(CN)_6]^{3-/4-}$. An oxidation peak current measuring 13.12 μA is observed for pRGO/ITO electrode, which increases to 24.0 μA when measured for SiO_2. It was observed that magnitude of the peak current enhanced to 30.7 μA in case of pRGOSHs/ITO electrode. The higher value of current obtained for pRGOSHs/ITO is due to the synergistically improved electro catalytic activity of pRGO and SiO_2 in pRGOSHs. The CV of ChOx/pRGOSHs/ITO shows a current of 27.8 μA, which is less than the pRGOSHs/ITO current (30.7 μA) that may be attributed to macro molecular and insulating nature of the covalently attached ChOx molecules.

Electrochemical impedance is encountered when the current flows through a circuit consisting of resistors and capacitors or inductors. The Randles circuit [Inset Fig.3B] is an equivalent circuit which can be used to measure the electrochemical impedance composed of solution resistance R_S in series with Rct (charge transfer resistance) in parallel combination of the double-layer capacitance C_{dl} or constant phase element (CPE) [32]. Fig. 3B shows the Nyquist plot used to find the R_{CT} for all the four electrodes. The magnitude of the R_{CT} (identified through the semicircle diameter) is correlated to the dielectric and insulating features across the electrode/electrolyte interface. It is observed that the SiO_2 particles show a R_{CT} value of 375 Ω, whereas, pRGO shows 225 Ω. In case of the hybrid pRGOSHs, the R_{CT} value is further decreased to 185 Ω denoted by the smallest semi-circle. This can be attributed to the faster charge transfer kinetics of pRGOSHs/ITO as compared to SiO_2/ITO and pRGO/ITO followed by a higher separation efficiency of electrons and holes. After immobilizing the enzyme ChOx over pRGOSHs, it is found that the R_{CT} value increased to 600 Ω and this increase in R_{CT} value attributed to the fact that most biological molecules,

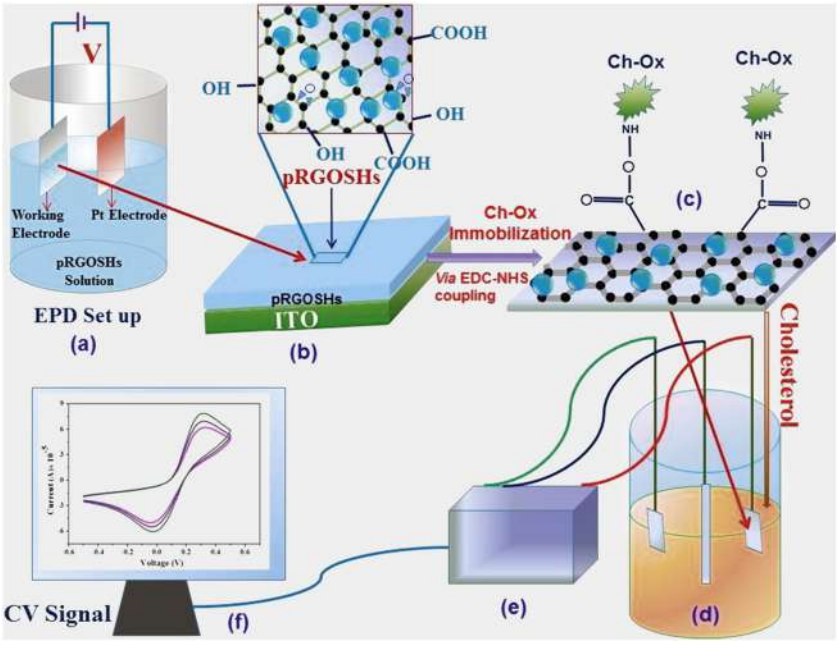

Scheme 1. Schematic representation of cholesterol sensing process: part; (a) EPD set up for the fabrication of pRGO and pRGOSHs thin films; (b) electrophoretically fabricated pRGOSHs thin film on ITO substrate having different functional groups; (c) immobilization of ChOx on pRGOSHs by EDC–NHS chemistry; (d) three electrode CV cell with pRGOSHs as working, Pt foil as counter and Ag/AgCl as reference electrodes; (e) electrochemical instrumentation; (f) display output (PC).

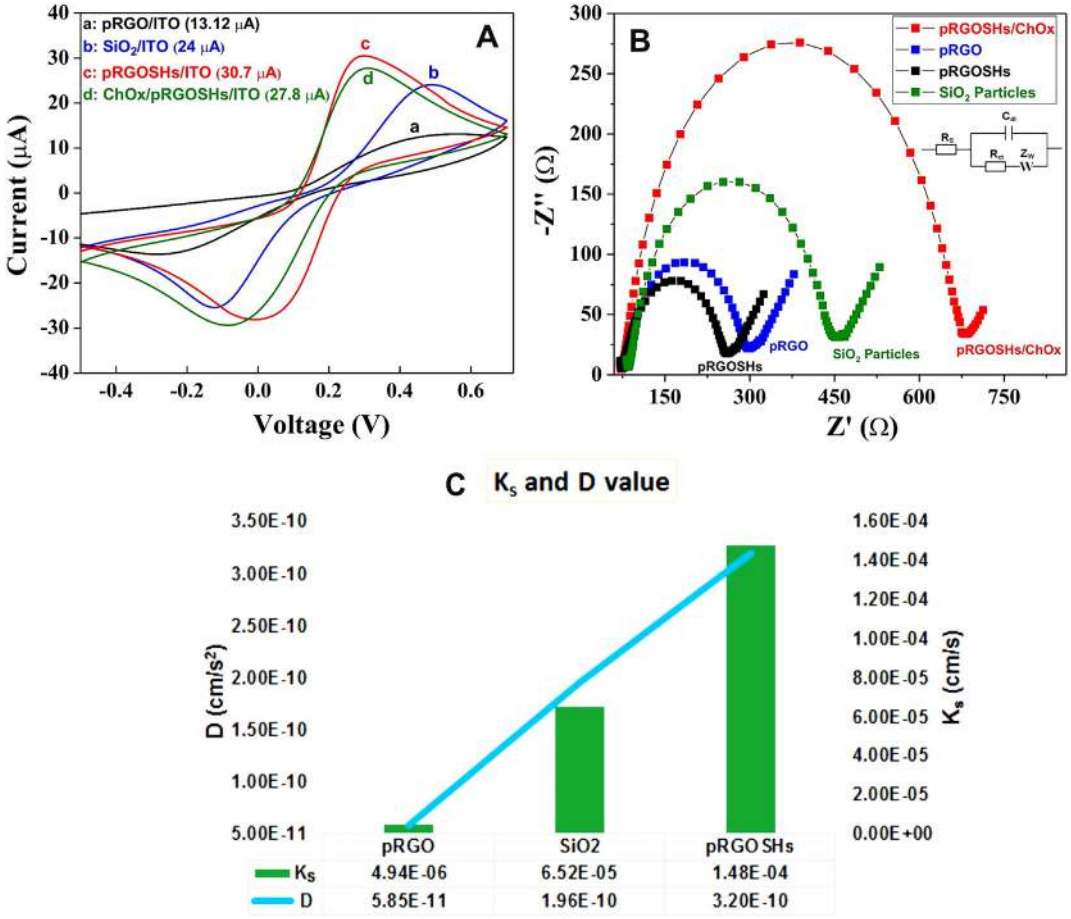

Fig. 3. (A); CV response of pRGO/ITO, SiO_2/ITO, pRGOSHs/ITO and ChOx/pRGOSHs/ITO electrodes^{-}; (B) Nyquist plot of SiO_2, pRGO, pRGOSHs and pRGOSHs/ChOx electrodes; (C) Comparative study of the K_s and D values for pRGO, SiO_2 and pRGOSHs electrodes.

including ChOx are poor electrical conductors and may cause hindrance to the electron transfer. This increase in R_{CT} indirectly supports the binding of ChOx onto pRGOSHs hybrid matrix.

Fig 3C shows the graphical representation of the calculated parameters; diffusion coefficient (D) [33] {using the Eq. (1) below} and the heterogeneous electron transfer rate constant (K_s) [34] {using the Eq. (2) below}for pRGO/ITO, SiO_2/ITO and pRGOSHs/ITO.

$$i_p = Constant\ nFAC\sqrt{\left(\frac{nFvD}{RT}\right)}\} \tag{1}$$

$$K_S = 2.18\sqrt{\left(\frac{D\alpha nFV}{RT}\right)}\, exp\left[-\frac{\alpha^2 nF}{RT}\left(E_p^a - E_p^c\right)\right] \tag{2}$$

Increase in the values of these parameters indicates a faster electron transfer kinetics. The pRGOSHs electrode shows a highest D value of 3.2×10^{-10} cm^2/s and K_s value of 1.48×10^{-4} cm/s, whereas for bare pRGO shows the least D and K_s values of 5.85×10^{-11} cm^2/s and 4.94×10^{-6} cm/s respectively. The SiO_2 electrode shows an intermediate D and K_s in comparison to the above two type of electrodes. The enhanced D and K_s values of pRGOSHs are originated from the synergistic effect of partially conductive 2-dimensional RGO sheets and the catalytic characteristics of silica particles. On the basis of these observations, pRGOSHs have been further used as efficient and cost effective electrode material for biosensing purpose.

3.2.2. Electron density distribution studies

In order to explain the results obtained in the CV measurements and the EIS, we have made density functional theoretical (DFT) calculation using Gaussian09 software to find the electron density distribution in the three different cases (pristine graphene, pRGO, pRGO + Si) and acknowledge the relative enhancement in the same for pRGO and pRGO + Si over pristine graphene, by calculating the difference in electron density using program ChemCraft (shown in Fig. 5). It is clear from the experiment that the deposition of the prepared material to the ITO substrate will depend on their negative charge density since the ITO electrode is attached to the positive terminal of the applied DC voltage. The surface having large electron density will attach more easily and strongly to the positive terminal electrode, favoring the overall sensing activity. The simulation studies are summarized in Fig. 4. Fig. 4(a), (b) and (c) show the electron densities distribution for pristine graphene (A), pRGO (B) and pRGO + Si (C) respectively. Now the Fig. 4(d), which is the subtraction of electron densities between pRGO and pristine graphene, show that as we go from the pristine graphene to the pRGO, the electron density slightly increases at the edges. Further, Fig. 4(e) and (f) attest that finally as the Si is added in the matrix of pRGO, the electron density at the edges increases significantly with respect to both pristine graphene and pRGO, which is evident from larger blue regions on C from both A or B respectively. This theoretically predicted substantial increase in electron density directly suggests enhancement in the binding affinity for much better sensing substrate in concordance with the experimental results obtained via the CV and EIS measurement studies.

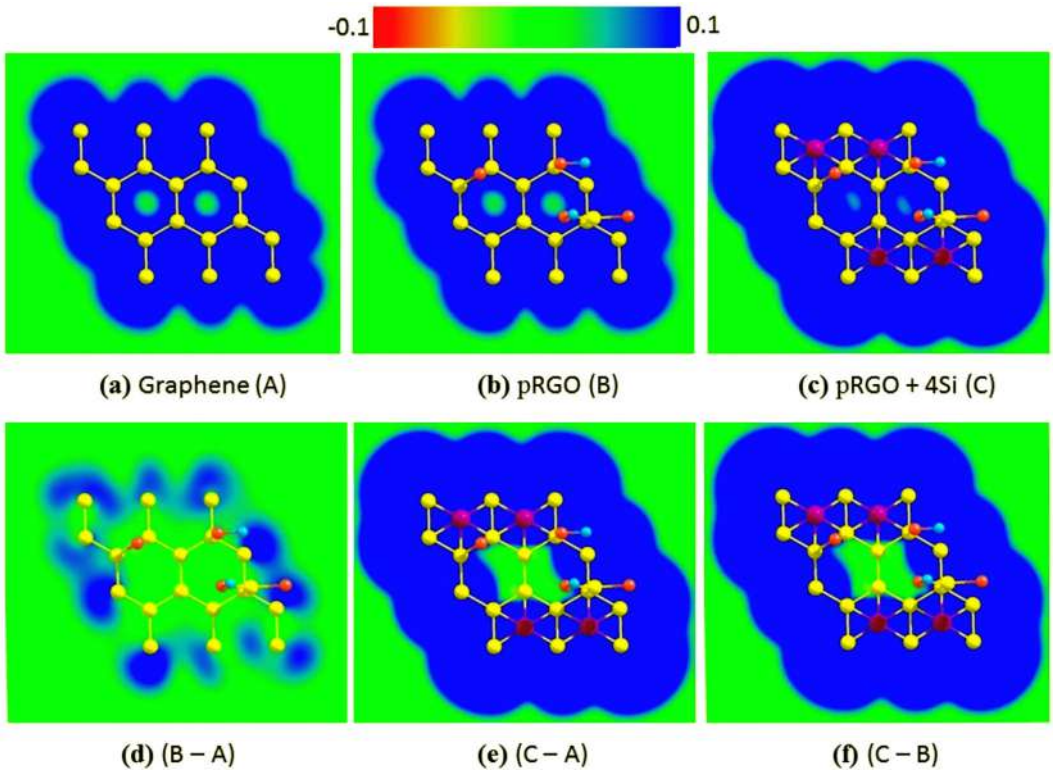

Fig. 4. Electron density distribution studies(Blue denotes the electron density region and Green denotes the neutral region) of (a) pristine graphene (b) pRGO, (c) pRGO + Si and the differences(d) pRGO-pristine graphene, (e) (pRGO + Si)-pristine graphene (f) pRGO + Si-pRGO.

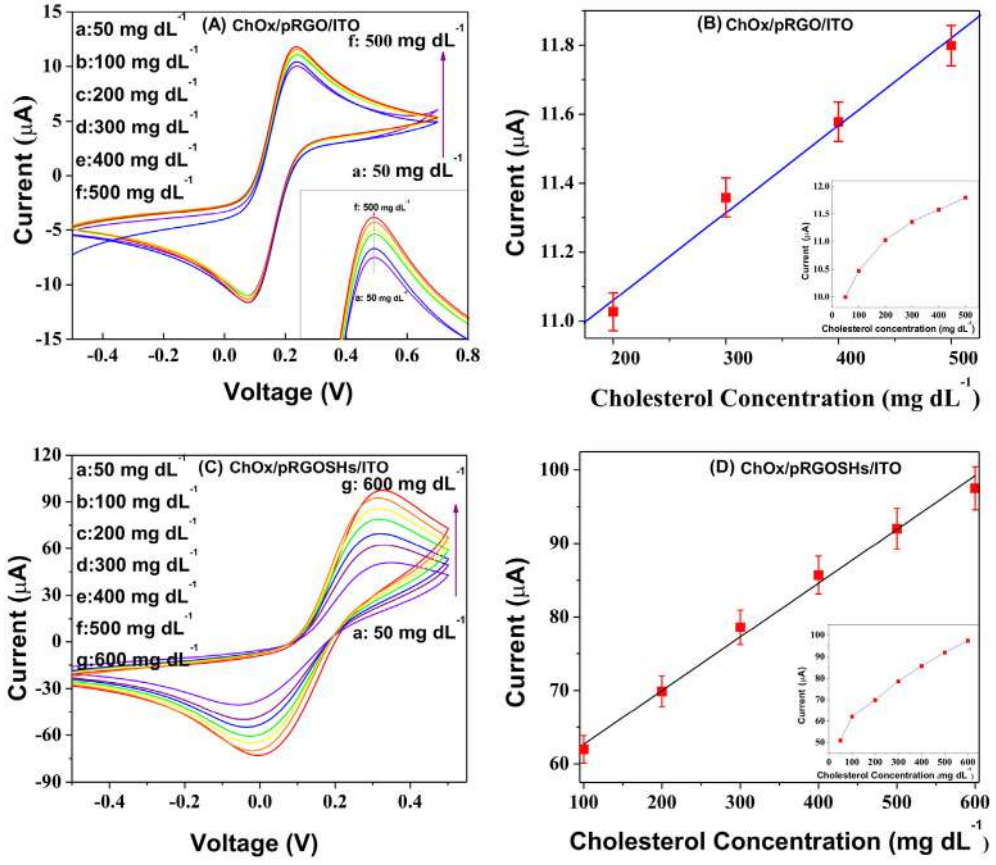

Fig. 5. Electrochemical response studies using CV of (A) the ChOx/pRGO/ITO bioelectrode as a function of cholesterol concentrations [50–500 mg dL^{-1}]; (B) Fitted calibration plot between anodic peak current and cholesterol concentrations for ChOx/pRGO/ITO (200–500 mg dL^{-1}); inset: calibration plot between anodic peak current and cholesterol concentrations (50–500 mg dL^{-1}). (C) Electrochemical response studies of the ChOx/pRGOSHs/ITO bioelectrode as a function of cholesterol concentrations [50–600 mg dL^{-1}]; (D) fitted calibration plot (the error bars with n = 3) for ChOx/pRGOSHs/ITO (100–600 mg dL^{-1}); inset: calibration plot between anodic peak current and cholesterol concentrations (50–600 mg dL^{-1}).

3.2.3. Cholesterol sensing studies

Electrochemical response studies of ChOx/pRGO/ITO and ChOx/pRGOSHs/ITO (Fig. 5(A) and (C) respectively) bio-electrodes have been studied as a function of cholesterol concentration using CV in PBS solution {50 mM PBS (pH 7, 0.9% NaCl) containing 5 mM $[Fe(CN)_6]^{3-/4-}$}. The mediated redox coupling electrochemical reaction was used as the sensing mechanism for this cholesterol biosensor. ChOx cannot directly transfer electrons to the electrode surface in electrochemical biosensors because its active site (FAD) is embedded within the enzyme layer [35]. Mediators are small molecules with lower redox potential, which can shuttle electrons between the embedded redox center of the enzyme and the electrode surface at its characteristic lower potential thereby increasing the sensitivity of the biosensor. In this work, potassium ferrocyanide/ferricyanide {$[Fe(CN)_6]^{3-/4-}$} was used as the mediator [36,37]. The ferro-ferri redox reaction can occur at ChOx-pRGOSHs/ITO electrode surface, which produces an oxidation and a reduction current. The fabricated cholesterol biosensor was based on the oxidation of cholesterol according to the following reactions (3–4).

$$Cholesterol + 2[Fe(CN)6]^{3-} + H_2O \xrightarrow{ChOx} Cholestenone + 2H^+ + 2[Fe(CN)6]^{4-} \quad (3)$$

$$[Fe(CN)6]^{4-} \xrightarrow{ChOx-pRGOSHs/ITO} [Fe(CN)6]^{3-} + e^{-1} \quad (4)$$

It is observed that the magnitude of current obtained for the bio-electrodes increases as the concentration of cholesterol increases (from 50 to 500 mg dL^{-1} for ChOx/pRGO/ITO and from 50 to 600 mg dL^{-1} for ChOx/pRGOSHs/ITO). It is distinctly visible from the CV response curves, [Fig. 5(a) and (c)], that the magnitude of current difference for ChOx/pRGOSHs/ITO is higher than ChOx/pRGO/ITO system. Here the pRGOSHs may acts as a good receptor of the electrons which generated during re-oxidation of ChOx. These electrons will be transferred to the electrode via $Fe(CN)_6)^{3-/4-}$ conversion to give an increased electrochemical signal. More numbers of electrons are generated when the concentration of the cholesterol in electrolyte solution increases and thereby an enhanced oxidation as well as reduction peak currents obtained for these bioelectrodes.

Fig. 5(B) and (D) show the linear calibration plot between anodic peak current and cholesterol concentrations for ChOx/pRGO/ITO as well as ChOx/pRGOSHs/ITO. The lower detection limit obtained in case of pRGO and pRGOSHs bioelectrode is of 1.3 mM, low enough to measure the cholesterol level in human serum systems. Detection limit is calculated by 3σ/m, where 'm' is the slope and 'σ' is standard deviation (SD) of the calibration graph. Linear range obtained for pRGO bioelectrode is from 5.17 to 12.93 mM, with a sensitivity of 0.39 μA/mM/cm^2, while in the case of pRGOSHs a much broader detection range from 2.58 mM to 15.51 mM was observed. Further the sensitivity is enhanced significantly to 11.1 μA/mM/cm^2 in case of ChOx/pRGOSHs/ITO as compared to that of ChOx/pRGO/ITO (0.39 μA/mM/cm^2).

The enzyme and substrate kinetics parameter, Michaelis–Menten constant (K_m), is estimated for both pRGO and pRGOSHs bioelectrode using the Lineweaver–Burke plot [38]. The low values of K_m indicate good affinity of immobilized enzyme on substrate towards the analyte. The K_m value calculated using the equation $\{\frac{1}{i_s} = \frac{k_m}{i_{max}}\frac{1}{C} + \frac{1}{i_{max}}\}$ for the ChOx/pRGO/ITO bioelectrode is 0.102 mg dL^{-1} (0.00264 mM) and for ChOx/pRGOSHs/ITO, it is further reduced to 0.019 mg dL^{-1} (0.00049 mM). The obtained higher sensitivity, lower detection limit and K_m value suggest ChOx/pRGOSHs/ITO is evidently a much better matrix than ChOx/pRGO/ITO for faster electron transfer between the immobilized enzyme and the electrode substrate, thereby promising a more sensitive cholesterol sensing platform.

The reproducibility, specificity and stability of developed pRGOSHs/ChOx/ITO cholesterol biosensor have been examined (see supplementary material S5). For specificity, the detection of cholesterol in the presence of other interfering analytes such as urea, ascorbic acid and glucose have been evaluated. The absence of any significant change in peak current response in presence of these interfering species shows the high specificity of pRGOSHs/ChOx/ITO biosensor towards cholesterol (see supplementary material, Figure S4 a). The stability of pRGOSHs/ChOx/ITO bio-electrode is monitored for eight weeks when stored in refrigerated conditions, and only ~9% decrease in current response have been noticed (Supplementary material, Figure S5 b). The reproducibility has been critically tested by taking five different pRGOSHs/ChOx/ITO bioelectrodes prepared under the same condition and the response current plot shows no major change in peak current response (see the supplementary material, Figure S5 c). These attest the potential of as fabricated cholesterol biosensor by showing appreciable reproducibility and stability at the same time. Results of the current study have been compared with some earlier reported studies for the same in Table 1 above as well as Figure S6 in the supplementary material.

The excellent electrochemical properties and large surface area of pRGOSHs is the key behind achieving high sensitivity for detection of cholesterol. Higher surface area of the nanohybrid allows several fold high loading of enzymes, which in turn enhances the detection of trace amount of cholesterol. Further, the synergistically improved electrochemical activities of pRGOSHs, increases the sensitivity of the proposed biosensor. The enhanced sensitivity and linear range of pRGOSHs, reflects the efficiency of the developed biosensor. As a future prospect, an attempt should be made to utilize this pRGOSHs/ITO based sensing platform in the detection of total cholesterol and low density lipoprotein for point-of-care diagnostic application.

4. Conclusions

The present work introduces a novel partially reduced graphene oxide (pRGO)-silica (SiO_2) particles hybrid system (pRGOSHs) for free cholesterol detection. Our pRGOSHs composite based biosensor, circumvents the disadvantages of compromised conductivity and reproducibility in case of biosensors fabricated using GO or SiO_2 nanoparticles. It simultaneously utilizes the unique sensing properties and restored conductivity offered by the pRGO, along with the efficient catalytic activity of SiO_2 particles proving its potential as the next generation biosensing platform for free cholesterol and several other bioanalytes detection. Further, the use of a facile, fast and reproducible synthesis route for pRGOSHs, without the generation of hazardous by products, further attests the potential of the proposed biosensing system to be brought on field. With commendable stability and reproducibility, these pRGOSH based biosensor, when tested for free cholesterol detection, show high sensitivity of 11.1 μA/mM/cm^2 and detection limit of 1.3 mM. Lower K_m value than most of the prior reported biosensors and enhanced K_s (rate constant) and D (diffusivity) attest the synergistic effect of combining conducting pRGO matrix having adequate functional groups, with the catalytic SiO_2 nanoparticles having high loading capacity and sensing performance. Further the presence of Si–OH bond (confirmed by FTIR and Raman) in the composite is found to be of cardinal importance for enabling the catalytic activity of the silica particles and for providing physically stable reactive sites in the composite. The theoretically predicted increased electron density in case of the pRGOSHs further corroborates the results attesting better affinity of substrates towards enzymes for enhanced sensing. Thus, with such efficient electrochemical sensing parameters, the proposed pRGOSHs composite shows definite potential for not only cholesterol sensing but for detecting several other clinically important biomolecules such as triglycerides, LDL etc. in the immediate future.

Conflict of interest

There is no conflict of interest among authors.

Preference

Color on the web (free of charge)

Table 1
A comparative table describing the cholesterol sensing characteristics of the bioelectrode fabricated along with some other reported in the literature:

Bio-electrode	Detection Range (mM)	Detection Limit (mM)	Sensitivity (μA/mM)	K_m value (mM)	Stability (days)	Ref.
ChOx/4-ATP SAM/Au	0.64–10.34		0.54	1.34	20 times	[39]
ChOx/MWCNTs	0.5–6.0	0.2	0.56	7.17		[40]
(PAH–MCNTs–GNPs/HRP)4/(PAH–MCNTs–GNPs/ChOx)4	0.18–11	0.02	0.3873		25 days	[41]
Grp/β-CD/methylene blue	0.001–0.10		10			[42]
ChOx-ZnO NP	10^(−6)–1	10 nm	1.08			[43]
ChOx/Polyaniline	1.29–12.92	0.64	1.62	1.94	6 weeks	[44]
ChOx/PANI/MWCNTs	1.29–10.34		6.8		12 weeks	[45]
CHIT/SiO_2/MWCNTs	0.15–7.68	.0164	3.8	0.052	70 days	[46]
ChOx/MUA/AuNPs/Dithiol/AuE	0.04–0.22	0.0346	9.02	0.062	30 days	[47]
ChOx/pRGO	5.17–12.93	1.3	0.39	0.0026	30 days	Present work
ChOx/pRGOSHs	2.58–15.51	1.3	11.1	0.00049	45 days	Present work

Acknowledgements

SA is thankful to University Grants Commission and Max Planck Institute of Solid State Research, Stuttgart for their financial support and providing some of characterization facilities. Authors are thankful to Christina Stefani of MPI Stuttgart for XRD measurements. AS acknowledges CAS, UPE and Networking programs sponsored by UGC and DST, New Delhi, India.

Appendix A. Supplementary data

Supplementary data to this article can be found online at http://dx.doi.org/10.1016/j.jelechem.2015.09.016.

References

[1] J. Motonaka, L.R. Faulkner, Anal. Chem. 65 (1993) 3258.
[2] I.C. Hwang, S.-Y. Suh, A.-R. Seo, H.Y. Ahn, E. Yim, Korean J. Fam. Med. 33 (2012) 229.
[3] C.S. Pundir, J. Narang, N. Chauhan, P. Sharma, R. Sharma, Indian J. Med. Res. 136 (2012) 633.
[4] L. Zhu, C. Deng, P. Chen, X. You, H. Su, Y. Yuan, M. Zhu, Carbon N. Y. 67 (2014) 795.
[5] A. Walcarius, S.D. Minteer, J. Wang, Y. Lin, A. Merkoçi, J. Mater. Chem. B 1 (2013) 4878.
[6] S. Abraham, N.R. Nirala, S.A. Panday, M. Srivastava, S.K. Srivastava, B. Walkenfort, A. Srivastava, Anal. Methods (2015).
[7] M.W. Ambrogio, C.R. Thomas, Y.-L. Zhao, J.I. Zink, J.F. Stoddart, Acc. Chem. Res. 44 (2011) 903.
[8] Q. He, J. Shi, F. Chen, M. Zhu, L. Zhang, Biomaterials 31 (2010) 3335.
[9] Y. Vida, M.I. Montañez, D. Collado, F. Najera, A. Ariza, M. Blanca, M.J. Torres, C. Mayorga, E. Perez-Inestrosa, J. Mater. Chem. B 1 (2013) 3044.
[10] B.C. Dave, B. Dunn, J.S. Valentine, J.I. Zink, Anal. Chem. 66 (1994) 1120A.
[11] H. Yang, Y. Zhu, Talanta 68 (2006) 569.
[12] Z. Dai, S. Liu, H. Ju, H. Chen, Biosens. Bioelectron. 19 (2004) 861.
[13] Z. Dai, X. Xu, H. Ju, Anal. Biochem. 332 (2004) 23.
[14] D. Chen, H. Feng, J. Li, Chem. Rev. 112 (2012) 6027.
[15] Y. Matsumoto, H. Tateishi, M. Koinuma, Y. Kamei, C. Ogata, K. Gezuhara, K. Hatakeyama, S. Hayami, T. Taniguchi, A. Funatsu, J. Electroanal. Chem. 704 (2013) 233.
[16] X. Wang, F. Zhang, J. Xia, Z. Wang, S. Bi, L. Xia, Y. Li, Y. Xia, L. Xia, J. Electroanal. Chem. 738 (2015) 203.
[17] K.-J. Huang, D.-J. Niu, X. Liu, Z.-W. Wu, Y. Fan, Y.-F. Chang, Y.-Y. Wu, Electrochim. Acta 56 (2011) 2947.
[18] Y. Xue, H. Zhao, Z. Wu, X. Li, Y. He, Z. Yuan, Biosens. Bioelectron. 29 (2011) 102.
[19] S. Abraham, V. Ciobota, S.K. Srivastava, R.K. Singh, J. Dellith, B.D. Malhotra, M. Schmitt, J. Popp, A. Srivastava, Anal. Methods (2014).
[20] X. Feng, R. Li, C. Hu, W. Hou, J. Electroanal. Chem. 657 (2011) 28.
[21] C. Zhu, P. Wang, L. Wang, L. Han, S. Dong, Nanoscale 3 (2011) 4376.
[22] J.-J. Shi, J.-J. Zhu, Electrochim. Acta 56 (2011) 6008.
[23] Z. Zheng, Y. Du, Q. Feng, Z. Wang, C. Wang, J. Mol. Catal. A Chem. 353 (2012) 80.
[24] P. Solís-Fernández, R. Rozada, J.I. Paredes, S. Villar-Rodil, M.J. Fernández-Merino, L. Guardia, A. Martínez-Alonso, J.M.D. Tascón, J. Alloys Compd. 536 (2012) S532.
[25] V. Kumar, S. Srivastava, S. Umrao, R. Kumar, G. Nath, G. Sumana, P.S. Saxena, A. Srivastava, RSC Adv. 4 (2014) 2267.
[26] Y. Zhang, J. Zhang, H. Wu, S. Guo, J. Zhang, J. Electroanal. Chem. 681 (2012) 49.
[27] D.C. Marcano, D.V. kosynkin, J.M. Berlin, a. Sinitskii, Z. Sun, a. Slesarev, L.B. Alemany, W. Lu, J.M. Tour, ACS Nano 4 (2010) 4806.
[28] W. Stöber, A. Fink, E. Bohn, J. Colloid Interface Sci. 26 (1968) 62.
[29] S. Park, J. An, J.R. Potts, A. Velamakanni, S. Murali, R.S. Ruoff, Carbon N. Y. 49 (2011) 3019.
[30] A.C. Ferrari, J.C. Meyer, V. Scardaci, C. Casiraghi, M. Lazzeri, F. Mauri, S. Piscanec, D. Jiang, K.S. Novoselov, S. Roth, A.K. Geim, Phys. Rev. Lett. 97 (2006) 187401.
[31] V.M. Bermudez, Langmuir 26 (2010) 18144.
[32] J.E.B. Randles, Discuss. Faraday Soc. 1 (1947) 11.
[33] P. Zanello, Inorganic Electrochemistry: Theory, Practice and Applications, Royal Society of Chemistry, 2003.
[34] R.J. Klingler, J.K. Kochi, J. Phys. Chem. 85 (1981) 1731.
[35] A. Chaubey, B.D. Malhotra, Biosens. Bioelectron. 17 (2002) 441.
[36] S. Dong, B. Wang, B. Liu, Biosens. Bioelectron. 7 (1992) 215.
[37] N. Pasco, K. Baronian, C. Jeffries, J. Webber, J. Hay, Biosens. Bioelectron. 20 (2004) 524.
[38] H. Lineweaver, D. Burk, J. Am. Chem. Soc. 56 (1934) 658.
[39] Z. Matharu, P.R. Solanki, V. Gupta, B.D. Malhotra, Analyst 137 (2012) 747.
[40] M. Guo, J. Chen, J. Li, L. Nie, S. Yao, Electroanalysis 16 (2004) 1992.
[41] X. Cai, X. Gao, L. Wang, Q. Wu, X. Lin, Sensors Actuators B Chem. 181 (2013) 575.
[42] N. Agnihotri, A.D. Chowdhury, A. De, Biosens. Bioelectron. (2014).
[43] S. Park, K. Cho, S. Kim, Trans. Electr. Electron. Mater. 15 (2014) 136.
[44] S. Singh, P.R. Solanki, M.K. Pandey, B.D. Malhotra, Sensors Actuators B Chem. 115 (2006) 534.
[45] C. Dhand, S.K. Arya, M. Datta, B.D. Malhotra, Anal. Biochem. 383 (2008) 194.
[46] P.R. Solanki, A. Kaushik, A.A. Ansari, A. Tiwari, B.D. Malhotra, Sensors Actuators B Chem. 137 (2009) 727.
[47] U. Saxena, M. Chakraborty, P. Goswami, Biosens. Bioelectron. 26 (2011) 3037.

Biosensors and Bioelectronics 90 (2017) 224–229

Contents lists available at ScienceDirect

Biosensors and Bioelectronics

journal homepage: www.elsevier.com/locate/bios

Excellent storage stability and sensitive detection of neurotoxin quinolinic acid

Ranjana Singh[a], Sunayana Kashyap[b], Suveen Kumar[c], Shiju Abraham[a], Tejendra K. Gupta[a], Arvind M. Kayastha[d], Bansi D. Malhotra[c], Preeti Suman Saxena[b,*], Anchal Srivastava[a,*], Ranjan K. Singh[a,*]

[a] Department of Physics, Institute of Science, Banaras Hindu University, Varanasi 221005, India
[b] Department of Zoology, Institute of Science, Banaras Hindu University, Varanasi 221005, India
[c] Department of Biotechnology, Delhi Technological University, Main Bawana Road, Delhi 110042, India
[d] School of Biotechnology, Institute of Science, Banaras Hindu University, Varanasi 221005, India

ARTICLE INFO

Keywords:
Quinolinic Acid
QPRT
Enzyme
Neurotoxin
Bio-electrodes

ABSTRACT

Quinolinic acid (QA) is a metabolite of tryptophan degradation obtained through kynurenine pathway, produced naturally in the mammalian brain as well as in the human cerebrospinal fluid. The presence of QA ~10–40 μM is a clear indicator of many neurological disorders as well as deficiency of vitamin B_6 in human being. In the present work; rapid, sensitive and cost-effective bio-electrodes were prepared to detect the trace amount of endogenous neurotoxin (QA). Cyclic voltammetry (CV) and differential pulse voltammetry (DPV) studies were carried out to measure the electrochemical response of the fabricated bio-electrodes as a function of QA concentrations. These devices were found to exhibit desirable sensitivity of ~7.86 mA μM^{-1} cm^{-2} in wide concentration range (6.5 μM-65 mM). The lower detection limit of this device is as low as 6.5 μM and it has excellent storage stability of ~30 days. The capability of the proposed electrochemical bio-sensor was also checked to detect QA in the real samples (human serum). These results reveal that the use of this electrochemical bio-sensor may provide a potential platform for the detection of QA in the real samples for the prior detection of many diseases.

1. Introduction

Quinolinic acid (pyridine 2,3-dicarboxilic acid, hereafter referred as QA) (Heyes et al., 1992) occurs naturally in the mammalian brain in nano-molar as well as in the human cerebrospinal fluid in several nano-molar to micro-molar amounts (Heyes et al., 1992; Chen et al., 2009; Schwarcz and Pellicciari, 2002). The presence of QA is found below 100 nM, whereas the increased level of this molecule (10–40 μM) can be detected in pathological conditions (Guillemin, 2012; Leipnitz et al., 2005). The increased level of this molecule is known to be responsible for many neurological disorders such as Alzheimer, (Guillemin and Brew, 2002) Huntington disease (Schwarcz et al., 2010) and HIV associated dementia (HAD) (Guillemin et al., 2004). The presence of QA also affects the function of neurons by the activation of *N*-methyl-D-aspartate (NMDA) receptors (Birley et al., 1982; Stone and Connick, 1985). Apart from these effects, its elevated level (30–164 μM) has also been recognized as a clear indicator of deficiency of vitamin B_6 in the human being (Brown et al., 1965). All these reports reveal that the elevated level of QA can be used to detect the presence of many diseases (Guillemin, 2012; Leipnitz et al., 2005; Guillemin and Brew, 2002; Schwarcz et al., 2010; Guillemin et al., 2004; Birley et al., 1982; Stone and Connick, 1985; Brown et al., 1965). Hence there is urgent need to fabricate; rapid, cost-effective, durable and sensitive sensor that can be used to detect the trace amount of QA for the early detection of many diseases as mentioned above (Guillemin, 2012; Leipnitz et al., 2005; Guillemin and Brew, 2002; Schwarcz et al., 2010; Guillemin et al., 2004; Birley et al., 1982; Stone and Connick, 1985; Brown et al., 1965).

Several detection techniques such as gas chromatography, mass spectrometry (During et al., 1989; Shoemaker and Elliott, 1991) liquid-chromatography (Patterson and Brown, 1980), thin layer chromatography (Taguchi et al., 1983), radio enzymatic assay (Foster et al., 1986) and capillary electrophoresis-mass spectrometry (Wang et al., 2013) can be utilized to determine the trace amount of QA in the biological samples. All these reported methods are time consuming as well as suffer from lack of selectivity, sensitivity and stability. Liquid

* Corresponding authors.
E-mail addresses: pssaxena@rediffmail.com (P.S. Saxena), anchalbhu@gmail.com (A. Srivastava), ranjanksingh65@rediffmail.com (R.K. Singh).

http://dx.doi.org/10.1016/j.bios.2016.11.053
Received 26 October 2016; Accepted 22 November 2016
Available online 23 November 2016
0956-5663/

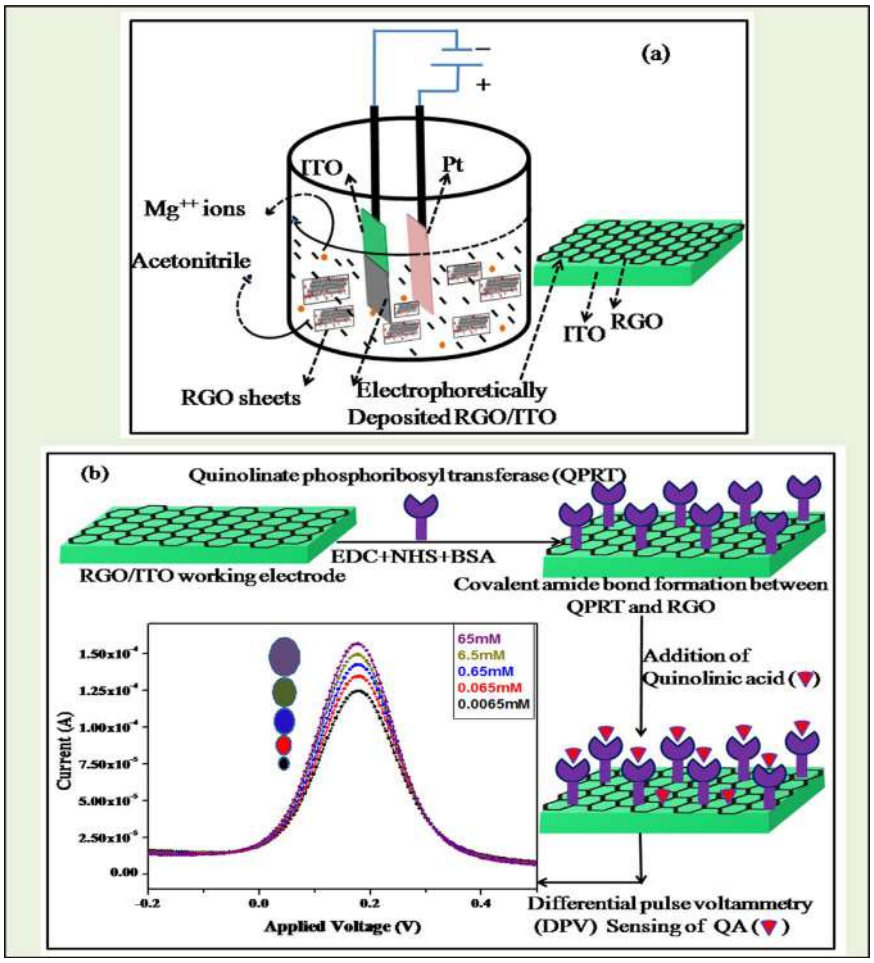

Fig. 1. Schematics for the (a) Fabrication of working electrode RGO/ITO by using electrophoretic deposition (EPD) technique and (b) immobilization of quinolinate phosphoribosyl transferase (QPRT) on working electrode RGO/ITO treated with EDC/NHS and BSA and sensing of QA via differential pulse voltammetry (DPV) technique.

chromatography with fluorimetric detection (Mawatari et al., 1995) has been reported to determine the trace amount of QA. However, this method suffers from certain limitations such as tedious procedure to handle the sample, to protect it from light and lack of selectivity. Fluorimetric detection of QA, based on catalytic activity of horseradish perioxidase (HRP) (Odo et al., 2009) in presence of hydrogen peroxide (H_2O_2) has been available to determine trace amount of QA. In this method; QA acquires fluorescing property but some reducing and oxidizing substances were found to affect the fluorescent derivatization of QA with HRP in presence of H_2O_2. Although sensitivity associated with this method is high but lack of selectivity, stability and time consuming procedure has remained as a challenge. Hence to remove all these short-comings, fabrication of such a sensing device having excellent storage stability and quick response is highly desirable for the early detection of the trace amount of QA.

Electrochemical bio-sensors have become more powerful sensing devices in recent years (Chikkaveeraiah et al., 2009) because of its quick response, sensitivity, simplicity, reproducibility and selectivity. These sensing devices require low reagents consumption, ease of fabrication, miniaturization and continuous monitoring of the analytes (Srivastava et al., 2011). As synthesized reduced graphene oxide (RGO, derivative of graphene) has become a promising material for biosensing applications recently in comparison to the graphene oxide (GO), (Srivastava et al., 2011; Schwierz, 2010; Park et al., 2012; Han et al., 2007; Pumera et al., 2010; Pumera, 2011; Huang et al., 2010, 2011; Srivastava et al., 2013). Chemically active RGO has large surface area, sufficient functional groups, potential to facilitate electron transfer from enzymes and proteins, cost-effective and easy to handle which are the essential properties of the electrochemical bio-sensors (Pumera et al., 2010; Pumera, 2011; Compton et al., 2011).

We have fabricated the cost-effective bio-sensor to detect the trace amount of QA. Various parameters (reproducibility, selectivity, magnitude of currents, linear coefficient and standard deviation) have been calculated for these devices. These bio-electrodes have good sensitivity of 7.86 mA μM^{-1} cm^{-2} with a wide range (6.5 μM– 65 mM) responses. It has good selectivity and excellent storage stability of ~30 days. The observed properties of the present bio-sensor are exciting and it can be useful to develop electrochemical bio-sensor for the early detection of QA. In the present work, we report results of the studies relating to the development of an electrochemical bio-sensing technique differential pulse voltammetry (DPV) to detect the trace amount of endogenous neurotoxin QA in the real samples (serum) also.

2. Experimental section

2.1. Materials

Quinolinate phosphoribosyl transferase (QPRT) enzyme was procured from KrishgenBiosystems, New Delhi India. Quinolinic acid (QA), 2, 6 pyridine di-carboxylic acid (PD), graphite flakes, acetonitrile, magnesium nitrate, sodium citrate, *N*-hydrooxysuccinimide (NHS), *N*-ethyl-*N*-(3-dimethylaminopropyl) carbodiimide (EDC), bovine serum albumin (BSA) and other analytical grade chemicals used in this work were procured from Sigma-Aldrich, India. All these materials were used without further purification.

2.2. Synthesis of reduced graphene oxide (RGO)

Graphene oxide (GO) was prepared by chemical route using Hummer's method (Marcano et al., 2010) and reduced graphene oxide (RGO) was obtained by reduction of GO with sodium citrate (Zhang et al., 2011). In this method, 100 mg sodium citrate was added into 10 ml aqueous suspension of GO (1 mg/ml) and the solution was stirred magnetically at 60 °C for ~6 h. Change in color from brown to black clearly indicates the reduction of GO to RGO. The RGO was treated in the following sequence; cooled down to room temperature, centrifuged at 10,000 rpm, washed with triple distilled water repeatedly and finally dried in the oven. The dried RGO powder was dispersed into water and acetonitrile for further use.

2.3. Preparation of RGO/ITO electrodes

Electrophoretic deposition (EPD) (Srivastava et al., 2013, 2012) technique was employed to fabricate RGO films on indium tin oxide (ITO) coated glass plate with sheet resistance ~30 Ω cm^{-1}. In this method, ITO-coated glass substrate acted as cathode and a platinum (Pt) foil (1 cm×2 cm) acted as an anode. These electrodes were kept parallel separated by 1 cm in a colloidal suspension of RGO prepared in acetonitrile (0.5 mg dl^{-1}). The 10^{-4}-10^{-5} M solution of Mg $(NO_3)_2 \cdot 6H_2O$ was added to the RGO suspension to enhance the deposition rate of RGO sheets on the cathode (ITO) (Wang et al., 2009; Compton et al., 2011). During the EPD process, DC voltage (150 V) was applied for two minutes. All these process involved in the preparation of working electrode has been depicted schematically in Fig. 1(a).

2.4. Immobilization of QPRT enzyme onto the RGO/ITO electrodes surface

An enzyme QPRT was covalently attached to RGO/ITO electrode. Prior to covalent attachment of the enzyme, COOH group of RGO was activated using EDC as a coupling agent and NHS as an activator. The COOH groups of RGO activated by following EDC/NHS chemistry (Srivastava et al., 2013; Sarkar and Nicholson, 1996) bind to the NH_2 groups of QPRT which results into the covalent amide bond (CONH) formation between RGO and QPRT. During the process of covalent attachment of QPRT to RGO/ITO electrode, 10 µl of QPRT enzyme (concentration 300 µg/ml) was freshly prepared in Tris HCl buffer (PH 8.0) and it was uniformly spread on the EDC/NHS activated RGO/ITO electrode [see Fig. 1(b)]. This electrode; immobilized with QPRT was incubated in humid chamber at room temperature for ~6 h. Since QPRT consisted of amino acids residues having NH_2 groups hence the formation of covalent immobilization was proposed via interaction between NH_2 functional groups of QPRT and COOH groups of RGO. Non-specific sites of the bio-electrodes were blocked by using bovine serum albumin (BSA). The amide bond formation was experimentally verified by FTIR spectra of QPRT/RGO. Schematic of immobilization of QPRT on working electrode RGO/ITO treated with EDC/NHS and BSA along with sensing of QA via differential pulse voltammetry (DPV) technique has been shown in Fig. 1(b).

3. Characterization

Structural and morphological characterizations were carried out using scanning electron microscopy (SEM, Philips XL 20), transmission electron microscopy (TEM-FEI Tecnai G2 electron microscope) and X-ray diffraction (XRD, Rigakuminiflex II). Raman (In-via Raman spectrometer, Renishaw), FTIR (Spectrum 65 FT-IR spectrometer, Perkin Elmer), UV–Visible (Lambda 25 UV–Visible spectrometer, Perkin Elmer) spectroscopic techniques were employed to characterize the as synthesized RGO. All the electrochemical measurements such as cyclic voltammetry (CV) and differential pulse voltammetry (DPV) were carried on Auto lab Potentiostat/Galvanostat (Eco Chemie, Netherlands) using three electrode cell configurations. Bio-electrode (QPRT/BSA/RGO/ITO), platinum foil and Ag/AgCl electrodes were used as working, counter and reference electrodes, respectively. The mixture of 5 mM $Fe(CN)_6^{4-}$ (Ferrocynide) and 5 mM $Fe(CN)_6^{3-}$ (Ferricynide) was used as the redox probe.

4. Results and discussion

4.1. Microstructural studies of RGO

SEM images of RGO shown in Fig. S1(a) indicates the uniform and sheet like morphology which is extended to several micrometers. Further, it is clearly visible that the thin layered RGO sheets consist of several wrinkles and folds. These wrinkles and folds might have developed due to defects and functional groups present in the carbon lattice. Fig. S1(b) shows TEM micrograph of RGO, which reveals a few layers of RGO sheets along with wrinkles and folds. HRTEM images in the inset of Fig. S1(b) indicates that the average inter-planar spacing of the lattice fringes of RGO is found to be ~3.5 Å.

The Raman spectrum of RGO has been shown in Fig. S1(c) containing four Raman bands observed at 1352, 1595, 2708 and 2930 cm^{-1}. The most prominent Raman band observed at 1352 cm^{-1} is assigned as D band which is attributed to the disorder present in the RGO. This structural disorder may be correlated to the oxygen functional groups as well as point defects present in the system. The Raman band centered at 1595 cm^{-1} is a well-defined; G band which represents the presence of sp^2 bonded carbon atoms. Overtone of D band i.e. 2D band is found at 2708 cm^{-1}. The presence of this overtone is clearly related to the dispersive nature as a function of frequency (Srivastava et al., 2012).

The X-ray diffraction (XRD) pattern of RGO which has been used as a working electrode for electrochemical bio-sensing studies recorded in the range of 10–75° is shown in Fig. S1(d). In the XRD pattern of RGO, an intense and broad peak with a 2θ value at around 25.28° is observed and assigned to the (00.2) (Srivastava et al., 2013) reflection plane corresponding to an inter-planner spacing of 0.352 nm, which is in good agreement with the HRTEM study [discussed in inset of Fig. S1(b)]. In addition to this, another peak of lower intensity is found at ~43.3° which is assigned to the (00.1) reflection plane of RGO (Srivastava et al., 2013). UV–Visible absorption spectrum of chemically synthesized RGO is shown in Fig. S1(e) where triple distilled water was taken as reference to record UV–Vis spectrum of RGO. The absorption peak at 268 nm can be assigned as π-π* transition of aromatic C=C bonds (Srivastava et al., 2013). Figs. S1(a), S1(b), S1(c), S1(d) and S1(e) have been provided in the Supplementary material.

4.2. FTIR spectroscopic studies of RGO, QPRT and QPRT/RGO electrodes

The IR spectra of RGO, QPRT and QPRT/RGO have been shown by (A), (B) and (C), respectively in Fig. 2(a). The IR bands observed at 1650 and 1400 cm^{-1} are attributed to stretching and bending mode vibrations of C=O and O-H bonds of carboxyl groups present in the RGO respectively. The COH and C=C stretching mode of vibrations are obtained at 1110 cm^{-1}, 1631 cm^{-1}, respectively. A broad band observed at 3453 cm^{-1} is assigned to stretching vibration of OH group. It is important to note that the IR spectra were taken in aqueous medium. The OH bonds of water strongly absorb at ~3453 cm^{-1} which overlaps with OH absorption of RGO. The OH stretching band of RGO is sharp. The OH stretching band of water being broad and strong hides the OH stretching band of RGO. New IR band of QPRT/RGO is obtained 985 cm^{-1} due to OH bending vibration of carboxylic group. While stretching vibrational mode corresponding to CN becomes prominent and is observed at 1215 cm^{-1}. The intensity of stretching mode of C=O in QPRT/RGO is found to be enhanced and blue shifted which confirms the amide bond formation between carboxylic and amino group of RGO

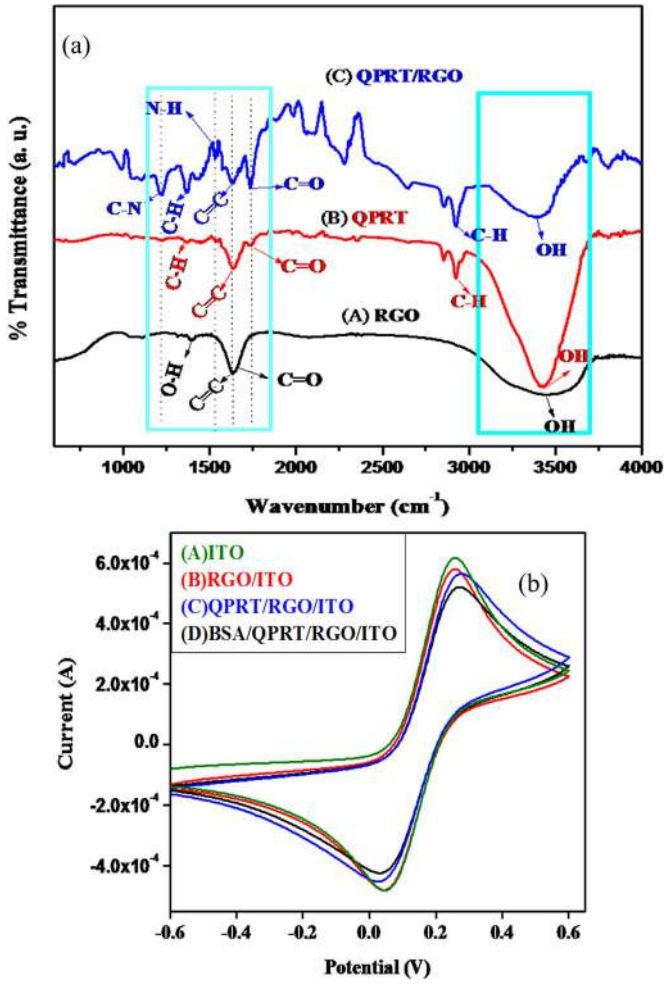

Fig. 2. (a) FT-IR spectrum of (A) RGO (B) QPRT and (C) QPRT/ RGO 3(b) CV curves of (A) ITO (B) RGO/ITO (C) QPRT/RGO/ITO and (D) BSA/QPRT/RGO/ITO electrodes.

and QPRT, respectively.

4.3. Electrochemical studies

The cyclic voltammetry (CV) studies of the fabricated electrodes were conducted in phosphate buffer solution (PBS) of pH 7.0 containing 0.9% NaCl and 5 mM solution of $[Fe(CN)_6]^{3-/4-}$. Fig. 3(b) shows cyclic voltammetry (CV) studies of ITO, RGO/ITO, QPRT/RGO/ITO and BSA/QPRT/RGO/ITO electrodes. It was found from the [Fig. 2(b)]

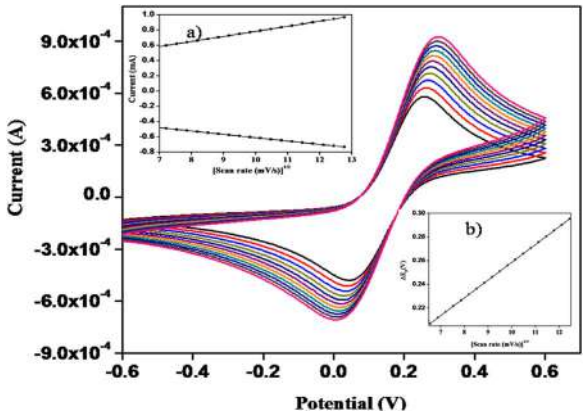

Fig. 3. Scan rate studies of RGO/ITO [Inset (a) magnitude of oxidation and reduction current generated as response of square root of scan rate (mV/s), Inset (b) potential as function of square root of scan rate] electrodes.

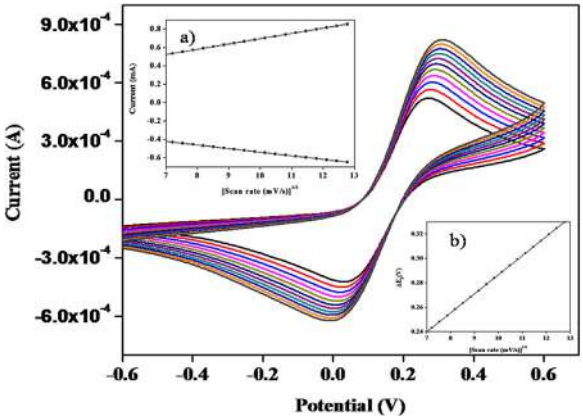

Fig. 4. Scan rate studies of BSA/QPRT/RGO/ITO [Inset (a) magnitude of oxidation and reduction current generated as response of square root of scan rate (mV/s), Inset (b) potential as function of square root of scan rate] electrodes.

that the magnitude of current for RGO/ITO electrode (Peak current 0.580 mA) is lower than that of bare ITO electrode (Peak current 0.616 mA), which indicated the reduction in electron transfer between solution and RGO/ITO interface. The immobilization of QPRT onto the RGO/ITO electrode further lowers the magnitude of peak current (0.565 mA) as compared to that of the RGO/ITO electrode. Bovine serum albumin (BSA) has been used for blocking of non-specific sites of QPRT/RGO/ITO bio-electrode. It was observed that magnitude of the peak current decreased again to 0.521 mA after coating of BSA on the surface of QPRT/RGO/ITO electrode. This reduction in peak current can be assigned due to adsorption of BSA on RGO/ITO sites of the QPRT/RGO/ITO immunoelectrode. To investigate the interfacial kinetics of the fabricated electrodes and bio-electrodes (RGO/ITO and BSA/QPRT/RGO/ITO) scan rate studies were conducted through CV. Fig. 3 and Fig. 4 show the observed CV response of RGO/ITO and BSA/QPRT/RGO/ITO electrodes respectively as a function of the scan rate (50–150 mV/s). A shift was observed in the redox peaks with increase in scan rate. It was also observed that cathodic (Ipc) and anodic peak (Ipa) currents both vary linearly with square root of the scan rate [insets (a) in Fig. 3 and Fig. 4], which indicated that the electrochemical reaction was a diffusion-controlled process (Kumar et al., 2015). The slopes and intercepts for the bio-electrodes RGO/ITO, and BSA/QPRT/RGO/ITO can be given by Eqs. (1–4):

$$I_{pc(RGO/ITO)} = [0.066\ mA(s/mV) \times (\text{scan rate}(mV/s))^{1/2}] + 0.119\ mA,\quad R^2 = 0.999,\ SD = 7.26 \times 10^{-3} \tag{1}$$

$$I_{pa(RGO/ITO)} = -[0.044\ mA(s/mV) \times (\text{scanrate}(mV/s))^{1/2}] - 0.175\ mA,\quad R^2 = 0.999,\ SD = 5.51 \times 10^{-3} \tag{2}$$

$$I_{pc(BSA/QPRT/RGO/ITO)} = [0.058\ mA(s/mV) \times (\text{scanrate}(mV/s))^{1/2}] + 0.120\ mA,\quad R^2 = 0.999,\ SD = 5.13 \times 10^{-3} \tag{3}$$

$$I_{pa(BSA/QPRT/RGO/ITO)} = -[0.039\ mA(s/mV) \times (\text{scan rate}(mV/s))^{1/2}] - 0.152\ mA,\quad R^2 = 0.999,\ SD = 4.45 \times 10^{-3} \tag{4}$$

The difference of cathodic (E_{pc}) and anodic (E_{pa}) peak potentials ($\Delta E_p = E_{pc} - E_{pa}$) and square root of scan rate for RGO/ITO and BSA/QPRT/RGO/ITO electrodes exhibit a linear relationship and follow Eqs. (5) and (6). A good linear relationship indicates the facile electron transfer from medium to the electrodes [inset (b) in Figs. 3 and 4].

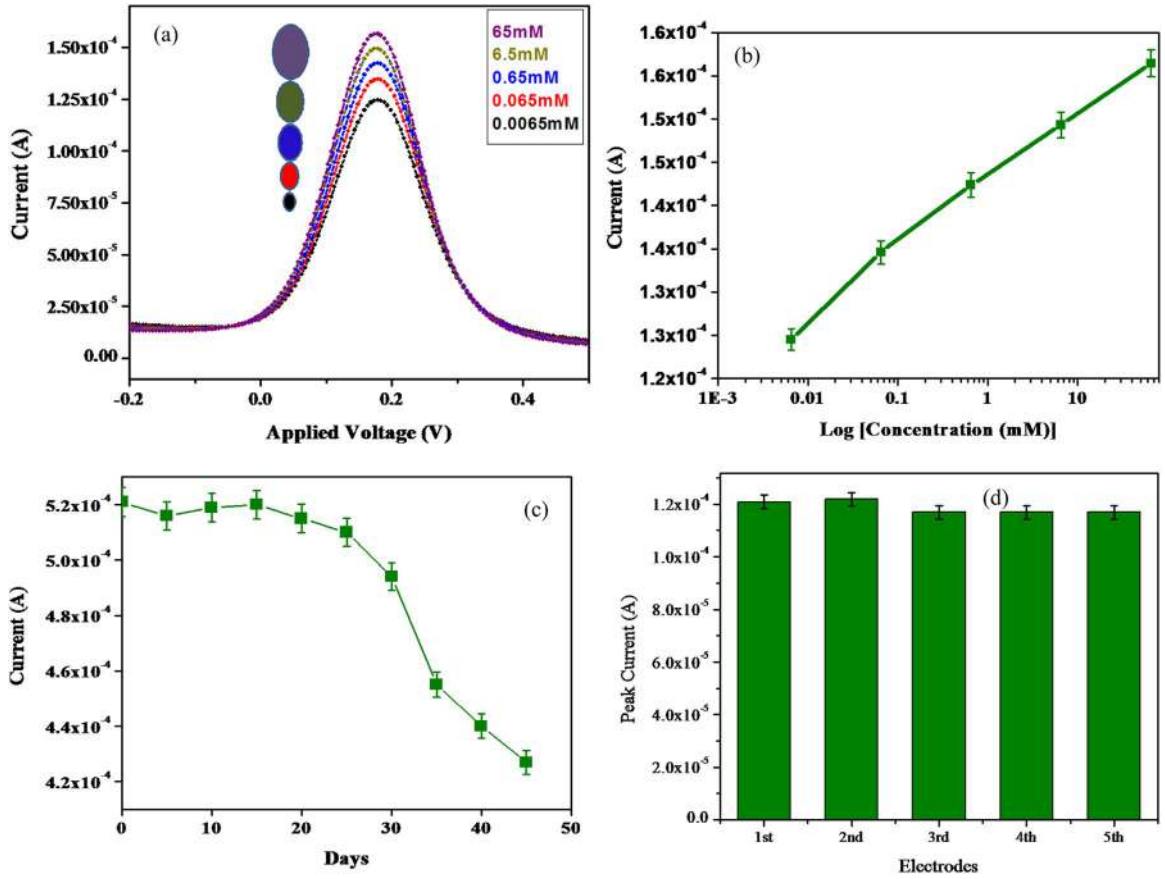

Fig. 5. (a) Electrochemical current response studies (differential pulse voltammetry, DPV) of BSA/QPRT/RGO/ITO electrode as a function of QA concentration [ranging from 6.5 μM to 65 mM] (b) Linearity between peak current of the bio-electrode measured by differential pulse voltammetry (DPV) and QA concentration has been shown on Log scale (c) Electrochemical current response studies (cyclic voltammetry, CV) of BSA/QPRT/RGO/ITO electrode as a function of time (days) and (d) Electrochemical current response studies (differential pulse voltammetry, DPV) of five different bio-electrodes BSA/QPRT/RGO/ITO fabricated via same set of procedure.

$$\Delta E_p(\mathrm{V})_{(\mathrm{RGO/ITO})} = [0.015\ \mathrm{V}(s/\mathrm{mV}) \times (\text{scan rate}(\mathrm{mV}/s))^{1/2}] + 0.11\ V,$$
$$R^2 = 0.999,\ \ SD = 1.31 \times 10^{-3}$$
$$\Delta E_p(\mathrm{V})_{(\mathrm{BSA/QPRT/RGO/ITO})} = [0.016\ \mathrm{V}(s/\mathrm{mV}) \times (\text{scanrate}(\mathrm{mV}/s))^{1/2}] + 0.13\ V, \quad (5)$$

$$R^2 = 0.998,\ \ SD = 1.78 \times 10^{-3} \quad (6)$$

where R is the correlation coefficient and SD is the standard deviation.

The diffusion coefficient (D) of bio-electrode BSA/QPRT/RGO/ITO was calculated using Randle Sevick equation (Kumar et al., 2016) (Eq. (7)) and found to be 0.31 $cm^2\ s^{-1}$.

$$I_p = (2.69 \times 10^5)\, n^{3/2} A\, D^{1/2} C\, \upsilon^{1/2} \quad (7)$$

where Ip is the peak current of immunoelectrode, n is the number of electrons (1) transferred, A is the active surface area of the immunoelectrode (0.25 cm^2), D is the diffusion coefficient, C is the concentration of redox species (5 mmol cm^{-2}) and υ is the scan rate (50 mV/s). Surface concentration (γ) of BSA/QPRT/RGO/ITO electrode was determined by using Laviron's theory (Sharma et al., 2012) given by

$$I_p = n^2 F^2 \gamma A \upsilon (4RT)^{-1} \quad (8)$$

where I_p represents the peak current of electrode, n is the number of electrons (1) transferred, F is the Faraday constant (96485 C mol^{-1}), γ is the surface concentration of the absorbed electro-active species, A is the surface area of the electrode, ν is the scan rate (V/s), R is the gas constant (8.314 J mol^{-1} K^{-1}) and T is room temperature (25 °C or 298 K). The Eq. (8) yields Υ to be 4.42×10^{-8} mol cm^{-2}.

4.4. Differential pulse voltammetry measurements

Differential pulse voltammetery (DPV) studies were carried out to measure the electrochemical response of the fabricated bio-electrodes (BSA/QPRT/RGO/ITO) as a function of QA concentration varying from 6.5 μM to 65 mM in PBS (pH 7.0, 0.9% NaCl) containing 5 mM $[Fe(CN)_6]^{3-/4-}$ [Fig. 5(a)]. It was observed that the magnitude of current increased with increase in concentration of QA which can be attributed to the formation of enzyme-ligand complex at the electrode surface. This process of complex formation leads to electron release at the electrode surface. QPRT; a member of the phosphoribosyl family of enzymes has been recognized to catalyze the formation of nicotinic acid mononuleotide from QA and substrate 5-phosphoribosyl-1-pyrophosphate (Bello and Grubmeyer, 2010). In this process, QA binds first to QPRT which may cause release of electron at the electrode surface. In the present work this process was monitored through differential pulse voltammetry measurements. Furthermore, a linear correlation was obtained in the wide concentration range of 6.5 μM to 65 mM (R^2 =0.993, SD =4.71×10^{-4}) and follow Eq. (9). Linearity between peak current of the bio-electrodes measured by differential pulse voltammetry (DPV) and QA concentration shown on log scale has been depicted in Fig. 5(b). The sensitivity of the electrode is found to be 7.86 mA μM^{-1} cm^{-2}.

$$I_p(\mathrm{mA}) = 7.86\ \mathrm{mA}\ \mu M^{-1}\mathrm{cm}^{-2} \times \log[\text{concentration}\ (\mu M)] + 0.143\ \mathrm{mA},$$
$$R^2 = 0.993,\ \ SD = 4.71 \times 10^{-4} \quad (9)$$

Several studies on different sensing techniques and sensing characteristic of the proposed electrochemical bio-sensor BSA/QPRT/

Table 1
Sensing characteristics of the proposed electrochemical bio-sensor BSA/QPRT/RGO/ITO summarized along with some results reported in the literature.

Detection techniques of quinolinic acid (QA)	Detection range	Detection limit	Sensitivity	Stability (days)	References
Radio enzymatic assay for quinolinic acid	–	2.5 pmol	–	–	Kumar et al. 2015
Capillary electrophoresis-mass spectrometry	0.4–40 μM	–	–	–	Kumar et al. 2016
Liquid chromatography with fluorimetric detection	0.36–68.8 nmol ml^{-1}	–	–	–	Leipnitz et al. 2005
Fluorimetric detection of quinolinic acid by catalytic activity of horseradish peroxidase	0.1–5 nmol ml^{-1}	0.04 nmol ml^{-1}	–	–	Mawatari et al. 1995
Electrochemical bio-sensor	**6.5 μM–65 mM**	**6.5 μM**	**7.86 mA $\mu M^{-1} cm^{-2}$**	**30**	**Present work**

RGO/ITO discussed above have been compared and summarized in Table 1.

The stability of the BSA/QPRT/RGO/ITO electrode was determined by CV studies at a regular interval of 5 days up to 45 days [Fig. 5(c)] and stored at 4 °C until further use. It was observed that magnitude of the peak current exhibited 95% response upto 30 days and there after the peak current decreased and reached to 80% at the end of 45 days. It indicates that the stability of the fabricated BSA/QPRT/RGO/ITO bio-electrode is upto ~30 days. In order to ensure reproducibility, five different bio-electrodes of constant surface area were prepared under similar conditions and their electrochemical responses were investigated by DPV studies. These bio-electrodes exhibit good reproducibility. Mean value of the current was found equal to ~119 μA. Each measurement was repeated for three times for each electrode and error bar was included accordingly. The relative standard deviation (RSD) for each bio-electrode was less than ~5% which showed the reproducibility of the fabricated bio-electrodes is high [Fig. 5(d)]. DPV measurements have also been carried out for the detection of QA in the real sample (serum) as shown in Fig. S3.

5. Conclusions

Early detection of endogenous neurotoxin, quinolinic acid may be helpful to the patients suffering from many neurological disorders such as Alzheimer's, Huntington's and HIV associated dementia (HAD) as well as deficiency of vitamin B_6. In this work selective, stable and reproducible bio-electrodes have been fabricated to detect quinolinic acid. The proposed bio-sensor based on electrochemical sensing may provide potential platform for the sensitive and selective detection of QA which can be used for the early detection of the neurological disorders and other diseases in the real samples in future.

Conflict of interests

The authors declare no competing financial interest.

Acknowledgements

Ranjana Singh is grateful to UGC, New Delhi, Govt. of India for providing financial support in terms of BHU research fellowship. One of the authors (TKG) is grateful to UGC for providing the research grant under the UGC Dr. D. S. Kothari Post-Doctoral Fellowship Scheme [No. F. 4-2/2006 (BSR)/PH/13–14/0108]. RKS is grateful to AvH Foundation, Germany, DST and CSIR, New Delhi, Govt. of India for support to procure Micro-Raman setup. AS is thankful to DST India (Project Code: DST/TSG/PT2012/68 & DST PURSE SCHEME 5050) and CAS-UGC, (Grant No. [F.530/7/CAS-V/2015/(SAPI)); Departmental Programme for providing financial assistance.

Appendix A. Supporting information

Supplementary data associated with this article can be found in the online version at doi:10.1016/j.bios.2016.11.053.

References

Bello, Z., Grubmeyer, C., 2010. Biochemistry 49, 1388–1395.
Birley, S., Collins, J.F., Perkins, M.N., Stone, T.W., 1982. Br. J. Pharmacol. 77, 7–12.
Brown, R.R., Yess, N., Price, J.M., Linkswiler, H., Sawan, P., Hankes, L.V., 1965. J. Nutr. 87, 419–422.
Chen, Y., Meininger, V., Guillemin, G.J., 2009. Cent. Nerv. Syst. Agents Med. Chem. 9, 32–39.
Chikkaveeraiah, B.V., Liu, H., Mani, V., Papadimitrakopoulos, F., Rusling, J.F., 2009. Electrochem. Commun. 11, 819–822.
Compton, O.C., Jain, B., Dikin, D.A., Abouimrane, A., Amine, K., Nguyen, S.T., 2011. ACS Nano 5, 4380–4391.
During, M.J., Freese, A., Heyes, M.P., Swartz, K.J., Markey, S.P., Roth, R.H., Martin, J.B., 1989. FEBS Lett. 247, 438–444.
Foster, A.C., Okuno, E., Brougher, D.S., Shwarcz, R., 1986. Anal. Biochem. 158, 98–103.
Guillemin, G.J., 2012. FEBS J. 279, 1356–1365.
Guillemin, G.J., Brew, B.J., 2002. Redox Rep. 7, 199–206.
Guillemin, G.J., Kerr, S.J., Brew, B.J., 2004. Neurotox. Res. 7, 103–123.
Heyes, M.P., Saito, K.J., Crowley, S., Davis, L.E., Demitrack, M., Der, A.M., Dilling, L.A., Elia, J., Kruesi, M.J.P., Lackner, A., Larsen, S.A., Lee, K., Leonard, H.L., Markey, S.P., Martin, A., Milstein, S., Mouradian, M.M., Pranzatelli, M.R., Quearry, B.J., Salazar, A., Smith, M., Strauss, S.E., Sunderland, T., Swedo, S.W., Tourtellotte, W.W., 1992. Brain 115, 1249–1273.
Huang, Y., Dong, Shi, X., Li, Y., Li, C.M., Chen, L.-J.P., 2010. Nanoscale 2, 1485–1488.
Han, M.Y., Oezyilmaz, B., Zhang, Y., Kim, P., 2007. Phys. Rev. Lett. 98, 206805–206809.
Huang, X., Yin, Z., Wu, S., Qi, X., He, Q., Zhang, Q., Yan, Q., Boey, F., Zhang, H., 2011. Small 7, 1876–1902.
Kumar, S., Kumar, S., Tiwari, S., Srivastava, S., Srivastava, M., Yadav, B.K., Kumar, S., Tran, T.T., Dewan, A.K., Mulchandani, A., Sharma, J.G., Maji, S., Malhotra, B.D., 2015. Adv. Sci. 2 (8), 1500048.
Kumar, S., J.G, Maji, S., Malhotra, B.D., 2016. Biosens. Bioelectron. 78, 497–504.
Leipnitz, G., Schumacher, C., Scussiato, K., Dalcin, K.B., Wannacher, C.M.D., Wayse, A.T.D., Dutra, C.S., Wagner, M., Latini, A., 2005. Int. J. Dev. Neurosci. 23, 695–701.
Mawatari, K.-I., Oshida, K., Iinuma, F., Watanabe, M., 1995. Anal. Chim. Acta 302, 179–183.
Marcano, D.C., Kosynkin, D.V., Berlin, J.M., Sinitsakii, A., Sun, Z., Slesarev, A., Alemany, L.B., Lu, W., Tour, J.M., 2010. ACS Nano 4, 4806–4814.
Odo, J., Inoguchi, M., Hirai, A., 2009. J. Health Sci. 55, 242–248.
Pumera, M., Ambrosi, A., Bonanni, A., Chng, E.L.K., Poh, H.L., 2010. Trac-Trend Anal. Chem. 29, 954–965.
Pumera, M., 2011. Mater. Today 14, 308–315.
Park, S.J., Kwon, O.S., Lee, S.H., Song, H.S., Park, T.H., Janng, J., 2012. Nano Lett. 12, 5082–5090.
Patterson, J.I., Brown, R.R., 1980. J. Chromatogr. 182, 425–429.
Schwarcz, R., Pellicciari, R., 2002. J. Pharmacol. Exp. Ther. 303, 1–10.
Schwarcz, R., Guidetti, P., Sathyasaikumar, K.V., Muchowski, P.J., 2010. Prog. Neurobiol. 90, 230–245.
Stone, T.W., Connick, J.H., 1985. Neuroscience 15, 597–617.
Shoemaker, J.D., Elliott, W.H., 1991. J. Chromatogr. 562, 125–138.
Srivastava, S., Solanki, P.R., Kaushik, A., Ali, M.A., Srivastav, A., Malhotra, B.D., 2011. Nanoscale 3, 2971–2977.
Schwierz, F., 2010. Nat. Nanotechnol. 5, 487–496.
Srivastava, S., Kumar, V., Ali, M.A., Solanki, P.R., Srivastava, A., Sumana, G., Saxena, P.S., Joshi, A.G., Malhotra, B.D., 2013. Nanoscale 5, 3043–3051.
Sarkar, P., Nicholson, P.S., 1996. J. Am. Ceram. Soc. 79, 1987–2002.
Srivastava, R.K., Srivastava, S., Narayanan, T.N., Mahlotra, B.D., Vajtai, R., Ajayan, P.M., Srivastava, A., 2012. ACS Nano 6, 168–175.
Sharma, A., Pandey, C.M., Sumana, G., Soni, U., Sapra, S., Srivastava, A., Chatterjee, T., Malhotra, B.D., 2012. Biosens. Bioelectron. 38 (1), 107–113.
Taguchi, H., Koyama, S., Shimabyashi, Y., Iwai, K., 1983. Anal. Biochem. 131, 194–197.
Wang, X., Davis, I., Liu, A., Miller, A., Shamsi, S.A., 2013. J. Chromatogr. A 1316, 147–153.
Zhang, Z., Chen, H., Xing, C., Guo, M., Xu, F., Wang, X., Gruber, H.J., Zhang, B., Tang, J., 2011. Nano Res. 4, 599–611.

RSC Advances

PAPER

Facile, rapid and upscaled synthesis of green luminescent functional graphene quantum dots for bioimaging†

Cite this: *RSC Adv.*, 2014, **4**, 21101

Vinod Kumar,[a] Vimal Singh,[a] Sima Umrao,[b] Vyom Parashar,[c] Shiju Abraham,[b] Anand K. Singh,[a] Gopal Nath,[d] Preeti S. Saxena*[a] and Anchal Srivastava*[b]

Received 27th February 2014
Accepted 24th March 2014

DOI: 10.1039/c4ra01735h

www.rsc.org/advances

We report here the upscaled synthesis of green luminescent functionalized graphene quantum dots (FGQDs) by using an inexpensive and commonly occurring natural precursor *viz.* graphite powder. We observed in our sample that photoluminescence increases for excitation wavelengths of 300 nm to 350 nm and then decreases when excited at 375 to 425 nm for FGQDs at neutral pH. We found that the synthesized FGQDs do not show a drastic change in emission properties when kept under different pH conditions, which makes them a potential candidate for *in vivo* imaging, where the pH of the culture media plays a crucial role in the maintenance of the fluorescence. Water solubility, and excellent photostability along with low cytotoxicity of FGQDs are manifested as a remarkable bioimaging material.

Introduction

Graphene, a single layer of graphite and a synthetic allotrope of carbon with its incredible debut in 2004, is lodging its presence in every realm of science. So far, a lot of work on graphene gravitated towards fundamental physics and electronic devices.[1] However, luminescence properties of graphene are not well explored. Due to the lack of a band gap, no optical luminescence is observed in pristine graphene. However, previous studies have found astonishing photoluminescence from zero band gap graphene and finite gap graphene oxide.[1] Recent experimental studies have shown the possibility of obtaining fluorescence from graphene.[2–4] To effectively tune the band gap of graphene, a promising approach is to convert the 2-D graphene sheets into 0-D graphene quantum dots (GQDs). Since the band gap depends on size,[5] shape[6] and fraction of the sp^2–sp^3 domains,[7] it has been found that photoluminescence emission may be tuned by controlling the nature and size of the extended sp^2 sites.[8] Although, theoretical physicists predicted the optical properties of GQDs,[9–11] experimental success has been achieved only very recently.

Furthermore, recent studies indicated that GQDs could have tremendous potential in bioimaging,[12,13] electrochemical biosensors,[14] catalysis[15,16] and in photovoltaic devices.[17] This leads researchers to explore the possibilities to fabricate GQDs by various routes, for example, arc discharge,[18] laser ablation,[19,20] electrochemical oxidation,[21] combustion/thermal,[22] supported synthesis,[23] microwave methods,[24] electro-beam lithography,[25] hydrothermal,[26–28] and by chemical oxidation.[29,30] However, these methods are limited by the prerequisite for special equipment and expensive starting materials such as carbon fibers and graphene oxide. Moreover, the low yield and multiple step process make these methods costly and time consuming. Hence, in the current study an attempt has been made to achieve a cost effective, quick, facile single-step large scale synthesis of wet chemically derived functionalized graphene quantum dots (FGQDs) through acidic treatment of graphite powder. As the source material, *i.e.* graphite, is devoid of any functional groups, the produced quantum dots have been termed as functional graphene quantum dots. The synthesized FGQDs have been further used in bioimaging of cancerous cells (*in vitro* study).

Experimental

Materials and methods

All chemicals and reagents used were of analytical grade. Graphite powder was purchased from Sigma Aldrich, Bangalore, India. H_2SO_4 and HNO_3 and all other chemicals were purchased from Merck limited, Mumbai, India. The dialysis bag was procured from Millipore Merck Limited, Mumbai, India.

[a]*Department of Zoology, Banaras Hindu University, Varanasi-221005, India. E-mail: pssaxena@rediffmail.com*

[b]*Department of Physics, Banaras Hindu University, Varanasi-221005, India. E-mail: anchalbhu@gmail.com*

[c]*Department of Applied Chemistry, University of Johannesburg, Johannesburg, South Africa*

[d]*Department of Microbiology, Institute of Medical Science, Banaras Hindu University, Varanasi-221005, India*

† Electronic supplementary information (ESI) available. See DOI: 10.1039/c4ra01735h

Synthesis of functionalized graphene quantum dots (FGQDs)

Graphite powder (0.20 g) was added into a mixture of concentrated H_2SO_4 (60 ml) and HNO_3 (20 ml). The solution was sonicated for 4 h at RT and stirred for 45 minutes at 90 °C. The obtained yellow colored solution was cooled to RT and its pH was set at 7 with Na_2CO_3. The solution was further dialyzed through a dialysis bag (retained molecular weight 2000 Da) for 3 days to get the final product as FGQDs.

Cytotoxicity evaluation

The cytotoxicity of the FGQDs has been studied with 3-(4,5-dimethylthiazol-2-yl)-2,5-diphenyl tetrazolium bromide (MTT) assays against human hepatic cancer cells (HuH-7 cells). The cells were cultured and maintained with DMEM medium (Invitrogen) containing 4.5 g ml^{-1} D-glucose, 4 mM L-glutamine, and 110 mg ml^{-1} sodium pyruvate, with 10% fetal bovine serum, 100 IU ml^{-1} penicillin and 100 μg ml^{-1} streptomycin. The cells were plated at 5000 cells per well on a 96 well plate and incubated for 24 h at 37 °C in a CO_2 incubator for proper adherence. FGQDs at a concentration range of 0–100 μg ml^{-1} were added to the culture media of each well followed by 24 h of incubation. Experiments were run in triplicate. After 20 h of incubation, 50 μl of 5 mg ml^{-1} MTT solution was added to each well. After a further 24 h of incubation, the culture media with MTT was removed and cells were treated with 200 μl of DMSO for 5 minutes at RT.

The optical density (OD) of solubilized formazan salts were measured at 490 nm. The cell viability was estimated according to the following equation:

$$\text{Cell viability [\%]} = (\text{OD treated/OD control}) \times 100\%$$

where, OD control was absorbance estimated without FGQDs while OD treated was absorbance estimated in the presence of FGQDs. Data were analyzed through SPSS software using one way ANOVA followed by the Duncan test to see the level of significance at $P < 0.01$ and $P < 0.05$.

Cellular imaging

Cellular uptake and bioimaging potential of FGQDs were investigated through a fluorescence microscope. For this, 5000 HuH-7 cells were plated in each well of 4 well sterile chamber slides with 200 μl of culture medium and incubated for 24 h at optimum culture conditions. 50 μl (5 μg ml^{-1}) of FGQDs were supplemented to this culture medium and incubation was continued for the next 24 h. Following incubation, FGQDs with medium were removed and the cells were washed twice with 1X PBS. Prior to inspection under the microscope, cells were fixed using 1% freshly prepared paraformaldehyde, counter stain with DAPI to localize chromatin and mounted in Canada balsam on a lysine pretreated glass slide. Cellular imaging was done with the help of a fluorescence microscope.

Characterization

UV-Visible spectra and fluorescence spectra were recorded with a Perkin Elmer UV-Visible-Lambda 25 spectrophotometer and a Perkin Elmer, LS-55 fluorescence spectrophotometer respectively. Fourier transform infrared spectroscopy (FTIR) characterization has been carried out using a Thermo scientific FTIR (Thermo Nicolet-6700). XPS analysis has been performed in a Perkin Elmer XPS chamber (PHI 1257) with a base pressure of 5×10^{-9} Torr. TEM images were taken with an HRTEM, Tecnaii-G2F30 STWIN, operated at an accelerating voltage of 200 keV. Cellular imaging was done using a Nikon Eclipse 90i microscope equipped with a Cool SNaP HQ2 CCD camera (Photometrics, AZ).

Results and discussion

We anticipate that during the sonication process exfoliation followed by cutting of the graphite results in the formation of FGQDs.[31] The Fig. 1a shows the optical image of yellow colored FGQDs solution under visible light which start giving green fluorescence (Fig. 1b) when observed under UV light (220–290 nm, mercury vapor lamp). This gives a primary indication about the green fluorescence of the FGQDs.

Fig. 2a shows the TEM image of FGQDs showing a narrow size distribution between 3 and 14 nm with the maximum fraction having average size of 7 nm, which is summarized in Fig. 2c. The high resolution transmission electron microscopic (HRTEM) image (Fig. 2b) shows parallel graphitic lines with spacing of ~3.4 Å indicating the crystalline behavior of 3–4 layered FGQDs in a nanodomain.

The UV-Visible absorption spectra of FGQDs (red curve) and graphite powder (black curve) dispersed in deionized water are shown in Fig. 3a. Two UV absorption peaks centered at λ_{max} 227 nm and λ_{max} 300 nm are observed. The absorption peak at λ_{max} 227 nm (5.5 eV) and a peak λ_{max} 300 nm (4.1 eV) are assigned to the π–π* transition of C=C band n–π* transitions of C=O bands respectively. Besides these main absorption bands a hump at λ_{max} 373 nm is also seen in FGQDs. The absorption peak at λ_{max} 227 nm (5.5 eV) in FGQDs is blue shifted with respect to the absorption band in graphite powder *i.e.* λ_{max} 271 nm, (4.5 eV). The appearance of absorption bands at λ_{max} 227 nm and λ_{max} 300 nm in highly oxidized graphite is a characteristic feature of FGQDs which is consistent with earlier reports.[32,26]

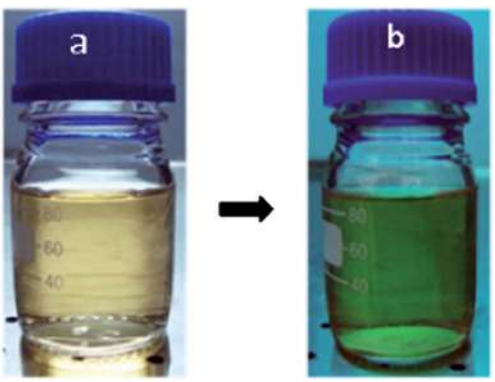

Fig. 1 Optical images of FGQDs, (a) under visible light, (b) under UV light.

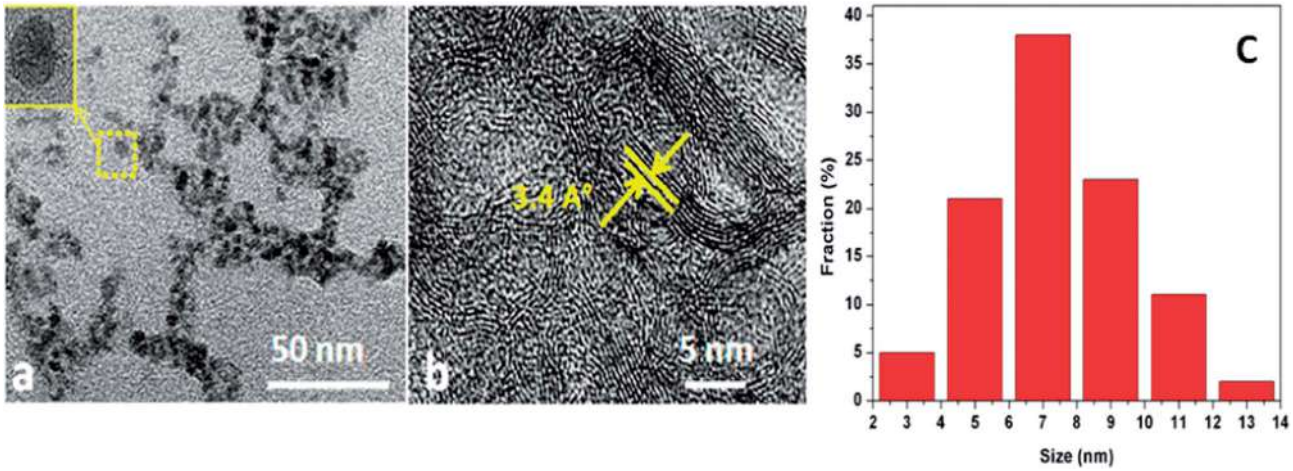

Fig. 2 (a) TEM image of FGQDs, with an average size of 7 nm, inset picture showing a typical single FGQD, (b) HRTEM image of FGQDs showing graphitic layers with spacing of 3.4 Å, (c) particle size distribution.

To get more insight into its optical properties, the band gap, *i.e.* the gap between the highest occupied molecular orbitals (HOMO) and the lowest unoccupied molecular orbitals (LUMO), of FGQDs were determined from the UV-Vis absorption spectra (Fig. 3a).

Equation (1) is used to calculate the band gap of both graphite and FGQDs from the absorption spectra.

$$\alpha h\nu = (h\nu - E_g)^2 \quad (1)$$

where α = the absorption coefficient, E_g = the bulk band gap energy.

The band gap energy has been calculated by plotting $(\alpha h\nu)^{1/2}$ *vs.* $h\nu$ and drawing tangents. The calculated band gap energies for FGQDs are 1.49 eV and 3.38 eV and for graphite is 0.30 eV. The calculated high band gap energy of FGQDs corroborate the observed band gap (Fig. 3b) exhibiting the quantum confinement.

The PL of GQDs is highly influenced by either synergism or competition between the intrinsic state emission such as quantum size effect, zigzag edge sites or recombination of localized electron–hole pairs and the defect state emission, *e.g.* energy traps.[33] In general, apart from the methods of synthesis, the PL of GQDs show high dependence on the size, excitation wavelength, pH and solvent, *etc.* The current study is also focused on the use of GQDs in bioimaging which demands pH and excitation independent fluorescence properties of GQDs. Keeping this point in view, we studied both the pH (acidic, basic and neutral conditions) and excitation dependent (λ_{ex} ranges from 300–425 nm) PL of FGQDs (Fig. 4).

Significant PL emission intensities have been observed in all pH conditions (acidic, basic and neutral) centered around ~500 nm. Which have been further exploited for fluorescence imaging of cancerous cells in our study. We have summarize the PL emissions in the tabular form as shown in Table 1 (ESI†). Along with a PL emission at 500 nm which is common in all cases a few additional PL emissions have also been observed in acidic and in neutral conditions. In both acidic and neutral conditions a broad PL emission band composed of multiple edges has also been observed at each λ_{ex} except 300 nm

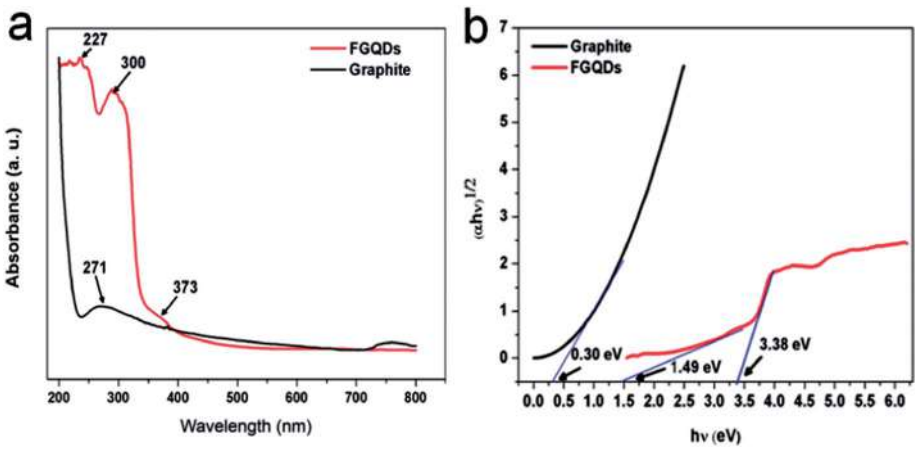

Fig. 3 (a) UV-Vis spectra of FGQDs and graphite powder, (b) band gap estimations from the absorption spectra.

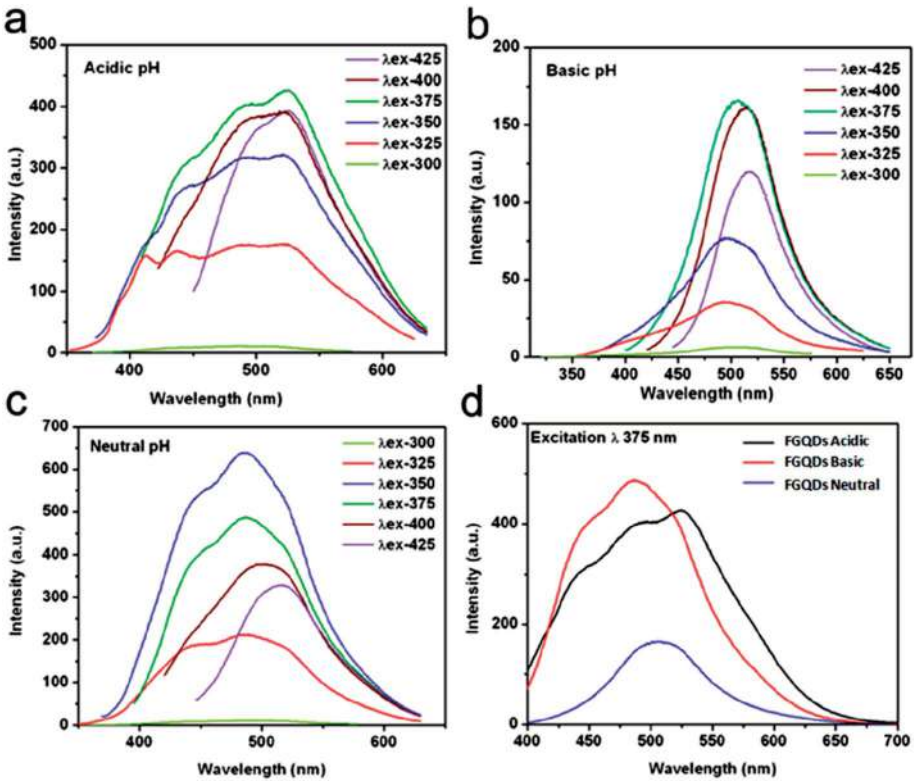

Fig. 4 PL spectra of synthesized FGQDs with different excitation wavelengths (λ_{ex} 300, 325, 350, 375, 400, and 425 nm) at different pH. (a) Acidic pH, (b) basic pH, (c) neutral pH, and (d) PL spectra of FGQDs with $\lambda_{ex} \sim$ 375 nm at acidic, basic, and neutral pH.

(Table 1a and b, ESI†). However, in basic conditions a sharp PL emission peak was noticed at each λ_{ex}, except for λ_{ex} 325 where one edge at 402 nm with a sharp peak at 496 nm has been observed (Table 1c, ESI†). The intensity of PL emission was found to increase with λ_{ex} up to 375 nm for both acidic and basic conditions but in neutral conditions it only increases up to 350 nm and then decreases at all pHs. It is noteworthy that the PL emission of FGQDs is pronounced at 500 nm in all pH conditions unlike earlier reports where PL was nearly or completely quenched under acidic and alkaline conditions.[26,34]

FGQDs undoubtedly follow a different PL mechanism to that reported in earlier studies.[33] It is presumed that strong acid oxidation results in the non-uniform breaking of the graphite sheet into different size GQDs with heavy oxygen functionalities at the edges and on the planes. A heterogeneous mixture with high oxygen functionalities in FGQDs plays a key role in stable PL behavior in all pH conditions, the exact mechanism is still under investigation. Using quinine sulfate as reference[35,36] PL quantum yields of FGQDs were measured and found to be 11.8% which is comparable to earlier reports.[37,38]

It is speculated that both the quantum size effect and surface defects contribute to the PL mechanism of GQDs.[25,39,40] To understand this, we performed Fourier transform infrared spectroscopy (FTIR) and X-ray photoelectron spectroscopy (XPS) measurements. During the FGQD formation, oxygen-containing groups, including carbonyl, carboxyl, hydroxyl, and epoxy groups were introduced to the edges and onto the basal plane, as shown in FTIR spectrum (Fig. 5a). XPS characterization is carried out to probe the composition of the FGQDs. XPS measurements showed that FGQDs are chiefly composed of C and O elements with a C/O atomic ratio of 1.3. The C1s XPS spectrum indicates that FGQDs have four types of C bonded atoms: C–C/C=C (284.6 eV), C–OH (285.7 eV), C–O–C (286.9 eV) and C–O/COOH (288.4 eV) (Fig. 5b).

The Raman technique is a practical method for the characterization of carbon based materials. In Raman spectra, the obtained G band represents the E_{2g} vibrational modes of the aromatic domains while the D band comes from the breathing modes of the graphitic domains.[41] Conventionally, the relative intensity of I_D/I_G was used to compare the structural order between the nanocrystalline and amorphous graphitic system and an increase in value indicated the decrease of the topological disorder in the graphite layer and the increase in the size of nanocrystalline graphite.[42] Therefore, the Raman spectroscopy characterization of the synthesized FGQDs was also carried out, as shown in Fig. 6. The Raman spectrum of FGQDs shows a D-band at 1363 cm^{-1} and a G band at 1582 cm^{-1} while the D band is absent in graphite (Fig. 6). The relative intensity of the "disorder" D band to the crystalline G-band (I_D/I_G) for the FGQDs is calculated as 0.86, which is comparable to other reports.[29] The high I_D/I_G indicates the decreased fraction of sp^2 domains with different degrees of GQD oxidation[43] as well as increased defect sites which arises during acid oxidation in FGQDs.

Although, these structural changes are present in the FGQDs synthesized in the current study, it is still debatable whether PL

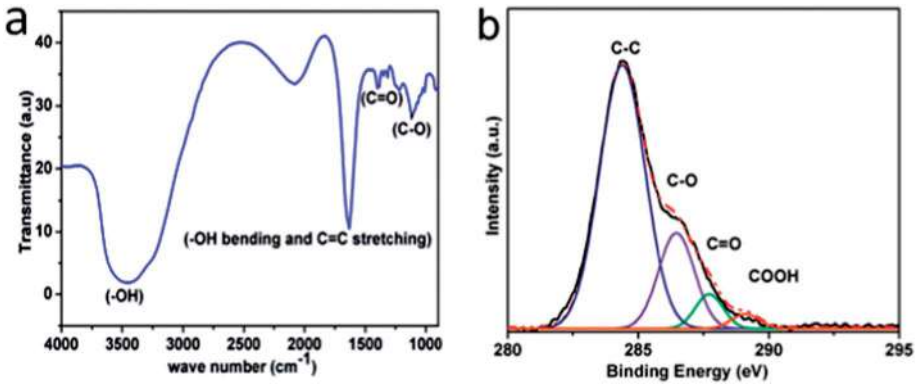

Fig. 5 (a) FTIR spectra of synthesized FGQDs, (b) the XPS C1s spectra of FGQDs.

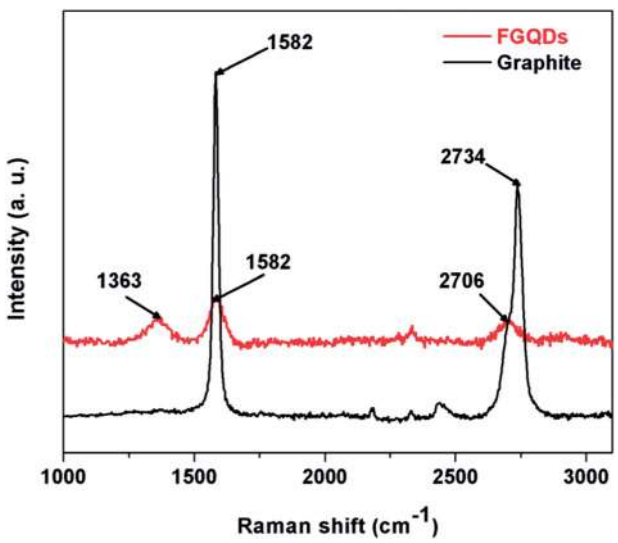

Fig. 6 Raman spectra of graphite and FGQDs.

is controlled by size effect and surface defects. It has been hypothesized that the presence of these oxygen-functional groups at the edges of FGQDs can possibly affect the PL behavior of FGQDs.[26,29] On the other hand, previous reports did not give any evidence that the population of the oxygen-functional groups relative to that of the C=C bond depends on the size of GQDs, suggesting that they have negligible effect on the size-dependent PL behavior of GQDs.[29,32] However, the presence of these groups makes the FGQDs soluble in water. This property of FGQDs is essential for making it a potential material for bioimaging.

Unlike organic dyes, the excellent photostability of GQDs imparts a better suitability to explore its further potential for bio-imaging. With this motivation, we have examined the imaging potential of FGQDs with human hepatic cancer cells (HuH-7 cells). Prior to imaging, the cytotoxicity of FGQDs was evaluated on HuH-7 cells by measuring mitochondrial dehydrogenase activity with 3-(4,5-dimethylthiazol-2-yl)-2,5-diphenyl tetrazolium bromide (MTT) assay followed by 24 h of incubation. As shown in Fig. 7, FGQDs at low concentrations (1–100 μg ml^{-1}) do not impose a considerable toxicity to HuH-7 cells compared to the control (untreated) groups.

On the basis of the toxicity evaluation, the bioimaging potential of green luminescent FGQDs was assessed through their treatment on HuH-7 cells. In this regard, the cells were cultured with FGQDs for 4 h and examined under a fluorescent microscope. The phase contrast image shows the presence of HuH-7 cells (Fig. 8a) and their corresponding nuclei, shown in blue color, are stained with DNA specific DAPI stain (Fig. 8b). The distribution of FGQDs in these HuH-7 cells was examined through their intrinsic stable green fluorescence (Fig. 8c). The merged image (Fig. 8d) clearly shows that the distribution of FGQDs is limited only in the cytoplasmic region of HuH-7 cells. This indicates that the synthesized FGQDs can be used as a fluorescent tag for bioimaging applications.

Unlike, routinely used organic dyes, FGQDs do not suffer with the problem of quenching and are highly stable under ambient conditions, which make them a strong candidate for bioimaging along with other biomedical applications.

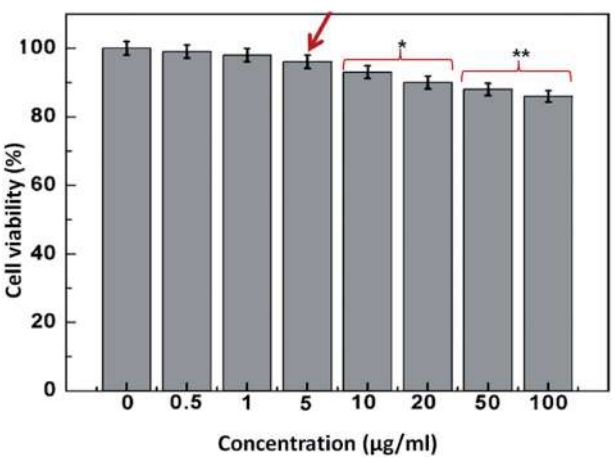

Fig. 7 Cell viability (MTT assay) of human hepatic cancer cells (Huh7 cells) incubated with different concentrations (0–100 μg ml^{-1}) of FGQDs after 24 h (**P < 0.01, *P < 0.05).

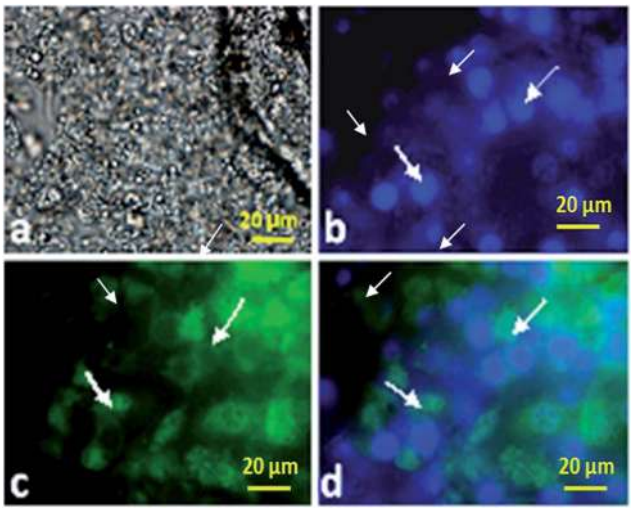

Fig. 8 Fluorescent images showing localization of FGQDs (green) in human hepatic cancer cells (Huh7 cells) following 4 h of treatment. (a) Phase contrast image of Huh7 cells, (b) DAPI stained nuclei (blue) of the corresponding cells shown in a, (c) localization of FGQDs (green) inside the cells, (d) merged image of DAPI and FGQDs in cells. Arrows show the cytoplasmic localization of FGQDs.

Conclusions

We have demonstrated a facile, rapid, cost effective and upscaled synthesis of green luminescent FGQDs directly from graphite powder. A pH dependent PL spectrum of FGQDs was measured to probe their photoluminescence properties and no drastic change in PL was observed. FGQDs have shown excellent biocompatibility and imaging potential when examined against human hepatic cancer cells (HuH-7 cells). Biocompatibility and photostability of synthesized FGQDs makes it most the suitable eco-friendly material for applications in bio-labeling and bioimaging.

Acknowledgements

This work was financially supported by UGC New Delhi, CAS Department of Zoology and Physics, BHU, Varanasi, India, NRF-South Africa. The authors also acknowledge Prof. S. C. Lakhotiya for fluorescence microscopy and Bio-Physics Lab., Department of Physics, BHU, for optical characterizations.

Notes and references

1 F. Bonaccorso, Z. Sun, T. Hasan and A. C. Ferrari, *Nat. Photonics*, 2010, **4**, 611–622.
2 S. Essig, C. W. Marquardt, A. Vijayaraghavan, M. Ganzhorn, S. Dehm, F. Hennrich, F. Ou, A. A. Green, C. Sciascia, F. Bonaccorso, K.-P. Bohnen, H. v Löhneysen, M. M. Kappes, P. M. Ajayan, M. C. Hersam, A. C. Ferrari and R. Krupke, *Nano Lett.*, 2010, **10**, 1589–1594.
3 D. Yu and L. Dai, *Appl. Phys. Lett.*, 2010, **96**, 143107–143109.
4 V. Parashar, K. Kumar, R. Prakash, S. K. Pandey and A. C. Pandey, *J. Mater. Chem.*, 2011, **21**, 6506–6509.
5 H. Li, X. He, Z. Kang, H. Huang, Y. Liu, J. Liu, S. Lian, C. H. A. Tsang, X. Yang and S.-T. Lee, *Angew. Chem., Int. Ed.*, 2010, **49**, 4430–4434.
6 X. Yan, B. Li, X. Cui, Q. Wei, K. Tajima and L. Li, *J. Phys. Chem. Lett.*, 2011, **2**, 1119–1124.
7 G. Eda, Y.-Y. Lin, C. Mattevi, H. Yamaguchi, H.-A. Chen, I.-S. Chen, C.-W. Chen and M. Chhowalla, *Adv. Mater.*, 2010, **22**, 505–509.
8 X. Yan, X. Cui and L.-S. Li, *J. Am. Chem. Soc.*, 2010, **132**, 5944–5945.
9 M. L. Mueller, X. Yan, B. Dragnea and L.-S. Li, *Nano Lett.*, 2011, **11**, 56–60.
10 M. L. Mueller, X. Yan, J. A. McGuire and L. Li, *Nano Lett.*, 2010, **10**, 2679–2682.
11 A. D. Güçlü, P. Potasz and P. Hawrylak, *Phys. Rev. B: Condens. Matter Mater. Phys.*, 2010, **82**, 155445–155449.
12 X. Sun, Z. Liu, K. Welsher, J. T. Robinson, A. Goodwin, S. Zaric and H. Dai, *Nano Res.*, 2008, **1**, 203–212.
13 S. Zhu, J. Zhang, C. Qiao, S. Tang, Y. Li, W. Yuan, B. Li, L. Tian, F. Liu, R. Hu, H. Gao, H. Wei, H. Zhang, H. Sun and B. Yang, *Chem. Commun.*, 2011, **47**, 6858–6860.
14 J. Zhao, G. Chen, L. Zhu and G. Li, *Electrochem. Commun.*, 2011, **13**, 31–33.
15 Y. Li, Y. Zhao, H. Cheng, Y. Hu, G. Shi, L. Dai and L. Qu, *J. Am. Chem. Soc.*, 2012, **134**, 15–18.
16 K. Gong, F. Du, Z. Xia, M. Durstock and L. Dai, *Science*, 2009, **323**, 760–764.
17 V. Gupta, N. Chaudhary, R. Srivastava, G. D. Sharma, R. Bhardwaj and S. Chand, *J. Am. Chem. Soc.*, 2011, **133**, 9960–9963.
18 X. Xu, R. Ray, Y. Gu, H. J. Ploehn, L. Gearheart, K. Raker and W. A. Scrivens, *J. Am. Chem. Soc.*, 2004, **126**, 12736–12737.
19 X. Wang, L. Cao, F. Lu, M. J. Meziani, H. Li, G. Qi, B. Zhou, B. A. Harruff, F. Kermarrec and Y.-P. Sun, *Chem. Commun.*, 2009, 3774–3776.
20 L. Cao, X. Wang, M. J. Meziani, F. Lu, H. Wang, P. G. Luo, Y. Lin, B. A. Harruff, L. M. Veca, D. Murray, S.-Y. Xie and Y.-P. Sun, *J. Am. Chem. Soc.*, 2007, **129**, 11318–11319.
21 J. Lu, J. Yang, J. Wang, A. Lim, S. Wang and K. P. Loh, *ACS Nano*, 2009, **3**, 2367–2375.
22 A. B. Bourlinos, A. Stassinopoulos, D. Anglos, R. Zboril, M. Karakassides and E. P. Giannelis, *Small*, 2008, **4**, 455–458.
23 R. Liu, D. Wu, S. Liu, K. Koynov, W. Knoll and Q. Li, *Angew. Chem.*, 2009, **121**, 4668–4671.
24 H. Zhu, X. Wang, Y. Li, Z. Wang, F. Yang and X. Yang, *Chem. Commun.*, 2009, 5118–5120.
25 L. A. Ponomarenko, F. Schedin, M. I. Katsnelson, R. Yang, E. W. Hill, K. S. Novoselov and A. K. Geim, *Science*, 2008, **320**, 356–358.
26 D. Pan, J. Zhang, Z. Li and M. Wu, *Adv. Mater.*, 2010, **22**, 734–738.
27 Q. Feng, Q. Cao, M. Li, F. Liu, N. Tang and Y. Du, *Appl. Phys. Lett.*, 2013, **102**, 013111–013114.
28 M. Li, W. Wu, W. Ren, H.-M. Cheng, N. Tang, W. Zhong and Y. Du, *Appl. Phys. Lett.*, 2012, **101**, 103107–103109.
29 J. Peng, W. Gao, B. K. Gupta, Z. Liu, R. Romero-Aburto, L. Ge, L. Song, L. B. Alemany, X. Zhan, G. Gao, S. A. Vithayathil,

B. A. Kaipparettu, A. A. Marti, T. Hayashi, J.-J. Zhu and P. M. Ajayan, *Nano Lett.*, 2012, **12**, 844–849.
30 Y. Sun, S. Wang, C. Li, P. Luo, L. Tao, Y. Wei and G. Shi, *Phys. Chem. Chem. Phys.*, 2013, **15**, 9907–9913.
31 H. A. Becerril, J. Mao, Z. Liu, R. M. Stoltenberg, Z. Bao and Y. Chen, *ACS Nano*, 2008, **2**, 463–470.
32 S. Kim, S. W. Hwang, M.-K. Kim, D. Y. Shin, D. H. Shin, C. O. Kim, S. B. Yang, J. H. Park, E. Hwang, S.-H. Choi, G. Ko, S. Sim, C. Sone, H. J. Choi, S. Bae and B. H. Hong, *ACS Nano*, 2012, **6**, 8203–8208.
33 L. Li, G. Wu, G. Yang, J. Peng, J. Zhao and J. Zhu, *Nanoscale*, 2013, **5**, 4015–4039.
34 Y. Dong, C. Chen, X. Zheng, L. Gao, Z. Cui, H. Yang, C. Guo, Y. Chi and C. M. Li, *J. Mater. Chem.*, 2012, **22**, 8764–8766.
35 Z. Xie, F. Wang and C. Y. Liu, *Adv. Mater.*, 2012, **24**, 1716.
36 S. Sahu, B. Behera, T. K. Maiti and S. Mohapatra, *Chem. Commun.*, 2012, **48**, 8835.
37 Q. Wang, H. Zheng, Y. Long, L. Zhang, M. Gao and W. Bai, *Carbon*, 2011, **49**, 3134.
38 R. Shen, K. Song, H. Liu, Y. Li and H. Liu, *Chem Phys Chem*, 2012, **13**, 3549.
39 Y.-W. Son, M. L. Cohen and S. G. Louie, *Nature*, 2006, **444**, 347–349.
40 X. Sun, D. Luo, J. Liu and D. G. Evans, *ACS Nano*, 2010, **4**, 3381–3389.
41 L. M. Malard, M. A. Pimenta, G. Dresselhaus and M. S. Dresselhaus, *Phys. Rep.*, 2009, **473**, 51.
42 Z. Lin, Y. Yao, Z. Li, Y. Liu, Z. Li and C.-P. Wong, *J. Phys. Chem. C*, 2010, **114**, 14819.
43 J. I. Paredes, S. Villar-Rodil, P. Solıs-Fernandez, A. Martınez-Alonso and J. M. D. Tascon, *Langmuir*, 2009, **25**, 5957.

Analytical Methods

PAPER

View Article Online
View Journal | View Issue

Cite this: *Anal. Methods*, 2015, **7**, 3993

Functional graphene–gold nanoparticle hybrid system for enhanced electrochemical biosensing of free cholesterol†

Shiju Abraham,[a] Narsingh R. Nirala,[b] Shobhit Pandey,[c] Monika Srivastava,[d] Sunil Srivastava,[e] Bernd Walkenfort[f] and Anchal Srivastava*[a]

Received 8th January 2015
Accepted 31st March 2015

DOI: 10.1039/c5ay00050e

www.rsc.org/methods

Realizing the unavailability of fast and reliable diagnostic techniques, especially for cholesterol measurement, the present work reports the development of cost effective bioelectrodes based on a reduced graphene oxide–functionalized gold nanoparticle (~25 nm) hybrid system (RGO–Fn Au NPs). The electrodes fabricated by the electrophoretic deposition technique attest a synergistically enhanced electrochemical sensing ability of 193.4 μA mM^{-1} cm^{-2} for free cholesterol detection, which is much higher than that of the traditional RGO system. The electrochemical impedance studies (EIS) show low charge transfer resistance, R_{CT}, for the hybrid system which is 57% and 60% lower than those of RGO and Au NPs respectively. Also higher loading capacity and enhanced kinetics have been realized for the hybrid system, owing to lower K_m value (0.005 mM) and enhanced rate constant (3.8×10^{-4} cm s^{-1}) in comparison with RGO and Au NPs. Moreover, the RGO–Fn Au NP platform promises a wider range of cholesterol detection (0.65–12.93 mM), while simultaneously being capable of detecting as low as 0.34 mM of free cholesterol. Apart from better sensitivity, loading capacity, kinetics and detection range, the system also has appreciable selectivity and stability. This supports its potential to be brought on field in the near future for cost effective and reliable detection from the complex system of human serum.

Introduction

Hypercholesterolemia, which is a repercussion of the present generation eating habits, occurs when the cholesterol level in the body rises above the safe level of 200 mg dL^{-1} (5.17 mM).[1] Failing to efficiently diagnose the increased level of cholesterol in the human blood plasma results in fatal issues such as cardiovascular diseases, coronary artery diseases, transient ischemic heart attacks and atherosclerosis.[2,3] This demands a better and efficient system which can work selectively in the complex system of blood, being affordable at the same time. The traditional chemical approaches for the analysis of cholesterol such as colorimetry, fluorimetry, gas chromatography/mass spectrometry and spectrophotometry suffer from common drawbacks such as low selectivity and specificity due to masking of the main chemical reaction with the interfering side reactions. This is further aggravated by the involvement of unstable and corrosive reagents.[4] In contrast, electrochemical-enzymatic biosensing procedures, unlike chemical methods, show good specificity and selectivity for determination of free cholesterol and other analytes in biological samples.[2,5]

It is important for a bioelectrode system to have better physico-chemical, catalytic and surface properties in order to ensure high loading of the analytes, enhanced electron transfer rate and several fold increase in the signal to noise ratio. Fulfilling these requirements, nanostructure based electrochemical biosensors were the first to have received wide attention in the last decade with the added advantage of portability and inexpensiveness.[6,7] Among the prominent candidates, gold nanoparticles (Au NPs), which have been extensively used in diverse biological applications owing to their appreciable biocompatibility, are the most promising ones.[8] These noble nanoparticles have unique properties such as the plasmonic properties, large surface area for larger loading of reactive molecules per particle and low cytotoxicity, which is why they have been applied in diagnostics and therapeutic work like labelling, delivery, sensing, and photothermal therapy.[9–11]

Above stated requirements for an efficient biosensor soon paved the way for the graphene family as yet another promising biosensing system owing to its ultra-high surface area and peculiar electronic properties.[12,13] Among the successful

[a]*Department of Physics, Banaras Hindu University, Varanasi, 221005, India. E-mail: anchalbhu@gmail.com; Fax: +91-542 2368174; Tel: +91-9453203122*

[b]*Department of Zoology, Banaras Hindu University, Varanasi, 221005, India*

[c]*Metallurgical Engineering Department, Indian Institute of Technology – (BHU), Varanasi, 221005, India*

[d]*School of Materials Science and Technology, IIT (B.H.U.), Varanasi, 221005, India*

[e]*Department of Pure and Applied Physics, Guru Ghasidas University, Main Campus, Koni, Bilaspur 495009, India*

[f]*Faculty of Chemistry, University of Duisburg, Essen, Germany*

† Electronic supplementary information (ESI) available. See DOI: 10.1039/c5ay00050e

candidates in the graphene family, reduced graphene oxide (RGO) based systems have shown appreciable potential for the detection and monitoring of different biomolecules.[14,15] This is due to their enhanced electrochemical activities, bulk production ability, enlarged conductivity, and high 2-D surface area along with sufficient functional groups. Although RGO, with restored conductivity, can perform comparatively well alone, highly improved electrochemical activities and enhanced sensitivity are reported when it is used as a matrix to combine with metal and metal oxide nanoparticles to form efficient hybrid systems. This diversifies and improves its applicability as required for current needs.[16–18] Particularly, the importance of combining RGO with Au NPs is prototypical providing better properties which have been utilized for biosensing recently, for *e.g.* in the detection of dopamine[19] and glucose sensing.[20]

Hence acknowledging the potential of fabricating a metal nanoparticle–RGO hybrid system, the present work proposes an efficient reduced graphene oxide–functionalized gold nanoparticle (RGO–Fn Au NPs) composite system for efficient free cholesterol sensing. For a comparative study the present work fabricates thin films of both RGO and RGO–Fn Au NP hybrid system separately on indium tin oxide (ITO) coated glass substrates. Additionally, the electrophoretic deposition technique (EPD) used for these electrodes' fabrication is both cost effective and shows bulk production potential. This can be understood from the estimated cost being as low as ~0.2$ for a single bioelectrode produced in our work. Typically, when immobilized by cholesterol oxidase (ChOx) for cholesterol detection *via* the cyclic voltammetry (CV) technique, a RGO–Fn Au NP based electrode shows enhanced electrochemical sensitivity in comparison to RGO. Finally this ecological system's potential to be applied on field is attested by its good biocompatibility, non-toxic nature and particularly high stability as expected from the chemically stable combination of RGO and Fn Au NPs in their composite form.[21–23] With these advantages, the system proves itself as a promising biosensing system which can be brought on field in the near future.

Experimental section

Materials

Graphite flakes (NGS Naturgraphit GmbH, Germany), tetrachloroauric acid ($HAuCl_4$), H_2SO_4, H_3PO_4, $KMnO_4$, H_2O_2, hydrazine hydrate, ammonia solution, ethanol, *etc.* used were of technical grade. All the chemicals employed for the fabrication of a cholesterol biosensor, namely, cholesterol oxidase (ChOx), cholesterol, *etc.* were procured from Sigma-Aldrich.

Preparation of graphene oxide (GO), reduced graphene oxide (RGO), gold nanoparticles (Au NPs) and their functionalization

GO has been synthesized by the method proposed by Marcano *et al.*[7,24] {see the ESI†}. RGO has been prepared by following the chemical method proposed by Dan Li *et al.*[25] Further gold nanoparticles were prepared by the trisodium citrate reduction of a gold precursor.[26] For the functionalization, 10 mL of Au NPs after centrifugation were re-suspended in 10 mL of DW as the first step. This Au NP solution was then treated with 1 mL of MUDA ($C_{11}H_{22}O_2S$, 20 mM) in ethanol and subsequently 5 mL of DW was added to it. This combination was sonicated at 50 °C for an hour and kept undisturbed for one day to obtain Fn Au NPs.

Fabrication of RGO–Fn Au NP thin film electrodes

First, the RGO–Fn Au NP hybrid system was prepared using a combination of sonication and stirring at specific temperatures {see the ESI†}. Thin films of nanostructured RGO as well as RGO–Fn Au NPs (2 mg dL^{-1} in acetonitrile) were then fabricated over ITO electrodes *via* the EPD technique. Typically, a pre-cleaned ITO-coated glass substrate having a sheet resistance of 30 Ω cm^{-1} was used as the working electrode and a platinum foil (1 cm × 2 cm) was used as the counter electrode. Keeping these electrodes parallel to each other in the desired RGO and RGO–Fn Au NP colloidal suspension, thin films of RGO and RGO–Fn Au NPs were deposited on the ITO-coated glass plates respectively. These thin film coated electrodes were then removed from the suspension, washed with deionized water and dried.

Solution preparation and immobilization

A stock solution of 500 mg dL^{-1} (12.93 mM) of cholesterol was prepared by dissolving cholesterol in a flask containing Triton X-100 placed in a heat bath of 60 °C. This stock solution was further diluted with a 0.02 M PB solution (pH 7.0) for preparing different cholesterol concentrations (25 mg dL^{-1} to 500 mg dL^{-1}). RGO as well as RGO–Fn Au NP electrodes' COOH groups were activated using the EDC–NHS coupling chemistry. For the immobilization of ChOx onto RGO/ITO and RGO–Fn Au NPs/ITO, 5 μl of ChOx (cholesterol oxidase (EC1.1.3.6 ≥ 50 U mg^{-1})) was used to cast films over the electrodes. These bioelectrodes were allowed to dry at 4 °C in a refrigerator. These activated electrodes were then washed thoroughly using a PB solution (pH ~ 7) and stored at 4 °C in a dry state until use. The MUDA molecules in the Au NPs possess acid groups on their edges providing extra binding points to the enzyme.

Characterization of the materials

The structural characterization of RGO and RGO–Fn Au NPs was done by the X-ray diffraction (XRD) technique (D8 ADVANCE, Bruker). The wavelength of Cu-Kα1 radiation of $\lambda = 1.5405$ Å was used for obtaining the XRD pattern. The morphological changes were investigated employing a scanning electron microscope [FE-SEM (Zeiss, Merlin)] instrument operated at an accelerating voltage of 20 V to 30 kV. The transmission electron microscope (TEM) images were obtained using a Zeiss EM 902 instrument. The UV-Vis absorption measurements were carried out with a Cary 5000 UV-Vis absorption spectrometer from Varian employing the double beam mode. Fourier transform infrared (FT-IR) spectroscopy (Perkin Elmer Spectrum 65, FT-IR spectrometer) was employed for the identification of molecular structures. The Raman measurements were performed on a micro-Raman setup (HR LabRam inverse system, Jobin Yvon

Horiba) using the 532 nm line from a frequency doubled Nd:YAG laser (Coherent Compass). Electrochemical studies (cyclic voltammetry) related to cholesterol detection were carried out on an Autolab potentiostat/galvanostat. Electrochemical impedance spectroscopy (EIS) for the electrodes was measured within the frequency range of 100 kHz to 1 Hz with a 5 mV amplitude using an applied potential of 0.2 V.

Results and discussion

Structural and spectroscopic studies

An X-ray diffraction (XRD) pattern was used to fingerprint the RGO–Fn Au NPs (see ESI, Fig. S3†). The XRD pattern of RGO exhibits an intense peak around 24.5°, which corresponds to the (002) plane, and, a weak peak around 10° due to the contribution from unreduced graphene oxide.[27] This d_{002} value along with the broadness of the reflection supports the restacking of graphene sheets due to the loss of oxygen-containing functional groups during the reduction process. Using Bragg's law, the value of the *d*-spacing is calculated as 0.35 nm, for the diffraction peak at 24.5°. The other four peaks of 2θ at 38°, 44°, 64° and 78° correspond to the Au NPs' reflections at (111), (200), (220) and (311) respectively.[28]

Fig. 1 shows the SEM micrographs of the RGO, Au NPs and RGO–Fn Au NPs. Fig. 1(a) represents the RGO nanosheets with their typical wrinkles and foldings. Furthermore the two dimensionality of RGO extending to several micrometers without losing uniformity can be observed. Fig. 1(b) indicates Au NPs having a particle size of ~25 nm, which sit on the Si/SiO_2 substrate with appreciable uniformity. As expected due to less adhesion of Au NPs with the Si/SiO_2 substrate, the particle density on the substrate is less. Sensitive backscattered electron (BSE) detectors are used to visualize a rich qualitative compositional contrast and internal structure information with similar resolution to that of secondary electron (SE) detectors.

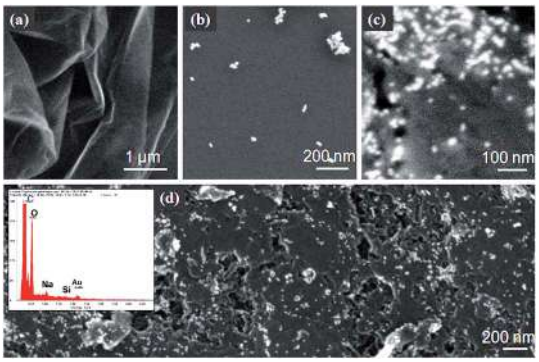

Fig. 1 Scanning electron microscopic (SEM) images of: (a) RGO nanosheets with folding and micrometers of uniformity in lateral dimensions; (b) Au NPs with an average size distribution of ~25 nm; (c) back scattered image of RGO–Fn Au NPs which shows clear contrast of Au NPs with respect to RGO sheets; and (d) RGO–Fn Au NP composite system with long range uniformity showing a nice distribution of Au NPs over as well as on the folding and defects of RGO. The inset shows the EDX of the RGO–Fn Au NP composite system showing the elemental combination of carbon, oxygen as well as Au.

Fig. 1(c) shows the BSE micrograph of RGO–Fn Au NPs. Here the Au NPs are strikingly identified owing to their enhanced contrast with respect to the fade RGO background. Fig. 1(d) shows the micrograph of a RGO–Fn Au NP hybrid system for a relatively longer region. The image illustrates the uniform distribution of the Au NPs which were adsorbed nicely on the surface of RGO. Again in contrast to the Au NP density on the Si/SiO_2 substrate, that on RGO is quite high owing to good adhesion properties between RGO and Au NPs. An EDX diagram can be seen in the inset figure confirming the elemental analysis of the RGO–Fn Au NP system. As expected mainly carbon, oxygen and gold were present in the composite system supporting the purity of the formed composite. The presence of sodium content in the spectrum is due to the unreacted reducing agent, trisodium citrate used for Au NP synthesis and also may be from the quality of acids used for the synthesis of graphene oxide.

TEM results of RGO, Au NPs and RGO–Fn Au NPs are depicted in Fig. 2. Few layered RGO nanosheets of long homogeneity with several nanometer-long wrinkles are visible in Fig. 2(a). Fig. 2(b) shows the TEM micrograph of Au NPs of ~25 nm in a more distinguishable manner, showing their almost spherical and oval shape. Fig. 2(c) indicates the RGO–Fn Au NP system in which Au NPs are well decorated on the RGO surfaces with some of them encapsulated by the RGO sheet.

Raman spectroscopy is a well-known, non-destructive technique to distinguish between sp^2 and sp^3 hybridization in carbonaceous materials as well as to identify the number of layers present in graphene.[29–32] The two main characteristic Raman bands present in almost all carbon-based materials are the G-band and D-band. Fig. 3 represents the optical micrograph and Raman mapping of RGO–Fn Au NPs taken in an area of 140 × 140 μm to get precise information about the chemical homogeneity on a larger scale. As the Au NPs do not show any significant signature in the composite system, the mapping shows information regarding the intensity distribution of different bands observed in RGO. Fig. 3(a) shows the optical micrograph of the RGO–Fn Au NP sheets on a glass substrate. Fig. 3(b) shows the Raman spectrum of the sample. Here, an intense G-band and prominent D as well as 2D bands can be observed. It is clearly visible that the intensity ratio of I_{2D}/I_G is less than 1 (~0.4), which is an indication of the system's decreased disorderness and better reduction while forming the composite. This also suggests that definitely a single layer reduced graphene oxide is not formed in the electrode; however, the full width at half maximum (FWHM) for the 2D band attests that the number of layers is restricted to ~5 or even less. The calculated FWHM at 2704 cm^{-1} is ~68 cm^{-1}, and according to the report of Hao *et al.*,[33] FWHM broadens with increasing number of layers, reaching a value of 66.1 ± 1.4 cm^{-1} for five layers of graphene, which almost matches with the calculated FWHM in our case. Alternatively, this broadening of FWHM (in comparison to ~27.5 ± 3.8 cm^{-1} FWHM for a single layer) could also be attributed to the presence of non-uniform number of layers which affects the double resonance process leading to such levels of broadening even when a combination of bi-layer and few layers is present. Fig. 3(c) shows the D-band region (1300–1380 cm^{-1}). While some areas in the mapping show the

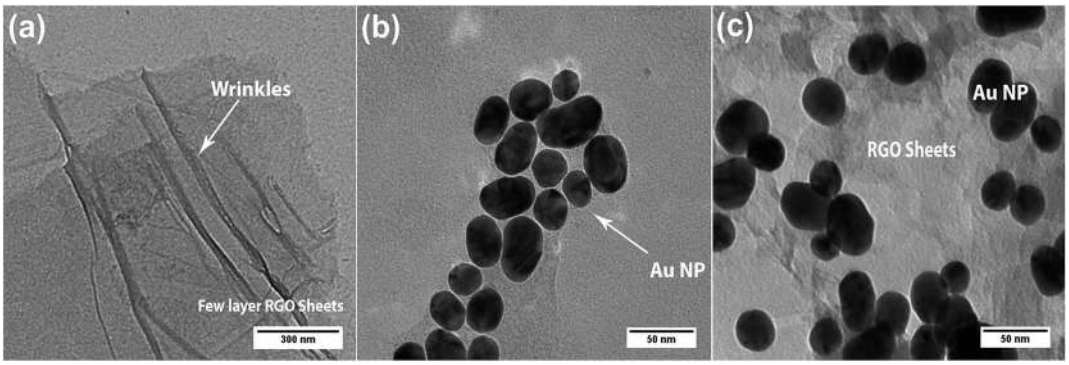

Fig. 2 Transmission electron microscopic (TEM) images of: (a) RGO nanosheets of few layers with wrinkles and folding; (b) Au NPs with an average size of ~25 nm; the shape of the particles are spherical and oval in nature. (c) RGO–Fn Au NP hybrid system with Fn Au NPs nicely attached to the surfaces and foldings of few layered RGO nanosheets.

presence of dense intensity distribution, the other areas have homogeneous distribution of disorderness. The dense areas indicate the oxidized regions of GO and the disorder induced through the presence of functionalized gold nanoparticles. Fig. 3(d) shows the G-band region (1550–1610 cm^{-1}). The corresponding intensity distribution map is in accordance with the optical image, indicating the system's purity. Fig. 3(e) indicates the 2D-band region (2650–2750 cm^{-1}), which is well pronounced, confirming RGO's few layered nature as attested by the considerable intensity of the 2D band to give the ratio I_{2D}/I_G an appreciable value (~0.4).[29]

Electrochemical characterization and cholesterol sensing

Amperometric biosensors work by the production and monitoring of current on the application of potential between two electrodes. In mediated biosensors enzymes donate electrons to mediators or electrochemically active artificial electron acceptors, which are effective in reducing the electrochemical interferences. The process requires the cycle of enzyme–substrate redox reaction followed by re-oxidization by the mediator. The electrodes measure the concentration of O_2 or the product H_2O_2 in the enzymatic reaction.

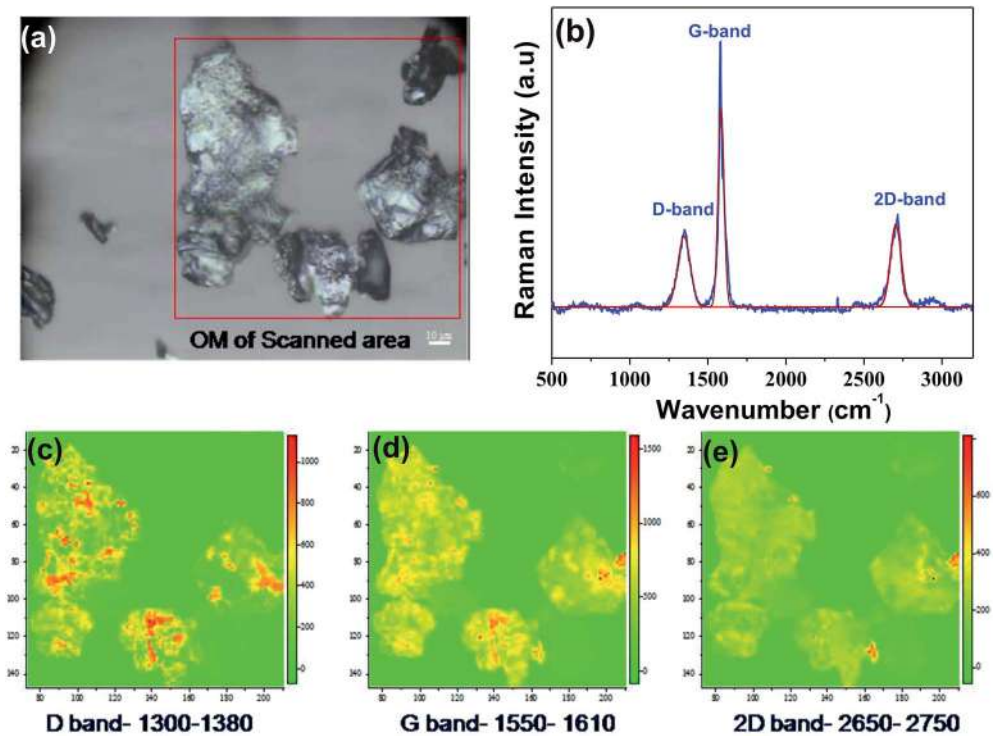

Fig. 3 Raman mapping of RGO–Fn Au NPs taken at a scanning area of 140 × 140 μm using an excitation source of 532.5 nm: (a) optical micrograph of the scanned area; (b) Raman spectra of RGO–Fn Au NPs; Raman intensity mapping for the (c) D-band region (1300–1380 cm^{-1}), (d) G-band region (1550–1610 cm^{-1}) and (e) 2D-band region (2650–2750 cm^{-1}).

The schematic representation of the electrochemical sensing set up used for cholesterol sensing is shown in Fig. 4. In this schematic, part (a) shows the EPD set up used for the fabrication of both RGO as well as RGO–Fn Au NP electrodes. One of the produced electrodes, *i.e.*, RGO–Fn Au NP thin film electrode on an ITO coated glass substrate, is shown in part (b), displaying the presence of functional groups. Part (c) shows the ChOx enzyme immobilization on RGO–Fn Au NPs through EDC–NHS coupling reaction. The resulting ChOx immobilised bioelectrode and the electrochemical reactions are illustrated in part (d). A known concentration of cholesterol is added to the electrochemical cell containing three electrodes. The cell comprises of RGO/ChOx/ITO or RGO–Fn Au NP/ChOx/ITO bioelectrodes as the working electrode, platinum foil as the counter electrode and Ag/AgCl as a reference electrode in 50 mM phosphate buffer saline (PBS) of pH 7.0 containing 5 mM of $[Fe(CN)_6]^{3-/4-}$. The current produced from the electrochemical reaction is interfaced through a potentiostat/galvanostat and finally the signals are interfaced to the computer.

The cyclic voltammogram (CV) studies of ITO, RGO/ITO, RGO–Au NP/ITO, RGO/ChOx/ITO and RGO–Au NP/ChOx/ITO electrodes, in PBS (pH $\sim$ 7) containing 5 mM $[Fe(CN)_6]^{3-/4-}$ are shown in Fig. 5(A). The oxidation peak current of 0.53 mA corresponding to the bare ITO based electrode is observed. However, the current increases to 0.77 mA in the case of a RGO/ITO electrode owing to its good electrical conductivity as well as the ability to function as a good platform for electron transfer. A RGO–Fn Au NP/ITO system shows much enhanced current (0.92 mA) than RGO/ITO due to the synergistically enhanced electrocatalytic activity on combining Au NPs with RGO. After the ChOx immobilization with RGO/ITO, the response current gets reduced to 0.59 mA and in the case of ChOx/RGO–Fn Au NPs/ITO, it comes down to 0.65 mA.

Here in these bioelectrodes, the redox active sites are deeply embedded in the ChOx bienzyme macromolecular structure. The insulating characteristics of these enzymes explain the above-mentioned reduction in current when compared to their non-immobilized counterpart. However, the dominant behavior of the composite system persists. Furthermore due to reduced conductivity of these bioelectrodes, the oxidation peak potential shifts towards a higher positive value as compared with that of the non-immobilised electrodes.

The electrochemical impedance is observed when current flows through a circuit consisting of resistors and capacitors or inductors. The equivalent circuit which can be used to measure the electrochemical impedance, *i.e.* the Randles circuit [inset Fig. 5(B)], is composed of solution resistance R_S, charge transfer resistance R_{CT} and double-layer capacitance C_{dl} or constant phase element (CPE).[34] The Nyquist plot used to find the R_{CT} for all electrodes is shown in Fig. 5(B). The semicircle diameter, which indicates the magnitude of the R_{CT}, is associated with the dielectric and insulating characteristics across the electrode/electrolyte interface. The RGO electrode shows an R_{CT} value of 350 Ω, whereas, Au NPs show 383 Ω as the R_{CT} value. However, in the case of the hybrid system, *i.e.* RGO–Fn Au NPs, the R_{CT} value is as low as 151 Ω as denoted by the smallest semi-circle. This supports the fast charge transfer kinetics of RGO–Fn Au NPs as compared to RGO as well as Au NPs, following higher separation efficiency of electrons and holes. Furthermore, as expected, the R_{CT} value of this composite system increases to 399 Ω after immobilization with ChOx owing to lower conductivity of ChOx. Evidently, the increase in the R_{CT} value indirectly supports the binding of ChOx onto RGO–Fn Au NPs.

Fig. 5(C) further supports RGO–Fn Au NPs' dominance over RGO for faster electron transfer owing to their much higher diffusion coefficient (D)[35] and standard heterogeneous rate

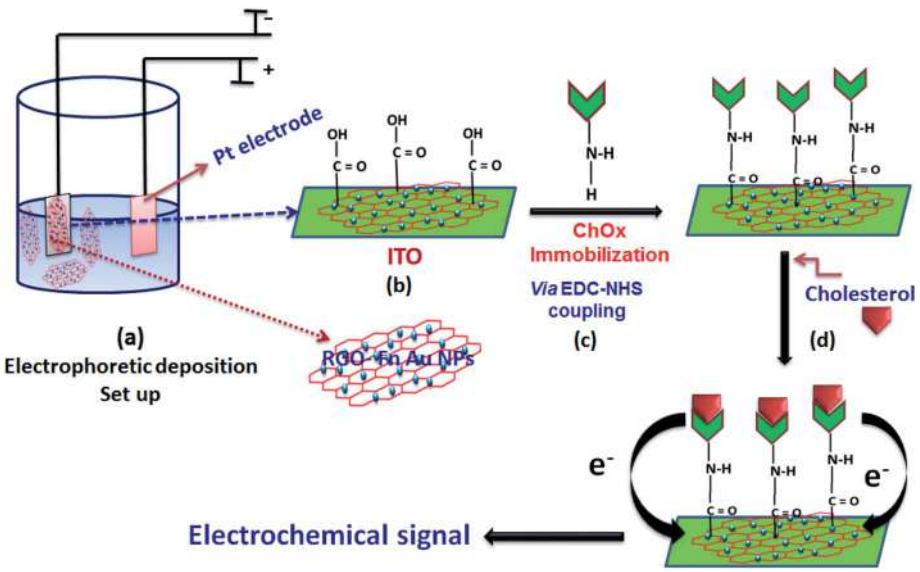

Fig. 4 Schematic representation of the cholesterol sensing process: EPD set up for the fabrication of RGO and RGO–Fn Au NP thin films; (b) electrophoretically fabricated RGO–Fn Au NP thin film on an ITO substrate; (c) immobilization of ChOx on RGO–Fn Au NPs by EDC–NHS coupling; and (d) the immobilized RGO–Fn Au NP bioelectrode and the electrochemical reaction while adding cholesterol to the electrochemical cell containing the bioelectrode.

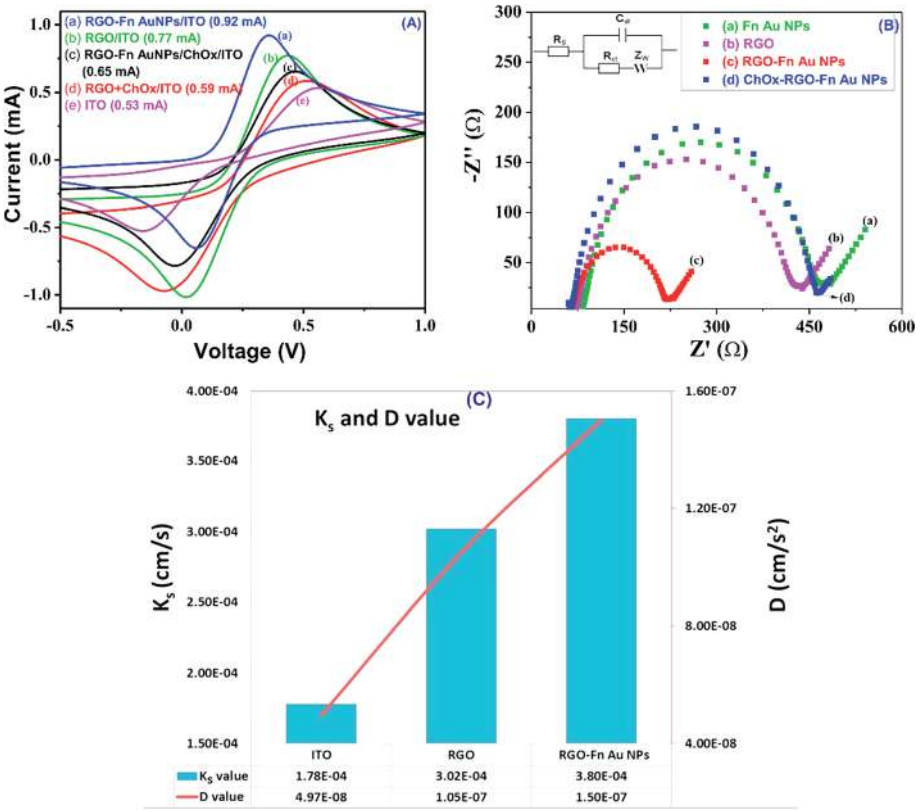

Fig. 5 (A) CV response of (a) RGO–Fn Au NP/ITO; (b) RGO/ITO; (c) RGO–Fn Au NPs/ChOx/ITO; (d) RGO/ChOx/ITO; and (e) ITO electrodes. (B) Nyquist plot of RGO, Au NP, RGO–Fn Au NP and RGO–Fn Au NP/Ch-Ox electrodes in PBS (pH = 7) containing 5 mM $[Fe(CN)_6]^{3-/4-}$. (C) Bar plot of parameters K_s and D for ITO, RGO and RGO–Fn Au NP electrodes.

constant (K_s) calculated using the Klingler and Kochi[36] equation, *i.e.* eqn (1).

$$K_s = 2.18\sqrt{\left(\frac{D\alpha nFv}{RT}\right)}\exp\left[-\frac{\alpha^2 nF}{RT}\left(E_p^a - E_p^c\right)\right] \quad (1)$$

$$i_p = \text{Constant } nFAC\sqrt{\left(\frac{nFvD}{RT}\right)} \quad (2)$$

In above equations, R is universal gas constant, F is Faraday constant in C mol^{-1}, α is transfer coefficient (for ITO: $\alpha = 0.165$, RGO/ITO: $\alpha = 0.215$ and RGO–Fn Au NPs/ITO: $\alpha = 0.268$), E_p is oxidation peak potential, ν is scan rate and T is the temperature in Kelvin. In the present study, the D value was determined using the Randles–Sevcik equation. Here the RGO–Fn Au NPs show a higher D value of 1.5×10^{-7} cm^2 s^{-1} and K_s value of 3.8×10^{-4} cm s^{-1} whereas bare ITO shows the least D and K_s values, 4.97×10^{-8} cm^2 s^{-1} and 1.7×10^{-4} cm s^{-1} respectively. Consistently, the RGO electrode showed intermediate D and K_s values of 1.05×10^{-7} cm^2 s^{-1} and 3.02×10^{-4} cm s^{-1} respectively. These enhanced D and K_s values for RGO–Fn Au NPs are aroused due to the synergistic effect of conductive 2-dimensional RGO sheets in combination with the good catalytic effect of Au NPs. These calculations further attest the selection of such a hybrid system as a much suitable electrode material for the fabrication of a highly sensitive and selective cholesterol biosensor.

Electrochemical response studies of RGO/ChOx/ITO and ChOx/RGO–Fn Au NPs/ITO have been summarized in Fig. 6. The measurements were carried out as a function of cholesterol concentration using cyclic voltammetry in a PBS solution {50 mM PBS (pH 7, 0.9% NaCl) containing 5 mM $[Fe(CN)_6]^{3-/4-}$}. The observations show an increase in the magnitude of current for the bioelectrodes as the concentration of cholesterol was increased (from 25 mg dL^{-1} to 500 mg dL^{-1}) in cases of both ChOx/RGO/ITO and ChOx/RGO–Fn Au NP/ITO bioelectrodes. Fig. 6(a) shows the CV response voltage *vs.* current plot of ChOx/RGO/ITO and the curves from 'a' to 'h' indicate different concentrations of cholesterol from 25 to 500 mg dL^{-1} which include the following concentrations: 25, 50, 100, 150, 200, 300, 400 and 500 mg dL^{-1}. In Fig. 6(b) fitting of the calibration plot relating the anodic peak current and cholesterol concentrations for RGO/ITO shows a distinct linear region within the concentration range of 50–500 mg dL^{-1}. Using this several electrochemical sensing parameters can be calculated. The detection range for the RGO/ITO bioelectrode comes out to be 25–500 mg dL^{-1} (0.65–12.93 mM) with a detection limit of 10 mg dL^{-1} (0.26 mM), low enough to measure the cholesterol level in human serum. The criterion used for the calculation of the detection limit is $3\sigma/m$, where 'm' is the slope and 'σ' is standard deviation (SD) of the calibration graph. Furthermore, the sensitivity of the RGO/ITO bioelectrode is found to be 116 μA mM^{-1} dL^{-1} which itself is better than several earlier reports (see Table 1). In

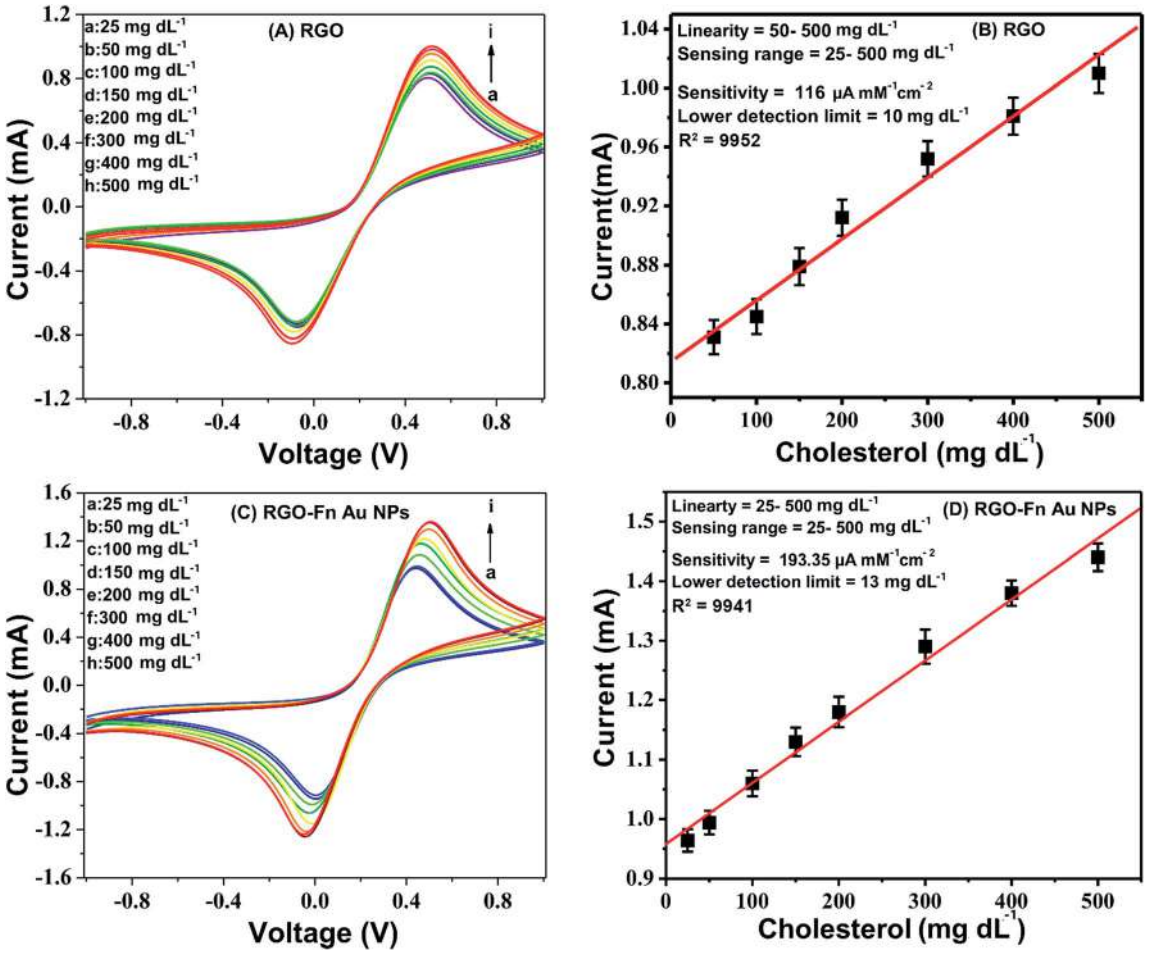

Fig. 6 Electrochemical response studies using CV of (A) the ChOx/RGO/ITO bioelectrode as a function of cholesterol concentrations (25–500 mg dL^{-1}); (B) fitted calibration plot between anodic peak current and cholesterol concentrations for RGO (50–500 mg dL^{-1}); (C) electrochemical response studies of the ChOx/RGO–Fn Au NP/ITO bioelectrode as a function of cholesterol concentrations (25–500 mg dL^{-1}); and (D) fitted calibration plot for RGO–Fn Au NPs (25–500 mg dL^{-1}).

addition, the accuracy of curve fitting can be acknowledged by the regression coefficient (R^2) value of 0.9952. Fig. 6(c) shows the CV response of RGO–Au NPs/ChOx/ITO for the cholesterol concentrations of 25 to 500 mg dL^{-1} denoted by the curves 'a' to 'h'. Clearly the magnitude of the current difference in ChOx/RGO–Fn Au NPs/ITO is higher than that of the ChOx/RGO/ITO system. The fitted calibration plot for ChOx/RGO–Fn Au NPs/ITO shows its linear behavior from 25 to 500 mg dL^{-1} as shown in Fig. 6(d). The linear range in this case is better than that of ChOx/RGO/ITO and so are the sensing parameters. The ChOx/RGO–Fn Au NP/ITO system shows a lower detection limit of 13 mg dL^{-1} (0.33 mM) fitted perfectly with an 'R^2' value of 0.9941. Additionally, an enhanced sensitivity of 193.35 μA mM^{-1} dL^{-1} is observed in this case which supersedes that of a bare RGO/ITO bioelectrode. This improvement is credited to the synergistic presence of the Au NPs along with the RGO matrix in improving the electrochemical properties.

Additionally, ferri/ferrocyanide was used as an inorganic mediator to work as an artificial electron transferring agent. This mediator can readily participate in the redox reaction with the biological molecule and boost the electron transfer. The specialty of these mediators lies in their ability to regenerate close to the electrode surface *via* electrochemical reaction thereby enabling the electrochemical reaction to take place at the characteristic potential of the mediator. Even in the presence of only a small amount of biological molecules, the current enhances significantly signifying a rapid chemical reaction. Hence clearly, as the fundamental premise, in this cholesterol sensing process, the observed current is related to the concentration of the biomolecules present (here cholesterol). The enzymatic reaction is as follows:

$$\text{Cholesterol} + 2\left[\text{Fe(CN)}_6\right]^{3-} + \text{H}_2\text{O} \xrightarrow{\text{ChOx}} \text{Cholestenone} + 2\text{H}^+ + 2\left[\text{Fe(CN)}_6\right]^{4-} \quad (3)$$

$$\left[\text{Fe(CN)}_6\right]^{4-} \xrightarrow{\text{ChOx–RGO–Fn Au NPs/ITO}} \left[\text{Fe(CN)}_6\right]^{3-} + \text{e}^{-1} \quad (4)$$

During the above biochemical reaction (shown in eqn (3) and (4)), ChOx catalyzes in the presence of oxygen and cholesterol gets oxidized to cholestenone and H_2O_2. The O_2 in this reaction

Table 1 Comparison table of sensing performance of different electrochemical biosensors for the determination of cholesterol[a]

System no.	Electrode material	Determination method	Detection range (mM)	Detection limit (mM)	Sensitivity ($\mu A\ mM^{-1}$)	K_m value (mM)	Stability (days)	Ref.
Present work	Ch-Ox/RGO–Fn Au NPs	Amperometric	0.65–12.93	0.33	193.3	0.005	9 weeks	Present work
Present work	Ch-Ox/RGO	Amperometric	1.3–12.93	0.26	116	0.01	6 weeks	Present work
System 1	Cu_2S NRS/CRIE	Amperometric	0.01–6.8	0.0001	62.5	—	30 days, 92.5%	38
System 2	PEO-*co*-PPy/ChOx/Pt foil	Amperometric	—	—	13.32	1.47	30 days	39
System 3	AuPt–Ch–IL/GCE	Amperometry	0.05–6.2, 6.2–11.2	0.01	90.7	0.24	30 days, 90%	40
System 4	MWCNT–chitosan–Pt–cholesterol	Amperometry	0.005–0.3	0.004	44	—	7 days, 60%	41
System 5	Ti/NPAu/ChOx–HRP–ChE	CV	0.97–7.8	0.012	29.33	0.64	60 days, 95%	2
System 6	ITO(PEI/Hb)5(PEI/COx)10	Amperometric	—	0.016	93.4	—	15 days	42
System 7	(PAH–MCNTs–GNPs/HRP)4/(PAH–MCNTs–GNPs/ChOx)4	CV	0.18–11	0.02	0.3873	—	25 days, 90%	43
System 8	G/PVP/PANI nanocomposites	Amperometry	0.05–10	0.001	34.77	—	14 days, 89.1%	44
System 9	AuE/dithiol/AuNPs/MUA/ChOx	CV	0.04–0.22	0.034	9.02	0.062	30 days, 95%	45
System 10	$NiFe_2O_4$/CuO/FeO–Ch/ChOx	DPV	0.13–12.95	0.81067	16.54	0.21	90 days	46

[a] Note: DPV – differential pulse voltammetry, NRS – nanostructure, CRIE – Cu rod integrated electrode, PEO-*co*-PPy – poly(ethyleneoxide)/polypyrrole, Ch – chitosan, IL – ionic liquid, GCE – glassy carbon electrode, HRP – horseradish peroxidase, PEI – poly(ethylene imine), Hb – hemoglobin, PAH – poly(allylamine hydrochloride), MCNTs – multiwalled carbon nanotubes, G – graphene, PANI – polyaniline, PVP – polyvinylpyrrolidone, GNPs and Au NPs – gold nanoparticles, MUA – 11-mercaptoundecanoic acid.

originates from the PBS buffer solution. The electro-oxidation current of H_2O_2 can be monitored by applying a suitable potential to this system. The extra potential required for the oxidation/reduction of H_2O_2 can be reduced by immobilizing the ChOx enzyme in a suitable immobilization matrix. Here the RGO/ITO and RGO–Fn Au NPs/ITO are found to be one of the most suitable and cost effective matrixes to serve the same purpose. During the electrochemical reaction, the electrons generated will be transferred to the electrodes *via* an Fe(III)/Fe(IV) redox probe that will result in translation of the signal in the form of current. So in this process, the corresponding increase in current is a direct indication of total cholesterol added to the system.

Michaelis–Menten constant (K_m), a well known enzyme and substrate kinetics parameter, has been estimated for the bio-electrodes in the present work using the Lineweaver–Burke plot[37] revealing the strong affinity of the enzyme towards the desired analyte. The K_m value has been calculated using eqn (5).

$$\frac{i}{i_s} = \frac{K_m}{i_{max}}\frac{1}{C} + \frac{1}{i_{max}} \quad (5)$$

where, 'C' is the concentration of mediator in mol cm^{-3}, 'i_{max}' is the maximum peak current and 'i_s' is the starting current. The calculated value of K_m for the ChOx/RGO/ITO bioelectrode is 0.4 mg dL^{-1} (0.01 mM) while for ChOx–RGO–Au NPs/ITO, it is 0.2 mg dL^{-1} (0.0051 mM), smaller than most of the earlier reports (Table 1). Such a low K_m value of ChOx–RGO–Au NPs/ITO suggests that the electrode matrix used here helps immobilized cholesterol oxidase to achieve a better conformation for faster enzymatic reaction. Thus, the ChOx–RGO–Au NPs/ITO provides a better platform for electron transfer between the immobilized enzyme and the electrode substrates and plays the major role in enhancement of electrochemical response. These results have been further corroborated by DFT calculations, which attest enhanced electron density distribution for the RGO–Au NP system in comparison with the bare RGO system (see the ESI†).

To investigate the viability of the fabricated biosensor, we have conducted the reproducibility, specificity and stability measurements and the results further confirm RGO–Fn Au NPs/ITO as a promising candidate in biosensing, which combines the advantages of both graphene as well as metal nanoparticles of gold, which themselves are good biosensing materials.

The specificity of cholesterol towards RGO–Fn Au NP/ChOx/ITO bioelectrodes along with other analytes has been checked. The negligible effect of interference on the corresponding peak current response of the RGO–Fn Au NP/ChOx/ITO biosensor inspite of the presence of interferents such as glucose (100 mg dL^{-1}), ascorbic acid (0.05 mM) and urea (1 mM) in phosphate buffer (0.2 M, pH 7.0), marks its high selectivity for effectively detecting cholesterol, which is important for the material to perform appreciably in complex human serum {ESI, Fig. S5(a)†}. The stability of the RGO–Fn Au NPs/ChOx/ITO biosensor is monitored for nine weeks by measuring the peak current response with respect to time at a regular interval of one week. The RGO–Fn Au NP/ChOx/ITO biosensor has shown a slightly decreased peak current response (~9.2%) after nine weeks when stored under refrigerated conditions (4 °C)

{ESI, Fig. S5(b)†}. This shows the good stability of the fabricated biosensor for a longer period of time and which in turn shows its potential to be brought on field with no degradation issue during transportation and long term use. Similarly, the reproducibility of the bioelectrodes of RGO–Fn Au NPs/ChOx/ITO used for the fabrication of cholesterol biosensors has been determined in terms of the peak current response. For checking this, five different RGO–Fn Au NP/ChOx/ITO bioelectrodes were prepared under the same set of conditions and procedures. No appreciable change in the peak current response was recorded confirming its high reproducibility {see ESI, Fig. S5(c)†}.

Table 1 attests better sensing parameters of the proposed RGO–Fn Au NP/ITO matrix as compared to the RGO/ITO system and the earlier reported data for various matrixes. The table places our electrode apart when compared to several types of materials systems. Clearly, the earlier reported metal/metal oxide nanostructure based systems (System 3, 5, 9 and 10) had a much better K_m value than that of a metal–polymer based system (System 2) but our RGO–Fn Au NP/ITO system beats the metal/metal oxide nanoparticle systems itself by an order of two in K_m value, thus attesting its good affinity for bioanalytes. Similarly, the comparison of sensitivity shows that our RGO–Fn Au NP/ITO system beats metal/metal oxide nanostructure system (Systems 1, 3, 5, 9 and 10), carbon–metal nanostructure system (System 4), and metal–carbon–polymer nanostructured system (System 7) by an order of one. Furthermore, it beats the polymer based system (System 6) by an order of three and carbon–polymer nanostructured system (System 8) by an order of two. This attests the system's commendable sensitivity in cholesterol detection. Moving ahead, the system has a good detection range covering normal plus excess levels of cholesterol usually found in human systems. Simultaneously, although the detection limit is not very low it is more than enough to cover the cholesterol range found in human systems. Thus, we have a sensor which can load analytes better (better K_m value), detect an appreciable range of cholesterol (good detection range), and do this at an enhanced rate (better K_s value), while promising great stability of about 9 weeks. These enhanced sensing parameters owing to the combination of large surface area of the RGO and conductive nature of gold nanoparticles, when combined with good biocompatibility and surface adsorbtion properties result in a commendable electrocatalytic system for cholesterol detection.

Conclusions

In conclusion, the present work reports a RGO–Fn Au NP hybrid system as a promising electrode platform for the electrochemical sensing of free cholesterol. Both the materials and the chemical synthesis route used are economical and the products have been well characterized by XRD, SEM, FTIR and Raman mapping. Bioelectrodes were fabricated by depositing thin films of RGO as well as RGO–Fn Au NPs on separate ITO substrates *via* a cost effective and fast EPD technique, having potential for bulk production. To attain maximum efficiency restacking of RGO was resisted by immobilizing with ChOx after EDC–NHS coupling. A comparative electrochemical sensing study of these bioelectrodes confirms synergistically enhanced sensing ability of the newly proposed RGO–Fn Au NP hybrid system over the traditional RGO system. A cyclic voltammetric study shows that when used alone, RGO's sensitivity is limited to 116 μA mM^{-1} cm^{-2}; however, when coupled with nanoparticles of Au, the resulting RGO–Fn Au NP hybrid system shows a much higher sensitivity of 193.35 μA mM^{-1} cm^{-2} when tested for the same range of cholesterol. These experimental findings have been corroborated by density functional theoretical (DFT) calculations using Gaussian09 software which attest enhanced electron density distribution in the case of the RGO–Fn Au NP hybrid system. Furthermore, the composite formation also favourably increases the chemical stability to about nine weeks, with good reproducibility and biocompatibility. Additionally, these enhanced sensing and stability benefits are achieved economically, with a single hybrid system based bioelectrode costing just ~0.2$. Thus, the proposed RGO–Fn Au NP hybrid system shows promising potential to be used on field for H_2O_2 sensing, enabling critical clinical diagnostics.

Acknowledgements

SA is thankful to University Grants Commission, New Delhi; Institute of Physical Chemistry, Jena, Germany and Alexander von Humboldt for necessary facilities and financial support. Authors are thankful to the laboratories of Prof. Sebastian Schlucker, University of Duisburg, Essen, Germany and Dr Valerian Ciobota, Rigaku Raman Technologies, Berlin, Germany for some of the characterizations. Authors are thankful to Dr Vellaichamy Ganesan and Pankaj K. Rastogi, Department of Chemistry, B.H.U. for EIS measurements. AS acknowledges CAS program sponsored by UGC at Department of Physics, B. H. U. and DST, New Delhi, India.

References

1 J. Motonaka and L. R. Faulkner, *Anal. Chem.*, 1993, **65**, 3258–3261.
2 A. Ahmadalinezhad and A. Chen, *Biosens. Bioelectron.*, 2011, **26**, 4508–4513.
3 M. Zhang, R. Yuan, Y. Chai, C. Wang and X. Wu, *Anal. Biochem.*, 2013, **436**, 69–74.
4 S. Brahim, D. Narinesingh and A. Guiseppi-Elie, *Anal. Chim. Acta*, 2001, **448**, 27–36.
5 B. Unnikrishnan, S. Palanisamy and S.-M. Chen, *Biosens. Bioelectron.*, 2013, **39**, 70–75.
6 A.-L. Liu, G.-X. Zhong, J.-Y. Chen, S.-H. Weng, H.-N. Huang, W. Chen, L.-Q. Lin, Y. Lei, F.-H. Fu and Z. Sun, *Anal. Chim. Acta*, 2013, **767**, 50–58.
7 S. Abraham, V. Ciobota, S. Srivastava, S. K. Srivastava, R. K. Singh, J. Dellith, B. D. Malhotra, M. Schmitt, J. Popp and A. Srivastava, *Anal. Methods*, 2014, **6**, 6711–6720.
8 T. R. Tshikhudo, Z. Wang and M. Brust, *Mater. Sci. Technol.*, 2004, **20**, 980–984.
9 P. Ghosh, G. Han, M. De, C. K. Kim and V. M. Rotello, *Adv. Drug Delivery Rev.*, 2008, **60**, 1307–1315.

10 R. A. Sperling, P. R. Gil, F. Zhang, M. Zanella and W. J. Parak, *Chem. Soc. Rev.*, 2008, **37**, 1896–1908.
11 X. Huang, P. K. Jain, I. H. El-Sayed and M. A. El-Sayed, *Nanomedicine*, 2007, **2**, 681–693.
12 K. S. Novoselov, A. K. Geim, S. V. Morozov, D. Jiang, Y. Zhang, S. V. Dubonos, I. V. Grigorieva and A. A. Firsov, *Science*, 2004, **306**, 666–669.
13 M. Pumera, *Chem. Soc. Rev.*, 2010, **39**, 4146–4157.
14 J. Wei, J. Qiu, L. Li, L. Ren, X. Zhang, J. Chaudhuri and S. Wang, *Nanotechnology*, 2012, **23**, 335707.
15 M. Zhou, Y. Zhai and S. Dong, *Anal. Chem.*, 2009, **81**, 5603–5613.
16 Q. Xu, S.-X. Gu, L. Jin, Y. Zhou, Z. Yang, W. Wang and X. Hu, *Sens. Actuators, B*, 2014, **190**, 562–569.
17 S. Cao, L. Zhang, Y. Chai and R. Yuan, *Biosens. Bioelectron.*, 2013, **42**, 532–538.
18 S. Abraham, V. Ciobota, S. K. Srivastava, R. K. Singh, J. Dellith, B. D. Malhotra, M. Schmitt, J. Popp and A. Srivastava, *Anal. Methods*, 2014, **6**, 6711–6720.
19 Y. Yan, Q. Liu, K. Wang, L. Jiang, X. Yang, J. Qian, X. Dong and B. Qiu, *Analyst*, 2013, **138**, 7101–7106.
20 X. Bai and K.-K. Shiu, *J. Electroanal. Chem.*, 2014, **720**, 84–91.
21 K.-J. Huang, D.-J. Niu, X. Liu, Z.-W. Wu, Y. Fan, Y.-F. Chang and Y.-Y. Wu, *Electrochim. Acta*, 2011, **56**, 2947–2953.
22 W. Hong, H. Bai, Y. Xu, Z. Yao, Z. Gu and G. Shi, *J. Phys. Chem. C*, 2010, **114**, 1822–1826.
23 Y. Xue, H. Zhao, Z. Wu, X. Li, Y. He and Z. Yuan, *Biosens. Bioelectron.*, 2011, **29**, 102–108.
24 D. C. Marcano, D. V. Kosynkin, J. M. Berlin, A. Sinitskii, Z. Sun, A. Slesarev, L. B. Alemany, W. Lu and J. M. Tour, *ACS Nano*, 2010, **4**, 4806–4814.
25 D. Li, M. B. Müller, S. Gilje, R. B. Kaner and G. G. Wallace, *Nat. Nanotechnol.*, 2008, **3**, 101–105.
26 J. Liu and Y. Lu, *Nat. Protoc.*, 2006, **1**, 246–252.
27 Y.-W. Liu, M.-X. Guan, L. Feng, S.-L. Deng, J.-F. Bao, S.-Y. Xie, Z. Chen, R.-B. Huang and L.-S. Zheng, *Nanotechnology*, 2013, **24**, 25604.
28 A. R. Biris, S. Pruneanu, F. Pogacean, M. D. Lazar, G. Borodi, S. Ardelean, E. Dervishi, F. Watanabe and A. S. Biris, *Int. J. Nanomed.*, 2013, **8**, 1429.
29 A. C. Ferrari, J. C. Meyer, V. Scardaci, C. Casiraghi, M. Lazzeri, F. Mauri, S. Piscanec, D. Jiang, K. S. Novoselov, S. Roth and A. K. Geim, *Phys. Rev. Lett.*, 2006, **97**, 187401.
30 K. N. Kudin, B. Ozbas, H. C. Schniepp, R. K. Prud'Homme, I. A. Aksay and R. Car, *Nano Lett.*, 2008, **8**, 36–41.
31 L. M. Malard, M. A. Pimenta, G. Dresselhaus and M. S. Dresselhaus, *Phys. Rep.*, 2009, **473**, 51–87.
32 D. A. C. Brownson, S. A. Varey, F. Hussain, S. J. Haigh and C. E. Banks, *Nanoscale*, 2014, **6**, 1607–1621.
33 Y. Hao, Y. Wang, L. Wang, Z. Ni, Z. Wang, R. Wang, C. K. Koo, Z. Shen and J. T. L. Thong, *Small*, 2010, **6**, 195–200.
34 J. E. B. Randles, *Discuss. Faraday Soc.*, 1947, **1**, 11–19.
35 P. Zanello, *Inorganic Electrochemistry: Theory, Practice and Applications*, Royal Society of Chemistry, 2003.
36 R. J. Klingler and J. K. Kochi, *J. Phys. Chem.*, 1981, **85**, 1731–1741.
37 H. Lineweaver and D. Burk, *J. Am. Chem. Soc.*, 1934, **56**, 658–666.
38 R. Ji, L. Wang, G. Wang and X. Zhang, *Electrochim. Acta*, 2014, **130**, 239–244.
39 H. B. Yildiz, D. O. Demirkol, S. Sayin, M. Yilmaz, O. Koysuren and M. Kamaci, *J. Macromol. Sci., Part A: Pure Appl.Chem.*, 2013, **50**, 1075–1084.
40 A. Safavi and F. Farjami, *Biosens. Bioelectron.*, 2011, **26**, 2547–2552.
41 Y.-C. Tsai, S.-Y. Chen and C.-A. Lee, *Sens. Actuators, B*, 2008, **135**, 96–101.
42 T. T. L. Souza, M. L. Moraes and M. Ferreira, *Sens. Actuators, B*, 2013, **178**, 101–106.
43 X. Cai, X. Gao, L. Wang, Q. Wu and X. Lin, *Sens. Actuators, B*, 2013, **181**, 575–583.
44 N. Ruecha, R. Rangkupan, N. Rodthongkum and O. Chailapakul, *Biosens. Bioelectron.*, 2014, **52**, 13–19.
45 U. Saxena, M. Chakraborty and P. Goswami, *Biosens. Bioelectron.*, 2011, **26**, 3037–3043.
46 J. Singh, M. Srivastava, P. Kalita and B. D. Malhotra, *Process Biochem.*, 2012, **47**, 2189–2198.

ACS APPLIED NANO MATERIALS

Article

Cite This: ACS Appl. Nano Mater. 2019, 2, 566−576

www.acsanm.org

In Situ Functionalized Fluorescent WS_2-QDs as Sensitive and Selective Probe for Fe^{3+} and a Detailed Study of Its Fluorescence Quenching

Vijay K. Singh,[†] Himanshu Mishra,[†] Rashid Ali,[‡] Sima Umrao,[§] Rajesh Srivastava,[†] Shiju Abraham,[#] Arvind Misra,[‡] Vidya Nand Singh,[⊥] Hirdyesh Mishra,[∥] R. S. Tiwari,*[,†] and Anchal Srivastava*[,†]

[†]Department of Physics, Institute of Science, Banaras Hindu University, Varanasi 221005, India

[‡]Department of Chemistry, Institute of Science, Banaras Hindu University, Varanasi 221005, India

[§]Department of Mechanical Engineering, School of Mechanical and Aerospace Engineering, Korea Advanced Institute of Technology (KAIST), Dajeon 34141, South Korea

[∥]Department of Physics (MMV), Banaras Hindu University, Varanasi 221005, India

[⊥]CSIR-National Physical Laboratory, Dr. K. S. Krishnan Marg, New Delhi 110012, India

[#]The Zuckerberg Institute for Water Research, The Jacob Blaustein Institutes for Desert Research, Ben-Gurion University of the Negev, Sede Boqer 8499000, Israel

Supporting Information

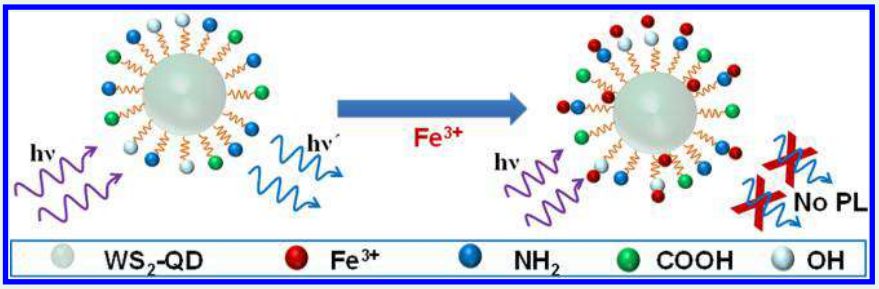

ABSTRACT: Most of the reports suggest that liquid exfoliated WS_2-QDs are unstable; therefore the need of present day is to develop a novel synthesis route for producing long-term stable WS_2-QDs. Herein, we report a bottom-up single-step hydrothermal growth of in situ functionalized blue fluorescent WS_2-QDs with stable fluorescence in aqueous media without subsequent treatments. Presence of various functional groups over the surface of f-WS_2-QDs provides high solubility and stability to f-WS_2-QDs in aqueous media preserving its fluorescence. Further, photoluminescence property of f-WS_2-QDs has been employed to devise an optical sensor with a high sensitivity ($K_D \sim 10^4\ M^{-1}$) and selectivity for ferric (Fe^{3+}) ions. Under the optimal condition, response of the sensor is found to be linear in the range of 0−55 μM with a limit of detection (LOD) of 1.32 μM, which is within the maximum permissible level of Fe^{3+} (~5.4 μM) in human drinking water by the USEPA. Further, we have also carried out a detailed evaluation on fluorescence quenching kinetics of f-WS_2-QDs. Nonlinear behavior of S−V plot and TRPL measurements suggest that quenching is a mixed phenomenon of dynamic as well as static processes. Finally we have proposed a mechanism for fluorescence quenching of f-WS_2-QDs in the presence of Fe^{3+}.

KEYWORDS: *WS_2, quantum dots, hydrothermal synthesis, quantum yield, TRPL, fluorescence quenching*

INTRODUCTION

In the post-graphene era, a great sensation has been observed in the current research on layered transition metal dichalcogenides (LTMDs) of few-to-monolayer nanocrystals (NCs) or quantum dots (QDs) of MoS_2, WS_2, $MoSe_2$, etc., which have been conceived as best substitutes of graphene and carbon QDs.[1−4] In this LTMDs series, 2D WS_2 has aroused even greater attention owing to its controllable band gaps as a function of layer numbers with remarkable optical and electronic properties.[5−7] WS_2 is a van der Waals layered material with hexagonal lattice structure arranged in triple layers (S−W−S); each layer has a thickness of 6 Å with strong in-plane covalent bonding and weak out-of-plane van der Waals interactions.[8] Further, by reducing the lateral size of 2D WS_2 sheet in 0D WS_2-QDs, one can acquire excellent electrical/optical behaviors from these NCs due to their strong quantum confinement and edge effects.[9] In addition to this, WS_2-QDs possess larger surface to volume ratio and much more active sites beyond monolayer 2D WS_2, which may be beneficial for sensing, catalysis, bioimaging, etc. To date,

Received: November 28, 2018
Accepted: December 14, 2018
Published: December 14, 2018

DOI: 10.1021/acsanm.8b02162
ACS Appl. Nano Mater. 2019, 2, 566−576

several "top-down" routes have been reported for producing WS_2-QDs, which include liquid phase exfoliation, intercalated exfoliation of bulk WS_2 followed by hydrothermal scissoring, ultrasonication, etc.[4,10−13] For instance, Lin et al. synthesized WS_2-QDs using potassium ions (K^+) intercalation of bulk WS_2 flakes followed by ultrasonication.[9] However, removal of the K^+ ions led to the instability to WS_2-QDs.[2,9,13] Zhao et al. reported synthesis of WS_2-QDs by exfoliating bulk WS_2 through H_2SO_4 intercalation.[14] This method requires a tedious and time-consuming post-treatment of lipoic acid conjugated poly(ethylene glycol) on the surface of WS_2-QDs. Zhang et al. synthesized WS_2-QDs through ultrasonic crushing of WS_2 powder for 12 h. But this synthesis approach also requires a second step of L-cysteine coating over WS_2-QDs surface for their protection.[15] In another report Xian et al. described the synthesis of water-soluble WS_2-QDs through ultrasonication of WS_2 powder in the presence of CTAB followed by hydrothermal scissoring.[10] CTAB (ionic surfactant) stabilizes WS_2-QDs in water and prevents its agglomeration; however, it is known to possess cytotoxicity which is not suitable for biological applications. Besides these, several other reports are available showing the importance of surface passivation/functionalization of QDs to make them stable and biocompatible. However, all these reported methods followed tedious and time-consuming post-processing of the sample to achieve the same. Moreover, earlier reports also suggest that QDs without passivation or surface functionalization lead to weak fluorescence due to agglomeration.[16,17] Therefore, for the best exploitation of WS_2-QDs potential, it must remain fluorescent and stably dispersed in water and biological fluids, which can be achieved through surface passivation/functionalization of it. Thus, there is a great challenge to develop a cost-effective, environment friendly, facile, and high yield strategy to produce water-soluble in situ functionalized WS_2-QDs with stable fluorescence.

Fe^{3+} is the most important and essential ion for the metabolic process of all the living systems. It is involved in oxygen metabolism, and by virtue of its redox chemistry as well as high affinity for oxygen, it facilitates electron transfer in DNA and RNA synthesis.[18] Its deficiency and excess both from normal permissible level can induce a variety of diseases. For example, iron deficiency (hypoferremia) causes anemia, liver damage, diabetes, cancer, and Parkinson's diseases and accumulation of iron (hyperferremia) causes oxidative stress, hemochromatosis, and Alzheimer's and neurodegenerative diseases due to over production of H_2O_2, etc.[19,20] Inappropriate treatment of metal ions can also lead to metal ion contamination, which has become a critical environmental issue in developing countries. Hence, the determination of Fe^{3+} in the biological systems and aquatic environment is of burgeoning interest for effectively monitoring and controlling the metal ion concentration. In this aspect, the development of metal ion sensors is a hot, yet challenging topic. In this context, many efforts have been devoted for developing accurate, sensitive, and selective approaches for metal ion detection, such as inductively coupled plasma mass spectrometry, voltammetry, fluorescent sensor, etc.[21−23] Among these, fluorescence based sensor is most appealing due to its inherent simplicity, high sensitivity, and freedom from sophisticated instrumentations.[18,24]

Although MoS_2-QDs has been synthesized using hydrothermal method,[25−27] however to the best of our knowledge, for the first time, we demonstrate a novel, scalable single-step "bottom-up" hydrothermal approach for producing nanometer sized, good quality, monodispersed in situ functionalized fluorescent WS_2-QDs. Owing to its nanometer size, the as-synthesized f-WS_2-QDs give highly intense blue fluorescence ($\lambda \sim 410$ nm) in UV-light which can be easily visualized by naked eye under UV lamp (~365 nm). The reagents used in present synthesis approach are $Na_2WO_4{\cdot}2H_2O$ and L-cysteine. Also the present method does not require any additional surface passivation agents and post-synthesis processing, which makes it more attractive as compared to the other reports on the synthesis of WS_2-QDs.[9,10] L-Cysteine causes the self-passivation of QDs and hence provides stability to the QDs in aqueous media. Further, for the proof of concept we have also demonstrated that our as-produced f-WS_2-QDs have potential to be applied as fluorescent probe for highly sensitive ($K_D \sim 10^4$ M^{-1}) and selective detection of Fe^{3+} ions. Under the optimal condition response of the sensor is found to be linear in the range of 0−55 μM with a LOD of 1.32 μM. Apart from this, we have also carried out a detailed kinetic study to unveil the interaction between f-WS_2-QDs and Fe^{3+} ions. S−V plot and time-resolved photoluminescence (TRPL) study reveal that fluorescence quenching is a mixed phenomenon of both static and dynamic processes. We have also proposed a mechanism for fluorescence quenching of f-WS_2-QDs in the presence of Fe^{3+}.

EXPERIMENTAL SECTION

Reagents and Chemicals. All the reagents used in the present work were of analytical grade and used without any further purification. Sodium tungstate dihydrate ($Na_2WO_4.2H_2O$) was obtained from Hi-media Chemicals, India. It was used as starting material for the synthesis of f-WS_2-QDs. L-Cysteine and hydrochloric acid (HCl) were procured from Merck, India, and Molychem Chemicals India, respectively. Deionized (DI) water was used as solvent material in hydrothermal synthesis as well as for all the optical and sensing measurements of f-WS_2-QDs. The stock solutions of different metal ions (0.1 M) such as Na^+, K^+, Ca^{2+}, Al^{3+}, Cd^{2+}, Zn^{2+}, Ni^{2+}, Hg^{2+}, Fe^{2+}, Pb^{2+}, Cu^{2+}, and Fe^{3+} were freshly prepared by dissolving their nitrate salts in water.

Techniques Used for Material Characterizations. Transmission electron microscopic (TEM) and high-resolution transmission electron microscopic (HR-TEM) images of f-WS_2-QDs were obtained through Tecnai G2 TEM (FEI, USA) operated at 200 kV. The atomic force microscopic (AFM) image of f-WS_2-QDs was acquired using JPK NanoWizard 4 (JPK Instruments AG, Germany) using gold-coated silicon tips (tip radius, 2−12 nm) (SNL-10 probe; Camarillo, CA) with a spring constant of 0.35 N/m in quantitative imaging (QI) mode. For AFM imaging, the sample was drop-cast on a freshly cleaved mica surface. For the evidence of the chemical composition of the f-WS_2-QDs, X-ray photoelectron spectra (XPS) were recorded in multiprobe surface analysis system (ESCA2000 VG Microtech Inc.) using monochromatic Mg Kα (1253.6 eV) radiation source. The base pressure of the instrument was maintained in the range of 10^{-10}−10^{-11} Torr during the sample analysis. The pass energy of the scans was fixed at 10 eV with a spectral resolution of ~0.1 eV. All the reported binding energies in the present work are calibrated to the C 1s peak at 284.6 eV. Raman spectra of the as-synthesized f-WS_2-QDs were recorded at room temperature with a Renishaw inVia Raman spectrophotometer (Germany), equipped with a diode pump solid-state laser of wavelength 532 nm. Laser beam was incident on the sample with a 50× objective at a constant laser power of 5 mW mm^{-2}. Absorption spectra of as-synthesized material were recorded using UV−vis spectrophotometer (PerkinElmer, USA) having a quartz cuvette of standard 10 mm path length. Static photoluminescence (PL) and lifetime spectra of f-WS_2-QDs were recorded using fluorescence spectrophotometer (PerkinElmer, USA)

DOI: 10.1021/acsanm.8b02162
ACS Appl. Nano Mater. 2019, 2, 566−576

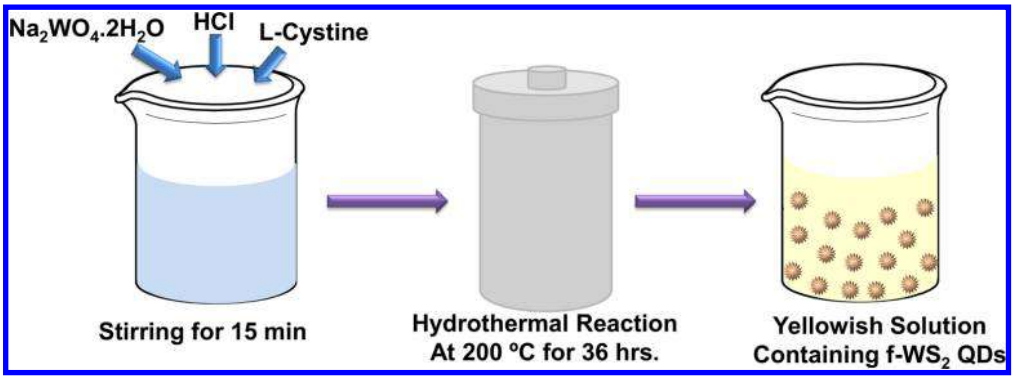

Figure 1. Schematic illustration showing the hydrothermal synthesis of f-WS_2-QDs.

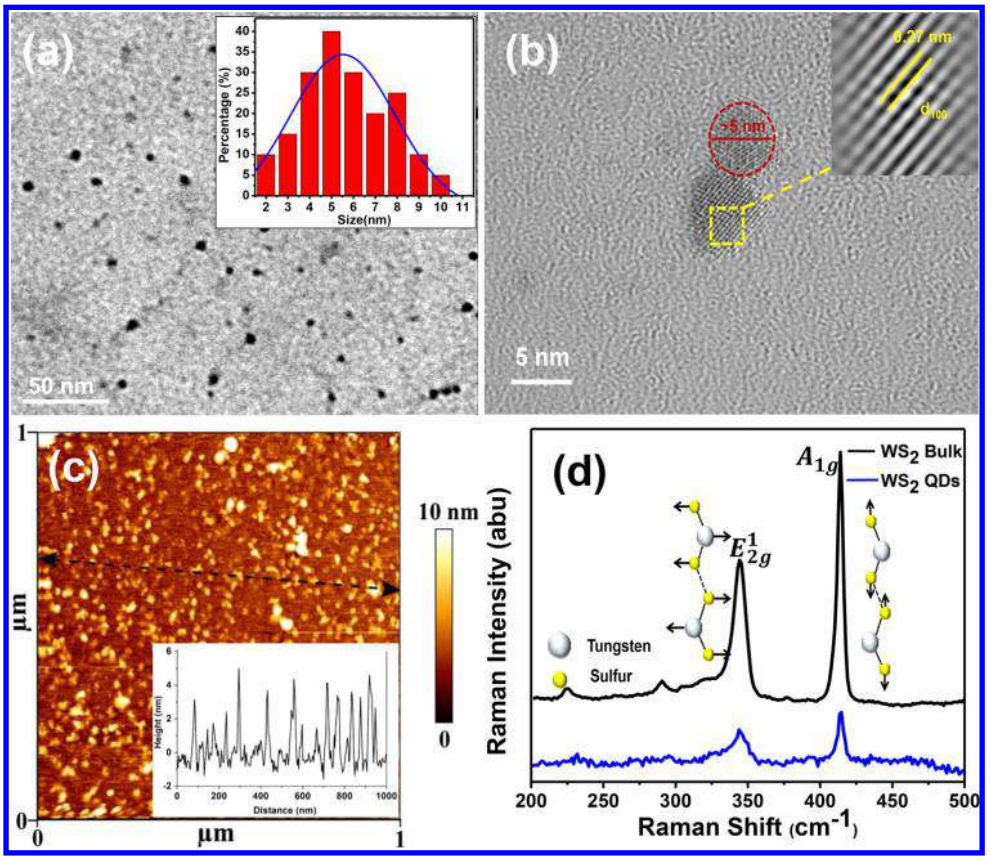

Figure 2. (a, b) TEM and HR-TEM images showing highly dispersed and crystalline f-WS_2-QDs. (c) AFM image and height profile (along the black line) of f-WS_2-QDs dispersed on mica sheet showing the monodispersed QDs with average height of ~4 nm. (d) Raman spectra of bulk as well as QDs of WS_2 showing characteristic peaks E^1_{2g} and A_{1g} phonon modes corresponding to the in-plane and out-of-plane vibrations of S−W−S atoms.

and time-resolved photoluminescence (TRPL) spectrophotometer (FLS920, Edinburgh, UK), respectively.

Synthesis of f-WS_2-QDs. As shown in Figure 1, f-WS_2-QDs were synthesized using a single step, facile, and scalable hydrothermal synthesis approach. Typically, 0.25 g of $Na_2WO_4{\cdot}2H_2O$ was dissolved in 25 mL of DI water. After the mixture was stirred for 15 min, the pH value of the solution was adjusted to ~4.0 using 0.1 M HCl solution. Further, 0.5 g of L-cysteine dissolved in 50 mL of distilled water separately was poured in the solution and sonicated for 10 min. Finally, the as-prepared solution was transferred into 100 mL Teflon-lined stainless steel hydrothermal vessel. After heating at 200 °C for 36 h followed by cooling down to room temperature, yellowish color solution containing f-WS_2-QDs was obtained. The proposed reaction during the hydrothermal synthesis is as follows:

$$HSCH_2CHNH_2COOH + H_2O \rightarrow CH_3COCOOH + NH_3 + H_2S \quad (R1)$$

$$4WO_4^{2-} + 9H_2S + 6CH_3COCOOH \rightarrow 4WS_2 + SO_4^{2-} + 6CH_3COCOO^- + 12H_2O \quad (R2)$$

Sensing Procedure of Metal Ions (Fe^{3+}) Using f-WS_2-QDs. Fluorescence quenching based sensitive and selective detection of Fe^{3+} using f-WS_2-QDs as fluorescent probe has been investigated. The metal ions interaction study was performed by the addition of freshly prepared solution of metal ions (0.1 M) into the quartz cuvette containing 3.0 mL solution of f-WS_2-QDs. After homogenization, the change in fluorescence intensity was recorded for the wavelength of ~410 nm under the excitation wavelength of ~310 nm. In addition to

DOI: 10.1021/acsanm.8b02162
ACS Appl. Nano Mater. 2019, 2, 566−576

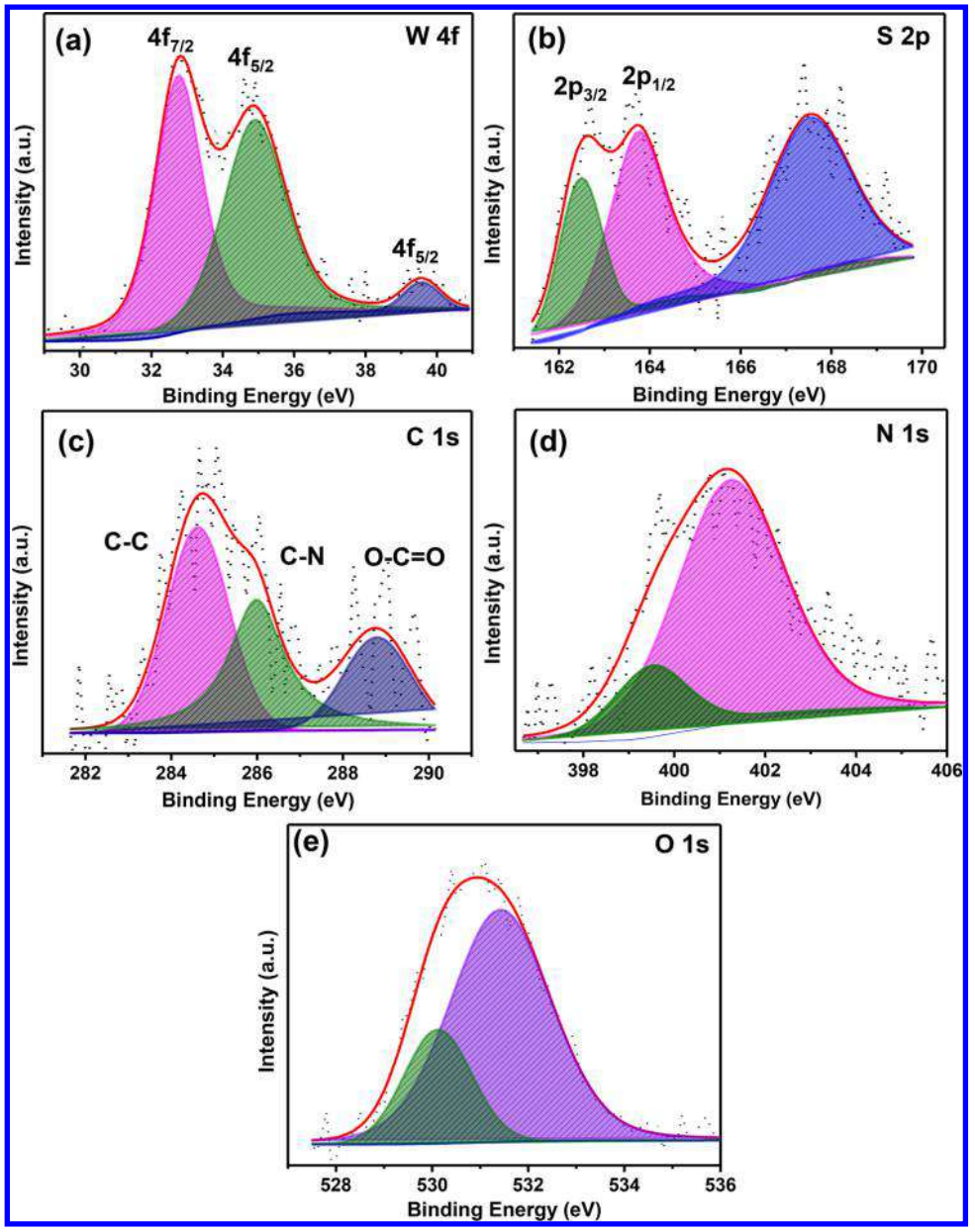

Figure 3. (a) W 4f, (b) S 2p, (c) C 1s, (d) N 1s, and (e) O 1s high resolution XPS spectra of f-WS_2-QDs.

this, the selectivity of sensing probe (f-WS_2-QDs) for Fe^{3+} was analyzed by addition of different metal ions to the solution of f-WS_2-QDs containing Fe^{3+} ions.

RESULTS AND DISCUSSION

As-prepared f-WS_2-QDs were characterized using various techniques such as TEM, HRTEM, AFM, and Raman spectroscopy to confirm and highlight their structural properties. Figure 2a shows TEM image of f-WS_2-QDs, revealing that as-prepared f-WS_2-QDs are uniform and monodispersed in nature. Variations in particle size have been plotted and presented in the inset of Figure 2a, which is well fitted with the Gaussian distribution function giving an average particle size of ~5.0 nm (n = 75). From here we can anticipate that such narrow distribution in particle size with superior homogeneous dispersion can significantly enhance the sensing performance of f-WS_2-QDs. High-resolution TEM (HR-TEM) image of typical f-WS_2-QDs (Figure 2b) confirms the growth of highly crystalline f-WS_2-QDs with a particle diameter of ~5 nm. A crystal lattice d-spacing (inset of Figure 2b) is identified to be 0.27 nm, which corresponds to the (100) lattice plane of f-WS_2 crystal.[28,29]

Furthermore, AFM analysis was performed to see the morphology and thickness of the as-synthesized f-WS_2-QDs. The topographic image and height profile obtained through AFM have been shown in Figure 2c. Similar to the TEM result, AFM analysis also reveals that QDs are monodispersed in nature. The height profile in Figure 2c shows the height of f-WS_2-QDs is ~4 nm, which confirms that QDs are few layered (~4−5 layers). Raman spectroscopic technique has been widely adopted for the characterization of the vibrational properties of TMDs and other layered materials because of its proven sensitivity and nondestructive nature. So we have also employed this technique to study the thickness and the vibrational modes present in the f-WS_2-QDs. Raman spectra of f-WS_2-QDs as well as its bulk counterpart have been shown in Figure 2d. In bulk WS_2 as well as in f-WS_2-QDs two prominent

DOI: 10.1021/acsanm.8b02162
ACS Appl. Nano Mater. 2019, 2, 566−576

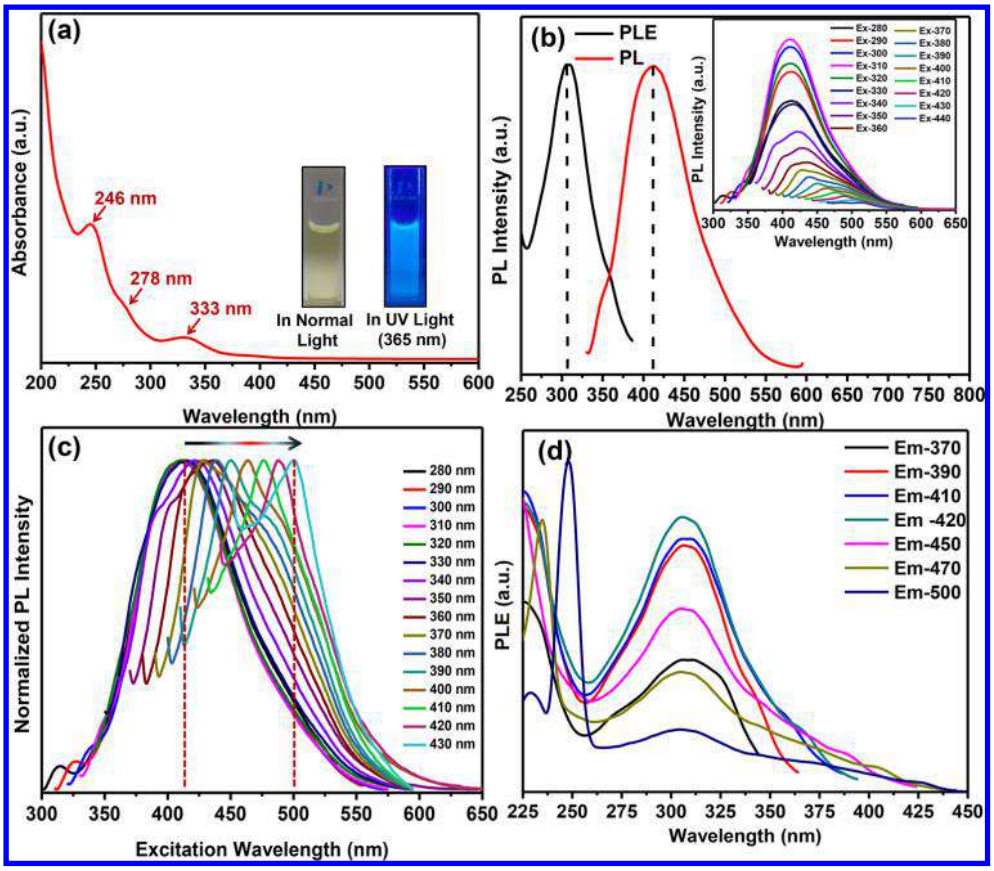

Figure 4. Photophysical properties of f-WS_2-QDs: (a) UV−vis absorption spectra and inset showing the f-WS_2-QDs liquid under normal and UV (~365 nm) light; (b) spectroscopic overlap between PL excitation spectra (PLE, black line, for an emission wavelength λ_{em} = 410 nm) and PL emission spectra (red line, for an excitation wavelength λ_{ex} = 310 nm) and inset showing PL spectra of f-WS_2-QDs at various excitation wavelengths; (c) normalized PL plot of excitation dependent PL spectra and (d) PL excitation (PLE) spectra for various emission wavelengths ranging from 370 to 500 nm.

peaks around ~348 cm^{-1} and ~418 cm^{-1} are observed, which correspond to the E^1_{2g} and A_{1g} phonon modes of 2H-WS_2, respectively, where E^1_{2g} and A_{1g} correspond to the in-plane and out-of-plane vibrations of S−W−S atoms, respectively.[30] It is evident from Figure 2d that the intensities of these peaks are much weaker in case of f-WS_2-QDs. The decrement in absolute intensity is due to the weaker interlayer attraction (water molecule interaction), which causes very narrow contribution toward the phonon restoring forces.[10] In addition to these, Fourier transform infrared (FTIR) spectroscopy was also performed to investigate the bonding composition of f-WS_2-QDs and presence of functional groups over the surface of these QDs (Figure S1). FTIR spectra confirmed the presence of various functional groups −COOH, $-NH_2$, −OH, $-SO_4^{2-}$, etc. over the surface of f-WS_2-QDs.

XPS Characterization. An XPS characterization was carried out to analyze the surface compositions and bonding characteristics of the as-synthesized f-WS_2-QDs. The high resolution core level spectra of W 4f, S 2p, C 1s, and O 1s have been shown in Figure 3. The region with binding energy (BE) from 30 to 38 eV can be fitted into doublet peaks located at 32.8 and 34.9 eV (Figure 3a), which can be attributed to the W $4f_{7/2}$ and W $4f_{5/2}$, respectively. These peaks are consistent with W^{4+} oxidation state of W in f-WS_2-QDs.[31] An additional peak at 39.3 eV is attributed to the W^{6+} oxidation state of W in tungsten hydroxide, which might be formed due to the surface oxidation of QDs during the hydrothermal synthesis process.[9,10] The BE of 2p core level of S in the range of 161 to 166 eV can be fitted into doublet peaks at 162.5 and 163.7 eV, which can be attributed to the S $2p_{3/2}$ and S $2p_{1/2}$ of S^{2-}, respectively (Figure 3b), suggesting the formation of WS_2. The peak at 167.9 eV signifies the presence of sodium sulfate, which is supposed to be present as residue after reaction in the colloidal suspension of f-WS_2-QDs.[32,33] The BE of C 1s spectra in range of 280−290 eV can be deconvoluted into three peaks at 284.6, 285.9, and 288.9 eV (shown in Figure 3c), which can be attributed to the C−C, C−N, and O−C═O, respectively. The BE of N 1s spectra in the range of 397−406 eV is deconvoluted into two peaks at 399.5 and 401.3 eV (shown in Figure 3d), which might be attributed to the C−N and O═C−N, respectively. These peaks confirm the presence of various functional groups such as carbonyl, carboxylic, etc. over the surface of as-synthesized WS_2-QDs,[34] which is also in good agreement with the FTIR analysis. Further, the BE of O 1s core level peak in the region 528−535 eV can be fitted into doublet peaks at 530.1 and 531.4 eV (shown in Figure 3d). The peak with BE = 530.1 eV can be assigned to the oxygen atoms (O^{2-}) of W═O bonds, and the peak with BE = 531.4 eV corresponds to the O−H group.[35] The presence of W═O and O−H group also confirms that edge of QDs is oxidized, which provides stability to it in water solution. From the XPS analysis we found that atom % values of W_{4f} and S_{2p} are 7.53 and 13.1, respectively. It shows that W and S atoms are in the ratio of approximately 1:2, which should be exactly 1:2 for pure

DOI: 10.1021/acsanm.8b02162
ACS Appl. Nano Mater. 2019, 2, 566−576

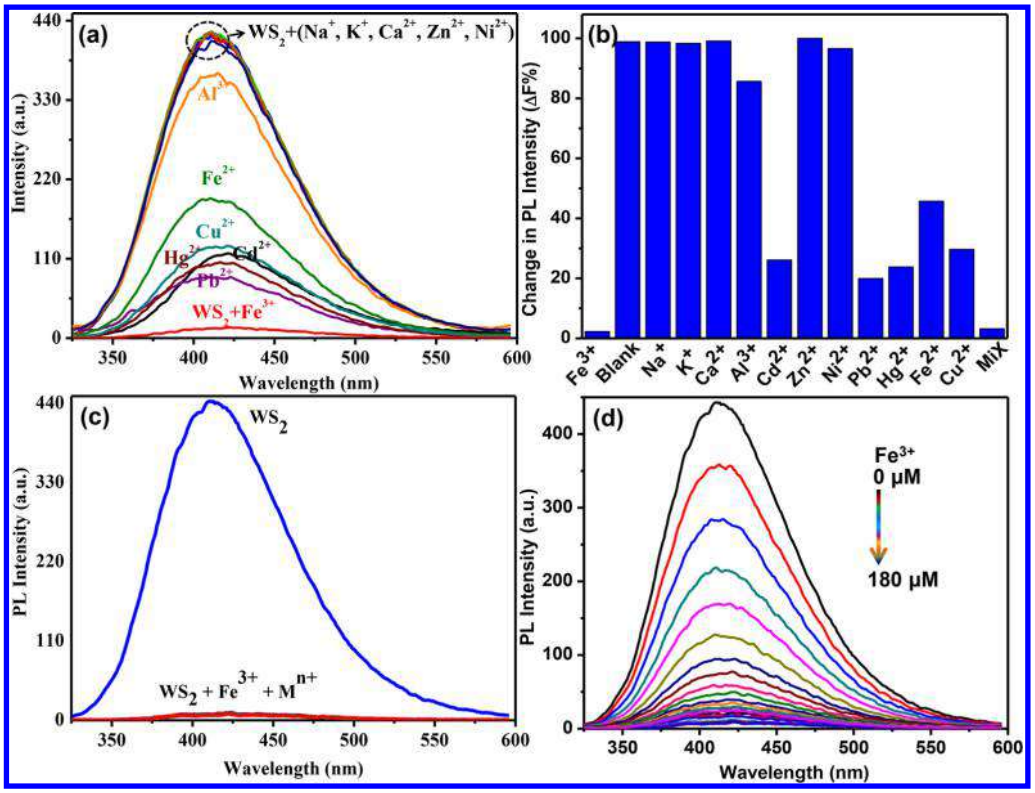

Figure 5. PL spectra of f-WS_2-QDs (a) upon interaction with various metal ions (180.0 μM), (b) percentage change in fluorescence intensity of f-WS_2-QDs in the presence of various metal ions, (c) interference of different metal ions to a solution of f-WS_2-QDs + Fe^{3+}, and (d) PL titration spectra of f-WS_2-QDs upon a gradual addition of Fe^{3+} (0−180.0 μM).

WS_2 crystal. This sulfur deficiency may be attributed to the surface oxidation of WS_2-QDs.

Photophysical Properties of f-WS_2-QDs. In order to unveil the photophysical properties of the as-synthesized f-WS_2-QDs, UV−vis absorption and photoluminescence (PL) characterizations were carried out, which have been shown in Figure 4. The absorption spectra of as-prepared f-WS_2-QDs is represented in Figure 4a, in which two intense absorption bands at 333 nm (3.72 eV) and 246 nm (5.04 eV), a hump at 278 nm (4.46 eV) along with a weak absorption at the red edge of the absorption spectra are observed. The band at 333 nm is attributed to the excitonic absorption band of f-WS_2-QDs arising from direct gap transitions at the K point. The absorption band at 278 nm (4.46 eV) is attributed to the optical transitions from the valence band to the conduction band.[9] The band at 246 nm (5.04 eV) might be attributed to the surface defects as well as surface adsorbed functional groups (−NH_2, −SO_4^{2-}, −OH^-, etc.) of f-WS_2-QDs.[26] A visual inspection shows that in normal light f-WS_2-QDs solution appears as light yellow in color, while it gives highly intense blue fluorescence under UV-lamp (λ = 365 nm) (inset of Figure 4a). To confirm this, the room temperature PL spectra of f-WS_2-QDs were recorded with PL spectrophotometer. Figure 4b shows the PL emission spectra recorded at various excitation wavelengths (λ_{ex}) ranging from 280 to 430 nm. It is observed that initially PL intensity increases when λ_{ex} varied from 280 to 310 nm and after that it starts decreasing (inset of Figure 4b); maximum PL intensity was observed at emission wavelength λ_{em} ∼ 410 nm with λ_{ex} ∼ 310 nm. It is also observed that at higher excitation wavelengths PL peak shifted toward the red edge of emission spectra. To verify this nature, the normalized PL intensities for different excitation wavelengths have been plotted and shown in Figure 4c. It clearly indicates the edge excitation red shifting of 90 nm starting from 410 to 500 nm. This edge excitation red shifting property indicate the polydispersity nature of f-WS_2-QDs. Further, photoluminescence excitation (PLE) spectra of f-WS_2-QDs for different λ_{em} ranging from 370 to 500 nm were also recorded and shown in Figure 4d. Weak excitation peaks at the red edge of the PLE spectra also support the edge excitation red shifting observed in PL spectra.

Detection of Ferric Ions (Fe^{3+}) by Using f-WS_2-QDs. The sensing behavior of f-WS_2-QDs in the presence of different metal ions such as Na^+, K^+, Al^{3+}, Ca^{2+}, Fe^{2+}, Fe^{3+}, Ni^{2+}, Cu^{2+}, Zn^{2+}, Cd^{2+}, Hg^{2+}, and Pb^{2+} (as their nitrate salts) has been examined through the PL spectrophotometer. Since the maximum PL intensity of f-WS_2-QDs was observed at 410 nm (λ_{ex} ∼ 310 nm) having Stokes shift of 8162 cm^{-1}, metal ion sensing application of f-WS_2-QDs has been performed at 410 nm. The quantum yield of f-WS_2-QDs with respect to anthracene as a reference was estimated by using eq 1 in Supporting Information and was found to be Φ_{WS_2} ∼ 4.04%, which is comparable to the WS_2-QDs obtained through the liquid phase exfoliation.[9]

The interaction studies have been performed by addition of 180 μM of different metal ions to the solution of f-WS_2-QDs separately. Interaction study showed that fluorescence intensity of f-WS_2-QDs centered at 410 nm quenched 60−75% with the addition of Fe^{2+}, Hg^{2+}, Cd^{2+}, Pb^{2+}, and Cu^{2+}, while it was quenched completely (∼98%) in the presence of Fe^{3+} (Figure 5a). Percentage change in fluorescence intensity (ΔF, %) in the presence of various metal ions is shown in Figure 5b, which also showed that PL intensity is totally quenched in the presence of Fe^{3+} ions. The change in fluorescence intensity of

DOI: 10.1021/acsanm.8b02162
ACS Appl. Nano Mater. 2019, 2, 566−576

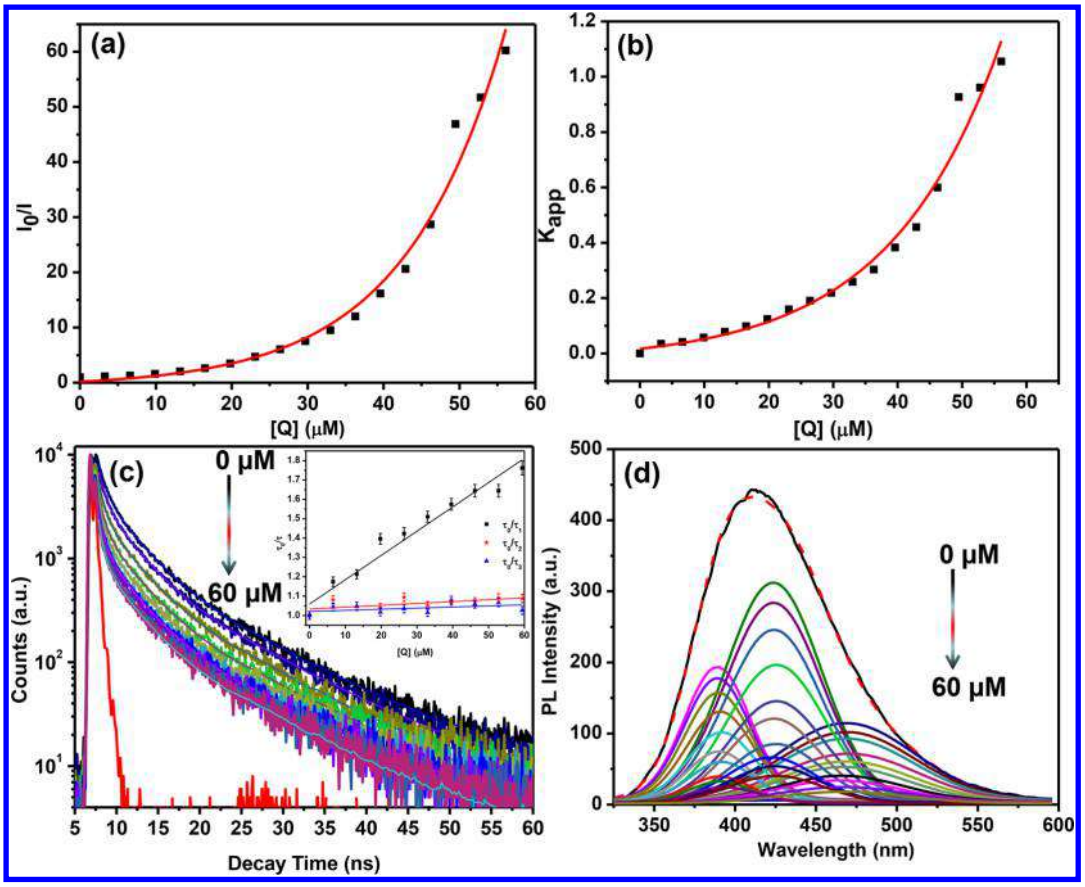

Figure 6. (a, b) Stern−Volmer plot, showing exponential increment in PL intensity ratio with the gradual addition of Fe^{3+} ions into the f-WS_2-QDs solution. (c) Picosecond time-resolved fluoroscence transient of fluorophore (f-WS_2-QDs), showing decrement in lifetime with the addition of quencher (Fe^{3+}) from 0 to 60 μM, under laser excitation of 375 nm, and inset showing the relative change in average lifetimes with the successive addition of Fe^{3+} ions. (d) Deconvoluted PL spectra corresponding to increasing Fe^{3+} concentration showing the presence of three types of quenching species.

f-WS_2-QDs in the presence of Fe^{2+}, Hg^{2+}, Cd^{2+}, Pb^{2+}, and Cu^{2+} may be attributed to the adsorption of these metal ions on the surface of f-WS_2-QDs.

In order to check the selectivity of sensing probe (f-WS_2-QDs) toward Fe^{3+} ions, the competitive metal ion interference experiments were performed with addition of Fe^{3+} in the solution of f-WS_2-QDs containing different metal ions and reversibly, upon addition of different metal ions (in excess, ~200.0 μM) to a solution of f-WS_2-QDs-Fe^{3+}. The insignificant change in emission intensity of f-WS_2-QDs-Fe^{3+} was observed, which suggests the high selectivity of f-WS_2-QDs for Fe^{3+} (Figure 5c). Further, to check the sensitivity of sensing probe toward Fe^{3+} ions, emission based titration experiments have also been performed by gradual addition of different concentrations (from 0 μM to 180 μM, in step of 3.3 μM) of Fe^{3+} ion to the solution of f-WS_2-QDs. It shows that the emission intensity of f-WS_2-QDs centered at 410 nm decreases and reached saturation limit up to addition of 180 μM Fe^{3+} ion (Figure 5d) and quantum yield decreases from ~4.04% to ~0.1% (Table S1).

Further, the detection limit of f-WS_2-QDs for Fe^{3+} was estimated from the respective fluorescence titration data based on the reported method.[36,37] According to the result of titration experiment, change in the fluorescence intensity of f-WS_2-QDs with Fe^{3+} was normalized in between the minimum to maximum intensity. A linear regression curve was obtained from the plot of these normalized fluorescence intensity of f-WS_2-QDs with Fe^{3+} versus log [Fe^{3+}] (Figure S2), and detection limit was calculated by using eq 1. Limit of detection was found to be as low as 1.32 μM. The plot of PL intensity on log scale versus the quencher (Fe^{3+}) concentration (shown in Figure S3) shows that the response of sensor is linear in the range of 0−55 μM.

$$\mathrm{LOD} = 10^{-[\mathrm{slope/intercept}]} \quad (1)$$

As it is well-known that depending on the nature of fluorescence probe and quencher, quenching of PL intensity may occur due to the formation of complex in ground state (static quenching) or through the diffusion collision process (dynamic quenching). So in order to unveil the fluorescence quenching behavior of f-WS_2-QDs in the presence of Fe^{3+}, the relative change in fluorescence intensity (I_0/I) has been plotted as a function of quencher concentration ([Q]) of Fe^{3+} described by Stern−Volmer (S−V) eq 2 and has been shown in Figure 6a, where K_{SV} is the S−V quenching constant.

$$\frac{I_0}{I} = 1 + K_{SV}[\mathrm{Q}] \quad (2)$$

In the present case, it is observed that relative fluorescence intensity deviates from linearity toward the y-axis with the successive addition of Fe^{3+}. This indicates that more than one type of quenching processes (static/dynamic quenching) are involved here. So by considering both the quenching processes, we plotted the modified S−V plot governed by eq 3, shown in

DOI: 10.1021/acsanm.8b02162
ACS Appl. Nano Mater. 2019, 2, 566−576

Table 1. Comparison of the Performance of Various Sensing Probes for the Detection of Fe^{3+}

SN	sensing probe	linearity	detection limit	K_{SV} (M^{-1})	ref
1.	CQDs	12.5−100 μM	9.79 μM	3.148×10^3	39
2	iridium(III)-based metal−organic frameworks		1.215 μM	1.165×10^4	40
3	dopamine functionalized GQDs	20 nM to 2 μM	7.6 μM		41
4	N, P co-doped CQDs	20−200 μM	20.0 μM		42
5	gold nanoclusters (AuNCs)	5.0−1280 μM	3.5 μM		43
6	nitrogen-doped carbon dots	0.5−1000 μM	79 nM		44
7	N, S CQDs	25−500 μM	4.0 μM	2.85×10^3	45
8	f-WS_2-QDs	0−55 μM	1.32 μM	1.1×10^4	present work

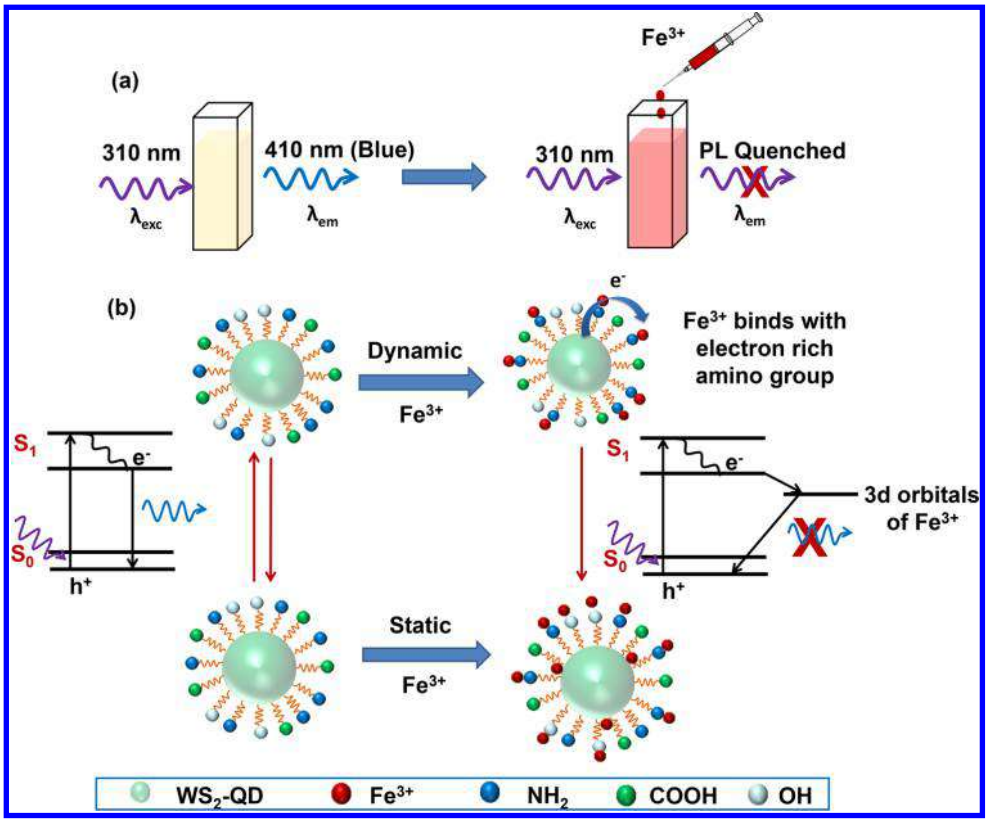

Figure 7. (a) and (b) showing the schematic representations of the fluorescence quenching of f-WS_2-QDs in the presence of Fe^{3+} ions and process of dynamic quenching and static quenching, respectively.

Figure 6b, where K_D and K_S are dynamic and static quenching constants.

$$K_{app} = \frac{\left(\frac{I_0}{I} - 1\right)}{[Q]} = (K_D + K_S) + K_D K_S[Q] \quad (3)$$

In this case again a positive deviation from S−V equation has been observed. This indicates that along with a ground state complex, few fluorophores are also present that do not form ground state complex but instead are quenched due to the presence of quencher in the close vicinity of fluorophore at the time of excitation. These closely spaced fluorophore−quencher pairs are quenched immediately at the time of excitation, resulting in dark complexes.[38] The formation of dark complexes in ground state is also supported from the absorption data of f-WS_2-QDs solution with gradual addition of Fe^{3+} ions, shown in Figure S4. From here it can be predicted that three types of fluorophores exist in the solution in which one is quenched through collisional and other two shows quenching in ground state.

Further, the specified quenching behavior can be determined through the time-resolved photoluminescence (TRPL) measurement. In order to distinguish the quenching behavior (dynamic/static), TRPL measurement was also carried out. Figure 6c represents the picosecond time-resolved transient with the successive addition of Fe^{3+} ion from 0 to 60 μM. It is observed from the fluorescence transients of f-WS_2-QD_S-Fe^{3+} system that the average lifetime (τ) decreases with the addition of Fe^{3+}. The exciton lifetime in TRPL measurement is fitted with eq 2 in Supporting Information, and it shows the triexponential decays. Lifetime corresponding to each triexponential decay (τ_1, τ_2, and τ_3) has been summarized in Table S2, and this triexponential decay signifies the presence of three types of fluorescing sites (as observed from modified S−V plot) present in the f-WS_2-QDs solution. It is observed that lifetime (τ_1) decreases from 0.74 to 0.42 ns with the increasing concentration of quencher (Fe^{3+}) from 0 μM to 60 μM. However, the decay times τ_2, and τ_3 remain nearly constant. Further, variation in relative change of fluorescence lifetime has been represented in the inset of Figure 6c. From here it is

DOI: 10.1021/acsanm.8b02162
ACS Appl. Nano Mater. 2019, 2, 566−576

evident that relative change in fluorescence lifetime corresponding to τ_1 shows linear variation and corresponding to τ_2 and τ_3 remaining nearly constant with increasing concentration of Fe^{3+} and fitted well with the eq 4.

$$\frac{\tau_0}{\tau} = 1 + K_q\tau_0[Q] = 1 + K_D[Q] \quad (4)$$

where K_q is the bimolecular quenching constant. From the slope of S−V plot in Figure 6c using eq 4, the obtained value of K_D is 1.1×10^4 M^{-1}. This indicates that ∼9.1 μM concentration of Fe^{3+} will be required to quench the 50% intensity of f-WS_2-QDs solution. The bimolecular quenching constant $K_q = 1.48 \times 10^{13}$ M^{-1} s^{-1} has been obtained using the values of fluorescence lifetime (τ_0) and S−V constant (K_D). The large value of K_q indicates the high efficiency of quenching and accessibility of the fluorophore to the quencher. Further, to verify the presence of three types of quenching species as obtained from TRPL characterization, PL spectra for different concentration of Fe^{3+} are deconvoluted and presented in Figure 6d. From here we can also see that each PL spectrum can be deconvoluted into three PL peaks, which also supports the presence of three types of quenching sites.

Various parameters obtained in the present work have been summarized in Table 1 and compared with other similar works, which suggest that our results are comparable to or better than the other reported works.

Mechanism for Fluorescence Quenching of f-WS_2-QDs in the Presence of Fe^{3+}. As discussed above from PL and TRPL data, we can conclude that the fluorescence quenching is taking place through both dynamic and static quenching process. Both quenching phenomena have been schematically represented in Figure 7. We hypothesized that the apparent static quenching can be attributed to the formation of iron hydroxide in ground state due to the presence of hydroxyl functional group over the surface of f-WS_2-QDs and also due to presence of Fe^{3+} in close proximity of f-WS_2-QDs.[46] However, the dynamic quenching can be attributed to the coordination of electron deficient Fe^{3+} with the electron (lone pair) rich amino groups present on the surface of f-WS_2-QDs in the excited state. Further, this coordination will support the electron transfer from the excited state S_1 of the f-WS_2-QDs to the half-filled 3d orbitals of Fe^{3+}. Now, since electron transfer from 3d orbitals of Fe^{3+} to the S_0 orbitals of f-WS_2-QDs is forbidden according to the selection rule, this leads to significant fluorescence quenching of f-WS_2-QDs.[47]

CONCLUSIONS

In summary, we demonstrated the "bottom-up" single-step hydrothermal growth of in situ functionalized fluorescent WS_2-QDs (average size of ∼5 nm), which are highly stable in aqueous medium without any subsequent treatments. Various structural and spectroscopic characterization techniques including TEM, HR-TEM, AFM, FT-IR, XPS, and Raman demonstrated that f-WS_2-QDs are few layered in nature having functional groups over its surface. The as-synthesized f-WS_2-QDs exhibited highly intense blue PL emission at λ_{em} ∼ 410 nm with an excitation wavelength of λ_{ex} ∼ 310 nm with a high PL quantum yield (Φ_{WS_2} ∼ 4.04%). This fluorescing nature of f-WS_2-QDs was successfully applied to devise an optical sensor for highly sensitive and selective detection of Fe^{3+} ions. Its fluorescence was quenched by ∼98% upon interacting with Fe^{3+}. Further, we elucidated in detail the fluorescence quenching kinetics of f-WS_2-QDs in the presence of Fe^{3+} ions. S−V plot (from PL titration data) and TRPL characterization revealed that the fluorescence quenching of f-WS_2-QDs is a mixed phenomenon of both static and dynamic in nature. The sensor response was found to be linear in the range of 0−55 μM with a lower detection limit of 1.32 μM, which is comparable to or better than those reported for the other fluorescent sensors for Fe^{3+}. Apart from this, S−V quenching constant $K_D = 1.1 \times 10^4$ M^{-1} was also calculated, which indicates that ∼9.1 μM concentration of Fe^{3+} would be required to quench 50% intensity of f-WS_2-QDs solution and larger value of $K_q = 1.48 \times 10^{13}$ M^{-1} s^{-1} indicates the high efficiency of quenching and accessibility of the fluorophore to the quencher. Hence, we believe that present investigation opened up a new avenue for the in situ growth of functionalized QDs with a potential for wide range of applications such as optical sensing, biosensing, and bioimaging, etc.

ASSOCIATED CONTENT

Supporting Information

The Supporting Information is available free of charge on the ACS Publications website at DOI: 10.1021/acsanm.8b02162.

FT-IR analysis of f-WS_2-QDs, quantum yield calculation of f-WS_2-QDs, LOD and linearity plot for the proposed optical sensor, UV−vis absorption titration data, and table containing decay life times of f-WS_2-QDs with increasing concentrations of Fe^{3+} ions (PDF)

AUTHOR INFORMATION

Corresponding Authors

*R.S.T.: e-mail, rstiwariphy@yahoo.com; phone, +91-9415991746.

*A.S.: e-mail, anchalbhu@gmail.com; phone, +91-9453203122.

ORCID

Arvind Misra: 0000-0003-2716-4139

Anchal Srivastava: 0000-0002-5804-6840

Notes

The authors declare no competing financial interest.

ACKNOWLEDGMENTS

V.K.S. acknowledges the UGC for providing Senior Research Fellowship (Fellowship Grant F.25-1/2014-15/(BSR)/5-127/2007/(BSR)). H.M. is thankful to CSIR, New Delhi, for providing an SRF fellowship (Fellowship Grant 09/013(0752)/2018-EMR-I). A.S. acknowledges DST, India (Project DST/TSG/PT/2012/68), DST-PURSE, SERB, India (Project EMR/2016/007720), and CAS-BHU for providing financial support. The authors acknowledge Bio-Physics Laboratory of Physics Department, Institute of Science, BHU, for access to the facilities for UV−vis, PL, and TRPL measurements.

REFERENCES

(1) Coleman, J. N.; Lotya, M.; O'Neill, A.; Bergin, S. D.; King, P. J.; Khan, U.; Young, K.; Gaucher, A.; De, S.; Smith, R. J.; et al. Two-Dimensional Nanosheets Produced by Liquid Exfoliation of Layered Materials. *Science* **2011**, *331*, 568−571.

(2) Chhowalla, M.; Shin, H. S.; Eda, G.; Li, L.-J.; Loh, K. P.; Zhang, H. The Chemistry of Two-Dimensional Layered Transition Metal Dichalcogenide Nanosheets. *Nat. Chem.* **2013**, *5*, 263.
(3) Xu, M.; Liang, T.; Shi, M.; Chen, H. Graphene-Like Two-Dimensional Materials. *Chem. Rev.* **2013**, *113*, 3766−3798.
(4) Butler, S. Z.; Hollen, S. M.; Cao, L.; Cui, Y.; Gupta, J. A.; Gutiérrez, H. R.; Heinz, T. F.; Hong, S. S.; Huang, J.; Ismach, A. F.; et al. Progress, Challenges, and Opportunities in Two-Dimensional Materials Beyond Graphene. *ACS Nano* **2013**, *7*, 2898−2926.
(5) Gutiérrez, H. R.; Perea-López, N.; Elías, A. L.; Berkdemir, A.; Wang, B.; Lv, R.; López-Urías, F.; Crespi, V. H.; Terrones, H.; Terrones, M. Extraordinary Room-Temperature Photoluminescence in Triangular WS_2 Monolayers. *Nano Lett.* **2013**, *13*, 3447−3454.
(6) Zhao, W.; Ghorannevis, Z.; Chu, L.; Toh, M.; Kloc, C.; Tan, P.-H.; Eda, G. Evolution of Electronic Structure in Atomically Thin Sheets of WS_2 and WSe_2. *ACS Nano* **2013**, *7*, 791−797.
(7) Jariwala, D.; Sangwan, V. K.; Lauhon, L. J.; Marks, T. J.; Hersam, M. C. Emerging Device Applications for Semiconducting Two-Dimensional Transition Metal Dichalcogenides. *ACS Nano* **2014**, *8*, 1102−1120.
(8) Molina-Sanchez, A.; Wirtz, L. Phonons in Single-Layer and Few-Layer MoS_2 and WS_2. *Phys. Rev. B: Condens. Matter Mater. Phys.* **2011**, *84*, 155413.
(9) Lin, L.; Xu, Y.; Zhang, S.; Ross, I. M.; Ong, A. C.; Allwood, D. A. Fabrication of Luminescent Monolayered Tungsten Dichalcogenides Quantum Dots with Giant Spin-Valley Coupling. *ACS Nano* **2013**, *7*, 8214−8223.
(10) Yan, Y.; Zhang, C.; Gu, W.; Ding, C.; Li, X.; Xian, Y. Facile Synthesis of Water-Soluble WS_2 Quantum Dots for Turn-On Fluorescent Measurement of Lipoic Acid. *J. Phys. Chem. C* **2016**, *120*, 12170−12177.
(11) Xu, S.; Li, D.; Wu, P. One-Pot, Facile, and Versatile Synthesis of Monolayer MoS_2/WS_2 Quantum Dots as Bioimaging Probes and Efficient Electrocatalysts for Hydrogen Evolution Reaction. *Adv. Funct. Mater.* **2015**, *25*, 1127−1136.
(12) Zhang, X.; Lai, Z.; Liu, Z.; Tan, C.; Huang, Y.; Li, B.; Zhao, M.; Xie, L.; Huang, W.; Zhang, H. A Facile and Universal Top-Down Method for Preparation of Monodisperse Transition-Metal Dichalcogenide Nanodots. *Angew. Chem., Int. Ed.* **2015**, *54*, 5425−5428.
(13) Nicolosi, V.; Chhowalla, M.; Kanatzidis, M. G.; Strano, M. S.; Coleman, J. N. Liquid Exfoliation of Layered Materials. *Science* **2013**, *340*, 1226419.
(14) Yong, Y.; Cheng, X.; Bao, T.; Zu, M.; Yan, L.; Yin, W.; Ge, C.; Wang, D.; Gu, Z.; Zhao, Y. Tungsten Sulfide Quantum Dots as Multifunctional Nanotheranostics for In Vivo Dual-Modal Image-Guided Photothermal/Radiotherapy Synergistic Therapy. *ACS Nano* **2015**, *9*, 12451−12463.
(15) Bai, X.; Wang, J.; Mu, X.; Yang, J.; Liu, H.; Xu, F.; Jing, Y.; Liu, L.; Xue, X.; Dai, H.; Liu, Q.; Sun, Y.-M.; Liu, C.; Zhang, X.-D. Ultrasmall WS_2 Quantum Dots with Visible Fluorescence for Protection of Cells and Animal Models from Radiation-Induced Damages. *ACS Biomater. Sci. Eng.* **2017**, *3*, 460−470.
(16) Gan, Z.; Liu, L.; Wu, H.; Hao, Y.; Shan, Y.; Wu, X.; Chu, P. K. Quantum Confinement Effects Across Two-Dimensional Planes in MoS_2 Quantum Dots. *Appl. Phys. Lett.* **2015**, *106*, 233113.
(17) Noh, M.; Kim, T.; Lee, H.; Kim, C.-K.; Joo, S.-W.; Lee, K. Fluorescence Quenching Caused by Aggregation of Water-Soluble CdSe Quantum Dots. *Colloids Surf., A* **2010**, *359*, 39−44.
(18) Sahoo, S. K.; Sharma, D.; Bera, R. K.; Crisponi, G.; Callan, J. F. Iron (III) Selective Molecular and Supramolecular Fluorescent Probes. *Chem. Soc. Rev.* **2012**, *41*, 7195−7227.
(19) Papanikolaou, G.; Samuels, M. E.; Ludwig, E. H.; MacDonald, M. L.; Franchini, P. L.; Dubé, M.-P.; Andres, L.; MacFarlane, J.; Sakellaropoulos, N.; Politou, M.; et al. Mutations in HFE2 Cause Iron Overload in Chromosome 1q-Linked Juvenile Hemochromatosis. *Nat. Genet.* **2004**, *36*, 77.
(20) Ong, W.-Y.; Farooqui, A. A. Iron, Neuroinflammation, and Alzheimer's Disease. *J. Alzheimer's Dis.* **2005**, *8*, 183−200.
(21) Tesfaldet, Z. O.; van Staden, J. F.; Stefan, R. I. Sequential Injection Spectrophotometric Determination of Iron as Fe(II) in Multi-Vitamin Preparations Using 1,10-Phenanthroline as Complexing Agent. *Talanta* **2004**, *64*, 1189−1195.
(22) Bobrowski, A.; Nowak, K.; Zarębski, J. Application of a Bismuth Film Electrode to the Voltammetric Determination of Trace Iron Using a Fe (III)−TEA−BrO_3− Catalytic System. *Anal. Bioanal. Chem.* **2005**, *382*, 1691−1697.
(23) Yokoi, K.; van den Berg, C. M. The Determination of Iron in Seawater Using Catalytic Cathodic Stripping Voltammetry. *Electroanalysis* **1992**, *4*, 65−69.
(24) Valeur, B.; Leray, I. Design Principles of Fluorescent Molecular Sensors for Cation Recognition. *Coord. Chem. Rev.* **2000**, *205*, 3−40.
(25) Wang, Y.; Ni, Y. Molybdenum Disulfide Quantum Dots as a Photoluminescence Sensing Platform for 2, 4, 6-Trinitrophenol Detection. *Anal. Chem.* **2014**, *86*, 7463−7470.
(26) Mishra, H.; Umrao, S.; Singh, J.; Srivastava, R. K.; Ali, R.; Misra, A.; Srivastava, A. pH Dependent Optical Switching and Fluorescence Modulation of Molybdenum Sulfide Quantum Dots. *Adv. Opt. Mater.* **2017**, *5*, 1601021.
(27) Li, X.; He, D.-W.; Wang, Y.-S.; Hu, Y.; Zhao, X.; Fu, C.; Wu, J.-Y. Facile and Controllable Synthesis of Molybdenum Disulfide Quantum Dots for Highly Sensitive and Selective Sensing of Copper Ions. *Chin. Phys. B* **2018**, *27*, No. 056104.
(28) Atkin, P.; Daeneke, T.; Wang, Y.; Carey, B.; Berean, K.; Clark, R.; Ou, J.; Trinchi, A.; Cole, I.; Kalantar-Zadeh, K. 2D WS_2/Carbon Dot Hybrids with Enhanced Photocatalytic Activity. *J. Mater. Chem. A* **2016**, *4*, 13563−13571.
(29) Ghorai, A.; Bayan, S.; Gogurla, N.; Midya, A.; Ray, S. K. Highly Luminescent WS_2 Quantum Dots/ZnO Heterojunctions for Light Emitting Devices. *ACS Appl. Mater. Interfaces* **2017**, *9*, 558−565.
(30) Zeng, H.; Liu, G.-B.; Dai, J.; Yan, Y.; Zhu, B.; He, R.; Xie, L.; Xu, S.; Chen, X.; Yao, W.; Cui, X. Optical Signature of Symmetry Variations and Spin-Valley Coupling in Atomically Thin Tungsten Dichalcogenides. *Sci. Rep.* **2013**, *3*, 1608.
(31) Martinez, H.; Benayad, A.; Gonbeau, D.; Vinatier, P.; Pecquenard, B.; Levasseur, A. Influence of The Cation Nature of High Sulfur Content Oxysulfide Thin Films Moysz (M= W, Ti) Studied by XPS. *Appl. Surf. Sci.* **2004**, *236*, 377−386.
(32) Audi, A. A.; Sherwood, P. X-Ray Photoelectron Spectroscopic Studies of Sulfates and Bisulfates Interpreted by X_α and Band Structure Calculations. *Surf. Interface Anal.* **2000**, *29*, 265−275.
(33) Volynsky, A. B.; Stakheev, A. Y.; Telegina, N. S.; Senin, V. G.; Kustov, L. M.; Wennrich, R. Low-Temperature Transformations of Sodium Sulfate and Sodium Selenite in the Presence of Pre-Reduced Palladium Modifier in Graphite Furnaces for Electrothermal Atomic Absorption Spectrometry. *Spectrochim. Acta, Part B* **2001**, *56*, 1387−1396.
(34) Hsieh, C.-T.; Tzou, D.-Y.; Hsieh, K.-Y.; Yin, K.-M. Photoluminescence from Amino Functionalized Graphene Quantum Dots Prepared by Electrochemical Exfoliation Method in the Presence of Ammonium Ions. *RSC Adv.* **2017**, *7*, 18340−18346.
(35) Bertus, L.; Faure, C.; Danine, A.; Labrugère, C.; Campet, G.; Rougier, A.; Duta, A. Synthesis and Characterization of WO_3 Thin Films by Surfactant Assisted Spray Pyrolysis for Electrochromic Applications. *Mater. Chem. Phys.* **2013**, *140*, 49−59.
(36) Shortreed, M.; Kopelman, R.; Kuhn, M.; Hoyland, B. Fluorescent Fiber-Optic Calcium Sensor for Physiological Measurements. *Anal. Chem.* **1996**, *68*, 1414−1418.
(37) Kim, M. H.; Jang, H. H.; Yi, S.; Chang, S.-K.; Han, M. S. Coumarin-Derivative-Based Off−On Catalytic Chemodosimeter for Cu^{2+} Ions. *Chem. Commun.* **2009**, 4838−4840.
(38) Mahata, P.; Mondal, S. K.; Singha, D. K.; Majee, P. Luminescent Rare-Earth-Based Mofs as Optical Sensors. *Dalton Transactions* **2017**, *46*, 301−328.
(39) Aslandaş, A. M.; Balcı, N.; Arık, M.; Şakiroğlu, H.; Onganer, Y.; Meral, K. Liquid Nitrogen-Assisted Synthesis of Fluorescent Carbon Dots from Blueberry and their Performance in Fe^{3+} Detection. *Appl. Surf. Sci.* **2015**, *356*, 747−752.

DOI: 10.1021/acsanm.8b02162
ACS Appl. Nano Mater. 2019, 2, 566−576

(40) Fan, K.; Bao, S.-S.; Nie, W.-X.; Liao, C.-H.; Zheng, L.-M. Iridium(III)-Based Metal−Organic Frameworks as Multiresponsive Luminescent Sensors for Fe^{3+}, $Cr_2O_7^{2-}$, and ATP^{2-} in Aqueous Media. *Inorg. Chem.* **2018**, *57*, 1079−1089.
(41) Dutta Chowdhury, A.; Doong, R.-a. Highly Sensitive and Selective Detection of Nanomolar Ferric Ions Using Dopamine Functionalized Graphene Quantum Dots. *ACS Appl. Mater. Interfaces* **2016**, *8*, 21002−21010.
(42) Chandra, S.; Laha, D.; Pramanik, A.; Ray Chowdhuri, A.; Karmakar, P.; Sahu, S. K. Synthesis of Highly Fluorescent Nitrogen and Phosphorus Doped Carbon Dots for the Detection of Fe^{3+} Ions In Cancer Cells. *Luminescence* **2016**, *31*, 81−87.
(43) Annie Ho, J.-a.; Chang, H.-C.; Su, W.-T. DOPA-Mediated Reduction Allows the Facile Synthesis of Fluorescent Gold Nanoclusters for Use as Sensing Probes for Ferric Ions. *Anal. Chem.* **2012**, *84*, 3246−3253.
(44) Lv, P.; Yao, Y.; Zhou, H.; Zhang, J.; Pang, Z.; Ao, K.; Cai, Y.; Wei, Q. Synthesis of Novel Nitrogen-Doped Carbon Dots for Highly Selective Detection of Iron Ion. *Nanotechnology* **2017**, *28*, 165502.
(45) Ding, H.; Wei, J.-S.; Xiong, H.-M. Nitrogen and Sulfur Co-Doped Carbon Dots with Strong Blue Luminescence. *Nanoscale* **2014**, *6*, 13817−13823.
(46) Zhu, X.; Zhang, Z.; Xue, Z.; Huang, C.; Shan, Y.; Liu, C.; Qin, X.; Yang, W.; Chen, X.; Wang, T. Understanding the Selective Detection of Fe^{3+} Based on Graphene Quantum Dots as Fluorescent Probes: the K_{sp} of a Metal Hydroxide-Assisted Mechanism. *Anal. Chem.* **2017**, *89*, 12054−12058.
(47) Wu, Q.; Wang, X.; Jiang, Y.; Sun, W.; Wang, C.; Yang, M.; Zhang, C. MoS_2-QD-Based Dual-Model Photoluminescence Sensing Platform for Effective Determination of Al^{3+} and Fe^{3+} Simultaneously in Various Environment. *ChemistrySelect* **2018**, *3*, 2326−2331.

DOI: 10.1021/acsanm.8b02162
ACS Appl. Nano Mater. 2019, 2, 566−576

Analytical Methods

PAPER

View Article Online
View Journal

Cite this: DOI: 10.1039/c4ay01303d

Mesoporous silica particle embedded functional graphene oxide as an efficient platform for urea biosensing

Shiju Abraham,[ab] Valerian Ciobota,[b] Saurabh Srivastava,[ac] Sunil K. Srivastava,[d] Rajesh K. Singh,[e] Jan Dellith,[f] B. D. Malhotra,[g] Michael Schmitt,[b] Jürgen Popp*[b] and Anchal Srivastava*[a]

The mesoporous silica particle embedded graphene oxide (GO) hybrid system is a promising platform for electrochemical biosensing owing to its large 2-dimensional structure, fast electron transfer kinetics, improved hydrophilic nature and surplus functional groups. Here, GO sheets were synthesized by Hummer's improved method and sub-micron sized homogeneous mesoporous silica (SiO_2) particles were prepared by Stober's method. The SiO_2 particles were embedded on the GO surfaces and were optimized with different concentrations for better applicability and hydrophilicity. Micro-structural and spectroscopic characterization of as-synthesized materials was carried out to confirm the successful synthesis as well as the functionalities required for biosensing. Scanning electron microscopy investigations suggest that the average size of the SiO_2 particles decorated on the GO surface is ~500 nm. Raman investigation provides information regarding the increase in defects and disorder on the GO surface with the increase in the SiO_2 content. The optimized GO–SiO_2 (GOS) composite electrode was prepared by the electrophoretic deposition technique and was used for the attachment of urease and glutamate dehydrogenase enzymes for urea detection employing the cyclic voltammetry method. The reproducibility, specificity and stability of the fabricated biosensor were found to be excellent for the urea sensing. Such an easy and cost effective material based GOS urea sensor showed a high sensitivity (2.6 μA mM^{-1} cm^{-2}) and a good detection limit (14 mg dL^{-1}).

Received 30th May 2014
Accepted 16th June 2014

DOI: 10.1039/c4ay01303d

www.rsc.org/methods

Introduction

The estimation of urea in serum, blood and urine is very important for the diagnosis of renal and liver diseases. An increase in the urea level (normal range in blood is 15–40 mg dL^{-1}) causes renal failure, urinary tract obstruction, dehydration, shock, burns, gastrointestinal bleeding, *etc.* Development of a sensitive, selective, reliable and low cost material based biosensor is of great importance for the diagnosis and management of urea. In recent years nanomaterial based electrochemical biosensors have attracted wide popularity and applicability due to their good selectivity, portability, inexpensiveness and simplicity. The two-dimensional (2D) nanomaterials, graphene and its derivative-graphene oxide (GO), have been attracting the attention of researchers from various disciplines in the last decade after the successful isolation of a single layer of graphite on an insulating silica (SiO_2) substrate.[1–4] Apart from graphene, there has been a great upsurge of interest towards studying GO, a heavily oxygenated graphene derivative.[5] These materials are now in the forefront of attention as a novel cousin of graphene.[6–9] The excellent solubility, stability against aggregation, large surface area, *etc.* of GO have led to many interesting applications, such as electrochemical sensing, electro catalysis, immunoassays, *etc.*[10–12] Further, since most of the atoms of the surface of the GO sheet are exposed, slight changes in the local charge environment due to the adsorption of biomolecules provide significant changes in their electrical properties.[13] This will be more pronounced when biocompatible, porous particles are embedded on the GO surfaces. These interesting properties by the synergetic effects may perhaps be utilized in the fabrication of more sensitive and selective biosensors.

In view of the special characteristics of GO, several nanoparticles (NPs) (such as SiO_2, Au, Ag, Pt, TiO_2 *etc.*)[14–18] have been

[a]Department of Physics, Banaras Hindu University, Varanasi, 221005, India. E-mail: anchalbhu@gmail.com; Fax: +91-542-2368174; Tel: +91-9453203122

[b]Institute of Physical Chemistry, Friedrich-Schiller-University Jena, Helmholtzweg 4, D-07743 Jena, Germany

[c]Department of Science and Technology Centre on Biomolecular Electronics, Biomedical Instrumentation Section, National Physical Laboratory, New Delhi 110012, India

[d]Department of Pure and Applied Physics, Guru Ghasidas University, Main Campus, Koni, Bilaspur 495009, India

[e]Department of Applied Physics, Indian Institute of Technology (B. H. U.), Varanasi, 221005, India

[f]Institute of Photonics Technology, Albert-Einstein-Str. 9, D-07445, Germany

[g]Department of Biotechnology, Delhi Technological University, Delhi 11042, India

introduced onto the surface of GO and thereby giving rise to novel nano-hybrid materials with unique properties and intriguing applications. SiO_2, a typical non-metallic oxide, is of special interest due to its widespread use as a cost-effective material in the construction of super hydrophilic/super hydrophobic surfaces. Among the various oxide NPs, it has been found that the control of size as well as porosity in SiO_2 particles is comparatively easy. The well-defined surface properties of SiO_2 particles are beneficial for site-specific delivery of different functional molecules of various sizes and shapes.[19] The high porosity of SiO_2 particles, which results in large surface area available for the encapsulation as well as for the immobilization of various sensing molecules leading to fast response time and low detection limit.[20,21] SiO_2 dispersion plays a major role in several applications like catalysts, membranes, biocompatible solid support, *etc.*[22,23] Further it has been found to be a suitable candidate for many biological applications owing to its good biocompatibility, enhanced electrochemical properties and excellent enzymatic activity in the respective enzyme reactions.[20,24,25] While considering the composite formulation and studies, silver NPs/functionalized SiO_2–GO composite is demonstrated to be a potential candidate for biosensing in glucose detection.[26] According to Watcharotone *et al.*,[27] graphene–silica composite thin films have several potential applications owing to their conducting and transparent properties. Kou and Gao[28] synthesized SiO_2 NPs covered GO hybrids and showed that GO–SiO_2 hybrids exhibit excellent hydrophilic nature and can be used as a building block to construct large area super hydrophilic surfaces. Liu *et al.*[29] studied the surface assembly of GO nanosheets on SiO_2 particles, and used this composite for the selective isolation of hemoglobin. Considering the above studies, the GOS composite system is of much interest because of its high solubility in water, easy synthesis, bulk production and abundant functional groups. The biocompatible, stable and porous SiO_2 particles combine with the compatible properties of GO, making the hybrid system (GOS) well suited for many applications, especially in biosensing where the composite has not been explored well.

While keeping all the above factors in mind, the work presented in this report is about the synthesis and fabrication of the thin film of the GOS composite onto an indium tin oxide (ITO) glass substrate by the electrophoretic deposition (EPD) technique. These thin films have been further used to immobilize urease (Urs) and glutamate dehydrogenase (GLDH) for urea detection by the cyclic voltammetry (CV) technique. The fabricated bioelectrode showed good stability, specificity as well as reproducibility. This GOS based urea sensor shows a high sensitivity (2.6 $\mu A\ mM^{-1}\ cm^{-2}$) and a good detection limit (14 $mg\ dL^{-1}$) compared to many other reports.

Experimental

Chemicals

Tetra ethyl *ortho*-silicate (TEOS, Aldrich, purity ≥ 99% with trace metal basis), graphite flakes (NGS Naturgraphit GmbH, Germany), ammonia solution, ethanol, H_2SO_4, H_3PO_4, $KMnO_4$, H_2O_2, *etc.* used were of analytical reagent grade. All the chemicals employed for the fabrication of the urea biosensor, namely, Urs, GLDH, nicotinamide adenine dinucleotide (NADH) and α-ketoglutarate (α-KG), were procured from Sigma-Aldrich.

Synthesis of GO and SiO_2 particles

Few years ago, an improved method for producing GO was proposed by Marcano *et al.*[30] This method has some distinct advantageous features over Hummers' method[6] in the sense that it yields a higher fraction of the hydrophilic carbon material. In the improved synthesis of GO, a 9 : 1 combination of concentrated H_2SO_4/H_3PO_4 (120 mL/13.33 mL) was added to 1 g of graphite flakes and 6 g of $KMnO_4$. The above mixing process created a slight exothermic reaction, and the mixture was stirred for 12 h keeping a constant temperature of 50 °C. The reaction was subsequently quenched by adding ~135 mL of ice with 30% H_2O_2. This mixture was then shifted, centrifuged and filtered. The solid material thus obtained (GO) was washed with 30% HCl and distilled water until pH ~ 7 was reached, then the material was dried. SiO_2 particles were synthesized by the well-known Stober's method.[21] Briefly, 120 mL of ethanol (98%) was taken in a round-bottom flask and 24 mL of ammonia solution was added to it. This solution was kept for stirring and after 20 minutes, the sol gel reaction was initiated by adding 12 mL of TEOS. The stirring was continued for 10 h until the solution gradually turned white in colour. The above colloidal solution of SiO_2 particles was used to decorate the surface of GO. The remaining solution was centrifuged at the rate of 3000 rpm for 30 minutes. The solid material collected was washed with ethanol and then dried at 80 °C. The final solid product obtained was used for further characterizations.

Production of GOS

The as synthesized GO was well dispersed (0.35 $mg\ mL^{-1}$) in double distilled water by continuous ultra-sonication for an hour. The SiO_2 dispersion was prepared in ethanol at a concentration of 20 $mg\ mL^{-1}$. Four composite solutions were prepared by taking a constant amount of the above GO solution (25 mL each) and varying the amounts of SiO_2 solution [250 μL (~5 mg), 500 μL (~10 mg), 750 μL (~15 mg) and 1000 μL (~20 mg)]. These composite solutions are abbreviated as GOS1, GOS2, GOS3 and GOS4 respectively. The mixture solution was then sonicated continuously for an hour by gradually increasing the temperature to 60 °C. The solution was then subsequently stirred for 4 h and centrifuged. Finally the solution was washed with ethanol, distilled water and then dried at 70 °C to get the solid product GOS. Among the four GOS composites, GOS3 was found to be more hydrophilic in nature and showed good film forming capabilities.

Fabrication of GOS thin film electrodes

Thin films of nanostructured GOS over ITO electrodes were formed by the EPD technique. Here a 10 mL colloidal solution of GOS3 (3 $mg\ dL^{-1}$) in acetonitrile is added to a two-electrode glass cell. A platinum foil (1 × 2 cm) was used as the counter electrode and a pre-cleaned ITO-coated glass substrate having a

sheet resistance of 30 Ω as the working electrode; both electrodes were separated by 1 cm. The film deposition was carried out onto the desired ITO-coated glass plate (0.25 cm^2) by applying a DC voltage of 120 V for 2 minutes. 10^{-5} to 10^{-4} mol of $Mg(NO_3)_2 \cdot 6H_2O$ was added to the colloidal suspension acting as an electrolyte and creating surface charge on the GOS3 desired for EPD. The two electrodes were placed parallel to each other and were dipped in the GOS3 colloidal suspension. The film was deposited onto the desired ITO-coated glass plate. The film was then removed from the suspension followed by washing with deionized water and drying.

Solution preparation and immobilization of enzyme

Urs (10 mg mL^{-1}) and GLDH (1 mg dL^{-1}) solutions were freshly prepared in the phosphate buffer (50 mM, pH ~ 7.0). A stock solution of urea (200 mg dL^{-1}) was prepared in deionized water and was kept at 4 °C. This stock solution was used to get different concentrations of urea by further dilution. NADH (3.7 mg dL^{-1}) and α-KG (47.5 mg dL^{-1}) were freshly prepared in double distilled water. Further, 10 μL of bienzyme solution containing Urs (10 mg mL^{-1}) and GLDH (1 mg mL^{-1}) in a 1 : 1 ratio was covalently immobilized by uniformly spreading on the activated electrode surface and incubating it for about 12 h. The immobilization occurs through the surface adsorption as well as through the formation of the amide bond between the terminal COOH group of GO and the terminal NH_2 group of the enzyme. The Urs-GLDH/GOS/ITO bioelectrode was then washed with PBS buffer and stored at 4 °C when not in use. This enzymatic electrode was utilized for urea detection using the cyclic voltammetric (CV) technique.

Characterization

The structures of GO, SiO_2 and GOS composites were characterized by the X-ray diffraction (XRD) technique (Rigaku miniflex-II diffractometer at 30 kV and 15 mA) using Cu-Kα1 radiation (λ = 1.5405 Å). The surface morphology of the samples prepared was investigated using scanning electron microscopy employing JEOL – Model JSM6300F-SEM. The molecular structure of the material was investigated using Fourier transform infrared (FT-IR) spectroscopy (Perkin Elmer Spectrum 65, FT-IR spectrometer). Raman spectroscopic measurement was made by using two different Raman spectrometers. One by using a single monochromator (TRIAX 550, JobinYvon, France) with the 514.5 nm line from an Ar laser (Innova 308 Series, Coherent, USA) as a Raman excitation source. Another Raman spectrometer (HR LabRam inverse system, JobinYvon Horiba) with a Raman excitation source of wavelength 532 nm from a frequency doubled Nd:YAG laser was used. The electrochemical studies related to urea detection were carried out on an Autolab potentiostat/galvanostat (Eco Chemie, The Netherlands). The measurements were carried out using a three electrode cell with the Urs-GLDH/GOS/ITO bioelectrode as the working electrode, platinum (Pt) as the counter electrode, and a Ag/AgCl electrode as the reference electrode in 50 mM phosphate buffer saline (PBS) of pH 7.0 containing 5 mM of $[Fe(CN)_6]^{3-/4-}$.

Results and discussion

Structural characterization

The XRD patterns of the three materials, namely GO, SiO_2 and GOS3 composite, are presented in Fig. 1.

The GO shows a peak at 10.4° (002) (corresponding to a *d*-spacing of 0.85 nm), which matches with the well-known XRD peak of GO.[28] GO also shows a weak broad peak at 22.7°, which has nearly one eighth of the integrated intensity of the main GO peak. This weak XRD peak interpreted in terms of the short-range order in the stacked graphene like sheets.[31] The XRD pattern of SiO_2 particles that the peak centered at 22.8° (JCPDS File no. 47-1301) is relatively broad and is attributed to its more amorphous nature as well as its quite large particle size distribution [between 300 and 500 nm, as seen from the SEM micrograph shown in Fig. 2(b)]. In the case of the composite system, GOS3, the analyzed XRD pattern gives rise to two peaks at 10.8 (corresponding to a *d*-spacing of 0.82 nm) and 22.7°. The interlayer spacing decreases (from 0.85 to 0.82 nm) when GO transforms into GOS.

SEM images of the GO, SiO_2 particles and their different composite systems presented in Fig. 2(a)–(f) reveal interesting features about their morphology and microstructure. The SEM micrograph shown in Fig. 2(a) supports the formation of a uniform GO sheet of different layers, with wrinkles marked by arrows. From Fig. 2(b), it is evident that the size of the SiO_2 particles is ~500 nm and the distribution of the particle size is quite narrow. For any practical application, optimization of the concentration of SiO_2 particles on the GO sheet is required. This provides an opportunity to study the properties of the GOS composite with varying concentration of SiO_2 particles. As the concentration of SiO_2 particles is varied from GOS1 to GOS4 (250 to 1000 μL), the density of the SiO_2 particles decorated on the GO sheet increases, which is evident from Fig. 2(c)–(f). Fig. 2(f) shows the extreme case wherein SiO_2 particles are densely packed one above another. The porous nature of the silica particles is visible from Fig. 2(f). The pore diameter varies

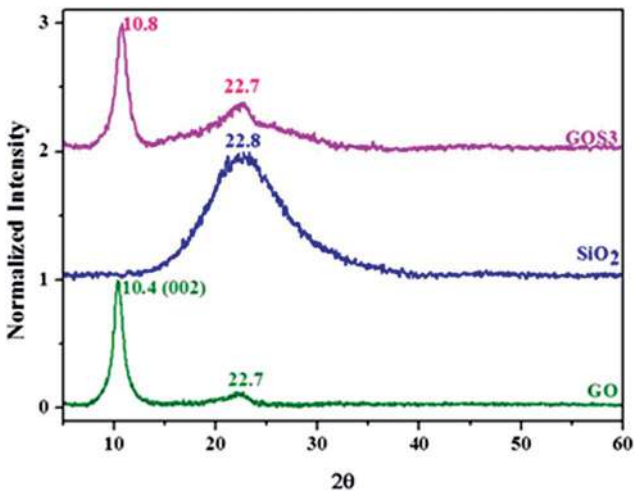

Fig. 1 X-ray diffraction (XRD) patterns of (i) GO sheets, (ii) SiO_2 particles, and (iii) GOS3.

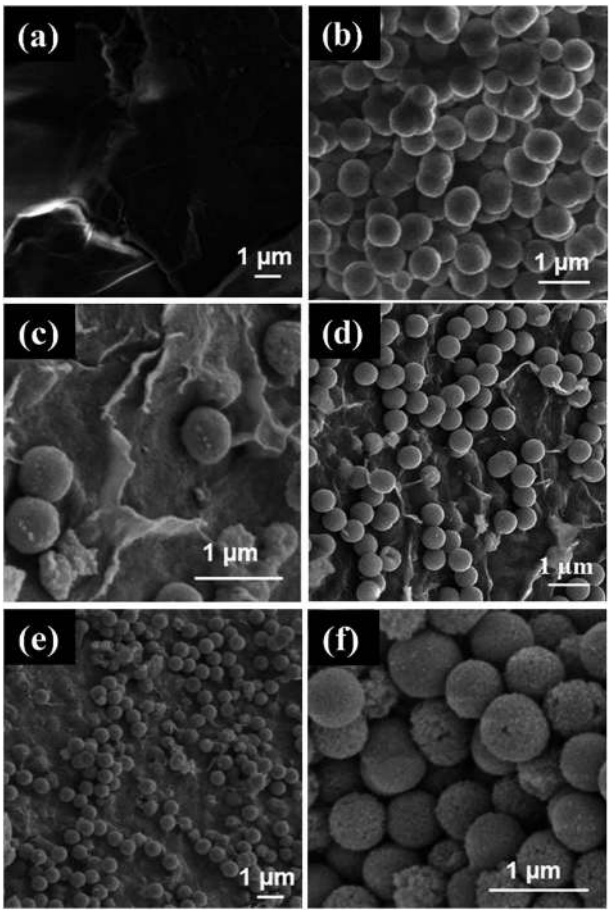

Fig. 2 SEM micrograph of (a) GO synthesized by improved Hummer's method, (b) Stober's SiO_2 particles, (c–f) SiO_2 particle decorated GO with increasing concentration of the SiO_2 content (c) GOS1, (d) GOS2, (e) GOS3, and (f) GOS4.

approximately in a range of 2–6 nm [Brunauer–Emmett–Teller (BET) pore size analysis gives an average pore diameter ~5 nm]. The porous nature enhances its surface area further and allows higher loading of biomolecules (enzymes) for the effective sensing of a particular analyte. Here the pores work as a better substrate for maximum loading.

Spectroscopic characterization

The FTIR spectra of GO, SiO_2 particles and the four GOS composites are presented in Fig. 3(a). Fig. 3(a)(i) shows the FTIR spectra of GO, which have different hydrophilic functional groups attached to graphene. A broad band extending from nearly 2800 to 4000 cm^{-1} appears in all the spectra [see spectra (i) to (vi) in Fig. 3(a)] due to O–H stretching vibration from the different species. A weak band at 2928 cm^{-1} observed in the IR spectra of GO [Fig. 3(a)(i)] is attributed to the C–H stretching mode of the carboxylic group. A band at 1110 cm^{-1} observed in GO corresponds to the C–O stretching vibration of the alkoxide group and the C–O stretching vibration due to the carboxylic group is observed at ~1400 cm^{-1}. An interesting feature of this study is that the intensity of the IR band arising due to the presence of the carboxylic functional group decreases as the concentration of SiO_2 increases. However, this decrease is accompanied by a simultaneous significant increase in the relative intensity of the IR band at ~1100 cm^{-1} corresponding to the C–O stretching vibration of the alkoxide group. It is worth mentioning that the carboxylic C–O stretching and the alkoxy C–O stretching vibrations which appear in the IR spectra are essentially due to the different functional groups situated at the edges of the GO sheet. Besides this, the spectra of the different GOS composites also show a prominent band at 1632 cm^{-1} which has been attributed to the scissor type O–H bending vibration of molecular H_2O. The intensity of this band is the largest in the case of GO and shows a decreasing trend for the increasing SiO_2 concentration. The broad peak around 1725 cm^{-1} represents the stretching vibration of the C=O bond of the carboxylic acid group. The three IR peaks, which appear in Fig. 3(a)(vi) below 1100 cm^{-1}, are the characteristic peaks of the Si–O–Si bonds. The most intense of these three peaks, which also appears at the highest wavenumber position at ~1070 cm^{-1}, corresponds to the anti-symmetric Si–O–Si stretching vibration (TO_3 mode).[32] The second IR band observed at 953 cm^{-1} can be assigned to the Si–OH stretching vibration.[33] The third IR peak at 803 cm^{-1} was assigned to the Si–O–Si symmetric stretching (TO_2 mode) vibration. These characteristic functional groups of GO and SiO_2 are beneficial for their nice binding and also for the immobilization of enzyme. The Raman spectra of SiO_2 have been recorded using 532 nm excitation (see the lower frame of Fig. 3(a)). Two prominent Raman bands at ~800 and ~970 cm^{-1} are observed, which match nicely with the IR absorption bands for the Si–O–Si symmetric stretching and Si–OH stretching vibrations, respectively. The Raman measurement was basically done to compare the IR and Raman wavenumber of the vibrational modes of SiO_2 alone. These peaks are well resolved and appear with sufficient intensity in the IR as well as Raman spectra of SiO_2, whereas in the IR spectra of the composite having different concentrations of SiO_2, the Si–OH stretching band appears with a very feeble intensity which diminishes drastically for decreasing SiO_2 concentration.

Raman spectroscopy is very well suited to distinguish between sp^2 and sp^3 hybridization in carbonaceous materials.[34,35] The two main characteristic Raman bands observed in almost all carbon-based materials are the G-band and the D-band. The G peak only disperses in more disordered carbon, where the dispersion is proportional to the degree of disorder. Kudin *et al.*[34] observed and reported the broadening of the G band in the functionalized graphene sheet and GO. The D-band (disorder-induced band) around 1350 cm^{-1} in the defected graphite originates from the one-phonon second order Raman scattering process. The Raman spectra of GO and GOS composites were excited with a 514 nm laser and are shown in Fig. 3(b)(i–v).

Raman spectra were fitted to three component bands namely D, G1 and G2 bands by using Spectra Calc software and the results are presented in Table 1. In Spectra Calc analysis, the guess values for the peak positions and line widths of the stipulated Raman bands are given as input. A non-linear least square fit assumes an appropriate intensity for each peak and the measured Raman profile is fitted (using a mixture of

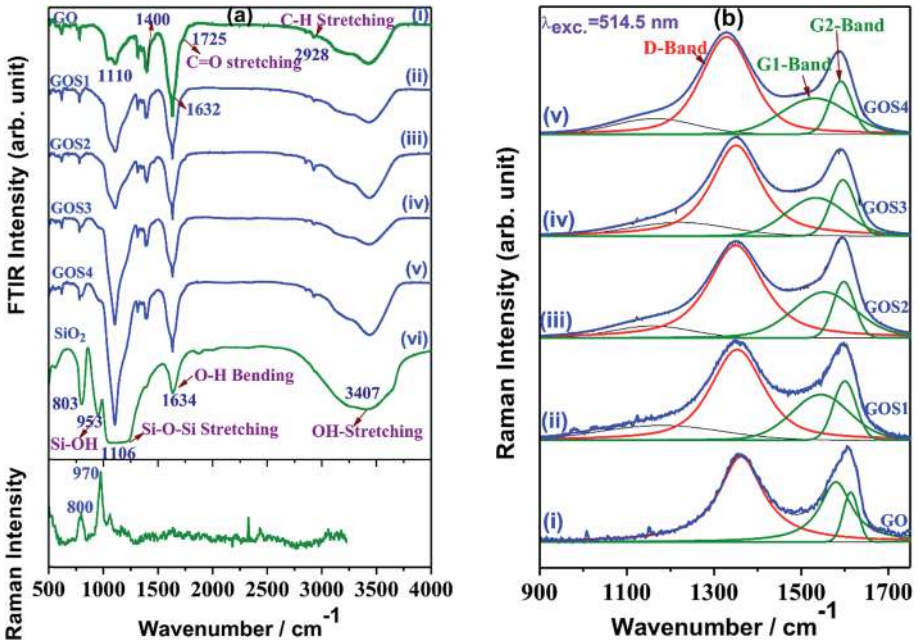

Fig. 3 (a) FTIR spectrum of (i) GO, (ii) GOS1, (iii) GOS2, (iv) GOS3, (v) GOS4, and (vi) SiO_2 particles and in the lower frame: Raman spectra of SiO_2 particles excited by 532 nm. (b) Raman spectra of (i) GO, (ii) GOS1, (iii) GOS2, (iv) GOS3 and (v) GOS4 showing the component bands D, G1 and G2.

Lorentzian/Gaussian) to get the peak position, linewidth and intensity of all the peaks. The analysis of the Raman spectra of GOS4 is missing in Table 1 as the GO surface is fully covered with SiO_2 particles [evident from the SEM image in Fig. 2(f)]. The G-band, which is the characteristic vibration of the sp^2 carbon in most of the carbon-based materials, is split into two components, G1 and G2. In a study[2] on functionalized multi-layered graphene (MLG), it has been pointed out that the splitting of the G band probably results from the presence of functional groups, which might change the curvature of the graphene layers. For the GO and GOS composite studied in the present case, this splitting is likely to be caused by the presence of the functional groups like epoxy, carbonyl, *etc.* Further, in the present study, for the SiO_2 decorated GO sheet, generally the G-band exhibits a shift towards lower wave number (from GO to GOS3) due to hybridization of GO sheets with the electron donor SiO_2. It has to be noted that such observation was also reported by Zhu *et al.*[36] in a study on GO enwrapped Ag/AgX composites.

Table 1 Peak position of the D and G (G1 and G2) Raman bands and I_D/I_G (by area) of GO and GOS composite measured using 514.5 nm excitation wavelength

Name of the sample	Peak position at 514.5 nm excitation wavelength			
	D	G1	G2	I_D/I_G
GO	1362	1580	1614	1.19
GOS1	1353	1545	1600	1.34
GOS2	1350	1553	1598	1.67
GOS3	1350	1534	1596	2.20

The intensity ratio, I_D/I_G, is a measure of the sp^3 disorder caused by functionalization and also the wrinkled morphology of GO. The increase in the value of the I_D/I_G ratio indicates the increase in disorder in the graphite material.[37] If we carefully examine the Raman spectra, when we go from GO to GOS3, the D-band shifts towards the lower wavenumber side, *i.e.* from 1362 to 1350 cm^{-1} and the G2 peak shows a similar red shift from 1614 to 1596 cm^{-1}. This indicates that upon increasing the SiO_2 content, the composite system modified significantly and has good impact on its increase in disorder. Keeping the above facts in mind, it is worth discussing the finding by Kou *et al.*[28] regarding the linkage between GO and SiO_2. According to them, silica particles non-covalently attached to carbon nanotubes did not lead to any significant band shift or relative intensity variation within the Raman D-band. The increase of the D band relative intensity in the GOS system indicates that the silica particles are deposited on the surfaces of GO through some covalent linkage. The above mentioned things are more clear from the I_D/I_G (by area) values, which increases from GO to GOS3 (1.19 to 2.20). This point can be further strengthened by the fact that the FWHM of the G1 and D-bands exhibits a broadening nature in most of the cases in our study while going from pure GO to GOS with higher SiO_2 concentration. Thus, one can conclude that the spectral features of SiO_2 decorated GO sheets clearly exhibit a shift from sp^2 hybridization on carbon atoms to sp^3 while going from GO to GOS3, and also they are binded to each other strongly.

Electrochemical characterization

The electrochemical biosensors function by the production and monitoring of current when a potential is applied between the two electrodes. In second generation biosensors (mediated

biosensors), the enzymes can donate electrons to electrochemically active electron acceptors. The efficiency and sensitivity of such biosensors can be greatly enhanced using a suitable mediator.[38,39] The $Fe^{3+/2+}$ redox couple utilized here exhibits well-defined redox properties. It helps in the facile electron transfer arising from the biochemical reactions between the analyte (urea here) and enzymes (Urs-GLDH here), at lower oxidation potentials.

Fig. 4 shows a schematic representation of the electrochemical sensing set up used for urea sensing. This schematic sketch illustrates the procedure for the GOS electrode formation, immobilization with Urs-GLDH and detection of analytes using the CV technique.

Fig. 5(a) shows CV studies of ITO, GO/ITO, SiO_2/ITO, GOS/ITO and Urs-GLDH/GOS/ITO electrodes that have been conducted in PBS (pH = 7) containing 5 mM $[Fe(CN)_6]^{3-/4-}$ using an Autolab, potentiostat/galvanostat. The oxidation peak current of ITO is 46.2 μA, being reduced to 43.3 μA for GO due to the insulating nature of GO and it is further decreased to 39.4 μA for SiO_2. However, it has been observed that the current increases to 49 μA in the case of the GOS/ITO electrode, indicating the electrocatalytic activity of SiO_2 that results in improved electron transport property of GO. Resulting in the high oxidation peak current among other electrodes fabricated, GOS is taken as the working electrode for the present investigation on urea sensing. After the enzyme immobilization on GOS, the response current further decreases to 35.3 μA. The Urs-GLDH bienzyme has the macromolecular structure and the redox active sites that are deeply embedded in this macromolecular structure. Besides this, the insulating characteristic of these enzymes results in reduced current. Furthermore because of the reduced conductivity of the Urs-GLDH/GOS/ITO bioelectrode, the oxidation peak potential shifts more towards a positive potential (0.371 V) as compared to that of the GOS/ITO electrode (0.347 V). Further, the peak separation between the oxidation and reduction peak currents obtained for the GOS/ITO electrode (90.3 μA) have been found to be higher as compared to their counterparts GO/ITO (77.8 μA) and SiO_2/ITO (74 μA). Fig. 5(b) shows CVs of the Urs-GLDH/GOS/ITO bioelectrode obtained as a function of the scan rate from 10 to 100 mV s^{-1}. A proportional increase of the redox current with respect to the square root of the scan rate is observed, indicating a diffusion controlled system following eqn (1) and (2).

$$I_a\,[A] = 2.1 \times 10^{-6}\,[A] + 5.9 \times 10^{-6}\,[A^2\ s\ mV^{-1}]^{1/2} \times \{\text{scan rate (mV s}^{-1})\}^{1/2} \quad (1)$$

$$I_c\,[A] = -8.6 \times 10^{-6}\,[A] - 3.3 \times 10^{-6}\,[A^2\ s\ mV^{-1}]^{1/2} \times \{\text{scan rate (mV s}^{-1})\}^{1/2}. \quad (2)$$

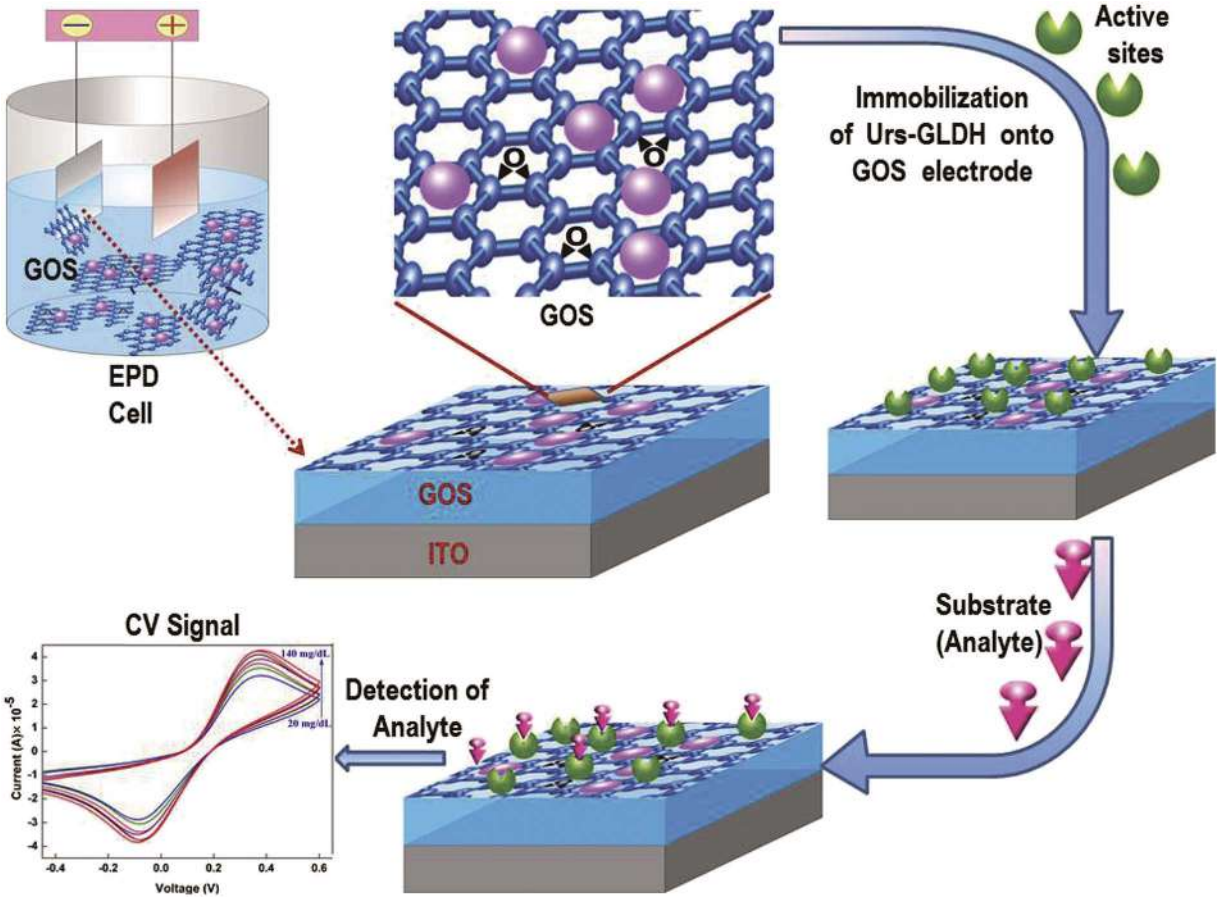

Fig. 4 Schematic representation of electrochemical sensing set up for urea sensing.

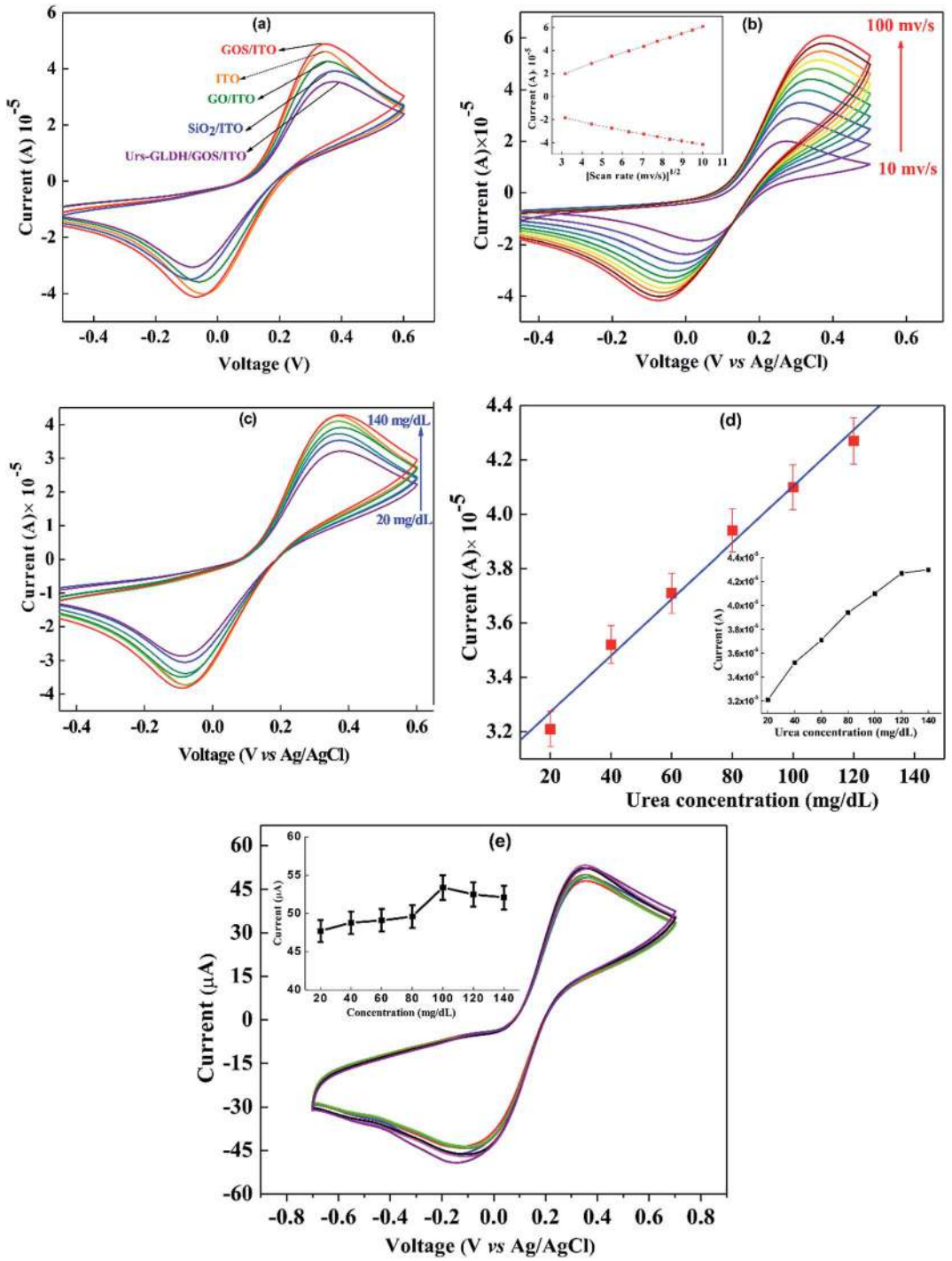

Fig. 5 (a) CV of ITO, GO/ITO, SiO_2/ITO, GOS/ITO and Urs-GLDH/GOS/ITO electrodes, in PBS (pH = 7) containing 5 mM $[Fe(CN)_6]^{3-/4-}$; (b) CV of the Urs-GLDH/GOS/ITO bioelectrode at different scan rates (10–100 mV s^{-1}) (inset: redox peak current as a function of square root of scan rate); (c) electrochemical response studies of the Urs-GLDH/GOS/ITO bioelectrode as a function of urea concentrations [20–140 mg dL^{-1} (3.3–23.2 mM)] using CV; (d) fitted calibration plot between anodic peak current and urea concentration (20–120 mg dL^{-1}); inset: calibration plot between anodic peak current and urea concentration (20–140 mg dL^{-1}); (e) control experiment of the GOS/ITO electrode as a function of urea concentration; inset: oxidation peak current *vs.* urea concentration plot of the GOS/ITO electrode.

The diffusion coefficient value (D) of the redox species for the Urs-GLDH/GOS/ITO bioelectrode has been estimated from the slope of I_p *versus* $v^{1/2}$ plot using the Randel–Sevcik equation:

$$I_p = (2.69 \times 10^5) n^{3/2} A D^{1/2} C v^{1/2}, \quad (3)$$

where, I_p is the peak current (I_{pa} anodic and I_{pc} cathodic), n is electron stoichiometry, A is the electrode area (0.25 cm^2), D is

the diffusion coefficient, C is the concentration of redox species (5 mM $[Fe(CN)^6]^{3-/4-}$) in mol cm^{-3}, and ν is the scan rate. The D value has been obtained as 3.6×10^{-7} cm^2 s^{-1}.

The electrochemical sensing studies of the Urs-GLDH/GOS/ITO bioelectrode have been carried out as a function of urea concentration in the presence of 30 μL of nicotinamide adenine dinucleotide (NADH, 3.7 mg dL^{-1}) and 70 μL of α-ketoglutarate (α-KG, 47.5 mg dL^{-1}) using cyclic voltammetry in PBS solution 50 mM PBS (pH 7, 0.9% NaCl) containing 5 mM $[Fe(CN)_6]^{3-/4-}$. It is observed that the magnitude of the response current obtained for the Urs-GLDH/GOS/ITO bioelectrode increases as the concentration of urea increases (Fig. 5(c)).

Fig. 5(d) shows the linear calibration plot between the anodic peak current and the urea concentration (20–120 mg dL^{-1}). The response current varies proportionally as a function of urea concentration in this detection range. The calibration curve displayed in Fig. 5(d) has been fitted between the urea concentration and the value of the anodic peak current that obeys eqn (3).

$$I_a(\text{Urs-GLDH/GOS/ITO})\ [\text{A}] = 3.06 \times 10^{-6}\ [\text{A}] + 1.04 \times 10^{-7}\ \text{A (mg dL)}^{-1} \times \{\text{urea concentration (mg dL}^{-1}\}\ (4)$$

At the next higher value of urea concentration (140 mg dL^{-1}), there is no significant increase in the response current and the Urs-GLDH/GOS/ITO bioelectrode is saturated[inset of Fig. 5(d)].

The lower detection limit for the GOS bioelectrode is 2.1 mM obtained using the $3\sigma/m$ criteria, where m is the slope and σ is the standard deviation of the calibration graph. The linear range lies between 3.3 and 19.9 mM with a good sensitivity of 2.6 μA mM^{-1} cm^{-2}.

Further, we have performed the control experiment using the GOS/ITO electrode as a function of urea concentration conducted in PBS containing 5 mM $[Fe(CN)_6]^{3-/4-}$ [Fig. 5(e)]. It has been observed that the response current obtained for GOS/ITO does not significantly change as a function of urea concentration [inset, Fig. 5(e)].

During the biochemical reaction (depicted in Fig. 6), Urs catalyzes the decomposition of urea into hydrogen bicarbonate (HCO_3^-) and ammonium (NH_4^+) ions. It has been found that ammonium ions simply diffuse into the solution. Thus, it is required to add GLDH as it catalyzes the reversible reaction between α-KG and NH_3 to NAD+ and linked oxidative deamination of L-glutamate in two steps. The first step involves a Schiff base intermediate formed between NH_3 and α-KG. Then the Schiff base intermediate protonated due to transfer of the hydride ions from NADH resulting in the formation of L-glutamate. NAD+ is utilized in the forward reaction of α-KG and free NH_3 that is converted to L-glutamate *via* hydride transfer from NADH to glutamate. NAD+ is utilized in the reverse reaction, involving L-glutamate being converted to α-KG and free (NH_3) *via* the oxidative deamination reaction.[2,38,40] The electrons generated during these reactions are transferred to the GOS/ITO electrode through a Fe(III)/Fe(IV) redox probe providing the signal in the form of current.

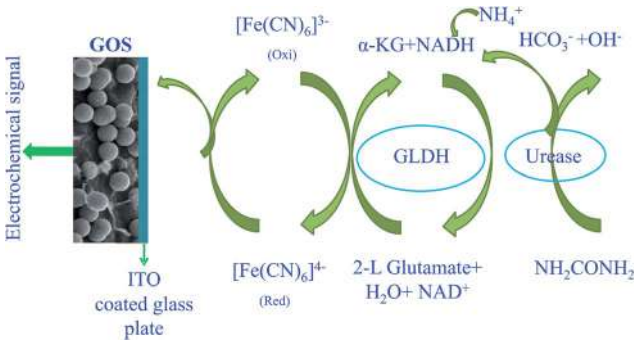

Fig. 6 Schematic representation of a electrochemical urea sensing mechanism using a GOS bioelectrode.

The biochemical reaction is formulated below:

$$(NH_2)_2CO + 3H_2O \xrightarrow{\text{Urs}} NH_4^+ + OH^- + HCO_3^- \quad \text{(step A)}$$

$$NH_4^+ + \text{α-ketoglutarate} + NADH \xrightarrow{\text{GLDH}} \text{L-glutamate} + NAD^+ + 2e \quad \text{(Step B)}$$

The Urs-GLDH/GOS/ITO urea biosensor has been checked for its accountability by different tests such as reproducibility, specificity and stability measurements (Fig. 7). The reproducibility of Urs-GLDH/GOS/ITO bioelectrodes has been determined by monitoring the maximum peak current response for the five similar electrodes made using the same protocol. It is found that there is no major change in the peak current response (see Fig. 7(a)) and confirms the reproducibility of the Urs-GLDH/GOS/ITO bioelectrode as a reliable urea biosensor. The stability of the biosensor was monitored for a period of eight weeks at an interval of one week to see the peak current response change with respect to aging. There was only ~6% decrease even after the eight week period when stored under refrigerated conditions (4 °C) (Fig. 7(b)). Further the Urs-GLDH/GOS/ITO urea biosensor's specificity towards urea has been measured to see the response with other analytes. For this, the interference monitored by checking the peak current response of Urs-GLDH/GOS/ITO in comparison with other interferants such as cholesterol, glucose and ascorbic acid. The absence of similar peak current response as in the case of urea is an indication of the high specificity of the Urs-GLDH/GOS/ITO biosensor towards urea (Fig. 7(c)).

The higher sensitivity obtained in our study as compared to the reported data (see Table 2) is due to the excellent electrochemical properties and the large surface area of GOS. Further, the mesoporous and biocompatible SiO_2 particles were found to exhibit good electrocatalytic properties, which further enhance the response current as compared to GO. Moreover, the mesoporous morphology of SiO_2 particles facilitate surface density of enzyme loading. The faster response time (10 s) is attributed to rapid electron transfer kinetics of GO with abundant edge-plane defects.

Conclusions

SiO_2 particles of uniform size ~500 nm embedded on the functional GO surface, which are quite useful for practical

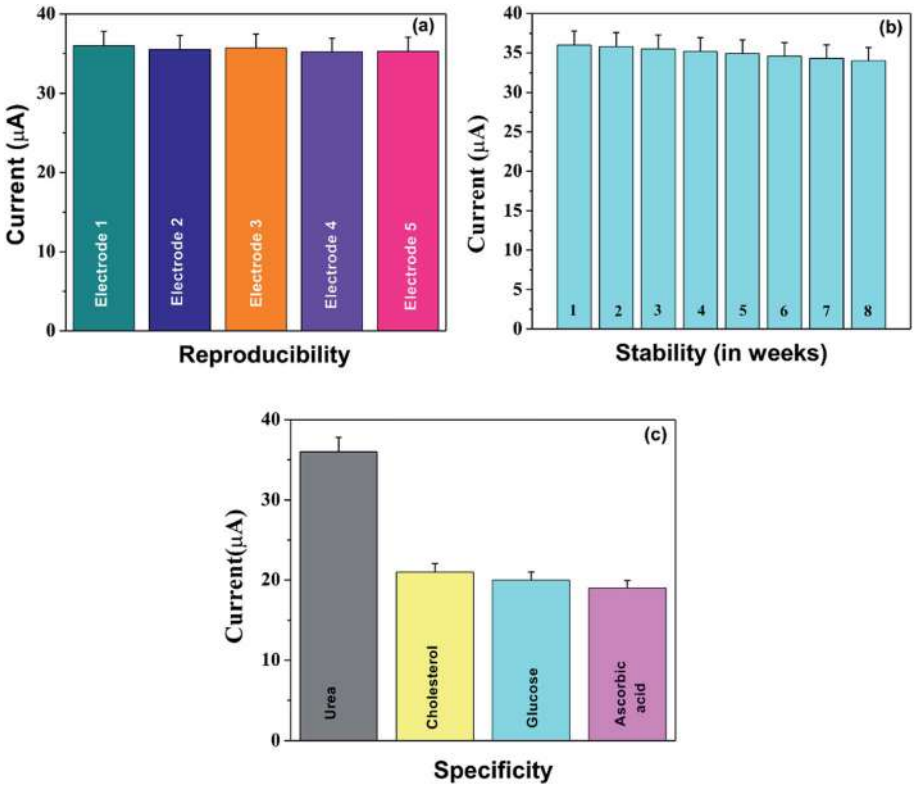

Fig. 7 (a) Different Urs-GLDH/GOS/ITO bioelectrodes fabricated *via* the same conditions applied to conduct the reproducibility test; (b) stability studies of the Urs-GLDH/GOS/ITO bioelectrode measured at a regular interval of one week upto eight weeks; (c) specificity plot describing the CV response of the Urs-GLDH/GOS/ITO bioelectrode in the presence of urea, cholesterol, glucose and ascorbic acid.

Table 2 A comparative table describing the urea sensing characteristics of the bioelectrode Urs-GLDH/GOS/ITO along with some other reported in the literature

Bioelectrode	Detection range (mM)	Detection limit (mM)	Sensitivity	Stability (days)	Ref.
Urs-GLDH/GOS/ITO	3.3–19.9	2.1	2.6 μA mM^{-1} cm^{-2}	35	Present work
Urs-GLDH/ZrO_2/ITO	0.8–16.6	0.8	0.07 μA mM^{-1} cm^{-2}	—	41
MWCNT/silica	2.18×10^{-2} to 1.07	—	2.3 mV mM^{-1} cm^{-2}	60	42
Urs-GLDH/ZnO-Ch/ITO	0.8–16.6	0.49	0.13 μA mM^{-1} cm^{-2}	90	39
Urs-PANi-nafion/Au	1–10	1	4.2 μA mM^{-1} cm^{-2}	—	43
Urs/PAPCP/ITO	0.16–5.02	—	0.47 μA mM^{-1} cm^{-2}	60	44

applications like biosensing, were synthesized and thoroughly characterized. The different techniques such as SEM, XRD used for structural characterization, and for vibrational spectroscopy, IR and Raman were used. SEM images clearly revealed an almost uniform size of mesoporous SiO_2 particles evenly distributed on the GO sheets. Raman study of the GO and GOS composites clearly reveals that the degree of disorder increases from GO to GOS3. This indicates that during the formation of GOS composites, more sp^3 disorder is introduced into the sp^2 structure of graphene, *i.e.* the GO sheets get significantly modified. The IR spectra of both GO and GOS show that different functional groups, such as epoxy, alkoxy and carboxylic are attached to the GO sheet, which is manifested by the observation of several characteristic peaks of these functional groups. Owing to its different functional groups and optimum concentration, GOS3 showed high hydrophilicity, film forming capabilities and thereby good enzyme loading. The as synthesized GOS were electrophoretically deposited and biofunctionalized with urease (Urs) and glutamate dehydrogenase (GLDH) enzymes. The Urs-GLDH/GOS/ITO bioelectrode has been utilized for the electrochemical biosensing of urea. The response studies of this urea sensor reveal a high sensitivity of 2.6 μA mM^{-1} cm^{-2}, a good detection limit of 2.1 mM and a good storage stability of 8 weeks. Further the reproducibility and specificity were found to be well promising for the Urs-GLDH/GOS/ITO bioelectrode to be used as an efficient urea biosensor. It should be interesting to utilize this easy and cost effective GO based platform, GOS for fabrication of other biosensors for application to clinical diagnostics.

Acknowledgements

The authors express their sincere gratitude to late Prof. B. P. Asthana. The authors are also thankful to Dr Andy Scheffel from IPHT, Jena for SEM measurements, Mrs Anna Schmidt from IPC, Jena for BET measurements and Department of Applied Physics, I. I. T. (B. H. U.) for XRD measurements. Two of us (SA, JP) are thankful to Deutsche Forschungs-Gemeinschaft (DFG PO 563/15-1) for providing funds for the "Intensification of Bilateral Scientific Cooperation". AS acknowledges the CAS program sponsored by UGC at Department of Physics, B. H. U. SA expresses his gratitude for the U.G.C. financial assistance and AvH fellowship.

References

1 K. S. Novoselov, A. K. Geim, S. V. Morozov, D. Jiang, Y. Zhang, S. V. Dubonos, I. V. Grigorieva and A. A. Firsov, *Science*, 2004, **306**, 666–669.
2 R. K. Srivastava, S. Srivastava, T. N. Narayanan, B. D. Mahlotra, R. Vajtai, P. M. Ajayan and A. Srivastava, *ACS Nano*, 2011, **6**, 168–175.
3 M. Veerapandian, M.-H. Lee, K. Krishnamoorthy and K. Yun, *Carbon*, 2012, **50**, 4228–4238.
4 X. Liu, X. Xu, H. Zhu and X. Yang, *Anal. Methods*, 2013, **5**, 2298–2304.
5 D. C. Marcano, D. V. Kosynkin, J. M. Berlin, A. Sinitskii, Z. Sun, A. Slesarev, L. B. Alemany, W. Lu and J. M. Tour, *ACS Nano*, 2010, **4**, 4806–4814.
6 W. S. Hummers Jr and R. E. Offeman, *J. Am. Chem. Soc.*, 1958, **80**, 1339.
7 D. R. Dreyer, S. Park, C. W. Bielawski and R. S. Ruoff, *Chem. Soc. Rev.*, 2010, **39**, 228–240.
8 Z. Wang, X. Zhou, J. Zhang, F. Boey and H. Zhang, *J. Phys. Chem. C*, 2009, **113**, 14071–14075.
9 W. D. Pu, L. Zhang and C. Z. Huang, *Anal. Methods*, 2012, **4**, 1662–1666.
10 T. Kuila, S. Bose, P. Khanra, A. K. Mishra, N. H. Kim and J. H. Lee, *Biosens. Bioelectron.*, 2011, **26**, 4637–4648.
11 M. Pumera, *Chem. Soc. Rev.*, 2010, **39**, 4146–4157.
12 A. M. V. Mohan, K. K. Aswini, A. M. Starvin and V. M. Biju, *Anal. Methods*, 2013, **5**, 1764–1770.
13 W. Yang, K. R. Ratinac, S. P. Ringer, P. Thordarson, J. J. Gooding and F. Braet, *Angew. Chem., Int. Ed.*, 2010, **49**, 2114–2138.
14 G. Goncalves, P. A. A. P. Marques, C. M. Granadeiro, H. I. S. Nogueira, M. K. Singh and J. Gracio, *Chem. Mater.*, 2009, **21**, 4796–4802.
15 I. V. Lightcap, T. H. Kosel and P. V. Kamat, *Nano Lett.*, 2010, **10**, 577–583.
16 S. Ge, M. Sun, W. Liu, S. Li, X. Wang, C. Chu, M. Yan and J. Yu, *Sens. Actuators, B*, 2014, **192**, 317–326.
17 A. F. de Faria, A. C. M. de Moraes, P. D. Marcato, D. S. T. Martinez, N. Durán, A. G. Souza Filho, A. Brandelli and O. L. Alves, *J. Nanopart. Res.*, 2014, **16**, 1–16.
18 Z. Luo, X. Ma, D. Yang, L. Yuwen, X. Zhu, L. Weng and L. Wang, *Carbon*, 2013, **57**, 470–476.
19 H. A. Ab Wab, K. A. Razak and N. D. Zakaria, *J. Nanopart. Res.*, 2014, **16**, 1–14.
20 B. G. Trewyn, S. Giri, I. I. Slowing and V. S.-Y. Lin, *Chem. Commun.*, 2007, 3236–3245.
21 W. Stöber, A. Fink and E. Bohn, *J. Colloid Interface Sci.*, 1968, **26**, 62–69.
22 M. Qhobosheane, S. Santra, P. Zhang and W. Tan, *Analyst*, 2001, **126**, 1274–1278.
23 G. Tolnai, F. Csempesz, M. Kabai-Faix, E. Kálmán, Z. Keresztes, A. L. Kovács, J. J. Ramsden and Z. Hórvölgyi, *Langmuir*, 2001, **17**, 2683–2687.
24 H.-H. Yang, S.-Q. Zhang, X.-L. Chen, Z.-X. Zhuang, J.-G. Xu and X.-R. Wang, *Anal. Chem.*, 2004, **76**, 1316–1321.
25 J. Wang, *Anal. Chim. Acta*, 1999, **399**, 21–27.
26 W. Lu, Y. Luo, G. Chang and X. Sun, *Biosens. Bioelectron.*, 2011, **26**, 4791–4797.
27 S. Watcharotone, D. A. Dikin, S. Stankovich, R. Piner, I. Jung, G. H. B. Dommett, G. Evmenenko, S.-E. Wu, S.-F. Chen and C.-P. Liu, *Nano Lett.*, 2007, **7**, 1888–1892.
28 L. Kou and C. Gao, *Nanoscale*, 2011, **3**, 519–528.
29 J. Liu, Q. Zhang, X. Chen and J. Wang, *Chem.–Eur. J.*, 2011, **17**, 4864–4870.
30 D. C. Marcano, D. V Kosynkin, J. M. Berlin, A. Sinitskii, Z. Sun, A. Slesarev, L. B. Alemany, W. Lu and J. M. Tour, *ACS Nano*, 2010, **4**, 4806–4814.
31 J. Yan, T. Wei, B. Shao, F. Ma, Z. Fan, M. Zhang, C. Zheng, Y. Shang, W. Qian and F. Wei, *Carbon*, 2010, **48**, 1731–1737.
32 P. Innocenzi, P. Falcaro, D. Grosso and F. Babonneau, *J. Phys. Chem. B*, 2003, **107**, 4711–4717.
33 R. M. Almeida and C. G. Pantano, *J. Appl. Phys.*, 1990, **68**, 4225–4232.
34 K. N. Kudin, B. Ozbas, H. C. Schniepp, R. K. Prud'Homme, I. A. Aksay and R. Car, *Nano Lett.*, 2008, **8**, 36–41.
35 H. M. Heise, R. Kuckuk, A. K. Ojha, A. Srivastava, V. Srivastava and B. P. Asthana, *J. Raman Spectrosc.*, 2009, **40**, 344–353.
36 M. Zhu, P. Chen and M. Liu, *ACS Nano*, 2011, **5**, 4529–4536.
37 D. Graf, F. Molitor, K. Ensslin, C. Stampfer, A. Jungen, C. Hierold and L. Wirtz, *Nano Lett.*, 2007, **7**, 238–242.
38 A. Chaubey and B. D. Malhotra, *Biosens. Bioelectron.*, 2002, **17**, 441–456.
39 P. R. Solanki, A. Kaushik, A. A. Ansari, G. Sumana and B. D. Malhotra, *Appl. Phys. Lett.*, 2008, **93**, 163903.
40 M. A. Ali, S. Srivastava, P. R. Solanki, V. Reddy, V. V. Agrawal, C. Kim, R. John and B. D. Malhotra, *Sci. Rep.*, 2013, **3**, 2661.
41 G. Sumana, M. Das, S. Srivastava and B. D. Malhotra, *Thin Solid Films*, 2010, **519**, 1187–1191.
42 T. Ahuja, D. Kumar, N. Singh and A. M. Biradar, *Mater. Sci. Eng., C*, 2011, **31**, 90–94.
43 Y.-C. Luo and J.-S. Do, *Biosens. Bioelectron.*, 2004, **20**, 15–23.
44 V. Bisht, W. Takashima and K. Kaneto, *Biomaterials*, 2005, **26**, 3683–3690.

Microwave Reduced Graphene Oxide as Efficient NIR Photothermal Agent

Article · June 2017

CITATIONS
0

READS
31

3 authors, including:

Sunayana Kashyap
Banaras Hindu University
11 PUBLICATIONS **6** CITATIONS
SEE PROFILE

Anchal Srivastava
Banaras Hindu University
95 PUBLICATIONS **4,396** CITATIONS
SEE PROFILE

Austin Journal of Biosensors & Bioelectronics

Open Access

Austin Publishing Group

Research Article

Microwave Reduced Graphene Oxide as Efficient NIR Photothermal Agent

Sunayana Kashyap[1], Vinod Kumar[2], Shiju Abraham[3], Sima Umrao[3], Siddharath Singh[4], Arpana Kamath[5], Rajala MS[5], Anchal Srivastava[3] and Preeti S Saxena[1]*

[1]Department of Zoology, Banaras Hindu University, India
[2]Institute of Nanoscience & Technology, India
[3]Department of Physics, Banaras Hindu University, India
[4]Departmentof Biotechnology, G.B. Pant Engineering College, India
[5]School of Biotechnology, Jawaharlal Nehru University, India

***Corresponding author:** Preeti S Saxena, Department of Zoology, Banaras Hindu University, Varanasi–221005, India

Received: April 10, 2017; **Accepted:** May 22, 2017; **Published:** June 07, 2017

Abstract

Current study reports the enhanced cancer cells photothermal ablation efficiency of Microwave Reduced Graphene Oxide (MRGO). Reduction of chemically exfoliated graphene oxide has been carried out using a microwave (700W for 5 minutes). The produced MRGO have been characterized with TEM, SEM, XRD, FTIR, RAMAN, AFM and UV-Vis spectroscopy. MRGO nano size sheets with average lateral dimension ~200nm, exhibited higher NIR absorption efficiency, in comparison to Graphene Oxide (GO). Photothermal efficacy (at optimized NIR laser 808 nm, power of 5.0W/cm^2 for 5 min) of MRGO have been tested against human alveolar epithelial carcinoma cell (A549) and human colorectal carcinoma cells (HCT116). As a result, a significant decrease in cell viability by 84% and 80% for A549 and HCT116 cell lines respectively has been estimated. No significant toxicity has been observed with MRGO (in absence of NIR treatment) at the concentrations well above the doses needed for photothermal heating against the same cancer cells. Our study introduces MRGO as a biocompatible and efficient photothermal agent.

Keywords: Photothermal therapy; Microwave assisted reduced graphene oxide; A549 and HCT116 cancerous cells

Introduction

Cancer is the leading cause of death worldwide. Around 14.1 million cases of cancer were found in the world in which 7.4 million were of men and 6.7 million of women in 2012 and it is expected this number can increase to 24 million till 2035 [1]. More than 200 types of cancer have been reported. Out of these, lung and colorectal cancer are the serious concern to both developed as well as developing countries. Lung cancer is the most frequently diagnosed cancer (1.61 million, 12.7% of the total) while, colorectal cancer is the third most common causes of cancer death (1.23 million, 9.7% of the total) [2]. There are several means for the treatment of cancer such as surgery, chemotherapy, radiotherapy, and sometimes a combination of them. But each of them suffers with certain drawbacks such as severe adverse reactions, low efficiency and occurrence of other health complications [3-6]. In past decades, photothermal therapy using near-infrared spectrum of light employing a photothermal agent has emerged as an alternative and effective tool for photo ablation of cancer cells with minimum side effects to nearby healthy cells [7-10].

In recent years, 2-D carbon nanomaterials i.e. Graphene Oxide (GO) and Reduced Graphene Oxide (RGO) owing excellent physicochemical properties, have been widely explored for NIR mediated photothermal ablation of cancer cells [11,12]. However, the issue of inherent toxicity of RGO acquired through the utilization of toxic reducing agents remains a matter of debate [12]. Up to now, in most of biomedical applications Chemically Reduced Graphene Oxide (CRGO) have been used. In chemical reduction of GO, several non-ecofriendly reducing agent like hydrazine hydrate, its derivatives like dimethyl hydrazine and various metal hydrides, *e.g.* sodium hydride, sodium borohydride ($NaBH_4$) and Lithium Aluminium Hydride ($LiAlH_4$) have been employed [13]. These chemical reducing agents are generally toxic in nature and not efficient for complete reduction of all functional groups present over GO. For *e.g.* $NaBH_4$, effectively reduces only C = O rather than epoxy groups, carboxylic acids groups and alcohol groups [14]. Usually RGO is obtained by graphene oxide reduction at high temperature, or by use of reducing agent [15]. Reduction of GO by unconventional heating resources as microwave irradiation is better alternative over the popular chemical reduction methods. It facilitates quick, inexpensive and mass production of RGO with little energy cost, overcoming the problems associated with chemically reduced RGO [16-18]. Further in the best of our knowledge, no reports are available towards the biomedical application of MRGO. In the current study, an attempt have been made to exploit the enhanced NIR absorption efficiency of MRGO for photothermal destruction of human alveolar epithelial carcinoma cell (A549) and human colorectal carcinoma cells (HCT116). This is the first study which reports the photothermal application of MRGO.

Experimental Details

Materials

Graphite flakes were obtained from NGS Naturgraphit GmbH (Germany). H_2SO_4, H_3PO_4 and all other chemicals were purchased from Merck limited, Mumbai, India. All the chemical reagents were of analytical grade.

Synthesis of graphene oxide (GO)

GO have been synthesized by improved Hummers method with a slight modification [19,]. In brief, 1 g of graphite powder have been pre-oxidized by reacting it with a mixture of 40 ml of 98% H_2SO_4, 5g $K_2S_2O_8$ and 5 g of P_2O_5 for 4h at 80^{0}C. Further oxidation have been achieved by adding the pre-oxidized graphite to a mixture of concentrated H_2SO_4–H_3PO_4 (v/v: 180: 13) with constant stirring.

Citation: Kashyap S, Kumar V, Abraham S, Umrao S, Singh S, Kamath A, et al. Microwave Reduced Graphene Oxide as Efficient NIR Photothermal Agent. Austin J Biosens & Bioelectron. 2017; 3(1): 1026.

After 5 min, 6 g of $KMnO_4$ have been added to the mixture and the stirring is continued for 15 h at 55°C. The reaction is stopped and the reactants were allowed to cool at RT followed by pouring of 200 ml of ice and 1.5 ml of H_2O_2 (30%). Multiple washings of the material have been carried out with DI water, 30% HCl and ethanol and finally coagulated with ether. The obtained semi-solid material has been vacuum dried overnight to obtain brown Graphene Oxide (GO) powder.

Reduction of graphene oxide (GO)

Reduced Graphene Oxide (RGO) has been obtained by reduction of Graphene Oxide (GO) by microwave reduction method. In microwave reduction, 100 mg of GO powder (kept in 250 ml conical flask) was irradiated with 700 W of microwaves for 5 minute (using a domestic microwave oven). The exfoliation of GO layers takes place and fluky lightweight MRGO was obtained (Figure S3).

Characterization

Transmission electron microscopy (TEM, Tecnaii-G2F30 STWIN), operated at an accelerating voltage of 200 KeV and scanning electron microscopy (SEM, JEOL–Model JSM6300F) have been used for structural characterization of GO and MRGO. The UV-Visible absorbance spectra of GO and MRGO solutions were recorded with Perkin Elmer UV-Visible-Lambda 25 spectrophotometer. FTIR and Raman spectrum have been recorded using Thermo scientific Fourier transform infrared spectroscopy (Thermo Nicolet-6700) and FT-Raman by Perkin Elmer Spectrum Raman instrument. The X-ray diffraction (XRD, Rigakuminiflex-II diffractometer at 30 kV, 15mA) was used to find the diffraction patterns of GO and MRGO (at wavelength of radiation Cu-Kα1~ 1.5405Å). AFM image was recorded by (Nanosurf Model: Easy scan 2 with scan rate of 0.5.Hz. Cellular imaging was done using a Primo vert Zeiss microscope. Hemocytometer-Superior Marienfeld Germany Plate Reader-TECAN Austria Gmb, Model-Sunrise Basic Tecan.were used for cell counting and cell viability assay.

Cell culture

Human Colorectal carcinoma cells (HCT116 cells) and human alveolar epithelial carcinoma cells. (A549 cells) were cultured separately in a 25cm² tissue culture flask with Dulbecco's Modified Eagle Medium (DMEM) and Ham's F12 containing 10% FBS (Fetal Bovine serum) 20mM D-glucose, penicillin (100 units/mL), and 100µg/mL streptomycin. Cells were allowed to grow in a humidified condition at 37 °C and 5% CO_2 atmosphere.

Cytotoxicity evaluation

3-(4, 5-dimethylthiazol-2-yl)-2, 5-diphenyl tetrazolium bromide (MTT) assays was carried out to evaluate the cytotoxic effects of MRGO against both A549 cells and HCT116 cells. For this, cells were cultured and maintained in DMEM and Ham's F12 medium, 5000 cells/well were seeded in 96 wells plates. Different concentrations (such as 0, 5, 10, 20, 50, 100 and 200µg/mL) of MRGO were added in separate wells followed by 24 hours of incubation at 37°C with 5% CO_2 atmosphere. Each concentration was added in triplicates. After 24 hours of incubation 20µL of 5.0 mg/mL MTT was added in each well and incubated for 4 hours, there after 200µL of DMSO was added to solubilize the resultant formazan crystals. Optical density was measured at 590-610 nm. The cell viability was estimated according to the following equation:

Cell Viability [%] = (OD treated/ OD control) ×100%

Where, OD control was absorbance value estimated from cells without incubation of MRGO and OD treated was absorbance estimated in the presence of MRGO.

NIR mediated phototherapy

NIR laser (Nd:YAG) of 808 nm with 5.0 W/cm² of power density was used for phototherapy experiment.5000 of each kind of cells/wells (A549 cells and HCT116) were seeded in 96 well plates in six different groups in triplicate separately. In first group, normal cell (without MRGO) with no laser treatment were taken. In second group, cells (without MRGO) after laser treatment were taken. The third group consists of cells with15.0µg/mL MRGO without laser treatment. The fourth, fifth and sixth group consist of cells with 15.0µg/mL MRGO exposed by NIR laser with different time interval as 2.0, 3.0 and 5.0 minutes respectively. After the NIR irradiation cells were washed with PBS (pH-7.4) and cell viability was estimated with trypan blue exclusion method.

Statistical analysis

Statistical analysis were done with SPSS-16 software using One way ANOVA and significant difference of means were determined using Duncan's multiple range test at the level of $p<0.05$ and $p<0.001$.

Results and Discussion

Structural characterization of MRGO has been carried out using Atomic Force Microscope (AFM), Scanning Electron Microscopy (SEM) and Transmission Electron Microscopy (TEM). The AFM image (Figure 1A) of MRGO showed uniform larger sheet with lateral dimension of 500 nm and average height profile of ~90nm, which has been reduced significantly i.e upto ~200 nm by ultra-sonication (Figure S1A) supporting information). The ultrasonicated MRGO sheets with ~200 nm of lateral dimension have been further used for photothermal experiments. The average height profile of the MRGO nanosheets has been found to be ~40nm (Figure S1.B supporting information). Well-exfoliated but crumpled and aggregated MRGO sheets are observable in the SEM image (Figure 1B) which is a

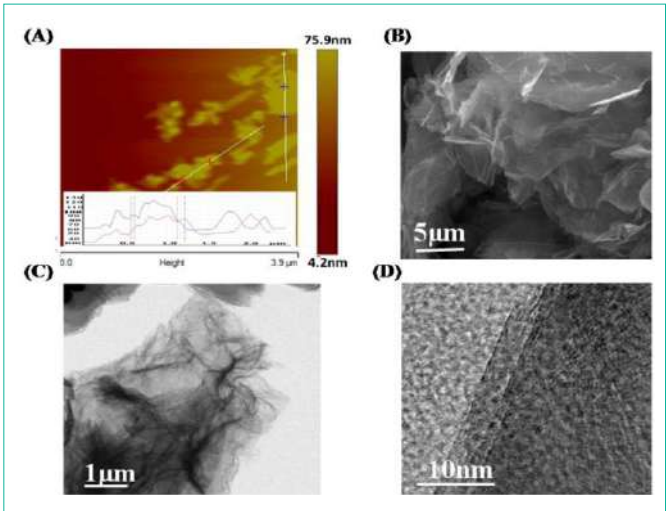

Figure 1: (A) AFM image of MRGO **(B)** SEM image of MRGO **(C)** TEM image of MRGO **(D)** HRTEM image of MRGO.

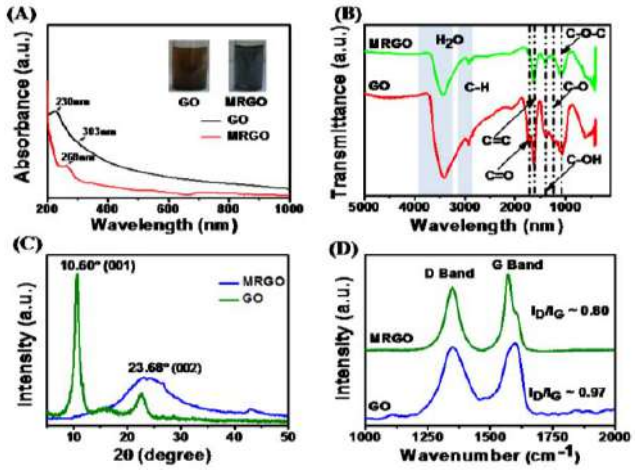

Figure 2: Characterizations of GO and MRGO, (A) UV-Vis absorption spectra, inset: Optical images of GO and MRGO dispersions, (B) FTIR spectrum, (C) XRD pattern, (D) RAMAN spectrum.

common feature of the RGO. TEM image of the MRGO (Figure 1C) shows the wrinkled structure of folded sheet with lateral dimension of ~1µm which break up into small sheet sizes with lateral dimension around ~200 nm after ultrasonication (Figure S2). Thus the results obtained in TEM image are in well agreement with the observation made in AFM. HRTEM (Figure 1D) of MRGO indicates its crystal and few layered nature [20,21].

In Figure 2A shows the UV-Vis absorption spectrum of GO and MRGO (Inset picture show the optical image of GO and MRGO Figure 2A). The absorption peak at 230 nm is due to π–π* transition of aromatic C-C bonds which is red shifted to 268 nm, indicating the electronic conjugation within the reduction of GO by exfoliation of GO layers due to microwave irradiation [22]. The RAMAN spectrums of as synthesized GO and MRGO were shown in Figure 2D. The GO and MRGO show G-band due to C-C vibration with sp^2 carbon which corresponds to the Eg^2 phonon at the centre of the Brillouinzone and D-band (sp^3 carbon) comes from the out-of-plane breathing mode of the sp^2 carbons, which is due to the presence of defects that were introduced in oxidization and reduction procedure. In case of GO, the G band was at 1571.7 cm^{-1}, while in case of MRGO the G band shifted to 1600.5 cm^{-1}. This indicated the reduction of GO is happening by exfoliation of layered structures of GO under microwave irradiation. The D band for GO and MRGO was sited at 1349 cm^{-1} and 1347cm^{-1} respectively. In case of MRGO, the I_D/I_G ratio was 0.80, which was smaller than the I_D/I_G ratio of GO. The reduced I_D/I_G value was attributed to the removal of defects originated due to oxygen containing functional groups and the conversion of sp^3 to sp^2 carbon [23].

In the FT-IR spectrum of the GO (Figure 2B), the peaks at, 3432, 1720,1410,1245 and 1045cm^{-1} were attributed to O-H, C=O stretch of COOH, C-OH, C-O and C-O-C bands, respectively. The absorption peaks at 2930 cm^{-1} and 2850 cm^{-1} show the symmetric and anti-symmetric stretching vibrations of C-H, while the presence of two absorption peaks observed at 1630 cm^{-1} can be attributed to the stretching vibration of C=C. Upon the exfoliation of GO by microwave irradiation, the C=O bands disappear and intensity of

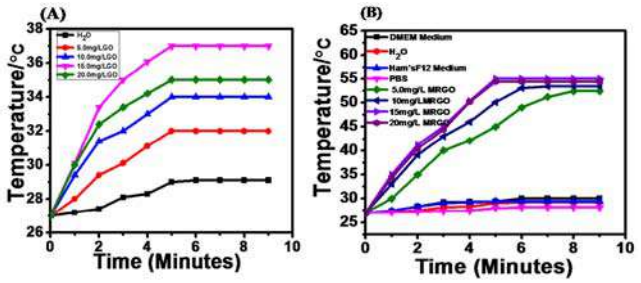

Figure 3: (A) Temperature response curves of aqueous suspension of GO at different concentrations **(B)** MRGO and medium with 808 nm laser irradiation for 5 minutes.

C-H stretching band increase. In the FTIR spectrum of MRGO (Figure 2B), the intensity of -OH vibrations observed at 3400 cm^{-1} is significantly reduced due to deoxygenation but it confirmed the presence of carboxylic functional group [24].

The powder X-Ray Diffraction (XRD) pattern (CuKα radiation) measurements were carried out to investigate the phase and structure of as synthesized RGO. In the XRD pattern of the GO (Figure 2C), a sharp peak at 10.60^0, corresponding to reflection of (001) plane (interlayer spacing of 0.83 nm) and the other one less intense peak at 22.12^0 was shown corresponding to (002) plane. After microwave reduction of GO, the sharp (002) peak of GO disappeared while another broad peak of around 23.68^0 shows up. The disappearance of the sharp peak in MRGO can be attributed to the exfoliation of layered structures of GO under microwave irradiation and the broad peak at 23.68^0 with interlayer spacing of 0.37 nm may originate from the partial restacking of exfoliated graphene layers [24].

The temperature response curves measured at different time points with different concentration of GO and MRGO after irradiating laser at 808 nm (5.0 W/cm^2) are shown in Figure 4**.** The laser irradiation effect (for 5 minutes) with the varying concentration of GO like 5.0 mg/L, 10.0 mg/L, 15.0 mg/L and 20.0 mg/L leads to rise in temperature as 32°C, 34°C, 37°C and 35°C respectively (Figure 3A). In contrast under same set of condition the temperature rise in case of MRGO was noticed to be 45°C, 50.1°C, 55°C and 54.4°C respectively (Figure 3B). DMEM media, Ham's12 media, Phosphate-Buffered Saline (PBS) and water did not show any response to the irradiation even at 5.0 W/cm^2. The above observations suggest the superior photothermal heating property in MRGO in comparison to GO.

Cytotoxic effect of MRGO on A549 and HCT116 cells were evaluated by MTT [3-(4,5-dimethylthiazol-2-yl)-2,5-diphenyl tetrazolium bromide] assays, result of which were shown in Figure 4A and B. Up to 200µg/mL concentration of MRGO, no significant toxicity has been estimated for both A549 cells and HCT116 cells, which describe the good biocompatibility of MRGO. The statistical analysis of the result was done by One way ANOVA followed by Duncan's test at the level of $p<0.05$. Cytotoxicity results reveal that there is no significant difference in the biocompatibility of MRGO and CRGO.

The photothermal effect of MRGO against A549 and HCT 116 cells were studied with the help of try pan blue exclusion method and

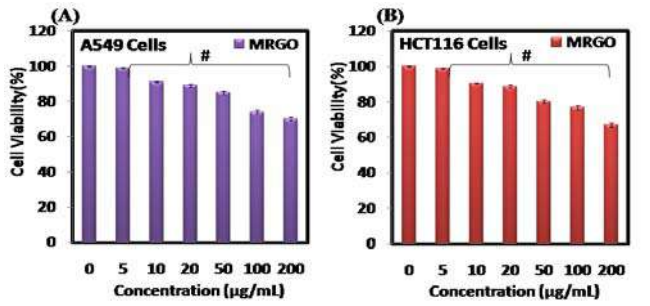

Figure 4: (A) MTT based colorimetric assay graph for cell viability of A549 cells and **(B)** HCT116 cells incubated for 24 hours with different concentration of MRGO as (0, 5,10, 20, 50, 100 and 200 µg/mL). The statistically not significant values are labelled with # at (p>0.05).

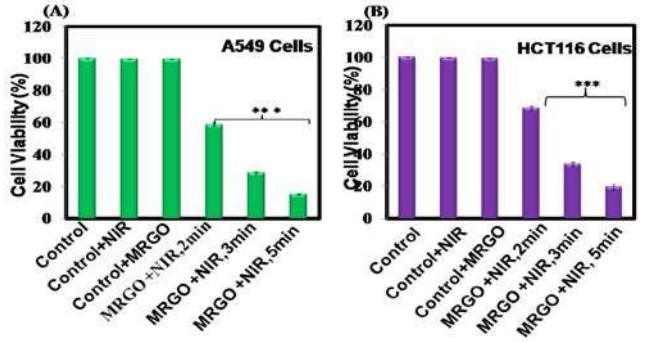

Figure 5: (A) Cell viability of A549 cells and (**B)** HCT116 cells after exposure of NIR laser (808 nm, 5.0 W/cm^2) at different time interval of 0, 2, 3, 5 min with 15µg/mL concentration of MRGO. The statistically significant values is labelled by *at (p<0.05).

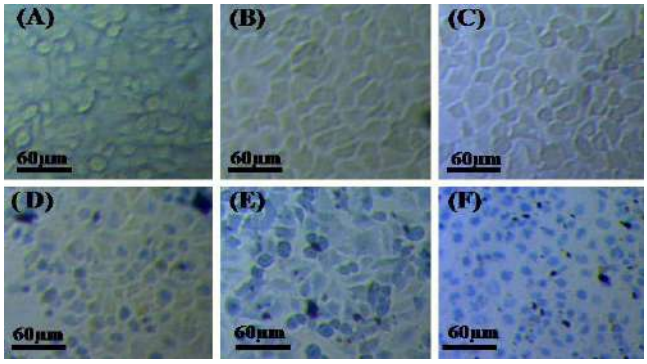

Figure 6: (A) Optical images of A549 Control cells, **(B)** Control cells after laser irradiation, **(C)** Cells with 15.0µg/mL MRGO, **(D)** Cells with 15.0µg/mL MRGO after 2 minutes of laser irradiation (5.0W/cm^2, 808 nm), **(E)** after 3 minutes of laser irradiation, **(F)** after 5minutes of laser irradiation**.** Blue.colour indicates dead cells (Trypanblue test). Scale bar = 60 µm.

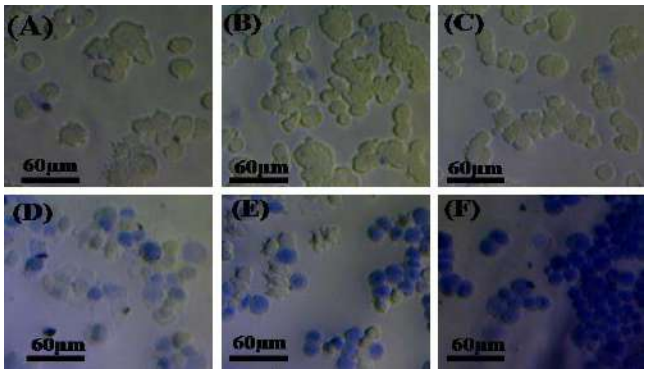

Figure 7: (A) Optical images of HCT 116 Control cells, **(B)** Control cells after laser irradiation, **(C)** Cells with 15.0µg/mL MRGO, **(D)** Cells with 15.0µg/mL MRGO after 2 minutes of laser irradiation (5.0W/cm^2, 808 nm), **(E)** after 3 minutes of laser irradiation, **(F)** after 5 minutes laser irradiation. Blue colour indicates dead cells (Trypan blue test). Scale bar = 60 µm.

the results were shown in Figure 5A and B. Percentage decrease in cell viability was calculated as 41%, 72% and 84% for A549 cells and 31.0%, 67% and 80% for HCT116 after 2.0, 3.0 and 5.0 minutes of NIR irradiation in the above cell suspensions containing MRGO. Further, negligible decrease in cell viability *i.e.* 99.6% and 99.4% for HCT116 and A549 cells respectively have been noticed after NIR irradiation for 5 minutes without MRGO in cell suspensions. Moreover, almost no decrease in cell viability *i.e.* 99.2% and 99.5% for HCT116 and A549 respectively was observed when only MRGO was incubated with cell for 5 minutes. The cell viability results shown above were calculated and were in respect of control cell's viability which was 100%.

After photothermal treatment mediated by MRGO both A549 and HCT116 were stained with trypan blue and further examination was made under light microscope (Figure 6 and 7). The cells with only MRGO (Figure 6C and 7C) and treated with NIR (Figure 6B and 7B), did not show any uptake the blue colour of trypan dye like control cells (Figure 6A and7A) which indicates that all the cells were viable, and this is because neither NIR laser nor MRGO itself may have potential to induce severe cell death. However, the presence of MRGO in cell suspension coupled with NIR radiation causes cell death which increases with time of irradiation for both kind of cells. Several blue stained dead cells appeared (Figure 6D and 7D) after 2 minute exposure of laser with MRGO treatment with preponderance of live cells, on the other hand almost all cells were blue stained 5.0 minutes of exposure (Figure 6E, F and 7E,F). Moreover, morphological changes can also be seen in microscopic examination of the cells with MRGO after NIR exposure.

In the current, study we could not explore the exact mechanism of cell death but it may be due to protein denaturation and coagulation as well as membrane destruction, which is primarily due to thermal disintegration up to 55°C expansion during NIR mediated phototherapy of MRGO. MRGO have shown better photothermal effect at lower laser power density *i.e.*5.0W/cm^2 in comparison to other nanomaterial based photothermal agent such as gold nano shell, and nanorod, which require high power density such as 35.0 W/cm^2 and 10.0W/cm^2 respectively [25, 26]. Further, study is underway to explore the mechanism of cell death and *in-vivo* application.

Facile and quick microwave assisted synthesis of MRGO with its high potential as photothermal agent will be an alternative therapeutic means for cancer therapy.

The high near infra-red absorption property of MRGO is solely attributed to the microwave assisted reduction of GO into MRGO. In the current study, we could not explore the exact mechanism of high NIR efficiency of MRGO but we propose similar mechanisms reported earlier [27].

Conclusion

In summary, our study establishes Microwave Reduced Graphene Oxide (MRGO) as a biocompatible and efficient NIR photothermal agent. Microwave assisted reduction of graphene oxide create nearly removal of oxygen functional groups in MRGO. It is presumed that reduction of oxygen functional group in MRGO nano sheets facilitates high NIR absorption by MRGO. Hence, MRGO nanosheets with lateral dimension of ~200 nm exhibited enhanced photohothermal effects at low power density in short time. Rapid and effective photothermal ablation of A549 and HCT 116 cancer cells by MRGO using NIR laser (808 nm at 5.0 W/cm^2 in 5 minutes) make it an interesting material for cancer phototherapy. The cost effective and ecofriendly production of MRGO with its high NIR absorption property can be further employed for *in vivo* photothermal application.

Acknowledgement

We are grateful to Prof. W. Kiefer University of Wurzburg (Germany) for gifting 808nm Laser. We acknowledge financial support from CAS program of Zoology Department, B.H.U., Varanasi and research fellowship from CSIR, New Delhi. Authors also acknowledge Biophysics laboratory, Department of Physics, B.H.U., Varanasi, for extending their laboratory facilities.

References

1. http://globocan.iarc.fr .2013.
2. Behera D. Epidemiology of lung cancer Global and Indian perspective. Journal Indian Academy of Clinical Medicine. 2012; 13; 131-137.
3. Schmid KE, Kornek GV, Scheithauer W, Binder S. Update on Ocular Complications of Systemic Cancer Chemotherapy. Survey of Ophthalmology. 2006; 51: 19-40.
4. Giordano SH, Kuo YF, Freeman JL, Buchholz TA, Hortobagyi GN, Goodwin JS. Risk of Cardiac Death After Adjuvant Radiotherapy for Breast Cancer. Journal of the National Cancer Institute. 2005; 97: 419-442.
5. Farrow DC, Hunt WC, Samet JM. Geographic variation in the treatment of localized breast cancer. The New England Journal of Medicine. 1992; 326: 1097-1101.
6. Polednak AP. Trends in and predictors of breast-conserving surgery and radiotherapy for breast cancer in Connecticut, 1988- 1997. International Journal of Radiation Oncology Biology Physics. 2002; 53: 157-163.
7. Moon HK, Lee SH, Choi HC. *In vivo* near-infrared mediated tumor destruction by photothermal effect of carbon nanotubes. ACS Nano. 2009; 3: 3707-3713.
8. Zhou F, Xing D, Ou Z, Wu B, Resasco DE, Chen WR. Cancer cell photothermal therapy in near infrared region by using single walled carbon nanotubes. Journal of Biomedical Optics. 2009; 142: 1-6.
9. Sherlock SP, Tabakman SM, Xie L, Dai H, Photothermally enhanced drug delivery by ultrasmall multifunctional FeCo/graphitic shell nanocrystals ACS. Nano. 2011; 5: 1505-1512.
10. Su Y, Wei X, Peng F, Zhong Y, Lu Y, Su S, et al. Gold nanoparticles-decorated silicon nanowires as highly efficient near-infrared hyperthermia agents for cancer cells destruction. Nano Letters. 2012; 12: 1845-1850.
11. Ghosh S, Dutta S, Gomes E, Carroll D, D'Agostino R, Olson J, et al. Increased heating efficiency and selective thermal ablation of malignant tissue with DNA-encased multiwall carbon nanotubes. ACS Nano. 2009; 3: 2667-2673.
12. Robinson JT, Tabakman SM, Liang Y, Wang H, Casalongue HS, Vinh D, et al. Ultrasmall reduced graphene oxide with nerar high near-infrared absorbance for photothermal therapy. Journal of the American Chemical Society. 2011; 133: 6825-6831.
13. Songfeng P, Hui-Ming C. The reduction of graphene oxide. Carbon. 2012; 50: 3210-3228.
14. Periasamy M, Thirumalaikumar M. Methods of enhancement of reactivity and selectivity of sodium borohydride for applications in organic synthesis. Journal of Organometallic Chemistry. 2000; 609: 137-151.
15. Gupta TK, Singh BP, Tripathi RK, Dhakate SR, Singh VN, Panwar OS, et al. Superior nano-mechanical properties of reduced graphene oxide reinforced polyurethane composites. RSC Advances. 2015; 5: 16921-16930.
16. Yang GH, Zhou YH, Wu JJ, Cao JT, Li L, Liu HY, et al. Microwave-assisted synthesis of nitrogen and boron co-doped graphene and its application for enhanced electrochemical detection of hydrogen peroxide. RSC Advances. 2013; 3: 22597-22604.
17. Yu H, Wang T, Wen B, Lu M, Xu Z, Zhu C,Chen Y, Xue X, Sun C, Cao M. Graphene/polyaniline nanorod arrays: synthesis and excellent electromagnetic absorption properties. Journal of Material Chemistry. 2012; 22: 21679.
18. Umrao S, Gupta TK, Kumar S, Singh VK, Sultania MK, Jung JH, et al. Microwave-Assisted Synthesis of Boron and Nitrogen co-doped Reduced Graphene Oxide for the Protection of Electromagnetic Radiation in Ku-Band. ACS Applied Materials Interfaces. 2015; 7: 19831-19842.
19. Marcano DC, Kosynkin DV, Berlin S, Sun JMA, Slesarev Z, Alemany A, et al. Improved synthesis of graphene oxide. ACS Nano. 2010; 4: 4806-4814.
20. Zhang H, Feng PX. Fabrication and characterization of few-layer graphene. Carbon. 2010; 48: 359-364.
21. Ortolani L, Cadelano E, Veronese GP, Boschi CD, Snoeck EE, Colombo L, et al. Folded graphene membranes: mapping curvature at the nanoscale. Nano Letters. 2012; 12: 5207-5212.
22. Thakur S, Karak N. Green reduction of graphene oxide by aqueous phytoextracts. Carbon. 2012; 50: 5331- 5339.
23. Thema FT, Moloto MJ, Dikio EDN, Kotsedi NN, Maaza LM, Khenfouch M. Synthesis and characterization of graphene thin films by chemical reduction of exfoliated and intercalated graphite oxide. Journal of Chemical Physics. 2012; 2013: 1-6.
24. Loryuenyong V, Totepvimarn K, Eimburanapravat P, Boonchompoo W, Buasri A. Preparation and Characterization of Reduced Graphene Oxide Sheets via Water-Based Exfoliation and Reduction Methods. Advances in Materials Science and Engineering. 2013; 2013: 1-5.
25. Huang X, El-Sayed MA. Gold nanoparticles: Optical properties and implementations in cancer diagnosis and photothermal therapy. Journal of Advanced Research. 2010; 1: 13-28.
26. Loo C, Lin A, Hirsch L, Lee M, Barton J, Halas N, et al. Nanoshell-enabled photonics-based imaging and therapy of cancer. Technology in Cancer Research and Treatment. 2004; 3: 33-40.
27. Acik M, Lee G, Mattevi C, Chhowalla M, Cho K, Chabal YJ. Unusual infrared-absorption mechanism in thermally reduced graphene oxide. Nature Materials. 2010; 9: 840-845.

Citation: Kashyap S, Kumar V, Abraham S, Umrao S, Singh S, Kamath A, et al. Microwave Reduced Graphene Oxide as Efficient NIR Photothermal Agent. Austin J Biosens & Bioelectron. 2017; 3(1): 1026.

Talanta 144 (2015) 745–754

Contents lists available at ScienceDirect

Talanta

journal homepage: www.elsevier.com/locate/talanta

Partially reduced graphene oxide–gold nanorods composite based bioelectrode of improved sensing performance

Narsingh R. Nirala [a], Shiju Abraham [b], Vinod Kumar [a], Shobhit A. Pandey [c], Umakant Yadav [a], Monika Srivastava [d], S.K. Srivastava [e], Vidya Nand Singh [f], Arvind M. Kayastha [g], Anchal Srivastava [b,*], Preeti S. Saxena [a,*]

[a] Department of Zoology, Banaras Hindu University, Varanasi 221005, India
[b] Department of Physics, Banaras Hindu University, Varanasi 221005, India
[c] Department of Metallurgical Engineering, IIT (BHU), Varanasi 221005, India
[d] School of Materials Science and Technology, IIT (BHU), Varanasi 221005, India
[e] Department of Physics, Mahila Mahavidyalaya (MMV), Banaras Hindu University, Varanasi 221005, India
[f] CSIR-National Physical Laboratory, New Delhi, India
[g] School of Biotechnology, Banaras Hindu University, Varanasi 221005, India

ARTICLE INFO

Article history:
Received 10 April 2015
Received in revised form
23 May 2015
Accepted 25 May 2015
Available online 8 July 2015

Keywords:
Partially reduced graphene oxide
Gold nanorods
Composite
Chitosan
Glucose K_m
K_s
Flavin adenine dinucleotide (FAD)
Electrochemical biosensors

ABSTRACT

The present work proposes partially reduced graphene oxide–gold nanorods supported by chitosan (CH–prGO–AuNRs) as a potential bioelectrode material for enhanced glucose sensing. Developed on ITO substrate by immobilizing glucose oxidase on CH–prGO–AuNRs composite, these CH–prGO–AuNRs/ITO bioelectrodes demonstrate high sensitivity of 3.2 μA/(mg/dL)/cm^2 and linear range of 25–200 mg/dL with an ability to detect as low as 14.5 mg/dL. Further, these CH–prGO–AuNRs/ITO based electrodes attest synergistiacally enhanced sensing properties when compared to simple graphene oxide based CH–GO/ITO electrode. This is evident from one order higher electron transfer rate constant (K_s) value in case of CH–prGO–AuNRs modified electrode (12.4×10^{-2} cm/s), in contrast to CH–GO/ITO electrode (6×10^{-3} cm/s). Additionally, very low K_m value [15.4 mg/dL(0.85 mM)] ensures better binding affinity of enzyme to substrate which is desirable for good biosensor stability and resistance to environmental interferences. Hence, with better loading capacity, kinetics and stability, the proposed CH–prGO–AuNRs composite shows tremendous potential to detect several bio-analytes in the coming future.

1. Introduction

With millions dying every year due to diabetes and hypercholesterolemia (average death of one person per six second from diabetes), increasing efforts have been put in to look for better biosensing techniques, which are not only efficient, unsophisticated and reliable, but also economical. Today, market is flooded with numerous diagnostic techniques [1], among which electrochemical analysis, owing to its high sensitivity, tight selectivity, operational simplicity and low cost, has triggered a never diminishing research interest in the field of biosensors [2,3]. In principle, it involves the use of electrochemical electrodes immobilized with Glucose oxidase, which on coming in contact with Glucose results in a redox reaction and the resulting electron transfer indirectly indicates the amount of glucose being detected. The transfer of electrons from the active site of GO_x, that is thick protein layer around flavin adeninine dinucleotide (FAD) to the electrode, thereby is the limiting factor for such detection process [4]. Research in this area therefore aims to ease this flow of electrons along with improvisation in stability, sensitivty and loading capacity of such bioelectrodes for an overall enhanced sensing performance.

Intially, the first generation glucose detection electrodes for electrochemical sensing were enzyme based and suffered from poor conductivity, thereby requiring typical environmental conditions for proper functioning [5–7]. This paved in the way for second generation glucose sensors which utilized metal catalysts to achieve enhanced conductivity and stability. Down this line, several publications have attested the potential of Au [8–11], Cu [12] and Ni [13] for electrochemical sensing of glucose. Metal alloy systems, specially Au alloys such as Au–Ag, Au–Ru, Au–Pb, and Au–Cd [14,15] have also been positively studied for this generation

* Corresponding authors. Fax: +91 0542 2368174.
E-mail addresses: anchalbhu@gmail.com (A. Srivastava), pssaxena@rediffmail.com (P.S. Saxena).

http://dx.doi.org/10.1016/j.talanta.2015.05.059
0039-9140/

electrodes. Further, with nanotechnology at its apex, nanomaterials with their high surface area and astonishing electrical properties, were the expected entries as potential biosensing platform, which lead to the development of third generation glucose sensors. Among the various metal nanoparticles, gold nanorods (AuNRs) have shown promising potential for electrochemical biosensing due to (1) one dimensional (1-D) structure, which provides better electron transfer platform and excellent electrocatalytic property and (2) congenial environment for biomolecules immobilization in order to retain their biological activity [16,17]. However, attaining uniform large area coating using such noble nanoparticles is not only difficult but highly expensive too.

With uniformity as an issue, 2D materials automatically came up as a solution to improvise the then available electrochemical sensors by forming nanocomposites with nanoparticles [18]. Down this line graphene and its chemical derivatives, emerged as potential substrates for fabricating bioelectrodes having novel sensing properties with very high stability, high conductivity and stability [19,20]. Among these graphene derivatives, biocompatible graphene oxide has shown great potential for improvising the loading capactity of bioelectrodes owing to the presence of its functional groups. Various nanomaterials have been grown on GO taking the benefit of its highly negatively charged surface due to the funcational groups, which can notably enhance the electrostatic binding of metal nanoparticles with GO, resulting in a hybrid supported by electro-static assembly [21,22]. However GO suffers with low conductivity due to distorted sp^3 hybradized geometry [23–25]. On the other hand great conductivity is achieved in case of reduced grapheen oxide with planar sp^2 hybradization, but this occurs at the cost of loss in the required functional groups [26]. Very recently a new class of graphene derivative known as partially reduced graphene oxide has emerged, in which unlike rGO, pi(π) conjugations are restored only partially. Thus prGOs take in the advantages of both GO and rGO at the same time.

Motivated by the success of highly stable Au nanostructure while simultaneously realizing the promising potential of GO based composites offering additional enhanced electrical conductivity benefits after getting reduced to prGOs, we are naturally inclined for combining these two together for a synergistically improved novel composite. The aim is to achieve better, faster, reusable and economic biosensors, with enhanced biomolecules loading capacity. We opt to choose chitosan (CH) for electrode fabrication due to two fold reasons, one, to prevent the re-stacking of prGO sheets and second to exploit it as a compatible matrix with strong film forming ability and enzyme loading [27]. To achieve the above said, glucose oxidase (GO_x) was immobilized on to CH–prGO–AuNRs composite film and the resulting electrodes demonstrated good linear response for glucose biosensing, with elevated sensitivity and stability. Further, improved loading capacity (lower K_m) and faster kinetics (higher K_s) ensures lower amount of required bio-analyte and oveall increase in the efficiency of sensing process. This attests the tremendous potential of the proposed prGO–AuNRs systems to detect not only glucose but several other bio-analytes in coming future.

2. Experimental

2.1. Reagents

All the chemicals used were of analytical grade and pure. H_2SO_4 (98%), H_3PO_4, $KMnO_4$, $AgNO_3$, $NaBH_4$, $AuHCl_4$(99.99%), N-cetyl-N, N,N-Trimethyl Ammonium Bromide (CTAB), L-Ascorbic acid, Chitosan, β-D Glucose, Glucose Oxidase (200 U/mg) were purchased from Sigma-Aldrich.

2.2. Synthesis of graphene oxide (GO)

Graphene oxide has been synthesized by the improved Hummers method [28]. In brief, 3.0 g graphite flakes were first added to a solution of concentrated H_2SO_4/H_3PO_4 (9:1). 18.0 g of $KMnO_4$ was then slowly added to the above formed mixture. The resulting mixture was stirred for 12 h at 50 °C. Obtained suspension was normally cooled down to room temperature and 400 mL of ice along with 3 mL of 30% H_2O_2 was subsequently added. This was then filtered to obtain acidic GO as the filtrate. Further, the filtrate was centrifuged (4000 rpm for 4 h) and the supernatant was decanted away. The material was washed in succession with 200 mL of distilled water, 200 mL of 30% HCl, and with 200 mL of ethanol. For each wash, the mixture was filtered and centrifuged (4000 rpm for 4 h) and the supernatant was decanted away repeatedly. Finally, the obtained brown colored semi-solid, that is GO was vacuum-dried at room temperature.

2.3. Synthesis of gold nanorods (AuNRs)

Gold nanorods were prepared by seed-mediated growth method [29]. For this 5 mL of CTAB solution (0.2 M) and 5 mL of $HAuCl_4$ solution (0.5 mM) were mixed by stirring. To the above solution, 0.6 mL of freshly prepared ice-cold $NaBH_4$ (0.01 M) solution was added to get a brownish yellow seed solution. Further growth solution was prepared by adding 5 mL of $AgNO_3$ (0.004 M) and 25 mL of $HAuCl_4$ (1 mM) to 25 mL of CTAB (0.2 M). Subsequently, 0.275 mL of ascorbic acid (0.1 M) was added to this solution resulting in the growth solution. Finally, to obtain AuNRs, seed solution (0.060 mL) was added to the growth solution (50 mL), and the mixture was gently shaken, resulting in a gradual color change from colorless to blue, within 20 min. To complete this growth process, the above obtained solution was then kept at 30 °C for 24 h. Finally, above obtained AuNRs suspension was centrifuged at 10,000 rpm for 10 min to obtain homogenous mixture of required AuNRs, which was stored at 30 °C in a dark room.

2.4. Preparation of prGO–AuNRs composite

10 mg of GO was first dispersed in 20 mL of deionized water via sonication (30 min) following which mild reducing reagent that is ascorbic acid (100 μL) was added and stirred for 2 h at 60 °C. A composite of prGO and AuNRs was then prepared by sonicating 10 mL of prGO with 4 mL of re-dispersed AuNRs in deionized water for 1 h at 50 °C. This composite solution was incubated overnight prior its use for biosensing purpose. A schematic representation of the synthesis of prGO–AuNRs composite has been shown in Fig. S1 (See in Electronic Supplementary Information (ESI)), which showcases electrostatic interaction between positive charge of AuNRs (red) and negative charge of prGO.

2.5. Preparation of CH–prGO–AuNRs electrode

A film of CH–prGO–AuNRs composite was fabricated on Indium Tin Oxide (ITO) coated glass substrate via spin coating technique. For this, a solution of chitosan was prepared by dissolving 50 mg of chitosan in 10 mL of distilled water with 2 mL acetic acid. Utilizing standardized concentration, 3 mL of prGO–AuNRs composite was thoroughly mixed with 6 mL of chitosan solution. A uniform thin film of prGO–AuRods composite was deposited on ITO electrode by spin coating, which was further dried at 40 °C. This CH–prGO–AuNRs electrode was finally washed with phosphate buffer saline (PBS) (0.2 M, pH 7.0) to remove any unbounded particles.

2.6. Preparation of $GO_{x/CH\text{-}prGO\text{-}AuNRs/ITO}$ bioelectrode

100 μL Of freshly prepared glucose oxidase (1 mg /mL) in PBS (0.2 M, pH 7.0) was added to CH–prGO–AuNRs composite solution and kept undisturbed at room temperature for 12 h, to ensure its immobilization and entrapment in CH matrix. A uniform thin film of GO_x–CH–prGO–Au Rods was deposited on ITO electrode by spin coating, which was subsequently dried at room temperature. The schematic representation of bioelectrode fabrication has been shown in Fig. S2 [see electronic supplimentry information (ESI)], where, the coil shape denotes CH (blue), the sheet shape represents prGO (brown), while the rod shape represents AuNRs (red). Finally, these obtained electrodes were washed with PBS (0.2 M, pH 7.0) to remove any unbounded GO_x enzyme from the electrode surface followed by drying at room temperature. These biosensor electrodes were then used for electrochemical glucose biosensing.

2.7. Characterization

The UV–Vis absorption spectra were collected using a Perkin Elmer UV-Visible-Lambda 25 spectrophotometer. The morphological changes were observed employing both scanning electron microscope [FE-SEM (Zeiss, Merlin), operated at 20 V–30 kV] and FEI Tecnai-G2 ransmission electron microscopy (TEM) techniques. Raman spectrometer (micro-Raman setup, Renishaw, Gloucestershire, UK) with an excitation source of Ar^+ laser (514.5 nm) was used to record the Raman spectrum of the material with a resolution of $\sim 1\ cm^{-1}$. Further, X-Ray diffraction (XRD) patterns were taken using the XRD instrument (Rigaku Desktop Miniflex II X-Ray diffractometer (Rigaku Corporation, Tokyo, Japan) equipped with Cu-Kα_1 as the source of X-ray along with a Ni filter. Fourier transform infrared spectroscopy (FTIR) measurements were performed using thermoscientific FTIR (Thermo Nicolet-6700). Finally, Cyclic voltammetry (CV) was performed using Autolab (PGSTAT101, Metrohm, The Netherlands) containing three electrode cells each having platinum foil as the counter electrode, Ag/AgCl (saturated KCl) as the reference electrode and Indium tin oxide (ITO) coated glass plate, modified with composite materials as the working electrode.

3. Results and discussion

3.1. Structural characterization

The X-ray diffraction (XRD) pattern of as synthesized GO can be seen in Fig. S3a (see ESI). Two intense peaks at 11.6° and 42.2°, corresponding to (002) and (001) reflection planes of GO can be clearly seen. Further a weak diffraction peak at 26° confirms complete conversion of graphite into GO through oxidative treatment. XRD results for prGO–AuNRs composite is seen in Fig. S3b (see ESI), where the peaks positioned at 38.21°, 44.41°, 64.61° and 77.61° depict (111), (200), (220) and (311) planes of AuNRs (JCPDS-04-0783). Further, the absence of peak at 11.6° [corresponding to (002) reflection plane of GO] in prGO–AuNRs indicates effective conversion of GO into prGO during the synthesis of composite. Finally, a broad and weak peak appearing at 25.6° signatures prGO.

Scanning electron microscopy (SEM) was carried out to characterize the surface morphology of GO, AuNRs and prGO–AuNRs composites and the micrographs are presented in Fig. 1. The micrograph of GO sheet as seen in Fig. 1(a) suggests several micrometers of homogeneity in lateral dimensions. Further, the wrinkled morphology can be visualized in the same image. The rod like structure of AuNRs with low aspect ratio can be seen in Fig. 1(b), with the inset Figure disclosing its magnified view. The AuNRs have average length of approximately 32 nm and average diameter of 16 nm, resulting in an average aspect ratio of 2.0. Fig. 1(c) shows the images of prGO–AuNRs, wherein again the inset image shows its magnified image. These images attest a clear decoration of AuNRs on the surfaces and in between the layers of prGO sheets. Finally, Fig. 1(d) shown energy dispersive X-ray (EDX) spectroscopy results of prGO–AuNRs. It confirms that the composite mainly contains carbon (C), oxygen (O) and gold (Au) elements, as expected on distributing AuNRs on the surface of prGO sheets. The copper (Cu) contribution comes from the copper grid used for the TEM measurements.

The morphology of AuNRs was further investigated using TEM and the micrographs are seen in Fig. 2. Fig. 2(a) signifies that the prepared AuNRs are quite uniform in shape and size with an average aspect ratio of about 2. Further, the selected area diffraction (SAED) pattern in Fig. 2(b) indicates that the grown particles

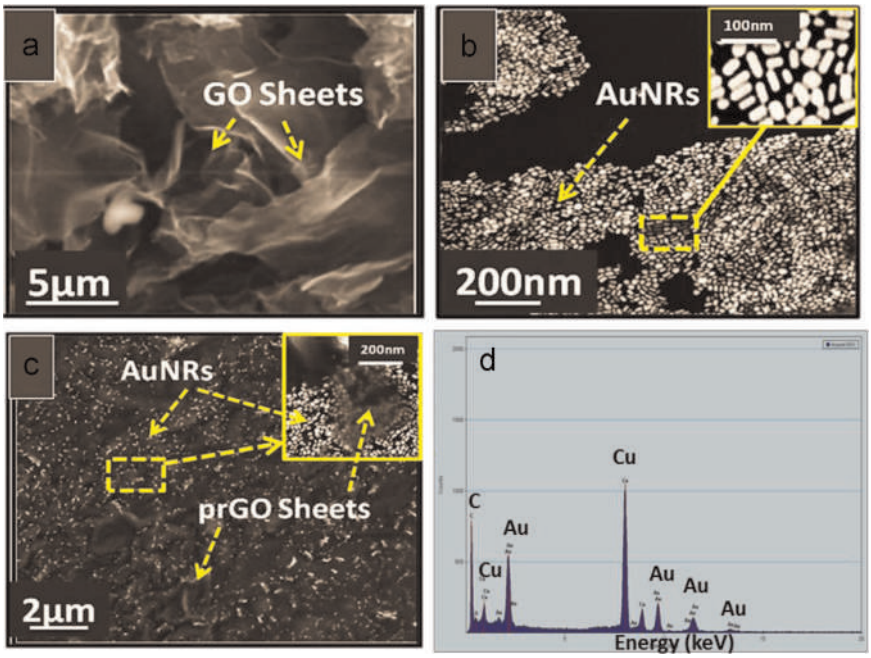

Fig. 1. SEM micrographs of (a) GO, (b) AuNRs, (c) prGO–AuNRs composite and (d) EDX spectrum of prGO–AuNRs composite.

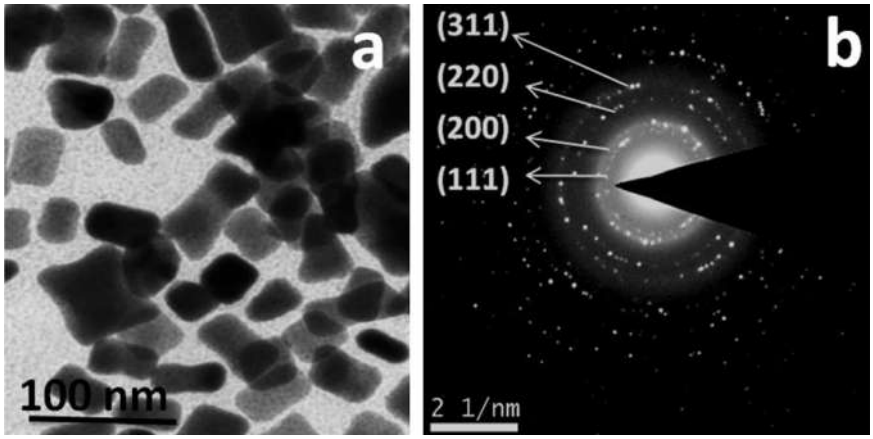

Fig. 2. (a) TEM image of AuNRs and (b) SAED pattern attesting crystallinity of the AuNRs with FCC lattice.

are crystalline in nature and have *FCC* lattice.

3.2. Spectroscopic characterization

Fourier Transform Infra Red spectroscopy (FTIR) study of GO and prGO–AuNRs composites has been summarized in Fig. 3. Fig. 3 (a) shows the FTIR spectra of GO where the peak at 1629 cm^{-1} corresponds to –C=C skeletal vibration, while the peaks at 1730 cm^{-1} and 1399 cm^{-1} are due to stretching vibrations of –C=O and –C–O bonds present in the carboxylic group. Further the epoxide (–C–O–C) group is confirmed by the peak found at 1220 cm^{-1}. Similarly, –OH functional groups reason out the peaks at 3439 cm^{-1} and 1070 cm^{-1}. In case of prGO–AuNRs composite, the peak intensity of these functional groups as seen in Fig. 3 (b) are reduced, attesting partial reduction of GO into prGO [XRD as well as FTIR data suggests the removal of functional groups between the planes of GO, and the controlled conversion of GO into prGO during the synthesis of prGO–AuNRs composite].

Fig. 4(A) shows the UV–Visible absorption spectra of GO, prGO and rGO solutions. In Fig. 4(A) (a), an absorption peak seen at λ_{max}~236 nm signatures the surface π-plasmon excitation (attributed to the π–π^* transition of carbon double bonds) of GO [30]. After partial reduction of GO, the absorption peak in comparison to GO slightly shifts (λ_{max}~236–254 nm) towards the red end as seen in Fig. 4(A)(b). On the other hand, the absorption peak in comparison to prGO shift even more in the case of rGO (λ_{max}~254–268 nm) as observed in Fig. 4(A)(c)].

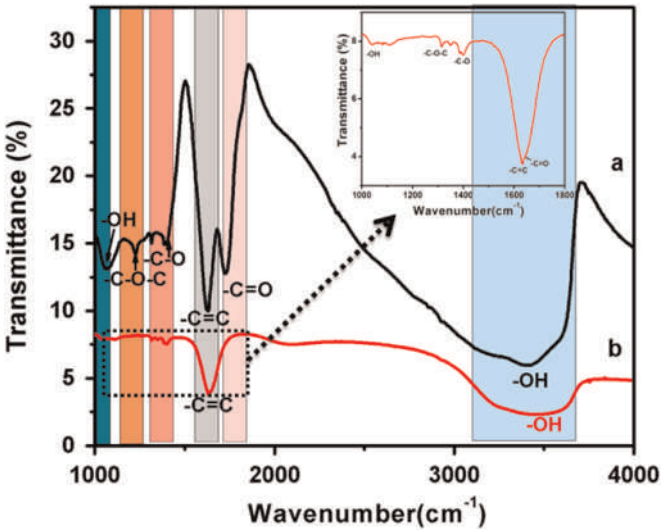

Fig. 3. FTIR spectra of (a) GO and (b) prGO–AuNRs.

The interaction of prGO with AuNRs is also confirmed by the UV–Vis spectroscopy result shown in Fig. 4(B). Curve b of Fig. 4 (B) attests that the surface plasmon absorption of synthesized AuNRs shows two bands: a strong long wavelength band (λ_{max} at 705 nm) due to the longitudinal oscillation of electrons and a weak short wavelength band (around 524 nm) in the visible region due to the transverse electronic oscillation. However, the optical absorption in the red region is not seen in case of GO as attested by curve a in Fig. 4(B). Finally, in case of prGO–AuNRs broad and red shifted (from 705 to 715 nm) plasmon band corresponding to the AuNRs loaded on prGO matrix can be seen in curve c in the same Figure. This is different from the spectra obtained for pure AuNRs due to the composite formation.

Raman spectrum of Graphite, GO, prGO and rGO have been shown in Fig. S4 (ESI). In case of graphite a prominent band at ~1576 cm^{-1} (G-band) can be seen along with a 2D band around 2700 cm^{-1}. Relatively low or negligible D-band at ~1340 cm^{-1} indicates near about absence of disordered/defected structure in graphite. In case of GO, the D band is broader in comparison to G band in case of graphite, prGO and rGO. Further, the intensity ratio (by area) I_D/I_G is also more (1.7) than that of graphite, prGO and rGO, indicating higher disordered nature due to both, high functionalization and high sp^3/sp^2 hybridization ratio. Additionally, the 2D band also disappears in case of GO. In case of prGO, the I_D/I_G ratio decreases to 1.13, which is driven by partial re-stacking of sp^2 hybridization and the removal of some functional groups. Further, in case of rGO, it is found that the I_D/I_G ratio further decreases to 1.0, which is an indication of the near about complete reduction of GO–rGO. The re-generation of 2D-band can also be noticed in case of both, prGO and rGO, attesting their increased graphitic nature.

Fig. 5(A) shows the FTIR spectra of the three graphene derivatives, GO, prGO and rGO with varying level of functional groups. Fig. 5(A)(a) represents the FTIR spectrum of GO and the various functional groups present. In Fig. 5(A)(b), that is in case of prGO, the peak intensity of these functional groups are found to be reduced, attesting partial reduction of GO into prGO Finally, in case of rGO as seen in Fig. 5(A)(c), the FTIR peak intensites reduce to much more significantly, indicating the removal of more oxygen containing functional groups in comparison to prGO.

Fig. 5(B) shows the FTIR spectra of pure chitosan (curve a), CH–prGO–AuNRs/ITO (curve b) and GO_x/CH–prGO–AuNRs/ITO (curve c) as bioelectrode materials. The peak around 3435 cm^{-1} in curve a represents the presence of $–NH_2$ functional group in case of pure chitosan. Further the mixing of prGO–AuNRs composite in chitosan (curve b), results in a peak around 3421 cm^{-1} indicating the stretching vibrational modes of –OH and $–NH_2$ functional groups.

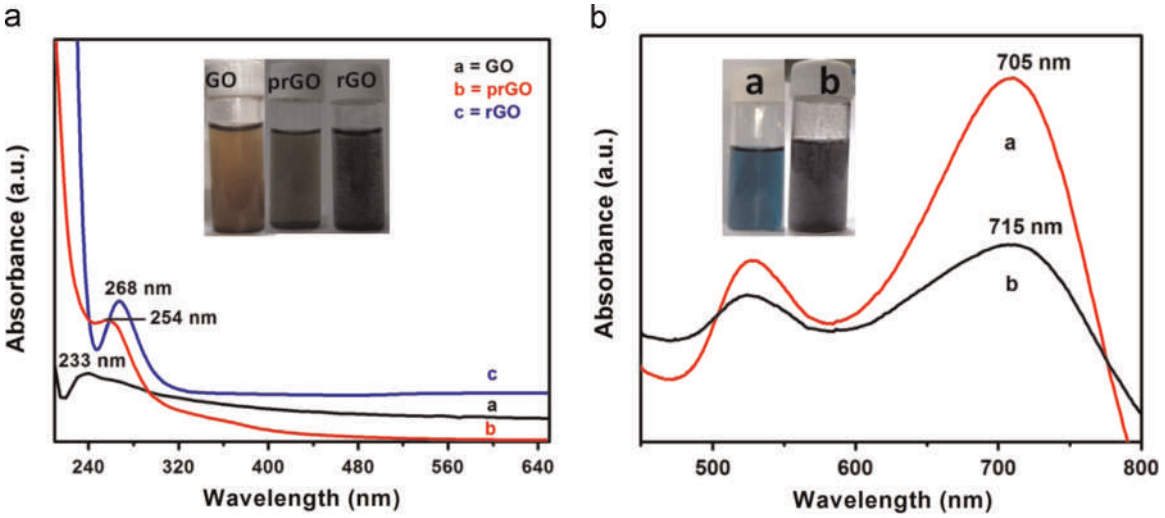

Fig. 4. Absorption spectra of (A) (a) GO, (b) prGO and (c) rGO solution and (B) (a) AuNRs and (b) prGO–AuNRs composite solution. Inset shows optical images.

Absence of any signature of negatively charged –COOH groups in prGO–AuNRs s probably due to its involvement in electrostatic interaction with positively charged gold nanorods. Further, the peaks at 1650 $cm^{-1}$and 1550 cm^{-1} (curve c) represent the –C=O (amide I) and –N–H (amide II) band, respectively suggesting the proper immobilization of GO_x on CH–prGO–AuNRs/ITO electrode.

3.3. *Electrochemical characterization of electrodes and bioelectrodes*

Cyclic voltammetry (CV) of these fabricated bioelectrodes has been obtained using Autolab with a three electrode system in phosphate buffer saline (PBS; 0.2 M, pH 7.0) containing 5 mM of $[Fe(CN)6]^{3-/4-}$ as conducting solution with a potential range of −1.00–1.00 V and a scan rate of 50 mV/s. Here platinum is used as the counter electrode, CH–prGO–AuNRs/ITO as the working electrode and Ag/AgCl as the reference electrode. Fig. 6 summarizes comparative study of peak current response of electrode materials. The results confirm higher peak current response for the composite material (CH–prGO–AuNRs/ITO) [9×10^{-4} A, (curve e)] in comparison to CH–GO/ITO [7.07×10^{-4} A, curve (b)], CH–prGO/ITO [7.9×10^{-4} A, (curve c)], CH–AuNRs/ITO [8.02×10^{-4} A, (curve d)] and ITO [6.3×10^{-4} A, (curve a)], attesting its potential to be used for fabricating bioelectrode for sensing purposes.

The anodic peak current obtained for CH–GO/ITO is 7.02×10^{-4} A, which increases to 9.0×10^{-4} A for CH–prGO–AuNRs /ITO electrode. The pronounced increment in the current

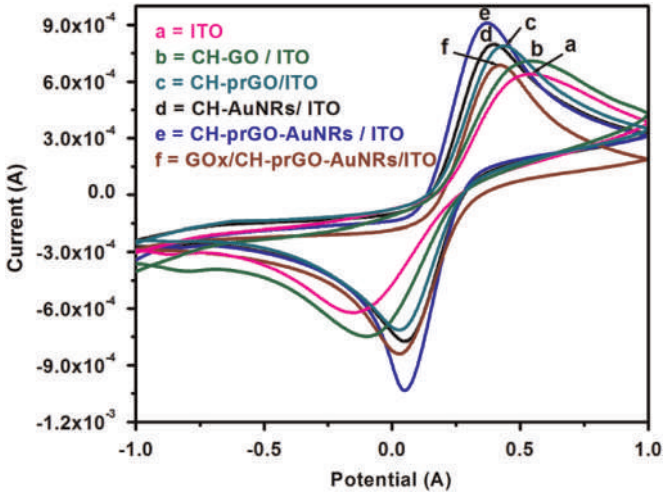

Fig. 6. Peak current response of ITO electrode (Curve a), CH–GO/ITO (curve b), CH–prGO/ITO (Curve c), CH–AuNRs/ITO (Curve d), CH–prGO–AuNRs/ITO (Curve e) and GO_x/CH–prGO–AuNRs/ITO bioelectrode (Curve f).

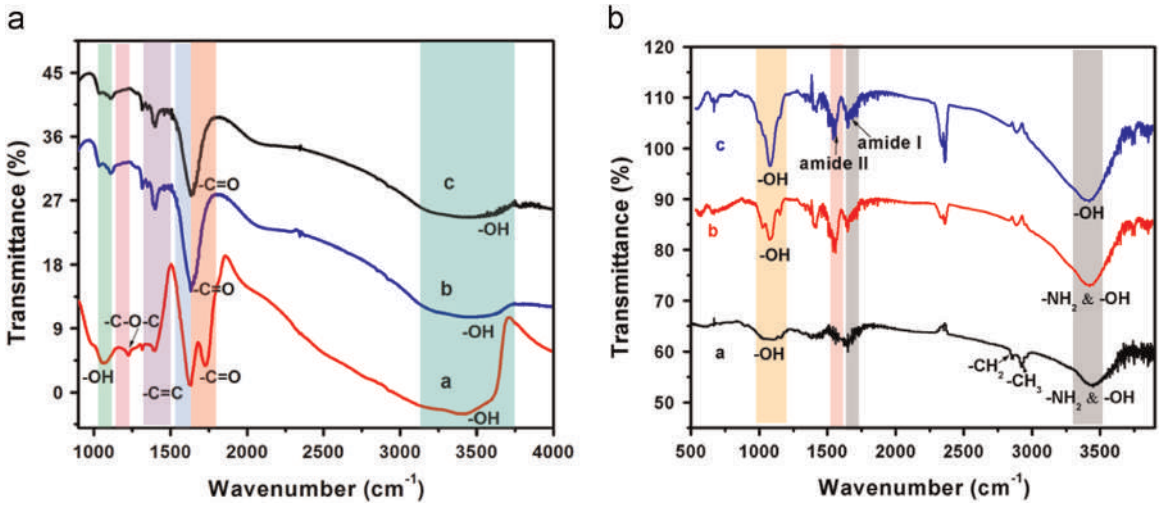

Fig. 5. FTIR spectra of (A) (a) GO, (b) prGO and (c) rGO and (B) (a) Chitosan, (b) CH–prGO–AuNRs/ITO electrode and (c) GO_x–CH–prGO–AuNRs/ITO bioelectrode.

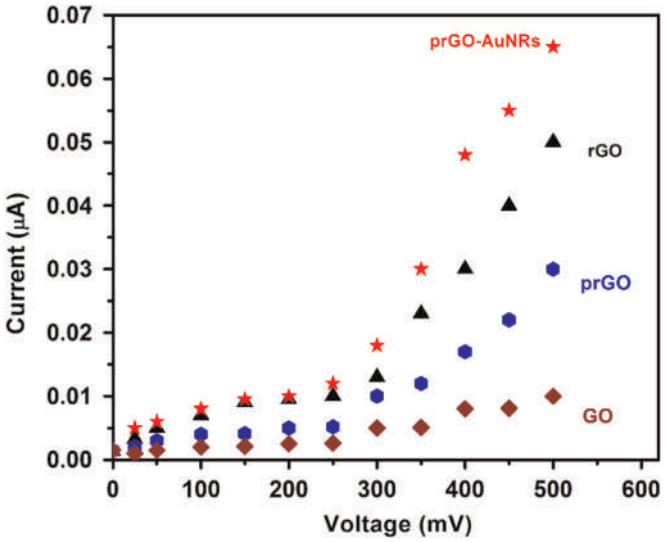

Fig. 7. *I–V* Characteristics of GO, prGO, rGO and prGO–AuNRs for the forward voltage region 0–500 mV.

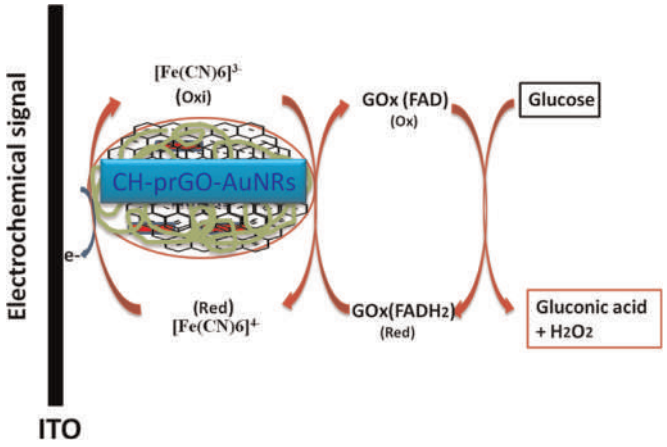

Fig. 8. Schematic diagram of electron transfer to ITO in red-ox electrochemical reaction.

value may be attributed to the excellent electrocatalytic property of the AuNRs along with further synergistic enhancement con their combination with prGO. This results in facile electron transfer, while simultaneously providing large surface area for an overall enhanced sensing performance. After GO_x attachment, the anodic peak current of GO_x/CH–prGO–AuNRs/ITO bioelectrode (curve f) decreases to 6.84×10^{-4} A as compared to CH–prGO–AuNRs /ITO (9.0×10^{-4} A), which may be attributed to the insulating nature of the attached enzyme (GO_x).

Fig. 7 shows *I–V* measurements of the four samples, GO, prGO, rGO and prGO –AuNRs using Keithley Instrument at room temperature. The forward scan results from 0 to 500 mV are shown below which suggest that the electrical conductivity of rGO is superior to prGO, which in turn has superior conductivity in comparison to GO. However, synergistically enhanced conductivity is obtained in case of prGO–AuNRs, which is higher than GO, prGO and rGO.

Further, surface concentration of the GO_x/prGO–AuNRs/ITO bioelectrode has been calculated using Brwon–Anston Model (Eq. (1)).

$$Ip = n^2F^2I^*AV/4RT \quad (1)$$

where, n is the number of electrons transferred, F is Faraday constant (96485.5 C/mol), I^* is the surface concentration (mol/cm^2), A is the surface area of the electrode (0.5 cm^2), V is the scan rate (50 mV/s), R is the gas constant (8.134/ mol K) and T is the room temperature (298 K). The surface concentration of GO_x/prGO–AuNRs/ITO bioelectrode is recorded as high as 4.7×10^{-1} mol/cm^2, suggesting higher loading of glucose oxidase onto prGO–AuNRs/ITO electrode, which undoubtedly leads to enhanced efficiency of the bioelectrode compared to other biosensors.

3.4. Study of electrochemical response of GO_x/CH–prGO–AuNRs/ITO bioelectrode

Realising the important parameters making up an impeccable biosensor, a meticulous electrochemical sensing study was performed and commendable results were obtained. As the first step, the peak current response was performed to check the positive biosensing nature. On obtaining positive results, tests for calculating detection limit, linearity and sensitivity, were carried out in order to determine how good a biosensor these proposed bioelectrodes are. Further, these biosensors' resistance to environmental interference, which remains one of the key disadvantages of present generation biosensors, was put to test. With good level of success in above tests, further its ability to require lesser input (loading capacity) to produce accurate desired output in lesser time (kinetics-K_s) was attested. To appreciate the important role of prGO–AuNRs matrix for better and effecient biosensing surpassing earlier reported biosensors, a study of the K_m value was also performed. With outstanding results in all above parameters, finally, to confirm the reliability of our study, commendable reproducibility of these bioelectrodes was chonfirmed.

The peak current response of GO_x/CH–prGO–AuNRs/ITO bioelectrode has been studied as a function of glucose concentration. The mechanism of electron transfer during the course of biosensing has been sketched in Fig. 8. In biochemical reaction, GO_x catalyses decomposition of glucose into gluconic acid and H_2O_2, as summarized in reaction Eqs. (2–4).

The biocatalytic reaction involves the reduction of the flavin adenine dinucleotide (FAD) group in the enzyme into $FADH_2$ by its reaction with glucose (Eq. (2)). The redox reaction is completed by further re-oxidation of the FAD by molecular oxygen to regenerate the oxidized form of the enzyme GO_x (FAD) (Eq. (3)).

$$GOx(FAD) + \beta\text{–D} - \text{Glucose} \rightarrow GOx(FADH_2) + \text{Gluconic acid} \quad (2)$$

$$GOx(FADH_2) + O_2 \rightarrow GOx(FAD) + H_2O_2 \quad (3)$$

$$H_2O_2 \rightarrow O_2 + 2e^- + 2H^+ \quad (4)$$

Oxidation of produced H_2O_2 results in increased response current at positive potential, while consumption of O_2 leads to decreased negative potential. The electrons generated during the biochemical reaction are transferred to the electrode via Fe(III)/Fe (IV) redox probe, ensuing a signal in the form of current. The calibration curve has been made by fitting the obtained value of glucose concentration and value of anodic peak current $I_{p,}$ as seen in Fig. 9(a). Further, from Fig. 9(b), it was found that the magnitude of current increases linearly as glucose concentration increases (biosensing ranges as 10–200 mg/dL), obeying Eq. (5).

$$I_p = 7.962 \times 10^{-4}[A] + 1.599 \times 10^{-6}\text{A/mg /dL (B)} \times \{\text{Glucose concentration(mg/dL)}\} \quad (5)$$

where $I_{p,}$ A and B indicate anodic current, intercept and slope respectively. Clearly, GO_x/CH–prGO–AuNRs /ITO bioelectrode exhibits increased linearity of 25–200 mg/dL with as low as 14.5 mg/dL detection limit. Further, sensitivity as high as

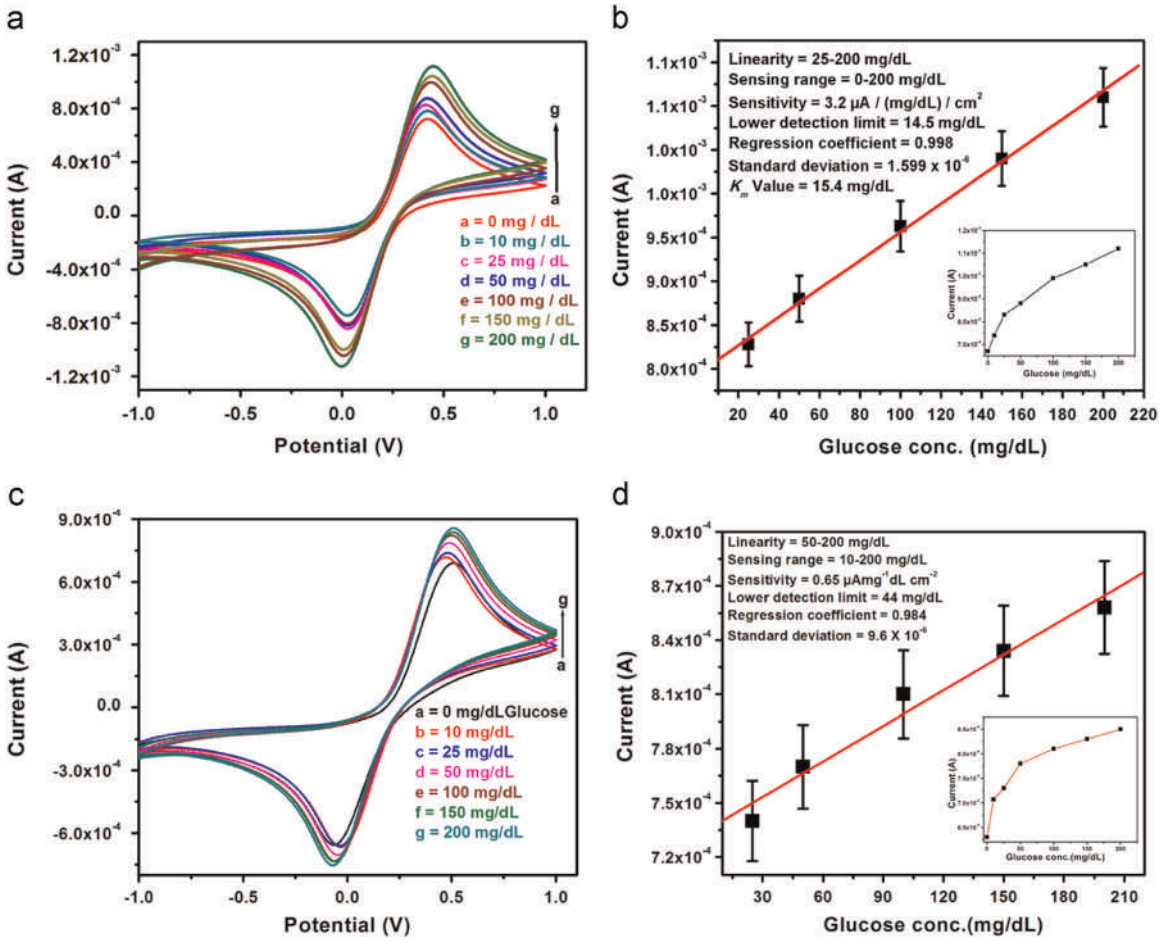

Fig. 9. Peak current response of (a) GO_x/CH–prGO–AuNRs/ITO and (c) GO_x/CH–AuNRs/ITO bioelectrodes as a function of glucose concentration; (b) and (d) Calibration curve between magnitude of anodic peak current (I_p) and glucose concentration (Inset glucose sensing range curve) for GO_x/CH–prGO–AuNRs/ITO and GO_x/CH–AuNRs/ITO bioelectrodes respectively.

Table 1
Sensing characteristics of GO_x/CH–prGO–AuNRs/ITO bioelectrode along with those reported in literature.

Bioelectode materials	Detection limit (mM)	Linearity (mM)	Sensitivity (μA/mM/cm^2)	K_m (mM)	References
Thiolated gold	–	2.7–22.20	–	3.70	[32]
ZnO nanocomb	0.02	2.02–4.00	15.30	2.10	[33]
ZnO nanorod	0.01	0.001–3.40	23.10	2.60	[34]
Au–CH/Pt	7.0	0.5–10	0.50	10.50	[35]
Au–CH	13.0	5×10^{-5} to 1.3×10^{-3}	–	3.50	[36]
CNT–CH	–	0–7.80	0.50	8.20	[37]
Pt–MWCNT–CH–SiO_2	1.0	1–20	58.90	14.40	[38]
Graphene–chitosan	0.02	0.08–12.00	37.93	8	[39]
rGO–GO_x	–	0.1–27	1.85	–	[40]
Pd–rGO	0.034	–	14.1	–	[41]
rGO–ZrO_2	–	0.29–14.00	11.65	–	[42]
Fn–GO	–	0.1–20	7.66	–	[43]
CH-prGO-AuNRs	**0.80**	**1.3–11.10**	**57.63**	**0.85**	**Present work**

3.2 μA/(mg/dL)/cm^2 (with regression coefficient of 0.998) has been calculated for GO_x/CH–prGO–AuNRs/ITO bioelectrode, further attesting the potential of the proposed bioelctrode composite system. A comparative study between GO_x/CH–prGO–AuNRs/ITO and GO_x/CH–AuNRs/ITO bioelectrode is shown in Fig. 9(c) and (d) respectively. It further suggests that in contrast to GO_x/CH–prGO–AuNRs/ITO, GO_x/CH–AuNRs/ITO shows lower sensitivity (0.65 μA/(mg/dL)/cm^2) as well as detection limit (44 mg/dL), resulting in an overall decreased response.

Lower detection limits (LODs) have been calculated based on the standard deviation of the response (SD) and the slope (B) of the calibration curve in Fig. 9(b). Post this approximation the LOD is calculated according to the formula: LOD = 3(SD/B). For doing so, the standard deviation of the response has been determined utilising standard deviation of y-intercepts of regression lines. The potential of the proposed system to work in complex biological systems was also put to test and compared with the conventioanal enzymetic based Auto Analyzer technique for glucose detection in human serum samples. The results are comparable with those obtained using conventional techniques, as attested by the low relative errors (relative to conventional techqniues) (Table S1, ESI).

Next, to develop an understanding of the electron kinetics involved, the standard electron transfer rate constant (K_s) value was calculated at the bioelectrodes during the reaction. The K_s value at

bare ITO, CH–GO/ITO and CH–prGO–AuNRs/ITO electrodes was calculated using Klingler and Kochi equation as shown in Eq. (6) [31].

$$K_s = 2.18\sqrt{\left(\frac{D\alpha nFv}{RT}\right)}\exp\left[-\frac{\alpha^2 nF}{RT}\left(E_p^a - E_p^c\right)\right] \quad (6)$$

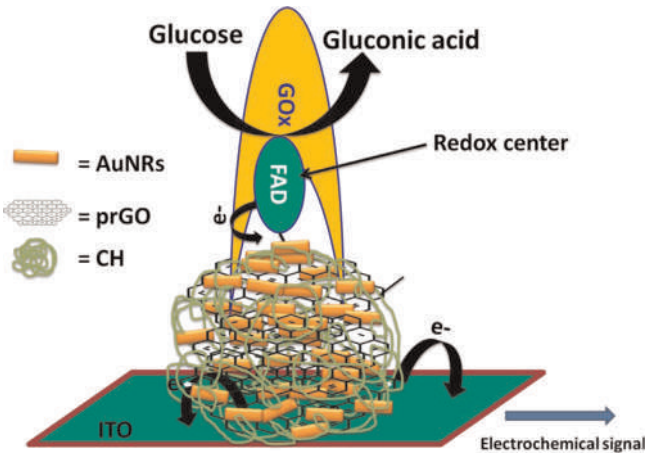

Fig. 10. Schematic diagram of electrical contact between electrode and redox center of GO_x.

where R, F, α (For ITO: $\alpha=0.19$, CH–GO/ITO: $\alpha=0.2$ and CH–prGo–AuNRs/ITO: $\alpha=0.23$) and T are the gas constant, Faraday constant, transfer coefficient and the temperature in Kelvin respectively. Similarly, K_s is standard heterogeneous rate constant, D is diffusion coefficient, E_p is oxidation peak potential, $E_{p/2}$ is half-wave oxidation peak potential and finally ν is scan rate. In present study, the D value was determined using Randles–Sevcik equation. The K_s value of bare ITO, CH–GO/ITO and CH–prGO–AuNRs/ITO electrodes have been estimated as 2.2×10^{-3} cm/s, 6.0×10^{-3} cm/s and 12.4×10^{-2} cm/s respectively. The K_s value obtained for the CH–prGO–AuNRs/ITO is relatively higher than that observed for Au-DTSSP-GOD (0.026 cm/s) [32] and oxidized copper electrodes ($5.0–9.0\times10^{-4}$ cm/s) [33] reported in literature. The obtained higher K_s value at CH–prGO–AuNRs/ITO electrode indicates that the oxidation of glucose was faster at the CH–prGO–AuNRs/ITO electrode than at the CH–GO/ITO and bare ITO electrode.

The K_m value which reveals the affinity of GO_x (lower the K_m, better it is) for glucose was estimated by Hanes–Woolf plot [34]. It should be noted that K_m is dependent both on the matrix as well as the method of enzyme immobilization which results in conformational changes. Also the value of K_m for the bound enzyme can be lower or higher than that of purified enzyme. In the present study, the calculated value of K_m for the GO_x/CH–prGO–AuNRs/ITO bioelectrode is 15.4 mg/dL (0.854 mM), which is much smaller than K_m of most of the earlier reported biosensing systems (Table 1).

The value of K_m compared to the reported values for metal

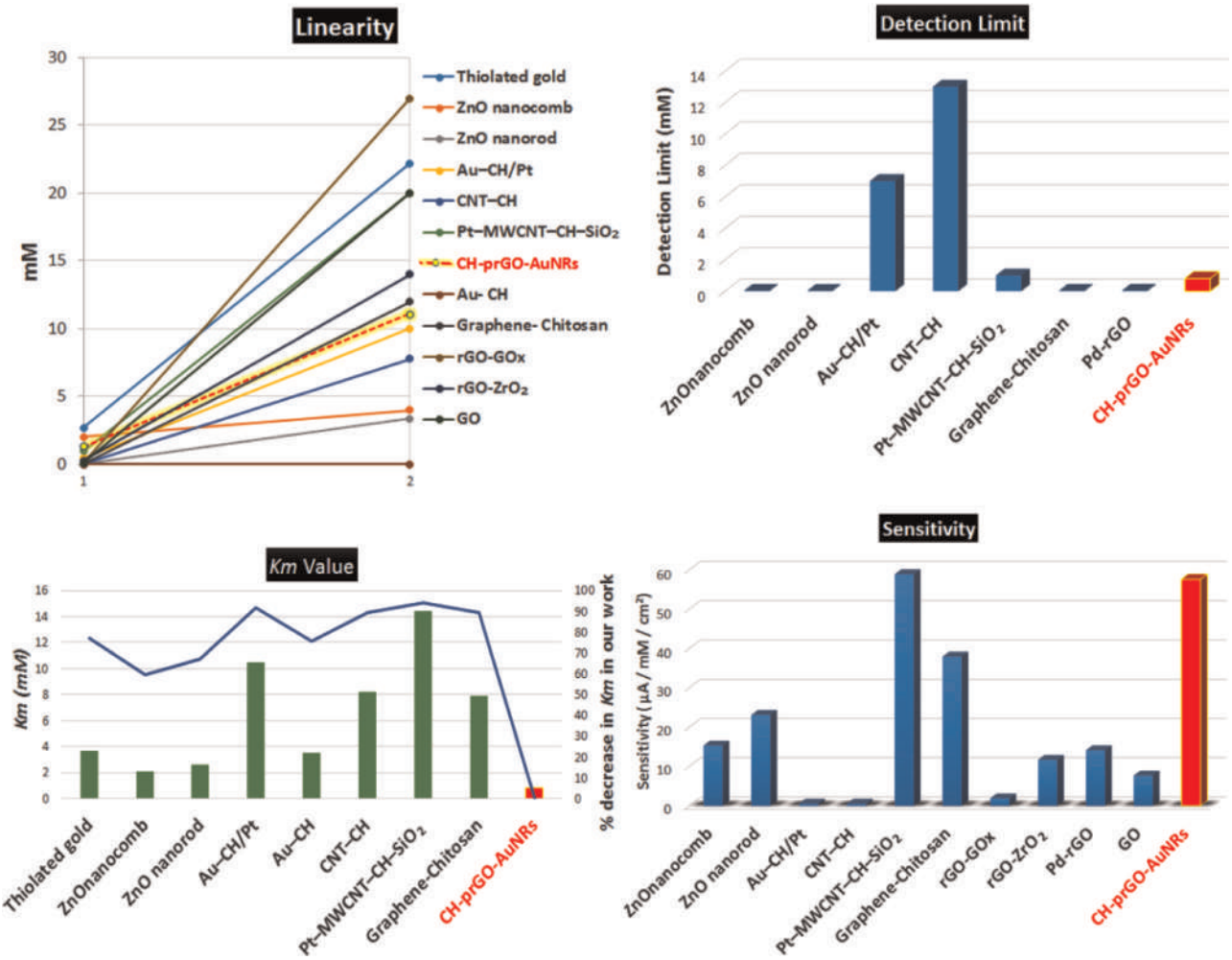

Fig. 11. Comparative study of discussed critical parameters (Detection Limit, Linearity, Sensitivity and K_m) with the earlier reported biosensors.

oxide and CH-based matrices (Table 1), suggests that the prGO–AuNRs matrix helps the immobilized GO_x to achieve better conformation for faster enzymatic reaction, resulting in the enhanced enzymatic activity. In earlier reports, it has been seen that glucose oxidase does not directly transfer electrons to conventional electrodes because of a thick protein layer surrounding its flavin adenine dinucleotide (FAD) redox center, thereby introducing an intrinsic barrier to direct electron transfer [35]. The present study circumvents this barrier as prGO–AuNRs provides better platform for electron transfer between the immobilized proteins and electrode substrates, resulting in better electrochemical response. This phenomenon is presented schematically in Fig. 10.

In order to appreciate the potential of our proposed biosensor system, a comparative study with the earlier reported biosensors, in terms of all the above discussed critical parameters (Detection limit, Linearity, Sensitivity and K_m) has been summarized in Fig. 11. It is evident that though the earlier reported Au–Ch and CNT–CHCH based biosensors have better detection limit, with comparable linearity, but our composite surpasses them and several others by showing extremely low K_m value and much higher sensitivity. Similarly those showing better linearity (ZnO nanocomb, Graphene–chitosan, rGO–GO_x, Pd–rGO, rGO–ZrO_2 and Thiolated gold based biosensor) fail to impress in terms of sensitivity, detection limit and K_m value.

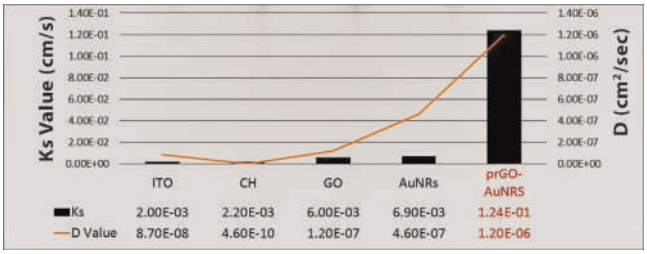

Fig. 12. Comparative study of K_s and D for bioelectrode.

Further, a comparison of the K_s parameter in Fig. 12 attests the ability of prGO–AuNRs composite to provide synergistically enhanced interaction between the enzyme (GO_x) and the bioelectrode for better biosensing activity. This is evident from the higher K_s value for the proposed prGO–AuNRs composite than bare ITO, CH, Au and prGO.

Resistance to interference is yet another important ability that is required for the biosensosr to be useful in real life complex system. The peak current response of $GO_{x/CH\text{-}prGO\text{-}AuNRs/ITO}$ biosensors upon addition of interferents like cholesterol (5 mM), ascorbic acid (0.05 mM), uric acid (0.1 mM) and urea (1 mM) with glucose (100 mg/dL) in phosphate buffer (0.2 M, pH 7.0) has been studied. No significant change in current response occurs by the presence of these interfering species, which confirms the proposed $GO_{x/CH\text{-}prGO\text{-}AuNRs/ITO}$ biosensor's high specificity for glucose (Fig. 13a).

Commendable stability of the $GO_{x/CH\text{-}prGO\text{-}AuNRs/ITO}$ bioelectrode was confirmed by measuring peak current response with respect to time at a regular interval of 1 week. The proposed biosensor showed only slight decrease in peak current response after 5 weeks, when stored in refrigerated conditions (4 °C) (Fig. 13b).

Finally, reproducibility, which often effects the biosensors adversely was put to test. For this four different $GO_{x/CH\text{-}prGO\text{-}AuNRs/ITO}$ bioelctrode were prepared under the same set of procedure. When tested for response, there was no change in peak current response (Fig. 13c). The % RSD values of inter-repeatability was calculated to be 1.13% and negligible variation was found for the intra % RSD values. The sensing performance of the GO_x/CH-prGO-AuNR/ITO bioelectrode based glucose biosensor is summarized in Table 1 along with those reported in the literature.

4. Conclusion

We have successfully tailored a composite of partially reduced graphene oxide and gold nanorods supported by chitosan (prGO–AuNRs) as an highly efficient electrode material for fabrication of

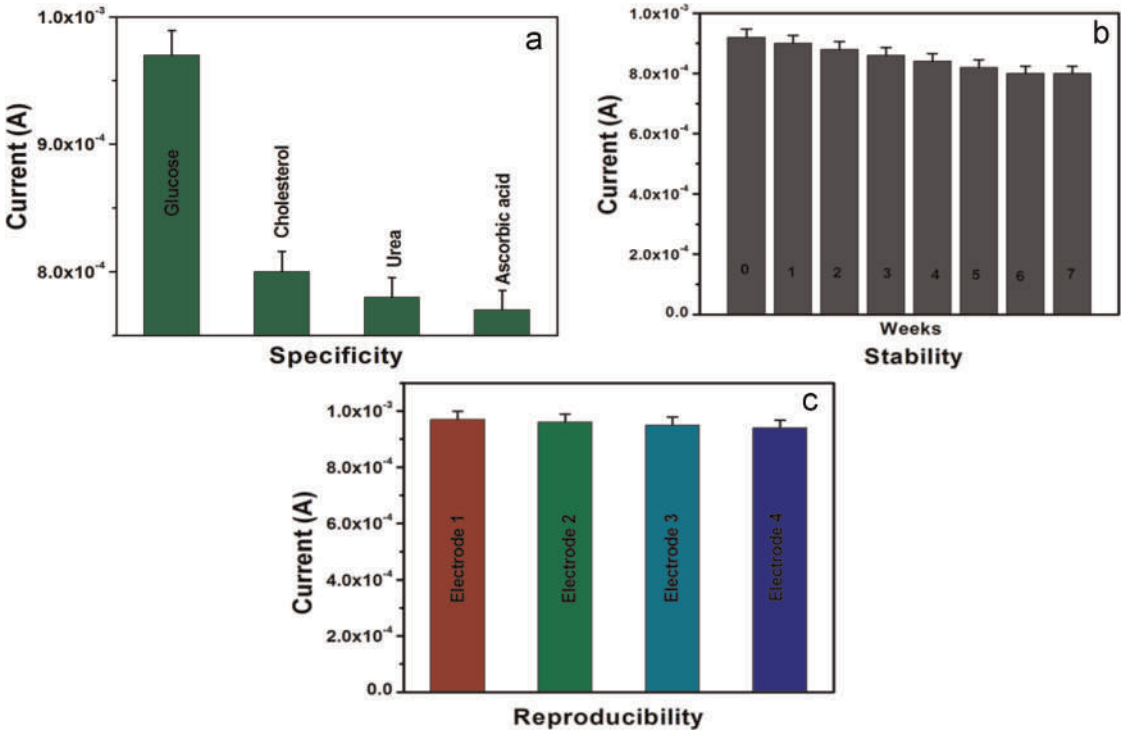

Fig. 13. (a) Peak current response of $GO_{x/CH\text{-}prGO\text{-}AuNRs/ITO}$ bioelectrode in presence of glucose, Cholesterol, Urea and Ascorbic acid, (b) peak current response of $GO_{x/CH\text{-}prGO\text{-}AuNRs/ITO}$ bioelectrode measured at regular interval of one week conducted in PBS, and (c) peak current response of different $GO_{x/CH\text{-}prGO\text{-}AuNRs/ITO}$ bioelectrode fabricated via the same set of procedure with GO_x (1 mg/mL), conducted in PBS (pH 7.4) containing 5 mM $[Fe(CN)6]^{3-/4-}$.

bioelectrode for electrochemical biosensing of glucose. Better electrochemical response for composite of prGO–AuNRs was confirmed by higher peak current response, which cannot be achieved by the use of parent materials individually. Further, improved sensitivity (3.2 μA/(mg/dL)/cm^2), ability to detect small amounts of glucose (due to lower detection limit of 14.5 mg/dL) and faster electron transfer i.e. kinetics (high K_s value $\sim 12.4 \times 10^{-2}$ cm/s) attests the composites true potential for biosensing applciations. The proposed biosensor surpasses the earlier reported biosensors by possesing better loading capacity signifying that lesser amount of blood sample would be required for detection. This is owing to much lower K_m value which also supports the synergistic interaction of prGO–AuNRs system with GO_x, that is enzyme for enhanced enzymatic activity. Finally with an ability to resist environmental interference, along with great stability and reproducibility, we propose that this composite has tremendous potential to be utilized as an efficient electrode material for electrochemical sensing of several clinically important bioanalytes (i.e. urea, cholesterol, and triglycerides, etc.) in the coming future.

Reporting ethical standards

Data Access and Retention: No data have been fabricated or manipulated (including images) to support our conclusions

Originality and Plagiarism: No data, text, or theories by others have been presented in manuscript. The statements in the text have been given with the study of the cited literature.

Multiple, Redundant or Concurrent Publication: This manuscript has not been submitted to more than one journal for simultaneous consideration

Acknowledgement of Sources: Research grants received from various funding agencies for all the authors have been acknowledged respectively in the manuscript.

Authorship of the Paper: Authors whose names appear on the submission have contributed sufficiently to the scientific work and therefore share collective responsibility and accountability for the results

Hazards and Human or Animal Subjects: The authors declare that there is no experiment has been done on any human or animal during the study of the manuscript

Disclosure and Conflicts of Interest: The authors declare that they have no conflict of interest.

Acknowledgments

NRN acknowledges the financial assistance from UGC (RJNF-JRF-SC-252).P. S. Saxena acknowledges CAS program in Zoology Department, B.H.U., Varanasi, India, funded by UGC. A.S. acknowledges the DST, New Delhi, India, UPE, CAS and networking program in Department of Physics, B.H.U., India.

Appendix A. Supplementary material

Supplementary data associated with this article can be found in the online version at http://dx.doi.org/10.1016/j.talanta.2015.05.059.

References

[1] P.B. Luppa, L.J. Sokoll, D.W. Chan, Clin. Chim. Acta 314 (2001) 1.
[2] O. Nekrassova, N.S. Lawrence, R.G. Compton, Talanta 60 (2003) 1085.
[3] T.-P. Sun, H.-L. Shieh, C.T.-S. Ching, Y.-D. Yao, S.-H. Huang, C.-M. Liu, W.-H. Liu, C.-Y. Chen, Int. J. Nanomed. 5 (2010) 343.
[4] A.L. Ghindilis, P. Atanasov, E. Wilkins, Electroanalysis 9 (1997) 661.
[5] A. Heller, Phys. Chem. Chem. Phys. 6 (2004) 209.
[6] O. Nekrassova, N.S. Lawrence, R.G. Compton, Electroanalysis 16 (2004) 1285.
[7] G.L. Luque, M.C. Rodríguez, G.A. Rivas, Talanta 66 (2005) 467.
[8] S. Park, H. Boo, T.D. Chung, Anal. Chim. Acta 556 (2006) 46.
[9] Y. Sun, H. Buck, T.E. Mallouk, Anal. Chem. 73 (2001) 1599.
[10] M. Tominaga, M. Nagashima, K. Nishiyama, I. Taniguchi, Electrochem. Commun. 9 (2007) 1892.
[11] Y. Bai, W. Yang, Y. Sun, C. Sun, Sens. Actuators B: Chem. 134 (2008) 471.
[12] H. Hassan, Z. Hamid, Int. J. Electrochem. (2011).
[13] S.S. Mahshid, S. Mahshid, A. Dolati, M. Ghorbani, L. Yang, S. Luo, Q. Cai, Electrochim. Acta 58 (2011) 551.
[14] M. Tominaga, T. Shimazoe, M. Nagashima, I. Taniguchi, J. Electroanal. Chem. 615 (2008) 51.
[15] A. Habrioux, E. Sibert, K. Servat, W. Vogel, K.B. Kokoh, N. Alonso-Vante, J. Phys. Chem. B 111 (2007) 10329.
[16] F. Li, J. Song, F. Li, X. Wang, Q. Zhang, D. Han, A. Ivaska, L. Niu, Biosens. Bioelectron. 25 (2009) 883.
[17] Y. Zhang, Y.-W. Tan, H.L. Stormer, P. Kim, Nature 438 (2005) 201.
[18] S. Abraham N.R. Nirala S.A. Panday M. Srivastava S.K. Srivastava B. Walkenfort A. Srivastava, Anal. Methods, 2015.
[19] A.T. Lawal, Talanta 131 (2014) 424.
[20] J. Li, H. Feng, J. Li, Y. Feng, Y. Zhang, J. Jiang, D. Qian, Electrochim. Acta 167 (2015) 226.
[21] Y.H. Lee, L. Polavarapu, N. Gao, P. Yuan, Q.-H. Xu, Langmuir 28 (2012) 321.
[22] Y. Fang, S. Guo, C. Zhu, Y. Zhai, E. Wang, Langmuir 26 (2010) 11277.
[23] A.A. Balandin, S. Ghosh, W. Bao, I. Calizo, D. Teweldebrhan, F. Miao, C.N. Lau, Nano Lett. 8 (2008) 902.
[24] Z. Wang, X. Zhou, J. Zhang, F. Boey, H. Zhang, J. Phys. Chem. C 113 (2009) 14071.
[25] Y. Liu, D. Yu, C. Zeng, Z. Miao, L. Dai, Langmuir 26 (2010) 6158.
[26] X. Huang, X. Qi, F. Boey, H. Zhang, Chem. Soc. Rev. 41 (2012) 666.
[27] M.D. Blankschien, L.A. Pretzer, R. Huschka, N.J. Halas, R. Gonzalez, M.S. Wong, ACS Nano 7 (2013) 654.
[28] W.S. Hummers, R.E. Offeman, J. Am. Chem. Soc. 80 (1958) 1339.
[29] B. Nikoobakht, M.A. El-Sayed, Chem. Mater. 15 (2003) 1957.
[30] W. Ren, Y. Fang, E. Wang, ACS Nano 5 (2011) 6425.
[31] R. Klingler, J. Kochi, J. Phys. Chem. (1981).
[32] L. Jiang, C.J. McNeil, J.M. Cooper, J. Chem. Soc. Chem. Commun. (1995) 1293.
[33] N. Torto, T. Ruzgas, L. Gorton, J. Electroanal. Chem. 464 (1999) 252.
[34] C.S. Hanes, Biochem. J. 26 (1932) 1406.
[35] I. Willner, E. Katz, Angew. Chem. Int. Ed. Engl. 39 (2000) 1180.
[36] S.A. Miscoria, J. Desbrieres, G.D. Barrera, P. Labbé, G.A. Rivas, Anal. Chim. Acta 578 (2006) 137.
[37] B.-Y. Wu, S.-H. Hou, F. Yin, J. Li, Z.-X. Zhao, J.-D. Huang, Q. Chen, Biosens. Bioelectron. 22 (2007) 838.
[38] X. Kang, Z. Mai, X. Zou, P. Cai, J. Mo, Anal. Biochem. 369 (2007) 71.
[39] X. Kang, J. Wang, H. Wu, I.A. Aksay, J. Liu, Y. Lin, Biosens. Bioelectron. 25 (2009) 901.
[40] B. Unnikrishnan, S. Palanisamy, S.-M. Chen, Biosens. Bioelectron. 39 (2013) 70.
[41] N. Cheng, Am. J. Anal. Chem. 03 (2012) 312.
[42] A.T.E. Vilian, S.-M. Chen, M.A. Ali, F.M.A. Al-Hemaid, RSC Adv. 4 (2014) 30358.
[43] M. Veerapandian, Y.-T. Seo, H. Shin, K. Yun, M.-H. Lee, Int. J. Nanomed. 7 (2012) 6123.

RSC Advances

PAPER

Cite this: *RSC Adv.*, 2015, **5**, 5406

Protein conjugated carboxylated gold@reduced graphene oxide for aflatoxin B_1 detection†

Saurabh Srivastava,[abc] Shiju Abraham,[b] Chandan Singh,[a] Md. Azahar Ali,‡[a] Anchal Srivastava,[b] Gajjala Sumana[a] and Bansi D. Malhotra*[ac]

A sensitive, reproducible, stable and label-free immunosensor has been prepared *via* simultaneous reduction of graphene oxide and gold(III) salt using an eco-friendly and non-toxic reducing agent sodium citrate resulting in uniformly distributed gold nanoparticles on reduced graphene oxide (rGO) sheets. The *in situ* grown gold@carboxylated reduced graphene oxide (Au@rGO) surface has been used for bioconjugation with monoclonal antibodies of aflatoxin B_1 using EDC-NHS chemistry. The *in situ* growth of AuNPs (gold nanoparticles) onto the rGO sheet results in improved electrocatalytic activity and loading of the antibodies due to the enhanced surface area. The monodispersion of the Au nanoparticles on the rGO sheets yields heterogeneous electron transfer (2.85×10^{-4} cm s^{-1}) resulting in improved biosensor efficacy compared to that based on the rGO electrode. This immunosensor is sensitive to detect as low as 0.1 ng mL^{-1} concentration of aflatoxin compared to the reported ELISA (enzyme-linked immunosorbent assay) standard method. The Au@rGO based immunosensor exhibits high sensitivity (182.4 μA (ng $mL^{-1})^{-1}$ cm^{-2}) in a wide linear detection range of 0.1–12 ng mL^{-1}. Results of the studies related to this immunosensor reveal that the Au@rGO nanocomposite is a suitable platform for the development of a compact biosensing device for food toxin monitoring.

Received 19th October 2014
Accepted 1st December 2014

DOI: 10.1039/c4ra12713g

www.rsc.org/advances

Introduction

Graphene, a single layer of sp^2 hybridized carbon atoms resembling a honeycomb lattice, is the fundamental building block of all carbonaceous nanomaterials. It is in increased demand owing to its unique electrical, optical and mechanical properties.[1–4] Reduced graphene oxide (rGO) synthesized by chemical methods has recently aroused much interest as an excellent candidate for biosensing applications. The abundant functional groups (hydroxyl and epoxies at the basal plane with carboxyl groups at edges), larger surface area, capability to facilitate direct electron transfer from enzymes and proteins, ease of processing and low cost reveal rGO as an interesting candidate compared to pristine graphene for electrochemical biosensing.[5–7] The oxygenated functional groups present in rGO have been found to be responsible for the heterogeneous charge transfer resulting in faster electron transfer kinetics.[6] Moreover, the oxygenated functional groups present in rGO facilitate direct covalent attachment of desired biomolecules onto the rGO surface providing high stability to the biosensor.

Compton *et al.* have recently reported the preparation of chemically active reduced graphene oxide (rGO) with a considerable amount of functional groups suitable for biomolecule attachment and with the desired conductivity for electrochemical sensing applications.[8] The rGO based materials have been employed for enzymatic analysis, genosensor development and food toxin detection *etc.*[9–16] Although rGO has been utilized in many electrochemical biosensing applications, there is considerable scope to improve the biosensing characteristics such as sensitivity, detection limit and stability. In this context, the nanocomposite of rGO with metal nanoparticles,[17–19] metal oxide nanoparticles[20,21] and conducting polymers[22,23] for biosensing applications have recently aroused much interest.

The functionalization of rGO with the noble metals such as gold (Au) and platinum (Pt) has been employed for the development of high performance electrochemical biosensing devices.[24–27] The noble metal nanoparticles are known to possess excellent electrocatalytic properties and the resulting Au@rGO nanocomposite has been found to exhibit an enhanced voltammetric current as compared to that of the bare rGO. Moreover, the high surface area and oxygenated moieties of rGO provide an efficient support for homogeneous dispersion of the metal nanoparticles without affecting their electrochemical activities. Chen *et al.* have reported a gold–graphene

[a]*Department of Science and Technology, Center on Biomolecular Electronics, Biomedical Instrumentation Section, CSIR-National Physical Laboratory, New Delhi-110012, India. E-mail: bansi.malhotra@gmail.com; Tel: +91-11-27871043 ext. 1609*

[b]*Department of Physics, Banaras Hindu University, Varanasi, U.P.-221005, India*

[c]*Department of Biotechnology, Delhi Technological University, Delhi-110042, India*

† Electronic supplementary information (ESI) available. See DOI: 10.1039/c4ra12713g

‡ Department of Electrical and Computer Engineering, Iowa State University, Ames, USA.

nanohybrid for the electrochemical detection of glucose with 400-fold enhanced sensitivity as compared to that of rGO.[27] Guo *et al.* have demonstrated that the platinum nanoparticles–graphene hybrid nanosheets show a higher voltammetric current and can be used to detect several organic and inorganic molecules with superior sensitivity in comparison to those based on pristine graphene.[25]

Aflatoxins (AFs) are a group of secondary fungal metabolites that are produced by *Aspergillus flavus* and *Aspergillus parasiticus* under certain conditions and are the most widely spread group of toxins resulting in contamination of food products. Among these, aflatoxin B_1 (AFB_1) is known to be the most toxic and is responsible for human hepatocellular carcinoma (the International Agency for Research on Cancer regards it as a human carcinogen).[28,29] Thus, sensitive and efficient detection of this food toxin is urgently needed to monitor food safety and human health. In this context, the development of an electrochemical biosensor has recently aroused much interest due to its high sensitivity, fast detection ability and simplicity. We have recently reported an rGO based immunosensor for the detection of a food toxin.[9]

We report *in situ* fabrication of a Au@rGO nanocomposite *via* the simultaneous reduction of GO and Au^{3+}. This Au@rGO nanocomposite material has been used as a sensitive platform for electrochemical detection of a food toxin (aflatoxin B_1). The proposed electrochemical detection strategy offers higher sensitivity, improved detection range and stability. The sodium citrate acts as a capping reagent for the effective reduction and stabilization of the Au@rGO nanocomposite.[27,30] Sodium citrate is considered to be a non-toxic reducing agent, as compared to hydrazine/sodium borohydride that is known to be highly toxic and explosive, for the reduction of GO. Moreover, unlike the rGO prepared *via* hydrazine which is known to agglomerate, the rGO obtained *via* sodium citrate is found to form a stable colloidal dispersion due to hydrogen bonding between the oxygenated functional groups on the surface of the rGO and the hydroxyl/carboxyl groups of sodium citrate.[30] Moreover, these functional groups allow enhanced loading of biomolecules for biosensing applications. To the best of our knowledge, this is the first report towards the application of an *in situ* derived carboxylated Au@rGO nanocomposite based platform for food toxin detection.

Results and discussion

Electron microscopy studies

Transmission electron microscopy (TEM) images of GO show good quality and thin layered graphene dispersed on a carbon coated copper grid (Fig. 1(i)). It can be clearly seen that the wrinkles and folds (marked regions) appear on the GO sheet due to defects and functional groups in the carbon lattice. It appears that the GO sheet is extended to several micrometers and the dark region corresponds to the multilayered GO. The TEM image of the Au@rGO nanocomposite is shown in Fig. 1(ii) wherein monodispersed Au nanoparticles (AuNPs) are clearly visible on the rGO surface. The rGO sheets possess defects and residual oxygenated functional groups that perhaps act as the nucleation sites for the formation of the AuNPs. The atomic scale image of a AuNP shows clear lattice fringes. The average inter-planar spacing of the lattice fringes is found to be 2.35 Å corresponding to the (111) plane (Fig. 1(iii)) which is in good agreement with the results of the X-ray diffraction studies. Fig. 1(iv) shows the particle size distribution of the AuNPs present at the rGO surface.

The surface morphology of the various modified electrodes has been investigated using scanning electron microscopy (SEM) as depicted in Fig. 2. Image (i) shows an SEM image of the rGO where the graphene sheets are found to be several microns in dimension. It appears that the rGO sheets stack together to form a larger sheet during coherent deposition on the ITO (indium tin oxide) electrode. However, the morphology of the Au@rGO/ITO electrode (image (ii)) reveals that the Au grains are incorporated throughout the rGO sheet. Some AuNPs are visible on the surface of the graphene sheets while some of them are found to be entrapped between the rGO sheets as is clearly visible in the enlarged image (iii). However, after functionalization with antibodies, the surface morphology of the Au@rGO/ITO electrode completely changes due to the high antibody loading on the electrode surface (image (iv)).

Structural studies

Fig. 3(i) shows the UV-visible spectra of (a) GO, (b) rGO and (c) the *in situ* synthesized Au@rGO nanocomposite dispersed in water. The UV-visible spectrum of GO shows an absorption peak at 232 nm due to π–π^* transition of aromatic C–C bonds. However, after rGO formation, the maximum absorption peak is found to be red shifted to 270 nm indicating reduction of GO.[9] The AuNPs exhibit the characteristic absorption peak at 530 nm (inset; Fig. 3(i)). The spectrum of the *in situ* synthesized Au@rGO nanocomposite shows two absorption peaks at 270 nm and 530 nm. This result indicates simultaneous reduction of Au^{3+} to Au as well as GO to rGO leading to Au@rGO nanocomposite formation.

Fig. 3(ii) shows XPS spectrum of the C 1s region of the Au@rGO nanocomposite. The spectrum has been deconvoluted into the characteristic binding energy peaks using peak fit 1 software. Background subtraction and peak fitting of the spectrum have been done using the Shirley function and Gaussian function, respectively. XPS measurements were carried out in a Perkin Elmer XPS chamber (PHI 1257) with a base pressure of 5×10^{-9} Torr. The chamber is equipped with a dual anode comprising of Mg-Kα (energy 1253.6 eV) and Al-Kα (energy 1486.6 eV) X-ray source and a high-resolution hemispherical energy analyzer for energy resolved electron detection. An Mg-Kα X-ray source has been used for this study. The samples were sputtered with 4 keV argon ions to remove surface contamination prior to the XPS studies. The binding energy peak found at 284.5 eV is assigned to graphitic C–C. The peaks found at 285.5 and 286.7 eV are due to the hydroxyl (C–OH) and epoxy (C–O) groups, respectively. Further, the binding energy peaks seen at 288.2 and 289.4 eV can be attributed to the carbonyl (C=O) and carboxylic acid (O–C=O) groups present in the samples, respectively. Table 1 details the binding energy position of the

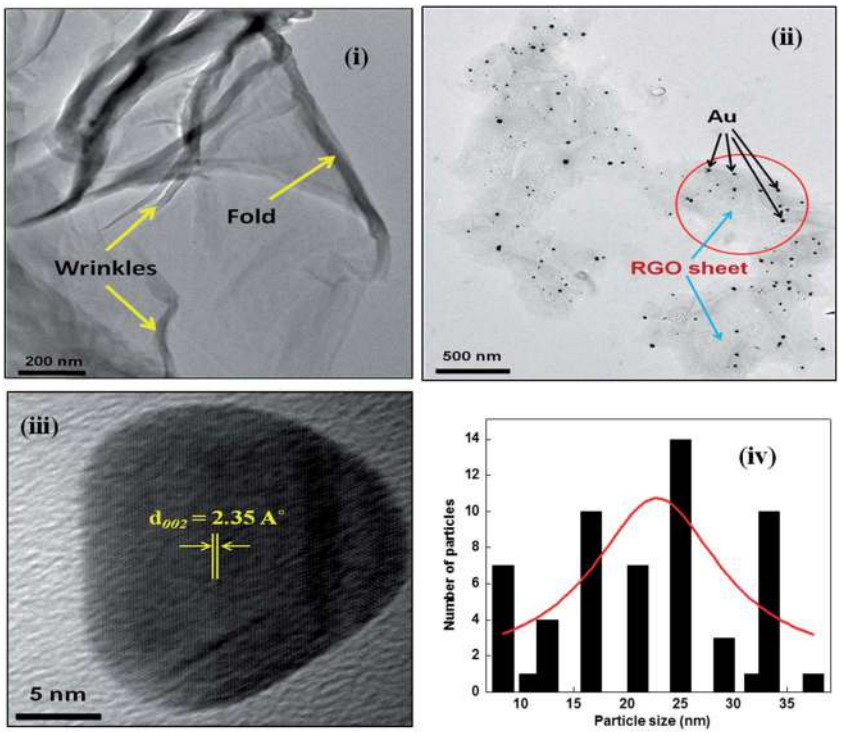

Fig. 1 Transmission electron micrographs of (i) graphene oxide, (ii) Au@rGO, (iii) high resolution transmission electron micrograph (HR-TEM) of a Au nanoparticle and (iv) particle size distribution of Au nanoparticles on the rGO sheet.

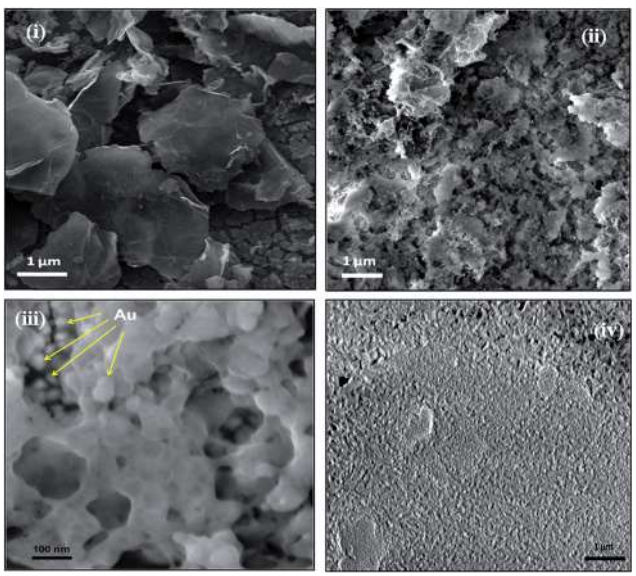

Fig. 2 Scanning electron micrographs of electrophoretically deposited (i) rGO/ITO film, (ii) Au@rGO/ITO film, (iii) enlarged view of the Au@rGO/ITO film and (iv) antibody functionalized anti-AFB_1/Au@rGO/ITO film.

various functional groups, FWHM and the corresponding relative percentage of these groups in the Au@rGO nanocomposite. These results indicate that the Au@rGO nanocomposite has abundant carboxylic acid functional groups as evidenced by their high relative atomic percentage (10.4%). These carboxylic acid groups have been used to bind with the amino terminal of the antibodies through the covalent immobilization process.

Fig. 3(iii) shows the Fourier transform infrared spectra (FT-IR) of the (i) rGO/ITO, (ii) Au@rGO/ITO and (iii) anti-AFB_1/Au@rGO/ITO films. The rGO and Au@rGO exhibit the characteristic peak at 1413 cm^{-1} corresponding to the O–H bending vibration of the carboxyl group. The band seen at around 1600 cm^{-1} is due to aromatic C=C stretching vibration. The broad band found at around 3300 cm^{-1} may be assigned to O–H stretching. Further, the band found in the region of 1000–1143 cm^{-1} corresponds to C–OH stretching vibration. From the FT-IR spectrum of the anti-AFB_1/Au@rGO/ITO film (spectrum c), it may be noted that the intensity of the 1413 cm^{-1} band (corresponding to O–H bending vibration of the carboxyl group) is considerably reduced as compared to that of the Au@rGO/ITO film (spectrum b). An additional peak corresponding to the amide I band appears at 1664 cm^{-1}. This indicates that carboxylic acid groups present in the nanocomposite have been utilized in amide bond formation with amino groups of the antibodies. The band seen at 3300 cm^{-1} becomes much broader and is shifted to 3400 cm^{-1} due to presence of the amide N–H stretching vibrations in the antibodies.

Fig. S1 (see ESI†) shows an X-ray diffraction (XRD) pattern of the electrophoretically deposited Au@rGO film on ITO substrate. The XRD pattern displays characteristic peaks corresponding to rGO, Au and ITO. A broad hump observed at $2\theta = 25^\circ$ represents the characteristic (002) plane (d_{002} = 3.56 Å) of rGO.[31] The characteristic peak occurring at 38° is assigned to the (111) reflection plane (d_{111} = 2.36 Å) of the fcc gold. Another

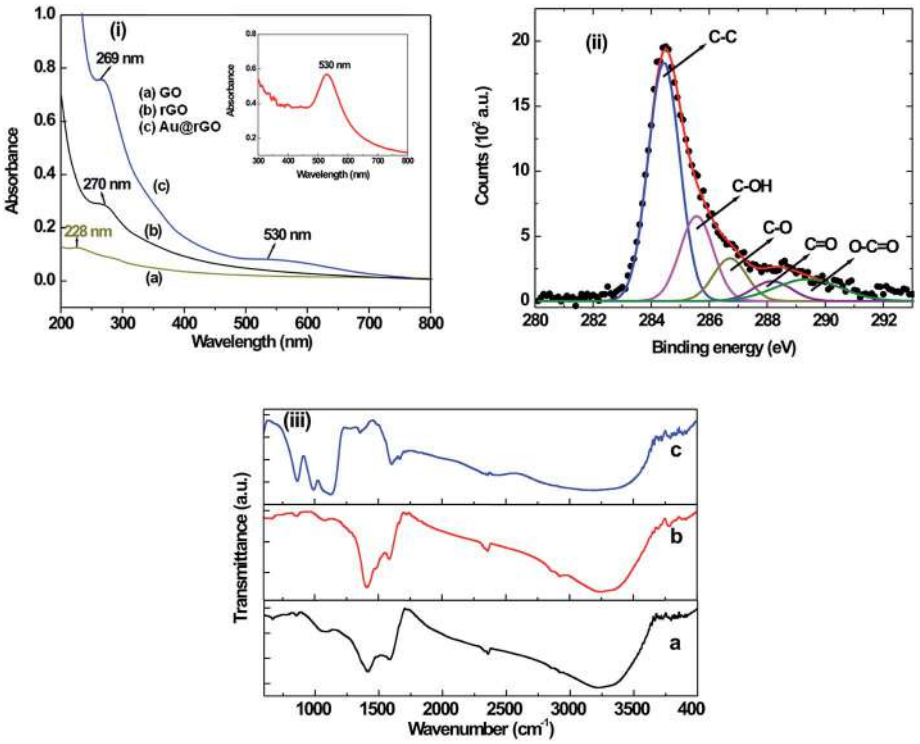

Fig. 3 (i) UV-visible spectra of (a) GO, (b) rGO and (c) the *in situ* synthesized Au@rGO, inset: UV-visible spectrum of the AuNPs showing the characteristic absorption peak at 530 nm. (ii) X-ray photoelectron spectrum (XPS) of the C 1s region of Au@rGO deconvoluted into characteristic peaks. (iii) Fourier-transform infrared spectra of (a) rGO/ITO, (b) Au@rGO/ITO and (c) anti-AFB_1/Au@rGO/ITO.

Table 1 The various functional groups on the Au@rGO nanocomposite, their binding energy position, FWHM and the relative percentage of these functional groups

Functional groups	Binding energy position (eV)	FWHM (eV)	Relative percentage (%)
C–C	284.4	1.3	53.7
C–OH	285.5	1.35	20.2
C–O	286.7	1.35	10.2
C=O	288.2	1.58	5.6
O–C=O	289.4	2.6	10.3

peak seen at 44° corresponds to the (200) plane ($d_{200} = 2.05$ Å) of Au (JCPDS 89-3697). The rest of the XRD peaks seen at 21.2°, 30.2°, 35.1° and 50.6° may be assigned to the (211), (222), (400) and (440) reflection planes, respectively, arising due to the ITO substrate (JCPDS 89-4596). The crystallite size of the AuNPs has been estimated to be 26 nm using the Debye–Scherrer equation.

Electrochemical studies

Fig. 4(i) shows cyclic voltammograms (CV) obtained for the various modified electrodes at 30 mV s^{-1} scan rate obtained using a three electrode system in phosphate buffered saline (PBS) at pH 7.4 containing 5 mM $[Fe(CN)_6]^{3-/4-}$. It can be seen that the magnitude of the oxidation peak current of the rGO/ITO electrode (255 μA) is higher as compared to that of the GO/ITO electrode. This is attributed to the higher conductivity of rGO arising due to reduction in the functional groups and defects compared to that of GO (curve a and b). Additionally, the peak-to-peak separation of rGO/ITO is found to be smaller as compared to that of the GO/ITO electrode indicating faster electron transfer. Moreover, the *in situ* synthesized Au@rGO/ITO electrode exhibits around 2-fold enhanced current (576.7 μA) indicating that decoration of rGO with Au nanoparticles increases the electroactive surface area providing the conducting bridges for the electron-transfer. Alternately, it may perhaps be attributed to the metallic conductivity as well as the excellent electrocatalytic activity of the gold nanoparticles-decorated rGO. After antibody functionalization, the oxidation current is found to decrease (468.4 μA) and the peak potential is shifted to a more positive value. This is indicative of the insulating nature of the immobilized antibody molecules. The anodic peak current further decreases to 335 μA in the case of the BSA/anti-AFB_1/Au@rGO/ITO electrode. This is due to the fact that BSA blocks most of the non-specific active sites present on the immunoelectrode surface. The electrochemical surface area[32] is related to the charge associated with a known adsorbate ($[Fe(CN)_6]^{3-/4-}$) on the electrode surface (ITO), q_m, and the charge associated with that of the various modified electrodes (monolayer coverage of the said adsorbate), q_{ad}, as

$$A_{ec} = q_{ad}/q_m \quad (1)$$

It has been found that the electrochemical surface area is significantly increased in the case of the Au@rGO/ITO electrode

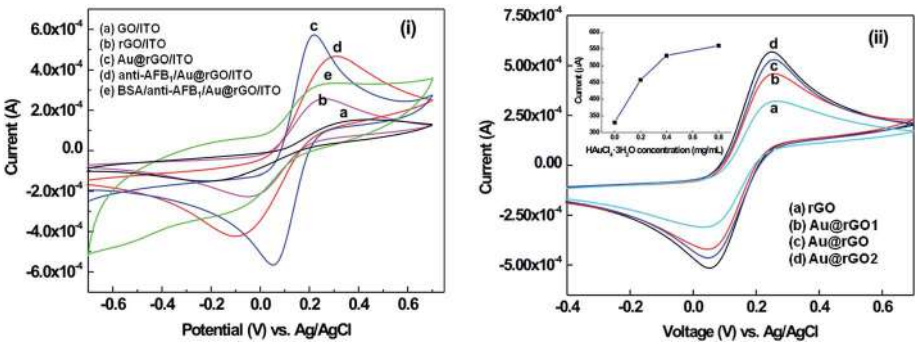

Fig. 4 (i) Cyclic voltammograms of the fabricated (a) GO/ITO, (b) rGO/ITO, (c) Au@rGO/ITO, (d) anti-AFB_1/Au@rGO/ITO and (e) BSA/anti-AFB_1/Au@rGO/ITO electrodes obtained using a three electrode system in PBS (pH 7.4) containing 5 mM $[Fe(CN)_6]^{3-/4-}$ at 30 mV s^{-1} scan rate. (ii) Cyclic voltammograms of the (a) rGO/ITO, (b) Au@rGO 1/ITO, (c) Au@rGO/ITO and (d) Au@rGO 2/ITO electrodes. The concentration of $HAuCl_4$ used was 0.2 mg mL^{-1} for Au@rGO 1, 0.4 mg mL^{-1} for Au@rGO and 0.8 mg mL^{-1} for Au@rGO 2 during the nanocomposite formation; inset (ii) indicates the variation of anodic peak current of different nanocomposite electrodes as a function of $HAuCl_4$ concentration.

(137 mm^2) as compared to that of the rGO/ITO (36.5 mm^2) and GO/ITO (29.4 mm^2) electrodes. This indicates that Au@rGO exhibits a higher electrochemical surface area leading to the large scale redox conversion of $[Fe(CN)_6]^{3-/4-}$ and an enhanced CV response.

Fig. 4(ii) shows the CV response of four nanocomposite electrodes as a function of $HAuCl_4 \cdot 3H_2O$ concentration. The concentration of rGO used was 1 mg mL^{-1} for all the four fabricated electrodes whereas the loading amount of AuNPs on the rGO sheet was controlled by taking different concentrations of $HAuCl_4 \cdot 3H_2O$ (0.2 mg mL^{-1} or 0.5 mM for Au@rGO 1, 0.4 mg mL^{-1} or 1 mM for Au@rGO and 0.8 mg mL^{-1} or 2 mM for Au@rGO 2). It has been observed that the redox peak current increases with increased Au loading on the rGO sheet. This is attributed to the increased electrochemical surface area and conductivity due to the increased amount of AuNPs. The concentration of the gold salt directly influences the size of the synthesized AuNPs which has a strong relationship with the electrochemical performance of the fabricated immunosensor. Ahmad *et al.* have concluded that increasing the concentration of gold salt results in larger AuNPs with agglomerated geometry while a low concentration results in smaller AuNPs.[33] In our case, with an increase in the concentration from 0.2 mM to 0.4 mM, the current increases significantly and then it becomes saturated due to the large agglomerated AuNPs. Keeping this in mind, 0.4 mM of gold salt has been utilized for the immunosensor fabrication.

Fig. S2(i) (see ESI†) shows cyclic voltammograms of the BSA/anti-AFB_1/Au@rGO/ITO immunoelectrode obtained as a function of scan rate (30–100 mV s^{-1}). It has been observed that redox peak current as well as potential increase linearly with the square root of the scan rate. This indicates that the redox reaction is controlled by semi-infinite linear diffusion resulting in faster electron transfer kinetics. The slope and intercept follow eqn (2)–(5):

$$I_a\,[A] = 4.06 \times 10^{-5}\,[A] + 4.4 \times 10^{-5}\,[A^2\ s\ mV^{-1}]^{1/2} \times \{\text{scan rate (mV s}^{-1})\}^{1/2};\ R^2 = 0.99 \quad (2)$$

$$I_c\,[A] = -8.4 \times 10^{-5}\,[A] - 3.3 \times 10^{-5}\,[A^2\ s\ mV^{-1}]^{1/2} \times \{\text{scan rate (mV s}^{-1})\}^{1/2};\ R^2 = 0.99 \quad (3)$$

$$V_{ap} = 7.4 \times 10^{-2}\ (V) + 1.7 \times 10^{-2}\ (V^{1/2}\ s^{-1/2}) \times \{\text{scan rate (mV s}^{-1})\}^{1/2};\ R^2 = 0.98 \quad (4)$$

$$V_{cp} = -1.2 \times 10^{-1}\ (V) - 1.4 \times 10^{-2}\ (V^{1/2}\ s^{-1/2}) \times \{\text{scan rate (mV s}^{-1})\}^{1/2};\ R^2 = 0.99 \quad (5)$$

The surface coverage of the BSA/anti-AFB_1/Au@rGO/ITO immunoelectrode has been estimated to be 3.96×10^{-8} mol cm^{-2} using the Brown–Anson model.[34]

Fig. S2(ii) (see ESI†) shows electrochemical impedance spectra (EIS, Nyquist plots) of the different modified electrodes in the frequency range of 10^4 to 10^{-1} Hz at a biasing potential of 10 mV. The electrochemical system can be modeled by an equivalent circuit (Randles circuit) comprised of the solution resistance (R_S), charge transfer resistance (R_{CT}), Warburg impedance (W) and double layer capacitance (C_{DL}) *etc.* The charge transfer process in this electrode has been investigated by measuring the charge transfer resistance (R_{CT}) that depends on the dielectric characteristics at the electrode/electrolyte interface. The maximum R_{CT} value of the rGO/ITO electrode is found as 721 Ω. However, the significant reduction in the R_{CT} value observed in the case of the Au@rGO/ITO electrode (136 Ω) may be attributed to the higher conductivity as well as the excellent electrocatalytic activity of the Au nanoparticles in the nanocomposite matrix. The antibody functionalized matrix (anti-AFB_1/Au@rGO/ITO) exhibits a higher R_{CT} (179 Ω) as compared to Au@rGO/ITO and is attributed to the insulating nature of the antibody molecules. Further, since BSA molecules cover most of the non-specific active sites of the immunoelectrode surface, the charge transfer process is again hindered, resulting in a higher R_{CT} (448 Ω) in the case of the BSA/anti-AFB_1/Au@rGO/ITO electrode.

The heterogeneous electron transfer rate constant (k_0) of the Au@rGO/ITO and rGO/ITO electrodes has been calculated using eqn (6)[35]

$$k_0 = \frac{RT}{n^2F^2AR_{CT}S} \quad (6)$$

where R is the gas constant, T is absolute temperature (K), F is the Faraday constant, A is the specific electrode area (cm^2), S is the bulk concentration of redox probe (mol cm^{-3}) and n is the number of transferred electrons per molecule of the redox probe. The k_0 value of the Au@rGO/ITO electrode has been estimated as 2.85×10^{-4} cm s^{-1} which is better than that of the rGO/ITO electrode (2.02×10^{-4} cm s^{-1}). This indicates that the Au@rGO/ITO electrode exhibits faster electron transfer kinetics compared to that of rGO/ITO leading to the superior analytical performance of the biosensor.

Response studies

Fig. 5(i) displays the results of the electrochemical sensing studies related to the BSA/anti-AFB_1/Au@rGO/ITO immunoelectrode as a function of AFB_1 concentration (0.1–12 ng mL^{-1}) in PBS (pH 7.4) containing 5 mM $[Fe(CN)_6]^{3-/4-}$. It has been observed that the magnitude of the peak current decreases with the increase in AFB_1 concentration in the detection range, 0.1–12 ng mL^{-1} after which it saturates. The reduction in response current may be attributed to the formation of electrically insulating antigen–antibody complexes produced from the specific interaction of the aflatoxin B_1 and antibody that may block the electron transfer *via* $[Fe(CN)_6]^{3-/4-}$.[36] Fig. 5(ii) displays the calibration plot relating to the change in the magnitude of the anodic peak current of the BSA/anti-AFB_1/Au@rGO/ITO immunoelectrode as a function of AFB_1 concentration in the detection range of 0.1–12 ng mL^{-1} (curve a). Furthermore, a control experiment has been performed to check the cross reactivity of the BSA/Au@rGO/ITO electrode with the AFB_1 antigens in the absence of antibodies (curve b, Fig. 5(ii)). However, no significant change in the current response was observed for the BSA/Au@rGO/ITO electrode as a function of AFB_1 concentration. This indicates that the AFB_1 antigens only interact with the BSA/anti-AFB_1/Au@rGO/ITO immunoelectrode resulting in a change in the CV response. It has been found that the current varies proportionally with the logarithmic AFB_1 concentration in the linearity range of 0.1–12 ng mL^{-1} according to eqn (7)

$$I_p = 2.7 \times 10^{-4} - 4.56 \times 10^{-5} \log[AFB_1 \text{ concentration (ng mL}^{-1})]; R^2 = 0.992 \quad (7)$$

The sensitivity of the immunosensor after the incorporation of AuNPs by the *in situ* reduction method has been estimated as 182.4 μA (ng $mL^{-1})^{-1}$ cm^{-2} which is found to be improved as compared to that of the rGO/ITO based biosensor (68 μA (ng $mL^{-1})^{-1}$ cm^{-2}).[9] This is attributed to the high electrocatalytic activity and larger electrochemical area of the Au decorated rGO matrix. Further, the wider linearity range (0.1–12 ng mL^{-1}) of the Au@rGO/ITO is due to the high loading of antibody molecules onto the rGO sheet as well as onto the surface of Au. Meanwhile for the rGO/ITO electrode, the linearity is only 0.25–1.25 ng mL^{-1} (Table 2).[9] This immunosensor can be used to detect AFB_1 at a concentration as low as 0.1 ng mL^{-1} in solution.

Fig. 6(i) shows the CV response of the BSA/anti-AFB_1/Au@rGO/ITO immunoelectrode in the presence of AFB_1 (1 ng mL^{-1}) obtained at regular intervals of 1 week. It has been found that the current value decreases to 2.43% after 8 weeks. This indicates that the fabricated BSA/anti-AFB_1/Au@rGO/ITO immunoelectrode exhibits good stability for at least two months.

Fig. 6(ii) indicates the CV response of five different BSA/anti-AFB_1/Au@rGO/ITO immunoelectrodes fabricated using similar procedure in presence of AFB_1 (1 ng mL^{-1}) concentration. The relative standard deviation (RSD) of reproducibility for these electrodes is estimated to be 2.32%, indicating good reproducibility and precision. The electrochemical sensing performance of this BSA/anti-AFB_1/Au@rGO/ITO based immunosensor for AFB_1 detection has been compared with those reported in the literature (Table 2).

Experimental

Materials

Gold(III) chloride trihydrate ($HAuCl_4 \cdot 3H_2O$; purity 99.99%), aflatoxin B_1 (AFB_1), anti-aflatoxin B_1 mouse monoclonal

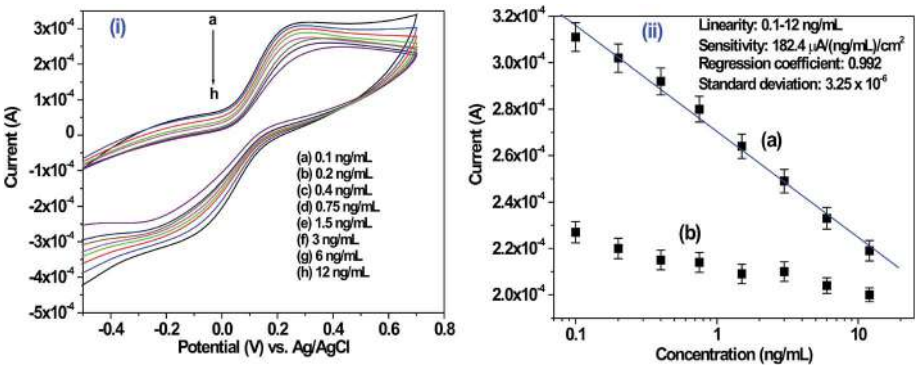

Fig. 5 (i) Electrochemical sensing response of the BSA/anti-AFB_1/Au@rGO/ITO electrode obtained as a function of AFB_1 concentration (0.1–12 ng mL^{-1}. (ii) Linear calibration plot of the immunoelectrode with respect to peak current as a function of AFB_1 concentration (curve a); control experiment in the absence of antibody (curve b).

Table 2 Response characteristics of the BSA/anti-AFB_1/Au@rGO/ITO based biosensor along with those reported in the literature

Bioelectrode	Sensitivity μA $(ng\ mL^{-1})^{-1}\ cm^{-2}$	Detection limit $(ng\ mL^{-1})$	Detection range $(ng\ mL^{-1})$	Stability (days)	Ref.
BSA/anti-AFB_1/MWCNTs/ITO	95	0.08	0.25–1.375	42	34
BSA/anti-AFB_1/rGO/ITO	68	0.15	0.125–1	45	9
BSA/anti-AFB_1/Ni–ITO	59	0.327	0.05–1	60	40
BSA/aAFB_1-C-AuNP/MBA/Au	45	0.18	0.1–1	—	41
BSA/AFB_1/PTH/AuNP/GCE	1.23	0.07	0.06–2.4	—	42
96-wellscreen printed microplate	—	0.03	0.05–2	30	43
BSA/anti-AFB_1/Au@rGO/ITO	182.4	0.1	0.1–12	56	Present work

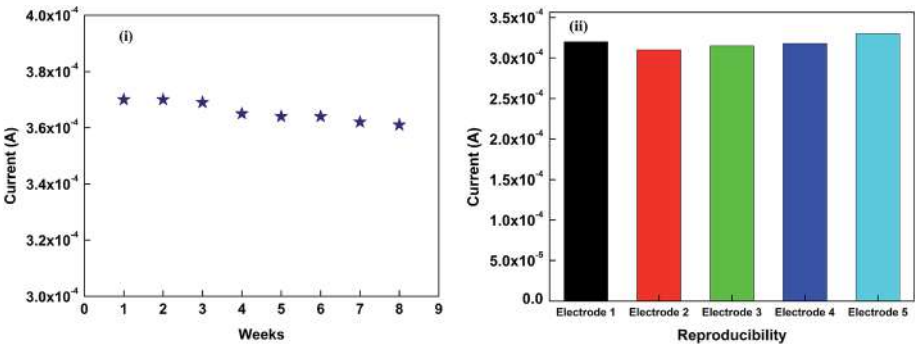

Fig. 6 (i) The current response of the BSA/anti-AFB_1/Au@rGO/ITO electrode as a function of time (weeks) and (ii) the current response of five different BSA/anti-AFB_1/Au@rGO/ITO immunoelectrodes fabricated using the same set of procedures in the presence of 1 ng mL^{-1} AFB_1 concentration.

antibodies (anti-AFB_1) and bovine serum albumin (BSA) have been purchased from Sigma-Aldrich USA. The graphite flakes (NGS Naturgraphit GmbH, Germany), H_2SO_4, H_3PO_4, $KMnO_4$, H_2O_2, ammonia solution, ethanol, *etc.*, are of technical grade. Deionized water has been used in all the buffer and solution preparation.

Synthesis of graphene oxide

The graphene oxide (GO) was synthesized using a method proposed by Marcano *et al.*[37] Briefly, a 9 : 1 combination of concentrated H_2SO_4/H_3PO_4, (240 mL/26.7 mL) was added to 2 g of graphite flakes and 12 g of $KMnO_4$. The $KMnO_4$ was mixed within 15 min in order to avoid any explosion, since the above mixing process is exothermic in nature. After that the reaction was subjected to magnetic stirring for 12 h at a temperature of 50 °C. This reaction was subsequently quenched by adding about 270 mL of ice with 2 mL of 30% H_2O_2. The yellowish slurry mixture was then shifted, centrifuged and filtered. The filtrate thus obtained was washed with 30% HCl and subsequently with distilled water until the pH ~7 and was dried at 70 °C to obtain solid GO.

Synthesis of reduced graphene oxide

The graphene oxide was converted into reduced graphene oxide (rGO) using sodium citrate. 10 mL (1 mg mL^{-1}) of a highly dispersed aqueous suspension of GO was added with 100 mg of sodium citrate and the solution was subjected to stirring for about 4 h at 60 °C. The colour of the solution changed from brown to black indicating conversion of GO to rGO. After the solution was cooled to room temperature the resultant homogeneous dispersion was centrifuged at 12 000 rpm and washed with Milli-Q water. Subsequently, the rGO was re-dispersed into 10 mL water for further characterization.

In situ synthesis of the Au@rGO nanocomposite

100 mg of sodium citrate was added to a 10 mL (1 mg mL^{-1}) aqueous suspension of GO and the solution was refluxed for 3 h at 60 °C. Further, 1 mL of $HAuCl_4 \cdot 3H_2O$ (10 mM) was added to the above solution and reflux was continued for another 1 h. Finally, the resulting homogeneous dispersion was centrifuged at 12 000 rpm and washed with Milli-Q water. Subsequently, the nanocomposite material (Au@rGO) was re-dispersed in 10 mL acetonitrile that had been used as a stock solution for electrophoretic deposition.

Fabrication of the Au@rGO/ITO electrodes

The Au@rGO nanocomposite film was deposited onto the ITO substrate using the electrophoretic deposition (EPD) technique. 100 μL of the stock solution of Au@rGO was re-dispersed in 10 mL of acetonitrile to prepare the colloidal suspension. A constant DC voltage source having two electrode systems was used for EPD. Pre-cleaned ITO coated glass substrate (sheet resistance 30 Ω cm^{-1}) and platinum foil were used as the anode and cathode, respectively. 10^{-4} mol of magnesium nitrate [$Mg(NO_3)_2 \cdot 6H_2O$] was taken as an electrolyte in the colloidal suspension that imparts surface charges to the Au@rGO

nanocomposite for uniform film deposition.[38] The electrodes separated by 1 cm distance were immersed into the colloidal suspension containing Au@rGO and subjected to a constant electric field (100 V cm^{-1}) for 90 s. The fabricated Au@rGO/ITO electrodes (0.25 cm^2), were removed from the suspension and dried.

Immobilization of monoclonal antibodies onto the Au@rGO/ITO electrodes

Monoclonal anti-aflatoxin B_1 (anti-AFB_1) antibody solution (10 μg mL^{-1}) was freshly prepared in phosphate buffer (PB, pH 7.4). Prior to antibody functionalization, the carboxyl groups present on the Au@rGO/ITO electrode were activated using *N*-ethyl-*N*-(3-dimethylaminopropyl) carbodiimide/*N*-hydroxysuccinimide (EDC-NHS) chemistry.[39]

10 μL of the antibody solution was uniformly cast onto the Au@rGO/ITO electrode surface and was incubated for 4 h under humid conditions at room temperature. It was then washed with bovine serum albumin (BSA) solution (0.1 mg mL^{-1}) prepared in PB. The BSA was used to block non-specific active sites present on the immunoelectrode surface. The BSA/anti-AFB_1/Au@rGO/ITO bioelectrode was then washed with PBS and stored at 4 °C when not in use. Fig. 7 demonstrates the fabrication of the carboxylated Au@rGO nanocomposite electrodes and its antibody functionalization strategy.

Characterization

The synthesized Au@rGO was characterized using X-ray diffraction (XRD, Rigaku) and UV-visible spectroscopy (Perkin-Elmer). The structural and morphological studies were carried out using scanning electron microscopy (SEM LEO 440) and transmission electron microscopy (TEM, Tecnaii-G2F30 STWIN). The XPS measurements were carried out in a Perkin Elmer XPS chamber (PHI 1257) with a base pressure of 5×10^{-9} Torr. An Mg-Kα X-ray source was used for this study. The chemical structure of Au@rGO was investigated using Fourier transform infrared spectroscopy (FT-IR, Perkin-Elmer, model spectrum BX). The electrochemical studies such as cyclic voltammetry (CV) and electrochemical impedance spectroscopy (EIS) were conducted using an Autolab, Potentiostat/Galvanostat (AUT-84275). The electrochemical studies were carried out using three electrode systems where ITO is the working electrode, platinum (Pt) is used as the counter electrode and Ag/AgCl is used as the reference electrode.

Conclusions

We have prepared a biosensing platform for aflatoxin detection consisting of uniformly dispersed Au nanoparticles on rGO sheets, with and without antibody conjugation. The Au@rGO nanocomposite has been fabricated onto an ITO electrode and subsequently functionalized with monoclonal anti-AFB_1. Sodium citrate helps in the simultaneous reduction of gold ions onto graphene sheets. The XPS and FT-IR analysis confirm the carboxylated nature of the Au@rGO sheets desirable for covalent interaction with antibodies *via* a strong amide bond leading to higher stability and a low detection limit. It has been found that incorporation of Au nanoparticles into rGO results in enhanced electrochemical activity and heterogeneous electron transfer rate as compared to the bare rGO. The shape, size, distribution and crystalline structure of Au@rGO has been investigated using electron microscopic, spectroscopic and optical techniques. The analytical performance of this immunosensor has been investigated using electrochemical techniques. The biosensor shows a higher sensitivity of 182.4 μA (ng $mL^{-1})^{-1}$ cm^{-2}, an extended linearity of 0.1–12 ng mL^{-1} and a good storage stability of 8 weeks along with high reproducibility. It should be interesting to use this novel bioelectrode for detection of other food toxins such as aflatoxin M_1, ochratoxin-A, *etc.*

Acknowledgements

We thank Director, CSIR-National Physical Laboratory, New Delhi, India for providing the facilities. C. S. and Md. A. A. are

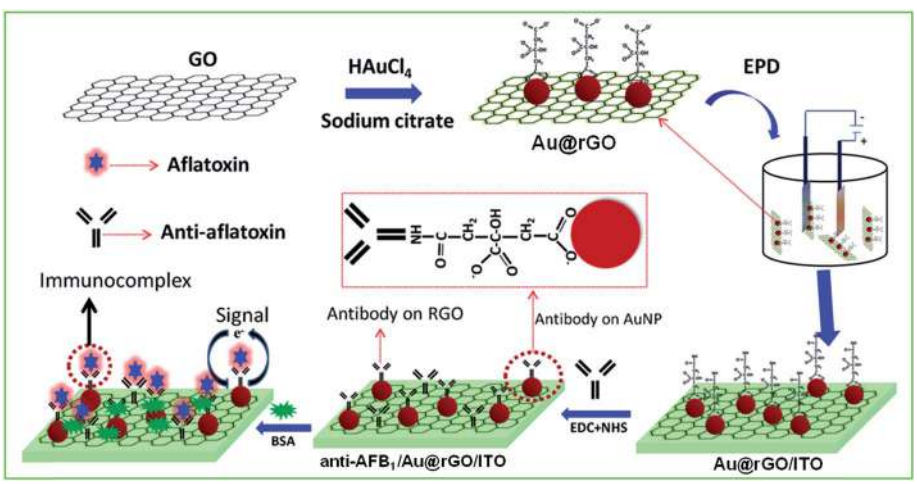

Fig. 7 Schematic representation of immunosensor fabrication.

thankful to the Council of Scientific and Industrial Research, India for providing senior research fellowships. S. S. acknowledges University Grant Commission, India for providing Dr D. S. Kothari Postdoctoral fellowship [no. F.4-2/2006 (BSR)/PH/13-14/0098]. The financial support received from Department of Science and Technology, India (Grant no. DST/TSG/ME/2008/18) and Indian Council of Medical Research, India (Grant no. ICMR/5/3/8/91/GM/2010-RHN) is gratefully acknowledged.

References

1 A. K. Geim and K. S. Novoselov, *Nat. Mater.*, 2007, **6**, 183–191.
2 G. Brumfiel, *Nature*, 2009, **458**, 390.
3 K. P. Loh, Q. Bao, G. Eda and M. Chhowalla, *Nat. Chem.*, 2010, **2**, 1015–1024.
4 C. Xu, X. Wang and J. Zhu, *J. Phys. Chem. C*, 2008, **112**, 19841–19845.
5 D. Chen, H. Feng and J. Li, *Chem. Rev.*, 2012, **112**, 6027–6053.
6 M. Pumera, *Chem. Soc. Rev.*, 2010, **39**, 4146–4157.
7 M. Pumera, *Mater. Today*, 2011, **14**, 308–315.
8 O. C. Compton, B. Jain, D. A. Dikin, A. Abouimrane, K. Amine and S. T. Nguyen, *ACS Nano*, 2011, **5**, 4380–4391.
9 S. Srivastava, V. Kumar, M. A. Ali, P. R. Solanki, A. Srivastava, G. Sumana, P. S. Saxena, A. G. Joshi and B. Malhotra, *Nanoscale*, 2013, **5**, 3043–3051.
10 C. Shan, H. Yang, J. Song, D. Han, A. Ivaska and L. Niu, *Anal. Chem.*, 2009, **81**, 2378–2382.
11 M. Zhou, Y. Zhai and S. Dong, *Anal. Chem.*, 2009, **81**, 5603–5613.
12 A.-M. J. Haque, H. Park, D. Sung, S. Jon, S.-Y. Choi and K. Kim, *Anal. Chem.*, 2012, **84**, 1871–1878.
13 Y. Wan, Z. Lin, D. Zhang, Y. Wang and B. Hou, *Biosens. Bioelectron.*, 2011, **26**, 1959–1964.
14 R. K. Srivastava, S. Srivastava, T. N. Narayanan, B. D. Mahlotra, R. Vajtai, P. M. Ajayan and A. Srivastava, *ACS Nano*, 2011, **6**, 168–175.
15 R. S. Dey and C. R. Raj, *J. Phys. Chem. C*, 2010, **114**, 21427–21433.
16 S. Alwarappan, C. Liu, A. Kumar and C.-Z. Li, *J. Phys. Chem. C*, 2010, **114**, 12920–12924.
17 T. Liu, H. Su, X. Qu, P. Ju, L. Cui and S. Ai, *Sens. Actuators, B*, 2011, **160**, 1255–1261.
18 S. Mao, G. Lu, K. Yu, Z. Bo and J. Chen, *Adv. Mater.*, 2010, **22**, 3521–3526.
19 T. T. Baby, S. Aravind, T. Arockiadoss, R. Rakhi and S. Ramaprabhu, *Sens. Actuators, B*, 2010, **145**, 71–77.
20 J. Xu, C. Liu and Z. Wu, *Microchim. Acta*, 2011, **172**, 425–430.
21 T. Kavitha, A. I. Gopalan, K.-P. Lee and S.-Y. Park, *Carbon*, 2012, **50**, 2994–3000.
22 X. M. Feng, R. M. Li, Y. W. Ma, R. F. Chen, N. E. Shi, Q. L. Fan and W. Huang, *Adv. Funct. Mater.*, 2011, **21**, 2989–2996.
23 Y. Bo, H. Yang, Y. Hu, T. Yao and S. Huang, *Electrochim. Acta*, 2011, **56**, 2676–2681.
24 W. Hong, H. Bai, Y. Xu, Z. Yao, Z. Gu and G. Shi, *J. Phys. Chem. C*, 2010, **114**, 1822–1826.
25 C. Zhu, S. Guo, Y. Fang and S. Dong, *ACS Nano*, 2010, **4**, 2429–2437.
26 X. Dong, W. Huang and P. Chen, *Nanoscale Res. Lett.*, 2011, **6**, 60.
27 Y. Chen, Y. Li, D. Sun, D. Tian, J. Zhang and J.-J. Zhu, *J. Mater. Chem.*, 2011, **21**, 7604–7611.
28 S. J. Daly, G. J. Keating, P. P. Dillon, B. M. Manning, R. O'Kennedy, H. A. Lee and M. R. Morgan, *J. Agric. Food Chem.*, 2000, **48**, 5097–5104.
29 L. Dunne, S. Daly, A. Baxter, S. Haughey and R. O'Kennedy, *Spectrosc. Lett.*, 2005, **38**, 229–245.
30 Z. Zhang, H. Chen, C. Xing, M. Guo, F. Xu, X. Wang, H. J. Gruber, B. Zhang and J. Tang, *Nano Res.*, 2011, **4**, 599–611.
31 L. Tang, Y. Wang, Y. Li, H. Feng, J. Lu and J. Li, *Adv. Funct. Mater.*, 2009, **19**, 2782–2789.
32 M. Watt-Smith, J. Friedrich, S. Rigby, T. Ralph and F. Walsh, *J. Phys. D: Appl. Phys.*, 2008, **41**, 174004.
33 T. Ahmad, I. A. Wani, J. Ahmed and O. A. Al-Hartomy, *Appl. Nanosci.*, 2014, **4**, 491–498.
34 C. Singh, S. Srivastava, M. A. Ali, T. K. Gupta, G. Sumana, A. Srivastava, R. Mathur and B. D. Malhotra, *Sens. Actuators, B*, 2013, **185**, 258–264.
35 A. Kaushik, P. R. Solanki, K. Kaneto, C. Kim, S. Ahmad and B. D. Malhotra, *Electroanalysis*, 2010, **22**, 1045–1055.
36 A. Kaushik, A. Vasudev, S. K. Arya and S. Bhansali, *Biosens. Bioelectron.*, 2013, **50**, 35–41.
37 D. C. Marcano, D. V. Kosynkin, J. M. Berlin, A. Sinitskii, Z. Sun, A. Slesarev, L. B. Alemany, W. Lu and J. M. Tour, *ACS Nano*, 2010, **4**, 4806–4814.
38 B. Gao, G. Z. Yue, Q. Qiu, Y. Cheng, H. Shimoda, L. Fleming and O. Zhou, *Adv. Mater.*, 2001, **13**, 1770–1773.
39 S. Srivastava, P. R. Solanki, A. Kaushik, M. A. Ali, A. Srivastava and B. Malhotra, *Nanoscale*, 2011, **3**, 2971–2977.
40 P. Kalita, J. Singh, M. Kumar Singh, P. R. Solanki, G. Sumana and B. Malhotra, *Appl. Phys. Lett.*, 2012, **100**, 093702–093704.
41 A. Sharma, Z. Matharu, G. Sumana, P. R. Solanki, C. Kim and B. D. Malhotra, *Thin Solid Films*, 2010, **519**, 1213–1218.
42 J. H. Owino, O. A. Arotiba, N. Hendricks, E. A. Songa, N. Jahed, T. T. Waryo, R. F. Ngece, P. G. Baker and E. I. Iwuoha, *Sensors*, 2008, **8**, 8262–8274.
43 S. Piermarini, L. Micheli, N. Ammida, G. Palleschi and D. Moscone, *Biosens. Bioelectron.*, 2007, **22**, 1434–1440.

THE JOURNAL OF PHYSICAL CHEMISTRY C

Article

Cite This: J. Phys. Chem. C 2018, 122, 22985−22995

pubs.acs.org/JPCC

Quantitative Description of the Vesicle Fusion Mechanism on Solid Surfaces and the Role of Cholesterol

Shiju Abraham, Tabea Heckenthaler, Dyuti Bandyopadhyay, Yakov Morgenstern, and Yair Kaufman*

The Zuckerberg Institute for Water Research, The Jacob Blaustein Institutes for Desert Research, Ben-Gurion University of the Negev, Sede Boqer, Israel

Supporting Information

ABSTRACT: Supported lipid bilayers on solid surfaces have promising potential for diverse applications, such as separation processes, biosensors, drug delivery, and more. However, the self-assembly of supported lipid bilayers via vesicle fusion—the commonly used preparation method for these lipid bilayers—is not fully understood. It is often found that lipid bilayers are patchy or exhibit holes/defects, which may hinder their applicability. Moreover, it is not fully understood whether these holes are transient, kinetically trapped, or thermodynamically stable (long-lasting). Here, we derived equations to *quantitatively* describe the mechanism of vesicle fusion on atomically smooth hydrophilic surfaces. The derived equations determine whether defectless lipid bilayers are thermodynamically stable/favorable and *qualitatively* predict the self-assembly rate. It is shown that vesicle fusion is governed by van der Waals and double layer interactions, as well as undulation repulsion between the lipid bilayers and the solid surface. Utilizing various experimental techniques, we confirmed the equation predictions by studying the self-assembly of lipid bilayers on silicon wafers using lipid mixtures that exhibited different electric potentials. Furthermore, we found that cholesterol increases the lipid bilayer resistivity—a crucial parameter for several applications—and the rate of self-assembly, by decreasing both the dielectric constant of the lipid bilayer and the undulation repulsion between the lipid bilayers and the solid surface. The derived equations can be used as quantitative guidelines for designing supported lipid structures on the surface, such as a layer of intact lipid vesicles, patchy or defectless lipid bilayers.

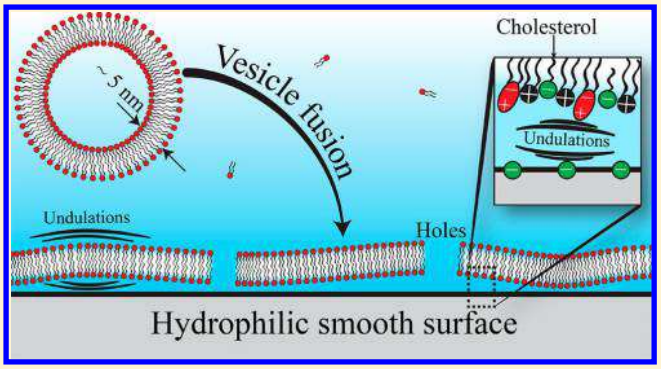

1. INTRODUCTION

Supported lipid bilayers (illustrated in Figure 1)—also called supported biomimetic membranes—are often considered as *simplified* models of biological membranes. Since supported lipid bilayers can self-assemble on different surfaces, as well as on different electrodes, they can be used to study the transport of different molecules or ions through membrane proteins,[1] and through peptides that self-assemble in biological membranes.[2] In other studies, the forces between supported lipid bilayers were measured in order to study different diseases that are related to the myelin sheath, such as multiple sclerosis.[3] Supported lipid bilayers can also be used for biosensing applications,[4] DNA ordering,[5] bioinspired surface coating,[6] and drug delivery,[7] and they have the potential to be used for diverse separation processes, such as energy-efficient water purification membranes.[8−14]

The self-assembly of supported lipid bilayers on different surfaces has been studied extensively.[15−25] Probably the simplest method to prepare supported lipid bilayers with or without membrane proteins is via vesicle fusion,[8,23,26−32] in which lipids are hydrated and self-assemble into vesicles. Then, the double layer interactions (electrostatic and entropic forces) between the vesicles and the surface attach the vesicles to the surface, which can rupture the vesicles and fuse them into a continuous lipid bilayer.[20,33] On the basis of quartz crystal microbalance with dissipation (QCM-D) and atomic force microscopy (AFM) studies, it is often assumed that on silica, for instance, the surface is fully covered by a lipid bilayer within ∼5 min.[17,22,29,34] However, QCM-D and AFM cannot overrule the existence of minor defects (e.g., 1%) throughout macroscopic areas. In addition, it was shown that, under certain conditions, vesicles can remain intact on the surface,[15,29] and patchy or defective (with holes) lipid bilayers can form,[35] as demonstrated in Figure 1.

For diverse applications, it is essential to control the configuration of the lipid bilayer that is on the surface, namely, whether it is defectless, or not, and whether it consists of intact vesicles. Biosensing applications and separation processes, for instance, require selective molecular transport through specific membrane proteins, and not through nonselective defects in the bilayer. Thus, these applications can only be achieved by defectless lipid bilayers. However, to the best of our

Received: July 9, 2018
Revised: September 17, 2018
Published: September 17, 2018

DOI: 10.1021/acs.jpcc.8b06566
J. Phys. Chem. C 2018, 122, 22985−22995

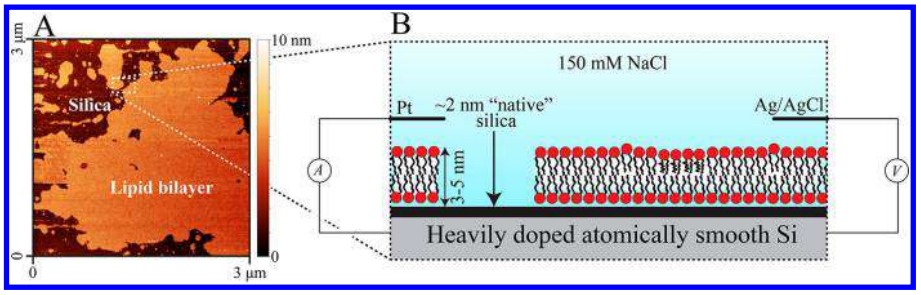

Figure 1. In this paper, we shed light on the conditions that render defectless lipid bilayers thermodynamically stable on atomically smooth hydrophilic surfaces. (A) AFM topography image demonstrating a patchy DMPC (zwitterionic headgroup) lipid bilayer on a silicon wafer (top layer ~2 nm of "native silica"). The bright area is the surface that was covered by the lipid bilayer, and the dark area is the silicon surface. The surface was scanned at 23 °C in a 150 mM NaCl solution, pH ~6. (B) Schematic illustration of a patchy lipid bilayer.

knowledge, the formation of the defects, or the fact that the defects do not "heal", is not fully understood; there is no *quantitative* model/mechanism that can be used to calculate whether the defects/holes are transient, kinetically trapped, or thermodynamically stable (long-lasting).

In section 3, we begin the discussion with a quantitative description of the vesicle fusion mechanism on atomically smooth hydrophilic surfaces. The proposed mechanism (1) quantitatively defines the parameters that determine whether a defectless lipid bilayer is thermodynamically favorable or not, (2) predicts the conditions under which intact vesicles are expected to remain on the surface (although they are expected to rupture eventually), and (3) correlates the effect of different parameters, such as the lipid bilayer bending modulus and the vesicle ζ-potential, with the rate at which the lipid bilayers self-assemble on the surface. Then, in section 4, we demonstrate how the mechanism can be used to calculate the thermodynamic stability of different lipid mixtures on a polished silicon wafer, which is a common substrate for supported lipid bilayers. In section 5, to test the proposed mechanism, we simultaneously measured the electrochemical impedance spectrum (which allows for measuring the capacitance, C_{LB}, resistance, R_{LB}, and the lipid bilayer surface coverage) and captured fluorescent images, atomic force microscopy (AFM) images, and force vs distance curves for different lipid bilayers. The combination of the four different techniques allowed us to determine the area fraction that was covered by the lipid bilayer after a specific vesicle fusion time; thus, these techniques allowed us to evaluate qualitatively the self-assembly rate. In the last subsection of section 5, we shed light on the effects of cholesterol on the self-assembly of supported lipid bilayers.

2. MATERIALS AND METHODS

2.1. Materials. 1,2-Dimyristoyl-*sn*-glycero-3-phosphocholine (DMPC), 1,2-dimyristoyl-3- trimethylammonium-propane (DMTAP), 1,2-dimyristoyl-*sn*-glycero-3-phospho-(1′-rac-glycerol) (DMPG), cholesterol, and 1,2-dimyristoyl-*sn*-glycero-3-phosphoethanolamine-*N*-(lissamine rhodamine B sulfonyl) (Rhod B) were purchased from Avanti Polar Lipids, Inc. (Alabama, USA) and used as received. Other chemicals, including chloroform (HPLC plus ≥99.9%, Sigma-Aldrich, USA), sulfuric acid (96%, CARLO ERBA Reagents, France), hydrogen peroxide (30%, Merck KGaA, Germany), ethanol, NaCl, etc., were of analytical grades. A Milli-Q gradient water purification system was used to purify the water to a resistivity of 18 MΩ·cm and was used in different stages of solution preparation and cleaning.

2.2. Preparation of Lipid Vesicles. Stock solutions of lipids (3 mg/mL), Rhod B (1 mg/5 mL), and cholesterol (5 mg/mL) were made in chloroform. The various lipid mixtures that are discussed in the paper were prepared by mixing these stock solutions. Vesicle solutions for the AFM, impedance spectroscopy, and ζ-potential measurements were prepared as follows. The desired lipid mixtures were initially prepared in chloroform and dried on a hot plate at 55 °C in a chemical hood for 1 h. A NaCl solution (150 mM, 1 mL) was added to the dried lipid combinations to reach a total concentration of 0.5 mM lipids (additionally, either 0.25 or 0.5 mM cholesterol and ≤1 mol % Rhod B were added in specific combinations). Ultrasonication for 2 min, followed by gradual heating (55 °C) for 20 min, was also performed to achieve a well-dispersed vesicle solution. The solutions were then extruded through a 100 nm pore size membrane ~10 times (at a temperature of ~55 °C) to have a final homogeneous vesicle solution for the experiments.

2.3. Self-Assembly of the Lipid Bilayer. Polished silicon wafers (p-type) of an electrical resistivity of 0.001−0.005 Ω·cm (University Wafer, South Boston, USA) were cut down to a size of 25 × 25 mm^2 to fit in the JPK electrochemical cell (EC-cell, Figure 2A) for the impedance spectroscopy, fluorescence imaging, AFM topography, and force vs distance measurements. Using the e-gun deposition technique, Ti (5 nm):Au (50 nm) coating was done on one of the edges (an area of ~5 mm × 5 mm) of the wafer to have better contact with the working electrode for the impedance spectroscopy measurements. Prior to the vesicle fusion, the SI substrate was immersed and rinsed well with a piranha solution (for 5 min), followed by rinsing with DDW, ethanol, and DDW and drying with a nitrogen gun. The Si substrate was immediately placed in the EC-cell and maintained at a constant temperature of 45 °C. Then, 400 μL of lipid solution was uniformly poured on the Si surface and maintained for 2 h for the vesicle fusion and the self-assembly of the lipid bilayer on the surface (the EC-cell inner substrate area is ~2.27 cm^2). The residual vesicles were then removed by an intense exchange (~15 times) of the vesicle solution by an electrolyte solution (150 mM NaCl without vesicles) in the EC-cell.

2.4. AFM Topography and Force Measurements. Topography and force vs distance measurements of the lipid bilayers were acquired using the atomic force microscopy (AFM) technique employing JPK NanoWizard 4 (JPK Instruments AG, Germany) at 26 ± 1 °C. Imaging was done by employing a quantitative imaging (QI) mode using V-shaped gold-coated silicon tips: SNL-10 (Bruker, Camarillo, CA, USA). The spring constant of the cantilever (~0.30 N/m)

DOI: 10.1021/acs.jpcc.8b06566
J. Phys. Chem. C 2018, 122, 22985−22995

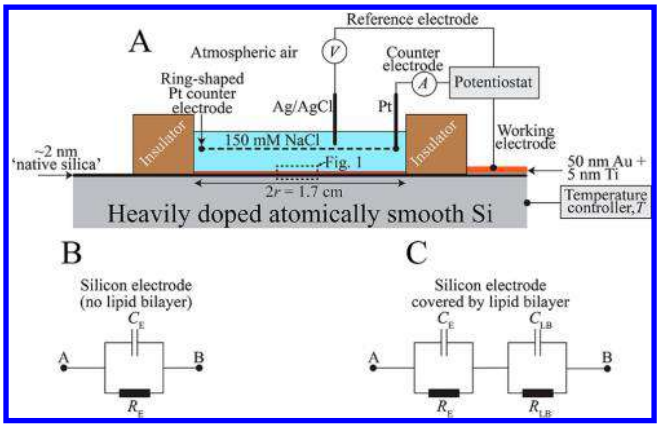

Figure 2. Schematic illustration of the experimental system. (A) AFM imaging, AFM force vs distance measurements, fluorescence imaging, and electrochemical impedance spectroscopy measurements were conducted simultaneously using the illustrated electrochemical cell. To analyze the electrochemical impedance spectra, two equivalent electrical circuits were used, (B) and (C), to model the bare silicon electrode and the electrode covered with a lipid bilayer, respectively. These two models allowed us to calculate C_E, R_E, C_{LB}, and R_{LB}, which are the silicon electrode capacitance and resistance and the lipid bilayer capacitance and resistance, respectively. Then, C_{LB} and R_{LB} were used to calculate the dielectric constant and the surface coverage of the supported lipid bilayer.

was estimated using the thermal noise method. All of the AFM measurements were done in a 150 mM NaCl solution. For the force vs distance measurements, the piezoelectric actuator was extended and retracted at a constant velocity of 10 nm·s^{-1}. The topography images and the force vs distance curves were analyzed using the JPK SPM-Data processing software.

2.5. Electrochemical Impedance Spectroscopy Measurements and Analysis. The electrochemical impedance spectroscopy (EIS) was performed at 26 ± 1 °C using a potentiostat (model: SP-300) from Bio-Logic Science Instruments, France. A three-electrode electrochemical system was used for these measurements (Figure 2A), consisting of a Si wafer that served as a working electrode, a reference electrode (Ag/AgCl), and a Pt 1.7 cm diameter ring shaped counter electrode. The Si wafer was ⟨100⟩ 380 μm thick, heavily doped, with a dopant concentration of 10^{19} cm^{-3} and a resistivity of 0.001−0.005 Ω·cm, which was purchased from University Wafer, South Boston, USA. EC-Lab software was used for the impedance and capacitance data analysis by fitting the equivalent circuits (Figure 2B and C) to the data. Prior to every impedance measurement with various lipid samples, the impedance spectrum of the bare Si electrode impedance measurement was considered as a control experiment.

2.6. Fluorescence Imaging. Fluorescent images of the samples on the substrates were captured at 26 ± 1 °C by an epifluorescent microscope (Axio Zoom, V16, Zeiss, Germany), which was coupled with the AFM. This provided a clear picture of the distribution and homogeneity of the lipid assembly on the surface. Fluorescent images were then cropped using Photoshop CC2018 (Adobe).

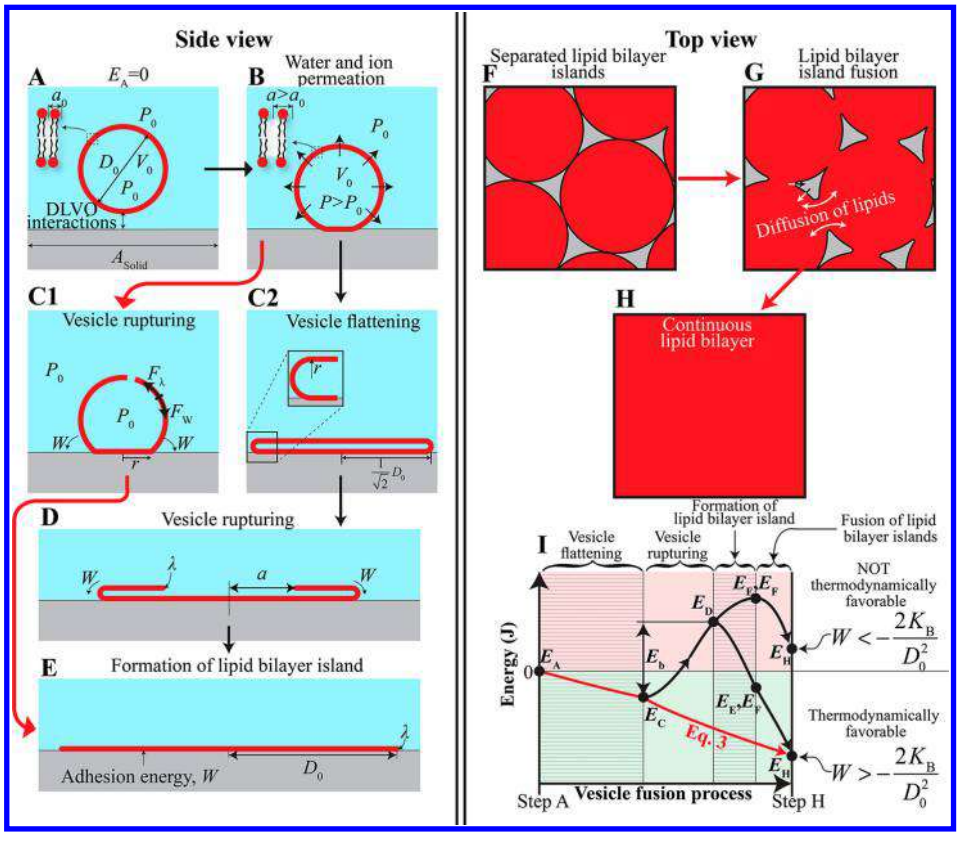

Figure 3. Proposed mechanism for the self-assembly of a lipid bilayer on hydrophilic surfaces via vesicle fusion. (A−E) Side view illustrations of the different stages of a single vesicle adhesion and rupturing on the surface. (F−H) Top view of the number of vesicles that fuse into a continuous defectless lipid bilayer. (I) A plot showing the conditions under which a defectless lipid bilayer is thermodynamically favorable (the energy in step H is lower than zero) or not.

DOI: 10.1021/acs.jpcc.8b06566
J. Phys. Chem. C 2018, 122, 22985−22995

2.7. ζ-Potential Measurements of the Vesicles. The ζ-potentials of the vesicles were measured at 45 ± 1 °C using the Nano ZS instrument from Malvern Panalytical Ltd. (United Kingdom) equipped with a He−Ne laser with a wavelength of 633 nm. These measurements were carried out in an ionic concentration of 150 mM (NaCl) at 45 °C by employing the principle of electrophoretic light scattering.

3. THEORETICAL SECTION: MECHANISM OF SELF-ASSEMBLY OF SUPPORTED LIPID BILAYERS VIA VESICLE FUSION

In this section, we calculated the energy of a vesicle and the solid surface at different stages of the vesicle fusion mechanism in order to determine whether the self-assembly of defectless lipid bilayers is thermodynamically favorable or not. Figure 3 illustrates the proposed mechanism of the self-assembly of a lipid bilayer on atomically smooth hydrophilic surfaces via vesicle fusion. For the following calculations, let us consider a single spherical vesicle with diameter D_0. The chemical structure of the lipids is assumed to favor the formation of a lipid bilayer; that is, the shape factor of a lipid in the vesicle is $v/(a_0 l_c) \sim 1$,[36] where v is the lipid headgroup volume, a_0 is the average area of a single lipid, and l_c is the length of the fully stretched hydrophobic tail of the lipid.

Equation 1 is a general equation that gives the energy of a vesicle (whether it is ruptured or not) and the solid surface in an aqueous solution

$$E = A_{SW}\gamma_{SW} + A_{LW}\gamma_{LW} + A_{LS}\gamma_{LS} + \frac{1}{2}\frac{K_B}{r^2}A_B + l\lambda \quad (1)$$

where A_{SW}, A_{LW}, and A_{LS} are the solid−water, lipid−water, and lipid−solid contact areas, respectively. γ_{SW}, γ_{LW}, and γ_{LS} are the solid−water, lipid−water, and lipid−solid surface energies (or surface tensions), respectively. K_B is the lipid bilayer bending modulus, r is the radius of curvature of the lipid bilayer, A_B is the area of the curved lipid bilayer, l is the length of the lipid bilayer edge for the case in which the vesicle is ruptured, and λ is the line tension of the lipid bilayer. We note that, for this derivation, the thickness of the lipid bilayer, t, is significantly smaller than D_0; thus, the inner and outer areas of the vesicle are assumed to be the same.

Figure 3A illustrates a vesicle that approaches a surface, and the adhesion energy between the vesicle and the surface, W (mJ·m^{-2}, positive for adhesion and vice versa), can be calculated using eq 12, which is discussed below. The volume of the vesicle is V_0, and its internal pressure, P_0, must be equal to the pressure of the bulk solution that surrounds the vesicle; otherwise, water and ions will be pushed in (low pressure) or out of the vesicle (high pressure). On the basis of eq 1, the energy in step A is given by

$$E_A = A_{solid}\gamma_{SW} + 2\cdot 4\pi\left(\frac{D_0}{2}\right)^2\gamma_{LW} + \frac{1}{2}\frac{K_B}{\left(\frac{D_0}{2}\right)^2}\cdot 4\pi\left(\frac{D_0}{2}\right)^2$$

$$= A_{solid}\gamma_{SW} + 2\pi {D_0}^2\gamma_{LW} + 2\pi K_B \quad (2)$$

where A_{solid} is the entire area of the solid surface.

In step B, the vesicle contacts the solid surface and W forces the vesicle to partially flatten. Since water is incompressible, the lost volume due to the vesicle flattening increases the internal pressure of the vesicle, which increases the average distance between the lipids, a_0, as illustrated in the inset of Figure 3B. The elevated pressure in the vesicle drives water and ions to permeate out of the vesicle, which decreases the volume of the vesicle. The vesicle area is assumed to be constant.

As water and ions permeate out of the vesicle, the vesicle continues to flatten, and the vesicle−surface contact area increases. As elaborated in Supporting Information section 1, a vesicle is expected to rupture without an energy barrier (i.e., the energy monotonically decreases) when the radius of the vesicle−surface contact area, r (see Figure 3C1), is larger than λ/W. Therefore, the vesicle is expected to rupture without an energy barrier when (see Supporting Information section 1)

$$D_0 > \sqrt{2}\frac{\lambda}{W} \quad (3)$$

For typical values of $\lambda = 1 \times 10^{-11}$ J·m^{-1} and $W = 1$ mJ·m^{-2}, all vesicles with $D_0 > 14$ nm are expected to rupture without encountering an energy barrier. We note that a different equation was proposed by Reviakine and Brisson,[21] which shows similar trends as the trends in eq 3; namely, the tendency of vesicles to rupture on the surface increases as D_0 and W increase and λ decreases. These trends were confirmed experimentally by Boxer et al.[37−39] Importantly, according to eq 3, small vesicles ($D_0 < \sqrt{2}\lambda/W$) are not expected to rupture; instead, as was also demonstrated experimentally by Boxer et al., these small vesicles flatten completely and form a disk-like vesicle, as illustrated in step C2. The energy in step C2 is given by

$$E_{C2} = \left(A_{solid} - \pi\left(\frac{1}{\sqrt{2}}D_0\right)^2\right)\gamma_{SW} + \pi\left(\frac{1}{\sqrt{2}}D_0\right)^2\gamma_{LS} + 3\pi\left(\frac{1}{\sqrt{2}}D_0\right)^2\gamma_{LW} + \frac{1}{2}\frac{K_B}{r^2}\cdot 4\pi r^2 \quad (4a)$$

Therefore,

$$E_{C2} - E_A = -\frac{1}{2}\pi {D_0}^2 W \quad (4b)$$

where the adhesion energy, by definition, is given by $W = \gamma_{SW} + \gamma_{LW} - \gamma_{LS}$. Since $E_{C2} - E_A$ is negative for $W > 0$, any adhesion energy will eventually force an unruptured vesicle to form a disk-like vesicle.

The energy that is required to rupture a disk-like vesicle is given by

$$E_D - E_{C2} = -\frac{\pi a^2}{2}\gamma_{LW} + \frac{\pi a^2}{2}\gamma_{LS} - \frac{\pi a^2}{2}\gamma_{SW} + 2\pi a\lambda \quad (5a)$$

$$E_D - E_{C2} = -\frac{\pi a^2}{2}W + 2\pi a\lambda \quad (5b)$$

where a is the radius of the hole that is opened in the vesicle, which can form anywhere on the vesicle, not necessarily at the center, as illustrated in Figure 3D. Importantly, as a hole is formed in the vesicle, i.e., $a \sim 0$, $E_D - E_{C2} > 0$; thus, the rupturing step is energetically unfavorable. However, there is a critical hole size, $a_C = \lambda/W$, at which $d(E_D - E_{C2})/da = 0$ and the rupturing process becomes favorable. Therefore, the energy barrier for rupturing a disk-like vesicle is given by

$$E_D - E_{C2}|_{a=a_C} = E_b = \frac{2\pi\lambda^2}{W} \quad (6)$$

DOI: 10.1021/acs.jpcc.8b06566
J. Phys. Chem. C 2018, 122, 22985−22995

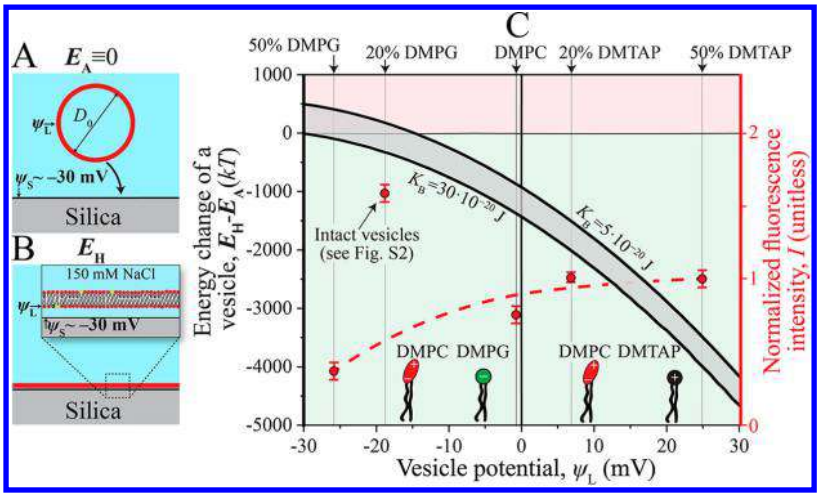

Figure 4. Demonstration of how the proposed mechanism can be used to calculate whether defectless lipid bilayers are thermodynamically favorable or not. (A) Illustration of a vesicle in an aqueous solution, where the energy is E_A, and (B) an illustration of a supported lipid bilayer, where the energy is E_H. (C) The bold black curves are based on eqs 10 and 12, showing the change in the energy of a vesicle that self-assembles to a supported lipid bilayer, $E_H - E_A$, for different (measured) vesicle potentials, $\zeta \sim \psi_L$, and for two extreme (but possible) bending moduli, K_B, taken from the literature.[46] For the specific system, supported lipid bilayers are thermodynamically favorable when $E_H - E_A < 0$. The thin vertical lines correspond to different lipid mixtures that were experimentally studied and discussed in section 4.2. The red dots are the measured fluorescence intensity of the lipid bilayers, where higher fluorescence intensity corresponds to higher lipid bilayer coverage. The fluorescence images are shown in Figure S2 in the Supporting Information. The dashed red line is a guideline.

We note that, for typical λ and W, E_b can exceed 100 kT (very high).

Lastly, the energy of the lipid bilayer island, step E, is given by

$$E_E = (A_{solid} - \pi {D_0}^2)\gamma_{SW} + \pi {D_0}^2 \gamma_{LS} + \pi {D_0}^2 \gamma_{LW} + 2\pi D_0 \lambda \quad (7)$$

Thus, the total change in the energy of a lipid bilayer island, in comparison to its energy as a vesicle in the bulk, is given by

$$E_E - E_A = -\pi {D_0}^2 W + 2\pi(D_0 \lambda - K_B) \quad (8)$$

Therefore, a single vesicle forms a lipid bilayer island when

$$W > 2\lambda/D_0 - 2K_B/{D_0}^2 \quad (9)$$

We note that, for typical values of K_B ($\sim 1 \times 10^{-20}$ J) and λ ($\sim 1 \times 10^{-11}$ J m^{-1}),[36,40] W has to exceed several μJ m^{-2} to render the formation of a lipid bilayer island thermodynamically favorable. This adhesion energy can be easily achieved on silica or mica, as elaborated in section 4.1.

When a number of vesicles rupture on the surface, which is a common case that is illustrated in Figure 3F, the ruptured vesicles can fuse into a continuous lipid bilayer in order to minimize the line tension, as illustrated in Figure 3G and H. The change in the energy of a single vesicle between step H and step A, after the vesicle fused with the other vesicles, is given by

$$E_H - E_A = -\pi {D_0}^2 W - 2\pi K_B \quad (10)$$

Importantly, $E_H - E_A$ can be considered as the "driving energy" for the vesicle fusion mechanism.

On the basis of eq 10, defectless lipid bilayers are thermodynamically favorable when

$$W > -2K_B/{D_0}^2 \quad (11)$$

Figure 3I depicts the energy profile of vesicle fusion on the basis of the proposed model, and it summarizes the conditions under which a defectless lipid bilayer is thermodynamically favorable or not. The red curve represents the energy profile when there is no energy barrier, whereas the black curve is the energy path that requires the vesicles to cross an energy barrier.

Lastly, W (notice that positive W corresponds to adhesion energy) can be estimated by[20,41]

$$W = \frac{A_{LWS}}{12\pi H^2} - \frac{\epsilon_0 \epsilon \kappa [2\psi_L \psi_S - (\psi_L^2 + \psi_S^2)\exp(-\kappa H)]}{\exp(\kappa H) - \exp(-\kappa H)} - \frac{3\pi^2}{128}\frac{k^2 T^2}{K_B H^2} \quad (12)$$

where the three terms correspond to the van der Waals, asymmetric double layer interactions at constant potentials,[41] and the undulation repulsion,[42] respectively. A_{LWS} is the Hamaker constant, ϵ_0 and ϵ are the vacuum permittivity and the dielectric constant of the aqueous solution, respectively, ψ_L and ψ_S are the surface potentials of the vesicle and the solid surfaces, respectively, H is the distance between the vesicle (or lipid bilayer) and the solid surface, k is the Boltzmann constant, T is the absolute temperature, and κ^{-1} is the Debye length.

For surface potentials lower than |25 mV| and aqueous solutions of low ionic strength, e.g., 150 mM NaCl, the Debye length is given by[36]

$$\kappa^{-1} = \left[\frac{\epsilon_0 \epsilon k T}{2Ce^2}\right]^{1/2} \quad (13)$$

where C is the ion concentration in the bulk (M) and e is the electron charge.

To summarize, the main conclusions that can be derived from the proposed vesicle mechanism are

(1) The self-assembly of defectless lipid bilayers on atomically smooth surfaces is thermodynamically favorable if $E_H - E_A < 0$, thus when $W > -2K_B/D_0$.
(2) The process of vesicle rupturing and fusion does not have an energy barrier when $W > \sqrt{2}\lambda/D_0$. Under these

DOI: 10.1021/acs.jpcc.8b06566
J. Phys. Chem. C 2018, 122, 22985−22995

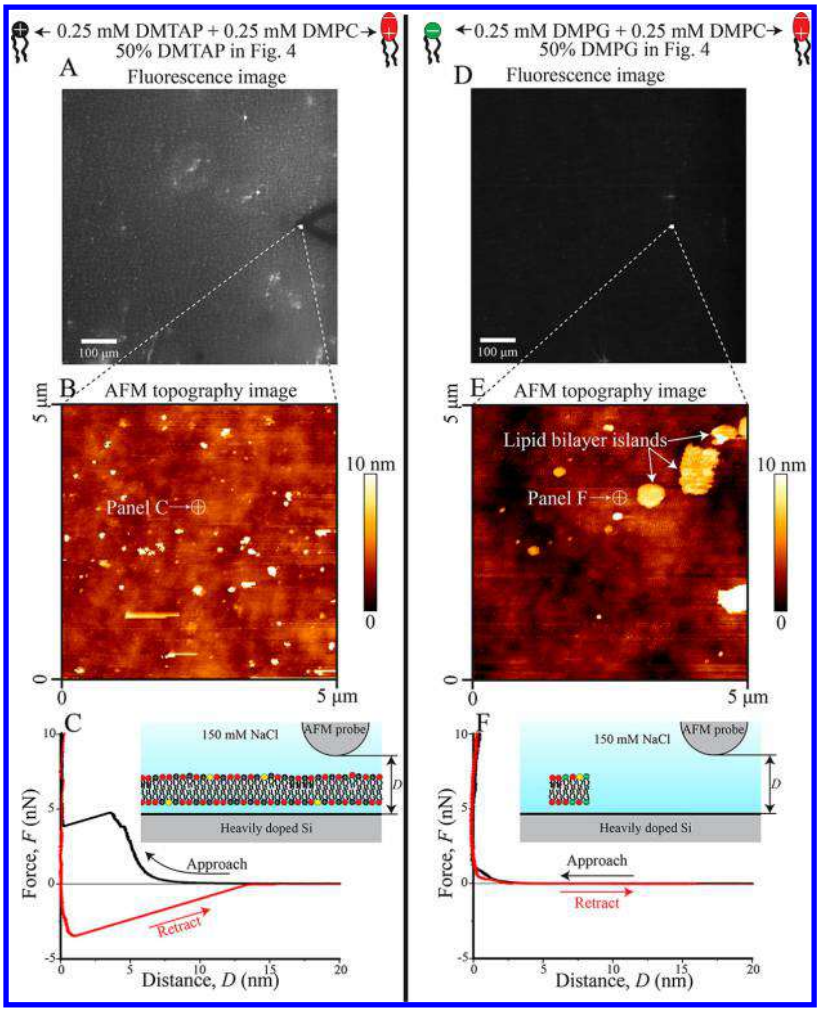

Figure 5. Experimental verification of the mechanism predictions. Comparison between two extreme vesicle solutions: (A–C) positively charged vesicles, the rightmost data point in Figure 4, (50% DMTAP), and (D–F) negatively charged vesicles, the leftmost data point in Figure 4 (50% DMPG). (A and D) Fluorescent images showing a higher average intensity for the positively charged mixture. (B and E) AFM topography images showing a lipid bilayer with no holes for the positively charged lipid vesicle and low lipid coverage for the negatively charged mixture. (C and F) Illustration of a clear indication of a typical lipid bilayer "penetration force" in the case of the positively charged lipid mixture and no "penetration force" in the case of the negatively charged mixture. These results are in agreement with the proposed model, showing that a lipid bilayer formed when $E_H - E_A < 0$ and did not form when $E_H - E_A > 0$ (see Figure 4).

conditions, defectless lipid bilayers are thermodynamically favorable, since K_B and λ are positive.

(3) The rate at which supported lipid bilayers self-assemble on surfaces, in the case of no energy barrier, is expected to be proportional to $\exp[-(E_H - E_A)/kT] = \exp[\pi(D_0^2W + 2K_B)/kT]$. Therefore, the rate is expected to increase with K_B and W (function of K_B). Importantly, W increases (adhesion increases) with K_B mainly due to the decrease in the undulation repulsion (see eq 12).

4. RESULTS AND DISCUSSION

4.1. Demonstration of How the Proposed Mechanism Can Be Used to Calculate the Thermodynamic Stability of a Supported Lipid Bilayer. In this section, we demonstrate how the proposed mechanism can be used to calculate whether a supported lipid bilayer is thermodynamically favorable or not. For this demonstration, let us consider binary mixtures of lipids, consisting of zwitterionic and positively charged lipids, DMPC + DMTAP(+), or of zwitterionic and negatively charged lipids, DMPC + DMPG(−). When these lipid mixtures are introduced into aqueous solutions, e.g., 150 mM NaCl, the lipids self-assemble to vesicles if the lipid concentration is above the critical micelle/aggregate concentration.[36] The maximum transition temperature of these binary lipid mixtures is ∼37 °C,[43,44] and therefore, the self-assembly of the supported lipid bilayer was conducted at 45 °C. As a first order approximation, let us assume that the ζ-potential of the different vesicles, which was measured (see Materials and Methods, section 2.7), was also the surface potential of the vesicles, i.e., $\zeta \approx \psi_L$ in eq 12.

The plot in Figure 4 summarizes the change in energy, or the "driving energy" of the vesicle fusion process, $E_H - E_A$ (eq 10), for five different lipid mixtures. According to the proposed mechanism, the lipid mixtures for which $E_H - E_A < 0$ are expected to yield thermodynamically stable defectless lipid bilayers. On the other hand, lipid mixtures for which $E_H - E_A > 0$ are not expected to yield supported lipid bilayers on the surface. Furthermore, the rate of the self-assembly of the lipid bilayer should increase as $E_H - E_A$ becomes more negative.

The following parameters were used to plot Figure 4: $\epsilon = 78$, $\epsilon_0 = 8.85 \times 10^{-12}$ C^2·J^{-1}·m^{-1}, $C = 0.15$ M NaCl, $\psi_S = -30$ mV

DOI: 10.1021/acs.jpcc.8b06566
J. Phys. Chem. C 2018, 122, 22985−22995

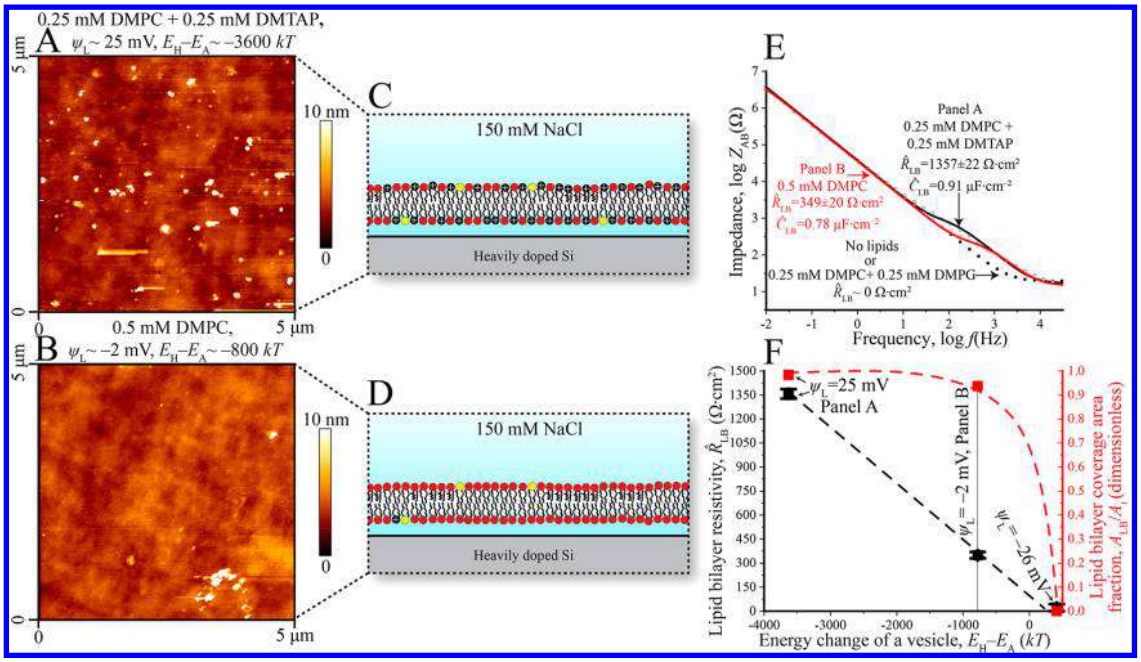

Figure 6. Effect of $E_H - E_A$ on lipid bilayer surface coverage. (A and B) Representative AFM topography images of 50% DMTAP and DMPC lipid mixtures showing no holes in the lipid bilayers. (C and D) Schematic illustrations of the two different lipid mixtures. (E) Representative Bode plots of the electrochemical impedance spectroscopy measurements for different lipid bilayers. (F) The black and red dots (errors are smaller than the red dot size) correspond to the measured resistivity, $\hat{R}_{LB}$, of the different lipid bilayers and the lipid bilayer area fraction, A_{LB}/A_t, respectively. (F) Each lipid bilayer is identified with a specific ψ_L, and the area fraction was calculated using eq 14. The dashed lines are guidelines (not a model).

(silica),[45] $A_{LWS} = 2 \times 10^{-21}$ J,[20] and $H = 0.5$ nm.[20] The measured ζ-potentials ($\approx\psi_L$) for the vesicles, from the left side of the plot to the right, were -26 ± 2, -19 ± 1, -2 ± 1, 7.0 ± 1, and 25 ± 2 mV. $D_0 = 100$ nm, $K_B = 5 \times 10^{-20}$ to 30×10^{-20} J,[46] and $\lambda = 1 \times 10^{-11}$ J m^{-1}.[36]

Figure 4C shows that only the most negatively charged vesicle, namely, 0.25 mM DMPC + 0.25 mM DMPG (50% DMPG), is NOT expected to yield a supported lipid bilayer.

4.2. Experimental Evaluation of the Proposed Mechanism. To experimentally evaluate the predictions of the mechanism proposed in section 4.1, the self-assembly processes of the lipid bilayers with the five different lipid mixtures mentioned in Figure 4 were studied using a fluorescence microscope, AFM topography imaging, force vs distance measurements, and electrochemical impedance spectroscopy. The self-assembly was carried out under the same conditions as those described in section 2.3; namely, the vesicle solution was left on the surface for 2 h at 45 °C, at which all of the different lipid mixtures were in the liquid phase. Then, the vesicle solution was rinsed, and the different measurements were carried out simultaneously at ~26 ± 1 °C, at which the lipids can be in the "solid" phase, or kinetically trapped in the liquid phase.

Figure S2 in the Supporting Information shows five typical fluorescence images of the different lipid mixtures specified in Figure 4. The normalized fluorescence intensity of the five images, I, is plotted in Figure 4C (red dots). The red dashed guideline shows that I increases as $E_H - E_A$ becomes more negative; thus, qualitatively, the self-assembly rate increases as $E_H - E_A$ becomes more negative, as predicted by the proposed mechanism. Notably, I in the case of 20% DMPG is significantly higher than the expected I based on the dashed guideline. The AFM topography image in Figure S2G shows that, for the 20% DMPG lipid mixture, about 50% of the surface was covered by intact vesicles, which can be approximated as an average of 1.5 lipid bilayers on the surface, and thus the high I. We note that, for the 20% DMPG mixture, the calculated adhesion energy, W (eq 12), is ~0.01 mJ·m^{-2} (weak adhesion). Under the experimental conditions, eq 3 and Reviakine and Brisson's equation[21] predict that D_0 must exceed 250 nm for the vesicles to rupture, whereas D_0 was ~100 nm; thus, both eq 3 and Reviankine and Brisson's equation support these results.

To elucidate the structure of the supported lipid bilayer, fluorescence images were combined with AFM topography images and force vs distance measurements. Figure 5 summarizes the results for the two extreme lipid mixtures, namely, the most positively charged vesicles (50% DMTAP in Figure 4) and the most negatively charged vesicles (50% DMPG in Figure 4). For the most positively charged vesicles, the mechanism predicts the fastest ($E_H - E_A$ is the lowest—most negative—among the studied lipid mixtures) self-assembly process that would ultimately yield a defectless lipid bilayer, and the left column in Figure 5 confirms this prediction. Figure 5A shows a fluorescent image that reveals fairly uniform brightness throughout the surface (~1 mm^2 in the fluorescent image); Figure 5B shows a representative topography image with no holes; and Figure 5C shows a force vs distance measurement, which reveals a typical penetration force into a lipid bilayer.[47,48] In addition, the resistivity of the lipid bilayer, $\hat{R}_{LB}$, was 1.2 ± 0.05 kΩ·cm^2, which is equivalent to ~0.96 surface coverage, as elaborated below.

On the other hand, the proposed mechanism predicts that the process of self-assembly should not be thermodynamically favorable for the negatively charged vesicles. The right column in Figure 5 confirms these predictions; Figure 5D shows a weak fluorescence signal in comparison to Figure 5A (the same exposure parameters as those in Figure 5A). The AFM

DOI: 10.1021/acs.jpcc.8b06566
J. Phys. Chem. C 2018, 122, 22985–22995

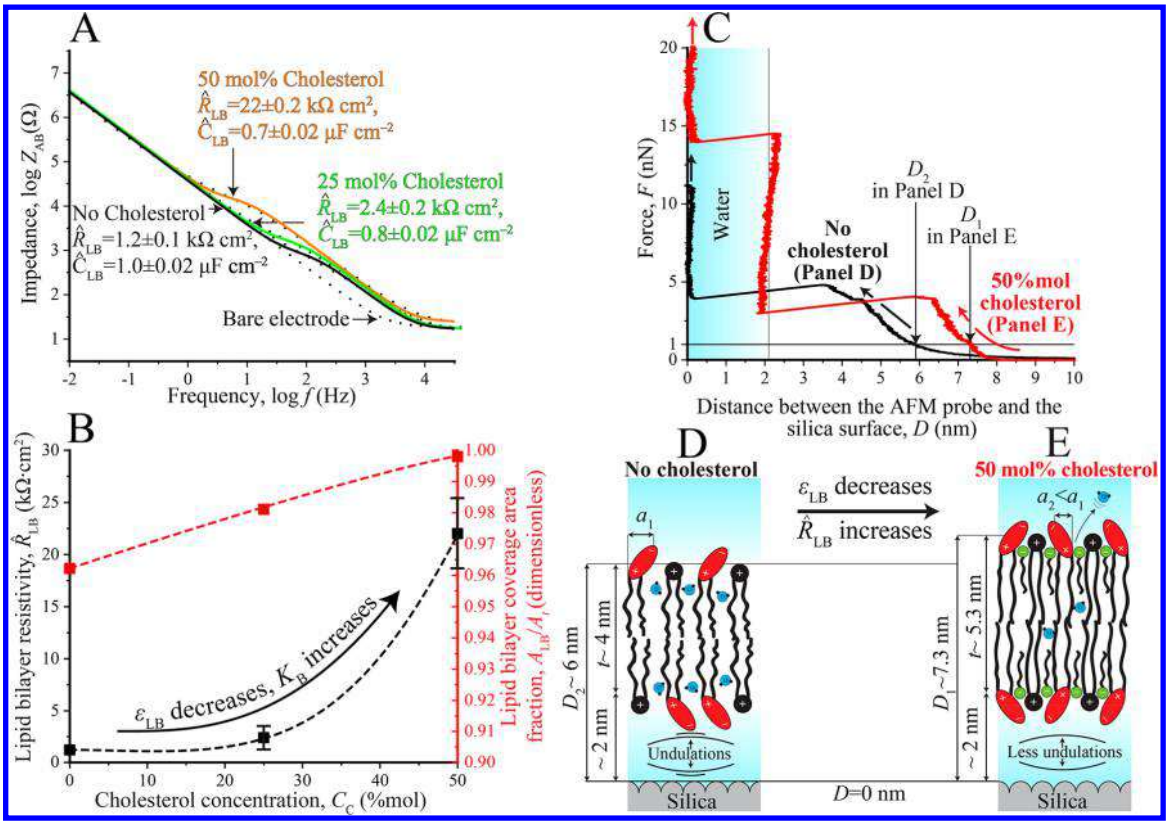

Figure 7. Effect of cholesterol on supported lipid bilayers. (A) Electrochemical impedance spectroscopy measurements of a lipid bilayer consisting of 0.25 mM DMPC + 0.25 mM DMTAP (most positively charged lipid mixtures in Figure 4) with three different cholesterol concentrations after 2 h of vesicle fusion at 45 °C. The curves represent the fit to the equivalent circuit shown in Figure 2B and C. (B) The plot shows the effect of cholesterol on the lipid bilayer resistivity, $\hat{R}_{LB}$, and on the lipid bilayer area coverage fraction, A_{LB}/A_t, which was calculated using eq 14. (C) Representative force vs distance curves measured between the AFM probe and the surface for a lipid bilayer without cholesterol (black curve) and with 50 mol % cholesterol (red curve). (D and E) Illustration of the effect of cholesterol on the lipid bilayer structure. The cholesterol decreases the average distance between the lipids, $a_2 < a_1$, and increases the lipid bilayer thickness, t. In the concentration range between 0 and 50 mol %, the cholesterol decreases ϵ_{LB}, which contributes to the increase in $\hat{R}_{LB}$. In addition, cholesterol also increases K_B, which decreases the undulation repulsion between the lipid bilayer and the surface, thus increasing W (see eq 12).

topography image in Figure 5E shows close-to-zero lipid coverage, and the force vs distance measurement in Figure 5F shows no typical penetration force. Furthermore, $\hat{R}_{LB} \sim 0$ (elaborated below).

Apart from the two extreme lipid mixtures, an AFM topography image of a pure DMPC lipid bilayer (centered data point in Figure 4) is shown in Figure 6B, revealing a continuous lipid bilayer. The case of 0.4 DMPC + 0.1 DMTAP (20% DMTAP in Figure 4) is shown in Figure S3 (Supporting Information), which also reveals a continuous lipid bilayer. Lastly, the case of 0.4 DMPC + 0.1 DMPG (20% DMPG in Figure 4) was already discussed above, and the AFM images are shown in Figure S2.

Importantly, AFM images can reveal defects at the nanometer scale, but this ability is limited to small areas (several dozens of μm^2). Electrochemical impedance spectroscopy, on the other hand, can be used to measure the lipid bilayer capacitance per area, $\hat{C}_{LB}$ ($F \cdot m^{-2}$), and resistivity, $\hat{R}_{LB}$ ($\Omega \cdot cm^2$), and can thus estimate the lipid bilayer coverage area over the *entire* electrode (~2.27 cm^2 for our system) without losing the sensitivity to minor defects in the lipid bilayer. Parts E and F of Figure 6 reveal a monotonic trend, showing that $\hat{R}_{LB}$ and the calculated lipid bilayer area fraction, A_{LB}/A_t, increased as $E_H - E_A$ decreased (became more negative). A_{LB}/A_t was calculated using the following equation, which is derived in section 4 in the Supporting Information

$$\frac{A_{LB}}{A_t} = 1 - \frac{\rho_S}{\hat{R}_{LB}} \quad (14)$$

where A_{LB} and A_t are the lipid bilayer and the total electrode area, respectively, and ρ_S is the measured resistivity of the electrode and the solution. As elaborated in section 4 of the Supporting Information, for the derivation of eq 14, it was assumed that $\rho_S \ll \rho_{LB}$, where ρ_{LB} is the resistivity of a defectless lipid bilayer. Indeed, it was shown before that the typical ρ_{LB} can be as high as 1 MΩ·cm²,[49] whereas ρ_S in our system was ~20 Ω·cm². As depicted in Figure S4 (Supporting Information), eq 14 yields the minimum area ("worst" coverage) fraction that is covered by the lipids; i.e., for the same $\hat{R}_{LB}$, when $\rho_S \sim \rho_{LB}$, A_{LB}/A_t would practically be higher than the prediction of eq 14.

4.3. Effect of Cholesterol on the Self-Assembly of Supported Lipid Bilayers. In this section, the effect of cholesterol on the rate at which lipid bilayers self-assemble on the surface is discussed. To evaluate the self-assembly rate, $\hat{R}_{LB}$ was measured for lipid bilayers consisting of 0.25 mM DMPC + 0.25 mM DMTAP with three different concentrations of cholesterol: (1) no cholesterol, (2) 25 mol % cholesterol, and (3) 50 mol % cholesterol. The results are summarized in

DOI: 10.1021/acs.jpcc.8b06566
J. Phys. Chem. C 2018, 122, 22985−22995

Figure 7A and B, which show that, after 2 h of vesicle fusion at 45 °C, $\hat{R}_{LB}$ increased from 1.2 to 22 kΩ cm^2 for lipids with no cholesterol and with 50 mol % cholesterol, respectively.

Two possible factors can increase $\hat{R}_{LB}$: (1) an increase in the lipid bilayer coverage area, A_{LB}/A_t, and/or (2) a decrease in the lipid bilayer dielectric constant, ϵ_{LB}, which increases the ion energy inside the lipid bilayer, thus slowing down the rate of ion transport according to the Born energy.[50] To determine the effect of each factor, namely, the surface coverage and the dielectric constant, we evaluated ϵ_{LB} by measuring the lipid bilayer capacitance, C_{LB}, and thickness, t.

Figure 7A shows that C_{LB} decreased with cholesterol concentration, and the capacitance is given by $C_{LB} = \epsilon_{LB}\epsilon_0 A_{LB}/t$, where $A_{LB} \sim 2.27$ cm^2. Therefore, two parameters could potentially have decreased C_{LB}: ϵ_{LB} and t (the change in A_{LB}, as discussed below, was negligible). In order to evaluate t, force vs distance measurements were conducted. Figure 7C shows two representative curves (out of 15 measurements at different locations) for lipid bilayers with no cholesterol (black curve) and lipid bilayers with 50 mol % cholesterol (red curve). Parts D and E of Figure 7 illustrate the interpretation of these measurements.

As illustrated in Figure 7D and E, the maximum height of the lipid bilayer, D, which includes the water layer under the lipid bilayer, was assumed to be the height where the repulsion force was 1 nN (see Figure 7C). $D \sim 6 \pm 0.1$ nm and $D \sim 7.3 \pm 0.4$ nm for the lipid bilayer without and with cholesterol, respectively. On the basis of the force measurements in the case of the cholesterol, the thickness of the water layer under the lipid bilayer was estimated to be ∼2 nm, which is in agreement with a previous publication.[51] Therefore, the thickness of the lipid bilayers was ∼4 ± 0.1 and 5.3 ± 0.4 nm for the lipid bilayer without and with 50 mol % cholesterol, respectively. Thus, the calculated ϵ_{LB} was 4.5 ± 0.1 and 4.2 ± 0.2 for the lipid bilayer without and with cholesterol, respectively. This minor decrease in ϵ_{LB} can only account for an increase of $\hat{R}_{LB}$ by a factor of ∼13 (see section 5 in the Supporting Information), whereas, in practice, cholesterol increased $\hat{R}_{LB}$ by a factor of ∼20.

We note that the increase in lipid bilayer thickness when cholesterol was added is in agreement with previous publications, showing that cholesterol "condenses" the lipid bilayer; i.e., cholesterol can decrease the average area of the lipids,[52,53] as illustrated in Figure 7D and E. Since the lipid bilayer is, to a large extent, incompressible (constant volume), t must increase as the average distance between the lipids decreases.

Importantly, since the reduction of ϵ_{LB} cannot explain the ∼20-fold increase in $\hat{R}_{LB}$, we concluded that cholesterol must have increased the lipid coverage area by increasing the rate of the self-assembly of the lipid bilayers on the surface. As shown in Figure 7B and on the basis of eq 14, A_{LB}/A_t increased from ∼0.962 to ∼0.998 for lipids without and with 50 mol % cholesterol, respectively. It is interesting to see that a difference of ∼3% in lipid coverage dramatically increases $\hat{R}_{LB}$. In addition, to increase $\hat{R}_{LB}$ to ∼1 MΩ·cm^2, as reported in the literature,[49] an additional 0.2% of surface coverage is needed; however, covering the extra 0.2% area may take an additional 24 h or more.[49] Apparently, the organization of the lipids on the surface into a defectless lipid bilayer is a relatively slow process, which can even take days.

The increased self-assembly rate in the presence of cholesterol can be explained by the reduction in the undulation repulsion between the lipid bilayers and the solid surface (notice the effect of K_B on $E_H - E_A$ in Figure 4C). It is well-known that cholesterol can increase K_B by a factor of ∼10,[46] which decreases the undulation repulsion ($\propto 1/K_B$, see eq 12) between the lipid bilayers and the solid surfaces, thereby increasing W. Increased W (stronger adhesion) increases the driving force for vesicle fusion on the surface, $E_H - E_A$, as plotted in Figure 4, which increases the self-assembly rate *exponentially*.

5. SUMMARY AND CONCLUSIONS

In previous publications, it was shown that vesicle fusion on solid surfaces is governed by electrostatic forces, i.e., by the double layer interactions between the vesicles/lipid bilayers and solid surfaces; however, to the best of our knowledge, this argument was not supported quantitatively. Here, we propose a quantitative description of the self-assembly mechanism of supported lipid bilayers via vesicle fusion on atomically smooth hydrophilic surfaces, such as polished silicon wafers (top layer is silica) or mica. It is confirmed that the double layer interactions indeed govern the self-assembly process, but when the double layer interactions are weak, such as the case of 20% DMPG in Figure 4, the van der Waals interactions cannot be neglected. Also, the bending/elastic modulus of the lipid bilayer, K_B, can significantly affect the undulation repulsion, which affects the thermodynamic stability and the rate of the self-assembly of the lipid bilayer.

The proposed mechanism defines the "driving energy" for the vesicle fusion on solid surfaces, $E_H - E_A$ (eq 10), which can be calculated using measurable parameters. When $E_H - E_A < 0$, defectless lipid bilayers are thermodynamically favorable, and the holes only constitute a transient state. The experimental results for lipid mixtures that yield $E_H - E_A < 0$ confirmed the self-assembly of lipid bilayers over more than 0.96 of the electrode area (∼2.27 cm^2) within 2 h. On the other hand, when $E_H - E_A > 0$, supported lipid bilayers are thermodynamically not favorable, and the experimental results showed close-to-zero lipid coverage. Lastly, the mechanism predicts that the rate of the self-assembly is proportional to $\exp[-(E_H - E_A)/kT]$, which is in agreement with the experimental results as well. *Importantly*, a simple way to accelerate the self-assembly of the supported lipid bilayer is to add cholesterol. Cholesterol increases K_B, and thus, it decreases $E_H - E_A$ (more negative).

Interestingly, on the basis of previous AFM and QCM-D studies, it is often assumed that the self-assembly of defectless lipid bilayers takes minutes to several hours. Our results indeed confirm the coverage of more than 0.96 of the surface area within 2 h of vesicle fusion for the specific conditions in our experimental system. However, the process of hole "stitching", i.e., the coverage of the last 0.04 area fraction, can take as long as a week or even more.[49,54]

■ ASSOCIATED CONTENT

Supporting Information

The Supporting Information is available free of charge on the ACS Publications website at DOI: 10.1021/acs.jpcc.8b06566.

Criterion for vesicle rupturing on a surface; fluorescence images of the five lipid bilayers; AFM images of the 20% DMTAP lipid bilayer; estimating the lipid bilayer area fraction, A_{LB}/A_t, using electrochemical impedance spectroscopy; effect of the lipid bilayer dielectric constant on the lipid bilayer resistivity (PDF)

DOI: 10.1021/acs.jpcc.8b06566
J. Phys. Chem. C 2018, 122, 22985−22995

AUTHOR INFORMATION

Corresponding Author

*E-mail: yairkau@bgu.ac.il.

ORCID

Yair Kaufman: 0000-0001-7771-8502

Notes

The authors declare no competing financial interest.

ACKNOWLEDGMENTS

We thank Mrs. Shaula C. Kaufman (TPP) for the fruitful discussions. This work was supported by the Adelis Foundation.

REFERENCES

(1) Khan, M. S.; Dosoky, N. S.; Berdiev, B. K.; Williams, J. D. Electrochemical Impedance Spectroscopy for Black Lipid Membranes Fused with Channel Protein Supported on Solid-State Nanopore. *Eur. Biophys. J.* **2016**, *45* (8), 843−852.

(2) García-Sáez, A. J.; Chiantia, S.; Salgado, J.; Schwille, P. Pore Formation by a Bax-Derived Peptide: Effect on the Line Tension of the Membrane Probed by AFM. *Biophys. J.* **2007**, *93* (1), 103−112.

(3) Lee, D. W.; Banquy, X.; Kristiansen, K.; Kaufman, Y.; Boggs, J. M.; Israelachvili, J. N. Lipid Domains Control Myelin Basic Protein Adsorption and Membrane Interactions Between Model Myelin Lipid Bilayers. *Proc. Natl. Acad. Sci. U. S. A.* **2014**, *111* (8), E768−E775.

(4) Nikoleli, G.-P.; Nikolelis, D. P.; Evtugyn, G.; Hianik, T. Advances in Lipid Film Based Biosensors. *TrAC, Trends Anal. Chem.* **2016**, *79* (C), 210−221.

(5) Avakyan, N.; Conway, J. W.; Sleiman, H. F. Long-Range Ordering of Blunt-Ended DNA Tiles on Supported Lipid Bilayers. *J. Am. Chem. Soc.* **2017**, *139* (34), 12027−12034.

(6) Yusko, E. C.; Johnson, J. M.; Majd, S.; Prangkio, P.; Rollings, R. C.; Li, J.; Yang, J.; Mayer, M. Controlling Protein Translocation Through Nanopores with Bio-Inspired Fluid Walls. *Nat. Nanotechnol.* **2011**, *6* (4), 253−260.

(7) Meng, H.; Wang, M.; Liu, H.; Liu, X.; Situ, A.; Wu, B.; Ji, Z.; Chang, C. H.; Nel, A. E. Use of a Lipid-Coated Mesoporous Silica Nanoparticle Platform for Synergistic Gemcitabine and Paclitaxel Delivery to Human Pancreatic Cancer in Mice. *ACS Nano* **2015**, *9* (4), 3540−3557.

(8) Kaufman, Y.; Berman, A.; Freger, V. Supported Lipid Bilayer Membranes for Water Purification by Reverse Osmosis. *Langmuir* **2010**, *26* (10), 7388−7395.

(9) Kaufman, Y.; Grinberg, S.; Linder, C.; Heldman, E.; Gilron, J.; Shen, Y.-X.; Kumar, M.; Lammertink, R. G. H.; Freger, V. Towards Supported Bolaamphiphile Membranes for Water Filtration: Roles of Lipid and Substrate. *J. Membr. Sci.* **2014**, *457* (C), 50−61.

(10) Licsandru, E.; Kocsis, I.; Shen, Y.-X.; Murail, S.; Legrand, Y.-M.; van der Lee, A.; Tsai, D.; Baaden, M.; Kumar, M.; Barboiu, M. Salt-Excluding Artificial Water Channels Exhibiting Enhanced Dipolar Water and Proton Translocation. *J. Am. Chem. Soc.* **2016**, *138* (16), 5403−5409.

(11) Kumar, M.; Grzelakowski, M.; Zilles, J.; Clark, M.; Meier, W. Highly Permeable Polymeric Membranes Based on the Incorporation of the Functional Water Channel Protein Aquaporin Z. *Proc. Natl. Acad. Sci. U. S. A.* **2007**, *104* (52), 20719−20724.

(12) Kumar, M.; Habel, J. E. O.; Shen, Y.-X.; Meier, W. P.; Walz, T. High-Density Reconstitution of Functional Water Channels Into Vesicular and Planar Block Copolymer Membranes. *J. Am. Chem. Soc.* **2012**, *134* (45), 18631−18637.

(13) Barboiu, M.; Gilles, A. From Natural to Bioassisted and Biomimetic Artificial Water Channel Systems. *Acc. Chem. Res.* **2013**, *46* (12), 2814−2823.

(14) Tunuguntla, R. H.; Henley, R. Y.; Yao, Y.-C.; Pham, T. A.; Wanunu, M.; Noy, A. Enhanced Water Permeability and Tunable Ion Selectivity in Subnanometer Carbon Nanotube Porins. *Science* **2017**, *357* (6353), 792−796.

(15) Biswas, K. H.; Jackman, J. A.; Park, J. H.; Groves, J. T.; Cho, N.-J. Interfacial Forces Dictate the Pathway of Phospholipid Vesicle Adsorption Onto Silicon Dioxide Surfaces. *Langmuir* **2018**, *34* (4), 1775−1782.

(16) Márquez, I. F.; Vélez, M. Formation of Supported Lipid Bilayers of Charged E. Coli Lipids on Modified Gold by Vesicle Fusion. *MethodsX* **2017**, *4*, 461−468.

(17) Zhang, Y.; Inal, S.; Hsia, C.-Y.; Ferro, M.; Ferro, M.; Daniel, S.; Owens, R. M. Supported Lipid Bilayer Assembly on PEDOT:PSS Films and Transistors. *Adv. Funct. Mater.* **2016**, *26* (40), 7304−7313.

(18) Lind, T. K.; Cárdenas, M. Understanding the Formation of Supported Lipid Bilayers via Vesicle Fusion—a Case That Exemplifies the Need for the Complementary Method Approach (Review). *Biointerphases* **2016**, *11* (2), 020801−020813.

(19) Wu, H.-L.; Tong, Y.; Peng, Q.; Li, N.; Ye, S. Phase Transition Behaviors of the Supported DPPC Bilayer Investigated by Sum Frequency Generation (SFG) Vibrational Spectroscopy and Atomic Force Microscopy (AFM). *Phys. Chem. Chem. Phys.* **2016**, *18* (3), 1411−1421.

(20) Anderson, T. H.; Min, Y.; Weirich, K. L.; Zeng, H.; Fygenson, D.; Israelachvili, J. N. Formation of Supported Bilayers on Silica Substrates. *Langmuir* **2009**, *25* (12), 6997−7005.

(21) Reviakine, I.; Brisson, A. Formation of Supported Phospholipid Bilayers From Unilamellar Vesicles Investigated by Atomic Force Microscopy. *Langmuir* **2000**, *16* (4), 1806−1815.

(22) Bailey, C. M.; Tripathi, A.; Shukla, A. Effects of Flow and Bulk Vesicle Concentration on Supported Lipid Bilayer Formation. *Langmuir* **2017**, *33* (43), 11986−11997.

(23) Lind, T. K.; Cárdenas, M.; Wacklin, H. P. Formation of Supported Lipid Bilayers by Vesicle Fusion: Effect of Deposition Temperature. *Langmuir* **2014**, *30* (25), 7259−7263.

(24) Tamm, L. K.; McConnell, H. M. Supported Phospholipid Bilayers. *Biophys. J.* **1985**, *47* (1), 105−113.

(25) Sackmann, E. Supported Membranes: Scientific and Practical Applications. *Science* **1996**, *271* (5245), 43−48.

(26) Hardy, G. J.; Nayak, R.; Zauscher, S. Model Cell Membranes: Techniques to Form Complex Biomimetic Supported Lipid Bilayers via Vesicle Fusion. *Curr. Opin. Colloid Interface Sci.* **2013**, *18* (5), 448−458.

(27) Leonenko, Z. V.; Carnini, A.; Cramb, D. T. Supported Planar Bilayer Formation by Vesicle Fusion: the Interaction of Phospholipid Vesicles with Surfaces and the Effect of Gramicidin on Bilayer Properties Using Atomic Force Microscopy. *Biochim. Biophys. Acta, Biomembr.* **2000**, *1509* (1−2), 131−147.

(28) Kaufman, Y.; Grinberg, S.; Linder, C.; Heldman, E.; Gilron, J.; Freger, V. Fusion of Bolaamphiphile Micelles: a Method to Prepare Stable Supported Biomimetic Membranes. *Langmuir* **2013**, *29* (4), 1152−1161.

(29) Dacic, M.; Jackman, J. A.; Yorulmaz, S.; Zhdanov, V. P.; Kasemo, B.; Cho, N.-J. Influence of Divalent Cations on Deformation and Rupture of Adsorbed Lipid Vesicles. *Langmuir* **2016**, *32* (25), 6486−6495.

(30) Jing, Y.; Trefna, H.; Persson, M.; Kasemo, B.; Svedhem, S. Formation of Supported Lipid Bilayers on Silica: Relation to Lipid Phase Transition Temperature and Liposome Size. *Soft Matter* **2014**, *10* (1), 187−195.

(31) Yanagisawa, M.; Iwamoto, M.; Kato, A.; Yoshikawa, K.; Oiki, S. Oriented Reconstitution of a Membrane Protein in a Giant Unilamellar Vesicle: Experimental Verification with the Potassium Channel KcsA. *J. Am. Chem. Soc.* **2011**, *133* (30), 11774−11779.

(32) Hain, N.; Gallego, M.; Reviakine, I. Unraveling Supported Lipid Bilayer Formation Kinetics: Osmotic Effects. *Langmuir* **2013**, *29* (7), 2282−2288.

(33) Garcia-Manyes, S.; Oncins, G.; Sanz, F. Effect of Ion-Binding and Chemical Phospholipid Structure on the Nanomechanics of Lipid Bilayers Studied by Force Spectroscopy. *Biophys. J.* **2005**, *89* (3), 1812−1826.

DOI: 10.1021/acs.jpcc.8b06566
J. Phys. Chem. C 2018, 122, 22985−22995

(34) Richter, R. P.; Brisson, A. R. Following the Formation of Supported Lipid Bilayers on Mica: a Study Combining AFM, QCM-D, and Ellipsometry. *Biophys. J.* **2005**, *88* (5), 3422−3433.
(35) Kurniawan, J.; Suga, K.; Kuhl, T. L. Interaction Forces and Membrane Charge Tunability: Oleic Acid Containing Membranes in Different pH Conditions. *Biochim. Biophys. Acta, Biomembr.* **2017**, *1859* (2), 211−217.
(36) Israelachvili, J. N. *Intermolecular and Surface Forces: Revised Third Edition*; 2011.
(37) Cremer, P. S.; Boxer, S. G. Formation and Spreading of Lipid Bilayers on Planar Glass Supports. *J. Phys. Chem. B* **1999**, *103* (13), 2554−2559.
(38) Johnson, J. M.; Ha, T.; Chu, S.; Boxer, S. G. Early Steps of Supported Bilayer Formation Probed by Single Vesicle Fluorescence Assays. *Biophys. J.* **2002**, *83* (6), 3371−3379.
(39) Schönherr, H.; Johnson, J. M.; Lenz, P.; Frank, C. W.; Boxer, S. G. Vesicle Adsorption and Lipid Bilayer Formation on Glass Studied by Atomic Force Microscopy. *Langmuir* **2004**, *20* (26), 11600−11606.
(40) Méléard, P.; Gerbeaud, C.; Pott, T.; Fernandez-Puente, L.; Bivas, I.; Mitov, M. D.; Dufourcq, J.; Bothorel, P. Bending Elasticities of Model Membranes: Influences of Temperature and Sterol Content. *Biophys. J.* **1997**, *72* (6), 2616−2629.
(41) Hogg, R.; Healy, T. W.; Fuerstenau, D. W. Mutual Coagulation of Colloidal Dispersions. *Trans. Faraday Soc.* **1966**, *62* (0), 1638−14.
(42) Abillon, O.; Perez, E. Swollen Lamellar Phases Between Two Solid Walls: Undulation Forces and Generation of Defects. *J. Phys. (Paris)* **1990**, *51*, 2543−2556.
(43) Zantl, R.; Baicu, L.; Artzner, F.; Sprenger, I.; Rapp, G.; Rädler, J. O. Thermotropic Phase Behavior of Cationic Lipid−DNA Complexes Compared to Binary Lipid Mixtures. *J. Phys. Chem. B* **1999**, *103* (46), 10300−10310.
(44) Gurtovenko, A. A.; Patra, M.; Karttunen, M.; Vattulainen, I. Cationic DMPC/DMTAP Lipid Bilayers: Molecular Dynamics Study. *Biophys. J.* **2004**, *86* (6), 3461−3472.
(45) Kirby, B. J.; Hasselbrink, E. F. Zeta Potential of Microfluidic Substrates: 1. Theory, Experimental Techniques, and Effects on Separations. *Electrophoresis* **2004**, *25* (2), 187−202.
(46) Pan, J.; Tristram-Nagle, S.; Nagle, J. F. Effect of Cholesterol on Structural and Mechanical Properties of Membranes Depends on Lipid Chain Saturation. *Phys. Rev. E* **2009**, *80* (2), 021931.
(47) Garcia-Manyes, S.; Redondo-Morata, L.; Oncins, G.; Sanz, F. Nanomechanics of Lipid Bilayers: Heads or Tails? *J. Am. Chem. Soc.* **2010**, *132* (37), 12874−12886.
(48) Garcia-Manyes, S.; Sanz, F. Nanomechanics of Lipid Bilayers by Force Spectroscopy with AFM: a Perspective. *Biochim. Biophys. Acta, Biomembr.* **2010**, *1798* (4), 741−749.
(49) Purrucker, O.; Hillebrandt, H.; Adlkofer, K.; Tanaka, M. Deposition of Highly Resistive Lipid Bilayer on Silicon−Silicon Dioxide Electrode and Incorporation of Gramicidin Studied by Ac Impedance Spectroscopy. *Electrochim. Acta* **2001**, *47* (5), 791−798.
(50) Dilger, J. P.; McLaughlin, S. G.; McIntosh, T. J.; Simon, S. A. The Dielectric Constant of Phospholipid Bilayers and the Permeability of Membranes to Ions. *Science* **1979**, *206* (4423), 1196−1198.
(51) Pan, J.; Mills, T. T.; Tristram-Nagle, S.; Nagle, J. F. Cholesterol Perturbs Lipid Bilayers Nonuniversally. *Phys. Rev. Lett.* **2008**, *100* (19), 198103.
(52) de Meyer, F.; Smit, B. Effect of Cholesterol on the Structure of a Phospholipid Bilayer. *Proc. Natl. Acad. Sci. U. S. A.* **2009**, *106* (10), 3654−3658.
(53) Hung, W.-C.; Lee, M.-T.; Chen, F.-Y.; Huang, H. W. The Condensing Effect of Cholesterol in Lipid Bilayers. *Biophys. J.* **2007**, *92* (11), 3960−3967.
(54) Gritsch, S.; Nollert, P.; Jähnig, F.; Sackmann, E. Impedance Spectroscopy of Porin and Gramicidin Pores Reconstituted Into Supported Lipid Bilayers on Indium−Tin-Oxide Electrodes †. *Langmuir* **1998**, *14* (11), 3118−3125.

DOI: 10.1021/acs.jpcc.8b06566
J. Phys. Chem. C 2018, 122, 22985−22995

Environmental Science & Technology

Article

Cite This: Environ. Sci. Technol. 2019, 53, 5202−5211

pubs.acs.org/est

Surface-Induced Silica Scaling during Brackish Water Desalination: The Role of Surface Charge and Specific Chemical Groups

Karthik Rathinam,[†,§] Shiju Abraham,[†,§] Yoram Oren,[†] Dietmar Schwahn,[‡] Winfried Petry,[‡] Yair Kaufman,*[,†] and Roni Kasher*[,†]

[†]Department of Desalination and Water Treatment, Zuckerberg Institute for Water Research, The Blaustein Institutes for Desert Research, Ben-Gurion University of the Negev, Sde Boqer Campus, Midreshet Ben-Gurion 8499000, Israel

[‡]Technische Universität München, Forschungs-Neutronenquelle, Heinz Maier-Leibnitz (FRM II), James-Franck-Straße 1, D-85748 Garching, Germany

Supporting Information

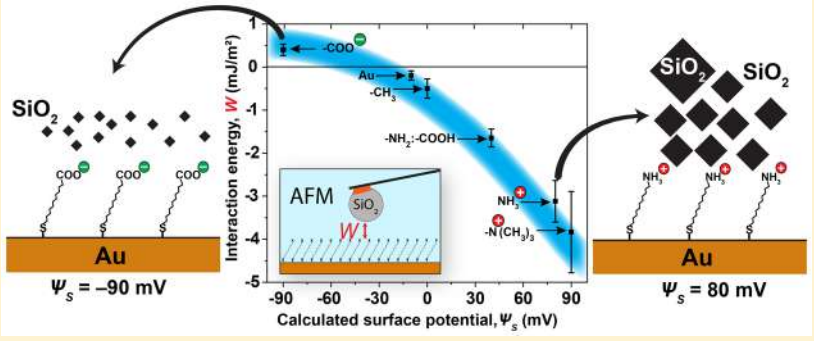

ABSTRACT: Silica scaling of membranes used in reverse osmosis desalination processes is a severe problem, especially during the desalination of brackish groundwater due to high silica concentrations. This problem limits the water supply in inland arid and semiarid regions. Here, we investigated the influence of surface-exposed organic functional groups on silica precipitation and scaling. A test solution simulating the mineral content of brackish groundwater desalination brine at 75% recovery was used. The mass and chemical composition of the precipitated silica was monitored using a quartz crystal microbalance, X-ray photoelectron spectroscopy, and infrared spectroscopy, showing that surfaces with positively charged groups induced rapid silica precipitation, and the rate of silica precipitation followed the order $-NH_2 \sim -N^+(CH_3)_3 > -NH_2/-COOH > -H_2PO_3 \sim -OH > -COOH > -CH_3$. Force vs distance AFM measurements showed that the adhesion energy between a silica colloid glued to AFM cantilever and the studied surfaces increased as the surface charge changed from negative to positive. Thus, for the first time direct measurements of molecular forces and specific chemical groups that govern silica scaling during brackish water desalination is reported here. The influence of the different functional groups and the effect of the surface charge on silica precipitation that were found here can be used to design membranes that resist silica scaling in membrane-based desalination processes.

1. INTRODUCTION

Desalinated inland brackish groundwater has become an important source of drinking water in arid and semiarid regions and is increasingly being used to resolve the worldwide water shortage. Reverse osmosis (RO) technology is the most widely used process for desalinating brackish water; however, a major limiting factor of this approach is silica scaling of the membrane, especially during the high recovery (>75%) used in brackish water desalination.[1−8] Silica scaling may occur when the concentration of dissolved silica in either the bulk water or in the vicinity of the membrane surface surpasses its solubility limit, which depends on the pH, ionic strength, temperature, and the hardness of the treated water.[9−11] Importantly, once silica scale is formed on the membrane surface, it is almost impossible to remove using an acid wash (unlike carbonate scaling) and processes that do remove it often damage the membrane.[1,12]

Silica scaling and nucleation are complex processes[9] due to the dynamic equilibrium in aqueous solutions between monomeric silicic acid (**1**) and higher molecular weight oligomers (**2**) formed by a self-condensation process.[9] Silica deposition on surfaces can occur through the polymerization of silicic acid after the direct deposition of silica monomer on the surface (heterogeneous deposition), or by the polymerization of silicic acid in the bulk solution, followed by the formation of

Received: October 31, 2018
Revised: March 10, 2019
Accepted: March 27, 2019
Published: April 8, 2019

DOI: 10.1021/acs.est.8b06154
Environ. Sci. Technol. 2019, 53, 5202−5211

silica oligomers, which deposit on the surface (homogeneous deposition).[9,13]

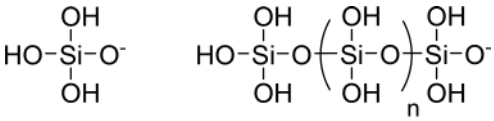

1 2

Silica precipitation and scaling can be alleviated by the use of commercial antiscalants,[14,15] or by reducing the silica concentration in the feedwater by using alumina adsorbents,[16,17] electrocoagulation,[2] or softening through a coagulation process.[18,19] However, such pretreatment methods increase operational costs and can induce organic fouling and biofouling[17,20−23] and thus various alternative approaches have been tested to deal with silica scaling. For example, the presence of sodium alginate in the feedwater reduces silica scaling during the desalination process.[24] In Israel, groundwater rehabilitation projects of the coastal aquifer aimed at reducing silica scaling have included altering the design features of the desalination units, and optimizing chemical treatment and operational conditions of the process.[8]

The effects of various membrane materials on silica scaling have also been studied. For example, silica scaling of RO membranes was found to be more pronounced on polyamide thin film composite membrane than on asymmetric cellulose triacetate membrane.[25,26] Bush and co-workers investigated pH adjustment of the feed stream as a strategy to prevent silica scaling during membrane distillation of water supersaturated with silica. They found that with feedwater at pH less than 5 or higher than 10, silica scaling impacts were negligible, and cleaning with solution pH above 11 was the most effective.[27] A study by Wallace et al.[28] found that the rate of silica precipitation on surfaces coated with mixed groups ($-NH_3^+$/$-COO^-$) was ∼18 times higher than the rate of silica precipitation on surfaces terminated with carboxyl ($-COO^-$) groups tested under similar conditions, with the amine group ($-NH_3^+$) terminated surface being highly resistant to silica precipitation. Conversely, polyamines extracted from the siliceous cell walls of diatoms, and synthetic polyamines, were shown to induce substantial silica precipitation.[29,30] More recently, investigations of the influence of reverse osmosis membrane surface properties on silica scaling during brackish water desalination demonstrated that membranes with positively charged groups on their surface showed reduced permeate flux due to high silica scaling, whereas membranes with a negatively charged surface showed a very limited flux decline.[31]

In this work, we studied the effects of membrane surface functional groups and charge on the extent of silica precipitation under conditions that simulate the desalination of brackish groundwater. We prepared self-assembled monolayers of alkyl thiols on gold with terminal $-NH_2$, $-N^+(CH_3)_3$, $-H_2PO_3$, $-OH$, $-COOH$, and $-CH_3$ groups and thus the surfaces bore positive, neutral, or negative charges; these surfaces were used as templates for silica precipitation tests. Brackish water desalination conditions were simulated using a model solution supersaturated with silica and with a mineral content equivalent to the stage at which 75% of the water in the brackish feed is recovered by desalination. In addition, using atomic force microscopy (AFM) we measured the molecular forces between the studied surfaces and a silica colloid glued to the AFM cantilever to simulate the molecular interactions between dissolved silica in solution and the studied surfaces. The measured forces and calculated interaction energies (calculated using the Derjaguin approximation) were then compared with the interaction energies predicted by the DLVO model,[32] which included double layer (electrostatic and entropic) and van der Waals forces. To the best of our knowledge, this is the first study that investigates molecular forces and specific surface interactions that affect silica scaling under conditions that simulate desalination of brackish groundwater.

2. MATERIALS AND METHODS

2.1. Materials. Sodium metasilicate nonahydrate ($Na_2SiO_3·9H_2O$), strontium chloride hexahydrate ($SrCl_2·6H_2O$), anhydrous magnesium chloride ($MgCl_2$), 1,4 piperazine *N*,*N*′-diethanesulfonic acid (PIPES), 1-dodecanethiol, 11-mercapto-1-undecanol, 11-amino-1-undecanethiol hydrochloride, (11-mercaptoundecyl)-*N*,*N*,*N*-trimethylammonium bromide, 11-mercaptoundecylphosphonic acid, and 11-mercaptoundecanoic acid were purchased from Sigma-Aldrich (St Louis, MO, U.S.A.). Sapphire wafers of 10 × 10 × 0.43 mm^3 size were purchased from Roditi (London, England). Sodium chloride (NaCl), sodium bicarbonate ($NaHCO_3$), anhydrous calcium chloride ($CaCl_2$), potassium sulfate (K_2SO_4), and sodium sulfate (Na_2SO_4) were obtained from Frutarom (Haifa, Israel). Aqueous hydrogen peroxide (30%), hydrochloric acid, absolute ethanol, and 25% ammonia solution were purchased from Bio-Lab (Jerusalem, Israel).

2.2. Preparation of a Model Solution Simulating Brackish Groundwater for Desalination (SBD Solution). The model solution (termed Simulated Brackish-water Desalination (SBD) solution) mimics brackish water at the stage at which 75% of the water in the brackish feed is recovered by desalination and is oversaturated with respect to amorphous silica. SBD solution was prepared by dissolving 355 mg sodium silicate ($Na_2SiO_3·9H_2O$) in 200 mL double-distilled water (DDW), followed by the addition of 1 N HCl to a pH value <6.5. Then, 875 mg NaCl, 343 mg $MgCl_2$, 625 mg $CaCl_2$, 520 mg Na_2SO_4, 44 mg K_2SO_4, 11.5 mg $SrCl_2·6H_2O$, and 53 mg of $NaHCO_3$ were added sequentially. The pH was adjusted to 6.5 by slowly adding 1 N HCl/1 N NaOH, then 5 mL 0.5 M PIPES buffer, pH 6.5, was added. Finally, DDW was added to give a final volume of 250 mL and the solution was filtered through a 0.22 μm filter. Plastic containers and vessels were used for all SBD solution preparation and filtration steps. The final concentrations of ions in the prepared SBD solution are given in Table S1 (Supporting Information, SI).

2.3. Preparation of Self-Assembled Monolayers of Alkyl Thiols with Different Terminal Functional Groups on Gold-Coated Surfaces. Gold-coated silicon and sapphire wafers (1 × 1 cm^2 and 0.5 × 0.5 cm^2, respectively) were prepared by coating silicon wafers (one side polished, 330 μm thick) and sapphire wafers (one side polished, 430 μm thick) with a 10 nm thick titanium (99.995%, Kurt J. Lesker, Jefferson Hills, U.S.A.) layer followed by coating with a 30 nm gold (99.999%, Kurt J. Lesker) layer. Both metals were deposited by thermal evaporation at a pressure of 2 × 10^{-6} bar using a thermal evaporator (Odem Ltd., Rehovot, Israel). Gold-coated quartz crystal microbalance (QCM) sensors (cat. no QSX-301) were purchased from Biolin Scientific (Gothenburg, Sweden).

DOI: 10.1021/acs.est.8b06154
Environ. Sci. Technol. 2019, 53, 5202−5211

Table 1. Water Drop Contact Angles and XPS Elemental Analyses of Self-Assembled Alkyl Thiol Monolayers on Gold-Coated Silicon Surfaces

			elemental ratio by XPS		
terminal group	functionalized alkyl thiol	contact angle (deg)[a]	N:C ratio (calculated)	O:C ratio (calculated)	P:C ratio (calculated)
$-NH_2$	$HS-(CH_2)_{11}-NH_2$	43 ± 1	0.06 (0.09)		
$-N^+(CH_3)_3$	$HS-(CH_2)_{11}-N^+(CH_3)_3\ Br^-$	42 ± 2	0.09 (0.07)		
$-NH_2/-COOH$	$HS-(CH_2)_{11}-NH_2/HS-(CH_2)_{10}-COOH$	47 ± 2	0.05 (0.05)	0.09 (0.09)	
$-H_2PO_3$	$HS-(CH_2)_{11}H_2PO_3$	78 ± 1		0.29 (0.27)	0.11 (0.09)
$-OH$	$HS-(CH_2)_{11}OH$	55 ± 1		0.14 (0.09)	
$-COOH$	$HS-(CH_2)_{10}COOH$	45 ± 1		0.25 (0.17)	
$-CH_3$	$HS-(CH_2)_{11}CH_3$	107 ± 2			

[a]Average values of four different locations.

Prior to thiol self-assembly, the wafers and QCM sensors were surface activated using a protocol developed by Biolin Scientific. First, the gold surfaces were exposed to UV for 10 min at room temperature, then immersed in a 5:1:1 mixture of ultrapure water, 25% aqueous ammonia, and 30% hydrogen peroxide at 348 K. After 5 min, the gold surfaces were rinsed 3 times with ultrapure water, then with absolute ethanol (2 times), dried under N_2 gas, and treated again with UV for 10 min.

The wafers or QCM sensors were then immediately immersed in a 1 mM ethanolic solution of alkyl thiol, each with a different functional group, for 24 h at room temperature. The following alkyl thiols were used for self-assembly (also specified in Table 1): 1-dodecanethiol ($HS(CH_2)_{11}CH_3$), 11-mercapto-1-undecanol ($HS(CH_2)_{11}OH$), 11-amino-1-undecanethiol hydrochloride ($HS(CH_2)_{11}NH_2{\cdot}HCl$), (11-mercaptoundecyl)-*N*,*N*,*N*-trimethylammonium bromide ($HS-(CH_2)_{11}N^+(CH_3)_3Br^-$), 11-mercaptoundecylphosphonic acid ($HS(CH_2)_{11}H_2PO_3$), and 11-mercaptoundecanoic acid ($HS-(CH_2)_{10}COOH$). The surfaces self-assembled with alkyl thiols (excluding the sensor with 1-dodecanethiol) were immersed for an additional 24 h in a 1 mM ethanolic solution of 1-dodecanethiol. Finally, the wafers were washed twice with ethanol and dried using N_2 gas. The gold surface self-assembled with 11-amino-1-undecanethiol hydrochloride was cleaned with 10 mM triethylamine in dichloromethane (DCM) followed by two washings with ethanol and dried using N_2 gas. The gold surface self-assembled with a mixture of 11-amino-1-undecanethiol hydrochloride and 11-mercaptoundecanoic acid was cleaned in the same manner. The self-assembled monolayers were characterized by water-drop contact angle measurements and their surface chemical compositions were analyzed by X-ray photoelectron spectroscopy (XPS), as shown in Table 1.

2.4. Surface Characterization. A dynamic contact angle instrument (OCA 20; DataPhysics Instruments, Filderstadt, Germany) was used to determine the surface wettability of the prepared surfaces using 0.3 μL of DDW as the probe liquid at room temperature. Contact angle measurements were performed at four locations on each sample, and the average is reported. Surface elemental composition was measured by XPS with an ESCALAB 250 (Thermo Fisher Scientific Inc., Waltham, U.K.) using an Al X-ray source and a monochromator. The chemical groups present on the surface were identified by attenuated total reflectance-Fourier transform infrared (ATR-FTIR) spectroscopy using a VERTEX 70 FTIR spectrometer (Bruker Optics, Ettlingen, Germany) with a resolution of 16 cm^{-1} complemented by a Miracle ATR attachment with a reflection diamond-coated KRS-5 element (Pike, Madison, WI, U.S.A.).

2.5. QCM Monitoring of Silica Precipitation. Silica precipitation on self-assembled monolayers on the gold sensors was monitored with an E4 QCM system (Qsense Biolin Scientific, Gothenburg, Sweden) under static conditions at 298 K. Open module cells were used containing gold-coated QCM sensors (QSX 301, with a fundamental frequency of ~5 MHz). Each experiment was initiated by adding 1 mL NaCl solution with the same ionic strength as the SBD solution and monitoring for 24 h, then the NaCl solution was replaced with SBD test solution and the system was monitored for an additional 24 h. Variations in frequency (Δf, Hz) were measured at overtones n = 5, 7, 9, 11, and 13; overtone n = 7, which represents a compromise between enhanced sensitivity at higher overtones and reduced interference of the solution properties at lower frequencies,[33] was used for calculating the average values of Δf for each surface. The QCM experiments were repeated twice for each sample and the average values are reported.

2.6. Silica Precipitation Experiments on Self-Assembled Monolayers on Gold-Coated Silicon and Sapphire Wafers. The gold-coated silicon or sapphire wafers self-assembled with alkyl thiols were horizontally immersed in 5 mL SBD solution in 10 mL plastic vials, then the vials were tightly sealed and maintained at 298 K for 24 h. The surfaces were then gently washed with ethanol/water (1:1) and dried under vacuum.

2.7. AFM Force Measurements. AFM images were acquired using a NanoWizard 4 (JPK Instruments, Berlin, Germany) and gold-coated silicon tips on a SNL-10 probe (Bruker, Camarillo, CA, U.S.A.) in quantitative imaging (QI) mode at room temperature (298 K). The spring constants of different cantilevers were estimated using the thermal noise method (0.35 N/m and 0.3 N/m, respectively, for imaging and force spectroscopy). AFM force vs distance curves were

DOI: 10.1021/acs.est.8b06154
Environ. Sci. Technol. 2019, 53, 5202−5211

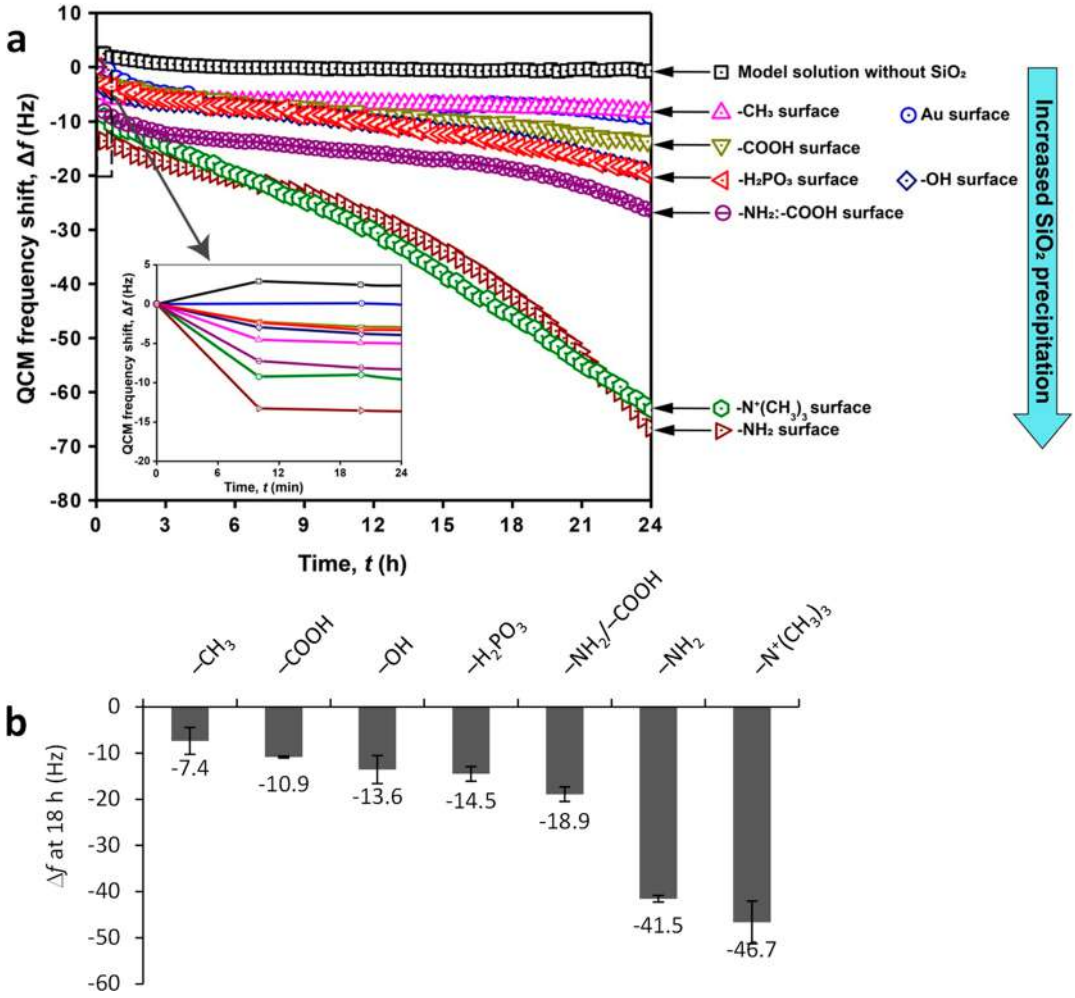

Figure 1. (a) QCM curves (averaged from two experiments) obtained to monitor silica precipitation from a SBD model solution onto self-assembled monolayers on gold sensors during a 24 h period at 25 °C. The inset shows the frequency changes between 0 and 24 min. The SBD solution was added to the system at $t = 0$. (b) The extent of frequency shift after 18 h for each of the self-assembled monolayers studied.

measured using a NovaScan cantilever (Novascan Technologies, Inc., Ames, IA, U.S.A.) with a 1 μm diameter silica colloidal probe glued to the AFM cantilever. The tip velocity was kept constant (100 nm/sec) throughout the measurements. All measurements were made in aqueous solution (225 mM NaCl). The deflection vs displacement data were converted into force vs relative distance graphs using SPM processing software (JPK Instruments, Berlin, Germany).

3. RESULTS AND DISCUSSION

3.1. Rational Behind the Chemical Composition of the Model Silica Solution. An aqueous solution was prepared to simulate the mineral content of brackish groundwater at the stage at which 75% of the water in the brackish feed is recovered by desalination, and with silica at 300 ppm concentration. This solution was termed Simulated Brackish-water Desalination (SBD) solution. The mineral content of SBD solution was based on the ion profile of the RO concentrate of brackish groundwater from the Negev Highlands, Israel, reported by Oren et al.[7] The silica concentration in the model solution was higher than that of the RO concentrate by a factor of 3.4 (see Table S1, SI) to obtain a saturation index of 2.5 for amorphous silica, as determined using OLI stream analyzer 9 software (OLI Systems, Morris Plains, NJ, U.S.A.). Silica concentration higher than the RO concentrate may represent a realistic condition where concentration polarization leads to increased solute concentrations near the membrane surface. The sulfate concentration was 50% lower than in the brackish water concentrate to keep the gypsum and strontium sulfate levels below saturation, whereas the concentrations of the other scale-causing compounds were maintained at the same level as in the RO concentrate. The stability of the silica in the prepared SBD solution was monitored for 4 days using turbidity measurements. At 24 h, the turbidity was low, 0.07 Nephelometric Turbidity Unit (NTU; Figure S1, SI), but after 4 days the turbidity increased dramatically from 0.07 NTU to 0.64 NTU. The SBD solution was also monitored by dynamic light scattering (DLS) and the concentration of dissolved silica in filtered aliquots of the solution was measured using the molybdenum blue spectrophotometric method.[34] No particles were detected in a 24 h period in the SBD solution and a slight decrease in the concentration of dissolved silica in the filtered samples, from 300 mg/L to 297 mg/L, was observed after 24 h. Hence, spectrophotometric measurements of silica concentrations and turbidity, and DLS analyses, all indicated that the prepared SBD solution (silica saturation index = 2.5) is stable for 24 h and therefore homogeneous precipitation of silica in

DOI: 10.1021/acs.est.8b06154
Environ. Sci. Technol. 2019, 53, 5202−5211

Table 2. XPS Elemental Analysis of Self-Assembled Monolayers on Gold-Coated Sapphire Surfaces after 24 h Immersion in a Model SBD Solution Supersaturated with Respect to Silica (saturation index = 2.5)

		XPS[a] (atomic %)						
terminal group	functionalized alkyl thiol	C	O	N	S	P	Au	Si
$-NH_2$	$HS-(CH_2)_{11}-NH_2$	30.42	43.58	1.20	2.69	-BDL-	0.35	21.76
$-N^+(CH_3)_3$	$HS-(CH_2)_{11}-N^+(CH_3)_3\ Br^-$	40.96	32.88	5.55	3.06	-BDL-	-BDL-	17.56
$-NH_2/-COOH$	$HS-(CH_2)_{11}-NH_2/HS-(CH_2)_{10}-COOH$	50.08	19.34	2.17	3.95	-BDL-	21.85	2.61
$-H_2PO_3$	$HS-(CH_2)_{11}H_2PO_3$	47.84	31.04	-BDL-	6.17	2.59	8.58	3.78
$-OH$	$HS-(CH_2)_{11}OH$	42.59	17.13	-BDL-	2.84	-BDL-	36.41	1.03
$-COOH$	$HS-(CH_2)_{10}COOH$	51.46	26.91	-BDL-	2.59	-BDL-	16.25	2.80
$-CH_3$	$HS-(CH_2)_{11}CH_3$	37.59	-BDL-	-BDL-	3.49	-BDL-	58.92	-BDL-

[a]BDL, below detection limit.

the bulk solution and sedimentation are unlikely to occur within 24 h after preparing the solution.

3.2. Silica Precipitation Rate As Measured by QCM. Self-assembled monolayers of alkyl thiols with different functional groups were prepared on gold-coated surfaces and used as substrates for studying the effect of surface-exposed functional groups on the extent of scaling, and particularly on silica precipitation, under conditions that simulate the desalination of brackish groundwater. The surface wettabilities of the prepared self-assembled monolayers were determined by measuring the water drop contact angle (Table 1) and were in accordance with the literature values.[35,36] The surface chemical compositions were analyzed by XPS and confirmed the presence of the expected elements on the gold surfaces (Table 1). Notably, the N/C and O/C atomic ratios obtained for the surface terminated with a mixture of $-NH_2/-COOH$ groups were in good agreement with the calculated value for a 1:1 ratio of $-NH_2$ and $-COOH$ groups. Overall, the water drop contact angle measurements and XPS analyses confirmed successful preparation of the self-assembled monolayers on gold-coated silicon wafers.[37]

The effect of the various surface-exposed organic functional groups on silica precipitation was studied by QCM (Figure 1). The above-described monolayers characterized by XPS and contact angle, listed in Table 1, were self-assembled on gold-coated quartz sensors for QCM measurements. The QCM frequency shift, Δf, was first monitored for 24 h at 298 K using NaCl solution with the same ionic strength as the SBD solution, then the solution was replaced with model SBD solution (silica saturation index = 2.5), and Δf was further monitored for 24 h at 298 K. A control experiment was carried out using SBD model solution lacking silica. No frequency decrease ($\Delta f = 0$) was observed in the control experiments whereas the model SBD solution resulted in a substantial decrease in frequency, with each self-assembled monolayer providing a different decrease in frequency (Figure 1). The QCM curves in Figure 1a indicate that the surfaces bearing $-NH_2$ or $-N^+(CH_3)_3$ groups showed the largest frequency decrease (Δf), suggesting the greatest amount of precipitation. Surfaces coated with $-NH_2/-COOH$, $-COOH$, $-OH$, $-CH_3$ or $-H_2PO_3$ groups showed smaller frequency shifts over the 24 h period, as shown in Figure 1a. On the basis of the QCM data, the extent of precipitation on surfaces with different terminal functional groups followed the order: $-NH_2 \sim -N^+(CH_3)_3 > -NH_2/-COOH > -OH \sim -H_2PO_3 > -COOH > -CH_3$. Figure 1b describes the extent of frequency shift after 18 h for each of the monolayers.

The results of the QCM experiments showed clear trends in the induction of precipitation by the different functional groups. As described below, silica was the main component of the precipitate, in accordance with the SBD solution being supersaturated with silica. The observed trend for precipitation in the presence of different terminal functional groups shows that silica precipitation is initiated by positively charged functional groups ($-NH_2$ is positively charged at pH 7) and inhibited by negatively charged groups ($-H_2PO_3$, $-COOH$), neutral groups ($-OH$), and hydrophobic groups ($-CH_3$). This result is in good agreement with the results reported for silica scaling by Tong et al.,[31] where reverse osmosis membrane surfaces modified with amine groups resulted in higher silica scaling and reduced membrane performance compared with other membranes during desalination of a solution simulating brackish water. In contrast, Wallace et al.[28] compared the rate of silica nucleation on surfaces coated with carboxyl groups ($-COOH$), amine groups ($-NH_2$), or a hybrid surface of carboxyl/amine groups, and observed that the amine terminated surface did not induce silica precipitation whereas the hybrid (carboxyl/amine) and carboxyl terminated surfaces did induce silica precipitation under similar conditions.

3.3. Surface Chemical Analysis and Elemental Composition of the Precipitate. Self-assembled monolayers of alkyl thiols on gold-coated silicon and sapphire wafers were immersed in the model SBD solution and the elements comprising the precipitate deposited on the surfaces were identified. After 24 h immersion, the surfaces were gently washed with 50% ethanol/water, dried, and characterized by ATR-FTIR and XPS. The ATR-FTIR spectra of the surfaces (Figure S2, SI) showed strong absorption peaks predominately in the 1000−1200 cm^{-1} region and were assigned to the Si−O−Si vibrations of silica based on the literature.[38,39] A peak at 1640 cm^{-1} was present in all the spectra and corresponded to the H−O−H vibrational frequency of adsorbed water.[39,40]

XPS analysis of the model surfaces after immersion in SBD solution (Table 2) showed various concentrations of silicon, in addition to other elements, confirming the presence of silica precipitate on the tested surfaces. The self-assembled $-NH_2$ and $-N^+(CH_3)_3$ groups (positively charged surfaces) provided the highest atomic percentage of Si of the seven surfaces studied, whereas the hydrophobic surface ($-CH_3$) showed no detectable silicon. These XPS analyses corroborate the observations from the QCM experiments. Other than Si, no elements related to scale formation, such as Ca, Mg, or Sr, were detected on the surfaces, clearly showing that SiO_2 was the major component in precipitate from SBD solution.

3.4. Effect of Surface Charge on the Forces between a Silica Colloid Glued to the AFM Cantilever and the Self-Assembled Monolayers. We used AFM to measure the

DOI: 10.1021/acs.est.8b06154
Environ. Sci. Technol. 2019, 53, 5202−5211

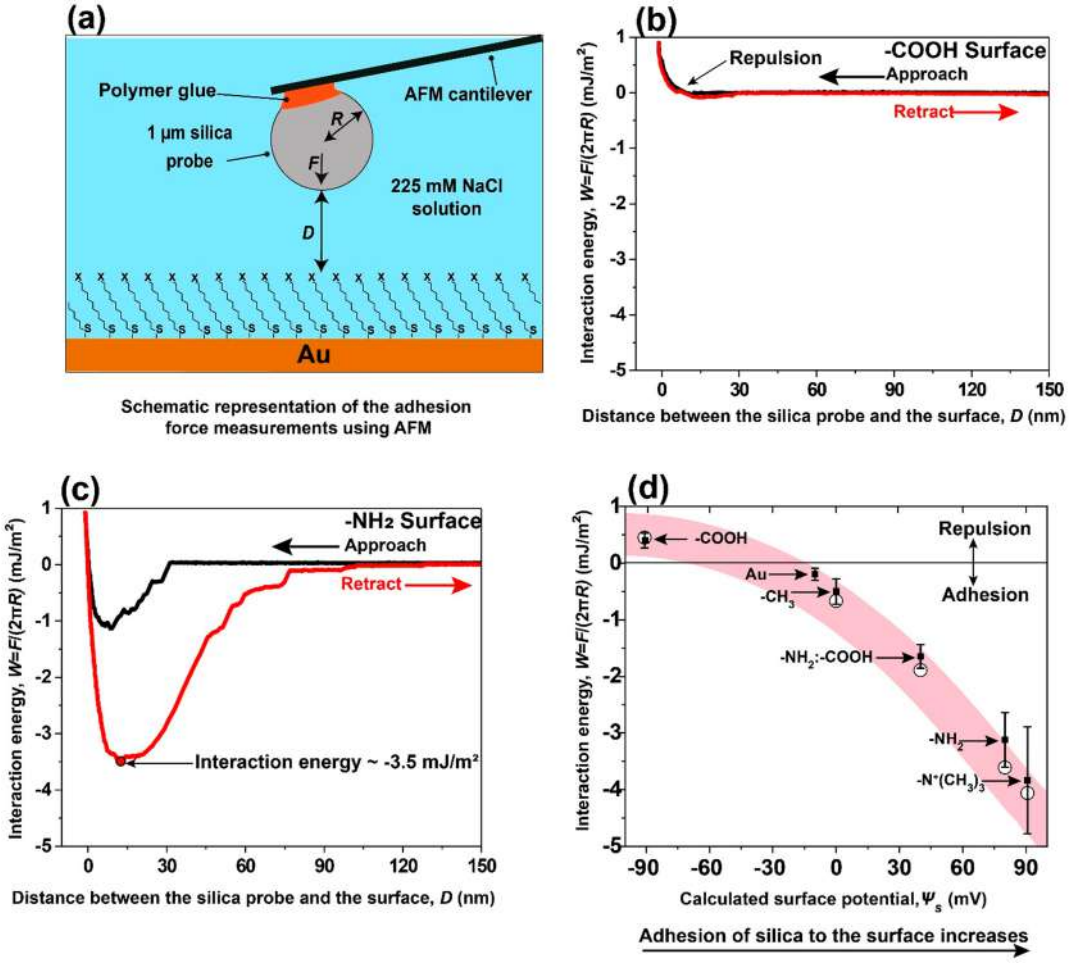

Figure 2. (a) Experimental setup for measuring the adhesion forces between silica colloid and the different surfaces using AFM, where X represents $-COOH$, $-CH_3$, $-NH_2$: $-COOH$, $-NH_2$, or $-N^+(CH_3)_3$. (b) Representative interaction energy vs distance measurement between the silica colloidal probe and the negatively charged $-COOH$ surface and (c) the positively charged $-NH_2$ surface. (d) Summary of the adhesion/repulsion energy between silica and the 6 surfaces, based on 10−15 force measurements on each surface, plotted against the calculated surface potential (eq 3). The white circles and black solid markers represent the calculated (eq 2) and measured energies, respectively.

forces between the studied surfaces and a silica colloid to shed light on the mechanisms by which surface-exposed functional groups affect the precipitation rate of silica (Figure 2a). Our aim was to mimic the initial adhesion forces between the different surfaces (Table 1) and dissolved silica species.

The interaction energy between the silica and the different surfaces were determined by measuring the force vs distance, $F(D)$, between a silica colloid (1 μm diameter) glued to the AFM cantilever and five self-assembled alkyl thiol monolayers on gold surfaces (together with an Au control surface) at 10−15 different locations, as illustrated in Figure 2a. The maximum adhesion force (the most negative value, see Figure 2c) was then converted to the adhesion energy between the surfaces using the Derjaguin approximation:[41]

$$W = \frac{F}{2\pi R} \quad (1)$$

where W is the adhesion energy (mJ·m^{-2}), F is the measured adhesion force (nN), and R is the radius of the colloidal probe (500 nm). Figure 2d summarizes the measured and calculated interaction energies for the six surfaces. Two representative interaction energy vs distance curves are shown in Figure 2b,c, and the other plots are presented in Figure S4a−d (SI). The $-COOH$ and $-NH_2$ terminated surfaces were chosen as two extreme model surfaces in Figure 2b,c due to the opposite surface charge on their head groups. The carboxyl ($-COOH$) group is negatively charged at pH 7 (the pH of the measured SBD solution), and the $-COOH$ terminated Au surfaces showed a repulsive interaction (~+0.4 mJ·m^{-2} at $D \approx 0.7$ nm, Figure 2b). This interaction was due to double layer repulsion between the negatively charged silica colloid with the negative surface charge of the carboxyl terminated Au surface, together with van der Waals (VDW) adhesion (positive Hamaker constant, as elaborated below). In contrast, the $-NH_2$ (positively charged at pH 7) and $-N^+(CH_3)_3$ modified Au-surfaces (Figures 2c and S4d) resulted in stronger adhesion forces (and energy).

All the retraction curves (red curves in Figure 2b,c, and in Figure S4) suggest that the silica probe detached from the surfaces at $D > 20$ nm for high adhesion energies ($W < -1$ mJ·m^{-2}). Neither the Au layer nor the thin (~1.5 nm) covalently attached layers could stretch this distance and thus we believe that the polymer used to glue the silica colloid to the cantilever (see Figure 2a) stretched during the retraction step, as schematically illustrated in Figure S5 (SI).

DLVO theory[32] was used to calculate the interaction energy, W, between the colloidal probe and the different modified surfaces in aqueous solution:

DOI: 10.1021/acs.est.8b06154
Environ. Sci. Technol. 2019, 53, 5202−5211

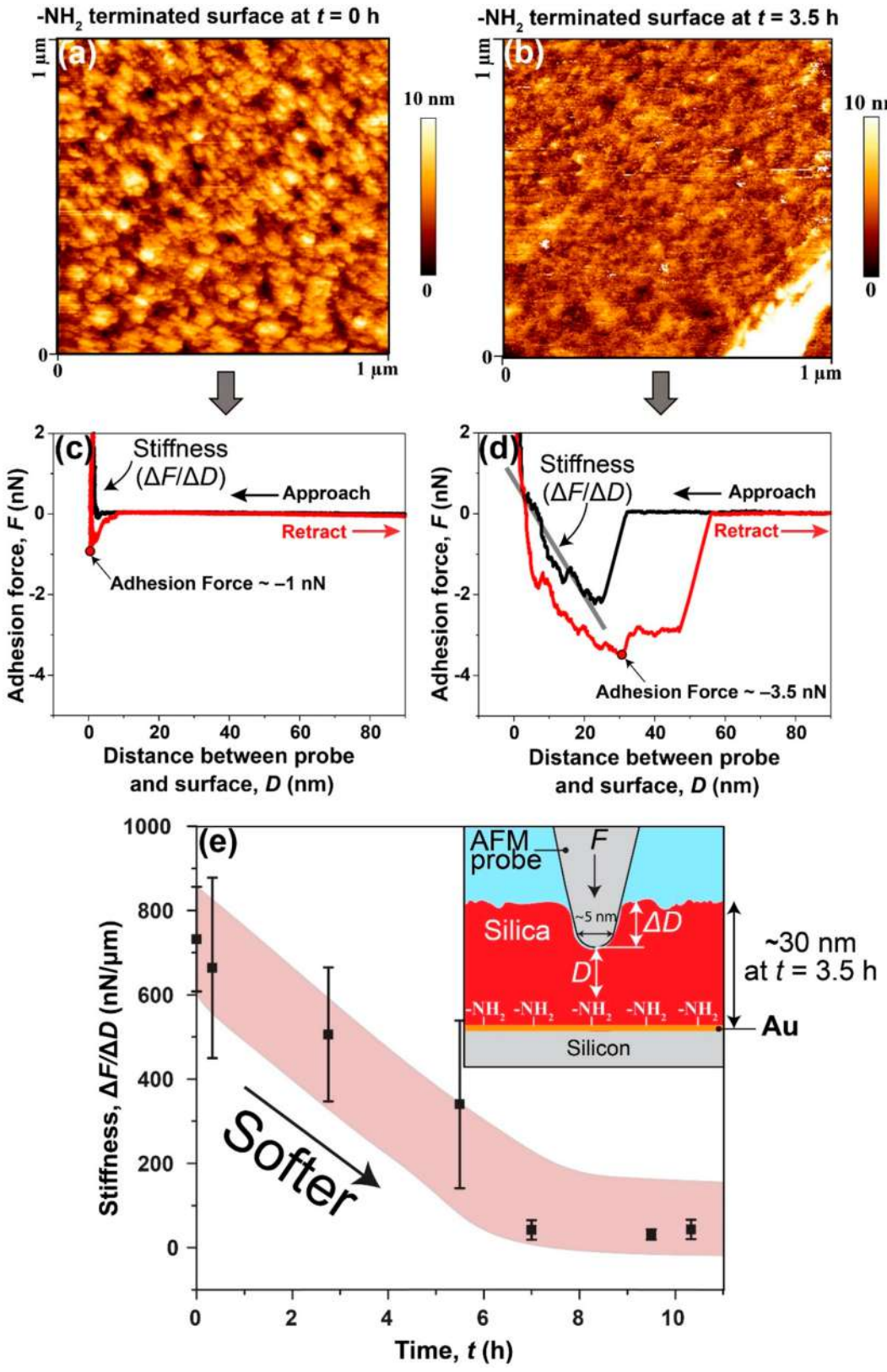

Figure 3. AFM topography images, and force and stiffness measurements of the silica layer that formed on the $-NH_2$ terminated surface. (a) Surface topography of the $-NH_2$ surface as it was initially soaked (t = 0 h) in model SBD solution supersaturated with silica. (b) The same location on the $-NH_2$ terminated surface at t = 3.5 h. The corresponding force vs distance curves (probe diameter ~5 nm) are shown in (c) for t ≈ 0 h and in (d) for t = 3.5 h. (e) Average silica layer stiffness measured at different precipitation times (inset: schematic of the AFM measurement setup using a sharp probe). Each data point in (e) is the average stiffness based on force measurements at 65 536 locations.

DOI: 10.1021/acs.est.8b06154
Environ. Sci. Technol. 2019, 53, 5202−5211

$$W = -\frac{A_{SWC}}{12\pi D^2} + \frac{\varepsilon_0 \varepsilon \kappa [2\psi_S \psi_C - (\psi_S^2 + \psi_C^2) e^{-\kappa D}]}{e^{+\kappa D} - e^{-\kappa D}} \quad (2)$$

where the first term is the VDW interaction and the second term is the double-layer interaction between a spherical and a flat surface exhibiting two different surface potentials.[42] A_{SWC} is the Hamaker constant for a surface water-colloidal probe system[32] and is ~1×10^{-20} J, $\varepsilon_0 = 8.85 \times 10^{-12}$ $C^2 \cdot J^{-1} \cdot m^{-1}$, and $\varepsilon = 80$ are the vacuum and medium (water) permittivities, respectively, and ψ_S and ψ_C are the modified surfaces and the colloidal probe (silica) surface potentials, respectively. ψ_C is ~−30 mV for a silica surface.[43] κ is the inverse of the Debye length and can be estimated by $\kappa = \frac{\sqrt{[NaCl]}}{0.304}$ [nm] for a monovalent aqueous solution[32] such as a NaCl solution, and D is the distance between the modified gold surface and the colloidal probe, (assumed to be 0.7 nm at contact).

The surface potentials, ψ_s, of self-assembled monolayers of alkyl thiols on gold were calculated using the Grahame equation[32,44] at 298 K:

$$\sigma = 0.117 \sinh(\psi_S/51.4)\sqrt{C} \quad (3)$$

where σ is the surface charge density (C m^{-2}), ψ_S is the surface potential (mV), and C is the NaCl concentration (0.225 M). σ was calculated by assuming a 1 nm average distance between two functional groups on the Au surface. On the basis of the pK_a values of the different ionizable groups and the pH of the SBD solution (between 6 to 7), the percentage of charged groups on each surface was assumed to be 80% for $-NH_2$ (as positively charged ammonium), 100% for $-N^+(CH_3)_3$, 100% for −COOH (negatively charged carboxylate ion), 30% for $-NH_2$/−COOH (best fit to the data), and 0% (not charged) for $-CH_3$. The calculated ψ_S and W values for the six surfaces are summarized in Figure 2d.

In addition to force measurements, AFM was used to measure topography and surface stiffness as the silica precipitated. The aim of that part was to understand what was the form of the precipitated silica on the studied surfaces. The topography and stiffness of a self-assembled $-NH_2$ monolayer on gold surface was measured before and during silica precipitation, and the results are summarized in Figure 3. These measurements were conducted while the surface was immersed in SBD solution supersaturated with silica. A topography image of the $-NH_2$ terminated surface as the surface was immersed in supersaturated silica solution (t = 0 h) is shown in Figure 3a. The topography at the same location after 3.5 h (Figure 3b) was significantly different, indicating silica precipitation on the surface. The probe in the force vs distance curve (Figure 3d) penetrated ~30 nm into the soft silica layer after 3.5 h of silica precipitation (see schematic in Figure 3e). Hence, we assume a silica precipitation rate of ~9 nm/h.

The precipitation of silica on the $-NH_2$ terminated surface also changed the surface stiffness, as calculated by $\Delta F/\Delta D$ when the probe presses the surface (see Figure 3c,d). Initially, at $t \approx 0$ h, the measured stiffness of the surface was 732 ± 124 nN·μm^{-1} whereas at $t \approx 11$ h, the stiffness decreased significantly (became softer) to 43 ± 23 nN·μm^{-1}. These results indicated that the precipitated silica formed a continuous gel layer which was much softer than the Au layer. Hence, a silica gel layer was formed during silica precipitation.

In this research we found that different surface organic chemical groups significantly influence silica precipitation under conditions that simulate the desalination of brackish groundwater. The QCM results revealed that surfaces terminated with positively charged $-NH_2$ and $-N^+(CH_3)_3$ groups induced more extensive silica precipitation than did surfaces terminated with negatively charged or neutral groups ($-NH_2$/−COOH, $-H_2PO_3$, −OH, −COOH, and $-CH_3$). In saturated solutions monosilicic acid is in equilibrium with solid silica:

$$SiO_{2(S)} + 2H_2O_{(l)} \rightleftharpoons Si(OH)_{4(aqueous)} \quad (4)$$

The equilibrium constant for eq 4 is $K = 1.95 \times 10^{-3}$ M (at 25 °C, for amorphous silica[28]), and is equal to the equilibrium activity of monosilicic acid. The silicate concentration in the experiments of the present study is 5×10^{-3} M, much higher than the equilibrium concentration, hence SBD solution is oversaturated with respect to silica. The surface of solid silica particles is negatively charged at pH 6.5.[45,46] Hence, a more intense scaling on positively charged surfaces may be explained by the attractive electrostatic forces between the positively charged surfaces and negatively charged solid silica, which stabilizes the precipitated silica and shifts the equilibrium (eq 4) toward precipitation. The attractive electrostatic interactions may also enhance adherence of silica particles to the positively charged surfaces. The observed large differences in the extent of silica precipitation on the different surfaces suggest that surface-induced precipitation (heterogeneous precipitation) processes dominate silica precipitation under the studied conditions, rather than processes that occur in bulk solution.

AFM measurements revealed that the adhesion forces (and energy) between a silica colloidal particle and the studied surfaces decrease when the surface charge changes from positive ($-NH_2$ and $-N^+(CH_3)_3$) to noncharged hydrophobic ($-CH_3$) and then to negatively charged (−COOH). We therefore conclude that surface chemistry, and particularly the surface charge density, affects the rate of silica precipitation. To the best of our knowledge, this is the first report of direct measurements that correlate electrostatic interactions with the rate of silica precipitation under conditions that simulate desalination of brackish groundwater. The effects of surface charge and surface chemistry identified in this study can be used to design surfaces that significantly decrease the rate of silica scaling and precipitation. Surfaces that can alleviate silica scaling are highly desirable for membrane-based water desalination, such as reverse osmosis desalination of brackish groundwater.

■ ASSOCIATED CONTENT

Supporting Information

The Supporting Information is available free of charge on the ACS Publications website at DOI: 10.1021/acs.est.8b06154.

The ion content of the model SBD solution and the Negev Highlands brackish groundwater; stability measurements of the SBD solution during 4 days; FTIR spectra of surface precipitates; AFM topography of the self-assembled gold surfaces; representative force vs distance measurement between the silica colloid and the tested surfaces; and an illustration of the colloidal probe fixed to the AFM cantilever (PDF)

DOI: 10.1021/acs.est.8b06154
Environ. Sci. Technol. 2019, 53, 5202−5211

AUTHOR INFORMATION

Corresponding Authors

*Phone: +972 52 6677228; e-mail: yairkau@bgu.ac.il (Y.K.).
*Phone: 972-86563531; fax: 972-86596889; e-mail: kasher@bgu.ac.il (R.K.).

ORCID

Karthik Rathinam: 0000-0003-2767-9319
Roni Kasher: 0000-0002-6429-9553

Author Contributions

§These authors contributed equally.

Notes

The authors declare no competing financial interest.

ACKNOWLEDGMENTS

The authors thank the Blaustein Center for Scientific Cooperation (Ben-Gurion University of the Negev) for a postdoctorate fellowship (K.R.) and the German-Israeli Foundation for Scientific Research and Development (GIF; Grant No. I-1240-307.8/2014) for financial support. We also thank Mrs. Rotem Manor and Mr. Costa Abarbanel for the preparation of gold-coated silicon and sapphire wafers, and Dr. Natalya Froumin (Ilse Katz Institute for Nanoscale Science) for the XPS analyses. This work was supported by the Adelis Foundation.

REFERENCES

(1) Koo, T.; Lee, Y. J.; Sheikholeslami, R. Silica fouling and cleaning of reverse osmosis membranes. *Desalination* **2001**, *139* (1−3), 43−56.
(2) Den, W.; Wang, C.-J. Removal of silica from brackish water by electrocoagulation pretreatment to prevent fouling of reverse osmosis membranes. *Sep. Purif. Technol.* **2008**, *59* (3), 318−325.
(3) Semiat, R.; Sutzkover, I.; Hasson, D. Scaling of RO membranes from silica supersaturated solutions. *Desalination* **2003**, *157* (1−3), 169−191.
(4) Salvador Cob, S.; Beaupin, C.; Hofs, B.; Nederlof, M. M.; Harmsen, D. J. H.; Cornelissen, E. R.; Zwijnenburg, A.; Genceli Güner, F. E.; Witkamp, G. J. Silica and silicate precipitation as limiting factors in high-recovery reverse osmosis operations. *J. Membr. Sci.* **2012**, *423−424*, 1−10.
(5) Lisitsin, D.; Hasson, D.; Semiat, R. Critical flux detection in a silica scaling RO system. *Desalination* **2005**, *186* (1−3), 311−318.
(6) Lunevich, L.; Sanciolo, P.; Dumee, L. F.; Gray, S. R. Silica fouling in high salinity waters in reverse osmosis desalination (sodium-silica system). *Environmental Science: Water Research & Technology* **2016**, *2* (3), 539−548.
(7) Oren, Y.; Korngold, E.; Daltrophe, N.; Messalem, R.; Volkman, Y.; Aronov, L.; Weismann, M.; Bouriakov, N.; Glueckstern, P.; Gilron, J. Pilot studies on high recovery BWRO-EDR for near zero liquid discharge approach. *Desalination* **2010**, *261* (3), 321−330.
(8) Bason, S.; Priel, M.; David, I.; Shulman, A.; Duer, A.; Bustan, L. Challenges and achievements in the expansion of the Granot BWRO plant: A part of Israel's coastal aquifer rehabilitation project. *Desalination and Water Treatment* **2017**, *61*, 206−214.
(9) Iler, R. K. *The Chemistry of Silica: Solubility, Polymerization, Colloid and Surface Properties, and Biochemistry*; Wiley: New York, 1979.
(10) Braun, G.; Hater, W.; Kolk, C. z.; Dupoiron, C.; Harrer, T.; Götz, T. Investigations of silica scaling on reverse osmosis membranes. *Desalination* **2010**, *250* (3), 982−984.
(11) Milne, N. A.; O'Reilly, T.; Sanciolo, P.; Ostarcevic, E.; Beighton, M.; Taylor, K.; Mullett, M.; Tarquin, A. J.; Gray, S. R. Chemistry of silica scale mitigation for RO desalination with particular reference to remote operations. *Water Res.* **2014**, *65*, 107−133.
(12) Latour, I.; Miranda, R.; Blanco, A. Silica removal in industrial effluents with high silica content and low hardness. *Environ. Sci. Pollut. Res.* **2014**, *21* (16), 9832−9842.
(13) Weres, O.; Yee, A.; Tsao, L. Kinetics of silica polymerization. *J. Colloid Interface Sci.* **1981**, *84* (2), 379−402.
(14) Neofotistou, E.; Demadis, K. D. Use of antiscalants for mitigation of silica (SiO2) fouling and deposition: fundamentals and applications in desalination systems. *Desalination* **2004**, *167*, 257−272.
(15) Salvador Cob, S.; Hofs, B.; Maffezzoni, C.; Adamus, J.; Siegers, W. G.; Cornelissen, E. R.; Genceli Güner, F. E.; Witkamp, G. J. Silica removal to prevent silica scaling in reverse osmosis membranes. *Desalination* **2014**, *344*, 137−143.
(16) Sanciolo, P.; Milne, N.; Taylor, K.; Mullet, M.; Gray, S. Silica scale mitigation for high recovery reverse osmosis of groundwater for a mining process. *Desalination* **2014**, *340*, 49−58.
(17) Latour, I.; Miranda, R.; Blanco, A. Silica removal from newsprint mill effluents with aluminum salts. *Chem. Eng. J.* **2013**, *230*, 522−531.
(18) Sheikholeslami, R.; Bright, J. Silica and metals removal by pretreatment to prevent fouling of reverse osmosis membranes. *Desalination* **2002**, *143* (3), 255−267.
(19) Zeng, Y.; Yang, C.; Pu, W.; Zhang, X. Removal of silica from heavy oil wastewater to be reused in a boiler by combining magnesium and zinc compounds with coagulation. *Desalination* **2007**, *216* (1−3), 147−159.
(20) Hermosilla, D.; Ordóñez, R.; Blanco, L.; de la Fuente, E.; Blanco, Á. pH and Particle Structure Effects on Silica Removal by Coagulation. *Chem. Eng. Technol.* **2012**, *35* (9), 1632−1640.
(21) Sweity, A.; Zere, T. R.; David, I.; Bason, S.; Oren, Y.; Ronen, Z.; Herzberg, M. Side effects of antiscalants on biofouling of reverse osmosis membranes in brackish water desalination. *J. Membr. Sci.* **2015**, *481*, 172−187.
(22) Gabelich, C. J.; Chen, W. R.; Yun, T. I.; Coffey, B. M.; Suffet, I. H. The role of dissolved aluminum in silica chemistry for membrane processes. *Desalination* **2005**, *180* (1-3), 307−319.
(23) Lunevich, L.; Sanciolo, P.; Milne, N.; Gray, S. R. Silica fouling in coal seam gas water reverse osmosis desalination. *Environmental Science: Water Research & Technology* **2017**, *3* (5), 911−921.
(24) Higgin, R.; Howe, K. J.; Mayer, T. M. Synergistic behavior between silica and alginate: Novel approach for removing silica scale from RO membranes. *Desalination* **2010**, *250* (1), 76−81.
(25) Mi, B.; Elimelech, M. Silica scaling and scaling reversibility in forward osmosis. *Desalination* **2013**, *312*, 75−81.
(26) Xie, M.; Gray, S. R. Silica scaling in forward osmosis: From solution to membrane interface. *Water Res.* **2017**, *108*, 232−239.
(27) Bush, J. A.; Vanneste, J.; Gustafson, E. M.; Waechter, C. A.; Jassby, D.; Turchi, C. S.; Cath, T. Y. Prevention and management of silica scaling in membrane distillation using pH adjustment. *J. Membr. Sci.* **2018**, *554*, 366−377.
(28) Wallace, A. F.; DeYoreo, J. J.; Dove, P. M. Kinetics of Silica Nucleation on Carboxyl- and Amine-Terminated Surfaces: Insights for Biomineralization. *J. Am. Chem. Soc.* **2009**, *131* (14), 5244−5250.
(29) Sumper, M.; Lorenz, S.; Brunner, E. Biomimetic Control of Size in the Polyamine-Directed Formation of Silica Nanospheres. *Angew. Chem., Int. Ed.* **2003**, *42* (42), 5192−5195.
(30) Brunner, E.; Lutz, K.; Sumper, M. Biomimetic synthesis of silica nanospheres depends on the aggregation and phase separation of polyamines in aqueous solution. *Phys. Chem. Chem. Phys.* **2004**, *6* (4), 854−857.
(31) Tong, T.; Zhao, S.; Boo, C.; Hashmi, S. M.; Elimelech, M. Relating Silica Scaling in Reverse Osmosis to Membrane Surface Properties. *Environ. Sci. Technol.* **2017**, *51* (8), 4396−4406.
(32) Israelachvili, J. N. *Intermolecular and surface forces*. Academic press: 2011.
(33) Salama, I. E.; Binks, B. P.; Fletcher, P. D. I.; Horsup, D. I. Adsorption of benzyldimethyldodecylammonium chloride onto stainless steel using the quartz crystal microbalance and the depletion methods: an optimization study. *Colloids Surf., A* **2014**, *447*, 155−165.

DOI: 10.1021/acs.est.8b06154
Environ. Sci. Technol. 2019, 53, 5202−5211

(34) Eaton, A. D.; Franson, M. A. H.; Association, A. P. H.; Association, A. W. W.; Federation, W. E. *Standard Methods for the Examination of Water & Wastewater*; American Public Health Association: 2005.
(35) Steiner, Z.; Rapaport, H.; Oren, Y.; Kasher, R. Effect of Surface-Exposed Chemical Groups on Calcium-Phosphate Mineralization in Water-Treatment Systems. *Environ. Sci. Technol.* **2010**, *44* (20), 7937−7943.
(36) Contreras, A. E.; Steiner, Z.; Miao, J.; Kasher, R.; Li, Q. Studying the Role of Common Membrane Surface Functionalities on Adsorption and Cleaning of Organic Foulants Using QCM-D. *Environ. Sci. Technol.* **2011**, *45* (15), 6309−6315.
(37) Bain, C. D.; Troughton, E. B.; Tao, Y. T.; Evall, J.; Whitesides, G. M.; Nuzzo, R. G. Formation of monolayer films by the spontaneous assembly of organic thiols from solution onto gold. *J. Am. Chem. Soc.* **1989**, *111* (1), 321−335.
(38) Pasternack, R. M.; Rivillon Amy, S.; Chabal, Y. J. Attachment of 3-(Aminopropyl)triethoxysilane on Silicon Oxide Surfaces: Dependence on Solution Temperature. *Langmuir* **2008**, *24* (22), 12963−12971.
(39) Kim, D.; Zuidema, J. M.; Kang, J.; Pan, Y.; Wu, L.; Warther, D.; Arkles, B.; Sailor, M. J. Facile Surface Modification of Hydroxylated Silicon Nanostructures Using Heterocyclic Silanes. *J. Am. Chem. Soc.* **2016**, *138* (46), 15106−15109.
(40) Asay, D. B.; Kim, S. H. Evolution of the Adsorbed Water Layer Structure on Silicon Oxide at Room Temperature. *J. Phys. Chem. B* **2005**, *109* (35), 16760−16763.
(41) Derjaguin, B.; Obuchov, E. Untersuchungen über die mechanischen Eigenschaften disperser Systeme und Oberflächenschichten. II. Die elastischen Eigenschaften und Dispersität der Schäume. *Colloid Polym. Sci.* **1934**, *68* (3), 243−246.
(42) Hogg, R.; Healy, T. W.; Fuerstenau, D. Mutual coagulation of colloidal dispersions. *Trans. Faraday Soc.* **1966**, *62*, 1638−1651.
(43) Kirby, B. J.; Hasselbrink, E. F., Jr Zeta potential of microfluidic substrates: 1. Theory, experimental techniques, and effects on separations. *Electrophoresis* **2004**, *25* (2), 187−202.
(44) Grahame, D. C. Diffuse double layer theory for electrolytes of unsymmetrical valence types. *J. Chem. Phys.* **1953**, *21* (6), 1054−1060.
(45) Kobayashi, M.; Juillerat, F.; Galletto, P.; Bowen, P.; Borkovec, M. Aggregation and charging of colloidal silica particles: Effect of particle size. *Langmuir* **2005**, *21* (13), 5761−5769.
(46) Emami, F. S.; Puddu, V.; Berry, R. J.; Varshney, V.; Patwardhan, S. V.; Perry, C. C.; Heinz, H. Force Field and a Surface Model Database for Silica to Simulate Interfacial Properties in Atomic Resolution. *Chem. Mater.* **2014**, *26* (8), 2647−2658.

DOI: 10.1021/acs.est.8b06154
Environ. Sci. Technol. 2019, 53, 5202−5211

ap

Asian Journal of Physics
Vol. 25, No 1 (2016) 121-126

Available on: www.asianjournalofphysics.in

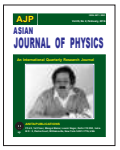

Two dimensional graphene derivatives supported isolated gold nanoparticles as an efficient SERS substrate

Shiju Abraham[a,b], Matthias König[b], Shobhit Pandey[c], Sunil K Srivastava[d], Bernd Walkenfort[b] and Anchal Srivastava[a]

[a]*Department of Physics, Banaras Hindu University, Varanasi-221 005, India*
[b]*Faculty of Chemistry, University of Duisburg, 45141 Essen, Germany*
[c]*Metallurgical Engineering Department, Indian Institute of Technology – (BHU), Varanasi-221 005*
[d]*Department of Pure and Applied Physics, Guru Ghasidas University, Bilaspur- 495 009, India*

(Dedicated to Professor Wolfgang Kiefer on the occasion of his 75th birthday)

The present work accomplishes surface enhanced Raman scattering (SERS) studies using the combination of stable, diluted and isolated gold nanoparticles (Au NPs) of tailored size (~ 50 nm) and distribution on two dimensional carbon nanostructures (2D-CNS) i.e. graphene oxide (GO) and reduced graphene oxide (RGO). Fabricated using a simple, quick and cost effective method, these SERS substrates have enough synergistic enhancement from each Au NPs and underlying CNS matrix with sensitivity enough to easily detect 10^{-6} molar concentrations of analyte, 4-mercaptobenzoic acid (4-MBA). Further, uniform distribution of Au NPs ensures great reproducibility showing potential for standardization in future.

Keywords: Surface enhanced Raman scattering (SERS), Nanoparticles, Graphene oxide (GO), 4-mercaptobenzoic acid (4-MBA)

1 Introdction

Surface-enhanced Raman scattering (SERS) is a surface selective and highly sensitive spectroscopic technique for molecular detection and surface analysis [1,2]. SERS offers higher magnitude of increased intensity and suppresses the fluorescence signal while selectively enhancing the Raman signal, and produces chemical fingerprinting with sensitivity enough to enable single-molecule detection [3]. Two widely accepted enhancement mechanisms are the dominant electromagnetic mechanism (EM) (contributing about 108 of enhancement) and the chemical mechanism (CM) (contributing one or two orders of enhancement), together contributing the overall enhancement [4]. The long range nature of EM relies on the roughness, high curves or gapped metal regions of the substrate in order to develop localized electromagnetic field regions called as “hot” spots. In this respect, rough noble metal nanoparticles substrates, especially Au NPs having good curvature and required optical properties for enhanced surface plasmons on excitation, proved out to be one of the most popular traditional SERS substrates with additional advantages such as biocompatibility, stability, controllable size and shape distributions [5,6]. Mostly, due to complex distribution of molecules on SERS substrate, molecules near the hot spots keep on fluctuating, which is further aggravated by other factors like chemical interactions between the molecules and the metal substrate, chemical adsorption-induced vibrations, molecular deformation and distortion, etc. [7,8]. These disadvantages demand new materials for SERS substrates, which can be fabricated uniformly and economically with particles size small enough that an isolated particle can give the required localized surface plasmon resonance effect.

Corresponding author :
e-mail: anchalbhu@gmail.com, phone:+91 9453203122 (Anchal Srivastava)

Often termed as a "first layer effect"; unlike EM, CM is a short range effect which requires the distance between the molecule and the substrate to be below 0.2 nm. Further, the charge transfer between molecule and substrate is possible by having the Fermi level of the metal substrate symmetrically aligned with the highest occupied molecular orbital (HOMO) and lowest unoccupied molecular orbital (LUMO) of the molecule [1,9]. These requirements mark the inefficiency of CM in case of noble nanoparticles based SERS substrates, but paved the way for graphene substrates based SERS; called now as Graphene Enhanced Raman Spectroscopy (GERS). In case of graphene, relatively smooth surface, visible range optical transitions [10], and lower surface plasmon [11] make EM ineffective, making CM as the dominant mechanism. However, unlike metal substrates, the Raman enhancements are limited and not enough for standardization [12]. Nevertheless, flexibility offered by graphene and its derivatives and particularly their ability to combine with metal nanoparticles attests its potential as a promising matrix for forming hybrids [13] which can take advantage of both EM and synergistically enhanced CM, for an overall commendable Raman enhancement; the prime motivation of the present work.

With this aim, the present work utilizes Au NPs supported 2D-CNS matrix, as a commendable SERS substrate for testing the efficacy of the Raman Marker; 4-MBA. Finally, in order to produce reproducibility enabling future standardization, the present work uses the enhancement upraised from isolated Au NPs of tailored size decorated at distances higher than the spectral resolution of the exciting source, still producing commendable enhancements without any signal degradation; enough for detecting smallest of the concentrations (10^{-6} M) of the Raman marker.

2 Experimental

Typically the 2D- CNS used here (GO and RGO) were produced using the earlier reports [14,15] (supplementary information). Further to produce non agglomerating Au NPs with tailored size, seeded-growth method proposed by Perrault *et al* was followed [16] (Supplementary information). However, in order to maximize the localized surface plasmon resonance (LSPR) effect for maximum enhancement from each Au NPs, the size was then tailored to 50 nm while simultaneously stabilizing with, polyvinylpyrrolidone (PVP).

The 2D- CNS- Au nanoparticles composites were prepared by simply adding 300 µL of diluted spherical Au NPs into 700 µl of 2 mg/ mL (in distilled water) dispersion of 2D- CNS, succeeded by sonication and storage in vibration stand until thin film formation (supplementary information). These two composites i.e RGO- Au NP and GO- Au NP were then uniformly spin coated covering entire (5×5) mm^2 silicon substrate to form the SERS substrate on which 5 µL of Raman marker solution of 4-MBA (1 µM) was then incubated for overnight at room temperature.

3 Results and Discussion

The transmission electron microscopy (TEM) image shown in Fig 1 manifests the homogenously stabilized Au NPs, which were well separated and spherical in shape (~50 nm). Figure 2(a) shows the TEM image of GO sheets, which is non-contaminated, continuous and few layered in nature. Figure 2 (b) corresponding to TEM of GO-Au NPs, clearly shows a single Au NP is decorated on ~(2 × 2) μm^2 area. The Au NPs have required shape (spherical) and size (50 nm) for effective Raman enhancement effect, while the distribution is such that, the distance between Au NPs exceeds the spectral resolution of the laser, enabling isolated particles enhancement. Figure 2(c) shows the TEM image of few layered RGO sheets of long lateral uniformity like GO. Similarly RGO-Au NPs shown in Fig 2(d) denotes the isolated Au NP distribution on the RGO surfaces as in case of GO.

In order to check the reproducibility and potential to be used as a standardized SERS substrate in future, the work involves Raman mapping (using confocal Raman microscope of WITec Alpha 300R, 632.8

nm laser line) of (100 × 100) μm^2 area on substrate scanned with an interval of 2 µm with an integration time of 1s. Figure 3 represents a simplified schematic of the SERS substrate and the SERS signal enhancement obtained.

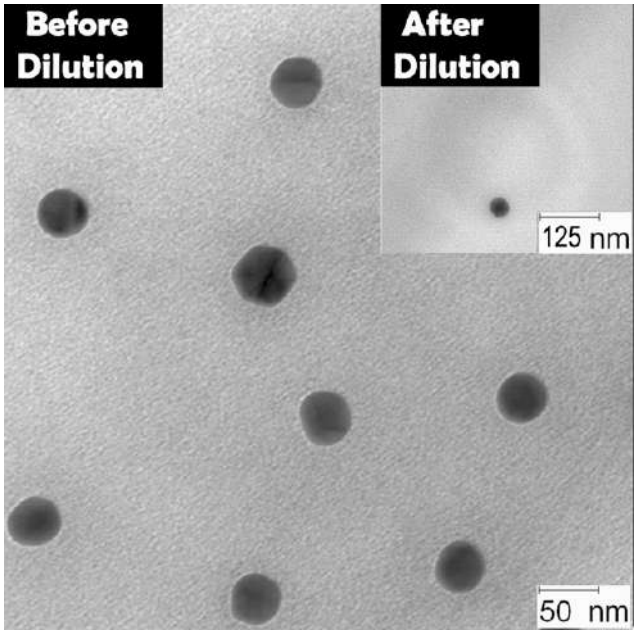

Fig 1. TEM Image of Au NPs; on inset, isolated Au N

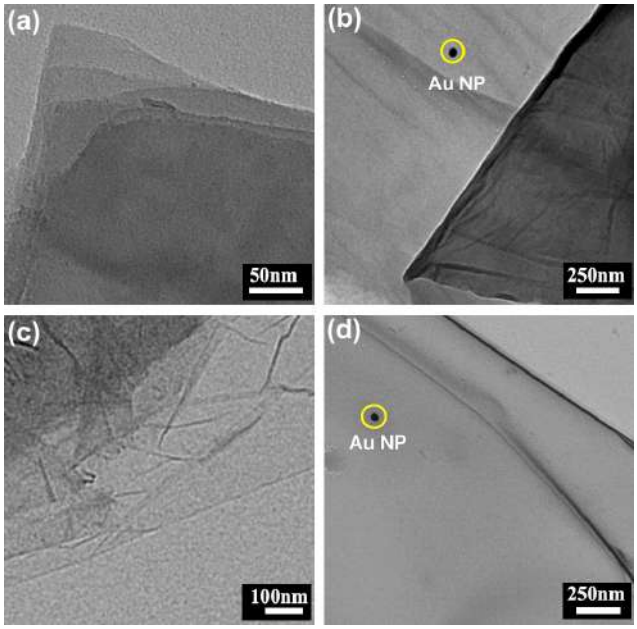

Fig 2. TEM Images of (a) Few layered GO, (b) GO-Au NPs (c) Few layered RGO, (d) RGO-Au NPs

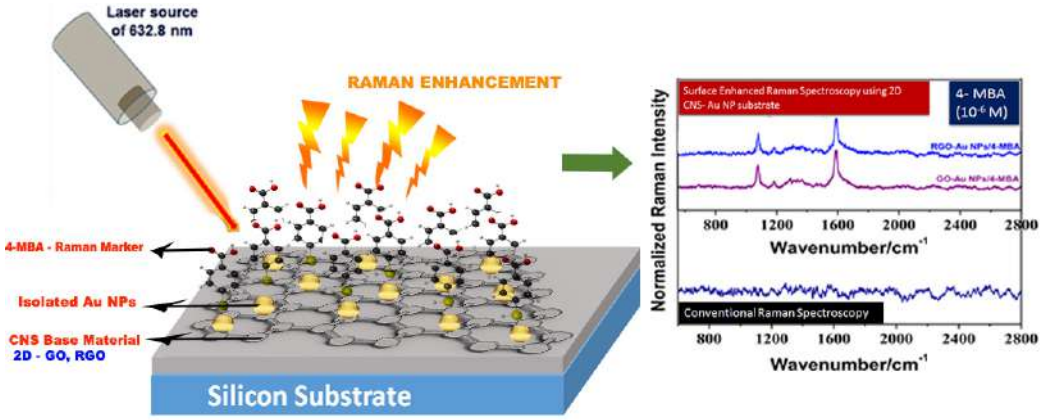

Fig 3. Schematic illustrating the SERS substrate and the Raman enhancement obtained

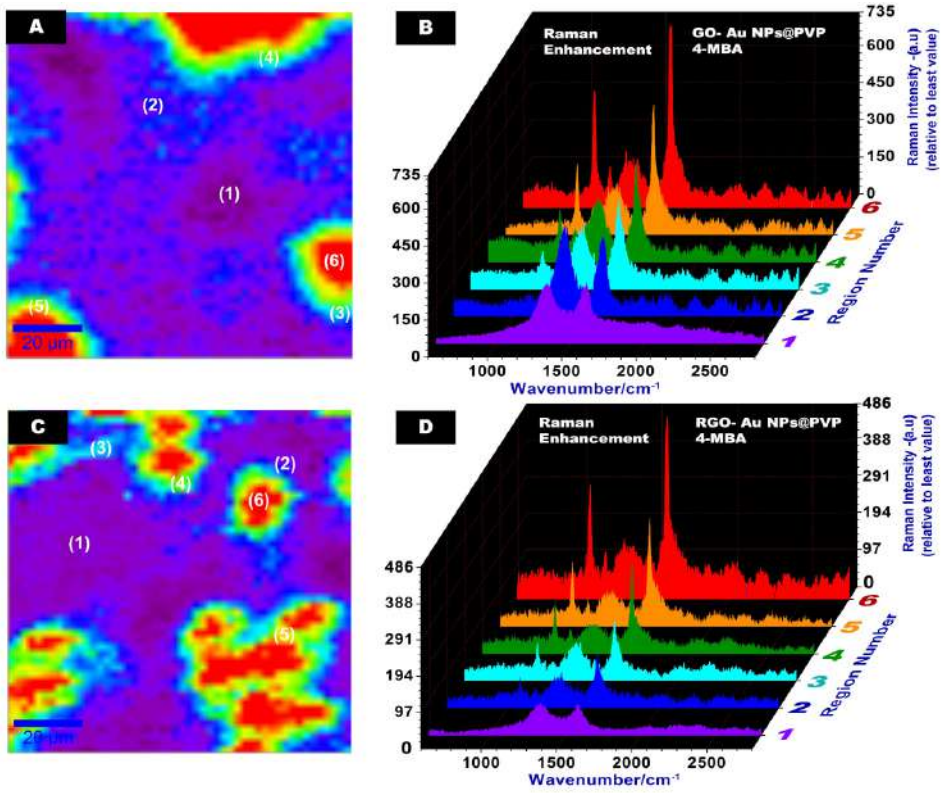

Fig 4. (a) Raman mapping image of GO-Au NPs-4-MBA; (b) Corresponding six point's 3D-SERS spectra. (c) The Raman mapping image RGO-Au NPs-4-MBA, (d) 3D- SERS spectra of RGO-Au NPs-4-MBA.

Raman imaging of GO-Au NPs- 4-MBA defined for the peak centered at 1585 cm^{-1} through the intensity color profile is shown in Fig 4 (a). The well-defined colored region is a profile for the prominent 4-MBA band centered ~ 1585 cm^{-1} (ν(CC) ring stretching). In the color profile, the intensity increases from violet to red. Evidently, the center part of the substrate is more or less occupied with violet and blue color, indicating its more GO nature rather than GO-Au NPs. So the maximum intensity (red color) region

indicates the maximum probable place where Au NPs were decorated and are bonded towards 4-MBA. These findings can be confirmed by the corresponding Raman spectrum of the six different regions (violet to red) (Fig 4 (b)). From the cyan to red color (marked 3 to 6), the corresponding Raman spectrum gives well defined peaks of the Raman marker 4-MBA at 1585, 1175, 1070 and 1340 cm^{-1} even for the low concentration (1 μM) and amount of Raman reporter molecule, attesting substantial Raman enhancement. Also a low profile D (~1350 cm^{-1}) and G-Band (~1580 cm^{-1}) of GO can be observed on the same spectrum. But in region 1 and 2, the D and G-Band are more prominent due to the CNS base material contribution. Figure 4 (c) represents the Raman mapping image of RGO-Au NPs-4-MBA and the 4-MBA field is more nicely distributed here (red region). In the corresponding Raman spectra (Fig 4(d)), a more defined 4-MBA characteristics peak can be observed throughout the region 2 to 5. So, both SERS substrates are observed to be good base materials utilizing both the EM and synergistically enhanced CM, to detect effectively and quickly even the very low concentration of Raman reporter molecule (1 μM), which is impossible to detect using normal RS [17].

4 Conclusions

The present work introduces a simple and quick chemical method to fabricate highly efficient SERS substrates based on Au NPs and 2D-CNS (graphene derivatives) combination. The proposed substrates have commendable Raman enhancement, taking the advantage of both; i.e. EM from the Au NPs and synergistically enhanced CM from Au NP decorated GO/RGO matrix. The tailored Au NPs have a size of 50 nm to ensure maximum enhancement at the used excitation source (632.5 nm). Further, their distribution is such that the distance between the nanoparticles is greater than the spectral resolution of the excitation source. These factors enable enhancement which is enough to detect 10^{-6} M concentrations of analyte with appreciable sensitivity. Further, the uniform distribution and isolated particle dependence for enhancement, cuts down the ambiguity of variations in hot spot regions, thereby powering these substrates with great reproducibility; suggesting great potential for standardization in future.

Acknowledgments

SA and SKSre thankful to Alexander von Humboldt for supporting this research work through AvH Research Group Linkage Program. AS acknowledges CAS program sponsored by UGC at Department of Physics, B. H. U and DST project (No.:DST/TSG/PT/2012/68), New Delhi, India for financial assistance.

References

1. Campion A, Kambhampati P, *Chem Soc Rev*, 27(1998)241-250.
2. Schlücker S, *Angew Chemie Int Ed*, 53(2014)4756-4795.
3. Nie S, Emory S R, *Science*, 275(1997)1102-1106.
4. Lin C -C, Yang Y -M, Chen Y -F, Yang T -S, Chang H -C, *Biosens Bioelectron*, 24 (2008)178-183.
5. Talley C E, Jackson J B, Oubre C, Grady N K, Hollars C W, Lane S M, Huser T R, Nordlander P, Halas N J, *Nano Lett*, 5(2005)1569-1574.
6. Song J, Cheng S, Li H, Guo H, Xu S, Xu W, *Mater Lett*, 135(2014)214-217.
7. Le Ru E, Etchegoin P, Principles of Surface-Enhanced Raman Spectroscopy: And Related Plasmonic Effects, (Elsevier), 2008.
8. Li J F, Huang Y F, Ding Y, Yang Z L, Li S B, Zhou X S, Fan F R, Zhang W, Zhou Z Y, Wu D Y, *Nature*, 464 (2010)392-395.
9. Otto A, J Raman Spectrosc, 36(2005)497-509.
10. Bruna M, Borini S, Appl. Phys Lett, 94(2009)31901; doi.org/10.1063/1.3073717.
11. Rana F, *Nanotechnology, IEEE Trans*, 7(2008)91-99.

12. Ling X, Wu J, Xie L, Zhang J, *J Phys Chem C*, 117(2013)2369-2376.
13. Khorasaninejad M, Raeis-Zadeh S M, Jafarlou S, Wesolowski M J, Daley C R, Flannery J B, Forrest J, Safavi-Naeini S, Saini S S, Sci. Rep, 3(2013) 2936: 1-7; doi:10.1038/srep02936
14. Marcano D C, Kosynkin D V, Berlin J M, Sinitskii A, Sun Z, Slesarev A, Alemany L B, Lu W, Tour J M, *ACS Nano*, 4 (2010)4806-4814.
15. Li D, Müller M B, Gilje S, Kaner R B, Wallace G G, *Nat Nanotechnol*, 3(2008)101-105.
16. Perrault S D, Chan W C W, *J Am Chem Soc*, 131(2009)17042-17043.
17. Hsieh C -W, Lin P -Y, Hsieh S, *J Nanophotonics*, 6 (2012)63501.1-6.

[*Received*: 30.09.2015; *accepted*:15.10.2015]

Supplementary Materials

Two dimensional graphene derivatives supported isolated gold nanoparticles as an efficient SERS substrate

Shiju Abraham[a,b], Matthias König[b], Shobhit Pandey[c], Sunil K Srivastava[d], Bernd Walkenfort[b] and Anchal Srivastava[a]

[a]*Department of Physics, Banaras Hindu University, Varanasi-221 005, India*

[b]*Faculty of Chemistry, University of Duisburg, 45141 Essen, Germany*

[c]*Metallurgical Engineering Department, Indian Institute of Technology, BHU, Varanasi-221 005, India*

[d]*Department of Pure and Applied Physics, Guru Ghasidas University, Bilaspur- 495 009, India*

e-mail: *anchalbhu@gmail.com* (*Anchal Srivastava*), *phone:+91 9453203122*

1 Experimental

1.1 Materials

Graphite flakes (NGS Naturgraphit GmbH, Germany), tetrachloroauric acid ($HAuCl_4$), polyvinylpyrrolidone (PVP), sodium citrate, hydroquinone, 4-MBA, H_2SO_4, H_3PO_4, $KMnO_4$, H_2O_2, hydrazine hydrate, ammonia solution, ethanol, etc. used were of technical grade and were procured from Sigma-Aldrich.

1.2 Preparation of Graphene Oxide (*GO*)

The protocol proposed by Marcano *et al* [1] has been applied for the synthesis of GO. Briefly, a 9 : 1 combination of concentrated H_2SO_4: H_3PO_4 was added to 2 g of graphite flakes and 12 g of $KMnO_4$. At a temperature of 50° C, the mixture was stirred for 12 h. The reaction was quenched after the mixture was cooled to room temperature (RT) by adding ~260 mL of ice with 2 mL of 30% H_2O_2. This mixture was then shifted, filtered and was washed with distilled water and 30% HCl. The final product obtained (GO) was then dried at 70°C.

1.3 Preparation of Reduced Graphene Oxide (*RGO*)

Chemical conversion of GO to RGO is achieved by following the method proposed by Dan Li *et al* [2]. Briefly, a 500 ml (0.25mg/mL) GO dispersion in distilled water was kept for ultra-sonication for 20 minutes to obtain a light yellowish dispersion. A pH≈10 is achieved for this GO dispersion by adding ~2 mL of ammonia solution (25%). Further, 400 µL of hydrazine hydrate solution (H_6N_2O) was added and the solution was kept under ultra-sonication at a temperature of 80°C for two hours. Successively, the solution stirred at 95°C for 12 hrs to continue the reduction reaction process and the solution turns black in color. This solution is then filtered, washed and dried at 80° C to collect the RGO.

1.4 Preparation of Gold Nanoparticles (*Au NPs*) *and the stabilization with PVP.*

Gold nanoparticles (Au NPs) were synthesized following seeded-growth method by Perrault *et al* [3]. Briefly 50 ml ultrapure water was heated under reflux. While boiling 300 µL gold(III) chloride solution (1 wt. %) is added followed by 900 µl sodium citrate solution (1 wt. %) after 2 mins of stirring. The solution is boiled for additional 2 minute and cooled at room temperature. The color changed to red during the reaction.

The obtained Au NPs seeds have a diameter of 20 nm. In a second step these seed particles were grown bigger to Au NPs stabilized by polyvinylpyrrolidone (PVP). In this regard, 250 ml ultrapure water, 10 ml of the seed solution, 2.5 ml gold (III) chloride solution (1 wt. %) and 2.5 g PVP were mixed in a Erlenmeyer flask. After the addition of 5 ml 0.03 M hydroquinone solution, the colloid is stirred for one day at room temperature. The obtained Au NPs have a diameter of 50nm.

1.5 Preparation of 2D-CNS-Au NPs composites

Both 2-Dimensional CNS materials (graphene derivatives GO and RGO) were taken at a concentration of 2 mg/mL in DW in separate vials. These dispersions were sonicated for 30 minutes to make a homogeneous dispersion. From the well dispersed CNS solution, 700 µl taken out in a 2 ml Eppendorf and added 300 µl of diluted spherical Au NPs of ~ 50 nm size. This was further sonicated for 10 minutes and kept in a vibrating stand until the thin film formation.

1.6 Fabrication of CNS, CNS-4-MBA and CNS-Au NPs-4-MBA thin film electrodes on Si-substrate

For fabricating a thin film of CNS and CNS-Au NPs on silicon (Si) substrate, all the silicon substrates were well cleaned by the standard protocol. On this Si substrate of 5mm × 5 mm dimensions, the CNS/ CNS-Au NPs were spin coated separately using 10 µL of hybrid solution. These substrates were dried at a temperature of 70 °C. On these CNS/ CNS-Au NPs substrates, 5 µl of Raman marker solution of 4-MBA (1 µM) was incubated for overnight at room temperature. These CNS-4-MBA and CNS-Au NPs- 4-MBA were further used for to conduct the SERS experiments.

2 Characterization of the materials

The structural characterization of GO and RGO, were characterized by X-ray diffraction (XRD) technique (Rigaku miniflex-II diffractometer at 30 kV, 15mA). The wavelength of Cu-Kα1 radiation of λ = 1.5405 Å was used for obtaining the XRD pattern.TEM images were obtained using a Zeiss EM 902 instrument. The SERS measurements through Raman mapping experiments were conducted with a confocal Raman microscope (WITec Alpha 300R, 30 cm focal length and 600 grooves per mm grating spectrometer) equipped with an EM-CCD. A 632.8 nm line from a He-Ne laser was focused onto the sample using a 40 × objective (Olympus) with a numerical aperture of 0.6 (5 mW laser power at the sample). For the Raman mapping, an area of (100 × 100) μm^2 is scanned with an interval of 2µm with an integration time of 1 s.

3 UV-Vis absorption studies

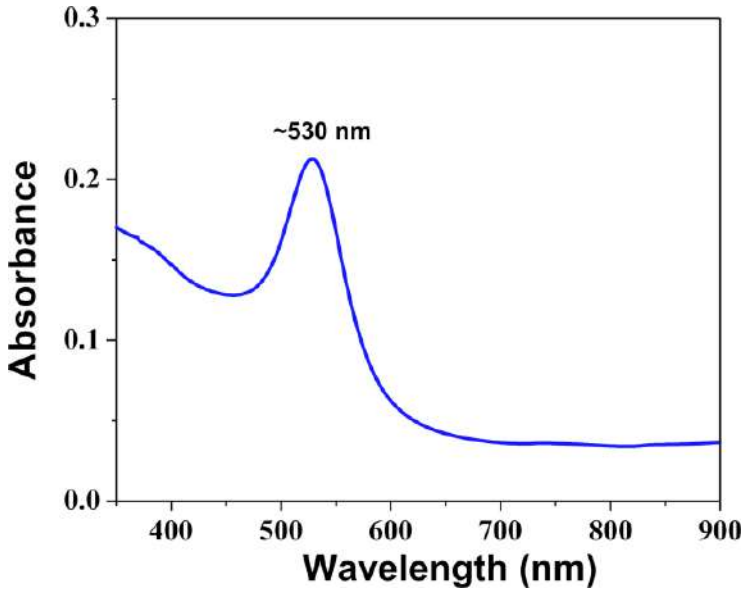

Fig S1. UV-vis absorption spectra of PVP stabilized Au NPs

Figure S1 shows the typical absorption UV-Vis spectrum of the PVP stabilized Au NPs in distilled water. The absorption peak due to the surface plasmon resonance of Au NPs is centered on 530 nm which

is more red shifted in nature comparing to nanoparticles of lesser particle size.

4 XRD studies of 2D-CNS base materials

The XRD pattern of the as-synthesized 2D CNS base materials, namely GO and RGO are presented in Fig S2. GO shows a strong diffraction peak at ~ 11° (Fig S2a), which corresponds to the (002)

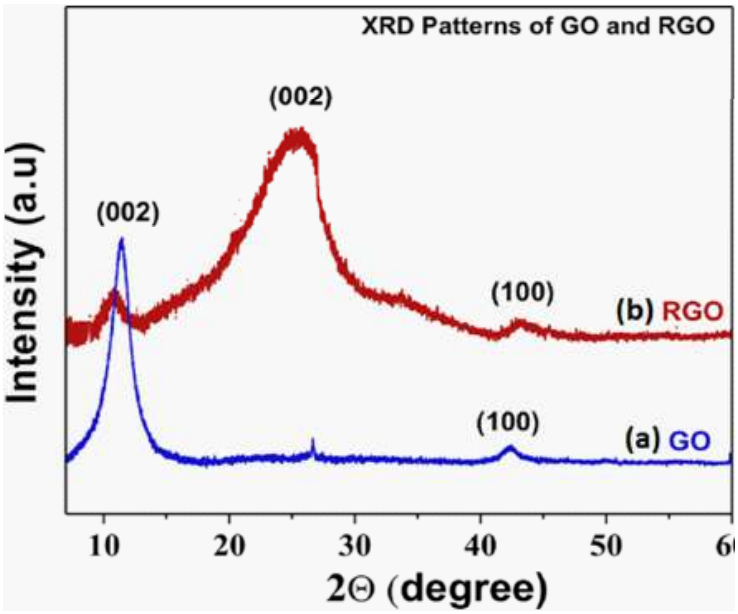

Fig S2. XRD Patterns of GO and RGO

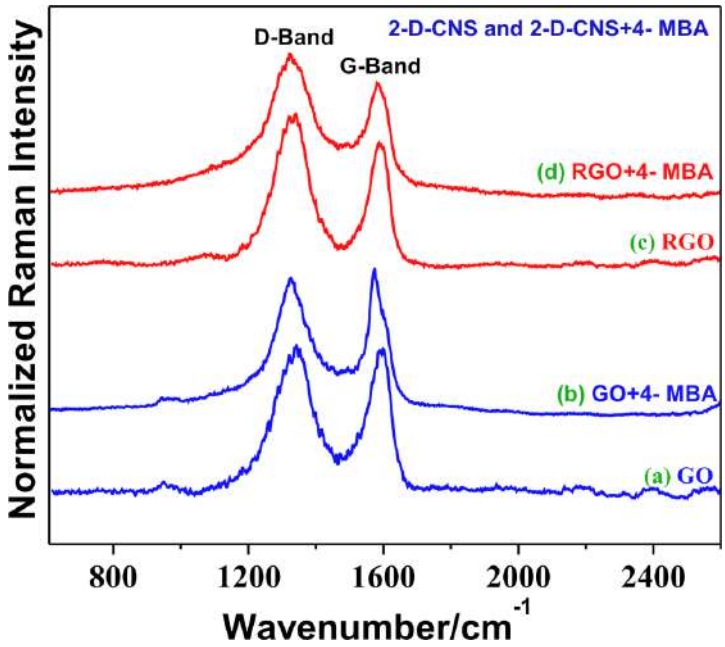

Fig S3. Normalized Raman spectra of (a) GO on Si-substrate where prominent D, G bands of CNS are marked; (b) GO base materials immobilized with Raman marker 4-MBA (5µL, 1 µM); (c) RGO on Si-substrate, (d) RGO base materials immobilized with Raman marker 4-MBA (5µL, 1 µM)

reflection. plane with a d-spacing of 8.0 Å [1].

The weak and broad band around 42º corresponding to the (100) reflection is due to the turbo static band of disordered carbon material. The most prominent diffraction peak of RGO is observed at ~24.5º (002) attesting the characteristic band of RGO ((Fig S2b) with an interlayer spacing of 3.4 Å. This value matches with the well-known XRD peak of RGO [4].

5 Raman spectra of 2D-CNS base materials and 2D-CNS+4-MBA

Figure S3 displays the Raman spectrum of 2D- CNS base materials (GO and RGO) which were spin coated on the Si-substrate. In Figs S3 (a) and (c), clearly shows the characteristic D and G bands centered around 1340 and 1580 cm^{-1}. The broad nature of D-band (disorder band) observed for both GO and RGO is due to their different functional groups and sp^3 hybridization present in these materials. Figures S3 (b) and (d) represent individual Raman spectrum of 2D CNS base materials, GO and RGO, respectively, which were immobilized with 1 μM of 4-MBA. The results attest GO and RGO both as SERS substrates due to the contributions from CM effect (as in GERS). Clearly, the G- band becomes sharper in nature due to the main Raman peak of 4-MBA centered around 1585 cm^{-1}, which is due to the ν(CC) ring stretching coinciding at the same position.

References

1. Marcano D C, Kosynkin D V, Berlin J M, Sinitskii A, Sun Z, Slesarev A, Alemany L B, Lu W, Tour J M,*ACS Nano*;4 (2010)4806-4814.
2. Li D, Müller M B, Gilje S, Kaner R B, Wallace G G, *Nat Nanotechnol*, 3(2008)101-105.
3. Perrault S D, Chan W C W, *J Am Chem Soc*,131(2009)17042-17043.
4. Park S, An J, Potts J R, Velamakanni A, Murali S, Ruoff R S, *Carbon,* 49(2011)3019-3023.

IOSR Journal of Business and Management (IOSR-JBM)
e-ISSN: 2278-487X, p-ISSN: 2319-7668. Volume 20, Issue 1. Ver. VIII (January. 2018), PP 66-70
www.iosrjournals.org

Random Walk Share Price Movements of Ashok Leyland Ltd. Irrespective of Active Corporate Initiatives

Mr.Shino P. Jose, Prof. Dr. T. Asokan
Assistant Professor St. Pius X College, Rajapuram Kerala
Pro Vice-Chancellor Kannur University Kerala
Corresponding author: Mr.Shino P. Jose

Abstract: *The corporate decisions are generally considered to be influencing the share price movements since the share price movements are found to be highly sensitive. There is literature support describing the association of corporate achievements, decisions, events and financial results with share price movements. Data have been collected from Ashok Leyland Ltd. during the period from January 2014 to December 2016. The decision study has been conducted based on the data collected. Each of the achievements, decisions, events have been analysed very closely and their impact on share price movements have been identified. Both percentage analysis and paired t-test have been applied in the methodology. The random walk of share price movement has been observed in spite of active initiatives from the part of Ashok Leyland Ltd.*

Date of Submission: 11-01-2018 Date of acceptance: 03-02-2018

This study is a close analytical effort into the corporate decisions of Ashok Leyland Ltd.. Various achievements, decisions, events and financial results of Ashok Leyland Ltd. during the period from January 2014 to December 2016 have been very closely and deeply analysed. The various corporate initiatives have been classified as under:

1. Acquisition/Merger/Collaboration – 01
2. Financial Results – 02
3. Certification/Awards/ Achievement– 03
4. General – 04
5. Production/Project/New Initiatives -05
6. Crisis/Disaster – 06
7. Divestment – 07
8. Patents -08

It has been observed that there are two classes of such major initiatives by the company and they are encoded as 2 and 5 as specified above. The financial results and production/project/new initiatives of Ashok Leyland Ltd. during January 2014 to December 2016 have been collected and linked with the share price movement of Ashok Leyland Ltd. in the same period. The pre-declaration and post declaration prices of Ashok Leyland Ltd. in connection with the declaration of thefinancial results and production /project/ new initiatives have been used for identifying the impact.

I. Research Methodology and Design

Data have been collected from secondary sources alone. The press release, publications and news paper coverage have been the main sources. The collected data are entered in various tables specifying the dates.

1. The percentage change in the share price in connection with the acquisitions /mergers/collaborations, financial results and production/project/new initiatives have been calculated and tabled.
2. Paired t-test using online graph pad was used to identify the impact of the acquisitions /mergers/collaborations, financial results and production/project/new initiatives on share price movement.

II. Data Analysis and Interpretation

1. Percentage Analysis

1.

Date	Date: 06th January 2014
Classification	Production/Project/New Initiatives -05 (1)
Decision	Ashok Leyland, the flagship of the Hinduja group, launched the **CAPTAIN series of next-generation heavy commercial vehicles**.
Percentage Change	-2.91
Share Price Movement	18.90 – 18.35, Downward, Negative by Rs..55.

2.

Date	Date: 21st January 2014
Classification	Financial Results – 02 (1)
Decision	Q3 was tough. Ashok Leyland's performance for the quarter closing at Rs.1,953 crores (Rs. 2,406 crores same period last year) with a net loss (PAT) of Rs. 167 crores (PAT Rs. 74 crores, same period last year). Slowdown in the Commercial Vehicle business and a YOY drop of 32% in Total Industry Volume (TIV) has reflected in the performance of Ashok Leyland also
Percentage Change	2.37
Share Price Movement	16.85 – 17.25, Upward, Positive by Rs..4.

3.

Date	Date:30th January 2014
Classification	Production/Project/New Initiatives -05 (2)
Decision	Ashok Leyland launches state-of-the-art LCVs A product of the Nissan-Ashok Leyland joint-venture Powered by the advanced, efficient ZD30 Common Rail diesel engine
Percentage Change	.92
Share Price Movement	16.30 – 16.45, Upward, Positive by Rs..15.

4.

Date	Date: 13th June 2014
Classification	Production/Project/New Initiatives -05 (3)
Decision	Ashok Leyland receives a huge order for 2,200 buses from the Government of Sri Lanka
Percentage Change	-2.96
Share Price Movement	33.75 – 32.75, Downward, Negative by Rs.1.

5.

Date	Date: 09th July 2014
Classification	Production/Project/New Initiatives -05 (4)
Decision	Ashok Leyland Ltd, flagship of the Hinduja Group, has raised Rs. 667 crores via a Qualified Institutions Placement (QIP).
Percentage Change	-7.2
Share Price Movement	35.20 – 32.65, Downward, Negative by Rs.2.55.

6.

Date	Date: 25th July 2014
Classification	Financial Results – 02 (2)
Decision	The Company registered a 4.8% increase in turnover - Rs. 2,477.80 crores for the quarter ended June 30, 2014, as against Rs. 2,363.81 crores of the corresponding quarter in 2013. Sale of M&HCV vehicles for the quarter stood at 14,949 numbers (14,900). Sale of Light Commercial Vehicles stood at 5,032 nos. (6,824)
Percentage Change	-4.10
Share Price Movement	34.15 – 32.75, Downward, Negative by Rs.1.4.

7.

Date	Date:09th September 2014
Classification	Production/Project/New Initiatives -05 (5)
Decision	Ashok Leyland has received orders for around 4000 buses from State Transport Undertakings (STUs) worth nearly INR 1500 Crores. A total of 22 STUs across the country have placed large orders on the company
Percentage Change	7.77
Share Price Movement	38.60 – 41.60, Upward, Positive by Rs.3.

8.

Date	Date:11th September 2014
Classification	Production/Project/New Initiatives -05 (6)
Decision	Ashok Leyland's Pantnagar manufacturing plant rolls out its 100,000th vehicle
Percentage Change	-.36
Share Price Movement	41.60 – 41.45, Downward, Negative by Rs..15.

9.

Date	Date: 06th November 2014
Classification	Financial Results – 02 (3)
Decision	**Ashok Leyland** recorded a net profit of Rs. 72.73 crores for the **first half** of FY 2014-15, as against a loss of Rs. 166.80 crores for the corresponding period last year. Revenues hiked by 16% and stood at Rs. 5,695.48 crores, as against Rs. 4913.43 crores for the same period last year.
Percentage Change	5.13
Share Price Movement	46.75 – 49.15, Upward, Positive by Rs.2.4.

10.

Date	Date: 17th November 2014
Classification	Production/Project/New Initiatives -05 (7)
Decision	Ashok Leyland bags major projects from Africa worth USD 79.2 mn
Percentage Change	-1.28
Share Price Movement	54.50 -53.80 , Downward, Negative by Rs..7.

11.

Date	Date: 29th January 2015
Classification	Financial Results – 02 (4)
Decision	Ashok Leyland reports 72 % growth in revenue and substantial improvement in profits. Ashok Leyland recorded revenues of Rs. 3361.00 crores, as against Rs. 1953.21 crores for the corresponding period last year. Net profit is reported as Rs. 32.09 crores for Q3, as against a net loss of Rs. 167.21 crores for Q3 in the previous year year.
Percentage Change	-3.67
Share Price Movement	68.20 – 65.70, Downward, Negative by Rs.2.5.

12

Date	Date: 12th May 2015
Classification	Financial Results – 02 (5)
Decision	Ashok Leyland FY'15 net profit at Rs.335Cr against Rs.29Cr in FY'14. Ashok Leyland recorded sales revenues of Rs.13562 Crores as against Rs.9943 Crores in the previous fiscal.
Percentage Change	-6.14
Share Price Movement	74.15 – 69.60, Downward, Negative by Rs.4.55.

13.

Date	Date: 22nd June 2015
Classification	Production/Project/New Initiatives -05 (8)
Decision	Ashok Leyland wins order for buses worth 82 mn USD from Senegal
Percentage Change	2.29
Share Price Movement	69.80 – 71.40, Upward, Positive by Rs.1.6.

Company :ASHOK LEYLAND LTD. 500477

Period: 19-Jun-2015 to 23-Jun-2015

All Prices in ₹

14.

Date	Date: 12th August 2015
Classification	Financial Results – 02 (6)
Decision	Ashok Leyland reports revenue growth of 55% and EBITDA grows by 287%. EBITDA for Q1 is reported as Rs.388.69 crores, against Rs.100.50 Crores same period last year, while Profit Before Tax (PBT) is reported to be Rs.234.90 Crores, against a loss of Rs.(70.45) Crores same period last year.
Percentage Change	1.78
Share Price Movement	86.90 – 88.45, Upward, Positive by Rs.1.55.

15.

Date	Date: 04th November 2015
Classification	Financial Results – 02 (7)
Decision	Q2 revenue grows 54%, EBITDA up 260% • H1 revenue grows 54%, EBITDA up 298%
Percentage Change	-3.93
Share Price Movement	90.35 – 86.80, Downward, Negative by Rs.3.55.

16.

Date	Date: 27th November 2015
Classification	Production/Project/New Initiatives -05 (9)
Decision	Ashok Leyland wins contract for 3600 vehicles worth $200Mn from Cote D'Ivoire
Percentage Change	.48
Share Price Movement	94.05 – 94.50 , Upward, Positive by Rs..45.

17.

Date	Date: 11th February 2016
Classification	Financial Results – 02 (8)
Decision	Ashok Leyland reports revenue growth of 22%, Net Profit growth of 519% in the Q3
Percentage Change	-4.75
Share Price Movement	87.35 – 83.20, Downward, Negative by Rs.4.15.

18.

Date	Date: 14th June 2016
Classification	Financial Results – 02 (9)
Decision	In the FY 2015 -16, Ashok Leyland standalone annual revenue grows 39% to Rs. 18,822 crores, Operating PAT up 3.75 times
Percentage Change	-1.95
Share Price Movement	105.10 – 103.05, Downward, Negative by Rs.2.05.

19.

Date	Date: 21st July 2016
Classification	Financial Results – 02 (10)
Decision	In the Q1 FY 2016-17,Ashok Leyland sales is up by 10%, Net Profit grows by 101%
Percentage Change	3.53
Share Price Movement	93.45 -96.75, Upward, Positive by Rs.3.3.

20.

Date	Date: 07th September 2016
Classification	Acquisition/Merger/Collaboration – 01 (1)
Decision	Nissan and Ashok Leyland to embark on new phase in business relationship. Nissan has agreed to sell to Ashok Leyland all of Nissan's shares in three joint venture companies that were formed in the year 2008. These joint ventures are for technology development, and manufacturing of power trains and vehicles
Percentage Change	2.45
Share Price Movement	85.75 – 87.85, Upward, Positive by Rs.2.1.

21.

Date	Date: 17th October2016
Classification	Production/Project/New Initiatives -05 (10)
Decision	Ashok Leyland launches 'Circuit' Series – first Electric Bus which is made in India
Percentage Change	3.91
Share Price Movement	80.65 – 83.80, Upward, Positive by Rs.3.15.

22.

Date	Date: 09th November 2016
Classification	Certification/Awards/ Achievement– 03 (1)
Decision	Ashok Leyland, Pantnagar manufacturing facility won the prestigious 2016 Deming Prize for the successful implementation of Total Quality Management
Percentage Change	-2.51
Share Price Movement	91.75 – 89.45, Downward, Negative by Rs.2.3.

2. Testing of Hypothesis

1. There is no significant difference between the pre-declaration share price and the post declaration share price when the financial results of Ashok Leyland Limited is announced.
2. There is no significant difference between the pre-declaration share price and the post declaration share price when the production/ project/ new Initiatives decisions of Ashok Leyland Limited is announced.

Ashok Leyland (Hinduja Group)

20 Ashok Leyland									
Decisions	**Pre**	**Post**	**% C**	**Pre- Mean**	**Post-Mean**	**t value**	**p value**	**Decision**	
1	85.75	87.85	2.45						
2	16.85	17.25	2.37						
2	34.15	32.75	-.4.10						
2	46.75	49.15	5.13						
2	68.2	65.7	-3.67						
2	74.15	69.6	-6.14						
2	86.9	88.45	1.78						
2	90.35	86.8	-3.93						
2	87.35	83.2	-4.75						
2	105.1	103.05	-1.95						
2	93.45	96.75	3.53	70.325	69.27	1.1876	0.2654	Not Significant	
3	91.75	89.45	-2.51						

5	18.9	18.35	-2.91						
5	16.3	16.45	0.92						
5	33.75	32.75	-2.96						
5	35.2	32.65	-7.2						
5	38.6	41.6	7.77						
5	41.6	41.45	-0.36						
5	54.5	53.8	-1.28						
5	69.8	71.4	2.29						
5	94.05	94.5	0.48						
5	80.65	83.8	3.91	48.335	48.675	0.6003	0.5631	Not Significant	

Decision 2

Group	Pre Declaration	Post Declaration
Mean	70.325	69.27
SD	28.7765	28.3292
SEM	9.0999	8.9585
N	10	10

Decision 5

Group	Pre Declaration	Post Declaration
Mean	48.335	48.675
SD	25.9292	26.7646
SEM	8.1995	8.4637
N	10	10

1. **The hypothesis is accepted**
2. **The hypothesis is accepted**

III. Findings

1. It has been noted that the financial results of Ashok Lyland Ltd. do not make any impact on the share price movements of Ashok Lyland Ltd.
2. It has been noted that the production/project/new initiatives decisions of Ashok Lyland Ltd. do not make any impact on the share price movements of Ashok Lyland Ltd.
3. There is a random walk in the share price of Ashok Lyland Ltd.

IV. Conclusion

The random walk theory is found to be very much applicable to the share price movements of Ashok Leyland Ltd.. During the years 2014, 2015 and 2016, the researcher has identified 2 categories of decisions of Ashok Leyland Ltd. and it has been noted that the share prices of Ashok Leyland Ltd. are not being significantly influenced by them. There is a random walk which could be yet again some external sources of power leading into this random walk.

References

[1]. Stulz, R. M. (1990). Managerial discretion and optimal financing policies. Journal of Financial Economics, 26(1), 3–27.
[2]. Tobin, J. (1969). A general equilibrium approach to monetary theory, Journal of Money, Credit and Banking, 1(1), 15–29.
[3]. Wilson, G. P. (1986). The relative information content of accruals and cash flows: combined evidence at the earnings announcement and annual report release date. Journal of Accounting Research, 24(1986), 165–200.
[4]. Xie, F. (2009). Managerial flexibility, uncertainty, and corporate investment: the real options effect. International Review of Economics and Finance, 18(4), 643–655.

Mr.Shino P. Jose "Random Walk Share Price Movements of Ashok Leyland Ltd. Irrespective of Active Corporate Initiatives." IOSR Journal of Business and Management (IOSR-JBM) 20.1 (2018): PP 66-70.

IMPACT FACTOR: 3.072 (SJIF)
ISSN 2348 – 0653 (Print)
ISSN -2347-856X (Online)

Ref No. IJBARR- Jan 2016 *Date: 20/01/2016*
Bangalore - 83.

To
Mr. Shino P. Jose
Assistant Professor, Department of Business Administration, St. Pius X College, Rajapuram, Kerala.

Sub: IJBARR- Acceptance Letter for Publication

Dear author, Thank you for your research paper submission, we appreciate your research paper quality and Standard, It is our pleasure to inform you that, your case study titled as **"An Empirical Investigation of the Purchasing Power Pass – Tnrough to Inflation and Stock Market Indices in India"** is accepted for our current publication, your paper will be published and accessible in Online (www.ijbarr.com) with ISSN -2347-856X on or before **30/01/16.**We will send your printed(**Two**) copy of IJBARR (ISSN 2348–0653 Print) Journal through professional courier on or before **19/02/16.** Please send your complete address to send your hard copy for postal purpose.

For any clarification please visit **www.ijbarr.com.**

Please send your scan copy of copy right form (available in our web portal) and publication charge **INR (₹) 2750**(Publication charge includes printing, online publication & logistics charge) on or before **23/01/16.**Your early confirmation may help us to edit your paper for our current publication.

You may use online transfer payment mode (or) directly deposit to any branch (Please send the payment details soon after your payment)

D.Loganathan
Saving Bank Acc. No: 20230803596,
IFSC: SBIN0014951,
State Bank of India,
Hulimavu Branch,
Bangalore -560076. India.

For additional copy you may pay INR(₹) 550 with publication charge.

For Correspondence
The Managing Editor
International Journal of Business and Administration Research Review,
Bangalore, Karnataka.
Mobi: 09500520177, 07204682715, 09986881177
E-mail: ijbarr2013@gmail.com

With Regards

The Editor

Copy to : Prof. (Dr.) T. Asokan, *Pro-Vice Chancellor, Kannur University, Thavakkara , Kerala.*

02

Effect of Decision Styles on Consumer Decision Making Process

Biju Joseph*
Dr. P Mohan**

Abstract

Decision making is the process of choosing the most appropriate alternative from the available set of alternatives. Individuals have certain consistent pattern of decision making known as decision styles. These styles are called directive, analytical, conceptual and behavioural. Selection of a product or service is a typical situation that involves complex decision making skills. In this study the effect of individual's decision style on the consumer's decision making process is explored in detail. The results show that there is no significant effect for the decision style on the consumer's purchase process.

Introduction

Decision making is a very pervasive function. In day-to-day life, human beings are confronted with frequent situations that warrant decisions. A purchase situation is a typical condition that requires a proper decision from the

* *Assistant Professor, Dept. of Business Administration, St. Pius X College, Rajapuram.*
** *Professor, Dept. of Commerce and Management Studies, University of Calicut.*

buyer. Studies of decision making have brought to light different versions of the decision making process that depend both on internal factors and external environment.

Review of Related Literature

Research on decision making produced numerous versions of decision making processes and styles. The word decision has been defined as "an answer to some question, a choice between two or more alternatives" (Rowe et al, 1984). According to Krumboltz and Hamel (1977) making a decision a series of steps, namely, defining the problem, creating a plan of action, examining possible alternatives and outcomes, and starting the action. Alker et. al., (1972) argued that the process of making decisions is based on the availability of information. Pitz and Harren (1980) pointed out that a decision maker faces at least two alternatives evaluated according to his or her values and preferences. Phillips (1997) argued that the process of decision making involves five stages: (a) identifying all possible alternatives; (b) valuing the alternatives; (c) assembling the information; (d) swapping between preferences and outcomes; and (e) selecting the most favorable alternative yields to the decision.

Rowe et al. (1984) suggested that decision-making is a process that includes the element of evaluating the merit of the potential consequences. Rowe and Mason (1987) referred to the decision making process as a cognitive process comprised of five elements: (1) the stimulus; (2) the individual's response to the stimulus; (3) the thinking about the problem; (4) executing the decision; and (5) determining the effectiveness of the decision.

Thunholm (2004) investigated the relationship between decision-making styles, self-esteem and self-regulation. Rowe et al. (1984) proposed the term decision style, which reflects the way a person uses information to reach a decision. Decision style focuses attention on the way one uses information and derives meaning from it. According to Rowe and Boulgarides (1992), identifying one's decision style may predict behavior such as reactions to stress, motivation, problem solving abilities, and general manner of thinking. The decision profile of any given individual reflects a combination of all four styles. It may be characterized as either one dominant style or as a balanced profile with all four styles at a similar strength. The four decision styles are described below.

The Directive style

This style is characterized by low tolerance for ambiguity and low cognitive complexity. The orientation is focused on task and technical concerns. Persons characterized with this style are described as practical, autocratic, rigid, impersonal, and have a strong desire for power and control. They have a need for

speed, efficient and satisfactory solutions because they have limited information and few alternatives. People with this style show preference for structure and specific information and facts, which are usually given in a verbal way (Connor & Becker, 2003).

The Analytical Style

This style demonstrates a much greater tolerance for context ambiguity and tends toward the need for greater volumes of information and the consideration of large sets of alternatives. Analytical style decision makers are best at coping with new, often unexpected situations and contexts. Their orientation toward detail often results in extended investigations of the problem context before a final decision is made. They analyze and examine details, desire to achieve the best possible solutions and are able to predict outcomes (Connor & Becker, 2003; Bou1garides & Cohen, 2001).

The Conceptual style

This orientation is connected to people and their social concerns. Such persons are creative and tend to take risks in finding answers. They have the ability to understand complex relationships. Intuition guides their search for information and examinations of multiple sources and alternatives. Persons characterized with this style are people-oriented, open and from truthful relationships with others. Such individuals do not look for control and power rather they like to share such things with others. They are very personable, flexible, and tend to be idealistic, having a strong emphasis on values and ethics (Connor & Becker, 2003; Boulgarides & Cohen, 2001; Rowe & Davis, 1996; Rowe & Mason, 1987).

The Behavioural style

Behavioural types display a people orientation. This style requires a relatively low amount of data input and as such generally demonstrates a relatively short range vision. They are conflict averse by nature and tend to rely on others opinion. This style is characterized by low tolerance for ambiguity and low cognitive complexity. Such people are supportive and friendly. They have open communication and are interactive, interested in others, open to suggestions, warm, and empathic. They enjoy being surrounded by people, and tend to avoid conflicts. (Connor & Becker, 2003; Boulgarides & Cohen, 2001; Rowe & Davis, 1996).

Consumer Decision making

A detailed analysis of consumer decision making situations will result in a typical consumer problem solving model consisting of four basic types of activities in the process of purchasing. These four steps are: (1) problem recognition, (2) information search and evaluation, (3) purchase decision, and (4) post

purchase behaviour. The following assumptions underlie the consumer problem solving model.

Problem Recognition

Problem recognition results when a consumer recognises a difference between the desired state of affairs and the actual state of affairs, enough to arouse and activate the decision process. The first stage in this process appears to be internal search that involves scanning memory for stored information that is relevant to the purchase situation under consideration. This available information has been previously acquired from passive reception experiences as well as through active external searches (Beales et al., 1981). In majority of cases, information acquired from an internal memory scan is sufficient for meeting the needs of the consumer. Consequently, a decision will be made without seeking any external information. Consumers become aware of the problem or need when they process the information arising internally or externally. They then become motivated. Thus, the process of problem recognition means that the consumer becomes aroused and activated to engage in some purposeful purchase decision activity.

The information Search Process

Once consumers have recognised the existence of a problem, and assuming there are no constraints preventing further behaviour, they move to the next stage of information search in the decision making process. The term search refers to mental as well as physical information seeking and processing activities which one engages in to facilitate decision making regarding some object in the market place. Search may be undertaken to find out about brands, prices, stores, and so on, related to the product. Search can be categorised as pre purchase or ongoing, based on the purpose and as internal or external, based on its sources. One study showed that most shoppers rely on experiential information sources in retail shopping trips (Elizabeth et al., 1980).

Evaluating Alternatives

There are two broad approaches followed by consumers for processing the information gathered during the search process: brand processing or attribute processing. In choice by processing brands, the buyer assesses one brand at a time. The consumer may decide to look at a particular brand, examine several attributes of that brand, then assess several attributes for a second brand and third brand and so on. In choice by processing attributes, the consumer examines a specific attribute and then compares several other brands on that attribute. Then, a second attribute may be selected for comparison, and so on.

January - December 2014 • ISSN 2231 - 3060

Purchasing Patterns

There are two important purchasing patterns. They are (1) the extent to which consumers exhibit repeat purchasing pattern, known as brand loyalty and (2) the extent to which the purchases are unplanned, known as impulse purchasing.

Brand Loyalty and Impulse Purchasing

Brand loyalty is the consumer's consistent preference and/or purchase of the same brand in a specified product or service category. It consists of both attitudes and actual behaviours toward a brand. Unplanned buying or impulse purchasing is another consumer purchasing pattern. As the word suggests, the purchase was not specifically planned (Stern, 1962).

Post Purchase Behaviour

Consumer decisions do not end with the act of purchase but continue as the consumer uses the product and assesses his or her purchase decision and experience with the item and carryout related purchases. After making a decision to purchase a product, there is some additional behaviour associated with that decision. Two important decisions are on the installation and use of the product and decisions on products or services related to the item purchased.

Post Purchase Evaluation

After making a purchase, the consumer engages in an evaluation of the purchase decision. He/she evaluates the decision in the post purchase stage. This stage serves to broaden the set of experiences stored in consumer's memory along with an evaluation on how well he is performing as a consumer in selecting products, stores etc. The feedback that the consumer gets from this evaluation is used for making adjustments in future buying strategies.

Consumer Satisfaction / Dissatisfaction

An important element in the evaluation stage is the satisfaction derived by the consumer from the buying process. Satisfaction refers to the buyer's impression that he/she is adequately rewarded in a purchase situation for the sacrifices made. Satisfaction is a result of matching the actual product/brand performance with the expected performance or reward from the brand in terms of its anticipated potential to satisfy the consumer's motives (Howard and Sheth, 1969). Once consumers purchase and use a product, they may become either satisfied, dissatisfied or neuteal. Research has revealed that several determinants including demographic variables, personality variables, expectations etc. influence satisfaction (Linda, 1979).

Objectives of the Study

The objectives of the study are as follows:

1) To understand the decision styles of young consumers.

2) To understand the relationship between the decision styles of a consumer and his/her approaches in various stages of purchase decision.

Methodology

This study is designed as a descriptive one based on primary data collected using a questionnaire designed for the purpose. The questionnaire has two parts: i) The Decision Style Inventory, and ii) Consumer Choice Scale.

Decision Style Inventory

The Decision Style Inventory (DSI) was developed by Rowe and Mason to measure the decision style of individuals. The DSI is composed of twenty questions regarding decision-making preferences. Each question has four response options corresponding to each of the decision styles. Individuals are asked to rate each of the four options (behavioral responses) in terms of the likelihood of its use. Individual scores for each decision-making style are computed by summing the scores for the options corresponding to that style (8=most preferred option; 4=option considered often, 2=option considered on occasion, 1=least preferred option). Thus, the raw scores for each dimension - Directive, Analytical, Conceptual, and Behavioral - range from 20 to 160. However, while the instrument is a forced choice instrument, individuals can employ more than one dominant style.

Consumer Choice Scale

A scale is developed by the researcher to evaluate the various aspects of the consumer decision making process. The scale contained 63 items on a five-point Likert scale ranging from 1 (strongly disagree) to 5 (strongly agree) which in turn measures 15 latent variables associated with consumer decision making. The reliability of the scale was calculated using Cronbach's alpha and it was found satisfactory (0.812). The reliability coefficients of all subscales were above 0.6.

Sample Design

110 undergraduate business management students belonging to Kasargod District were selected as the sample for the study using judgment sampling method. The following table shows the classification of the sample on

the basis of gender, and socio-economic class. The latest Socio Economic Classification (SEC) has 12 grades arranged in 5 classes. Under the classes A and E, there are three grades each as A1, A2, A3 and E1, E2, E3 respectively. In all other classes there are two grades each. (B1, B2, C1, C2, D1, and D2).

Table 1 : Profile of the Sample

		Frequency	Percent
Gender	Male	48	43.6
	Female	62	56.4
	Total	110	100.0
Socio Economic Class (SEC)	A	54	49.09
	B	30	27.27
	C	16	14.55
	D	7	6.36
	E	3	2.73
	Total	110	100.0

Source : Primary data

Hypotheses

Eight hypotheses were formulated for the study. They are given below.

H1: There is no association between gender and decision style.

H2: There is no significant difference in need recognition approache among consumers having different decision styles.

H3: There is no significant difference in information search of consumers with different decision styles

H4: The motivations of consumers with different decision styles are the same.

H5: The intensity of evaluation of alternatives of consumers with different decision styles is the same.

H6: There is no significant difference in the product choice strategies of consumers with different decision styles.

H7: There is no significant difference in impulse purchase orientation of consumers with different decision styles.

H8: There is no significant difference in post purchase satisfaction of consumers with different decision styles.

Tools of Analysis

Various mathematical and statistical tools such as percentage, mean, Chi-square test, and ANOVA are used for the analysis of data.

Table 2 : Decision styles of the respondents

Style	Frequency	Percent
Directive	6	5.5
Analytical	22	20.0
Conceptual	26	23.6
Behavioural	52	47.3
Analytic Conceptual	3	2.7
Conceptual Behavioural	1	.9
Total	110	100.0

Source : Primary data

The most pervasive decision style among the respondents (47.3 percent) is Behavioural style which reflects a people orientation. Conceptual style occupies the second position (23.6 percent) and is closely followed by the analytical style (20 percent). The directive style is the least preferred (5.5 percent) style among the respondents. Four respondents who have a combination of two styles were excluded from further analysis.

umers with different

choice strategies of

chase orientation of

hase satisfaction of

s percentage, mean,
ta.

dents

Percent
5.5
20.0
23.6
47.3
2.7
.9
100.0

spondents (47.3 per-
ion. Conceptual style
followed by the ana-
referred (5.5 percent)
a combination of two

Table 3 : Mean scores of respondents for variables related with consumer choice

Variables	Male		Female		Combined	
	Mean	S.D.	Mean	S.D.	Mean	S.D.
Intrinsic Need	3.64	0.72	3.93	0.71	3.78	0.72
Extrinsic Need	3.13	0.88	2.98	0.84	3.05	0.86
Extensive Information Search	3.74	0.80	3.41	0.78	3.58	0.79
Internal Information Search	3.32	0.84	3.33	0.88	3.32	0.86
External Information Search	3.11	0.89	3.39	0.79	3.25	0.84
Intensity of Evaluation	3.25	1.08	3.06	0.99	3.16	1.03
Choice by Processing Brands	3.07	0.96	3.25	0.82	3.16	0.89
Choice by Processing Attributes	3.49	0.83	3.66	0.63	3.58	0.73
Hedonic Motivation	2.99	1.02	3.34	0.91	3.17	0.96
Utilitarian Motivation	3.35	1.03	3.07	0.96	3.21	1.00
Post Purchase Satisfaction	3.28	0.91	2.75	0.85	3.01	0.88
Impulsive Purchase	2.87	0.85	3.13	0.69	3.00	0.77

Source : *Primary data*

The table shows that males have higher mean scores in the areas like extrinsic need recognition, extensive information search, intensity of evaluation of alternative brands, the utilitarian motivation of shopping and post purchase satisfaction. Females have a higher proclivity in the areas of intrinsic need recognition, external information search.

Testing of Hypothesis 1

Table 4 : Cross Tabulation of Gender and Decision Style

Gender		Decision Style of the Person				Total
		Directive	Analytical	Conceptual	Behavioural	
Male	Count	4	10	11	21	46
Female	Count	2	12	15	31	60
Total	Count	6	22	26	52	106

The chi-square test of independence was applied and the result is given below

Table 5 : Chi-Square Tests

	Value	df	Asymp. Sig. (2-sided)
Pearson Chi-Square	1.57	3	.667

The Pearson chi-square value is 1.57 with 3 degrees of freedom and p values is 0.667 > 0.05 which is not significant. So the hypothesis that there is no association between gender and decision style is accepted.

Table 6 : Cross tabulation of Decision Styles and Consumer Choice Variables

Consumer choice variables	Decision Style of the Person				Total
	Total	Directive	Analytical	Conceptual	
Intrinsic Need Recognition	3.21	4.01	3.88	3.74	3.80
Extrinsic Need Recognition	3.08	2.92	3.05	3.09	3.04
Extensive Information Search	3.54	3.60	3.52	3.55	3.55
Internal Search	3.08	3.36	3.36	3.32	3.32
External Search	3.33	2.91	3.39	3.35	3.27
Intensity of Evaluation	3.29	3.42	3.05	3.06	3.14
Choice by brand processing	2.46	3.41	3.16	3.16	3.17
Choice by attributes	3.54	3.50	3.53	3.66	3.59
Hedonic Motivation	3.33	3.09	3.35	3.13	3.19
Utilitarian Motivation	2.89	3.35	3.06	3.22	3.19
Post purchase satisfaction	2.13	3.34	3.08	2.87	2.98
Impulsive purchase	2.92	3.02	3.04	3.02	3.02

Analysis of variance was performed to see whether any significant difference exist between different decision styles in relation to various consumer choice variables. The results are summarized in the table below.

Table 7 : Test statistic and significance value of ANOVA

Variables	F	Sig.
Intrinsic Need Recognition	2.269	.085
Extrinsic Need Recognition	.204	.893
Extensive Information Search	.042	.988
Internal Search	.182	.908
External Search	1.746	.162
Intensity of Evaluation	.763	.517
Choice by brand processing	1.891	.136
Choice by attributes	.335	.800
Hedonic Motivation	.396	.756
Utilitarian Motivation	.520	.669
Post purchase satisfaction	3.460	.019
Impulsive purchase	.040	.989

Testing of Hypothesis 2

Analysis of variance shows that the effect of decision styles on intrinsic need recognition is not significant, $F(3,102) = 2.269$, $p < 0.05$. Similarly the effect of decision styles on extrinsic need recognition is also not significant, $F(3,102) = 0.204$, $p > 0.05$. Therefore the hypothesis that there is no significant difference in need recognition of consumers with different decision styles is accepted.

Testing of Hypothesis 3

Statistical test using ANOVA shows that the effect of decision styles on extensive search of information is not significant, $F(3,102) = 0.42$, $p > 0.05$. Therefore the hypothesis that there is no significant difference in information search of consumers with different decision styles is accepted.

Testing of Hypothesis 4

Analysis of variance shows that the effect of decision styles on consumer's hedonic purchase motivation is not significant, $F(3,102) = 0.396$, $p > 0.05$. Similarly the effect of decision styles on consumer's utilitarian motivation of purchasing is also not significant, $F(3,102) = 0.52$, $p > 0.05$. Therefore the hypothesis that the buying motives among the consumers with different decision styles are the same is accepted.

Testing of Hypothesis 5

Statistical test using ANOVA shows that the intensity of evaluation of alternatives among consumers with different decision styles is the same. The test statistic $F(3,102) = 0.42$, $p > 0.05$, shows that the difference mean scores is not significant. Therefore the hypothesis that the intensity of evaluation of alternatives among consumers with different decision styles is the same is accepted.

Testing of Hypothesis 6

Consumers are said to follow the strategies of processing by brands and processing by attributes in selecting a particular alternative. The application of ANOVA shows that the difference among the consumers with different decision styles in the strategy of choice by processing brands is not significant, $F(3,102) = 1.89$, $p > 0.05$. Similarly the difference among the consumers with different decision styles in the strategy of choice by processing attributes is also not significant, $F(3,102) = 0.34$, $p > 0.05$. Therefore the hypothesis that there is no significant difference in the product choice strategy adopted by the consumers with different decision styles is the same is accepted.

Testing of Hypothesis 7

Analysis of variance shows that the effect of decision styles on impulse purchase orientation is not significant, $F(3,102) = 0.40$, $p > 0.05$. Therefore the hypothesis that there is no significant difference in impulse purchase orientation of consumers with different decision styles is accepted.

Testing of Hypothesis 8

Analysis of variance shows that the difference in post purchase satisfaction of consumers with different decision styles is significant, $F(3,102) = 0.3.46$, $p < 0.05$. Therefore the hypothesis that there is no significant difference in post purchase satisfaction of consumers with different decision styles is rejected.

Summary and Conclusion

The decision styles of individuals are categorized as directive, analytic, conceptual and behavioural. Each style is characterized by unique orientations and approaches. In a business perspective, every individual is a consumer in some or other way; and each one has to take various decisions as part of his/her role as a consumer. The effect of decision styles on various aspects of consumer decision making process is analysed in this research. It is found that there is no association between gender and decision style. Further application of statistical test have confirmed that there is no effect of decision styles on the consumer decision areas such as need recognition, level and sources of information search,

purchase motives, intensity of evaluation of alternatives, product choice strategies adopted by consumers and orientation for impulsive purchase. But the study reveals that there is difference in post purchase satisfaction among the consumers having different decision styles.

The above finding is contrary to the general perception that decision style has an effect in the consumer's decision making process. The contradictory finding in this study may be due to the problem of the sample chosen for the study. The sample size was only 106 and it was a homogenous group of students belonging to the age group of eighteen to twenty one. This might have reflected in the findings of the study. Therefore the researchers suggest further explorations in this regard.

References

1. Alker, H. N., Rao, V. R., & Hughes, G. D. (1972). Value consistent and expedient decision making. American Psychological Association Proceeding, 7, 149-150.
2. Boulgarides, D. J., & Cohen. W. A. (2001). Leadership style vs. leadership tactics. Journal of Applied Management and Entrepreneurship, 6, 59-73.
3. Connor, P. E., & Becker, R. W. (2003). Personal value system and decision-making styles of public managers. Public personal management, 32, 155-180.
4. Elizabeth C. Hirschman and Michael K. Mills. (1980). Sources Shoppers Use to Pick Stores. Journal of Advertising Research, 20, 47-51.
5. Gerald Linda. (1979). New Research Works on Consumer Satisfaction/Dissatisfaction Model. Marketing News, 21, p.8
6. Hawkins Stern. (1962). The Significance of Impulse Buying Today. Journal of Marketing, 26, 59-60.
7. Howard Beales et al. (1981). Consumer Search and Public Policy. Journal of Consumer Research. 8, 11-22.
8. John A. Howard and Jagdish N. Seth. (1969). The Theory of Buyer Behavior. Wiley, New York.
9. Krumboltz, J. D., & Hamel, D. A. (1977). Guide to career decision making skills. New York: College Entrance Examination Board.
10. Phillips, S. D. (1997). Toward an expanded definition of adaptive decision making. The Career Development quarterly, 45, 275-287.

The Macrotheme Review
A multidisciplinary journal of global macro trends

Rhetoric or Reality: Perception of Sustainability Practices by Practicing Managers of SMEs in South India.

Siji Cyriac* and T Asokan**
**St Pius X College, Rajapuram, India*
***Department of Management Studies, Kannur University*

Abstract

The Small and Medium Enterprises (SMEs) play a vital role in triggering economic growth and equitable development, particularly in developing countries like India. Though their significant economic contribution of SMEs is well understood, their responsible business practices have not been extensively studied for any meaningful interpretation. Individually each of these SMEs may not have a significant influence like large corporate whose cumulative social and environmental impacts are significant. Many company's Sustainability initiatives, particularly CSR are disparate and uncoordinated, run by a variety of managers without the active engagement of the CEO. Such firms cannot maximise their positive impact on the economic, social and environmental systems in which they operate. The main question is how the SMEs are socially, economically and environmentally responsible to their stakeholders and external constituents and how they perceive and act on their other normative responsibilities. How SMEs are responsible to their external stakeholders including their cultural, social or governmental relationships in ways that coincide or conflict with their obligations to the other primary stakeholders, eg. their employees, owners, customers, and suppliers. There is an urgent need therefore to understand the responsible business practices adopted by the SMEs. Much of the Anecdotal evidence on SMEs in the world over appears to suggest that the ethical orientation of the SMEs is a product of the ethical orientation of its owner. What they do is what they believe. Therefore this paper attempts to examine the perception of Sustainability Practices on SMEs by analysing the ethical and CSR orientation of their managers.

Keywords: Sustainability Practices, SMEs, South India

1. Introduction

Small and Medium enterprises have been playing an important role in the overall economic development of a country like India, where millions of people are unemployed or underemployed. As per a recent survey SSI Sector comprises of 95% of the total industrial units in the country. In India Small and Medium industries occupy 12.3 million units, contribute to 40 percent of industrial production and 35% of their exports.(Facts for you Pge.24). In countries like India where the disparity levels in income are quite stark and the industrial growth has not been widespread and uniform, the role of the SMEs in creating employment is quite significant. They also provide lively hood opportunities through simple, value – adding processing activities in

agriculture based economics, nurture entrepreneurship and economic systems, through linkages with the large enterprises. (Vasanthy IIMB 2010). Many large scale organizations depend on the SMEs for the supporting spare parts and raw materials

While their economic contribution is well understood with their supporting available data, their responsible business practices have not been extensively studied. Within the business ethics field, the presumption of the unit of analysis as a large firm has always been the norm. Unfortunately, there is much less to report in terms of research on CSR or Sustainability practices on Small and Medium sized enterprises. SMEs are facing many ethical challenges that seriously compromise the contributions they could make to the long term economic well being of their communities. Ethics is always concerned with the good, the self and the other (Rossouw, 2002).SMEs emerge as a response to personal or community need in the absence of other opportunities of formal employment, or other access to goods and services. (Mollie painter).

2. SMEs vs large Corporations

There is a growing consensus that SMEs demonstrate distinctive characteristics which make them different from large organizations According to Wynarczyk etl(1993) there are three ways in which small firms differ characteristically from large firms :- they are in terms of uncertainty and vulnerability, active engagement in innovation, and in terms of evolution and change. Compared to large corporations SMEs are :-

- Independent and owner managed
- Stretched by a broad range of tasks
- Limited cash flow
- Facing persistent survival challenges
- Built on personal relationships
- Mistrustful of bureaucracy and controlled by informal mechanisms

SMEs have to juggle the normative concerns that are part of their every day practices much more carefully, and without the necessary institutional support and resources to which larger companies have access. Therefore the content, nature and extent of their participation in SR practices and ethics is likely to be different. (Jenkins, 2006).

3. Definition of SMEs

SMEs are defined in different ways in different parts of the world. Some define them in terms of assets, while others use employment, shareholder funds or sales as criteria. Some others use a combination of revenue and employment as a hybrid criterion. In India, it is defined in terms of investment in plant and machinery. The MSME act of 2006 defines them as

- Enterprises engaged in the production/manufacturing of goods for any industry
- Enterprises engaged in rendering/providing services

Enterprises in the manufacturing sector are defined in terms of investment in plant and machinery (excluding land and buildings) and further classified into

Small enterprise – investment up to Rs. 2.5 million and Rs. 50 million

Medium enterprises – investment between Rs. 50 million and Rs. 100 million.

Service Enterprises : defined in terms of their investment in equipment and further classified into

Small enterprises – Investment above Rs. 1 million and up to Rs 20 million

Medium enterprises – Investment above Rs 20 million and up to Rs. 50 million

The clarity in definitions help in clearly charting various focused programmes and policy interventions for the various categories of firms.

4. The Concept of Sustainability

According to Global Reporting Initiative (GRI) the goal of sustainable development is to 'meet the needs of the present without compromising the ability of future generations to meet their own needs'. The Key indicators of sustainability are Economic Performance, Social performance and Environmental Performance. It is also knows what is being with regard to the three Ps ie, People, Profit and Planet. Another term generally used is triple bottom line performance.

The economic dimension of sustainability concerns the organization's impacts on the economic conditions of its stakeholders and on economic systems at local and national level. Financial performance is fundamental to understanding an organization and its own sustainability. The Environmental dimension of sustainability concerns organizations' impacts on living and non living natural systems, including ecosystems, land, air, and water. Society performance focuses attention on the impacts organizations have on the local communities in which they operate. It is the risks associated with bribery and corruption, undue influence in public policy – making etc.

Large scale firms are guided by GRI to publish annual sustainability reports based on the triple bottom line parameters. Several studies have been done to analyse the quality of the sustainability reports published by them. The GRI now has come out with certain guidelines for the SMEs to follow certain codes of conduct using the GRI G4 guidelines and make a report on the sustainability practices.

5. Sustainability Practices and Ethics in India

There is a clear documentation of sustainability practices in large organizations in India. (Mitra, 2007, Sood & Arora, 2006). In recent years, CSR in SMEs in India has been gaining increased attention from practitioners, NGOs and international agencies, but not significantly scholars. In a recent study conducted on CSR practices it was found that while large multinationals had formulated a CSR policy, which they make it public, CSR is not at all institutionalised in SMEs. The reason for the lack of institutionalisation of CSR include limited resources to CSR, lack of pressure from the customer and inability of see any direct benefit in doing CSR.

Much of the documented evidence suggest that the ethical orientation of SMEs is a product of the ethical orientation of its owner. And therefore we can conclude that the owners/managers in SMEs determine the ethical orientation of the firm.

There are a few studies examining the value orientation and ethical dimensions of Indian managers in large corporations. Chavan & Lamba, 2007 examined the cultural influences on the

judgement of Australian, Malasian and Indian SME managers to whistle bowling as an internal control mechanism.

In another study done conducted in the Pune Industrial belt in Western India, it was found that compliance to the Government laws was seen as being socially responsible. Many SME owners were of the opinion that philanthropy and CSR are one and the same. Ravenkar, 2004 said that many of the SMEs are at a stage where they are struggling to establish themselves and do not have the manpower or resources to address these issues. In a comparative study undertaken on constraints and contingencies of small businesses in Bangladesh and India, the authors found that many SMEs had similar constraints and contingencies across countries and bribery related variables tended to be fairly similar (Amin & Bannerjie, 2007).

Tarun Kumar, 2004 conducted a survey in an Industrial cluster in northern India, and he found that since most SMEs were led by owners, the value system and philosophy of the owner played a significant role in determining the CSR practices undertaken. Many of the SMEs were unable to see any clear benefits by following or practicing CSR. Very few companies had social reports, codes of conduct or stated ethical practices. But the study explores that many of the SMEs are involved in some kind of developmental activities. Many CEOs of these SMEs were members of Rotary or Lions Clubs and supported various developmental activities initiated by these clubs.

In a study conducted by the UNIDO (2008) on CSR perceptions and activities in SMEs in five industrial clusters in India, it was found that regardless of the geographical region they hailed from, SMEs tended to behave similarly towards CSR. Many of them considered 'taking care of their employees internally' and 'being involved in community welfare' as their CSR responsibility. Vasanthy Srieenivas IIMB, says that 'the influence of the personal values of the entrepreneurs in determining the choice of CSR activities found support'. When markets and large businesses put pressure of the SMEs, they are forced to follow certain CSR practices such as worker education, health and safety compliance which are undertaken in the normal course of business.

The role of cluster wise sustainability practices assumes relevance now. The leather cluster for example is plagued by pollution. The operations in leather tanning – washing, stripping, bleaching, chrome tanning and basification – involve the use of very toxic chemicals and its effluents tend to pollute ground water. The adoption of common effluent treatment plants and eco-friendly technologies has not become very widespread due to the lack of awareness among small firms and also partly due to lack of enforcement of environmental laws among small players (EXIM, 2000).

6. Why SMEs?

The Small and Medium Enterprises significantly contribute to India's economic growth. These serve independently and as ancillary to a large firms and help generate employment and industrialise the rural and backward regions of India. They employee nearly 40% of India's work force and contribute around 45% of India's manufacturing output.

The field of Business ethics and sustainability is usually centred around large, specially multinational corporations (MNCs) as the primary unit of analysis. Some of the aspects are transferable to SMEs also. Still, these small companies have their own frames of reference. They

are almost always close to the communities they operate. They are usually local, not global companies. They are family-owned or owned by a small group of investors or entrepreneurs rather than by anonymous shareholders. So the internal and external stakeholder relationships have to be redefined for SMEs.

The business activities of SMEs are performed in proximity to the locals. This enables them to be aware of local needs, manage expectations and develop sustainability programmes appropriately. Now that the CSR clause in the Companies Act, 2013 covers companies that have a net profit of five crore INR and above, it is expected that while micro enterprises will not qualify, many small and medium enterprises (SMEs) will.

The sustainability practices of these enterprises are driven by the personal interests of promoters who hold a significant financial stake in the business. They tend to be in clusters and engaged in similar business activities. While the quantum of revenue available for CSR with individual SMEs is expected to be small, all eligible companies in a specific geographical cluster, who single handed as well as collectively impact the same community, can pool their resource to create a sizeable CSR fund.

7. Methodology.

A questionnaire was developed including the motives and business benefits arising out of sustainability practices based on academic literature and business benefits on the activities that were pursued as CSR. It was distributed to organizations in Kerala and Tamil Nadu, tow south Indian states and some telephonic interviews also were carried out. The information is collected using both primary and secondary data.

Kerala is a small state in the southern most part of India which accounts for only 1.2 percentage of the total geographic area in India. Kerala claims 10.5% of the SME units in the country. Tamil Nadu also is situated in the southernmost past of the country and accounts for a large area and it accommodates large portion of the industrial units in the country.

8. Results

The respondents were asked to identify 3 most important motives for implementing sustainability practices and the benefits they perceive as a result of implanting sustainability practices. These motives were to be identified without ranking them. 90% of the said that CSR has a positive impact. 78% of them agreed that it has a long term sustainability impact. Many of them (50%) agreed that enhancing community trust and support is a major motive in implementing Sustainability practices.

Important motives for Implementing Sustainability Practices

No	Motives	Frequency	Percentage
1.	CSR has a positive impact	98	90.50
2	Long term sustainability	78	65
3	Enhance community trust & support	50	41.67
4	It is only a survival morality	48	40
5	It is only honesty and straight dealing	45	37.5
6	Retaining employees	45	37.5
7	Competitors are doing this	24	20
8	Favourable media coverage	24	20
9	Altruism	23	19.16
10	Avoid regulation	20	16.6
11	Company tradition	15	12.5
12	Buyer expectation	10	08.33
13	Increase profits	7	05.88

9. Analysis

When asked about the impact of SMEs in society all respondents' answers focused on the positive impact, predominantly in job creation. SMEs play a role in meeting the needs of their country, community, and closer circle of family and dependents.

SMEs emerge as a response to personal or community need in the absence of other opportunities of formal employment, or other access to goods and services. Sustainability could be positioned at the very heart of SME activity. Sustainability concerns go far beyond the sustainability rhetoric employed by some larger corporations in the first world.

Some SMEs are involved in activities that play an important role in supporting their immediate communities. This ranges from supporting schools and the aged, or even providing community infrastructure such as water wells. These activities are mostly undertaken by individual businesses (un-coordinated) and are not as 'hyped' as corporate CSR projects.

The dark side of the responsiveness to need is the fact that many SMEs might be operating as 'survival morality', which by definition is concerned with 'bread first, morals later'. The argument is that ethics will be compromised if there is any business advantage to be had. Business pressure, and sometimes pressure from an unethical environment, leads companies to 'cut corners', reduce product quality, and over-promise or over-commit, which eventually impacts negatively on the sustainability of these operations.

Regarding the understanding of the notion of 'ethics in SMEs', the theme that emerged most strongly related to 'honesty', straight dealing' and 'not cheating'. Another prominent theme referred to governance issues such as proper accounting, auditing and honest taxpaying. Another issue was labour issues which reflects on 'how they treat their staff'

On important ethical problems or issues for SMEs - responses were related to administrative dishonesty and labour issues. The issues which are highlighted in administrative dishonesty are

corruption, tax avoidance, misrepresentation in audits, and ignoring licensing procedures. These issues relate to relationship with Government institutions. The labour issues are centred on fair wages and the treatment of the staff. It includes disrespect for the staff as well as poor working conditions. Other issues are employing under aged workers, not allowing freedom of associations, not providing proper benefits or job security and indulging in tribalism. The third ethical concern relate to the quality of goods and services. These include over pricing, misrepresentation in terms of product quality, and selling pirated goods.

When enquired about the factors that make ethics difficult, it was found that unethical behaviour is very often is a reaction to an environment in which unethical business practices are widespread. The existence of systemic corruption in the broader environment in which SMEs operate was consistently highlighted as one of the most serious challenges they face. Of these, the most serious factor was corruption in interactions with the government as they have to constantly interact with the government as they have little or no bargaining power.

Competing with unethical competitors is another concern. There is a shortage of positive stories and role-models. Lack of quality controls, delays, and inconsistency in pricing are inevitable side-effects of SMEs emerging in such an environment.

Respondents in the study indicate that many of the ethical problems have a direct impact on the sustainability of businesses. According to them the following factors hinder long term business relationships – poor quality products, short term thinking, lack of business experience or management skills, and inconsistent delivery from suppliers. On the other hand, honesty, reliability and professionalism amongst small business owners were identified as factors that facilitate long term business relationships.

The factors identified as central in establishing a culture of ethics include: encouraging competition, developing strong reputations and nurturing long term relationships with clients, encouraging freedom of association of employees, and less political

10. Findings and Conclusions

Since SMEs contribute significantly to the economy and are geographically widely spread in a country like India, their adoption of Sustainability and ethical practices is crucial for a balanced development. The present clearly identifies the fact that there are many differences among the sustainability practices of SMEs and large scale organizations. While large scale organization or companies with more than 5 crore profit for a period of three consecutive years, have to set apart 2% of their profit for CSR activities. Therefore SMEs' understanding of sustainability practices depends on how they view their purpose, what their specific needs are, and what they can afford.

Bibliography

1. Amin, M.R & Bannerjee, S. 2007 Constraints and contingencies of the Small business: A comparative perspective. *Indian Business and Economic Research Journal. 6(9)*
2. Chavan, M. & Lamba. A.S 2007 An International perspective on internal controls in small and medium enterprises. *The Business Review*. 8(1).
3. Jenkins, H 2006. Small business Champions for corporate social responsibility. *Journal of Business Ethics*. 67
4. Mitra, M.2007. It's only business: India's corporate social responsiveness in a globalized world. New Delhi*: Oxford University Press*

5. Revenkar, A.V 2004. *Corporate social responsibility in small and medium scale industries*. New Delhhi, Business Community Foundation Publication
6. Russo, F. 1999. *Strengthening Indian SME clusters: UNIDO's experience*. New Delhi: UNIDO
7. Tarun, K. 2004. *CSR in industrial areas/SMEs: Activities, policies and strategies in Delhi India.* New Delhi, Business Community Foundation.
8. V. Sreenivasan. India: CSr and Ethics in MSMEs in India*,.Ethics in Small and Medium Enterprises,* Springer,2010.
9. www.gri.com

Research Paper *IJBARR*
Impact Factor: 4.729 *E- ISSN -2347-856X*
Refereed, Listed & Indexed *ISSN -2348-0653*

SUSTAINABILITY WITHIN SMES: AN OVERVIEW OF THE PERCEPTION OF ENTERPRISE SOCIAL RESPONSIBILITY BY PRACTICING SME MANAGERS.

Mr Siji Cyriac* **Prof (Dr) T Asokan ****
**Assistant Professor, St Pius X College, Rajapuram, Kasaragod, Kerala.*
***Professor, Department of Management Studies , Kannur University.*

Abstract
The Small and Medium Enterprises (SMEs) play a vital role in triggering economic growth and equitable development, particularly in developing countries like India. Though their significant economic contribution of SMEs is well understood, their responsible business practices have not been extensively studied for any meaningful interpretation. Individually each of these SMEs may not have a significant influence like large corporates whose cumulative social and environmental impacts are significant. Many company's Sustainability initiatives, particularly CSR are disparate and uncoordinated, run by a variety of managers without the active engagement of the CEO. Such firms cannot maximise their positive impact on the economic, social and environmental systems in which they operate. The main question is how the SMEs are socially, economically and environmentally responsible to their stakeholders and external constituents and how they perceive and act on their other normative responsibilities. How SMEs are responsible to their external stakeholders including their cultural, social or governmental relationships in ways that coincide or conflict with their obligations to the other primary stakeholders, eg. their employees, owners, customers, and suppliers. There is an urgent need therefore to understand the responsible business practices adopted by the SMEs. Much of the Anecdotal evidence on SMEs in the world over appears to suggest that the ethical orientation of the SMEs is a product of the ethical orientation of its owner. What they do is what they believe. Therefore this paper attempts to examine the perception of Sustainability Practices on SMEs by analysing the motives of implementing ethical and CSR practices by practicing SME managers.

Introduction

Small and Medium enterprises have been playing an important role in the overall economic development of a country like India, where millions of people are unemployed or underemployed. As per a recent survey SSI Sector comprises of 95% of the total industrial units in the country. In India Small and Medium industries occupy 12.3 million units, contribute to 40 percent of industrial production and 35% of their exports.(Facts for you Pge.24). In countries like India where the disparity levels in income are quite stark and the industrial growth has not been widespread and uniform, the role of the SMEs in creating employment is quite significant. They also provide lively hood opportunities through simple, value – adding processing activities in agriculture based economics, nurture entrepreneurship and economic systems, through linkages with the large enterprises. (Vasanthy IIMB 2010). Many large scale organizations depend on the SMEs for the supporting spare parts and raw materials

While their economic contribution is well understood with their supporting available data, their responsible business practices have not been extensively studied. Within the business ethics field, the presumption of the unit of analysis as a large firm has always been the norm. Unfortunately, there is much less to report in terms of research on CSR or Sustainability practices on Small and Medium sized enterprises. SMEs are facing many ethical challenges that seriously compromise the contributions they could make to the long term economic well being of their communities. Ethics is always concerned with the good, the self and the other (Rossouw, 2002).SMEs emerge as a response to personal or community need in the absence of other opportunities of formal employment, or other access to goods and services. (Mollie painter).

SMEs vs large Corporations

There is a growing consensus that SMEs demonstrate distinctive characteristics which make them different from large organizations According to Wynarczyk etl(1993) there are three ways in which small firms differ characteristically from large firms :- they are in terms of uncertainty and vulnerability, active engagement in innovation, and in terms of evolution and change. Compared to large corporations SMEs are :-

- Independent and owner managed
- Stretched by a broad range of tasks
- Limited cash flow
- Facing persistent survival challenges
- Built on personal relationships
- Mistrustful of bureaucracy and controlled by informal mechanisms

SMEs have to juggle the normative concerns that are part of their every day practices much more carefully, and without the necessary institutional support and resources to which larger companies have access. Therefore the content, nature and extent of their participation in SR practices and ethics is likely to be different. (Jenkins, 2006).

Definition of SMEs

SMEs are defined in different ways in different parts of the world. Some define them in terms of assets, while others use employment, shareholder funds or sales as criteria. Some others use a combination of revenue and employment as a hybrid criterion. In India, it is defined in terms of investment in plant and machinery. The MSME act of 2006 defines them as

- Enterprises engaged in the production/manufacturing of goods for any industry
- Enterprises engaged in rendering/providing services

Enterprises in the manufacturing sector are defined in terms of investment in plant and machinery (excluding land and buildings) and further classified into

Small enterprise – investment up to Rs. 2.5 million and Rs. 50 million

Medium enterprises – investment between Rs. 50 million and Rs. 100 million.

Service Enterprises : defined in terms of their investment in equipment and further classified into

Small enterprises – Investment above Rs. 1 million and up to Rs 20 million

Medium enterprises – Investment above Rs 20 million and up to Rs. 50 million

The clarity in definitions help in clearly charting various focused programmes and policy interventions for the various categories of firms.

The Concept of Sustainability

According to Global Reporting Initiative (GRI) the goal of sustainable development is to 'meet the needs of the present without compromising the ability of future generations to meet their own needs'. The Key indicators of sustainability are Economic Performance, Social performance and Environmental Performance. It is also knows what is being with regard to the three Ps ie, People, Profit and Planet. Another term generally used is triple bottom line performance.

The economic dimension of sustainability concerns the organization's impacts on the economic conditions of its stakeholders and on economic systems at local and national level. Financial performance is fundamental to understanding an organization and its own sustainability. The Environmental dimension of sustainability concerns organizations' impacts on living and non living natural systems, including ecosystems, land, air, and water. Society performance focuses attention on the impacts organizations have on the local communities in which they operate. It is the risks associated with bribery and corruption, undue influence in public policy – making etc.

Large scale firms are guided by GRI to publish annual sustainability reports based on the triple bottom line parameters. Several studies have been done to analyse the quality of the sustainability reports published by them. The GRI now has come out with certain guidelines for the SMEs to follow certain codes of conduct using the GRI G4 guidelines and make a report on the sustainability practices.

Sustainability Practices and Ethics in India

There is a clear documentation of sustainability practices in large organizations in India. (Mitra, 2007, Sood & Arora, 2006). In recent years, CSR in SMEs in India has been gaining increased attention from practitioners, NGOs and international agencies, but not significantly scholars. In a recent study conducted on CSR practices it was found that while large multinationals had formulated a CSR policy, which they make it public, CSR is not at all institutionalised in SMEs. The reason for the lack of institutionalisation of CSR include limited resources to CSR, lack of pressure from the customer and inability of see any direct benefit in doing CSR.

Much of the documented evidence suggest that the ethical orientation of SMEs is a product of the ethical orientation of its owner. And therefore we can conclude that the owners/managers in SMEs determine the ethical orientation of the firm.

There are a few studies examining the value orientation and ethical dimensions of Indian managers in large corporations. Chavan & Lamba, 2007 examined the cultural influences on the judgement of Australian, Malasian and Indian SME managers to whistle bowling as an internal control mechanism.

In another study done conducted in the Pune Industrial belt in Western India, it was found that compliance to the Government laws was seen as being socially responsible. Many SME owners were of the opinion that philanthropy and CSR are one and the same. Ravenkar, 2004 said that many of the SMEs are at a stage where they are struggling to establish themselves and do not have the manpower or resources to address these issues. In a comparative study undertaken on constraints and

contingencies of small businesses in Bangladesh and India, the authors found that many SMEs had similar constraints and contingencies across countries and bribery related variables tended to be fairly similar (Amin & Bannerjie, 2007).

Tarun Kumar, 2004 conducted a survey in an Industrial cluster in northern India, and he found that since most SMEs were led by owners, the value system and philosophy of the owner played a significant role in determining the CSR practices undertaken. Many of the SMEs were unable to see any clear benefits by following or practicing CSR. Very few companies had social reports, codes of conduct or stated ethical practices. But the study explores that many of the SMEs are involved in some kind of developmental activities. Many CEOs of these SMEs were members of Rotary or Lions Clubs and supported various developmental activities initiated by these clubs.

In a study conducted by the UNIDO (2008) on CSR perceptions and activities in SMEs in five industrial clusters in India, it was found that regardless of the geographical region they hailed from, SMEs tended to behave similarly towards CSR. Many of them considered 'taking care of their employees internally' and 'being involved in community welfare' as their CSR responsibility. Vasanthy Srieenivas IIMB, says that 'the influence of the personal values of the entrepreneurs in determining the choice of CSR activities found support'. When markets and large businesses put pressure of the SMEs, they are forced to follow certain CSR practices such as worker education, health and safety compliance which are undertaken in the normal course of business.

The role of cluster wise sustainability practices assumes relevance now. The leather cluster for example is plagued by pollution. The operations in leather tanning – washing, stripping, bleaching, chrome tanning and basification – involve the use of very toxic chemicals and its effluents tend to pollute ground water. The adoption of common effluent treatment plants and eco-friendly technologies has not become very widespread due to the lack of awareness among small firms and also partly due to lack of enforcement of environmental laws among small players (EXIM, 2000).

Why SMEs

The Small and Medium Enterprises significantly contribute to India's economic growth. These serve independently and as ancillary to a large firms and help generate employment and industrialise the rural and backward regions of India. They employee nearly 40% of India's work force and contribute around 45% of India's manufacturing output.

The field of Business ethics and sustainability is usually centred around large, specially multinational corporations (MNCs) as the primary unit of analysis. Some of the aspects are transferable to SMEs also. Still, these small companies have their own frames of reference. They are almost always close to the communities they operate. They are usually local, not global companies. They are family-owned or owned by a small group of investors or entrepreneurs rather than by anonymous shareholders. So the internal and external stakeholder relationships have to be redefined for SMEs.

The business activities of SMEs are performed in proximity to the locals. This enables them to be aware of local needs, manage expectations and develop sustainability programmes appropriately. Now that the CSR clause in the Companies Act, 2013 covers companies that have a net profit of five crore INR and above, it is expected that while micro enterprises will not qualify, many small and medium enterprises (SMEs) will.

The sustainability practices of these enterprises are driven by the personal interests of promoters who hold a significant financial stake in the business. They tend to be in clusters and engaged in similar business activities. While the quantum of revenue available for CSR with individual SMEs is expected to be small, all eligible companies in a specific geographical cluster, who single handed as well as collectively impact the same community, can pool their resource to create a sizeable CSR fund.

Enterprise Social Responsibility

Not only Corporations which are major firms, be responsible for CSR activities, Small and Medium Enterprises too need to lend their share in carrying out responsible business. As the study is based on CSR in SMEs, the term is coined to suit to the SMEs.

Methodology.

A questionnaire was developed including the motives and business benefits arising out of sustainability practices based on academic literature and business benefits on the activities that were pursued as ESR. It was distributed to organizations in north Kerala and some telephonic interviews also were carried out. The information is collected using both primary and secondary data.

Sample Profile. Table 1.

		Frequency	Percent
Age	less than 30	37	11.2
	31-35	45	13.6
	36-40	30	9.1
	41-45	52	15.8
	46-50	102	30.9
	more than 50	64	19.4
	Total	330	100.0
		Frequency	Percent
Education	SSLC/Plus Two	33	10.0
	Graduate	84	25.5
	Post Graduate	86	26.1
	Diploma	73	22.1
	Technology	48	14.5
	6	6	1.8
	Total	330	100.0

		Frequency	Percent
Gender	Male	274	83.0
	Female	56	17.0
	Total	330	100.0

		Frequency	Percent
Education	SSLC/Plus Two	33	10.0
	Graduate	84	25.5
	Post Graduate	86	26.1
	Diploma	73	22.1
	Technology	48	14.5
	6	6	1.8
	Total	330	100.0

Descriptive Statistics . Table 2.

	Mean	Std. Deviation	Analysis N
Increase profits	3.00	1.205	330
Long term sustainability	4.02	.969	330
Company tradition	3.43	.944	330
Recruit/retain employees	3.51	1.005	330
Attract Investors	3.42	1.122	330
Promote transactions/partnerships	3.33	1.053	330
Enhance community trust and support	4.11	.973	330
Avoid regulation	2.76	1.119	330
Enhance reputation	3.85	1.065	330
Favourable media coverage	3.15	1.186	330
Improve public welfare	4.03	.987	330
Altruism	3.90	1.003	330
External pressures	2.83	1.148	330
Competitors are doing	2.90	1.250	330
Buyer expectations	3.22	1.074	330

Results

Among the factors described above Improve public welfare scored the highest mean of 4.03.Followed by Long term sustainability. Enhance community trust and support holds a major opinion of 4.11 mean. Avoiding regulation and competitors are doing holds the least mean. The summaries and respondents with their mean score and standard deviation has been given in the table 2 descriptive analysis.

A factor analysis has been carried out to explore latent factors that motives in undertaking ESR activities. A total of 5 factors has been identified and explained. These factors have been named as External stakeholder management, Internal stakeholder management, long term sustainability and reputation. These five factors disclose the overall perception of ESR by practicing managers. A summary of the factor analysis has been given in Table.3.

Table 3. Rotated Component Matrix[a]

	Component				
	External stakeholder management	Internal Stakeholder management	Public Welfare	Long term Sustainability	Reputation
Increase profits		.538			
Long term sustainability				.627	
Company tradition				.685	
Recruit/retain employees		.768			
Attract Investors				.497	
Promote transactions/partnerships		.540			
Enhance community trust and support			.647		
Avoid regulation					.592
Enhance reputation					.720
Favourable media coverage					.467
Improve public welfare			.693		
Altruism			.642		
External pressures	.800				
Competitors are doing	.752				
Buyer expectations		.565			

Findings and conclusions

The study supports the earlier studies that long term sustainability, Enhance community trust and support, Improve public welfare are some of the motives that have been mostly picked by the SME managers.

SMEs emerge as a response to personal or community need in the absence of other opportunities of formal employment, or other access to goods and services. Sustainability could be positioned at the very heart of SME activity. Sustainability concerns go far beyond the sustainability rhetoric employed by some larger corporations in the first world.

Some SMEs are involved in activities that play an important role in supporting their immediate communities. This ranges from supporting schools and the aged, or even providing community infrastructure such as water wells. These activities are mostly undertaken by individual businesses (un-coordinated) and are not as 'hyped' as corporate CSR projects.

The dark side of the responsiveness to need is the fact that many SMEs might be operating as 'survival morality', which by definition is concerned with 'bread first, morals later'. The argument is that ethics will be compromised if there is any business advantage to be had. Business pressure, and sometimes pressure from an unethical environment, leads companies to 'cut corners', reduce product quality, and over-promise or over-commit, which eventually impacts negatively on the sustainability of these operations.

Regarding the understanding of the notion of 'ethics in SMEs', the theme that emerged most strongly related to 'honesty', straight dealing' and 'not cheating'. Another prominent theme referred to governance issues such as proper accounting, auditing and honest taxpaying. Another issue was labour issues which reflects on 'how they treat their staff'On important ethical problems or issues for SMEs - responses were related to administrative dishonesty and labour issues. The issues

which are highlighted in administrative dishonesty are corruption, tax avoidance, misrepresentation in audits, and ignoring licensing procedures. These issues relate to relationship with Government institutions. The labour issues are centred on fair wages and the treatment of the staff. It includes disrespect for the staff as well as poor working conditions. Other issues are employing under aged workers, not allowing freedom of associations, not providing proper benefits or job security and indulging in tribalism. The third ethical concern relate to the quality of goods and services. These include over pricing, misrepresentation in terms of product quality, and selling pirated goods.

When enquired about the factors that make ethics difficult, it was found that unethical behaviour is very often is a reaction to an environment in which unethical business practices are widespread. The existence of systemic corruption in the broader environment in which SMEs operate was consistently highlighted as one of the most serious challenges they face. Of these, the most serious factor was corruption in interactions with the government as they have to constantly interact with the government as they have little or no bargaining power.

Competing with unethical competitors is another concern. There is a shortage of positive stories and role-models. Lack of quality controls, delays, and inconsistency in pricing are inevitable side-effects of SMEs emerging in such an environment. Respondents in the study indicate that many of the ethical problems have a direct impact on the sustainability of businesses. According to them the following factors hinder long term business relationships – poor quality products, short term thinking, lack of business experience or management skills, and inconsistent delivery from suppliers. On the other hand, honesty, reliability and professionalism amongst small business owners were identified as factors that facilitate long term business relationships.

The factors identified as central in establishing a culture of ethics include: encouraging competition, developing strong reputations and nurturing long term relationships with clients, encouraging freedom of association of employees, and less politicalSince SMEs contribute significantly to the economy and are geographically widely spread in a country like India, their adoption of Sustainability and ethical practices is crucial for a balanced development. The present clearly identifies the fact that there are many differences among the sustainability practices of SMEs and large scale organizations. While large scale organization or companies with more than 5 crore profit for a period of three consecutive years, have to set apart 2% of their profit for CSR activities. Therefore SMEs' understanding of sustainability practices depends on how they view their purpose, what their specific needs are, and what they can afford.

Bibliography

1. Amin, M.R & Bannerjee, S. 2007 Constraints and contingencies of the Small business: A comparative perspective. *Indian Business and Economic Research Journal. 6(9)*
2. Chavan, M. & Lamba. A.S 2007 An International perspective on internal controls in small and medium enterprises. *The Business Review*. 8(1).
3. Jenkins, H 2006. Small business Champions for corporate social responsibility. *Journal of Business Ethics*. 67
4. Mitra, M.2007. It's only business: India's corporate social responsiveness in a globalized world. New Delhi*: Oxford University Press*
5. Revenkar, A.V 2004. *Corporate social responsibility in small and medium scale industries*. New Delhhi, Business Community Foundation Publication
6. Russo, F. 1999. *Strengthening Indian SME clusters: UNIDO's experience*. New Delhi: UNIDO
7. Tarun, K. 2004. *CSR in industrial areas/SMEs: Activities, policies and strategies in Delhi India.* New Delhi, Business Community Foundation.
8. V. Sreenivasan. India: CSR and Ethics in MSMEs in India,.*Ethics in Small and Medium Enterprises,* Springer,2010.
9. Nagadevara V &V. Sreenivasan : Rhetoric vs Reality: How do practicing managers view CSR in India, 2013
10. www.gri.com

RESEARCH REVIEW JOURNALS
Volume-04
Issue-06
June-2019

ISSN: 2455-3085 (Online)
RESEARCH REVIEW International Journal of Multidisciplinary
www.rrjournals.com[UGC Listed Journal]

A Study on the Behaviour of Volatility of Nifty Index Options

Nidhin Mathew

Assistant Professor, St. Pius X College Rajapuram, Kasaragod (India)

ARTICLE DETAILS

Article History
Published Online: 10 June 2019

Keywords
Options, Index Options, Volatility, Lead-Lag, Arbitrage, Spot Market.

***Corresponding Author**
Email: nidhinkmathew857[at]gmail.com

ABSTRACT

An option is a financial derivative that gives the holder the right, but not the obligation, to buy or sell a basket of stocks at an agreed-upon price on or before a certain date. Index options are similar to other options contracts, where the underlying instruments are stock market indices. This study is an attempt to analyse the relationship between spot and options markets in order to find out whether there exists any lead-lag relationship between these two. The study focuses on the relationship between the NIFTY Index Options and the underlying stock index - NIFTY 50. The study mainly focuses on analysing the dynamic relationship between options and spot market volatilities in the NIFTY. The relationships such as long term, short term and causality between spot and options market volatilities are analysed with the help of various econometric models. This study intrepidly says that the relationship between the options and spot markets is so dynamic. It is seen that there is a very smooth way of passing information from the options market to spot market and both are highly linked.

1. Introduction

An option is a financial derivative that gives the holder the right, but not the obligation, to buy or sell a basket of stocks at an agreed-upon price on or before a certain date. A call option is an option that gives the holder the right, but not the obligation, to buy underlying assets at an agreed-upon price on or before a specific future date. A put option is an option that gives the holder the right, but not the obligation, to sell underlying assets at an agreed-upon price on or before a specific future date. Index options are similar to other options contracts, where the underlying instruments are stock market indices. Index options deliver the investor a chance either to capitalize on an expected market move or to protect holdings in the underlying assets. The degree of exposure changes with the specific index option. The risk associated with the index option is limited and it is known to buyers in advance. If the index does not move as anticipated, the buyer's risk is limited to the premium paid, which is the price of the option. An index call option is said to be 'in-the-money' when its strike price is less than the underlying index. An index call option is said to be 'at-the-money' when its strike price is the same as the underlying index and 'out-of-the-money' when its strike price is greater than that underlying index. An index put option is said to be in-the-money when its strike price is greater than the reported level of the underlying index. It is 'at-the-money' when its strike price is the same as the underlying index and 'out-of-the-money', when its strike price is less than the underlying index.

The efficiency of the financial markets can be analysed different models, tests or by exploring arbitrage pricing relationships. According to Brunetti and Torricelli, if there is an absence of arbitrage, two assets providing identical future profits must trade at the same price in an efficient market. If there is any possibility for arbitrages, there will be an immediate reaction from market participants resulting in withdrawal arbitrage opportunities. The efficiency of the Options market can be analysed in two ways - Cross markets efficiency and Internal option market efficiency. Cross market efficiency is based on tests of the joint efficiency of the option and the underlying market and internal option market efficiency aims at assessing the existence of arbitrage opportunities within the very same option market.

The National Stock Exchange of India Ltd. (NSE), which is the leading stock exchange in India, was established in 1992 as a tax paying company in Mumbai. NSE has provided a number of financial services such as listings of securities, trading, clearing and settlement services, indices, market data, financial education, etc. The NIFTY 50 is the flagship index of NSE, which was launched on 3rd November 1995 with a base value of 1000. The index itself covers all the major sectors of the Indian economy and it includes 50 stocks. The derivatives trading at India's National Stock Exchange (NSE) commenced on 12thJune 2000 with futures trading on NIFTY Index. National Stock Exchange (NSE) introduced trading in index options on 4th June 2001. The options contracts are European style and cash settled and are based on the popular market benchmark NIFTY Index.

This study is an attempt to analyse the relationship between spot and options markets in order to find out whether there exists any lead-lag relationship between these two. The study focuses on the relationship between the NIFTY Index Options and the underlying stock index - NIFTY 50. The study mainly focuses on analysing the dynamic relationship between options and spot market volatilities in the NIFTY. The relationships such as long term, short term and causality between spot and options market volatilities are analysed with the help of various econometric models.

2. Review of literature

Fleming, Ostdiek and Whaley (1996) examine the interactions between the S&P500 index, options and futures contracts on this index. They conclude that the derivatives markets lead systematically the spot market, while the futures market precedes the options market, in particular, due to more

important liquidity, and therefore to less high transaction costs on the former.

Hemler and Miller (1997) in their study examined the efficiency of European style S&P 500 Index options traded on the Chicago Board Options Exchange (CBOE). From their study, Hemler and Miller found significant arbitrage opportunities for S&P 500 European options. However, they warned that some quotes might not have been executed, due to stale prices, indicating some arbitrage profits may have been virtually impossible to achieve.

De Jong and Donders (1998) examined the relationship between the Dutch options market and the spot market. They found that the futures contracts lead both the options and the index by about 10 minutes. Their results proved that the relationship between the options market and the spot market is not unidirectional.

Booth and Tse (1999), examining the relationship between the German derivative markets and the DAX index, find cross linkages among the three markets. In particular, they conclude that the spot market lead the options market. In the case of French markets, Capelle-Blancard and Vandelanoite (2002), using Granger linear and non-linear causality tests between European options and the CAC40 index, find that the spot market leads the options market.

Fung (2004) in his study examined the pricing efficiency of the Hang Seng Index options market in Hong Kong, by making use of the Box spread Strategy. It was found that there were very few arbitrage opportunities and upon further examination based on the reporting time of quotes, it was found that all the apparent mispricing were deceptive and they could be explained by stale quotes. The absence of real arbitrage opportunities confirmed the efficiency of the Hong Kong options market.

Benzion(2005) in his study examined the efficiency of the Israeli options market by examining the box spread strategy. They made use of a real-time computer program to find Arbitrage gain opportunities by considering the sample of index options traded on the Tel-Aviv Stock Exchange. It was found that only a few arbitrage opportunities were possible which disappeared rapidly and substantiated the efficiency of the Israeli options market.

Vipul (2009) examined themarket efficiency for the European style Nifty index options of the National Stock Exchange (NSE) India, by making use of a box-spread strategy. Time-stamped transaction data provided by NSE between 1 January 2002 and 31 December 2003 was used for this study. It was found that profit opportunities, after accounting and incorporating for transaction cost, was quite frequent, but, they did not persist even for 2 minutes. The fact that the arbitrage opportunities do not persist even for two minutes, indicates that the arbitrageurs do not ignore the mispricing for a long time..

3. Objectives of the study

1. To examine whether there exists any lead-lag relationship between the spot and options market in NSE.
2. To analyses the pricing efficiency of the NIFTY Index Options by comparing the linkage in volatilities between the spot and options market.

4. Data and methodology

For the present study, NIFTY 50 Index is the underlying index and NIFTY Index options are considered to test the internal market efficiency of NSE India.In order to assess the relationship between spot and options market, the daily at the money implied volatility of the options price along with the daily historical volatility of the underlying asset have been collected from the BLOOMBERG database and NSE website for NIFTY 50 indices for five years from 1st January 2014 to 31st December 2018. The historic volatility (HVol) is based on the standard deviation of daily price movements. On the other hand, the implied volatility (IVol) is found by using the Black-Scholes model on the at the money option prices.

The analysis of the study is done with the help of the econometrics software E-Views through the following steps:

1. The preliminary analysis is done through descriptive statistics.
2. The unit root test has been adopted in order to ensure that the variables HVol and IVol are stationary, which is a pre-requisite for determining the short-term as well as the long-term relationship among the variables.
3. Long term relationship between the spot and options market is determined by using the Johansen co-integration model.
4. Short-term relationship and lead-lag between the spot and options market are defined through the Vector Error Correction model.
5. The causality of the spot and options volatility series is established by employing the Granger Causality/ Block Exogeneity Test on the variables included in the study.

Using the above mentioned models/tests, the following null hypotheses can be tested to accomplish the objectives of the study.

H_{01}: There is no significant relationship between the spot and options market in a long and short period.

H_{02}: The option price has no information to pass on to spot market

H_{03}: There is no significant lead-lag effect between the spot and options market.

5. Limitations of the study

The study is based on secondary data and therefore errors in the collection, compilation of data, etc. are dependent on the process and perfection decided by others. Daily volatilities, both historic and implied volatilities are directly obtained from Bloomberg database. Seasonality effect, Monday effect, expiration effects, cyclical effects and celebration effects effect are not taken into consideration in the study. Microeconomic factors like GDP, interest rate, inflation rate and other country-specific factors are not included here.

6. Analysis and interpretations

Identifying the established relationship among the spot market and options market for a long period is important to explain the efficiency of the market to predict the movement of another market. Long run relationship between the options market and its underlying market has an important effect on forecasting and hedging models to reduce the risk involved in the underlying asset.

6.1 Results from Summary Statistics

Table -1
Summary Statistics for NIFTY Index

VARIABLES	OPTION	SPOT
Mean	27.64493	30.43304
Median	23.47200	25.68300
Std. Dev.	13.51401	15.52703
Skewness	1.640008	1.784281
Kurtosis	6.249030	6.739794

Table No.1 shows the descriptive statistics of spot and option variables for the NIFTY options market. In order to understand the behaviour of raw data series included in the study, mean, median, standard deviation, skewness, kurtosis and Jarque-Bera measured and presented. During the period of study, the options and spot variables show the coefficients of variation of 0.4887 and 0.51025 respectively for the NIFTY index. It indicates that the options market shows comparatively lower variation. Also, the average volatility in the option prices is lower than that of the spot market volatility. The skewness for both the market shows values around 2 which indicate that most values are concentrated on the left of the mean with extreme values to the right. Kurtosis is above 3 for both HVol and IVol and it should be said that the series is leptokurtic which means that the distribution is sharper than a normal distribution with values clustered around the mean. This means a high probability for extreme values.

6.2 Result of Stationary Test

Table -2 Results of Stationary Tests

INDEX	VARIABLES	LEVEL	
		ADF	PP
NIFTY	OPTION	-2.92874**	-3.78437***
	SPOT	-2.60406*	-3.74055***
*, **,*** indicates the significance at 10%,5%, and 1% level.			

Stationary is the important property of time series data which shows the ability of the data series to explain the long and short term information. As a preliminary test, it is necessary to test the stationarity of the time series variables such as HVol and IVol by applying Augmented Dickey-Fuller (ADF) and Philip Perron (PP) Unit Root Test. Table no. 2 shows the results of the ADF and PP test for HVol and IVol. HVol and IVol variables are stationary in its level form. It indicates that HVol and IVol are capable to test the role of one variable on the other. The significance of these statistical results says that there is no possibility of accepting the null hypothesis that there is a unit root in the variable. While rejecting the null hypothesis, it is absolutely confirmed that the data series are losing their long-term informational content.

6.3 Result of VAR Criteria for the Lag Selection Procedure

Table -3 Result of VAR Criteria Adopted for Selection of Lag Length for Model

Index	Lag	LogL	LR	FPE	AIC	SC	HQ
NIFTY	0	-9268.61	NA	10687.68	14.95260	14.96086	14.95571
	1	-6204.11	6114.184	76.74950	10.01630	10.04109	10.02562
	2	-6189.35	29.40235*	75.42894*	9.998945*	10.04026*	10.01448*
* indicates lag order selected by the criterion at 5% level. LR-sequential modified LR test statistic, FPE- Financial Prediction Error, AIC-Akaike Information Criterion, SC- Schwarz information Criterion, HQ- Hannan-Quinn information criterion.							

Table no. 3 shows the result of VAR criteria adopted for the selection of optimal lag length for the statistical methodology used to determine the relationship between option and spot market. As per the Likelihood Ratio (LR), final protection error and Akaike Information Criterion (AIC), HQ, SC and FPE the optimal lag length for NIFTY is 2. The error term of each variable is stationary at this point. The optimal lag length helps to avoid the auto correlation problem from the time series data set up to an extent.

6.4 Long Term Relationship Between Option and Spot Markets

Table -4 Results of Unrestricted Co-integration Rank Test applied through Johansen Co-integration Methodology

Index	Hypothesis	Eigen Value	Trace Statistics	Critical Value at 5%	Max- Eigen Statistic	Critical Value at 5%
NIFTY	r=0	0.064351	91.08453**	15.49471	82.41228**	14.26460
	r≤1	0.006975	8.672250	3.841466	8.672250	3.841466
**denotes the rejection of the hypothesis at a 5% level. Trace test indicates one cointegration equation at a 5% level. Max-Eigenvalue test indicates 1 cointegrating equation at the 5% level.						

Table No. 4 provides the result of the unrestricted co-integration rank test applied through Johansen co-integration methodology. The results of Johansen co-integration are explaining through the Trace Statistics and the Max- Eigen test Statistics. For the NIFTY Index options market, the null hypothesis that there is no co-integration equation among Spot and Options is rejected at 5% level of significance. Both test statistics like Trace statistics and Max-Eigen statistics reject

the null hypothesis at a 5% significance level. So the alternative hypothesis that there is atleast one co-integration equation between the options and spot market is accepted. This long-run relationship between options and spot market helps the traders in hedging their portfolio risk and to exploit the arbitrage opportunities. This result reveals that the movement of one market can be predicted by another market during the long term period.

6.5 Short Term Relationship between Spot and Options Market

Table -5 Results of Normalized Co-integration Vector Error Correction Model

Index	Error Correction	D(HVOL)	D(IVOL)
NIFTY	Co-integration Equation-1 [1.00000]	0.00631	0.119247
		[0.63397]	[9.04097]

Table No.5 shows the results of the Vector Error Correction Model applied to determine the short-run relationship between the option and spot markets for various options market during the study period. In NIFTY, the speed of adjustment of the spot market is around 0.6%, at the same time the options market shows around 11%. It indicates that when the options market responds and adjusts around 11% to the new information, the speed of adjustment of the spot market is only 0.6%. From this result, it is proved that the options market is adjusting to the new information very soon than the spot market. The reactions of the spot prices and option prices to the disequilibrium errors captured by the speed of adjustment show that within one time period 11% of disequilibrium errors are corrected in options market, which shows the leading behaviour of the options market. The result shows that the options market responds faster to the previous period's deviation from the long run equilibrium. Thus it should be concluded that the options market is adjusting to the new information faster than spot markets and they are more volatile to the market conditions than the latter.

6.6 Causal Relationship between Spot and Options Markets

Table -6 Results of Normalized Co-integration Vector Error Correction Model

Index	Dependent Variable	Chi-square Value
NIFTY	HVOL	9.418739***
	IVOL	3.646289**

Table-6 shows the result of VAR Granger Causality/ Block Exogeneity Wald Test for a causal relationship between spot and options market in different economies. The Chi-Square values are significant which means that while restricting the lag values of options and residuals of the spot, the null hypothesis of options market does not cause spot volatility is rejected at 5 percentage level of significant and accepted the alternative hypothesis of options market causes spot market for all the options market. Both variables are causing each other, in other sense, there is bidirectional causality between the options market and spot market. This result is supported by the theory and literature that there is bidirectional causality between the options market in India and abroad.

With the help of these empirical results, the null hypotheses of the study such as there are no significant relationship between spot and options market in a long and short period, the option price has no information to pass on to spot market and no significant lead-lag effect between spot and options market are rejected. The study clearly reveals that there is co-integration between the spot and options market. Even though there is a bidirectional relationship between the spot and options market, the options market shows the dominant and leading roll on the spot market.

7. Conclusion

The study mainly focuses on analysing the dynamic relationship between options and spot market volatilities in the NIFTY. The relationships such as long term, short term and causality between spot and options market volatilities are examined in this study. Due to data movement and market trends, the established relationships among markets may be changed. The causal relationship reveals the lead-lag positions between the options and spot markets.

Co-integration results for all the economies under study indicate the possibility of rejection of the null hypothesis that there is no co-integration between options and spot markets. This indicates that there is a long term relationship between both the markets. On the basis of Johansen Co-integration Methodology, the study, thus, proves that there are long term relationship and co-integration between the options market and its underlying market. The speed of adjustment parameters of options and spot markets to the disequilibrium in the co-integration is analysed by using the Vector Error Correction Model. On the basis of the speed of adjustment parameters, it is possible to explain the leading behaviour of the market or the ability of the market to adjust and respond to the new information. It is found that the options market is leading the spot market. It can be said that options markets lead the spot market always and spot markets attract the options market often. The dominant role of the options markets is witnessed through the empirical results of the study. The causality relationships between options and spot markets reveal the position of lead-lag among options and spot markets. Results of the Wald test indicate that there are bidirectional causality relationships between spot and options markets. Both markets are performing like indicators and followers. It can be said that options markets lead the spot markets in most of the cases.

On the basis of empirical results, the null hypothesis such as spot volatility pays a very negligible role in determining options volatility is rejected. It is found that spot market volatility is the key factor that can be considered as the determinant of the options market due to the informational efficiency of the options market. To conclude, this study intrepidly says that the relationship between the options and spot markets is so dynamic. It is seen that there is a very smooth way of passing information from the options market to spot market and both are highly linked.

References

1. Damoder.N. Gujarathi and Sangeetha, Basic Econometrics, *Tata McGraw Hill Education Pvt Ltd*, Fourth edition.
2. John C. Hull and Sankarshan Basu, Option, Futures and Other Derivatives, *Pearson*, Seventh edition
3. Billingsley, R. S., & Chance, D. M. (1985). Options market efficiency and the box spread strategy. The Financial Review, 20 (4), 287 - 301. DOI:10.1111/j.1540-6288.1985.tb00309.x
4. Dixit, A., Yadav, S. S., & Jain, P. K. (2009). Violation of lower boundary condition and market efficiency: An investigation into the Indian options market. Journal of Derivatives & Hedge Funds, 15 (1), 3 - 14. DOI:10.1057/jdhf.2008.30
5. Dixit, A., Yadav, S. S., & Jain, P. K. (2011). Testing lower boundary conditions for index options using futures prices: Evidences from the Indian options market. Vikalpa, 36 (1), 15 - 32. DOI: 10.1177/0256090920110102
6. Girish, G. P., & Rastogi, N. (2013). Efficiency of S&P CNX Nifty index option of the National Stock Exchange (NSE), India, using Box spread arbitrage strategy. GadjahMada International Journal of Business, 15 (3), 269 - 285.
7. Sol Kim, In Joon Kim, Seung Oh Nam, (2009) "The lead-lag relationship between stock index options and the stock index market: Model, moneyness, and news", International Journal of Managerial Finance, Vol. 5 Issue: 3, pp.311-332
8. Bloomberg Data Base
9. www.nseindia.com

A COMPARATIVE ANALYSIS OF NSE SECTORAL INDICES

Nidhin Mathew
Assistant Professor
Department of Commerce
St. Pius X College Rajapuram, Kasaragod, Kerala, India

Abstract: Risk and returns are the two important variables that determine the future financial benefits of an investment. This paper studies the relationship between risk and return of different Sectoral Indices on NSE using Capital Asset Pricing Model (CAPM). CAGR and Beta of the nine Sectoral indices such as Auto Index, Bank, Financial Services, FMCG Index, IT Index, Media Index, Metal Index, Pharma Index and Realty Index were calculated and compared. The results of the study revealed that, both risk and the return have been higher for the Bank, Financial Services, Realty and Metal sectors as compared to the market.

Keywords: Sectoral Indices, Risk, Return, Beta, CAPM

I. INTRODUCTION

Risk and returns are the two important variables that determine the future financial benefits of an investment. Risk and return is based on market risk and also investors' decision for investment. Naturally rational investors would expect a high return but they did not mind for high risk. The investors and stake holders of the equity stock are analyses the share price and earnings per share value in the past years. Assessing the required rate of return on an investment to be made in the stock market is a challenging task for an ordinary investor. Number of market models and techniques are being used to calculate required return for taking suitable investment decisions. Investors are always cautious about the future return on their investment. However, any investment in any types of assets must have risk of uncertainty. Risk is defined as the probability that an investor will not realize the expected return; i.e actual return will be different than expected. This includes the chance of losing some or all of the original investment. To determine the right choice of a security or portfolio to an investor, it depends on the level of risk that the stock carries. Therefore an estimation of the risk return profile of a security or portfolio is a significant phase before making any investment decision.

The National Stock Exchange of India Ltd. (NSE), is the leading stock exchange in India, located in Mumbai. The NSE was established in 1992 as a tax paying company. NSE was the first stock exchange in India to offer a fully automated screen-based electronic trading system. NSE has provided a number of financial services such as listings of securities, trading, clearing and settlement services, indices, market data, financial education, etc. The NIFTY 50 is the flagship index of NSE, which was launched on 3rd November, 1995 with a base value of 1000. The index itself covers all the major sectors of the Indian economy and it includes 50 stocks. In addition to the NIFTY 50 Index, the NSE maintains market indices that track market capitalizations, volatility, specific sectors, etc.

Sectoral indices are generally used to provide information about price movements or general behavior of the sector or industry in the economy. The sectoral index is created by selecting a group of most actively traded stocks that represent a specified sector of the market. The sectoral indexes are designed to provide a single value for the overall performance of a number of stocks representing a group of similar industries or a sector of the economy. The indices provide a historical view of stock market performance, giving investors more awareness on their investment decisions. Ordinary investor who does not have much knowledge about individual stocks to make right investment, can use indexing as a method of selecting stocks for investments. Therefore an analysis of the historical performance of the stock market indices will help the investor to forecast trends in the market. However, the degree of this risk would probably vary from industry to industry or market to market.

This paper studies the relationship between risk and return of different sectoral Indices on NSE over the last 5 years with the help of Capital Asset Pricing Model (CAPM). To get an accurate measure of the market risk of various sectors, generally investors use Beta as a measure of the volatility as compared to the whole market.Sectoral indices selected for the study are The NIFTY Auto Index, The NIFTY Bank, The Nifty Financial Services, The NIFTY FMCG Index, The NIFTY IT Index, The NIFTY Media Index, The NIFTY Metal Index, NIFTY Pharma Index and NIFTY Realty Index along with The NIFTY 50 as the market indicator.

Table 1: Sectoral Indices

INDEX	No. of Constituents	Launch Date	Base Date	Base Value
NIFTY Auto	15	July 12, 2011	January 1, 2004	1000
NIFTY Bank	12	September 15, 2003	January 1, 2000	1000
NIFTY Financial Services	20	September 7, 2011	January 1, 2004	1000
NIFTY FMCG	15	September 22, 1999	January 1, 1996	1000
NIFTY IT	10		January 1, 1996	100
NIFTY Media	15	July 19, 2011	December 30, 2005	1000
NIFTY Metal	15	July 12, 2011	January 1, 2004	1000
NIFTY Pharma	10	July 1, 2005	January 1, 2001	1000
NIFTY Realty	10	August 30, 2007	December 29, 2006	1000
NIFTY 50	50	April 22, 1996	November 3, 1995	1000

II. REVIEW OF LITERATURE

Rakesh Kumar and Raj S Dhankar (2011) studied the normality of return and risk in Indian stock market, in their article titled, "Distribution of Risk and Return - A test of normality in Indian stock market" using parametric and non-parametric test to prove these objectives. They have selected different indexes like Sensex, BSE 100 and BSE 500 from BSE for the period 1996 to 2006. Their study results show that, the returns are negatively skewed for all the indices over the study period.

Shanmugasundram and Benedict (2013) conducted a study on the volatility of the sectoral indices with reference to NSE. They have studied the risk-return relationship of the NSE NIFTY index and five sectoral indices such as NSE AUTO Index, NSE BANK Index, NSE FMCG Index, NSE INFRA Index and NSE IT Index was examined. The results did not show any significant difference in the risk across of sectoral indices and NIFTY.

Bora and Adhikary (2015) examined the risk-return relationship using BSE Sensex companies. The monthly closing price of the 30 stocks was used to evaluate the risk and returns for the period between 2010 and 2013. Their findings revealed positive relation between stock returns and market returns and betas (systematic risk) were found to be unstable during the study period.

Shaini Naveen & T. Mallikarjunappa (2016) conducted a study on the risk and return in banking sector, using NIFTY Bank Index as the benchmark. They examined and compared the performance of 12 banks listed in the NSE. The study evaluates the performance of banking stocks mainly to identify the required rate of return and risk associated to a particular stock based on different risk elements prevailing in the market. Their study revealed that the banking sector is more volatile than the market (NSE).

Dr. S Poornima and Swathing (2017) evaluated the performance of selected stocks from automobile sector and IT sector. Five stocks in both automobile and IT sector have been taken for the sample. The risk and return analysis of any industry reveals the complexities associated with that particular industry. Study revealed that automobile industry showing positive return and low risk whereas IT sector showing negative return and high risk during the study period.

III. OBJECTIVES OF THE STUDY

The study aimed to analyse the risk and returns of the sectoral indices on NSE. The nature of returns and risk will also be examined. This is expected to throw light on the behaviour of the major sectors.

1) To examine the risk and return associated to different sectoral indices on NSE.
2) To compare average return of sectoral indices with expected return using CAPM.

IV. RESEARCH METHODOLOGY

Data and sources of data:

Daily closing prices of the NSE NIFTY 50 and nine sectoral indices on NSE have been taken for a period of five years from April 1, 2014 to March 29, 2019 from NSE website. To determine the risk free rate, 91 days Treasury Bill rate is collected from RBI website.

Tools Used For Analysis:

Return

To calculate the five year average return, first daily returns of the sectoral indices and the NIFTY index is computed as a percentage. The difference between the closing index value of two consecutive days divided by the preceding day was taken.

Return = [(closing Price - Opening Price) / (opening Price)] * 100
Average return = (Return/ N)

Compound Annual Growth Rate (CAGR):

Average return does not include any measure of the overall risk involved in the investment. CAGR reduces the effect of volatility of periodic returns. The Compound Annual Growth Rate is the average rate at which value of the investment grows over a certain period assuming the value has been compounding over that period. The formula for Compound Annual Growth Rate is:

$$\mathbf{CAGR} = (\mathbf{V_1} - \mathbf{V_0})^{(\mathbf{1/n})} - \mathbf{1}$$

Where $\mathbf{V_0}$ is the initial value of the investment, $\mathbf{V_1}$ is the value of the investment at the end of the period and **n** is the number of investment periods.

Volatility

Risk associated to the indices is measured by using standard deviation (σ) of the returns and by calculating beta (β) values of the sectoral indices to show the sensitivity of the sector returns. Here standard deviation is used to measure volatility in return. If the volatility is high, the risk of the sector is considered high as well. The formula for standard deviation is:

$$\boldsymbol{\sigma} = \sqrt{\frac{\Sigma(X - \bar{X})^2}{N - 1}}$$

Where $\boldsymbol{\sigma}$ is the standard deviation, X is the daily return of indices, $\bar{X}$ is the average and N is the number of values in the data set.

Beta:

Beta (β) (also known as systematic risk) measures the volatility of the sectoral index to the market index (NSE NIFTY). Beta (β) indicates whether sectoral indices are more or less volatile than the NIFTY. If beta is more than 1, it indicates that the index is more volatile than the market. The Beta (β) can be computed as follows:

$$\beta = \frac{\text{COV(market returns, Sectoral Index returns)}}{\text{VAR(market returns)}}$$

Where $'COV(market\ returns,\ Sectoral\ Index\ returns)'$ is the covariance between the market return and sectoral index return and $'VAR(market\ returns)'$ is the variance of the market returns.

If Beta < 1, then stock / index is less volatile than market, Beta > 1, then stock / index is more volatile than the market and Beta < 0, then stock / index is losing money while market as a whole is gaining.

Capital Asset Pricing Model (CAPM)

Capital Asset Pricing Model (CAPM) is a model created by Harry Markowitz (1959) to find out the expected return. CAPM assumes that the investors are risk averse and they always search for the "mean-variance efficient portfolio". In such a portfolio, the risk will be minimized for given expected return or the expected return will be maximized for the given level of risk. The calculation used in CAPM can be described as following:

$$\mathbf{E(R)} = \mathbf{Rf} + \boldsymbol{\beta}(\mathbf{Rm} - \mathbf{Rf})$$

Where,

E(R) is the expected return
R_f means risk free rate of return i.e., return given by government T- bills
β is Beta (Systematic risk)
R_m is the market return

V. RESULTS AND DISCUSSION

1) Risk – Return Relationship

Table 2: Risk – Return Comparison

INDEX	CAGR (%)	Standard Deviation	Beta
NIFTY Auto	7.51	18.42	1.12
NIFTY Bank	19.02	18.14	1.17
NIFTY Financial Services	18.92	17.50	1.18
NIFTY FMCG	10.89	16.33	0.74
NIFTY IT	10.94	17.31	0.60
NIFTY Media	6.84	22.87	0.96
NIFTY Metal	3.85	25.54	1.31
NIFTY Pharma	4.14	19.74	0.77
NIFTY Realty	7.32	31.10	1.52
NIFTY 50	**11.64**	**13.36**	**1.00**

Chart 1: Risk – Return Relationship

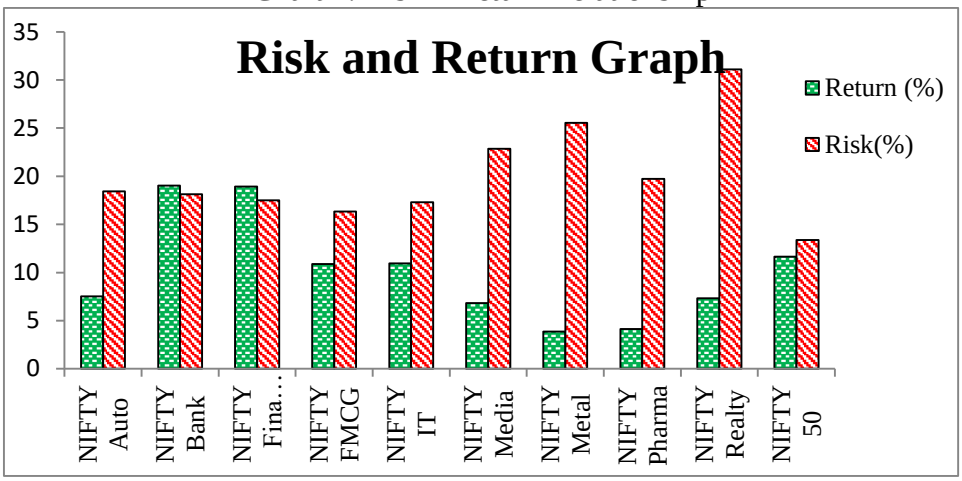

The maximum return during the study period has been from the Bank index, followed by Financial Services, IT, FMCG and Auto sectors, in that order. The least returns have come from the Metal, Pharma, Media and Realty sectors in that order. The mean value of return of NIFTY 50 index is 11.64 percent. NIFTY Bank index and NIFTY Financial Services index have return above market return. All other indices have return less than market return during the study period. Therefor if an investor is not concerned about the risk factors he can invest in NIFTY Bank or NIFTY Financial Services stocks to earn a better return than the market.

An analysis of the standard deviation values shows that the Realty sector, Metal, Media, Pharma, Auto, Bank and Financial services in that order have higher standard deviations meaning have relatively higher risks. As reflected in the standard deviation values, the high risk industries such as Realty, Metal, Financial services, Bank and Auto show higher beta values of more than one, means that these indices are more volatile than the market (NIFTY).

2. Expected Return

Table 3: Expected Return

INDEX	Beta	E(R)
NIFTY Auto	1.12	12.28
NIFTY Bank	1.17	12.55
NIFTY Financial Services	1.18	12.60
NIFTY FMCG	0.74	10.25
NIFTY IT	0.60	9.51
NIFTY Media	0.96	11.43
NIFTY Metal	1.31	13.29
NIFTY Pharma	0.77	10.41
NIFTY Realty	1.52	14.41

Chart 2: Security Market Line

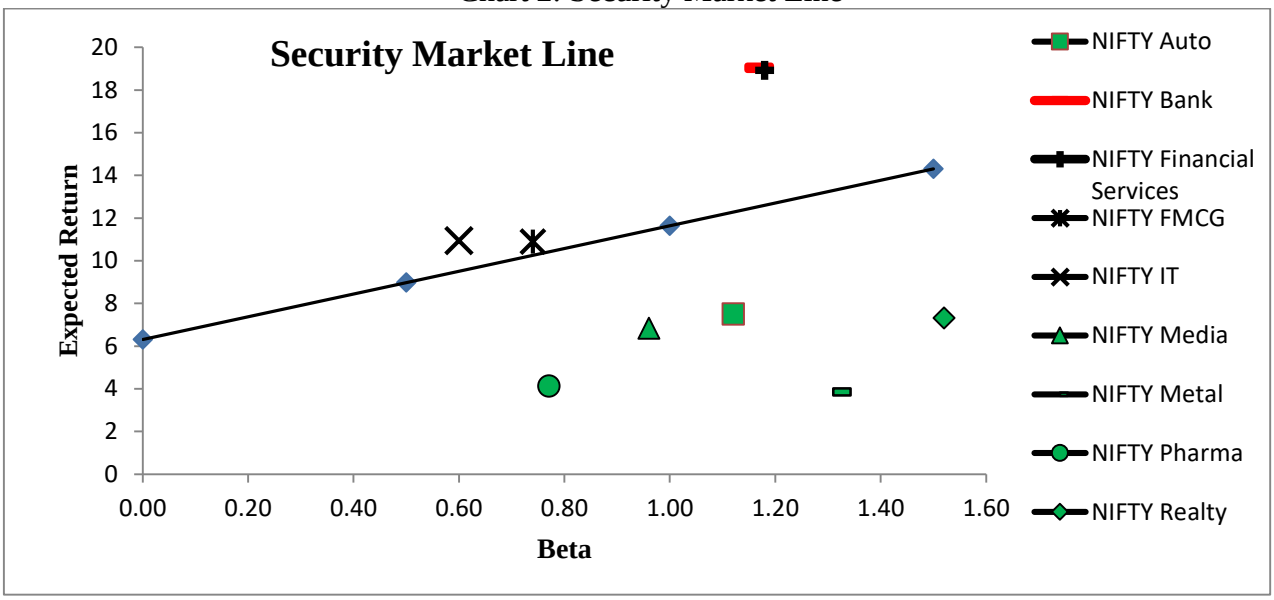

The above table shows the expected return of different sectors computed using CAPM model. An analysis of the expected return values shows that the Realty, Metal, Financial services, Bank, and Auto in that order have higher expected return. The security market line (SML) is a pictorial representation of the Capital Asset Pricing Model. It shows the expected return of a stock for any given beta or it reflects the risk associated with given expected return. The securities which are above the SML are undervalued securities since they give the higher expected return for a given amount of risk. The securities which are below the SML are overvalued securities since they have lower expected returns for the same amount of risk. Above graph shows that IT, FMCG, Bank and Financial Service sectors are undervalued and all other sectors are overvalued. Therefore a portfolio made up of stocks from these sectors will give more return to an investor as compared to the market.

VI. CONCLUSION

Risk and returns are the two important variables that determine the future financial benefits of an investment. Return on any investment is depends on the market risk and also the risk tolerance of the investors. In this paper the researcher has examined the volatility associated to various sectoral indices on NSE for five years from April 1, 2014 to March 29, 2019. The results of the study revealed that, both risk and the return have been higher for the Bank, Financial Services, Realty and Metal sectors as compared to the market. The analysis of Beta reveals the change in the return on the indices over the change in return on the market. The Beta value of Realty, Metal, Financial services, Bank and Auto is more than one, which indicates that these indices are more volatile than the market. Analysis of Security Market Line shows that IT, FMCG, Bank and Financial Service sectors are undervalued and all other sectors are overvalued. Therefore a portfolio made up of stocks from these sectors will give more return to an investor as compared to the market.

VII. REFERENCES

1. Shaini Naveen & T. Mallikarjunappa (2016) "A Study On Comparative Analysis of Risk and Return With Reference To Stocks of CNX Bank Nifty" International Journal of Scientific Research and Modern Education, 1(1), 737-743.
2. Dr. S Poornima and Swathiga (2017) "A study on relationship between risk and return analysis of selected stocks on NSE using capital asset pricing model" International Journal of Applied Research 2017; 3(7): 375-378.
3. Bora, B, & Adhikary, A. (2015), Risk and Return Relationship -An Empirical Study of BSE Sensex Companies in India. Universal Journal of Accounting and Finance, 3(2), 45–51.
4. Shanmugasundram. G and Benedict John (2013), "Volatility of the Indian Sectoral Indices - a study with reference to National Stock Exchange", Financial Services & Management Research, 2(8),36-47.
5. Jarrett J and Kyper E (2005), "Daily variation, Capital market efficiency and predicting stock market returns", Management Research News, Vol. 28, No.8, pp. 34- 47
6. Karmakar M and Chakraborty M (2003), "Stock market anomalies: Evidence from India", Prajnan, Vol.32, No.1
7. Avadhani V. Security Analysis and Portfolio Management, Himalaya Publishing House. 2013.
8. https://in.finance.yahoo.com
9. https://www.nseindia.com
10. https://www.moneycontrol.com

A COMPARATIVE ANALYSIS OF ASSET QUALITY OF PUBLIC, PRIVATE AND FOREIGN BANKS IN INDIA

Nidhin Mathew
Assistant Professor
Department of Commerce
St. Pius X College Rajapuram, Kasaragod, Kerala, India

Abstract: The commercial banks in India have made significant contributions to the development of almost all sectors such as agriculture, trade and commerce, infrastructure, etc. The Indian banking sector has seen tremendous changes and many positive developments during the last decade. Some of the major recommendations of the Narasimham Committee for strengthening the banking system were asset classification, income recognition & provisioning and capital adequacy norms. The banking sector in India comprises of public sector banks, private sector banks and foreign banks. NPAs are considered to be an important parameter to judge the performance and financial health of banks. In this context, the present study has been undertaken to evaluate and compares the NPA of public, private and foreign banks during the recent years and makes some suggestions for NPA management. The data has been analyzed using percentage and ratio method, and the statistical tool one-way ANOVA is used to test the hypothesis.

Keywords: Asset Quality, NPA, Public Sector Banks, Private Sector Banks, Foreign Banks, ANOVA

I. INTRODUCTION

A strong, healthy, viable and sustainable banking system is very essential for the overall development of an economy, the failure of which may lead to an adverse effect on various segments and spheres of the economy. The commercial banks in India have made significant contributions to the development of almost all sectors such as agriculture, trade and commerce, infrastructure, etc. The Indian banking sector has seen tremendous changes and many positive developments during the last decade. The policy makers such as the Reserve Bank of India and the Ministry of Finance have made several notable efforts to improve the efficiency and profitability of the banking sector. With a view to strengthening the banking system, the Narasimham Committee has suggested various reforms to meet the challenges of growing expectations of the masses. Some of the major recommendations of the Narasimham Committee were asset classification, income recognition & provisioning and capital adequacy norms. As per RBI directives an asset account (term loan/ cash credit/ overdraft/ bills purchase or discount) is classified as Non-Performing Asset if it remains irregular or out of order for a period of 90 days or more. A bank's profitability is greatly affected by the amount of Non-performing assets in its balance sheet. When loan account becomes overdue and banks are neither able to recover the capital nor earn interest income, then in real terms they become non-performing. The banking sector in India comprises of public sector banks, private sector banks and foreign banks. The future of all of these banks would be based on the capability the banks in maintaining good quality assets, capital adequacy and stringent prudential norms. NPAs are considered to be an important parameter to judge the performance and financial health of banks. The level of NPA is one of the drivers of financial stability and the growth of the banking sector. In this context, the present study has been undertaken to evaluate and compares the NPA of public, private and foreign banks during the recent years and makes some suggestions for NPA management. As of 31st March 2018, twenty-one public sector banks, twenty-one private sector banks and forty-five foreign banks were functioning in India. The loan asset details of all these banks under each category were considered for this study.

RBI Master Circular, dated July 1, 2015, defined Non Performing Assets as, "An asset, including a leased asset, becomes non- performing when it ceases to generate income for the bank. A non -performing asset (NPA) is a loan or an advance where interest and/ or installment of principal remain overdue for a period of more than 90 days in respect of a term loan, the account remains 'out of order' in respect of an Overdraft/Cash Credit, the bill remains

overdue for a period of more than 90 days in the case of bills purchased and discounted, the installment of principal or interest thereon remains overdue for two crop seasons for short duration crops, the installment of principal or interest thereon remains overdue for one crop season for long duration crops."

Non-Performing Assets are classified into the following three categories based on the period for which the asset has remained non- performing - Sub-standard Assets, Doubtful Assets and Loss Assets. A sub-standard asset is one, which has remained as non-performing for a period one year or less. A doubtful asset is one, which has remained in the category of the sub-standard asset for a period of one year. A loss asset is a loan asset in which loss has been identified by the bank but the amount has not been written off wholly. Gross NPAs are the total amount of loans that are classified as NPAs as per RBI guidelines. It consists of all the sub-standard, doubtful, and loss assets. Gross NPA is the total amount of advance accounts where interest and principal are outstanding for a period of ninety days and more. Net NPA refers to the amount arrived at after reducing the provisions for bad and doubtful debts from Gross NPA. Net NPA means GNPA minus total provision for bad and doubtful debts.

II. REVIEW OF LITERATURE

Das. S. (2010) has tried to analyse the parameters that are actually the reasons of NPAs and those are, willful defaults, market failure, poor follow-up and supervision, poor Legal framework, non-cooperation from banks, lack of entrepreneurial skills and diversion of funds. **Rajeev. M.** (2010) examines the Indian trends of NPA's from various dimensions and explains how the recognition of problem continuous observing can reduce it to a greater extent. They also discuss the functions of the joint liability groups or self-help groups in enhancing the loan recovery rate. **Kaur, H**. (2011) attempt was made in the paper to know about NPA, the magnitude and reasons for high NPA's, the factors responsible for the contribution towards NPA's and their impact on the banking systems.

Vohra and Dhamu (2012) emphatically point out that the NPAs have a direct impact on profitability, liquidity and equity of the banks. The authors observe that the NPAs of Indian banks are relatively very high by global standards. Thus, they recommend restricting of lending operations only to secured advances with adequate collateral securities. They also list a few common reasons for an asset turning NPA, considering economy, industry, borrower and lender sides separately. **Rai, K.** (2012) made an effort to evaluate the NPA of the selected banks and their trends and issues, also the measures taken for managing the NPA's like a reformulation of banks' credit appraisal techniques, the establishment of monitoring cell, etc.

Ahmad, Z. (2013) have written on the NPA and causes for NPA. Secondary data was collected for a period of five years and analysed by CAGR, average, ANOVA and ranking banks. The banks were ranked according to their performance to manage the NPA's. The efficiency in managing the NPA by the nationalised banks was tested. **Ranjan, R. and Dhal**. (2013) explore an empirical approach to the analysis of Indian commercial banks' non-performing loans by regression analysis. The empirical analysis evaluates as to how the NPA's are influenced by some economic and financial factors, i.e., terms of credit, macroeconomic shocks and bank size induced risk preferences.

Joseph, A. L., (2014) deals with trends of NPA in the banking industry, internal, external and some other factors that mainly responsible for NPA rising in the banking industry and also provides some suggestions for overcoming the burden of NPA. **Arora, N. and Ostwal, N**., (2014) analyse the comparison and classification of loan assets of private and public sector banks. The study concluded that the NPA's are a big issue for the banks. According to them, the financial companies and public sector banks have higher NPA's as compare to Private sector banks. **Kavitha, N. A**. (2016) said that the extent of NPA is comparatively very high in public sector banks as compared to private banks. **Singh, V. R**., (2016) said that Non-Performing Assets have always created a big problem for the banks in India and the NPAs level of our banks is still high as compared to the foreign banks.

III. OBJECTIVES OF THE STUDY

The main objective of this paper is to understand the significant difference in the occurrence and management of NPA of the public sector, private sector and foreign banks in India. Therefore the objectives of the study are as follows:

1) To examine the asset quality of public sector, private sector and foreign banks in India
2) To analyze various categories of loan assets that contribute to NPA
3) To evaluate the performance of the public sector, private sector and foreign banks via NPA analysis

IV. RESEARCH METHODOLOGY

Data and sources of data:

The data related to the various categories of loan assets have been collected from the RBI database for a period of ten years ranging from 2008-09 to 2017-18. Information about asset classification, Income Recognition, etc. has been compiled from RBI circulars and various issues of RBI Report on Trends and Progress of Banking in India.

Tools Used For Analysis:

The study is analytical in nature, is related to asset quality of the Public sector, private sector and foreign banks in India. The analysis of various categories of loan assets of the banks has been carried out for a period of ten years ranging from 2008-09 to 2017-18. The data has been analyzed using percentage and ratio method, and the statistical tool one-way ANOVA is used to test the hypothesis. To analyze the NPA factor and NPA based performance, GNPA% (Gross NPA as a percentage of total advances) and NNPA% (Net NPA as Percentage of Net Advances) are used. To determine the significant difference in the various parameters of NPA between Public sector, private sector and foreign banks, the ANOVA test is used by formulating the following hypotheses:

H_{01}: There is no significant difference in GNPA ratio between Public sector, private sector and foreign banks

H_{11}: There is a significant difference in the GNPA ratio between the Public sector, private sector and foreign banks.

H_{02}: There is no significant difference in the NNPA ratio between the Public sector, private sector and foreign banks.

H_{12}: There is a significant difference in the NNPA ratio between the Public sector, private sector and foreign banks.

V. RESULTS AND DISCUSSION

1) Standard Advances as a percentage of total advances

Table – 1: Standard Assets

Year	Standard Advances as a percentage of total advances		
	Public Sector Banks	Private Sector Banks	Foreign Banks
2017-18	85.4	95.4	96.2
2016-17	88.3	95.9	96.0
2015-16	90.7	97.2	95.8
2014-15	95.0	97.9	96.8
2013-14	95.6	98.2	96.1
2012-13	96.4	98.2	97.0
2011-12	97.0	98.1	97.3
2010-11	97.8	97.8	97.5
2009-10	97.8	97.3	95.7
2008-09	98.0	97.1	95.7

Chart – 1: Standard Assets

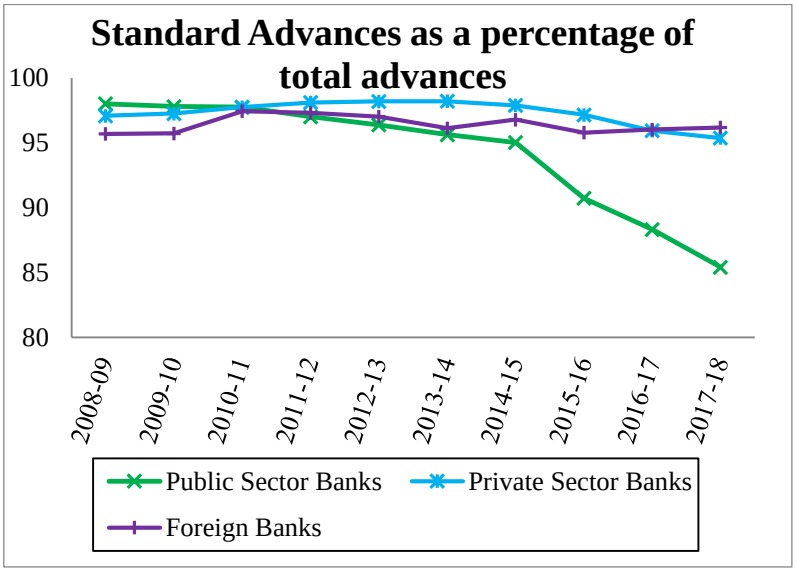

Source: RBI Report on Trends and Progress of Banking in India

A standard asset is an asset that is not classified as Non-Performing. It represents a healthy financial condition in the normal course of business. Analysis of Table – 1 shows that the percentage of standard assets is getting reduced during the study period for all three categories. In the case of public sector banks, the percentage of standard assets is significantly reduced to 85.4% from 98%. It implies that the financial conditions of the banks are getting down year after year.

2) Sub-Standard Advances as a percentage of total advances

Table – 2: Sub-Standard Assets

Year	Sub-Standard Advances as a percentage of total advances		
	Public Sector Banks	Private Sector Banks	Foreign Banks
2017-18	3.5	1.2	1.1
2016-17	3.0	1.4	1.2
2015-16	3.4	0.9	1.7
2014-15	1.9	0.7	0.7
2013-14	1.8	0.6	1.4
2012-13	1.8	0.6	1.1
2011-12	1.6	0.5	0.9
2010-11	1.1	0.6	0.9
2009-10	1.1	1.4	2.9
2008-09	0.9	1.8	3.5

Chart – 2: Sub-Standard Assets

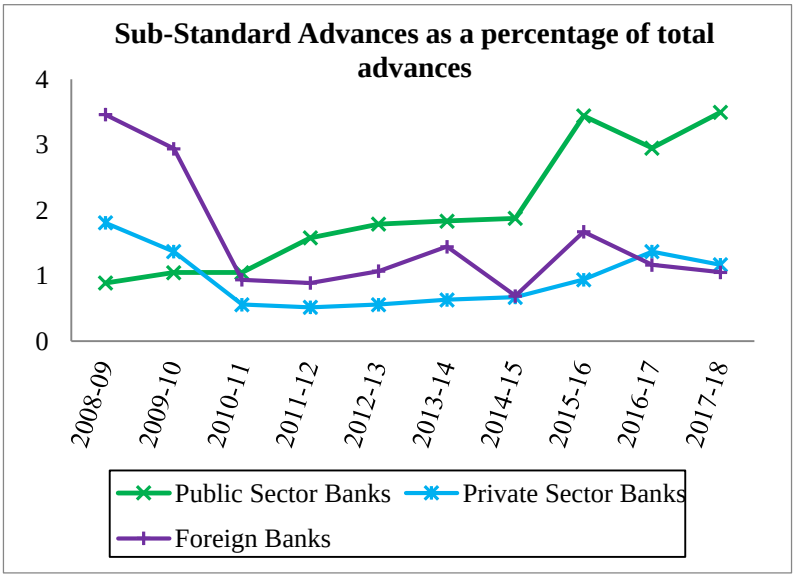

Source: RBI Report on Trends and Progress of Banking in India

A sub-standard asset is one, which has remained as non-performing for a period one year or less. Analysis of table - 2 reveals that the percentage of sub-standard assets of public sector banks is significantly increasing from 0.9% to 3.5%. However private sector banks and foreign banks reduced its percentage of sub-standard assets during the study period and thereby improved its asset quality and financial strength.

3) Doubtful Advances as a percentage of total advances

Table – 3: Doubtful Assets

Year	Doubtful Advances as a percentage of total advances		
	Public Sector Banks	Private Sector Banks	Foreign Banks
2017-18	10.2	3.2	2.3
2016-17	8.4	2.3	2.4
2015-16	5.5	1.6	1.6
2014-15	2.9	1.1	1.6
2013-14	2.3	0.8	1.4
2012-13	1.7	1.0	1.0
2011-12	1.2	1.1	1.0
2010-11	1.0	1.3	1.1
2009-10	0.9	1.0	0.9
2008-09	0.9	0.9	0.6

Chart – 3: Doubtful Assets

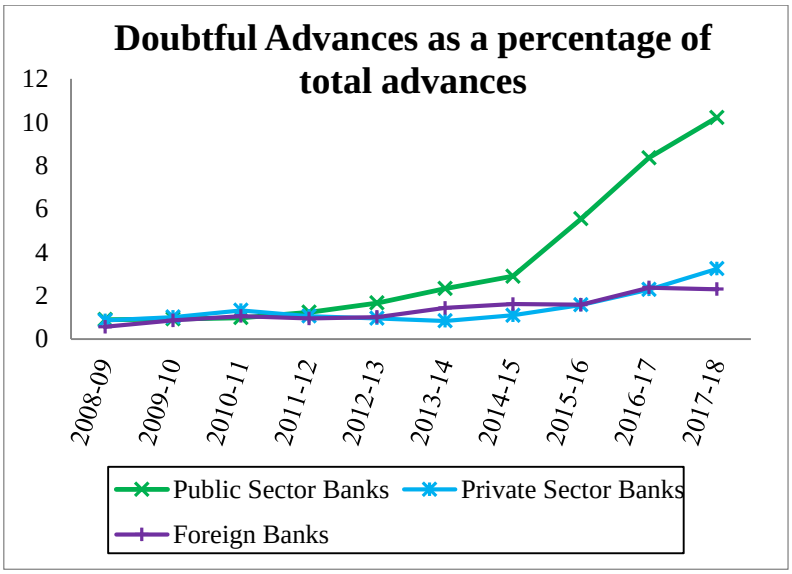

Source: RBI Report on Trends and Progress of Banking in India

A doubtful asset is one, which has remained in the category of a sub-standard asset for a period of one year. Table – 3 shows that the doubtful asset of all the three categories of the banks getting increased during the study period. The growth rate of doubtful assets of the public sector banks is much higher than that of the private sector and foreign banks. It indicates that the chance of assets becoming non-performing is increasing year after year.

4) Loss Advances as a percentage of total advances

Table – 4: Loss Assets

Year	Loss Advances as a percentage of total advances		
	Public Sector Banks	Private Sector Banks	Foreign Banks
2017-18	0.9	0.2	0.5
2016-17	0.4	0.4	0.4
2015-16	0.3	0.3	0.9
2014-15	0.2	0.3	0.9
2013-14	0.2	0.3	1.0
2012-13	0.2	0.3	0.9
2011-12	0.2	0.3	0.8
2010-11	0.2	0.4	0.6
2009-10	0.2	0.3	0.5
2008-09	0.2	0.2	0.3

Chart – 4: Loss Assets

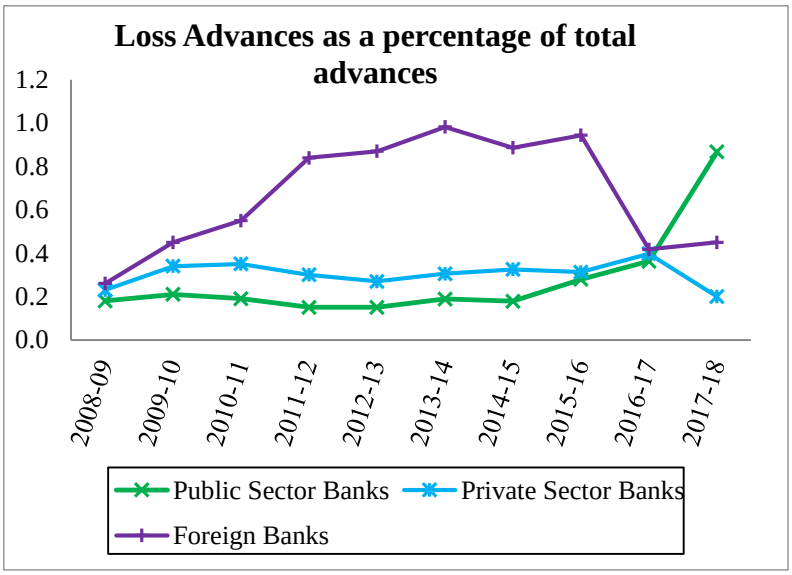

Source: RBI Report on Trends and Progress of Banking in India

A loss asset is a loan asset in which loss has been identified by the bank but the amount has not been written off wholly. The percentage of loss assets of public sector banks is much higher than the other two categories. Private Sector Banks shows better control over loss assets. The increasing percentage of loss assets will adversely affect the asset quality of the banks.

5) Gross NPA as a percentage of total advances

Table – 5: Gross NPA

Year	Gross NPA as a percentage of total advances		
	Public Sector Banks	Private Sector Banks	Foreign Banks
2017-18	14.6	4.6	3.8
2016-17	11.7	4.1	4.0
2015-16	9.3	2.8	4.2
2014-15	5.0	2.1	3.2
2013-14	4.4	1.8	3.9
2012-13	3.6	1.8	3.0
2011-12	3.0	1.9	2.7
2010-11	2.2	2.2	2.5
2009-10	2.2	2.7	4.3
2008-09	2.0	2.9	4.3

Chart – 5: Gross NPA

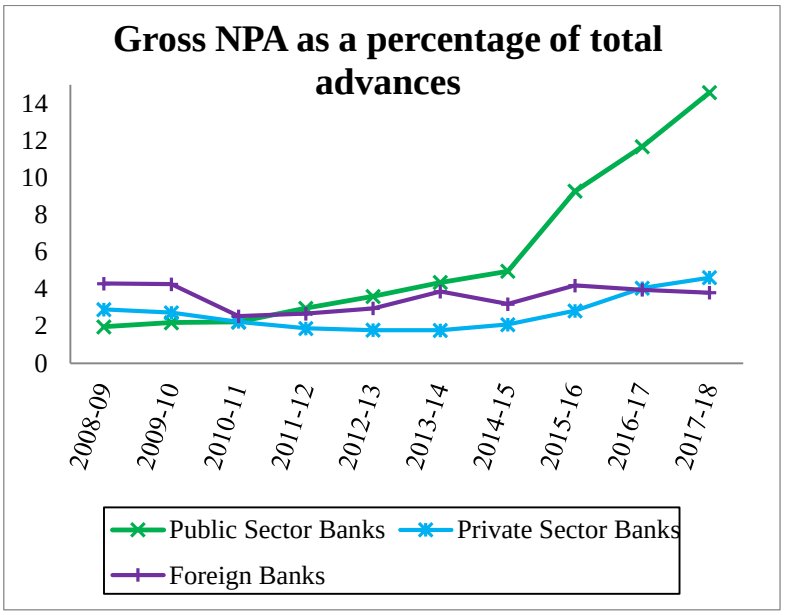

Source: RBI Report on Trends and Progress of Banking in India

GNPA Ratio is the ratio of gross NPA to total advances of the bank. In respect of public sector banks, the GNPA ratio shows an increasing trend, which was 2% in 2008-09, increased to 14.6 % in 2017-18. However, the GNPA ratio of the private sector and foreign banks were 4.6 % and 3.8 % respectively in 2017-18, which was much better as compared to public sector banks. A high GNPA ratio indicates deterioration in the quality of the loan assets of the bank.

6) Net NPA As a Percentage of Net Advances

Table – 6: Net NPA

Year	**Net NPA As a Percentage of Net Advances**		
	Public Sector Banks	**Private Sector Banks**	**Foreign Banks**
2017-18	8.0	2.4	0.4
2016-17	6.9	2.2	0.6
2015-16	5.7	1.4	0.8
2014-15	2.9	0.9	0.5
2013-14	2.6	0.7	1.1
2012-13	2.0	0.5	1.0
2011-12	1.5	0.5	0.6
2010-11	1.1	0.6	0.7
2009-10	1.1	1.0	1.8
2008-09	0.9	1.3	1.8

Chart – 6: Net NPA

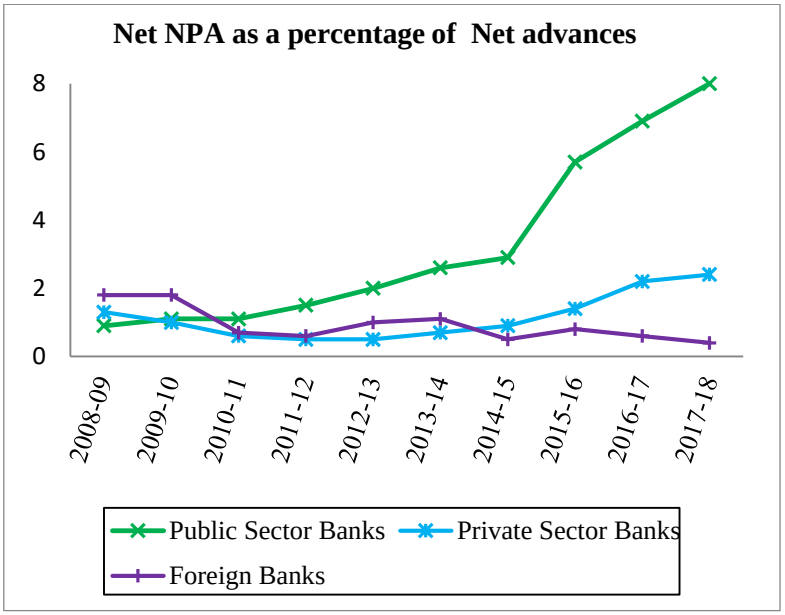

Source: RBI Report on Trends and Progress of Banking in India

The Net NPA (NNPA) to net advances ratio is the most standard measure of assets quality. To find this ratio, Net NPAs are measured as a percentage of Net Advances. The NNPA ratio in respect of public sector banks increased substantially from 0.9% to 8.0% in 2017-18 and it shows a fluctuating trend in respect of private sector banks and stood at 2.40% in 2017-18. However, the NNPA of foreign banks gets reduced to 0.4 % in 2017-18 from 1.8 % in 2008-09, which indicates improvement in the asset quality of foreign banks.

7) Testing of Hypothesis

a) H_{01}: There is no significant difference in the GNPA ratio between the Public sector, private sector and foreign banks.

ANOVA						
Source of Variation	SS	df	MS	F	P-value	F crit
Between Groups	50.61872633	2	25.30936316	3.555092432	0.042606	3.354131
Within Groups	192.2180136	27	7.119185689			
Total	242.8367399	29				

The results of one way ANOVA revealed that the F-value (3.555092432) is greater than the F-critical value (3.354131) for the alpha level selected, i.e P-value is less than 0.05. Therefore, the null hypothesis 'there is no significant difference in the GNPA ratio between the Public sector, private sector and foreign banks' is rejected and the alternative hypothesis accepted. That means there is a significant difference between the GNPA ratio of the Public sector, private sector and foreign banks.

b) H_{02}: There is no significant difference in the NNPA ratio between the Public sector, private sector and foreign banks.

ANOVA						
Source of Variation	SS	df	MS	F	P-value	F crit
Between Groups	33.39466667	2	16.6973333	6.60002635	0.00464	3.35413
Within Groups	68.307	27	2.52988889			
Total	101.7016667	29				

The ANOVA table revealed that F-value (6.60002635) is greater than the F-critical value (3.354131) for the alpha level selected, i.e P- value is less than) 0.05. Therefore, the null hypothesis 'there is no significant difference in the NNPA ratio between the Public sector, private sector and foreign banks' is rejected and the alternative hypothesis accepted. That means there is a significant difference between the NNPA ratio of the Public sector, private sector and foreign banks.

VI. CONCLUSION

The presence of Non- Performing Assets has been significantly affected the profitability and expansion of banks. All three categories - public sector banks, private sector banks and foreign banks showing an increasing trend of non-performing assets during the study period. From the study, it is clear that the asset quality of public sector banks has significantly deteriorated. The gap between public sector banks and other banks has widened in terms of Gross NPA and Net NPA significantly since 2008. Foreign banks and private sector banks are comparatively better performers than public sector banks as their Gross NPA and Net NPA are comparatively quite low than public sector banks. Asset quality is also foreign banks and private sector banks as compared to public sector banks.

Thus, the current situation has raised an important question which demands more researches in addressing the issues of rising Non-Performing Assets in public sector banks. The banks should evaluate the creditworthiness of customers by analyzing their risk-bearing capacity before issuing loans and advances. Banks should also focus on improving the NPA recovery policies, standardization of norms, post – disbursement supervision and credit monitoring. The Government and RBI have the duty of identifying and addressing the gaps in the legal and regulatory framework so as to reduce NPA level in banks' balance sheet. The government and RBI should also incorporate/amend suitable provisions for the settlement of NPAs, maintaining asset quality and competitiveness of the banks from time to time.

VII. REFERENCES

1. Borio, C and P Lowe (2002), "Assessing the Risk of Banking Crises", BIS Quarterly Review, December, pp 43–54.
2. Kabra, G and Dash, M. K(2010), "The Determinants of Non-Performing Assets in Indian Commercial Banks", Middle Eastern Finance and Economics, Issue 7.
3. Selvaraju, R., Vasanthi, G. and Michael, JN(2006), "Effect of Non-Performing Assets on Operational Efficiency of Central-Cooperative Banks", Indian Economic Panorama, Vol. 16(3). 33-39.
4. N. K. Saddy and H. Kaur(2011), "A Comparative study of non-performing assets of public and private sector banks", International Journal of Research in Commerce and Management, Vol-2, Issue-9, 82-89.
5. Kavitha, N(2012), "The Impact of Non-performing Assets on the Profitability of Indian Scheduled Commercial Banks: An Empirical Evidence", International Journal of Research in Commerce and Management, Vol.3, Issue 1, pp. 27-30.
6. Mohnani Priyanka, and Deshmukh Monal(2013), "A Study of Non-Performing Assets on Selected Public and Private Sector Banks", International Journal of Science and Research, Vol. 2, Issue 4,
7. S. Sirisha and P. Malyadri(2011), "A Comparative Study of Non-Performing Assets in Indian Banking Industry", International Journal of Economic Practices and Theories, Vol. 1, Issue 2, pp.77-87.
8. Sultan Singh, Mohina, and Sahila Choudhry, "Analysis of asset quality of private sector Indian Banks", Vol. 3, Issue 1, 2013, pp. 58-60.
9. RBI Master Circular - Prudential norms on Income Recognition, Asset Classification and Provisioning pertaining to Advances as on July 1, 2015.
10. https://dbie.rbi.org.in/DBIE/dbie.rbi?site=statistics

CORPORATE GOVERNANCE AND EMPLOYEE SATISFACTION – A CASE STUDY OF KOTTAYAM TEXTILES, VEDAGIRI.

Name: Nikhil Mohan
Asst.Professor on Contract, St.Pius X College.

ABSTRACT

"Happy workers are productive workers", based on the idea that job performance is a widely studied area of job satisfaction. Job satisfaction refers to an employee's attitude towards his job. It is very important because most of the people spend a major portion of their life at their work place: more over job satisfaction has its impact on the general life of the employee also. Employee satisfaction is the end feeling of a person after performing a task. Corporate governance ensures that company treats every employee equal and provides employee with reasonable monetary and non-monetary benefits. So here we study the various factors of corporate governance and check these factors influence the satisfaction level of employees in "kottayam Textiles, Vedagiri".

Key Words: Job satisfaction, Corporate Governance.

INTRODUCTION

Corporate governance may be defined as a set of systems, process and principles which ensures that a company is governed in the best interest of all stakeholders. It is the system by which companies are directed and controlled. It is about promoting corporate fairness, transparency and accountability.

On the other hand employee satisfaction means end feeling of an employee after performing a job. The low job satisfaction is a sign of the inefficiency, work get slowed down because of the low job satisfaction.

An employee is any person hired by the owner to perform a particular job. Employees contribute their labour and expertise to achieve the desired output. The interest of employees includes wages, salary, job security, relationship and other financial and non-financial benefits from the business. Corporate governance ensures that company treats every employee equally and provides employees with reasonable monetary and non-monetary benefits.

OBJECTIVES

1) To know the various factors of corporate governance.
2) To know whether these factors influence the satisfaction level of employees.

HYPOTHESIS

H0 (Null Hypothesis): There is no significant association between corporate governance factors and satisfaction level of employees.

Ha (Alternative Hypothesis): There is significant association between corporate governance factors and satisfaction level of employees.

METHODOLOGY

The primary and secondary data were used for the study. Primary data were collected by using structural questionnaire and schedule. The secondary data were collected from books, websites, company records and reports.

SAMPLE DESIGN

The total number of workers in the organisation is 360. Out of them researcher collected data from 60 workers. Researcher mainly depend upon the simple random sampling method.

TOOLS FOR ANALYSIS

Data were tabulated and analysed with appropriate tools like tabulation, percentage and hypothesis tested using Chi-square test.

SIGNIFICANCE OF THE STUDY

This study helped to identify the factors of corporate governance and whether these factors influence the satisfaction level of employees in kottayam textiles, vedagiri. Therefore the various inference derive from this study will help both the management and workers for framing various policies.

PROFILE OF THE ORGANISATION

Kottayam textiles were established in the year 1962 in the private sector and started commercial production in 1968. Company was inaugurated by then deputy prime minister of India Sri. Moraji Desai on 12/06/1968 and started registered production on 01/11/1968. Due to several financial crisis, mill was closed on 1976 and later it was nationalised by the Govt. of Kerala on 1983. The mill is manufacturing superfine variety combined cone yarn in counts ranging 100’s 90’s 80’s wrap.

Total number of workers in this mill is 360. Out of them there are 156 permanent workers and remaining are casuals and apprentice trainees.

FACTORS INFLUENCING CORPORATE GOVERNANCE

I. Working conditions:

Working condition refers to the working environment. It includes proper air conditioning, drainage system and there should be proper safety regulations.

II. Welfare measures:

Welfare includes anything that is done for the comfort and improvement of employees and is provided over and above the wages. Eg: medical facility, housing facility, education facilities to children of employees, recreation, canteen etc.

III. Code of conduct:

A code of conduct is a set of rules outlining the responsibilities of, or proper practices for, an individual party or organisation. It means having a manner of moral conduct, observing particular principle and employing ethics habitually as a way of life.

IV. Business ethics:

The basic concept and fundamental principle of decent human conduct. It includes study of universal values such as the essential quality of all men and women, human or natural rights, obedience to the law of land, concern for health and safety, also for the natural environment.

V. Fair wage

A wage is defined as remuneration in monetary form computed on hourly, daily, weekly, or piece work basis. It could also be defined as a payment for labour or services to a worker.

DATA ANALYSIS AND INTERPRETATION

Working condition		
opinion	No. of workers	Percentage
Excellent	10	16.66
Good	10	16.66
Poor	40	66.66
Total	60	100

Source: Primary Data *Table No: 1*

After analysing the working conditions of the organisation, the researcher got a clear idea that, majority workers are not happy with the present working conditions.

Welfare measure		
opinion	No. of workers	Percentage
Highly satisfied	30	50
Satisfied	10	16.66
Dissatisfied	20	33.66
Total	60	100

Source: Primary Data *Table No: 2*

Regarding the welfare measures provided by the organisation, 50% of the respondents are highly satisfied. Only a few are dissatisfied.

Code of conduct		
opinion	No. of workers	Percentage
Excellent	15	25
Good	10	16.66
Poor	35	58.33
Total	60	100

Source: Primary Data *Table No: 3*

By analysing the opinion of the employees about code of conduct in the organisation, majority workers are not happy with the present code of conduct.

Business ethics		
opinion	No. of workers	Percentage
Excellent	25	41.66
Good	25	41.66
Poor	10	16.66
Total	60	100

Source: Primary Data *Table No: 4*

After analysing the ethical activities of the organisation, majority (83.32%) workers are satisfied with the present ethical activities.

Fair wages		
opinion	No. of workers	Percentage
Highly satisfied	30	50
Satisfied	20	33.33
Dissatisfied	10	16.66
Total	60	100

Source: Primary Data *Table No: 5*

Regarding the wage system followed by the organisation, we can understand that most of the respondents are satisfied with the present remuneration system.

TESTING OF HYPOTHESIS

H0 (Null Hypothesis): There is no significant association between corporate governance factors and satisfaction level of employees.

H1 (Alternative Hypothesis): There is significant association between corporate governance factors and satisfaction level of employees.

Hypothesis was tested by using Chi-Square Test.

OBSERVED FREQUENCIES

Corporate governance factors	Satisfied	Not satisfied	Total
Work conditions	20	40	60
welfare measures	40	20	60
Code of conduct	25	35	60
Business ethics	50	10	60
Fair wages	50	10	60
Total	185	115	300

Table No: 6

EXPECTED FREQUENCIES

Corporate governance factors	Satisfied	Not satisfied	Total
Work conditions	37	23	60
welfare measures	37	23	60
Code of conduct	37	23	60
Business ethics	37	23	60
Fair wages	37	23	60
Total	185	115	300

Table No: 7

TABLE FOR OBSERVED FREQUENCIES AND EXPECTED FREQUENCIES

O	E	O-E	$(O-E)^2$	$(O-E)^2/E$
20	37	-17	289	7.810
40	37	3	9	0.243
25	37	12	144	3.891
50	37	13	169	4.567
50	37	13	169	4.567
40	23	17	289	12.56
20	23	-3	9	0.391
35	23	12	144	6.260
10	23	-13	169	7.347
10	23	-13	169	7.347
Total				54.983

Table No: 8

Table value of x^2 with degrees of freedom (r-1) (c-1)

(5-1) (2-1) = 4 @ 5%of level of significance = 9.488

The computed value of x^2 is more than the table value of x^2 @ 5% level with degree of freedom = 4

Therefore the H0 (Null Hypothesis) is rejected and Ha (Alternative Hypothesis) is accepted. That means there is significant association between corporate governance factors and satisfaction level of employees.

FINDINGS

After analysing the working conditions of the organization the researchers got a clear idea that, majority of the workers are not satisfied due to inadequate dust and sound control system, temperature ventilation and lighting, outdated training facilities, insufficient safety measures.

1. After analysing the working conditions of the organization the researchers got a clear idea that, majority of the workers are not satisfied due to inadequate dust and sound control system, temperature ventilation and lighting, outdated training facilities, insufficient safety measures.
2. Regarding the welfare measures provided from the organization out of the total sample size a majority of the respondents are satisfied with the available welfare facilities such as recreational club, library, canteen,

cooperative society, and tour programs twice in a year, sports and arts day etc. But a few of them are dissatisfied.

3. By analysing the opinion of the employees about code of conduct of the organization they said that they are maintaining a hormonal relationship among themselves and to the management. Rules and regulations implemented by the organization are beneficial to the employees.
4. About ethical activities of the organization the workers said that they are satisfied the impartial attitude of the management to the workers and a good grievance redressel system for the employees.
5. Regarding the wage system of the textiles out of total respondent's majority of respondents said that they are getting sufficient wages when compared to other same level of industry.

SUGGESTIONS

1. Ensure adequate safety measures like proper health care facilities, dust and sound control system, proper ventilation and temperature control facilities.
2. Employees and management should strictly follow the rules and regulations framed by the Govt.
3. Maintaining high morale and better human relations inside on organization by sustaining and improving the working conditions.
4. The management should improve the wage scale of workers to increase the satisfaction level and thereby increase their efficiency.
5. To provide adequate training facilities for their employees, it improve their carrier advancement

CONCLUSION

The existence of a good corporate governance system is vital for organizational progress and positive employee behaviour. We found in this study that good corporate governance significantly and positively predicted employee job satisfaction; and the three dimensions of corporate governance (i.e. corporate structure, corporate code of governance and internal control) significantly and positively predicted job satisfaction. The establishment of a good corporate governance system is therefore necessary to elicit good behaviours from employees. This is because a satisfied employee is a productive employee. So if a good corporate governance system is capable facilitating job satisfaction, the need to create one, maintain and improve it is a clarion call on all organizational leaders.

REFERENCE

1. Al-Qudah, M.Y. (2012). The effect of corporate governance on customer relationship quality and marketing performance. An unpublished master's degree thesis submitted to the department of business administration, Middle East University.
2. Chiang, H. (2005). An empirical study of corporate governance and corporate performance. The Journal of Law and Economics, 31(1), 122-140.
3. Collier, P. M. (2005). Management Accounting Risk and Control Strategy. CIMA Publishing: Oxford Combined Code Reviewed.
4. Donaldson, L. & Davis, J. H. (1991). Stewardship Theory or Agency Theory: CEO Governance and Shareholder Returns. Retrieved from www.agsm.edu.au/eajm/9106/pdf/donaldson.pdf
5. Davis, J.H., Schoorman, F.D., & Donaldson, L. (1997). Toward a Stewardship Theory of Management. The Academy of Management Review, 22(1), 20-47.
6. Donald, C. & Dowling, Jr. (2000-2001). How to Ensure Employment Problems Don't Torpedo Global Mergers and Acquisitions. 13 DePaul Bus. L.J. 159.
7. Duke II, J. & Kankpang, K. (2011). Linking corporate governance with organizational performance: New insights and evidence from Nigeria. Global Journal of Management and Business Research, 11(12), 47-58.
8. Ellickson, M.C. & Logsdon, K. (2001). Determinants of job satisfaction of Municipal Government employees. State and Local government Review. 33(3):173-184.

A case study on financial performance of Panathadi-vanitha service Co-operative society.

Nikhil Mohan
Asst.Professor on Contract, St.Pius X College.

ABSTRACT

In India the co-operative movement was started at the beginning of the present century. It was the result of the economic distress caused to the peasants during this period. Although the idea of forming co- operative societies was first suggested by Frederic Nicholson to solve the problem of rural indebtedness, a real beginning of the co-operative movement was made when the Cooperative Societies Act was passed in 1904. This was done with a view to encouraging thrift, self-help and co-operation amongst agriculturists, artisans and persons of limited means. Societies formed under the Act were given legal status and were authorized to raise funds and carry on business in a corporate capacity. They were classified as rural and urban; rural societies were bound to accept the principle of unlimited liability. This Act however, was deficient in many respects. The Act of 1912 was therefore, passed to make good these deficiencies. It regularized certain practices of doubtful legal validity and made provision for further expansion under proper safeguards. The distinction between rural and urban societies was removed and a more scientific classification based on limited or unlimited liability was adopted. Co-operative societies other than credit were allowed to be formed. Registration of unions and federal bodies like central banks was expressly legalized and a number of minor improvements were introduced. The simplicity and elasticity of the old Act were at the same time retained and a wide rule-making power was left to provinces to develop on their own lines.

KEY WORDS: Financial Analysis, Co-operative society.

OBJECTIVES OF THE STUDY

1. Assessment of past performance and current situation.
2. To study the financial performance
3. To compare the financial position of last 5 year.

SCOPE OF THE STUDY

It covers mainly the deposit and financial performance of the Vanitha service co-operative society ltd. The continuous data of the last 5 year that is from 2013-14 to 2017-18 are used to analyze the performance of the society

RESEARCH METHODOLOGY

The study is based on the case method and importance is given to secondary data as sources of information. The data requires for the study are collected through the discussion with the officials of the society. The data are collected from records, registers and annual statements of

the society. Appropriate statistical tools are being used in order to explain the real working of the society.

TOOLS AND TECHNIQUES

Various tools are used to evaluate the significance of financial statement data. Three commonly used toots are these

- Ratio Analysis
- Comparative Income Statements

RATIO ANALYSIS

One of the method for analyzing financial statements is the use of many kinds of ratios. You use ratios to calculate the relative size of one number in relation to another. After you calculate a ratio, you can then compare it to the same ratio calculated for a prior period, or that is based on an industry average, to see if the company is performing in accordance with expectations. In a typical financial statement analysis, most ratios will be within expectations, while a small number will flag potential problems that will attract the attention of the reviewer. The methods to be selected for the analysis depend upon the circumstances and the users' need. The user or the analyst should use appropriate methods to derive required information to fulfil their needs.

COMPARATIVE FINANCIAL STATEMENTS

Comparative financial statements are those statements which have been designed in a way so as to provide time perspective to the consideration of various elements of financial position embodied in such statements. In these statements figures for two or more periods are placed side by side to facilitate comparison.

Comparative Income Statement

This statement discloses the net profit or net loss resulting from the operations of business. Such statement shows the operating results for a number of accounting periods so that changes in absolute data from one period to another period may be stated in terms of absolute change or in terms of percentage.

Comparative Balance Sheet

This statement, prepared on two or more different dates, can be used for comparing assets and liabilities and to find out any increase or decrease in these items.

PERIOD OF THE STUDY

The performance of the society during the year 2013-14,2014-15,2015-16,2016-17,2017-18 are covered by this study.

LIMITATION OF THE STUDY

- ★ The study is mainly depend on secondary data, which were collected from books and records of the society.
- ★ Short time period
- ★ Less budget

CURRENT RATIO

YEAR	CURRENT ASSET	CURRENT LIABILITY	CURRENT RATIO
2013-14	25545535	6599109	3.87
2014-15	32687735	8735106	3.74
2015-16	40913934	8772277	4.66
2016-17	44131583	17428724	2.66
2017-18	55776752	25950953	2.53

INTERPRETATION

As a conversion, the standard current ratio is 2:1. From the above table we can see that the society's current ratios in all years are above the standard ratio. Therefore in the society too much money is blocked.

LIQUIDITY RATIO

YEAR	LIQUID ASSET	CURRENT LIABILITY	LIQUIDITY RATIO
2013-14	1621879	6599109	0.24
2014-15	2401106	8735106	0.27
2015-16	6684763	8772277	0.76
2016-17	1383630	17428724	0.08
2017-18	1836149	25950953	0.07

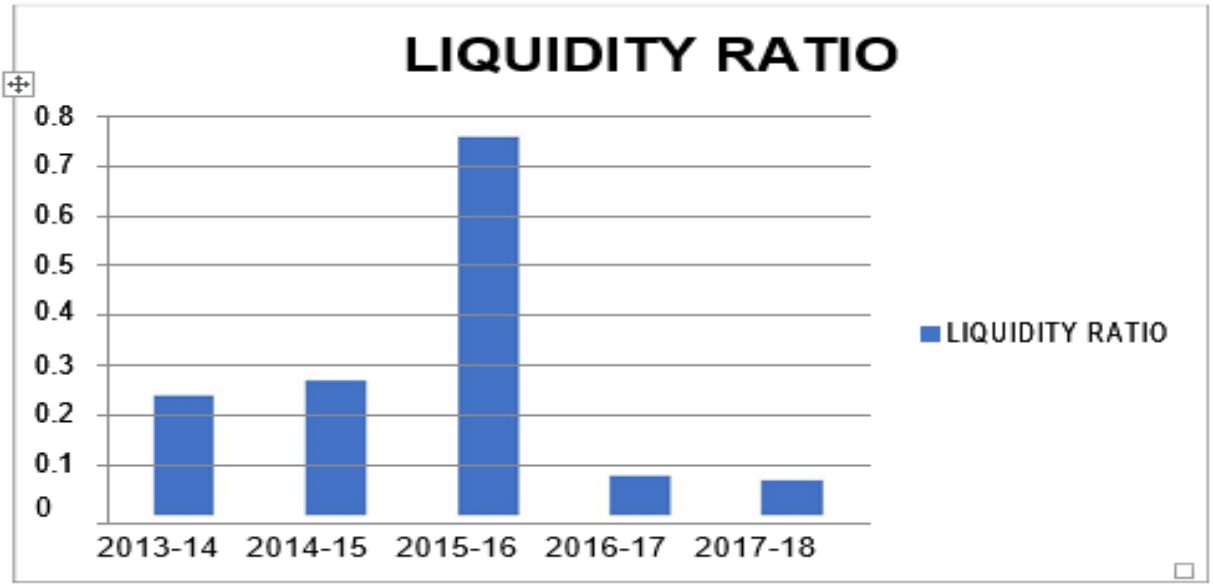

INTERPRETATION

The standard liquid ratio is 1. Here the society's liquid ratio is lower than the standard ratio.

So the society have insufficient quick assets.

DEBT EQUITY RATIO

YEAR	LONG TERM DEBT	SHAREHOLDERS FUND	DEBT-EQUITY RATIO
2013-14	17859295	4522328	3.95
2014-15	25856560	5282559	4.89
2015-16	35143987	6751824	5.20
2016-17	30201505	10758892	2.81
2017-18	33782919	10771768	3.14

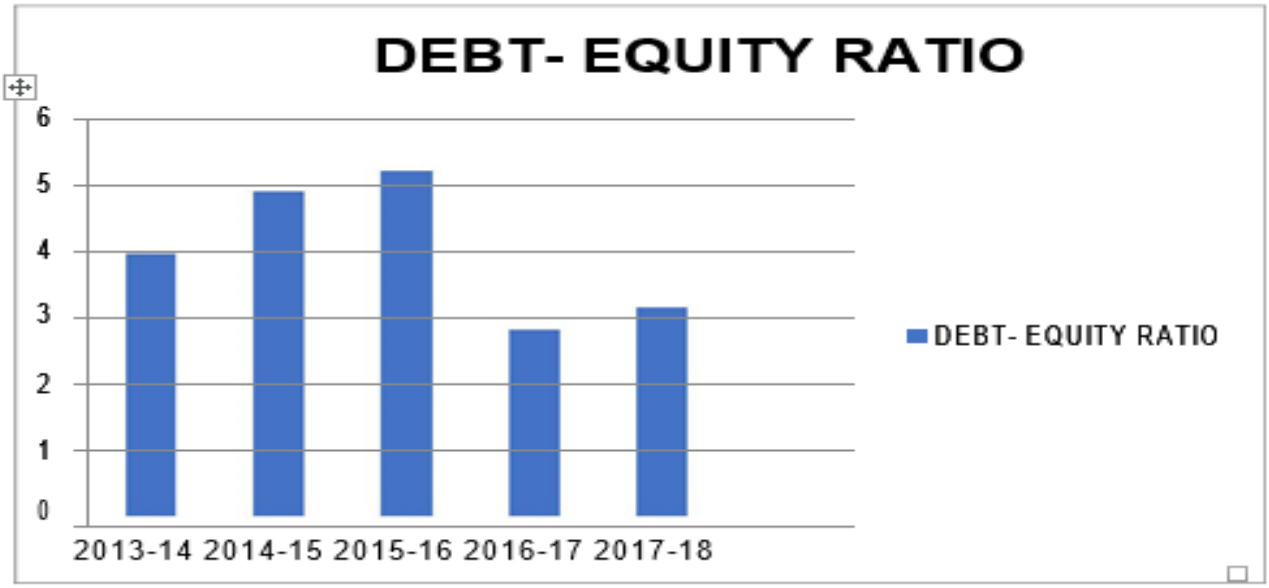

INTERPRETATION

The standard or ideal debt equity ratio is 1:1. Here the society's debt equity ratio is higher than the standard ratio. Therefore the society may be adopted to take advantage of cheaper debt capital.

PROPRIETARY RATIO

YEAR	SHAREHOLDERS FUND	TOTAL ASSET	PROPRIETARY RATIO
2013-14	4522328	26814111	0.17
2014-15	5282559	36912472	0.14
2015-16	6751824	46506407	0.14
2016-17	10758892	51136054	0.21
2017-18	10771768	63354478	0.17

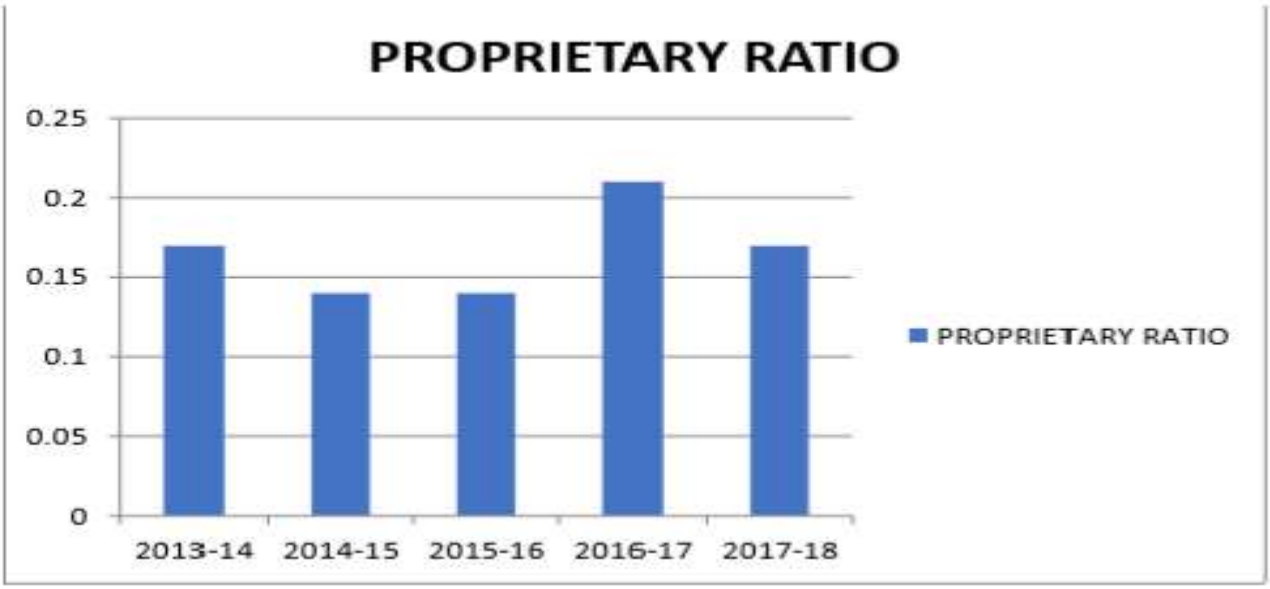

INTERPRETATION

The standard proprietary ratio is 0.5:1. Here the society's proprietary ratio is lower than the standard ratio. So the society shows greater risk to the creditors.

SOLVENCY RATIO

YEAR	TOTAL ASSET	TOTAL DEBT	SOLVENCY RATIO
2013-14	26814111	22224920	1.21
2014-15	36912472	30541906	1.21
2015-16	46506407	40544503	1.15
2016-17	51136054	36077956	1.42
2017-18	63354478	4079002	1.55

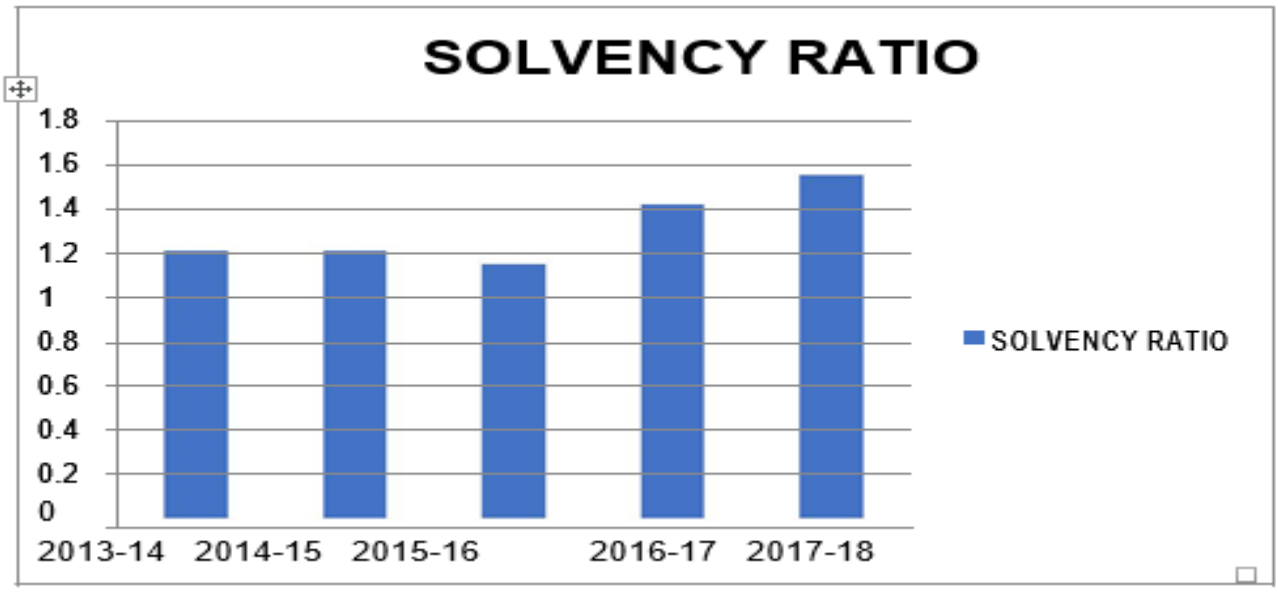

INTERPRETATION

The solvency ratio indicates the degree of solvency of a society. Here the solvency ratio is more than 1. If the ratio is more than 1, the lenders can breathe a free air as their investment is secured. In the society the solvency and the financial position are strong.

COMPARATIVE BALANCESHEET

COMPARATIVE BALANCESHEET OF PANATHADI VANITHA SERVICE CO-OPERATIVE SOCIETY LTD									
	AMOUNT					PERCENTAGE OF INCREASE OR DECREASE IN			
PARTICULARS	**2014**	**2015**	**2016**	**2017**	**2018**	**2015**	**2016**	**2017**	**2018**
FIXED ASSETS									
LAND AND BUILDING	447396	447396	1778796	1778796	1778796	0	298	298	298
OTHER	3629009	7409040	8693537	13309895	13755745	104	140	267	279
TOTAL FIXED ASSETS	4076405	7856436	10472333	15088691	15534541	93	157	92	281
CURRENT ASSETS									
CASH IN HAND	304798	859646	480805	306486	682008	182	58	1	124
CASH AT BANK	1291666	1512545	6142372	1012782	1064779	17	376	-22	-18
CASH AT OTHER BANK	25415	28915	61586	64362	89362	14	142	153	252
SHORT TERM LOANS	15994471	20547138	25470296	25584655	27719974	28	59	60	73
MID TERM LOANS	976634	654453	708874	955190	837413	-33	-27	-2	-14
NORMAL LOANS	654345	1328535	1142395	757320	1082658	103	75	16	65
INTEREST RECEIVABLE	1362614	1520959	2215645	2790381	2611576	12	63	105	92
ADVANCE RECEIVABLE	1453272	1479947	2312836	11180275	20446498	2	59	669	1307
DEFICITE STOCK	76040	76040	76040	76040	76040	0	0	0	0
MDS DUE TO	3291847	4563191	1960178	1287726	1050078	39	-40	-61	-68
OTHER	114433	116366	342907	116366	116366	2	200	2	2
TOTAL CURRENT ASSETS	25545535	32687735	40913934	44131583	55776752	28	60	73	118
TOTAL ASSET	**29621940**	**40544171**	**51386267**	**59220274**	**71311293**	**37**	**73**	**100**	**141**
CAPITAL AND LIABILITIES									
SHARE CAPITAL	724990	878435	1024145	1376765	1415105	21	41	90	95
RESERVES	3523320	4064383	5326283	8879773	8729495	15	51	152	148
EMPLOYEE PROVIDENT FUND	145880	211603	273258	374216	492168	45	87	157	237
PROFESSIONAL EDUCATION FUND	38138	38138	38138	38138		0	0	0	-100
EMPLOYEE SECURITY FUND	90000	90000	90000	90000	135000	0	0	0	50
SHAREHOLDERS FUND	4522328	5282559	6751824	10758892	10771768	17	49	138	138
FIXED LIABILITIES	17859295	25856560	35143987	30201505	33847429	45	97	69	90
OTHERS	641208	669946	718179	831153	741143	4	12	30	16
CURRENT LIABILITIES									
SAVING DEPOSITS	2014651	2330442	2677021	3206555	3161013	16	33	59	57
CURRENT DEPOSITS	2075847	2078497	2447328	2144769	3289393	0	18	3	58
GROUPS	7702	7702	7702	7702	7702	0	0	0	0
THRIFT	267425	268705	268465	267425	266465	0	0	0	0
GOV.AGENCIES				250000	225000				
MDS DUE BY	1456367	3243268	606268	44153	8800	123	-58	-97	-99
ADVANCE PAYABLE	777117	806492	2765493	11508120	18992580	4	256	1381	2344
TOTAL CURRENT LIABILITIES	6599109	9405052	8772277	17428724	25950953	43	33	164	293
TOTAL LIABILITIES	**29621940**	**40544171**	**51386267**	**59220274**	**71311293**	**37**	**73**	**100**	**141**

INTERPRETATION

From the above comparative balance sheet 2014 is taken as base year. In 2015, total fixed assets have increased by 93%, total current assets have increased by 28%, shareholders fund have increased by 17% and total current assets have increased by 43%.Generally there is an overall increase in total assets in 2015 over 2014 only by 37%. In 2016, total fixed assets have increased by 157%, total current assets have increased by 60%, shareholders fund have increased by 49% and total current assets have decreased by 33%.Generally there is an overall increase in total assets in 2016 over 2014 only by 73%. In 2017, total fixed assets have increased by 270%, total current assets have increased by 73%, shareholders fund have

increased by 138% and total current assets have increased by 164%.Generally there is an overall increase in total assets in 2017 over 2014 by 100%. In 2018, total fixed assets have increased by 281%, total current assets have increased by 118%, shareholders fund have increased by 138% and total current assets have increased by 293%.Generally there is an overall increase in total assets in 2018 over 2014 only by 141%.

FINDINGS:

1) A current ratio of 2:1 is considered as an ideal one. In all the 5 years the current ratio is above the standard. It indicates that too much money is blocked in the society.
2) A liquid ratio of 1:1 is considered as an ideal one. In all the 5 year except one year the ratio is below the standard.
3) In all the five years the society's debt equity ratio is above the standard. It indicates higher proportion of debt contents in the capital structure.
4) A proprietary ratio of 0.5:1 is considered as ideal. All the five years proprietary ratio is below the standard. It shows greater risk to the creditors.
5) A higher solvency ratio indicates that the financial positions are strong. All the five year the society's solvency ratio is more than 1.
6) The membership position of the society is increasing during the study period. Most of the members are belongs to A-class members.
7) The share capital position of the society shows a fluctuating trend.
8) Loan position of the society is fluctuating one.
9) Paid up share capital position of the society shows decreasing and increasing trend.
10) Current asset and liability position of the society shows a fluctuating trend during the study period.
11) Saving bank deposit performance of the society shows in increasing trend.
12) Day deposit, group deposit and tariff deposit, position of the society shows a fluctuating trend.
13) Current asset and liability position of the society shows increasing trend.
14) The major source of finance of the bank consists of share capital reserve fund deposits.

SUGGESTIONS:

- ★ The society should increase its membership position.
- ★ In order to avoid overdue, sufficient field staff should be appointed to see that the loans sanctioned are utilized for specific purpose only.
- ★ The society should take effective measures to the utilization of loan availed. The society should conduct inspection regularly.
- ★ Effective measures should be taken to increase the net profit of the society.
- ★ Loan should be given by right base, right purpose and only to eligible member
- ★ The society should reduce over expenditure.
- ★ In order to raise working capital, society should encourage the members to deposit their savings in the society.
- ★ Current asset and liability position of the society should increase.
- ★ Saving bank deposit performance of the society should increase.

CONCLUSION

Panathadi-Vanitha Service Co-operative Society is in its state as able to satisfy the needs of its members. The society has the full support of the people of that area, which help the society for grown with a good performing condition. The society is working efficiently for serving the people. The reason behind the savers of the society is hard work of employs and managing committee. Co-operation is based on the value of self-help, self- responsibility, democracy; Co-operation was the chaotic situation in the political and economic spheres of the industrial life. The education of the members on the principle and practice of co-operation is one of the prerequisite for the success of a co-operative society.

On the basis of various techniques applied for the financial analysis of Panathadi Vanitha Service Co-operative society we can arrive at a conclusion that the financial position and overall performance of the society is satisfactory. Though the income of the society has increased over the period but not in the same pace as of expenses but the society has succeeded in maintaining a reasonable profitability position. The overall financial position of the company is quite healthy and over the last years which covered the period of the study, the financial position has improved.

BIBLIOGRAPHY

1) BOOKS:

Robert Kaplan and Antony A. Atkinson: –Advanced management accounting

Alasdair Gilchrist :–Management accounting

R P Rustagi:-Financial Management

Deepak Gupta:-Best Management Accounting

Dr.Vinod Kumar:-Management Accounting

2) JOURNALS AND MAGAZINES

Record of Panathadi Vanitha Service Cooperative Society Private Ltd

3) WEBSITES

https://en.m.wikipedia.org/wiki/financial _analysis

www.shodhganga.inflibnet.ac.in

https://www.investopedia.com/terms/f/financial-analysis.asp

MEASURING THE AWARENESS ABOUT IMPLEMENTATION OF GST: A SURVEY ON PUBLIC

By

NIKHIL MOHAN

Asst.Professor on Contract,
St.Pius X College, Kerala

Abstract

Tax is a way of collecting revenue from individuals, companies or other entities by the government in order to finance state expenditure.It is considered as the most important sources of government's incometo drive the economic growth and achieve the status of a developed country and high income. Thus, there are various taxes levied on the users such as direct taxes and indirect taxes. Direct taxes are taxes on income, while indirect taxes are taxes on goods andservices of both types of taxes mentioned, GST is included in the second type of tax, where it is a system of taxation of expenses or use of goods and services. The idea behind having one consolidated indirect tax to subsume multiple currently existing indirect taxes is to benefit the Indian economy in a number of ways. There will now be a single tax on goods and services. In addition to the above, the Goods and Services Tax Law aims at streamlining the indirect taxation regime. As mentioned above, GST will subsume all indirect taxes levied on goods and service, including State and Central level taxes. The GST mechanism is advancement on the VAT system, the idea being that a unified GST Law will create a seamless nationwide market. In this research, the researcher is trying to understand the awareness level of general public about Goods and Service Tax (GST).

Key words: GST, Goods and Service Tax, Awareness.

STATEMENT OF THE PROBLEM

GST is considered the world's best tax system based on the implementation of the country which has implemented the GST.GST has just being applied in India. The government and its crew are still in their way to spread out the information of GST in order to combat confusion among people. It is an issue if people are still unaware or confuse with the tax system of GST. GST is a popular issue that is being discussed by people day to day, it is necessary to know whether the public are aware of the government's plan and do they have knowledge on this issue. Therefore this study makes an effort to test the awareness of the public on the implementation of Goods and Services Tax (GST)

OBJECTIVES OF THE STUDY

1. To have an overview about the Goods and Service Tax (GST).
2. To have a study on public awareness towards GST
3. To provide suggestions based on the findings of the study.

RESEARCH METHODOLOGY

The research was based on both primary data and secondary data. Primary data was collected by using questionnaire and secondary data have been collected from journals, websites etc. The researcher was not possible to study the entire population of Public Awareness about GST in KASARAGOD district. So the researcher has collected only limited respondents i.e. 200 respondents.

* **Region Of Research**

  The geographical area of the research is KASARAGOD district, Kerala. Since there is a lack of time, the region is restricted to a small area.

* **Research design**

  The research is an analytical study. The design is based on the objectives of the study and the hypothesis of the study. Selection of respondents was made randomly. The method used in this study was quantitatively using questionnaire as the main instrument. A set of questionnaire which consists of 10questions designed to gain primary data. Data in relation to provisions for goods and service tax would be collected from the existing law. The data collected through the interviews and questionnaires will be subject to further statistical methods of analysis.

* **Sampling**

  The population of the study consists of students,accountants, tax payers and the general public. Out of the population a sample of 200 persons are to be recognized as the sample size. The sample will be collected based on purposive sampling. A limited number of sample is only practicable since the lack of time. Thus the sample size is limited to 40 based on convenient sampling.

* **Tools for data collection**

  The study involves collection of both primary and secondary data. Primary data is being collected by using structured questionnaire. The questionnaire before actual use is analyzed through pilot testing. The difficulties identified in pilot testing are

removed before finalizing the final questionnaire. This questionnaire will be distributed to the selected sample.Secondary data were collected through published and unpublished reports on GST impacts on Indian economy, various journals, and various websites related with GST etc….

* **Hypothesis**

  H_0: Public are well aware about GST

  H_1: Public are unaware about GST

* **Tools for Data Analysis**
  - Percentage Analysis
  - Chi-Square Test

DATA ANALYSIS & INTERPRETATION

The present study is mainly based on primary data. A detailed questionnaire was prepared for collecting data from the Merchants and service providers in KASARAGOD DISTRICT. The sample size is limited to 200 and all works are performed on the basis of these samples.

The data collected by using questionnaire were analyzed and tabulated extensively using different graphs and diagrams. The analysis is mainly based on percentage analysis. The secondary data is mainly obtained from websites, journals and newspapers. The term interpretation is used to give explanation and significance of collected data.

Table No: 1

SOURCE OF INFORMATION ABOUT GST		
OPINION	**NO OF RESPONDENS**	**PERCENTAGE**
Friends	15	7.5
Family	35	17.5
Mass media	120	60.0
Online access	30	15
TOTAL	200	100.00

Source: Primary Data

The above table shows the respondents source of awareness about GST. Out of the totalrespondents taken for the study, 60 % of the public are aware of GST through mass media, 7.5 % ofthe public are through friends, 17.5 % of the public are through family

discussion and the remaining15% of the public are through online sources. Majority of the public are aware of GST throughmass media.

Table No: 2

GST CHECKS THE TAX EVASION PERIODICALLY		
OPINION	**NO OF RESPONDENTS**	**PERCETAGE**
YES	30	15
NO	50	25
NO IDEA	120	60
TOTAL	200	100

Source: Primary Data

The table above shows the opinion of the public against the term tax evasion.It is seen that many of the people are not aware about the concept of tax evasion.15 percentage are respond that GST checks tax evasion periodically. 25% are of the opinion that GST doesn't check tax evasion periodically and it is seen that majority of the respondents i.e.; 60 % are having no oipinion about the problem.

Table No: 3

ITEMS NOT SUBJECT TO GST		
OPINION	**NO OF RESPONDENTS**	**PERCENTAGE**
COOKING OIL	5	2.5
BOOKS	20	10.0
PETROL	100	50.0
CLINIC	15	7.5
TOBACCO	60	30.5
TOTAL	200	100.00

Source: Primary Data

The above table and pie diagram shows various opinions on which item is excluded from the charge of GST from the given options. It is seen that about 30% of the respondents agree that 'tobacco' is excluded from GST, 7.5 % are agree upon 'clinic' 50% are belongs to 'petrol' and 10% are on 'books' . Remaining 2.5 % are with the opinion of 'cooking oil'

Table No: 4

WHETHER ALL PERSONS NEED TO BE REGISTERED UNDER GST		
OPINION	**NO OF RESPONDENTS**	**PERCENTAGE**
YES	65	32.5
NO	135	67.5
TOTAL	200	100

Source: Primary Data

The above table shows the opinion of respondents on 'whether all the business need to be registered under GST ?.' it can be understood from the above table that more than half of the respondents are aware that all the business are not taxable person according to law. 67.5% are supporting that all 'person' are not taxable. Remaining 32.5% are provided their opinion as all business are taxable and need to be registered under GST.

Table No: 5

GST WILL ELIMINATE CASCADING EFFECT		
OPINION	**NO OF RESPONDENTS**	**PERCENTAGE**
YES	75	37.5
NO	65	32.5
NO OPINION	60	30.0
TOTAL	200	100.0

Source: Primary Data

The above tables describes the responces by the respondents on one of the feature of GST i.e,; removal of cascading effect. It is the fact that 37.5 % of the respondents are agrees that GST will remove cascading effect . but the remaining 62.5% of the respondents are either of the opinin of it will not eliminate cascading effect or no opinion. 12 respondents are doesn't having any opinion on this matter.

Table No: 6

NEED MORE AWARENESS PROGRAMES ABOUT GST		
OPINION	**NO OF RESPONDENTS**	**PERCENTAGE**

YES	170	85
NO	30	15
TOTAL	200	100

Source: Primary Data

The above table provides the opinion of the public on the issue of awareness programmes . it shows a clear picture that 85% of the respondents are in need of various awareness programmes about GST. Only remaining 15% of the respondents are aginst such opinion .

Table No: 7

AWARENESS LEVEL ABOUT GST		
OPINION	**NO OF RESPONDENTS**	**PERCENTAGE**
Very Well	10	5
Well	25	12.5
Adequate	40	20
Poor	50	25
Very Poor	75	37.5
TOTAL	200	100

Source: Primary Data

CHI-SQUARE TEST

O	**E**	**O-E**	**$(O-E)^2$**	**$(O-E)^2/E$**
10	40	-30	900	22.5
25	40	-15	225	5.63
40	40	0	0	0
50	40	10	100	2.5
75	40	35	1225	30.63
		TOTAL:		**61.26**

X^2=**61.26**

Degree of Freedom= r-1 = 5-1 = **4**

α =0.05 = **5%**

Critical value (Table Value) = **9.488**

Calculated value (61.26) is in rejection area, hence we can reject the Null Hypothesis and accept Alternative Hypothesis.

FINDINGS

- From the test result, we can find out that public are unaware about GST.
- General public are demanding for more awareness programs.
- Majority of the public getting information of GST through mass media.
- Majority of the respondents are not at all aware about the term tax evasion and the role of GST tax authority on checking tax evasion regularly.
- From the data derived from the opinion of the public it is concluded that half of the total respondents are not aware about the items excluded from GST. The GST law of India states that GST would be applicable to all goods other than alcoholic liquor for human consumption and five petroleum products, viz. petroleum crude, motor spirit (petrol), high speed diesel, natural gas and aviation turbine fuel. Only 50% of the respondents provided with correct option remaining are not aware about the items excluded in the GST.
- More than half of the respondents are known the fact that all person need not be registered under GST. But a portion of the respondents are on the opinion that every person is taxable person. Thus it is concluded that there need more clarification on this issue among the public.
- From the opinion given by the respondents it is understood that majority of the respondents are in need of further awareness about GST. It is clear that many of them are not aware about the concepts of GST and who are interested in knowing GST further. It is assumed that remaining 15% of the respondents are knowledgeable persons on the concepts and terms of GST. Thus there is a need of various awareness programs.
- Elimination of cascading effect is one of the main feature of GST. Many of the respondents are doesn't have any opinion on this matter. Thus it is concluded that people need to be aware about the concept of cascading effect. The working of such effect and how GST would eliminate cascading effect of tax.

CONCLUSION

GST is considered the world's best tax system based on the implementation of the country which has implemented the GST.GST has just being applied in India. The government and its crew are still in their way to spread out the information of GST in order to combat confusion among people.After analyzing the information and result of Chi-square test, we can conclude that most of the common people are unaware about GST.

BIBLIOGRAPHY

https://services.gst.gov.in/services/login

https://timesofindia.indiatimes.com

www.cbic.gov.in/htdocs-cbec/gst/index

https://www.gst.gov.in

https://economictimes.indiatimes.com

www.gstcouncil.gov.in/state

****

Research Paper
Impact Factor: 4. 695
Peer Reviewed & Indexed Journal

IJMSRR
E- ISSN - 2349-6746
ISSN -2349-6738

A STUDY ON CUSTOMER SATISFACTION OF INTERNET BANKING SERVICE QUALITY

Mrs.Reshma.B.K
Assistant Professor in Commerce, St.Pius X College,Rajapuram,Kasaragod, kerala.

Abstract
The banking industry has been rapidly developing the use of Internet banking as an efficient and viable tool to create customer value. It is one of the popular services offered by the traditional banks to provide speedier and reliable services to online users. With the rapid development of computer technology as a commercial too Internet banking can be used to attract more customers to perform banking transactions in related banks. However, the main problem of Internet banking faced by the providers is that a large number of the banks' customers are not willing to use the Internet banking services offered. This happened due to the services offered through Internet banking have yet to satisfy their customers. Customer satisfaction is an important factor to help banks to sustain competitive advantages. Therefore, the purpose of this research is to search and examine the customer satisfaction towards Internet banking.

***Keywords: Internet Banking, Service Quality, Customer Satisfaction, Security*.**

Introduction

Banking sector plays a significant role in the development of an economy. The advent of Information Technology (IT) and its convergence with communication technology have drastically changed the landscape of banking services across the globe. Over the past few decades, banks all over the world have been investing substantial amounts of money in IT with the avowed objectives of improving operational efficiency, competitive position and product innovation. The use of IT in the banking sector has contributed to the emergence of more flexible and user friendly Self Service Banking Technologies (SSBT) to address the rapid and changing needs of banking customers. It has changed the face of global banking sector radically altering the manner in which customers conduct their banking transactions. Indian banking sector too has followed the same path and the gap between Indian banks and their counterparties in the technology advanced countries is vanishing.

Statement of Problem

Customer satisfaction is a complicated mix of "hardware" (technology, product, price, quality etc.) and "software" (attitude, responsiveness, deliverance, communication etc.). Today's customers are not satisfied with care and courtesy alone, they expect concern and commitment. In this competition environment not the oldest, not the strongest and not the first can survive, but only the "best" can survive. The success of Internet Banking not only depends on the technology but also on the large extend the attitude, commitment and involvement of the operating at all levels and how far the customers reap the benefits from Internet banking services. The purpose of this study is to examine the customer satisfaction with various service quality dimensions.

Objectives

1. To identify the factors affecting customer satisfaction on Internet Banking service quality.
2. To evaluate the satisfaction level of Internet Banking users.
3. To examine the major problems faced by users while using Internet Banking services.
4. To identify the level of trust and awareness level on the security features of Internet Banking.

Significance of the Study

Internet has established its role as a powerful economic force multiplier with a new studyprojecting that its contribution to India's GDP will explode to $100 billion (Rs 5 lakh crore) .The increasing usage of internet in Kerala is evident from the fact in the previous years. People ofKerala are becoming e-literate through 'Akshaya' project undertaken byGovt. of Kerala in 2005, which imparts training to one person from one family to makepeople aware of the basics and scope of IT, hands-on-skill in operating a computer and use ofinternet. Both availability of access to internet and e-literacy are essential prerequisites for theadoption of internet banking. More access to computers and the internet, the greater is the possibility of the use of internet banking. Similarly, the more people are becoming e-literate,the more is the possibility of doing internet banking.

At present, public utility service providers are encouraging their customers to make payment of their utility bills online.. However, research studies indicate thatcustomers' security and risk are the major inhibitors to the adoption of IB. therefore, in order to ally the apprehensions of customers about the risk associated with the use of IB, the providers need to educate and enlighten customers regarding the safe use of IB by asking them to take the required precautions. However, a comprehensive research investigating the extent of IB use, precautions taken by IB users for safe banking over internet, awareness and trust

of customers on the security features adopted by banks to guard them against the risk of fraud, the service quality dimensions and their effect on customer satisfaction, problems encountered by IB users during service delivery etc. Hence, the present study is quite relevant and timely from the point of view of both academic and banking industry.

Research Methodology

Research methodology refers to the theoretical analysis of the methods appropriate to a field of study or to the body of methods and principles particular to a branch of knowledge.

Data Sources

The study makes use of primary and secondary data. The primary data is collected from the IB users through a structured questionnaire. Secondary data collected from various sources like Articles, websites, Lecture books etc

Period of Study: The study is conducted for a period of 21 days from 2nd week of April 2018.

Research Instrument: A well-structured questionnaire was prepared with a view to collect information from Internet banking Users.

Population: Population comprises all the customers who were using Internet Banking Services in kasaragod.

Sample Size: Due to the limited period of study, only 100 customers selected as sample unit from the population.

Method of Sampling: Random Sampling Method is used for selecting the Sample Unit.

Types of Analysis

Bi-variable analysis was done for establishing relationship among the variables under study.
Tools used for analysis

1. Friedman Test.
2. Kruskal-Wallis Test.

Limitations of the Study

1. Selected Sample is limited to 100. Hence findings cannot be generalized.
2. Respondents may be biased. So the collected data may not be reliable.
3. Customers' preferences and opinions are supposed to change from time to time.

RahmathSafeena et al (2011) found that banks need to highlight the benefits of IB, make IB easy to use, and enhance IB security to improve consumers' trust. They also need to make the consumers aware about the system by providing them about the details of the benefits associated with it and also ensuring security of the system.

Dixit N. &Datta S.K., (2010) in their study, they found that country like India, there is need for providing better and customized services to the customers. Banks must be concerned the attitudes of adult customers with regard to acceptance of online banking. It is shows that adult customers are more reluctant to join new technologies or methods that might contain little risk.

Khan M.S. &Mahapatra S.S., (2009), explored the service quality of internet banking operative in India from customer's perspective. It is observed that customers are satisfied with the reliability of the services provided by the banks but are not very much satisfied with the dimension 'User friendliness'.

Srivastava, (2007), reveals that the perception of the consumers can be changed by awareness program, friendly usage, less charges, proper security, and the best response to the services offered. The study also provides the kind of correlation between different factors. As per our basic assumptions we consider only those consumers who know how to use Internet and have an access to Internet, and our study considered only the situation wherein banks provide Internet banking of their colleagues or friends who surround him using Internet banking then it may influence his decision to follow Internet banking option.

Sohail et al (2007), the results of the factor analysis in the present study produced three dimensions. While this result reveals that "efficiency and security" is the most influencing factor in users' evaluation of service quality, the factor group produces a combination of diverse measures which may be due to the highly correlated nature of service quality dimensions.

Analysis of Data

The analysis is presented in four parts

1. Demographic profile of respondents.
2. Reasons for using IB services.
3. Problems faced by IB users.
4. Level of trust on security features available in IB.

Friedman Test and Kruskal-Wallis Test are used for making these Analyses.

Table No.1: Demographic Profile of Respondents

	Category	**No .Of Respontents**	**Cumulative Frequency**
AGE	LESS THAN/=25	24	24
	26 TO 30	25	49
	31 TO 40	25	74
	GREATER THAN/=41	26	100
GENDER	MALE	64	64
	FEMALE	36	100
EDUCATION QUALIFICATION	UP TO PLUS TWO	13	13
	GRADUATE	10	23
	POST GRADUATE	70	93
	PROFESSION	7	100
OCCUPATION	UNEMPLOYED	16	16
	PUBLIC SECTOR	25	41
	PRIVATE SECTOR	32	73
	BUSINESS/PROFESSION	27	100
AVERAGE MONTHLY INCOME	LESS THAN/=10000	21	21
	10001TO 20000	33	54
	20001TO 30000	19	73
	GREATERTHAN/=30001	27	100
TYPES OF ACCOUNT	SAVINGS	77	77
	CURRENT	23	100
USAGE OF BANKING SERVICE	LESS THAN/=5	34	34
	6 TO 10	27	61
	11 TO 15	18	79
	GREATERTHAN/=16	21	100
USAGE OF IB SERVICE	LESS THAN/=2	31	31
	3TO 5	33	64
	6TO 8	26	90
	GREATERTHAN/=9	10	100
AVG MONTHLY USAGE OF IB	LESS THAN/=3	25	25
	4 TO 7	29	54
	8 TO 10	19	73
	GREATERTHAN/=11	27	100
ACCESSABILITY OF IB	VERY GOOD	21	21
	GOOD	67	88
	AVERAGE	10	98
	POOR	2	100
	VERY POOR	0	100
WEBSITE PRESENTATION	VERY GOOD	16	16
	GOOD	62	78
	AVERAGE	20	98
	POOR	2	100
	VERY POOR	0	100

Table 1.exhibit the profile of the sample respondents selected for the study. The majority of IB users belong to the age group greater than 40. Gender wise classification shows that out of the 100 respondents, majority (64percent) are male. As to education Qualification 70 percent are post graduate and only 7 percent are professionally qualified. From the table it can be seen that majority (32 percent) are belong to private sector followed by business and profession. The monthly income classification of the respondents reveals that majority of them falls under the income group 10001-20000 and almost 73 percent respondents were receiving less than 30000 as monthly income. The table shows that 77 percent respondents having Savings bank a/c. the classification of the sample based on the usage of IB services shows that majority of respondents are using IB for about 3 to 5 years and also, it may be seen that most of them (46 percent) using IB services for almost 8 and above times. From the table it can be seen that majority of respondents have better perception and opinion about the accessibility of IB services and Website presentation of Bank.

Reason for Using IB Services

Using of IB services is influenced by many factors. It might be because of speed, convenience, transaction efficiency, user friendly characteristics etc…Friedman test is used to test the following hypothesis.

H0: there is no significant difference in the reason for using IB services of users.

H1: there is significant difference in the reason for using IB services of users.

The test results are presented in the following table.

Table No.2: Mean Ranks Obtained For the Reason behind In Using IB Services

Ranks		
	Mean Rank	**Rank**
Speed	2.25	2
Convenience	2.01	1
Transaction Efficiency	2.49	3
User Friendly	3.25	4

The mean ranks obtained for the reason behind the using of IB services are stated above. The lower the ranks, the higher will be the preference or preferable reason. As per table given that the highest preference is given to convenience (mean rank 2.01), followed by speed (mean rank 2.25) and transaction efficiency (mean rank 2.49).

Table No.3: Friedman Test

Test Statistics	
N	100
Chi-Square	51.912
Df	3
Asymp. Sig.	0.000
a. Friedman Test	

The chi-square static provides a value of 51.912, which is significant at 5 percent level of significance (0.000<0.05). Therefore, the null hypothesis of "no difference in the reason for using IB services among selected users" is rejected. This indicates the variation in the preference of users in the selection of IB service.

Problems Faced by Users while Using Internet Banking Services

Friedman test is used to find out the major problems faced by the users among the selected sample based on their perception and experience and test the following hypothesis too.

H0: there is no difference in the perception on the problems faced by the IB users while using IB service

H1: there is difference in the perception on the problems faced by the IB users while using IB service

Table No.4: Mean Ranks Obtained For the Problems Faced By the IB Service Users

Ranks		
	Mean Rank	**Rank**
Inability to login of a/c	6.38	6
Account temporarily locked	7.05	8
Transaction failed and amount	7.12	9
Money lost without	8.39	12
Low speed	4.61	1
Connection problems	4.64	2
Personal information leaked	8.02	11
Inadequate customer support	6.66	7
Transaction details missing	7.14	10
Lengthy procedure	6.29	5
Inability to get one time	5.72	3
Delay in getting new	6.02	4

The mean ranks obtained for the problems faced by the users while using of IB services are stated above. The lower the ranks, the higher will be the major problem. As per table given that the highest or major problem faced by the users is Low Speed (mean rank 4.61), followed by Connection Problems (mean rank 4.64) and Inability to get One Time Password (mean rank 5.72).

Table No.5: Friedman Test

Test Statistics	
N	100
Chi-Square	135.868
Df	11
Asymp. Sig.	0.000
a. Friedman Test	

The chi-square static provides a value of 135.88, which is significant at 5 percent level of significance ($p = 0.000<0.05$). Therefore, the null hypothesis of "no difference in the perception on the problems faced by users while using IB services" is rejected. This indicates the variation in the preference or perception on the problems faced by the IB users.

Level of Trust towards the Security Features of IB

Kruskal Wallis test is used to find the level of trust and to test the following hypothesis

H0: There is difference in the perception on the security features of IB among users having different Education Qualification

H1: There is no difference in the perception on the security features of IB among users having different Education Qualification.

Table No.6: Education Qualification-wise means ranks on Security Features of IB services

Ranks			
	Qualification	**N**	**Mean Rank**
VeriSign	Up to plus two	13	46.85
	Graduate	10	52.00
	Post graduate	70	50.61
	Profession	7	54.07
Padlock symbol	Up to plus two	13	51.96
	Graduate	10	47.75
	Post graduate	70	50.61
	Profession	7	50.64
THE LETTER 's' IN THE URL	Up to plus two	13	49.92
	Graduate	10	48.00
	Post graduate	70	49.49
	Profession	7	65.29
Virtual keyboard	Up to plus two	13	59.38
	Graduate	10	32.40

	Post graduate	70	52.81
	Profession	7	36.71
Sms/email alert	Up to plus two	13	59.27
	Graduate	10	51.40
	Post graduate	70	50.11
	Profession	7	36.79
Sign on password expiry	Up to plus two	13	49.81
	Graduate	10	52.65
	Post graduate	70	48.59
	Profession	7	67.79
Automatic lockout on multiple password incorrect	Up to plus two	13	42.04
	Graduate	10	65.10
	Post graduate	70	48.29
	Profession	7	67.50
Automatic timeout	Up to plus two	13	48.08
	Graduate	10	55.80
	Post graduate	70	49.36
	Profession	7	58.79
Mandatory use of special characters in password	Up to plus two	13	41.69
	Graduate	10	51.95
	Post graduate	70	51.09
	Profession	7	58.86
Address bar turning green	Up to plus two	13	56.62
	Graduate	10	54.10
	Post graduate	70	49.05
	Profession	7	41.21

Table No.7: Kruskal Wallis Test

Chi-Square										
	Verisign	P S	Letter 'S' In The Url	V K	Sms/Email Alert	S P E	Almip	Atianost	Muscp	Abtg
ChiSquare	.409	.141	2.155	8.423	3.749	7.918				
Df	3	3	3	3	3	3	3	3	3	3
Asymp. Sig.										
a. Kruskal Wallis Test										
b. Grouping Variable: QUALIFIACTION										

The Education Qualification wise mean rank table shows that users with professional Education Qualification have the better perception and high level of trust on all the security features available in IB except Virtual Keyboard, SMS alert, Automatic Lockout on Multiple Incorrect Password. All hypothesis except related to Virtual keyboard, Automatic Lockout on Multiple Incorrect Password (ALMIP) are not rejected as the P values are 0.038 and 0.048. As related to hypothesis, other security features are rejected as the P values are 0.938, 0.986, 0.541, 0.290, 0.331, 0.737, 0.499 and 0.611 (P>0.05) Therefore it can be concluded that based on Education Qualification wise, there is significant difference among IB users in relation to level of trust on security features – Virtual Keyboard and Automatic Lockout on Multiple Incorrect Password

Findings

1. Demographic profile of the Selected IB Users : Majority of respondents have better perception and opinion about the accessibility of IB services and Website presentation of Bank.
2. Reason for Using IB Service: Out of the different factors that motivate the customer to use the IB service, Convenience factor is most considered. The mean rank variation of all the motivating factors or reasons is statistically significant in the output of Friedman test (P=0<0.05). Lowest mean rank is highly preferred. Here convenience factor has the lowest mean rank (2.01), followed by speed (2.25).

3. Problems Faced by the IB Users: The mean ranks obtained for the problems faced by the users while using of IB services shows that the highest or major problem faced by the users is Low Speed and Connection Problems due to Server Error. Friedman test is used for this purpose. The lower the ranks, the higher will be the major problem where mean rank of Low Speed is 4.61, followed by Connection Problems (mean rank 4.64) and Inability to get One Time Password (mean rank 5.72).
4. Level of trust of customers on Security Features available in IB : Majority of respondents are not aware of VeriSign security and Padlock Symbol security. The Education Qualification wise mean rank table shows that users with professional Education Qualification have the better perception and high level of trust on all the security features available in IB except Virtual Keyboard, SMS alert, Address bar turning to green. Kruskal-Wallis used for this purpose. As a result, it is observed that based on Education Qualification wise, there is significant difference among IB users in relation to level of trust on security features – Virtual Keyboard and Automatic Lockout on Multiple Incorrect Password.

Suggestions

1. Respondents are dissatisfied with online customer service representative. So there is a need to rectify the online connectivity of the customer service representative.
2. People are so much conscious about the security measures whether it might provide privacy andsecurity for the information that entered.
3. Out of the mentioned problems, it is founded that Low Speed and Connection problem due to server errors are the major problems faced by Users. Therefore banks need to take corrective measures to improve their server efficiency.
4. Banks has to conduct various awareness programs in order to improve the level of awareness and knowledge of customers about the functioning of IB and its attributes.

Conclusion

The results of this research indicated that transaction efficiency, ease of use, service content are important determinants of customers' satisfaction with internet banking. However, privacy and security problems, low speed and connection problems due to server errors are the main/major problems faced by the IB users. It indicates that as cost and time customers spent on internet banking increases, customers' satisfaction will decrease. Therefore, this paper suggests certain policy implications for the banking industry. Thus, the proposed model can be of help in planning efforts towards increasing consumers' satisfaction. By improving these factors, bank management may increase adoption and satisfaction among internet bank users. These also imply initiating appropriate actions to enhance basic facilities and improve privacy and security on internet banking. This in essence will improve business transaction and thus increase overall customer satisfaction.

Bibliography

1. Bughin J (2004), "The Success of Internet Banking: An Economic Investigation of Its Pattern of Diffusion Within Western Europe".
2. Md. Mahtab Alam (2010), "Customers Satisfaction Measurement of Internet Banking".
3. Rangsan Nochai (2010), "The Impact of Internet Banking Service on Customer Satisfaction In Thailand: A Case Study In Bankok".
4. Minjoon Jun, Shaohan Cal, "The Key Determinants of Internet Banking Service Quality: A Content Analysis".
5. M E Doddaraju, "A Study on Customer Satisfaction towards Public and Private Sector Banking Service".
6. Nakanjakko Lydia, "Electronic Banking and Customer Satisfaction- Case Study: Centenary Bank".
7. Mohsin Zafar, Arshad Zaheer, "Impact of Online Service Quality on Customer Satisfaction In Banking Sector".
8. Itoro Moses Ikoh, "Determinants of Customer Satisfaction with Internet Banking Services".
9. Books.
10. "Banking with Technology" – R.K. Uppal "Commercial Banks in India: Growth, Challenge And Strategies"- Benson Kunjukunju.

Websites

1. www.shodhganga.inflibnet.ac.in.
2. www.isaet.org.
3. www.ijstr.org.
4. www.researchgate.net.
5. www.scribd.com.
6. www.aicit.org.
7. www.academia.edu.
8. www.investopedia.com.
9. www.wikipedia.com.

Research Paper *IJBARR*
Impact Factor: 5.471 *E- ISSN -2347-856X*
Refereed, Listed & Indexed *ISSN -2348-0653*

A STUDY ON FACTORS INFLUENCING TEACHERS' MOTIVATION AND JOB SATISFACTION

Mrs.Reshma.B.K
Assistant Professor in Commerce, St.Pius X College,Rajapuram,Kasaragod, kerala.

Abstract
The general objective of this study was to identify factors influencing teachers' motivation and job performance in schools Kasaragod,Kerala. Specifically, the study sought to identify factors of motivation that can lead to teacher's job satisfaction and dissatisfaction, assess factors of motivation. The study employed some descriptive survey research design & research techniques employed were mini questionnaires. The sample consisted 100 teachers randomly selected from schools. Data were analysed descriptive statistics such as tables, and percentages while the qualitative responses were coded, categorized and analysed into themes. The findings of the study show that motivation of teachers was affected by factors such as poor working conditions, low salary/pay, unfavourable policies of school management, delays in promotions and in general a negative perception towards teaching. Based on the findings, the study recommends various development measures to be undertaken by school managements to improve job satisfaction as well teacher retentivity.

Keywords: Promotions , Training, Salary, Satisfaction.

Introduction

Teachers are arguably the most important group of professionals for our nation's future. High quality education is emphasized as the key tool for the development of students with the competences they need to adapt to the globalized society and becoming global achievers. Several inputs contribute to the quality of education, which in turn determines the student's learning outcomes. However, the success and failure in achieving quality education lies primarily on teachers. Hence, Teachers play a vital role in ensuring high quality education. Nyakundi (2012) explains teacher motivation is the most important factor in the promotion of teaching and learning excellence. He adds, motivated teachers are more likely to motivate students to learn and to ensure the implementation of education goals. The quality of an educational system cannot outperform the quality of its teachers. While teacher motivation is fundamental to the academic process, research studies show that many teachers in the developing countries are not highly motivated. According to Michaelowa (2002), several factors negatively influence teacher motivation and job satisfaction in developing countries. This should be taken seriously and an investigation into teachers 'motivation and job satisfaction is therefore necessary to achieve the educational goals. Ali and Ahmed (2009) explained the strong positive effects of rewards and recognition on job motivation and satisfaction. Same was applied with the findings of Katou (2008) who stated that motivation and job performance of employees can be increased considerably if extra attention is given on employee's reward and their recognition (Satisfaction, motivation, knowledge, collaboration with partner sand colleagues, dedications, holding and participation may be in the order of the most important aspects of human resource management results. Performance cannot be judged through a single yardstick and that is dependent on various behavioural dimensions of an employees. There are no rules by which unusually good actions could be gauged, and it can be pleasant behaviour, helping colleagues or punctuality (Flynn, 1998; Ali & Ahmed, 2009). Considering recognition, it can be said that it is an important factor affecting employee motivation. Recognition is a public expression of appreciation given by a group to individuals who undertake desired behaviours (Fisher, & Ackerman, 1998).

Literature Review

Related literature on teacher motivation and job satisfaction both national and international were reviewed. Various theories were also explored and the main factors that influence teacher motivation and job satisfaction were examined. Several researchers, for their studies have developed a working definition for teacher motivation and job satisfaction. Richardson (2014) defines teacher motivation as the internal and external factor that stimulate desire in teaching to be continuously interested and committed to make their best efforts to support students' learning goals. Whereas Guajardo (2011) describes motivation as the willingness, drive or desire to engage in good teaching. According to Gulnazet al. (2015) the word "motivation" can be defined as the intrinsic and extrinsic drives or forces that determine focus, and direct behaviour of the learners towards a specific target or goal. Further, Nyakundi (2012) defines job satisfaction as the feeling by the employee towards the job they do about conditions of work and the rewards accrued. Employees' satisfaction in their jobs is essential for the company, which will prevent bad performance and huge losses. Several studies found that teacher motivation and job satisfaction play key roles in the success of teaching and learning process. According to Ololube (2005) teacher motivation and job satisfaction are crucial to the long-term growth of any educational system but as well very essential in the lives of teachers as they form the fundamental reason for working. Further, Nyakundi (2012) indicates that teacher motivation is the important factor for classroom effectiveness and school improvement. He asserts that higher levels of job dissatisfaction,

stress and burn out negatively influence motivation and job performance. Sharif & Nazir (2016) ascertain that working environment, pay and promotion, job security, and level of fairness have significant relationship with job satisfaction. They further extend Low job satisfaction of the employees' leads to lack of productivity, job stress, poor overall performance, & employee turnover rate. They suggest by giving decent salaries and promotional opportunities, the performance of the organization, service quality and job satisfaction among employees can be increased. The review of empirical studies on teacher motivation in low income countries indicate that teacher motivation and job satisfaction is low and decreasing. Further, Arachchi and Edirisinghe (2011) emphasize that, motivation and satisfaction of teachers are vital to play their role in schools effectively. The present study was designed to explore motivation and job satisfaction of teachers in Hyderabad, India.

Research Objectives

The study was designed to address the following objectives.

1. To identify the factors that related to teachers for the choice of their profession.
2. To examine teachers' satisfaction in relation to their job.
3. To investigate the special objectives that teachers have in their job.
4. To suggest ways to improve job satisfaction of teachers.

Research Methodology & Significance of The Study

Sample

The sample of the study comprised of 100 Teachers from various colleges (Males=56 and Females=44) randomly drawn from different schools in Kasaragod. Their age ranged from 28-55 years and their experience ranged from 1-22 years. The study is a mix of descriptive and exploratory research design. Sample of 100 teaching staff/ administrators has been randomly selected from various schools at kasaragod. Survey method was used for collecting the data from the respondents. Researcher designed survey questionnaire was used to collect data from teachers. The quantitative data from the questionnaire survey was analysed using simple descriptive techniques such as frequencies and percentages whereas the qualitative data for the open-ended questions were analysed by coding and categorizing into emerging themes.

Significance: The purpose of the study was to examine teachers' motivation and job satisfaction.

Results And Discussion

The questionnaire survey was used to understand, analyse as well explore the motivation and job satisfaction of teachers. Table 1 summarizes the demographic information of the teachers participated in the study.
Table II of the questionnaire survey deals with the factors related to teachers for the choice of teaching profession and their motivation towards teaching.

The following table illustrates the findings.

Table 1: Demographics of The Participants

	Independent Variable	**Frequency**
GENDER	MALE	56
	FEMALE	44
AGE	28 – 35 years	42
	36- 45 years	47
	46 – 60 years	11
STATUS	ADMINISTRATORS	3
	TEACHERS	97
AREA OF SPECIALIZATION	SCIENCES	34
	COMMERCE	38
	ARTS & LANGUAGES	28
LENGTH OF SERVICE	1- 5 years	22
	5- 15 years	64
	16 – 25 years	14

Table 2: Factors Related To The Choice of The Profession And Motivation

#	Item	Yes (%)	No (%)
1	Did you select teaching profession on your own choice?	**89**	**11**
2	Do you want to go to any other profession?	**21**	**79**
3	Are you involved in teaching with full satisfaction?	**34**	**66**
4	Did you leave any other job to continue teaching?	**43**	**57**
5	Do you like yourself as a teacher?	**96**	**4**
6	Are you satisfied with your present performance?	**93**	**7**
7	Do you feel yourself better than others?	**83**	**17**

The findings in the above table indicates that, 89% of the teachers agreed that they selected teaching profession by their own choice. On the other hand, all of them stated that nobody has pressurized them to choose this profession. Surprisingly, 21% of the respondents indicated that teaching was not their most preferred profession and they wanted to go to some other profession.

However, 43% of the teachers said that, they got some other jobs and left it and joined in teaching. Teachers have also responded to an open-ended question regarding the reasons for choosing teaching profession and their reasons are as follows:

1. Love to teach kids and be with them.
2. Has vacations more compared to other professions and relatively less working hours comparing to other jobs.
3. No transfers.
4. Almost a permanent job.
5. 32% stated that they could not get any other job and so opted for this.
6. Can be a part of service to society.

The following table 3 explains the factors related to the job satisfaction of teachers.

Table 3: Factors Related To The Job Satisfaction Of Teachers

#	**Reasons for the satisfaction**	**Yes (%)**	**No (%)**
1	Teaching is passion	84	16
2	Getting awards through improving students' achievement	21	79
3	Self-satisfaction	14	86
4	Monetary benefits	34	66
5	Like to teach students and to improve their lives	88	12
6	Feeling happy to be with students	94	6

1. Among the respondent teachers 84% indicated they involved in teaching with full satisfaction. They were asked to indicate the reasons for their satisfaction.
2. From the above data, teachers preferred teaching as it is passion for them and they are interested in attaining student achievement & also they feel happy in being with students.
3. Comparing to males, more female teachers stated that they loved teaching. 21% satisfied by getting awards through improving students' achievement. Most of the male teachers indicated this reason. Less than 15% stated that they involve in teaching for their self-satisfaction.
4. For the open-ended questions regarding the special objectives of teachers in their job, table 4 shows the responses

Table 4: Teachers' Objectives In Their Jobs

#	Teacher's objective	Yes (%)	No (%)
1	Would like to be a great inspiring teacher	97	3
2	Develop society and create responsible citizens	98	2
3	Teach students for their high achievement	92	8
4	For my personal growth only	89	11

Most of the teachers (98%) expressed that their objective in teaching is to develop good citizens. While 97% of them said they like to be a good teacher. Others stated that their aims in teaching are to teach students for high achievement and to create good society. 11% of the teachers' objective is their personal development. It can once again be seen that teaches are a lot dedicated professional.

Teachers were asked to respond to a question regarding their expectations to improve their job satisfaction and they have suggested the following ways.

1. Conducting seminars and training workshops by the management to update their knowledge and to learn new technologies.
2. Participating in the in-service professional development programmes and learning communities and be rewarded for them.
3. Hike in teachers' salary.
4. Motivating parents, society and other stakeholders to respect teachers and to value their service.
5. Transfer to nearby schools from the distant school
6. Should not be involved in govt related projects other than teaching

Table 5 summarizes the data of satisfaction of teachers in their profession.

Table 5: Satisfaction of Teachers In Their Profession

#	Item	Satisfied (%	Just Okay (%)	dissatisfied/disagree (%)
1	Are you satisfied with your job?	28	62	12
2	Are you satisfied with the treatment by administrators of your schools?	9	45	36
3	Are you satisfied with the working conditions?	10	34	56
4	Are there adequate learning and teaching materials in your schools?	29	71	10
5	Are you satisfied with the training or orientation programs conducted by your school for your academic as well technology advancement?	41	23	36
6	Are you satisfied with the rewards you get from school authorities?	13	36	51
7	Are you satisfied with the salaries?	14	21	65

Are our Teachers Satisfied: Regarding job satisfaction, the results illustrate that, most of the teachers, (62%) said their level of job satisfaction was "just okay" meaning they were neither satisfied nor unsatisfied, and 28 % are satisfied while 12 % are not satisfied. By comparing the percentage of teachers who were neutral about their level of job satisfaction and that of teachers who were satisfied, it is evident that the teachers' level of job satisfaction was low. Referring to the findings on teachers' level of motivation above, one can deduce that there is a direct relationship between motivation and job satisfaction as low motivation might be a result of job dissatisfaction.

Working Conditions: Teachers' working conditions and basic infrastructure were reported not to be satisfactory. For example, only 10% are satisfied with the working conditions in their respective schools were satisfactory while 90 % of the teachers disagreed with the statement. This presents a serious and immediate need for teachers working conditions to be improved to facilitate effective teaching in schools.

Teaching and learning Materials: Adequate availability of teaching and learning materials is important for teachers to perform their work effectively thus producing results. However, results from this mini- survey indicate that teaching and learning materials are inadequate. School managements must focus on these, which are extremely important for the teacher to develop their skills.

Teachers' Promotions: Being promoted on time not only improves teachers' motivation and satisfaction but also helps to develop their careers. Results from this mini-survey show more than half of teachers (65 %) were promoted. However, only 20 % of the teachers reported that they were promoted on time.

Teachers' Salaries: Results show that teachers are not satisfied with their salaries as only 14 % of the teachers reported that their pay as teachers was satisfactory while 86% reported that their pay was poor or just manageable. Low salaries is one of the factors that cause teachers to quit profession. Challenges such as low salary and poor working conditions are thus among the reasons for teachers' job dissatisfaction. Unfortunately, it's a fact that teachers were always lowly paid as compared to other professions demanding same educational qualifications. A slow decline in respect for teachers in society is a concern and is a factor for many teachers to quit profession.

According to teachers' view, Poor pay, frequent disputes between teachers & administrators, extreme expectations from parents & school managements, very low working conditions, overcrowded classrooms, very less training and inadequate materials for teaching, disrespect in society are all factors, which contribute to de motivating of teachers.

Teachers' Views on Motivation Factor And Improving Job Satisfaction

An analysis of the proceedings of focus group discussions shows that most of the participants were of the view that improving the working conditions and paying of extra allowances to teachers is one way of improving teachers' motivation and job satisfaction.

They also added that promoting teachers on time and paying their salary adjustments on time would improve their motivation and job satisfaction.

The participants also said that treating teachers with some respect would help to improve their motivation and job satisfaction.

Other participants believed that the government must take efforts to improve its relationship with teachers by framing teacher friendly procedures.

Recommendations

The following are the key recommendations, which need to be considered to improve teachers' motivation and job satisfaction.

Salaries have a direct impact on the attractiveness and prestige of teachers. Hence, to improve teachers' motivation and job satisfaction, the school management should take serious measures to improve teachers' salaries to enable them to improve their living conditions by enabling them to cope with the high costs of living.

Also, schools must include mechanisms to recognize and reward teachers who perform exceptionally well compared to others should be put in place to motivate them.

To motivate teachers, promote teacher's retention and better work performance the school management should consider paying hardship allowances/incentives to teachers working in difficult environments like in remote areas. Also, performance-based incentives must be introduced.

Schools must provide a compulsory grant for every teacher and every year for their professional training or furthering their academic qualifications. Also, a Certain amount of money must be allocated to buy their necessary teaching materials required in addition to the school supplies.

To achieve better learning outcomes, the working and living of teachers in difficult environments should be improved. This includes making available housing, water, electricity, free education to children of teachers and necessary insurances etc.

From this data, some people have considered joining teaching profession as the last resort, after plans to join other careers have failed. Teaching is the easiest career to join and therefore attracts people who are not devoted to the profession. Therefore, selection processes of those entering the teaching profession should be made rigid to attract more highly qualified and dedicated candidates from diverse backgrounds. This will help to improve the status of the teaching profession. Also, in service training programs should be well designed to allow more teachers to improve their professionalism and competence.

Also, students must be encouraged to take up this profession. In countries like USA, a program called Teach for America was designed for young students with bachelor's degree. They work in school and the Board of education support for their fee for pursuing further courses along with their regular salary. Teach for India is also another program started in India and may be this program can be given more thrust by the necessary authorities to address the shortage of serious teaching professionals.

Non-financial factors like; Good communication channels, value employees, positivity and secrecy of teachers' issues must be taken care properly by school management.

Encouraging teamwork, propagating job security and good retirement plans. Providing a good retirement plan, family health insurance plans etc. Will certainly become motivational factors to take this profession seriously especially for teachers working in private schools. Although Government school teachers may enjoy these benefits, but it still at large for private school establishments.

Teachers' schedules need to allow for time to improve and reflect on their practice. Teachers who are overworked and are not given this time to reflect on their teaching are unable to review lessons taught, make necessary adjustments, and monitor and revise based on student needs. Teachers who aren't given time to prepare for and review their classes are also at high risk of burnout. Curriculum standards should be clearly articulated for the teachers, so that the skills addressed remain consistent from classroom to classroom, but teachers should be given the freedom to work beyond those standards to best meet the needs of their students.

Teachers also need to be provided sufficient, high-quality professional development programs to perfect their skills. Few teachers already attend professional development sessions each year, but many of these are one-size-fits-all presentations that may not necessarily translate into a teacher's classroom engagement .Professional development needs to be differentiated as we differentiate for our students. Teachers should be able to dictate their needs and problems and work through them in small professional learning communities with master guides to advise them. Key teaching concepts of assessment, differentiation, and core content should be worked through in these learning groups, with relevance as close to the individual classroom experience as much as possible. If teachers are given the opportunity in teacher-centered learning environments to master their skills, then they will be more able to transfer these skills into their students. -

Employees' welfare services such as lunch, tea, good furniture, spacious & ventilated offices and a distinct corporate image will be good for the professional pride. Respect and fair administration to the code of conduct by the school will ensure that teachers own the professional conduct. The employer should enlighten teachers on the code of regulations and ensure that they are conversant with it & deal with their issues with meaningful privacy.

Conclusion

Observing this data, it is recommended that awareness should be raised among parents and other stakeholders to respect and recognize the status and importance of teachers in education. Further, Teachers should be provided with appropriate training and professional development opportunities and be offered a better scale of pay at par with other professions. Employees must be given tasks as per their expertise, which may cause high satisfaction and motivation. Precisely, management should focus at transparent, equitable & competitive compensation system. The periodical salary increments, allowances, and other compensations on regular & specific periods keep their morale high and make them more motivated and satisfied. In summary, the school managements must put in place a sound professional and ethical management system for all teachers' welfare issues that envisage teacher's motivational needs, with a view of adequately meeting them. There are certain limitations or constraints to the generaliz ability of the study, for example, consideration of inflation rate and unemployment rate. However, there search is very important in building the relationship between teachers and their respective management in local environment.

References

1. Ali, R. & Ahmed, M.S. (2009). The Impact of Reward and Recognition Programs on Employee's Motivation and Satisfaction: An Empirical Study. International Review of Business Research Papers, 5, 270-279.
2. Arachchi, C.K. &Edirisinghe, D., (2011). An investigation into Motivation of Teachers in the Colombo District Government Schools in Sri Lanka, Annual Academic Sessions, Open University of Sri Lanka. pp 30-32. Flynn, G. 1998. Is your recognition program understood? Workforce, 77 (7), 3035.
3. Fisher, R.J. & Ackerman, D. (1998). The Effects of Recognition and Group Need on Volunteerism: A Social Norm Perspective. Journal of Consumer Research,25, 3, 262-275.
4. Guajardo, J., (2011). Teacher motivation: Theoretical Framework, Strategies, Analysis of Save the Children Country offices and recommended strategies, Save the Children Basic Education Reform.
5. Gulnaz, F., Ahmad, A and Mandouh, S.A. (2015). An Exploration of the Demotivational Factors Affecting Teaching and Learning of English as a Foreign Language of EFL Learners in Gulf Countries. PEOPLE: International Journal of Social Sciences, 2(1). pp 17-32.
6. Katou, A.A. (2008) Measuring the impact of HRM on Organisational performance. Journal if Industrial Engineering and Management, 1, 2, 119-142. Retrieved 21 September, 2011 from Google search.
7. Michaelowa, K., (2002). Teacher Job Satisfaction, Student Achievement and the Cost of Primary Education in Francophone Sub- Saharan Africa, HWWA Discussion Paper, Humberg Institute of International Economics. Retrieved from http://ageconsearch.umn.edu/bitstream/26273/1/dp020188.pdf on 10.08.2016.
8. Nyakundi, T. K., (2012). Factors Affecting Teacher Motivation in Pacific Secondary Schools in Thika West District, Kiambu Country, M.Ed project, School of Education of Kennyatta University.
9. Ololube, N.P., (2005). Teachers Job Satisfaction and Motivation for School Effectiveness: An Assessment. Retrieved from http://files.eric.ed.gov/fulltext/ED4 96539.pdf on 10.08.2016.
10. Richardson, E., (2014). Teacher motivation in Low income Contexts: An Actionable Framework for Intervention, Teacher Motivation Working Group. Retrieved from http://www.teachersforefa.unesco.org/tmwg/blog2/wp-content/uploads/2015/03/Teacher-Motivation-in-Low-Income-Contexts.pdf on 10.08.2016.
11. Sharif, U.F. and Nazir, A. (2016). An Investigative Study on Job Satisfaction Level of Employees Working in Software Industry: A View Point of Employees in Pakistan, PEOPLE: International Journal of Social Sciences, 2(1), pp 415-432. Retrieved from http://dx.doi.org/10.20319/pijss.2016.s21.415432.

DOI: 10.21917/ijsc.2018.0251

ENSEMBLE CLASSIFICATION BASED MICROARRAY GENE RETRIEVAL SYSTEM

Thomas Scaria[1] and T. Christopher[2]
[1]*Department of Computer Science, St. Pius X College, India*
[2]*Department of Information Technology, Government Arts College, Coimbatore, India*

Abstract

Data mining plays an important role in the process of classifying between the normal and the cancerous samples by utilizing microarray gene data. As this classification process is related to the human lives, greater sensitivity and specificity rates are mandatory. Taking this challenge into account, this work presents a technique to classify between the normal and cancerous samples by means of efficient feature selection and classification. The process of feature selection is achieved by Information Gain Ratio (IGR) and the selected features are forwarded to the classification process, which is achieved by ensemble classification. The classifiers being employed to attain ensemble classification are k-Nearest Neighbour (k-NN), Support Vector Machine (SVM) and Extreme Learning Machine (ELM). The performance of the proposed approach is analysed with respect to three different datasets such as Leukemia, Colon and Breast cancer in terms of accuracy, sensitivity and specificity. The experimental results prove that the proposed work shows better results, when compared to the existing techniques.

Keywords:

Data Mining, Classification, Feature Selection

1. INTRODUCTION

Data mining is the technology that aims to gain knowledge from the datasets and the gained knowledge is represented in an intelligible fashion. Most of the research processes involve data analysis to come up with a research solution. Due to the advancement in medical science and technology, most of the biological researches rely on data analysis. Data analysis in biomedical field helps the experts to study and understand the patterns of normal and abnormal cases without any special effort.

Cancer is the most life-threatening disease, which is found prevalently these days. Ignorance is the major cause for the progression of this disease. Several computer based technologies contribute in detecting different kinds of cancer. Among them, image processing and data mining techniques prove remarkable contribution in detecting cancer at an earlier stage. Advanced image processing techniques deal with digital images to detect the stage of the cancer. On the other hand, data mining techniques utilize biological data to detect the cancer.

The interrelationship between the gene expression and the health condition of an individual is greater. Hence, this work utilizes the microarray gene expression datasets to distinguish between the normal and the abnormal genes. The normal and the cancerous gene expressions are studied and classified by machine learning algorithms. With the help of these microarray gene expressions, the type of cancer can be determined. The microarray gene expression data can be analysed in three different ways, which are supervised, unsupervised and semi-supervised techniques.

Hence, the microarray technology utilizes the data mining approaches for analysing the microarray data. The microarray technology relies on the DNA (Deoxyribo Nucleic Acid), which is present in the nucleus of the cell. The DNA possesses two different segments called coding and non-coding segments. The coding segment is popularly known as genes, which is a vital component. The advancements of genetic engineering help in visualizing the entire structure of the cell. With the help of DNA microarrays, the genes can be analysed effectively and the expression level of genes is utilized to study the nature of disease. This is accomplished with the help of retrieving similar expression profiles.

The supervised learning technique relies on prior knowledge that has been gained from the dataset. The classification system is trained with the dataset initially, followed by which the classification techniques can differentiate between the classes of the gene expression. Some of the popular classifiers for achieving the task of classification are k-Nearest Neighbour (k-NN) [1], Support Vector Machine (SVM) [2] and Relevance Vector Machine (RVM) [3]. The unsupervised techniques do not require any prior knowledge about the dataset and the related gene expressions are grouped together. Some of the popular gene based clustering techniques are observed in the works of [4-9]. Semi-supervised techniques are the combination of supervised and unsupervised techniques.

This research article aims to present a system for retrieving the microarray gene data of a particular class by employing supervised algorithm based on ensemble classification. The dimensionality of gene expression data is greater, such that it consumes more time to process the data and involves computational complexity. In order to make the microarray gene retrieval system efficient in terms of computation and time consumption, this work reduces the feature dimension by means of Information Gain Ratio (IGR). The IGR selects the necessary features from the dataset and the classification is carried out by ensemble classifier. The classifiers being utilised are k-NN, SVM and Extreme Learning Machine (ELM) respectively. The main contributions of this work are listed below.

- The reduction of feature dimensionality helps in attaining reduced computational and time complexity.
- The feature dimensionality of the microarray gene dataset is reduced by IGR.
- The incorporation of ensemble classification results in enhanced accuracy rates and reduced misclassification results.

The remaining sections of the paper are organized as follows. Related review of literature with respect to microarray gene classification is presented in section 2. The proposed microarray gene retrieval system is described in section 3. The performance of the proposed approach is analysed and the experimental results

are presented in section 4. Finally, the concluding points about the work are presented in section 5.

2. REVIEW OF LITERATURE

This section reviews the state-of-the-art related literature with respect to microarray gene classification techniques.

In [10], a multiple objective model is designed on the basis of analytical hierarchy process. A multi-objective heuristic algorithm is proposed, which is an enhancement of Univariate Marginal Distribution Algorithm. This model works by framing two important rules, which are 'Higher rule' 'Fewer rule' and 'Forcibly decrease rule'. The higher and lower rule intends to analyse and sort the gene data. The 'Forcibly decrease rule' produces the better individuals with maximum classification accuracy. This work gives more importance to the classification accuracy, rather than to reduce the gene count.

A centroid based feature discrimination principle for selecting better genes is presented in [11]. The centroid of the class is computed by the kernel based expectation. The feature selection problem is designed as the L1-regularized optimization problem by considering the linear discriminant analysis principle. The centroid of the class is computed by the kernel based technique, which can define the between and within class separability.

In [12], a work to classify between the cancer types is proposed. The proposed technique is based on information gain and genetic algorithm. The features are selected by information gain, followed by the employment of genetic algorithm to reduce features and finally, the classification of cancer is attained by genetic programming. This work concludes that the performance of genetic algorithm maximizes the accuracy rates.

In [13], an unsupervised technique based on Ant Colony Optimization (ACO) algorithm is proposed for selecting genes. This technique applies the ACO algorithm in the filter based approach, in order to maximize the gene relevance and minimize the gene redundancy rates. Additionally, the fitness function being proposed by this work does not require any prior knowledge about the gene dataset. The classification is attained by the filter based approach and is proven to be better than SVM, naïve bayes and decision trees.

A hybrid classification technique is proposed for classifying the gene microarray data [14], which is based on Principal Component Analysis (PCA) and Brain Emotional Learning (BEL) network. This work states that BEL is suitable for high dimensional features. The proposed work proves better results in terms of accuracy. In [15], a technique to classify between the microarray data for drug response is proposed and is based on feature selection and classification. The feature selection of this work is carried out by a metaheuristic approach, which selects the top ranking relevant genes based on max relevance and min redundancy is proposed. The metaheuristic approaches being employed are Particle Swarm Optimization (PSO), Cuckoo Search (CS) and Artificial Bee Colony (ABC) algorithms. The classifiers being employed by this work are k-NN and SVM. This work concludes that the CS algorithm works better than PSO and ABC algorithms respectively.

In [16], a two stage classification model which relies on pre-processing and classification is proposed. ReliefF is utilized in the pre-processing stage, such that the top ranking genes are selected. The selected genes are mapped into a dissimilarity space and the classification process is carried out. The classification results of this work are compared against artificial neural network, SVM and Fisher's linear discriminant classifier by varying the number of genes. In [17], a faster feature selection technique is proposed that is based on recursive feature elimination by simulated annealing and square root. This approach eliminates several features instead of removing a single feature, hence the count of features being removed as the iteration progresses. This technique concludes that this approach of feature reduction does not affect the classification accuracy of the work. In [18], a hybrid feature selection algorithm is proposed for microarray gene expression data. The features are selected from the mutual information maximization and adaptive genetic algorithm.

In [19], a novel gene selection technique is proposed for cancer classification, which is based on genetic algorithm and artificial intelligence. Initially, the dimensionality of the features is reduced by integer coded genetic algorithm. Laplacian and Fisher score are employed to compute similarity between the features. This work is applied over several classifiers and the performance of the proposed gene selection technique is tested. In [20], the microarray gene dataset is classified by means of kernel ridge regression techniques such as wavelet kernel ridge regression and radial basis kernel ridge regression. The features of the microarray gene dataset are reduced by means of modified cat swarm optimization technique. The performance of this approach is compared against simple ridge regression, SVM and random forest classifer.

In [24], the microarray gene retrieval system that relies on Local Fisher Discriminant Analysis (LFDA) and Support Vector Machine (SVM) is proposed. A supervised microarray gene retrieval system based on Kernel Local Fisher Discriminant Analysis (KLFDA) and Extreme Learning Machine (ELM) classifier is presented in [25].

Motivated by the above related works, this article aims to present a gene retrieval system for microarray gene data. The dimensionality of microarray gene data is huge and hence the dimensionality of the data is reduced by selecting the necessary features by means of IGR. The selected features are then processed to classify between the cancer types by means of ensemble classification. The following section elaborates the proposed approach in addition to the overview of the proposed approach.

3. PROPOSED MICROARRAY GENE DATA CLASSIFICATION SYSTEM

The intention of this work is to present a microarray gene data classification system based on Information Gain Ratio (IGR) and the process of classification is carried out by ensemble classifiers. The entire work is segregated into two phases, which are feature selection and classification. The feature selection process selects the relevant and necessary features, which makes the classification process to the point. The IGR is an improvisation of information gain and the main reason for the choice of IGR is that it takes all the unique entities into account. This idea weeds out all the redundant and irrelevant entities from the feature set and conceives all the necessary set of features. This kind of feature

selection improves the classification accuracy and reduces the overall time consumption of the work.

The classification process relies on ensemble classifiers, which are k-NN, SVM and ELM classifiers. k-NN is the classical classifier which takes certain number of samples for training and the classification results are returned by taking the nearest neighbours into account. This k-NN classifier is the simplest classifier with minimal computational complexity. SVMs are the promising classifiers which consider a reasonable set of samples for training and SVM can perform non-linear classification. ELM is chosen as one of the ensemble classifiers, owing to its faster learning ability and efficiency. The decisions of all the individual classifiers are collected and the maximum occurred decision is declared as the final decision. This way of classification increases the accuracy rate. The following sub-sections of the work describe the feature selection and classification process.

3.1 FEATURE SELECTION

This phase of the work intends to select the necessary features from the high dimensional dataset. The main reason is to avoid redundant and irrelevant features, which can reduce time and computational complexity considerably. The IGR is employed for selecting the features, which considers the unique entities into account and is computed as follows. In order to calculate IGR, information gain is computed.

$$IG_S = -\left[\frac{r \cdot f(c_1, S)}{|S|}\right] \log_2 \left[\frac{r \cdot f(c_1, S)}{|S|}\right] \quad (1)$$

In the above equation, $\left[\frac{r \cdot f(c_1, S)}{|S|}\right]$ is the probability of the repetitive occurrence of a sample, which is present in the class c_1. Let the feature f contains q unique values, which can be represented as $\{f_1, f_2, f_3, \ldots, f_q\}$. For a dataset with f features, the training dataset is formed as follows $\{c_1, c_2, c_3, \ldots, c_q\}$ and the information gain of the feature is computed by the following formula,

$$IG(F) = \left[\frac{|F_i|}{|F|}\right] \times IG(F_i). \quad (2)$$

The *IGR* of the feature is then computed with the help of information gain and is presented below,

$$IGR(F) = \left[\frac{|IG_S - IG(F)|}{|IG_S + IG(F)|}\right] \times 100. \quad (3)$$

The IGR makes it possible to extract the features with high correlation degree, which makes sense that the features required to distinguish between the samples alone are extracted. Hence, the IGR selects the genes with high correlation degree and the rest are not considered. As soon as the feature selection process is over, the classification process is triggered and is carried out by ensemble classification.

3.2 ENSEMBLE CLASSIFICATION

Ensemble classification is achieved by clubbing different classifiers in order to achieve greater classification accuracy. This kind of classification is efficient, as the classification decision depends on multiple classifiers, rather than a single classifier. Ensemble classification is reliable and effective. This work utilizes k-NN, SVM and ELM classifiers to make the final classification decision.

The reason for selecting three classifiers is that the time conservation is improved, as the count of classifiers increases. Hence, this work employs three reliable classifiers and the reasons for the choice of classifiers are presented above. All the classifiers gain knowledge from the input database during the process of training and the classifiers distinguish between the microarray data during the testing phase. The following sub-sections present the working principles of the three different classifiers. The classification is diagrammatically represented in the following figure.

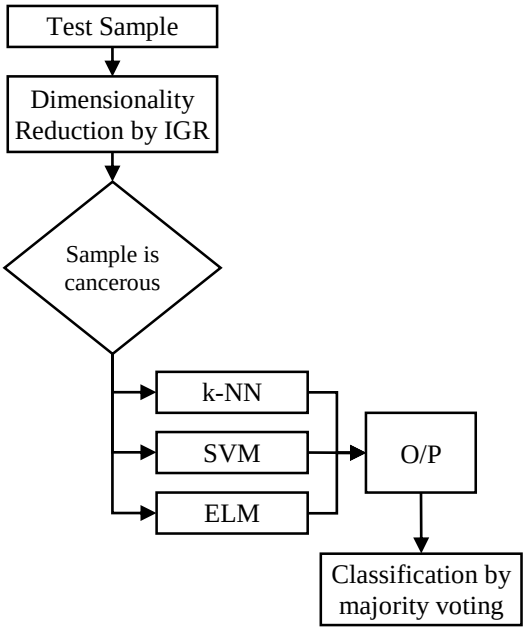

Fig.1. Overall flow of ensemble classification

3.2.1 k-NN Classifier:

The k-NN classifier is one of the basic classifiers, which distinguish between the normal and abnormal gene data. The k-NN classifier distinguishes between the normal and the abnormal data by computing Euclidean distance between the data, which is computed by,

$$E_{Dis} = \sum_{i=1}^{N} \sqrt{x_i^2 - y_i^2} \quad (4)$$

The efficiency of this classifier depends on the choice of the value '*k*'. The value of *k* decides the classification accuracy of the classifier and choosing the right value of *k* is a challenging problem. Additionally, the value of *k* differs for every dataset and prior knowledge about the dataset is necessary for fixing the value of *k*. This makes it ineffective and this work utilizes *k* fold cross validation, which automatically chooses the *k* value. In the process of *k* value fixation is carried out by decomposing the training data into multiple *k* samples, among which a single sample is treated as the test sample and the remaining samples are considered as the training samples. This operation is repeated for *k* times, till all the samples are treated as testing sample atleast once. When this operation is over, the mean value of the computed *k* results and the mean value is fixed as *k*. This technique is

optimal and the need to choose the value of k by the users is eliminated. Additionally, this technique does not require any prior knowledge about the dataset and is feasible for any kind of dataset.

3.2.2 SVM Classifier:

SVM is a promising classifier and is trained with a set of training samples. The SVM classifies between the microarray gene data by means of a separating margin. Let the group of training samples are to be classified as either normal or abnormal. The samples are included in the corresponding class by means of a hyperplane. This hyperplane is necessary to separate the samples belonging to the normal and abnormal classes. The differentiation between the classes can be represented as follows.

$$\psi.j_i + b \geq +\text{ve for } cl_i = \text{Positive} \quad (5)$$

$$\psi.j_i + b \leq -\text{ve for } cl_i = \text{Negative} \quad (6)$$

The distance between the hyperplane decides the accuracy of the classification results.

$$\text{Distance between the hyperplanes} = \frac{2}{\|\psi\|}. \quad (7)$$

The lesser the value of $\|\psi\|$, the better is the classification results. Hence, the distance between the hyperplane is optimized by means of Lagrange's function.

$$lf(x) = \sum_{i=1}^{Q} \alpha_i \psi_i (j_i \cdot j) + th \quad (8)$$

In Eq.(8), α_i is the lagrange multiplier which partitions the hyperplane $\psi_i(j_i \cdot j)$ and th is the threshold to partition the hyperplane. Hence, if the value of $lf(x)$ is greater than 0, then the sample is abnormal, otherwise normal.

3.2.3 ELM Classifier:

The striking point about this classifier is its faster learning ability [20]. Consider the microarray gene data is represented by (a_i,b_i), where $a_i = [a_{i1},a_{i2},\ldots,a_{in}]^T \in D^n$ and a_{in} is the i^{th} training sample in n dimension. The i^{th} label in c^{th} dimension of the training dataset is represented by $b_i = [b_{i1},b_{i2},\ldots,b_{ic}]^T \in D^c$ and c is the total count of classes in the process of classification. As far as this work is taken into consideration, the total count of class is two. The Single hidden Layer Feed Forward Neural Network (SLFN) is formed by

$$\sum_{j=1}^{N} \gamma_i q\left(w_j \cdot a_i + y_j\right) = y_i; i = 1,2,...,n \quad (9)$$

In Eq.(9), w_j is the weight of the samples that are represented by $[w_{j1},w_{j2},..w_{jn}]^T$. The w_j is responsible for interconnecting the j^{th} neuron with the input neurons and the j is presented by $j = [j_1,j_2,\ldots,j_c]^T$. Additionally, the w_j links the hidden neuron with the output neurons. The bias of the j^{th} hidden neuron is given by y_j. Let HL be the hidden layer output matrix of the classifier, in which the j^{th} column of HL signifies the j^{th} hidden neurons output vector by taking the input a_{i1}, $a_{i2},\ldots$, a_{in} into account.

$$HL = \begin{bmatrix} a_{fn}\left(w_1 \cdot a_1 + y_j\right) & \cdots & a_{fn}\left(w_N \cdot a_1 + y_N\right) \\ \vdots & \ddots & \vdots \\ a_{fn}\left(w_1 \cdot a_n + y_j\right) & \cdots & a_{fn}\left(w_N \cdot a_n + y_N\right) \end{bmatrix} \quad (10)$$

$$\gamma = \begin{bmatrix} \gamma_1^T \\ \vdots \\ \gamma_N^T \end{bmatrix} \quad (11)$$

$$R = \begin{bmatrix} r_1^T \\ \vdots \\ r_N^T \end{bmatrix} \quad (12)$$

The matrix format of the SLFN is represented as follows.

$$HL\gamma = R \quad (13)$$

The output weights are computed by normalized least-square solution as follows

$$\gamma = HL^{\dagger}R \quad (14)$$

where $HL^{\dagger}$ is the HL's Moore-Penrose generalized inverse. When the training process is initialized, the total count of classes, hidden neurons and activation function a_{fn} are fed into the classifier. The training samples are given by $\{a_i,b_i\}$ and the classifier is made to get trained by γ, as given in Eq.(14). By this way, the ELM classifies between the normal and abnormal data.

As soon as the decisions of all the classifiers are obtained, the decision with maximum count is computed. For instance, any two of the classifiers may classify the sample as normal and one classifier may arrive at the decision as abnormal. In this case, the sample is declared as normal as per the maximum voting strategy. As this work employs three different classifiers, there can be nine different combinations of solutions and the final decision is made accordingly. Each classifier can end up the decision with normal and abnormal. The abnormal class is denoted by 1 and the normal class is denoted by 0. Each column of the decision matrix (D_{mat}) denotes the classifier. The first column of the D_{mat} indicates the k-NN classifier, the second and third column of the matrix denotes the SVM and ELM classifiers. Based on the D_{mat}, the final decision is computed by taking the repeatedly occurring decision.

$$D_{mat} = \begin{bmatrix} 1 & 0 & 0 \\ 0 & 1 & 0 \\ 0 & 0 & 1 \\ 1 & 1 & 0 \\ 1 & 0 & 1 \\ 1 & 1 & 0 \\ 0 & 0 & 0 \\ 1 & 1 & 1 \\ 0 & 1 & 1 \end{bmatrix} \Rightarrow \begin{bmatrix} 0 \\ 0 \\ 0 \\ 1 \\ 1 \\ 1 \\ 0 \\ 1 \\ 1 \end{bmatrix} \quad (15)$$

Thus, the final decision is made by taking the D_{mat} into consideration. This way of classification is not prone to misclassification and so the classification accuracy of this technique is greater. The following section analyses the performance of the proposed approach in terms of standard performance measures.

4. RESULTS AND DISCUSSION

The performance of the proposed approach is analysed in terms of classification accuracy, sensitivity and specificity. The datasets being utilized for evaluating the performance of the

proposed approach are leukemia [21], colon [22] and breast cancer [23] datasets. The leukemia dataset consists of 3571 genes, which are derived from 72 individuals. Colon dataset contains 2000 genes collected from 62 instances. In this dataset, forty samples are normal and the remaining twenty two samples are abnormal. The breast cancer dataset contains 24481 genes with 78 samples. Out of the 78 samples, 34 samples are considered as abnormal and the remaining 44 are considered as normal.

The proposed algorithm is applied in Matlab environment with version 8.1. All the experiments are carried out in a standalone system with 16GB RAM and 7th generation Intel core processor with 4MB cache, 3.5GHz. This work divides the dataset into ten parts and each part act as a testing part, while the remaining nine parts are the training parts. Hence, all the parts of the dataset are tested. The performance of the proposed approach is tested with respect to classification accuracy, sensitivity, specificity and misclassification rate.

The accuracy rate of the classification approach is very important, as the correct classification between normal and cancerous cases is necessary. As this work is related to human disease diagnosis, the accuracy rates are given more importance. The accuracy rate is computed by taking the True Positive (*TP*), True Negative (*TN*), False Positive (*FP*) and False Negative (*FN*) rates. The formula for computing accuracy rate is presented as follows.

$$Ac = \frac{TP + TN}{TP + TN + FP + FN} \times 100 \quad (16)$$

The sensitivity and specificity measures are other important performance measures of a classification algorithm. The formulae for computing sensitivity and specificity are presented in the following equations.

$$Sen = \frac{TP}{TP + FN} \times 100 \quad (17)$$

$$Spec = \frac{TN}{FP + TN} \times 100 \quad (18)$$

$$MC = 100 - Ac \quad (19)$$

The sensitivity and specificity rates of the classification algorithm must be greater. It is important to achieve greater sensitivity and specificity rates rather than to achieve better accuracy rates. The accuracy rates consider all the *TP*, *TN*, *FP* and *FN* rates but the sensitivity and specificity rates consider *FN* and *FP* rates respectively. The impact of wrong classification is serious when it comes to diagnosis of disease. The sensitivity rates of the algorithm increase, when the false negative rates decrease. False negative rates are dangerous because the abnormal sample is classified as normal and this is serious because the next process of the treatment may be delayed.

The specificity rates of the work can be improved, provided the *FP* rates are reduced. In this scenario, the abnormal samples are classified as normal, which may hold back the treatment procedure of the affected case. Hence, it is necessary to minimize *FP* and *FN* rates, as much as possible. The greater the sensitivity and specificity rate, the more reliable is the classification system. The performance of this work is evaluated in two aspects. The first aspect aims to prove the efficiency of ensemble classification over the application of individual classifiers. The second aspect of performance analysis compares the performance of the proposed approach with the related state-of-the-art techniques.

4.1 PERFORMANCE ANALYSIS BY VARYING THE CLASSIFIERS

The aim of this section is to justify the choice of ensemble classifier over several individual classifier such as k-NN, SVM and ELM. However, it is not good to determine that the performance of ensemble classifier is the best, on applying it over a single dataset. Considering this, the performance of ensemble classifier is tested over three different datasets and all the analysis prove that ensemble classifier shows better performance than the individual classifiers. As shown below, the ensemble classifier shows greater accuracy, sensitivity and specificity rates. The ensemble classifier proves better results for all the datasets, as the classification decision does not based on a single classifier. The performance of the proposed approach is evaluated for all three datasets by varying the feature selection and classification techniques. The experimental results of the proposed ensemble classification are tabulated in Table.1.

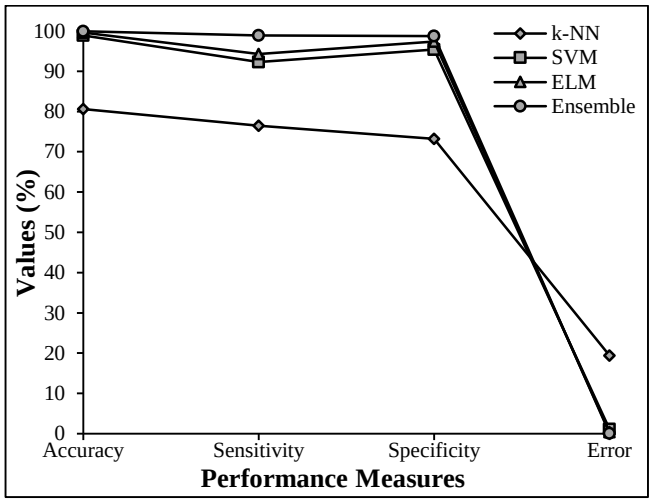

Fig.2. Performance analysis on ALL-AML

Table.1. Performance analysis by varying classification techniques

Dataset – ALL-AML				
Performance Metrics / Classifiers	**k-NN**	**SVM**	**ELM**	**Ensemble**
Accuracy (%)	80.6	98.9	99.4	99.9
Sensitivity (%)	76.5	92.3	94.3	98.9
Specificity (%)	73.2	95.4	97.4	98.7
Error Rate (%)	19.4	1.1	0.6	0.1
Dataset – Colon Tumor				
Performance Metrics / Classifiers	**k-NN**	**SVM**	**ELM**	**Ensemble**
Accuracy (%)	73.6	78.6	98.5	99.4
Sensitivity (%)	60.25	81.7	99.7	99.8
Specificity (%)	65.6	75.4	96.4	98.9

Error Rate (%)	26.4	21.4	1.5	0.6
Dataset – Breast Cancer				
Performance Metrics / Classifiers	**k-NN**	**SVM**	**ELM**	**Ensemble**
Accuracy (%)	66.73	76.8	92.17	98.3
Sensitivity (%)	73.2	74.6	94.2	97.8
Specificity (%)	72.9	79.6	93.28	98.7
Error Rate (%)	33.27	23.2	7.83	1.7

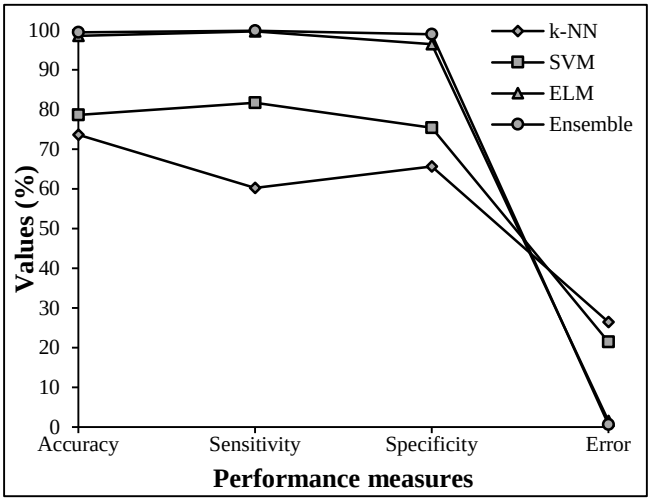

Fig.3. Performance analysis on Colon tumor dataset

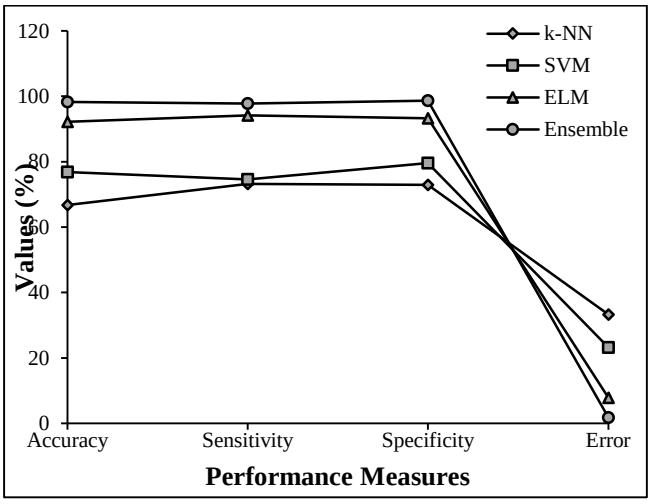

Fig.4. Performance analysis on Breast cancer dataset

The above presented performance analysis proves the efficiency of ensemble classifier in the place of employed individual classifier. The ensemble classifier proves better results with greater sensitivity and specificity rates. The maximum accuracy rate being proven by the ensemble classifier is 99.9% for the Leukemia dataset.

The accuracy rates of the colon tumor and breast cancer of the ensemble classification technique are 99.4% and 98.3% respectively. The average sensitivity rate of the ensemble classification technique is 98.83%. On the other hand, the average sensitivity rate of the SVM and ELM are 82.86% and 96.06% respectively. The specificity rate of the proposed approach is 98.76%. The experimental results prove the efficacy of the proposed approach.

4.2 PERFORMANCE ANALYSIS

This section aims to compare the performance of the proposed approach and compares it with the recent exiting approaches such as dissimilarity measure based microarray gene data classification [16], heuristic algorithm based microarray gene data classification [10]. The dissimilarity based microarray gene data classification takes the top ranking gene into account without concerning the features of the gene data. The heuristic based microarray data classification focuses on classification accuracy, rather than the process of gene selection. The experimental results are presented in Table.2.

Table.2. Comparative analysis with the existing approaches

Datasets/Performance metrics	**Colon Tumor**		
	Dissimilarity based	**Heuristics based**	**Proposed**
Accuracy	82.3	89.6	**99.01**
Sensitivity	73.6	81.9	**99.4**
Specificity	77.3	78.96	**97.2**
Misclassification rate	17.7	10.4	**0.99**
Datasets/Performance metrics	**Breast cancer**		
	Dissimilarity based	**Heuristics based**	**Proposed**
Accuracy	82.3	89.6	**99.01**
Sensitivity	73.6	81.9	**99.4**
Specificity	77.3	78.96	**97.2**
Misclassification rate	17.7	10.4	**0.99**
Datasets/Performance metrics	**ALL-AML**		
	Dissimilarity based	**Heuristics based**	**Proposed**
Accuracy	82.3	89.6	**99.01**
Sensitivity	73.6	81.9	**99.4**
Specificity	77.3	78.96	**97.2**
Misclassification rate	17.7	10.4	**0.99**

This work has proven the performance of the proposed approach by comparing with the recent existing techniques. The proposed approach is tested up on three different datasets however, the performance of the proposed approach is stable and promising. The major reason for the better results being shown by the proposed approach is the feature dimensionality reduction and ensemble classification. The feature dimensionality reduction aims in selecting the most prominent features rather than the entire feature set. This helps in achieving better classification results. In addition to this, ensemble classifier takes the final decision by considering the decisions of all the individual classifiers. The maximal occurring decision is declared as the final decision, which improves the classification accuracy.

5. CONCLUSIONS

This paper presents a retrieval system for microarray gene data, which relies on information gain ratio and ensemble classification. As the dimensionality of the gene data is greater, this work intends to select the optimal features by means of IGR and then the classification phase is initiated. Initially the ensemble classifier is trained with the dataset, which makes it able to classify between the normal and the abnormal samples. The efficiency of the proposed approach is evaluated against different datasets and the power of ensemble classification is justified. In future, this work plans to introduce multiclass classification system for microarray gene data.

REFERENCES

[1] D. Coomans and D.L. Massart, "Alternative k-Nearest Neighbour Rules in Supervised Pattern Recognition: Part 1. k-Nearest Neighbour Classification by using Alternative Voting Rules", Analytica Chimica Acta, Vol. 136, pp. 15-27, 1982.

[2] C. Cortes and V. Vapnik, "Support-Vector Networks", *Machine Learning*, Vol. 20, No. 3, pp. 273-297, 1995.

[3] G.B. Huang, Q.Y. Zhu and C.K. Siew, "Extreme Learning Machine: Theory and Applications", *Neurocomputing*, Vol. 70, No. 1, pp. 489-501, 2006.

[4] S. Bandyopadhyay, A. Mukhopadhyay and U. Maulik, "An Improved Algorithm for Clustering Gene Expression Data", Bioinformatics, Vol. 23, No. 21, pp. 2859-2865, 2007.

[5] U. Maulik, A. Mukhopadhyay and S. Bandyopadhyay, "Combining Pareto-Optimal Clusters using Supervised Learning for Identifying Coexpressed Genes", *BMC Bioinformatics*, Vol. 10, No. 1, pp. 20-27, 2009.

[6] A. Mukhopadhyay, S. Bandyopadhyay and U. Maulik, "Multi-Class Clustering of Cancer Subtypes through SVM based Ensemble of Pareto-Optimal Solutions for Gene Marker Identification", *PLoS ONE*, Vol. 5, No. 11, pp. 1-8, 2010.

[7] U. Maulik and A. Mukhopadhyay, "Simulated Annealing based Automatic Fuzzy Clustering Combined with ANN Classification for Analysing Microarray Data", *Computers and Operations Research*, Vol. 37, No. 8, pp. 1369-1380, 2010.

[8] A. Mukhopadhyay and U. Maulik, "Towards Improving Fuzzy Clustering using Support Vector Machine: Application to Gene Expression Data", *Pattern Recognition*, Vol. 42, No. 11, pp. 2744-2763, 2009.

[9] U. Maulik, "Analysis of Gene Microarray Data in a Soft Computing Framework", *Applied Soft Computing*, Vol. 11, No. 6, pp. 4152-4160, 2011.

[10] Jia Lv, Qinke Peng, Xiao Chen and Zhi Sun, "A Multi-Objective Heuristic Algorithm for Gene Expression Microarray Data Classification", *Expert Systems with Applications*, Vol. 59, pp. 13-19, 2016.

[11] Shun Guo, Donghui Guo, Lifei Chen and Qingshan Jiang, "A Centroid-based Gene Selection Method for Microarray Data Classification", *Journal of Theoretical Biology*, Vol. 400, pp. 32-41, 2016.

[12] Hanaa Salem, Gamal Attiya and Nawal El-Fishawy, "Classification of Human Cancer Diseases by Gene Expression Profiles", *Applied Soft Computing*, Vol. 50, pp. 124-134, 2017.

[13] Sina Tabakhi, Ali Najafi, Reza Ranjbar and Parham Moradi, "Gene Selection for Microarray Data Classification using a Novel Ant Colony Optimization", *Neurocomputing*, Vol. 168, pp. 1024-1036, 2015.

[14] Ehsan Lotfi and Azita Keshavarz, "Gene Expression Microarray Classification using PCA-BEL", *Computers in Biology and Medicine*, Vol. 54, pp. 180-187, 2014.

[15] Nur Shazila Mohamed, Suhaila Zainudin and Zulaiha Ali Othman, "Metaheuristic Approach for an Enhanced MRMR Filter Method for classification using Drug Response Microarray Data", *Expert Systems with Applications*, Vol. 90, pp. 224-231, 2017.

[16] Vicente Garcia and J. Salvador Sanchez, "Mapping Microarray Gene Expression Data into Dissimilarity Spaces for Tumor Classification", *Information Sciences*, Vol. 294, pp. 362-375, 2015.

[17] Aiguo Wang, Ning An, Guilin Chen, Lian Li and Gil Alterovitz, "Improving PLS–RFE based Gene Selection for Microarray Data Classification", *Computers in Biology and Medicine*, Vol. 62, pp. 14-24, 2015.

[18] Huijuan Lu, Junying Chen, Ke Yan, Qun Jin and Yu Xue, Zhigang Gao, "A Hybrid Feature Selection Algorithm for Gene Expression Data Classification", *Neurocomputing*, Vol. 256, pp. 56-62, 2017.

[19] M. Dashtban and Mohammadali Balafar, "Gene Selection for Microarray Cancer Classification using a New Evolutionary Method Employing Artificial Intelligence Concepts", *Genomics*, Vol. 109, No. 2, pp. 91-107, 2017.

[20] Guang-Bin Huang, Hongming Zhou, Xiaojian Ding and Rui Zhang, "Extreme Learning Machine for Regression and Multiclass Classification', *IEEE Transactions on systems, Man and Cybernetics-Part B*, Vol. 42, No. 2, pp. 513-529, 2012.

[21] PMC-NCBI-NIH, Available at: http://www.ncbi.nlm.nih.gov/pmc/articles/PMC151171

[22] Gene Expression Project, Available at:http://microarray.princeton.edu/oncology

[23] Lt. Thomas Scaria and T. Christopher, "Microarray Gene Retrieval System based on LFDA and SVM", *International Journal of Intelligent Systems and Applications*, Vol. 1, pp. 9-15, 2018.

[24] Lt. Thomas Scaria and T. Christopher, "Supervised Microarray Gene Retrieval System based on KLFDA and ELM", *International Journal of Advanced Intelligent Paradigms*, 2018.

I.J. Intelligent Systems and Applications, **2018, 1, 9-15**
Published Online January 2018 in MECS (http://www.mecs-press.org/)
DOI: 10.5815/ijisa.2018.01.02

Microarray Gene Retrieval System Based on LFDA and SVM

Lt. Thomas Scaria[1]
[1]Department of Computer Science, St. Pius X College, Kerala, India
E-mail: thomasscaria.pu@gmail.com

Dr. T. Christopher[2]
[2]Asst Professor, PG and Research Department of Information Technology, Government Arts College, Coimbatore, India

Received: 10 May 2017; Accepted: 06 July 2017; Published: 08 January 2018

Abstract—The DNA microarray technology enables the biologists to observe the expressions of multiple thousands of genes in parallel fashion. However, processing and gaining knowledge from the voluminous microarray gene data is serious issue. It is necessary for the biologists to retrieve the required data in a reasonable time. In order to address this issue, this work presents a gene retrieval system, which is based on feature dimensionality minimization and classification of the microarray gene data. The feature dimensionality minimization is achieved by Local Fisher Discriminant Analysis (LFDA), which inherits the merits of both Fisher Discriminant Analysis (FDA) and Locality Preserving Projection (LPP). Support Vector Machine (SVM) is employed as the classifier to classify between the genes. The LFDA is chosen for reducing the dimensionality of the features, owing to its better performance on multimodal data. The SVM is trained with the feature dimensionality reduced microarray gene data, which improves the efficiency and overthrows the computational complexity. The performance of the proposed approach is compared with the LPP and FDA. Additionally, the performance of SVM is compared with the k-Nearest Neighbour (k-NN) classifier. The combination of LFDA and SVM serves better in terms of accuracy, sensitivity and specificity.

Index Terms—DNA microarray technology, feature reduction, SVM classification, LFDA.

I. Introduction

Data mining is the process of examining a vast amount of data to provide well-defined information. Hence, the process of transformation from raw data to clear-cut information is called as knowledge discovery process. Recognising the superiority of data mining, several applications utilize the technology. Some of the noteworthy applications are business platforms, finance, biomedicine, networks, education and so on [1].

Microarray technology enables the life scientists to study and analyse the genomic expression of a living organism [2, 3]. DNA microarray technology makes it possible to observe the expression level of several thousands of genes in a concurrent fashion [4,5]. Numerous research activities exploit the microarrays for definitive solution. For instance, toxicology, medical diagnosis, gene regulative studies depend on the microarrays [6-8].

Data mining techniques intend to gain knowledge from the microarray data by means of data clustering, classification and association mining. The overall process of microarray data analysis consists of data normalization, data processing and post-processing. Based on the operative nature of data mining techniques, the learning algorithms are classified into supervised and unsupervised learning.

Supervised learning is comprised of two phases and they are training and testing. In the training phase, the classifier is fed with knowledge of the subject samples of several categories. The testing stage aims to find the category of the test sample being passed. Unsupervised learning techniques do not require any prior knowledge about the processing data.

Irrespective of the presence of several data mining techniques, it is still difficult to gain knowledge from the voluminous microarray data [9]. It would be beneficial for the scientists to have a system that can fetch the data being searched and is popularly called as information retrieval system. The microarray information retrieval system strongly depends on the gene classification process. However the classification process is not simple, as the microarray data is quite voluminous and high dimensional [10, 11].

Understanding the necessity of the information retrieval from microarray gene data, this article proposes a microarray gene information retrieval system. The entire work is decomposed into two different phases, which are microarray feature reduction and classification. The initial phase aims to reduce the dimensionality of the microarray data and the next phase engages itself in gene classification. This work employs Local Fisher Discriminant Analysis (LFDA) to reduce the dimensions of the features. The reasons for the employment of LFDA

are it preserves the local structure of the data and clearly separates different classes [12].

The Support Vector Machine (SVM) is trained with the dimensionality reduced feature set. SVM is employed owing to its margin optimization and exclusion of local maxima [13]. The key points of the proposed work are listed below.

- Incorporation of LFDA to minimize the dimensionality of the features, which makes the entire process simpler.
- The classifier SVM is trained with the dimensionality reduced set of features, which enhances the speed of learning.
- The information retrieval is faster, as LFDA reduces the feature dimension to train the SVM.
- The computational complexity is overthrown, as the process of classification is done after feature dimensionality minimization.

The rest of the paper is organized as follows. Section 2 presents the related review of literature with respect to the microarray gene data classification. The proposed information retrieval system for microarray gene data is presented in section 3. The performance of the proposed approach is analysed in section 4. The conclusions are drawn in section 5.

II. Related Works

This section reviews the related literature with respect to the classification of microarray gene data.

In living organisms, all the cells possess nucleus which in turn contains DNA. Every DNA contains the coding and decoding segments. These coding segments are called as genes and the genes describe the structure of proteins. The formation of proteins is achieved in two steps. Initially, the gene is converted to mRNA and mRNA is converted to proteins.

DNA microarray is the advanced technology that renders a provision to have a global insight of the cell and this paves way for measuring the expression level of several thousands of genes concurrently [14]. However, the serious challenge associated with the microarray gene data is the data dimensionality and this issue leads to misclassification [15, 16].

Effective gene selection is the remedy to this issue and the gene selection is the process of detecting and eliminating unwanted features during the training phase. As the knowledge is gained by the system without unwanted features, the knowledge discovery process is more effective [17]. Feature selection is the most important step, as it decides the efficiency of the work.

A perfect feature selection technique reduces the time consumption and computational complexity involved in the gene classification. However it is not an easy task, as it is difficult to determine which are relevant features and irrelevant features. On successful gene selection, the researchers can analyse the data to classify between the normal and the gene expression related to some diseases. Understanding the significance of this issue, several researchers engage themselves in this research.

Globally, the feature selection techniques are classified into filter, wrapper and embedded techniques. Filter based approaches depend on the overall features of the training data for feature selection. Wrapper based approaches involve in the optimization process of the predictor for feature selection. Finally, the embedded techniques employ machine learning algorithms to extract the relevant set of features. However, it is reported that the wrapper and embedded approaches show computational burden [18].

The filter based approaches measure the relevancy of the genes by examining the fundamental features of the data, where a single gene or a subgroup of genes is analysed against the class labels. The advantage of filter based approach is its minimal time consumption and the drawback is that the classification results are not up to the mark.

Wrapper approaches failed to grab the attention of the researchers, as the computational overhead is high. Embedded techniques utilize machine learning for feature selection and the mostly used classifier is the Support Vector Machine (SVM). Besides these traditional feature selection techniques, there are several ensemble and hybrid approaches.

Fisher Discriminant Analysis (FDA) classifies the entities by organizing the entities in a single dimensional space and then the classification process is done by fixing threshold. The fisher criterion is utilized to reduce the dimensionality. However, the results produced by FCA are not convincing, when the samples in a class form multiple clusters [19, 20].

Local Preserving Projection (LPP) conserves the local structure of the data, while minimizing the data dimensionality [21]. The local structure is preserved, as the embedding transformation takes the neighbouring pair of data in the embedding space. However, the LPP doesn't take the label information into account such that it does not work well in the supervised environment.

In [22], an associative classification algorithm is proposed for microarray gene classification. This work clubs both the association rule and classification mining. This work is based on four different phases, which are statistical gene filtering, discretization, class association rules and prediction. The initial phase is meant for distinguishing between the genes and to choose the important genes in the gene expression. The discretization phase is for converting the continuous values to discrete values. The next phase is responsible for producing a group of association rules by utilizing closed frequent itemset. Finally, the classification process is carried out by employing a scoring function. The performance of the proposed approach is tested against Linear Discriminant Analysis (LDA), SVM and decision tree.

In [23], a technique for gene selection and classification is proposed. This work is based on Random Forest Ranking (RFB) and Binary Balck Hole Algorithm (BBHA). The experimental results of this work are

compared with several classification techniques and the proposed work is proved to be better.

Motivated by these works, this article intends to present an information retrieval system for microarray data with two stages, which are data dimensionality reduction and classification. This work produces expected results, as the dimensionality of the features are minimized prior to the classification stage, which is achieved by LFDA.

The dimensionality minimization stage reduces the computational complexity and time consumption. The SVM is trained with the obtained feature reduced microarray data, which improves the learning speed and performance. The following section presents the proposed approach in a detailed fashion.

III. Proposed Gene Retrieval System with LFDA and SVM

This section elaborates the phases involved in the proposed approach along with the overall working principle.

A. Overall Idea

The microarray gene expression data is complex to manage, owing to the nature and the high dimensionality of the data [24]. As the microarray gene data contains numerous expressions, it is difficult to manage the data. For this sake, this article proposes a gene retrieval system by utilizing the LFDA and SVM for the biomedical applications.

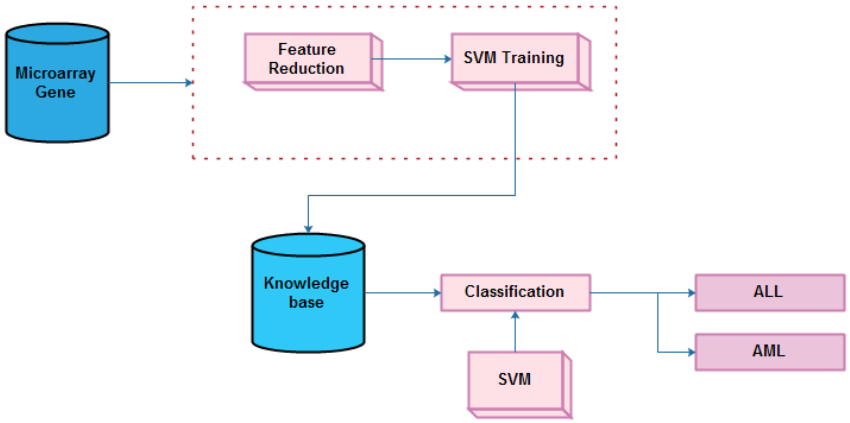

Fig.1. Overall flow of the proposed approach

To achieve the goal, the research is carried out in two steps, which are feature dimensionality minimization and classification. The initial step intends to reduce the data by means of LFDA. The SVM is then trained by the data with minimized dimensionality. The overall flow of the proposed work is presented in figure 1.

The LFDA is chosen by this work, as it clearly increases the class partitions and conserves the local structure of the data. Thus, LFDA works well both between-class and within-class scenarios. This dimensionality minimized data is utilized for the purpose of training the SVM. SVM is selected as the classifier, as the learning ability is better with few samples. The gene retrieval system yields better results, as the feature reduction and classification phases are employed together. The following subsections explain the phases involved in the proposed gene retrieval technique.

B. Feature Dimensionality Minimization by LFDA

The major goal of dimensionality minimization is to acquire a low dimensional depiction of high dimensional data along with the preservation of the local structure of the original data [25]. A perfect dimensionality minimization paves way for better classification. Recognizing the importance of feature dimensionality minimization, this work utilizes LFDA which inherits the ideas of both FDA and LPP. FDA is the traditional technique for dimensionality reduction but it cannot perform well with multimodal data.

LPP addresses this issue by minimizing the dimension of multimodal data while it preserves the local structure of the data also. Basically, LPP is an unsupervised dimensionality reduction technique and so it does not take the class labels into consideration. This implies that this technique does not suit supervised dimensionality reduction.

LFDA combines the idea of both FDA and LPP [26], such that it works well for multimodal data. LFDA can address the dimensionality minimization issue by solving the generalized eigenvalue issue. Let the microarray gene data possess k' labelled entities and is represented as $\{(a_i, b_i)\}_{i=1}^{k'}$, where $b_i \in \{1,2,\dots,cc\}$ which is the class label related to the entity a_i and cc is the count of classes.

Consider k'_n as the count of labelled entities which are in class $n \in \{1,2,\dots cc\}$ and this can be represented as

$$k' = \sum_{n=1}^{cc} k'_n \quad (1)$$

The local between-class and local within-class matrices are denoted by SM^{lbet} and SM^{lwit} respectively and are represented as follows.

$$SM^{lbet} = \frac{1}{2}\sum_{i,j=1}^{k'} P_{i,j}^{lbet}\left(a_i - a_j\right)\left(a_i - a_j\right)^{\mathrm{T}} \quad (2)$$

$$SM^{lwit} = \frac{1}{2}\sum_{i,j=1}^{k'} P_{i,j}^{lwit}\left(a_i - a_j\right)\left(a_i - a_j\right)^{\mathrm{T}} \quad (3)$$

Here, $P_{i,j}^{lbet}$ and $P_{i,j}^{lwit}$ are the $k' \times k'$ matrices and represented in the following equation.

$$P_{i,j}^{lbet} = \begin{cases} X_{i,j}\left(\frac{1}{m'} - \frac{1}{k'_{b_i}}\right) & if\ b_i = b_j \\ \frac{1}{k'} & if\ b_i \neq b_j \end{cases} \quad (4)$$

$$P_{i,j}^{lwit} = \begin{cases} \frac{X_{i,j}}{k'_{b_i}} & if\ b_i = b_j \\ 0 & if\ b_i \neq b_j \end{cases} \quad (5)$$

Where $X_{i,j}$ is the affinity value between a_i and a_j, subject to the local scaling heuristic. The local scaling is performed on class by class basis, such that the local structure of the microarray gene data is maintained. In eqns 4 and 5, $X_{i,j}\left(\frac{1}{m'} - \frac{1}{k'_{b_i}}\right)$ is negative. On the other hand, $\frac{X_{i,j}}{k'_{b_i}}$ and $\frac{1}{k'}$ are positive. This means that the entities present in the same class are closer to each other and the entities of different class are farther. This local scaling operation reduces the computational cost as well. The transformation matrix for microarray gene data TM^{LFDA} is formed as

$$TM^{LFDA} = \underset{TM \in Z^{s \times z}}{argmax}[t(TM^{\mathrm{T}} SM^{lbet} TM (TM^{\mathrm{T}} SM^{lwit} TM)^{-1}] \quad (6)$$

The LFDA forms the transformation matrix of the genes, which maximizes the local between-class scatter ($TM^{\mathrm{T}} SM^{lbet} TM$) and minimizes the local within-class scatter ($TM^{\mathrm{T}} SM^{lwit} TM$) in the embedding space. The generalized eigen value issue is solved by

$$C = SM^{(lbet)}; D = SM^{(lwit)} \quad (7)$$

Suppose if the value of $X_{i,j} = 1\ \forall\ i,j$, then the $SM^{(lbet)}$ and $SM^{(lwit)}$ are minimized to $SM^{(bet)}$ and $SM^{(wit)}$ respectively. Thus, the scatter matrices are formed for the microarray gene data and the dimensionality reduced data is obtained.

C. Gene Classification by SVM

As soon as the feature dimensionality reduction is achieved on microarray gene data, the SVM is trained with that data. The goal of SVM is to separate the entities by considering the hyperplane.

Let the training entities for SVM is denoted as TE, with which the SVM is trained. The SVM gains knowledge from the training entities and classify the entities into either class A or class B, by means of hyperplane. The hyperplane is formed by solving the below given equation.

$$f(x) = \sum_{i=1}^{cc} \beta_i \rho_i (x_i . x) + l \quad (8)$$

Where β_i is the lagrange multipler that aims to segregate the hyperplane $\rho_i (x_i . x)$. l is the threshold that determines the classification policy by the hyperplane. With respect to the threshold value, the entities are classified to be either in class A or B and this can be represented as

$$\begin{cases} f(x) \geq 0; Class\ A \\ f(x) < 0; Class\ B \end{cases} \quad (9)$$

By this way, the SVM classifies between the entities present in the microarray gene data. The next section analyses the performance of the proposed gene retrieval system.

IV. Experimental Analysis

This section evaluates the performance of the proposed approach. Initially, a short description about the dataset is presented, followed by which the performance of the proposed work is analysed.

A. Dataset Descripton

The experiments are carried out on the Leukemia dataset, which is publicly available [27]. This dataset is formed by collecting the microarray data from Affymetrix chip, which contains 6817 genes. The genes are filtered after which the gene count is reduced to 3051. The training data contains 38 cases, which constitutes 27 Acute Lymphoblastic Leukemia (ALL) and 11 Acute Myeloid Leukemia (AML).

B. Results and Discussion

The proposed approach is implemented in Matlab environment (version 8.2). The feature dimensionality of the microarray gene data is minimized by LFDA. The obtained feature dimensionality minimized data is passed for SVM classification. The performance of the proposed technique is analysed by varying the feature reduction techniques and classification techniques in terms of accuracy, sensitivity, specificity and misclassification rates.

Accuracy is the most important measure of any classification technique, and is the ratio of the correctly classified samples to the total number of samples being involved in classification. Sensitivity rate is computed by the ratio of correctly classified samples to be in the correct class to the sum of correctly classified samples in the correct class and the samples which are misclassified to be the members of the wrong class.

Specificity is the rate of samples which are correctly classified as non-native samples of the class to the sum of samples that are wrongly classified as the member of a specific class and the samples that are correctly classified as non-native samples of the class. All the above stated performance measures are represented as follows.

$$accuracy = \frac{True_p + True_n}{True_p + True_n + False_p + False_n} \times 100 \quad (10)$$

$$sensitivity = \frac{True_p}{True_p + False_n} \times 100 \quad (11)$$

$$specificity = \frac{True_n}{False_p + True_n} \quad (12)$$

$$misclassification = 100 - accuracy \quad (13)$$

In the above equations, $True_p$, $True_n$, $False_p$ and $False_n$ are the true positive, true negative, false positive and false negative rates. Initially, the feature reduction techniques are varied and the performance of the proposed approach is analysed.

The proposed work is compared by implementing LPP [21] and FDA [19] individually against LFDA. The second round of performance analysis deals with the classifiers. This work compares the performance of SVM against k-NN classifier. The experimental results are presented below. The experimental results present the accuracy, sensitivity, specificity and misclassification rates with respect to both ALL and AML.

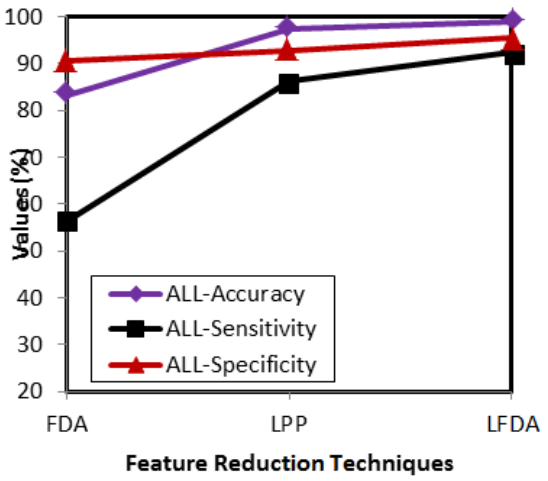

Fig.2. Comparative analysis w.r.t feature reduction techniques for ALL

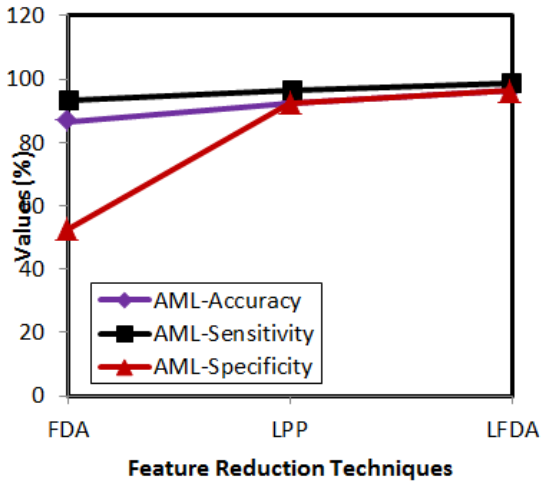

Fig.3. Comparative analysis w.r.t feature reduction techniques for AML

The above presented graphs show the experimental results of both ALL and AML cases with respect to the feature reduction techniques. The attained results prove that the accuracy, sensitivity and specificity rates of the LFDA are better than the FDA and LPP. LFDA achieves better results, as it works well for both between and within class relationships of entities.

Besides this, the LFDA addresses the dimensionality minimization issue by solving the generalized eigen value effectively. All these factors help the LFDA to perform better than the analogous techniques. FDA does not serve well for multimodal data and this issue is addressed by LPP.

However, LPP cannot perform well for supervised environment and thus, LFDA inherits the merits of both the techniques to render better results. The following graphs (fig 4 and 5) present the accuracy, sensitivity and specificity rates by varying the classifiers for ALL and AML.

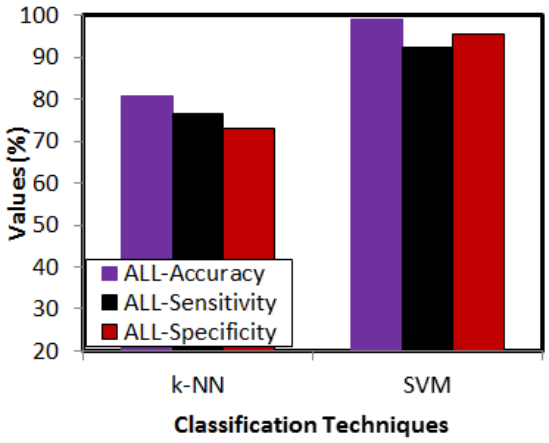

Fig.4. Comparative analysis w.r.t classification techniques for ALL

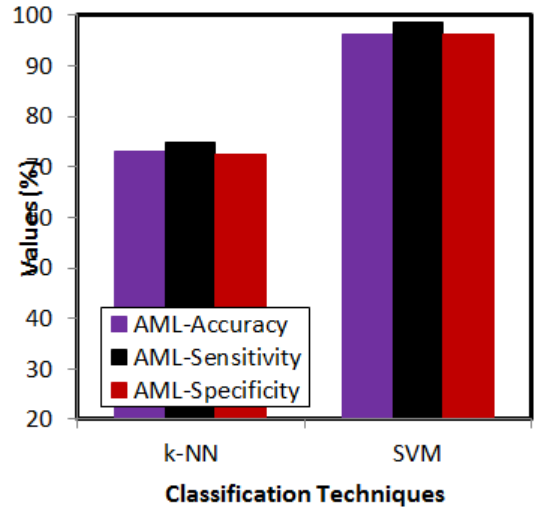

Fig.5. Comparative analysis w.r.t classification techniques for AML

The performance of the classification technique is needed to be justified. In order to achieve this, the feature dimensionality reduced microarray gene data is fed to k-NN and SVM for checking the performance. The learning ability of the k-NN classifier is not upto the mark, when compared to SVM.

Besides this, the learning speed of SVM is greater than k-NN. For these reasons, the choice of SVM is justified

in the above presented experimental results. SVM shows the greatest accuracy rates in both ALL and AML cases. The maximum accuracy rate being shown by SVM is 98.9. The highest sensitivity and specificity rates being shown by SVM are 98.6 and 96.3 respectively. This shows the efficacy of the SVM over k-NN classifier. The following graphs (fig 6 and 7) present the misclassification rates by taking the feature reduction and classification techniques into account.

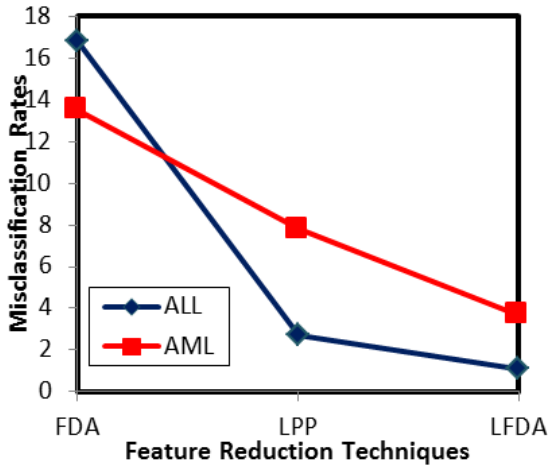

Fig.6. Misclassification rate analysis w.r.t feature reduction techniques

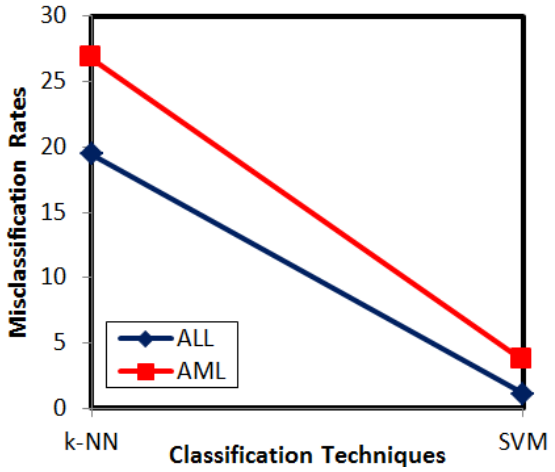

Fig.7. Misclassification rate analysis w.r.t classification techniques

Misclassification rate is indirectly proportional to the accuracy rate. Hence, it is obvious that the misclassification rate of LFDA is comparatively lower than the analogous techniques. LFDA shows the least misclassification rates for both ALL and AML, which are 1.1 and 3.7 respectively. This proves the efficacy of the LFDA over FDA and LPP.

On varying the classifiers, SVM shows the least misclassification rates, when compared to k-NN. From the experimental results, it is evident that the proposed approach serves better with LFDA for feature dimensionality reduction followed by SVM classification. This results in better retrieval rates for both ALL and AML cases.

V. Conclusion

This article presents an effective gene retrieval system, which is based on LFDA and SVM. LFDA is utilized for reducing the feature dimensionality of the microarray gene data. This activity of feature reduction helps in removing the unwanted data and thereby saves memory and reduces computational complexity of the forthcoming phase. The learning speed improves, as the SVM gains knowledge from the feature dimensionality reduced microarray data. The performance of the proposed approach is analysed by varying the feature reduction and classification techniques.

LFDA outperforms the LPP and FDA, as it inherits the benefits of both feature extraction techniques. The SVM proves its efficiency over k-NN in terms of classification accuracy. The experimental results prove the efficacy of the proposed approach in terms of accuracy, sensitivity and specificity rates. In future, we plan to continue the research by analysing several feature reduction and classification techniques for microarray gene data.

References

[1] H. Chen, "Homeland Security Data Mining Using Social Network Analysis". In: Ortiz-Arroyo D., Larsen H.L., Zeng D.D., Hicks D., Wagner G. (eds) Intelligence and Security Informatics. *Lecture Notes in Computer Science*, Vol. 5376, pp. 4-4, 2008.

[2] M.M. Babu, "Introduction to microarray data analysis". *Computational genomics: Theory and application*. Vol. 17, No.6, pp.225-49, 2004.

[3] V. Filkov, S. Skiena and J. Zhi, 'Analysis Techniques for Microarray Time Series Data', *Journal of Computational Biology*, Vol. 9, No. 2, pp. 317-330, 2002.

[4] M. Schena, D. Shalon, R.W. Davis, and P. O. Brown, "Quantitative monitoring of gene expression patterns with a complementary DNA microarray," *Science*, Vol. 270, No. 5235, pp. 467–470, 1995.

[5] J. L.DeRisi, V.R. Iyer, and P.O.Brown, "Exploring themetabolic and genetic control of gene expression on a genomic scale," *Science*, vol. 278, no. 5338, pp. 680–686, 1997.

[6] "The chipping forecast I," *Supplement to Nature Genetics*, vol. 21, no. 1, 1999.

[7] "The chipping forecast II," *Supplement to Nature Genetics*, vol. 32, 2002.

[8] D.P. Berrar, W. Dubitzky, M. Granzow, editors. A practical approach to microarray data analysis. Boston, Mass, USA: *Kluwer academic publishers*; 2003.

[9] I. Slavkov, S. Džeroski, J. Struyf, S. Loskovska. "Constrained clustering of gene expression profiles". *In : Proc. of the Conference on Data Mining and Data Warehouses at the Seventh International Multi-Conference on Information Society*, pp. 212-215, 2005.

[10] Y.Y. Leung, Y.S. Hung, "An integrated approach to feature selection and classification for microarray data with outlier detection, *In: Proc. of 8th Annual International Conference on Computational Systems Bioinformatics*, Aug. 10-12, Stanford, CA, USA, pp. 1-4, 2009.

[11] A. Osareh and B. Shadgar, "Classification and Diagnostic Prediction of Cancers using Gene Microarray Data Analysis", *Journal of Applied Sciences*, Vol. 9, No. 3, 459-468, 2009.
[12] M. Sugiyama, "Dimensionality reduction of multimodal labeled data by local Fisher discriminant analysis". *Journal of Machine Learning Research*, Vol.8, pp.1027–1061, 2007.
[13] J. Shawe-Taylor, and Cristianini N. "Kernel methods for pattern analysis". *Cambridge university press*, 2004.
[14] G. Piatetsky-Shapiro, P. Tamayo, Microarray data mining: facing the challenges, *ACM SIGKDD Explor. Newsl.* Vol. 5, No. 2,pp. 1-5, 2003.
[15] T. Golub, D. Slonim, P. Tamayo, C. Huard, M. Gaasenbeek, J. Mesirov, H. Coller, M. Loh, J. Downing, M. Caligiuri, et al, "Molecular classification of cancer: class discovery and class prediction by gene expression monitoring", *Science*, Vol. 286, No.5439, 531–537, 1999.
[16] A. Jain, D. Zongker, Feature selection: evaluation, application, and small sample performance, *IEEE Trans. Pattern Anal. Mach. Intell*. Vol.19, No. 2, pp.153–158, 1997.
[17] I. Guyon, S. Gunn, M. Nikravesh, L.A. Zadeh, editors. "Feature extraction: foundations and applications". *Springer*, Vol. 207, 2008.
[18] V. Bolón-Canedo, N. Sánchez-Maroño, A. Alonso-Betanzos, J.M. Benítez, F. Herrera, "A review of microarray datasets and applied feature selection methods", *Information Sciences*, vol.282, pp.111-135, 2014.
[19] R. A. Fisher. "The use of multiple measurements in taxonomic problems". *Annals of Eugenics*, Vol. 7, No. 2, pp. 179–188, 1936.
[20] K. Fukunaga. "Introduction to Statistical Pattern Recognition". *Academic Press*, Inc., Boston, second edition, 1990.
[21] X. He and P. Niyogi. "Locality preserving projections". In S. Thrun, L. Saul, and B. Sch ¨olkopf, editors, *Advances in Neural Information Processing Systems* 16. MIT Press, Cambridge, MA,2004.
[22] S Alagukumar, R Lawrance, "Classification of microarray gene expression data using associative classification", *International Conference on Computing Technologies and Intelligent Data Engineering*, 7-9 Jan, Kovilpatti, 2016.
[23] Elnaz Pashaei, Mustafa Ozen, Nizamettin Aydin, "Gene selection and classification approach for microarray data based on Random Forest Ranking and BBHA", *IEEE-EMBS International Conference on Biomedical and Health Informatics*, 24-27 Feb, Las Vegas, USA, 2016.
[24] S. Dehuri and S. Cho, "Multiobjective Classification Rule mining Using Gene Expression Programming", *In : Proc of the International Conference on convergence and Hybrid Information Technology*, 11-13 November, Busan, Vol. 2, pp. 754-760, 2008.
[25] G.E. Hinton and R.R. Salakhutdinov, "Reducing the dimensionality of data with neural networks", *Science*, Vol. 313, pp. 504–507, 2006.
[26] M. Sugiyama, M. Krauledat and K.R. Muller. "Covariate shift adaptation by importance weighted cross validation". *Journal of Machine Learning Research*, Vol. 8, pp. 985–1005, 2007.
[27] http://ligarto.org/rdiaz/Papers/rfVS/.

Authors' Profiles

Lt. Thomas Scaria is presently working as Assistant professor of Computer Science at Department Of computer Science, St.Pius College, Rajapuram, Kerala, India and an active Research Scholar at periyar University Salem. His Area of Interest Includes Data Mining in Bio Sciences and Bio Informatics. He Received his MCA degree from Periyar University in the Year 2003 and M.Phil in Computer Science from Annamalai University in the Year 2008. He Did his M.Sc Applied Psychology from Annamalai University in the Year 2012. He has to Credit 13 Years of teaching and 6 years of research experience.

Dr. T. Christopher is presently working as Assistant Professor of Computer Science, at Post Graduate and Research Department of Information Technology, Government Arts College (Autonomous), Coimbatore, Tamilnadu, India. He has published 40 research papers in International/National Journals; His area of interest includes knowledge mining and Network security. He has to credit 26 years of teaching and research experience.

How to cite this paper: Lt. Thomas Scaria, T. Christopher, "Microarray Gene Retrieval System Based on LFDA and SVM", International Journal of Intelligent Systems and Applications(IJISA), Vol.10, No.1, pp.9-15, 2018. DOI: 10.5815/ijisa.2018.01.02

ISSN 2319 – 1953
International Journal of Scientific Research in Computer Science Applications and Management Studies

Analysis of Microarray Gene Retrieval System Based On KFVM and SKFLM

Thomas Scaria[1], Dr.T Christopher[2]

[1]*Research Scholar, Department Of CS, Periyar University,Salem,Tamilnadu.India.*

[2] *Department Of CS,Government Arts College,Coimbatore,TamilNadu,India*

[1]ts.stpius@gmail.com

***Abstract*— Gene retrieval from microarray is exceptionally troublesome assignment in microarray innovation. A few microbiologists checked the articulations in a huge number of qualities in parallel mode. Handling and acquiring information from microarray information is a difficult task. LPP, LDA, FDA, LFDA, KLFDA, IGR are portions of the strategies utilized for highlighting the decrease. K-NN, SVM, ELM and so forth are portions of the systems utilized for Classification. Through this examination, we intend to propose two calculations KFVM and SKFLM, which are endeavours to distinguish the impact of different portions and highlight the choice issues of existing methods. The execution of the proposed methodology is applied in breast cancer Dataset.**

***Keywords*— DNA Microarray, Features Selection, Kernel Selection, KFVM, SKFLM.**

I. INTRODUCTION

Death rate of cancer-affected patients is very high in recent years. The real cause of cancer is not identified until now. The reasons for cancer are manifold and they are not found cited accurately in the past. The life cycle of the malignancy influenced persistent relies upon the phase of the disease. If we could distinguish or identify the malady in the beginning, the life expectancy of the patient might be increased. With the end goal of identifying the disease in the beginning itself, a few computer aided system dependent on image processing and data mining are developed. The image processing systems detect cancer by dealing with the Computerized Tomography (CT), Magnetic Resonant Imaging (MRI) technology, X-rays etc. Microarray gene retrieval is the process that aims to gain knowledge from the gene datasets and the gained knowledge is represented in an intelligible fashion. Most of the research processes in this area are using feature selection and classification for the data mining technique. Data analysis fields related with microarray system helps the experts to study and understand the patterns of normal and abnormal genes without any special effort.

The process of extracting essential information from the dataset is known as dimensionality reduction or feature selection. The scientific portrayal of the issue is characterized as pursues: Let us consider the high dimensional dataset X with D-dimensional data. Highlight extraction includes finding the low dimensional dataset Y with d-dimensional data, which are significant in low dimensional information, where d>D, that is we convert X→Y and D→d.

The quality articulations assist us by identifying human diseases as they are connected with one another. At the point when the quality articulations break down, the interrelationship between the quality articulations and carcinogenesis can be perceived [1]. Study and break down of the genomic articulation of a living being is done with the assistance of Microarray technology [2,3]. DNA microarray technology makes it possible to watch the expression level of a large number of qualities in a simultaneous manner. Various research exercises abuse the microarrays for authoritative arrangement [4]. The main points of the proposed work are listed herewith.

- Analysis, Identification and Application of best feature selection and solve the linearity problem in LFDA, KLFDA and IGR, which makes the entire process simpler.
- Analysis, Identification and Application of best kernel in K-NN, SVM and ELM, which enhances the speed of learning.
- The information retrieval is faster, with the help of feature reduction techniques and classification is took place with the help of Machine learning methods.
- The computational complexity is overthrown, as the process of classification is done after feature dimensionality minimization.
- Two new two algorithms KFVM (Kernel Feature Vector Machine) and SKFLM (Supervised Kernel Feature Learning Machine) are introduced for avoiding the Feature Selection Problem and Kernel Selection Problems.

The rest of the paper structure is organized as follows. Section 2 presents the related review of literature with respect to the microarray gene data classification. The proposed information retrieval system and overall flow of the work for microarray gene data is presented in section 3.The performance of the proposed approach is analysed in section 4.Analysis of combined effect and conclusions are drawn in section 5.

II.BACKGROUND

In this work, we try to implement the concepts of feature selection and kernel selection that is directly related to

dimensionality reduction and classification techniques. Dimensionality reductions reduce the number of parameters of the particular dataset, which increase the speed of classification. Real world data are mainly divided into two types such as Linear Data and Non Linear Data.

A. Dimensionality Reduction Methods

1) Linear Dimensionality Reduction Methods

The suitable method used for better separation is convert the high dimensional space is into low dimensional subspace [5].One of the important technique for unsupervised dimensionality reduction is Principal Component Analysis and it plays important role in pattern recognition and machine learning. The projection provides the low dimensional subspace, which can represent all the data without losing the any information [6].

The fisher rule is used to diminish the dimensionality. In any case, the outcomes delivered by FCA are not convincing, when the examples in a class frame numerous clusters [7, 8]. Neighbourhood Preserving Projection (LPP) saves the nearby structure of the data, while limiting the data dimensionality. Local Preserving Projection (LPP) conserves the local structure of the data, while minimizing the data dimensionality [9].The reasons for the employment of LFDA are it preserves the local structure of the data and clearly separates different classes [10].

2) Non Linear Dimensionality Reduction Methods

In real world, most of the data are in the form of non-linear. Handling these types of data for further analysis is difficult. There are many techniques, which can handle this type of non-linear data.

Support Vector Machine is a supervised technique for classification that classifies the data into different classes based on the hype plane and it considers only the support vectors for the problem of classification [11]. Generally, SVM is used for two-class classification and its class may be 0 or 1 otherwise -1 or 1. Let us consider X=(x1…xD) be a high dimensional data and each xi has its own class labels Y= [- 1, 1]. In the case of linear data, SVM tries to find the hyper plane with minimum distance from the data points from the boundary. If the data is non-linearly distributed, the data is transformed by using non-linear transformation functions[12].

Motivated by the existing research works, this works aims to propose a microarray gene retrieval system based on KFVM and SKFLM. The results of the proposed approach are satisfactory in terms of classification accuracy and execution time as well. The following section elaborates the proposed approach.

B. Feature Selection Methods

Feature Selection techniques are characterized in to three sorts; they are Filter Methods, Wrapper methods and Embedded method. The Specific algorithms are given underneath

- Pearson's Correlation: Identifying the linear dependence between two factors X and Y. Its esteem fluctuates from -1 to +1.
- ANOVA: ANOVA is used for Analysis of variance.
- Chi-Square: It is a Statistical test connected to the unions of clear-cut highlights to assess the probability of relationship or relationship between them utilizing their frequency distribution.
- The significant objective of dimensionality minimization is to secure a low dimensional data along with the preservation of the local structure of the original data. LFDA, which acquires the thoughts of both FDA and LPP. FDA is the conventional method for dimensionality decrease yet it cannot perform well with multimodal data.
- On the negative side, we can implement LFDA only in the case of linear data. It is difficult for it to deal with non-linear data. In this case, we implement a new method known as KLFDA.
- The IGR is employed for selecting the features, which considers the unique entities into account and is computed as follows.

  $IGR(F) = (IG_S - IG(F) / IG_S + IG(F)) * 100,$

  Here, IG_S means information Gains and IG(F) means information gain of features.

As soon as the feature selection process is over, the classification process is triggered and is carried out by ensemble classification.

C. Types of Kernels

Now we discuss some of the important kernel functions only

K: X×X→R, is called Kernel such that

$\Phi(x) \cdot \Phi(y) = K(x, y)$

Efficiency: K is often more efficient to compute than Φ and the dot product.

Flexibility: Flexibility can be chosen arbitrarily so long as the existence of Φ is guaranteed

The important types of kernels are,

1. Linear Kernel
2. Gaussian Kernel
3. Polynomial Kernel
4. Normalized Polynomial Kernel
5. Radial Basis Function Kernel:RBF

D. Classification Methods

In Machine Learning Classification is a supervised learning approach in which the computer programs learns from the inputs and then uses this learning to classify new observations. Important classification algorithms in machine learning's are

1) Linear Classifier: Logistic Regression, Naive Base Classification
2) Support Vector Machine

How We Classify in SVM

Training data: sample drawn from set X⊆RN

According to some distribution,
S= ((x1, y1). . . (xm, ym)) ∈ X× {−1, +1}.
Support Vector-Points along the Margins or outliers
Canonical hyperplane: 'a' and 'b' chosen such that for closest points Mod (ax+b) =1
Here,
Y=ax+b = 0 Means hyper plane
Y=ax+b = +1 Means Features above the hyper Plane
Y=ax+b= -1 Means Features below the hyper Plane.

3) Decision Trees
4) Boosted Trees
5) Random Forest
6) Extreme Learning Machine (Neural Networks)
7) K Nearest Neighbour

III. Proposed Supervised Microarray Gene Retrieval System

Examination on the high dimensional information is the principle issue in Microarray, to enhance the performance of the system the measurements to be diminished into lower measurement. There are numerous procedures for linear and nonlinear dimensionality decrease. A portion of the systems are reasonable linear information and not appropriate for nonlinear information. This work presents the various techniques used to reduce the dimensions of the data.

Here we portray the working rule of the proposed methodology notwithstanding the general stream of the work. The fundamental point of this research proposal related to feature selection in kernel methods. Nevertheless, a large portion of the past work uses kernel to help select features in the original space. Interestingly, we will likely choose includes in the portion space, since we cannot change non-separability nature of the data through feature selection in the first space. In any case, include choice in a part space can deal with this issue.

A. Overall flow of the work

Microarray gene retrieval system aims to return the results to the user with respect to the queried data. The general flow of this work is presented below,

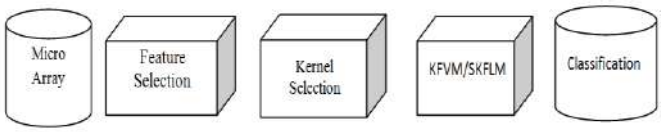

Microarray-->Feature Selection-->Kernel Selection
-->KFVM/SKFLM-->Classification

The objective of this proposed research work is to identify a better feature selection and classification accuracy rate within the time. This accuracy rate is achieved by employing KFVM and SKFLM and the execution time of the work is reduced by feature reduction and faster learning ability of the classifier. The entire retrieval system is divided into two phases, which are feature reduction with the help of best Linearity reduction and classification with the help of best kernel selection. The Linearity reduction phase tends to reduce the dimensionality of the features. This step is manipulated carefully, such that the limited significant features alone are selected for further processing. This step is followed by the classification phase, with the help of best kernel, which aims to distinguish between the classes.

B.Microarray Feature dimensionality minimization and classification by KFVM and SKFLM

Kernel Feature Vector Machine is an improvisation of LFDA and SVM .Supervised Kernel Feature Learning Machine is an improvisation of KLFDA and ELM. Through this, algorithms we try analyse and identify the best feature selection methods and try to identify which classification technique is suitable for the classification .Linearity Problem and Selection of Kernel are the biggest challenge associated with Microarray gene retrieval. Goal of dimensionality minimization is to acquire a low dimensional depiction of high dimensional data along with the preservation of the local structure of the original data. Processing all the data is unnecessary and minimizing the feature dimensionality paves way for several benefits such as reduced computational overhead and time consumption.

Proposed algorithm

```
//Training
Input: Microarray  Dataset
Output : knowledge base construction
Begin
  For data (1 to n)
 Extract f Features ;
   Best Kernel Selection for Classification;
  Implementation of KFVM and SKFLM
   Build knowledge base;
 End for;
End;
// Testing
Input : Class Types;
Output : Ranked results;
Begin
 If (query=Class Type)
   List all the types of the class;
 Else
   Compute the Difference Between the Class and Within the class dataset;
   Return top ranking records;
 End if;
End;
```

IV. EXPERIMENTS AND EVALUATIONS

A.The Data Set

Publicly available breast cancer data set is used for this research.

http://csse.szu.edu.cn/staff/zhuzx/Datasets.html[15].

This Data set contains 24481 genes with 97 instances separated with 2 classes.

B. Analysis of Kernel Functions

In this research, we are using different classifiers like K Nearest Neighbour (K-NN), Support Vector Machine (SVM), Extreme Learning Machine (ELM) and Linear Classifier (LC).These classifier has been tested by taking five different Kernel Selection methods on high dimensional data set. From Table I and Figure 1, it is clear that "Normalised Polynomial Kernel (NPK)" is best Kernel selection method for SVM classification and RBF kernel is best selection method for ELM classification. These Kernel selection methods give 98.9% accuracy for high dimensional data features.

TABLE I.
ACCURACY OF KERNEL SELECTION METHOD IN ASSOCIATE WITH CLASSIFICATION TECHNIQUE

Types Of Kernels	Classification Method			
	K-NN	SVM	ELM	LC
	Accuracy (%)	Accuracy (%)	Accuracy (%)	Accuracy (%)
PK	97.5	97.5	97.5	97.5
NPK	98.2	98.9	98.5	98.2
RBF	97.8	98.2	98.9	96.8
GK	95.7	95.7	95.7	94.2
LK	94.4	95.2	95.2	94.4

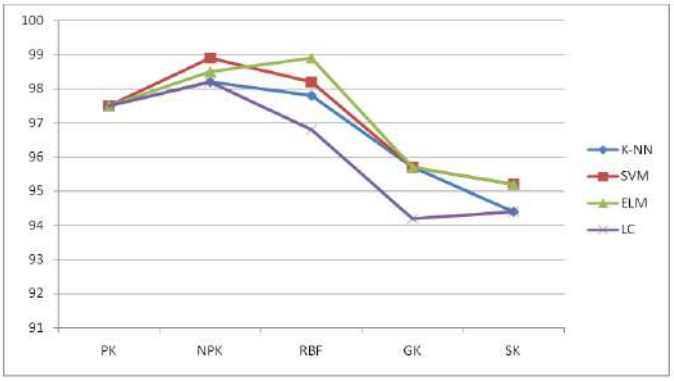

Fig .1-Accuracy of Kernel Selection method in associate with Classification Technique

C. *Analysis of Feature Selection Methods*

From the table data, we can see that the Filter feature selection method is good feature selection technique and in the previous studies reported that the wrapper and embedded approaches are shows computational burden [11].

TABLE 2

ANALYSIS AND IDENTIFICATION OF BEST FEATURE SELECTION METHOD

Feature Selection Techniques	Feature Selection Methods		
	Filter Method	Wrapper Method	Embedded Method
	F-Value (%)	F-Value (%)	F-Value (%)
PC	98.5	94.5	93.5
LDA	97.2	95.9	95.5
LFDA	96.8	93.2	94.9
KLFDA	97.7	95.7	95.7
IGR	98.4	95.2	95.2

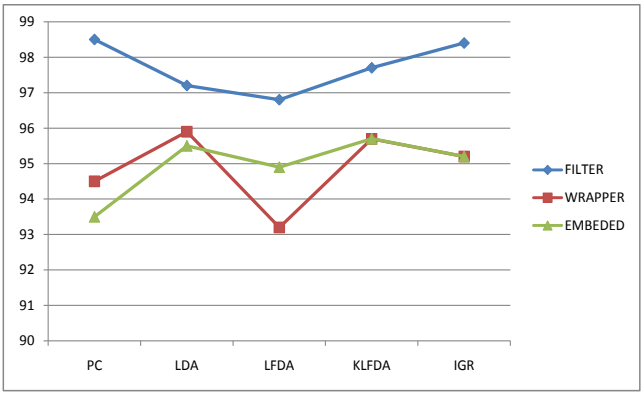

Figure 2: Analysis and Identification of Best feature Selection method

V.ANALYSIS OF THE COMBINED EFFECT AND CONCLUSION

Through this research, we can see that the effect of the Kernel function varies significantly depending on the dimensionality of the data set. Various types of Kernel functions tested in this work, NPK has shown best SVM performance across a wide range of dimensions when used with a variety of feature selection techniques. The RBF kernel shows variable performance depending on dimensionality in ELM.

The results show that the choices of the Kernel function and feature selection technique have profound effect on the performance of SVM, ELM and other classifiers. In future, some other Kernel functions and feature selection techniques may be tested with different datasets. The best Feature selection method is Filter wrapper and it is suitable for all the feature selection techniques. If we analyse the overall performance of kernel selection and feature selection methods, we can see that LFDA feature selection method is suitable for SVM classification and KLFDA feature selection method is suitable for ELM classification.

REFERENCES

[1] S. Bandyopadhyay, R. Mitra, U. Maulik, and M. Q. Zhang, *Development of the human cancer microRNA network*,BMC Silence, vol. 1, no. 1, p. 6, 2010.

[2] Madan Babu M. ,*An Introduction to Microarray Data Analysis*,Chapter 11, pp 225-249, Accessed January 2008.

[3] Vladimir Filkov, Steven Skiena and Jizu Zhi (2002),*Analysis Techniques for Microarray Time Series Data*, Journal of Computational Biology, Vol. 9, No. 2, pp. 317-330.

[4] M. Schena, D. Shalon, R.W. Davis, and P. O. Brown,*Quantitative monitoring of gene expression patterns with a complementary DNA microarray*,Science, vol. 270, no. 5235, pp. 467–470, 1995.

[5] Zizhu Fan; Yong Xu; Zhang, D.,*Local Linear Discriminant Analysis Framework Using Sample Neighbors*, IEEE Transactions on Neural Networks, , On page(s): 1119 - 1132 Volume: 22, July 2011.

[6] Yuxi Hou; Iickho Song; Hwang-Ki Min; Cheol Hoon Park, Complexity-*Reduced Scheme for Feature Extraction With Linear Discriminant Analysis* , IEEE Transactions on Neural Networks and Learning Systems, page(s): 1003 - 1009 Volume: 23, Issue: 6, June 2012.

[7] R. A. Fisher,The use of multiple measurements in taxonomic problems. Annals of Eugenics,7(2): 179–188, 1936.

[8] K. Fukunaga,*Introduction to Statistical Pattern Recognition*. Academic Press, Inc., Boston, second edition, 1990.

[9] X. He and P. Niyogi. *Locality Preserving Projections*.,Advances in Neural Information Processing Systems 16. MIT Press, Cambridge, MA,2004.

[10] Sugiyama, M. (2007),Dimensionality reduction of multimodal labeled data by local Fisher discriminant analysi,. Journal of Machine Learning Research, 8, 1027–1061.

[11] V. Bolón-Canedo, N. Sánchez-Maroño, A. Alonso-Betanzos, J.M. Benítez, F. Herrera,*A review of Microarray datasets and applied Feature selection methods*, Information Sciences, vol.282, pp.111-135, 2014.

[12] M. Dashtban, Mohammadali Balafar,*Gene selection for microarray cancer classification using a new evolutionary method employing artificial intelligence concepts*, Genomics, Volume 109, Issue 2, March 2017, Pages 91-107

[13] Abubakhari Sserwadda, Ömer Sinan Saraç**,***Gene selection and classification of pancreatic microarray datasets***,**Signal Processing and Communications Applications Conference, Antalya, Turkey, 15-18 May, 2017**.**

[14] S Alagukumar, R Lawrance,*Classification of microarray gene expression data using associative classification***,** International Conference on Computing Technologies and Intelligent Data Engineering, Kovilpatti, India, 7-9 Jan, 2016

[15] *http://csse.szu.edu.cn/staff/zhuzx/Datasets.html*

A Bio-inspired Algorithm based Multi-class Classification Scheme for Microarray Gene Data

LT. Thomas Scaria & T. Christopher

Journal of Medical Systems

ISSN 0148-5598
Volume 43
Number 7

J Med Syst (2019) 43:1-8
DOI 10.1007/s10916-019-1353-y

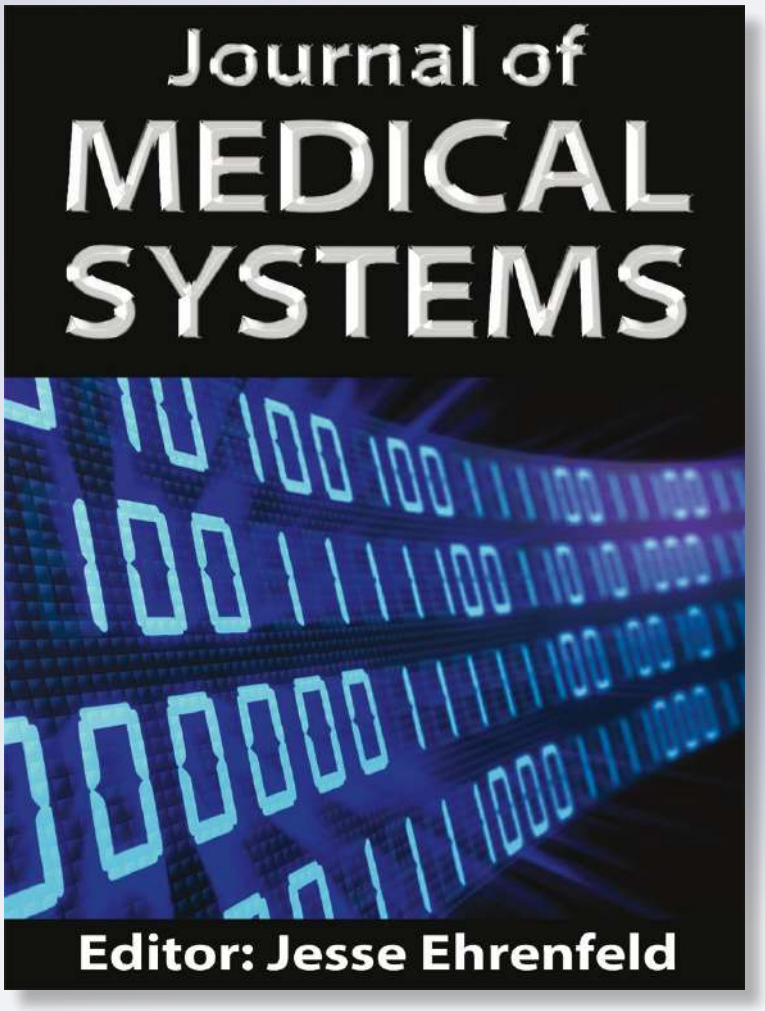

Springer

Journal of Medical Systems (2019) 43:208
https://doi.org/10.1007/s10916-019-1353-y

TRANSACTIONAL PROCESSING SYSTEMS

A Bio-inspired Algorithm based Multi-class Classification Scheme for Microarray Gene Data

LT. Thomas Scaria[1] · T. Christopher[2]

Received: 14 March 2019 / Accepted: 20 May 2019

Abstract
Microarray gene data is widely known for its high dimensionality and volume. The utilization of microarray gene data is increasing now-a-days, owing to the advancement of medical science. Microarray gene data helps in diagnosing diseases quite accurately. However, processing microarray gene data is difficult and is usually not understandable. Taking this challenge into account, this work presents a user-friendly rule based classification model, which is easily understandable and does not demand users to have prior knowledge. The classification rules are formed with the help of cuckoo search optimization algorithm and the rules are pruned by the associative rule mining. Finally, the classification is performed with the help of the pruned rules. The performance of the proposed approach is satisfactory in terms of accuracy, sensitivity, specificity and time consumption.

Keywords Microarray gene · Disease analysis · Cancer classification · Association rules

Introduction

Microarray gene expression is widely utilized by the biological experts to track the gene expression level of a living being. Microarrays are utilized for assessing the gene expression by performing several different operations and one of the most common operations is the comparison between the genes of a cell, which are retained in different conditions. Hence, the microarray gene analysis has gained considerable research interest. However performing microarray gene analysis is not easier, as it involves voluminous data.

Usually, the process of microarray gene analysis intends to analyse the microarray data for gaining beneficial knowledge from the data. Data classification is one of the most common operations performed over data and can be attained by the classifiers. The classifier is trained with the sample data, such that it can differentiate between the entities with respect to the class. Though there are numerous classifiers to perform analysis by differentiating the entities, rule based classification is quite rare in the microarray data analysis field.

The rule based classification model requires a set of well formed rules, such that the healthcare professionals can diagnose the disease and the suitable treatment for the disease can be figured out. However, it is a difficult task to figure out the effective rules from a voluminous dataset with noise. In addition to this, the dimensionality of microarray data is quite larger and hence, there rule based classification technique may require greater number of rules to perform classification.

The bio-inspired algorithms prove better performance over the complex problems with greater search space. There are so many bio-inspired algorithms presented in the literature. Hence, it is better to utilize the bio-inspired algorithms to mine the rules being framed. Now-a-days, rule mining with the help of bio-inspired algorithms is becoming the new research trend and some of the samples are ABCMiner [1] and BeeMiner [2].

Recognizing the need of better classification technique and to present an aid to the healthcare professionals, this article intends to propose a rule based classification model based on Cuckoo Search Optimization Algorithm (CSOA). The main task of CSOA is to detect the perfect interval upon the rule based classification scheme to classify between the microarray gene data. The proposed work considers the microarray gene datasets with both binary and multi-classes of cancer. The

This article is part of the Topical Collection on *Transactional Processing Systems*

✉ LT. Thomas Scaria
lttscaria.19@gmail.com

[1] Department of Computer Science, St. Pius X College, Kasaragod, Kerala, India

[2] PG and Research Department of Information Technology, Government Arts College, Coimbatore, India

Published online: 29 May 2019

rules framed by the proposed approach are understandable and effective.

This article presents a web application to perform disease classification based on rules, which is beneficial for the healthcare professionals. This work aims to predict the disease by means of the association rules formed with respect to the association between the entities and the Cuckoo Search Optimization Algorithm (CSOA). The proposed approach classifies the microarray gene expression data.

This work considers different gene expression data with binary and multi-class datasets. The performance of this approach proves that this work shows better classification accuracy and hence, the proposed model can be utilized as an aid for biologists. Some of the work contributions are presented as follows.

- This work presents a rule based classification model, which is quite rare in the existing literature.
- The framed rules help in extracting better knowledge and train the classification model accordingly.
- The accuracy rate of the proposed approach is better, which is evident in the performance analysis.

The rest of the content is organized in the following way. Section 2 presents the review of literature with respect to microarray gene data analysis. The proposed rule based classification technique for microarray gene data is elaborated in section 3. The performance of the proposed approach is evaluated in section 4. Finally, section 5 concludes the article with the future possible enhancements.

Review of literature

This section reviews the related literature with respect to microarray gene data analysis.

A gene expression analysis for early lung cancer prediction technique is presented with the help of machine learning techniques in [3]. This work analyses the microarray gene expression data of the Kent Ridge bio-medical dataset to detect the lung cancer. The most optimal set of genes is selected from the microarray gene data to predict the cancer causing agent.

A microarray image gridding and segmentation technique is proposed in [4], which is executed on Graphics Processing Unit (GPU). This work intends to achieve better performance by utilizing the available resources in the Computed Unified Device Architecture (CUDA). It is claimed that the proposed approach shows better performance by consuming minimal time period.

A faster cDNA microarray gene expression data classifier is proposed for diagnosing the diseases in [5]. This work enhances the Gene Expression Graph based classifier for minimizing the computation time. This work filters the genes by means of the edge weight, in order to increase the classification accuracy and to reduce the false-positive rates.

In [6], a consensus gene selection criteria is proposed on the basis of distributed GPU with partial least-square based microarray data analysis is presented. This work measures the consistency and distinctiveness of gene expressions and the genes associated with the specific disease are figured out. The process of gene selection is accelerated as the work is implemented in distributed GPU. This work utilizes Diffused Large B Cell Lymphoma (DLBCL) and Prostrate cancer datasets.

A grouped gene selection of cancer based on adaptive sparse group lasso with respect to conditional mutual information is proposed in [7]. Initially, the genes are grouped by means of weighted gene co-expression network for the cancer microarray data. The conditional mutual information is utilized to compute the integrated and data driven weights. This paves way for enhancing the correlation between the genes in all the groups. By this way, the genes are classified and selected.

In [8], a microarray based cancer diagnostic system is proposed on the basis of repeated cross validation based ensemble feature selection. This work resamples the data by means of ensemble techniques and the features are selected by Repeated Cross Validation (RCV). The performance of this work is compared against Support Vector Machine (SVM) and recursive feature elimination techniques. The performance of this approach is evaluated in four different datasets.

A local nearest neighbour based feature weighting system is proposed for gene selection in [9]. This work considers the nearest neighbours based weighting approach by minimizing and maximizing the distances of within-class and between-class locally with respect to k nearest neighbour rule. This approach can be utilized in both binary and multi-class problems.

In [10], the feature selection and feature extraction techniques are combined together by utilizing deep learning in order to predict the outcome of the breast cancer. This work presents an unsupervised feature learning model by combining the Principal Component Analysis (PCA) and autoencoder neural network to detect the unique features of gene expressions. The AdaBoost algorithm based ensemble classifier is employed to predict the clinical outcomes of breast cancer.

The significance and functional similarity of gene identification with respect to the disease is proposed in [11]. This gene selection algorithm combines the information acquired from the protein interaction network and the gene expression profile. The significance of the gene is computed by comparing it with the other gene by utilizing mutual information. This work performs analysis on different cancer microarray datasets.

In [12], a system to predict the progression of cancer by employing gene interaction regularized elastic net is proposed. This work considers both the measurement and interaction information of the gene by establishing the elastic net. The discriminate features are chosen with the help of the grouping

effect. This work is evaluated over ovarian and breast cancer datasets.

An auto-weighted least square method is presented for predicting the missing values in the microarray data in [13]. This work weights the neighbourhood genes with respect to a corresponding gene in terms of the gene significance. The convergence is enhanced with the help of an accelerating strategy. The missing values on the microarray data is predicted by this work as well.

In [14], a fast and scalable feature selection technique is proposed for gene expression data based on Hilbert-Schmidt independence criterion. The correlation between the gene expression data and the response variables are figured out by detecting the informative genes with the help of multivariate algorithm. This algorithm can be utilized on different response variables and is suitable of binary and multi-class classification.

A large-scale microarray data analysis meant for cloud-scale genomic signals is presented in [15]. This work is based on the cloud-scale distributed parallel based one dimensional wavelet based transformation for declaring a threshold. This idea retains the genes by means of denoising process to classify between the cancer types. However, this work processes the image based data.

In [16], an unsupervised gene selection technique is proposed on the basis of matrix factorization framework. This work introduces an unsupervised two-stage gene selection technique, in which the first stage clusters the genes by removing the redundant gene with the help of k-NN algorithm. The second stage selects the significant genes out of all the genes with the help of matrix factorization.

In [17], a gene retrieval system is presented on the basis of Local Fisher Discriminant Analysis (LFDA) and Support Vector Machine (SVM) is proposed. The LFDA is utilized for reducing the dimensionality of the microarray data and SVM is utilized for classification. A microarray data gene retrieval system based on Kernelized LFDA and Extreme Learning Machine (ELM) is proposed in [18]. In [19], an ensemble classification based technique is proposed on the basis of Information Gain Ratio (IGR) and classifiers k-NN, SVM and ELM.

Motivated by these existing works, this article intends to propose a gene classification system based on rule based classification model. The intention of this work is to make the entire process simpler with better understandability and is achieved by the meaningful rules.

Proposed approach

This section elaborates the proposed web application for disease prediction by forming rules. Initially, the overview of the work is presented as follows.

Work overview

Data classification is one of the widespread problems being faced by the data mining applications. It is a complex task to classify between the data, as the effectiveness of the classification system depends on the knowledge imparted to the classifier. Microarray data is quite voluminous and is pretty hard to impart knowledge to classifier. In addition to this, the microarray cancer data analysis is completely related to the human lives.

The objective of the microarray cancer data classification is to form a classification model, which enables the classifier to decide the best possible class of the entity. As this work handles the data related to human lives, the accuracy of the system is the main concern. Though there are numerous disease prediction and diagnostic systems available in the literature, the microarray data based classification techniques are scarce. Additionally, the classification techniques are hard to understand and in order to deal with this issue, this work attempts to propose a rule based classification scheme. The overall flow of the work is presented in Fig. 1.

The proposed approach deals with the voluminous microarray data for framing the rule set, such that the class associated with the entity can be figured out in the forthcoming process. There are several classification algorithms for microarray data, which are based on classifiers such as k-NN, SVM,

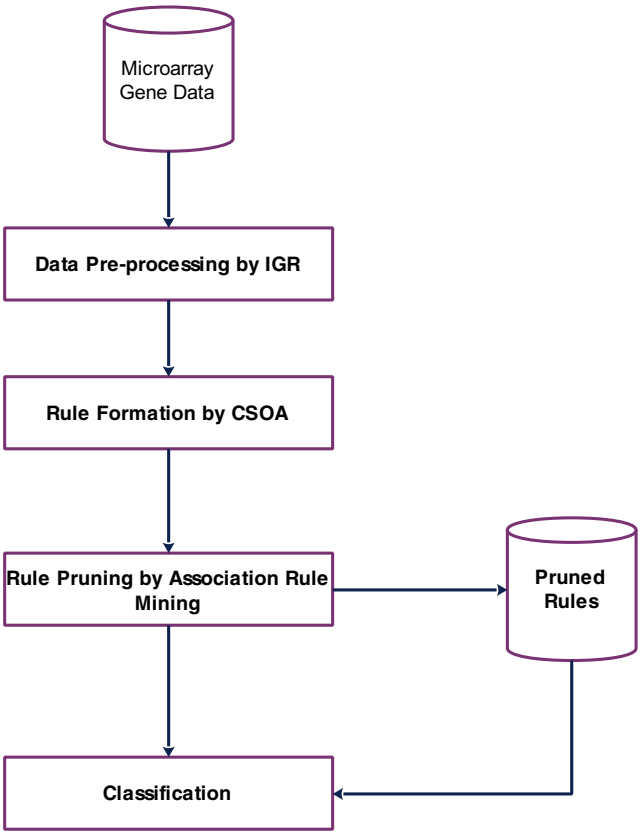

Fig. 1 Overview of the proposed approach

ELM, decision tree and so on. These classifiers perform better, however learning process of the classifiers depend on the statistical and mathematical ideas that can applied irrespective of the nature of domain. The classifiers are common for all sorts of classification problems and so the classifiers cannot derive problem specific knowledge with respect to the datasets.

Understanding the benefits of rule based classification techniques, this article presents a rule based classification scheme for microarray data. The proposed approach involves four significant phases and they are data pre-processing, rule formation, rule pruning and classification. The rules are framed by means of the bio-inspired algorithm namely CSOA. This work generates the significant rules for better classification accuracy. The proposed approach is elaborated in the following section.

Proposed Rule based Classification Approach

The rule based classification scheme requires more rules to ensure better classification but, it is quite tough to save more number of rules and to handle them. In addition to this, it is challenging to detect the appropriate rules for performing classification. The proposed work intends to address the above stated issues by forming dynamic rules with the help of CSOA.

The CSOA is completely based on the behaviour of cuckoo with the levy flight concept, as discussed in [20]. Basically, the CSO algorithm involves three significant phases and they are egg laying phase, quality of egg assessment and nest maintenance. The cuckoo bird lays eggs on the nest in a random fashion and the quality of eggs is assessed in the quality assessment phase. The eggs with better quality alone are suitable for the next generation. Suppose, if the nest contains eggs with poor quality, then the nests are discarded.

The proposed work achieves the goals in four different phases and they are data pre-processing, rule formation, rule pruning and classification phases. All these phases are explained as follows.

Microarray Data Pre-processing

The microarray dataset is high dimensional and hence, the dimensionality has to be reduced for better data processing. The high dimensionality of the microarray dataset slows down the process and degrades the performance of the system. Understanding the issue of high dimensionality, this work reduces the dimensionality by selecting the significant genes by employing Information Gain Ratio (IGR), as performed in our previous work [19].

The IGR chooses the significant genes by considering the information gain and the gene with maximal correlation level are chosen as significant genes. The IGR is computed by

$$IGR(F) = \left[\frac{IG_S - IG(F)}{IG_S + IG(F)}\right] \times 100 \tag{1}$$

Where IG_s and IG_F are given by

$$IG_S = -\left[\frac{r.o(c_1, S)}{|S|}\right] log_2 \left[\frac{r.o(c_1, S)}{|S|}\right] \tag{2}$$

$$IG(F) = \left[\frac{|F_i|}{|F|}\right] \times IG(F_i) \tag{3}$$

In the above equations, $\left[\frac{r.o(c_1,S)}{|S|}\right]$ denotes the probability of the repetitive occurrence of a gene, which is present in the class c_1. Let the feature f contains q unique values, which can be represented as $\{f_1, f_2, f_3, \ldots, f_q\}$. For a dataset with f features, the training dataset is formed as follows $\{c_1, c_2, c_3, \ldots, c_q\}$.

Hence, the IGR selects the genes with more significance by considering the correlation and information gain and these virulent genes are utilized for the forthcoming phases.

Rule Formation Phase

Rule formation is the heart of the proposed approach, which is meant for building the meaningful rule set and paves way easy classification. Hence, this work pays more attention to form better rules and the rules framed by the proposed work follows a specific structure. Consider that all the rules formed by the proposed work are represented in a standard format as given below.

$$Rl(rl_{i_1}, rl_{i_2}, \ldots CL, rl_{i_n}) \tag{4}$$

Here, rl_{i_n} is the different attributes and n is the total count of entities being present in each rule and is fixed on the basis of the count of genes. Suppose, if the user employs five genes to perform classification, then the classification rule is framed with the help of five genes. Each rule of the system involves two important parts and the standard form of the rule is as follows.

$$Rl : rl_i \rightarrow CL \tag{5}$$

Each and every rule is identified with the help of an identifier and is called as the index. Apart from this, each rule is treated with the operations such as max, min and mean. These operations are performed over the expression with respect to the class. The max and min are the two basic and significant operations, which can reveal the upper and the lower limit of the values.

Hence, the optimal upper and lower limits help in attaining better results and the limits are fixed by the CSO algorithm. The second important stage of rule formation is the rule detection, which intends to detect a particular kind of cancer out of the whole entities in the microarray data. The rules are detected in the following way. As mentioned earlier, each and every rule is computed with the max and mix values for

every rule in the solution space. The lower and upper limit of a rule is computed by the following equations.

$$rl_i(lowl) = rl_i.m - q_1 \times (rl_i.max - rl_i.min) \quad (6)$$

$$rl_i(upl) = rl_i.m + q_2 \times (rl_i.max - rl_i.min) \quad (7)$$

In the above equations, $rl_i.max$ and the $rl_i.min$ are the maximum and minimum values of the rule item denoted as rl_i. With the upper and lower limits, the general range can be figured out. $rl_i.m$ denotes the mean value of the microarray expression with specific identifier and is computed with respect to all the entities present in a specific class. q_1 and q_2 are the values ranging between 0 and 1. It is always ensured that the *lowl* and *upl* are unequal to each other and *lowl* is always lesser than the *upl*. As soon as the rules are detected, the fitness of the rules is figured out with the help of standard performance indicators such as True Positive (TP), True Negative (TN), False Positive (FP) and False Negative (FN), as presented in eq. 8.

$$R_{fit} = \frac{TP}{TP + FN} \times \frac{TN}{TN + FP} \quad (8)$$

The gene data with respect to index is evaluated and when the value of the gene data exists between the *lowl* and *upl*, then it can be included in the rule. The class is predicted with the help of TP, TN, FP and FN. TP indicates that the total count of entities with predicted class and are included in the rule. TN denotes that the total count of entities with unpredicted class and are not included in the rule. FP indicates that the total count of entities with unpredicted class and are not included in the rule. FN indicates that the total count of entities with predicted class and are not included in the rule.

When the rules are formed by this way, the optimal solution to the problem is figured out by the CSO algorithm. This algorithm is based on the concept of egg laying by cuckoo on a randomly picked nest. The nests with high quality eggs alone are suitable for the next generation and the nests with poor quality eggs are discarded. In this case, the rules are eggs and the nests are randomly chosen.

For the rule item ri_1, the position of the cuckoo is randomly selected with the help of levy flights.

$$X_i^{(t+1)} = X_i^{(t)} + \alpha \oplus Levy(\lambda) \quad (9)$$

$$Levy(\lambda) = t^{-\lambda}; \lambda \in [0, 3] \quad (10)$$

Where λ is the step-length. In equation (9), $X_i^{(t+1)}$ is the microarray data identifier of a new rule item, which is on the nest t. $X_i^{(t)}$ is the microarray data identifier of a rule item on the nest t, which is the neighbour of the current solution. ᅫ represents the step size and is greater than 0, mostly set as 1. $\oplus$ indicates the entry-wise multiplication, which is similar to the PSO algorithm. Employment of Levy flight boosts up the efficiency of navigating through the search space [20].

Suppose, when the position of egg has to be modified and it can be attained by changing the limit of the rule item as follows.

$$X_i^{(t+1)}.upl = X_i^{(t+1)}.max - \gamma \quad (11)$$

$$X_i^{(t+1)}.lowl = X_i^{(t+1)}.min + \gamma \quad (12)$$

$X_i^{(t+1)}.upl$ and $X_i^{(t+1)}.lowl$ denote the upper and the lower limit of the new rule and γ is the random number between 0 and 1. Hence, the rules are formed by considering the range of the data. Though, it is unnecessary to maintain all the rules and hence, the rules with optimal fitness rates are to be chosen and saved for future reference. This is done by the rule pruning step and is explained in the following section.

Rule Pruning Phase

The total count of rules computed by the rule formation phase is more and the count can be reduced with the help of this phase. The main task of this phase is to remove the duplicate and ineffective rules. Let the microarray training data is represented as MTD and CL is the class label. Each rule rl_i can be represented as in equation 5 and the support (*SUP*) and confidence (*CON*) rates of the rules are computed as follows.

$$SUP(Rl_i) = \frac{TP}{CL} \quad (13)$$

$$CON(Rl_i) = \frac{TP}{TP + FP} \quad (14)$$

The support of a rule is computed by the count of entities in the training dataset with matching items Rl_i for a given class label CL. The total count of matching rule items Rl_i with class label CL with the total count of matching rule items Rl_i is computed to determine the confidence of the rule. The overall algorithm of this work is presented as follows.

Proposed Algorithm
Input: Microarray gene dataset
Output: Disease classification
Begin
//Pre-processing
Pre-process the dataset by employing eqn.1;
//Rule formation
Rule set = NULL;
Choose a class from a set of classes;
Detect the rules and compute the fitness;
Add the rules with greatest fitness to the rule set;
//Rule pruning
Prune the rules by eqns (13) and (14);
//Classification
Compute the feasibility of the sample and forecast;
Return the result;
End;

Hence, the rules with maximal confidence are taken into account and stored for future classification. The data classification is presented as follows.

Table 1 Dataset details

Dataset	Classes	Total entities	Gene count
Colon	2	62	2000
Leukemia	2	72	7129
Lung	2	96	7129
SRBCT	4	83	2308
Lymphoma	3	62	4026
Leukemia	3	72	7129

Classification Phase

The entity is classified by computing the feasibility of the sample with respect to a particular class and is computed by the following

$$Feasibility = \frac{TP}{C_{cl}} \tag{15}$$

The feasibility of the sample is the ratio of the TP rate and the count of the entities with respect to a specific class being forecasted. The test entity is treated with the forecasting value of the rules as follows.

$$Forecast = \left(w1 \times R_{fit}\right) + \left(w2 \times feasibility\right) \tag{16}$$

In the above equation, w1 and w2 are the weighted parameters with respect to the fitness and the feasibility level. W1 is a random number between 0 and 1, w2 is computed by $(1 - w1)$. The test sample is treated with these equations, so as to forecast the appropriate class for the sample. The class with the greatest feasibility is taken into account and suggested to the user. The classification accuracy of the microarray dataset is computed by the ratio of the perfectly classified test sample (CC_{Ts}) to the total count of samples in the dataset being classified correctly (N_c).

$$Classification\ accuracy = \frac{CC_{Ts}}{N_c} \tag{17}$$

By this way, the rule is provided with the classification accuracy. The performance of the proposed approach is evaluated in the forthcoming section.

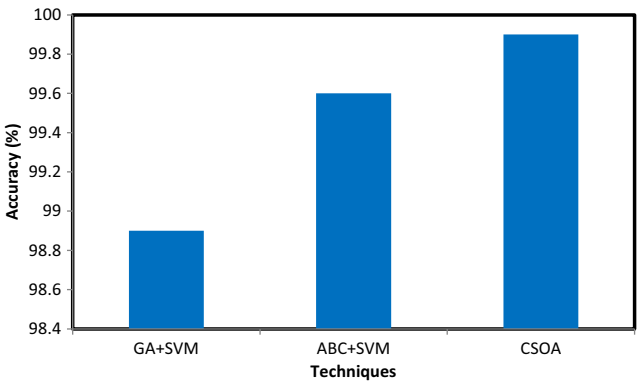

Fig. 2 Accuracy rate analysis

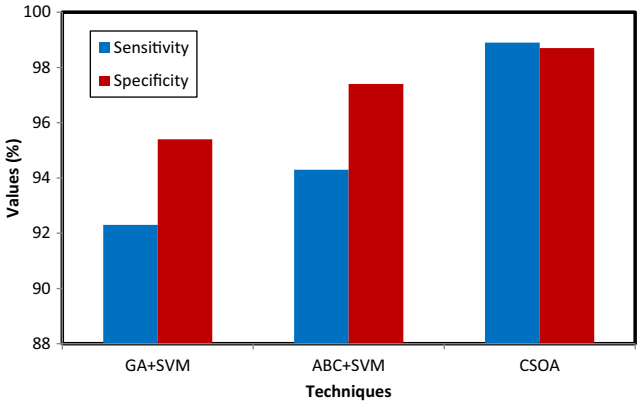

Fig. 3 Sensitivity and specificity rate analysis

Results and discussion

The performance of the proposed approach is evaluated over both binary and multiclass datasets. The binary class microarray datasets include colon, leukemia and lung cancer [21–23]. The considered multi-class microarray datasets are SRBCT, lymphoma and leukemia [24–26]. The initialized cuckoos are 200 and the termination condition is fixed by considering the count of iterations, which is 2500. The count of gene and classes available in the dataset are presented in Table 1.

The performance of the proposed work is tested and the experimental results are computed and compared with the existing approaches. The performance metrics considered are accuracy, sensitivity, specificity and time consumption. The experimental results attained by the proposed approach are as follows (Figs. 2, 3 and 4).

The performance of the proposed approach is compared against two recently proposed algorithms found in [27, 28] respectively. When the performance of the proposed approach is tested, the accuracy, sensitivity, specificity rates are proven to the maximum when compared to the existing approaches, while consuming minimal time period. The main reason for the better performance of the proposed approach is the utilization of CSOA and the rule pruning phase. This work can be applied to datasets with any classes without any prior

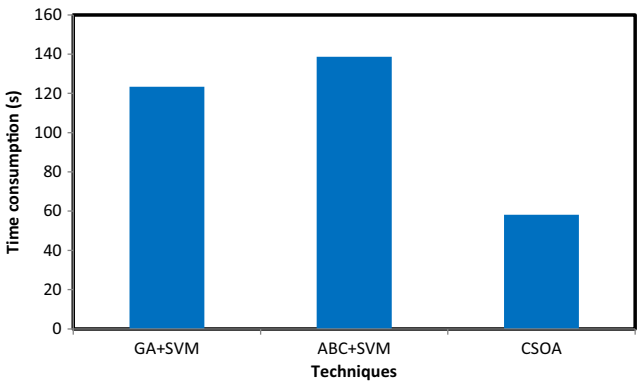

Fig. 4 Time consumption rate analysis

knowledge. As the rules are pruned with respect to the effectiveness, the performance of the proposed approach is enhanced. The following section concludes the paper.

Conclusions

This article proposes a rule based classification model that relies on CSOA, which is meant for microarray gene data. The microarray gene data is highly voluminous and is difficult to perform classification, which is required to distinguish between the type of cancer. This work trains the system with the sample train data obtained from the publicly available datasets and the proposed approach forms rules with the help of CSOA. The formed rules are then pruned with the help of associative rule mining, in order to select the efficient rules alone. Finally, the classification is performed by computing the feasibility and forecast values. The main advantages of this work are that the users need not to possess any prior knowledge and the classification can be done for any dataset. As the classification is based on rules, the proposed work is user-friendly and easily understandable. In future, this work is planned to be extended by considering the microarray image. In addition to this, the performance of different bio-inspired algorithms are planned to be incorporated into the system.

Compliance with ethical standards

Conflict of Interest The authors declare that they have no conflict of interest.

Ethical Approval This article does not contain any studies with human participants or animals performed by any of the authors.

References

1. Celik, M., Karaboga, D., Koylu, F., Artificial bee colony data miner (abc-miner). In: 2011 International Symposium on Innovations in Intelligent Systems and Applications (INISTA), June. pp. 96–100, 2011.
2. Talebi, M., Abadi, M., Beeminer: a novel artificial bee colony algorithm for classification rule discovery. In: 2014 Iranian Conference on Intelligent Systems (ICIS), February, pp. 1–5, 2014.
3. Pati, J., Gene Expression Analysis for Early Lung Cancer Prediction Using Machine Learning Techniques: An Eco-Genomics Approach. IEEE Access 7:4232–4238, 2018.
4. Katsigiannis, S., Zacharia, E., and Maroulis, D., MIGS-GPU: Microarray Image Gridding and Segmentation on the GPU. IEEE Journal of Biomedical and Health Informatics 21(3):867–874, 2017.
5. Hsieh, S.-Y., and Chou, Y.-C., A Faster cDNA Microarray Gene Expression Data Classifier for Diagnosing Diseases. IEEE/ACM Transactions on Computational Biology and Bioinformatics 13(1):43–54, 2016.
6. Wu, H.-C., Wei, X.-G., and Chan, S.-C., Novel Consensus Gene Selection Criteria for Distributed GPU Partial Least Squares-Based Gene Microarray Analysis in Diffused Large B Cell Lymphoma (DLBCL) and Related Findings. IEEE/ACM Transactions on Computational Biology and Bioinformatics 15(6):2039–2052, 2018.
7. Li, J., Dong, W., and Meng, D., Grouped Gene Selection of Cancer via Adaptive Sparse Group Lasso Based on Conditional Mutual Information. IEEE/ACM Transactions on Computational Biology and Bioinformatics 15(6):2028–2038, 2018.
8. Güney, H., and Öztoprak, H., Microarray-based cancer diagnosis: repeated cross-validation-based ensemble feature selection. Electronics Letters 54(5):272–274, 2018.
9. An, S., Wang, J., and Wei, J., Local-Nearest-Neighbors-Based Feature Weighting for Gene Selection. IEEE/ACM Transactions on Computational Biology and Bioinformatics 15(5):1538–1548, 2018.
10. Zhang, D., Zou, L., Zhou, X., and He, F., Integrating Feature Selection and Feature Extraction Methods With Deep Learning to Predict Clinical Outcome of Breast Cancer. IEEE Access 6:28936–28944, 2018.
11. Maji, P., and Shah, E., Significance and Functional Similarity for Identification of Disease Genes. IEEE/ACM Transactions on Computational Biology and Bioinformatics 14(6):1419–1433, 2017.
12. Zhang, L., Liu, H., Huang, Y., Wang, X., Chen, Y., and Meng, J., Cancer Progression Prediction Using Gene Interaction Regularized Elastic Net. IEEE/ACM Transactions on Computational Biology and Bioinformatics 14(1):145–154, 2017.
13. Yu, Z., Li, T., Horng, S.-J., Pan, Y., Wang, H., and Jing, Y., An Iterative Locally Auto-Weighted Least Squares Method for Microarray Missing Value Estimation. IEEE Transactions on NanoBioscience 16(1):21–33, 2017.
14. Gangeh, M. J., Zarkoob, H., and Ghodsi, A., Fast and Scalable Feature Selection for Gene Expression Data Using Hilbert-Schmidt Independence Criterion. IEEE/ACM Transactions on Computational Biology and Bioinformatics 14(1):167–181, 2017.
15. Harvey, B. S., and Ji, S.-Y., Cloud-Scale Genomic Signals Processing for Robust Large-Scale Cancer Genomic Microarray Data Analysis. IEEE Journal of Biomedical and Health Informatics 21(1):238–245, 2017.
16. Li, J., and Wang, F., Towards Unsupervised Gene Selection: A Matrix Factorization Framework. IEEE/ACM Transactions on Computational Biology and Bioinformatics 14(3):514–521, 2017.
17. Lt. Scaria, T., and Christopher, T., Microarray Gene Retrieval System based on LFDA and SVM. International Journal of Intelligent Systems and Applications (1):9–15, 2018.
18. Lt. Thomas Scaria, Christopher, T., Supervised Microarray Gene Retrieval System Based on KLFDA and ELM, International Journal of Advanced Intelligent Paradigms, Accepted, In Press, 2018.
19. Lt. Scaria, T., and Christopher, T., Ensemble Classification based Microarray Gene Retrieval System. ICTACT Journal on Soft Computing 9(1):1806–1812, 2018.
20. Yang, X. S., Nature-Inspired Metaheuristic Algorithms 128, (2008).
21. Alon, U., Barkai, N., Notterman, D., Gish, K., Ybarra, S., Mack, D., and Levine, A., Broad patterns of gene expression revealed by clustering analysis of tumor and normal colon tissues probed by oligonucleotide arrays. Proc. Nat. Acad. Sci. 96(12):6745–6750, 1999.
22. Golub, T., Slonim, D., Tamayo, P., Huard, C., Gaasenbeek, M., Mesirov, J., Coller, L., Downing, J., Caligiuri, M., Bloomfield, C., and Lander, E., Molecular classification of cancer: class discovery and class prediction by gene expression monitoring. Science 286(5439):531–537, 1999.
23. Beer, D. G., Kardia, S. L., Huang, C.-C., Giordano, T. J., Levin, A. M., Misek, D. E., Lin, L., Chen, G., Gharib, T. G., Thomas, D. G. et al., Gene-expression profiles predict survival of patients with lung adenocarcinoma. Nature Med. 8(8):816–824, 2002.
24. Khan, J., Wei, J. S., Ringner, M., Saal, L. H., Ladanyi, M., Westermann, F., Berthold, F., Schwab, M., Antonescu, C. R., Peterson, C. et al., Classification and diagnostic prediction of cancers using gene expression profiling and artificial neural networks. Nature Med. 7(6):673–679, 2001.

25. Alizadeh, A., Eisen, M., Davis, M., Rosenwald, A., Boldrick, J., Sabet, T., Powell, Y., Yang, L., Marti, G., Moore, T., Hudson, J., Lu, L., Lewis, D., Tibshirani, R., Sherlock, G., Chan, W., Greiner, T., Weisenburger, D., Armitage, J., Warnke, R., Levy, R., Wilson, W., Grever, M., Byrd, J., Botstein, D., Brown, P., and Staudt, L., Distinct types of diffuse large b-cell lymphoma identified by gene expression profiling. Nature 403(6769):503–511, 2000.
26. Armstrong, S. A., Staunton, J. E., Silverman, L. B., Pieters, R., den Boer, M. L., Minden, M. D., Sallan, S. E., Lander, E. S., Golub, T. R., and Korsmeyer, S. J., Mll translocations specify a distinct gene expression profile that distinguishes a unique leukemia. Nature Genet. 30(1):41–47, 2001.
27. Alshamlan, H. M., Badr, G. H., and Alohali, Y. A., Genetic bee colony (gbc) algorithm: a new gene selection method for microarray cancer classification. Comput. Biol. Chem. 56:49–60, 2015b.
28. Alshamlan, H. M., Badr, G. H., and Alohali, Y. A., Abc-svm: artificial bee colony and svm method for microarray gene selection and multi class cancer classification. Int. J. Mach. Learn. Comput. 6(3): 184, 2016.

International Journal of Applied Engineering Research ISSN 0973-4562 Volume 11, Number 7 (2016) pp 5338-5341

Survey on Web Content Extraction

Jincymol Joseph
Assistant professor Department of Computer Science
St.Pius X College Rajapuram Kasargod, Kerala, India
E-mail: jincyjosek@gmail.com

Dr.J R Jeba
Associate Professor & HOD, Department of Computer Applications
Noorul Islam Centre for Higher Education
Kumaracoil, Tamil Nadu, India
E-mail: jrjeba@rediffmail.com

Abstract-
World wide web has become one of the most significant resources nowadays. It brings the information mainly in the form of web pages. It may contain informative contents as well as non-informative contents. The non-informative contents like advertisements, header, footer, copyright statements, etc are called noisy parts. It has been proved that almost 40-50% contents are these types of noisy data. Web mining is an application of data mining technique to extract informative contents from non-informative contents. Web content mining is a subdivision under web mining. It is defined as the process of extracting informative content from non-informative contents known as noise. The advantage of eliminating non-informative content will saving in storage and indexing. This paper describes various methods for extracting web information from the huge volume of data present in world wide web.

Keywords: Hierarchical pattern based clustering, vision based approach, support vector, noisy data

INTRODUCTION

Web content mining is the process of extracting core contents from web documents. The term content extraction was introduced by Rahman[13]. As the internet grows rapidly, anyone can upload or download any information at any time. This leads to the continuous expansion of irrelevant, redundant, structured and unstructured information on the web pages. A web document may contain audio, video, text, images, tables etc. Extracting useful information from these types of unstructured data is a complex task. Some algorithms were developed for this purpose and each one has its advantages and disadvantages.

Content extraction has many advantages. It is easier for accessing useful information in a timely and efficient manner. Irrelevant and redundant information is removed. Since it will not waste their time and memory for indexing and storing irrelevant content, the performance of search engine is increased. So it can be considered as a pre-processor for search engine. It also helps users to browse internet through small screen devices. It also helps in generating rich site summary from blogs or articles.

Normally a web content extractor, extracts all the information on the web pages including text, graphics, audio, video, links, advertisements, contents, etc. During the extraction process, noisy data are discarded and useful information is preserved. Many algorithms were developed for eliminating these noisy information and extracting the core contents of the web pages.

LITERATURE REVIEW

Many authors have tried to exploit content extraction tools for web documents. Some highlights of the relevant work are outlined here.

Sandip et al [1] proposed the automatic identification of informative sections of web pages. Here four simple yet powerful algorithms called Contentextractor, FeatureExtractor, K-FeatureExtractor an L-Extractor were proposed to identify and separate content blocks from non-content blocks. FeatureExtractor is based on the characterization and uses heuristics based on the occurance of certain features to identify content blocks. K-FeaureExtractor is a special modification of FeatureExtractor which perform better in a wide variety of web pages. ContentExtractor identifies non-content blocks based on the appearance of the same block in multiple web pages. L-Extractor uses various block features and train a support vector(SV) based classifier to identify a informative block versus a non-informative block. First, the algorithm partition the web page into blocks based on heuristics. Second, the algorithm classifies each block as either a content block or non-content block. It has the advantage that both K-FeatureExtractor and ContentExtractor produce excellent precision and recall values and runtime efficiency. It also reduces the complexity and increases the effectiveness of the extraction process. It has the disadvantage that it will increase the storage requirement for indices and the efficiency of the markup algorithm are not improved.

Yinghui et al[2] proposed a methodology called Hierarchical pattern based clustering algorithm. Based on using item sets to represent patterns in web transactions, Greedy Hierarchical item set based clustering (GHIC) has been presented. At first, the set of frequent item sets in the unclustered data is obtained. After that, a new dataset (Binary item sets dataset) was generated where the rows represent the original transactions and the columns represent the presence or absence of a frequent item set. This is represented as the new set of transactions. The problem was converted into clustering these binary vectors. Then GHIC is presented to solve the clustering problem in the new set of transactions. It has the

advantage that a set of item sets was allowed to describe a cluster instead of just a set of items and it has the ability to explain the clusters and the differences between clusters. Difference or similarity matrix was not considered here.

Jinbeom Kang et al[3] proposed a new method of web page segmentation by recognizing tag patterns in the DOM tree structure of a page. These repetitive HTML tag patterns are called key patterns. Repetition based page segmentation(REPS) algorithm is proposed to detect key patterns in a page and to generate virtual nodes to correctly segment nested blocks. REPS proceeds in four phases. First a web page is represented by a DOM tree structure after removing less meaningful tags such as <a>, <b>, <script>, etc from the HTML source of the page. In the second phase, REPS generates a sequence from the DOM tree by using the tags in the child nodes of the root node. The third phase is to find the key patterns from the sequence and recognize candidate blocks by matching the sequence with the key patterns. The final phase of REPS is to generate blocks in a page by modifying the DOM tree into a more deeply hierarchical structure by introducing virtual nodes.

Chia-Hui Chang[4] done a survey of web information extraction systems. They noticed some points like to automate the translation of input pages into structured data, a lot of efforts have been devoted in the area of information extraction(IE). IE produces structured data ready for post processing, which is critical to many application of web mining and searching tools. The web IE processes online documents that are semi-structured and usually generate automatically by a server-side application program. Web IE usually applies machine learning and pattern mining techniques to exploit the syntactical patterns of the template based documents. They found disadvantages like the extraction precision is greatly decreased in case of missing or multiple order attributes.

Wei Liu et al [5] proposed a method called Vision based approach for deep web data extraction. It is primarily based on the visual features human users can capture on the deep web pages while also utilizing some simple non-visual information such as data types and frequent symbols to make the solution more robust. It consists of two main components, vision based data record extractor(ViDRE) and vision based data item extractor(ViDIE). First, given a sample deep web page from a web database, obtain its visual representation and transform into a visual block tree. Second, extract data records from the Visual Block tree. Third, partition extracted data records into data items and align the data items of the same semantic together. Fourth, generate visual wrappers (a set of visual extraction rules) for the web database based on sample deep web pages. ViDE can easily distinguish the misaligned data items due to their different fonts or positions. Visual information of web pages helps to implement web data extraction. Demerits like either precision or recall is not 100 percent. Also this measure indicates the percentage of web databases the automated solution fails to achieve perfect extraction.

Badr Hssina et al[14] proposed a method to extract required pattern by removing noise that is present in the web document using hand-crafted rules. Hand-crafted rules use string manipulation functions to extract information from HTML. Since the source of information is a mixture of image, audio, presentation, etc, it is not easy to separate out the informative content effectively and intelligently. First, connect to any website and get data from that site. Then choose options like extract links, extract image, extract media, extract HTML schemas, extract content.

R.Gunasundari[15] developed a method to extract content from web pages, which is based on links present in a web site. In this method, algorithm judges the contents by several parameters in the nodes. They are Link Text Density(LTD), Link Amount(LA), Link Amount Density(LAD) and Node Text Length(NTL).LTD and NTL are very important parameter for content location judgement and LA & LAD are indicators for accurate content judgement. The following methods are used for extracting the main contents. First, standardize the web page tags. Second, pre-processing the web page tags. Third, judging the location of the content. Four, extracting the content. Five, Adjusting the extraction results. This method can reduce quantity of data transmission and complexity. Also it is suitable for data collection workers and other professionals. Concept retrieval and the expansion of semantic and synonyms are needed for further work.

According to S.S. Bhamare [16] noise on the
web pages are not the part of the main content and this irrelevant information in web pages can really affect web mining task. Two categories of noise group are formed. They are global noise and local noise. There are web cleaning techniques or methods.

1. Page segmentation manually or automatically segments a web page into small blocks focusing on coherant subtopics.
2. Block matching identifies logically comparable blocks in different web pages.
3. Importance evaluation measures the importance of each block accrding to different information or measurements.
4. Noise determination distinguishes noisy blocks from non-noisy blocks based on the importance evaluation of blocks

Pralhad S Gamre et al[17] organize a set of documents into categories through clustering. Grouping of similar documents into clusters will help the users to find the information easily. Objects in the same cluster should be similar. Also, objects in one cluster should be dissimilar from objects in other cluster. Hybrid approach uses concept based mining model. In this model, it analyses terms on the sentence, document, corpus level and Hierarchical Agglomerative Clustering(HAC) to group similar documents in clusters and the documents are arranged in hierarchical structure to make easy access of web documents.

Requirements for document clustering methods are identified. They are extraction of informative features, overlapping cluster model, scalability, noise tolerance, incremental and result presentation[17]. Some properties of clustering algorithm are data model, similarity measure and cluster model. The proposed system works in the following manner.

1. Retrieve the results obtained for a search query from search engine.

2. Select the most important results from all the retrieved URLs.
3. Preprocess the documents using concept based model.
4. Measure the importance of each concept with respect to semantics of sentences.
5. Use Hierarchical Agglomerative Clustering (HAC) to group the similar documents in clusters and the documents are arranged in hierarchical structure.

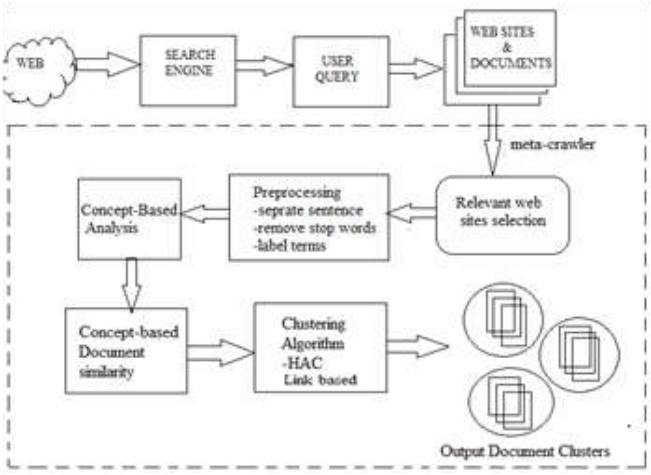

Categorizing similar documents together into clusters will help the users to find useful information quicker. Each cluster contains documents that are very similar to each other and very dissimilar to the documents in other clusters. Clustering can increase the efficiency of information retrieval. So, it will reduce the time and get high precision. An important issue is incrementality, because web pages changes frequently and new pages are added frequently.

CONCLUSION

Each of these model examines web content present in the internet and extract information using various methods. All these methods have some pros and cons. The review on several existing models is examined and the pitfalls explored are identified during the review. As future work, research is to be continued on alternative method for extracting core contents from web pages.

REFERENCES

[1] Sandip, prasenjit, Nirmal Pal and C.Lee Giles, "Automatic Identification of Informative Sections of web pages", IEEE Transactions on knowledge and data Engineering, Vol 7, No 9, 2005.

[2] Yinghui Yang and Balaji Padmanabhan "A Hierarchical Pattern-Based Clustering Algorithm for Grouping Web Transactions", IEEE Transactions on knowledge and data Engineering, Vol 7, No 9, 2005.

[3] Jinbeom Kang, Jaeyoung Yang, Nonmember and Joongmin Choi, "Repetition-based Web Page Segmentation by Detecting Tag Patterns for Small-Screen Devices", IEEE Transactions on Consumer Electronics, Vol. 56, No. 2, May 2010

[4] Chia-Hui Chang, Moheb Ramzy Girgis, "A Survey of Web Information Extraction Systems", IEEE Transactions On Knowledge And Data Engineering, Vol. 18, No. 10, October 20006.

[5] Wei Liu, Xiaofeng Meng and Weiyi Meng, "ViDE: A Vision-Based Approach for Deep Web Data Extraction", IEEE Transactions On Knowledge And Data Engineering, Vol. 22, No. 3, March 2010

[6] Badr Hssina, Abdelkarim Merbouha, Hanane Ezzikouri, Mohammed Erritali, Belaid Bouikhalene "An implementation of web content extraction using mining techniques", Journal of Theoretical and Applied Information Technology 31st December 2013. Vol. 58 No.3, ISSN: 1992-8645

[7] Ms. Pranjali G. Gondse, Professor Anjali B. Raut "Main Content Extraction From Web Page Using Dom", International Journal of Advanced Research in Computer and Communication Engineering Vol. 3, Issue 3, March 2014

[8] K. Nethra1, J. Anitha2 and G. Thilagavathi "Web Content Extraction Using Hybrid Approach", ICTACT Journal On Soft Computing, January 2014, VOLUME: 04, ISSUE: 02

[9] Rajni Sharma, Max Bhatia, "Eliminating the Noise from Web Pages using Page Replacement Algorithm ", International Journal of Computer Science and Information Technologies, Vol. 5 (3), 2014, 3066-3068

[10] J.R jeba, S.P.Victor, "A novel approach for finding item sets with hybrid strategies", International Journal of Computer Applications., Vol.17, No.5, 2011

[11] J.R.Jeba, S.P.Victor, " Comparison of frequent item set Mining algorithms", International Journal of Computer Science and Information Technologies, Vol 2 (6), 2011

[12] J R Jeba, S.P.Victor, "Effective measures in Association Rule mining", International Journal of Scientific and Engineering research, Vol 3, Issue 8, 2012.

[13] A.F.R Rahman, H.Alam and R.Hartono, "Content extraction from HTML documents", International workshop on Web document Analysis, pp.7-10, 2001.

[14] Badr Hssina, " An implementation of web content extraction using mining techniques", Journal of Theoretical and Applied Information Technology, Vol. 58 No.3

[15] R.Gunasundari, "A study of content extraction from web pages using links"International Journal of Data Mining & knowledge management process, Vol.2, No.3, May2012

[16] S.S. Bhamare, Dr.B.V., "Survey on Web Page Noise Cleaning for Web Mining", International Journal of Computer Science and Information Technologies, Vol. 4 (6), 2013

[17] Pralhad S. Gamare, G. A. Patil, "Web document clustering using hybrid approach in data mining"

International Journal of Advent Technology, Vol.3, No.7, July 2015

[18] Lambodar Jena, Narendra Kumar Kamila "Data Extraction and Web Page Categorization using Text Mining", International Journal of Application or Innovation in Engineering & Management, Vol 2, Issue 6, June 2013.

Noise Reduction using Character Density Approach

Jincymol Joseph, J R Jeba

Abstract--- Web mining is an application of data mining to extract informative content from World Wide Web(WWW). It has become one of the most significant resources nowadays. It may contain informative as well as non-informative contents. Non-informative contents may be header, footer, advertisements, copyright information, etc. These are called noisy data. A user needs only main contents. Web mining methods are useful for removing noisy parts and extract main contents from a web page, The advantage of using web mining methods is reduced time. Also, it provides users the needed information. This paper describes various methods for eliminating non-informative content from the large volume of data present in World Wide Web.

Keywords- Noisy data, web mining, cluster, outlier

I. INTRODUCTION

In WWW, meaningful data is extracted using data mining application called web mining. Anyone can upload or download any information at any time. So, internet grows rapidly and it leads to continuous expansion of irrelevant, redundant, structured and unstructured data on the web. In current development of data, extraction is a difficult work. Many algorithms were developed for extracting core contents from web pages. Using web mining methods, the needed information can be accessed timely and efficient manner.

A web content extractor extracts the core contents by removing the noises such as header, footer, copyright information, advertisements, etc. In this algorithm, character_density of each tag is calculated and compares it with threshold value.

II. WEB MINING CATEGORIES

It has 3 classes: Web usage mining, Web structure mining and Web content mining.

A. Web content mining

It is the process of extraction of meaningful data from huge quantity of material available on the web pages. Web page consists of information in the form of text, audio, images, tables, video etc. Most of the data present on the web is structured, semi-structured or unstructured form. Data extraction from structured pages is easy when compared with semi-structured or unstructured pages. Web content mining follows two approaches.

a. Agent based approach

The objective of agent based approach is to find relevant and significant information available.

(a) Intelligent search agents- It searches for information automatically besides a particular query.
(b) Information filtering/categorizing agents- Filters the data present on web.
(c) Personalized web agents-IT discovers those documents which are any how related to the user profiles.

b. Database Approach

Database approach consists of databases which contain attributes, tables and schema. By using standard query, organize the semi-structured data present on the web pages into structured data.

B. Web structure mining

A web graph structure contains nodes and edges. Here nodes represent web pages and edges represent hyperlinks which connect two interrelated pages. Web structure mining uses graph theory for analyzing the node and link structure of a web site. Web structural mining can be classify on the basis of web structural data types:

1. Hyperlink analysis- It links the webpage from current page to some other location or page.
2. Document structure- It is the process of mining document structure which includes analysis of the tree-like structure of page structures to describe XML or HTML tag usage.

C. Web Usage Mining

A web consists of inter-related files on one or more servers. Web usage mining is used to find interesting and meaningful usage pattern from data on web to understand the requirements of web based applications. Web usage mining can be classified upon the type of usage data considered.

- Web server data: Web server data includes user logs, access time, page reference and IP address.
- Application server data: To build an e-commerce websites and applications is a feature of commercial application server. Create application server log is a key attribute or feature of application server data.
- Application level data: New type of event is defined and then logging of that event is turned on. [1]

Revised Manuscript Received on December 22, 2018.
Jincymol Joseph, Department of Computer Science, St.Pius X College Rajapuram, Kasargod,Kerala, India (E-mail-jincyjosek@gmail.com)
Dr. J R Jeba, Department of Computer Applications, Noorul Islam Centre for Higher Education, Kumaracoil, Tamil Nadu, India

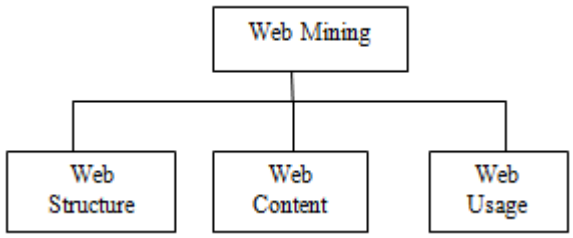

Fig 1:

This page covers enormous volume of undesirable material, named as noisy information. The header, footer, copyright, navigational panel and advertisements are known as noisy content. Noises can be classified as :

- Global noise: Global noises are redundant web pages on the internet. Global noises spread over websites such as duplicate page, Mirror sites and so on.
- Local noise: Local noises are also known as intra page noise. These are unimportant information in a web pages such as copy right, advertisements, footer, header, navigation bar and so on

Web content extraction is to identify the main content blocks by removing global and local noises from a web page [2].

It extracts valuable information by exploring the hyperlinks, audio, text, video, metadata, image and so on. It aids to know customer behavior and analyze the performance of a web site. It aids to develop companies indirectly. Web content mining estimates the hunt outcome of search engine and extracts the core contents from web pages. It takes more time manually. If analyzed information is in huge quantity, tough to discover out appropriate data [3].

Web sites may contain structured, unstructured, semi structured and multimedia data. Web content mining becomes complicated when it has to analyse these types of data. Unstructured data mining techniques are Information extraction, topic tracking, summarization, categorization, clustering and information visualization. Web crawler, wrapper generation and page content mining are structured data mining techniques. Semi- structured methods are OEM, Top down extraction and web data extraction language. Color histogram matching, multimedia miner and Shot Boundary Detection are multimedia data mining methods.

Categorization classified documents into various classes. It aids to recognize the key subject of a document pool.

Cluster is the collection of associated documents. The clustering is process of clustering documents depend on the similarity measure. Some common clustering algorithms available are hierarchical, binary relational and fuzzy. Similarity measure is the most important factor in clustering algorithms.

Summarization reduces the amount of text in a document. For this, the user defined a parameters list. [4]

III. WEB MINING METHODS

Some methods are developed for web content mining. Each and every method has advantages as well as disadvantages. Some of them are:

a. Hybrid Approach

It includes rule generation and automatic extraction methods. Mining of useful content from HTML pages called rule generation method. DOM tree is built to know the visual content of the web page along with features initially. Feature extraction technique is used between and <td> tags. To generate rules and well-formed document, machine learning methods like Decision tree classification and Naïve Bays Classification are applied Rules generated from these methods are used for extracting the core content from the web pages.

b. Outliers Detection Method

Outlier detection is a process for detecting the noises that are irrelevant to the informative content. First the documents are preprocessed for outlier detection. A list of word are generated by tokenizing the document and these are stored in the repository. These tokens are presented in the repository is used to generate a vector numerically representing the preprocessed document. Outliers are identified in the data set depends on the distance to their k nearest neighbors. It uses a distance search through the k-th nearest neighborhood, so it implements some type of locality as well. Those objects with the largest distance to their k-th nearest neighbors are considered as outlier respective to the data set. [5]

IV. PROPOSED METHOD

The objective of the proposed method is to extract informative content from a web page. So, proposed system, the non-informative contents are eliminated and display only the informative contents. A set of web pages is given as input and set of informative contents within the web page provides as output.

Depends on the contents of HTML tags, tags can be classified into two types: positive tag and negative tag. Positive tag contains useful or core content in a web page. Negative tags are also called noises and all tags except the

positive tags are negative tags. Negative tag does not contain any useful information and it reduces the performance of web pages. Removing the negative tags or noisy data will improve the performance of web content mining. Some negative tags are Anchor tag(<a>), Style tag(<style>), Link tag(<link>), Script tag(<script>), Comment tag(<!--…-->), Noscript tag(<noscript>), Horizontal ruler(<hr>) and Line Break(
).

A. Algorithm Noise Removal

Input: An HTML page

1. Convert HTML into XHTML
2. Remove tags<script>, <img>, <style>, <declaration>, <option>, <comment> and <meta>.
3. Construct a DOM Tree T for web page.
4. Compute threshold for web page
5. For every child node c in T do

Published By:
Blue Eyes Intelligence Engineering
& Sciences Publication

Compute character_density(c)
6. If character_density(c) > threshold then
6.1 content = c
7. else remove (c)
8. end if
9. end for

Output: Web page without noises.

Noise in the web page contains less text. Also content contains lengthy texts. In a tree structure , <body> is the root node and it contains noise as well as content. So, it has more text than noise and more hyperlinks than content. Its character_density should be an intermediate value for compare each node's density. Character_density of <body> tag is considered as threshold for our study. If character_density of a node is greater than given threshold then we can say that the node is a content node and not a noise block. If it is a noise block, discard that block.

B. DOM Tree construction

[17]Document Object Model (DOM) is a standardized and language independent interface for accessing and updating content and structure of documents. It is a logical structure of a document. A DOM tree is constructed corresponding to each HTML page. Tags are internal nodes and the information within these tags are leaf nodes.

[18] DOM tree structure permit dynamic access of programs and scripts. It is used to update the content and structure of a page. DOM defines the logical structure of documents and the way for accessing and manipulating the document. Using DOM method , structure of the web page can be constructed. Web pages include noise and relevant data. Consider the example given below.

Example 1.

```
<html>
        <head>
                <title> Welcome:DOM Tree</title>
        </head>
        <body>
           <table>
                <tr>
                        <td> Character Number</td>
                </tr>
           </table>
           <div>
                <p>Tag</p>
           </div>
        </body>
</html>
```

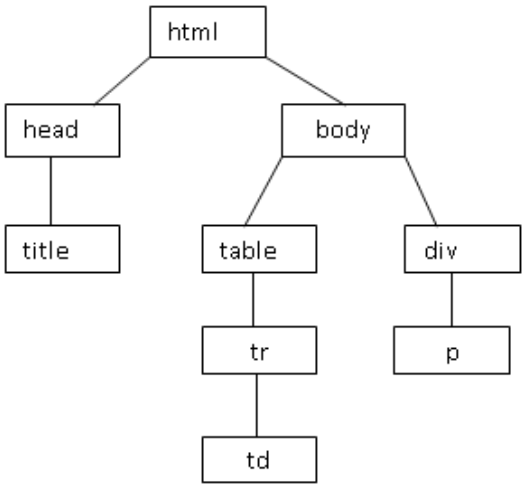

Fig 2: DOM tree construction

Algorithm character_density(c)
Input: Node c
1. for all child node i under c do
2. c.CharNum=CountChar(c)
3. c.TagNum= CountTag(c)
4. if i.TagNum=0 then
5. i.TagNum=1
6. End if
7. Calculate
character_density(c) = i.CharNum / i.TagNum
Output: character_density(c)

Here CharNum is the number of characters present in the subtree.

TagNum is the number of tags in the subtree. Character_density is the ratio of CharNum to TagNum. TagNum value is set to 1 if TagNum equal to 0.

V. RESULT

Character_density for the tags in example1 can be calculated as follows.

1. <body>: CharNum=41, TagNum=5 ,Character_Density=8.2
2. <td>: CharNum=16, TagNum=1,Character_Density=16
3. : CharNum=3,TagNum=1,Character_Density=3

Threshold value is 8.2, Character_Density of each tag is compared and the tag with below this threshold value is considered as noise.

VI. ISSUES IN WEB MINING

- Large Data Sets- Web data sets can be very large. It require huge amount of storage on the database.
- Large no. of Servers- A single server can not mine all the data.
- Hardware and Software Management- Proper organization of software and hardware is required to mine multitera byte data set which is not an easy task.

- Data Cleaning- Automated data cleaning is required on large scale to find out useful information from data.
- Relevant Information- Difficult to find out important information from large database on web.
- New knowledge Mining- Extracting new knowledge from the web by using traditional methods.[1]

VII. CONCLUSION

The technique is proposed for content extraction from web pages in this paper. In this method, the HTML tags are analysed and we divide the tags as Positive tag and Negative tag. All the negative tags are removed, since negative tags are considered as noises present in the web pages. To find out negative tags, character_density is calculated for each tags. After removing all the noises, the informative contents are extracted. It produces effective result for user query and thus the user get accurate information. This method takes less time considering the other methods.

REFERENCES

1. Kavitha,Priyanka Mahani, Dr.Neelam Ruhil, "Web Data Mining Aperspective of research and challenges", IEEE Transactions on knowledge and data Engineering, October 2016.
2. Sandeep Kaur and Abhishek Tyagi "Noise reduction and Content Extraction from web pages using DOM Based Page Segmentation", International Journal of Computer Technology & Application, Vol 5(6),2022-2027, December 2014.
3. Faustina Johnson and Santosh Kumar Gupta, "Web content mining techniques: A survey", International Journal of Computer Applications, Vol. 47, No. 11, June 2012
4. Vishal Gupta, Gurpreet S. Lehal, "A Survey of Text Mining Techniques and applications.", Journal of emerging technologies in web intelligence, Vol. 1, No. 1, August 2009.
5. Surabhi Lingwal, "Noise Reduction and content retrieval from web pages ", International Journal of Computer Applications, Vol. 73, No. 4, July 2013
6. Ms. Pranjali G. Gondse, Professor Anjali B. Raut "Main Content Extraction From Web Page Using Dom", International Journal of Advanced Research in Computer and Communication Engineering Vol. 3, Issue 3, March 2014
7. D.S.Misbha, J.R.Jeba, "Scheduling Effective Cloud Updates in Streaming Data Warehouses using RECSS Algorithm" IJAER Vol.11 No.7
8. K. Nethra1, J. Anitha2 and G. Thilagavathi, "Web Content Extraction Using Hybrid Approach", ICTACT Journal On Soft Computing, January 2014, VOLUME: 04, ISSUE: 02
9. Fei Sun,Dandan Song and Lejian Liao ,"DOM based Content extraction via Text Densiy ", International Journal of Computer Science and Information Technologies, Vol. 5 (3) , 2014, 3066-3068
10. J.R Jeba, S.P.Victor,"A novel approach for finding item sets with hybrid strategies", International Journal of Computer Applications., Vol.17,No.5,2011
11. [12] J.R.Jeba, S.P.Victor," Comparison of frequent item set Mining algorithms", International Journal of Computer Science and Information Technologies, Vol 2 (6), 2011
12. Jincymol Joseph, J.R.Jeba , "Survey on web Content Extraction" , IJAER Vol.11 No.7
13. J R Jeba, S.P.Victor, "Effective measures in Association Rule mining", International Journal of Scientific and Engineering research, Vol 3,Issue 8,2012.
14. A.F.R Rahman, H.Alam and R.Hartono, "Content extraction from HTML documents", International workshop on Web document Analysis, pp.7-10, 2001.
15. CincyW.C,J.R.Jeba, "A method of A-BAT Algorithm based Query Optimization for crowed Sourcing System, IJ Intelligent Systems and applications, March 2018.
16. R.Gunasundari, "A study of content extraction from web pages using links"International Journal of Data Mining & knowledge management process, Vol.2,No.3,May2012
17. S.S. Bhamare,Dr.B.V.Pawar, "Survey on Web Page Noise Cleaning for Web Mining", International Journal of Computer Science and Information Technologies, Vol. 4 (6) , 2013
18. Pralhad S. Gamare, G. A. Patil, "Web document clustering using hybrid approach in data mining" International Journal of Advent Technology, Vol.3, No.7, July 2015
19. CincyW.C,J.R.Jeba, Performance Analysis of Novel Hybrid A-BAT Algorithm in Crowdsourcing Environment" , IJAER, Vol.12 No.24
20. W3C document object model. Website, 2009.
21. http://www.w3.org/DOM.
22. Bhavdeep Mehta,Meera Narvekar, "DOM Tree based approach for web content extraction", IEE

Published By:
Blue Eyes Intelligence Engineering
& Sciences Publication

IJCSE International Journal of Computer Sciences and Engineering Open Access
Research Paper Vol.6, Issue.10, Oct. 2018 E-ISSN: 2347-2693

Diabetes Mellitus Prediction on Obese Adult Ladies Using Data Mining Techniques

Manumol Thomas[1*], Chandra J[2]

[1]Dept. of Computer Science, Christ University, Bengaluru, India
[2]Dept. of Computer Science, Christ University, Bengaluru, India

[*]*Corresponding Author:* manumol.thomas22@gmail.com

Available online at: www.ijcseonline.org

Accepted: 10/Oct/2018, Published: 31/Oct/2018

Abstract—The research deals with prediction of Diabetes Mellitus in Pregnant and Non pregnant obese adult ladies using the data mining classification algorithms such as J48, Naïve Bayes, and SVM. Comparative study of classification algorithm is done by using Naïve Bayes, J48 and SVM. The results obtained by J48 and Naïve Bayes were found to be more satisfactory when compared to SVM classification. Naïve Bayes and J48 can be used as a predictor classifier for doing the diabetes mellitus prediction.

Keywords-Medical data mining, Support Vector Machine, J48, Naïve Bayes, Diabetes mellitus

I. INTRODUCTION

Diabetes is a very severe health issue, when the level of blood glucose becomes unregulated. Glucose acts as fuel of human body. When the body uses glucose as a fuel, insulin is essential to get the glucose into cells. Diabetes happens because either production of insulin is insufficient or the cells don't react accurately to insulin or both. The symptoms are increased thirst and hunger [8]. There are three types of diabetes mellitus. Type 1 Diabetes is known as "Insulin dependent diabetes mellitus" (IDDM). It is also known as "Juvenile Diabetes". IDDM is very common among children. Type 1 diabetes causes the body's failure to produce sufficient insulin. Type 2 Diabetes known as "Non-insulin dependent diabetes mellitus" or "Adult onset diabetes" is a condition caused by producing insufficient insulin to the body demands and it does not respond to the same. Type 3 Diabetes is gestational diabetes is caused by the development of high blood glucose level during pregnancy due to undiagnosed diabetes [1].

In general Diabetes is seen in all kinds of age group so it is often known as queen of all diseases. The research focuses on identifying standard set of parameters that directly contribute to diabetes and selecting an efficient algorithm would greatly aide patients to identify their possibility of getting diabetes without the need for doctors or other expensive equipment.

Data mining is process of identifying valuable information from large amounts of heterogeneous data and identifying and determining patterns and rules. Currently health organizations produce huge amount of data mainly in the area of cancer which are very difficult to analyses. Medical data mining helps extract hidden patterns, thereby opening the door to an enormous source of analysis of medical data including classification, clustering, regression, and so on. Data mining Classification is an information technique which is used to do lot of prediction. Classification is a technique which is every so often used for predicting valuable patterns and it helps to reduce the time required to identify these patterns. It also helps to extract some efficient rules from the proposed dataset [3].

Prediction on diabetes can be done with the help of three classification algorithms such as J48, SVM and Naïve Bayes. J48 builds a classification model by using Decision Tree from a set of labeled training data with the concept of information entropy. The Naïve Bayes Algorithm is based on conditional probabilities [4].

Few studies have focused on comparing data mining classifiers such as Support vector machine (SVM), Regression, BayesNet, Naïve Bayes and Decision Table for the grouping of diabetic patient dataset. Data mining techniques is utilized as a part of healthcare field for diagnosis of diabetes and treatment [1].The healthcare associations use Data mining techniques like classification, clustering and association to build their ability for decision making regarding patient health. A patient classified as "high risk" and "low risk" on the basis of the seriousness of the sickness[4].The researchers' concentrates on recognizing the

best classification algorithm for the combining of data that functions better on various data sets and they have observed the correctness of the tool may vary depending on the data set has been used. The results of the few studies shows that the execution of a classifier depends upon the data set, especially when there are number of attributes which are used in the data set [6].Most of the researchers have done comparison of classification algorithms by using different data set. Researchers highlight the application challenges and future issues of data mining in the field of health and care filed and Data mining methods are also used in management of healthcare for diagnosis and treatment, Healthcare resource management and Customer relationship Management. According to the author's experimental work it is found that the Naïve Bayes and decision tree are the best and efficient Data mining classifiers.

The remaining of the paper is formulated as follows; Section 2 discusses the methodology of research, Brief description about dataset and classification algorithms. In section 3 Result and discussion compares the accuracy of three different classification algorithms with PIMA Indian dataset. Finally the paper concludes in section 4.

II. METHODOLOGY

The Decision Tree and Naïve Bayes are the most popular classifiers in the field of Data mining. The current research focuses on Diabetes Mellitus prediction in Pregnant and Non pregnant obese adult ladies using the data mining classifiers such as J48, Naïve Bayes, and SVM. So these different classification algorithms were taken into consideration for experimental comparison.

2.1. Decision Tree (DT)

DT classifier is an efficient Data mining classification algorithm. Quinlan's ID3, C4.5, J48 and CART are some of the popular DT algorithms. As the name suggests DT is a tree which helps to make powerful decisions and it consists of root node, branches and leaf nodes. Internal node contains questions. Each branch denotes the result of a test and each leaves represents decision. The main aim of applying decision tree is to anticipate the estimation of target attribute based on input values. Usually tree creates from top to bottom.

To implement DT classifier there are different steps involved: they are,

1. Given dataset S, select an attribute as class Label (Dependent variable) to splitting tuples in partitions.
2. To decide a splitting criterion to generate a partition in which all tuples have a place with a single class and select best split to create a node
3. Repeat above steps until complete tree is grown.

DT Classifier helps to extract IF-THEN rules, thus it is also known as rule based classifier.

2.2. J48 Algorithm

The algorithm J48 has two inputs T and A where T is the training record and A is the Attributes. It expands the leaf node until criteria is met and works recursively selecting the best node to split the data.

Step 1 : BuildTree (T, A)
Step 2 : IF End_Cond (T,A)=false THEN
Step 3 : Root=CNode ()
Step 4 :Root.TCondition=findbest-partition (T, A);
Step 5 : Let X = {v}//v is the possible outcome of Root.TCondition
Step 6 : For each v ε X do
Step 7 : Tv = {t} // Root.TCondition (t) =v and t ε
Step 8 : Leaf= BuildTree (Tv, A)
Step 9 : Add leaf as descendent of root node
Step 10 : End for loop
Step 11 : End IF
Step 12 : Return root
Step 13 : ELSE
Step 14 : Child=CNode ();
Step 15 : Child. Label=Classify (T); Return child.
End_Cond:

This function terminates the build tree process by checking whether all the records have the child label or the same attribute values

CNode ():
This function creates the new node
Findbest-partition (T, A):
This function selects the best attribute for splitting the records
Classify ();
This function assigns the Class label to the child node [9].

2.3. Naïve Bayes

Naïve Bayes classification algorithm is a probability based classifier. Naive Bayes predicts the future activities based on some historical data. Naïve Bayes gives high accuracy and speed when it applied on large data set.

Algorithm mainly based on three concepts. They are ,
Prior => all the information from day to day and past experiences
Likely hood =>possibility of information
Posterior =>predicting some particular information based on the information

2.3.1. Algorithm

1. Assume D is a training set of data along with its associated class labels and each tuple represented by T. Each tuple consists of n dimensional attributes T= (T_1, T2….$T_{n)}$.

2. Suppose there are M classes C_1, C2……C_M. Given a tuple T, the classifier will predict that T belongs to the class having the highest posterior probability conditioned on T.
   $P(C_i \mid T) > P(C_j \mid T)$

3. As P (T) is constant for all classes only $P(T \mid C_i)\ P(C_i)$ need to be maximized.

4. Dataset D with many attribute would be computationally expensive, so compute $P(T \mid C_i)$ based on equation 1

   $$P(T \mid C_{i)} = P(T_1 \mid C_{i)}.\ P(T_2 \mid C_{i)} \ldots\ldots\ P(T_n \mid C_i) \text{ ---------} \textbf{(1)}$$

5. Compute the maximized posterior hypothesis as in equation 2
   $P(C_i \mid T) = P(T \mid C_{i)} P(C_{i)} / P(T)$ **----------(2)**

2.4. Support Vector Machine (SVM)

SVM Classifier can be applied on linear and non-linear data. It transforms the original data set into larger dimensions by making use of non-linear mapping and searches for a linear separable hyper plane within the new dimensions. This hyperplane is a decision boundary separates tuples of different classes. Data from two classes (for example, data of patients with and without diabetes) can always be separated by a hyper plane. Support vectors and margins are used order to find the hyper plane. Support vectors are subsets of the actual training tuples. SVM is used for both prediction and classification.

Maximum marginal hyper plane separates two classes correctly. Hyper planes with larger margins will be more accurate as compared to those with smaller margins. A hyper plane will always be equally distant from both sides of the margin. Separating hyper plane can be written as:

$$Wv * X + B = 0 \text{ ----------} \textbf{(3)}$$

In equation 3 where,

Wv: weight of the vector
B: Biase
X: Training tuple

III. RESULTS AND DISCUSSION

3.1. Dataset Description

The data set collected from UCI machine learning repository. It consists of 768 instances and 9 Attributes. All patients here are females at least 21 years old of Pima Indian heritage.

	A	B	C	D	E	F	G	H	I
1	pregnant	plasma	bp	skin	insulin	mass	pedegree	age	class
2	3	126	88	41	235	39.3	0.704	27	tested_negative
3	3	158	76	36	245	31.6	0.851	28	tested_positive
4	3	180	64	25	70	34	0.271	26	tested_negative
5	4	129	86	20	270	35.1	0.231	23	tested_negative
6	3	171	72	33	135	33.3	0.199	24	tested_positive
7	1	120	70	30	135	42.9	0.452	30	tested_negative
8	3	170	64	37	225	34.5	0.356	30	tested_positive
9	4	154	62	31	284	32.8	0.237	23	tested_negative
10	1	136	74	50	204	37.4	0.399	24	tested_negative
11	1	153	82	42	485	40.6	0.687	23	tested_negative
12	3	148	66	25	0	32.5	0.256	22	tested_negative
13	6	134	70	23	130	35.4	0.542	29	tested_positive
14	5	139	80	35	160	31.6	0.361	25	tested_positive
15	5	158	84	41	210	39.4	0.395	29	tested_positive
16	4	148	60	27	318	30.9	0.15	29	tested_positive
17	1	138	82	0	0	40.1	0.236	28	tested_negative
18	3	162	52	38	0	37.2	0.652	24	tested_positive
19	1	142	86	0	0	44	0.645	22	tested_positive
20	4	122	68	0	0	35	0.394	29	tested_negative
21	1	171	72	0	0	43.6	0.479	26	tested_positive
22	2	146	76	35	194	38.2	0.329	29	tested_negative
23	3	141	0	0	0	30	0.761	27	tested_positive
24	1	128	64	42	0	40	1.101	24	tested_negative

Figure 1. Screenshot of Pima Indian Dataset

The Figure 1 depicts an overview of the sample Pima Indian Dataset. The attributes are Number of times pregnant, Plasma glucose concentration a two hours in an oral glucose tolerance test, Diastolic blood pressure (mm Hg), and Body Mass Index, Age (years) etc.

The figure creates a mining structure which excludes some of the fields of Dataset, in favor of a model that is filtered on particular attributes such as Plasma greater than 120 , BMI greater than 40 who belongs to the target group of 20-30 again dataset divides into two based of pregnant and Non-pregnant ladies. The performance of classifiers has been analyzed and prediction has been done on the basis of possibility of getting diabetes in pregnant and non-pregnant ladies. The dataset is used to train and test the diabetic data set by dividing training data and test data using 90-10 ratio. The experiment results with J48, Naïve Bayes, and SVM show the improvement in accuracy.

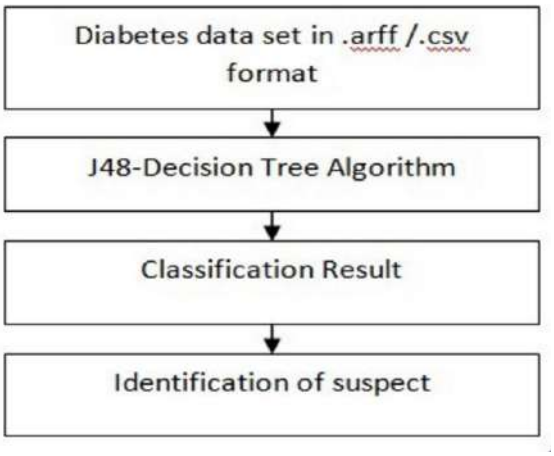

Figure 2. Block Diagram of J48

The Figure 2 depicts the block diagram of j48 classifier. After collecting the dataset the implementation is done with J48 Decision Tree. Then decision rules are extracted for predicting the diabetes in pregnant and non-pregnant ladies separately.J48 is a kind of decision tree which generates some relevant rules by proposed dataset. The J48 decision tree for diabetes diagnosis in pregnant ladies using Pima Indian diabetes dataset is depicted in Figure 3.

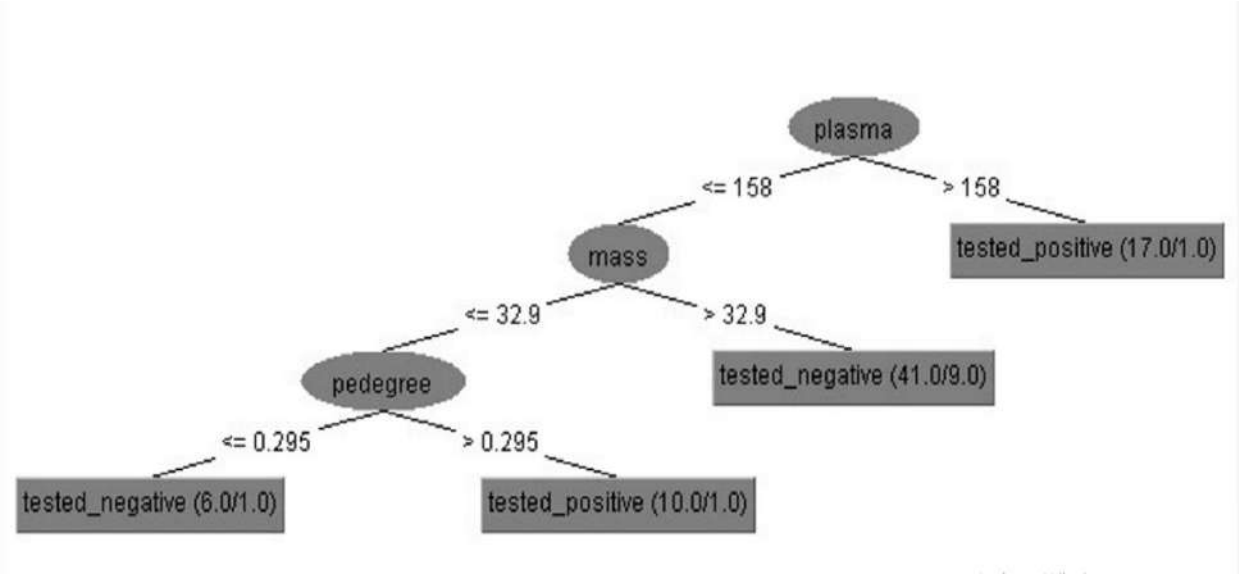

Figure 3.The J48 decision tree for diabetes in pregnant ladies

Rule 1. If plasma> 158 then Class=> Tested Positive
Rule 2. If plasma<= 158 & BMI >32.9 then Class=> Tested Negative
Rule 3. If plasma<= 158 & BMI <= 32.9 & Pedegree > 0.295 then Class=>Tested Positive
Rule 4. If plasma<= 158 & BMI <= 32.9 & Pedegree <= 0.295 then Class=>Tested Negative

Certain rules have been extracted while executing J48 decision tree algorithm for pregnant ladies. If a person has plasma concentration above 158 then the person will be a diabetic patient. If plasma concentration is less than 158 and BMI greater than 32.9 then that particular person will not be a diabetic patient. If plasma is less than or equal to 158 and BMI is less than or equal to 32.9 and pedegree greater than 0.295 then the patient will be tested positive, but if pedegree is less than or equal to 0.295 then that person will be non-diabetic for the same.

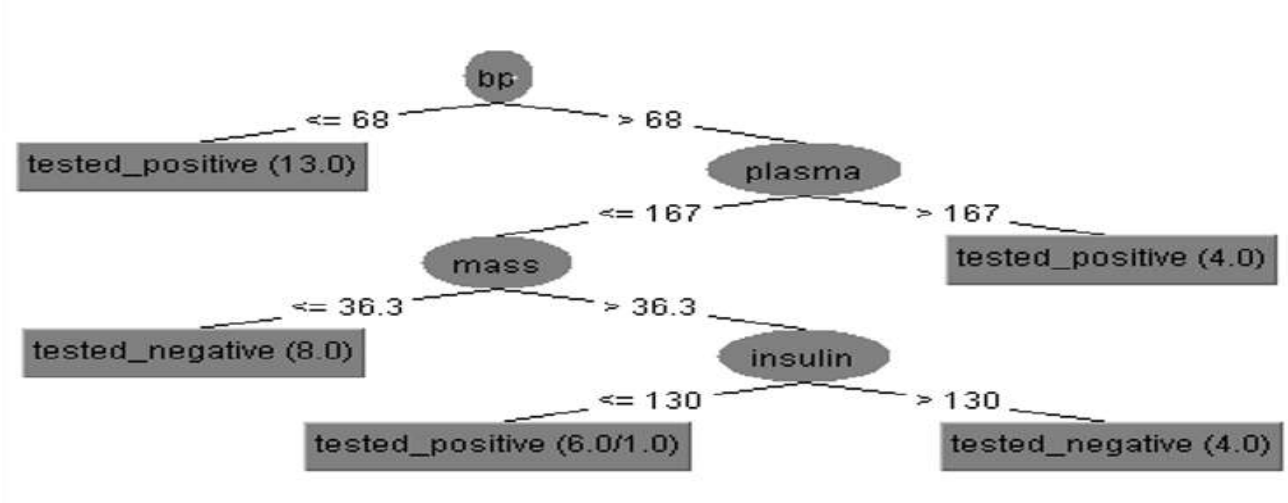

Figure 4. The J48 decision tree for diabetes in non- pregnant ladies

The Figure 4 depicts the visualization of rule based tree which is extracted by J48 with proposed dataset related to non-pregnant ladies. The extracted IF-THEN rules follow,

Rule 1. If bp<= 68 then Class=>Tested Positive
Rule 2. If bp> 68 & plasma> 167 then Class=>Tested Positive
Rule 3. If bp> 68 & plasma<= 167 & mass <= 36.3 then Class=>Tested Negative
Rule 4. If bp> 68 & plasma<= 167 & mass > 36.3 & Insulin>130 then Class=>Tested Negative
Rule 5. If bp> 68 & plasma<= 167 & mass > 36.3 & Insulin<=130 then Class=>Tested Positive

From Rule 1 to Rule5, it is achieved that if the blood pressure is less than or equal to 68 then the particular patient will be diabetic. If the blood pressure is greater than or equal to 68 and plasma is less than or equal to 167, Body mass index is greater than 36.3 then the particular patient will not be diabetic.

Table. 1: Performance result of classifiers

	Classifier	Correctly classified instances	Incorrectly classified instances	Time (sec)	Kappa statistic	Mean absolute error	Root mean squared error
Pregnant Ladies	Naïve Bayes	85.71 %	14.28 %	0.01	0.72	0.2221	0.2778
	J48	85.71 %	14.28 %	0.01	0.72	0.2175	0.3464
	SVM	42.85%	57.14 %	0.01	0	0.5714	0.7559
Non-Pregnant Ladies	Naïve Bayes	75 %	25 %	0.01	0.3846	0.2608	0.4555
	J48	68.75 %	31.25 %	0.02	0.3103	0.3542	0.5408
	SVM	66.66%	33.33 %	0.00	0	0.3333	0.5774

The Table 1 shows the performance of Naïve Bayes, J48 and SVM based on correctly classified instances, incorrectly classified instances, computing time, Kappa Statistic, Mean absolute error and Root mean squared error. Naïve Bayes and J48 have more accuracy compared to that of the SVM. The table above shows that the SVM classifier is not suitable for this particular dataset. Percentage split is used as the test option.90 % of data used for training and the remaining 10 % for testing. Graphical representation of above table is given below in Figure5.

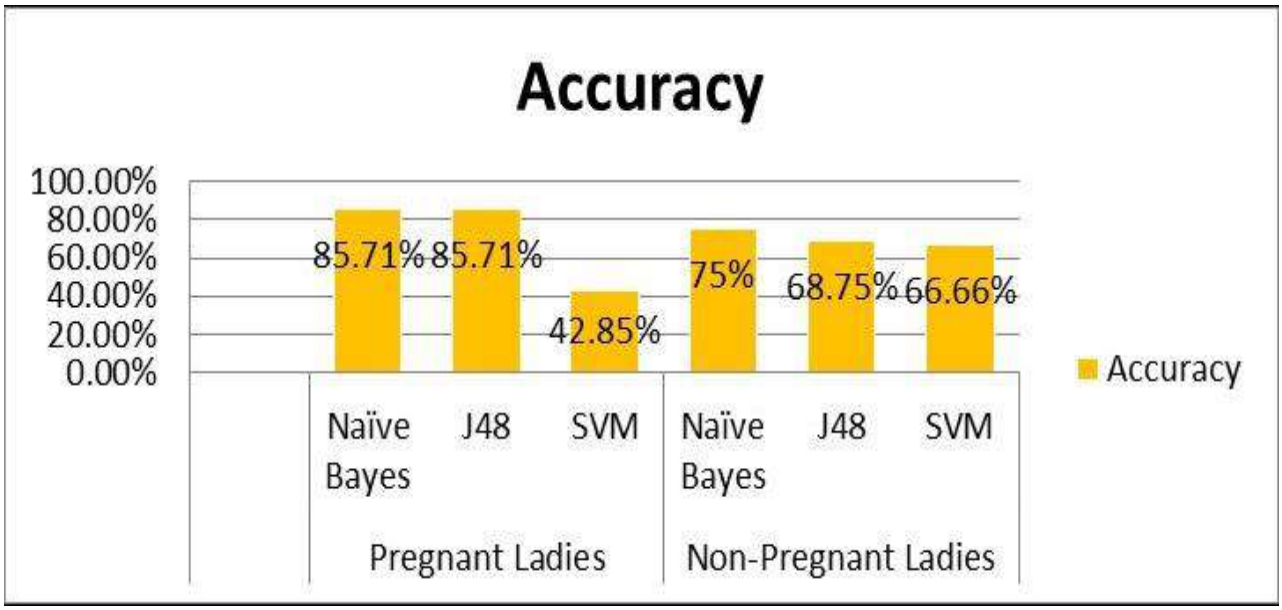

Figure 5. Performance evaluation on Naïve Bayes, J48 and SVM

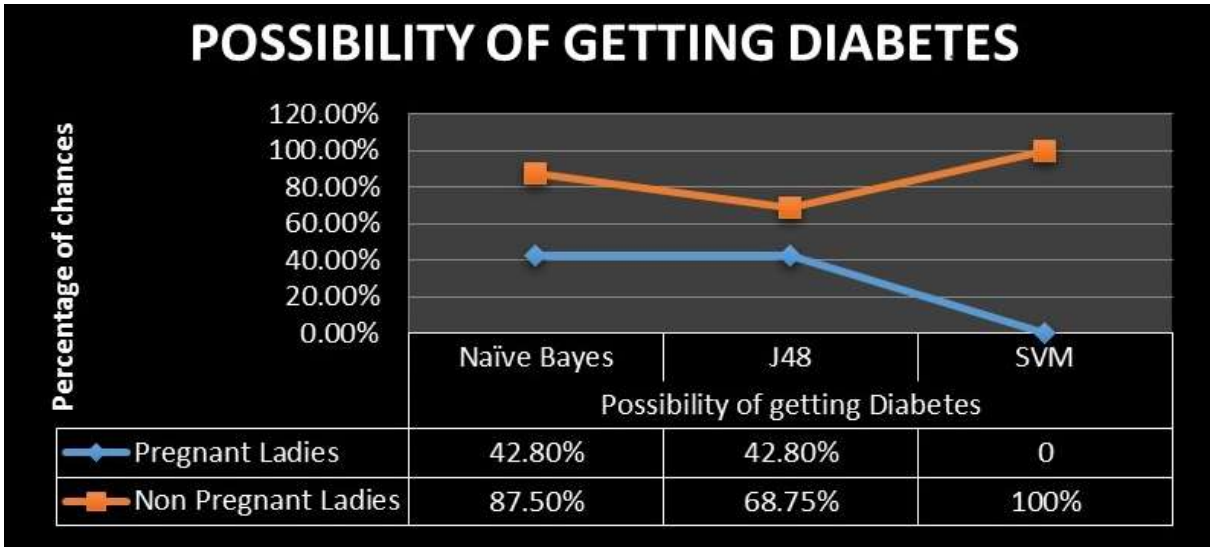

Figure 6. Diabetes prediction in pregnant and non-pregnant ladies

The Figure 6 depicts the possibility of getting diabetes in pregnant and non-pregnant ladies with the help of three classifiers. Naïve bayes classifier predicts that, 42.8% chances is there for getting diabetes in pregnant ladies but in the case of non-pregnant ladies the possibility is more, that is 87.5 %.while running J48 classifier possibility of getting diabetes in pregnant ladies is 42.8% but in non-pregnant ladies it is 68.75%.In the case of SVM chances of getting diabetes in pregnant ladies is 0% but in non-pregnant ladies it is 100%.

IV. CONCLUSION

In this work, we discussed the possibility of getting diabetics in pregnant and non-pregnant adult obese ladies based on some relevant attributes such as Age, BMI and Plasma concentration. Through this research work we can conclude that Naïve Bayes and J48 as an efficient predictable classifier than SVM for diabetes data set and also predicted the chances of getting diabetes in Non-Pregnant Ladies are greater than that for pregnant Ladies.

ACKNOWLEDGMENT

First and foremost we would like to express our deep gratitude to Prof. Joy Paulose, Head of the Department Computer Science, Christ University, for constantly monitoring and providing us with constructive feedback.

REFERENCES

[1] D. A Kumar and R. Govindasamy," Performance and Evaluation of Classification Data Mining Techniques in Diabetes", International Journal of Computer Science and Information Technologies, Vol. 6 (2), 2015.

[2] Chandra. J, Nachamai.M, and A.S Pillai, "Predicting Cervical Carcinoma Stages Identification Using SVM Classifier", International Journal of Computer Trends and Technology, Volume (22) Number(3), 2015.

[3] C.Shah, A.G. Jivani," Comparison of Data Mining Classification Algorithms for Breast Cancer Prediction", IEEE – 31661

[4] D.Tomar and S.Agarwal ,"A survey on Data Mining approaches for Healthcare", International Journal of Bio-Science and Bio-Technology,Vol(5), No(5), pp. 241-266,2013.

[5] G.Kaur and A.Chhabra,"Improves J48 classification algorithm for prediction of diabetes", International journal of computer Applications,Volume(98) ,No(22), July 2014.

[6] G.K.M.Nookala, B.K.Pottumuthu, N.Orsu, and S.B. Mudunuri," Performance Analysis and Evaluation of Different Data Mining Algorithms used for Cancer Classification", International Journal of Advanced Research in Artificial Intelligence,Vol(2), No(5), 2013.

[7] M.A. Khaleel, S. K. Pradham, G.N. Dash," A Survey of Data Mining Techniques on Medical Data for Finding Locally Frequent Diseases", International Journal of Advanced Research in Computer Science and Software Engineering, Volume(3), Issue(8), August 2013.

[8] M.kumari, R.Vohra ,Anshularora," Prediction of Diabetes Using Bayesian Network", International Journal of Computer Science and Information Technologies, Volume(5), Number(4) , pp(5174-5178), 2014.

[9] N.Nandkumarsakhare, s.joshy, "Classification of Criminal Data Using J48 Decision", International journal forum of researchers students and Academician,2012

[10]V.Karthikeyan, I.ParvinBegum, K.Tajudin, I.S.Begam, "comparative of data mining classification algorithm(CDMCA)in diabetes disease prediction",International journal of computer applications(0975-8887) Volume(60),No.(12),December 2012.

Authors Profile

Ms.Manumol Thomas pursed Bachelor of Science from University of Kannur, Kerala in 2014 and Master of Computer Application from Christ University in year 2017. Currently working as Assistant Professor in Department of Computer Science, at St.pius X college Rajapuram,Kerala since 2017.

Mrs. Chandra J pursed Bachelor of Science and Master of Computer Application from University of Bharathidasan University, Tamilnadu in year 1996.Completed MPhil from Vinayaka Missions University in 2009 And completed Phd from Hindustan University in 2016. She is currently working as Assistant Professor in Department of Computational Sciences at Christ University, Bangalore,Karnataka.

IJCSE International Journal of Computer Sciences and Engineering Open Access
Review Paper Vol.-7, Issue-1, Jan 2019 E-ISSN: 2347-2693

Malayalam Questions Classification in Question Answering Systems using Support Vector Machine

Bibin P.A[1]*, Babu Anto P[2]

[1] Department of Computer Science, St. Pius X College, Rajapuram, Kerala, India
[2] Department of Information Technology, Kannur University, Kerala, India

**Corresponding author: bibinpa@gmail.com, Tel: +91 9447877128*

Available online at: www.ijcseonline.org

Accepted: 26/Jan/2019, Published: 31/Jan/2019

***Abstract*—** We consider Question answering systems (QAS) as the next step in information retrieval, allowing users to create questions in natural language and get concise answers. Researches show that exact classification of questions with respect to the expected answer type is imperative to make a successful QAS. The duty of classifying distinctive questions becomes hard and challenging because there are variety of Natural Language Questions. Due to the agglutinative nature researchers find so many difficulties in Malayalam based QAS. So a very limited researches have been done in classifying Malayalam Questions with the help of Machine Learning Techniques. In this paper, we have used Support Vector Machines (SVM) to classify Questions. In Malayalam we can classify the question into following types എന്ത് (what), എപ്പോൾ (when), എങ്ങനെ (how), എവിടെ(where), എന്തുകൊണ്ട്(why), എത്ര (how many/how much) and ആര്(who). For Malayalam Question classification using SVM 1is the average precision, 0.93 is the average recall and the average F1 Score is 0.95. So the outcome that we obtained shows the effectiveness of Support Vector Machines in classifying the question.

***Keywords*—** Malayalam Question Classification, Support Vector Machine, Machine Learning, Question Answering

I. INTRODUCTION

With the invention of computers the life of human has become much easier. In this century with the help of any web search engines any person can access any data, which is at any place of the world at his/her a finger tip. We expect the computers to act like an intelligent human being. Because of this a new stream called Artificial Intelligence (AI) has emerged in the field of Computer Science.

Natural Language Processing (NLP) is a branch of AI, where a user is interacting in his own language such as English, Malayalam etc to an intelligent system. Since there are many languages in the world, understanding of Natural Language become an important hurdle in making the computers intelligent. Question Answering is one of the major tasks in NLP. Question Answering in natural languages can be done using various techniques in NLP such as Information Retrieval (IR), Machine Learning, Knowledge Representation, etc [1],[2],[3].

Based on the application domain the Question Answering System (QAS) can be classified into: Restricted domain QAS and General domain QAS. Restricted domain QAS answers only domain specific questions [4]. Here the answers will be searched only within a specific document collection. General domain QAS answers questions from all domains, but the answer will not be very precise [5]. In our research we are mainly concentrating on the Restricted domain, which is tourism.

One of the most challenging problem in question answering is to classify the question which is given by the user [6]. A Question Classification module has two main advantages. 1) It provides an outlook on the type of the answer which helps us to proceed further to find out and confirm the answer. 2) It gives us the information that help downstream processes in finding answer selection strategies that may be answer type specific, rather than uniform.

Usually, Question Classification can be achieved by two approaches: Rule-based approach and machine learning approach. In this paper with the help of machine learning approaches we are deriving the expected answer types. This work contains three parts: (i) A scheme of classification of answer types into which questions should be arranged (ii) With the correct answer type scheme of classification a corpus of questions are to be disposed and (iii) an algorithm that gain knowledge from this corpus and makes the correct prediction [7]. With the help of supervised machine learning techniques, we could train a classifier using the corpuses that are manually annotated with their question and its

corresponding answer type. Creating corpus for training and testing is a much time-consuming and a tedious task, but the advantage is that we do not require any rule-writing skills [8].

Section 1 contains the introduction of NLP and QAS, Section 2 contains the motivation for QAS and importance of Malayalam language, Section 3 contain the related work of QAS, Section 4 contain the architecture and essential steps of Question Classification, section 5 describes Effectiveness and Efficiency, Section 6 describes results and discussion of question classification and Section 7 concludes research work.

II. MOTIVATION FOR QUESTION ANSWERING SYSTEM(QAS)

From the very beginning itself, human beings are always in search of information. With the aid of web search engines or other IR techniques appropriate information is available to everyone at their finger tips. Question answering can be considered as a specialized type of IR. When we are using web search engine, we are getting only the relevant pages but we are interested in getting the precise answer to the questions. Question answering helps us to obtain the exact answer, and it includes NLP, IR, Machine Learning (ML), Knowledge Representation, Logic and Inference, Semantic Search, etc. So we can say that almost every branches of AI is contained in Question Answering. QAS can be used in any domain, such as tourism, teaching, personal assistants, medical science, etc. It can be used in every situation where we are in need of help from the computers. So this research is very much relevant in the current scenario.

In India there are 22 scheduled languages and many more unscheduled languages. Malayalam is one among the scheduled languages. Malayalam belongs to the Dravidian family of languages and is the official language of south Indian state Kerala. Malayalam Language is rich in Morphological inflections ie, adding of suffixes, prefixes and infixes to the root or the stem word. Due to its agglutinative nature, researchers find so many difficulties in Malayalam based QAS. The literacy rate of Kerala is 96.7 percentages, which is the highest literacy rate in India. Most of the Keralites knows only Malayalam language and are not so good in using English language. Kerala is known as God's own Country. Kerala is famous for its Ayurvedic treatments, high mountains, gorges and deep-cut valleys, lush and evergreen rain forests, coconut palms, backwaters, and food items. Keralites also want to know a lot of things about the different tourism spots and its related things. Getting exact answer from a set of documents in Malayalam for a particular question is very difficult. They required a system that can help them to find a precise or short answer to their questions.

III. REVIEW OF LITERATURE

Nowadays to get the correct answer to a question from internet with the help of a web browser using own language we are in need of QAS. L. Hirschman *et al.* gives us a brief idea of the upcoming research trends in QA in English. The background of the TREC QA evaluations, the results obtained from it, the methodology used for evaluation, the four important methods which are most important in QA, etc. are discussed in this paper [9].

Dell Zhang *et al.* had done a comparison between the different algorithms used for Machine Learning. The algorithms which they used were Support Vector Machine (SVM), Nearest Neighbours (NN), Naïve Bayes (NB), Decision Tree (DT) and Sparse Network of Winnows (SNoW). They found that SVM can achieve performance improvement over other Machine Learning algorithms [10].

Bhoir V *et al.* proposed solution of QAS works for a specific domain of tourism. The crawler developed in the system gathers web page information which is processed using NLP and procedure programming for a specific keyword. The system returns precise short string answers or list to natural language questions related to tourism domain like distance, person, date, list of hotels, list of forts, etc [11].

Pragisha K. *et al.* given the system which finds answers of Malayalam factual questions by analyzing a repository of Malayalam documents for handling the four classes of factual questions in Malayalam for closed domain. The QA system is divided into three modules as Question Analysis, Text Retrieval and answer snippet extraction and Answer identification [12].

Raji Sukumar *et al.* presented a model for developing intelligent query processing in Malayalam. For this they had selected a time enquiry system in Malayalam language. Natural Language Query Processing System is a restricted domain system, deals with the natural Language Queries on time enquiry for different modes of transportation. The system performs a shallow syntactic and semantic analysis of the input query. After the knowledge level understanding of the query, the system triggers a reasoning process to determine the type of query and the result slots that are required [13].

IV. PROPOSED MALAYALAM QUESTION CLASSIFICATION

SVM is a supervised machine learning method that examines the given data and arrange them into one of the two categories. It is a clever method to overcome over fitting and can deal with a large number of features with less computation. Using SVM we are trying to find out different

question keywords in Malayalam from our question phrase and then classify them based on the training data which we have already created. We have used testing data sets which are translated from Text REtrievial Conference (TREC 10) and then assigned labels to them.

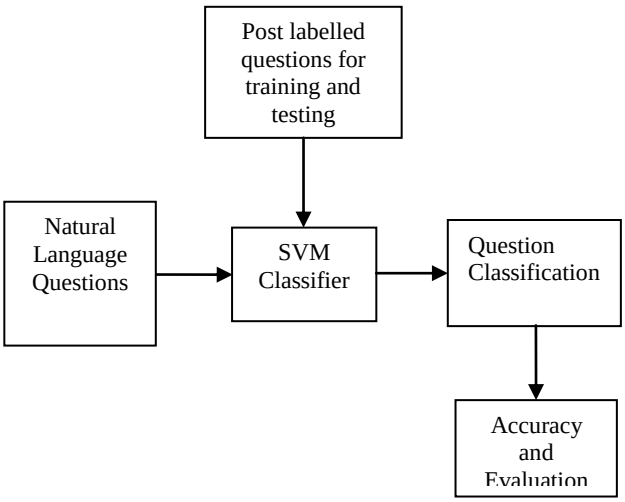

Figure 1: Question Classification using SVM

In Malayalam we can classify the question into the following types: എന്ത് (what), എപ്പോൾ (when), എങ്ങനെ (how), എവിടെ (where), എന്തുകൊണ്ട് (why), എത്ര (how many/how much) and ആര് (who).The following table shows the different types of questions and their assigned labels with examples.

Table 1: Question type

Question Type	*Expected Answer Type*	*Example and label*
എന്ത് (what)	കാര്യം (Thing)	Eg. ബോട്ടിൽ എന്ത് ഇന്ധനമാണ് ഉപയോഗിക്കുന്നത്? (What fuel does the boat use?) *For this question the main class is* ENTITY *and sub class is* Substance
	നിർവ്വചനം *(Definition)*	Eg. എന്താണ് ടൂറിസം? (what is tourism) *For this question the main class is* DESCRIPTION *and sub class is* Definition
എപ്പോൾ(when)	സമയം *(time)*	*Eg.* എപ്പോൾപ്രദർശനംആരംഭിക്കും? (*When does the show start?)* *For this question the main class is* NUMERIC *and sub class is* Date/Time
എങ്ങനെ(how)	വിധത്തിൽ *(manner)*	Eg. എനിക്ക് മൂന്നാറിൽ എങ്ങിനെ എത്തിച്ചേരാം? (How can I reach Munnar?) *For this question the main class is* DESCRIPTION *and sub class is Manner*
എവിടെ(where)	സ്ഥലം *(Location)*	Eg. തജ്മഹൽ എവിടെയാണ്? (Where is taj mahal?) *For this question the main class is* LOCATION *and sub class is City or* Country
എന്തുകൊണ്ട് (why)	കാരണം *(Reason)*	Eg. നിങ്ങൾഎന്തിനാണ്കണ്ണൂരിലേക്ക് പോകുന്നത്? (Why are you going to Kannur?) *For this question the main class is* DESCRIPTION *and sub class is* Reason

എത്ര (how many / how much)	എണ്ണം *(Count)/*അളവ് (Quantity)	Eg. ഇൻഡ്യയിൽ എത്ര സംസ്ഥാനങ്ങൾ ഉണ്ട്? (How many states are there in India?) *For this question the main class is* NUMERIC *and sub class is* Count
ആര്(who)	വ്യക്തി *(Person)*	Eg. കേരളത്തിന്റെ ടൂറിസം മന്ത്രി ആര്? (Who is the tourism minister of Kerala?) *For this question the main class is* HUMAN *and sub class is* Individual

V. EFFECTIVENESS AND EFFICIENCY

In our Malayalam Question classifier system, the user will provide a natural language question to the system. The Malayalam Question classifier will train the system based on the 200 training data set which we had already labelled. Then it will test it using the testing data set. Based on this, the question posed will be classified and will be assigned a label. The effectiveness and efficiency of the system is measured with the help of precision and recall system.

Precision can be defined as in what ratio we could predict positive identifications was actually correct? Precision (P) is the total count of True Positives (TP) divided by the total count of True Positives (TP) plus the total count of False Positives (FP).

$$P = \frac{TP}{TP + FP} \quad (1)$$

Recall can be defined as in what ratio we could predict actual positives was identified correctly? Recall (R) is the total count of True Positives (TP) divided by the total count of True Positives (TP) plus the total count of False Negatives (FN).

$$R = \frac{TP}{TP + FN} \quad (2)$$

A True Positive (TP) is a result where the system correctly forecast the positive class. A True Negative (TN) is a result where the system correctly forecast the negative class. A False Positive (FP) is a result where the system incorrectly forecast the positive class. A False Negative (FN) is a result where the system incorrectly forecast the negative class. In Binary Classification, we can have either positive class or negative class. Positive class denotes the object we are searching and the negative class denotes the other chance.

F1 score or F Measure is required when we are in need to find a balance between Precision and Recall. F1 score can be defined as the weighted average of Precision and Recall.

$$\text{F1 Score} = 2\,\frac{P * R}{P + R} \quad (3)$$

Various 200 questions for training and 100 questions for testing are utilized with SVM and classified effectively with precision of 1.

Table 2: Performance Evaluation for SVM

Question Type	Precision	Recall	F1 Score
എന്ത് (what)	1	0.92	0.95
എപ്പോൾ (when)	1	0.95	0.97
എങ്ങനെ (how)	1	0.89	0.94
എവിടെ (where)	1	0.94	0.96
എന്തുകൊണ്ട് (why)	1	0.91	0.95
എത്ര (how many/how much)	1	0.94	0.96
ആര് (who)	1	0.96	0.97
Average	1	0.93	0.95

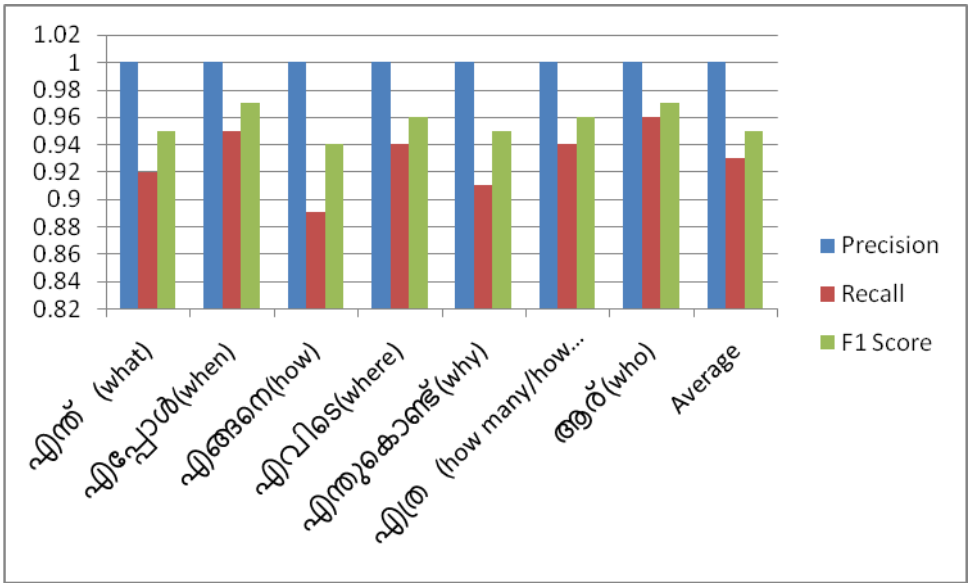

Figure 2: Graphical Performance Evaluation for SVM

VI. RESULTS AND DISCUSSION

The precision, recall and F1 score for the recorded question types obtained by SVM for classifying the questions are demonstrated on table 2 and figure 2. The obtained average precision by SVM is 1 the recall is 0.93 and the F1 Score is 0.95. The outcome is extraordinarily encouraging compared to some current research on QAS of English language with average precision 0.7 and recall 0.63 [14] and precision 0.73 and recall 0.73 [15]. Consequently, the result we obtained shows the effectiveness of SVM in classifying the questions.

VII. CONCLUSION

For Question classification, average precision, recall and F1 score are 1, 0.93 and 0.95 respectively. Hence, the result that we obtained shows the effectives of Support Vector Machines in classifying the question. The Question classification has an important role in determining the techniques used for extracting the correct answer. So we can expect that with the help of Question Classification method we could develop a Malayalam QAS with much better accuracy and precision.

REFERENCE

[1] V. Lopez, V. Uren, M. Sabou and E. Motta, "*Is question answering fit for the Semantic Web? A survey* " , Semantic Web, Vol. **2**, Issue. **2**, pp. **125-155**, **2011**.

[2] S. K. Dwivedia, V. Singhb, "*Research and reviews in question answering system*", International Conference on Computational Intelligence: Modeling Techniques and Applications (CIMTA), **India**, pp.**417-424**, **2013**

[3] G. Suresh kumar, G. Zayaraz, "*Concept relation extraction using Naïve Bayes classifier for ontology-based question answering systems*", Journal of King Saud University - Computer and Information Sciences, Vol. **27**, Issue. **1**, pp. **13-24**, **2015**.

[4] D. Mollá, J.L. Vicedo "*Question answering in restricted domains: an overview* ", Computational Linguistics, Vol. **33**, issue. **1**, pp. **41-61**, **2007**.

[5] N. Indurkhya, F.J. Damereau., "*Handbook of Natural Language Processing (second ed.)*" , Chapman & Hall/CRC, Boca **Raton** , **2010**.

[6] V. Punyakanok, D. Roth, and W.-t. Yih., "*Natural language inference via dependency tree mapping: An application to question answering*", Computational Linguistics, Vol. **6**, Issue. **9** pp. **1-10**, **2004** .

[7] H Sundblad, "*Question Classification in Question Answering systems*", Phd Thesis Submitted to Department of Computer and information Science at **Linkoping University**, **2007**.

[8] O. Kolomiyets , M.F. Moens., "*A survey on question answering technology from an information retrieval perspective*", Information Sciences—Informatics and Computer Science, Intelligent Systems, Applications: An International Journal, Vol.**181**, Issue.**24**, pp. **5412-5434**, **2011**

[9] L. Hirschman, R. Gaizauskas, " *Natural language question answering: The view from here*", Natural Language Engineering, Vol.**7**, Issue.**4**, pp. **275-300**, **2001**.

[10] D.Zhang, W.S. Lee, "*Question Classification Using Support Vector Machines*", Proceedings of the 26th Annual International ACM SIGIR Conference on Research and Development in Informaion Retrieval, ACM, Toronto, **Canada**, pp.**26-32**, **2003**.

[11] V. Bhoir, M. A. Potey, "Question answering system: A heuristic approach," *The Fifth International Conference on the Applications of Digital Information and Web Technologies (ICADIWT 2014)*, **Bangalore**, pp. **165-170**, **2014**.

[12] K. Pragisha, P. C. Reghuraj, "*A Natural Language Question Answering System in Malayalam Using Domain Dependent Document Collection as Repository",* International Journal of Computational Linguistics and Natural Language Processing, Vol. **3** Issue. **3**, pp.**534-539**, **2014**.

[13] S. A. Raji , B. P. Anto , " *Intelligent Query Processing In Malayalam*", International Journal on Computational Sciences & Applications (IJCSA), Vol.**3**, Issue.**2** pp. **51-59**, **2013**.

[14] B. Samei, H. Li, F. Keshtkar, V. Rus, A. C. Graesse, "*Context-Based Speech Act Classification in Intelligent Tutoring Systems*", Intelligent Tutoring Systems. ITS 2014. Lecture Notes in Computer Science, Vol.**8474**, pp. **236-241**, **2014**

[15] C. Unger, C. Forascu, V. Lopez, A.C. Ngonga Ngomo, E. Cabrio, P. Cimiano, S. Walter, *" Question Answering over Linked Data (QALD-4)*" , In L. Cappellato, N. Ferro, M. Halvey, & W. Kraaij (Eds.), Working Notes for CLEF 2014 Conference Sheffield, **United Kingdom** pp. **1172-1180**, **2014**.

Authors Profile

Bibin P A pursued Bachelor and Master of Computer Application from Marian College Kuttikkanam, Mahatma Gandhi University, Kottayam, Kerala, India in 2004 and 2007. He is currently pursuing Ph.D. from Kannur University, Kerala, India and currently working as Assistant Professor in Department of Computer Science, St. Pius X College, Rajapuram, Kannur University, Kasargod, Kerala since 2011. His main research work focuses on Machine Learning, Natural Language Processing, Data Mining, Information Reterival and Artificial Intelligence. He has 8 years of teaching experience and 3 years of Research Experience.

Babu Anto P pursued Bachelor of Science from Calicut University in 1980. 2. Completed Master of Science from Cochin University in 1982. 3. Awarded Ph.D. from Cochin University of Science And Technology in 1992. Currently working as an Assosiate Professor in Department of Information Technology, Kannur University ,Kerala, India from 2003 onwards. He is a life member of CSI, ISTE, ASI, International Association of Computer Science and Information Technology and International Association of Engineers. He has published more than 75 research papers in reputed international and national jouranals. Under his supervision and guidance 6 Ph.D. degree were awarded and 5 are pursuing Ph.D. His main research work focuses on Machine Learning, Natural Language Processing, Image Processing and Speech Processing. He has 28 years of teaching experience apart from 08 years of exclusive Research Experience.

"An Analysis of Cashless Economy Initiatives in India and Its Impact on Rural People: A Case Study of Kallar Grama Panchayath of Kasaragod District"

Mr Edwin Jerard
Assistant professor on contract,
St Pius X College, Rajapuram, Kerala

Abstract

This paper examined the views of people on introduction of cashless economy in India. Digital India programme is a pioneering programme of the Government of India with a vision to transform India into a digitally empowered society and knowledge economy. "Cashless, Paperless, Faceless," is one of declared role of Digital India.

The study was conducted in rural areas of Kasaragod district and data was collected with the help of structured questionnaire and analyzed using simple random sampling techniques. It carried out with objectives of understanding the importance of cashless economy, how cashless economy is effective in rural economy and to study the current position of cashless economy in India s shows that cashless economy will help in curbing black money, counterfeit's fake currency, fighting against terrorism, reduce cash related robbery, helps in improving economic growth of our country. The study carried out 50 respondents including both youngsters and aged groups.

Key words: Demonetisation, digital transactions, financial literacy

Introduction

A cashless economy is an economy in which all type of transaction is carried out through digital means. Here the major role is that of, banks and policymakers. It includes e - banking (mobile banking, banking through computers) debit cards, credit cards and swipe cards etc. Adopting these initiatives all over the nation irrespective of urban or rural disparity decides the success of cashless economy initiatives. In rural areas government have more importance role to encourage poor and illiterate people. In rural areas to make digital payments more common government is taking initiative by promoting Aadhar payment which ensures financial transaction by just using finger print. Digital India programme is a pioneering programme of the Government of India with a vision to transform India into a digitally empowered society and knowledge economy. "Faceless, Paperless, Cashless" is one of professed role of Digital India.

The term cashless economy was first introduced in India economy by former Prime Minister Dr. Manmohan Singh later Mr. Narendra Modi gave more importance in cashless economy. The RBI and the Government are making several measures to reduce the use of cash in the economy by promoting the digital/payment devices including prepaid instruments and cards. Government with the help of RBI tries to make the country cashless in transactions. Here, the term less cash society and cashless transaction economy indicate the same thing of reducing cash transactions and settlement rather doing transactions digitally. Cashless transaction economy indicates a culture of people settling transactions digitally and not going shortage of cash. In a modern economy, money moves electronically. Expansion of e payment landscape along with people who takes digital payment as a culture is the base to fulfill the target of the government.

As Mahatma Gandhi said the soul of the nation is in the rural India. Since 66 % of the total population of the country is still in Rural India as per the WTO Calculation, Mahatma Gandhi's statement is still valid. And the success of any initiative in India to be a successful one, it has to be reached into the rural area. So the study focus on a village to analysis how far the cashless India initiative has reached to the soul of the nation.

Objectives

- To understand the government initiatives to implement cashless economy concept in India.
- To examine effectiveness and reach of cashless economy initiatives in rural area.

Hypothesis

1. H0: There is no significant influence of cashless economy initiatives on rural people.

Methodology

An analysis of cashless economy initiative in rural India and its impact on rural people in Kallar Grama Panchayath is based on following aspects: Awareness of cashless economy in rural people, how it is effective in rural economy and what are

the different cashless transactions techniques used by rural people. The area of study is the Kallar Grama Panchayath. The primary data is the core part it has been collected through the use of definitely structured questionnaire. The subsidiary data is collected from magazines, Journals, Books and various websites. The analytical part of the study is based on statistical tools and methods, graphs and charts etc.

Analysis

Infusion of technology into transactions brings paradigm shift to the society and paves way for cashless economy in any economy. Indian banks have advanced to the global level in adopting technology due to the government support as well as to compete with the foreign counterparts. Technology has become a business driver. Banking has moved to a new dimension once the internet and mobiles become so wider along with speedy net connection.

The ultimate aim of the government is make the country a fully cashless payment based economy. But to accomplish this task is not easy. Cashless transactions, basically for a country where cent percentage literacy is a distant dream, have their downsides for consumers. On the other hand, for those who have access to digital payments, discarding cashless options or hesitating to use technology is also not the answer, especially in the wake of the financial crisis brought on by the government's demonetisation move. A cashless economy has its benefits. Moving to cashless options provides the consumers a convenient and customer friendly business atmosphere. For the government it reduces not issuing cost, fake currency and black money concerns. Traditionally, debit cards, credits cards, internet banking and telephone were the online transactions provisions. But the introduction of smart phones brought a paradigm shift. But the security of transactions has also increased manifold. India has witnessed faster growth and transition in digital payment initiatives, from e-Wallets to the Unified Payment Interface to a combination of the two. Cashless payment options available in India are.

1) **E Wallets** – Electronic Wallets have become very common these days. At the outset of demonetisation itself, use of e wallets has been implemented at a very large-scale. These e wallets permit the users to make payments using your mobile number or by scanning a QR code which takes place in a second.

2) **UPI** –UPI (Unified Payments Interface) is another great way to go cashless. Using unified payments interface, people can do transactions using their smart phones. People having a bank account, which is already ensured through financial inclusion and a smart phone, can do transactions.

3) **Plastic Money** – Card payments, using either debit card or credit card are classified as Plastic Money. The wide network of POS (Point of Sale) machines and ATM cards increases the cashless transactions. Now a days ATM machines are replaced by POS in shops so as to use the cards to swipe and thereby encouraging cashless transactions. Transaction of money to various e wallets and payments are possible using the ATM cards.

4) **Net Banking** – Internet banking is another stepping stone towards cashless transaction. It is the base for most for the mobile application as well as e wallets. Net banking provides almost all the banking services and it can be called as the small branch of a bank.

5) **Aadhaar Card** – Aadhaar Card enabled payment system allows a person to pay using his aadhaar card if it is linked to his bank account. A person whose Adhar is linked with bank account can make transaction with a biometric detection device mostly finger print reader instead of carrying any cards instruments etc.

National Payments Corporation of India reported that there is tremendous increase in usage of cards at Point of Sale (POS) terminals at retail outlets and shops. The value of transactions almost doubled. Immediate Payment Service (IMPS) and Unified Payments Interface (UPI) usage has also manifolded. Number of POS in India is around 14 lakh and all the terminals accept all brands of debit and credit cards.

Contemporary footsteps towards cashless economy

Green banking, Digital India and less-cash economy are the keen focus of the Indian Government. By 2020 the average age of Indians are expected to be 29 years and smart phones are common. Youth everywhere are tech savvy. With the number of mobile owners are one million plus, 30% among them are smart phone users. Banks are focusing on adopting latest technologies and providing a number of applications and products to improve customer service and withstand in the cutthroat competition. Provide the best digital solution for all banking activities especially payments anywhere any time is the present agenda of all the banks. The demonetisation process aimed less cash society along with all stated goals and the government is pressing the banks to implements the same through, POS machines, mobile banking, mobile wallets, Adhar enabled payments systems, Jandhan accounts etc. Government of India even set a target of 25 billion digital transactions in the year 2017. Cheap availability of internet facilities especially by Jio also helped in gaining momentum in the digitalisation process and e-banking as well as m-banking.

The digitalisation process in India gained momentum and pace recently. The technological infrastructure also increases rapidly and more and more people are into it day by day. And it is expected that the no cash payment which is 22% of the total payment will overtake cash payment by 2023. Thus in order to make cash less economy and digital India banks is focusing technological up gradation and innovations.

Portable POS machines are latest up gradation in the banking industry. Basically they are now wifi enabled and so the internet connection is possible without connecting to the modem. The advantage is that even the customers can connect the POS machines to their mobile phone wifi and fund transfer is possible with that connection. Near Field Communication (NFC) technology enabled Terminal are given for Point of Sale for safe and trouble free banking. Near Field Communication (NFC) technology is the next generation short-range high frequency wireless communication technology. NFC is handy for customers as this technology make transactions simpler, exchange the digital content, and connects those electronic devices with a touch. It

is an amalgam today's diverse contactless technologies, enabling current and future solutions in various areas like payment, transportation & digital exchange

Social media in Banking: The presents generation youngsters are chained to social media such as Face book, twitter etc. The latest technology in banking is that linking social media accounts of its customers with the bank accounts. So that the social media accounts of the customers can be used as a platform for basic banking activities. Most of the Indian banks are started making use of this innovation. SBI has also makes use of this technology so that the youngsters are finding more comfort with the bank.

Platforms Like "SBI Mingle" – its social media banking platform for Face book and Twitter users. Using SBI Mingle, its customers can do a host of banking services like checking balance and requesting mini statements on their Face book or Twitter accounts. The Bank is also planning to introduce more services like request for chequebook, stop cheque, register for mobile banking, internet banking, and SMS alerts and block ATM/Debit Card on this platform soon.

m-Wallet is latest technological addition to the Indian banking system. The heavy rush of smart phone users and the demand for the mobile based banking technology paved the way for m-Wallet. This is a mobile based app which is designed for effortless authentication and transfer of money. In this common plat form once the app is installed the user can transfer money from his account and keep the money in this account for e-trade and e-shopping and so on. Since online shopping and e- payments are gaining momentum instead of keeping liquid money in pocket people shit to the m-Wallets. M-Wallets provide bill payment facilities, recharge options and much more. It is been followed by other banks mobile apps like Fedmobile etc.

The BHIM app: The BHIM application inaugurated by Prime Minister in India on 30 December 2016 has been downloaded by over 16 million customers within a short time of six months. BHIM another initiative and innovation by the National Payments Corporation of India, based on the Unified Payment Interface. Using BHIM, a customer can receive, send, collect money using virtual payment address (VPA), Account number and IFSC. In June 2017, there were more than 4.6 million transactions under BHIM app amounting to Rs 14,867 crores across 49 banks.

Aadhaar based payments: The introduction of Aadhaar card and Aadhaar authentication UIDAI has been a new light for the banking technology in India. The Aadhaar authentication brought a new payment system ie Aadhaar Enabled Payment System (AEPS) and BHIM Aadhaar, a digital POS system that requires a Smartphone with biometric device for the merchant and not even required a phone from the customer. BHIM Aadhaar is an extension of AEPS.

QR code based payment: Quick Response code (QR) based transaction is one of the latest innovation to bank payments. A QR based payment technology represents a new channel of initiating and accepting payments between buyers and sellers using the mobile phone. Bharat QR is a QR code based solution wherein the customer makes payment to merchant by scanning a static or dynamic QR code. It is interoperable among major Card schemes i.e. Visa, MasterCard and RuPay.

Digital mobile banking platforms: This innovation another integrated mobile based application where a verity of financial services are available. This platform offers series from a number of e-commerce companies plus almost all banking services. YONO (You Only Need One) is the integrated and innovative digital banking platform provided by State Bank of India (SBI) to enable users to access a variety of financial and other services using a smart phone. This innovation is been introduced 24 November 2017. YONO provides services over 60 e-commerce companies. All the leading banks have these type of mobile apps like fedmobile.

Chatbot service: Chatbot is a computer program designed to simulate conversation with human users, especially over the Internet. This innovation is been first used by HDFC. SBI has very recently launched its Intelligent Assistant (SIA) to address customer enquiries and help them with every day banking task. There is many more innovation which exist ant developed countries banking sector which are yet to introduce in Indian banks such as DIGIPASS. DIGIPASS is security ensuring device which act as One Time Password (OTP) generator. This device helps in preventing fraudulent activities related with OTP which the bankers receive as SMS.

Analysis of the study area in a nutshell reveals the following results.

Figure No 1: Awareness on Cashless economy concept

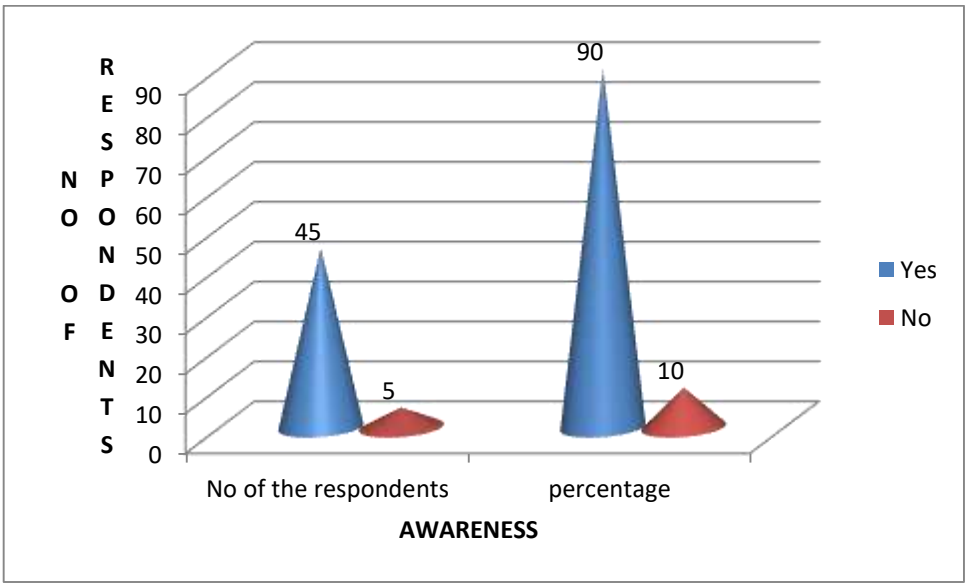

Source: data collected

It is evident from the above information that 90 % of the samples possess basic information on cashless India initiatives by Government. Only 10 % does not know much on the concept. It reveals the fact that Government initiatives of cashless India campaign are fruitful in the study area and if the authorities are ready to take up little more initiatives 100 % will get basic information.

Table No1: Factors restricting to cashless initiatives

SL NO	Restricting factors	No of the respondents	Percentage
1	Un awareness	5	35.71
2	Poor security	5	35.71
3	Any other	4	28.58
	Total	14	100

Source: data collected

It was clear from the earlier analysis that 28 % that is 14 people are not supporting cashless India concept and the reason is being shown above figure. 35.71 % who are against cashless says that they don't have clear idea about the cashless India concept. Another 35.71 % believe that the security aspect of cashless payment is not as safe as cash payments. 28.58 % have some other reasons such as resistance mentality to change, their age blocks them etc. It shows that more wide campaigns is required to reach the idea to entre people of the

Hypothesis Testing

1. H0: There is no significant influence of cashless economy initiatives on rural people.

Ho: $p=0.5$ against $p<0.5$

Analysis

	Proportion of satisfied customers in sample	z value	Conclusion
Test for proportion	0.39	-2.985	Reject the Hypothesis

There is significant influence of cashless initiatives on rural people.

Conclusion

Cashless economy means all the people in the economy uses digital means of transaction so that there is no visible money in the market. It is basically a utopian concept since it could not be a reality even in any developed country. Once it is a reality or even a good percentage of transaction is trough digital form it reduces printing and maintenance cost of notes and coins and also drives away black money and fake currency. The nation wants easy and more reliable economic and financial transaction since physical transaction is not secure, more time consuming and expensive than cashless or digital transaction. The digital transaction needs financial literacy and e-literacy or digital literacy among the population.

India has almost 150 crores of population. The Govt. should make a proposal to for almost 2 or 3 decades to create a full e-literacy among the population. Now the young generation of the population is using the cashless transaction or digital transaction more than the elder population. For that Govt. should provide basic e-literacy from the primary level of education and people those who have completed the education also. Policy makers and regulators jointly take more initiatives to boost digital transactions in India. Demonitisation and other initiatives by the government increased the digital transactions.

The effort was to analyse the impact or importance of cashless economy or digitalization in the present era and to evaluate government efforts and its success rate. The study area is rural in nature hence it reveals that the awareness of cashless economy is very limited to the respondents of the study. So it reveals that real side of the cashless economic structure in India. The study points out that in the rural area people are not aware of cashless economy transaction in a better manner. The study reveals that young generation is more demanding and ready to accept changes. So the government focus must be on youngsters. Provide them enough financial literacy since they are the future. Aim a complete cashless economy after a century as only the youngsters with basic financial literacy.

Reference

1. Abubakar, F.M., & H.B. Ahmad (2013). The Moderating Effect of Technology Awareness on the Relationship between UTAUT Construct and Behavioral Intention to Use Technology: A Conceptual Paper. Australian Journal of Business and Management Research, 2 (3), 14-23.

2. Adeoti, O., & Osotihemin, K. (2012). Adoption of Point of Sale: Assessment of Consumers' Level of Satisfaction. Research Journal of Finance and Accounting, 1 (3), 1-5.

3. Adesina, A.A., & Ayo, C.K. (2010). An Empirical Investigation of the Level of Users' Acceptance of E-Payment System. Journal of Internet Banking and Commerce,

4. Kumar, Aravind. (2017). Demonetization and Cashless Banking Transactions in India. International Journal of New Innovations in Engineering and Technology.

5. Gujarati Rashmi. (2017), India's march towards faceless, paperless, cashless economy. International Journal of Commerce and Management

6. Roth, B. L. (2010).―The Future of Money: The Cashless Economy – Part 1‖. [Online] Available: https://www.x.com/.../future- money-cashless-economy—part-i.

7. www.sbi.com

8. https://nfc-forum.org/

"A STUDY ON IMPACT OF HIGHER EDUCATION LOAN ON HUMAN CAPITAL DEVELOPMENT OF KERALA ECONOMY AND CURRENT TRENDS"

Mr Edwin Jerard
Assistant professor on contract,
St Pius X College, Rajapuram, Kerala

Abstract

Higher Education is a fundamental driving force for growth of an economy, and of paramount importance in economic and social mobility which ultimately lead to social welfare. Escalating cost of higher Education is a crucial problem to be tackled by common people as well as the government. Effective credit access for education attainment is an important issue for the policy makers and the people who are economically meagre. Kerala being cent per cent educated state has much more to go ahead in higher education segment. Poor strata still depends on banks, other financial institutions and even money lenders to meet the higher education expenses.

This paper aims at analysing the role of education loans by the financial institutions, especially banks on human capital formation and its impact on and the magnitude of the beneficiaries of education loans. The current trends in education loan availability as well as the providers along with public policy are also being analysed.

Key words: College density, Gross Enrolment Ratio, NPA

INTRODUCTION

Education is all about discovering novel things which, one doesn't know about and increases his knowledge. It has a constructive role in the life of every person and it gives the potential to show their best by their mind and spirit. For determining what is good and what is bad of you education will help you out. The incompleteness of a person without education is shown in the following words, a person with good education will become good citizen, more dependable worker, a right thinker and correct decision maker. (Carl Rogers)

Education is the key to Human capital formation and development. Additionally, education is one of the crucial factors in advancements, equal opportunity and life chances. It is the most powerful instrument for empowering and developing the citizens to master their cultural and social environment and compete for survival. It increases individual's chances for employment in the labour market and allows them to secure monetary and non-monetary returns and gives them opportunity for job mobility (Schultz).

Economic growth currently rest on the capability to produce knowledge based goods. However, the future of knowledge economy is subjected more on economy's capacity to produce knowledge through research and development, rather than on knowledge based goods. Hence, knowledge economies have much greater value and accord higher priority to the production and distribution of knowledge. Higher Education Institutions are a major source for producing the human capital required for knowledge production. It is however noteworthy today, that even if much knowledge is available at very low cost, its accessibility and use depends on human capacity to process and absorb it. If a nation's capacity to produce knowledge is weak, its capacity to access and absorb it determines the pace at which that country develops (IIEP, 2007). Higher education therefore, plays a crucial role in enhancing a nation's human capacity to absorb and use knowledge. Then, if knowledge is a source of economic growth, disparities in its distribution become a source of inequalities among nations.

Higher Education is a fundamental driving force for growth of the economy, and of paramount importance in economic and social mobility which ultimately lead to human capital development and social welfare. Escalating cost of higher Education is a crucial problem to be tackled by common people as well as the government. Effective credit access for education attainment is an important issue for the policy makers and the people who are economically meagre. Kerala being cent per cent educated state has much more to achieve in higher education segment. Poor strata still depends on banks, other financial institutions and even on money lenders to meet the higher education cost.

This study is intended to know, the extent of education loan availed by beneficiaries of the loan, for their higher education and the current trends of education loans in Kerala. Every year there are many developments or revolutions and modification in education loan segment and loan product. All these alterations in the education loan sector are based upon the productivity of the loan for the banks and government to ensure the real intention of the loan. The Government address education loan issues in Kerala and brings some remarkable change year to year.

Objectives

1. To understand magnitude of human capital development in Kerala Economy through education loan.
2. To evaluate the current trends in education loan segment from all three angles, that is of beneficiaries, loan providing banks and the government.

Methodology

The study is basically based on secondary data. The subsidiary data is collected from magazines, Journals, Books and various websites like government of Kerala website, RBI website, SLBC website and so on. The analytical part of the study is based on statistical tools and methods, percentage method and charts as and when it is required.

ANALYSIS

Higher Education (HE) is the crucial in attaining sustainable development and growth. The above statement is supported by the Gross Enrolment Ratio of developed countries. Indis's Gross Enrolment Ratio (GER) in higher education has registered an increase from 24.5% in 2015-16 to 25.2% in 2016-17, according to the latest edition of the All India Higher Education Survey (AIHES) launched by Union Human Resource Development (HRD). The importance of GER can be under stood by examining the GER of developed countries. USA's GER in HE is 85.8 per cent. India has still much more to go at least to reach half of the GER of developed countries. India aims to attain GER of 30 per cent in HE by 2020.

Tamil Nadu has highest GER in HE among other states in India and Kerala holds third position below Himachal Pradesh with a GER of 34.2 per cent in HE. This ranking is not at all favourable for the state since it is the first one to attain 100 per cent literacy long back comparing to other states. Six states have registered GER higher than national average (25.2%), with their share of students entering higher education is growing twice as fast as overall rate. Bihar has lowest GER with just 14.4% of its eligible population, in an age group of 18 to 23 years, pursuing higher education. Comparing with Bihar, Kerala is far better but yet to grow much to be at par with USA and other developed countries.

States in south India have higher college density. College density is defined as number of colleges per lakh eligible population. The college density in top three states/UTs is Puducherry (49), Telangana (59) and Karnataka (53). Bihar (7 colleges/1lakh population), Jharkhand (8) and West Bengal (11) on the other hand are the bottom in terms of college density. But a favourable odd is that though Kerala is not there in the top three, the number of Kerala students enrolled for higher education in other south Indian states than Kerala is very high.

The low rate of GER in Kerala for HE is due to many factors and one of the factors making hindrance for higher education is the cost for the HE. The Higher Education sector in India has witnessed tremendous change in the last few years. Growing demand, lack of capacity in public sector institutions and withdrawal of government's budgetary support has led to

exponential growth in the private higher education institutions. The essentiality of a robust system of the higher education financing arises on account of demographic challenges, trend towards privatization, and poor budgetary support. Since the privatisation took place in its full swing the cost of HE also mounted up. Ultimately the lower middle class and poor strata of students has to depend on financial institution ie education loan to meet the HE expenses. Student debt is currently a topic of much discussion, this is not the first time policymakers and higher education leaders have expressed concern about the negative consequences of student borrowing. The education loan has grown at a rate of 32.3 per cent in 2009-10 and at 39.8 per cent each in 2010-11 and 2011-12 and 44.8 per cent during the period 2012-13 to 2014-15(Chakraborty).

Since a large number of the students find it difficult to meet the expense of their education, the financial institutions have a great role. The sole purpose of education loan itself is to provide financial assistance to meritorious students to pursue their education. Both central and state governments also always extend their hands to support education loan scheme in the nation. It is evident that if education loan is available easily and at a lower rate of interest it will boost HE effectively. Right now in Indian Banks are providing educational loan for Higher Education only.

Table No 1 – Interest rate of education loan last 5 Years

Year	STUDENT LOAN SCHEME	
	Upto 7.50 Lacs	Above 7.50 lacs
01.01.2014	15.75%	14.75%
01.01.2015	15.60%	14.60%
01.01.2016	10.80%	10.75%
01.01.2017	10.00%	10.75%
01.01.2018	10.15%	10.90%

Source – SBI Data Base (www.sbi.com)

From the above table it is clear that though education loan is crucial for human capital development in the state the interest loan is very high. Up to 2015 the interest rate is on an average above 15 per cent. But there after a notable reduction around 5 per cent reduction in interest rate is imposed on education loan by the banks. Increased NPA rate and government intervention caused this reduction in the rate of interest. Comparing to agricultural and differential interest rate scheme (DIRS) loans, which have an annual interest rate of 4 per cent, the education loan rate is very high. HE being most crucial thing the rate of interest should be reduced to a minimal rate.

In order to understand more about the significance of education loans in Kerala, one should analyse the demand for education loan from the students and the sanctioned loan by the banks. The following table deals with this aspect.

Table No 2 – Statistics of Loan application, Sanction and Outstanding amount and number of loans (Amount in lakhs)

Year	Applications No	Sanctioned		Outstanding	
		No	Amount	No	Amount
March 2012	63667	62690	138062	353795	705788
March 2013	51277	50277	140560	380295	829454
March 2014	56102	55314	126069	390237	919917
March 2015	50111	47305	115774	393849	956843
March 2016	43662	41042	153199	369829	969182

Source: Performance report of various years by SLBC Kerala

From the table we can see that the number education loan applications are coming down continuously. In the year 2012 there were 63667 applications but in 2016 it has come down to 43662. 31.42 per cent reduction in the demand for education loan.

It is rather a good sign it shown that the financial condition of the people are increasing. In the case of sanctioned loan also the trend is same, 34.53 per cent reduction in the sanctioned loan. Total number of outstanding loans showed a continuous rise till 2015. But in the year 2016 the number has declined. The fact is that though the number of outstanding loans is reduced the amount outstanding is increased in 2016.

Table No 3 – Growth in education loan NPA (Amount in lakhs)

Year	Outstanding		NPA	
	No	Amount	No	Amount
March 2012	353795	705788	28367	49045
March 2013	380295	829454	47661	76225
March 2014	390237	919917	48098	95842
March 2015	393849	956843	34398	74647
March 2016	369829	969182	43644	109389

Source: Performance report of various years by SLBC Kerala

The above table explains the increase in education loan NPA of the banks in Kerala. The shocking fact is that 223.04 per cent is the growth rate in NPA of the education loan segment of banks. It is a serious issue to be tackled. Since provision is to be made for the NPA it affects very badly on the banks and in turn they become reluctant to sanction education loans. Every loan is sanction based up on the repayment capacity of the borrower. In the case of education loan this principle will not work. Because the students are consuming ends and they don't have repayment capacity. So the loan is sanctioned on the expected income once the course for which loan is sanctioned is completed and they get job. The education system and the job market are not favourable in India so the HE earned students find it hard to get a job. It leads to high NPA rate in the education loan segment.

Table No 3 – Loan Amount based NPA segregation (Amount in lakhs)

Year	Below 4 Lakhs		4 lakh to 7.5 Lakhs		Above 7.5 Lakhs		Total Due	
	No	Amount	No	Amount	No	Amount	No	Amount
Mar – 12	312664	524485	27201	88111	19168	103163	359013	721603
Mar – 13	348149	662045	21124	85698	10003	76647	380295	829454
Mar – 14	291937	593075	36127	148012	10409	77407	334873	818494
Mar – 15	327007	681374	48767	169663	18076	105806	393849	956843
Mar – 16	304415	650261	43943	185075	21471	133845	431624	991423

Source: Performance report of various years by SLBC Kerala

The education loan given by the banks are classified into three categories as per the instructions from RBI and Ministry of Finance. Up to 4 lakhs the loan need any security, between 4 to 7.5 lakhs the guarantee required is the co-borrower-ship by parents or guardian and above 7.5 lakhs collateral security is required. Total due is NPA plus the instalment due. A loan is classified as NPA when three consecutive EMIs are not paid. But for a loan if only one or two EMIs are due they are not considered as NPA. From the table it is clear that in all three segments the due amount is increasing but in the case of loans below 4 lakhs there is reduction in 2016.

Since NPA is a great loss and big nail on the profit of the banks they hand over the NPAs to the Reliance Asset Reconstruction Company (R ARC), who promises to recover the NPA from the education loan defaulters. Purchase of NPAs by Reliance ARCs from SBT Student loans are becoming a crisis in Kerala where parents are under tremendous pressure to avail higher education after borrowing money from banks and private money lenders and pledging jewellery. Statistics show that banks have sanctioned a total of Rs77, 885 crore to 331663 student borrowers in Kerala until March 2015, which is second only to Tamilnadu where Rs1, 63130 crore was given to 960202. The economic slowdown triggered by the global financial crisis of 2008 has meant there are fewer jobs in many sectors, including software services. There have been drastic job-cuts across the industrial

sector, and the once-flourishing nursing sector, to which Kerala was a major supplier of human resource until recently, still now it has not been able to recoup back. In July 2017, public sector bank State bank of Travancore has sold its education NPAs of Rs 130 crore, to be recovered from 8568 defaulters, to R-ARC for Rs 63 crore. Reliance paid Rs 9 crore to the bank immediately and gave security receipt for Rs 54 crore. It could pay the money to the bank within a time frame of 15 years. R-ARC was sending notices and threatening that the property of borrower's families will be pledged.

Relief to the Beneficiaries - Recently in 2017 Chief Minister Pinarayi Vijayan has announced a support scheme to help students from financially backward families repay education loans. This scheme was designed to help families facing revenue recovery (especially those who are facing threats from the ARC's) after finding themselves unable to repay the loan. The scheme would be effective from April 2016 and would be applicable to loans up to Rs 9, 00,000. The government would share 90% of the repayment liability in the first year, 75% in the second year, 50% in the third year and 25% in the fourth year. For bad loans up to Rs 4, 00,000 availed before April1, 2016 the government would bear 60% of the repayment liability if the bank waived the interest. For loans between Rs4, 00,000 and Rs 9, 00,000 the government would 50% of the principal amount up to a maximum of Rs 24000 on a special package for closure of the loan. Mr. Pinarayi Vijayan said that the government would bear the repayment liability in the case of student's demise or handicap due to an accident, provided the bank was ready to waive the interest. According to an estimate prepared by the State Level Bankers Committee, Kerala, this scheme would cost the government Rs 900 crore.

CONCLUSION

Higher Education is most crucial sector for the growth and development of human resource which can take responsibility for economic, social and scientific development of the country. The vision of the higher education in India is to realize the country's human resource potential to its fullest with equity and inclusion. The importance of higher education is evident in the aim of XII Five Year Plan i.e. to increase the enrolment ratio from the level of about 15 % to 30 % by the end of XII Plan. To materialize these objectives providing financial assistance to the meritorious and needy students is important. The banks in the country have a greater role in backing the students who are in need of financial support.

The Rate of interest of the education loan is quite high and an immediate reduction of the interest has to be done by the banks. Initiatives are to be taken by the government considering the importance of the education loan. Government has to take initiatives to increase GER in HE in the state and GER should bring at par with the developed countries in the HE sector. Above all since the NPA is mounting up it is the right time for the government to interfere and tackle the issue, so that the banks will be more favourable in providing education loans. Different studies are also proves that the mushrooming self-financing colleges has to be strictly monitored by the government, so that quality education in the higher education level is ensured and students gets job, so that the education loans are easily replayed on time.

REFERENCES

1. www.indianexpress.com
2. www.decanherald.com
3. Tilak, J. B. (2001). Jandhyala B G Tilak. Kochi: Centre for Socio-economic & Environmental Studies.
4. Vinayan (2012). Student's loans in financing higher education: levels of Indebtedness among student's borrowers in Kerala. Hyderabad Social development Papers
5. Varghese K.X & Manoj P.K, Efficacy of Educational Loans: Employability of the Borrowers is the most important Predictor. Volume: 2 Issue: 1 ISSN No 2277-8160
6. Shultz, T (1988) "Education Investment and Returns". In: Chenery H. and Srinivasan T. Handbook of Development Economics. North Holland.
7. Carl Rogers, the famous American author, authored books Like "Psychologist"
8. International Institute for Educational Planning Newsletter (IIEP) Vol. xxv, No.1, January – March, 2007.
9. All India Higher Education Survey (AIHES) January 2018, HRD Ministry
10. Chabraborthy K C, Ex- RBI, Deputy Governor, "Paper on Indian Education System – Issues and Challenges". 2011

IMPACT: International Journal of Research in Humanities, Arts and Literature (IMPACT: IJRHAL)
ISSN (P): 2347-4564; ISSN (E): 2321-8878
Vol. 7, Issue 2, Feb 2019, 117-124

"A STUDY ON IMPACT OF TECHNOLOGICAL UP GRADATION AND INNOVATION IN INDIAN BANKING SECTOR WITH SPECIAL REFERENCE TO SBI"

Edwin Jerard

Assistant Professor, St Pius X College, Rajapuram, Kerala, India

Received: 02 Feb 2019 **Accepted:** 06 Feb 2019 **Published:** 12 Feb 2019

ABSTRACT

The banking sector is the backbone of any economy since it acts as the convertor of savings into investment. Irrespective of other sources, the banking sector has a leading role in the capital formation and thereby the acceleration of growth and development. How effectively the banks bag the savings from the people and convert it as capital leads the growth rate of the nation into a larger extent. Technological up gradation and innovations play a vital role in the efficiency and effectiveness of the banking sector. The transformation from the ledger system to the computerization have increases the pace and efficiency of the banking sector. Since the government is focusing more on digital India and No cash economy Banks have still miles to go. The inclusion of banking services to each and everyone, reduction of the cost of banking and Easy banking ie less time consuming for bankers as well as customers and banking services anywhere at any time are the aims of modern banking. But a developing country like India, having infrastructural deficiencies and poor literacy rate, technological changes, and innovations in the banking sector is a herculean task. This paper is about the technological up gradation and innovation in banking sector taken place in the last five few years. These initiatives are to capture the valuable pie of the new gen.

KEYWORDS: *Fin-Tech Companies, Innovative Banking, Recent Technological Innovations*

INTRODUCTION

Capital formation is the stepping stone and it fosters the development of any nation. India being a developing nation the pace of its development is decided by the availability of capital and proper investment of the same. Irrespective of other sources, the banking sector has a leading role in the capital formation and thereby the acceleration of growth and development. How effectively the banks bag the savings from the people and convert it as capital leads the growth rate of the nation into a larger extent. The banking system in India has done a crucial role in the growth and development of the economy. The Indian banking system has been stable even after seeing change and surviving without any major crisis. During the last few decades, India's banking system has bagged several outstanding achievements to its credit. Extensive coverage of the entire nation under the banking network is the greatest among them. It is no longer confined to metropolitans or cosmopolitans centers, but also reached even in all the nuke and corner of the nation. This wide coverage and inclusion of all the sect and sector of the country is the key to the success of the Indian banking sector.

Technological up gradation and innovations play a vital role in the efficiency and effectiveness of the banking sector. The transformation from the ledger system to the computerization have increases the pace and efficiency of the banking sector. Since the government is focusing more on 'Digital India' and 'Cashless economy' Banks have still miles to go. The Inclusion of banking services to each and everyone, reduction of the cost of banking and Easy banking ie less time consuming for bankers as well as customers and banking services anywhere at any time are the aims of modern banking. But a developing country like India, having infrastructural deficiencies and poor literacy rate, technological changes, and innovations in the banking sector is a herculean task. Banks have been working towards a Digital India, adopting the latest technologies and introducing a number of products and applications to improve customer convenience.

Less time consumption and more convenience and availability of banking services at any time ie 24X7 banking and banking anywhere is the need for high tech generation. All the banks are aiming technological advancement to this extend keeping security and safety main concern. The shift from going to banks for each and every banking activity to virtual banking anywhere any time is, though convenient, convincing and catchy attracted numerous security issues such as high tech ATM robbery, juice jacking, hacking, cyber-attacks relating internet banking, mobile banking, phishing,

State Bank of India (SBI) being India's largest bank and one of the top 10 among the largest banks in the world with balance sheet size Rs 33 trillion around 25,000 branches. Its presence is seen in around 50 countries. The bank which is founded in 1806 as Imperial Bank of India now owns 25% market share of banking activities in India. Being one of the most reputed banks in the world and largest in the nation it has a crucial role in technological advancement and innovations in banking activities. This paper is an attempt to coin out and analyze the latest technological up gradation and innovations from SBI.

REVIEW OF LITERATURE

(Aruna R. Shet, 2015) To tackle the challenges of needs and perception of the customers most of the banks took technological initiatives to withhold in the cutthroat competition. Indian banks have become globally competitive in terms of technology as well as services. Technical efficiency and advancement in Indian banking is a result of technological up gradation of foreign banks. The aforesaid phenomena grabbed the pace after the liberalization. Developing the most efficient technologies at the lower cost and attracting people more by it to the bank is the key to the success of the banks. A better understanding of the customer needs and better solution is the base. (Dr. T Sreelatha and C H Chandra Sekhar) Technology has caused a paradigm shift in the banking sector and the delivery of banking services. Information technology and related innovations costly and complex on the outset, but they are 'energy guzzlers'. Since cost reduction and attracting new and potential customers is the need of the hour, innovation, as well as technological up gradation, is the only strategy for the banks to survive.

STATEMENT OF PROBLEM

The Banking system is changing rapidly due to technological up gradation of mankind. The last two decade witnessed tremendous changes in banking technology. The customer demand for up gradation, customer technological up gradation, and people being more techno-savvy are the pillars of this change along with cost reduction, customer retention and attraction from the bankers view. This present study analyses very recent innovations and technological changes in the banking field giving special reference to SBI.

OBJECTIVES

1. To study how innovations have contributed to the development of Indian banking. 2. To examine the impact of recent banking sector innovations on the Indian economy

METHODOLOGY

The study is basically based on secondary data. The subsidiary data is collected from magazines, Journals, Books and various websites like RBI website, SBI website and so on. The analytical part of the study is based on collected data and percentage method.

ANALYSIS

Over the years the banking sector in India has undergone tremendous changes. Entry of technology in the Indian banking sector can be traced back to the Raganarajan Committee report, way back in the mid of the 1970s. In 1979, the RBI has put forward the Talwar Committee on Consumer Services in Banks and it suggested that computerization of some functions is required to speed up customer service in Indian banks. While the automation process has not kicked off till 1993, it was due to strong opposition against bank automation process. Opponents argued that automation may increase unemployment sine technology reduces human labor. However, in 1993, the Unions of Bank employees agreed an agreement with Bank Managements under the assurance of Indian Banks Association (IBA) that they back up the employees. This agreement paved way for the introduction of computerization and the development of communication networks in Banks.

EARLIER TECHNOLOGICAL CHANGES IN INDIAN BANKINGSYSTEM

Core banking was the initial step in the banking sector in India. Once computerization has introduced in Indian banks also adapted the same. Under Core banking system all the branches under a bank are computerized and interconnected them using a network. This helped the customers to do banking transitions from any of the branches of the same bank irrespective of the home branch. So the customer is the no more the customer of the branch but the bank.

Core banking is been followed by a card system. A debit card was the first into it. In this system, a plastic card is used to the withdrawal of money from Automated Teller Machines. This initiative was basically for cost reduction of the

withdrawals as well as to reduce the customers' inconvenience of visiting the bank for each and every withdrawal. Now a customer can withdraw cash 24X7 from any of the ATM irrespective of the bank.

A credit card was another addition to banking innovation. A credit card is nothing but a debit card for the overdraft account. In this initiatives customer can avail easy loan from the banks up to a certain limit. More up gradation was added to the plastic card system and ATMs. Now the cards can be used for e payments, fund transfer using many applications and in POS machines. Automated Teller Machines (ATM) are now upgraded into small bank branch itself. Cash deposit, cash withdrawals, ATM pin generation and pin change, balance enquiry, mobile banking activation, transfer of fund and many more banking activities are possible.

Another up gradation to the plastic card is instead of magnetic strips which are used to keep the account details is now been replaced by the chips. Gift card and travel card are other two important additions to the plastic cards. Even debit card is upgraded on the base of the volume of day to day transaction and geographical are of the usage of the card. Gold cards, platinum cards, international cards etc are some of them. This bifurcation provides different withdrawal limits on a daily base and uses the same card in different countries facility.

Electronic Clearing System (ECS) is introduced in the late 1990s. It was another stepping innovation for the inter-bank transactions. ECS facilitates paperless credit debit transactions directly linked to the customer accounts. This facility is an RBI initiative.

Electronic fund transfer in the early 2000s is another see change in the banking sector. Real Time Gross Settlement (RTGS) and National Electronic Fund Transfer (NEFT) added the pace of the inter-bank transactions. Under this innovation, the fund can be transferred easily and consuming less time. Earlier the financial instruments like Cheques and demand drafts were used and were time-consuming and costly. Encashing cheques and demand drafts of different banks for the bank customer usually takes days together. But RTGS is real-time based so the fund to another banks can be transferred in no time. NEFT facility is also used for interbank fund transfer, but basically, this facility is used for less amount transfer and most of the cases amount less than Rs 2,00,000/-.

RECENT INNOVATIONS AND UP GRADATION IN INDIAN BANKING SECTOR

Cheque Truncation System (CTS): This is the latest technological addition to the Indian banking system. This system is designed for speedy and timely clearness of negotiable instruments especially Cheques and Demand Draft. Earlier system was sending these instruments to the clearing centers and using Electronic Cheque Clearing System (ECCS) interbank settlement is done. This always takes days together. CTS are introduced to tackle this delay. Under this system, these financial instruments are scanned and the scanned images are sent to the clearing centers and clearance is done within a day.

Internet banking: Your bank at the tip of your finger is the base of internet banking concept. This service provided by bank facilitates its customer, who is having this facility, with banking services such as balance enquiry, fund transfer, RTGS and NEFT facilities, an opening of fixed deposits, bill payments and tax payment and so on. Many up gradations are done in the internet banking facility. This facility ensures uninterrupted banking ie 24X7 banking without the time and places barrier. SBI online is an online banking portal SBI. It provides banking assistance such as spend analyzer, State Bank Rewardz, CIBIL

score estimator, ATM card request and duplication, PPF account opening, Stop Cheque and new cheque book request, and many more

Point of Sale machines (POS): POS is an electronic device used for money transaction using ATM card. Basically, it is a computer terminal connected to a customer account and magnetically encodes creditor's debit cards and makes the transaction from cardholders to POS connected accounts. POS machines are used basically for cashless transactions in different business ventures. SBI also promote POS intensively with the slogan to make card payments safe and hassle-free.

Telephone banking and SMS banking: These are the facilities to provide limited banking services to the account holders of the bank. In this setup customer can dial to a particular phone no any time to know the account balance, requesting new cheque books, ATM card blocking, Duplication and renewal. SMS facility also provides the above-mentioned services using SMS service. The most recent up gradation in this SMS banking is generating ATM pin (personal identification number) for new ATM cards and regeneration of the same. For most of the online transaction, one-time password (OTP) also comes as SMS to ensure a secure transaction.

LATEST TECHNOLOGY LANDSCAPE

Green banking, Digital India and less-cash economy are the keen focus of the Indian Government. By 2020 the average age of Indians are expected to be 29 years and smartphones are common. Youth everywhere are tech savvy. With the number of mobile owners is one million plus, 30% among them are smartphone users. Banks are focusing on adopting the latest technologies and providing a number of applications and products to improve customer service and withstand in the cutthroat competition. Provide the best digital solution for all banking activities especially payments anywhere any time is the present agenda of all the banks. The demonetization process aimed less cash society along with all stated goals and the government is pressing the banks to implements the same through, POS machines, mobile banking, mobile wallets, Adhar enabled payments systems, Jandhan accounts etc. A government of India even set a target of 25 billion digital transactions in the year 2017. Cheap availability of internet facilities especially by 'Gio' also helped in gaining momentum in the digitalization process and e-banking as well as m-banking.

The digitalization process in India gained momentum and pace recently. The technological infrastructure also increases rapidly and more and more people are into it day by day. And it is expected that the no cash payment which is 22% of the total payment will overtake cash payment by 2023. Thus in order to make cashless economy and digital India banks are focusing technological up gradation and innovations.SBI, being the largest bank in India, trying to be a forerunner of technological adaption and innovation in the nation.

Portable POS machines are a latest up gradation in the banking industry. Basically, they are now wifi enabled and so the internet connection is possible without connecting to the modem. The advantage is that even the customers can connect the POS machines to their mobile phone wifi and fund transfer is possible with that connection. SBI provides the facility of 'mPOS'. Near Field Communication (NFC) technology enabled Terminal are given for POS for safe and hassle-free banking. NFC (Near Field Communication) technology is the next generation short-range high-frequency wireless communication technology. NFC creates life easier and more convenient for customers around the world by making it simpler to make

transactions, exchange digital content, and connect electronic devices with a touch. It harmonizes today's diverse contactless technologies, enabling current and future solutions in various areas like payment, transportation & digital exchange.

Social media in Banking: The presents generation youngsters are chained to social media such as Facebook, twitter etc. The latest technology in banking is linking social media accounts of its customers with the bank accounts. So that the social media accounts of the customers can be used as a platform for basic banking activities. Most of the Indian banks are started making use of this innovation. SBI has also made use of this technology so that the youngsters are finding more comfort with the bank.

SBI has launched 'SBI Mingle' – its social media banking platform for Facebook and Twitter users. Using SBI Mingle, its customers can do a host of banking services like checking the balance and requesting ministatements on their Facebook or Twitter accounts. The Bank is also planning to introduce more services like a request for chequebook, stop cheque, register for mobile banking, internet banking, and SMS alerts and block ATM/Debit Card on this platform soon.

m-Wallet is the latest technological addition to the Indian banking system. The heavy rush of smartphone users and the demand for the mobile-based banking technology paved the way for m-Wallet. This is a mobile-based app which is designed for effortless authentication and transfer of money. In this common platform once the app is installed the user can transfer money from his account and keep the money in this account for e-trade and e-shopping and so on. Since online shopping and e- payments are gaining momentum instead of keeping liquid money in pocket people shit to the m-Wallets. M-Wallets provide bill payment facilities, recharge options and much more.

The BHIM app: The BHIM application launched by the Prime Minister on 30 December 2016 has been downloaded by over 16 million customers within a short time of six months. BHIM is a mobile app developed by National Payments Corporation of India, based on the Unified Payment Interface. Using BHIM, a customer can send, receive, collect money using virtual payment address (VPA), Account number plus IFSC. In June 2017, there were more than 4.6 million transactions under BHIM amounting to Rs 14,867 crores across 49 banks. SBI pay BHIM is the SBI version of BHIM payment portal. It enables an SBI merchant to accept payments for goods/services using his Android smartphone and fingerprint reader, from customers having Aadhaar seeded bank accounts, by authenticating the customer's biometrics. The transaction will be interoperable in nature

Aadhaar based payments: The introduction of aadhaar card and aadhaar authentication UIDAI has been a new light for the banking technology in India. The aadhaar authentication brought a new payment system ieAadhaar Enabled Payment System (AEPS) and BHIM Aadhaar, a digital POS system that requires a smartphone with a biometric device for the merchant and does not require even a phone from the customer. BHIM Aadhaar is an extension of AEPS. BHIM SBIPay is the app developed by the SBI for easy, secure and instant payments.

QR code-based payment: Quick Response code (QR) based transaction is one of the latest innovation to bank payments. A QR based payment technology represents a new channel of initiating and accepting payments between buyers and sellers using the mobile phone. Bharat QR is a QR code based solution wherein the customer makes payment to the merchant by scanning a static or dynamic QR code. It is interoperable among major Card schemes i.e. Visa, MasterCard, and RuPay. Bharat QR-SBI is the application for these services launched by the SBI.

Digital mobile banking platforms: This innovation another integrated mobile based application where a verity of financial services is available. This platform offers series from a number of e-commerce companies plus almost all banking services. YONO (You Only Need One)is an integrated digital banking platform provided by State Bank of India (SBI) to enable users to access a variety of financial and other services. This innovation is been introduced on 24 November 2017. YONO provides services to over 60 e-commerce companies.

Chatbot service: Chatbot is a computer program designed to simulate a conversation with human users, especially over the Internet. This innovation is been first used by HDFC. SBI has very recently launched its Intelligent Assistant (SIA) to address customer enquiries and help them with everyday banking task.

There is many more innovation which exist ant developed countries banking sector which is yet to introduce in Indian banks such as DIGIPASS. DIGIPASS is security ensuring device which acts as One Time Password (OTP) generator. This device helps in preventing fraudulent activities related to OTP which the bankers receive as SMS.

FINDINGS AND SUGGESTIONS

- Banking sector innovations and up gradation increased the pace of banking activities.
- Innovations helped the customers to perform banking activities through various electronic devices and SBI is taking due initiatives to grab the advantages of all banking sector technologies.
- Latest technologies in banking are basically to attract new generation and an increasing number of customer who opts the new technology is high in SBI.
- Innovation in banking activities focuses more on the security aspect of transactions.
- Bank has to take care more efficiently and effectively the roll of financial awareness dispersal.

CONCLUSIONS

The scopes of innovation and technological advancement have sea scope in the banking sector. Indian banks are gaining momentum to on at par with other international banks to survive in the competition. India is one of the largest countries its diversity always counts. The main hindrance to the speedy shift entire banking system is the literacy deficiency. In the case of financial literacy Indian population is lagging far behind. Compelling them to the technological innovations in the banking will bounce bank and its negative effects like intermediaries cheating etc keep the people away from banking activities. Another aspect of concern is the cost aspect as well as the security of the innovations and up gradations. One the one side FinTech companies are mushrooming and a number of technologies introduced. For a small error in the banking sector, banks have to pay a big price and customer belief in the bank will be questioned. So along with innovations and up gradations, the banks have to promote financial awareness among the people. SBI being the largest PSU bank of the country eagerly adapting technological advancement in the banking sector and the response towards these technologies are quite high from the customer base of the bank.

REFERENCES

1. *"Banking on Technology - perspectives on the Indian Banking Industry",(2014, January) Indian Banking Association, http://www.ey.com/Publication*
2. *"Banking Technology in India: Present Status & Future Trends",(2017 September 1) Institute For Developmentand Research In Banking Technology, http://www.idrbt.ac.in/assets*
3. *Dr Sreelatha T, Chandra Sekhar C H, (2012 October) "Role of Technology in Indian Banking Sector", Indian Journal of Management and Business studies.Vol 2, Issue 4.*
4. *Nanda, S. (2016). The Role of Knowledge Management in Indian Banking Sector. IMPACT: International Journal of Research in Business Management (IMPACT: IJRBM), 4(7), 37-44.*
5. *Shekhar K C, ShekharLekshmy, (2013) "Banking: Theory and Practice" Noida, Vikas Publishing House Pvt. Ltd.*
6. *Shet R Aruna, (2015) "Technological Innovations in Indian Banking Sector", International Journal of Scientific Engineering and Research*
7. *mab.sbi.co.in*
8. *www.economictimes.indiatimes.com*
9. *www.onlinesbi.com*
10. *www.rbi.org.in*
11. *www.sbi.co.in*
12. *www.economictimes.indiatimes*

IMPACT: International Journal of Research in Humanities, Arts and Literature (IMPACT: IJRHAL)
ISSN (P): 2347-4564; ISSN (E): 2321-8878
Vol. 6, Issue 11, Nov 2018, 292-297

PATTERN OF OCCUPATIONAL SHIFT AMONG MALABAR MIGRANTS – A CASE STUDY OF KALLAR GRAMA PANCHAYATH IN KASARAGOD DISTRICT

PRAVEENKUMAR P

Assistant professor, Department of development Economics

St. Pius X College Rajapuram, Kasaragod, Kerala

Received: 20 Oct 2018 **Accepted:** 27 Oct 2018 **Published:** 15 Nov 2018

ABSTRACT

The impact of the migration on the economy of Kerala in general and of Malabar in particular needs special mention. Large scale production of commercial crops like rubber, ginger, pepper, arecanut and coconut, advanced methods of cultivation and the introduction of new agricultural crops are some of the aspects to be highlighted. Migration to Malabar turned out to be a mass movement, as migration of half a million people took place without any design, organisation or leadership. Famine was a driving force behind large scale migration to Malabar. Land prices in Malabar were very low as compared with the land price in Travancore. The low price of land in Malabar and increasing tendency of cultivation of commercial crops, coupled with the aforesaid situations in Travancore, helped the migration of small peasants to Malabar. Malabar migration is a form of agriculture to agriculture migration, anticipating a long run improvement and can be perceived as a human capital decision. Migration often leads to change of traditional occupation to other and substantial socio economic development. The immigrant people change their occupation from agriculture or agricultural labour to industrial labour or some other jobs. The present study focuses the changes that take place in the occupational pattern of the Malabar migrants in Kallar Grama Panchayath in Kasaragod district. The study makes use of secondary data for meeting the objectives.

INTRODUCTION

Movement of people from one place to another for temporary or permanent settlement due to social, economic, political, religious or other reasons is a familiar phenomenon. Although migration is as old as human history, the massive population movements of the modern times have wider social, economic, political, demographic and ecological implications. Migration has multi faced and varies from one to another. Loss of resources, diffidence to the resources, and lack of employment in surroundings where people living, causes for migration of communities from one place to another. Migration is a significant factor in social and economic change of primitive subsistence economies into capitalist economies through accelerating the process of economic development.

The impact of the migration on the economy of Kerala in general and of Malabar in particular needs special mention. Migration often leads to transform of traditional occupation to other. Large scale production of commercial crops like rubber, ginger, pepper, arecanut and coconut, advanced methods of cultivation and the introduction of new agricultural crops are some of the aspects to be highlighted. Special mention should be made of the introduction of tapioca, a food crop, which was generally unknown in Malabar. Tapioca, introduced by the immigrants was so widely cultivated. The presence and the influence of the Travancore migrants altogether changed the cultural, social, educational, religious political and economic conditions of the

existing society and produced a mixed culture in which migrants hold the lead. Along the routes of the migration settlements were started, Roads and bridges followed them.

Migration of farmers from central Kerala to Malabar region is unique while considering any other migration. It's a community or cluster migration; wherein a group homogeneous people along with their close kin migrated together for a better livelihood. Most of them sold away their entire property in the motherland and settled in several parts of Malabar. In the initial phase they faced hurdles and constraints. The peasant migration from Travancore to Malabar made a significant addition to the agricultural labour force. Gradually they flourished in this new land. There have been substantial changes that have taken place in the economic sphere of Malabar region. They not only boosted agricultural sector but also themselves benefited out of that. Thus migration to Malabar involved a revolution of great magnitude and formed an important phase in the social, economic and cultural history of Kerala.

Malabar migration is a form of agriculture to agriculture migration, anticipating a long run improvement and can be perceived as a human capital decision. The socio-economic conditions of the settlers were generally very backward during the initial years of migration. The migrants disposed whatever possessions they were having at the original land, which varied from few cents of few acres of land plus cattle and a small house.

OBJECTIVES AND METHODOLOGY

Primarily, the study intends to get an understanding of the socio-economic advancement and occupational transformation of the farmers who have migrated from Travancore to Kallar Grama Panchayath, Kasaragod district. The specific objective of the study is,

- To understand occupational shift among the Malabar migrant farmers in Kallar Grama Panchayath Kasaragod district.

In order for this, Life history method was used to trace the entire process of migration and the changes that are noted today. The study is non-qualitative, historic and descriptive in nature. The first-hand and in-depth data was collected from the older members of the farming households through informal and intensive personal interviews, discussions and interaction. Life history approach was used to understand the occupational changes in the migrant farming households of Kallar Grama Panchayath over two successive generations. Kallar is an area, where the peasant farmers from Travancore started settling, in significant number. Several migrant colonies surround this locality. 42 farmers were selected for the case study through simple random sampling. 42 samples from 14 wards are selected as 3 samples from each ward of Kallar Grama Panchayath. Details regarding the occupational aspects of the sons of the respondent as well as his siblings were collected from him. All the respondents were Roman Christians. The study is basically two- generational which attempts to trace the occupational details of the father (First generation) and the sons (second generation).

HISTORY MIGRATION TO MALABAR

The migration to Malabar started from early decades of the 20th century, and continued up to the 1970s or even to 1980s when almost the whole area of the uncultivated wastelands were occupied by the peasant migrants as noted by Joseph (1988, 2002).

The first organized migration to Malabar was envisaged by the Knanaya Catholic Diocese of Kottayam under the direction the then Bishop Mar Alexander Chulaparambil in 1943(Joseph). Two settlements or colonies were started. The first was the Rajapuram Colony in the present Kasargod District. A group of 72 selected families from Kidangoor, Koodalloor, Punnathura and Pala came by train to Kanjangad and proceeded

to their destinations at Chullikara, Kallar and Malakkallu.The second settlement was in Madampam,30 Kilometers East of Kannur. 100 families mostly from Meenachil Taluk traveled by train to Kannur and settled at Madampam and Payyavoor. The settlement was named after the bishop, Alexnagar colony, in the present Kannur District. The idea of organized migration was envisaged and presented to the Bishop by Professor Joseph Kandoth, who was then a professor at the St. Alosius College in Manglore. This migration had a significant demographic and social impact as the Christian population of Malabar increased 15-fold from 31,191 in 1931 to 4,42,510 in 1971. (Kumbattu Varkey Joseph) The distance travelled by majority of the in migrants was more than 300 kms away from their native villages and settled in the hinterlands of the erstwhile Malabar district, which included prominent places like Rajapuram,Chullikara,Malakkallu-, Malom, Chittarikkal Madampam,Payyavoor,Chamathachal,Chemperi,Chempathotty, Cherupuzha, Kudianmala, Iritty, Ulikkal, Peravoor etc in Kannur Kasaragod districts.

The huge majority of the migrants were Syrian Christians, mainly (Syrian Malabar Nasrani) from erstwhile Travancore state. The migrants were mostly from present day Kottayam such as Pala, Chaganacherry, Kanjirapally, Kuravillagadu, Ramapuram, Bharananganam etc. and Idukki districts (Thodupuzha Taluk) with many from hill areas of Ernakulam district also, like Kothamangalam, Moovattupuzha etc. Several Hindu Nairs also migrated. Settlements were established in various hill areas of Malabar region.

ANALYSIS OF OCCUPATIONAL SHIFT IN THE STUDY AREA

In this section, an attempt is made to analyze the shift in occupation over the two successive generations and the changes that has been take place in the cropping pattern of the study area. The following analyses were conducted to reach a conclusion.

A. Two –generational occupation shift

Here occupation means the principal occupation followed by the father and that of his Sons. In general there is a clear shift of occupation from agriculture to non-agriculture over two successive generations.

Table 4.1

Two –generational occupation shift

Generation	Agriculture	Non-agriculture	TOTAL
I Generation	30 (71.42%)	12 (28.58%)	42 (100%)
II Generation	4 (9.52%)	38 (90.48%)	42 (100%)

Source: Sample survey

Data regarding the pattern of occupation (table 4.1) indicates that there is a clear shift of occupation from agriculture to non-agriculture over two successive generations. While most of the first generation respondents were depending on agriculture, 90.48 % of their sons (2nd generation) have moved to non-agricultural occupations. Further analysis indicates that majority of the non-agriculturists follow agriculture as their supplementary occupations. But very few of the agriculturists ensue non- agriculture even as supplementary occupations.

A. PATTERN OF OCCUPATION

The following Tables (4.2 and 4.3) indicate the intensity of the occupational shift over two successive generations. The occupational diversity is highly pronounced among the sons of first generation respondents. The improved educational status also impacted on the occupational pattern of second generation.

Table 4.2

Occupational categories of first generations

NO	OCCUPATION	NO. OF RESPONDENTS	PERCENTAGE
1	FARMER	30	71.42%
2	COOLIES	5	11.9%
3	SMALL BUSINESS	4	9.52%
4	PENSIONERS	2	4.76%
5	GOVT. JOB	1	2.38%
	TOTAL	42	100%

Source: Sample survey

From the above table it is clear that apparently, an over whelming majority (71.42%) of the first generation respondents is engaged in agriculture and agriculture labour occupations. 11.9% of migrants are cooli workers and 9.52% doing business. 4.76% of respondents are pensioners. Only 2.38% of respondents have Government job.

Table 4.3

Occupational categories of second generation

NO	OCCUPATION	NO.OF RESPONDENTS	PERCENTAGE
1	FARMERS	4	9.52%
2	NURSES	9	21.42%
3	BUSINESS	26	61.9%
4	GOVT. JOB	2	4.76%
5	ENGINEERS	1	2.38%
	TOTAL	42	100%

Source: Sample survey

Conclusion

Migration of farmers from central Kerala to Malabar region is unique while considering any other migration. It's a community or cluster migration; wherein a group homogeneous people along with their close kin migrated together for a better livelihood. One of the striking impacts of migration is the socio-economic development it had brought about in Malabar. The fearful forest region was transformed in to agricultural lands and later became semi-urban centers or village towns. The migration of peasants and the new land use pattern introduced by them could lead to the development of Malabar region in general and of the centers where migrants settled down in particular. The roads, schools and hospitals constructed by them could contribute to the progress of the region.

There is significant change in the socio economic condition of migrated farmers in the study area. They are socially and economically well developed. Education has been a major factor in improving the socio-economic status of the households, which in turn, enabled them occupy lucrative jobs outside the villages or even outside the state or country. The first generation respondents are less educated. 54.76% of them got only basic education. The second generation members have reportedly attained higher educational qualifications. 71.42 % of second generation is studied above degree level. Education has been a major factor in improving the socio-economic status and change in occupation of the households in the study area.

REFERENCE

- K.V. Joseph, Migration and Economic Development of Kerala, Mittal Publications, 1988 Joshy Mathew, Tradition, Migration and Transformation, Agrarian Migration to Wayanad, A Socio-Historical Perspective 1928-2000,
- Sebastian Valloppilly, Malabarile Kudiyettathinde Katha, Kulathuvayal Bhootha Varthamanangal, Suvarna Jubilee Smaranika, Kulathuvayal St. George Forona Palli, 1992,
- V. J. Varghese, Land, Labour and Migration: Understanding Kerala's Economic Modernity, Working Paper Series 420
- Kuravilangad Joseph, „Kudiyettathinde Vazhiyile Chadikkuzhikal", Koodaranji Edavakayude Suvarna Jubilee Smaranika, 1949-1999
- K. V. Joseph, Keralites on the Move, A Historical Migration from Kerala.
- K. V. Joseph, „Migration and the Changing Patterns of Land Use in Malabar", Journal of Indian school of Political Economy, Vol. XIV, Jan-March,
- P. K. Michael Tharakan, Dimensions and Characteristics of the Migration of Farmers from Travancore to Malabar, 1930-1950," Journal of Kerala Studies, June, Vol. 5.
- K. V. Joseph, Socio Cultural Determinants and the Peasant Migration from Travancore to Malabar", K. S. Mathew (eds.), Migration in South India
- K. C. Zachariah, S. Irudaya Rajan, (eds.), Kerala Demographic Transition, Determinants and Cosequences
- P. T. Sebastian, „Peasant Migration to Malabar", Charles Dias, (ed.), Kerala Spectrum, Aspects of Cultural Inheritance, Dr. K. J. John Felicitation Volume, The Indo Portugal Cultural Inheritance.

IMPACT: International Journal of Research in Humanities, Arts and Literature (IMPACT: IJRHAL)
ISSN (P): 2347-4564; ISSN (E): 2321-8878
Vol. 7, Issue 1, Jan 2019, 292-297

FINANCIAL INCLUSION AND FINANCIAL LITERACY AMONG TRIBAL PEOPLE - A CASE STUDY OF KALLAR GRAMA PANCHAYATH IN KASARAGOD DISTRICT

Praveenkumar .P

Guest Lecturer, Department of Development Economics

St. Pius X College Rajapuram, Kasaragod, Kerala

ABSTRACT

Indian economy has been recording high growth rates in the last two decades compared to earlier period, impacting livelihood of many people. However, questions have been raised about inclusiveness of various sections of society, particularly the poor, in the growth process so that India can achieve equitable and sustainable development. A major problem in achieving inclusive growth seems to be lack of access to key services such as banking. Financial inclusion can be expected to provide universal access to a wide range of financial services at a reasonable cost. These contain not only banking products but also other financial services such as insurance and equity products (Planning Commission, 2009). But the problem is that the inclusiveness of various sections of society, particularly the tribal people. Most of the financial products and services are still not reaching to the poor. One of the reasons for the exclusion of such people is the illiteracy regarding the financial terms. The present study focuses the extent of financial inclusion and the level of awareness regarding financial terms among the tribal people in Kallar Grama Panchayath in Kasaragod district.

INTRODUCTION

Access to finance, especially by the poor and vulnerable groups, is an essential requisite for employment, economic growth, poverty alleviation and social upliftment. Financial inclusion means the provision of affordable financial services by the formal financial system to those who tend to be excluded. Financial inclusion will enable the poor and the rustics of our country to open a bank account to save and invest, to borrow and to repay, to insure and to take part in the credit. This will enable them to break the chain of poverty. In the Annual Policy Statement of the RBI (2005-06), policies were made to encourage banks to provide extensive banking services to the unbanked mass of the country. Even though there are people who desire the use of financial services, but are denied access to the same. The financially excluded sections largely comprise of the marginalized people in the society especially the tribal people. In this scenario, the need for financial literacy is become more important than ever before as it determines the success of financial inclusion programs of every country.

Financial literacy means the ability of a person to understand financial matters. In other words it means the awareness, knowledge and skills of individuals to make decisions about savings, investments, borrowings and expenditure in an informed manner. In India, the need for financial literacy is greater because a large section of the population still remains out of the formal financial setup. With a view to increase the level of financial literacy the Reserve Bank of India has undertaken a project titled 'Project Financial Literacy'. The objective of this project is to disseminate information regarding the central bank and general banking concepts to various target groups, including, school and college going children, women, rural and urban poor, defense personnel and senior citizens. Even then, a large segment of the population is still excluded from the purview of formal financial setup due to the lack of financial literacy.

Historically, it has well been proved that always the social groups deprived of adequate entitlements both physical and human who are labeled, in official parlance, as the marginalized and weaker sections, would be excluded from social and economic environment in which they are destined to live. In this context, the study tries to analyze the level of awareness and level of financial inclusion among the tribal people in Kallar Grama Panchayath

OBJECTIVES OF THE STUDY

1. To analyze the level of awareness of tribal people with regard to various financial terms.
2. To identify the level of financial inclusion among tribal people in the study area. The present study focuses on a detailed view on financial inclusion and the awareness of tribal people regarding the financial services. The study used primary data to evaluate the level of financial inclusion and literacy.

FINANCIAL LITERACY AMONG THE TRIBAL PEOPLE

The level of financial literacy among the tribal people is analyzed in terms of their awareness with regard to various financial terms. Degree of awareness is measured on a three point scale such as high awareness, average awareness and low awareness. The result of the analysis is presented in the following table.

Table 3.1

Level of Awareness about various Financial Services

Sl. No.	Various financial services	Level of awareness in %		
		high awareness	average awareness	low awareness
1	Bank Deposit/Bank loans	30(100%)	-	
2	Cheque	3(10%)	2(6.6%)	25(83.3%)
3	Usage of ATM	3(10%)	6(20%)	21(70%)
4	LIC /Insurance	3(10%)	2(6.6%)	25(83.3%)
5	Pension Funds	9(30%)	6(20%)	15(50%)
6	Post Office Savings	2(6.7%)	3(10%)	25(8.3%)
7	Internet Banking	0	6(20%)	24(80%)
8	Mobile banking	9(30%)	5(16.7%)	16(53.3%)
9	Awareness of Digital Financial Inclusion	5(16.7%)	6(20%)	19(63.3%)

Source: Sample survey

It can be observed from the table that most of the respondent has low awareness with regard to various digital financial services like internet and mobile banking, Usage of Banking Applications etc. Their awareness level is higher with regard to the term 'Bank deposits'. The respondents have average awareness about various financial terms such as, ATM, LIC /Insurance, Cheque etc. The tribal people have a low level of financial literacy while looking at the overall financial awareness.

USAGE OF VARIOUS FINANCIAL SERVICES

The financial inclusion is measured on the basis of the usage of various financial services by the tribal people in the study area. Among the total sample of 30 individuals only 28 persons having a bank account. Therefore the usage of financial services is measured only from these 28 sample persons.

Table 1

Usage of financial services

Sl no	Digital Financial services	using	Not using
1	Usage of chequ book	6(22%)	22(78%)
2	Usage of ATM	3(10.7)	25(89.3)
3	Usage of Internet Banking	0	28(100%)
5	Usage of mobile based services	5(17.9%)	23(82.1%)
6	Usage of Banking Applications	4(14.3%)	24(85.7%)
7	Post office deposits	2(7.1)	26(92.9)
9	Others	2(7.1)	26(92.9)

Source: sample survey

Out of the 30 sample respondents, 93% having a bank account. But the problem is that majority of them are not using various financial services. The facilities like internet banking are note used by any of the respondents. Only 17.9% using the mobile based services like e-valet and e-payment. 14.3% of the respondents using banking applications like Fed-mobile, google Pay etc. Since digital financial services naturally rely on mobile communications networks, right of entry to mobile technology and the capability to use it, how and when desired, are critical factors in determining financial inclusion.

From this above discussion it is clear that the financial inclusion is higher in quantitatively among the tribal people, but most of them are not using such services regularly. Large number of tribal people is excluded from the financial services even though they are financially included. This type of exclusion is mainly because of the illiteracy regarding the financial services and the fear to use it.

CONCLUSION

Financial literacy is considered as an important adjunct for promoting financial inclusion and ultimately financial stability. The present study reveals that the tribal people are poorly informed about various financial products and practices. Even though they are financially included most of them are fear to use the banking services. Majority of the tribal people have their own bank account but it is not regularly using. The tribal people are not interested to use the financial services like ATM because of their low awareness. Many of them are not aware about the modern banking services like internet banking mobile banking etc. As far as the reason for exclusion from having bank accounts is concerned, self-exclusion has come out to be the prominent reason. Financial awareness programmes will be helpful to bring a practice of recording of incomes and expenditures among tribal people and it will helpful to bring them fully financially included. So the governmental agencies have to re-design the financial literacy programmes in such a manner to reach the tribal people

REFERENCE

1. World Bank. (2015). Innovative Digital Payment Mechanisms Supporting Financial Inclusion: Stocktaking Report. World Bank Group. Planning commission (2009) government of India.
2. Asian Development Bank (2016). Digital Financial Services in the Pacific Experiences and Regulatory Issues. Mandaluyong City, Philippines: Asian Development Bank
3. Tejil Thomas & Suresh T. S A study to assess the knowledge on digital financial inclusion among scheduled castes and scheduled tribes, IMPACT: International Journal of Research in Humanities, Arts and Literature 2018
4. Shem Alfred Ouma, Teresa Maureen Odongo and Maureen Were, Mobile financial services and financial inclusion: Is it a boon for savings mobilization?, review of development finance
5. Niranjan JN, A Case Study of Barriers to Digital Financial Inclusion of Auto-Rickshaw Drivers in Viman Nagar, Pune, Maharashtra, Journal of Political Sciences & Public Affairs

IMPACT: International Journal of Research in Humanities, Arts and Literature (IMPACT: IJRHAL)
ISSN (P): 2347-4564; ISSN(E): 2321-8878
Vol. 6, Issue 11, Dec 2019, 292-297

AN OVERVIEW OF RETURN MIGRATION IN KERALA

Praveen kumar P
Guest lecturer, Department of development Economics
St. Pius X College Rajapuram, Kasaragod, Kerala

Received: 23 Nov 2018 **Accepted:** 27 Nov 2018 **Published:** 2 Dec 2018

ABSTRACT

An absolute static population exists nowhere in this world. The movement of people in search of better living conditions and a more secure environment is as old as human civilization. Such movements not only transform the lives of the migrants profoundly, but also lead to significant economic and social changes in the regions of origin and destination of the migrants. The expansion and developments in transport and communication along with industrialisation have paved way for large-scale movement of people from villages to towns, from towns to other towns and from one country to another country in search of new job opportunities and avenues. Industrialisation has widened the gap between rural and urban areas, inducing a shift of the workforce towards the industrializing areas. Kerala is one of the Indian States with large number of international migrants. The main reason for the achievement of higher level of human development in Kerala can be attributed to the migration to foreign countries, but return migration can affect negatively by reducing the investment in the home country (Anje Wiesbrock, 2008).The return migration has the strength to reduce positive impact of migration. The reason for return migration varies from country to country. The government policies in the destination countries influence the magnitude of return (Richard Black, Russel 2005).

Key word: Return migration, Remittance

INTRODUCTION

In the past few decades, the world has witnessed an alarming increase in the number of migrants. Globalization has led to a significant increase in human mobility within and across the countries (IOM, 2013). As per the latest WHO reports it has been estimated that about 1billion people of the world's population are constituted by migrants, of which 214 million are international migrants and the remaining 740 million constituted by internal migrants.

The major driving forces behind migration are better employment opportunities and a better living standard away from home. Bhagwati (1972) argue that migration process carries human capital to regions of destination, involves investment in the employment of migrants, enables acquiring of new skills and emphasizes the economic cycle. Short-term or seasonal migration has played a crucial role in allowing the rural populace to cope with the consequences of agrarian distress and devastated rural economies in many parts of India. Chandrasekhar (2007) argued that short-term migration is distress-led, driven by the complete collapse of rural employment generation, the economic difficulties of cultivation and also inadequate employment opportunities in towns. Short-term migration for work has evidently increased rapidly in recent times in India.

Kerala is one of the Indian States with large number of international migrants. The main reason for the achievement of higher level of human development in Kerala can be attributed to the migration to foreign countries. Higher migrant's earnings compared to non-migrants brought positive distributional impact. Educated unemployment rate in Kerala is very high and migration reduces unemployment pressure to a large extent.

Kerala has been a major exporter of the workforce to gulf countries since the 1970s with the dramatic increase in oil prices. The State who has formed an important labour source for the construction sectors in the Gulf countries.

Non Resident Keralites

Non resident Keralites play a vital role in the development of the State. Their contribution to the development can be seen at family level, community level and state/country level. At family level it has improved household earnings, food, consumption, health care, housing and educational attainments and for over three decades remittances have been meeting the current account deficit of the country. The Non-Resident Malayali Census 2013 of Economics and Statistics Department, Government of Kerala, identified that out of the 16.25 lakh Non-Resident Malayalis, 14.26 are working in different jobs. Around 50 lakh people in Kerala are dependent on Non Resident Malayalis. Country wise, 90% of Non-Resident Malayalis are working in the Gulf region

As per the survey conducted by Economics and Statistics Department of Government of Kerala, the largest number of NRKs is reported from Malappuram, their proportion to the total NRKs being 18 per cent. Thrissur is in the second position accounting for 11per cent of the total followed by Kannur and Kozhikide with 10per cent share each. Idukki and Wayanad are the two low NRK reporting districts and their share to the total NRKs are 1per cent each.

Out of the total Non-Resident Keralites, 87.77per cent are engaged in different economic activities. Among those employed, 93.04per cent are men and 6.96per cent are women. District wise, Malappuram has the highest proportion of 19.51per cent NRKs employed followed by Thrissur and Kozhikode at 10.50per cent and 10.37per cent respectively. Even though Idukki reported the lowest share in employed NRKs women NRKs employed is 32.83per cent of total working women NRKs. Second highest proportion of female working NRKs is reported from Kottayam (31.68per cent).

Return migration in Kerala

Return migration can be defined as a migratory movement when people return to their place of origin after spending a significant period in another country. Return Emigrants are individuals who have returned permanently after living at least for two years abroad (NORKA, GOK). The reasons for return are several. Some have returned because they are terminated from their job, difficult working and living conditions in Gulf countries, ill health, injury, and accidents, other important reasons such as recent financial crisis and strict nationalization policies adopted by the Saudi Government.

The global economic crisis and new labor policies in the gulf countries have created a context in which return of low and unskilled migrant workers to the State. Return emigrants have became demographically, politically and economically a significant component of Kerala's population. The policies of giving larger share of jobs for natives, abandonment of large scale construction made the return of unskilled labours to their home country

If we look at the state wise distribution of these return migrants in India from abroad, Kerala has nearly 50 percent of these return migrants. It seems the emigrants from Kerala are also higher, and which has been persistent from 1970's has the higher tendency of migrants returning back. The statistical data related to migrants in Kerala bring us to its importance in the social and economic scenario of Kerala population. Now one out of every 29 persons in Kerala, one out of every 22 adult population of Kerala, one out of every 19 working age population of Kerala, and one out of every 9 working age male population of Kerala are return emigrants.

Corresponding to every 100 households in Kerala, there are 16 return emigrants; 12 of them have at least one return emigrant. About 1.3 percent households have more than one return emigrant. At present, there are roughly over 1.3 million return emigrants in Kerala. (Zachariah, Rajan, 2012).

During the 1970's and the early years of the 1980's, annual return flows were relatively small. But after the end of the 1980'sfavourable conditions in gulf countries began to decline due to factors as, decline in oil prices, depletion of petro-dollar stocks, increasing competition among expatriates from different countries for work opportunities in the Gulf region, cuts in the wage and salary levels and the tightening of rules relating to immigration and employment of foreign workers perpetuated the return of migrant workers to their native places (Nair, 1986). However, such developments did not, in fact, reduce the volume of the emigration. Most countries in the Middle East became havens for thousands of illegal immigrants from several countries in Asia, the share of Kerala among such illegal immigrants being especially high. The UAE and the Kingdom of Saudi Arabia have sent back thousands of illegal immigrants to countries of origin by granting them amnesty. Hostilities in Kuwait also led to an increased flow of return migration in 1990.

Thus, since 1980's not only has there been a steady increase in the annual inflow of return migrants after termination of jobs or expiry of visa, there has also been sudden spurts in the flow of emigrants arising from ad hoc reasons such as sudden war and abrupt decisions by host countries to compulsorily repatriate illegal immigrants. Among the migrant sending states in India, Kerala has borne the brunt of such forced repatriation. But the return of emigrants from the Gulf Countries has assumed large dimensions in Kerala only in recent years. The time series flow of emigrants, return emigrants and NRKs are depicted in the following table 2.

Table no 1: Migration Trend in Kerala, 1982-2014

YEAR	EMI	REMI	NRK
1990	510214	197732	707946
1991	566668	219856	786524
1992	637103	253733	890836
1993	754544	287610	1042154
1994	819025	331166	1150191
1995	957388	379562	1336950
1996	1062376	433489	1495865
1997	1178589	486033	1664622
1998	1318489	553096	1871585
1999	1412649	620851	2033500
2000	1501917	684457	2186374
2001	1600465	739766	2340231
2002	1717695	794385	2512080
2003	1838478	893940	2732418
2004	1900025	925990	2819727
2005	1961573	958041	2907036
2006	2023121	990092	2994345

2007	2084669	1022143	3081654
2008	2146216	1054194	3168963
2009	2207764	1086245	3256272
2010	2269312	1118296	3343581
2011	2330860	1150347	3430890
2014	2400375	1252471	3652845

Source: Migration and Development: The Experience of Kerala, KC Zachariah, S.Irudaya Rajan and Kerala Migration Survey, 2011

Since 1993, when there were only 1.24 lakh Gulf returnees in the State, the size of the annual flows seems to have been growing rapidly. At present, there are roughly over 1.3 million return emigrants in the state. In 2008, there were about 1.157 million return emigrants; Ten years earlier, in 1998 this was reported to be 7.4 lakhs return emigrants (Zachariah and Rajan,2014). Over the past few years, return emigrants have become a significant component of Kerala's population. They are everywhere in the state. The time series flow of emigrants, return emigrants and NRKs are depicted in table 1. Return emigrants are significant demographically, economically, culturally and politically (Zachariah and Rajan, 2011).

Districts that send out more emigrants tend to receive more return emigrants. Thus Malappuram district had the largest number of return emigrants in all years except 2011. Wayanad and Idukki districts send out a few emigrants and they had a few return emigrants too (Kerala Migration Survey, 2011). Return emigrants as percentage of emigrants is the highest in Thiruvananthapuram district. Thiruvananthapuram, Malappuram, Thrissur, Kannur and Kollam districts received moderate share of return emigrants and other districts received less percentage of return migrants.

Pull factors

The pull factors of gulf migration evaluate the reasons for return from gulf countries. Various reasons were found out according to the responses of respondents. Important among them are unfavorable working conditions, expiry of contract, compulsory expatriation, low wages, family problems, hostile climate, etc. The following table shows the main reasons that are pulling the migrants back to Kerala based on primary data.

Table no 2: Table - Pull factors

Reasons	Responses	
	N	Percent
Unfavourable working conditions	22	15
Expiry of contract	24	16
Compulsory expatriation	18	12
Low wages	15	10
Family problems	35	23
Hostile climate	32	21
Other reasons	4	3
Total	150	100

It could be seen that majority of migrants that is 23 percent returned to Kerala due to their family problems. Similarly 21 percent returned due to hostile climate, 16 percent returned due to expiry of contract, 15 percent returned due to unfavourable working conditions and 12 percent returned due to compulsory expatriation.

Concluding remarks

This paper attempted to understand the strength and spread of Gulf returnees in Kerala and the pull factors taking them back to Kerala. from the secondary information collected, it could be noticed that since 1980's not only has there been a steady increase in the annual inflow of return migrants after termination of jobs or expiry of visa, there has also been sudden spurts in the flow of emigrants arising from ad hoc reasons such as sudden war and abrupt decisions by host countries to compulsorily repatriate illegal immigrants. Data reveal that Malappuram district is having maximum number of gulf returnees followed by Thiruvananthapuram.

The push and pull factors of migration to Kerala are also examined in this chapter. It could be seen that majority of migrants that is 23 percent returned to Kerala due to their family problems. Similarly 21 percent returned due to hostile climate, 16 percent returned due to expiry of contract, 15 percent returned due to unfavourable working conditions and 12 percent returned due to compulsory expatriation. Thus it can be seen that there are several reasons pulling them back to Kerala among which the family problems lie on the front.

REFERENCE

- *Anje Wiesbrock (2011).The Integration of Immigrants in Sweden: a Model for the European Union?. Malden. Blackwell Publishing Ltd*
- *Prof. Richard Black (2005), Workshop on Sustainable Return of Professional and Skilled Migrants organized by Refugee and Migratory Movements Research Unit.. University of Sussex.*
- *Chandrasekhar (2007), Short-term migration in rural India: The Impact of nature and extent of partcipation in agriculture*
- *K. C. Zachariah, S. Irudaya Rajan (2012), Migration and Development: The Kerala Experience Hardcover, CDS working Paper*

Demographic Changes and Replacement Migration in Kerala

OPEN ACCESS

Volume: 6

Special Issue: 1

Month: November

Year: 2018

ISSN: 2319-961X

Impact Factor: 4.005

Citation:
Praveenkumar, P. "Demographic Changes and Replacement Migration in Kerala." *Shanlax International Journal of Economics*, vol. 6, no. S1, 2018, pp. 82–88.

DOI:
https://doi.org/10.5281/zenodo.1488525

P.Praveenkumar
Guest Lecturer, Department of Development Economics
St. Pius X College Rajapuram, Kasaragod, Kerala

Abstract
Kerala, a state of southern India is witnessing large inflow of migrant labour from different parts of the country in the recent years. One of the main reasons for such a trend is the demographic and social character of the state. Kerala is one of the states in India which ranks highest with respect to social and human indices. Kerala experiencing an advanced demographic transition as the mortality and fertility levels have come down. During 1950 -60 the life expectancy at birth for Kerala were only 46.15 years which advanced to 75.2 years during 2011-15. The aged population constitute 13.3 % of the total population 2016.This changes in the demographic structure leads a shortage of labours born out of demographic transition and increase the number of aged people in the state. The recent phenomenon of replacement migration is a result of a rapid decline in the number of workers in the young working ages caused by the demographic transition, emigration of a large number of young person's to the gulf countries and the aversion of youth towards the low paid unskilled jobs. The shortage of labours as a result of ageing population and out-migration is met by labourers from other parts of the country. In this context, the present study focuses the reasons that are responsible for the evolution of replacement migration, along with the consequences resulting out of it. The study makes use of secondary data for meeting the objectives.
Keywords: migration, demographic transition, replacement migration

Introduction

Individual migration is the movement by people from one place to another with the intentions of settling, permanently or temporarily in a new location. The movement of people in look for of better living situation and a more protected environment is as old as human civilisation. Such movements not only change the lives of the migrants deeply but also lead to major economic and social changes both at the place of origin and destination of the migrants. The development in the transport and communication sectors along with industrialisation have smoothed the way for large-scale movements of people from villages to towns, from towns to other towns and from one country to another country in search of new job opportunities. Industrialisation has widened the gap between rural and urban areas, inducing a shift of the workforce towards industrialising areas (Arun and Ajay, 2017).

Migration from Kerala to the other states in India and to countries outside has now become so rampant that its impact is felt in every aspect of life in the State. (K.C.Zachariah E.T. Mathew S. Irudaya Rajan) Migration has been the single-most dynamic factor in the otherwise dreary development scenario of Kerala in the last quarter of the twentieth century. Kerala is approaching the end of the millennium with a little cheer in many people's homes, a major contributing factor for which has been migration. Migration has contributed more to poverty alleviation in Kerala than any other factor, including agrarian

reforms, trade union activities and social welfare legislation (K.C.Zachariah E.T. Mathew S. Irudaya Rajan) Kerala is in front in the experience of demographic transition compared to all other Indian states which manifests itself in quantum and model of both internal and international migration. Kerala is in the third stage of demographic transition. Demographic transition leads to an expansion of the working age population in the state and it leads to huge migration from the state to other parts of the nation and to other nations. On the other hand as a result of the demographic transition, the state is facing the problem of aging population. The 2011 census reveals that 60+ age group constitute about 12.6% of the state's total population as against 8.6% that of India and by 2061, it is estimated that this share would increase to 40% of Kerala's population.. The composition of aging population in total population and large outmigration from the state leads to the phenomenon of replacement migration in Kerala.

The fact or the concept of replacement migration is of recent origin. As a result of the demographic transition, turn down in working-age population or people to meet the required labour force along with increasing ageing population etc leads to the process of replacement migration. United Nations defines replacement migration as 'the migration that would be needed to offset declines in the size of population, the declines in the population of working age, as well as to offset the overall ageing of a population' (United Nations, 2000).

According to the 2011 Census, there are 457 million internal migrants in India. It accounting for 37.8 per cent of the total population and in Kerala this percentage was 48.9 per cent. One out of two persons in Kerala is an internal migrant. Over the years, Kerala's external (international) migrants were replaced by internal (in) migrants. According to the latest Kerala Migration Survey (2014) conducted by the Centre for Development Studies (CDS), Kerala has an estimated 2.4 million international migrants and 0.7 million internal migrants accounting for the absence of 3.1 million. Incidentally, the in-migrants to Kerala is estimated at 3.4 million in 2017 as per the GIFT (Gulati Institute of Finance and Taxation), which almost matches the quantum of internal and international migrants from Kerala giving rise to the phenomenon of "Replacement Migration" (Arun Perumbilavil Anand).

Objectives of the Study

- To analyze the phenomenon of migration in the state of Kerala;
- To recognize the reasons that are responsible for the evolution of replacement migration

An Overview of Migration in Kerala

Indian state of Kerala had received much attention in the 1970s and 1980s in view of the large number of emigrants to the gulf countries. The state has a work force of around 83 lakhs, out of which 19 lakhs are women workers. The vast majority work in the unorganised, or informal sector. Sometimes people work in conditions of partial employment, often without adequate access to decent wages or Social Security protection. The concentration of Government has been mainly focused on protecting the working conditions and the rights of the relatively privileged minority of workers in the organised sector.

Unemployment is one of the basic problems confronting the State, and Government has to spur the creation of new employment opportunities. There are presently around 43 lakhs of young people registered on the unemployment rolls of the State. Productive employment is being created in the State's economy at very low rates. Despite the relatively high skill and adaptability levels of the State's workforce, labour market has not been perceived as a positive factor by prospective investors in Kerala. The competitive market reform policies have turned many industrial units unviable. The plantation sector is also facing a grave situation due to unremunerative prices for commodity products like Coffee, Tea and Rubber. All this has led to retrenchment and closure of many industrial units and estates in the plantation sector.

Urbanization is one of the key "pull" factors of migration: "Contrary to conventional wisdom on urbanization and migration, high rates of migration (permanent and temporary) into urbanized areas have

continued despite rising levels of (formal) unemployment and persistent urban poverty. It shows that the expanding urban informal sector is representing a significant pull factor" (Deshingkar and Grimms, 2004). In many instances, large migrant population provokes substantial popular unease translated into xenophobia, racism, or lesser forms of hostility toward migrants. While the inflow of migrants has grown exponentially in recent years into the rapidly urbanizing and rapidly growing- South Western and Punjab Haryana- Delhi belt, policy makers have not woken up to this reality, except for knee-jerk reactions following Bangalore exodus, or Suzuki violence. It is politically imperative that policy makers pay attention to living conditions in the migrant centres.

External Migration

Migration has been a significant factor in helping reduce poverty and unemployment in Kerala. For over three decades there has been steady migration from the state of Kerala to countries in the Gulf and different parts of India and the world. It is estimated that today over 10 percent of the population of Kerala lives outside the state, in various parts of India and abroad particularly in the Gulf region, the US and Europe. According to the latest study 'Kerala Migration Survey 2011', 22.8 lakh Kerala emigrants are living abroad in 2011. The number of Kerala migrants living in other States of India in 2011 is estimated at 9.31 lakhs. There are two types of migration. They are external migration and internal migration. These are discussed below.

Internal Migration

A recent trend in the employment sector in the State is the inflow of interstate migrant labour from other States. Migrants are coming to Kerala from states like West Bengal, Bihar, Orissa, Chattisgarh, Jharkhand etc,. There are various factors leading to this in migration. They are

- Higher wages for unskilled labour in the State,
- Large opportunities for employment and
- Shortage of local labour,

These workers are less advantaged group in the labour market working for a subsistence living. Even though a comprehensive data on migrant labour is not available, different studies show that the incidence of migrant labour is increasing in the State. Since they are not engaged through a contractor or an intermediary, the legal protections envisaged under the Interstate Migrant Workmen (Regulation of Employment and Conditions of Service) Act, 1979 are alien to them in their employment. According to Census, 2001, among the districts, Ernakulam district, recorded the highest inflow of migrants from other States.

The migrant labourers get much higher monetary wages than in their native places and they work for longer hours and their real wages may be lower. They live in shanty houses/rooms in slums like localities often on a sharing basis. They have limited access to sanitation facilities and safe water and the working and living conditions and habits make them suffer from a number of diseases. But their access to public services like health and education is limited and they enjoy very limited protection from labour laws. They also face problems of social integration in Kerala.

Though these workers are predominantly engaged in the construction, plywood and steel industries, their presence is noticeable in almost all employments including service sector in the State. Because of their lower levels of reservation wages; and they do not have organization and union and lack of 'voice', recently there is an increasing tendency to employ migrant labour; especially in the field of constructions. Since measures had not been developed to improve the weak conditions of these labour, Social Security, compensation in case of job loss, health problems etc, the State Government have envisaged a scheme called "Inter State Migrant Workers Welfare Scheme" through Kerala Building and Other Constructions Workers Welfare Fund Board.

Non Resident Keralites

Non resident Keralites play a vital role in the development of the State. Their contribution to the development can be seen at family level, community level and state/country level. At family level it has improved household earnings, food, consumption, health care, housing and educational attainments and for over three decades remittances have been meeting the current account deficit of the country. The Non-Resident Malayali Census 2013 of Economics and Statistics Department, Government of Kerala, identified that out of the 16.25 lakh Non-Resident Malayalis, 14.26 are working in different jobs. Around 50 lakh people in Kerala are dependent on Non Resident Malayalis. Country wise, 90% of Non-Resident Malayalis are working in the Gulf region

As per the survey conducted by Economics and Statistics Department of Government of Kerala, the largest number of NRKs is reported from Malappuram, their proportion to the total NRKs being 18 per cent. Thrissur is in the second position accounting for 11per cent of the total followed by Kannur and Kozhikide with 10per cent share each. Idukki and Wayanad are the two low NRK reporting districts and their share to the total NRKs are 1per cent each.

Out of the total Non-Resident Keralites, 87.77per cent are engaged in different economic activities. Among those employed, 93.04per cent are men and 6.96per cent are women. District wise, Malappuram has the highest proportion of 19.51per cent NRKs employed followed by Thrissur and Kozhikode at 10.50per cent and 10.37per cent respectively. Even though Idukki reported the lowest share in employed NRKs women NRKs employed is 32.83per cent of total working women NRKs. Second highest proportion of female working NRKs is reported from Kottayam (31.68per cent).

Table Number of Emigrants and Its Change during 1998-2013

Year	Emigrants	Increase/Decrease
1998	1361919	--
2003	1838478	476559
2008	2193412	354934
2013	2400375	206963

Source: Kerala Migration surveys 1998-2013

According to the Kerala Migration Survey 2013, Kerala has 2.4 million emigrants compared to 1.4 million in 1998. Over last 20 years, emigration has augmented although exhibiting a gradual decline in its growth. About 4.7 lakh emigrants were estimated as new emigrants in 2003 compared to 1998. The inter-survey increase in 2003-2008 showed a decline with 3.5 lakh migrants compared to that in 1998-2003. Again there was a reduction in inter-survey estimates of 2.1 lakh over a five year period. Over the years there has been a drop in the number of emigrants and some districts witnessed a negative growth in terms of numbers. One of the probable reasons points to the global recession of 2008 that gripped the Gulf countries. Many people returned to their home state after losing their jobs during the crisis.

While looking at the phenomenon of Kerala's massive Gulf emigration, thus evolved and flourished from the latter half of the twentieth century onwards, it is obvious that in the initial phase the emigrants were predominantly non-agricultural labourers with low educational attainments. Nevertheless, the emigration of labour did not create any major hurdles and conspicuous deficiencies in the home economy in the early phase, but in later the continuous emigration resulted in a scarcity of labour especially in the construction sector, which was followed inevitably by a hike in the wage rate (Prakash, 1998). Interestingly, at present, Kerala has the highest wage rates among the states in India.

The chronic shortage of labour felt in the construction sector in Kerala and the resultant higher wage rates received the attention of workers from other states and they started flocking Kerala in large numbers. This

has opened a new era of replacement migration to Kerala as the state once again becoming a fertile ground for migrating population after a break of about 60 years since the 1960s. Though initially, the migrants were primarily from the states like Tamil Nadu and that mostly characterised seasonal and short-duration migration, at a later period the state started receiving migrants from far distant states like Bihar, Assam and West Bengal.

Demographic Transition and its Effect

District-wise Decadal Growth of Population by Residence and Sex in Kerala (2001-2011) (In Percentage)

Districts	Total		
	Persons	Male	Female
Kasaragod	8.58	6.89	10.19
Kannur	4.73	2.48	6.80
Wayanad	4.71	2.66	6.78
Kozhikode	7.20	5.12	9.16
Malappuram	13.45	11.73	15.06
Palakkad	7.35	7.30	7.40
Thrissur	4.94	4.13	5.69
Ernakulam	5.69	5.28	6.09
Idukki	-1.79	-2.45	-1.13
Kottayam	1.07	0.35	1.77
Alappuzha	0.88	-0.14	1.83
Pathanamthitta	-2.97	-4.70	-1.38
Kollam	1.94	-0.21	3.95
Thiruvananthapuram	2.07	0.75	3.32
Kerala	4.91	3.61	6.14

Source: Office of the Registrar General and Census Commissioner, India.

The above Figure depicts district wise decadal population growth rate experienced by Kerala during the period 2001 to 2011. Today the state experiences one of the lowest population growth rates in the country, i.e., only 4.91%. It is glaring to note that some districts of Kerala like Idukki (-1.93%) and Pathanamthitta (-3.12%) have stated witnessing population decline as per the recent census records. It is important to note that the state's population growth rate always remained higher than that of the India's until 1971. Since 1971, the population growth of the state started to decrease drastically marking the onset of demographic transition. So the demographic transition in Kerala leads to a shortage of labour force in Kerala now and in future.

District-wise Decadal Growth Rate of Child Population (Age Group 0-6 Years) by Residence in Kerala (2001-2011)

Districts	Total		
	Persons	Male	Female
Kasaragod	-2.01	-2.08	-1.94
Kannur	-1.96	-2.43	-1.47
Wayanad	-11.28	-11.53	-11.02

Kozhikode	-3.31	-3.83	-2.78
Malappuram	4.08	3.80	4.38
Palakkad	-5.20	-5.36	-5.03
Thrissur	-8.58	-8.20	-8.97
Ernakulam	-10.23	-10.51	-9.94
Idukki	-21.27	-21.08	-21.46
Kottayam	-17.94	-18.03	-17.84
Alappuzha	-15.18	-14.95	-15.41
Pathanamthitta	-23.76	-24.11	-23.41
Kollam	-13.10	-13.64	-12.55
Thiruvananthapuram	-16.68	-16.73	-16.62
Kerala	-8.44	-8.62	-8.26

Source: Office of the Registrar General and Census Commissioner, India.

The above figure shows that the District-wise Decadal Growth Rate of Child Population (Age Group 0-6 Years) by Residence in Kerala. It is clear from the table that, all district in kerala having negative growth rate its child population. This phenomenon is an outcome of the demographic transition in the state. This will leads to a The chronic shortage of labour in the state and in future the condition become serious.

Replacement Migration in Kerala

Replacement migration in Kerala simply means that the ones who have gone outside Kerala for job will be replaced by someone who came from outside Kerala. The relatively higher wages, large employment opportunities and shortages of local labours due to mass out migration, the changes in demography and resultant decrease in working age population make Kerala a lucrative job destination for workers from outside the State. This has made Kerala an emerging destination of internal migrants from other states in India, while Kerala continues to sending its own people as workers to the Middle East and Europe. At the same time, Kerala's lagging productive sectors and its major economic activities find a renewal with the current inflow of migrant workers to the state. The diverse roles played by the internal migrants to the state not only in terms supplementing its work force but also in terms of maintaining the vibrancy of state's economy have far reaching socio-economic implications.

In recent years, replacement migrants account for a significant proportion of workers in several sectors, especially among casual labourers in the construction sector. survey based study conducted by Gulati Institute of Finance and Taxation on behalf of the Department of Labour and Rehabilitation, Government of Kerala in 2013 estimated that there are over 25 lakhs inter-state migrants currently employed in the state with an annual arrival rate of 2.35 lakhs. This number constitutes about 9% of the State's total population. Moreover, the study also estimated that about Rs. 17,500 crores move out of the State in the form of remittances made by migrant labourers to their home states annually.

Conclusion

Migration as a component in interpreting demographic structure of the population has not been pronounced till recently. The process of demographic transition has been nearing its final stage, with fertility and mortality levels representing a near perfect replacement level of growth in population. Migration, both internal and international, together with the advances made with regard to demographic transition has undoubtedly been a distinct feature of the state of Kerala. A visible consequence of such distinction is its

share of elderly population which is one of the highest among Indian states (Rajan and Aliyar, 2012). As a result of the demographic transition, decline in working-age population or people to meet the required labour force due to huge out migration along with increasing ageing population etc leads to the process of replacement migration in Kerala. According to the Kerala Migration Survey 2013, Kerala has 2.4 million emigrants compared to 1.4 million in 1998. In the initial phase the emigrants from kerala the migrants are predominantly non-agricultural labourers with low educational attainments. Nevertheless, the emigration of labour did not create any major hurdles and conspicuous deficiencies in the home economy in the early phase, but in later the continuous emigration resulted in a scarcity of labour especially in the construction sector, which was followed inevitably by a hike in the wage rate (Prakash, 1998). Interestingly, at present, Kerala has the highest wage rates among the states in India. The chronic shortage of labour felt in the construction sector in Kerala and the resultant higher wage rates received the attention of workers from other states and they started flocking Kerala in large numbers.

The relatively higher wages, large employment opportunities and shortages of local labours due to mass out migration, the changes in demography and resultant decrease in working age population make Kerala a lucrative job destination for workers from outside the State. At present, the in migrants in Kerala are replacing not only Gulf emigrant workers but also population deficits caused by the rapid fertility decline in Kerala which begun since the late 1960s.

References

Anand, Arun Perumbilavil. "Ageing Population and Replacement Migration: A Case Study of Kerala."

Arun, P. A. and P.A Ajay. "Migrant Labour in Kerala: A Study on Interstate Migrant Workers." PESQUISA-International Journal of *Research. 2(2), (2017). 45-53.*

Joseph, V K. "Factors and Patterns of Migration: The Kerala Experience." Journal of Indian *School of Political Economy. (13), 2001. 55–72.*

Paper to be presented in the 28th International Population Conference of IUSSP to be held at Cape Town, South Africa, October 29- November 4, 2017.

Zachariah, K.C., E.T Mathew and *Rajan, S.Irudaya. "Impact of* Migration on Kerala's Economy and Society." International Migration. 39: 2001 63–87. doi:10.1111/1468-2435.00135.

Zachariah, K. C. and K. P Kannan. "Kerala*'s Gulf connection." Thi*ruvananthapuram: Centre for Development Studies. 2002.

Zachariah, K.C. and R.S. Kurup. "Determinants of Fertility Decline in Kerala, in Tim Dyson and Nigel Grook (Ed). India"s Demo*graphy: Essays on the Contemporary Population." New Jer*sey: Humanities Press. Available at http//: www.popline.org/docs/030352.

Zachariah, K.C. and S. Irudaya Rajan. "Unemployment in Kerala at the turn of the Century: Insights from CDS Gulf Migration Studies." Working Paper 374, Centre for Development Studies (CDS), Thiruvan*anthapuram. 2005.*

Zachariah, K. C. "Demographic Transition in Kerala in the 1980s." Thiruvananthapuram: Centre for Development Studies. 1994.

"Department of Labour and Rehabilitation. Domestic Migrant Labour in Kerala." Thiru*vananthapuram: Government of Kerala. 2013.*

"State Planning Board." Kerala Human Development Report 2016. Thiruvananthapura*m: Government of Kerala.*

*"United Nations Pop*ulation Council. The UN Population Division o*n Replacement Migration. Population and Development Review." 2000, 26, 413-417.*

ejbps, 2017, Volume 4, Issue 10 309-312 Research Article SJIF Impact Factor 4.382

EUROPEAN JOURNAL OF BIOMEDICAL AND PHARMACEUTICAL SCIENCES

http://www.ejbps.com

ISSN 2349-8870
Volume: 4
Issue: 10
309-312
Year: 2017

DETECTION, ISOLATION AND MOLECULAR CHARACTERIZATION OF LEPTOSPIRA FROM SOIL AND WATER SAMPLES OF CENTRAL KERALA

K. J. John[1]*, K. K. Anilkumar[2], Ramesh Kumar[3] and D. Nisha[4]

[1]Research Scholar, Meenakshi University of Higher Education & Research (MAHER), Chennai.
[2]Associate Professor, Department of Microbiology, St.Pius X College, Rajapuram, Kasargod.
[3]Lab Director, EI Lab Metropolis, Ernakulam.
[4]Head of the Department, Serology & Immunology Department, Lab Metropolis, Ernakulam.

***Corresponding Author: K. J. John**
Research Scholar, Meenakshi University of Higher Education & Research (MAHER), Chennai.

Article Received on 23/07/2017 **Article Revised on 13/08/2017** **Article Accepted on 02/09/2017**

ABSTRACT

Leptospirosis has been repeatedly reported from the State of Kerala since 1989 and is one of the commonest diseases among the 14 notifiable diseases in the district level communicable disease surveillance system. As there are no field studies on human leptospirosis in Kerala, we have proposed this sero-epidemiological study of leptospirosis in the Ernakulam district in Kerala to identify locally prevalent serogroups, and to understand local epidemiological features of the disease. In spring of 2015, 75 samples, which includes water samples (50), soil samples (25), were collected from the sewage and paddy field of central part of Ernakulam district located in Kerala. Some parts of agricultural land, which had stagnant waters such as: streams, water channels, were focused to collect sample. Leptospira spp. is to be isolated using culture method and then identified by phenotyping tests. Identification of Leptospiras is possible through culture in the Leptospira Enrichment medium. PCR technique is used to confirm the Leptospira species in all the collected samples. This method is able to differentiate between the saprophytic and pathogenic Leptispiras. The results revealed the ubiquity of Leptospira in the environment and highlight the need to develop formal approaches for systematic monitoring. This study concluded that the collected water and soil samples have only limited significance in the distribution of Leptospira. This study also provides important information regarding the identification of the pathogenic serovars and saprophytic serovars.

KEYWORDS: Leptospirosis, sero-epidemiological, agricultural land, saprophytic, pathogenic.

1. INTRODUCTION

Leptospirosis is a disease caused different strains of bacteria of the genus Leptospira which are related with animals.[1] It is more widespread in the tropical countries. Of all the diversity that causes disease, *Leptospira icterohaemorrhagiae* is the most serious type. If not treated properly, it could lead to severe complications.[2-4] Leptospirosis is a disease of animals that can spread to humans. Rats are common carriers of leptospirosis. Soil contaminated with urine of infected animals can also transmit the disease to humans. All people working as Sewage workers, agricultural workers, butchers, meat inspectors or workers in contact with contaminated waters are generally prone to this disease. Leptospirosis can also be spreaded due to contact with urine, blood or tissues of infected persons.[5,6]

Leptospirosis is a serious emerging disease in Kerala but also there is no technical publication on this.[1-3] Leptospira interrogans is infective as long as it is moist and can remain outside the host in water or moist soil for six months or more. The primary hosts are rodents especially rats.[7,8] Common rats in Kerala are *Rattus rattus*, *Rattus norvegicus*, *Mus musculus*, *Bandicoota indica*, *B. malabaricus*, *B. bengaliensis*, *Nosokia bengaliensis* and *Tetera sp*. *Bandicoots* usually visit drains, sewage canals and roadside water collections after rains and are responsible for urban infections.[9-11] *Mus musculus* are generally found in residential area's store rooms or warehouse infection through edible items. *Rattus rattus* is peridomestic and domestic and has great epidemiological bearing.

Kerala is in the wet tropical area with annual rainfall of above 3000 mm and optimum temperature from 21 to 35°C throughout the year. April and May experience the temperature up to 36°C to 38°C.[12] This mixed type of climate encourage group II epidemiology prototype among residential area, where many hosts act as carriers with multiple serogroups in an limited area and cause disease throughout the year.[13] Industrialized area in contrast has group I epidemiology prototype, where exposure is occupational /recreational, the animal act as reservoir or cause of infecting. Here serogroups are

Table 1: Results of isolates obtained from the collected samples.

Name of the Samples	No. of samples collected	Positive samples	No of isolates obtained	% acheived
Water	50	39	8	78
Soil	25	19	4	76

4. CONCLUSIONS

In Kerala, there are an increasing number of reported leptospirosis cases which led to mortality. The infection is usually spread through the urine of infected animals and may contaminate the environmental soil and water. This study was conducted to conclude the frequency of leptospira species in selected environmental soil and water samples. In conclusion, this study suggests important information concerning the infection levels and identification of the pathogenic serovars and saprophytic serovars. The results obtained suggests that water and soil have only limited significance in the persistence and dissemination of Leptospira in central part of Kerala. Increased awareness, continuous monitoring and efficient preventive measures should be taken by concerned authorities to control the occurrence of leptospirosis.

Author Contributions

The authors have no competing interests with the work presented in this manuscript.

ACKNOWLEDGEMENTS

The authors wish to express their gratitude to RND BIO Solutions and El Lab Metropolis, Ernakulam, for their input, valuable discussions and accessibility.

REFERENCES

1. John TJ, Rajappan K, Arjunan KK. Communicable diseases monitored by Disease Surveillance in Kottayam district, Kerala state, India. Indian J Med Res, 2004; 120: 86-93.
2. Speelman P. Leptospirosis. 16th ed., In: Kasper D L, Braunwald E, Hauser S, Lougo D, Jameson L, Fauci AS, (eds) Harrison's principles of internal medicine, McGraw-Hill Professional, USA, 2005; 988-991.
3. W. H. O. International Leptospirosis. 2003; 23-24.
4. Faine S, Adler B, Bolin C, Perolat P. Leptospira and leptospirosis. 2nd ed., Victoria: Medisci press, Melbourne, Australia, 1999; 138-139p.
5. Kariv R, Klempfner R, Barnea A, Sidi Y, Schwartz E. The changing epidemiology of leptospirosis. Emerg Infect Dis, 2001; 7(6): 990-992.
6. Pappachen MJ, Sheela M, Aravindan KP. Relation of rainfall pattern and epidemic leptospirosis. J Epidemiol Community Health, 2004; 58(12): 1054-1055.
7. Bal AE, Gravekamp C, Hartskeerl RA, De Meza-Brewster J, Korver H, et al. Detection of leptospires in urine by PCR for early diagnosis of leptospirosis. J clin Microbiol, 1994; 32(8): 1894-1898.
8. Ridzlan FR, Bahaman AR, Khairani-Bejo S, Mutalib AR. Tropical biomedicine. detection of pathogenic Leptospira from selected environment in Kelantan and Terengganu, Malaysia. 2010, Trop Biomed; 27(3): 632-638.
9. Laurichesse H, Gourdon F, Smits HL, Abdoe TH, Estavoyer JM, et al. Safety and immunogenicity of subcutaneous or intramuscular administration of a monovalent inactivated vaccine against *Leptospira interrogans* serogroup Icterohaemorrhagiae in healthy volunteers. Clin Microbiol Infect, 2007; 13(4): 395-403.
10. Ananthanarayan R and Panicker CKJ. Textbook of Microbiology. 8th ed. Orient Longman, Hyderabad, 2009; 389-394.
11. Heymann DL. Control of Communicable Diseases (20th edition), Washington: APHA press, USA, 1980; 433 p.
12. Levett PN. Leptospirosis. Clinical Microbiology Review, 2001; 14(2): 296-326.
13. Cohen ML. Resurgent and Emerging Diseases in a changing world. Br Med Bull, 1990; 54(3): 523-532.
14. NICD. Communicable Diseases CD, Alert Newsletter, 1997; Vol 14.
15. W.H.O. The Veterinary Contribution to Public Health, Tech. 1975, Report Series No.573.
16. W.H.O. Bacterial and Viral Zoonosis, Tech. 1982, Report Series No.682.
17. W.H.O. Human Leptospirosis Guidance for Diagnosis, Surveillance and Control, 2003; 92: 4.
18. Yasouri SR, Moghadam RG and Ghane M. Identification of Pathogenic and Saprophytic Leptospira spp from the Rice Fields of Tonekabon Township Using PCR Technique. Adv Stud Biol, 2013; 5(10): 437–445.
19. Koay TK, Nirmal S, Noitie L and Tan E. An epidemiological investigation of an outbreak of leptospirosis associated with swimming, Beaufort, Sabah. Med J Malaysia, 2004; 59(4): 455–459.

Isolation of Leptospira from soil, water, Rodent feces and Blood samples

John K J[1] , Anilkumar K K[2], Rameshkumar[3], Nisha D[4]

Research scholar, Meenakshi University Of Higher Education & Research (MAHER), Chennai
Associate Professor & HOD, Dept of Microbiology, St.Pius X College, Kasargod
Department of Biochemistry, EI Lab Metropolis, Cochin
Department of Microbiology & Serology, EI Lab Metropolis, Cochin

Abstract

Leptospirosis is recurrent epidemic and is one of the commonest diseases among the 14 notifiable diseases in the district level communicable disease surveillance system. As there are no field studies on human Leptospirosis in Kerala, we have proposed this sero-epidemiological study of Leptospirosis in the Emakulum district in Kerala to identify locally prevalent serogroups, and to understand local epidemiological features of the disease. Samples were collected from various sources, which included water samples (50), soil samples (25) feces of the rodents (15) and blood samples, of farmers (30) that was collected from the rice farms located in central part of Emakulum District of Kerala. Since presence of Leptospira was expected in stagnant water bodies agricultural land, that had stagnant waters such as: streams, water channels, were focused to collect sample. Leptospira spp.was isolated using culture method.

Key word: *Leptospirosis, sero-epidemiological, agricultural land, saprophytic, pathogenic*

Introduction

Leptospirosis is a disease caused by different strains of bacteria of the genus Leptospira which are related with animals. It is more widespread in the tropical countries. Of all the diversity that causes disease, *Leptospira icterohaemorrhagiae* is the most serious type. If not treated properly, it could lead to severe complications[1]. Leptospirosis is a disease of animals that can spread to humans. Rats are common carriers of Leptospirosis. Soil contaminated with urine of infected animals can also transmit the disease to humans. All people working as Sewage workers, agricultural workers, butchers, meat inspectors or workers in contact with contaminated waters are generally prone to this disease. Leptospirosis can also be spreaded due to contact with urine, blood or tissues of infected persons [2].

Kerala is in the wet tropical area with annual rainfall of above 3000 mm and optimum temperature from 21 to 35 °C throughout the year. April and May experience the temperature up to 36°C to 38°C[1]. This mixed type of climate encourage group II epidemiology prototype among residential area, where many hosts act as carriers with multiple serogroups in an limited area and cause disease throughout the year[3]. Industrialized area in contrast has group I epidemiology prototype, where exposure is occupational /recreational, the animal act as reservoir or cause of infection. Here serogroups are limited except at the time of any natural calamities. Often every year April to October Kerala gets heavy rains and intermittent floods. Irregular flooding of geographically lower areas show the way to repeated wash out of the forests and farmlands soil and rodent burrows thus wastes reach there into all water resource including streams, ponds, canal and rivers where microbes like *leptospires* can survive for days. This leads to not only monsoon outbreaks but also periodic disease cases throughout the year.

Many reports from Kerala shows the Epidemics of Leptospirosis during monsoon months Pappachen 20043. Emakulam district is situated in central part of Kerala that lies between the Western Ghats and the coastal strip of Arabian Sea. Emakulam district have many streams, ponds and irrigation canals which flowing together during monsoon flooding. These canals are nourishing during dry months by the irrigation project namely the Periyar Valley Irrigation Project. Uninterrupted cultivation of food crops like rice and pineapple provide rodents with enough food that enable them to survive4.

Materials and Methods

Sample collection (Ghane and Yasouri, 2013)

In the season June to December of 2015, 120 samples, which includes water samples (50), soil samples (25), feces of the rodents (15) and blood samples of farmers (30) were collected from the rice farms of CENTRAL part of Emakulam DISTRICT located in KERALA. Parts of agricultural land, which had stagnant waters such as: streams, water channels, were focused to collect sample using 50 ml sterile tubes. Also, soil and feces samples were collected from agricultural lands and transferred to the sterile tubes. For blood culture, heparinized blood was collected and plasma was separated and directly added to culture bottles containing culture medium for leptospires. Then, the samples were transferred to laboratory

Preparation of samples and isolation of Leptospira.

Each one of the water samples into the tube was mixed thoroughly and transferred to 4 sterile short test tubes. Then, the tubes were centrifuged with 4000 rpm for 10 minutes. Surface contents of the tubes were extracted and the liquid was filtered through sterile 0.45 µm bacteria filter to filter out unwanted microorganisms. Since Leptospira pass through the filter they were expected in the filtrate collected in 1.5 ml Micro tube. This samples were then, aseptically inoculated in to liquid Leptospira Enrichment medium.

The soil sample was first transformed into phosphate buffered saline, mixed well, filtered through sterile bacteria filter. Filtrate was and transferred to the Leptospira Enrichment medium and incubated at 30°C for 15 days. After incubation , contents of liquid Leptospira Enrichment medium were inoculated in to the solid Leptospira Enrichment medium with sterile loop. Again, plates were incubated at 30°C incubator for 15 days.

20–40 drops (500–1000 µl) of plasma from heparinized blood were transferred into tubes containing 9 ml of Leptospira enrich liquid medium. Cultures were incubated at 30°C and examined weekly. After incubation time, contents of liquid Leptospira Enrichment medium were inoculated in to the solid Leptospira Enrichment medium. Plates were then incubated at 30°C for 15 days.

Identification of pathogenic species of Leptospira with Beta Hemolysis of Blood Agar (Iola et al (1979), and palmer et al., (2000)

The production of hemolysin by some strains of pathogenic *Leptospira* sp., were also studied using blood agar. After streaking of culture, the plates were sealed and incubated aerobically at 30°C until colonies became visible (2 to 3 weeks). A blood agar overlay method was used due to the long incubation period required for obtaining colonies. After the overlay solidified, plates were incubated at 30°C until small, clear zones of hemolysis appeared surrounding individual colonies (24 to 48 h). The plates were transferred to the cold (4°C) for 12 h and then reexamined for zones of hemolysis.

Results

Out of the fifteen fecal samples two isolates were obtaind,from fifty water samples eight isolates were obtained and from twenty five soil samples four isolates were obtained. They were preserved as pure cultures in blood agar and nutrient agar plates respectively. Similarly from 30 blood samples five cultures were isolated and maintains as pure culture.

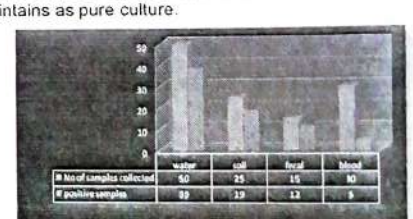

Discussion & Conclusion

Leptospirosis has become the most commonly reported notifiable communicable disease in Kerala[1]. Since 1989 several cases of *Leptospirosis* have been diagnosed among the local people here[2,3]. Monthly reports of the District Medical Officer, Ernakulam, shows an 20 confirmed Leptospiral deaths in the year 2006. There might be many more unreported and unconfirmed cases too. Most of the patient history of subjects says that the major occupations of these families are agriculture and animal rearing. Depending on the level of exposure of organism, Leptospiral infection may be subclinical or clinical depending. So the identification and characterization of the subspeciacies are of utmost importance.

Reference:

1. John, T. J, Rajappan K, Arjunan KK. (2004) "Communicable diseases monitored by Disease Surveillance" 120 86-93
2. Speelman, P (2005) "Leptospirosis" In: Kasper, D. L, Fauci, A. S, Braunwald, E, Longo, D. L, Hauser, S. L, Jameson, J. L, editors. *Harrison's principles of internal medicine* 16th ed p 988-91
3. W.H.O. (1982) "Bacterial and Viral Zoonosis" Tech. Report Series No 682
4. W.H.O. (2003) Human Leptospirosis: Guidance for Diagnosis, Surveillance and Control Vol 92 No.4

ISOLATION OF AMYLASE PRODUCING BACTERIA FROM BIOGAS PLANT SYSTEM

SHARATH KRISHNAN PV, Dr. K.K ANILKUMAR
DEPARTMENT OF MICROBIOLOGY, St. PIUS X COLLEGE

ABSTRACT:

Amylase is an enzyme obtained from the microbes has been used by many industries for production of foods and beverages. With the utilization of microorganisms it is possible to produce this enzyme in large scale and also easily manipulated it for desired purposes in general, enzymes produced from fungal and bacterial sources have many applications in industries. The main objective of the present Study Concentrated on isolation of Bacteria from different layers of Biogas plant and a preliminary assessment on their amylolytic activity. In this study the Bacteria sample from Biogas plant in the college canteen were collected from different depth after keeping it undisturbed for 24hrs using a "Sample Collector". Then the collected sample were first streaked onto Nutrient Agar plates to isolate pure colonies from the samples in this study. Twenty isolates were obtained from 5 different samples A, B, C, D and E that was collected from different depths of biogas plant. From sample A, 4 isolates were obtained and that was named as A1, A2, A3 and A4. From sample B, 5 isolates were obtained and they were named as B1, B2, B3, B4, and B5. From sample C, 2 isolates were obtained and was named C1 and C2. 5 isolates obtained from sample D were named as D1, D2, D3, D4 and D5. 4 isolates obtained from sample E was named as E1, E2, E3 and E4. All the Twenty cultures were isolated on Starch Agar media. Out these twenty isolates only 7 cultures (B2, B3, B4, C2, D2, D3 and D4) was showing amylolytic activity. From the sample A and E none of the isolates were amylolytic. Efficiency of starch hydrolysis are evaluated by the diameter of zone of hydrolysis produced by each isolate. Gram's iodine was used to identify the Amylase activity. The Gram Staining for the Seven Isolates were also done. Moreover, Colony Characteristics of each of the seven isolates were analyzed and its Biochemical Tests were also done. The effects of Temperature on Bacteria Culture Growth were also studied by incubating Bacterial culture in Room temperature and Temperature above 45 degree Celsius and results were noted. Out of the Seven isolates that was obtained Five isolates were Cocci Species(Gram positive Cocci) and Two isolates were Bacillus species(One was Gram -ve and other one was Gram +ve). From the Study it was noted that Amylase producing Bacteria were absent at 1 metre depth and at 2.00 cm depth indicating Amylase activity mainly occurs in mid region of the Biogas plant. All the Isolates didn't survived at Temperature more than 45 degree Celsius. This indicated that Amylase producing Bacteria needs an Optimum Temperature to show its greatest activity.

OBJECTIVE OF STUDY:

The biogas plants which are fed mainly with kitchen waste, which is rich in starch, should have amylase producing organisms for the utilization of these rich carbon and energy source. The commercial importance of amylase enzyme makes it valuable to look for new amylase producers from biogas plants that are fed with kitchen waste. In the light of this following objectives are selected for the present study. Thus the Primary objective of this study is to isolate bacteria which have amylolytic activity from samples collected from different depths of biogas plant. Second objective is to compare and analyze the diversity of amylase producers isolated from various levels of sample collected. The third objective is to study their morphological and biochemical characters. The fourth objective of the study is to analyze influence of temperature on the growth of these isolates.

Thus the main objective of the present study concentrates on isolation of bacteria from different layers of Biogas plant and a preliminary assessment on their amylolytic activity.

BIOGAS PLANT

SAMPLE COLLECTOR

ISOLATES SHOWING AMYLOLYTIC ACTIVITY

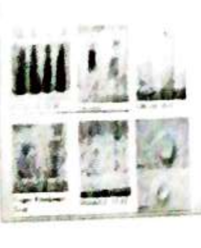

BIOCHEMICAL TEST RESULTS

METHODS:

Biogas plant that was established in the college campus five years back was used as the source of sample for the present study. Since this biogas plant is running on college canteen waste this will be regularly introduced with starchy materials thus will be a natural enrichment system for amylolytic microorganisms.

SAMPLE COLLECTION

In order to collect the samples from the Biogas Plant a Sample Collector was designed which was composed of a 2metre long PVC pipe that can be inserted in to the biogas plant. On this pipe 5 polythene tubes with 3mm diameter was attached with the help of tags. The polythene tubes were of different lengths so that sample can be obtained by sucking out from different depths of the biogas plant. The polythene tubes were of different length i.e. from A(1m), B(0.8m), C(0.6m),D(0.4m) and E(0.2m). The free end of the polythene tubes were closed by tags that was removable whenever it required. It was tagged so to make the polythene tubes air tight and thus preventing the entry of sample in to the tube. A stone with a weight of 50 grams was tied at the tip of the PVC pipe so that it remains immersed in the biogas tank at standstill. Thus samples from different depth were collected.

ISOLATION OF MICROORGANISMS

The serial dilutions all five samples (A, B, C, D and E) in the ratio 1/10,1/100 and 1/1000 were made. 1ml each of aliquots was added into sterile plates and pour plate was performed. Parallel to that samples were also streaked onto nutrient agar plates to get isolated pure colonies of bacteria present in the samples. All the isolates obtained by streaking them in Nutrient Agar were Gram Stained. The colony characters of the isolates were noted further subjected to various biochemical tests and culture characteristic analysis.

SCREENING OF POTENTIAL AMYLASE PRODUCING BACTERIA AND USING STARCH HYDROLYSIS TEST

All bacterial strains were isolated from Biogas plant system by using serial dilutions. From each of Test tubes, 0.1 ml was transferred into Starch Agar plates. Then, the sample was distributed evenly by using L-shaped glass rod and incubated at normal room temperature for 24hrs. After incubation period, colonies were further sub-cultured on the respective medium to obtain pure isolates and they were maintained in a refrigerator for further investigation. The isolates were screened for amylolytic activity by streaking on the starch agar plates and incubated at normal room temperature for 24 hrs. Plates were observed for starch hydrolysis. Iodine solution was flooded on the starch agar plates on which starch hydrolysis was suspected. After 30s plates observed for colorless area around the colony in a dark blue background due to the starch iodine reaction. Presence of clear zone around the growth of isolates were considered as amylase producers and subcultured on starch agar slants for further investigation.

Study on Influence of Temperature on the Amylolytic Activity of Bacteria

The pure cultures of the isolates that showed amylolytic activity in the Starch Agar plates were further streaked on the newly prepared Starch agar plates. These plates were placed on the incubator in temperature range 45°C and kept it for 24hours and the results were observed and noted down.

RESULT AND DISCUSSION:

From the present isolation and Screening of the biogas Sample it was evident that Biogas Plant is Rich in Amylase Producing Bacteria. Out of the 20 isolates 7 were showing amylolytic activity, which means about 35 % are amylase producers. Moreover 4 out of this 7 amylolytic isolates were from the upper middle layers of the biogas plant. The results shows that deepest layers, sample A, do not have any amylolytic organisms. Absence of amylolytic bacteria from that sample is very much in agreement with the expected result. As per the biochemical events the deepest parts of biogas plant is the place where methanogens dominate and the final steps of methane production take place. Depolymerization, acidogenesis and acetogenesis may have completed before the methane production. Thus starch like biopolymers will be scare in such layers. Similarly samples from the uppermost layers, sample E, was also having no amylolytic organisms. This may be due to the availability of readily usable simple sugars that promote yeast and sugar fermenting organisms thus competitively excluding starch hydrolyzing bacteria. However this can only be confirmed by analyzing the availability of free sugars and density of microorganisms that can rely totally on such carbon source. Isolates obtained from sample D, which is the uppermost middle layer (0.4M), showed best amylolytic activity. Four out of five isolates were amylase positive and isolate D3 and D2 showed maximum activity (maximum zone of starch hydrolysis). These isolates showed 38mm and 37 mm respectively that is the highest zone of starch hydrolysis among the positive samples. This shows that amylolytic activity is maximum in this layer and most efficiently starch hydrolysis take please here. One out of two isolates obtained from layer C, which is the middle layer (0.6M), was amylase positive. The hydrolytic activity was also good but less than that of the isolates from sample D (34mm). Three out of Four isolated from the sample B, which is from the lower middle layer/ upper bottom layer, showed amylolytic activity. However the efficiency of these isolates is lesser in comparison with the isolates from other samples. 26mm, 31 mm and 34mm starch hydrolysis zone for B2, B3 and B4 respectively. We can observe that there is a gradual decrease in the starch hydrolytic efficiency of the isolates obtained from upper to lower layers. This may be due to the concentration of starch molecules may be getting decreased in the lower layers. As per the results obtained by the biochemical test conducted for all the amylase positive isolates all of them were motile. VP, citrate and coagulase negative. MR test was positive for B2, B3, C2 and D2. Urease test was found to be positive for B2, B4 and D3 isolates. Except D2 and D4 all other isolates were catalase positive. B2 and B3 were found to be oxidase negative and all other isolates were positive for oxidase test. This may be an indication of their aerobic nature.

Effect of temperature on amylase activity

Temperature is one of the environmental factors for amylase production which is usually varies from one organism to another. In the present study, maximum amylase activity was observed normal Room Temperature i.e. in the range 37-40°C. The result also showed a positive correlation between the amylase activity and the incubation temperature up to normal room temperature, followed by a gradual decrease. At higher temperature i.e. in 45°C, bacterial growth got suppressed and consequently amylase activity was also inhibited. The isolates grown well and revealed high amylase activity in the temperature ranged from 35 to 40°C. Thus it was shown the present study that all the amylase producing bacteria obtained from Biogas plant system are not Thermoduric and further more they are mesophilic in nature.

ACKNOWLEDGEMENT

I am highly obliged and express my profound sense of gratitude to my project supervisor Dr. K.K Anil Kumar (HOD, Department of Microbiology) for his incessant supervision, continues support, and illuminating guidance, throughout the period of this work and for providing necessary facilities for the project work.

I express my sincere gratitude towards Dr.Sarala Gopalakrishnan, Associate Professor, Department of Microbiology and Dr. N.V Vinod, Assistant Professor, Department of Microbiology, St.Pius X[th] College, Rajapuram for the resources and support provided to gain experience in this field of study.

I am obliged for the support received from Mr.Shelvin T Kuriakose, Guest Lecturer, Department of Microbiology St.Pius X[th] College Rajapuram.
I am thankful to my Lab assistant Smt.Elsamma V.J for providing me with all the necessary Lab equipments as and when required.

I would also like to unfold my gratitude to my classmates who have been with me throughout my work thereby helping me to complete my work on time.

CONTACT

SHARATH KRISHNAN PV
EMAIL : [illegible]

Dr. K.K ANILKUMAR
EMAIL : [illegible]

ISSN 2320-5407 International Journal of Advanced Research (2015), Volume 3, Issue 6, 792-797

Journal homepage: http://www.journalijar.com

INTERNATIONAL JOURNAL OF ADVANCED RESEARCH

RESEARCH ARTICLE

Predisposing factors in Polycystic Ovarian Syndrome for Cardiovascular disease

*** Deepthi T[1], Jiju JS[2], Aswathy Sundaresh[2], Sharmila K[2], Sarala Gopalakrishnan[3], Abdul Gafoor C[4], Jeyapal V[4] and Dinesh Roy D[4]**

1. Department of Medical Microbiology, Sree Gokulam Medical College, Thiruvananthapuram- 695607, Kerala.
2. Research Scholars, Meenakshi University, West K K Nagar, Chennai- 600078, TN.
3. Department of Microbiology, St. Pius X College, Kasargod- 671532
4. Genetika, Centre for Advanced Genetic Studies, Pettah P O, Thiruvananthapuram-695 024, India.

Manuscript Info

Manuscript History:

Received: 14 April 2015
Final Accepted: 22 May 2015
Published Online: June 2015

Key words:

Cardiovascular disease, DNA repair, Lipid profile, Mean break per cell value, Obesity, Polycystic ovarian syndrome.

Corresponding Author

Deepthi T

Abstract

Polycystic ovarian syndrome (PCOS) is a heterogeneous, multifactorial, complex genetic and endocrine disorder, characterized by menstrual disturbances, clinical and biochemical manifestations of hyperandrogenism and polycystic ovaries. It is a common endocrinopathy affecting 6–10% of reproductive aged women. 28 infertile women were selected as study subjects and 25 asymptomatic healthy fertile women as control subjects in this study. The goal of the present study was to evaluate the predisposing risk factors leading to cardiovascular disease (CVD) in subjects with polycystic ovarian syndrome. Various biochemical parameters such as blood sugar, lipid profiles and hormones such as Follicle Stimulating Hormone (FSH) and Luteinizing Hormone (LH) were assessed in the sera of all these subjects. Decreased high density lipoprotein (HDL) and elevated levels of all other biochemical and endocrinological parameters were observed in the study subjects. Elevated level of break per cell value (b/c) in the study subjects along with the above parameters and raised body mass index (BMI) is suggestive of increased risk of CVD in PCOS. The findings imply that there is a strong evidence for increased risk of developing CVD in subjects suffering from PCOS. Lifestyle modifications by increasing physical exercise and dietary control will help in modifying the CVD risk factors in PCOS.

Introduction

Polycystic ovary syndrome (PCOS) is a heterogeneous, multi-factorial, complex genetic and endocrine disorder, characterized by menstrual disturbances, clinical and biochemical manifestations of hyperandrogenism and polycystic ovaries (Witchel, 2006). It is a common endocrinopathy affecting 6–10% of reproductive aged women (Azziz et al., 2004).

PCOS is associated with 10 fold risk for developing type 2 diabetes in adulthood (Nestler, 2008) and 2 fold increased rate of metabolic syndrome (Essah et al., 2007). According to a recent study, more than half of adolescent PCOS patients had high density lipoprotein levels below the normal reference range for their sex (Bekx et al., 2010) which is a strong predictor of future cardiac risk. PCOS is the most common endocrinopathy in women of reproductive age, with a prevalence ranging from 5 to 10% in the general population and almost 30% among obese women (Azziz et al., 2004; Alvarez et al., 2006).

PCOS is associated with an approximately 7-fold increased risk of type 2 diabetes mellitus (DM) (Jakubowski, 2005). Insulin resistance (IR) and pancreatic β cell dysfunction are major risk factors for the development of type 2 DM. Defects in insulin action and insulin secretion are critical determinants in the pathogenesis of glucose intolerance in PCOS and both are influenced by genetic and environmental factors (Carmina, 2009). Women with PCOS are predisposed to develop Impaired Glucose Tolerance (IGT) and type 2 diabetes mellitus (Legro et al., 1999). Obesity, insulin resistance, and impaired pancreatic cell function contribute to this predisposition. In addition to these recognized factors, racial origin and the presence of type 2 diabetes in a first degree relative influence the risk of glucose intolerance, although this issue has been examined in a limited number of studies involving women with PCOS (Yildiz et al., 2003).

Dyslipidemia is a disorder of lipoprotein metabolism, including lipoprotein overproduction or deficiency. These changes may be manifested by the elevation of serum total cholesterol (TC), low density lipoprotein (LDL) cholesterol and triglycerides (TG) concentration and a decrease in the high density lipoprotein (HDL) cholesterol concentration. As compared to women without PCOS, 85% of PCOS women have dyslipidemia characteristic of the metabolic syndrome. Obesity has an important influence on the lipid profile with approximately 50% of patients with PCOS being overweight or obese with abdominal fat accumulation. Insulin is positively correlated with total cholesterol, LDL and TG, and negatively correlated with HDL in IR patients. Dyslipidemia was found to be a major prognostic risk factor for cardiovascular disease (Legro et al., 1999).

PCOS is classically associated with an atherogenic lipoprotein profile, characterized by elevated triglyceride rich lipoproteins, accumulation of small dense LDL and depressed HDL. All these changes were reported to be due to insulin resistance, although elevated androgens may contribute to small HDL size by stimulating hepatic lipase activity (Rajkhowa et al., 1997). Early subclinical atherosclerotic disease, as evidenced by carotid intimal media thickness (Talbott et al., 2000) and increased coronary artery calcification (Talbott et al., 2004) were reported in women with PCOS. Studies had shown the association of PCOS with hyperinsulinemia and IR which may lead to CVD (Carmina, 2009; Shaw et al., 2008).

Menstrual cycle irregularity may be a marker of metabolic abnormalities predisposing women to an increased risk for cardiovascular disease (CVD). The most well known correlation between metabolic syndrome and reproductive disorders is in women with PCOS. IR is the most common metabolic abnormality in PCOS patients followed by obesity and dyslipidemia with an incidence of 31.5% for the metabolic syndrome (Zeyneloglu et al., 2006). The major risk factors leading to the metabolic syndrome or cardiovascular dysmetabolic syndrome are physical inactivity and an atherogenic diet, and the cornerstone clinical feature is abdominal obesity or adiposity (Lahbadia et al., 2008).

The PCOS is a familial disorder, but the genetic basis of the syndrome remains controversial. Determining the mode of inheritance of this syndrome is difficult because there has been no clearly described male phenotype and because it is a disorder that affects principally women of reproductive age there is now a larger focus on the management of the metabolic outcomes of PCOS, essentially through lifestyle intervention to achieve weight loss and developing physical activity (Carey et al., 1993). There are only few studies concerning the association between phenotypic expression, body make up and PCOS, and association with the processes of sexual maturation, growth and various environmental factors (stress, nutrition, physical activity and other factors). There is a lack of information about further PCOS development and prognosis, considering the environmental and individual factors. Hence the present study was undertaken to evaluate the various CVD risk factors and their DNA repair efficiency in women with PCOS by investigating the endocrinological, biochemical and genetic influence (Zabuliene and Tutkuviene, 2010).

Materials and Methods

Twenty eight infertile women in the age group of 17 to 37 years with a clinical diagnosis of PCOS referred from various gynecology and infertility centers of Kerala formed the test group of this study. Twenty five asymptomatic age matched healthy fertile women in the age group of 17 to 35 years formed the control group. Informed consents were obtained from all the subjects of the study according to the norms laid down by the institutional ethical committee.

Eight ml of venous blood was collected aseptically from all the subjects by venepuncture after overnight fasting. 3 ml of blood was collected in sodium heparinised vacuutainers and mutagen induced bleomycin sensitivity assay was performed as described by Hsu et al., 1997. The remaining 5 ml of blood was allowed to clot and serum separated immediately. Blood sugar and lipid profile were estimated using semi-automated clinical chemistry analyzer. The

level of the serum lipid peroxide marker, malondialdehyde (MDA) was determined using thiobarbituric acid as main reagent by measuring these values on photoelectric colorimeter at 540nm.

For mutagen sensitivity analysis, set up the lymphocyte cultures using RPMI 1640 as the medium supplemented with 15 % fetal bovine serum, 10µg/ml phytohaemagglutinin. 0.03 units/ml of bleomycin treatment was given 6 hrs before harvesting to induce chromosome breakage. At the end of 70th hour, the culture was treated by colchicine (0.04µg/ml) to arrest the cell division at metaphase. Then the culture was incubated for 72 hours at 37^{0}C. For mutagen sensitivity, the slides were stained with Giemsa and look for chromosomal lesions such as breaks, gaps, accentric fragments, ring chromosome etc, were also scored. The frequency of chromatid breaks were considered as a measure of an individual's DNA repair capacity. For chromosome sensitivity analysis the mean number of break per cell (b/c) was calculated. The frequencies of breaks were expressed as b/c for comparison. Any individual expression <0.8 was considered hyposensitive, between 0.8 and 1.0 as sensitive and those >1.0 was considered hypersensitive. A minimum of 100 metaphases per culture was scored and data were analyzed.

Result

Table (1)
Demographic and anthropometric characteristics of the Study and Control subjects

Category		Study		Control	
		N	%	N	%
Age range	≤20	7	25%	4	16%
	21 to 30	8	28.57%	15	60%
	>30	13	46.42%	6	24%
Birth order	1 to 3	27	96.42%	19	76%
	>3	1	3.57%	6	24%
Place of residence	Rural	13	46.42%	15	60%
	Coastal	2	7.14%	2	8%
	Urban	13	46.42%	8	32%

The demographic and anthropometric characteristics of the study and the control subjects were given in the table 1. The age of study subjects in the current study ranged from 17 to 37 years with a mean age of 28. The age of the control subjects ranged from 17 to 35 years with mean age of 27.08. The birth order of study subjects ranged from 1 to 5 and the majority of study subjects belonged to group 1 to 3 followed by others. Majority of the study subjects belonged to both rural (n=13; 46.42%) and urban (n=13; 46.42%) followed by coastal area. 16 subjects had sedentary type of occupation and 12 have non- sedentary type of occupation. The mean b/c value (0.802) was higher in urban area. Among the twenty eight study subjects, 16 subjects (57.14%) had irregular menstrual period and 12 subjects (42.85%) had regular menstrual period. The irregular menstrual period had higher chance of infertility. Also, 13 of the study subjects showed (46.42%) menarche at the age of ≤12 and 15 subjects showed (53.57%) menarche at the age of ≥13. The body mass index of the infertile women with PCOS was found to be higher than that of the age matched control subjects which indicate that BMI is commonly associated with PCOS.

The following biochemical evaluations revealed a statistically significant difference between the study subjects and the control subjects. The mean total cholesterol was found to be 195.82 mg/dl in study subjects and 190.28 mg/dl in the control subjects and this difference had statistical significance. The HDL value was found to decrease with increasing b/c value in the PCOS patients. A statistically significant difference was observed among the study and control subjects. In the case of LDL value and triglyceride, it was found to be increased with increasing b/c value.

The following hormones also revealed a statistically significant difference between the study subjects and the control subjects. FSH, LH, prolactin and estradiol showed a statistically significant difference. The mean value of FSH among the study subjects and control subjects was 24.89 IU/mL and 9.72 IU/mL respectively. The follicle stimulating hormone was increased in PCOS patients. The prolactin level was 27.35 ng/ml and 17.11 ng/ml respectively for the study and control subjects. The mean LH level was 52.61 IU in study subjects and 15.9 IU in control subjects. The LH was also found to be increased in PCOS patients.

Table (2)
Distribution of mean b/c value and MDA value among the Study and Control Subjects

Category	Number	Mean b/c value	MDA value
Study	28	0.7919	1.6
Control	25	0.7203	0.86

Among the 28 study subjects the mean break per cell value was found to be 0.7919 and that of control subjects was 0.7203. This indicates that the subjects with PCOS had a defective DNA repair capacity / DNA damage than the control subjects. Thus there is an increased chance of DNA damage and defective DNA repair system with increased severity of risk factors among the PCOS subjects than control subjects.

Discussion

Polycystic ovarian syndrome (PCOS) is a common endocrinopathy affecting 6–10% of reproductive aged women (Azziz et al., 2004) and manifested by hyperandrogenism, ovulatory dysfunction, and polycystic ovaries in its complete phenotype (Azziz et al., 2006). Although evidence for cardiovascular events in women who were affected by PCOS during fertile age is limited, available data suggest more frequent cardiovascular disease (CVD) in classic PCOS (Carmina, 2009). More than 50% of PCOS patients have metabolic syndrome, including obesity, insulin resistance and dyslipidemia.

With increased adiposity in two thirds of American PCOS women (Azziz et al., 2009), the degree to which obesity and PCOS interact to promote premature atherosclerosis and increase cardiovascular mortality is a worldwide concern (Shaw et al., 2008; Christian et al., 2003).

PCOS is characterized by chronic anovulation (failure or absence of ovulation) and hyperandrogenism (excessive production of male hormones in women) with clinical manifestations of irregular menstrual cycles, infertility, hirsutism, and acne (Kahn and Gordon, 1999) which is a common condition affecting women of reproductive age in 5 to 10% (Carmina and Lobo, 1999). Schuring et al., (2008) reported that the elevated GnRH pulses further increase LH level and reduce FSH, which converts excess androgen into estrogens via aromatase activity in normal women. The present study is not in agreement with this report as the mean FSH level in the study group was significantly higher than that of the controls.

Charnvises et al., (2005) reported that menstrual irregularity is the most common gynecological presentation of PCOS, oligomenorrhea being observed in approximately 85–90% of women with PCOS, while as many as 30–40% of amenorrheic patients have PCOS. This fact is supported by the present study that 57.14% of study subjects showed irregular menstrual periods. Jamal and Ozgur, (2006) reported that long term hyperinsulinemia in humans, as is the case in PCOS patients, stimulates leptin secretion from adipose tissue (Conn et al., 2000). Although both insulin resistance and hyperinsulinemia have significant pathogenic roles in PCOS, women with hyperinsulinemia are not necessarily all hyperandrogenic and only 52% of those with type 2 diabetes mellitus have clinical manifestations of androgen excess.

Essah et al., (2008) reported that there is some evidence of a more atherogenic lipid profile (increased levels of TC, LDL cholesterol and triglycerides, and decreased levels of HDL cholesterol) among women with certain ovulatory disorders, specifically among women with PCOS. The present study also observed elevated levels of triglyceride and low density lipoprotein and decreased level of high density lipoprotein. These findings imply the fact that women with PCOS have certain predisposing factors for developing cardiovascular disease.
Balen et al., (1995) and Kiddy et al., (1990) reported that obesity and excess weight are major chronic diseases in Western world countries. Obesity increases hyperandrogenism, hirsutism, and infertility and pregnancy complications both independently and by exacerbating PCOS. Thus the present study suggests that obesity has become one of the major factors not only for both metabolic syndrome and cardiovascular disease; but also for PCOS.

Conclusion

The clinical abnormalities observed in the study subjects with PCOS include irregular menstruation, obesity and type 2 diabetets mellitus. The mean break per cell value of study subjects were significantly higher than that of control subjects, indicating that the subjects with PCOS showed a defective DNA repair capacity. The anthropometrics and demographic characteristics of the present study revealed that the life style factors like lack of physical exercise, increased lipids, obesity and poor glycemic control may contribute significantly to PCOS. The present study found a diabetogenic pattern in PCOS subjects to develop IGT or Type 2 DM by the later stages of life. The findings imply that there is a strong evidence for increased risk of developing CVD in subjects suffering from PCOS. Life style modification by increasing physical exercise and dietary control will help in modifying the CVD risk factors in PCOS.

References

[1] **Witchel, SF., (2006).** Puberty and polycystic ovary syndrome. Mol Cel Endocrinol 254–255:146–53. 243.

[2] **Azziz, R., Woods, K.S., Reyna, R., Key, T.J., Knochenhauer, E.S. and Yildiz, B.O. (2004).** The prevalence and features of the polycystic ovary syndrome in an unselected population, J Clin Endocrinol Metab 89: 2745–2749.

[3] **Nestler, J.E., (2008).** Metformin for the treatment of the polycystic ovary syndrome. N Engl J Me 358, 47–54.

[4] **Essah, P.A., Wickham, E.P. and Nestler, J.E. (2007).** The metabolic syndrome in polycystic ovary syndrome. Clin Obstet Gynecol 50: 205- 225 125.

[5] **Bekx, M.T., (2010).** Connor EC, Allen DB, Characteristics of adolescents presenting to a multidisciplinary clinic for polycystic ovarian syndrome, J Pediatr Adolesc Gyneco l23, 7–10.

[6] **Alvarez-Blasco, F., Botella-Carretero, J.I., San Millan, J.L., Escobar- Morreale, H.F. (2006).**Prevalence and characteristics of the polycystic ovary syndrome in overweight and obese women, Arch Intern Med 166, 2081–2086.

[7] **Legro, R., Kunselman, A., Dodson, W. and Dunaif, A. (1999).** Prevalence and predictors of risk for type 2 diabetes mellitus and impaired glucose tolerance in polycystic ovary syndrome: a prospective, controlled study in 254 affected women. J Clin Endocrinol Metab 84:165–169.

[8] **Jakubowski, L. (2005).** Genetic aspects of polycystic ovary syndrome, Endokrynol Pol 56, 285–93.

[9] **Carmina, E. (2009).** Cardiovascular risk & events in polycystic ovary syndrome, Climateric 12 (Suppl 1): 22–25.

[10] **Yildiz, B.O., Yarali, H., Oguz, H. and Bayraktar, M. (2003).**Glucose intolerance, insulin resistance, and hyperandrogenemia in first degree relatives of women with polycystic ovary syndrome. J Clin Endocrinol Metab 88: 2031–2036.

[11] **Rajkhowa, M., Neary, RH., Kumpatla, P., et al., (1997).** Altered composition of high density lipoproteins in women with the polycystic ovary syndrome. J Clin Endocrinol Metab 82: 3389–94

[12] **Talbott, E.O., Guzick, D.S., Sutton-Tyrrell, K., et al., (2000).** Evidence for association between polycystic ovary syndrome and premature carotid atherosclerosis in middle-aged women, Arterioscler Thromb Vasc Biol 20: 2414–2421.

[13] **Talbott, E.O., Zborowski, J.V., Rager, J.R., Boudreaux, M.Y. et al., (2004).** Evidence for an association between metabolic cardiovascular syndrome and coronary and aortic calcification among women with polycystic ovary syndrome, J Clin Endocrinol Metab, 89:5454–5461.

[14] **Shaw, L.J., Bairey Merz, C.N., Azzi,z R., Stanczyk, F.Z., Sopko, G., et al., (2008).** Postmeno-pausal women with a history of irregular menses and elevated androgen measurements at high risk for worsening cardiovascular event-free survival: results from the national institutes of health—national heart, lung, and blood institute sponsored women's ischemia syndrome evaluation. J Clin Endocrinol Metab, 93:1276-1284.

[15] **Zeyneloglu, H.B. and Esinler. I. (2006).** Chronic complications of polycystic ovary syndrome, In: Allahbadia GN, Agrawal R, Editors. Polycystic Ovary Syndrome, UK: Anshan Publishers P-102–12

[16] **Lahbadia, G.N. and Merchant, R. (2008).** PCOS in the Indian Subcontinent. Semin Reprod Med 26: 22–34. 6.

[17] **Carey AH, Chan KL, Short F, White DM, Williamson R., Franks S.,** Evidence for a single gene effect causing polycystic ovaries and male pattern baldness. Clin Endocrinol (Oxf) 1993; 38:653-8

[18] **Zabuliene, L.1. and Tutkuviene, J. (2010).** Body composition and polycystic ovary syndrome 46(2):142-57.

[19] **Azziz, R., Carmina, E., Dewailly, D., Diamanti-Kandarakis, E. et al., (2006).** Positions statement: criteria for defining polycystic ovary syndrome as a predominantly hyperandrogenic syndrome: an androgen excess society guideline. J Clin Endocrinol, Metab 91:4237 –4245.

[20] **Azziz, R., Carmina, E., Dewailly, D., Diamanti-Kandarakis, E. et al., (2009).** The androgen excess and PCOS society criteria for the polycystic ovary syndrome: the complete task force report. Fertil Steril 91:456–488.

[21] **Christian, R.C., Dumesic, D.A., Behrenbeck, T., Oberg AL., et al., (2003).** Prevalence and predictors of coronary artery calcification in women with polycystic ovary syndrome. J Clin Endocrinol Metab 88:2562–2568.

[22] **Kahn, J.A. and Gordon, C.M.** (1999). Polycystic Ovary Syndrome. Adolesc Med 10:321–336.

[23] **Carmina, E., Lobo, RA. (1999).** Polycystic Ovary Syndrome (PCOS): arguably the most common endocrinopathy is associated with significant morbidity in women. J Clin Endocrinol Metab 84:1897–1899. 42.

[24] **Charnvises, K., Weerakiet, S., Tingthanatikul, Y., Wansumrith, S., Chanprasertyothin, S. and Rojanasakul, A. (2005).** Acanthosis nigricans: clinical predictor of abnormal glucose tolerance in Asian women with polycystic ovary syndrome, Gynecol Endocrinol 21, 161–4.

[25] **Jamal, K. and Ozgur, K.** (2006). Predictors of dyslipidemia in women with polycystic ovary syndrome. In: Allahbadia GN, Agrawal R, Editors. Polycystic Ovary Syndrome, UK: Anshan Publishers 193–202.

[26] **Conn, J.J., Jacobs, H.S., and Conway, G.S., (2000).** The prevalence of polycystic ovaries in women with type 2 diabetes mellitus. Clin Endocrinol (Oxf); 52:81–6

[27] **Essah, P.A., Nestler, J.E., and Carmina,** E. (2008). Differences in dyslipidemia between American and Italian women with polycystic ovary syndrome, J Endocrinol Invest 31,35–41.

[28] **Balen, A.H., Conway, G.S., Kaltsas, G., Techatrasak, K., Manning, P.J., West. et al., (1995).** Polycystic ovary syndrome, The spectrum of the disorder in 1741 patients, Hum Reprod 10(8), 2107-11.

[29] **Kiddy, D.S., Sharp, P.S., White, D.M., Scanlon, M.F., Mason, H.D., Bray, C.S., Polson, D.W., Reed, M.J., and Franks, S. (1990).** Differences in clinical and endocrine features between obese and non-obese subjects with polycystic ovar syndrome: an analysis of 263 consecutive cases, Clin Endocrinol (Oxf) 32, 213-220.

ISSN 2320-5407 International Journal of Advanced Research (2015), Volume 3, Issue 6, 984-989

Journal homepage: http://www.journalijar.com

INTERNATIONAL JOURNAL OF ADVANCED RESEARCH

RESEARCH ARTICLE

Genetic Instabilities and Oxidative Stress in Congenital TORCH Infected Children

* Swapna C Senan[1], Aswathy Sundaresh[2], Jisha P[3], Sarala Gopalakrishnan[4], Anjali K[5], Dinesh Roy D[5]

1. Department of Medical Microbiology, Sree Gokulam Medical College, Thiruvananthapuram- 695607
2. Department of Medical Biochemistry, Sree Gokulam Medical College, Thiruvananthapuram- 695607
3. School of Health Sciences, Kannur University- 670661
4. Department of Microbiology, St. Pius X College, Kasargod- 671532
5. Genetika, Centre for Advanced Genetic Studies, Pettah P O, Thiruvananthapuram-695 024, India

Manuscript Info

Manuscript History:

Received: 14 April 2015
Final Accepted: 25 May 2015
Published Online: June 2015

Key words:

CBMN assay, Congenital Anomalies, DNA damages, Malondialdehyde, Oxidative stress, TORCH infection.

*Corresponding Author

Swapna C Senan

Abstract

The maternal infections that are transmissible in utero at several stages of the pregnancy can be caused by a group of infectious organisms, namely TORCH. These are associated with multiple abortions, sterility, intrauterine foetal death or malformations because of the foetus's inability to resist infectious organisms and the DNA damages caused by them. The oxidative stress plays a role in the pathophysiology of these abnormalities. The aim of the present study was to evaluate the role of oxidative stress and DNA damages in congenitally TORCH infected children. The study measured the level of oxidative stress by Malondialdehyde (MDA) test and the DNA damages are quantified by CBMN assay. Detailed demographic, lifestyle and clinical characteristics were compared with the results obtained. The mean CBMN frequencies as well as MDA values are observed to be higher in 47 congenitally TORCH infected children than the 16 control children. The present study observed a positive correlation between congenital TORCH infection and the oxidative DNA damage and thereby measures the effect of teratogens in pregnant women. This aids to aware the people about the cytogenetic effects of the environmental factors.

Introduction

During gestation, many microorganisms can infect the foetus, causing severe birth defects. Such organisms and the resulting clinical syndromes have been categorized as TORCH infections (Franca and Mugayar, 2004). The maternal infections that are transmissible in utero at several stages of the pregnancy can be caused by many organisms, of which the members of the TORCH complex, namely Toxoplasma gondii (T. gondii), Rubella virus (RV), Cytomegalovirus (CMV), the Herpes Simplex Virus (HSV) occupy prominent positions. These infections are associated with inadvertent outcomes like multiple abortions, sterility, intrauterine foetal deaths, still births, congenital malformations and other reproductive failures, especially when they are acquired during the first trimester of the pregnancy (Li et al., 2009).

Every year, an estimated 7.9 million children are born with a serious birth defect of genetic or partly genetic origin. Over 1 million more infants are born with serious birth defects of post-conception origin including those that result from maternal exposure to environmental agents (teratogens) such as alcohol, rubella, syphilis, and iodine deficiency that can harm the developing foetus (MOD, 2006).

Congenital anomalies represent a significant cause of premature birth of child morbidity and mortality. From 200,000 new borns per year, over 10,000 presented malformations. Epidemiologic studies have shown that the incidence of malformations is increasing and varies upon geographic features, race and gender. Perinatal mortality is generated in 66.66% of cases by congenital malformations; illnesses from perinatal period and the rest of them are generated by birth (Rodica et al., 2009). Congenital malformations can be divided into broad categories, one being malformations attributed to discrete environmental factors. Environmental causes of congenital anomalies are referred to as teratogenic. These are generally problems with the mother's environment (Gilber, 2002).

Infectious agents can create intrauterine infections leading to birth defects, abortion and stillbirth (Golalipour et al., 2009). The ability of the foetus to resist infectious organisms is limited and the foetal immune system is unable to prevent the dissemination of infectious organisms to various tissues (Mladina et al., 2000).

Oxidative stress is a condition in which the delicate balance existing between prooxidant (free radicals) production and their subsequent amelioration via the antioxidant defense system becomes skewed in favor of free radical expression (Cross and Halliwell, 1994). Oxidative stress is manifested at the maternal foetal interface from early pregnancy onwards. It plays a role in both the normal development of the placenta as well as in the pathophysiology of complications such as miscarriage, preeclampsia, intrauterine growth restriction (IUGR), and premature rupture of the membranes (Burton and Jauniaux, 2004).

At molecular level, the oxidative damage to DNA cause polysaccharide ring cleavage, base modification or chain breakage, damage to cellular constituents etc. Damage to lipids leads to formation of lipid aldehydes, lipid peroxides (Kohen and Nyska, 2002; Valko et al., 2007; Lipinski, 2011). MDA is a byproduct of lipid peroxidation; therefore, an elevation in MDA levels may reflect an overproduction of lipid peroxides and/or impaired antioxidant defense mechanism.

These lipid peroxides are produced mainly in the placenta due to membrane disruption by Reactive Oxygen Species (ROS) (Routledge, 2000). ROS are released from phagocytic cells that destroy cells infected with viruses, or bacteria, although surrounding tissue can also be affected leads to DNA damage.

In India, the studies relating oxidative stress and TORCH infection that leads to DNA damage and the resulting congenital anomalies in children, was not carried out. This throw light to the fact that people are unaware about the impact of such infection and the extent of genetic instability it can cause. Hence the present study was undertaken to assess the effect of increased oxidative stress and to quantify the extent of somatic DNA damages in congenitally TORCH infected children. This may aid to aware the people about the effect of the environmental factors and thereby the prevention of congenital anomalies due to TORCH infection.

Materials and Methods

The study was carried out in forty seven children suffering with varying degrees of congenital TORCH infection. Sixteen healthy children were also selected as control for this study. The samples were recruited from various maternity centers of Kerala for genetic testing to Genetika, Centre for Advanced Genetic Studies, Trivandrum, Kerala. Detailed demographic, lifestyle, and clinical characteristics were recorded using proforma. Cytokinesis-Block Micronuclei (CBMN) Assay was performed on each sample by using Cytochalasin B for quantitating the extent of somatic DNA damages.

Eight ml of venous blood was collected aseptically from all the subjects by venepuncture after overnight fasting. 4ml was transferred into the vacuutainer containing sodium heparin to perform the CBMN assay. The remaining 4ml was transferred into plain tube and allowed to clot. With the serum, malondialdehyde test is performed to detect the frequency of oxidative stress in the study subjects. MDA was determined using thiobarbituric acid as main reagent and the values are measured on semi-auto analyser at 540nm.

Two parallel cultures were set up for each sample, culture A & B. The culture A was for detecting constitutional chromosome anomalies by using peripheral blood lymphocyte culture method described by Moorhead et al., (1960), and GTG banded karyotypes were prepared according to ISCN pattern 1995. The culture B was for quantitating the extent of somatic DNA damages by Cytokinesis Block Micronuclei (CBMN) assay.

Lymphocyte cultures were prepared for each subject and were performed in 10 ml RPMI 1640 supplemented with 100 units/ ml penicillin, 100 units/ml streptomycin, 15% foetal bovine serum and 1% phytohemagglutinin. At 44th hr after initiation, cells were blocked in cytokinesis by adding cytochalasin B (Sigma, final concentration, 4.5µg/ml). The total incubation time for all cultures was 72 hr. After incubation, the cells were fixed in 3:1 methanol/glacial acetic acid, dropped onto clean microscopic slides, air dried, and stained with Giemsa stain. For each sample, 1,000 binucleated cells were scored at 100X magnification. The number of micronuclei per 1,000 binucleated cells was recorded.

Results

Forty seven children with varying degrees of congenital abnormalities or clinical abnormalities viz cleft lip, low set ears, webbed neck, dysmorphism, depressed nasal bridge, congenital heart disease, developmental delay, cystic hygroma, etc who were suffering from congenital TORCH infections were selected. The age of these children ranged from 4 days to 2 years. Sixteen, age and sex matched healthy childrens were selected as control study. The maternal age of these children ranged from 20 to 38 years with a mean age of 27.1 and the paternal age was 22 to 41 years with a mean age of 32.04. Various demographic, clinical, lifestyle and physiological condition were recorded and correlated with the extent of DNA damages and oxidative stress.

The Cytokinesis block micronuclei assay revealed that there is a statistical significant increase in the mean CBMN frequency among the study subjects (12.89) than the control subjects (10.16). In the case of MDA value, it was found to be 1.7 in study subjects and 1.35 in control subjects. The present study observed a significantly high level of MDA in study subjects when compared to the control subjects (Table: 1).

TABLE 1:
DISTRIBUTION OF MDA VALUE AND MEAN CBMN FREQUENCY AMONG STUDY AND CONTROL SUBJECTS

Variable	Number	MDA Value	Mean CBMN Frequency
Study	47	1.7	12.89
Control	16	1.35	10.16

The distribution of CBMN frequency and MDA value in study subjects according to age were given in the table 2. The age of the children were ranged from 4 days to 2 years. Among the 47 study subjects, 19.14% above the age of one year showed the highest mean CBMN frequency of 12.96. The study showed significant relationship between the paternal age and the mean CBMN frequency. As the paternal age (32 to 41) and maternal age (>35) increased, the study showed significant relationship with mean CBMN frequency .i.e, the older the parents the greater the mean CBMN frequency. The study observed that there is a significant relationship between the mean CBMN frequencies and increased duration of married life.

TABLE 2:
DISTRIBUTION OF MDA VALUE AND MEAN CBMN FREQUENCY ACCORDING TO THE AGE OF THE STUDY SUBJECTS

Category	Variable	Number	Percentage	MDA	Mean CBMN Frequency
Age of Children	<1	31	65.95%	1.61	12.48
	1	7	14.89%	1.81	12.85
	>1	9	19.14%	1.89	12.96

Subjects with the history of drug intake and the history of chronic illness among parents showed higher mean CBMN frequency. This clearly indicates a significant relationship between the mean CBMN frequency and the history of drug intake and illness.

Regarding the TORCH investigation 18 (38.29%) of the children reported toxoplasma IgG positivity, 33 (70.21%) showed rubella IgG positivity, 37 (78.72%) showed CMV IgG positivity and 15 (31.91%) showed HSV IgG positivity. Eight out of forty seven study subjects reported IgG positivity in toxoplasma, rubella, CMV, HSV and the rest showed one or two IgG positivity.

The study frankly observed that subjects with CMV IgG positivity showed increased CBMN frequency as well as increased MDA level than the IgG negative subjects. This is also true among subjects with toxoplasma, rubella, CMV, HSV. The mean CBMN frequency was found to be increased with increased severity of the clinical conditions moreover the children born to advance paternal age, history of chronic illness among parents and the history of various drug intake also showed increased mean CBMN frequency.

Discussion

The purpose of the present study was to investigate the oxidative stress and DNA damages in children with congenital TORCH infection. It is well known that the best time to identify and address risk factors for poor reproductive health outcomes for mothers and babies is not after but before conception through preconception care (Johnson et al., 2006). Infections are one of those risks, because certain infectious diseases carry a real threat to mothers and the foetus in utero (Lassi et al., 2014).

The development of the cytokinesis-block (CB) technique has made the human lymphocyte micronucleus assay (MN) a reliable and precise method for assessing chromosome damage. The level of genetic integrity of human populations is increasingly under threat due to industrial activities that result in exposure to chemical and physical genotoxins (Fenech and Morley, 1985).

In the present study it was observed that children above 1 year age had high mean CBMN frequency. It was analyzed that the severity of TORCH infection gets increased when the age of the children increases. They show congenital abnormality with increasing mean CBMN frequency. Paternal age and maternal age had influenced in the TORCH positive babies. The mean CBMN frequency was higher in increasing age compared to others. In the present study the duration of married life also influenced the TORCH infected babies.

Some studies show that foetal infection may manifest in case of an infection in an immunized pregnant woman when she has been immunized for that particular agent (Toxoplasma Gondii, Cytomegalovirus) before pregnancy, although it is much lower in intensity (Guerina, 2005). A reliable diagnosis of acute T. gondii, RV, or CMV infection in pregnant women is the main objective of the TORCH diagnostic assays. Generally, detection of IgM antibodies is a sensitive indicator of an ongoing or recent infection (Bobic et al., 1991; Gras et al., 2004). Improvements in IgM and IgG avidity assays assist the clinician in detecting acute infection and distinguishing between a primary and secondary immune response (Grangeot et al., 1997; Lazzarotto et al., 1997).

Conclusion

TORCH infection cause severe birth defects. The children who had reported TORCH infection showed increased mean CBMN frequency and MDA value. The mean CBMN frequency was increased with increasing paternal age, chronic illness and history of drug intake. The mean CBMN frequency and MDA value was increased in toxoplasma, rubella, CMV, HSV, IgG positivity than the subjects with IgG negativity. Also the TORCH infected children showed increased DNA damages and increased level of oxidative stress that leads to severe congenital anomalies. Avoiding contact with pet animals may help to get rid of the chance of TORCH infection.

References

Bobic, B., Sibalic, D. and Djurkovic Djakovic, O. (1991). High levels of IgM antibodies specific for Toxoplasma gondii in pregnancy 12 years after primary toxoplasma infection, Gynecol. Obstet. Invest, 31182–184.

Burton, G.J. and Jauniaux, E. (2004). Placental oxidative stress; from miscarriage to preeclampsia, J Soc Gynecol Invest, 11, 342–352.

Fenech, M. and Morley, A. (1985). A measurement of micronuclei in lymphocytes, Mutat, Res, 147, 29-36.

Franca, C.M. and Mugayar, L.R. (2004). Intrauterine infections: a literature review Spec Care Dentist, 24(5), 250-3.

Gilbert, G.L. (2002). Infections in pregnant women, Med J Aust, 176(5), 229-36.

Golalipour, M.J., Khodabakhshi, B. and Ghaemi, E. (2009). Possible role of TORCH agents in Congenital malformations in Gorgan, northern Islamic Republic of Iran, Eastern Mediterranean Health Journal, 15(2).

Grangeot-Keros, L., Mayaux, M.J., Lebon, P., Freymuth, F., Eugene, G., Stricker, R. and Dussaix, E. (1997). Value of cytomegalovirus (CMV) IgG avidity index for the diagnosis of primary CMV infection in pregnant women, J. Infect. Dis, 175, 944 –946.

Gras, L., Gilbert, R.E., Wallon, M., Peyron, F. and Cortina-Borja. (2004). Duration of the IgM response in women acquiring Toxoplasma gondii during pregnancy: implications for clinical practice and Cross-sectional incidence studies, Epidemiol. Infect, 132, 541–548.

Guerina, N. (2005). Management of Cytomegalovirus and Toxoplasma Gondii in pregnancy, In: S.D. Craigo, E.R. Baker. eds. Medical complication in pregnancy, Practical pathways in obstetrics and gynecology', McGraw-Hil Medical Publishing Division, , 359-381.

Halliwell, B. and Cross C.E. (1994). Oxygen-derived species, their relation to human disease and environmental stress, Environ Health Perspect, 102(Suppl 10), 5-12.

Johnson, V.A., Brun-Vézinet, F., Clotet, B., Kuritzkes, D.R., Pillay, D., Schapiro, J.M. and Richman, D.D. (2006). Update of the drug resistance mutations in HIV-1: Fall 2006, Top HIV Med, 14(3), 125-130.

Kohen, R. and Nyska, A. (2002) 'Oxidation of biological systems: oxidative stress phenomena, antioxidants, redox reactions, and methods for their quantification', Toxicol Pathol, 30, 620–50.

Lassi Zohra, S., Ayesha, M. Imam., Sohni, V. Dean., Zulfiqar, A. Bhutta., Lassi et al., (2014). Preconception care: preventing and treating infections, Reproductive Health, 11(Suppl 3), S4, 12-16.

Lazzarotto, T., Spezzacatena, P., Pradelli, P., Abate, D.A., Varani, S. and Landini, M.P. (1997). Avidity of immunoglobulin G directed against human cytomegalovirus during primary and secondary infections in immunocompetent and immunocompromised subjects, Clin. Diagn. Lab. Immunol. 4, 469–473.

Li, Z., Yan, C., Liu, P., Yan, R. and Feng Z. (2009). The prevalence of the serum anti-bodies to TORCH among women before pregnancy or in the early period of pregnancy in Beijing, Clinica Chimica Acta, 403, 212-15.

Lipinski, B. (2011). Hydroxyl radical and its scavengers in health and disease, Oxid Med Cell Longev, 809696.

Mladina, N., Mehikic, G. and Pasic, A. (2000). Torch infections in mothers as a cause of neonatal Morbidity, Medical Archives, 54(5–6), 273–276.

MOD (March of Dimes), (2006). The March Of Dimes Global Report on Birth Defects: The Hidden Toll of Dying and Disabled Children, March of Dimes Birth Defects Foundation.

Moorhead, P.S., Nowell, P.C., Wellmann, W.J., (1960). Chromosome preparation of leu-kocytes, Cultured from Human Peripheral Blood, Exp Cell Res, 20: 613-617.

Rodica Radu., Anamaria Molnar., Tudor Mirza., Stefan, I.. and Tigan. (2009). Congenital Malformation Prevalence in Cluj District between 2003-2007, Applied Medical Informatics, 25(4), 37-46.

Routledge, M.N. (2000). Mutations induced by nitrogen species in the supF forward mutation Assay. Mutat. Res, 450, 2000, 95–105.

Valko, M., Leibfritz, D., Moncol, J., Cronin, M.T., Mazur, M. and Telser, J. (2007). Free radicals and antioxidants in normal physiological functions and human disease, Int J Biochem Cell Biol, 39(1), 44-84.

ANTI OXIDANT, ANTI INFLAMMATORY AND ANTINOCICEPTIVE STUDY ON ARECA NUT

Jeena sharafudheen[1], Sarala Gopalakrishnan[2], J.K.Mukkadan[3]

ABSTRACT

The objective of study is to evaluate the anti oxidant activity and the total phenolic and falvanoid content of areca nut aqueous extract. Areca nut extract scavenged super oxide, DPPH, hydroxyl radicals and inhibited tissue lipid peroxidation *in vitro*. Oral administration of areca nut extract for one month, significantly increased super oxide dismutase, glutathione and glutathione reductase enzymes level($p<0.001$) in blood of rat and glutathione -s-transferase, glutathione peroxidise and superoxide dismutase enzyme in liver. The result showed mild scavenging ability against stable free radicals DPPH and ABTS and good antioxidant activity through enzymatic system possessing 68±0.007mg GAE/g and 7.03±CE mg/g phenolic and flavanoid content respectively.

Key words: *Areca catechu,* Antioxidant activity, Total phenolic and flavanoid compounds.

INTRODUCTION

In many Asian cultures such as India, Taiwan, and Southeast Asia, betel nut , *Areca catechu* L. (family Palmaceae), is traditionally masticated either alone or as a quid along with a large variety of ingredients, such as betel leaf (*Piper betel*; family Piperaceae), slaked lime, different types of tobacco besides additives, perfumes and stimulants (1). In herbal medicine, the areca nut has been used medicinally as a drug against parasitic worms (2). In old Indian scripts such as Vagbhata (4th century), and Bhavamista (13th century), betel nut was described as a therapeutic agent. Its use was recommended in many diseases such as leucoderma, leprosy, anaemia and obesity. It was also reported to have de-worming properties (3).The present study is to evaluate the total phenolic and flavanoid contents in areca nut and in order to determine their health-promoting antioxidant property.

MATERIALS AND METHODS

Drugs

Sample of areca nut (*Areca catechu*) obtained locally from areca nut farmers of Angamaly, Kerala were used for the study. The nuts were dehusked and nut portion was collected. This was further crushed to get coarse powder with help of mortar and pestle. The powder was weighed and soaked in the methanol in a ratio of 1gm in 2.5 ml. It was covered with aluminium foil and kept overnight. After soaking overnight, sample was again stirred and filtered through Whatsman No.4 filter paper. Filtrate was then collect separately and evaporated to dryness. Red colored flakes were obtained which were crushed and powdered. In order to get a uniform suspension of areca extract, the extract was dissolved in hexane (100 mg/10 ml) and 10µ of Triton X 100 (Sigma-Aldrich) was added and

1&3 - Little Flower Medicinal Research Center, Angamaly, Ernakulam
2 - St.Pius college, Rajapuram, Kasargod

further evaporated to dryness and finally made up to 10ml with distilled water. The extract was dissolved in paraffin oil for *in vivo* studies.

Animals

Wilstar albino rats (20-25 g) were used in the study. They were purchased from Little Flower Medical Research Centre (LFMRC) Animal Breeding Station, Angamaly, Kerala,India and were housed in well ventilated cages under controlled conditions of light and humidity and provided with normal mouse chow and water ad libitum. All the animal experiments were done as per the instructions prescribed by the Committee for the Purpose of Control and Supervision of Experiments on Animals (CPCSEA), Ministry of Environment and Forest, Government of India, and implemented through the Institutional Animal Ethical Committee of the Research Centre.

Chemicals and reagents

Nitroblue tetrazolium (NBT), glutathione, glutathione oxidized (GSSG), nicotinamide adenine dinucleotide phosphate reduced (NADPH) and 5-5'dithiobis 2-niotrobenzoic acid (DTNB) were purchased from Sisco Research Laboratories Pvt. Ltd., (Mumbai, India), catechin, gallic acid, 2,2-Diphenyl-1-picryl hydrazyl (DPPH) and 2,2-azobis-3-ethylbenzthiozoline-6-sulphonic acid (ABTS) were purchased from Sigma Aldrich (St.Louis, USA). All other chemicals and reagents used were of analytical reagent grade.

Estimation of total phenolic and flavanoid content of areca nut

Total phenolic content (TPC) of plant extracts was determined using the *Folin Ciocalteu* assay by Kahkone *et al* (1999) with some modifications. *Folin-Ciocalteu* reagent (1.5 ml; diluted 10 times) and sodium carbonate (1.2 ml, 7.5% w/v) were added to the extracts (300 µl, triplicate). The tubes were vortexed and allowed to stand for 30 min at 40°C for color development. Absorbance was then measured at 765 nm using UV-VS spectrophotometer. Total phenolic content were expressed as mg gallic acid equivalents/g dry weight (GAE).

The total flavanoid content was determined using colorimetric method. 0.25ml of sample (catechine for standard or extract)was mixed with 1.25 ml of distilled water in a test tube, followed by addition of 0.075ml of 5% sodium nitrate solution. After 6 minutes, 0.15ml of 10% aluminium chloride solution was added and the mixture was allowed to stand for 5 minutes before the addition of 0.5 ml of 1M sodium hydroxide solution. 2.5 ml of distilled water was added and the absorbance was measured immediately at 510 nm.

Determination of antioxidant activity of areca nut extract by in vitro method

Superoxide radical scavenging activity

Superoxide radical scavenging activity was determined by the NBT reduction method (7). Different concentrations of areca nut extract (10-200 µg) were added to the reaction medium containing 3 µg NaCN in 6 mM EDTA, riboflavin (2 µM), NBT (50 µM) and phosphate buffer (67 mM, pH 7.8) in a final volume of 3 ml. The tubes containing reaction mixture were uniformly illuminated with an incandescent lamp for 15 minutes. The optical density was measured at 560 nm before and after illumination. The percentage inhibition of superoxide generation was evaluated by comparing the absorbance value of the control and experimental tubes.

Hydroxyl radical scavenging activity

The hydroxyl radical scavenging activity was measured by studying the competition between deoxyribose and the extract for hydroxyl radicals generated from the Fe_3+/ascorbate/EDTA/H_2O_2 system (Fenton reaction). The reaction mixture (1.0 ml final volume) contained deoxyribose (2.8 mM), $FeCl_3$ (0.1 mM), EDTA (0.1 mM), H_2O (1 mM), ascorbate (0.1 mM), KH_2PO_4 - KOH buffer (20 mM, pH 7.4) and different concentrations of areca nut extract (10-200 µg). The reaction mixture was incubated for 1 hr at 37°C. Deoxyribose degradation was measured as TBARS and percentage inhibition calculated (8). The percentage inhibition was calculated according to the formula: Inhibition percentage (Ip) = [(AB-AA)/AB] x 100 where A and B are absorbance values of the blank sample and of areca extract solution, respectively.

Determination of inhibition of lipid peroxidation

Different concentrations of the areca nut extract (10- 200 µg) were added to rat liver homogenate (0.1 ml, 25% w/v), ascorbic acid (0.06 mM), 30 mM KCl, 0.16 mM $FeSO_4$ solution and final volume made up with Tris buffer (40 mM, pH-7) to 0.5 ml. Tubes were incubated for one hour at 37°C. Aliquots of the incubation mixture (0.4 ml) were treated with sodium dodecyl sulphate (SDS-8%, 0.2 ml), thiobarbituric acid (TBA-0.8%, 1.5 ml), and acetic acid 20%, pH-3.5, 1.5 ml). The total volume was then made up to 4 ml with distilled water and incubated for 1 hr at 100 4°C in a water bath. After cooling, 1 ml of distilled water and 5 ml of mixture of n-butanol and pyridine (15:1, v/v) were added and vortexed. After centrifugation the absorbance of the organic layer was measured at 532 nm. Percentage inhibition of lipid peroxidation was determined by comparing the results of the test compound with those of the control (8).

Determination of DPPH radical scavenging activity

Different concentrations of areca nut extract (0.1-1 mg) were mixed with 0.375 ml methanolic solution of DPPH (1, 1-diphenyl- 2-picrylhydrazyl-0.25 g/L). Total volume was made up to 2 ml with methanol. The disappearance of DPPH was read spectrophotometrically at 515 nm after 20 min of incubation at room temperature in dark (9).

Determination of ABTS radical scavenging activity

ABTS radical scavenging activity of the extract was determined using ferryl myoglobin/ABTS protocol (10). The stock solutions and 500 µM ABTS diammonium salt, 400 µM myoglobin (MbIII), 740 µM potassium ferricyanide and 450 µM H_2O_2 was prepared in phosphate-buffered saline (PBS, pH 7.4). Metmyoglobin was prepared by mixing equal volumes of myoglobin and potassium ferricyanide solutions. The test tubes contained ABTS (150 µM), MbIII (2.25 µM), varying concentrations of areca nut extract (10-200 µg) and PBS (pH-7.4) in volume of 2 ml. The reaction was initiated by adding 75 µM H_2O_2 and lag time was recorded in seconds before absorbance of ABTS at 734 nm began to increase.

Ferric reducing antioxidant power (FRAP) assay

The ferric reducing ability was measured at low pH. FRAP reagent contained 25 ml 0.3 M acetate buffer, 2.5 ml 4,6-Tris-2-pyridyl- (s)-Triazine (TPTZ) and 2.5 ml ferric chloride. Different concentration of areca nut extract (10-200 µg) was made up to one ml with freshly

prepared FRAP reagent. The mixture was incubated at 37°C for 15 minutes and absorbance read at 595 nm against distilled water at 595 nm. Standard graphs were constructed using known concentrations of ferrous salt in water/methanol to replace $FeCl_3$ and expressed as EC1 values. EC1 is defined as concentration of an antioxidant having a ferric reducing ability equivalent to that of 1 mM ferrous salt (11)

Determination of effect of Areca extracts on antioxidant enzyme levels in vivo.

Wilstar albino rats (5-6 weeks)weighing 20-25 g were divided into 4 groups of five animals and they were fed orally with areca nut extract dissolved in paraffin oil at different doses for 30 days. Group I was kept as normal. Group II was kept as control treated with paraffin oil only. Group III and Group IV were treated respectively with 100 mg and 500 mg areca nut extract/kg body weight.

At the end of the feeding trial, animals were sacrificed by ether anesthesia, and blood was collected by heart puncture, liver was excised and washed in ice-cold Tris Hcl buffer (0.1 M, pH-7.4), and cytosolic samples of liver homogenate were prepared by centrifuging at 10,000 rpm for 30 mins at 4°C. Whole blood was used for determination of superoxide dismutase, catalase and glutathione levels. Serum was used for glutathione reductase estimation. Liver tissue homogenate was used for super oxide dismutase, catalase, glutathione peroxidase, glutathione reductase, glutathione -S-transferase and glutathione assays.

Superoxide dismutase activity was measured by the NBT reduction method (7). Catalase activity was estimated by the method of Aebi, 1974(12) by measuring the rate of decomposition of hydrogen peroxide at 240 nm. Glutathione activity was assayed by the method of Moron, Depierre and Manner, 1979(13) based on the reaction with DTNB. The assay of glutathione peroxidase was done by the method of Hafeman, Sundae and Houestra, 1974(14) based on the degradation of H_2O_2 in the presence of GSH. Glutathione reductase activity was measured by the method of Racker, 1955 (15). The method of Habig, Pabst and Jakoby, 1974 (16) was followed assay of glutathione -S-transferase (GST) activity which is based on the rate of increase in conjugate formation between GSH and 1-chloro-2, 4- nitrobenzene (CDNB).

Statistical analysis

The values were expressed as mean ±standard deviation (SD). Statistical evaluation of data was done by one way ANOVA followed by Dunnet's test.

RESULTS

Determination of total flavanoid and phenol content

The total phenolic and flavanoid content values in the areca nut seeds were 7.03±0.12 CE mg/g extract and 68±0.007GAE mg/g extract estimated respectively (Table. I)

TABLE I: ESTIMATION OF TOTAL FLAVANOID AND PHENOL CONTENTS OF AREACA NUT

Total flavanoids(CE)mg/g	Total phenol content(GAE)mg/g
7.03±0.12	68±0.007

alues are the mean ±SD of different determinations

Antioxidant activities of areca nut extract in vitro

Areca nut extract was found to scavenge superoxide, hydroxyl radicals and inhibit tissue lipid peroxidation (Fig. 1). Areca nut extract gave an IC50 of 36 µg/ml for scavenging superoxide radicals but IC50 for inhibition of hydroxyl radicals and lipid peroxidation was found to be greater than 200 µg/ml and 400 µg/ml respectively and so could not be calculated. The ferric reducing activity for 50 µg of areca nut extract was found to be 1.8 mM for areca nut extract. Areca nut extract possessed only mild DPPH radical scavenging ability as IC50 was more than 1000 µg/ml. It showed only a mild capacity to scavenge ABTS radical.

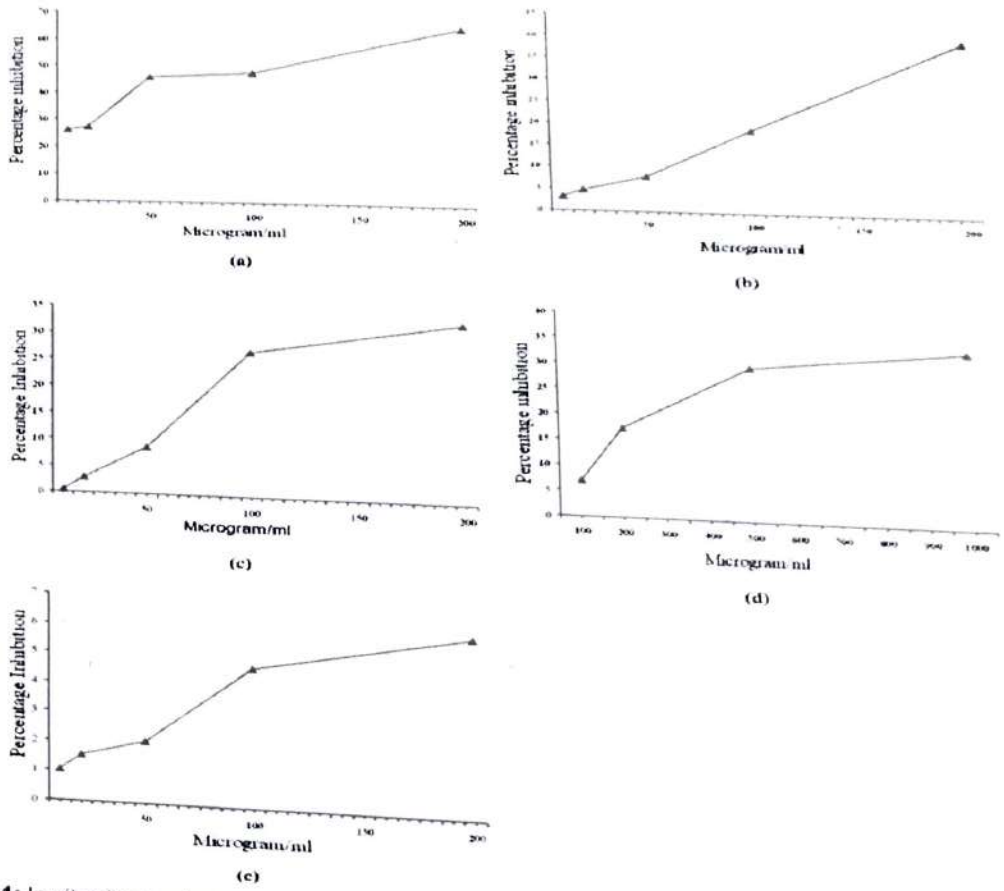

Fig. 1: In vitro free radical scavenging activity of areca nut extract. (A) Superoxide radical scaver activity. (B) Hydroxyl radical scavenging activity. (C) Inhibition of lipid peroxidation (D) DPPH ra scavenging activity (E) ABTS radical scavenging activity

Effect of administration of areca nut extract on antioxidant enzymes and glutathione

Antioxidant enzymes in blood and serum of mice were increased after administration of areca nut extract for a period of 30 days (Table II). Catalase was found to be increased in all animals treated with 100 and 500 mg/kg body weight of areca nut extract ($P<0.05$). The essential oil body weight ($P<0.01$) areca nut extract. The level of glutathione peroxidase enzyme was significantly increased by areca nut extract at 500 mg/kg body weight. ($P<0.01$). Even though glutathione was found to be increased, it was not found significant. The level of glutathione reductase was found to be unaltered in both the treated groups. Glutathione-S-transferase (GST)

TABLE I I: EFFECT OF ORAL ADMINISTRATION OF ARECA NUT EXTRACT FOR ONE MONTH ON ANTIOXIDANT SYSTEMS IN BLOOD.

Treatment	Catalase (k/g Hb)	Super oxide dismutase (U/g Hb)	Glutathione reductase (U/g Hb)	Glutathione (nmol/ml)
Normal	34.74±8.18	473±42.65	2.88±0.54	46.3±4.7
Control	32.57±7.43	444±38.89	2.75±0.26	44.2±7.2
100mg/kg body weight	56.91±8.43*	605±31.00***	6.64±0.83*	68.7±6.5**
500mg/kg body weight	50.36±19.18*	865±23.76***	8.08±1.57***	77.9±5.6***

Each value represents the mean±S.D (n=5). *P<0.05 compared with control, **P<0.01 compared with control,***P<0.001 compared with control.

administration significantly elevated superoxide dismutase ($P<0.001$) at both doses. Glutathione level was also found to be significantly increased in treated groups at 100 mg/kg body weight ($P<0.01$) and 500 mg/kg body weight ($P<0.001$). Glutathione reductase was elevated by the administration of areca nut extract ($P<0.05$) in all animals treated with 100 mg/kg body weight and significant activity was shown at 500 mg/kg body weight ($P<0.001$). Areca nut extract also showed a significant effect on some of the antioxidant enzymes in liver tissue of mice after treatment for 30 days (Table III). Catalase level did not change significantly in any of the treated groups. Superoxide dismutase activity was elevated in the group treated with 500 mg/kg level was found to be elevated in animals and significant activity was shown at 500 mg/k body weight ($P<0.01$) treated group.

DISCUSSION

Reactive Oxygen Species (ROS) are involved in the cell growth, differentiation, progression and death. Low concentrations of ROS may be beneficial or even indispensable in processes such as intracellular signalling and defence against micro-organisms. Nevertheless, higher amounts of ROS are indicated in the aging process as well as in a variety of human diseases including cardiovascular and inflammatory disease, cataract, cancer, ischemia and failures in immunity and endocrine functions.

TABLE I II: EFFECT OF ORAL ADMINISTRATION OF ARECA NUT EXTRACT FOR ONE MONTH ON ANTIOXIDANT SYSTEMS IN LIVER.

Treatment	Catalase (U/mg protein)	Super oxide dismutase (U/mg protein)	Glutathione peroxidase (U/mg protein)	Glutathione -s-transferase (nmol/mg protein)	Glutathione reductase^	Glutathion (nmol/ml)
Normal	5.29±0.66	0.84±0.12	8.16±0.65	42.57±1.66	88.83±12.03	13.8±1.7
Control	4.97±0.7	0.82±0.04	8.98±1.54	39.46±3.43	79.0±20.16	11.4±1.7
100mg/kg body weight	5.68±0.98	0.90±0.16	13.12±5.65	32.46±3.43	19.79±17.48	12.3±2.2
500mg/kg body weight	8.36±0.45	1.10±0.13*	19.2±7.53**	102.09±11.9***	69.56±9.53	13.9±3.3

*P<0.05 compared with control, **P<0.01 compared with control, ***P<0.001 compared with control. Each value represents the mean ±S.D (n=5), ^ (nmol of NADPH consumed/min/mg Protein)

As a safeguard against the accumulation of ROS, several non enzymatic and enzymatic antioxidant mechanisms exist naturally in each cell. Latter include antioxidant enzymes and anti oxidant systems. Major antioxidant enzymes are superoxide dismutase (SOD), catalase and peroxidases, of which glutathione peroxidises is thought to be most important. Glutathione (GSH) and numerous GSH dependent enzymes, metal binding proteins and vitamins are the important antioxidant enzyme systems.

Result of this study shows lower amount of phenolic (68±0.007mg GAE/g) and flavanoid (7.03±CE mg/g) in the areca nut seed aqueous extract compared to earlier report (17, 18). Study reveals the ability of areca nut seed to inhibit oxygen radicals as seen from the inhibition of lipid peroxidation, scavenging of superoxide and hydroxyl radical in vitro. However showed only a mild scavenging activity against stable free radicals as DPPH and ABTS making confusion with earlier studies and reports. Even in the low concentration of phenolic and flavanoid constituents, administration of areca nut seed extract increase serum antioxidant status for protecting cell from intracellular oxidative damage

Various literature and research findings suggest that the polyphenolic and flavanoid constituents of areca seed varies depending up on the geographical region where it is grown or cultivated, species and its maturity(19). Sufficient research data about its phenolic and flavanoid contents are not available to compare this result. However, little variation was observed in the amount of constituents when compared with the available data. This variation may be due to th above mentioned reasons.

Antioxidant activity of this study highlig the mild scavenging activity of areca se aqueous extract act against stable free radica such as DPPH and ABTS. DPPH is a fr

radical compound that has been widely used to determine the free radical scavanging ability of various sample (20,21). DPPH decreases significantly up on exposure to proton radical scavengers(22) 2,2'-Azinobis-3 ethylbenzothiazoline-6-sulfonic acid radical (ABTS+) is a stable organic radical that has gained general acceptance as the organic radical for use in measuring radical scavenging activity as an expression of hydrogenating antioxidative activity in plant crude extract(23). The reducing capacity of a compound may serve as a significant indicator of its potential antioxidant activity. A higher absorbance indicates a higher ferric reducing power (24, 25). Therefore DPPH scavanging,ABTS scavenging and reducing power assay were used to analyse the antioxidant activity of the areca seeds. Many studies clearly reported the high scavenging activity of areca seed against stable free radicals DPPH and ABTS(18,26). This strong scavenging activity of areca seed extract was possibly due to its high content of phenolic and flavanoid compounds which could act as a hydrogen donor antioxidant(19). This point confusing our result that areca seed aqueous extract shows mild scavenging activity with the lower amount of phenolic and flavanoid constituents but the administration of same areca seed aqueous extract shows good antioxidant activity by increasing serum antioxidant status. It implies the capacity of areca seed to act as an antioxidant through enzymatic system independent with the concentration of phenolic and flavanoid constituents.

Numerous publications report excellent linear correlations between "total phenolic profile" and "antioxidant capacity" (27). It should be noted that the correlation of IC50 radical scavenging activity of enzymes to total phenolic and flavanoid was not studied. So it is possible that the relation between the antioxidant activity through enzymatic system to total phenolic and flavanoids of areca seed extract is still need in our further study. All these experimental evidence suggests that the areca seed aqueous extract is a potential source of natural antioxidant through enzymatic and non enzymatic antioxidant mechanisms. However further investigation require to identify the actual component responsible for its enzymatic and non enzymatic antioxidant activity prior to the development in to the drug.

REFERENCE

Anonymous. "Betel-quid and areca-nut chewing: review," IARC monographs on the evaluation of the carcinogenic risk of chemicals to humans, no. 37, pp. 137-202, 1985.

GW Staples and RF Bevacqua , "Areca catechu (betel nut palm)," in Species Profiles for Pacific Island Agroforestry, ver.1.3., CR Elevitch, Eds. H_lualoa Hawai'i: Permanent Agriculture Resources (PAR) Press, pp.1-17, August 2006(http:// www tradition- altree.org .pdf).

RN Sharan,"Association of areca nut with carcinogenesis: a review," *Cancer Journal* ,no. 9, pp. 1, 1996.

AOAC (Association of Official Analytical Chemists), "Official Method 979. 09, Protein in grains," in Official Methods of Analysis of the Association of Official Analytical Chemists, S Delwiche, Eds. 17th edn, Gaithersburg, MD, USA: AOAC International Press, 2000, pp. 1-30.

AOAC (Association of Official Analytical Chemists), "Official Method 960.39. Fat (crude) or ether extract in meat," in Official Methods of Analysis of the Association of Official Analytical Chemists, 17th edn, Gaithersburg, MD, USA: AOAC International Press, 2000, pp. 1-2.

SS Nielsen, Food analysis, 2nd ed. Gaithersburg: Aspen Publication,1998.

Mc Cord JM, Fridovich I. Superoxide dismutase enzyme function for erythrocaprein. J Biochem 1969; 244: 6049-6056.

Ohkawa H, Oshishi N, Yagi K. Assay for lipid peroxide in animal tissue by thiobarbituric acid reaction. Anal Biochem 1979; 95: 351-358.

Aquino R, Morellis S, Lauro MR, Abdo S, Saija A, Tomaino A. Phenolic constituents and antioxidant activity of an extract of Anthurium vesicular leaves. J Nat Prod 2001; 64: 1019- 1023.

Alzoreky N, Nakahara N. Antioxidant activity of some edible Yemeni plants evaluated by Ferryl myoglobin/ABTS assay. J Food Sci Technol Res 2001; 7: 144-146.

Benzie IFF, Strain JJ. The ferric reducing ability of plasma (FRAP) as a measure of "antioxidant power" - The FRAP assay. Anal Biochem 1996; 239: 70-76.

Aebi M. Catalase estimation. In: HV Berg Meyer, eds. Methods of enzymatic analysis New York, Verlag, Chemie 1974: 673-684.

Moron MA, Depierre JW, Manner Vick B. Levels of glutathione, glutathione reductase and glutathione-S-transferase activities in rat liver. Biochim Biophys Acta 1979; 582: 67-68.

Hafeman DG, Sundae RA, Houestra WG. Effect of dietary selenium on erythrocyte and liver glutathione peroxidase in the rat. J Nutr 1974; 104: 580-587.

Racker E. Glutathione reductase (Liver and yeast). In: Sidney PC, Nathen OK, eds. Methods of Enzymology. New York, Academic Press 1955: 722-725.

Habig WH, Pabst MJ, Jakoby WR. "Glutathione-S-transferase, the first enzymatic step in mercapturic formation". J Biol Chem 1974; 247: 7130-7139.

Hamsar,M N, Ismail, Mordi, Ramanadan, Mansor. Antioxidant af activity of different part of *Areca catechu* extract on Glutathion-S- Transferase activity in vitro.Free Radicals and Antioxidants vol 1,2011,28-33.

Wei-Min Zhang,Jing Wei,Wen-xue chen,Hai-De Zhang."The chemical composition and phenolic antioxidants of *Areca catechu* L seeds". 2011 *International conference on agricultural and biosystems Engineering Advances in Biomedical Engineering Vols.* 1-2, 16-22.

Abdul Hannan, saumen Karan,Tapan Kumar Chatterjee."A comparative of in -vitro antioxidant activity of different extracts of areca seed collected from Areca catechu plant grown in assam".I J of pharmacy and pharmaceutical sciences,vol 4,2012,421-427.

R, Amarowicz, RB Pegg, P Rahimi-Moghaddam, B Barl and JA Weil,"Free radical-

scavenging capacity and antioxidant activity of selected species from the Canadian prairies." Food Chemistry. March 2004,Vol 84,551-562

T Hatano, H Kagawa, T Yasuhara and T Okuda, "Two new flavonoids and other constituents in licorice root: Their relative astringency and radical scavenging effects."Chemical & Pharmaceutical Bulletin, june 1988, Vol 36, 2090-2097

T Yamaguchi, H Takamura, T Matoba and J Terao, "HPLC method for evaluation of the free radical-scavenging activity of foods by using 1,1-diphenyl-2-picrylhydrazyl," Bioscience, Biotechnology, and Biochemistry, June 1998,Vol 62, 1201-1204

MJTJ Arts, JS Dallinga, H-P Voss, GRMM Haenen and A Bast, "A critical appraisal of the use of the antioxidant capacity (TEAC) assay in defining optimal antioxidant structures,"Food Chemistry, March 2003, Vol 80, 409-414

PD Dgh, "Antioxidant activity of Bidens [illegible] laeva Linn) its scavenging effect [illegible] radical and active oxygen [illegible] American Oil Chemists' Soci[illegible] Vol 75, 455, 461

S Meir, J Kanner, B Akiri and S [illegible] "Determination and involvement [illegible] aqueous reducing compounds [illegible] oxidative defense systems of [illegible] senescing leaves," Journal of Agricultural and Food Chemistry, July [illegible] 1813-1819

Periyasamy Prathiban, Veerachamy [illegible] Gobi Anjana "Estimation of [illegible] and antioxidant activity of [illegible] of areca nut and betel [illegible] Pharmacy and Pharm[illegible] Analysis,2014,Vol 01(01),[illegible]

D Huang, B Ou and RL Prior, "The [illegible] behind antioxidant [illegible] assays," Journal of Agricultural [illegible] Chemistry, February 2005,[illegible] 1856

*****

Original Research Paper

Volume : 5 | Issue : 11 | November 2016 • ISSN No 2277 - 8179 | IF : 3.508 | IC Value : 69.48

ROLE OF INFECTIONS AND GENETIC INSTABILITIES AMONG LOW BIRTH WEIGHT BABIES

Medical Science

KEYWORDS: Low birth weight, Chromosomal abnormalities, Cytokinesis-Block Micronuclei (CBMN) Assay

Swapna C Senan	Research Scholar, Meenakshi University, West KK Nagar, Chennai- 600 078. TN. India.
Sarala Gopalakrishnan	Department of Medical Microbiology, St Pius X College, Kasargod -671532, India.
Sadiya Ahammed	Genetika, Centre for Advanced Genetic Studies, Pettah P O, Thiruvananthapuram-695 024, India.
Dinesh Roy D	Genetika, Centre for Advanced Genetic Studies, Pettah P O, Thiruvananthapuram-695 024, India.

ABSTRACT

Birth weight is one of the most sensitive and reliable predictors of health of any community. Low birth weight (LBW) is an important factor for high prenatal and infant morbidity and mortality. The health of the mother is of prime importance in the outcome of pregnancy and health of the baby. Prenatal diagnosis enables early diagnosis of congenital anomalies and genetic disorders in utero. The proper diagnosis of chromosomal abnormalities can lead to the prevention of future birth of similarly affected children. The aim of the present study was to determine the role of infection and genetic instabilities among low birth weight babies. The study was carried out in 42 study subjects and 18 subjects without any chronic illness were also selected as control for this study. Cytokinesis-Block Micronuclei (CBMN) Assay was performed on each sample by using cytochalasin B for quantitating the extent of somatic DNA damages. The present study demonstrated that micronuclei frequency was significantly elevated in the study subjects than control subjects. The mean CBMN frequency of the subjects was statistically higher than that of the healthy control subjects. This study clearly demonstrated that the mean CBMN frequency of study subjects increases with respect to demographic and clinical risk factors such as maternal and paternal age, duration of married life, history of maternal infection, maternal illness and drug intake. LBW babies usually need extra hospital care, and there is a constant concern and uncertainty over future health outcomes. However, little attention is paid to birth weight improvement as a means of reducing child mortality. An affordable health care service, the preconception counseling and care for young women is strongly needed for a healthy future outcome.

INTRODUCTION

Low Birth Weight (LBW) baby is defined as baby having weight less than 2.5 kg within 24 hours of birth[1]. LBW is an important public health problem in developing world[2]. The proportion of LBW reported from India is 21.5%[3]. Birth weight of a child is an important indicator of its vulnerability for childhood illness and chances of survival[4].

In developing countries, LBW is a major determinant of perinatal mortality and morbidity[5]. According to Neonatal mortality, LBW babies are 20 times more likely as compared to babies heavier than 2.5kg[6]. The incidence of LBW was significantly higher in the group of teenage mothers[7]. A high incidence of LBW babies among women living in rural areas with low coverage of safe water supply. This could be because of increased episodes of gastro intestinal infections impairing normal fetal development[8]. Significantly higher incidence of LBW babies among anemic as compare to non anemic mothers[9].

There are certain risk factors which are strongly associated with LBW babies[2]. Young maternal age was a significant risk factor for LBW[10]. A baby's birth weight is related to birth weight of both parents and more strongly through the line. Women born with LBW have a higher risk of having LBW babies. Cigarette smoking, tobacco and chewing is also a risk factor for LBW[11]. Prenatal growth retardation, premature birth and congenital malformations appear the most important factors that determine low birth weight[12].

During gestation, many microorganisms can infect the foetus, causing severe birth defects and the resulting clinical syndrome have been categorized as TORCH infection[13]. Genital tract infection during pregnancy can cross into the amniotic fluid and result in prelabour rupture of the membranes and preterm labour. Globally, at least 7.6 million children are born annually with severe genetic or congenital malformation, 90% of these infants are born in mild and low income countries. Congenital anomalies are associated with premature labour. In fact, many of these foetus are spontaneously aborted very early in pregnancy[14].

Low birth weight constitutes about 17% of all live births globally. Children of low birth weight are at an increased risk from neurosensory, developmental, physical and physiological problems. Chromosomal abnormalities and various other syndromes are one of the most common causes of low birth weight. Maternal infections also cause major birth defects in new born babies. These infections are most serious during pregnancy and when transmitted in utero, can cause congenital malformation in neonates. A detailed evaluation for the etiology of these low birth weight babies is necessary and has good clinical implications. No serious attempts were made earlier to correlate between the role of infection and genetic instabilities among low birth weight babies. Hence the present study was undertaken to evaluate the role of infection and genetic aspects of children born with low birth weight.

MATERIALS AND METHODS

Forty two subjects suffering with low birth weight were selected for this study. The samples were referred from various maternity centres of kerala for genetic testing to Genetika, Centre for Advanced Genetic Studies, Trivandrum, Kerala. Eighteen subjects without any chronic illness were also selected as control for this study. Detailed demographic, clinical and lifestyle characteristics were recorded using proforma. In this study, Cytokinesis Block Micronuclei (CBMN) assay was carried out in each subject. CBMN assay was performed by using Cytochalasin B for quantitating the extent of somatic DNA damages.

The fresh blood collected by venepuncture was transferred to vacuutainer containing sodium heparin as anticoagulant. Added 5 to 6 drops of whole blood samples to a vial containing 10 ml. RPMI 1640

supplemented with 100 units/mL penicillin, 100µg/mL streptomycin, 15% fetal bovine serum and 100µg/mL phytohemagglutinin. Cytochalasin B was added to the cultures at a final concentration of 4.5µg/mL (Sigma) after 44th hours of initiation of cells with phytohaemagglutinin. Cells were harvested after 72 hr incubation, and they were treated with a hypotonic solution (0.075M KCl) for 1 min and fixed in fresh fixative solution (methanol: acetic acid, 3:1). The cells were dropped onto slides and the slides were air dried and stained with 10% Giemsa. Micronucleated cells were analyzed under light microscopy at 100X magnification. The number of micronuclei is not less than 1000 binucleated cells were scored and the distribution of micronuclei among binucleated cells was recorded.

Table 1- Distribution of mean CBMN frequency according to various demographic characteristics of the study subjects

Category	Variables	Total	Percentage (%)	Mean CBMN Frequency
Age (Years)	<1	22	52.3	14.25
	1 to 15	12	28.5	14.26
	16 to 30	2	4.7	13.94
	New born	6	14.2	14.28
Sex	Female	20	47.5	14.28
	Male	22	52.3	14.19
Birth weight (Kg)	<2	14	33.3	14.28
	≥2	28	66.6	14.26
Paternal age (Years)	20 to 40	31	73.80	14.25
	41 to 60	11	26.19	14.33
Maternal age (Years)	20 to 40	40	95.23	13.94
	41 to 60	2	4.76	14.29
Duration of married life of parents(Years)	<1	2	4.76	13.94
	1 to 15	38	90.47	14.28
	16 to 30	2	4.76	14.59

Distribution of mean CBMN frequency according to various demographic characteristics of the study subjects were showed in Table 1. The subjects were grouped on their demographic characteristics such as age, sex, birth weight, paternal age, maternal age and duration of married life of parents. Among the 42 study subjects, 22 subjects (52.3%) were belonged to <1 years of age and showed a mean CBMN frequency of 14.25. 12 subjects (28.5%) with age between 1 to 15 years and showed a mean CBMN frequency of 14.26. 2 subjects (4.7%) were belonged to age between 16 to 30 years and showed a mean CBMN frequency of 13.94. New born babies showed highest mean CBMN frequency of 14.28. 20 female subjects showed mean CBMN frequency of 14.28 and 22 male subjects showed mean CBMN frequency of 14.19. Birth weight of the subjects were divided in to <2 kg and ≥2 kg. Subjects with <2 kg of birth weight showed highest mean CBMN frequency of 14.28. Paternal age and maternal age between 41 to 60 years were showed highest mean CBMN frequencies (14.33 and 14.29). Parents having 16 to 30 years duration of married life showed mean CBMN frequency 14.59.

Table 2- Distribution of mean CBMN frequency according to the various clinical characteristics of the study subjects

Category	Variables	Total	Percentage (%)	Mean CBMN
Clinical conditions	Congenital abnormalities	9	21.4	14.42
	Cleft palate	2	4.7	13.87
	Developmental delay	8	19.04	14.39
	Dysmorphism	19	45.2	14.07
	Multiple anomalies	4	9.5	14.87
H/o maternal infection	Yes	16	38.09	14.3
	No	26	61.90	14.26
H/o illness	Yes	14	33.33	14.31
	No	28	66.66	14.26
H/o drug intake	Yes	16	38.09	14.35
	No	26	61.90	14.23
CMV IgG antibody	Positive	6	14.28	14.36
	Negative	36	85.71	14.26
Rubella IgG antibody	Positive	6	14.28	14.28
	Negative	36	85.71	14.25
USS finding	Normal	20	47.61	14.25
	Abnormal	22	52.38	14.3

Distribution of mean CBMN frequency according to the various clinical characteristics of the study subjects were showed in Table 2. The subjects were grouped on their clinical characteristics such as clinical conditions, H/o of maternal infection, H/o of illness, H/o drug intake, CMV IgG antibody, Rubella IgG antibody and USS finding. According to their clinical conditions, 19 subjects (45.2%) had dysmorphism, 9 subjects (21.4%) had congenital abnormalities, 8 subjects (19.04%) had developmental delay, 4 subjects (9.5%) had multiple anomalies and remaining 2 subjects (4.7%) had cleft palate. The highest mean CBMN frequency (14.42) was showed by subjects with congenital abnormalities. 16 subjects have history of maternal infection and they showed the mean CBMN frequency of 14.3. 14 subjects have history of illness showed a mean CBMN frequency of 14.31. History of drug intake was showed by 16 subjects and they showed mean CBMN frequency of 14.35. Subject with CMV IgG antibody was positive and showed a mean CBMN frequency of 14.28. Subject with Rubella IgG antibody was positive and showed a mean CBMN frequency of 14.28. Normal USS finding subjects showed mean CBMN frequency of 14.25 and abnormal USS finding subjects showed mean CBMN frequency of 14.3.

DISCUSSION

Low birth weight infants fail to achieve their ultimate growth potential as a result of intrauterine and postnatal growth failure. In 2012, an estimated 15 million babies (11.3 % of live births) worldwide were born preterm, about 13 million of these infants survived beyond the first month of life[15]. In the present study, newborn babies had high risk of low birth weight compared with other ages and they showed highest mean CBMN frequency.

Birth weight is a technically simple parameter to monitor prenatal health in a population. Prenatal growth retardation, premature birth, and congenital malformations appear the most important factors that determine low birth weight[16]. In the present study, 33.3% of the study subjects have birth weight less than 2 kg. Babies with birth weight less than 2kg showed highest mean CBMN frequency of 14.28.

In the cross sectional study conducted by Rizvi et al.,[18], the newborns were assess for congenital anomaly (CA). In the present study, it was analyzed that majority of the subjects (n=19) have dysmorphism. Among these clinical conditions, the highest mean CBMN frequency showed by subjects had multiple anomalies (14.87).

Rizvi et al.,[18] reported increased risk of LBW with increasing maternal age. A study from India failed to find any association between LBW and increasing maternal age as significant risk factors[17]. According to Dinesh Roy et al.,[18] the incidence of chromosome anomalies was significantly increased after 30 years. The observation found in the present study was the mean CBMN frequency increases with increasing maternal age.

In some maternal conditions, the risk lies with the drugs used for treatment, rather than the illness itself. Some drug may induce teratogenic effects that are clinically evident until many years after birth[19]. In the present study, it was observed that the distribution of mean CBMN frequency was higher in those subjects with the history of drug exposure and the history of illness.

Presence of IgM antibodies is associated with acute infection. IgG avidity test may have a higher specificity in the detection of acute infection; however, it still cannot identify a neonatal infection[20]. Rahav et al.,[21] demonstrated a vertical transmission of CMV in about 30% of mothers infected by CMV during pregnancy. However,

Volume : 5 | Issue : 11 | November 2016 • ISSN No 2277 - 8179 | IF : 5.508 | IC Value : 69.48

abortion rate is relatively high in pregnancies complicated by CMV infection. In the present study showed that 14.28% subjects were CMV IgG antibody positive with a mean CBMN frequency of 14.36 and 85.71% showed CMV IgG antibody negative.

Risk for congenital rubella syndrome happens when infection occurs in early stages of pregnancy. Specifically, the percentage of infants with congenital rubella syndrome exceeds 50% in cases of infection during the first trimester of pregnancy while the relative percentage is significantly reduced after the 20th gestational week[20]. In the present study, subjects with Rubella IgG antibody positive showed increased mean CBMN frequency than the subjects with Rubella IgG antibody negative.

CONCLUSION

In short, the present study involves the role of infection and genetic instabilities among low birth weight babies. The distribution of mean CBMN frequency according to demographic and clinical factors of the study subjects was observed. Age, sex, birth weight, paternal age, maternal age etc. showed increased level of CBMN frequency. The level of mean CBMN frequency was higher among those who have the history of maternal infection and history of illness. CMV IgG antibody and Rubella IgG antibody were also found to be significantly elevated in study subjects. These findings suggest that the Low birth weight have a high incidence of infection and genetic instability but these are the major contributors to infant mortality. Efforts towards preventing early marriage would contribute significantly in reducing the prevalence of low birth weight. Public education and awareness are on how to carry a healthy pregnancy. Likewise; women should be linked to the appropriate maternal health services including antenatal care and nutritional counseling services.

REFERENCE

1. Yilgwan CS, Abok II, Yinnang WD, Vajime BA. Prevalence and risk factors of low birth los. Jos J Med. 2009; 4(1):13–15.
2. Jitendar Nagpal, Ajay kumar and Siddarth Ramji Anterior Lens Capsule Vascularity in Evaluating Gestation in Small for Gestation Neonates. Indian Pediatrics.(2004) 817-821.
3. Mumbare SS, Maindarkar G, Darade R, Yenge S, Tolani MK, Patole K. Maternal risk factors associated with term low birth weight neonates: a matched-pair case control study. Indian Pediatr. 2012;49(1):25–28.
4. Sudesh Raj Sharma, Smith, Giri, Utsav Timalsina, Sanjiv Sudarshan Bhandari, Bikash Basyal, Kusum Wagle, and Laxman Shrestha. Low Birth Weight at Term and Its Determinants in a Tertiary Hospital of Nepal: A Case-Control Study PLoS One. 2015; 10(4):e0123962.
5. Ayesha Khan, Farah Deeba Nasrullah, and Riffat Jaleel. Frequency and risk factors of low birth weight in term pregnancy Pak J Med Sci. 2016; 32(1): 138–142.
6. UNICEF and WHO. Low Birth weight: Country, Regional and Global Estimates. NY: UNICEF Editorial and publication center ; 2004. division of communication.
7. Banerjee B, Pandey GK, Dut D, Sengupta B, Mondal M. Teenage Pregnancy: A Socially Inflicted Health Hazard. Indian J Community Med. 2009; 34(3):227–231.
8. Kayode GA, Amoakoh-Coleman M, Agepong IA, Anash AE, Grobbee DE, Klipstien-Grobusch K. Contextual risk factors for LBW:A multilevel analysis. PLoS ONE. 2014; 9(10):e109333.
9. Badshah S, Mason L, Mckelvie K, Payne R, Lisboa PJG. Risk factors for Low Birth Weight in the Public Hospitals at Peshawar, NWFP-Pakistan. BMC Public Health. 2008; 8: 197–206.
10. Viengsakhune L, Yoshida Y, Harun-or-Rashid M, Sakamoto J. Factors affecting low birth weight at four central hospitals in Vientiane, Lao PDR Nagoya J Med Sci. 2010; 72:51–58.
11. Gupta PC, Sreevidya S. Smokeless tobacco use, birth weight, and gestational age: population based cohort study of 1217 women in Mumbai, India. BMJ. 2007;328(7455):1538.
12. Paliwa ASV, Mohan I, Choudhary RM, Sharma BN. Risk factros associated with low birth weight in newborns: a tertiary care hospital based study. Int J Cur Res Rev. 2013;05(11):42–8.
13. Franca CM and Mugayar LR. Interanterine infection: a literature review.(2004) 24(5):250-253.
14. Creasy RK and Resnik R. Maternal-Fetal Medicine: Principles and Practice. 5th ed. Philadelphia PA:WB Saunders 2004.
15. Lawn JE, Blencowe H, Oza S, You D, Lee AC, Waiswa P, et al. Lancet every newborn study group. every newborn: progress, priorities, and potential beyond survival. Lancet. 2014; 384(9938):189–205.
16. Rizvi SA, Hatcher J, Jehan I, Qureshi R. Maternal risk factors associated with low birth weight in Karachi: a case control study. Eastern Mediterranean Health J. 2007; 3(6):1343–1352.
17. Mumbare SS, Maindarkar G, Darade R, Yenge S, Tolani MK, Patole K. Maternal risk factors associated with term low birth weight neonates: a matched-pair case control study. Indian Pediatr. 2012;49(1):25–28.
18. Roy D, Dinesh, K, Pavithran, P. Y, Henry, K. E, Elizabeth, P, Sindhu, T, Vijayakumar. Correlation of Age and Birth Order of Parents with Chromosomal Anomalies in Children. 2003, Volume 39, Issue 6, pp 695 - 699.
19. Hussen N, Stoll BJ, Fanaroff AA, etal. Changes in pathogens causing early-onset sepsis in very-low-birth-weight infants. N Engl J Med. 2002; 347:240-247
20. Yamada H, Nishikawa A, Yamamoto T, Mizue Y, Yamada T, Morisawa M, et al. Prospective study of congenital toxoplasmosis screening with use of IgG avidity and multiplex nested PCR methods J Clin Microbiol. 2011; 49:2562–6.
21. Bahar G, Gabbay R, Ornoy A, Shechtman S, Arnon J, Diav-Citrin O. Primary versus nonprimary cytomegalovirus infection during pregnancy. Israel. Emerg Infect Dis. 2007; 13:1791–3.
22. Namavi MH, Ziaee M, Naseh N. Congenital rubella syndrome in infants of women vaccinated during or just before pregnancy with measles-rubella vaccine. Indian J Med Res. 2008; 127:551–4.

IJSRM
INTERNATIONAL JOURNAL OF SCIENCE AND RESEARCH METHODOLOGY
An Official Publication of Human Journals

Human Journals
Research Article
August 2018 Vol.:10, Issue:2

IF - 3.925

Anti-Bacterial, Anti-Inflammatory and Anti-Nociceptive Activities of Areca Nut Components (Arecoline and Polyphenol)

IJSRM
INTERNATIONAL JOURNAL OF SCIENCE AND RESEARCH METHODOLOGY
HUMAN

***[1]Jeena Sharafudheen, [2]Sarala Gopalakrishnan, [3]J.K.Mukkadan, [4]Kayal Vizhi**

[1]Microbiology, Research assistant, Little Flower Medical Research Center, Angamaly, Kerala, India, 683572.

[2] Microbiology, Assistant Professor, St.PiusX[th]College, Rajapuram, Kasargod, Kerala, India, 671532.

[3]Physiology, Research director, Little Flower Medical Research Center, Angamaly, Kerala, India, 683572.

[4]Physiology, Assistant professor, Meenakshi Medical College, Enathur, Tamil Nadu, India,671552

Submission: 22 July 2018
Accepted: 29 July 2018
Published: 30 August 2018


www.ijsrm.humanjournals.com

Keywords: *Areca catechu*, Arecoline, Anti-bacterial, Anti-inflammatory, Anti-nociceptive, polyphenols.

ABSTRACT

The aim of the present study was to evaluate and compare the anti-bacterial, anti-inflammatory and anti-nociceptive properties of two important components of *Areca catechu* seed (Areca nut). i.e., Arecoline and Polylphenols. Polyphenols and Arecoline were separated by solvent extraction and characterized by IR and NMR spectroscopy. Anti-bacterial properties of these two separated components were carried out in three different concentrations (10, 20 and 50µg) by agar diffusion method. Both the components of areca nut showed prominent anti-bacterial activities in a dose dependent manner against the different bacterial culture ($p<0.05$). Among the six bacterial culture tested Gram positive bacterial cultures showed susceptibility to arecoline and Gram negative bacteria showed more susceptibility to polyphenols. Carrageenan induced paw edema method used for evaluation of anti-inflammatory activities of two components. Both the components tested in two concentrations (200 and 400 µg) showed significant reduction in the paw edema volume ($p<0.001$) in a dose dependent manner. Even though, the result clearly suggested that, phenolic component is more effective anti-inflammatory agent than alkaloid in every dose. Antinociceptive activity was carried out using acetic acid induced rat models. Both components of areca nut in two doses (200 and 400µg) showed significant reduction ($p<0.001$) of writhing induced by the acetic acid after oral administration in a dose dependent manner. However two doses of both components showed the significant reduction, administration of phenolic components decrease the number of writhing compared to alkaloid fraction administrated groups. The present study report evaluated that areca nut have a good anti-bacterial, anti-inflammatory and anti-nociceptive activities that are hidden in its separated components.

INTRODUCTION

Plants which have one or more of its organs containing substances that can be used for therapeutic purposes are called medicinal plants. Throughout history, natural products from plants have played major sustaining role in the lives of human beings especially as food sources and also medicinal products. Areca nut or betel nut is the seed or endosperm of palm *Areca catechu* Linn (Family-*palmaceae*) is a handsome slender single trunked monoecious medium-sized palm tree. This palm is also called the betel tree because the areca nut is often chewed along with the betel leaf, a leaf from a vine of the family *Piperaceae*. The areca nut is not a true nut, but rather a fruit categorized as a berry. Areca nut is one of plant has got an important place in the ancient system of medicines in several countries such as India, China, Bangladesh and Philippines. Chewing the mixture of areca nut and betel leaf is a tradition, custom or ritual which dates back thousands of years in much of the geographical areas from South Asia eastward to the Pacific. It constitutes an important and popular cultural activity in many Asian and Oceanic countries.

Comprehensive analysis of the chemical composition of areca nut have been reported and reviewed. The percentage of each chemical components of areca nut may vary depending-on the region where *Areca catechu* is grown, its degree of maturity and its processing method (1). Polyphenols *(flavonols, tannins)* constitute a large proportion of the dry weight of the nut. The polyphenols mostly flavonoids include catechine (10%), epicatechin (2.5%) and leucocyanidin (12%). The remaining percentage of flavonoids occurring as complex flavonoids with varying degree of polymerization (2).

Areca catechu is only one of the species of areca contain alkaloid. Among the chemical constituents, alkaloids are the most important biologically. Among the nut has been shown to contain at least six related alkaloids, of which four have been conclusively identified in biochemical studies (3). 15-17.7% of weight of areca nut is fat. The fatty acid of areca-nut contains moderate level of both unsaturated fatty acid and saturated fatty acid. It also contains 36 elements and vitamins (B_6 and C) (4). Most of the folklore medicinal properties of areca nut are now validated and proved by several scientific observations. Our present study aimed to separate the arecoline and polyphenolic components of areca nut and to find out the anti-microbial, anti-inflammatory and anti-nociceptive properties of separated components.

MATERIALS AND METHODS

This study was conducted in Department of Life Science at Little Flower Medical Research Center (LFMRC) Angamaly, Kerala, India during the period 2012-2013. All experiments were carried out under the supervision of guides.

MATERIALS

1. Plant materials: Ripened areca nut (*Areca catechu*) samples were obtained from local areca nut farmers of Angamaly, Kerala, India for the study.

2. Microorganisms: The pathogenic strains of bacteria were obtained from the Department of Microbiology, Aswani Diagnostic Centre, Calicut, Kerala. Organisms used were *Staphylococcus aureus, Streptococcus pyogenes, Klebsiella pneumoniae, Pseudomonas aeruginosa, Salmonella typhi,* and *Escherichia coli.* The bacterial cultures were maintained on nutrient agar (NA).

3. Animals used: Wistar albino rats (200–250 g) were used for the study were purchased from Little Flower Medical Research Centre (LFMRC) Animal Breeding Station, Angamaly, Kerala, India (Rodent house Register number: 496/01/a/CPCSEA). This study was approved by Institutional Animal Ethical Committee of the Research Centre.

4. Drug used: Carrageenan, diclofenac, acetic acid, indomethacin, chloramphenicol

5. Chemicals and Reagents: peptic digest of animal tissue, sodium chloride, beef extract, yeast extract and agar were purchased from Hi Media laboratories (Mumbai, India). All other chemicals and reagents used were of analytical reagent grade.

METHODS

1. Separation of areca nut components

Alkaloid arecoline and polyphenolic components of areca nut separated by solvent extraction (1).

2. Determination of Anti-bacterial activity

Well diffusion assay (5) on nutrient agar used to determine the anti-bacterial properties. Bacteria used for the study were inoculated into nutrient broth (NB) and incubated at 37°C

for 6 hours. The turbidity of the resulting suspension was diluted with NB to obtain transmittance of 74.3% (absorbance of 0.132) at 600 nm. The percentage was found spectrometrically comparable to 0.5 McFarland turbidity standards. This level of turbidity is equivalent to approximately 1.5×10^8 CFU/ml. Then the bacterial cultures were inoculated on the surface of Nutrient agar (NA) plates. Subsequently, wells of 6 mm diameter was prepared on NA using sterile cork borer and 50 µl of alkaloid and phenolic samples in different concentrations (10 µg/ml, 20 µg/ml & 50 µg/ml) were loaded in each well. Antibiotics Chloramphenicol used as positive control (25 µg). The tests were carried out in triplicates. The plates were incubated at 37°C for 24 hours. At the end of incubation, zones of inhibition were measured with a transparent ruler. Zones of clearing greater than 6 mm were considered susceptible to the test component.

3. Determination of Anti-inflammatory activity

Carrageenan-induced paw edema method (6) was performed for the evaluation of anti-inflammatory activity. Six groups of rats used for the study having six animals in each group. Animals of group-1 (carrageenan control group) received normal saline solution, animals of group-2 (standard drug treated group) received indomethacin (10 mg/kg, i.p), animals of group-3 and 4 received alkaloid fraction 200 µg and 400 µg /kg b.w, group 4 and 5 received phenolic fraction 200 µg and 400 µg /kg b.w respectively p.o. Vehicle, standard drug and test compound were administered 30 minutes prior to carrageenan injection. After 30 minutes, 0.1 ml of 1% (w/v) solution of carrageenan in 0.9% normal saline solution was injected subcutaneously into the plantar region of right hind paw and the paw volume of each rat from all groups was measured at 0, 30, 60, 120 and 240 minutes using vernier caliper after carrageenan challenge.

4. Determination of Anti-nociceptive activity

Experiments were carried out using acetic acid induced rat models (7). Rats used for study were divided into six groups with six animal in each group, group 1 as normal control received only vehicle (0.9% w/v NaCl), group 2 received Diclofenac (10mg/kg b.w) orally, animals of group-3 and 4 received alkaloid fraction 200 µg and 400 µg /kg b.w, group 4 and 5 received phenolic fraction 200 µg and 400 µg /kg b.w respectively 30 minutes before the administration of 0.8% acetic acid intraperitoneally. Abdominal constriction (writhes) per animal was counted over a period of 20 minutes just 5 minutes after the intraperitoneal

administration of anti-nociceptive agent. Index of anti-nociceptive activity was referred to as the percentage protection against abdominal constriction. It is calculated as:

No. of writhing in control group-No. of writhing in treated group x 100
No. of writhing in control group

Statistical analysis

The values were expressed as mean standard deviation (SD). Statistical evaluation of the data done by one way ANOVA followed by Pairwise test, Tukey's test and Dunnet's test for anti-bacterial, anti-inflammatory and anti-nociceptive activities respectively.

RESULTS AND DISCUSSION

Arecoline and polyphenols separated from ripened areca nut used for the present study. Polyphenols characterised by IR (Figure: 1a) and arecoline by NMR (Figure: 1b) from department of Analytical Chemistry, Cochin University, Cochin. Kerala.

Polyphenols-IR spectra: KBr, δ(cm-1)=3473 cm-1,3152 cm-1,1725 cm-1,1598 cm-1
Arecoline-NMR spectra: C^{13}NMR (400MHZ, DMSO, 25°C,TMS), δ=2.61(d,2H), 2.89(s,3H), 3.47(s,2H),3.73(s,3H), 3.92(s,2H), 7.08(t,1H)

Effect of antibacterial activity

Microorganisms are responsible for most of the diseases. Anti-bacterial activity of two components of areca nut was carried out using agar diffusion method. The effect of various concentration of two important component of areca nut that is, arecoline and polyphenol were tested against *Salmonella typhi, Staphylococcus aureus, Streptococcus pyogenes, Escherichia coli, Klebsiella pneumoniae* and *Pseudomonas aeruginosa*. Results obtained were tabulated in Table: 1, (Figure: 2a and 2b). Both components of areca nut showed prominent anti-bacterial activity to different bacterial cultures in different doses. Among the six bacterial culture tested alkaloid component showed significant activity against to only two bacterial culture *Staphylococcus aureus* and *Streptococcus pyogenes* at higher dose-50 µg/ml compared to standard. That is, 15.27±0.04 and 23.37±0.26 respectively. In case of phenolic component, dose 50 µg/ml is active against *Salmonella typhi, Escherichia coli* and *Klebsiella pneumoniae* compared to standard. But 10 µg/ml is active against *Pseudomonas aeruginosa* (11.23±0.45). 50 µg/ml is more active against *Salmonella typhi* (11.1±0.11) and

least active to *Klebsiella pneumoniae* (8.40±0.00). The activity of two components said that alkaloid components shows activity against Gram positive bacterial cultures and phenolic components are active against Gram negative cultures.

The Gram-positive bacterial species showed higher susceptibility value for alkaloid components and the zone of diameter increasing with the concentration of alkaloids. Whereas phenolic components showed the susceptibility value higher for the Gram negative bacterial strains than Gram positive with the increasing concentration. The lower zone of inhibition observed in the Gram negative bacterial strains by alkaloid components compared to Gram positive is not at all together surprising. This is very likely due to the peptidoglycan containing periplasmic space and outer membrane lipopolysaccharide layer of Gram negative bacteria. The Gram negative outer membrane acts as a barrier, preventing the penetration of numerous substances, including anti-microbial substances into the organisms. The periplasmic space also containing enzymes capable for breaking down foreign molecules attempting to gain entry into the microorganisms (8 and 9). Here the gram negative bacterial species tested were not allowed to enter the alkaloid components of areca nut due to its structure compared to phenolic. Our study shows phenolic concentrates significantly

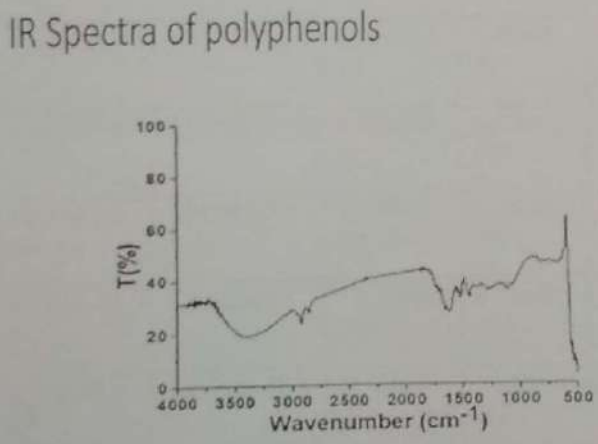

Figure 1a: IR spectra of polyphenols

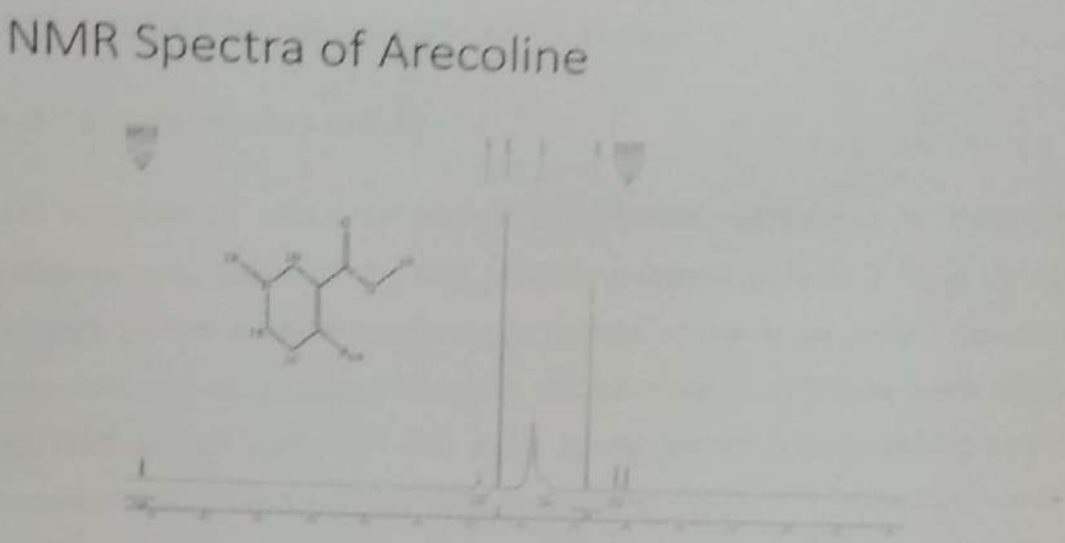

Figure 1b: NMR spectra of arecoline

Table 1: Anti-bacterial activity of alkaloid and phenolic components

SL. NO	ORGANISMS	POLYPHENOLS (µg)			ALKALOID (µg)			
		10	20	50	10	20	50	standard
1	*Salmonella typhi*	10.78± 0.23*	13.85±0.04 *	16.65±0. 13*	9.52±0. 24	10.73±0 .15	11.1±0.1 1*	16.92±0. 03
2	*Staphylococcus aureus*	5.57±0.19	5.92±0.11	8.00±0.3 1*	6.90±0. 00*	8.80±0. 09*	11.25±0. 23*	15.27±0. 04
3	*Streptococcus pyogens*	4.42±0.19	4.90±0.13	6.60±0.2 3*	6.30±0. 09*	9.03±0. 12*	10.47±0. 16*	23.37±0. 26
4	*Escheritia coli*	10.55±0.0 7*	12.62±0.12 *	12.93±0. 19*	8.55±0. 05	9.12±0. 04	9.40±0.0 0*	21.02±0. 36
5	*Klebsiella pneumoniae*	8.28±0.12 *	8.93±2.88*	12.52±0. 12*	6.15±0. 14	8.05±0. 12	8.40±0.0 0*	19.08±0. 08
6	*Pseudomonas aurogenosa*	15.38±0.2 0*	18.48±0.06 *	21.73±0. 14*	11.23±0 .45	10.32±0 .17	10.35±0. 05	9.83±0.0 5

Values were expressed as mean ± SEM (n=6), *p<0.05 denotes significance with respect to the standard group using one way ANOVA followed by pairwise test. inhibited the growth of *Pseudomonas aeruginosa*. This also showed increasing zone of inhibition with increasing the doses. Therefore areca nut phenolic components hold promise in management of *Pseudomonas aeruginosa* infection. *Staphylococcus aureus* is one of the most common

bacteria implicated in food poison. Alkaloid components showed good inhibitory activity against this pathogens and also to *Streptococcus pyogens.*

Effect of Anti-inflammatory activity

The anti-inflammatory effects of alkaloid and phenolic components of Areca nut in carrageenan-induced edema in rat's hind paws are presented in Table: 2 Figure 3a and 3b. There was a gradual increase in edema paw volume of rats in the control groups. Both components of areca nut possessed maximum anti-inflammatory activity in a dose dependent manner. That is, 200 µg/kg and 400 µg/kg in carrageenan induced animal models in comparison to that of Control group. There is significant reduction in paw edema volume by all tested group compares to control group after 240 minutes. The result showed that phenolic components 400 µg administrated group shows significant reduction in paw edema from the time of administration with significant to standard group. But 200 µg administrated group shows reduction after 30 minutes only. In case of alkaloid component reduction in paw edema occur 30 minutes and 60 minutes after the administration of 200 µg and 400 µg respectively. The paw volume after 240 minutes of 200 mg phenolic components administrated group (28.60±0.05) was found to be near to the 400 µg administrated alkaloid group (28.49±0.13).

Table 2: Anti-inflammatory activity of alkaloid and phenolic components

SL.NO	GROUP	DOSE	PAW VOLUME AFTER ADMINISTRATION OF DRUG/EXTRACT				
			0 min	30 min	60 min	120 min	240 min
			mean±SEM	mean±SEM	mean±SEM	mean±SEM	mean±SEM
1	CONTROL	0.01 ml	12.66±0.07	19.44±0.12	28.57±0.10	34.30±0.21	42.77±0.14
2	STANDARD	10 mg	12.35±0.05*	15.58±0.19*	17.65±0.13*	18.49±0.03*	19.54±0.06*
3	ALKALOID	200 µg	12.46±0.04	19.58±0.08	24.29±0.15*	28.32±0.10*	30.88±0.36*
4	ALKALOID	400 µg	12.42±0.06	17.53±0.09*	22.67±0.08*	25.60±0.17*	28.49±0.13*
5	PHENOLIC	200 µg	12.47±0.02	17.57±0.12*	24.94±0.17*	25.86±0.02*	28.60±0.05*
6	PHENOLIC	400 µg	12.45±0.45*	16.90±0.09*	20.77±0.09*	23.64±0.09*	26.63±0.11*

Values were expressed as mean ± SEM (n=6), *p<0.001 denotes significance with respect to the control group using one way ANOVA followed by Tukey's test.

The values of reduction in paw volume, 26.63±0.11, 28.49 ± 0.13 for 400 µg administration of phenolic and alkaloid and 19.54±0.06 for standard drug were found significantly at 240

minutes after carrageenan administration. Administration of 200 µg phenolic and alkaloid also found significant in the reduction of paw edema that is, 28.60±0.05 and 30.88±0.36 respectively with the standard drugs after 240 minutes of carrageenan administration. Even though the two components of areca nut shows the significant reduction in paw edema result suggest that phenolic component is more effective anti-inflammatory agent than alkaloid in every dose.

In the present study, treatment with areca nut water extract was effective in reducing the oedematogenic response evoked by carrageenan in a dose dependent manner. Comparative study carried out using the two components of areca nut, both components showed maximum anti-inflammatory activities in dose dependent manner. However, the significant reduction showed in paw edema volume of phenolic treated group with increasing time reveals phenolic components are more effective in the anti-inflammatory properties of areca nut. Result of the present study also indicates that areca nut plays a crucial role as protective factors against the carrageenan-induced acute inflammation with its phenolic group. Result of work carried out on anti-inflammatory properties of areca nut water extract and its two components increasing the medicinal properties of areca nut.

Effect of Antinociceptive activity

Table: 3 and figure 4 show the effects of phenolic and alkaloid fraction of areca nut on acetic acid-induced writhing in mice. Both fractions of areca nut showed significant reduction ($p<0.001$) of writhing induced by the acetic acid after oral administration in a dose dependent manner. After oral administration of phenolic fractions in different doses (200 and 400 mg/kg body weight), the percent inhibition was 43.75% and 59.51% respectively. Alkaloid fractions showed 24.10% and 37.80% for 200 mg and 400 mg/kg administration. The result showed that however, two doses of both doses showed the significant reduction, administration of phenolic components decrease the number of writhing compared to alkaloid fraction administrated groups. The inhibitory effect of diclofenac (79.46%) was greater than that of the highest inhibition of test group. However two doses of both doses showed the significant reduction, administration of phenolic components decrease the number of writhing compared to alkaloid fraction administrated groups. The inhibitory effect of diclofenac (79.46%) was greater than that of the highest inhibition of test group.

Table 3: Anti-nociceptive activities of alkaloid and phenolic components

SL.NO	GROUP	DOSE	NO. OF WRITHING	INHIBITION
1	CONTROL	10	56.00 ± 1.34	.....
2	STANDARD	10 mg	11.50 ± 0.34*	79.46
3	ALKALOID	200 µg	42.50 ± 0.56*	24.10
4	ALKALOID	400 µg	34.83 ± 0.40*	37.80
5	PHENOLIC	200 µg	31.50 ± 0.50*	43.75
6	PHENOLIC	400 µg	22.67 ± 0.33*	59.51

Values were expressed in Mean ± SEM(n=6), *p<0.01 was considered as significant with respect to the control group using one way ANOVA followed by Dunnett's test.

Present study with areca nut water extract showed dose dependent and significant inhibition of acetic acid induced writhes in mice. Study carried out to compare and find out the components responsible for anti-nociceptive activity, both components showed decrease in number of writing in the dose dependent manner. But the significant inhibition of acetic acid induced writhes found in phenolic group administrated group compared to alkaloid group. The mechanism of analgesic activity of areca nut could be probably due to the blockage of the effect or the release of endogenous substances that excite pain in nerve endings similar to that of indomethacin.

Graphical Representations

ANTIBACTERIAL ACTIVITY

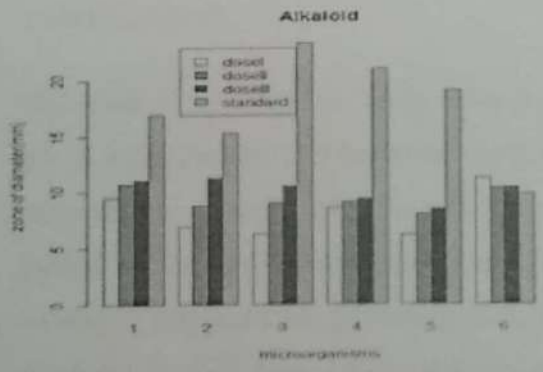

Fig: 2a

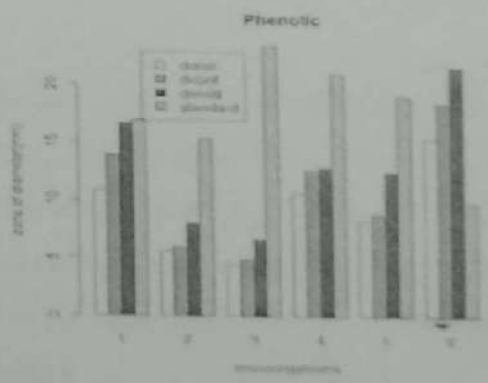

Fig: 2b

2) ANTI-INFLAMMATORY ACTIVITY

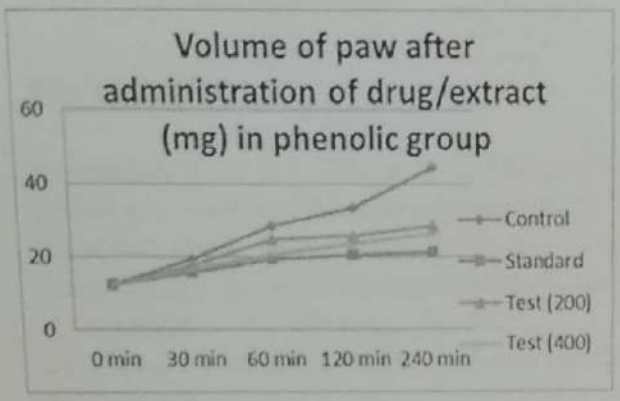

Fig: 3a

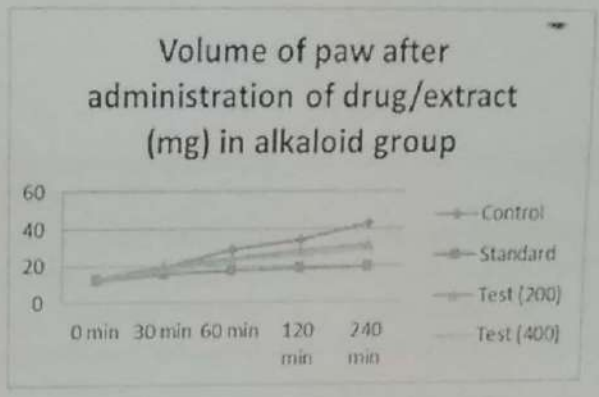

Fig: 3b

3) ANALGESTIC ACTIVITY

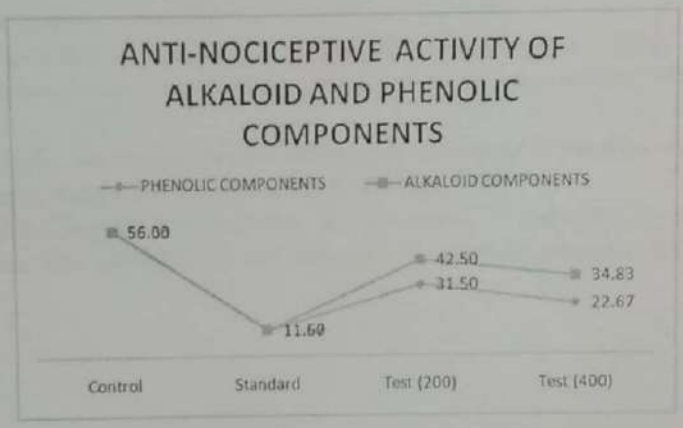

Fig: 4

CONCLUSION

The result of anti-bacterial study using the two components of areca nut revealed that areca nut is effective for anti-bacterial agent with promising anti-bacterial leads alkaloid and polyphenols, depends upon the percentage of these two components in it. Output of work carried out on anti-inflammatory and anti-nociceptive properties of areca nut components increasing the medicinal properties of areca nut. Among the raising controversy on areca nut result of our work opened a new door for areca nut research.

ACKNOWLEDGMENT

The authors would like to thanks the Faculty of Department of Analytical Chemistry, Cochin University, Cochin, Kerala for providing compound analysis. We assure you that this

manuscript has not been published already in part or whole in any journal or magazine for private or public circulation.

REFERENCES

1) Jayalakshmi. A, and Mathew. A. G. Chemical composition and processing.-The Areca nut Palm. Central Plantation Crops Research Institute, Kerala;1982.pp. 225–244.

2)Wei-Min Zhang, Wu-Yang Huang,Wen-Xue Chen, Lin Han and Hai-De Zhang. Optimization of Extraction Conditions of Areca Seed Polyphenols and Evaluation of Their Antioxidant Activities. (2014); pp. 16416-16427

3)Shivashankar. S, Dhanaraj. S, Mathew. A. G., Srinivasa Murthy. S., Vyasamurthy. M. N., Govindarajas.V.S.Technol.Physical and chemical characteristics of processed areca nut.pp.113– J. Food Sci; 1969:113-116

4)Huang.J.L, McLeish.M.J. High-performance liquid chromatographic determination of the alkaloids in betel nut. *J. Chromatogr;* 1989: 447–450.

5)Rojas J.J, Ochoa.V.J, Munoz.J.F. Screening for antimicrobial activity of ten medicinal plants used in Colombian folkloric medicines possible alternate in the treatment of nosocomial infections: BMC complement altern Med.;2006

6)Phyllis.E, Whiteley, Stacie.A, Dalrymple..model of inflammation:carrageenan-induced paw edema in the rat.current protocol in pharmacology;2001.

7)Dharmsiri.MG, Jayakody.J.R, Galhena.G, Liyanage.SS, Ratnasooriya. WD.J. ethanopharmacol. Anti-inflammatory and analgestic activities of mature fresh leaves of *vitexnegundo*.J.of .ethanopharmacol;2003:199-206

8)Cheruiyot.K.R, Olila.D, Kateregga.J.*In-vitro* antibacterial activity of selected medicinal plants from Longisa region of Bomet district, Kenya. Afr. Health Sci, 2009:42–46

9)Holetz.F.B,Pessini.G.L,Sanches.N.R, A Cortez D., Nakamura.C.V ,Filho.B.P.D . Screening of some plants used in the Brazilian folk medicine for the treatment of infectious diseases. Mem. Inst. Oswaldo Cruz; 2002:1027–1031

RESEARCH PAPER | Medical Science | Volume : 6 | Issue : 6 | June 2016 | ISSN - 2249-555X | IF : 3.919 | IC Value : 74.50

Evidence of Teratogenicity and DNA Damage among Women with Second Trimester Abortions

KEYWORDS: Second trimester pregnancy loss, Teratogenicity, Cytokinesis-block Micronuclei (CBMN) assay

Swapna C Senan
Department of Medical Microbiology, Sree Gokulam Medical College, Thiruvananthapuram- 695607

Sumitha Prabhu PS
Research Scholar, Meenakshi University, West KK Nagar, Chennai-600 078. TN, India

Sumina Cherian
Department of Biochemistry, Pushpagiri Institute of Medical Science and Research Centre, Tiruvalla, Pathanamthitta- 689101

Sarala Gopalakrishnan
Department of Microbiology, St. Pius X College, Kasargod- 671532

Dinesh Roy D
Genetika, Centre for Advanced Genetic Studies, Pettah P O, Thiruvananthapuram-695 024, India

ABSTRACT *Second trimester pregnancy loss is uncommon, but it should be regarded as an important event in a woman's obstetric history. The exposure of various teratogen lead to DNA damage and subsequent chromosomal abnormalities. These factors play a major role in second trimester abortion. The study consists of 40 women with second trimester abortion/s and 15 healthy subjects without any chronic illness were selected as control for the study. The goal of the present study was to evaluate the effect of teratogenicity and extent of somatic DNA damage in subjects with second trimester abortion. The extent of somatic DNA damage is quantified by Cytokinesis Block Micronuclei (CBMN) assay. Detailed demographic and clinical characteristics were recorded and compared. The present study demonstrated that micronuclei frequency was significantly elevated in the study subjects than control subjects. Maternal problems such as history of infection, increased duration of married life, thyroid disorders, diabetes etc can leads to foetal loss. Modification of lifestyle along with proper preventive measures against teratogenic infection and awareness of the role of genetics in the etiology of recurrent pregnancy loss will help in reducing the risk for miscarriage.*

INTRODUCTION

Second trimester pregnancy loss is defined as pregnancy loss after the 14th week of gestation and before the 24th week of gestation (Wyatt et al., 2005). It is uncommon, but it should be regarded as an important event in a woman's obstetric history. Foetal abnormalities including chromosomal problems, maternal anatomic factors, immunologic factors, and teratogenic factors should be considered. However a cause and effect relationship may be difficult to establish (Thomas et al., 2007). 12–15% of conceptions result in clinically recognized pregnancy loss. The majority of these are first trimester miscarriages and fewer than five percent of pregnancies are lost after 10 weeks of gestation (Robert and Silver, 2007). The incidence of miscarriage in the second trimester varies depends on the gestational weeks. In low risk women the risk of miscarriage in the second trimester is approximately 0.5% (Westin et al., 2007).

Various indications for the termination of pregnancy are foetal demise, risk to the pregnant woman, such as severe preeclampsia, eclampsia, renal disease and uncontrolled gestational diabetes, severe foetal congenital anomalies, intrauterine infection such as rubella, premature rupture of membrane, malignant diseases and other medical disorders like severe heart diseases (Chia et al., 2002).

Teratogenic infection can create intrauterine infections leading to birth defects, abortion and stillbirth. The common teratogenic infectious agents are toxoplasmosis, other agents, rubella virus, cytomegalovirus (CMV) and herpes simplex virus (HSV), etc. These are the most important infectious agents that can cause congenital malformations (Golalipour, 2009).

Several drugs and chemicals are known to be teratogenic to the human embryo when administered during pregnancy, especially during the period of organogenesis. The evidence for their teratogenicity has been shown by human epidemiologic and clinical studies. These teratogenic insults occurring during embryonic life may be present immediately after birth, at infancy or even later in life, especially if the damage involves the central nervous system (CNS) (Ornoy, 2003) such damage can lead to aberrant gene expression and apoptosis. Higher levels of DNA damage are detected among women with complicated pregnancies (Furness et al., 2011; Harma et al., 2005). Hence the present study was undertaken to evaluate the effect of teratogenicity and DNA damages in couples experiencing second trimester abortions.

MATERIALS AND METHODS

Forty subjects suffering with second trimester abortion were selected as study subjects and 15 normal healthy subjects without any chronic illness were selected as control for the present study. Detailed demographic and clinical characteristics were recorded using profoma. They were referred from various infertility clinics and maternity centers of Kerala to Genetika, Centre for Advanced Genetic studies, Trivandrum.

Seven ml of blood sample was collected by venepuncture. Two ml of blood was transferred into sodium heparinized vacuutainers for quantifying the extent of somatic DNA damages by Cytokinesis-Block Micronuclei (CBMN) assay. The remaining five ml of blood was transferred into a plain tube, allowed to clot, serum separated immediately. Blood

Volume : 6 | Issue : 6 | June 2016 | ISSN - 2249-555X | IF : 3.919 | IC Value : 74.50

sugar and lipid profile were estimated using semi-automated clinical chemistry analyzer.

Two ml blood was added to a culture tube containing 10 mL RPMI 1640 supplemented with 100units/mL penicillin, 100µg/mL streptomycin, 15% fetal bovine serum and 100µg/mL phytohemagglutinin. Cytochalasin B was added to the cultures at a final concentration of 4.5µg/mL (Sigma) after 44th hours of initiation of cells with phytohaemagglutinin. Cells were harvested after 72 hr incubation, and they were treated with a hypotonic solution (0.075M KCl) for 1 min and fixed in fresh fixative solution (methanol: acetic acid, 3:1). The cells were dropped onto slides and the slides were air dried and stained with 10% Giemsa. Micronucleated cells were analyzed under light microscopy at 100X magnification. The number of micronuclei is not less than 1000 binucleated cells were scored and the distribution of micronuclei among binucleated cells was recorded.

RESULTS

Table1- Distribution of mean CBMN frequency according to various demographic characteristics

Category	Variables	Number (Percentage)	Mean CBMN frequency
Age of husband (Years)	25 to 35	19 (47.5%)	12.70
	36 to 45	19 (47.5%)	12.76
	>45	2 (5%)	13.01
Age of wife (Years)	<30	26 (65%)	12.70
	30 to 40	12 (30%)	12.80
	>40	2 (5%)	13.01
Duration of married life (Years)	1 to 5	23 (57.5%)	12.74
	6 to 10	13 (32.5%)	12.47
	11 to 15	1 (2.5%)	12.61
	16 to 20	3 (7.5%)	12.82

Table 2- Distribution of mean CBMN frequency according to various clinical characteristics

Category	Variables	Number (Percentage)	Mean CBMN frequency
Number of gestations	<3	5 (12.5%)	12.42
	3 to 6	33 (82.5%)	12.52
	>6	2 (5%)	12.81
Number of spontaneous abortions	0 to 2	18 (45%)	12.52
	3 to 5	2 (5%)	12.59
	6 to 8	20 (50%)	12.91
Number of MTPs	<2	5 (12.5%)	12.5
	≥2	35 (87%)	12.78
History of infection	Yes	6 (15%)	12.77
	No	34 (85%)	12.59
History of illness	Yes	11 (27.5)	12.75
	No	29 (72.5%)	12.72
History of drug intake	Yes	7 (17.5%)	12.75
	No	33 (82.5%)	12.70
Ultrasound Scan (USS) findings	Cardiac anomalies	5 (12.5%)	12.25
	Maternal abnormalities	2 (5%)	12.61
	Growth retardation	3 (7.5%)	12.12
	Congenital anomalies	30 (75%)	12.90
Cytogenetic Analysis	Abnormal karyotype	24 (60%)	13.13
	Normal karyotype	16 (40%)	12.15

The demographic and clinical characteristic findings are given in the table 1 and table 2. The age of husbands were grouped into 25 to 35, 36 to 45 and >45 years. The highest mean CBMN frequency 13.01 was showed by the age of husband >45 years. Age of wives were grouped into <30, 30 to 40 and >40 years. The highest mean CBMN frequency of 13.01 were showed in the age group >40 years. The age of the couples was increased and the mean CBMN frequency was also increased. The duration of married life, the couples those who had duration of 16 to 20 years of married life were showed mean CBMN frequency of 12.82. The number of gestations of the study subjects was observed and the highest mean CBMN frequency (12.81) was showed in subjects with more than 6 times of gestations. Moreover the subjects with more than six times spontaneous abortions were showed an increased mean CBMN frequency of 12.91. Simultaneously subjects with ≥2 times medical termination of pregnancies (MTP) was showed a mean CBMN frequency of 12.78. In short, increase in number of gestations, spontaneous abortions and MTPs were showed an increased incidence of mean CBMN frequency among the study subjects. Subjects with history of infection, history of illness and history of drug intake were showed increased incidence of abortions and their mean CBMN frequencies are 12.77, 12.75 and 12.75. More over 75% of Ultrasound Scan (USS) findings were showed congenital anomalies. Cytogenetic analysis was showed 60% abnormal karyotype and a mean CBMN frequency of 13.13.

DISCUSSION

In a retrospective study (De La Rochebrochard et al., 2002) estimate of the spontaneous abortion among women aged 35–44 years was higher when paternal age was 40–64 years. The interpretation of this increase in terms of the paternal age effect is uncertain, because the distribution of female age between 35 to 44 years may be shifted toward higher values when comparing partners of men aged 35–39 years with partners of men aged 40 or more years. In the present study, the paternal age >45 years and maternal age >40 years were observed with increased mean CBMN frequency. The result from the current study suggests that increased age of couples plays an important role in second trimester abortions.

Infections play a critical role in pregnancy wastage and their occurrence in patients with bad obstetric history (BOH) or complicated pregnancy is a significant risk factor (Stegmann et al, 2002; Kishore et al, 2003; Kishore et al, 2000). All viral pathogens usually cause a primary maternal viremia which may infect the placenta and thereby the foe-

Volume : 6 | Issue : 6 | June 2016 | ISSN - 2249-555X | IF : 3.919 | IC Value : 74.50

tus with the exception of HSV-I or II, which causes an ascending infection via the genital tract to foetal membranes and then to the foetus (Ajayi et al., 2010). In the present study, among the 40 study subjects, 15% had the history of infection and they were observed with high micronuclei frequency indicating an increased DNA damage in them.

In addition to their role in first trimester miscarriage, chromosomal abnormalities also cause pregnancy loss in the second trimester. About 24 percent of pregnancy losses in the second trimester are caused by chromosomal abnormalities, and about 12 percent of late second trimester losses are attributed to this cause (Warburton et al., 1986). Chromosomal abnormalities found in second trimester losses are similar to those found in live births; the most common are trisomies 13, 18, and 21, monosomy X (i.e., Turner syndrome), and sex chromosome polysomies (Simpson et al., 1996). In the present study, it is analysed that 24 study subjects had abnormal karyotype and 16 study subjects had normal karyotype. Subjects with chromosomal abnormalities or abnormal karyotype showed an increased mean CBMN frequency.

Proximity to commercial pesticide applications was associated with an elevated risk of foetal death due to congenital anomalies. Furthermore, a consistent pattern was found with respect to timing of exposure; the largest risks for foetal death due to congenital anomalies were from pesticide exposure during the 3rd to 8th weeks of pregnancy (Erin et al., 2001). In the present study, it was observed that the mean CBMN frequency was highest in those who had congenital anomalies suggesting an increased DNA damage in them.

Human teratogens generally increase rates of specific defects or spectrum of defects. For example, thalidomide cause limb, spine, and central nervous system defects; isotretinoin causes ear, CNS, and cardiac defects; valproic acid causes neural tube defects; and angiotensin II converting enzyme (ACE) inhibitors cause renal functional effects (Mitchell, 2000). The present study is in agreement with above mentioned statement. Subjects with increased exposure to drugs during their pregnancy period were observed with increased mean CBMN frequency. Thus it can be suggested that lowering the exposure to various drugs among pregnant mothers can be avoided in order to prevent the teratogenic effect of all these drugs, chemicals, toxins towards the developing foetus.

CONCLUSION

The present study involves teratogenicity and DNA damage in second trimester abortions. The distribution of mean CBMN frequency according to demographic and clinical factors of the study subjects was observed. Age of the couples, duration of married life, number of gestations, number of spontaneous abortions, number of MTPs, etc. were showed an increased level of mean CBMN frequency. The level of mean CBMN frequency was highest among those who have the family history of infection, history of illness, history of drug intake. Abnormal karyotype of the study subjects showed increased mean CBMN frequency. The main preventive measures of second trimester pregnancy loss including vaccination and folic acid supplementation are recommended regardless of risk. The fruits and vegetables contain pesticides are the main teratogenic factor so should be well washed prior to consumption. Pregnant women should be advised to avoid contact with soil, pet animals and also avoid with toxic substances like chemicals, radiations, heavy metals, pesticides etc. These preventive measures may help from exposure to various teratogenic agents and thus reduce the risk of DNA damage and subsequent pregnancy loss/congenital anomalies.

REFERENCE

1. Ajayi, G.O. and Omilabu, S.A.; Prenatal diagnoses of cytomegalovirus (CMV), rubella, toxoplasmosis, varicella, parvovirus, herpes simplex and syphilis. The Lagos programme experience. Clin Exp Obstet Gynecol; 2010. 37: 37-38.
2. Chia, P.; Chia, H.; Subramaniam, R.; Failed medical and surgical termination of pregnancy. JOG; 2002. 4: 212.
3. De La Rochebrochard, E.; Thonneau, P.; Paternal age and maternal age are risk factors for miscarriage; results of a multicentre European study. Hum Reprod2002, 17:1649–56.
4. Enrique, Donoso.; Jorge, A.; Carvajal.; Claudio Vera.; Jose, A.; The women's age as a risk factor for maternal mortality, fetal, newborn and child.Rev.med.Santiago Chile vol.142 Feb; 2014.
5. Erin, M.; Irva, Hertz-Picciotto, and James, J.; Beaumont. A Case-Control Study of Pesticides and Fetal Death Due to Congenital Anomalies.Epidemiology; 2001. 12:148–156.
6. Furness, D.L.; Dekker, G.A.; Roberts, C.T.; DNA damage and health in pregnancy. J Reprod Immunol; 2011.89: 153–162
7. Harma, M.; Kocyigit, A.; Erel, O.; Increased DNA damage in patients with complete hydatidiform mole.Mutat Res; 2005. 583: 49–54.
8. Kishore, J.; and Kapoor, A.; Erythrovirus B19 infection in humans. Indian J Med Res; 2000.112: 149-154.
9. Kishore, J.; Agarwal, J.; Agrawal, S.; Ayyagari, A.; Seroanalysis of Chlamydia trachomatis and S-TORCH agents in women with recurrent spontaneous abortions; 2003.
10. Mitchell, A.A.; Special Considerations in Studies of Drug-Induced Birth Defects, In: Strom, BL, editor, Pharmacoepidemiology, third edition, England: John Wiley & Sons, Ltd., pp; 2000. 749-63.
11. Ornoy, A.; The impact of intrauterine exposure versus postnatal environment in neurodevelopmental toxicity: long-term neurobehavioral studies in children at risk for developmental disorders. Toxicol Lett; 2003. 140–141:171–181.
12. Robert, M.; Silver, Fetal Death Obstet Gynecol; 2007. 109:153–67.
13. Saker, M.; Mokhtari, N.S.; Merzouk, S.A.; Merzouk, H.; Belarbi, B.; Narce, M.; Oxidant and antioxidant status in mothers and their newborns according to birthweight. Eur J Obst Gynecol Reprod Bio; 2008, 141, 95–99.
14. Simpson, J.L.; Mills, J.L.; Kim, H.; Holmes, L.B.; Lee, J.; Metzger, B.; et al. Infectious processes:an infrequent cause of first trimester spontaneous abortions. Hum Reprod; 1996. 11:668–72.
15. Stegmann, B.J and Carey, J.C.; TORCH Infections: Toxoplasmosis, Other (syphilis, vancella zoster, parvovirus B19, Rubella, Cytomegalovirus (CMV), and Herpes infections. Curr Womens Health Rep; 2002. 2: 253-258.
16. Thomas, C.; Michels, and Alvin, Y.; Second Trimester Pregnancy Loss, American Academy of Family Physicians; 2007.
17. Warburton, D.; Kline, J.; Stein, Z.; Strobino, B.; Cytogenetic abnormalities in spontaneous abortions of recognized conceptions. In: Porter IH, Hatcher NH, Willey AM, eds. Perinatal Genetics: Diagnosis and Treatment. Orlando, Fla.: Academic Press; 1986.23-40.
18. Westin, M., Kallen, K., Saltvedt, S., Amstrom, M., Grunewald, C. and Valentin, L. Miscarriage after a normal scan at 12-14 gestational weeks in women at low risk of carrying a fetus with chromosomal abnormalities according to nuchal translucency screening. Ultrasound Obstet Gynecol; 2007. 30 (5), 720-736.
19. Wyatt PR, Owolabi T, Meier C, et al. Agespecific risk of fetal loss observed in a second trimester serum screening population. Am J Obstet Gynecol 2005; 192:240-6.

Streaming instability in negative ion plasma

Ajith Kumar, and Vincent Mathew

Citation: Physics of Plasmas **24**, 092107 (2017); doi: 10.1063/1.4989427
View online: http://dx.doi.org/10.1063/1.4989427
View Table of Contents: http://aip.scitation.org/toc/php/24/9
Published by the American Institute of Physics

Streaming instability in negative ion plasma

Ajith Kumar[a] and Vincent Mathew[b]
Department of Physics, Central University of Kerala, Padannakkad, Kasaragod, 671314, India

(Received 9 June 2017; accepted 11 August 2017; published online 28 August 2017)

The streaming instability in an unmagnetized negative ion plasma has been studied by computational and theoretical methods. A one dimensional electrostatic Particle In Cell Simulation and fluid dynamical description of negative ion plasma showed that, if the positive ions are having a relative streaming velocity, four different wave modes corresponding to Langmuir wave, fast and slow ion waves and ion acoustic waves are produced. Below a critical wave number, instead of two distinct fast and slow ion waves, we observed a coupled wave mode. The value of the critical wave number is strongly determined by the ion streaming velocity. The thermal velocities of electrons and ions influence the growth rate of instability. *Published by AIP Publishing.*
[http://dx.doi.org/10.1063/1.4989427]

I. INTRODUCTION

Plasma systems which contain positive ions, negative ions, and electrons are considered as negative ion plasma. The presence of heavier negatively charged constituents and reduced number of electrons leads to peculiar wave natures and instabilities in negative ion plasma. Space and planetary[1] plasma environments such as earth's ionosphere,[2] cometary coma,[3] etc. are the examples for natural negative ion plasma systems.[4] Pair ion plasma is a special case of negative ion plasma and it is significant in recent plasma physics.[5,6] There have been many experimental and theoretical studies on the production and characteristics of negative ion plasma. Study of ion acoustic solitons and the wave breaking mechanism in negative warm ion plasma was carried out by Das and Tagare,[7] Das,[8] and Ludwig *et al.*[9] They observed a critical density ratio of negative and positive ions for the generation of solitary waves. A theoretical study of ion acoustic solitary waves in negative ion plasma with adiabatic positive and negative ion temperature and isothermal electrons was performed by Tagare based on the perturbation method.[10] The properties of ion acoustic solitons in warm plasma with non isothermal electrons were also studied by Tagare and Reddy.[11] Wong *et al.* carried out an experimental study of fast ion modes generated by the out of phase motion between positive and negative ions in a multi species plasma consisting of SF_6^-, Ar^+, and electrons.[12] Experimental and theoretical study of beam plasma instability in negative ion plasma containing SF_6^-, Ar^+, and a very small fraction of electrons was done by Intrator *et al.*[13] Song *et al.* investigated the propagation and damping characteristics of ion acoustic waves in the Q machine consisting of Ar^+, SF_6^-, and electron components.[14] The shock formation in collisional negative ion plasma for different cases of relative density was experimentally studied by Luo *et al.*[15] Another experimental study of shock formation in negative ion plasma was performed by Takeuchi *et al.*[16]

In the present work, we performed a one dimensional particle in cell simulation[17] of streaming instability in a negative ion plasma consisting of positive ions, negative ions, and electrons. In order to justify the simulation results, we numerically solved the dispersion relationship and observed identical characteristics. The positive and negative ions have equal and opposite charges, but different masses. The electron concentration is very much less than that of the negative ion concentration and satisfies the charge neutrality condition, $n_p = n_n + n_e$, where n_p, n_n, and n_e are the positive ion density, negative ion density, and electron density, respectively. The electrons and positive ions have a relative streaming velocity with respect to negative ions. The plasma was treated as unmagnetized and collisionless.

An outline of the simulation setup and observations are given in Sec. II and the theoretical model is given in Sec. III. Section IV contains the numerical solution of the dispersion relationship and Sec. V is the conclusion.

II. PARTICLE IN CELL SIMULATION (PIC) SIMULATION

One dimensional electrostatic PIC simulation was carried out by using the PIC code KEMPO1(Kyoto Electro Magnetic Pic cOde)[18] with periodic boundary conditions. The space and time were normalized to the Debye length (λ_D) and plasma time period (ω_{pe}^{-1})of electrons, respectively. The simulation domain was taken as $2048\lambda_D$ with grid length $1\lambda_D$. The total number of super particles corresponding to electrons, positive ions, and negative ions was 65 536, 262 144, and 196 608, respectively. The charge to mass ratios of the electrons, positive ions, and negative ions were -1, 0.01, and -0.001, respectively. In order to avoid the numerical instability and also our main objective was the qualitative understanding of the phenomena, the numerical values in the simulations were taken as little different from the real particle plasma system. The oscillation frequencies of electrons, positive ions, and negative ions were ω_{pe}, $0.24\omega_{pe}$, and $0.068993\omega_{pe}$, respectively. For the first run, the streaming velocities of electrons and positive ions were chosen as $10\lambda_D\omega_{pe}$ and $3\lambda_D\omega_{pe}$, respectively. The electron thermal velocity was $0.1\lambda_D\omega_{pe}$ and the positive ion thermal velocity

[a]Present address: Department of Physics, St Pius X College, Rajapuram, Kasaragod, Kerala 671532, India. Electronic mail: kannothajith@gmail.com.
[b]Electronic mail: vincent@cukerala.ac.in.

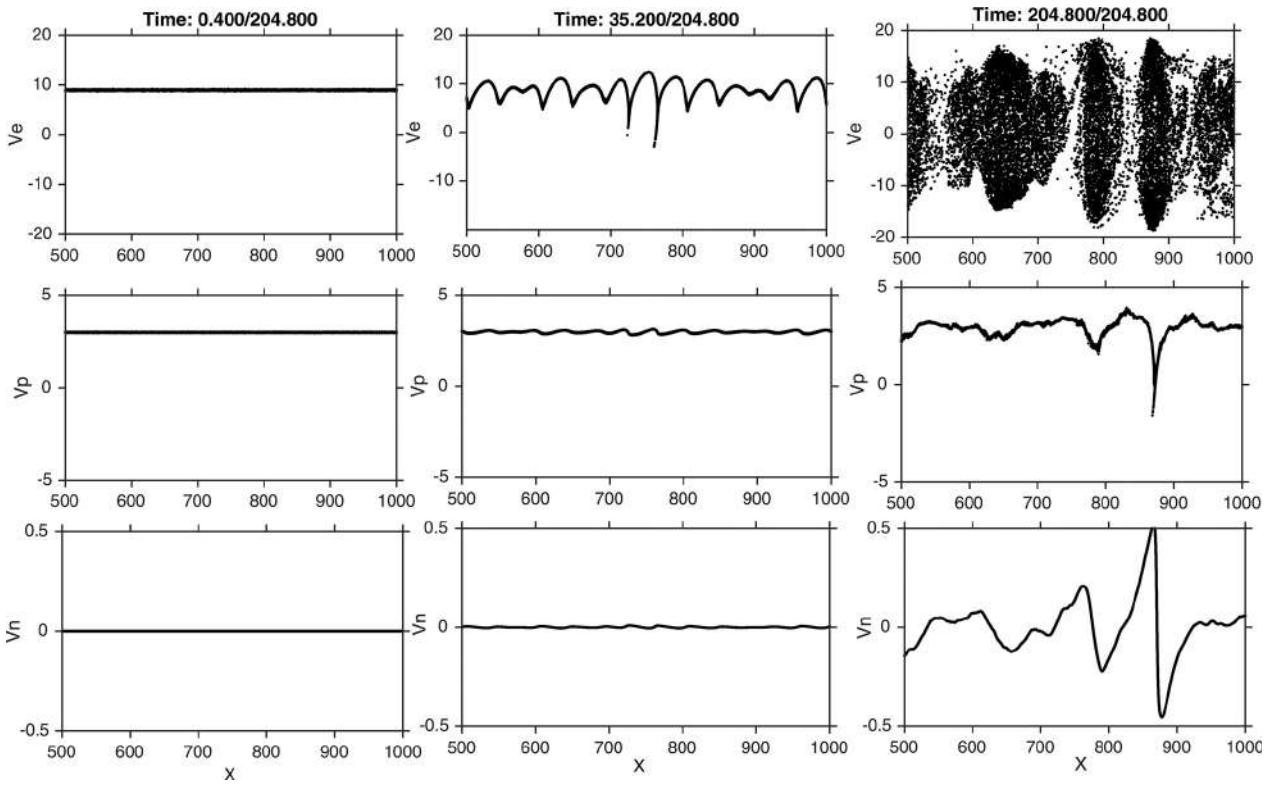

FIG. 1. Phase space diagram of plasma constituents at different time intervals.

was $0.01\lambda_D\omega_{pe}$. The total computational time was $204.8\omega_{pe}^{-1}$ with 4096 steps and $\Delta t = 0.05\omega_{pe}^{-1}$.

It has been observed that the streaming instability in negative ion plasma has two phases. The initial phase of instability was driven by the streaming of electrons and it had a very high growth rate and peaks at time $40\omega_{pe}^{-1}$. At the beginning of the simulation, the electric field was zero and as the time evolves it started to grow by acquiring energy from the streaming electrons. During this stage, we observed the Langmuir wave generation associated with vortex formation in the electron velocity phase space. After the saturation of the initial phase, the second phase of instability started to grow with a comparatively small growth rate. In the course of this time, fast and slow ion waves and ion acoustic waves are generated. The phase space diagrams of plasma components at different intervals of time and the evolution of electric field during the simulation are shown in Figs. 1 and 2, respectively. The dispersion diagram ($\omega - k$) obtained by the space time Fourier transform of the electric field shows the presence of four prominent frequency modes corresponding to Langmuir wave (ω_e), fast and slow ion modes (ω_{+a} and ω_{+b}), and very low frequency ion acoustic waves (ω_-) (Fig. 3). We cannot observe two distinct, fast and slow ion waves below a critical wave number, $k*$. Below the critical wave number, there are only three kinds of waves, Langmuir wave, coupled ion wave, and ion acoustic wave. The value of critical wave number is strongly determined by the ion streaming velocity. The dispersion diagram for the second and third run of simulations with increased ($4\lambda_D\omega_{pe}$) and reduced ($1\lambda_D\omega_{pe}$) ion velocity is shown in Fig. 4. For the first run, the value of the critical wave number was observed at $0.045\lambda_D^{-1}$ and that reduced to $0.02\lambda_D^{-1}$ for the second run

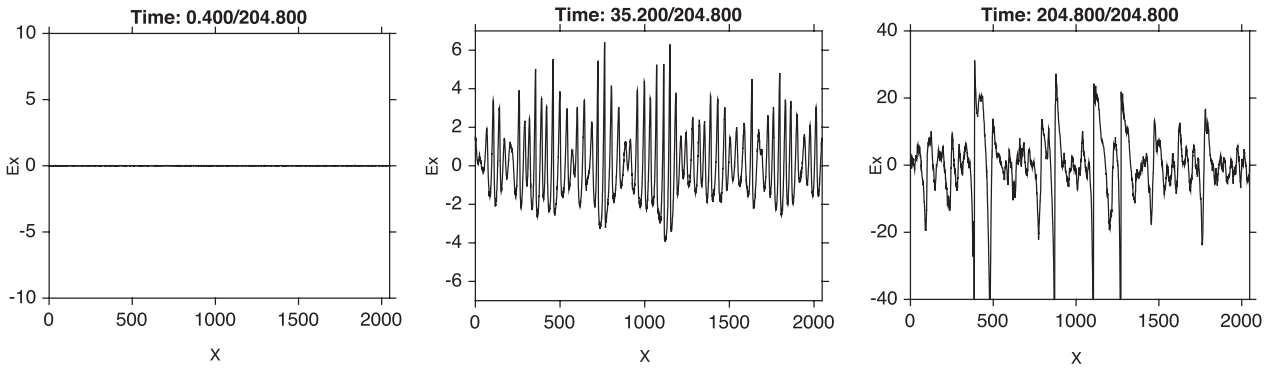

FIG. 2. Electric filed at different time intervals.

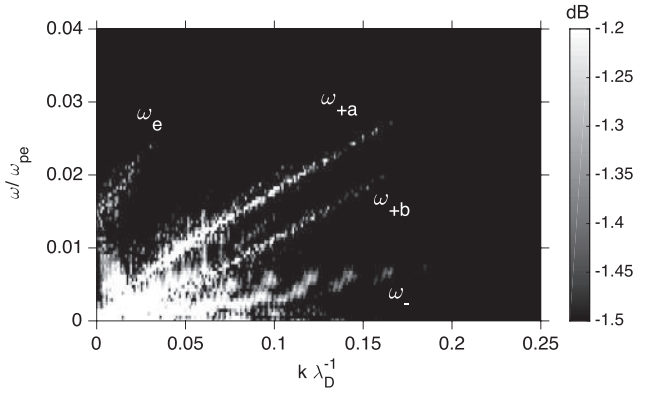

FIG. 3. $\omega - k$ diagram.

[Fig. 4(a)]. When the ion streaming velocity is less than a minimum value, we can observe only three distinct frequencies corresponding to the Langmuir wave, coupled ion wave, and ion acoustic wave [Fig. 4(b)].

The thermal velocities of electrons and ions influence the growth rates of the instability. Figure 5 shows the evolution of electrostatic energy during the simulations for different cases of electron thermal velocities. The increased value of electron thermal velocity leads to growth of the initial phase of instability faster and we can observe a more rapid electron vortex formation and Langmuir wave generation. But, for the second phase, the electron thermal velocity causes a reduced growth rate. The ion thermal velocity enhances the growth rate for both the first and second phases of instability (Fig. 6).

III. DISPERSION RELATIONSHIP

We considered a plasma system comprising positive ions, negative ions, and electrons with densities n_p, n_n, and n_e, respectively. m_e, m_p, and m_n are the masses of electrons, positive ions, and negative ions, respectively. The heavier negative ion species are initially at rest ($v_{n0} = 0$). The relative speeds of electrons and positive ions to the negative ions are v_e and v_p, respectively. The temperatures of electrons and positive ions are T_e and T_p, respectively.

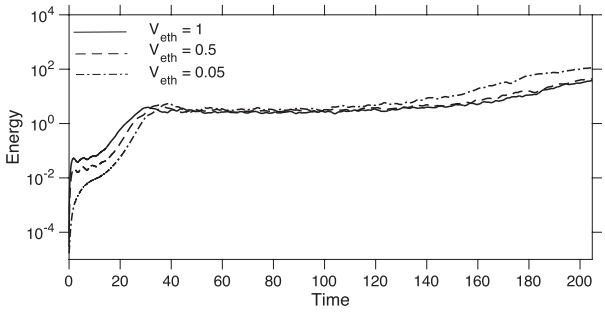

FIG. 5. Dependence of electron thermal velocity on the instability.

One dimensional continuity and momentum equations can be applied to the plasma components, electrons, positive ions, and negative ions. The continuity equations are,

$$\frac{\partial n_e}{\partial t} + n_e \frac{\partial v_e}{\partial x} + v_e \frac{\partial n_e}{\partial x} = 0, \tag{1}$$

$$\frac{\partial n_p}{\partial t} + n_p \frac{\partial v_p}{\partial x} + v_p \frac{\partial n_p}{\partial x} = 0, \tag{2}$$

$$\frac{\partial n_n}{\partial t} + n_n \frac{\partial v_n}{\partial x} + v_n \frac{\partial n_n}{\partial x} = 0. \tag{3}$$

The momentum equations are,

$$m_e n_e \frac{\partial v_e}{\partial t} + m_e n_e v_e \frac{\partial v_e}{\partial x} + KT_e \frac{\partial n_e}{\partial x} + en_e E = 0, \tag{4}$$

$$m_p n_p \frac{\partial v_p}{\partial t} + m_p n_p v_p \frac{\partial v_p}{\partial x} + KT_p \frac{\partial n_p}{\partial x} - en_p E = 0, \tag{5}$$

$$m_n n_n \frac{\partial v_n}{\partial t} + m_n n_n v_n \frac{\partial v_n}{\partial x} + en_n E = 0. \tag{6}$$

Here, K is the Boltmann constant.

We assumed that, all the variables n_j, v_j, and E can be written in the form: $f = f_0 + f_1$, where f_0 is the value at its equilibrium state and f_1 is the perturbed value ($f_1 \ll f_0$). The quasi-neutrality condition of plasma is given as,

$$n_{p0} = n_{e0} + n_{n0}. \tag{7}$$

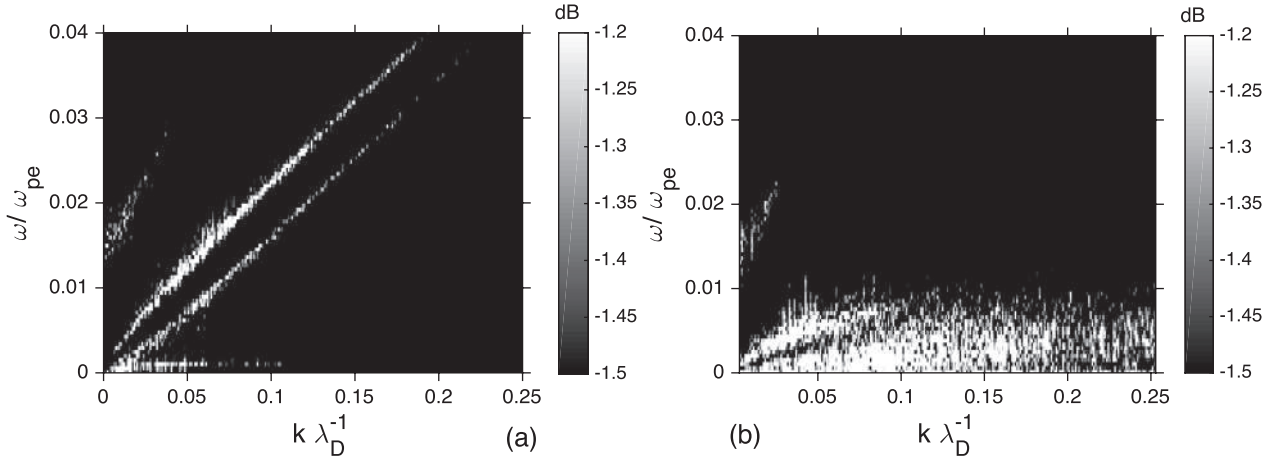

FIG. 4. Dispersion diagram for Increased and reduced values of ion streaming velocity.

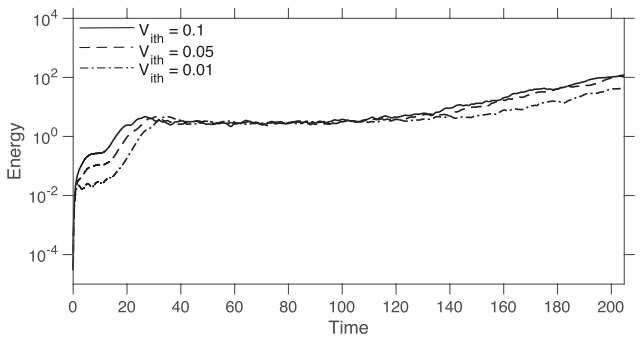

FIG. 6. Dependence of Ion thermal velocity on the instability.

Equations are linearized and all first order quantities are taken to have the dependence, $e^{i(kx-\omega t)}$. From the linearized continuity equations,

$$v_{e1} = \frac{\omega - kv_{e0}}{k}\left(\frac{n_{e1}}{n_{e0}}\right), \tag{8}$$

$$v_{p1} = \frac{\omega - kv_{p0}}{k}\left(\frac{n_{p1}}{n_{p0}}\right), \tag{9}$$

$$v_{n1} = \frac{\omega}{k}\left(\frac{n_{n1}}{n_{n0}}\right). \tag{10}$$

Applying the above equations in the linearized first order momentum equations, we get,

$$n_{e1} = -\frac{iekn_{e0}/m_e}{(\omega - kv_{e0})^2 - k^2(KT_e/m_e)}E_1, \tag{11}$$

$$n_{p1} = \frac{iekn_{p0}/m_p}{(\omega - kv_{p0})^2 - k^2(KT_p/m_p)}E_1, \tag{12}$$

$$n_{n1} = -\frac{iekn_{n0}}{m_n\omega^2}E_1. \tag{13}$$

We have Poisson's equation

$$\nabla \cdot E_1 = \frac{e}{\epsilon_0}(n_{p1} - n_{e1} - n_{n1}). \tag{14}$$

Substituting for perturbed particle densities in the above equation and using the relationship $\frac{1}{2}mv_{eth}^2 = \frac{1}{2}KT_e$ and $\frac{1}{2}mv_{pth}^2 = \frac{1}{2}KT_p$, where v_{eth} and v_{pth} are the thermal velocities of electrons and positive ions, respectively,

$$\frac{\omega_p^2}{(\omega - kv_{p0})^2 - k^2v_{pth}^2} + \frac{\omega_e^2}{(\omega - kv_{e0})^2 - k^2v_{eth}^2} + \frac{\omega_n^2}{\omega^2} = 1. \tag{15}$$

Here, ω_p, ω_e, and ω_n are the plasma frequencies of positive ions, electrons and negative ions, respectively.

IV. NUMERICAL SOLUTION

For the numerical illustrations, we took a more realistic example of plasma containing, SF_6^-, Ar^+, and electrons. We considered a stream of this negative ion plasma in which negative ions lag behind the electrons and positive ions because of their higher inertia. The relative streaming velocities of positive and negative ions were considered as very large and hence, we treated the SF_6^- as initially at rest. The input parameters for solving the dispersion relationships were $n_{p0} = 10^{13}\text{m}^{-3}$, $n_{e0} = 10^{10}\text{m}^{-3}$, $n_{n0} = 9.99 \times 10^{12}\text{m}^{-3}$, $m_e = 9.1 \times 10^{-31}\text{kg}$, $m_p = 6.6 \times 10^{-26}\text{kg}$, $m_n = 2.3 \times 10^{-25}\text{kg}$, $v_{eth} = 10^4\text{m/s}$, $v_{pth} = 10^3\text{m/s}$, $v_{p0} = 4.5 \times 10^5\text{m/s}$, and $v_{e0} = 10 \times v_{p0}$.

The ω–k diagram drawn from the numerical solutions of the dispersion relationship is shown in Fig. 7. The real part of ω gives the possible wave frequencies and the imaginary part shows their damping or growth rates. The numerical solutions yielded both positive and negative complex roots corresponding to wave growth and wave damping, respectively. In the case of streaming instability, there is a greater amount of energy transfer from particles to the waves which causes the wave growth. Since our computational study also shows the growing characteristics of instability, only positive complex roots are considered as a physically relevant solution. For the given set of input parameters, we observed different stable frequency components labelled as ω_e, ω_{+a}, ω_{+b}, and ω_- corresponding to the Langmuir wave (ω_e), fast and slow ion waves (ω_{+a} and ω_{+b}), and ion acoustic wave (ω_-). Below a critical wave number, we cannot observe these fast and slow ion plasma oscillations; instead, we get a combined wave mode. The observed value of the critical wave number is 6m^{-1}. The magnitude of the critical wave number is strongly determined by the ion streaming velocity. In other

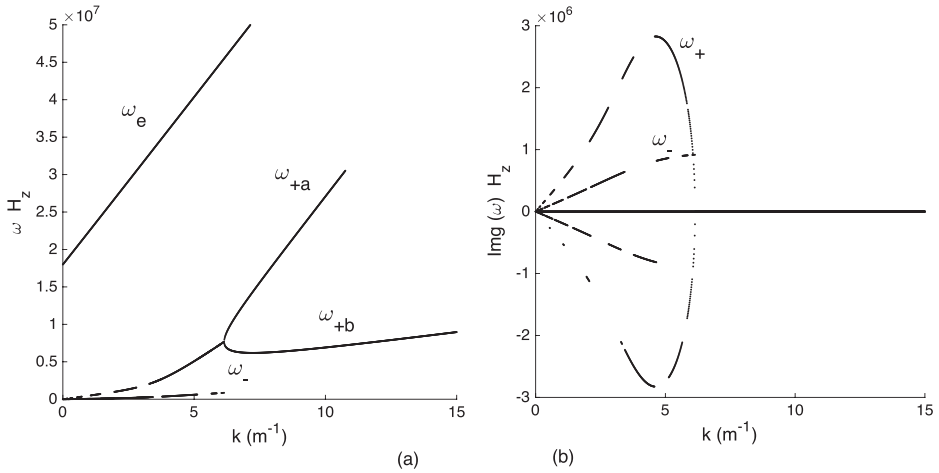

FIG. 7. $\omega - k$ diagram obtained from the numerical solution of the dispersion relationship for $v_{op} = 4.5 \times 10^5\text{m/s}$.

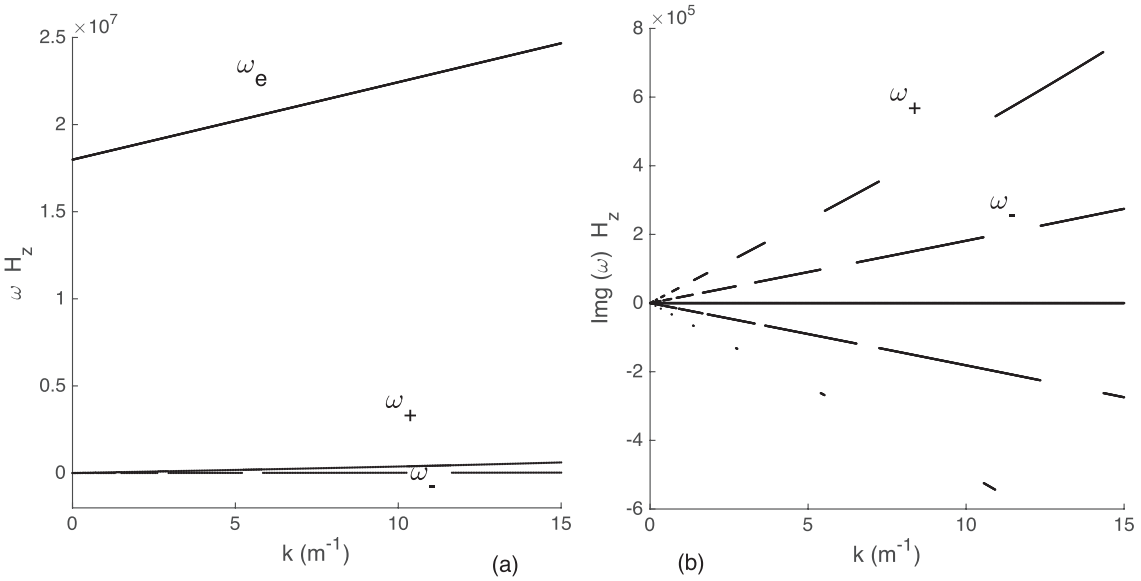

FIG. 8. $\omega - k$ diagram obtained from the numerical solution of the dispersion relationship for $v_{op} = 4.5 \times 10^4$m/s.

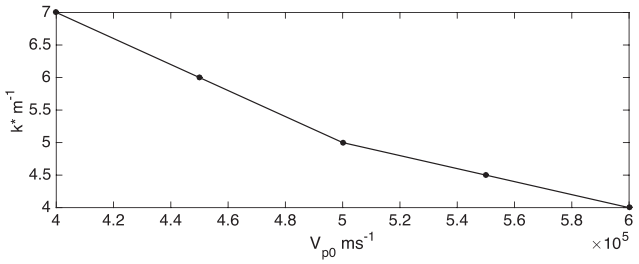

FIG. 9. Dependence of ion streaming velocity on the critical wave number.

words, if the ion velocity is less than the critical value, we can observe only three modes of waves or the critical wave number shifted towards the higher values. Figure 8 shows the dispersion diagram when the ion streaming velocity reduced to $4.5 \times 10^4 \text{ms}^{-1}$. Here we observe only three modes of frequencies. The dependence of the critical wave number on ion velocity is shown in Fig. 9.

V. CONCLUSION

In an unmagnetized, collisionless, negative ion plasma, if the electrons and positive ions have a streaming velocity with respect to negative ions, it will generate the instability and produce different stable wave frequencies corresponding to the Langmuir wave, fast and slow ion waves, and ion acoustic wave. Below a critical wave number, instead of two distinct fast and slow ion waves, we can observe only a coupled wave mode. The magnitude of the critical wave number depends on the streaming velocity of ions. Both our one dimensional electrostatic PIC simulation and one dimensional fluid dynamical model show the identical behaviour. The electron and ion thermal velocities influence the growth rate of instability.

[1]A. Coates, F. Crary, G. Lewis, D. Young, J. Waite, and E. Sittler, "Discovery of heavy negative ions in titan's ionosphere," Geophys. Res. Lett. **34**, L22103, doi:10.1029/2007GL030978 (2007).
[2]F. Fehsenfeld, D. Albritton, J. Burt, and H. Schiff, "Associative-detachment reactions of O^- and O_2^- by $O_2(^1\Delta_g)$," Can. J. Chem. **47**, 1793–1795 (1969).
[3]P. Chaizy and H. Reme *et al.*, "Negative ions in the coma of comet Halley," Nature **349**, 393 (1991).
[4]D. Sheehan and N. Rynn, "Negative-ion plasma sources," Rev. Sci. Instrum. **59**, 1369–1375 (1988).
[5]W. Oohara and R. Hatakeyama, "Pair-ion plasma generation using fullerenes," Phys. Rev. Lett. **91**, 205005 (2003).
[6]W. Oohara, D. Date, and R. Hatakeyama, "Electrostatic waves in a paired fullerene-ion plasma," Phys. Rev. Lett. **95**, 175003 (2005).
[7]G. Das and S. Tagare, "Propagation of ion-acoustic waves in a multicomponent plasma," Plasma Phys. **17**, 1025 (1975).
[8]G. Das, "Ionic thermal effects on ion-acoustic waves in plasmas with negative ions," Plasma Phys. **19**, 363 (1977).
[9]G. Ludwig, J. Ferreira, and Y. Nakamura, "Observation of ion-acoustic rarefaction solitons in a multicomponent plasma with negative ions," Phys. Rev. Lett. **52**, 275 (1984).
[10]S. Tagare, "Effect of ion temperature on ion-acoustic solitons in a two-ion warm plasma with adiabatic positive and negative ions and isothermal electrons," J. Plasma Phys. **36**, 301–312 (1986).
[11]S. Tagare and R. V. Reddy, "Effect of ionic temperature on ion-acoustic solitons in a two-ion warm plasma consisting of negative ions and non-isothermal electrons," Plasma Phys. Controlled Fusion **29**, 671 (1987).
[12]A. Wong, D. Mamas, and D. Arnush, "Negative ion plasmas," Phys. Fluids **18**, 1489–1493 (1975).
[13]T. Intrator, N. Hershkowitz, and R. Stern, "Beam–plasma interactions in a positive ion–negative ion plasma," Phys. Fluids **26**, 1942–1948 (1983).
[14]B. Song, N. DÕAngelo, and R. L. Merlino, "Ion-acoustic waves in a plasma with negative ions," Phys. Fluids B: Plasma Phys. **3**, 284–287 (1991).
[15]Q. Luo, N. DÕangelo, and L. R. Merlino, "Shock formation in a negative ion plasma," Phys. Plasmas **5**, 2868–2870 (1998).
[16]T. Takeuchi, S. Iizuka, and N. Sato, "Ion acoustic shocks formed in a collisionless plasma with negative ions," Phys. Rev. Lett. **80**, 77 (1998).
[17]C. Birdsall and A. Langdon, *Plasma Physics via Computer Simulation*, Series in Plasma Physics and Fluid Dynamics (Taylor & Francis, 2004).
[18]H. Matsumoto and Y. Omura, *Computer Space Plasma Physics* (Terra Scientific Publishing, Tokyo, 1993).

Physica B 464 (2015) 38–43

Contents lists available at ScienceDirect

Physica B

journal homepage: www.elsevier.com/locate/physb

The pinning effect in a polar semiconductor quantum dot with Gaussian confinement: A study using the improved Wigner–Brillouin perturbation theory

Monisha P J [a,*], Soma Mukhopadhyay [b]

[a] School of Physics, University of Hyderabad, Hyderabad 500046, India
[b] Department of Physics, D V R college of Engineering and Technology, Hyderabad 502285, India

ARTICLE INFO

Article history:
Received 7 November 2014
Received in revised form
12 February 2015
Accepted 16 February 2015
Available online 17 February 2015

Keywords:
Quantum dots
Pinning effect
Improved Wigner–Brillouin perturbation theory
Gaussian confinement

ABSTRACT

The effect of electron–phonon interaction on a few low-lying energy levels in a polar semiconductor quantum dot with Gaussian confinement is studied by using an improved Wigner–Brillouin perturbation theory (IWBPT). In the absence of the electron–phonon interaction, the electronic ground state plus one phonon state is degenerate with the first excited electronic state plus the zero-phonon state at some value of the confinement length. Similarly, the electronic ground state plus one phonon state is also degenerate with the second excited electronic state plus the zero-phonon state at a larger value of the confinement length. It is shown that the electron–phonon interaction lifts these degeneracies and as a result, the excited state energy levels bend downward and get pinned to the ground state plus one phonon state as the confinement frequency is increased. Our calculations are finally applied to GaAs and InSb quantum dots.

1. Introduction

Interest in the subject of quantum dots has continued unabated for the last three decades mainly for two reasons. First and foremost, quantum dots provide an excellent laboratory where the predictions of quantum mechanics can be tested. Secondly and probably more importantly, quantum dots exhibit very many novel physical properties which are quite different from those of their bulk counterparts [1] and have tremendous potentiality for applications [2] in nano-electronic technology, opto-electronic devices, quantum transport at nano-scale and spintronics. Any theoretical investigation on a quantum dot (QD) requires a prescription for the attractive confinement potential. Initial studies considered square well potential models to simulate a QD [3]. Later, a number of magneto-optical experiments together with the generalized Kohn's theorem [4] suggested that a QD can be mimicked by a parabolic confinement potential (PCP). This led to a host of investigations on parabolic QD's [5]. Some recent experiments [6] have however suggested that the confining potential in a QD is not really parabolic but is rather anharmonic in nature. Adamowsky et al. [7] have successfully used an attractive Gaussian confining potential (GCP) for the investigation of the properties of excess electrons in QD's. This potential has a finite depth and in the neighborhood of the dot centre behaves like a parabolic potential and also approximately satisfies the generalized Kohn theorem. Furthermore, in contrast to the rectangular potential well, it is continuous at the dot boundaries, and this makes it easier to handle mathematically. Also, it has a central minimum as required for a physical potential, and furthermore, the force experienced by the particles within this potential well is nonzero, which is also a desirable feature. Another advantage with the Gaussian confining potential (GCP) over the parabolic confining potential (PCP) is that the former allows for, in addition to excitations, ionization and tunneling processes. Of course, one can also use power law anharmonic potentials, but these potentials suffer from divergence syndrome at large distances, while the Gaussian potential is by construction bound to give convergent results. One may, however, argue that in a quantum dot the spatial coordinates never extend to a very large value to lead to any divergence problem, nevertheless, it is always appealing to work with a prescription that is mathematically sound and works in all limits. We would like to mention in passing that the Gaussian potential has proved to be a useful potential in various branches of physics and has been solved approximately for a single-particle problem by several authors (see [8] and references therein). We will refer to a QD with a GCP as a Gaussian QD (GQD). Because of the realistic nature of the Gaussian potential as a confining potential, a good number of investigations have been reported in recent years on GQD's [9].

* Corresponding author.
E-mail address: pjmonisha@gmail.com (M. P J).

http://dx.doi.org/10.1016/j.physb.2015.02.013
0921-4526/

The electron–phonon (e–p) interaction is known to play an important role on the electronic properties of QD's [10]. A number of studies have also predicted several polaronic effects in polar semiconductor QD's [11]. One of the challenges in this context has been to suggest polaronic properties that could be measured so that the existence or otherwise of the polaronic effect in a QD can be verified experimentally. In an endeavor to achieve this goal, Mukhopadhyay and Chatterjee have studied the phonon-induced Zeeman splitting in a polar semiconductor QD [12]. Krishna et al. [13] have studied the optical absorption and oscillator strength of a QD. Mukhopadhyay and Peeters have studied the so called "pinning effect" in a parabolic QD (PQD) [14]. For a polar semiconductor in a magnetic field, the first excited state (ES) Landau level plus a zero-phonon state is degenerate with the ground state (GS) Landau level plus a one-phonon state at, $\omega_0 = \omega_c$, where ω_c is the cyclotron frequency. In the presence of e–p interaction, this degeneracy is lifted and if the magnetic field is sufficiently large, the first excited state (ES) Landau level may asymptotically approach the ground state (GS) Landau level plus one longitudinal optical (LO) phonon energy. This is known as the pinning effect. In bulk polar systems, the splitting and pinning of the Landau levels in the presence of a magnetic field had been observed experimentally in the sixties [15]. Since a magnetic field provides an effective parabolic potential for the electron, a PQD is expected to show the pinning effect even in the absence of a magnetic field. This has been precisely shown by Mukhopadhyay and Peeters [14]. Since the Gaussian potential is a more realistic confining potential, it would be more appropriate to study the pinning effect in a GQD. The polaronic effect has been studied in general by Yanar et al. [16] in GQD. The purpose of the present work is to investigate the pinning effect in a GQD in two dimensions. Since GQD has two parameters to play with, namely the depth and the range, one would expect much richer pinning behavior in the case of a GQD.

2. The model Hamiltonian and its solution

The Hamiltonian of an electron moving in a GQD and interacting with the LO phonons of frequency ω_0 is given by

$$H' = \frac{\vec{p}'^2}{2m^*} + V'\left(\vec{\rho}'\right) + \hbar\omega_0 \sum_{\vec{q}'} b^{\dagger}_{\vec{q}'} b_{\vec{q}'} + \sum_{\vec{q}'} \left(\xi_{\vec{q}'} e^{-i\vec{q}'\cdot\vec{\rho}'} b^{\dagger}_{\vec{q}'} + hc\right) \tag{1}$$

where all the vectors are two-dimensional. In (1), the first term is the electron kinetic energy with $\vec{p}'$ as the momentum operator of the electron and m^* its effective mass, the second term is the confinement potential which we take as $V'\left(\vec{\rho}'\right) = -V_0' e^{-\rho'^2/2R'^2}$, where $\vec{\rho}'$ is the position vector of the electron, V_0' the depth and R' the range of the potential, the third term is the phonon Hamiltonian, $b^{\dagger}_{\vec{q}'}\left(b_{\vec{q}'}\right)$ being the creation (annihilation) operator of a phonon of wave vector $\vec{q}'$with dispersionless frequency ω_0 and the fourth term is the electron–phonon interaction with $\xi_{\vec{q}'}$ as the electron–phonon interaction coefficient. We shall work in the Feynman units [16] in which the energy is scaled by the phonon energy $\hbar\omega_0$, length by the weak-coupling polaron radius $r_0 = (\hbar/m^*\omega_0)^{1/2}$ and the wave vector by $q_0 = 1/r_0$. This is equivalent to putting $\hbar = m^* = \omega_0 = 1$. In these units the dimensionless Hamiltonian reads

$$H = \frac{H'}{\hbar\omega_0} = \frac{\vec{p}^2}{2} - V_0 e^{-\rho^2/2R^2} + \sum_{\vec{q}} b^{\dagger}_{\vec{q}} b_{\vec{q}} + \sum_{\vec{q}} \left(\xi_{\vec{q}} e^{-i\vec{q}\cdot\vec{\rho}} b^{\dagger}_{\vec{q}} + hc\right), \tag{2}$$

where everything is dimensionless, $\rho = \rho'/r_0$, $\vec{q} = \vec{q}'/q_0$, $\vec{p} = \vec{p}'/\hbar q_0$, $V_0 = V_0'/\hbar\omega_0$, $R = R'/r_0$ and $\xi_{\vec{q}} = \xi_{\vec{q}'}/\hbar\omega_0 = \left(\sqrt{2}\pi\alpha/vq\right)^{1/2}$ where v is the dimensionless volume in two dimensions and α is the dimensionless electron–phonon coupling constant.

To make progress, we consider the Gaussian potential as a parabolic potential plus a perturbation. It is reasonable to make such an assumption since the deviation of the Gaussian potential from the parabolic potential would be very small for small values of r. So we rewrite the Hamiltonian (2) as

$$H = H_0 + H_1 + H_2 \tag{3}$$

where

$$H_0 = \frac{\vec{p}^2}{2} + \left[\frac{1}{2}\omega_h^2\rho^2 - V_0\right] + \sum_{\vec{q}} b^{\dagger}_{\vec{q}} b_{\vec{q}}, \tag{4}$$

$$H_1 = -\lambda\left[\frac{1}{2}\omega_h^2\rho^2 + V_0\left(e^{-\rho^2/2R^2} - 1\right)\right], \tag{5}$$

$$H_2 = \sum_{\vec{q}} \left(\xi_{\vec{q}} e^{-i\vec{q}\cdot\vec{\rho}} b^{\dagger}_{\vec{q}} + hc\right) \tag{6}$$

where $\lambda = 0$ for PQD, $\lambda = 1$ for GQD, $\omega_h^2 = V_0^2/R^2$, H_1 and H_2 are the perturbations. We include the contribution from H_1 within the mean field approximation as

$$H_1 = \lambda\left[\frac{V_0}{\left\langle\rho^2\right\rangle} - \frac{1}{2}\omega_h^2 - V_0\frac{\left\langle e^{-\rho^2/2R^2}\right\rangle}{\left\langle\rho^2\right\rangle}\right]\rho^2 \tag{7}$$

where the expectation values are calculated with respect to the GS wave function Ψ_{GS} of the space part of the unperturbed harmonic oscillator Hamiltonian with frequency ω_h i.e., $\Psi_{GS} = (\omega_h/\pi)^{1/2}\exp\left(-\omega_h\rho^2/2\right)$. With this Ψ_{GS} we obtain $\left\langle\rho^2\right\rangle = 1/\omega_h$ and $\left\langle e^{-\rho^2/2R^2}\right\rangle = 2\omega_h R^2\left(1 + 2\omega_h R^2\right)^{-1}$. The total Hamiltonian then reads

$$H = \frac{\vec{p}^2}{2} + \frac{1}{2}\omega^2\rho^2 - V_0 + \sum_{\vec{q}} b^{\dagger}_{\vec{q}} b_{\vec{q}} + \sum_{\vec{q}} \left(\xi_{\vec{q}} e^{-i\vec{q}\cdot\vec{\rho}} b^{\dagger}_{\vec{q}} + hc\right) \tag{8}$$

with the effective harmonic confinement frequency, $\omega = \left[(1-\lambda)\omega_h^2 + 2\lambda V_0\omega_h\left\{1 - 2\omega_h R^2\left(1 + 2\omega_h R^2\right)^{-1}\right\}\right]^{1/2} = \omega'/\omega_0$, where ω' is the effective confinement frequency in actual units. The effective unperturbed energy (in Feynman units) is thus given by $E^0_{j_1 j_2} = \left(j_1 + j_2 + 1\right)\omega - V_0$, and we write the total energy corresponding to H as $E_n = E_n'/\hbar\omega_0$, where E_n' is the energy in actual units and E_n is the energy in Feynman units. We shall study the effect of H_2 using the perturbation theory and calculate the correction ΔE_n to the electronic energy. Because of the presence of degeneracy in our problem, we need to use a degenerate perturbation theory and we shall employ the Improved Wigner–Brillouin Perturbation theory (IWBPT) [17]. The advantage with IWBPT is that it gives the correct pinning behaviour for weak electron–phonon interaction. The second-order correction to the unperturbed energy due to the electron–phonon interaction is given by

$$\Delta E_n = -\sum_j \sum_{\vec{q}} \frac{\left|\left\langle\varphi_j^0\left(\vec{\rho}\right)\right|\xi_{\vec{q}} e^{-i\vec{q}\cdot\vec{\rho}}\left|\varphi_n^0\left(\vec{\rho}\right)\right\rangle\right|^2}{E_j^0 - E_n^0 - \Delta_n + 1}, \tag{9}$$

where, $\Delta_n = \Delta E_n - \Delta E_0^{RSPT}$ and $\varphi_j^0\left(\vec{\rho}\right)$ is the wave function of a harmonic oscillator with frequency ω. Because of the presence of

ΔE_n on the right hand side, we need to calculate the energy self-consistently. Eq. (9) with $\Delta_n = 0$ gives the RSPT result which works well for the GS when $\omega << 1$. To perform the summation in Eq. (9) we use the relation

$$\frac{1}{E_j^0 - E_n^0 - \Delta_n + 1} = \int_0^\infty e^{-\left(E_j^0 - E_n^0 - \Delta_n + 1\right)t} dt \tag{10}$$

On simplifications, Eq. (9) yields the energy corrections to the GS and the first two ES's as

$$-\frac{\Delta E_{GS}}{16\gamma} = B\left(\frac{1}{\omega}, \frac{1}{2}\right), \tag{11}$$

$$-\frac{\Delta E_{1ES}}{4\gamma} = B\left(\frac{1-\Delta_1}{\omega} - 1, \frac{1}{2}\right) + 3B\left(\frac{1-\Delta_1}{\omega}, \frac{1}{2}\right), \tag{12}$$

$$-\frac{\Delta E_{2ES}}{\gamma} = 5B\left(\frac{1-\Delta_2}{\omega} - 2, \frac{1}{2}\right) + 6B\left(\frac{1-\Delta_2}{\omega} - 1, \frac{1}{2}\right) + 13B\left(\frac{1-\Delta_2}{\omega}, \frac{1}{2}\right), \tag{13}$$

where $\gamma = [\alpha\sqrt{\pi}/32\sqrt{\omega}]$ and $B(x, y)$ is the beta function. In general, for an N-dimensional case the expressions are as follows:

$$-\frac{\Delta E_{GS}^{ND}}{8\beta} = B\left(\frac{1}{\omega}, \frac{1}{2}\right) \tag{14}$$

$$-\frac{\Delta E_{1ES}^{ND}}{4\beta} = B\left(\frac{1-\Delta_1}{\omega} - 1, \frac{1}{2}\right) + (2N-1)B\left(\frac{1-\Delta_1}{\omega}, \frac{1}{2}\right), \tag{15}$$

$$-\frac{\Delta E_{2ES}^{ND}}{\beta} = \left(2N^2 - 4N + 5\right)B\left(\frac{1-\Delta_2}{\omega} - 2, \frac{1}{2}\right) + (4N-2)B\left(\frac{1-\Delta_2}{\omega} - 1, \frac{1}{2}\right) + \left(2N^2 + 4N - 3\right)B\left(\frac{1-\Delta_2}{\omega}, \frac{1}{2}\right), \tag{16}$$

where

$$\beta = -\frac{\alpha}{32\sqrt{\omega}}\left[\Gamma\left(\frac{N-1}{2}\right)/\Gamma\left(\frac{N}{2}+1\right)\right]$$

In the present problem, the region of interest is $1 - \Delta_n \cong n\omega$ and we consider the term which contributes maximum to the energy in this region, for each state ($n = 1, 2, \ldots$) and we obtain

$$\Delta E_{1ES} = -\frac{\alpha\sqrt{\pi}}{8}\frac{\sqrt{\omega}}{1 - \Delta_1 - \omega} \tag{17}$$

$$\Delta E_{2ES} = -\frac{5\alpha\sqrt{\pi}}{32}\frac{\sqrt{\omega}}{1 - \Delta_2 - 2\omega} \tag{18}$$

To see the pinning of the energy levels E_{1ES} and E_{2ES} to $[E_0^0 + 1$ phonon state], we have to consider the large ω limit. In this limiting case, a self-consistent calculation leads us to the following results:

$$E_{1ES} = \frac{N}{2}\omega + 1 + \Delta E_{GS} - \frac{\alpha\sqrt{\pi}\sqrt{\omega}}{8(\omega - 1 - \Delta E_{GS})} \tag{19}$$

$$E_{2ES} = \frac{N}{2}\omega + 1 + \Delta E_{GS} - \frac{5\alpha\sqrt{\pi}\sqrt{\omega}}{32(2\omega - 1 - \Delta E_{GS})} \tag{20}$$

3. Numerical results and discussions

Our calculation is valid for any polar semiconductor quantum dot. We shall be however more interested in GaAs and InSb quantum dots in the present work. For GaAs, we take $\alpha = 0.07$, $\omega_0 = 5.5 \times 10^{13}$/s and $m^* = 0.6 \times 10^{-28}$ gm so that we have $\hbar\omega_0 = 36.25$ meV and $r_0 = 5.63$ nm. Thus for GaAs,$V_0 = 0.4$ means: $0.4 \times \hbar\omega_0 = 14.5$ meV and $R = 3$ means $3 \times r_0 = 16.9$ nm. For InSb, we take $\alpha = 0.02$, $\omega_0 = 3.7 \times 10^{13}$/s and $m^* = 0.128 \times 10^{-28}$ gm so that for InSb we have $\hbar\omega_0 = 24.38$ meV and $r_0 = 14.93$ nm. First of all, we notice that the relationship between the effective confinement frequency ω and the range of the Gaussian potential R is not so simple. In Fig. 1, we plot ω vs. $1/\sqrt{R}$ for a GaAs QD and interestingly enough, the behavior is almost linear unless R is extremely large. In this work, we shall always mean the confinement potential to be GCP unless otherwise mentioned. In Fig. 2, we plot the GS and the first two ES energies (E_0, E_1 and E_2) of an electron confined in a GaAs QD as a function of the effective QD size R for two values of the depth of the Gaussian potential, V_0. For a particular value of V_0 and the electron–phonon coupling constant α, as R increases, energies decrease monotonically. However, at small values of R, as R increases, the energies decrease very rapidly for all the states and at large values of R, the energies decrease very slowly, ultimately saturating to the bulk limits.

When the QD size is small, the uncertainty in the momentum is expected to be large and as a result the kinetic energy itself will be large and hence the total energy increases as R decreases. Thus the polaronic effect is extremely significant for small QD's as has been predicted by a host of investigations [11]. It is also interesting to note that at small R energies increase with increasing V_0, while above a certain QD size (which is different for different states), energies decrease with increasing V_0. This behavior can be roughly understood from the results of the finite square potential well problem. If the depth of the potential is V_0 and width of the well is R, then the GS energy can be written as $E_0 = V_0\cos^2\left(m^*R^2E_0/2\hbar^2\right)$. When R is small, the kinetic energy is large and therefore E_0 can be approximated by the kinetic energy on the right hand side of the above equation and then as V_0increases, E_0 increases almost linearly. On the other hand, when R is large, the kinetic energy may be neglected and the particle can be expected to lie at the bottom of the potential well and so E_0 can be approximated by $[-V_0]$ on the right hand side of the above equation. In this case, as V_0 increases, E_0 decreases, at least for the parameter values considered in this work.

In Fig. 3, we compare the energies of a GaAs QD with GCP and

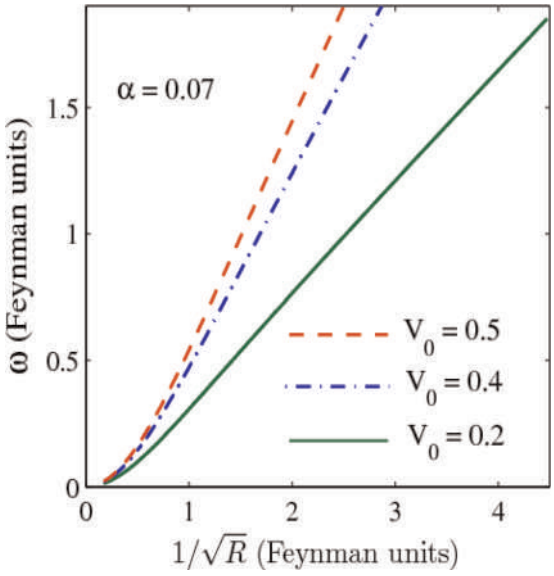

Fig. 1. ω vs. $1/\sqrt{R}$ for a GaAs QD for three values of V_0.

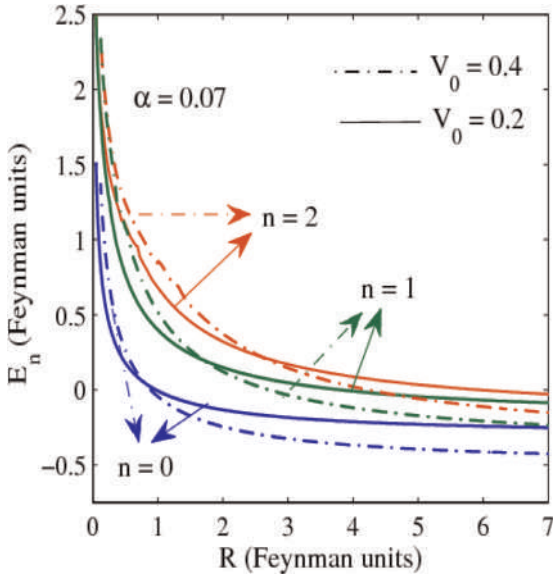

Fig. 2. GS and first two ES energies (E_0, E_1 and E_2) of a GaAs QD as a function of R, for two values of V_0.

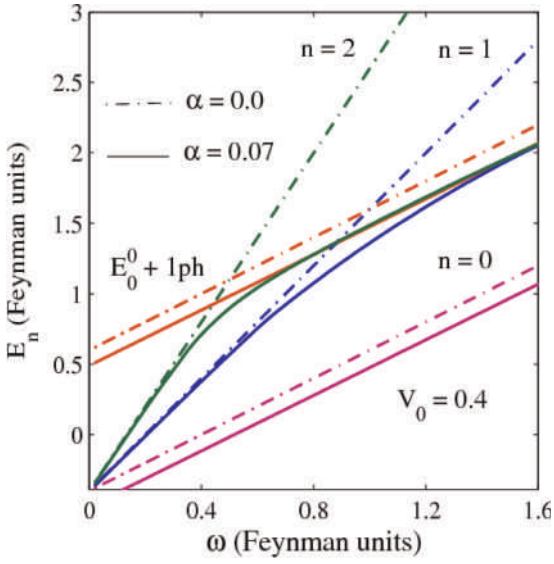

Fig. 4. E_0, E_1 and E_2 vs. ω for a GaAs QD with and without electron–phonon coupling for $V_0 = 0.4$.

PCP. It is clearly evident that the PCP model, in general, overestimates the energy. At large values of R however, the results, as expected, become independent of the confinement potential models and consequently both the models give the same results which are, of course, the bulk limits.

In Fig. 4, we have plotted the energies of an electron confined in a GaAs QD as a function of ω both in the presence and absence of the electron–phonon interaction. The dashed-dotted lines represent the unperturbed energies and the solid lines indicate the energies of the electron when the electron–phonon interaction is taken into account. The unperturbed first and second electronic ES's plus zero-phonon are degenerate with electronic GS plus one phonon state at $\omega = 1$ and $\omega = 0.5$ respectively. In the presence of the electron–phonon interaction, these degeneracies are lifted and the energy values are lowered. One can see from the figure that as ω approaches 1, the first ES energy (the solid curve) starts bending downward and with further increase in ω gets pinned to the GS plus one-phonon energy. The removal of degeneracy by the electron–phonon interaction and the subsequent lowering of energy values are clear indications of the polaronic effects in a QD. Experimentally one should be able to observe the splitting and the pinning behavior of the energy levels and verify the existence of the polaronic effect in a QD.

In Fig. 5, we plot $\Delta E_{n,n-1} = (E_n - E_{n-1})$ for $n = 1$ and $n = 2$ as a function of ω. $\Delta E_{1,0}$ seems to approach the one phonon energy as ω is increased, while $\Delta E_{2,1}$ initially increases, reaches a maximum and then decreases to zero under the same condition. This happens because in this limit, both the ES energies get pinned to the GS plus one phonon energy.

In Fig. 6, we plot E_0, E_1 and E_2 of a GaAs QD as a function of $1/\sqrt{R}$ for $V_0 = 0.4$ and $V_0 = 0.2$ to see the effect of V_0 on the pinning effect. One can see that the degeneracies at two different values of R (for the two ES energies) are lifted and the energies are lowered in the presence of electron–phonon coupling. The pinning effect is also clearly visible. Experimentally, this might be a more direct and useful way of observing the pinning effect as compared to Fig. 3. It is interesting to observe that the pinning occurs for a lower value of ω as we increase V_0. In Fig. 7, we plot $(E_n - E_{n-1})$ as a

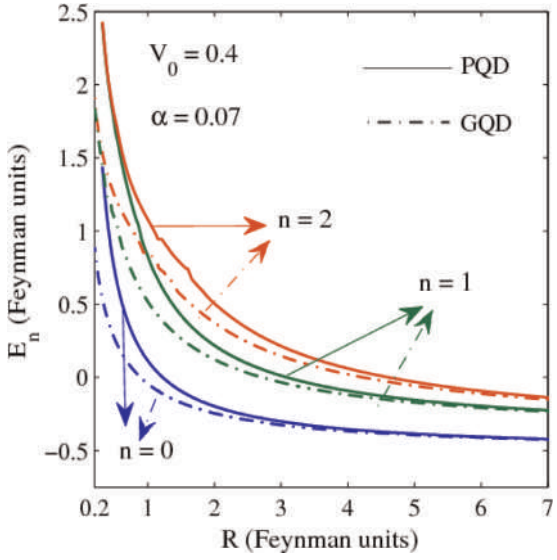

Fig. 3. Variation of E_0, E_1 and E_2 of a GaAs QD with GCP and PCP as a function of R for $V_0 = 0.4$.

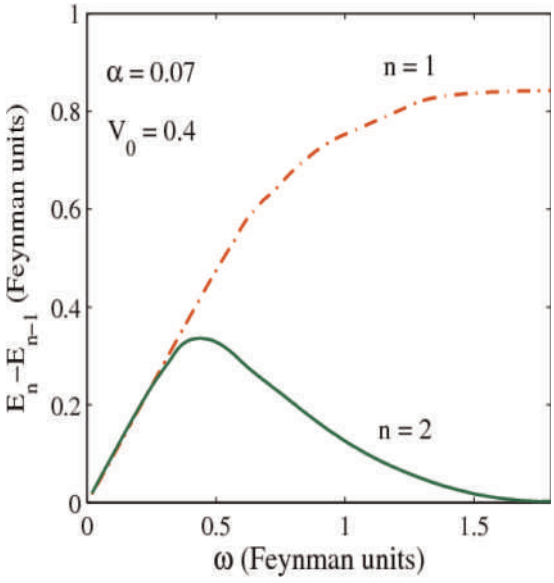

Fig.5. $\Delta E_{n,n-1}$ for $n = 1$ and $n = 2$ vs. ω for a GaAs QD for $V_0 = 0.4$.

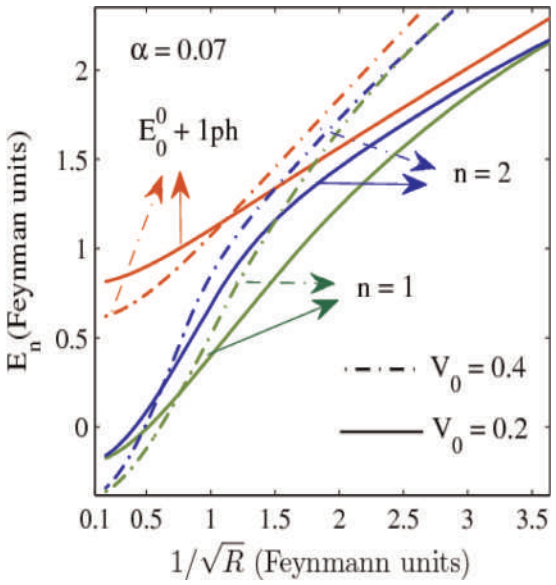

Fig. 6. E_1 and E_2 as a function of $1/\sqrt{R}$ for a GaAs QD with GCP for $V_0 = 0.4$ and 0.2.

function of $1/\sqrt{R}$ for $V_0 = 0.4$ and $V_0 = 0.2$. The behavior is more or less similar to Fig. 5. As R is reduced, $(E_2 - E_1)$ saturates to a constant which is expected to be an LO-phonon energy in an ideal case and $(E_1 - E_0)$ goes through a maximum and finally reduces to zero. The reason for this behavior has already been explained earlier.

Fig. 8 shows the comparison of electronic energies as a function of ω' for GaAs and InSb QD's. For GaAs, the energy levels bend more and consequently the reduction in the energy values becomes more pronounced. Also the pinning occurs at a higher value of ω'. This becomes even more evident from Fig. 9 where we have plotted $(E'_n - E'_{n-1})$ as a function of ω'. In Fig. 10, we have compared the pinning behavior in a GaAs QD as a function of $1/\sqrt{R}$ with both GCP and PCP models. As we can see from the figure, the pinning occurs at a large ω value for the GCP model.

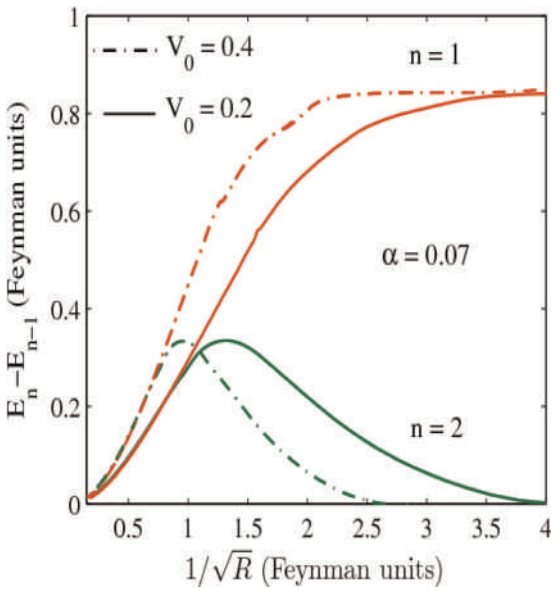

Fig. 7. $(E_2 - E_1)$ of a GaAs QD as a function of $1/\sqrt{R}$ for $V_0 = 0.4$ and 0.2.

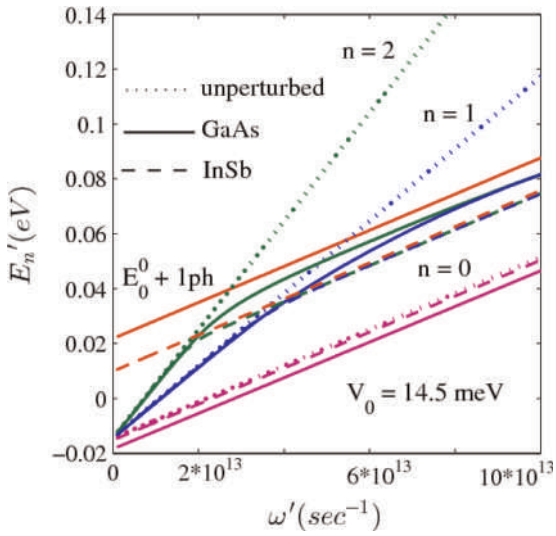

Fig. 8. E'_0, E'_1 and E'_2 vs. ω' for GaAs and InSb QD's.

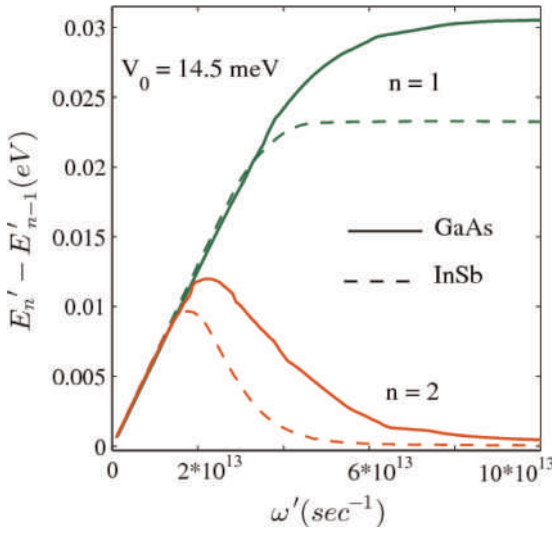

Fig. 9. $(E'_n - E'_{n-1})$ as a function of ω' for GaAs and InSb QD's.

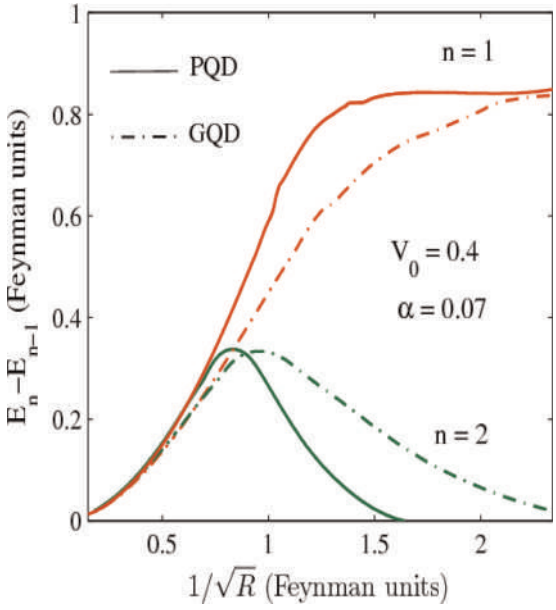

Fig. 10. The energy difference as a function of $1/\sqrt{R}$ for PQD and GQD of GaAs.

4. Conclusions

We have studied the effect of electron–phonon interaction on a few low-lying energy levels in a QD with GCP model and applied our results to GaAs and InSb QD's. We have particularly addressed ourselves to one of the most important polaronic effects called the pinning effect. We have shown that as the effective size, R of the QD is decreased, at certain R the degeneracies in the energy levels are lifted because of the electron–phonon interaction giving rise to splitting in the energy levels and the energy levels are shifted down. With the further reduction in the QD size, bending of the energies causes the ES levels to get pinned to the GS plus one phonon energy. As the electron–phonon interaction is increased, the bending of the energy levels becomes more pronounced and the energy levels are further shifted down and pinning occurs at a larger value of the QD size. This splitting and pinning can be observed in the laboratory and the existence or otherwise of the polaronic effect in a polar QD can be tested experimentally. We have also studied the effect of the strength of the Gaussian confining potential V_0 on the pinning effect. We find that as V_0 increases, pinning occurs at larger values of R. Also it turns out that the pinning takes place at a smaller confinement length in the case of a GQD as compared to that in PQD.

References

[1] P. Moriarty, Rep. Prog. Phys. 64 (2001) 297.
[2] (a) M.A. Kastner, Rev. Mod. Phys. 64 (1992) 849;
(b) N.F. Johnson, J. Phys. Condens. Matter 7 (1995) 965;
(c) R.C. Ashoori, Nature 379 (1996) 413;
(d) U. Woggon, Optical Properties of Semiconductor Quantum Dots, Springer, Berlin, 1997;
(e) D. Bimberg, M. Grundmann, N.N. Ledentsov, Quantum Dot Heterostructures, Wiley, New York, 1998.
[3] (a) F. Geerinckx, F.M. Peeters, J.T. Devreese, J. Appl. Phys. 68 (1990) 3435;
(b) Jia-Jiong Jia-Lin Zhu, Xiong, Bing-Lin Gu, Phys. Rev. B 41 (1990) 6001;
(c) T. Takagahara, Phys. Rev. B 47 (1993) 4569;
(d) N. Porras-Montenegro, S.T. Perez-Merchancano, A. Latge, J. Appl. Phys. 74 (1993) 7624;
(e) J.L. Marín, R. Riera, S.A. Cruz, J. Phys. Condens. Matter 10 (1998) 1349.
[4] W. Kohn, Phys. Rev. 123 (1961) 1242.
[5] (a) F.M. Peeters, Phys. Rev. B 42 (1990) 1486;
(b) P.A. Maxym, T. Chakraborty, Phys. Rev. Lett. 65 (1990) 108;
(c) N.F. Johnson, M.C. Payne, Phys. Rev. Lett. 67 (1991) 1157;
(d) N.F. Johnson, F.C. Payne, Phys. Rev. B 45 (1992) 3819;
(e) R. Egger, W. Hausler, C.H. Mak, H. Grabert, Phys. Rev. Lett. 82 (1999) 3320;
(f) L. Lu, W. Xie, S. Liang, Curr. Appl. Phys. 11 (2011) 1302.
[6] D. Heitmann, K.K. Bollweg, V. Gugmundsson, T. Kurth, S.P. Riege, Physica E 1 (1997) 204.
[7] J. Adamowsky, M. Sobkowicz, B. Szafran, S. Bednarek, Phys. Rev. B 62 (2000) 4234.
[8] (a) N. Bessis, G. Bessis, B. Joulakian, J. Phys. A: Math. Gen. 15 (1982) 3679;
C.S. Lai, J. Phys. A: Math. Gen. 16 (1983) L181;
R.E. Crandall, J. Phys. A: Math. Gen. 16 (1983) L395;
M. Cohen, J. Phys. A: Math. Gen. 17 (1984) L101;
A. Chatterjee, J. Phys. A: Math. Gen. 18 (1985) 2403;
(f) A. Chatterjee, Phys. Rep. 186 (1990) 249.
[9] (a) Paul-Antoine TokueiSako, Hervieux, Geerd H.F. Diercksen, Phys. Rev. B 74 (2006) 045329;
(b) WenfangXie, Solid State Commun. 127 (2003) 401;
(c) B. Boyacioglu, M. Saglam, A. Chatterjee, J. Phys. Condens. Matter 19 (2007) 456217;
(d) S.S. Gomez, R.H. Romero, Cent. Eur. J. Phys. 7 (2009) 12.
[10] (a) O. Verzelen, R. Ferreira, G. Bastard, Phys. Rev. B 64 (2001) 075315;
(b) T. Inoshita, H. Sakaki, Phys. Rev. B 56 (1997) R4355–R4358;
(c) M.A. Odnoblyudov, I.N. Yassievich, K.A. Chao, Phys. Rev. Lett. 83 (1999) 4884;
(d) L. Jacakl, J. Krasnyj, D. Jacak, P. Machnikowski, Phys. Rev. B 65 (2002) 113305.
[11] (a) M.H. Degani, G.A. Farias, Phys. Rev. B 42 (1990) 11950;
(b) L. Wendler, A.V. Chaplik, R. Haupt, O. Hipolito, J. Phys. Condens. Matter 5 (1993) 8031;
(c) K.D. Zhu, S.W. Gu, Phys. Rev. B 47 (1993) 12947;
(d) K.D. Zhu, T. Kobayashi, Solid State Commun. 92 (1994) 353;
(e) S. Mukhopadhyay, A. Chatterjee, Phys. Lett. A 204 (1995) 411;
(f) S. Mukhopadhyay, A. Chatterjee, Phys. Rev. B55 (1997) 9297;
(g) C.Y. Chen, P.W. Jin, W.S. Li, D.L. Din, Phys. Rev. 56 (1997) 14913;
(h) S. Mukhopadhyay, A. Chatterjee, Phys. Rev. B 58 (1998) 2088;
(i) S. Mukhopadhyay, A. Chatterjee, Phys. Lett. A 240 (1998) 100;
(j) S. Mukhopadhyay, A. Chatterjee, J. Phys.: Condens. Matter 11 (1999) 2071;
(k) M.A. Odnoblyudov, I.N. Yassievich, K.A. Chao, Phys. Rev. Lett. 83 (1999) 4884;
(l) N. Kervan, T. Altanhanand, A. Chatterjee, Phys. Lett. A 315 (2003) 280;
(m) P.M. Krishna, A. Chatterjee, Physica E 30 (2005) 64;
(n) P.M. Krishna, S. Mukhopadhyay, A. Chatterjee, Phys. Lett. A 360 (2007) 655.
[12] (a) S. Mukhopadhyay, A. Chatterjee, Phys. Rev. B 59 (1999) R7833;
(b) S. Mukhopadhyay, A. Chatterjee, Int. J. Mod. Phys. B 14 (2000) 3897;
(c) S. Mukhopadhyay, B. Boyacioglu, M. Saglam, A. Chatterjee, Physica E 40 (2008) 2776–2782.
[13] P.M. Krishna, S. Mukhopadhyay, A. Chatterjee, Int. J. Mod. Phys. B 16 (2002) 1489.
[14] S. Mukhopadhyay, F.M. Peeters, J. Phys. Condens. Matter 14 (2002) 8005–8010.
[15] (a) E.J. Johnson, D.M. Larsen, Phys. Rev. Lett. 16 (1966) 655;
(b) D.H. Dickey, E.J. Johnson, D.M. Larsen, Phys. Rev. Lett. 18 (1967) 599;
(c) G. Lindemann, R. Lassing, W. Seidenbusch, E. Gornik, Phys. Rev. B 28 (1983) 4693.
[16] Sonay Yanar, et al., Superlattices Microstruct. 43 (2008) 208.
[17] (a) F.M. Peeters, J.T. Devreese, Phys. Rev. B 31 (1985) 3689;
(b) G.Q. Hai, F.M. Peeters, J.T. Devreese, Physica B 184 (1993) 289;
(c) Francisco A.P. Osorio, Marcelo Z. Maialle, O. Hipolito, Phys. Rev. B 57 (1998) 1644.

Persistent current and the existence of a metallic phase flanked by two insulating phases in a quantum ring with both electron–electron and electron–phonon interactions

ARTICLE *in* PHYSICA E LOW-DIMENSIONAL SYSTEMS AND NANOSTRUCTURES · MAY 2015

Impact Factor: 1.86 · DOI: 10.1016/j.physe.2015.05.029

4 AUTHORS, INCLUDING:

I.V. Sankar
University of Hyderabad
5 PUBLICATIONS **2** CITATIONS
SEE PROFILE

Monisha P j
University of Hyderabad
5 PUBLICATIONS **0** CITATIONS
SEE PROFILE

Ashok Chatterjee
University of Hyderabad
111 PUBLICATIONS **925** CITATIONS
SEE PROFILE

Physica E 73 (2015) 175–180

Contents lists available at ScienceDirect

Physica E

journal homepage: www.elsevier.com/locate/physe

Persistent current and the existence of a metallic phase flanked by two insulating phases in a quantum ring with both electron–electron and electron–phonon interactions

I.V. Sankar [a], P J Monisha [a], Shreekantha Sil [b], Ashok Chatterjee [a,*]

[a] School of Physics, University of Hyderabad, Hyderabad 500046, India
[b] Department of Physics, Visvabharathi University, Shantinekatan, Birbhum, India

HIGHLIGHTS

- A quantum ring threaded by a magnetic flux is studied including electron–phonon interaction.
- The system is modeled by the Holstein-Hubbard Hamiltonian.
- The persistent current is found to be suppressed by electron–phonon interaction.
- The persistent current decreases continuously as the number of atoms increases.
- The metallic phase is found to be flanked by CDW and SDW phases.

ARTICLE INFO

Article history:
Received 4 February 2015
Received in revised form
23 April 2015
Accepted 26 May 2015
Available online 29 May 2015

Keywords:
Quantum ring
Holstein-Hubbard model
Persistent current
CDW and SDW phases

ABSTRACT

The persistent current in the ground state of a quantum ring threaded by a magnetic flux is calculated within the framework of the Holstein-Hubbard model. It is found that the persistent current is suppressed by both the electron–electron and electron–phonon interactions. Calculation of Drude weight reveals that the persistent current is diamagnetic in nature. It is observed that as the number of atoms in the quantum ring increases, the persistent current decays in a continuous way. It is finally predicted that there exists an intervening metallic phase flanked in real time by two insulating phases, the SDW phase and the CDW phase.

A magnetic flux Φ piercing through a quantum ring (QR) generates a periodic persistent current (PC) $I(\Phi)$ with a period Φ_0 equal to hc/e in its ground state (GS) [1] due to the quantum mechanical phase coherence effect. Thus a QR threaded with a magnetic flux can behave as an artificial spin [2] and can be used as a qubit. Several experiments [3] have already confirmed the existence of PC in QR's. Though several studies have been made on PC in a Hubbard QR (HQR), no study has been reported, to our knowledge, on the Holstein-Hubbard QR (HHQR). The HHQR is more interesting because the electron–phonon (e–p) interaction can change the nature of the GS altogether. It is generally believed that the GS of a HH system can be either an antiferromagnetic (AF) spin–density wave (SDW) Mott insulator or a bipolaronic charge–density wave (CDW) Peierls insulator [4]. However, recently, Takada and Chatterjee and Krishna and Chatterjee [5] have shown the existence of an intervening metallic phase at the cross-over region of SDW–CDW phases in a one-dimensional (1D) HH model at half filling. This observation has understandably attracted a lot of attention in recent years and consequently this phenomenon has been studied in 1D [6] as well as in two and higher dimensions [7]. One expects a wider metallic phase in higher dimensions because of the larger phase space dimensionality and greater scope for mobility.

In the present paper, we shall study the combined effect of electron–electron (e–e) and e–p interactions on PC in HHQR and unravel the GS phase diagram at $T = 0$. We assume that the magnetic flux passes through the ring axially and the electrons move in a field-free region so that the phase of the wave function of the electron changes by the Aharonov-Bohm (AB) effect.

* Corresponding author.
E-mail address: acsp@uohyd.ernet.in (A. Chatterjee).

http://dx.doi.org/10.1016/j.physe.2015.05.029
1386-9477/

The 1D HHQR pierced by an AB flux can be modelled by the Hamiltonian

$$\mathcal{H} = -\ te^{i\phi}\sum_{\langle ij\rangle\sigma} c_{i\sigma}^{\dagger} c_{j\sigma} + U\sum_{i} n_{i\uparrow}\, n_{i\downarrow} + \omega_0 \sum_{i} b_i^{\dagger}\, b_i + g_0 \sum_{i\sigma} n_{i\sigma}\left(b_i^{\dagger} + b_i\right) + g_1 \sum_{\langle ij\rangle\sigma} n_{i\sigma}\left(b_j^{\dagger} + b_j\right). \quad (1)$$

The first term in (1) refers to the kinetic energy where $c_{i\sigma}^{\dagger}$ ($c_{i\sigma}$) is the creation (annihilation) operator for an electron of spin σ (with N$\sigma = \uparrow, \downarrow$) at site i, $\langle ij\rangle$ indicates that the summation is over nearest-neighbour (NN) sites i and j, t is the hopping parameter, and $\phi = 2\pi\Phi/\mathrm{N}$, Φ being the total magnetic flux passing through the ring (measured in units of flux quantum $\Phi_0 = h/e$) and N is the total number of sites. The second term is the onsite e–e Coulomb interaction, U being the corresponding correlation strength and $n_{i\sigma} = c_{i\sigma}^{\dagger} c_{i\sigma}$ is the number operator for electrons of spin σ at site i. The third term is the phonon Hamiltonian where $b_i^{\dagger}$ (b_i) is the phonon creation (annihilation) operator and ω_0 is the dispersionless phonon frequency. The last two terms represent respectively the onsite and NN e–p interactions with the corresponding strengths g_0 and g_1.

We first eliminate the phonon degrees of freedom using the conventional Lang-Firsov transformation [8] with the generator:S=$g_0\sum_{i\sigma} n_{i\sigma}\left(b_i^{\dagger} - b_i\right) + g_1\sum_{\langle ij\rangle\sigma} n_{i\sigma}\left(b_j^{\dagger} - b_j\right)$, and perform zero-phonon averaging to obtain the effective electronic Hamiltonian as

$$\mathcal{H}_e = -\ \varepsilon_e \sum_{i\sigma} n_{i\sigma} - t_e e^{i\phi}\sum_{ij\sigma} c_{i\sigma}^{\dagger} c_{j\sigma} + U_e \sum_{i} n_{i\uparrow}\, n_{i\downarrow}, \quad (2)$$

where $t_e = t\ \exp\left[-\left\{\left(g_0 - g_1\right)^2 + (\,z-1)g_1^2\right\}/\omega_0^2\right]$, $U_e = U - 2\left(g_0^2 + zg_1^2\right)/\omega_0$, $\varepsilon_e = -\left(g_0^2 + zg_1^2\right)/\omega_0$ and z is the number of NN sites. The last two terms in Hamiltonian (2) provide competing dynamics. The hopping term drives an electron to move from one site to another leading to a Peierls state whereas the Coulomb term opposes double occupancy favouring the formation of local spin moments. We shall use the mean-field (MF) Hartree–Fock approximation (HFA) to obtain the energy corresponding to the effective Hamiltonian $\mathcal{H}_e$. This is a reasonable approximation so long as the band energy dominates over the e–e interaction.

For simplicity and without loss of generality, we consider a system with even number of sites and divide the system into two sub-systems, namely, even-numbered sites (A sublattice) and odd-numbered sites (B sublattice). We next define charge density (n), CDW order parameter (c) and SDW order parameter (s) (per site) as [9]: $2n = n_{A\uparrow} + n_{A\downarrow} + n_{B\uparrow} + n_{B\downarrow}$, $2c$ where $n_{A\sigma}$ and $n_{B\sigma}$ are the

$$= n_{A\uparrow} + n_{A\downarrow} - n_{B\uparrow} - n_{B\downarrow},\ 2s$$

$$= n_{A\uparrow} - n_{A\downarrow} - n_{B\uparrow} + n_{B\downarrow},$$

expectation values of $n_{i\sigma}$ for $i \in A$ and $i \in B$, respectively. We can express $\mathcal{H}_e$ in terms of the above parameters and c and s can be found by self-consistency conditions. The effective Coulomb correlation term can be decoupled using MF HFA [10] and $\mathcal{H}_e$ finally reduces to

$$\mathcal{H}_e = -\ t_e e^{i\phi}\sum_{\langle ij\rangle\sigma} c_{i\sigma}^{\dagger} c_{j\sigma} + \varepsilon_{A\sigma}\sum_{i\in A} n_{i\sigma} + \varepsilon_{B\sigma}\sum_{i\in B} n_{i\sigma} + \mathrm{N}U_e\left(n^2 - c^2 - s^2\right), \quad (3)$$

where $\varepsilon_{A\uparrow} = -\varepsilon_0 + U_e(n + c - s)/2$, $\varepsilon_{A\downarrow} = -\varepsilon_0 + U_e(n + c + s)/2$, $\varepsilon_{B\uparrow} = -\varepsilon_0 + U_e(n - c + s)/2$, $\varepsilon_{B\downarrow} = -\varepsilon_0 + U_e(n - c + s)/2$. Next we make Fourier transformation to the momentum space and perform the Bogoliubov transformations: $c_{k\sigma} = \cos(\theta_{k\sigma})\alpha_{k\sigma} - \sin(\theta_{k\sigma})\beta_{k\sigma}$; $c_{k+(\pi/a),\sigma} = \sin(\theta_{k\sigma})\alpha_{k\sigma} + \cos(\theta_{k\sigma})\beta_{k\sigma}$, with $\theta_{k\sigma} = \tan^{-1}\left[-\left(\Delta_-^{\sigma}/\varepsilon_k\right)\right]/2$ to diagonalize $\mathcal{H}_e$ which then reads

$$\mathcal{H}_e = \sum_{k\in \mathrm{BZ},\sigma}\left[E_{k\sigma}^{\alpha}\alpha_{k\sigma}^{\dagger}\alpha_{k\sigma} + E_{k\sigma}^{\beta}\beta_{k\sigma}^{\dagger}\beta_{k\sigma}\right] + K, \quad (4)$$

where $E_{k\sigma}^{\alpha} = \Delta_+^{\sigma} - x_k^{\sigma}$, $E_{k\sigma}^{\beta} = \Delta_+^{\sigma} + x_k^{\sigma}$, $x_k^{\sigma} = \varepsilon_k^2 + \Delta_-^{\sigma}$, $\varepsilon_k = 2\,t_e\,\cos(ka + \phi)$, $K = \mathrm{N}U_e\left(n^2 - c^2 - s^2\right)$ and $\Delta_{\pm}^{\sigma} = (\varepsilon_{A\sigma} \pm \varepsilon_{B\sigma})/2$. The order parameters c and s are given by

$$c = -\frac{1}{\mathrm{N}}\sum_{k\in \mathrm{BZ},\sigma}\left(\frac{\Delta_-^{\sigma}}{x_k^{\sigma}}\right)\left[f_{\alpha,\sigma} - f_{\beta,\sigma}\right], \quad (5)$$

$$s = -\frac{1}{\mathrm{N}}\sum_{k\in \mathrm{BZ}}\left\{\left(\frac{\Delta_-^{\uparrow}}{x_k^{\uparrow}}\right)\left[f_{\alpha\uparrow} - f_{\beta\uparrow}\right] - \left(\frac{\Delta_-^{\downarrow}}{x_k^{\downarrow}}\right)\left[f_{\alpha\downarrow} - f_{\beta\downarrow}\right]\right\}, \quad (6)$$

where $f_{i\sigma} = \alpha_{k\sigma}^{\dagger}\alpha_{k\sigma} = 1/[1 + e^{\left(E_{k\sigma}^{i} - \mu\right)/k_B T}]$. PC ($I_{PC}$) and the Drude weight (DW) (D) [11] are defined as

$$I_{PC}(\Phi) = -\frac{1}{2\pi}\frac{dE(\Phi)}{d\Phi},\ \mathrm{D} = \frac{\mathrm{N}}{4\pi^2}\left.\frac{d^2E(\Phi)}{d\Phi^2}\right|_{\Phi=\Phi_m}, \quad (7)$$

where Φ_m is the location of the minimum of $E(\Phi)$ which can be 0 or 1/2 depending on the parity of the number of electrons.

The average electron density or the occupation per site n is defined as: $n = N_e/N$, where N_e is the total number of electrons in the 1D tight-binding (TB) QR and N as defined earlier, is the total number of sites. In the present work, $N = 200$ and $N_e = N - 2$ (unless otherwise specified). The GS energy ($E(\Phi)$), PC ($I_{PC}(\Phi)$) and DW for a non-interacting (NI) TB QR are found to be periodic in Φ with period Φ_0, as expected. We also find that as t increases, $E(\Phi)$ decreases but $|I_{PC}|$ increases. Furthermore DW turns out to be positive which implies that the QR is metallic and diamagnetic. From the behaviour of $I_{PC}(\Phi)$ vs. Φ for $N_e = 200$ and $N_e = 198$, we clearly see that PC has opposite phases in the two cases. This can be attributed to the parity effect predicted earlier by Cheung et al. and Sticlet et al. [12] in the case of Dirac electrons in 1D continuum. The explanation of the parity effect in a QR is simple. Due to the removal of one electron each from A and B, each sublattice contains 99 electrons. This lowers the Fermi energy and causes a downward shift in PC and as a result, PC in a QR with 198 electrons has an opposite phase to that with 200 electrons. We also observe a similar parity effect in $D(\Phi)$.

In the recent past, the variation of I_{PC} with Φ for different values of U has been studied for a HQR [13] in which they

have considered a HQR. In Fig. 1, we show the I_{PC} vs. U taking the maximum value of $|I_{PC}|$ from the I_{PC} vs. Φ curve. It is evident that up to a certain critical value of $U(U_c)$ (which depends on t), PC

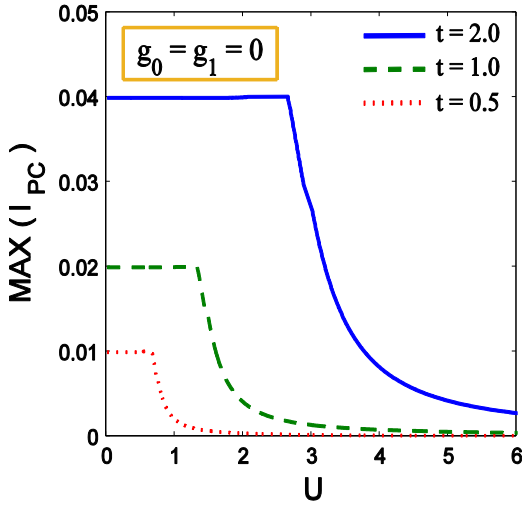

Fig. 1. $(I_{PC})_{max}$ vs. U for a Hubbard QR for different values of t.

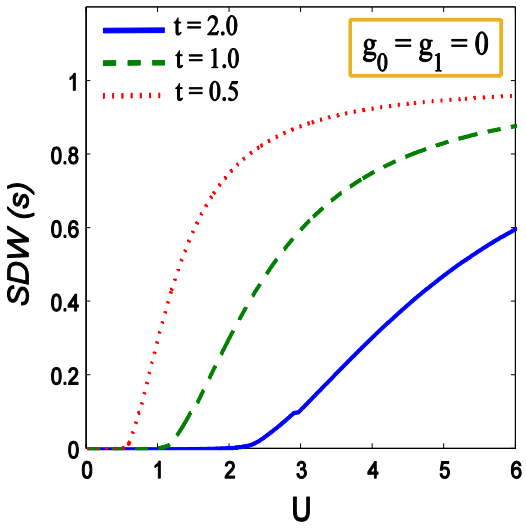

Fig. 2. Variation of the SDW order parameter (s) for HQR as a function of U.

remains independent of U. This can be understood in the following way. For a given t, there exists a critical U up to which the hopping dominates over the Coulomb correlation and so the contribution to PC comes essentially from the hopping process. The use of MF HFA which neglects the quantum fluctuations, further underestimates the role of correlation. Above U_c, however, the Coulomb correlation starts influencing the electron dynamics more and more and as a result PC begins to decrease with further increase in U. According to [13] which deals with only 7 atoms, $U_c = 0$. At $U = 4.4$, the SDW order parameter s is found to have a value 0.791 for $t = 1$. The existence of a nonzero value of U_c may be an artefact of the mean field theory used in the present work. As U is increased further, s approaches 1 confirming that the GS is then an AF SDW Mott insulator. This is shown in Fig. 2 which reveals how s grows with U in a HQR. The figure clearly shows that there does exist a critical $U(U_c)$ for a given t such that $s = 0$ for $U < U_c$. For $t = 1$, $U_c \sim 1.3$ which agrees with the result we have obtained from the I_{PC} vs. U graph (not shown here). The result that U_c increases with increasing t is easily understandable from the fact that a larger value of t leads to a larger mobility. The figure furthermore shows that as t decreases, s approaches 1 at a smaller value of$U$. In other words, as U is increased, the system goes into a SDW state at a relatively smaller value of t. We conclude that the system undergoes a quantum phase transition at this point from a diamagnetic metallic state ($D > 0$) to the AF Mott insulating state.

In Fig. 3 we plot PC as a function of the onsite e–p coupling constant g_0 for a HHQR in the absence of e–e and NN e–p interactions. The figure shows that the onsite e–p interaction has a stronger effect on PC compared to the e–e interaction. Thus, even at values much smaller than t, the onsite e–p interaction has an observable effect on PC. Consequently, a considerable suppression in PC occurs at much smaller values of g_0 as compared to that of U. The behaviour of the CDW order parameter (c) as a function of g_0 is shown in Fig. 4. The figure clearly indicates that up to a critical g_0, c is essentially zero. As g_0 increases, c increases rather rapidly and reaches 1 at a critical value of g_0 which is more or less independent of t. The $c = 1$ state corresponds to a pure CDW (Peierls) insulating state. Thus here the QR system undergoes a quantum phase transition from a diamagnetic metallic state to the Peierls CDW insulating state in a continuous and smooth way.

In Fig. 5 we show the variation of PC with g_1 for three values of t with $g_0 = 0 = U$. The magnitude of PC reduces in a similar way as happens with respect to g_0, but the reduction appears to be more rapid in the present case. The variation of CDW order parameter (c) as a function of g_1 is shown in Fig. 6. The qualitative effect of the

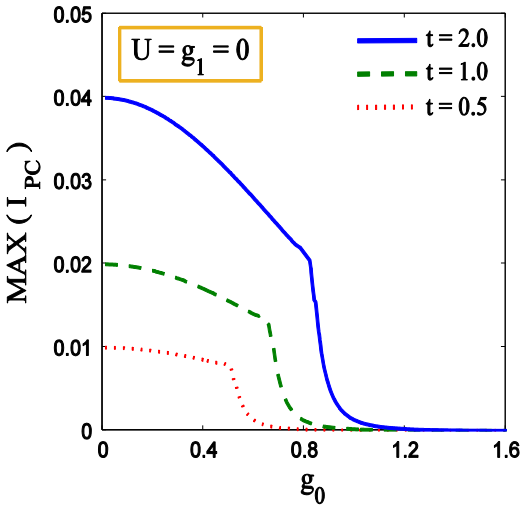

Fig. 3. PC vs. g_0 in HHQR with $U = 0 = g_1$.

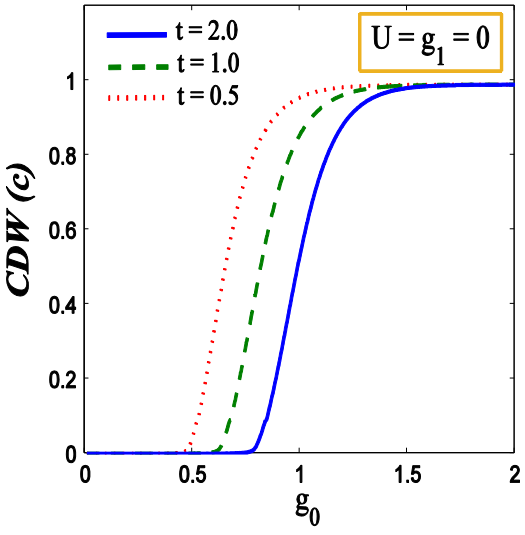

Fig. 4. CDW order parameter (c) vs. g_0 with $U = 0 = g_1$.

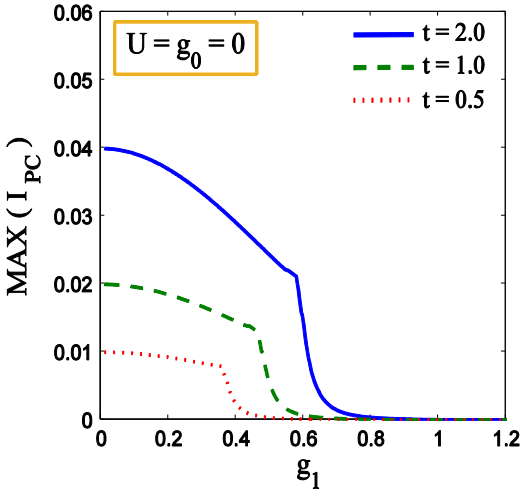

Fig. 5. PC vs. g_1 in HHQR with $U = 0 = g_0$.

NN e–p interaction is essentially the same as that of the onsite e–p interaction but in the present case the transition from $c = 0$ to $c = 1$ occurs at a little lower values of g_1.

PC as a function of U for different combinations of g_0 and g_1 is

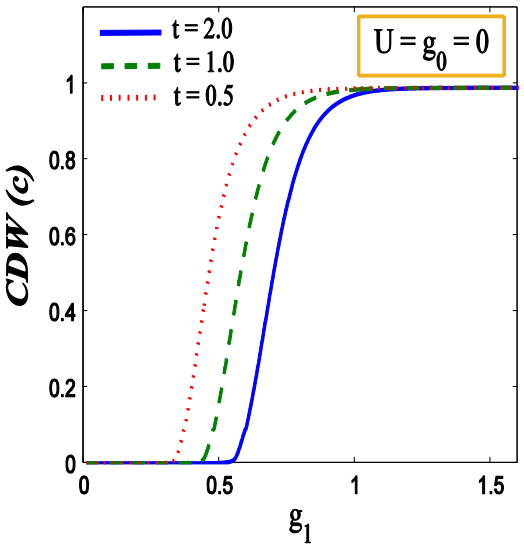

Fig. 6. Variation of the CDW order parameter (c) as a function of g_1 in the absence of e–e and NN e–p interactions.

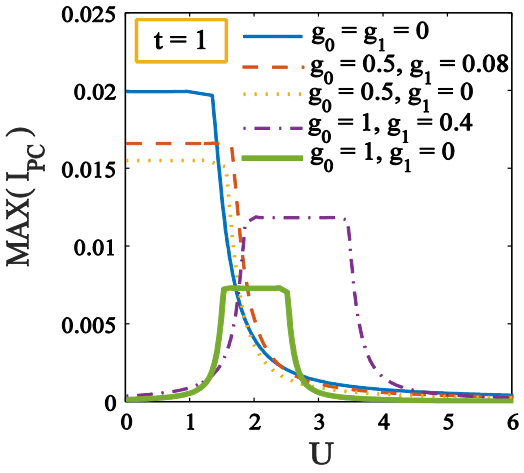

Fig. 7. PC vs. U for various combinations of g_0 and g_1.

plotted in Fig. 7. For small values of g_0 the behaviour is qualitatively similar to that for $g_0 = 0$. When g_0 becomes of the order of 1, the behaviour of PC becomes qualitatively different. For example, now even for small values of U, PC may be zero. This is due to the formation of CDW state induced by the electron–phonon interaction.

In Fig. 8 we plot a three-dimensional (3D) diagram to show more explicitly the effect of both the onsite and the NN e–p interactions together on c. The figure clearly shows that the NN e–p interaction has a more dominant effect than the onsite e–p interaction.

Next we study the combined effect of the e–e and e–p interactions on the SDW–CDW transition. The presence of both the e–e and e–p interactions makes the situation a bit more complicated. Before we deal with this situation we shall make a few comments on the effective onsite e–e interaction potential U_e. The value of U_e can be used to define the nature of the phase of a system. If U_e is less than 0, the interaction between two electrons at a particular site will be attractive and the system is more likely to be found in the CDW phase, while if $U_e > 0$, the effective e–e interaction will be repulsive and for a large positive U_e, the GS of the system is expected to be a SDW state. In both cases, the hopping parameter would be smaller than U_e. Thus there exists a possibility of

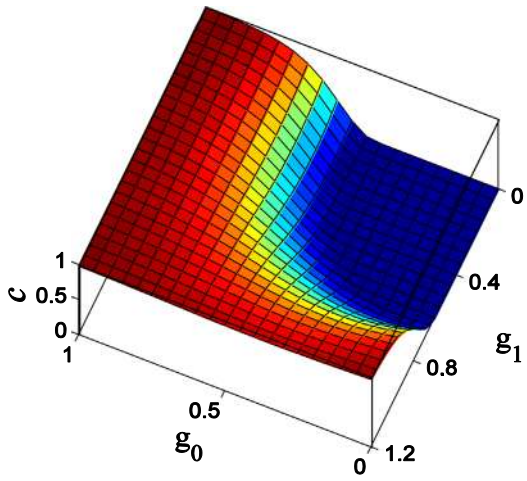

Fig. 8. Variation of the CDW parameter (c) with g_0 and g_1.

occurrence of an intermediate state for the system for which one would expect U_e~0. In this case, the system could be found in a metallic state [4–7]. Here we take $g_1 = 0$ for the sake of simplicity and first consider the $U_e = 0$ case i.e., we determine the values of U and g_0 that yield $U_e = 0$. The effective Hamiltonian then describes just a tight-binding model with the effective hopping parameter and the site energy as t_e and ε_e respectively. Thus the GS of the system does turn out to be metallic in this case with $c = 0 = s$. The numerical results also confirm this assertion. (We do not however show these graphs to save space). Next we consider the $U_e < 0$ case. For large negative U_e, the GS of the system is found to be a CDW state which is possible for small U and large g_0 values. For large negative U_e, the GS of the system is found to be a CDW state which is possible for small U and large g_0 values. Finally, we consider the $U_e > 0$ case which is seen to correspond to a SDW GS. In Fig. 9 the 3D diagram showing $|(I_{PC})_{max}|$ as a function on g_0 and U, which is obviously a surface. The surface lying above the $g_0 - U$ plane corresponds to the metallic state whereas the one that lies on the same plane corresponds to the insulating phase. To uncover the explicit nature of the phase transition we plot the 2D phase diagram in the $g_0 - U$ plane. We draw the phase diagrams by calculating DW which is positive for a diamagnetic metallic phase and zero for an insulating phase. The insulating phase can be either a CDW phase (c~1) or an SDW phase (s~1) depending on the relative interaction strengths.

$g_0 - U$ c~1s~1 Fig. 10 shows the phase diagram for a half-filled ($n = 1$) band. The figure clearly shows the existence of an

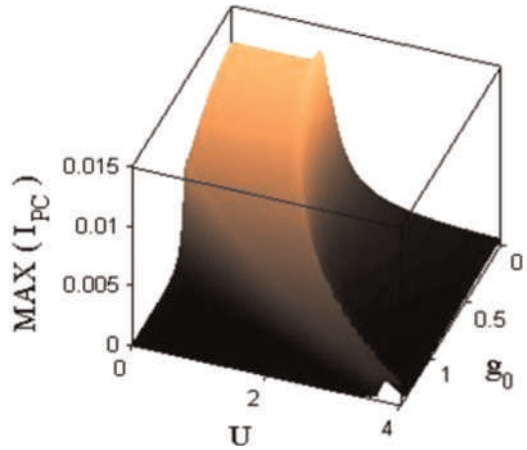

Fig. 9. Effect of both onsite e–e and e–p interactions on PC for $t = 1$ and $g_1 = 0$ for quarter filled band ($N = 200$, $N_e = 100$).

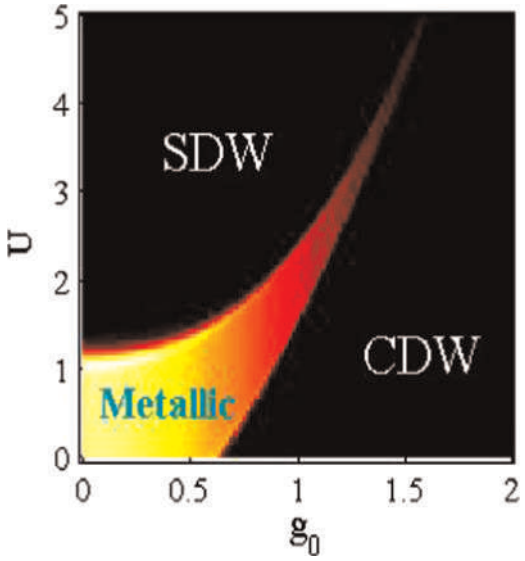

Fig. 10. Phase diagram of HHQR for a half-filling band ($n = 1$) for $t = 1$ and $g_1 = 0$.

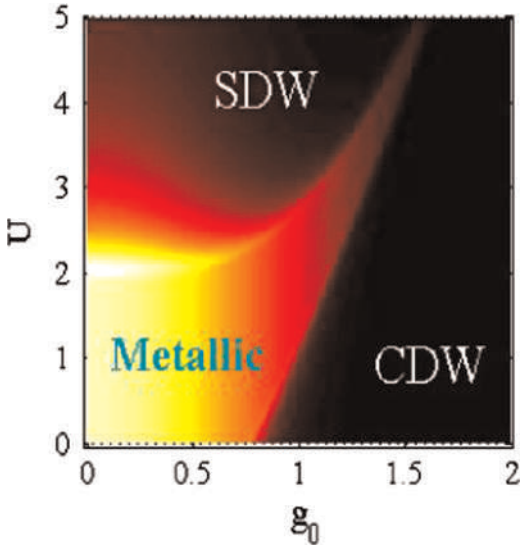

Fig. 11. Phase diagram of HHQR for a non-half-filled band ($n = 0.95$) for $t = 1$ and $g_1 = 0$.

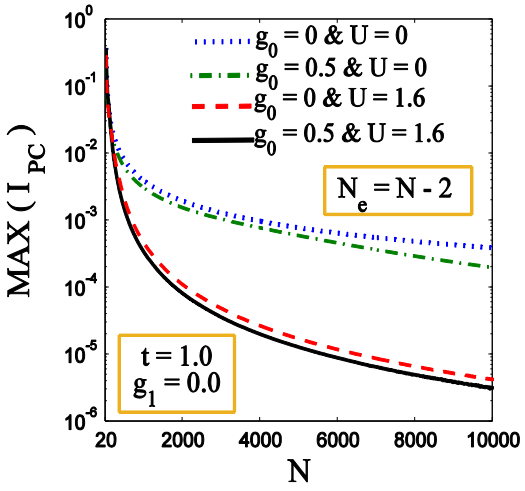

Fig. 12. PC vs. N for HHQR.

intermediate metallic phase in between the two insulating phases. It is evident that the metallic phase is favoured at small values of g_0 and U. For a band which is slightly less than half-filled the metallic phase turns out to be wider (Fig. 11). This implies that correlation is stronger at half-filling. For a band with still lesser band-filling ($n = 0.9$) the metallic phase becomes even wider. Thus we conclude that the intermediate metallic phase becomes wider as the band-filling decreases from 1. The reason is easily understandable because when the band is less than half-filled, more sites are available for the electrons to avoid double occupancy and lower the energy. One can also observe that the metallic phase widens more towards the SDW phase as the band-filling decreases from the half-filled case. The reason for this is, however, not very clear (Fig. 11).

In Fig. 12, we plot PC vs. N for different combinations of g_0 and U. PC clearly decreases with increasing N. The reason is understandable. For a small system, the electron wave function is coherent over the entire ring and this causes a larger current in the QR.

In conclusion, we have studied the combined effect of e–e and e–p interactions on PC in a 1D HHQR pierced by an AB magnetic flux. First the phonon degrees of freedom are eliminated by using the conventional Lang-Firsov transformation to obtain an effective Hubbard model which is subsequently studied using the HF decoupling scheme. The resulting linearized Hamiltonian is then written in terms of CDW and SDW order parameters which are calculated by a self-consistent approach. We observe that PC is diamagnetic and there exists the so called parity effect in a QR. We have shown that e–e and e–p interactions cause suppressions in PC in a HHQR. However the e–p interaction plays a more dominant role as compared to the e–e interaction. We have also shown that PC increases with decreasing N. This is due to the increasing coherence of the electron wave function as the system size decreases. The enhancement in PC with decreasing system size appears to be continuous precluding any possibility of an abrupt transition from the bulk to the nano-phase. Finally we have obtained the phase diagram in the $g_0 - U$ plane which predicts the existence of an intervening metallic phase which can sustain persistent current in the presence of a AB magnetic flux in a HHQR in between the CDW–SDW phases. The vicinity of the CDW or the SDW phase can possibly be used for switches. In general the phenomenon observed in this work can have far-reaching implications from the point of view of device technology as well as superconductivity in nanosystems.

References

[1] M. Bűttiker, Y. Imry, R. Landauer, Phys. Lett. A 96 (1983) 365.
[2] O.V. Kibis, O. Kyriienko, I.A. Shelykh, Phys. Rev. B 87 (2013) 245437.
[3] (a) L.P. Levy, G. Dolan, J. Dunsmuir, H. Bouchiat, Phys. Rev. Lett. 64 (1990) 2074;
(b) V. Chadrasekhar, et al., Phys. Rev. Lett 67 (1991) 3578;
(c) D. Mailly, C. Chapelier, A. Benoit, Phys. Rev. Lett. 70 (1993) 2020;
(d) E.M.Q. Jariwala, P. Mohanty, M.B. Ketchen, R.A. Webb, Phys. Rev. Lett. 86 (2001) 1594;
(e) R. Deblock, R. Bel, B. Reulet, H. Bouchiat, D. Mailly, Phys. Rev. Lett. 89 (2002) 206803;
(f) H. Bluhm, Phys. Rev. Lett. 102 (2009) 136802;
(g) A.C. Bleszynski-Jayich, et al., Science 326 (2009) 5950;
(h) G.M. Souche, et al., Phys. Rev. B 87 (2013) 115120;
(i) M.A. Castellanos-Beltran, et al., Phys. Rev. Lett. 110 (2013) 156801;
(j) B.B. Wei, S.J. Gu, H.Q. Lin, J. Phys.: Condens. Matter 20 (2008) 395209;
(k) A. Moskova, M. Mosko, J. Tobik, Phys. Status Solidi B 250 (2013) 147.
[4] (a) E.A. Nowadnick, S. Johnston, B. Moritz, R.T. Scalettar, T.P.D. Devereaux, Phys. Rev. Lett. 109 (2012) 246404;
(b) S. Kumar, J. van den Brink, Phys. Rev. B 78 (2008) 155123.
[5] (a) Y. Takada, A. Chatterjee, Phys. Rev. B 67 (R) (2003) 081102;
(b) A. Chatterjee, Y. Takada, J. Phys. Soc. Jpn. 73 (2004) 964;
(b) P.M. Krishna, Ashok Chatterjee, Physica C 457 (2007) 55.
[6] (a) R.T. Clay, R.P. Hardikar, Phys. Rev. Lett. 95 (2005) 096401;

(b) R.P. Hardikar, R.T. Clay, Phys. Rev. B 75 (2007) 245103;
(b) M. Tezuka, R. Arita, H. Aoki, Phys. Rev. B 76 (2007) 155114;
(c) H. Fehske, G. Hager, E. Jackelmann, Europhys. Lett. 84 (2008) 57001;
(d) S. Ejima, H. Fehske, J. Phys.: Conf. Ser. 200 (2010) 012031.
[7] (a) J. Bauer, Europhys. Lett. 90 (2010) 27002;
(b) W. Koller, D. Meyer, Y. Ono, A.C. Hewson, Europhys. Lett. 66 (2004) 559;
(c) G.S. Jeon, Tae-Ho Park, J.H. Han, H.C. Lee, Han-Yong Choi, Phys. Rev. B 70 (2004) 125114;
(d) J. Bauer, A.C. Hewson, Phys. Rev. B 81 (2010) 235113;
(e) Y. Murakami, P. Werner, N. Tsuji, H. Aoki, Phys. Rev. B 88 (2013) 125126.
[8] (a) I. Lang, Y.A. Firsov, Sov. Phys. JETP 16 (1963) 1301;
(b) I.V. Sankar, S. Mukhopadhyay, A. Chatterjee, Physica C 480 (2012) 55;
(c) I.V. Sankar, A. Chatterjee, Eur. Phys. J. B 87 (2014) 154.
[9] D. Cabib, E. Callen, Phys. Rev. B 12 (1975) 5249.
[10] A.N. Das, S. Sil, J. Phys.: Condens. Matter 5 (1993) 8265.
[11] (a) W. Kohn, Phys. Rev. A 133 (1964) 171;
(b) B.S. Shastry, B. Sutherlland, Phys. Rev. Lett. 65 (1990) 243.
[12] (a) Ho-Fai Cheung, Y. Gefen, E.K. Riedel, Wei-Heng Shih, Phys. Rev. B 37 (1988) 6050;
(b) D. Sticlet, B. Dora, J. Cayssol, Phys. Rev. B 88 (2013) 205401.
[13] P. Koskinen, M. Manninen, Phys. Rev. B 68 (2003) 195304.

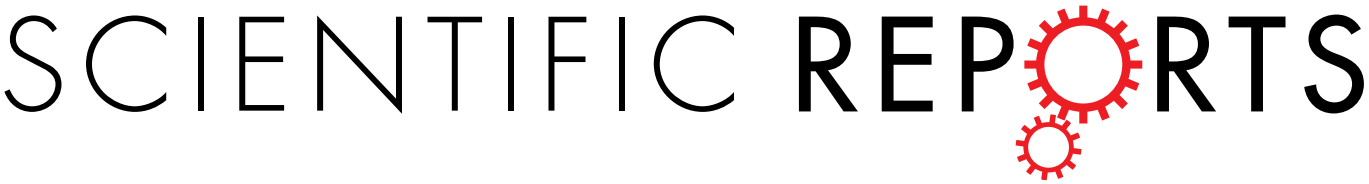

OPEN

Received: 23 June 2015
Accepted: 07 December 2015
Published: 01 February 2016

Persistent current in a correlated quantum ring with electron-phonon interaction in the presence of Rashba interaction and Aharonov-Bohm flux

P. J. Monisha[1], I. V. Sankar[1], Shreekantha Sil[2] & Ashok Chatterjee[1]

Persistent current in a correlated quantum ring threaded by an Aharonov-Bohm flux is studied in the presence of electron-phonon interactions and Rashba spin-orbit coupling. The quantum ring is modeled by the Holstein-Hubbard-Rashba Hamiltonian and the energy is calculated by performing the conventional Lang-Firsov transformation followed by the diagonalization of the effective Hamiltonian within a mean-field approximation. The effects of Aharonov-Bohm flux, temperature, spin-orbit and electron-phonon interactions on the persistent current are investigated. It is shown that the electron-phonon interactions reduce the persistent current, while the Rashba coupling enhances it. It is also shown that temperature smoothens the persistent current curve. The effect of chemical potential on the persistent current is also studied.

The existence of a persistent current (PC) in a normal metal ring was first proposed by Buttiker, Imry and Landauer[1]. Cheung *et al.*[2] have studied the effects of temperature, chemical potential and randomness on PC in strictly one-dimensional (1D) normal rings. Several theoretical studies[3–7] have been subsequently carried out on PC in mesoscopic systems. Since the energy would be periodic in the flux, one expects the PC to show the similar behavior. With the advent of nano-fabrication techniques, several experimental investigations have been made to confirm the existence[8,9] and the periodicity[10–14] of PC in semiconductor quantum rings (QRs). The periodicity of PC in a finite ring can be shown using continuum or discrete models[15]. The period is found to be $\Phi_0 = hc/e$ for non-interacting spinless electrons. The most useful model to study PC is the Hubbard model in which the ring consists of discrete lattice sites and the electrons can hop from one site to another. Several works[16–19] have been carried out on the Hubbard ring to understand the magnetic response and the behavior of PC. But most of them have neglected the electron-phonon (*e-p*) interaction which can actually play quite an important role in the low-dimensional systems. The effect of *e-p* interaction on PC can be captured by considering the Holstein-Hubbard (HH) model[20,21]. Another important interaction that has come to light in the context of nano-systems in recent years is the spin-orbit (SO) interaction which is at the heart of the emerging field of spintronics. New devices are being contemplated which would use the spin degrees freedom instead of charge. There can be two kinds of SO interactions in solids. One originates due to the structural inversion asymmetry which is known as the Rashba spin-orbit (RSO) interaction and the other is due to the bulk inversion asymmetry which is called as the Dresselhaus spin-orbit (DSO) interaction. The effects of SO interaction[22–24] are found to be pronounced in QR's. By tuning the external electric field the electron spin can be controlled and consequently, the Rashba effect can be manipulated, which is precisely the idea behind spintronics[25]. In the present paper we shall study the effects of RSO interaction on PC in a 1D HH ring threaded by an Aharonov-Bohm (AB) flux. Since the number of electrons in a QR also changes the magnitude and phase of PC[2], the chemical potential is expected to have an interesting effect on PC. As the temperature increases, the electrons may occupy higher energy levels that are close and can have opposite currents and therefore, as a net result, the higher positive and negative contributions

[1]School of Physics, University of Hyderabad, Hyderabad 500046, India. [2]Department of Physics, Visva-Bharati-Santiniketan, West Bengal-731235, India. Correspondence and requests for materials should be addressed to A.C. (email: acsp@uohyd.ernet.in)

to PC may cancel out. Buttiker has indeed observed a decrease in the amplitude of the PC with temperature[26]. We shall therefore study the effects of chemical potential and temperature as well on PC in a 1D HH ring in the presence of RSO interaction.

Theoretical Formalism

The Hamiltonian for a HH ring threaded by a magnetic flux Φ can be written in the presence of RSO interaction as

$$H = H_0 + H_{so} = H_e + H_p + H_{ep} + H_{so}, \tag{1}$$

where

$$H_e = \varepsilon_0 \sum_i c_i^\dagger c_i - te^{i\theta} \sum_{\langle ij \rangle} [c_i^\dagger c_j + \text{h.}c] + U \sum_i n_{i\uparrow} n_{i\downarrow}, \tag{2}$$

$$H_p = \hbar\omega_0 \sum_i (b_i^\dagger b_i + 1/2\,), \tag{3}$$

$$H_{ep} = \mathrm{g}_1 \sum_i n_i (b_i + b_i^\dagger) + \mathrm{g}_2 \sum_{\langle ij \rangle} n_i (b_j + b_j^\dagger), \tag{4}$$

$$H_{so} = -\sum_{ij} [c_i^\dagger t_{so} e^{i\theta} c_j + \text{h.}c\,]. \tag{5}$$

Eq. 2 represents the electronic Hamiltonian H_e which consists of three terms. The first term represents the site energy, ε_0 being the site energy, $c_i = \begin{pmatrix} c_{i\uparrow} \\ c_{i\downarrow} \end{pmatrix}$, $c_{i\sigma}^\dagger (c_{i\sigma})$ being the creation (annihilation) operator for an electron at site i with spin σ, and $i = 1, 2, 3, \ldots N$, N being the total number of sites in the system. The second term describes the hopping term where t is the hopping integral between the nearest-neighbour (NN) sites, $\langle ij \rangle$ denotes that the summation is to be performed over NN sites i and j and $\theta = (2\pi\Phi/\mathrm{N})$ is the AB phase due to the magnetic flux Φ, which is an integral multiple of the elementary flux quantum $\Phi_0 = hc/e$. The third term is the onsite repulsive electron-electron (e-e) Coulomb interaction where U measures the strength of the interaction and $n_{i\sigma} = c_{i\sigma}^\dagger c_{i\sigma}$ is the number operator for the electrons at site i with spin σ. Eq. 3 gives the unperturbed phonon Hamiltonian where $b_i^\dagger (b_i)$ is the creation (annihilation) operator for a phonon with dispersionless frequency ω_0 at site i. Eq. 4 represents the onsite and NN e-p interactions with g_1 and g_2 measuring the respective coupling constants. Thus g_1 measures the strength of the interaction of an electron with the phonons at the i-th site, whereas g_2 gives the strength of the interaction of an electron at the i-th site with the phonons at the $(i+1)$-th site. The value of g_2 is in general expected to be smaller than that of g_1 and typically for a real material one may take the value of g_2 about one order less than that of g_1. In general, an electron is supposed to interact with phonons at all sites. But we restrict our study of e-p interaction up to NN terms assuming that beyond NN's, interactions will be small enough to be ignored. [If the onsite e-p interaction is so strong that the electron gets trapped in a deep potential well created at the i-th site, then its interaction with the NN phonons will be very small. In such cases the effective NN e-p interaction can be neglected]. In real systems the effects of g_1 and g_2 manifest themselves through the localization-delocalization transition. Finally, Eq. 5 describes the SO interaction with

$$t_{so} = i\alpha \left(\sigma_x \cos\varphi_{ij} + \sigma_y \sin\varphi_{ij}\right) - i\beta \left(\sigma_y \cos\varphi_{ij} + \sigma_x \sin\varphi_{ij}\right) \tag{6}$$

where $\varphi_{ij} = (\varphi_i + \varphi_j)/2$ and $\varphi_i = 2\pi(i-1)/N$ so $\varphi_{ij} = 2\pi(i-1/2\,)/N$, σ_x and σ_y are the Pauli spin matrices. And $i = 1, 2, \ldots, N$ is the site index along the azimuthal direction φ of the ring.

In the present problem we are interested in RSO interaction only and so we take $\beta = 0$. We first perform a Lang-Firsov transformation (LFT) with a generator $R = [\mathrm{g}_1 \sum_{i\sigma} n_{i\sigma} (b_i^\dagger - b_i) + \mathrm{g}_2 \sum_{\langle ij \rangle \sigma} n_{i\sigma} (b_j^\dagger - b_j)]/\hbar\omega_0$. LFT is a displaced oscillator (also called a coherent state) transformation and its purpose is to eliminate the phonons to obtain an effective electronic Hamiltonian. Performing a LFT physically means assuming a coherent state for phonons where the coherence strength is determined by the electron density. The LFT works well in the strong-coupling limit. Next we employ a unitary transformation with the matrix

$$U_m = \frac{1}{\sqrt{2}} \begin{bmatrix} 1 & -1 \\ e^{\frac{2\pi i}{N}\left(m-\frac{1}{2}\right)} & e^{\frac{2\pi i}{N}\left(m-\frac{1}{2}\right)} \end{bmatrix}, \tag{7}$$

so that the transformed Hamionian reads

$$\begin{aligned} H_{eff} \;=\; & e_0^e \sum_{i\sigma} \tilde{n}_{i\sigma} - \frac{1}{2} e^{i\theta} \sum_{\langle ij \rangle \sigma} \tilde{c}_{i\sigma}^\dagger [t_e + i\alpha_e] \mathbb{B} \tilde{c}_{j\sigma} + U_e \sum_i \tilde{n}_{i\uparrow}\, \tilde{n}_{i\downarrow} \\ & + \frac{\tilde{n}_i}{4} [\tilde{c}_{i\uparrow}^\dagger \tilde{c}_{i\downarrow} + \tilde{c}_{i\downarrow}^\dagger \tilde{c}_{i\uparrow}] - [\tilde{c}_{i\uparrow}^\dagger \tilde{c}_{i\downarrow} + \tilde{c}_{i\downarrow}^\dagger \tilde{c}_{i\uparrow}] \left(\frac{\tilde{n}_i}{4}\right) \end{aligned} \tag{8}$$

where

$$e_0^e = -(g_1^2 + z\ g_2^2)/\hbar\omega_0, \quad (z = \text{number of NNs}) \tag{9}$$

$$t_e = te^{-\left[(g_1-g_2)^2+(z-1)\ g_2^2\right]/(\hbar\omega_0)^2}, \tag{10}$$

$$U_e = U - 2(g_1^2 + z\ g_2^2)/\hbar\omega_0, \tag{11}$$

$$\alpha_e = \alpha e^{-\left[(g_1-g_2)^2+(z-1)g_2^2\right]/(\hbar\omega_0)^2}, \tag{12}$$

$$\mathbb{B} = \begin{bmatrix} 1 + e^{\frac{2\pi i}{N}} & -1 + e^{\frac{2\pi i}{N}} \\ -1 + e^{\frac{2\pi i}{N}} & 1 + e^{\frac{2\pi i}{N}} \end{bmatrix}. \tag{13}$$

$$\widetilde{O} = \mathbb{B}^{-1} O \mathbb{B} \tag{14}$$

We now use a mean-field approximation (MFA) to deal with the *e*-*e* interaction. This approximation neglects the fluctuations and is known to be a meaningful approximation if the correlation is not strong. Using MFA, we get after some algebra[27]

$$H_{eff}^M = \sum_{i=1}^{N} \tilde{c}_i^\dagger [\mathbb{C} + (-1)^i \mathbb{D}] \tilde{c}_i - e^{i\left(\theta + \frac{\pi}{N}\right)} \sum_{ij\sigma}^{N} \tilde{c}_{i\sigma}^\dagger [t_e \mathbb{E} + i\alpha_e \mathbb{F}]\ \tilde{c}_{j\sigma} + K \tag{15}$$

where,

$$\begin{aligned} \varepsilon_{A\uparrow} &= e_0^e + U_e(c-s)/2, \quad \varepsilon_{B\uparrow} = e_0^e - U_e(c-s)/2, \\ \varepsilon_{A\downarrow} &= e_0^e + U_e(c+s)/2, \quad \varepsilon_{B\downarrow} = e_0^e - U_e(c+s)/2, \end{aligned} \tag{16}$$

$$\mathbb{C} = \begin{bmatrix} \varepsilon_{AB\uparrow}^+ & 0 \\ 0 & \varepsilon_{AB\downarrow}^+ \end{bmatrix}, \ \varepsilon_{AB\uparrow}^+ = (\varepsilon_{A\uparrow} + \varepsilon_{B\uparrow})/2, \quad \varepsilon_{AB\downarrow}^+ = (\varepsilon_{A\downarrow} + \varepsilon_{B\downarrow})/2, \tag{17}$$

$$\mathbb{D} = \begin{bmatrix} \varepsilon_{AB\uparrow}^- & 0 \\ 0 & \varepsilon_{AB\downarrow}^- \end{bmatrix}, \ \varepsilon_{AB\uparrow}^- = (\varepsilon_{A\uparrow} - \varepsilon_{B\uparrow})/2, \quad \varepsilon_{AB\downarrow}^- = (\varepsilon_{A\downarrow} - \varepsilon_{B\downarrow})/2, \tag{18}$$

$$\mathbb{E} = \begin{bmatrix} \cos(\pi/N) & i\ \sin(\pi/N) \\ i\ \sin(\pi/N) & \cos(\pi/N) \end{bmatrix}, \tag{19}$$

$$\mathbb{F} = \begin{bmatrix} \cos(\pi/N) & i\ \sin(\pi/N) \\ -i\ \sin(\pi/N) & -\cos(\pi/N) \end{bmatrix}, \tag{20}$$

$$K = NU_e(n^2 - c^2 + s^2)/4, \tag{21}$$

$$n = [(n_{A\uparrow} + n_{A\downarrow}) + (n_{B\uparrow} + n_{B\downarrow})]/2, \tag{22}$$

$$c = [(n_{A\uparrow} + n_{A\downarrow}) - (n_{B\uparrow} + n_{B\downarrow})]/2, \tag{23}$$

$$s = [(n_{A\uparrow} - n_{A\downarrow}) - (n_{B\uparrow} - n_{B\downarrow})]/2. \tag{24}$$

Using the Fourier transform: $\tilde{c}_{m\sigma} = \frac{1}{\sqrt{N}} \sum_k e^{i\ kma}\ \tilde{c}_{k\sigma}$, where a is the lattice constant and redefining $\tilde{c}_{i\sigma}(\tilde{c}_{i\sigma}^\dagger)$ as $c_{i\sigma}(\ c_{i\sigma}^\dagger\ )$ and $\tilde{c}_{k\sigma}(\tilde{c}_{k\sigma}^\dagger)$ as $c_{k\sigma}(c_{k\sigma}^\dagger)$ and separating the Hamiltonian into even and odd sited terms, we obtain after some rearrangement of terms

$$H_{eff}^M = \sum_{k=-\pi/a}^{\pi/a} c_k^\dagger \mathbb{G} c_k + \sum_{k=-\pi/a}^{\pi/a} c_k^\dagger \mathbb{H} c_{k+(\pi/a)} + K, \tag{25}$$

where

$$\mathbb{G} = \begin{bmatrix} \varepsilon^{+}_{AB\uparrow} + \alpha_{11} & \alpha_{12} \\ \alpha_{21} & \varepsilon^{+}_{AB\downarrow} + \alpha_{22} \end{bmatrix}, \tag{26}$$

$$\mathbb{H} = \begin{bmatrix} \varepsilon^{-}_{AB\uparrow} & 0 \\ 0 & \varepsilon^{-}_{AB\downarrow} \end{bmatrix}, \tag{27}$$

$$\alpha_{11} = -2t_e \cos(\pi/N)\cos(ka + \theta + \pi/N) + 2\alpha_e \cos(\pi/N)\sin(ka + \theta + \pi/N), \tag{28}$$

$$\alpha_{12} = 2t_e \sin(\pi/N)\sin(ka + \theta + \pi/N) + 2\alpha_e \sin(\pi/N)\cos(ka + \theta + \pi/N), \tag{29}$$

$$\alpha_{21} = 2t_e \sin(\pi/N)\sin(ka + \theta + \pi/N) - 2\alpha_e \sin(\pi/N)\cos(ka + \theta + \pi/N), \tag{30}$$

$$\alpha_{22} = -2t_e \cos(\pi/N)\cos(ka + \theta + \pi/N) - 2\alpha_e \cos(\pi/N)\sin(ka + \theta + \pi/N). \tag{31}$$

We shall work in the reduced zone scheme i. e., we choose k to lie in the range: $-\pi/2a \le k \le \pi/2a$. In this scheme, the matrix elements $\alpha's$ can be written as: $\alpha_{ij}(k + \pi/a) = -\alpha_{ij}(k)$. The effective mean-field Hamiltonian can now be written as

$$H^{M}_{eff} = \sum_{k=0}^{\pi} (c^{\dagger}_{k\uparrow} \; c^{\dagger}_{k\downarrow} \; c^{\dagger}_{k+\pi,\uparrow} \; c^{\dagger}_{k+\pi,\downarrow}) \mathbb{W} \begin{pmatrix} c_{k\uparrow} \\ c_{k\downarrow} \\ c_{k+\pi,\uparrow} \\ c_{k+\pi,\downarrow} \end{pmatrix} \tag{32}$$

where

$$\mathbb{W} = \begin{bmatrix} \varepsilon^{+}_{AB\uparrow} + \alpha_{11} & \alpha_{12} & \varepsilon^{-}_{AB\uparrow} & 0 \\ \alpha_{21} & \varepsilon^{+}_{AB\downarrow} + \alpha_{22} & 0 & \varepsilon^{-}_{AB\downarrow} \\ \varepsilon^{-}_{AB\uparrow} & 0 & \varepsilon^{+}_{AB\uparrow} - \alpha_{11} & -\alpha_{12} \\ 0 & \varepsilon^{-}_{AB\downarrow} & -\alpha_{21} & \varepsilon^{+}_{AB\downarrow} - \alpha_{22} \end{bmatrix}. \tag{33}$$

The exact numerical diagonalization of H^{M}_{eff} yields four energies E_1, E_2, E_3, E_4 and the four distribution functions $f(E_1), f(E_2), f(E_3), f(E_4)$, where $f(E_i) = [e^{\beta(E_i-\mu)} + 1]^{-1}$. The GS energy is now given by

$$E_{GS} = \sum_i E_i f(E_i) + K \tag{34}$$

and the PC (I_{pc}) can be calculated from the relation

$$I_{pc} = -\frac{1}{2\pi}\left(\frac{\partial E_{GS}}{\partial \Phi}\right). \tag{35}$$

Numerical results and Discussions

For the sake of convenience, we set $t = 1$ and measure all energies in units of $\hbar\omega_0$. In Fig. 1(a), we plot the GS energy E_{GS} as a function of the flux Φ for various values of α in the absence of all other interactions. We can see that the GS energy increases with α. The periodicity of the energy with Φ is also clearly evident. In Fig. 1(b) we plot PC vs. Φ for different values of α. The RSO interaction clearly enhances I_{pc}. Also, the phase of PC changes, when α exceeds a critical value (α_c). In the present case, $\alpha_c > 1$. The variation of I_{PC} as a function of α is explicitly shown in Fig. 1(c). I_{PC} increases with α monotonically, though its derivative can have a more interesting behavior.

Figure 2 shows the behaviour of PC as a function of U with and without RSO interaction. The MFA employed here may be considered to be a reasonable approximation since we have studied the effect of U from $U = 0$ to $U = 4$ which lies in the weak correlation regime since $\hbar\omega_0 = 1$ is set as the energy scale. The solid line describes the behavior for $\alpha = 0$ and the dashed-dotted line for $\alpha = 2$. One can easily notice that PC decreases as U increases. The explanation is quite simple. As U increases, the electrons experience a larger onsite repulsion and thus find it more difficult to go from one site to another. This reduces PC. In the absence of RSO interaction, there seems to exist some critical value of $U(U_c)$ below which PC remains constant and unaffected by U. This implies that the effective hopping parameter t_e remains predominant over U below U_c and thus U does not play any significant role. Above U_c, PC dies out extremely sharply. In the presence of RSO interaction, however, there is a qualitative difference in the behavior of PC as a function of U. The figure shows the behavior for $\alpha = 2$. It is evident that, though even now, the decrease of PC with increasing U is quite rapid, it is smooth and there is no

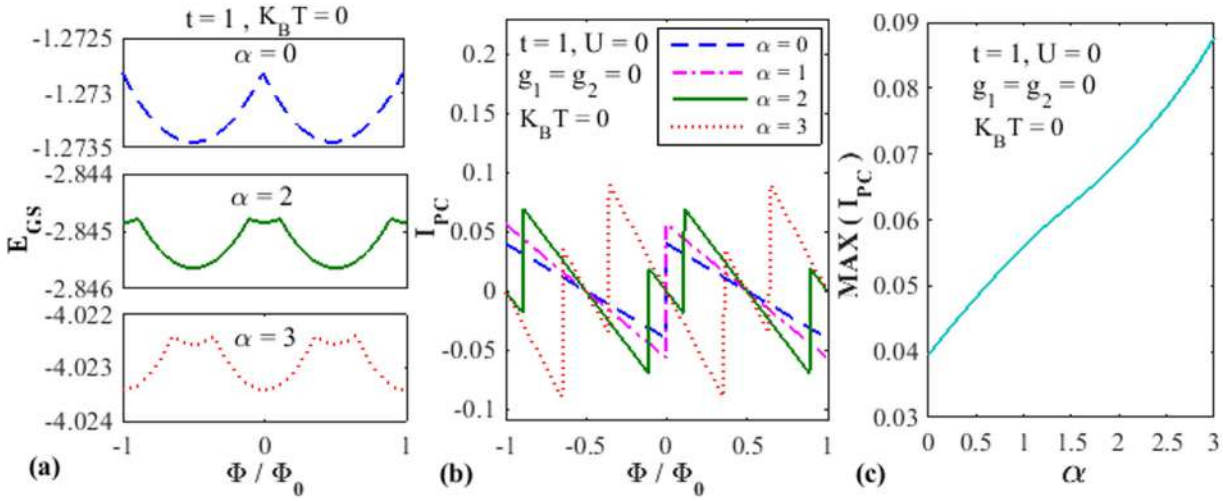

Figure 1. The GS energy and PC in the presence of SO interaction for $U = g_1 = g_2 = 0$. (**a**) The GS energy as a function of the flux Φ for different α. (**b**) Persistent current I_{PC} as a function of Φ for different α. **(c)** Variation of I_{PC} as a function of α.

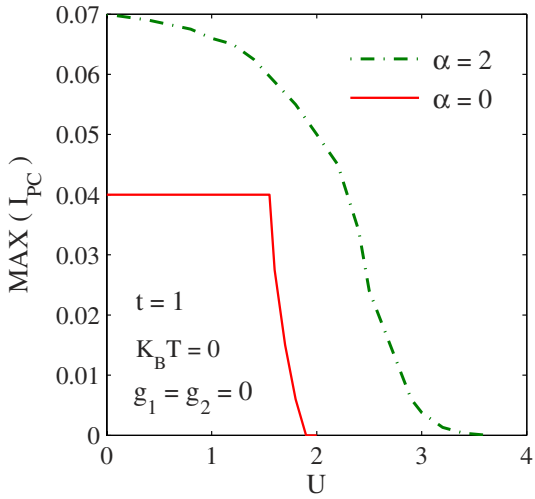

Figure 2. The effect of *e-e* interaction on the PC. I_{PC} as a function of U for $\alpha = 2$ and $\alpha = 0$.

indication of existence of any critical value of U. One possible explanation for this behavior may be the following. In the presence of the Rashba interaction, the PC undergoes a significant enhancement as can be seen from Fig. 1(c) and the correlation effect also increases because of a second-order contribution from the RSO interaction. Because of the higher effective U, even at small U, the correlation plays an important role and consequently PC decreases with U from $U = 0$ itself and thus shows a smooth behavior as a function of U. Use of a better method to include the quantum fluctuations may make the PC vs. U curve smooth even in the case of $\alpha = 0$ and rule out the existence of any critical U_c. A final answer on this issue requires more critical investigations.

Next we look into the effects of onsite and NN *e-p* interactions on PC. In Fig. 3 we plot PC as a function of g_1. It is evident that PC decreases as g_1 increases. This reduction in PC is understandable. Since g_1 gives the strength of the onsite *e-p* interaction, as g_1 is increased, the *e-p* interaction will distort the lattice more around that site leading to a deeper polarization potential for the electron causing electron self-trapping or localization at that site[28–30]. This will inhibit conduction. The gradient of the curve is however not monotonic which may have some interesting physical implications. One may also notice that the resistive effect of the *e-p* interaction is more pronounced than that of the *e-e* interaction.

In Fig. 4(a), we wish to study the effect of NN *e-p* interaction on PC keeping $\alpha = 0$. So we plot I_{PC} vs. Φ for several values of g_2. To see the sole effect of g_2 we first study the case with $U = 0 = g_1$. We find that the effect of g_2 on PC is stronger that of that of g_1, which is clearly suggested by Eq. 10. According to Eq. 10, t_e contains an additional Hoslstein reduction factor solely dependent on g_2. Figure 4(a) also shows that the periodicity of PC decreases with increasing g_2. The behavior is qualitatively similar (not shown here) even with g_1, but again the

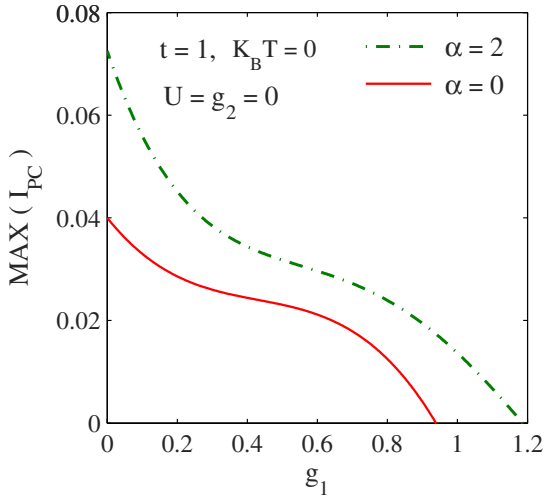

Figure 3. The effect of *e-p* interaction on the PC. I_{PC} vs. g_1 for $\alpha = 0$ and $\alpha = 2$ (with $U = 0 = g_2$).

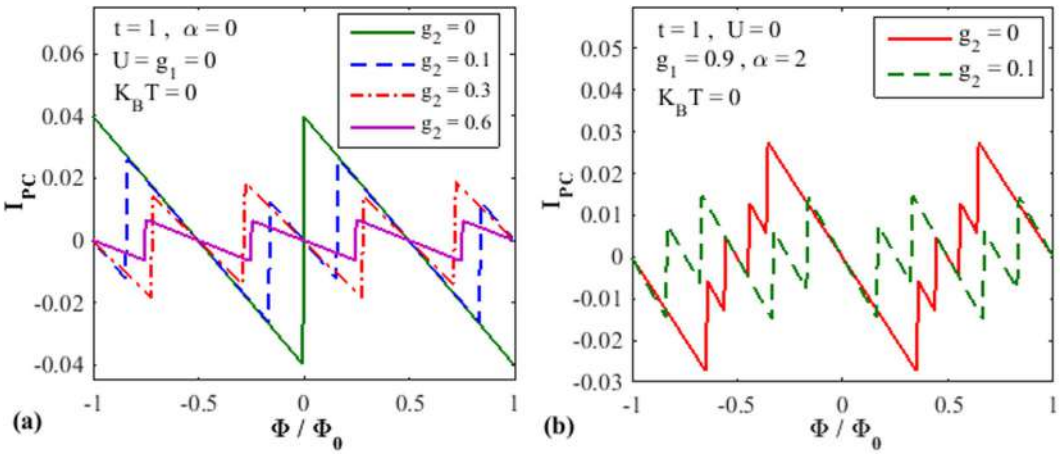

Figure 4. The effect of NN *e-p* interaction on the PC. (**a**) I_{pc} vs. Φ for different values of g_2 with $\alpha = 0$. (**b**) PC vs Φ for $g_2 = 0$ and 0.1 with $g_1 = 0.9$.

effect of g_2 is stronger. In Fig. 4(b) we show PC vs. Φ for $g_2 = 0$ and 0.1 in the presence of onsite *e-p* interaction ($g_1 = 0.9$). Of course, the reduction in PC is now more pronounced and furthermore the periodicity also decreases. We do not plot PC vs. g_2 because the behavior is infested with a lot of fluctuations.

The effect of temperature on PC is plotted in Fig. 5(a) for both $\alpha = 0$ and $\alpha = 2$ and it is clear that as the temperature increases, PC decreases in both cases as our commonplace notion would justify. The exact numerical behavior is however a little more complicated eluding any simple explanation. As established earlier, PC is larger in the presence of the RSO interaction. Interestingly enough, PC develops a peak at very low temperature. In Fig. 5(b) we plot PC vs. temperature in the presence of RSO interaction for $g_1 = 0.5$ and compare with the graph for $g_1 = 0$. It is evidently clear that in the presence the *e-p* interaction, the peak in PC becomes sharper and acquires a greater value. This happens because as *e-p* interaction increases, polaronic quasiparicle weight increases leading to a sharper peak in the PC.

Finally we wish to study the effect of chemical potential μ on PC. In Fig. 6(a), we plot PC as a function of Φ for different values of μ. As expected, the magnitude and the phase of PC change with μ. Direct dependence of PC on μ is shown in Fig. 6(b) both in the presence and absence of the RSO interaction. In both cases, PC decreases with increasing μ, the values of PC being greater for the $\alpha = 2$.

Conclusions

In this work, the effect of RSO interaction on PC is studied in a one-dimensional Holstein-Hubbard ring threaded by an Aharonov-Bohm flux. First, the phonon degrees of freedom are eliminated by performing the conventional Lang-Firsov transformation and then the spin-dependence is removed by performing another unitary transformation. The effective electronic Hamiltonian is finally diagonalized by using a mean-field Hartree-Fock

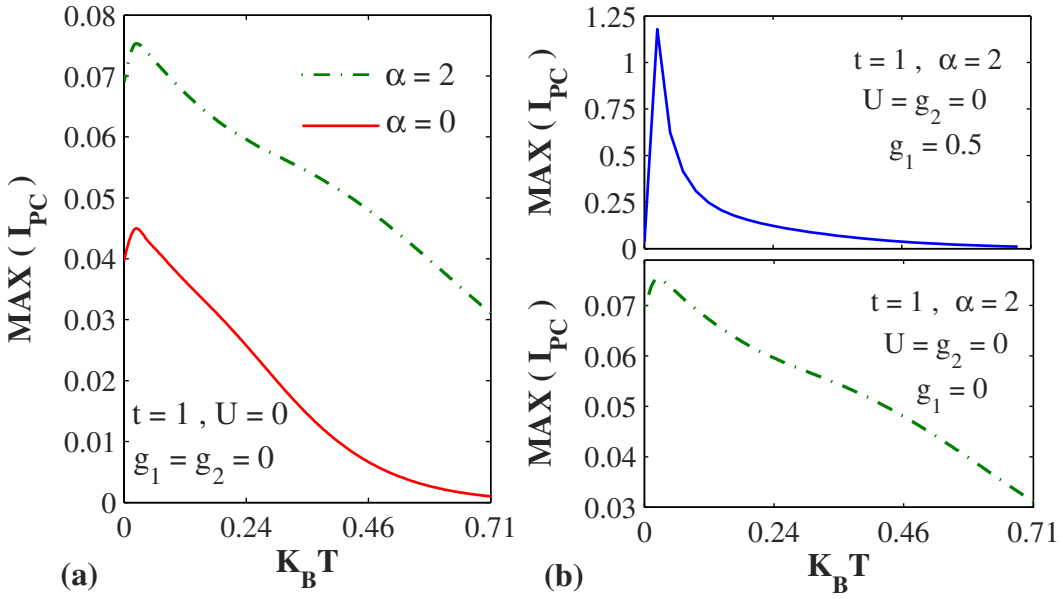

Figure 5. The effect of temperature on the PC. (**a**) I_{pc} as a function of temperature for $\alpha = 0$ and $\alpha = 2$. (**b**) I_{pc} as a function of temperature for different values of g_1 with $\alpha = 2$.

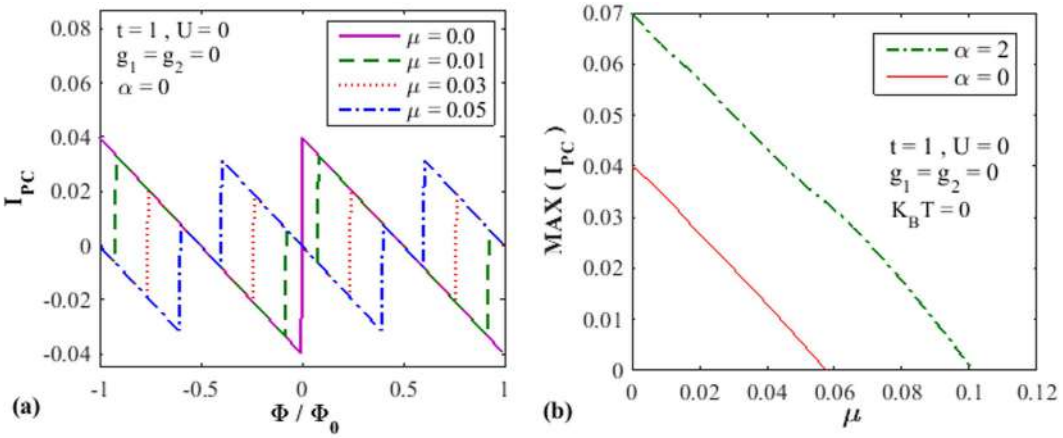

Figure 6. The effect of chemical potential on the PC. (**a**) The persistent current as a function of flux for different μ. (**b**) PC vs μ for $\alpha = 2$ and $\alpha = 0$.

approximation and PC is calculated by differentiating the GS energy with respect to the flux. We show that the magnitude of PC is enhanced as we switch on the RSO interaction α. Also, for large values of $\alpha(\alpha > 1)$, the phase of PC is observed to change. We notice that both the *e-e* and *e-p* interactions reduce the value of PC. We also observe that the NN *e-p* interaction has a stronger effect on PC than the onsite *e-p* interaction has. We furthermore show that PC decreases with temperature and in the presence of *e-p* interaction develops a sharp peak at a low temperature. We finally show that the magnitude of PC decreases with increasing chemical potential and its phase also changes (as the number of particles change).

References

1. Büttiker, M., Imry, Y. & Landauer, R. Josephson behavior in small normal one-dimensional rings. *Phys. Lett. A* **96,** 365–367 (1983).
2. Cheung, H.-F., Gefen, Y., Riedel, E. K. & Shih, W.-H. Persistent currents in small one-dimensional metal rings. *Phys. Rev. B* **37,** 6050–6062 (1988).
3. Altshuler, B. L., Gefen, Y. & Imry, Y. Persistent differences between canonical and grand canonical averages in mesoscopic ensembles: Large paramagnetic orbital susceptibilities. *Phys. Rev. Lett.* **66,** 88–91 (1991).
4. von Oppen, F. & Riedel, E. K. Average persistent current in a mesoscopic ring. *Phys. Rev. Lett.* **66,** 84–87 (1991).
5. Abraham, M. & Berkovits, R. Persistent currents in an interacting 1D disordered ring: Manifestations of the Mott-Hubbard transition. *Phys. Rev. Lett.* **70,** 1509–1512 (1993).

6. Giamarchi, T. & Shastry, B. S. Persistent currents in a one-dimensional ring for a disordered Hubbard model. *Phys. Rev. B* **5,** 10915–10922 (1995).
7. Castelano, L. K., Hai, G.-Q., Partoens, B. & Peeters, F. M. Control of the persistent currents in two interacting quantum rings through the Coulomb interaction and interring tunneling. *Phys. Rev. B* **78,** 195315–195315-4 (2008).
8. Lévy, L. P., Dolan, G., Dunsmuir, J. & Bouchiat, H. Magnetization of mesoscopic copper rings: evidence for persistent currents. *Phys. Rev. Lett.* **64,** 2074–2077 (1990).
9. Chadrasekhar, V. *et al.* Magnetic response of a single, isolated gold loop. *Phys. Rev. Lett.* **67,** 3578–3581 (1991).
10. Timp, G. *et al.* Suppression of the Aharonov-Bohm effect in the quantized Hall regime. *Phys. Rev. B* **39,** 6227–6230 (1991).
11. Mailly, D., Chapelier, C. & Benoit, A. Experimental observation of persistent currents in GaAs-AlGaAs single loop. *Phys. Rev. Lett.* **70,** 2020–2024 (1993).
12. Liu, J. *et al.* Correlations between Aharonov-Bohm effects and one-dimensional subband populations in GaAs/$Al_xGa_{1-x}As$ rings. *Phys. Rev. B* **48,** 15148–15157 (1993).
13. Jariwala, E. M. Q., Mohanty, P., Ketchen, M. B. & Webb, R. A. Diamagnetic Persistent Current in Diffusive Normal-Metal Rings. *Phys. Rev. Lett.* **86,** 1594–1597 (2001).
14. Deblock, R., Bel, R., Reulet, B., Bouchiat, V. & Mailly, D. Diamagnetic Orbital Response of Mesoscopic Silver Rings. *Phys. Rev. Lett.* **89,** 206803-1–206803-4 (2002).
15. Viefers, S., Koskinen, P., Singha Deo, P. & Manninen, M. Quantum rings for beginners: energy spectra and persistent currents. *Physica E* **21,** 1–35 (2004).
16. Gupta, S., Sil, S. & Bhattacharyya, B. Half-filled Hubbard ring with alternating site potentials in a magnetic field. *Phys. Lett. A* **324,** 494–500 (2004).
17. Maiti, S. K., Chowdhury, J. & Karmakar, S. N. Strange behavior of persistent currents in small Hubbard rings. *Phys. Lett. A* **332,** 497–502 (2004).
18. Wei, B.-B., Gu, S.-J. & Lin, H.-Q. Persistent currents in the one-dimensional mesoscopic Hubbard ring. *J. Phys.: Condens. Matter* **20,** 395209–395205 (2008).
19. Maiti, S. K. Magnetic response in mesoscopic Hubbard rings: A mean field study. *Solid State Commun.* **150,** 2212–2217 (2010).
20. Das, A. N. & Sil, S. A study of the polaronic band width and the small-to-large-polaron transition in a many-polaron system. *J.* Phys.: Condens. Matter **5,** 8265–8276 (1993).
21. Takada, Y. & Chatterjee, A. Possibility of a metallic phase in the charge-density-wave–spin-density-wave crossover region in the one-dimensional Hubbard-Holstein model at half filling. *Phys. Rev. B* **67,** 081102-1–081102-4(R) (2003).
22. Koga, T., Nitta, J., Akazaki, T. & Takayanagi, H. Rashba Spin-Orbit Coupling Probed by the Weak Antilocalization Analysis in InAlAs/InGaAs/InAlAs Quantum Wells as a Function of Quantum Well Asymmetry. *Phys. Rev. Lett.* **89,** 046801-1–046801-4 (2002).
23. Premper, J., Trautmann, M., Henk, J. & Bruno, P. Spin-orbit splitting in an anisotropic two-dimensional electron gas. *Phys. Rev. B* **76,** 073310-1–073310-4 (2007).
24. Maiti, S. K., Dey, M., Sil, S., Chakrabarti, A. & Karmakar, S. N. Magneto-transport in a mesoscopic ring with Rashba and Dresselhaus spin-orbit interactions. *Europhys. Lett.* **95,** 57008-p1–57008-p6 (2011).
25. Bellucci, S. & Onorato, P. Crossover from the ballistic to the resonant tunneling transport for an ideal one-dimensional quantum ring with spin-orbit interaction. *Phys. Rev. B* **78,** 235312-1–235312-6 (2008).
26. Büttiker, M. Small normal-metal loop coupled to an electron reservoir. *Phys. Rev. B* **32,** 1846–1849 (1985).
27. Cabib, D. & Callen, E. Charge order and antiferromagnetic order in the Hubbard model with nearest-neighbor Coulomb interaction: Weak coupling. *Phys. Rev. B* **12,** 5249–5254 (1975).
28. Krishna, R. P. M., Mukhopadhyay, S. & Chatterjee, A. Nature of the self-trapping transition in a one-dimensional Holstein– Hubbard model. *Phys. Letts. A* **327,** 67–72 (2004).
29. Sankar, I. V., Mukhopadhyay, S. & Chatterjee, A. Localization–delocalization transition in a two-dimensional Holstein–Hubbard model. *Physica C* **480,** 55–60 (2012).
30. Sankar, I. V. & Ashok, Chatterjee Self-trapping phase diagram for the strongly correlated extended Holstein-Hubbard model in two-dimensions. *Eur. Phys. J. B* **87,** 154–163 (2014).

Author Contributions

A.C. gave the idea. S.S. and M.P.J. carried out the analytical calculation. M.P.J. and I.V.S. performed the numerical computation. M.P.J. wrote the manuscript. A.C. reviewed the manuscript.

Additional Information

Competing financial interests: The authors declare no competing financial interests.

How to cite this article: Monisha, P. J. *et al.* Persistent current in a correlated quantum ring with electron-phonon interaction in the presence of Rashba interaction and Aharonov-Bohm flux. *Sci. Rep.* **6**, 20056; doi: 10.1038/srep20056 (2016).

Solid State Communications 166 (2013) 83–86

Contents lists available at SciVerse ScienceDirect

Solid State Communications

journal homepage: www.elsevier.com/locate/ssc

Exact distribution function of a one-dimensional Fröhlich–Toyozawa–Luttinger liquid

Monisha P.J.[a], Soma Mukhopadhyay[b], Ashok Chatterjee[a,*]

[a] School of Physics, University of Hyderabad, Hyderabad 500046, India
[b] Department of Physics, Kashipur, Sangareddy Mandal, Hyderabad 502 285, India

ARTICLE INFO

Article history:
Received 12 March 2013
Accepted 8 April 2013
by P. Sheng
Available online 26 April 2013

Keywords:
D. Luttinger liquid
D. Electron–phonon interactions
D. Momentum distribution

ABSTRACT

An exact analytical expression for the electron momentum distribution function of a one-dimensional Frohlich–Toyozawa–Luttinger (FTL) liquid is obtained. It is explicitly shown that the residual Fermi surface disappears when the electron–electron interaction is increased. It is furthermore shown that the electron–phonon interactions also flatten the distribution function, the optical phonons having a larger effect than the acoustic phonons. However, it is found that the nature of the distribution function of an FTL liquid is qualitatively different from that of the corresponding Luttinger liquid above k_F.

1. Introduction

The one-dimensional (1D) many-electron problem has generated renewed interest after the discovery of quasi-one dimensional solids such as carbon nanotubes, quantum wires and other one-dimensional systems. Luttinger-liquid behaviour has indeed been observed in carbon nanotubes and other quasi-one dimensional conductors [1]. The usual Fermi liquid theory based on quasi-particle picture breaks down in these systems because of the Peierls instability and spin-charge separation. Tomonaga [2] first solved the one-dimensional interacting fermion problem exactly using bosonization and certain approximations regarding the commutator of the density operators. Later Luttinger [3] proposed a better model for this problem introducing some new states and this model is also exactly soluble. But the ground state of the Luttinger model is not bounded from below and Lieb and Mattis [4] rectified this error and again solved the problem exactly. Luther and Peschel [5] calculated the electron spectral density, susceptibility and pair propagation of an interacting electron system within the framework of the Luttinger model. Haldane [6] used the Luttinger model for the description of the general interacting Fermi gas in one dimension and called it a Luttinger liquid. Yoshioka and Ogata [7] obtained the asymptotically exact ground state for a 1D electrons and studied the transition from a Luttinger liquid behaviour to a non-Luttinger liquid behaviour as a function of some parameter which appears in the electron–electron interaction coefficient. Photoluminescence experiments from real quantum wires show the existence of sharp Fermi surface [8]. Hu and Das [9] suggested that virtual plasmon emissions that are present in systems would be inhibited in dirty systems leading to the restoration of the Fermi surface. Adding to the Luttinger Hamiltonian a parametrised term that accounts for the scattering of plasmons by the impurities existing in real systems Melgarejo and Vericat [10] showed that Fermi surface was indeed restored in the presence of the impurities. Wonneberger [11] have investigated the density and the electron distribution function of a Luttinger liquid confined to a harmonic trap. Wang et al. [12] presented accurate expressions for the effect of the long-range electron–electron interaction on momentum distribution, density of states, electron spectral function etc. of a 1D Luttinger liquid. Schönhammer [13] also obtained the momentum distribution function of electrons and the spectral function of a Luttinger liquid. Sen and Chakrabarti [14] employed density functional theory to establish the Luttinger liquid behaviour of a sodium-doped quasi-1D trans-polyacetylene chain. All these investigations, however, neglected the lattice excitations like phonons and their interactions with electrons, which actually play an important role in the transport phenomena and are relevant in polar semiconductors. Several investigations [15] were however made on 1D many-polaron problem using the quadratic electron dispersion. Baldea [16] was probably the first to study an interacting electron system including phonons using the linear electron dispersion. He considered the interaction of electrons with long-wavelength acoustic phonons within the framework of the Tomonaga model and calculated the momentum distribution function. Marino [17] considered a 1D acoustic many-polaron Hamiltonian within the framework of the Luttinger model and showed that for a certain range of the coupling constants the system would exhibit

* Corresponding author.Tel.: +91 40 2313 4356.
E-mail address: acsp@uohyd.ernet.in (A. Chatterjee).

0038-1098/$ - see front matter © 2013 Elsevier Ltd. All rights reserved.
http://dx.doi.org/10.1016/j.ssc.2013.04.007

a metallic behaviour since the spectrum contains gapless collective excitations of polaronic plasmons. Later, Martins [18] considered a problem with both electron–optical–phonon interaction and the electron–acoustic–phonon interaction but neglected the electron–electron interaction. Recently, Rao et al. [19] have exactly solved the 1D interacting electron problem within the framework of Luttinger model incorporating both the electron–optical–phonon interaction and the electron–acoustic–phonon interaction along with the electron–electron interaction to obtain the energy spectrum. This system can be referred to as the Fröhlich–Toyozawa–Luttinger (FTL) liquid. It seems that metallicity of the system depends crucially on the nature of the electron-electron interaction in one dimension. To our knowledge, however, no investigation has so far been made to obtain the momentum distribution function of electrons in a Luttinger liquid in the presence of the electron–phonon interactions. The purpose of the present paper is to make an attempt in this direction.

The FTL liquid can be modelled by the Hamiltonian

$$\begin{aligned} H = & -i\hbar v_F \int \psi^+(x)\sigma_3\partial_x\psi(x)dx \\ & + \frac{1}{2}\int \left[\dot{\phi}^2(x) + \hbar^2\omega_0^2\phi^2(x)\right]dx \\ & + \frac{1}{2}\int \left[\dot{\tilde{\phi}}^2(x) + \hbar^2 v_s^2(\partial_x\tilde{\phi}(x))^2\right]dx \\ & + g'\hbar\omega_0\int \psi^+(x)\psi(x)\phi(x)dx \\ & + \lambda'\hbar v_s\int \psi^+(x)\psi(x)\partial_x\tilde{\phi}(x)dx \\ & + \iint \psi^+(x)\psi^+(y)\frac{V|x-y|}{2}\psi(y)\psi(x)dxdy \end{aligned} \quad (1)$$

where the first term is the free electron Hamiltonian with σ_3 as the Pauli matrix, v_F the Fermi velocity, $\psi(x)$ is the two-component field operator given by $\psi = \begin{pmatrix} \psi_1(x) \\ \psi_2(x) \end{pmatrix}$, with $\psi_i(x) = 1/\sqrt{L}\sum_k e^{ikx}a_{ik}$, where $\psi_1(x)$ is the field operator for the electrons of type-1 with the energy dispersion, $\epsilon_k = kv_F$ and $\psi_2(x)$ represents the field operator for electrons of type-2 with $\epsilon_k = -kv_F$, L being the length of the system. The second term is the free optical phonon Hamiltonian with $\phi(x) = \sum_k (1/\sqrt{2L\hbar\omega_0})(b_k + b_{-k}^+)e^{ikx}$ as the optical phonon field operator and ω_0 the dispersionless optical phonon frequency. The third term is the free acoustic phonon Hamiltonian with $\tilde{\phi}(x) = \sum_k (1/\sqrt{2L\hbar v_s|k|})(\tilde{b}_k + \tilde{b}_{-k}^+)e^{ikx}$ as the acoustic phonon field operator and v_s the velocity of sound. The fourth term is the electron–optical–phonon interaction with $g' = \sqrt{8\pi\hbar g}\times(\hbar\omega_0/2m)^{1/4}$, g being the dimensionless electron–optical–phonon coupling constant [20] and the fifth term represents the electron–acoustic–phonon interaction with $\lambda' = -i\sqrt{8\pi\hbar v_s\lambda}$, λ being the dimensionless electron–acoustic–phonon coupling constant [20]. The last term denotes the electron–electron interaction where $V|x-y|$ represents the electron–electron interaction potential. It has been shown in [19] that by employing suitable transformations both the phonon fields can be eliminated from the problem to obtain an effective electronic Hamiltonian given by

$$\begin{aligned} H = & \sum_{k>0} D_+(k)[\rho_1(k)\rho_1(-k) + \rho_2(-k)\rho_2(k)] \\ & + \sum_{all\ k} D_-(k)\rho_1(k)\rho_2(-k) \end{aligned} \quad (2)$$

where

$$\begin{aligned} D_\pm(k) = & \frac{1}{2L}\Big[\pm\{2g'^2(v_F^2k^2 \mp \omega_0^2)/\omega_0^2 + (2\pi\hbar v_F \pm 2\pi\hbar v_F)\} \\ & \pm 2\lambda'^2(v_F^2 \mp v_s^2)/v_s^2 + V_{1k}\Big] \end{aligned} \quad (3)$$

$\rho(q)$ is the Fourier transform of $\rho(x) = \psi_i^+(x)\psi_i(x)$, satisfying: $[\rho_i(-k), \rho_j(k')] = (-1)^{i+1}\delta_{ij}\delta_{kk'}\ (kL/2\pi)$ (with $k,k'>0$, $i,j=1,2$), and $V_{1k} = V_k + V_{-k}$, where V_k is the Fourier transform of $V|x-y|$ and the free electron Hamiltonian has been replaced by $(2\pi v_F/L)\sum_{k>0}[\rho_1(k)\rho_1(-k) + \rho_2(-k)\rho_2(k)]$ as usual. Hamiltonian (2) can be diagonalized by a transformation with the generator $S = (2\pi i/L)\sum_{all\ k}[\phi(k)/k]\rho_1(k)\rho_2(-k)$, where $\phi(k) = (1/2)\ tanh^{-1}\{-D_2(k)/D_1(k)\}$, k being real and even. The energy spectrum is given by

$$\begin{aligned} \epsilon(k) = & \hbar v_F|k|\left[1 - \frac{g'^2 + \lambda'^2}{\pi\hbar v_F} + \frac{V_{1k}}{2\pi\hbar v_F}\right]^{1/2} \\ & \times\left[1 + \frac{g'^2k^2v_F}{\pi\hbar\omega_0^2} + \frac{\lambda'^2v_F}{\pi\hbar v_s^2}\right]^{1/2} \end{aligned} \quad (4)$$

which is valid only if: $[g_c'^2 + \lambda_c'^2] < [\pi\hbar v_F + V_{1k}/2]$. To plot the the energy spectrum $\epsilon(k)$ we need an explicit form for V_{1k}. The form: $1/k^2$ does not give proper description of the excitation spectrum. We choose following Wang et al. [12]: $V_{1k} = 4\pi\mu e^2\ \ln(1 + k_F/k)$, where μ is the electron–electron coupling constant. In Fig. 1 we plot the dimensionless excitation energy $\epsilon(k)$ (in units of Rydberg) for various interactions. We define the effective eletron–optical–phonon coupling constant as $\alpha_{op} = (4\pi g(\omega_0')^{3/2}/L')^{1/2}$ and the effective electron–acoustic–phonon coupling constant as $\alpha_{ac} = (16\pi\lambda(v_s')^2/L')^{1/2}$, where the primed quantities are dimensionless in Rydberg units. As expected, the electron–electron interaction increases the energy, while the polaron formation decreases it.

In the present paper we obtain for the first time the electron distribution function, $\bar{n}_k$ for the FTL liquid. Since $\bar{n}_k$ is an even function of k, we need to consider only $k>0$ and also it will suffice to calculate $\bar{n}_k$ only for particle type-1. It may however be noted that our calculation also includes the Coulomb interaction between the two types of electrons. We write: $\bar{n}_k = \langle a_{1k}^+ a_{1k}\rangle = \langle c_k^+ c_k\rangle$, where $c_k^+(c_k)$ creates (destroys) a type-1 particle for $k>0$ with positive energy. c_k, c_k^+ are related to ψ 's through

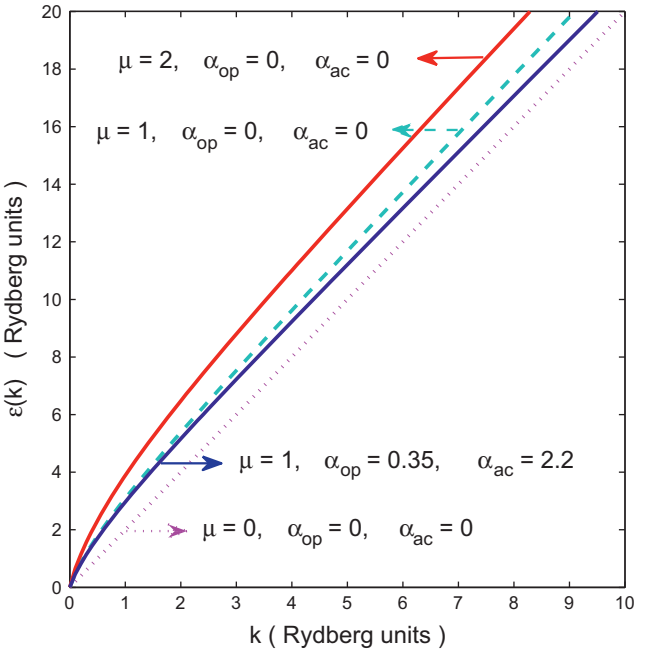

Fig. 1. (Color online) Energy spectrum of a Luttinger liquid for various interactions and interaction strengths.

Fourier transformations and thus we have

$$\bar{n}_k = \frac{1}{L}\iint_0^L I(x,x')e^{ik(x-x')}dxdx', \tag{5}$$

where $I(x,x') = \langle \Psi|\psi_1^+(x)\psi_1(x')|\Psi\rangle$, $|\Psi\rangle$ being the GS of the interacting system. Using the transformations: $e^{iS}He^{-iS} = \tilde{H}$, $e^{iS}|\Psi\rangle = |\Psi_0\rangle$, the Hamiltonian becomes diagonal and we get: $I(x,x') = \langle \Psi_0|e^{iS}\psi_1^+(x)e^{-iS}e^{iS}\psi_1(x')e^{-iS}|\Psi_0\rangle$, where $|\Psi_0\rangle$ is the new GS of the non-interacting system. To calculate $I(x,x')$ we introduce as usual the operator: $f_\sigma(x) = e^{i\sigma S}\psi_1(x)e^{-i\sigma S}$, so that we can write: $f_\sigma(x) = W_\sigma(x)R_\sigma(x)\psi_1(x)$, where $W_\sigma(x) = \exp\{\sum_{k>0}(2\pi/kL)\eta_1(k,x)(cosh\sigma\phi(k) - 1)\}$, $R_\sigma(x) = \exp\{\sum_{k>0}(2\pi/kL)\eta_2(k,x)sinh\sigma\phi(k)\}$, $\psi_1(x) = c(x)\times\exp\{\sum_{k>0}(2\pi/kL)\eta_1(k,x)\}$, $\eta_i(k,x) = [\rho_i(-k)e^{ikx} - \rho_i(k)e^{-ikx}]$. Thus we have: $I(x,x') = \langle \Psi_0|\psi_1^+(x)R_1^+(x)W_1^+(x)W_1(x')R_1(x')\psi_1(x')|\Psi_0\rangle$, where $R(x)$ and $W(x)$ are unitary and commute with each other. Since there are two types of electrons in our system, the GS is a product state, $|\Psi_0\rangle = |\Psi_1\rangle|\Psi_2\rangle$ and consequently, we have: $I(x,x') = I_1(x,x')I_2(x,x')$, where: $I_1(x,x') = \langle \Psi_1\left|\psi_1^+(x)W^{-1}(x)W(x')\psi_1(x')\right|\Psi_1\rangle$, and $I_2(x,x') = \langle \Psi_2|R^{-1}(x)R(x')|\Psi_2\rangle$. Using the Becker-Hausdroff identity and the properties of $\rho(k)$, one can show that: $I(x,x') = \prod_{i=0}^3 Z_i(x,x')$, where $Z_j(x,x') = e^{\sum_{k>0}(2\pi/kL)\varphi_j(k)\xi_j(k)}$, $(j = 0,1,2)$ with, $\varphi_1(k) = \varphi_0^2 = (cosh\phi(k) - 1)^2$, $\varphi_2(k) = sinh^2\phi(k)$, $\xi_0(k) = \xi_1(k) = (e^{ik(x-x')} - 1) = \xi_2(-k)$, and $Z_3(x,x') = \langle \Psi_1\left|\psi_1^+(x)\psi_1(x')\right|\Psi_1\rangle = (1/L)\sum_{p\le k_F} e^{ip(x'-x)}$. Then we obtain: $\bar{n}_k = \frac{1}{L}\sum_{p\le k_F}\int_{-L}^{L} dr\, e^{i(k-p)r}\, e^{-Q(r)}$, where $e^{-Q(r)} = \prod_{i=0}^2 Z_i(x,x')$, with $Q(r) = \int_0^\infty 2\varphi_2(k)((1-coskr)/k)dk$, $r = (x-x')$. Finally, in the limit $L\to\infty$, we get

$$\bar{n}_k = \int_{(k-k_F)}^{0} F(k)\,dk + d \tag{6}$$

where

$$F(k) = \frac{1}{2\pi}\int_{-\infty}^{\infty} dx\, e^{-Q(x)}\, e^{ikx},$$

$$Q(x) = \int_0^\infty dk\, \frac{1-\cos(kx)}{k}|u(k)|^2$$

$$\left|u(k)\right|^2 = \frac{D_+(k) - \sqrt{D_+^2(k) - D_-^2(k)}}{\sqrt{D_+^2(k) - D_-^2(k)}} \tag{7}$$

and "d" is a constant. It can be easily seen analytically that for $\mu = \alpha_{op} = \alpha_{ac} = 0$, $\bar{n}_k$ becomes the usual Fermi–Dirac distribution function with a sharp Fermi surface. Furthermore, if we include only V_{1k}, and put $\alpha_{op} = \alpha_{ac} = 0$, we get back the analytical result of Lieb and Mattis. It was also observed by Lieb and Mattis that if the Coulomb interaction were very small, there would still exist a residual Fermi surface at $k = k_F$, while a strong Coulomb interaction would destroy the Fermi surface completely. Here we wish to study how $\bar{n}_k$ is particularly modified by the electron–phonon interactions. Using the expressions for $|u(k)|^2, Q(r)$ and $F(k)$ we can obtain the exact momentum distribution function $\bar{n}_k$ numerically. Again we choose for V_{1k} the prescription of Wang et al. [12]. In Fig. 2 we plot $\bar{n}_k$for several values of μ with α_{op}=α_{ac}=0. For $\mu = 0$ the usual Fermi–Dirac distribution with a sharp Fermi surface is clearly visible. Wang et al. [12] have studied the behaviour of $(0.5-\bar{n}_k)$ vs. $(k-k_F)$ for $k\ge k_F$. To compare our results qualitatively with theirs we plot $(0.5-\bar{n}_k)$ in Fig. 3. Our results clearly show the same behaviour as those of Wang et al.

In Fig. 4 we plot the derivative of the momentum distribution function i. e., $[-(d\bar{n}_k/dk)]$ as a function of k. It is evident from the behaviour of $[-(d\bar{n}_k/dk)]$ that for $\mu = 1$, the distribution function has a singularity at the Fermi surface and thus there still exists a residual Fermi surface for weak Coulomb correlations. However for $\mu = 3$, the residual Fermi surface disappears completely. This result is in agreement with the analytical observation of Lieb and Mattis.

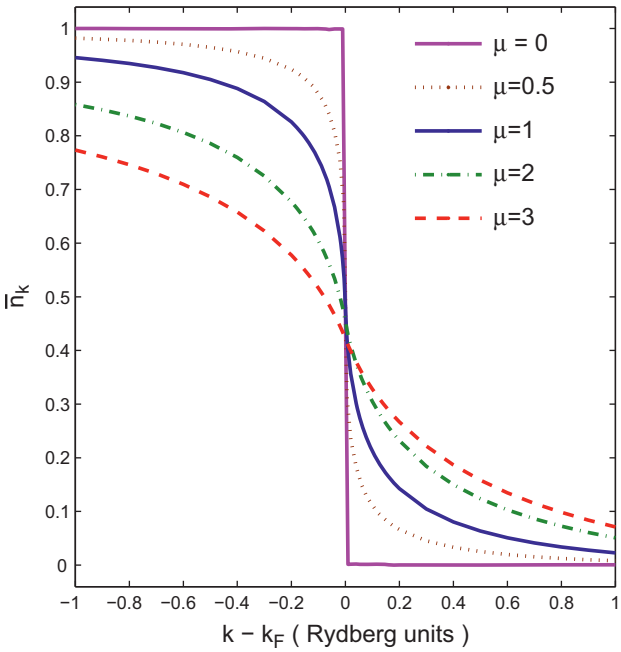

Fig. 2. (Color online) Momentum distribution function of electrons in a Luttinger liquid for various values of the electron–electron interaction coefficient.

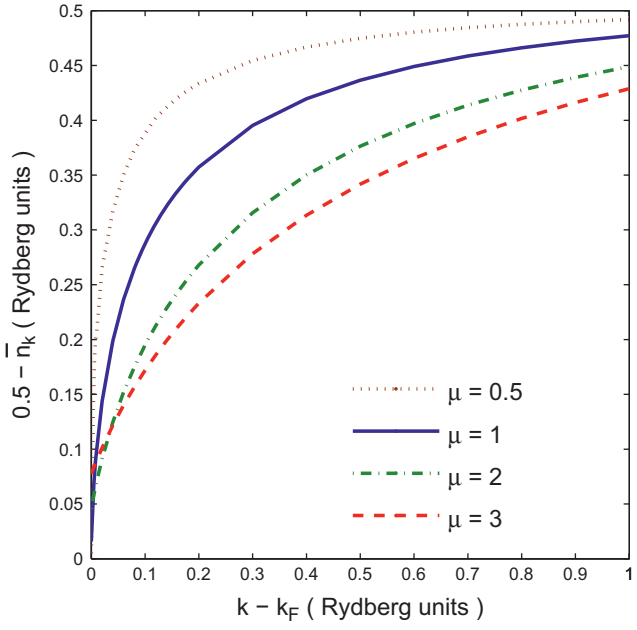

Fig. 3. (Color online) Variation of $(0.5-\bar{n}_k)$ as a function of $(k-k_F)$.

In Fig. 5 we show the behaviour of the momentum distribution of the electrons in an FTL liquid i. e., when both the acoustic and optical electron–phonon interactions are present in the Luttinger liquid. For the sake of comparison, we plot the distribution function for the electrons for four cases, namely, for $\mu = 1$, $\alpha_{ac} = 0$, $\alpha_{op} = 0$; $\mu = 2$, $\alpha_{ac} = 0$, $\alpha_{op} = 0$; $\mu = 1$, $\alpha_{ac} = 2.2$, $\alpha_{op} = 0$, and $\mu = 1$, $\alpha_{ac} = 2.2$, $\alpha_{op} = 0.35$. It is clear that like electron–electron interaction, electron–phonon interactions also flatten the distribution function, the optical phonons, of course, having a larger effect than the acoustic phonons. It is also evident that the

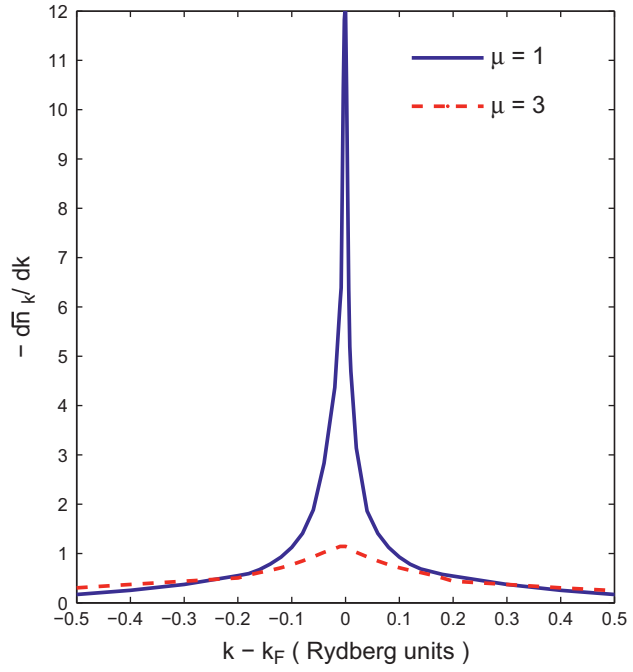

Fig. 4. (Color online) Variation of $[-d\bar{n}_k/dk]$ as a function of $(k-k_F)$.

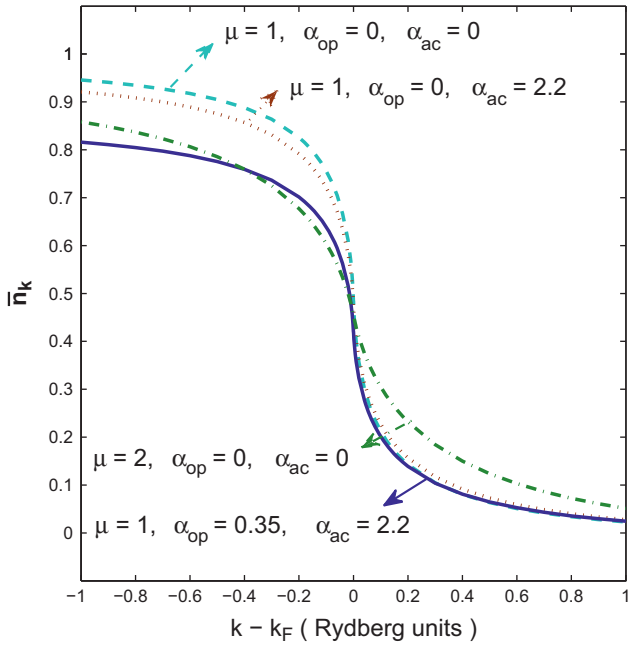

Fig. 5. (Color online) Distribution function for the FTL liquid.

nature of the residual Fermi surface of a FTL liquid is more or less the same as that of the corresponding Luttinger liquid.

It is important to note that in the presence of electron-phonon interactions, the distribution function has a rather long tail which remains more or less unaffected by the coupling constants, particularly for low-lying excitations. Thus the behaviour of the distribution function of an FTL liquid is qualitatively different from that of a Luttinger liquid above k_F.

In conclusion, we have studied the momentum distribution function for the electrons in a Luttinger liquid in the presence of both electron–acoustic–phonon and electron–optical–phonon interactions. Such a system can be referred to as an FTL liquid. We have shown that in the case of a Luttinger liqud strong Coulomb interactions destroy the residual Fermi surface completely. We find that in the case of an FTL liquid, the residual Fermi surface is also destroyed by the electron–phonon interactions. Furthermore, the optical phonon interaction is observed to have a larger effect on the distribution function than the acoustic phonon interaction. Interestingly enough, the distribution function has a very long tail above k_F in an FTL liquid, which is apparently unaffected by the strengths of the electron–phonon interactions. Thus the momentum distribution function an FTL liquid shows a qualitatively different behaviour from that of a Luttinger liquid above k_F particularly for low-lying excitations. This will have important consequences on the thermodynamic and other physical quantities that depend on averaging.

References

[1] B. Dardel, D. Malterre, M. Grioni, P. Weibel, Y. Baer, J. Voit, D. Jerome, Europhys. Lett. 24 (1993) 687;
M. Bockrath, D.H. Cobden, A.G.L.u.J. Rinzler, R.E. Smalley, L. Balents, P. L. McEuen, Nature 397 (1999) 598;
S. Sen, S. Chakrabarti, Physica E 40 (2008) 2736.
[2] S. Tomonaga, Prog. Theory Phys. (Kyoto) 5 (1950) 544.
[3] J.M. Luttinger, J. Math. Phys. 4 (1963) 1154.
[4] D.C. Mattis, E.H. Lieb, J. Math. Phys. 6 (1965) 304.
[5] A. Luther, I. Peschel, Phys. Rev. B 9 (1974) 2911.
[6] F.D.M. Haldane, J. Phys. C 14 (1981) 2585.
[7] D. Yoshioka, M. Ogata, J. Phys. Soc. Jpn. 9 (1993) 2990.
[8] J.M. Calleja, A.R. Goñi, B.S. Dennis, J.S. Weiner, A. Pinczuk, S. Schmit-Rink, L. N. Pfeiffer, K.W. West, Solid State Commun. 79 (1991) 911.
[9] B.Y. Hu, S. Das Sarma, Phys. Rev. Lett. 68 (1992) 1750;
ibid, Phys. Rev B 48 (1993) 5469.
[10] A.A. Melgarejo, F. Vericat, Physica E 8 (2000) 57.
[11] W. Wonneberger, Phys. Rev. A 63 (2001) 063607.
[12] D.W. Wang, A.J. Millis, S. Das Sarma, Phys. Rev. B 64 (2001) 193304.
[13] K. Schönhammer, J. Phys. Condens. Matter 14 (2002) 12783.
[14] S. Sen, S. chakrabarti, Physica E 40 (2008) 2736.
[15] G. Whitfield, P.B. Shaw, Phys. Rev. B 14 (1976) 3346;
F.M. Peeters, J.T. Devreese, Phys. Rev. B 36 (1987) 4442;
T.K. Mitra, A. Chatterjee, S. Mukhopadhyay, Phys. Rep 153 (1987) 91;
J. Voit, H.J. Schulz, Phys. Rev. B 36 (1987) 968.
[16] I. Baldea, Phys. Sripta 31 (1985) 606.
[17] E.C. Marino, Phys. Rev. Lett. 55 (1985) 2991.
[18] M.J. Martins, J. Phys. C 20 (1987).
[19] C.S. Rao, P.M. Krishna, S. Mukhopadhyay, A. Chatterjee, J. Phys.: Condens. Matter 13 (2001) L919.
[20] M.H. Degani, O. Hipolito, R. Lobo, G.A. Farias, J. Phys. C 19 (1986) 2919.

RSC Advances

PAPER

View Article Online
View Journal | View Issue

Cite this: *RSC Adv.*, 2014, **4**, 59890

A possible mechanism for the emergence of an additional band gap due to a Ti–O–C bond in the TiO_2–graphene hybrid system for enhanced photodegradation of methylene blue under visible light†

Sima Umrao,‡[a] Shiju Abraham,‡[abc] Frank Theil,[bc] Shobhit Pandey,[d] Valerian Ciobota,[b] P. K. Shukla,[e] Caroline J. Rupp,[f] Sudip Chakraborty,[g] Rajeev Ahuja,[g] Jürgen Popp,[bc] Benjamin Dietzek*[bc] and Anchal Srivastava*[a]

Received 16th September 2014
Accepted 22nd October 2014

DOI: 10.1039/c4ra10572a

www.rsc.org/advances

Here we report the experimental and theoretical study of two TiO_2–graphene oxide (TG) and TiO_2–reduced graphene oxide (TR) composites synthesized by a facile and ecological route, for enhanced visible light (~470 nm) photocatalytic degradation of Methylene Blue (MB) (99% efficiency), with high rate constant values (1800% over bare TiO_2). TG couples TiO_2 nanopowder with Graphene Oxide (GO) while TR couples it with reduced graphene oxide (RGO). The present study, unlike previous reports, discusses never-before-reported double absorption edges obtained for both TG (3.51 eV and 2.51 eV) and TR (3.42 eV and 2.39 eV) composites, which represents the reason behind feasible visible light (2.56 eV) induced photocatalysis. TiO_2 domains in the composites dominate the higher band edge, while GO/RGO domains explain the lower band edge. Formation of Ti–O–C bonds in both TG and TR drives the shifting upwards of the valence band edge and reduction in band gap. Further, these bonds provide a conductive pathway for charge carriers from TiO_2 nanopowder to the degraded species *via* the GO/RGO matrix, resulting in decreased charge carrier recombination in TiO_2 and enhanced efficiency. To attest that the developed theory is correct, density function theory (DFT) calculations were performed. DFT obtained energetics and electronic structures support experimental findings by demonstrating the role of the Ti–O–C bond, which results in double band edge phenomenon in composites. Finally, the mechanism behind MB degradation is discussed comprehensively and the effect of the weight percent of GO/RGO in the composite on the rate constant and photodegradation efficiency has been studied experimentally and explained by developing analytical equations.

Introduction

Hazardous waste management of organic dyes like Methylene Blue (MB), rhodamine B and crystal violet through photo-degradation has remained a never-diminishing area of research.[1–3] Heterogeneous photocatalysts have a commendable efficiency for degrading organic pollutants, and along this line, TiO_2 is one of the most exhaustively studied materials owing to its excellent photo-functional properties, strong oxidizing power, absence of toxicity, long term photo and chemical stability, high refractive index and low production cost.[1,4–7] Comprehensive reports showing photodegradation of MB *via* the exclusive use of TiO_2 are present, but it is well understood that TiO_2 alone fails to achieve high photocatalytic efficiency, because of its compromised quantum efficiency, due to the relatively fast recombination of electrons and holes, which adversely affects the surface redox reaction.[8] Furthermore, TiO_2 is activated only by ultraviolet light (<385 nm), as its band gap

[a]*Department of Physics, Banaras Hindu University, Varanasi, 221005, India. E-mail: anchalbhu@gmail.com*

[b]*Institute of Physical Chemistry and Abbe Center of Photonics, Friedrich-Schiller-University, Helmholtzweg 4, D-07743, Jena, Germany. E-mail: benjamin.dietzek@ipht-jena.de*

[c]*Leibniz-Institute of Photonic Technology Jena (IPHT), Albert-Einstein-Str. 9, D-07745, Jena, Germany*

[d]*Department of Metallurgical Engineering, Indian Institute of Technology-B. H. U., Varanasi, 221005, India*

[e]*I.T.S. Engineering College, Greater Noida, 201308, India*

[f]*Departamento de Física, Universidade Federal de Santa Maria, 97105-900, Santa Maria, RS, Brazil*

[g]*Condensed Matter Theory Group, Department of Physics and Astronomy, Uppsala University, Box-516, Sweden*

† Electronic supplementary information (ESI) available: The supporting file includes the Raman and FTIR spectra and the XRD diffraction patterns of as-synthesized GO, RGO, TiO_2, and composites as well as PL emission spectra with explanations. See DOI: 10.1039/c4ra10572a

‡ These authors contributed equally to this work.

lies in the UV light energy range, which constitutes only about 3–5% of the solar spectrum.[9] Practically, this factor strongly limits the use of solar spectrum light as a light source for photocatalysis purposes. This limitation can be circumvented by tailoring the absorption capacity of TiO_2 in the visible range, which constitutes about 50% of the energy of the whole solar spectrum. The wide band gap of a TiO_2 photocatalyst can be modified to extend its photoresponse into the visible region for degradation of organic dyes in several ways, including coupling with noble metals,[10–12] quantum dots,[13,14] non-metal doped semiconductors,[6] carbon nanotubes (CNTs)[15,16] and fullerenes.[17] Further, reports attest that such composite formations,[12,18–20] especially with carbon materials can inhibit the electron–hole pair recombination, thereby enhancing the photocatalytic performance of TiO_2.[15,21–23]

Among the various carbon nanostructures, graphene and its derivatives, GO and RGO have captured much attention, owing to their modified optoelectronic properties, high surface area, superior electron mobility, lower cost and easy chemical modification to change surface properties, which is favorable for composites fabrication.[24–27] Therefore, the combination of TiO_2 and graphene is very promising as it simultaneously possesses excellent absorptivity, transparency, conductivity and permeability, which could assist effective photodegradation of pollutants.

There are a number of reports showing the enhanced photocatalytic activity of composites of TiO_2 nanoparticles with graphene for the degradation of organic molecules and the photocatalytic splitting of water under UV light.[22,28–38] The enhanced photocatalytic activity was attributed to the synergetic effect between graphene and TiO_2 nanoparticles, because graphene acts as an excellent electron acceptor and transporter, and the Ti–O–C bond opens up an easy path for charge transfer which remarkably decreases the recombination of electron–hole pairs.[3] Although claiming good efficiency, many of these reports are based on usage of un-ecological UV light and suffer from slow kinetics (k value).[28–30]

Realizing the importance of efficient visible light photodegradation, there are a few reports which show the enhanced photocatalytic activity of TiO_2–GO/RGO composites under visible light.[39–42] The results and application aspects are well understood in numerous articles for TiO_2–graphene based composites; some of which attest the formation of Ti–O–C bonds in such composites,[43] but there are none which provide a clear explanation for the mechanism behind the enhanced photocatalytic effect. To do a meticulous study of the reasons behind the successful visible light degradation of MB using such composites, we report two chemically bonded TiO_2 nanopowder composites, of which one couples TiO_2 nanopowder with GO and other with RGO using a facile synthesis route. Uniquely, using FT-IR analysis, the existence of a Ti–O–C bond between TiO_2 and GO/RGO is confirmed. Because of such bond formations, never-before-discussed double absorption edges are obtained for both TG (3.51 eV and 2.51 eV) and TR (3.42 eV and 2.39 eV) composites. The TiO_2 domains dominate the higher end of range, while the GO/RGO domains explain the lower end of range. Again the effect of a Ti–O–C bond represents the reason behind the depression of the higher value compared to that of bare TiO_2 (3.68 eV) and the increase of lower end of range compared to pure GO/RGO (2.10 eV/1.83 eV). Two such absorption edges were earlier reported in the graphene-h-BN system.[44] The existence of such double band edges in our composites is the novel reason behind the possibility of photocatalytic degradation upon irradiation with 470 nm visible light.

To provide support for our developed understanding, theoretical modeling of optical spectra based on density functional theory (DFT) and utilizing the projector augmented wave method (PAW) implemented in the VASP (Vienna *ab initio* Simulation Package) program for the theoretical prediction of the energetics and the electronic structure of the individual systems GO, RGO and TiO_2 along with the composites of GO and RGO with TiO_2 was performed. A comparable trend has been found between the experimentally and theoretically obtained optical responses, attesting to multiple absorption edges being present in the composites, with a similar trend in the band edge range when compared with bare TiO_2 and GO/RGO, while as expected only a single absorption edge is obtained for TiO_2, GO and RGO separately. Furthermore, the DFT obtained structure confirms the presence of Ti–O–C bonds in exact correspondence to the data obtained experimentally *via* FT-IR, whose formation due to the bonding between the free electrons on the surface of TiO_2 with some unpaired π-electrons, shifts upward the valence band edge and reduces the band gap. Simultaneously, in harmony with the experimental results, better photo-efficiency in the case of TR than in the case of TG is confirmed *via* theoretical modelling, owing to better bond formation in case of modelled TR, compared to TG. This is further supported by a greater band edge shift and an even greater reduction in band gap as expected.

For a diligent study, the effect of the ratio of the two components, weight percentages of GO/RGO in both TG and TR composites have been studied. A photocatalytic investigation of the degradation of MB using bare TiO_2, TG composites (both 5 : 1 wt% (TG1) and 2 : 1 wt% (TG2)) and TR composites (both 5 : 1 wt% (TR1)and 2 : 1 wt% (TR2)) has been accomplished in this work. The composites under normal visible light (470 nm) show astonishing photodegradation efficiency in comparison to bare TiO_2 owing to the role of Ti–O–C bond formation as discussed above. Furthermore, the composites are significant for their high rate constants. The mechanism behind MB degradation is discussed comprehensively and an analytical model to explain the effect of the ratio of concentration of GO/RGO in the composites on the rate constants has been developed. Furthermore, our TR2 composite synthesized by the proposed fast, facile, ecological and economical route, achieves an astonishingly high MB degradation efficiency of 99% with an 1800% increase in the photocatalytic degradation rate constant value compared to bare TiO_2.

Experimental section

Materials

Titanium(IV) butoxide, ($C_{16}H_{36}O_4Ti$, Sigma-Aldrich Chemicals Pvt Limited, Germany, purity ≥97%), graphite flakes (1–2 mm,

NGS Naturgraphit GmbH, Germany), potassium permanganate ($KMnO_4$, ≥99.0%, Fluka), ethanol (CH_3CH_2OH, ≥98% Sigma-Aldrich, Germany), ammonia solution, H_2SO_4, H_3PO_4, H_2O_2 and H_6N_2O were used.

Preparation of graphene oxide

GO was synthesized *via* an improved Hummers method.[45] Briefly, a 9 : 1 ratio of concentrated H_2SO_4/H_3PO_4 was added to 2 g of graphite flakes and 12 g (76 mM) of $KMnO_4$. The mixture was isothermally stirred for 12 h at 50 °C. The mixture was cooled to room temperature, and subsequently the reaction was quenched by adding approximately 270 mL of ice with 2 mL of 30% H_2O_2. The obtained mixture was then filtered and centrifuged. The solid material was washed with distilled water, 30% HCl and ethanol until a pH ≈ 7 was attained and then dried at 80 °C in an oven. Finally the desired GO dispersion was procured by continuous ultra-sonication for an hour.

Preparation of reduced graphene oxide

RGO was synthesized by reducing the above as-obtained GO with the aid of hydrazine hydrate solution (H_6N_2O) as the reducing agent.[46] Briefly, a 1000 mL (0.25 mg mL^{-1}) solution of as-synthesized GO in double-distilled (DD) water was kept under ultra-sonication for an hour, to obtain a light-yellowish homogeneous solution. 3.92 mL of ammonia solution (25%) was added to the above-obtained GO solution to achieve a pH ≈ 10. Thereafter, 700 μL of H_6N_2O was added and the solution was kept under ultra-sonication at a temperature of 80 °C for three hours, followed by magnetic stirring at 95 °C for 2 h. In the final step, the yellowish GO solution turned black upon reduction. The solution was then filtered, followed by washing with DD water and drying at 80 °C.

Preparation of TiO_2 nanopowder

TiO_2 nanopowder was prepared using a sol–gel method[13] employed with slight modifications. Typically, the solution A was prepared by dissolving 17 mL of $Ti(OBu)_4$ (50 mM) in 40 mL of absolute ethanol. Solution B was obtained by mixing 3 mL of concentrated HNO_3, 35 mL of absolute ethanol and 15 mL of deionized water. The solution B was mildly stirred and subsequently added dropwise to solution A over a time span of 25 minutes. The obtained mixture was further stirred for 90 minutes and left untouched for 30 h. This resulted in light white TiO_2 gels, which were dried at 200 °C for 6 h. Ultimately the obtained pale yellow nanopowder was used for subsequent characterizations and photocatalytic measurements.

Preparation of composites

For the preparation of composites, 200 mg of TiO_2 nanopowder was well dispersed in 200 mL of ethanol (96%) by sonication for an hour at ~50 °C. Similarly, GO as well as RGO dispersions (1 mg mL^{-1}) were prepared in ethanol (96%). The four combinations of composite materials were prepared by mixing 50 mL of TiO_2 dispersion (1 mg mL^{-1}) with 10 and 25 mL dispersions (1 mg mL^{-1}) of GO as well as RGO. The composite solutions were sonicated for an hour at ~70 °C and then dried at 45 °C. The solid materials thus obtained are abbreviated as TG1 (TiO_2 : GO = 5 : 1 wt%); TG2 (TiO_2 : GO = 2 : 1 wt%); TR1 (TiO_2 : RGO = 5 : 1 wt%) and TR2 (TiO_2 : RGO = 2 : 1 wt%).

Characterization

The morphologies of the as-synthesized samples were investigated using scanning electron microscopy (SEM) on a JEOL – Model JSM6300F-SEM instrument and transmission electron microscopy (TEM) using a FEI – Tecnai-20 electron microscope. The crystalline structures of GO, RGO, TiO_2, TG and TR composites were characterized by X-ray diffraction (XRD) (diffractometer system-XPERT-PRO) using Cu-$K_{\alpha 1}$ radiation (λ = 1.5405980 Å). For Brunauer–Emmett–Teller (BET) measurements, nitrogen adsorption–desorption isotherms were measured at 77 K using the Autosorb 1-C instrument from Quantachrome Instrument Corp., USA. Raman measurements were performed on a micro-Raman setup (HR LabRam inverse system, JobinYvon Horiba). The 532 nm line from a frequency doubled Nd:YAG laser (Coherent Compass) was used as the excitation wavelength. Fourier transform infrared spectra (FTIR) of the samples were recorded using a Perkin Elmer Spectrum 65 FT-IR spectrometer. Photoluminescence (PL) spectra were measured on a fluorescence spectrophotometer (PerkinElmer) with an excitation wavelength of 300 nm. The EIS measurements were carried out on a PARSTAT 2273 potentiostat/galvanostat (Advanced Measurement Technology Inc., NPL, Delhi) by using three-electrode cells. The dye degradation level was measured using a UV/Vis/NIR Spectrophotometer (JASCO-V-670, with PMT and PbS detectors).

Computational methodology

The electronic structure calculations of the model systems were performed based on density functional theory.[47,48] The projector augmented wave method (PAW) implemented VASP (Vienna *ab initio* Simulation Package) program[49,50] was used throughout for the theoretical prediction of the energetics and the electronic structure. The Perdew–Burke–Ernzerhof (PBE) type of generalized gradient approximation (GGA) was employed as the exchange–correlation functional[51,52] for the structural optimization of the structures. It is worth mentioning here that the generalized gradient approximation (GGA) tends to underestimate the binding energies, while local density approximation (LDA) tends to overestimate the binding energies. The Brillouin zone was sampled by a 3 × 3 × 1 *k*-mesh using the Monkhorst-Pack scheme and the optimal energy cutoff of 400 eV was used for the individual systems of the GO, RGO and TiO_2 surfaces, while for the composite systems the gamma point was used. For the surface calculations, we used a vacuum of 15 Å in the *z* direction in order to avoid quenching of the wave functions for all the isolated systems, and for the nanocomposites the vacuum was 30 Å. A denser *k*-mesh was used to produce the density of states, and the smearing width was 0.05 eV. All the structures were optimized until the Hellman–Feynman forces acting on them reduced to 0.005 eV $Å^{-1}$. For the electronic relaxation, the conjugate gradient algorithm was used.

Photocatalytic activity test

All four composites were separately dispersed in absolute ethanol (1 mg mL^{-1}) by ultra-sonication. 10 ppm MB solution was prepared by dissolving 10 mg of MB powder in 1000 mL of distilled water. For the optimization of the individual composites, the catalytic measurements were carried out with three different proportions of MB and catalyst (CAT). The combinations of catalyst (TiO_2), co-catalyst (GO or RGO) and distilled water (DW) used in the work are as listed below:

P1: (MB solution in DW (10 mg/1000 mL) = 2800 μL) + (CAT solution in ethanol (1mg mL^{-1}) = 87.5 μL) + (DW = 612.5 μL).

P2: (MB solution in DW (10 mg/1000 mL) = 2800 μL) + (CAT solution in ethanol (1mg mL^{-1}) = 175 μL) + (DW = 525 μL).

P3: (MB solution in DW (10 mg/1000 mL) = 2800 μL) + (CAT solution in ethanol (1mg mL^{-1}) = 350 μL) + (DW = 350 μL).

All three solutions were then irradiated (central wavelength at 470 nm) under constant stirring using LED torches (power ~0.1 mW mm^{-2}, Innotas Elektonik, GmbH Germany). UV-Vis absorption spectroscopy was used to study the variation in the absorption maximum of MB. Every hour the absorption measurement was taken, and the catalytic degradation was continued for five hours.

Results and discussion

Structure and morphology of TiO_2 and TiO_2–GO/RGO composites

We systematically investigated the quantitative effect of GO/RGO on photocatalytic activity and band gap modification of the as-synthesized composites. First, all samples were characterized both structurally and spectroscopically. The XRD patterns of GO, RGO, TiO_2, TG, and TR are shown in Fig. S1 (see ESI).† In the diffraction pattern of GO, the peak around 2θ = 10.62° corresponds to the (001) reflection (interlayer spacing of 0.83 nm), while the other peak at ~24° having lower intensity compared to the previous peak is due to short-range order in the stacked graphene-like sheets with spacing of around 0.36 nm. The diffraction peak of RGO at 24.04° corresponds to the (002) reflection, with a *d*-spacing of 0.37 nm. The XRD pattern of TiO_2 nanopowder shows six distinct diffraction peaks at 20.78°, 25.1°, 30.39°, 37.94°, 48.21°, and 54.15°. These can be indexed respectively as the (102), (101), (101), (004), (200), and (105) planes of TiO_2 (JCPDS no. 21-1272) having a fcc crystal structure. Among the above mentioned peaks, the small obtuse peak around 30.39° corresponds to the rutile (R) phase, while the other peaks denote the anatase (A) phase of TiO_2. The diffraction peak at around 2θ = 20.78° corresponds to the (102) reflection for the Ti_4O_7 phase of titanium oxide (JCPDS no. 18-1402). The presence of broad peaks and the absence of unidentified peaks confirm the small size and high purity of the prepared nanopowder. Notably, in the diffraction pattern of TG, the sharp peak of GO becomes less intense, suggesting the disruption of the GO layers due to formation of a partially reduced GO structure and the formation of the composite material itself. Furthermore, it can be found that the XRD patterns of TG and TR show peaks which are similar to the diffraction pattern of TiO_2. This indicates that the anatase phase is predominant in the composite samples. The XRD pattern of TR exhibits clear peaks of pure TiO_2, but the peak at 25° in TiO_2 is broadened due to its superimposition with the diffraction peak of RGO at 24.04°.

The morphologies of TiO_2, TG and TR were characterized by using TEM and SEM. Fig. 1(a–d) show the TEM images of TiO_2 and TG, whereas Fig. 1(e and f) show the SEM images of TR. From Fig. 1(a) it is clear that the TiO_2 nanopowder consists of 2–15 nm sized TiO_2 particles. Furthermore, the higher-magnification image (Fig. 1(b)) of the same sample delineates several crystal planes of TiO_2 nanopowder which are randomly oriented across the particles. Fig. 1(c) shows the micrograph of TG, where TiO_2 nanopowder can clearly be seen uniformly decorated on the surface of GO. Furthermore, the well resolved adjacent image (Fig. 1(d)) depicts the crystal planes of TiO_2 nanopowder on the GO surface. From the SEM images of TR

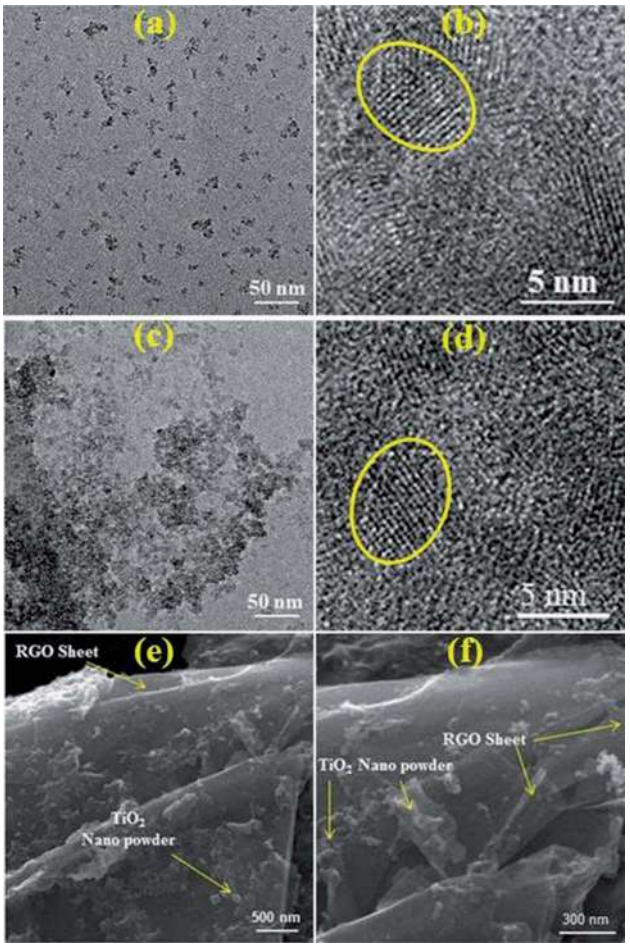

Fig. 1 (a) TEM images of TiO_2 nanopowder; (b) HRTEM image of TiO_2 nanopowder showing several crystal planes randomly oriented across the particles; (c) TEM image of TG; (d) HRTEM image of TG showing crystal planes. (e and f) SEM images of TR at different magnifications.

(Fig. 1(e) and (f)) it can be seen that the TiO_2 nanopowder is well attached to the RGO surfaces. Thus, both TEM and SEM images (Fig. 1(c and f)) attest to the intimate contact between the TiO_2 nanopowder and the GO and RGO sheets, which probably constitutes the basis for the electronic interactions between the components.[53] These results further reveal that GO and RGO inhibit the aggregation of TiO_2 nanopowder. The specific surface area of TiO_2 nanopowder was measured by Brunauer–Emmett–Teller (BET) analysis, which showed the presence of a high specific surface area of TiO_2 nanopowder of around ~250 $m^2\ g^{-1}$, attesting to the inhibition of TiO_2 agglomeration (see ESI†). Additionally, the test also provided results for average pore diameter, which in the present case came out to be 0.24 nm. The Raman investigation (See ESI, Fig. S2†) supported the successful synthesis of GO, RGO, TiO_2, TG and TR. Furthermore, Fourier transform infrared (FT-IR) spectra of the TiO_2 nanopowder, TG and TR composites were measured to study the different functional groups and chemical bonds present, such as Ti–O–Ti vibrations and Ti–O–C vibrations in the system (Fig. S3, See ESI†), which were further confirmed by DFT calculations.

In order to study the formation of the chemical bonds Ti–O–C and Ti–C after loading TiO_2 with GO and RGO, the interactions between TiO_2 and GO/RGO were also investigated by the analysis of XPS results of TG and TR as shown in Fig. 2. The core level O 1s XPS spectra of TG and TR are shown to prove the existence of the Ti–O–C bond (Fig. 2(a and d)). The main peaks centered at 529.08 and 530.09 eV correspond to Ti–O–Ti (lattice O).[54] The peaks with higher binding energy located at 530.02 and 530.89 eV are attributed to Ti–O–C for both TG and TR respectively.[54] The other peaks centered at 532.11 eV and 532.89 eV correspond to Ti–OH and C–O groups for TG.[54] Furthermore, in the case of TR, the peak centered at 531.65 eV was attributed to the C–O groups. Fig. 2(c) shows the core level spectra of C 1s for the TG hybrid with its peak positions observed at binding energies of 284.18, 284.94 and 287.44 eV, corresponding to C–C, C=O, and C–OH bonds, respectively.[55] For the TR hybrid (Fig. 2(f)), three peaks centered at 284.21, 285.27, and 287.10 eV correspond to C–C in aromatic rings, C=O, and C–OH groups, respectively.[2] Additionally, in TR, another peak at 282.5 eV (Ti–C) was observed, which could be because of the chemical bonding between titanium and carbon.[55] Fig. 2(b) and (e) show the chemical states of the Ti(IV) species in TG and TR respectively. The Ti 2p core levels can be deconvoluted to a doublet (Ti 2p3/2 and Ti 2p1/2), exhibiting a binding energy difference (ΔE_{BE}) of 5.61 and 5.71 eV for TG and TR respectively, which indicates the presence of normal states of Ti(IV), and is consistent with an earlier report.[56] The binding of GO/RGO and TiO_2 may be advantageous for the transport of electrons through the TG and TR hybrids. However, the increase in (ΔE_{BE}) of TR reveals that the interaction between TiO_2 and RGO is stronger than between TiO_2 and GO.

Modified optical band gap study

The UV-Vis absorption spectra and PL spectra of the TiO_2, TG and TR were measured in order to investigate the optical energy gaps of the samples. After the addition of GO/RGO, the synergistically interacting GO/RGO matrix modifies the electronic band gap structure of TiO_2 and opens up an energy level between the conduction and valence bands, as a consequence of which the band gap energy of TiO_2 is reduced, and an additional band edge originates. This result was explained analytically and supported by the similar double band edge structures obtained for the composites through DFT calculations.

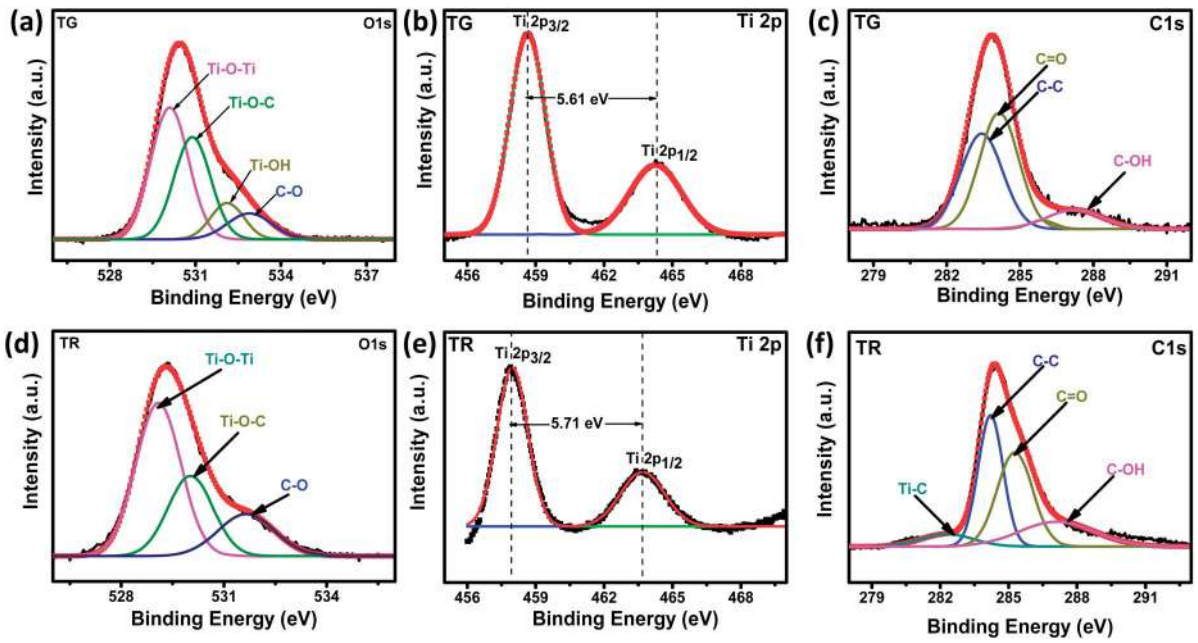

Fig. 2 XPS analysis. O 1s (a and d), C 1s (c and f) and Ti 2p (b and e) core level XPS spectra of TG and TR hybrids, respectively.

Experimental study of the optical band gap

To determine the optical band gap, we plotted the modified Kubelka–Munk function, *i.e.*, $[\alpha h\nu]^{1/2}$ (α is the absorption coefficient, h is Planck's constant, ν is the light frequency) *versus* the photon energy of the exciting light ($h\nu$). The absorption spectrum of bare TiO_2 (Fig. 3(a)) shows one absorption edge corresponding to a band gap of 3.68 eV. The absorption spectra of GO and RGO show a weak absorption band of about 2.10 eV and 1.83 eV respectively (Fig. 3(b) and (c)). Uniquely, the absorption spectra of TG and TR composites show double absorption edges. For TG, the first absorption edge corresponds to an optical band gap of 3.51 eV, which must be driven by TiO_2 domains in the composite. The value, as speculated, is less than that of bare TiO_2 (3.68 eV), signifying the effect of the synergistic interaction of TiO_2 and the underlying GO matrix on the TiO_2 domains, caused by the Ti–O–C bond formation which was confirmed from the FT-IR spectra. In the case of the TR composites, this higher band edge value reduces to 3.42 eV, owing to enhanced interactions between TiO_2 and the RGO matrix. This is attested to by the FT-IR analysis results, which show improved Ti–O–C bond signals in the case of the TR composites, in contrast to the case of the TG composites. The second (lower) absorption edge is obtained at 2.51 eV and 2.39 eV for the TG and TR composites respectively. The prominent driving force behind these absorption edges is the GO and RGO domains in the case of the TG and TR composites, respectively. Again as expected, the values of 2.51 eV (TG) and 2.39 eV (TR) are greater than those of pure GO (2.10 eV) and RGO (1.83 eV), which is a direct effect of TiO_2 on the GO and RGO matrices, *via* Ti–O–C bond formation. Further, the quenching in the photoluminescence spectra of the TiO_2 nanopowder after the addition of GO and RGO supports the reduction in the active band gap of TiO_2 (see ESI, Fig. S4†). The above incisive explanation for multiple band gaps observed in the TG and TR results evinces the pioneering result of achieving the degradation of MB under normal visible light. This validates these composites as much better candidates, due to their better ecological profile compared to earlier UV-light-based MB degradation using TiO_2 composites.

Computational study of the optical band gap

In order to support the experimental results outlined above, we calculated the optical spectra based on density functional theory (DFT) for the individual systems GO, RGO and TiO_2 along with the composite systems GO and RGO with TiO_2 (Fig. 4 and 5). The anatase TiO_2 surface, which is a tetragonal crystal structure, was constructed with a slab size of $4 \times 4 \times 4$, with an interlayer distance of 3.95 Å. The optical gap of any system is directly related to the first absorption peak of its optical spectrum. Therefore, determining the optical response is quite intuitive from the optical gap perspective. The visible-light-driven photocatalytic activity of the experimentally synthesized TiO_2 nanopowder, TG and TR composites were compared from the optical spectra analysis, which is an consequence of the optical absorption gap of these materials. The calculated optical spectra can be compared to the UV-Vis spectra of experimentally synthesized TiO_2 nanopowder, GO, RGO and their respective composites with TiO_2 as depicted in Fig. 4 and 5. A similar trend was found between the experimentally and theoretically obtained optical responses. The absorption peak strength can also vary if one goes from an individual system to the composite systems. We started calculating the composites by introducing 3 Å distance between surface and

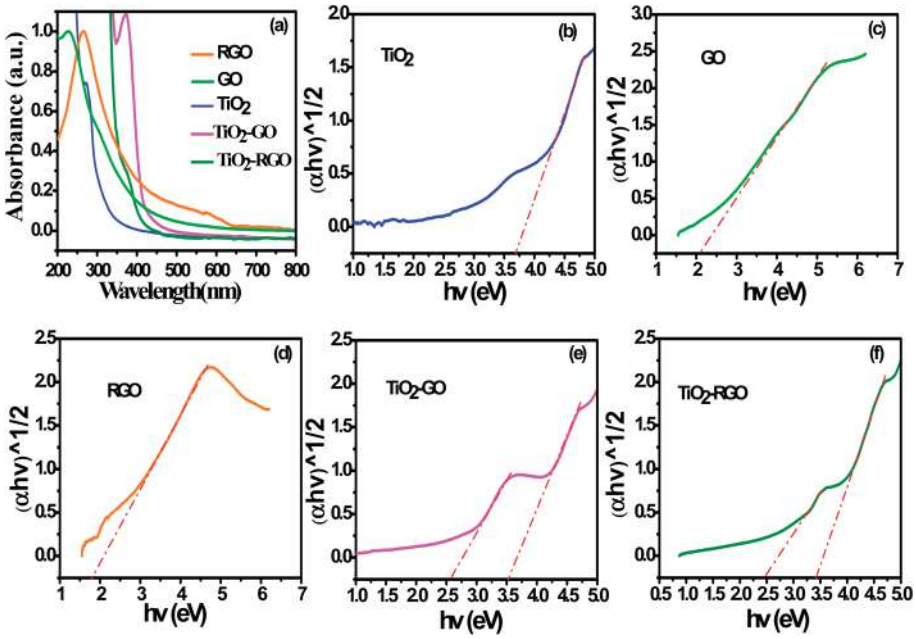

Fig. 3 (a) UV-Vis spectra of as-prepared TiO_2 nanopowder, GO, RGO, TG and TR composites. The plot of the transformed Kubelka–Munk function *versus* the energy of light for the calculation of E_g, (b)–(f) for as-synthesized TiO_2, GO, RGO, TG and TR composites respectively.

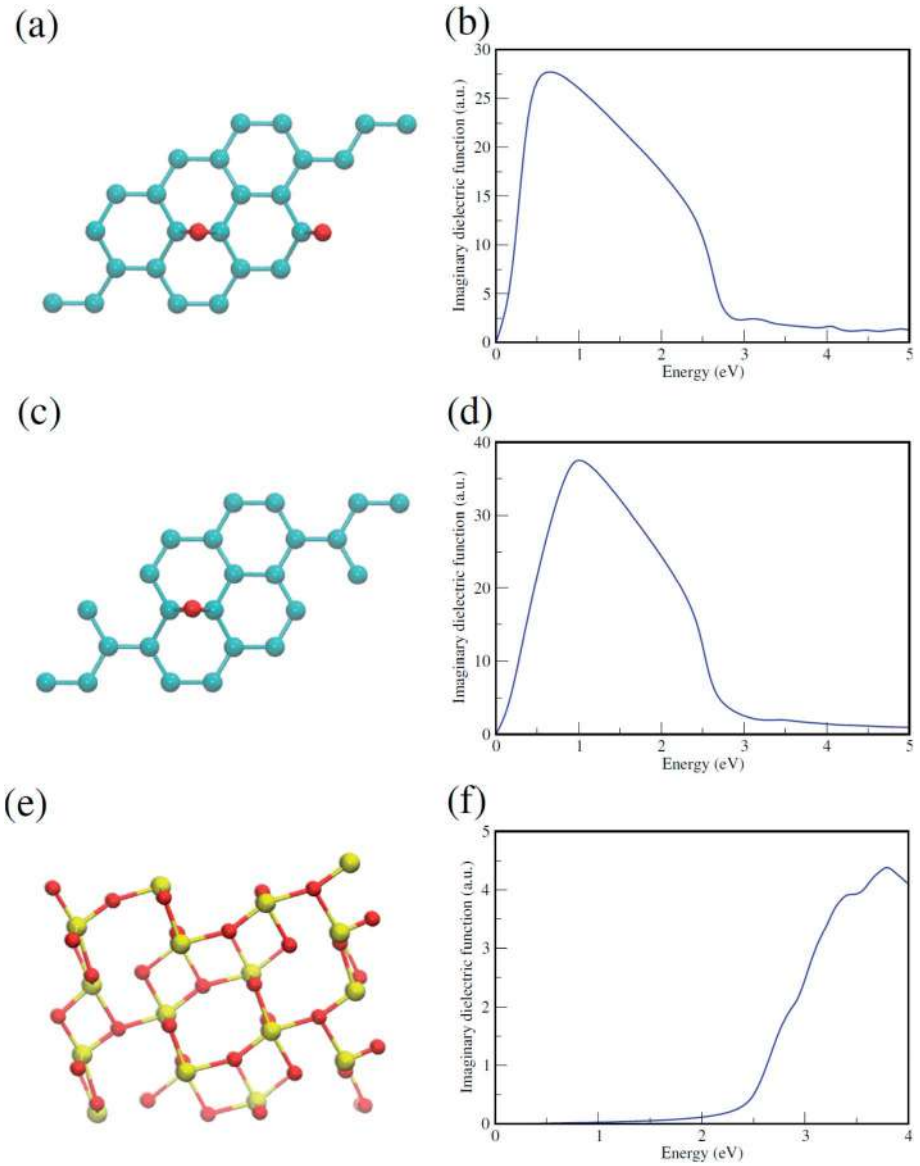

Fig. 4 Optimized structures and calculated imaginary dielectric functions (a.u.) as functions of energy for GO [(a) and (b), respectively], RGO [(c) and (d), respectively] and TiO_2 [(e) and (f), respectively]. The cyan, red and yellow balls represent the carbon, oxygen and titanium atoms, respectively.

adsorbate. This distance was chosen to be between physisorption and chemisorption binding. It was found that in the relaxed structures, this distance decreased to 2.4 Å and 2.1 Å for the TG and TR systems, respectively, as the shortest distance between adsorbate and surface. This leads to the inference that RGO binds more with anatase TiO_2 than GO does, hence the charge transfer between the surface and the adsorbate is more significant in the case of TR than TG, which is in agreement with experimental findings. This influences the optical absorption peak for the nanocomposites as well. We can assume that the formation of the Ti–O–C bond is due to the bonding between the free electrons on the surface of TiO_2 with some unpaired π-electrons, which then shift upward the valence band edge and reduce the band gap. Hence coinciding with the experimental findings, multiple absorption edges were found in the nanocomposites of TG and TR, whereas the single absorption edge is observed for the individual systems of TiO_2, GO and RGO.

Enhanced photocatalytic activity

To study the effect of the wt% ratio of TiO_2 : GO/RGO on both the photodegradation efficiency of MB and the photocatalytic rate constants, five as-synthesized samples, abbreviated as bare TiO_2 nanopowder, TG1, TG2, TR1, TR2 (for details see Section 2.5) were analyzed for their photocatalytic behavior in five equal time intervals (each of 60 min), under visible light (470 nm) irradiation. The observed change in normalized temporal concentration (C/C_0) of MB during photodegradation is proportional to the normalized maximum absorbance (A/A_0).

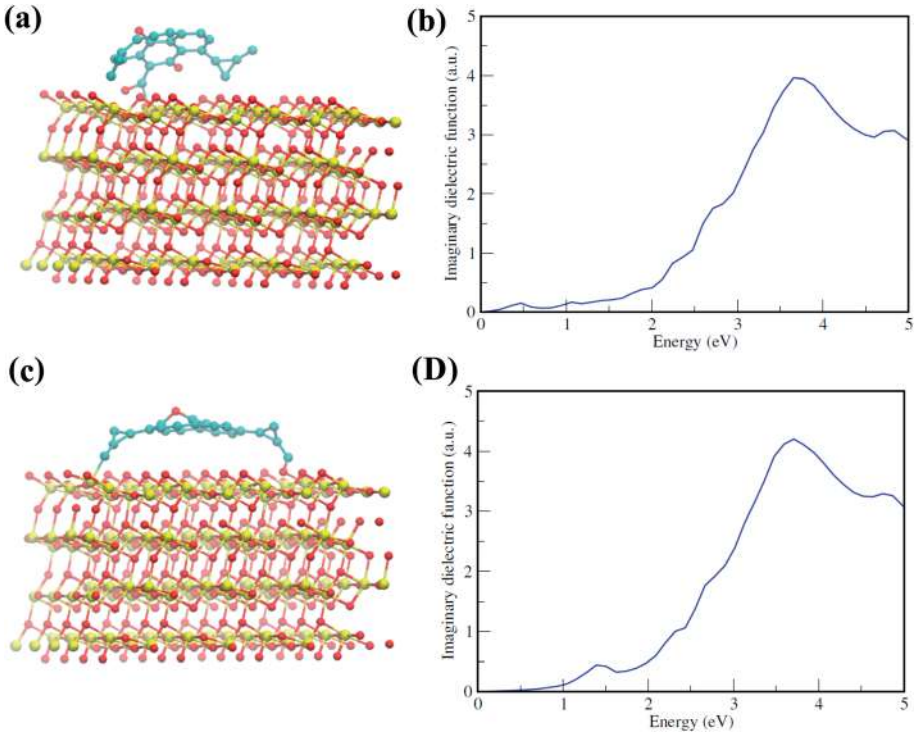

Fig. 5 Optimized structure (a) and calculated imaginary dielectric function (a.u.) as a function of energy (b) for GO + TiO_2 heterojunction. Optimized structure (c) and calculated imaginary dielectric function (a.u.) as a function of energy (d) for RGO + TiO_2 heterojunction. The cyan, red and yellow balls represent the carbon, oxygen and titanium atoms, respectively.

Here initial concentration (C_0) is regarded as the concentration of MB after adsorption equilibrium.

Fig. 6 illustrates the measured photodegradation performance of different photocatalysts with varying concentration under the same reaction conditions. Fig. 6(a) shows the remaining percentage of MB in solution after irradiation with visible light, and Fig. 6(b) depicts the photodegradation performance of MB with respect to time. It was found that the composites, TG and TR, exhibit faster and better photodegradation capability than pure TiO_2 nanopowder. Multiple concentrations of TG1, TG2, TR1 and TR2 were studied for photodegradation of MB (Fig. 6(c) and 6(d)). An increase in the concentration of the TR composites in MB solution (P1, P2 and P3) improves the photocatalytic activity, while decreased photocatalytic activity is observed upon increasing the concentration of the TG composite (P1 to P3); (For details see Section 2.8). The TR2–P3 composite shows the highest photocatalytic activity with an average degradation of MB of 98.72% within 300 min, while with pure TiO_2 nanopowder this value drops down to 36.84% and for GO or RGO, it is ~38% for the same period of time. Without the use of a catalyst, the concentration of MB changes slightly both under exposed (around 5% during 300 min exposure) and dark (only 3%) conditions.

Fig. 7 summarizes the meticulous comparative analysis of photodegradation efficiencies and rate constants of all four as-synthesized TiO_2 composites (TG1, TG2, TR1, TR2), with as-synthesized bare TiO_2 nanopowder and the previously reported[26] TiO_2–graphene composite for MB degradation, carbon nanotubes/TiO_2 nanotubes[15] and M-fullerene/TiO_2 for MO and MB degradation respectively.[17] Fig. 7 clearly shows that the k value and photodegradation efficiency of our synthesized composites is high in comparison to previously reported TiO_2–graphene composites even though they have used UV light which has a higher energy than visible light. For determining the rate constant, the degradation of dye could be assigned to a pseudo-first-order kinetics reaction by a linear plot with a simplified Langmuir–Hinshelwood model when C_0 is low.[57] That is,

$$\ln(C_0/C) = kt$$

where k is the apparent first-order rate constant.

Clearly both TG (TG1 and TG2) and TR (TR1 and TR2) composites surpass bare TiO_2 in terms of efficiency and rate constant. For the TR2 composite, the highest k value is 0.0621 min^{-1} (with efficiency ~99%) and for the TG2 composite it is 0.0236 min^{-1} (with efficiency ~76%), which is about 1780% and 614% higher than that of bare TiO_2 (36% efficiency with k value 0.0033 min^{-1}). Clearly both TR1/TG1 have lower rate constant values compared to TR2/TG2 respectively, attesting to the enhanced effect of decreasing wt% TiO_2 in both composites on the rate constant. In contrast, the effect of decreased wt% TiO_2 in composites on photodegradation efficiency, is the opposite for TG (a decrease), than in the case of TR (an increase). A detailed analytical model explaining the probable reasons behind such dependence of rate constant and

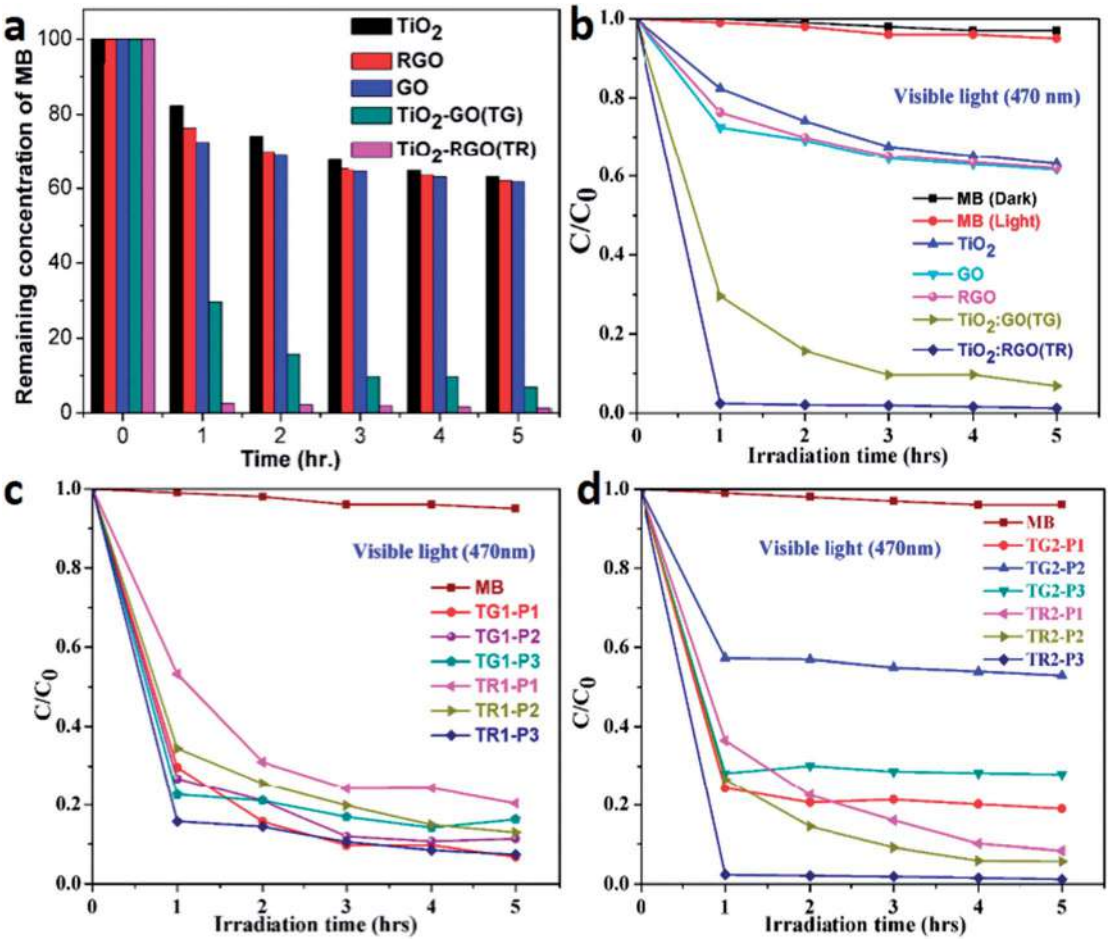

Fig. 6 The bar plot showing the remaining MB in solution after the irradiation with visible light (470 nm) over the as-synthesized TiO_2 nanopowder, GO, RGO, TG and TR composites (a), in liquid phase maximum photocatalytic degradation of MB under visible light (470 nm) over TiO_2, GO, RGO, TG and TR composites (b), photodegardation of MB over TG (5 : 1) and TR (5 : 1) (c) and photodegradation of MB over TG (2 : 1)and TR (2 : 1) (d) under visible light.

photodegradation efficiency on the wt% of GO/RGO in TG and TR composites has been provided in the ESI.†

Mechanism of enhanced photodegradation efficiency

The schematic (Fig. 8(a)) illustrates the mechanism of charge transfer from TiO_2 to GO and RGO *via* the interfaces supported by Ti–O–C bonds, which give a path for the charge transfer from TiO_2 to the GO/RGO matrix and hinder the recombination of electron–hole pairs. After irradiation with visible light, photoexcitation in TiO_2 occurs from O-2p orbital on the valance band (VB) to the Ti-3d orbital on the conduction band (CB), generating holes at the O-2p state with a very high redox potential.[58] Due to the high redox potential of the holes, hydroxyl radicals ($^{\bullet}OH$) are produced from water, having the potential to degrade the organic pollutants. The photo-generated electrons in the TG or TR photocatalyst can now easily migrate from the inner region to the surface and react with adsorbed O_2 on the surface, resulting in generation of radicals such as $O_2^{\bullet-}$, thereby increasing the overall efficiency. The reaction mechanism behind the degradation of MB by the TR composite (also valid for TG composite by replacing RGO with GO) can be expressed as follows:

$$TiO_2\text{–RGO} + h\nu \rightarrow TiO_2\,(e^-) - RGO + TiO_2\,(h^+) - RGO$$

$$TiO_2\,(e^-) - RGO \rightarrow TiO_2 - RGO\,(e^-)$$

$$RGO\,(e^-) + O_2 \rightarrow RGO + O_2^{\bullet-}$$

$$TiO_2\,(h^+) + H_2O \rightarrow H^+ + OH^{\bullet}$$

$$O_2^{\bullet-} + OH^{\bullet} + MB \rightarrow \text{Degradation of MB}$$

The enhancement of charge carrier separation clearly results in an increased concentration of more reactive oxidizing species (such as $OH^{\bullet}$, $O_2^{\bullet-}$), which enhances the photodegradation of MB.[25] The typical electrochemical impedance spectra (Fig. 8(b)) of ITO, TiO_2, TG and TR clearly attest to enhanced photocatalytic degradation in TG and TR. Here the impedance spectra in the frequency range varying from 0.01 Hz to 10 kHz were recorded in the three electrode configuration using the catalytic materials as the working electrode, Ag/AgCl as the reference

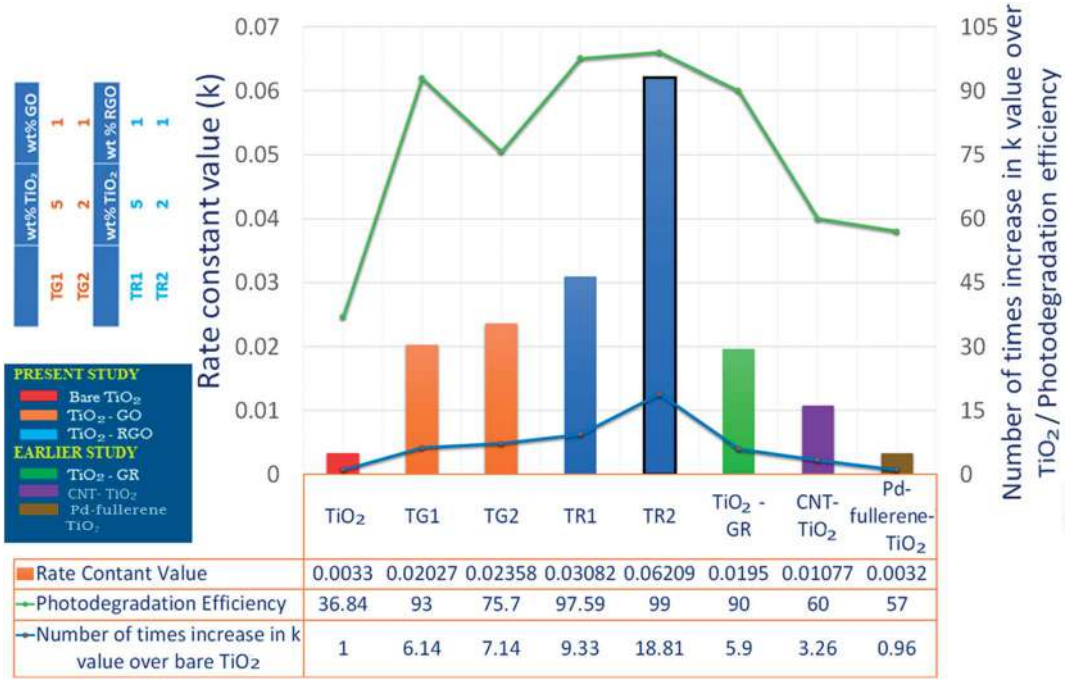

Fig. 7 Comparative study of rate constants (k) and photodegradation efficiencies of TG and TR composites (present work) *vs.* bare TiO_2 (present work)/previously reported TiO_2–graphene composites, CNT-TiO_2 composites and Pd-fullerene TiO_2 hybrids for photocatalytic degradation of methylene blue.

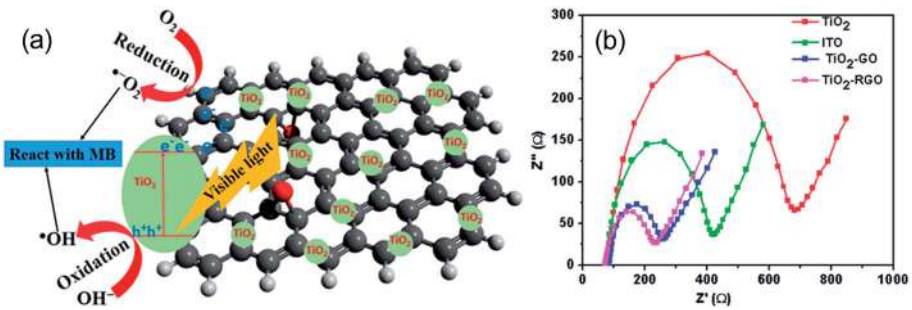

Fig. 8 (a) Schematic illustration of the enhanced photocatalytic activity of TR composites for the photodegradation of MB under visible light irradiation. (b) EIS changes of TiO_2, TG and TR electrodes. The EIS measurements were performed in the presence of a PBS solution (pH 7) containing 5 mM $[Fe(CN)_6]^{3-/4-}$.

electrode, platinum as the counter electrode and PBS solution (pH 7) containing 5 mM $[Fe(CN)_6]^{3-/4-}$ as the electrolyte. A single semicircle at the high frequency region and a straight line at the low frequency region indicate a mixed charge transfer and charge diffusion process.[59] It is observed that, with the introduction of GO/RGO into TiO_2, though in small amounts, the span of the semicircle is reduced, which indicates a decrease in both the solid state interface layer resistance and the charge transfer resistance (R_{ct}) on the surface. The R_{ct} values of the TG/TR electrodes were much smaller than that of the TiO_2 electrode, which illustrates that TG/TR lead to a much lower charge transport resistance and a much higher separation efficiency of electrons and holes, both together resulting in enhanced photocatalytic degradation of MB.

Conclusions

Distilling the above work, we developed two classes of chemically bonded TiO_2–GO/RGO hybrids with different weight-percent-ratios using a facile, economic, ecological and fast route, exhibiting high photocatalytic activities (for TR2 – 99%) and high rate constant values (for TR2 – 1900% more than bare TiO_2) under visible light. FT-IR analysis confirms the formation of Ti–O–C bonds in both the TR and TG composites, resulting in the emergence of new a optical band edge in both TG (3.51 eV and 2.51 eV) and TR (3.42 eV and 2.39 eV) composites. Complementary DFT calculations again confirm, both a similar trend of double band edges for composites and the existence of Ti–O–C bonds, which shift upwards the valence band edge and reduce the band gap. Furthermore, these bonds provide a

conductive pathway for charge carriers, inhibiting their recombination in TiO_2 (confirmed by EIS and PL spectra), resulting in enhanced efficiency compared to bare TiO_2. Greater narrowing of the band gap and better conductivity in the case of TR is observed compared to TG. Also, theoretically better binding of RGO with anatase TiO_2, than of GO with anatase TiO_2 is observed. The consequence is a better photocatalytic response of TR compared to TG composites.

Author contributions

S.U. and S.A. equally contributed on this work. A.S. conceived the experiment. S.U. and S.A. contributed to sample fabrication. S.U. carried out the UV absorption, PL measurement and FTIR spectra. V.C. carried out the Raman measurements. S.A. and F.T. performed the photocatalytic experiments. B.D. and J.P. discussed regularly the measurement results while conducting the experiments. C.J.R., S.C. and R.A. performed theoretical analysis by DFT. P.K.S. discussed all the optical measurement results. S.P. has corroborated the work with an analytical model for enhanced photocatalytic activity. S.U., S.A., S.P. and A.S. co-wrote the manuscript. All authors discussed the results and commented on the paper.

Conflict of interests

The authors declare no competing financial interest.

Acknowledgements

The authors express their sincere gratitude to the late Prof. B. P. Asthana, who had initiated this project. The authors are thankful to Andy Scheffel and Dr Jan Dellith from IPHT, Jena for SEM measurements, Mrs Anna Schmidt from IPC, Jena for BET measurements, Christa Schmidt from IPHT and Mr Vineet Srivastava from IIT Kanpur for XRD measurements, Dr Il-Kwon Oh from KAIST, South Korea for TEM measurements, and Prof. Snajay Kumar from Bio-physics lab, BHU, for PL and some of UV-Vis measurements. The authors are thankful to Dr Preeti Suman Saxena, Department of Zoology, Banaras Hindu University for providing some of her laboratory facilities. Two of us (SA, JP) are thankful to Deutsche Forschungs-Gemeinschaft (DFG). AS acknowledges the CAS program sponsored by UGC at Department of Physics, B. H. U and DST, New Delhi, India. SU, SA and RKS express their gratitude for the U.G.C. financial assistance. BD and FT gratefully acknowledge funding of the research project 'Photonic Nanomaterials' – PhoNa (Grant no. 03IS210EA) within the framework 'Spitzenforschung und Innovation in den Neuen Ländern' from the Bundesministerium für Bildung und Forschung (BMBF). CR would like to acknowledge CNPq and CAPES for the financial support. SC and RA would like to acknowledge the Carl Tryggers Stiftelse for Vetenskaplig Forskning (CTS), Swedish Research Council (VR), Swedish Energy Agency, and Stiffelsen J. Gust Richerts Minne (SWECO) for financial support. SNIC is also acknowledged for providing computing time.

References

1 M. A. Al-Ghouti, M. A. M. Khraisheh, S. J. Allen and M. N. Ahmad, *J. Environ. Manage.*, 2003, **69**, 229–238.
2 M. R. Hoffmann, S. T. Martin, W. Choi and D. W. Bahnemann, *Chem. Rev.*, 1995, **95**, 69–96.
3 A. Fujishima and K. Honda, *Nature*, 1972, **238**, 37–38.
4 H. S. Wahab, T. Bredow and S. M. Aliwi, *Chem. Phys.*, 2008, **353**, 93–103.
5 A. Yamakata, T.-a. Ishibashi and H. Onishi, *Chem. Phys.*, 2007, **339**, 133–137.
6 Y. Ni, Y. Zhua and X. Ma, *Dalton Trans.*, 2011, **40**, 3689–3694.
7 R. M. D. Hernandez-Alonso, F. Fresno, S. Suarez and J. M. Coronado, *Energy Environ. Sci.*, 2009, **2**, 1231–1257.
8 A. L. Linsebigler, G. Lu and J. T. Yates, *Chem. Rev.*, 1995, **95**, 735–758.
9 A. Kudo, K. Omori and H. Kato, *J. Am. Chem. Soc.*, 1999, **121**, 11459–11467.
10 S. Kim, S. J. Hwang and W. Choi, *J. Phys. Chem. B*, 2005, **109**, 24260–24267.
11 X. Zhang, Y. Liu, S.-T. Lee, S. Yang and Z. Kang, *Energy Environ. Sci.*, 2014, **7**, 1409–1419.
12 T. Tong, J. Zhang, B. Tian, F. Chen, D. He and M. An, *J. Colloid Interface Sci.*, 2007, **315**, 382–388.
13 E. A. Kozlova, N. S. Kozhevnikova, S. V. Cherepanova, T. P. Lyubina, E. Y. Gerasimov, V. V. Kaichev, A. V. Vorontsov, S. V. Tsybulya, A. A. Rempel and V. N. Parmon, *J. Photochem. Photobiol., A*, 2012, **250**(103), 103–109.
14 X. Yu, J. Liu, Y. Yu, S. Zuo and B. Li, *Carbon*, 2014, **68**, 718–724.
15 M. L. Chen, F. J. Zhang and W. C. Oh, *J. Korean Ceram. Soc.*, 2008, **45**, 651–657.
16 J. Yu, T. Ma and S. Liu, *Phys. Chem. Chem. Phys.*, 2011, **13**, 3491–3501.
17 Z.-D. Meng, F.-J. Zhang, L. Zhu, C.-Y. Park, T. Ghosh, J.-G. Choi and W.-C. Oh, *Mater. Sci. Eng., C*, 2012, **32**, 2175–2182.
18 M. Wang, J. Ioccozia, L. Sun, C. Lin and Z. Lin, *Energy Environ. Sci.*, 2014, **7**, 2182–2202.
19 Z. Zhang, C. Shao, X. Li, Y. Sun, M. Zhang, J. Mu, P. Zhang, Z. Guo and Y. Liu, *Nanoscale*, 2013, **5**, 606–618.
20 P. A. DeSario, J. J. Pietron, D. E. DeVantier, T. H. Brintlinger, R. M. Stroud and D. R. Rolison, *Nanoscale*, 2013, **5**, 8073–8083.
21 W. Ren, Z. Ai, F. Jia, L. Zhang, X. Fan and Z. Zou, *Appl. Catal., B*, 2007, **69**, 138–144.
22 W. Wang, J. Yu, Q. Xiang and B. Cheng, *Appl. Catal., B*, 2012, **119–120**, 109–116.
23 Y. Yao, G. Li, S. Ciston, R. M. Lueptow and K. A. Gray, *Environ. Sci. Technol.*, 2008, **42**, 4952–4957.
24 K. S. Novoselov, A. K. Geim, S. V. Morozov, D. Jiang, Y. Zhang, S. V. Dubonos, I. V. Grigorieva and A. A. Firsov, *Science*, 2004, **306**, 666–669.
25 A. K. Geim, *Science*, 2009, **324**, 1530–1534.

26 K. Krishnamoorthy, R. Mohan and S.-J. Kim, *Appl. Phys. Lett.*, 2011, **98**, 244101–244103.
27 T.-F. Yeh, J.-M. Syu, C. Cheng, T. T.-H. Chang and H. Teng, *Adv. Funct. Mater.*, 2010, **20**, 2255–2262.
28 N. Zhang, Y. Zhang and Y.-J. Xu, *Nanoscale*, 2012, **4**, 5792–5813.
29 N. Yang, Y. Liu, H. Wen, Z. Tang, H. Zhao, Y. Li and D. Wang, *ACS Nano*, 2013, **7**, 1504–1512.
30 G. Jiang, Z. Lin, C. Chen, L. Zhu, Q. Chang, N. Wang, W. Wei and H. Tang, *Carbon*, 2011, **49**, 2693–2701.
31 Y. Gao, X. Pu, D. Zhang, G. Ding, X. Shao and J. Ma, *Carbon*, 2012, **50**, 4093–4101.
32 H. Zhang, X. Lv, Y. Li, Y. Wang and J. Li, *ACS Nano*, 2009, **4**, 380–386.
33 X. Yin, H. Zhang, P. Xu, J. Han, J. Li and M. He, *RSC Adv.*, 2013, **3**, 18474–18481.
34 Q. Xiang, J. Yu and M. Jaroniec, *Chem. Soc. Rev.*, 2012, **41**, 782–796.
35 X. An and J. C. Yu, *RSC Adv.*, 2011, **1**, 1426–1434.
36 Q. Xiang, J. Yu and M. Jaroniec, *Nanoscale*, 2011, **3**, 3670–3678.
37 X. Zhou, T. Shi, J. Wua and H. Zhoua, *Appl. Surf. Sci.*, 2013, **287**, 359–368.
38 S. M. -Torres, L. M. P. -Martínez, J. L. Figueiredo, J. L. Faria and A. M. T. Silva, *Appl. Surf. Sci.*, 2013, **275**, 361–368.
39 C. Chen, W. Cai, M. Long, B. Zhou, Y. Wu, D. Wu and Y. Feng, *ACS Nano*, 2010, **4**, 6425–6432.
40 G. S. Anjusree, A. S. Nair, S. V. Nair and S. Vadukumpully, *RSC Adv.*, 2013, **3**, 12933–12938.
41 S. D. Perera, R. G. Mariano, K. Vu, N. Nour, O. Seitz, Y. Chabal and K. J. Balkus, *ACS Catal.*, 2012, **2**, 949–956.
42 N. R. Khalid, E. Ahmed, Z. Hong, L. Sana and M. Ahmed, *Curr. Appl. Phys.*, 2013, **13**, 659–663.
43 Q. Huang, S. Tian, D. Zeng, X. Wang, W. Song, Y. Li, W. Xiao and C. Xie, *ACS Catal.*, 2013, **3**, 1477–1485.
44 L. Ci, L. Song, C. Jin, D. Jariwala, D. Wu, Y. Li, A. Srivastava, Z. F. Wang, K. Storr, L. Balicas, F. Liu and P. M. Ajayan, *Nat. Mater.*, 2010, **9**, 430–435.
45 D. C. Marcano, D. V. Kosynkin, J. M. Berlin, A. Sinitskii, Z. Sun, A. Slesarev, L. B. Alemany, W. Lu and J. M. Tour, *ACS Nano*, 2010, **4**, 4806–4814.
46 D. Li, M. B. Muller, S. Gilje, R. B. Kaner and G. G. Wallace, *Nat. Nano.*, 2008, **3**, 101–105.
47 P. Hohenberg and W. Kohn, *Phys. Rev.*, 1964, **136**, 864–871.
48 W. Kohn and L. Sham, *Phys. Rev. A: At., Mol., Opt. Phys.*, 1965, **140**, 1133–1138.
49 G. Kresse and J. Hafner, *Phys. Rev. B: Condens. Matter Mater. Phys.*, 1994, **49**, 14251–14269.
50 G. Kresse and J. Furthmüller, *Comput. Mater. Sci.*, 1996, **6**, 15–50.
51 J. P. Perdew, J. A. Chevary, S. H. Vosko, K. A. Jackson, M. R. Pederson, D. J. Singh and C. Fiolhais, *Phys. Rev. B: Condens. Matter Mater. Phys.*, 1992, **46**, 6671–6687.
52 J. P. Perdew and Y. Wang, *Phys. Rev. B: Condens. Matter Mater. Phys.*, 1992, **45**, 13244–13249.
53 T. Xu, L. Zhang, H. Cheng and Y. Zhu, *Appl. Catal., B*, 2011, **101**, 382–387.
54 T. Lu, R. Zhang, C. Hu, F. Chen, S. Duo and Q. Hu, *Phys. Chem. Chem. Phys.*, 2013, **15**, 12963–12970.
55 H.-N. Kim, H. Yoo and J. H. Moon, *Nanoscale*, 2013, **5**, 4200–4204.
56 N. K. Allam, F. Alamgir and M. A. El-sayed, *ACS Nano*, 2010, **4**, 5819–5826.
57 X. H. Wang, J. G. Li, H. Kamiyama, Y. Moriyoshi and T. Ishigaki, *J. Phys. Chem. B*, 2006, **110**, 6804–6809.
58 W. Geng, H. Liu and X. Yao, *Phys. Chem. Chem. Phys.*, 2013, **15**, 6025–6033.
59 Y. Liu, D.-P. Wang, Y.-X. Yu and W.-D. Zhang, *Int. J. Hydrogen Energy*, 2012, **37**, 9566–9575.

Sensors & Actuators: B. Chemical 273 (2018) 455–465

Contents lists available at ScienceDirect

Sensors and Actuators B: Chemical

journal homepage: www.elsevier.com/locate/snb

Carbon nanostructure (*0-3 dimensional*) supported isolated gold nanoparticles as an effective SERS substrate

Shiju Abraham[a,1], Matthias König[b,2], Sunil K. Srivastava[c], Vinod Kumar[d], Bernd Walkenfort[b], Anchal Srivastava[a,*]

[a] Department of Physics, Institute of Science, Banaras Hindu University, Varanasi, 221005, India
[b] Faculty of Chemistry, University of Duisburg, Essen, 47057, Germany
[c] Department of Physics, Mahatma Gandhi Central University, Motihari, 845 401, India
[d] Department of Materials Engineering, Ben-Gurion University of the Negev, Beersheba, 84105, Israel

ARTICLE INFO

Keywords:
SERS
Raman marker
Carbon nanostructures
Isolated gold nanoparticles

ABSTRACT

The present work reports a comparative surface enhanced Raman scattering (SERS) study of nanohybrids of spatially isolated gold nanoparticles (Au NPs) with different carbon nanostructures (CNS). For a meticulous comparative analysis, different CNS covering from zero dimensional to three dimensions were used. SERS activities of developed nanohybrids platforms were evaluated with a Raman marker i.e. Mercaptobenzoic acid (4-MBA, 1 μM). Synergistic Raman signal enhancement from each Au NP (electromagnetic enhancement) and underlying CNS matrix (chemical enhancement) was observed in nanohybrid enabling detection of very small concentration of 4-MBA i.e. 1 μM convincingly. Among the different underlying matrix, GQDs-Au NPs based SERS platform have shown highest SERS enhancement by a factor of 10^7, followed by GO-Au NPs combination ($\sim 3 \times 10^6$) and others. Enhanced SERS activity of GQDs -Au NPs -4-MBA nanohybrid platform is attributed to the D and G bands of GQDs, overpowering the strong fluorescent background of GQDs alone. Reported nanohybrids; specially GQDs-Au NPs offers numerous possibilities to be used as sensitive and reproducible SERS platform for the detection of other biologically/chemically important analytes, showing potential for standardization in near future.

1. Introduction

Beside its numerous usefulness in analytics, traditional Raman spectroscopy (RS) is limited for detecting low concentrations of target analytes with weak vibrational bands due to lower scattering cross-section [1–3]. To overcome such limitation, Resonant Raman spectroscopy (RRS) [1] and Surface-Enhanced Raman Spectroscopy (SERS) [4–10] have been explored in last few decades. However, RRS suffers with a drawback of the simultaneous increase in the fluorescence background as the excitation coincides with the absorption [11]. On the other hand SERS is both surface selective and highly sensitive technique, which offers higher magnitude of increased intensity (10^8-10^{14}), suppresses the fluorescence signal while selectively enhancing the Raman signal, producing chemical fingerprint with sensitivity enough to enable single-molecule detection [12,13]. Electromagnetic enhancement (EE) and chemical enhancement (CE) are two well accepted mechanisms that explain the SERS activity. Surface plasmon resonance effect of plasmonic nanostructures are the chief contributor to the EE [4,14] while CE is based on the charge transfer between a nanomaterial and adsorbed analytes [15]. And the combination of both EE and CE resulted to $\sim 10^{14}$ times enhancement in SERS signal.

In last few years, nanostructures of certain metals like gold (Au) and silver (Ag) with their roughened surfaces have shown interesting SERS activities attributed to the enhanced surface plasmons resonance on excitation [16,17]. In most of the SERS studies, gold nanoparticles (Au NPs) have been used as a popular SERS substrate and it is due to their certain beautiful properties like long term stability, better control over size and shape and biocompatibility [18,19]. However, the SERS potentials of Au NPs have not been fully exploited in previous studies due to less control on particles orientation and aggregations while fabricating their SERS substrates. Some well-known techniques like electrochemical routes, vacuum evaporation and nano-lithography were employed to overcome above mentioned challenges for fabrication of Au NPs based SERS platform. But these techniques are costly and

* Corresponding author.
E-mail address: anchalbhu@gmail.com (A. Srivastava).
[1] Current address: Zuckerberg Institute for Water Research, Ben-Gurion University of the Negev, Sede Boqer Campus, 8499000, Israel.
[2] Institute of Chemistry of new Materials, University of Osnabrück, Barbarastraße 7, D-49076 Osnabrück, Germany.

https://doi.org/10.1016/j.snb.2018.06.066
Received 23 December 2017; Received in revised form 7 June 2018; Accepted 13 June 2018
Available online 18 June 2018
0925-4005/

tedious in operation. Therefore, some alternate strategies for making efficient Au NPs based SERS substrates are highly required. In recent years, carbon nanomaterials have been used as a unique support matrix for manipulation of plasmonic properties of metallic nanoparticles, which have been used in several applications ranging from light-emitting devices [20], to data storage [21] and in bio-sensing [22,23]. Adding to this, monolayer single-crystalline graphene grown by CVD method was reported as a flexible and transparent substrate for SERS [24]. Apart from the suitability as a supportive matrix [25], the combination of unique properties of carbon nanomaterials with metallic nanoparticles, not only provide a synergy of CE and EE, but also offers several exciting future applications, which is not possible individually. An relevant example is the application of Ag-SiO_2-CNT based nanoporous freestanding SERS substrate for detection of trinitrotoluene [26]. Several recent studies have demonstrated the SERS potential of different carbon nanostructures with metal nanoparticles [27–32]. Most importantly, carbon nanomaterials have shown their unique ability to provide the ultimate dielectric spacer which is very crucial for high optical field-enhancements in plasmonics, arises due to sub-nanometer gaps among metallic nanostructures [33,34]. With this background information, the SERS study of these metallic nanoparticles becomes more important in their spatially isolated state. And it is believed that carbon nanostructures will not only work as an efficient support matrix for spatial isolation of Au NPs, but also contribute significantly in SERS signal enhancement *via* CE. With this motivation, the current study is aimed to explore the SERS activities of spatially isolated Au NPs on different carbon nanostructures i. e. covering zero dimensional (0D) graphene quantum dots (GQDs), 1D carbon nanotube (CNTs), 2D graphene oxide (GO) and reduced graphene Oxide (RGO), and 3D graphene hydrogels (GHs). Thus to compare the dimensionality effect of on spatial distribution, hence SERS activities of Au NPs, different carbon nanostructures have been used for the study.

2. Material and methods

2.1. Materials

Graphite flakes (NGS Naturgraphit GmbH, Germany), tetrachloroauric acid ($HAuCl_4$), polyvinylpyrrolidone (PVP), 4-MBA, 5,5′-Dithiobis (2-nitrobenzoic acid) (DTNB), H_2SO_4, H_3PO_4, $KMnO_4$, H_2O_2, hydrazine hydrate, ferrocene, xylene, ammonia solution, ethanol, etc. used were of technical grade and were procured from Sigma-Aldrich.

2.2. Synthesis of different carbon nanostructures and PVP stabilized gold nanoparticles

The synthesis procedures for all the CNS base materials and the PVP stabilized gold nanoparticles were elaborated in detail in the supporting information (SI).

2.3. Preparation of CNS-Au NPs composites

All CNS materials used except GQDs were taken at a concentration of 2 mg/mL in DW in separate vials. 2 mL of GQDs solution taken in another vial. All these six dispersions were sonicated for 30 min to make a homogeneous dispersion. From the well dispersed CNS solution, 700 μL taken out in a 2 mL eppendorf and added 300 μL of diluted spherical Au NPs of ~ 50 nm size. This was further sonicated for 10 min and kept in a vibrating stand until the thin film for SERS is made on silicon.

2.4. Fabrication of CNS-Au NPs nanohybrid SERS platform and immobilization of Raman marker

Pre-cleaned silicon (Si) of 5 × 5 mm dimension were used for fabrication of SERS platform. A 10 μL of hybrid solution was spin coated at 1000 rpm to get a uniform nanohybrid films over entire substrate. These substrates were dried at 70 °C for 30 min. Several optimization experiments were carried out before developing a uniform SERS platform. 5 μL of 4-MBA (1 μM Raman marker) was added on to the developed platform and incubated for overnight at RT and further used for the SERS study. Here, Si substrate is used to spin coat the material rather than SiO_2/Si substrate in order to reduce the interference-enhanced Raman scattering (IERS) effect which usually arises from Si substrate with metal oxide layer of specific thickness.

2.5. Characterization of the materials

The structural characterization of CNTs, GO, RGO and GHs were carried out by X-ray diffraction (XRD) technique (Rigaku miniflex-II diffractometer at 30 kV, 15 mA). The wavelength of Cu-Kα1 radiation of λ = 1.5405 Å was used for obtaining the XRD pattern. TEM characterization of CNS and CNS-Au NPs nanohybrid were carried out by using a Zeiss EM 902 instrument. The Raman and SERS measurements were conducted with a confocal Raman microscope (WITec Alpha 300R, 30 cm focal length and 600 grooves per mm grating spectrometer) equipped with an EM-CCD. A 632.8 nm line from a He-Ne laser was focused onto the sample using a 40x objective (Olympus) with a numerical aperture of 0.6 (5 mW laser power at the sample; laser spot diameter ~1.286 μm). For the Raman mapping, an area of 100 × 100 μm is scanned with an interval of 2 μm with an integration time of 1 s. Raman mapping data were processed by the *WITecProject* software and the graphs were plotted by *Origin* software. The intensity scale bar in the Raman mapping images are in the unit of CCD cts.

3. Results and discussion

3.1. XRD studies of the CNS base materials

The XRD pattern of the as-synthesized CNS base materials except GQDs, namely CNTs, GO, RGO and GHs are presented in Fig. S1 (Supporting Information). The XRD peak observed at ~25.9° (Fig. S1a) corresponds to the characteristic peak of CNTs (002). GO shows a strong diffraction peak at ~ 11° (Fig. S1b), which corresponds to the (002) reflection plane with an interlayer spacing of ~8.0 A° [35]. Further the weak and broad band around 42° in GO corresponding to the (100) reflection and is due to the turbo static band of disordered carbon material. The most prominent diffraction peak of RGO is observed at ~24. 5° (002) attesting the characteristic band of RGO (Fig. S1c) with an interlayer spacing of ~3.4 A°. This value matches with the well-known XRD peak of RGO [36]. Fig. S1 (d) shows the diffraction pattern of GHs with a peak centered at ~25.7° (002). The XRD profile of GHs matches with that of the earlier report [37].

3.2. Transmission electron microscopy (TEM) studies

The Fig. 1 is a representative TEM micrograph of Au NPs, GQDs, CNTs and their nanohybrid which were used for the SERS study. In Fig. 1(a), a uniform distribution of PVP stabilized Au NPs is seen. The size of the particles was measured to be ~ 50 nm. In Fig. 1(b), an isolated Au NP is shown which were achieved through the dilution of Au NPs stock solution. Fig. 1(c) showed the TEM images of homogeneously packed and well separated GQDs with lateral size ~10 nm (height profile ranging from ~1–5 nm: from AFM topography in Fig. S3 of Supporting Information). The nanohybrid of GQDs-Au NPs as shown in Fig. 1(d) is an indication of very unique phenomenon took place during the synthesis of this nanohybrid. In close observation, it was noticed that each Au NP is surrounded by several GQDs because the size of GQDs are much smaller than the Au NPs. Fig. 1(e) showed the well separated CNTs. Here the individual CNTs are of approximately 30 nm in diameter and in micrometers in length. Further, these CNTs are of quite good in its homogeneity and are almost free from impurities. In

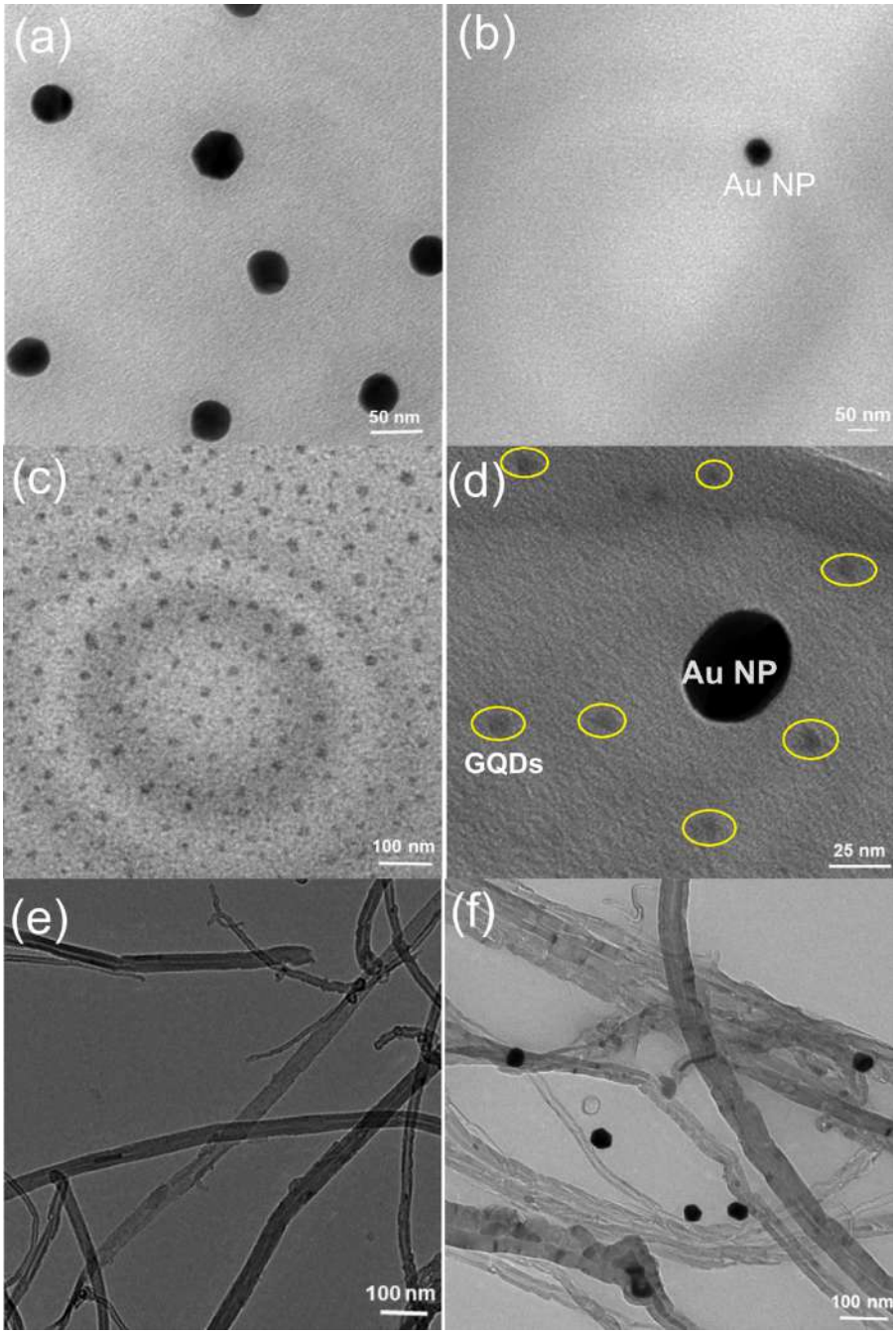

Fig. 1. TEM Image of (a) Au NPs, stabilized through PVP with an average size of ~50 nm (b) Single Au NP isolated on the same scale through dilution, (c) GQDs, with an approximate diameter of 10 nm, (d) GQDs-Au NPs, where a single Au NP is surrounded by few GQDs; (e) CNTs, with an outer diameter ~30 nm; (f) CNTs-Au NPs, where Au NPs are distributed on the CNTs surfaces in isolated regions.

the TEM image of CNTs-Au NPs nanohybrid (Fig. 1f), well decorated monomers of Au NPs on the CNTs surfaces are seen with quite large separation and some of the CNTs were aligned themselves to form bundles of CNTs.

Fig. 2(a) shows the TEM image of GO sheets which are multilayer in nature with lateral dimensions of several hundreds of nm. The TEM micrograph of GO-Au NPs nanohybrid is shown in Fig. 2(b) clearly indicate the decoration of isolated Au NP (encircled with yellow circle) on a nearly $2 \times 2\,\mu m$ area of GO. The optimized concentration of Au NPs and their stabilization with PVP results in their spatial isolation on the CNS matrix. PVP is an important stabilizing agent which help in spatial isolation of Au NPs without sacrificing the required SERS properties. Fig. 2 (c) shows the TEM image of RGO sheets where it appeared to be single or bilayer in its nature. In TEM micrograph of RGO-Au NPs nanohybrid as shown in the Fig. 2(d), the decoration of few isolated Au NPs (monomers) on the RGO surfaces were observed similar to GO-Au NPs. Fig. 2(e) represent the TEM image of GHs with wrinkles, folding and pores, etc. Characteristics features of 3D hydrogels made up of graphene sheets make it like a 3D graphene network, which can be observed from the figure. In the TEM micrograph of GHs-Au NPs shown in Fig. 2(f), the Au NPs are distinctly attached to the GHs network through the cavities, holes, folding and so on, ie. a better physical binding capability of the 3D network is clearly visible in the same fig. Further the isolation of Au NPs on GHs can be observed through this micrograph.

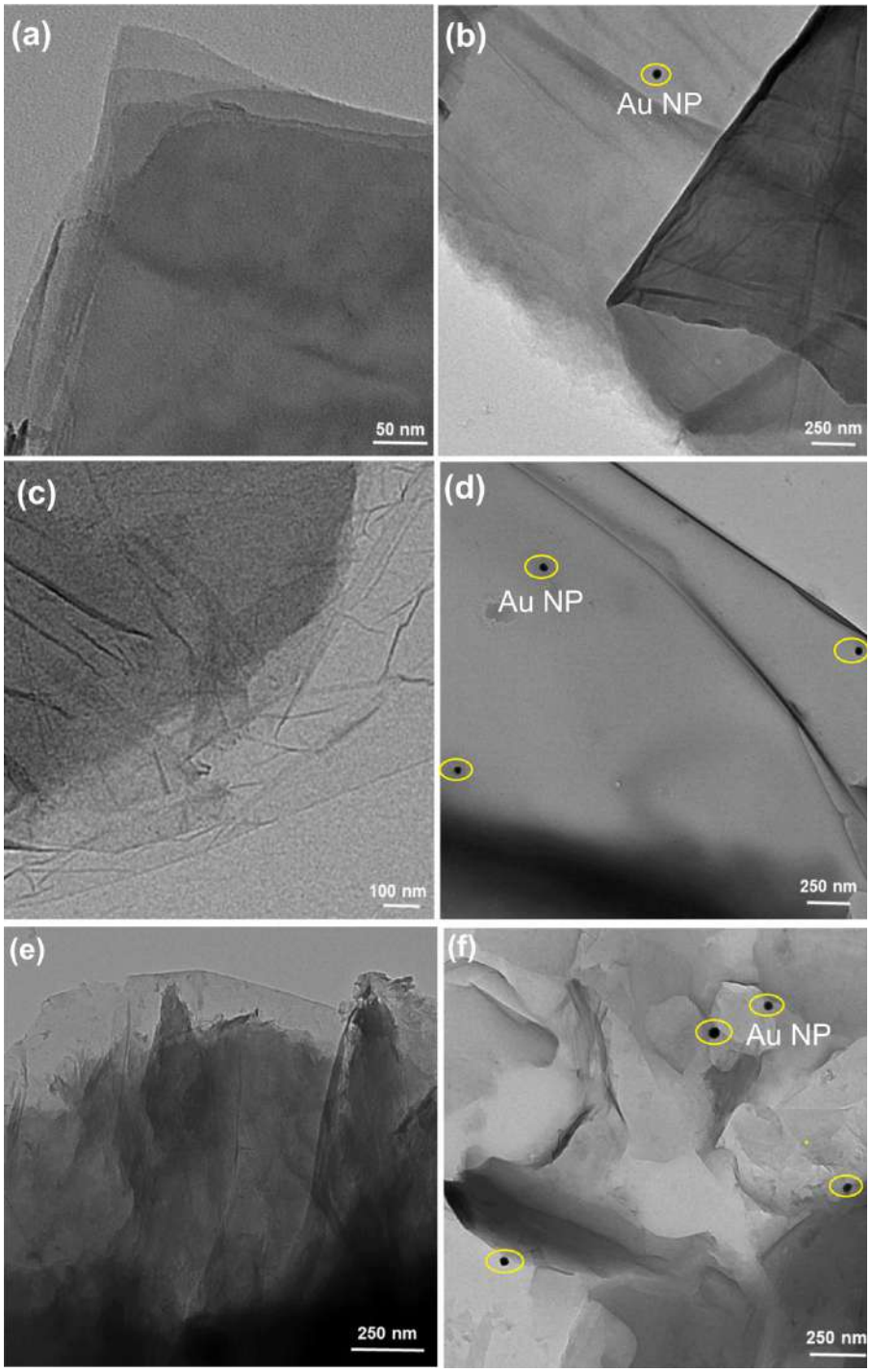

Fig. 2. TEM Images of (a) Few layer GO, (b) GO-Au NPs, where Au NPs distributed distinctly in isolated positions (c) Few layered RGO sheet with a long lateral uniformity, (d) RGO-Au NPs, where individual Au NPs can be easily distinguishable (encircled); (e) GHs, with graphene network is grown in 3-D direction (f) GHs-Au NPs, where Au NPs (encircled) are distributed on and inside the GHs in isolated regions.

3.3. Raman spectroscopy studies

Many sets of Raman measurements were done on the developed nanohybrid SERS platforms to evaluate their SERS activities altogether in similar experimental condition and parameters. Fig. 3(a) shows the Raman spectrum of all the five CNS base materials (on Si-substrate) used in the present investigation. All CNS materials except GQDs showed the characteristic D and G bands centered around 1340 cm^{-1} and 1580 cm^{-1} respectively. In case of GQDs, which showed a broad curve over the entire region owing to its high fluorescing nature, thereby hiding the characteristic bands. A broad nature of D-band (disorder band) is observed in these samples, especially for both GO and RGO; owing to the presence of different oxygen functional groups and combined sp^2 - sp^3 hybridization. Here, the observed Raman intensity (in arbitrary units) is least for CNTs (~250 a.u) and most for GO (~1750 a. u.). Raman spectrum of CNS-Au NPs nanohybrid is shown in Fig. 3(b). A clear enhancement in the Raman intensity (both for D-band and G-band) for all nanohybrid is observed. While on decoration; in case of CNTs, the Raman intensity increased from ~250 to ~750 and for GO it was ~1750 to ~4000 a. u. However, the fluorescence noise

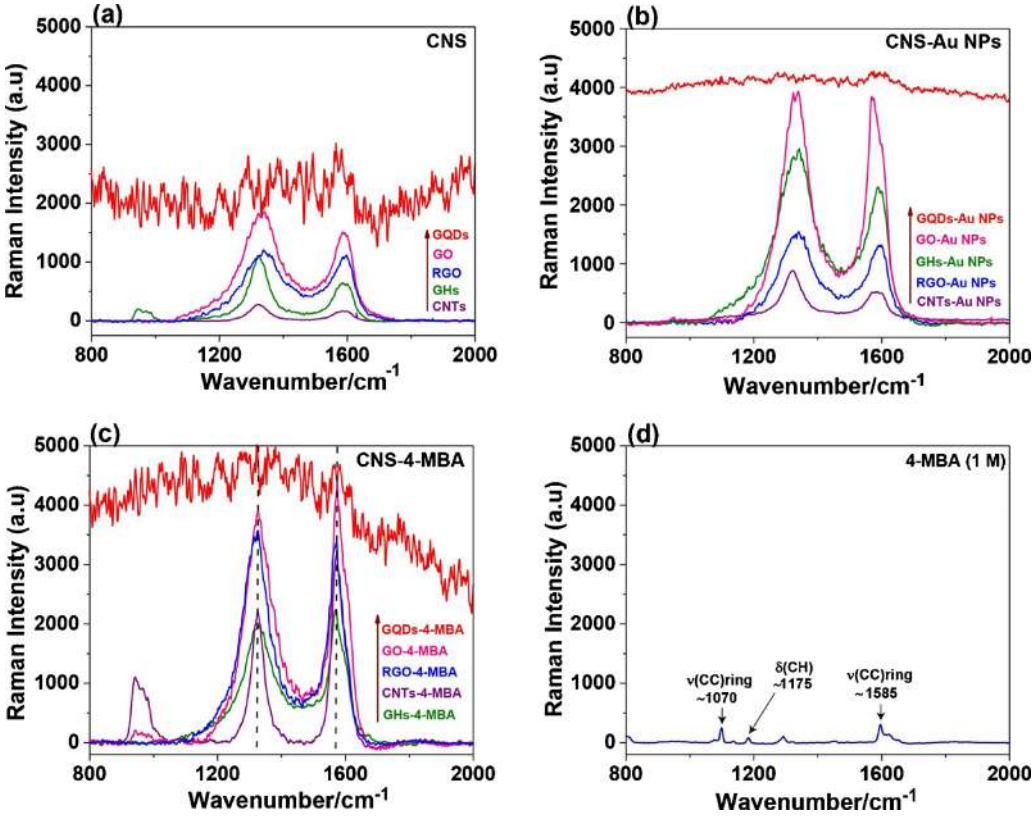

Fig. 3. Raman spectra of (a) all the five CNS base materials on Si-substrate; (b) CNS-Au NPs nanohyrid on Si-substrate; (c) CNS base materials with 4-MBA (5 μL, 1 μM) Raman marker on Si-substrate; (d) 4-MBA (1 M) immobilized on Si-substrate.

level reduced dramatically in case of GQDs-Au NPs nanohybrid comparing to the bare GQDs. In Fig. 3(c), Raman spectrum of CNS with Raman marker i.e. 4-MBA (1 μM) is presented. With Raman marker, G band for all CNS (except GQDs) become sharper due to the prominent Raman peak of 4-MBA centered at ~1585 cm^{-1} {v $(CC)_{ring}$ stretching}, which is coinciding on the same position. With Raman marker, an enhancement in Raman intensity for D band was also noticed for all CNS (except GQDs) as the coinciding band of Raman marker around 1350 cm^{-1} {ν_s (COO-)} is presented on the same position as that of D band. These enhancements in the G and D band may attributed to the chemical enhancement (CM) originated from the parent CNS moiety. Fig. 3(d) denotes the Raman spectra of 4-MBA (1 M) on Si-substrate as a control where all characteristic bands of 4-MBA can be seen with much reduced Raman intensity.

Fig. 4 is a schematic illustration of the proposed study. In part (a) of schematic, molecular structure ($C_7H_6O_2S$) of 4-MBA is shown while in part (b) is the tabular form of the prominent Raman bands of 4-MBA. Part (c) represents the reported Raman spectra of 4-MBA at varying concentration [38]. Part (d) is showing the main SERS strategy adopted in this study. Part (e) is the enhanced Raman spectrum of 4-MBA of 10^{-6} M concentration with and without CNS-Au NPs SERS substrate.

3.4. Surface enhanced Raman spectroscopy (SERS) studies

The Raman mapping for an area of 100 × 100 μM and corresponding SERS results of GQDs-Au NPs-4-MBA and CNTs-Au NPs-4-MBA are shown in Fig. 5. Fig. 5(a) shows the Raman mapping image of GQDs-Au NPs-4-MBA, where the Raman band color profile of 4-MBA centered at 1070 cm^{-1} is presented and the profile is distributed throughout the area in a diffused manner. As the GQDs size (~10 nm) is not as much of the Au NPs (~50 nm) used here, it will be difficult to decorate Au NPs on the GQDs surfaces, rather an opposite manner of decoration (GQDs on Au NPs) or composite formation of GQDs-Au NPs has been taken place. Hence a diffused Raman mapping image is seen in the Fig. 5(a). The Raman spectrum of different regions of GQDs-Au NPs SERS platform with -4-MBA is shown in Fig. 5(b). A significant Raman signal enhancement (for mapped regions 3–6) is observed in prominent bands of 4-MBA at 1585, 1350, 1175, and 1070 cm^{-1} corresponding to v $(CC)_{ring}$ stretching, ν_s(COO-), δ(CH), v$(CC)_{ring}$, respectively which are quite distinguishable from each other. As shown by Hsieh et.al. [38], the prominent peaks of 4-MBA can be obtained with high concentration of 4-MBA i.e. (10^{-3}–10^{-4} M). However, in our study, the reported SERS nanohybrid platforms can precisely detect even 1 μM of 4-MBA with readable signals (Fig. 5). Yet another interesting thing observed was the appearance of both D and G bands in GQDs-Au NPs along with the peaks of 4-MBA. The D and G band were not distinguishable in case of the pure GQDs or GQDs-4-MBA {Fig. 3(a) and (c)} due to strong fluorescence background of GQDs which is masked by the presence of Au NPs.

Raman mapping image and SERS activity CNTs-Au NPs-4-MBA is shown in Fig. 5(c) & (d). In Fig. 5(c), an intense and localized red, yellow and green colored regions are seen, which are directly related to the intensity of Raman signal with an increasing intensity from violet to red. The one dimensionality of CNTs with a diameter of ~ 30 nm limits the degrees of freedom of Au NPs stability on their surfaces, leading to a disproportionate anchorage of Au NPs. The corresponding Raman spectrum (of selected six points) is shown in Fig. 5(d). Interestingly it was noticed that, in case of CNTs-Au NPs nanohybrid, both D and G-bands are almost disappeared (characteristics bands of CNTs) and in the same time, the appearance of two intense and sharp bands of 4-MBA located at 1585 cm^{-1} and 1070 cm^{-1}. Another low intensity peak of 4-MBA centered at ~1175 cm^{-1} is also seen in the spectrum corresponding to 4, 5 and 6 regions in the mapping, probably due to the chemical enhancement caused by the CNTs. Moreover, disproportionate anchorage of Au NPs on CNTs surfaces hinders the synergism between the electromagnetic enhancement (EM, due to Au NPs) and chemical

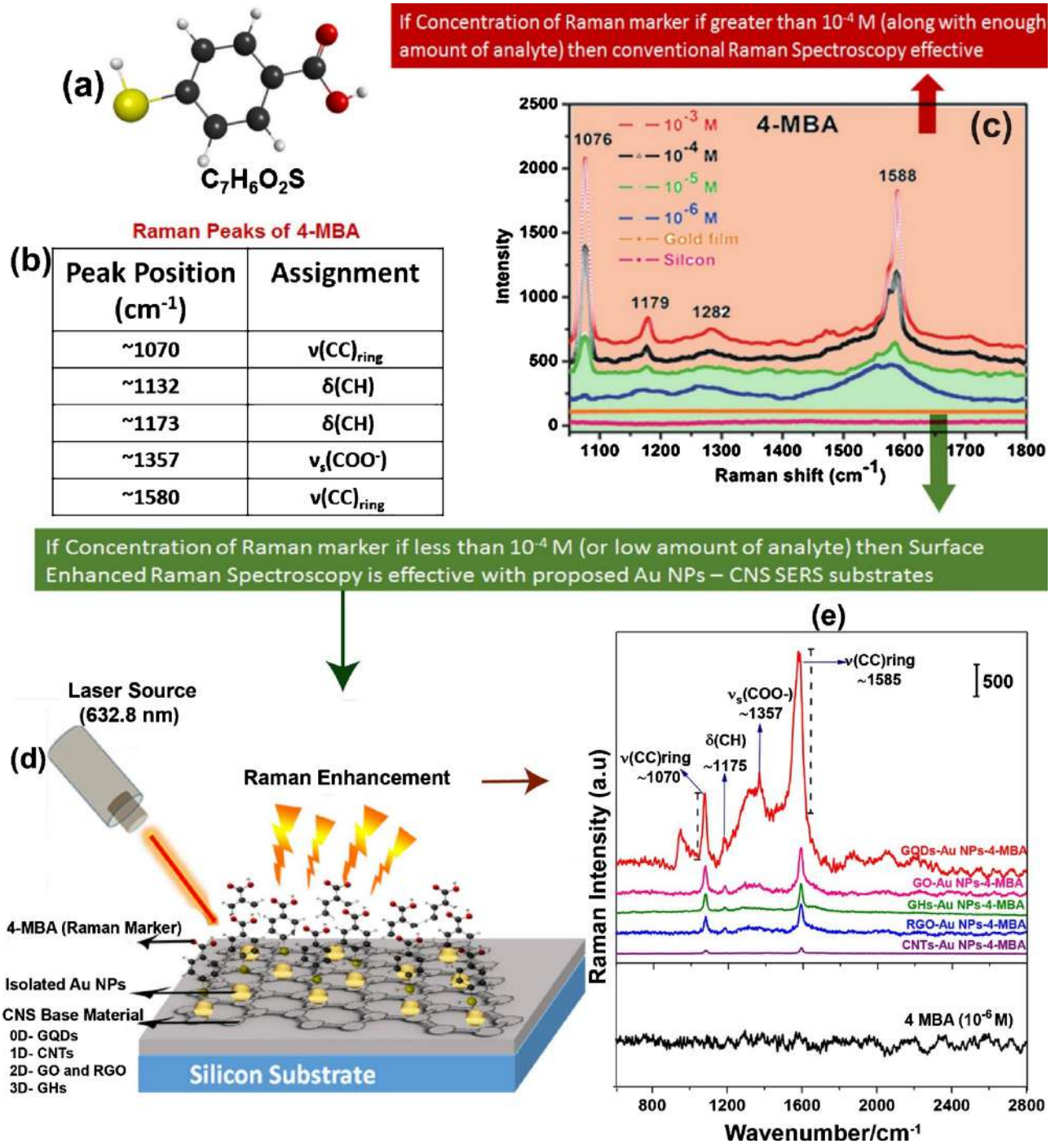

Fig. 4. Schematic illustration of (a) the molecular structure of 4-MBA, (b) the table indicating the Raman bands of 4-MBA; (c) reported Raman spectra of 4-MBA at varying concentration; (d) the SERS system using the laser beam of 632.8 nm with ~5 mw of laser power at the sample and (e) enhanced Raman spectrum of 4-MBA at 10^{-6} M concentration with and without CNS-Au NPs SERS substrate.

enhancement (CM, due to underlying CNTs networks).

Fig. 6 represents the Raman mapping image and corresponding SERS spectra of GO-Au NPs-4-MBA and RGO-Au NPs-4-MBA. The well-defined colored regions (in Fig. 6(a)) from violet to red is a direct indication of the presence of 4-MBA. Obviously, the center part of the substrate is relatively occupied with violet and blue color indicating its more GO nature rather than GO-Au NPs. High intensity (red color) region clearly indicates the probable places of isolated Au NPs over CNS matrix presented, leading to a synergism between electromagnetic enhancement (due to Au NPs) and chemical enhancement (from the underlying CNS matrix). These findings were supported by corresponding Raman spectra of the six different region defined {violet to red, Fig. 6(b)} in the image. From cyan to red color region (marked 3 to 6), the Raman spectra peaks of 4-MBA located at ~1585, 1175, 1070 and 1340 cm^{-1} are well defined even for such a low concentration of Raman reporter molecule. In addition, a weak D and G-band can also be noticed on the same spectrum from the GO matrix. But in region 1 and 2 (violet and blue), the D and G-band are more prominent due to the enhancement from the CNS base material alone, pointing towards a distinct anchorage of Au NPs on the GO matrix. Similar Raman mapping results were obtained for 4-MBA using the same concentration and conditions using RGO-Au NPs SERS substrate {Fig. 6(c)}. Mapping of

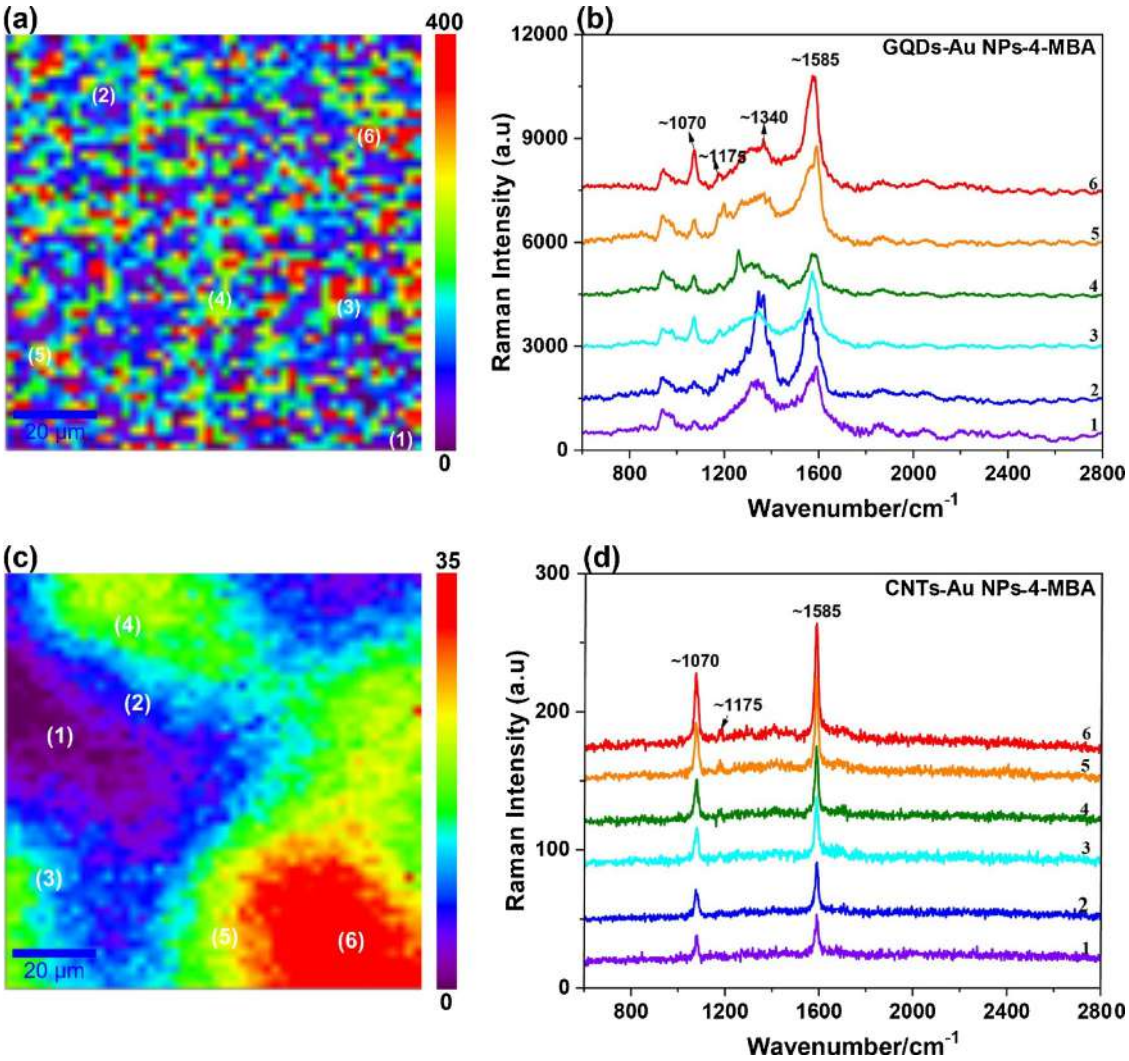

Fig. 5. Raman mapping and SERS spectra for the 0 and 1D CNS-Au NPs-4-MBA SERS substrate; (a) Raman mapping image of GQDs-Au NPs-4-MBA on Si-substrate where six points are marked for corresponding SERS spectra; (b) Corresponding six point's SERS spectra of GQDs-Au NPs-4-MBA;(c) Raman mapping image of CNTs-Au NPs-4-MBA on Si-substrate; (b) Corresponding six point's SERS spectra of CNTs-Au NPs-4-MBA.

Raman marker is more pronounced, which can be visualized through the red regions in the image and corresponding Raman spectra of different points is represented in Fig. 6(d). A more distinct characteristics peaks of 4-MBA were observed throughout the region 2 to 5 in the spectra. Thus, not only GQDs-Au NPs hybrid but, both GO-Au NPs and RGO-Au NPs nanohybrid have shown good SERS performances as they can also detect 1 μM of 4-MBA. And it is due a synergism between electromagnetic (due to Au NPs) and chemical enhancement (due GO and RGO network) in these nanohybrid.

Fig. 7(a) demonstrate the Raman mapping image of the GHs-Au NPs-4-MBA. In this mapping, the signature of 4-MBA is seen at the edges and corners of the scanned area. The central part of the scanned area (violet region) is more occupied with the low profile 4-MBA regions and it is a representation of the GHs-4-MBA rather than GHs-Au NPs-4-MBA. The corresponding Raman spectra of six different regions selected in the scanned area are shown in Fig. 7(b). In this spectra, the prominent bands of 4-MBA can be seen throughout the regions 2 to 6 and the spectra are almost free from various noise disturbances. Hence, 3D GHs-Au NPs do exhibit a good SERS activity for the detection 4-MBA at low concentration (1 μM).

Fig. 8(a) shows a comparative SERS spectrum of all CNS-Au NPs nanohybrid platforms tested against 1 μM of 4-MBA. From this spectra GQDs-Au NPs have shown maximum SERS intensity for 4-MBA and it measured to be ~2500 a. u. (taking the $\nu(CC)_{ring}$ mode as an example).

The enhancement factor (EF) is a parameter to quantify the enhancement ability of the SERS substrate in which each individual molecule that is absorbed on the substrate. Considering the equation from the literature for calculating the enhancement factor (EF) [39];

$$EF = (I_{SERS}/I_{bulk}) \times (N_{bulk}/N_{SERS}) \quad (1)$$

here, I_{SERS} and I_{bulk} are the Raman intensity attained from the SERS substrate and the bulk 4-MBA (here it is taken 1 M). Whereas N_{SERS} and N_{bulk} represent the number of 4-MBA molecules contributed for the SERS signal and the number of molecules contributed for the Raman signal respectively in the proximity of the Raman laser spot.

N_{SERS} and N_{bulk} were calculated using different parameters such as Avogadro's number (6.022×10^{23}), area of the Si wafer used for fabricating the SERS substrate (2.5×10^{-5} m^2), concentration of the Raman marker used (1 M for bulk Raman and 1 μM for SERS) and radius of the laser spot (~643.5 nm). I_{bulk} measured was 250 (a. u.) and I_{SERS} obtained were ~2500 (a. u.) for GQDs-Au NPs-4-MBA, ~750 (a. u.) for GO-Au NPs-4-MBA, ~400 (a. u.) for RGO-Au NPs-4-MBA and GHs-Au NPs-4-MBA and ~100 (a. u.) for CNTs-Au NPs-4-MBA based SERS substrate.

So, applying the values to equation (1) gives the maximum EF for GQDs-Au NPs substrate with an enhancement factor of 10^7. We

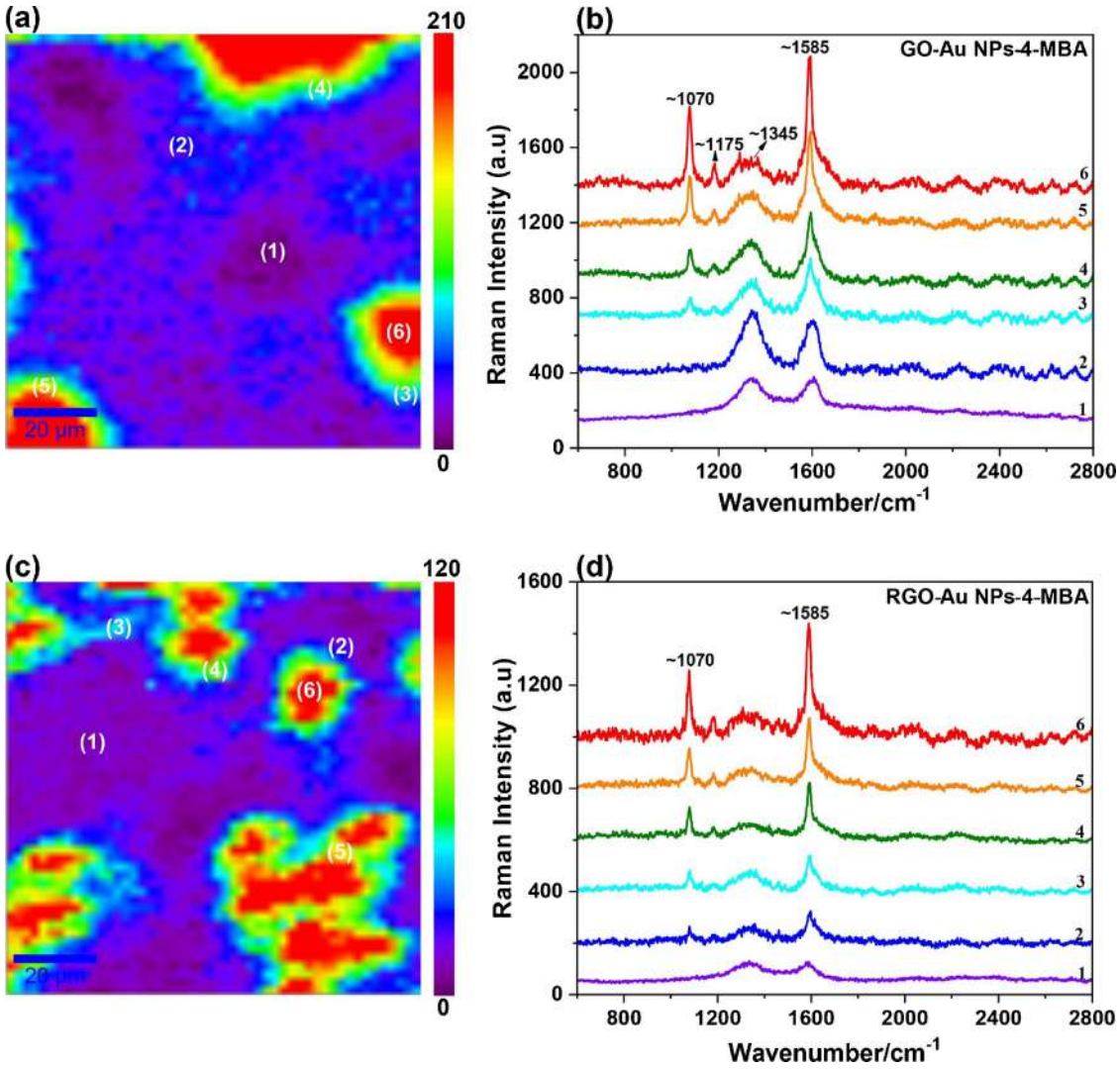

Fig. 6. Raman mapping image and SERS spectra for the 2D CNS-Au NPs-4-MBA substrate of GO-Au NPs-4-MBA and RGO-Au NPs-4-MBA. (a) Raman mapping image of GO-Au NPs-4-MBA on Si-substrate where six points are marked according to different intensity color code; (b) Corresponding six point's SERS spectra. (c)The Raman mapping image RGO-Au NPs-4-MBA on Si-substrate, (d) SERS spectra of RGO-Au NPs-4-MBA.

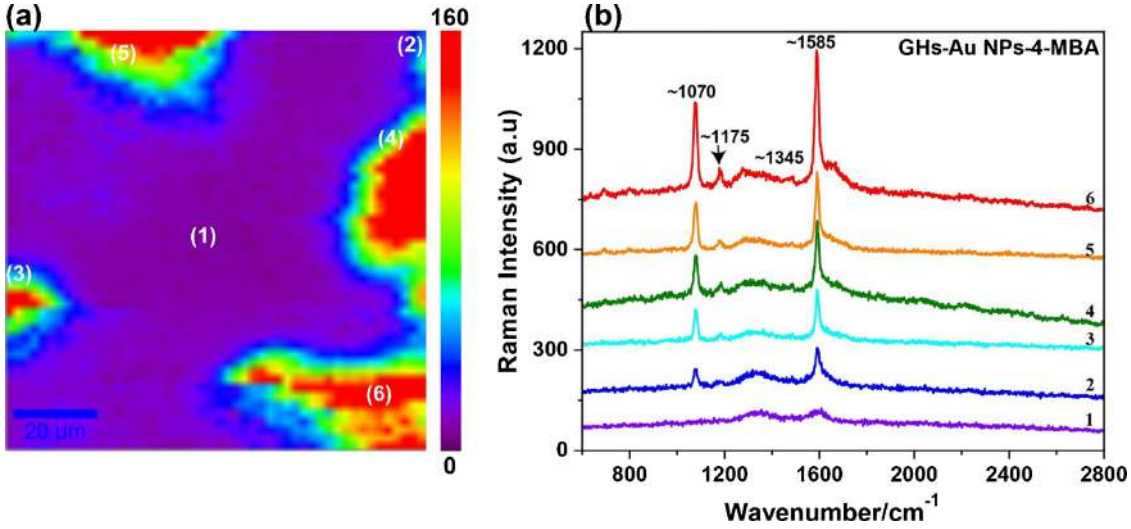

Fig. 7. Raman mapping image of and SERS spectra for the 3D CNS substrate of GHs-Au NPs-4-MBA. (a) Raman mapping image of GHs-Au NPs-4-MBA on Si-substrate where six points are marked for measuring the SERS spectra; (b) Corresponding six point's SERS spectra of GHs-Au NPs-4-MBA.

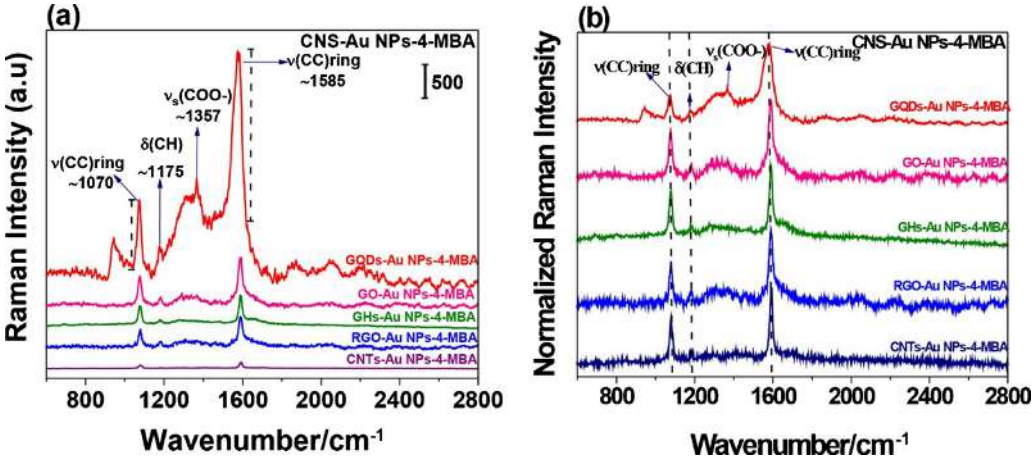

Fig. 8. SERS spectrum of (a) the best five results of different CNS-Au NPs-4-MBA combination; (b) corresponding normalized SERS spectrum.

hypothesis, it may be due to the reverse decoration of GQDs on Au NPs owing to its smaller size along with its abundant functional groups and large number of edges available. This unique architecture of GQDs-Au NPs might ensure an improved charge transfer between the reporter molecules 4-MBA and the GQDs and thereby produce stronger SERS effect [40]. Supporting to this, Liu et al. [41] recent study discusses about this GQDs based SERS enhancement, and according to that report, the enhancement is attributed to the presence of Van Hove singularities in the electronic density of states. The EF of other substrates were also comparatively better and for GO-Au NPs, it is $\sim 3 \times 10^6$; for GHs-Au NPs and RGO-Au NPs, it is $\sim 1.6 \times 10^6$(same for both) and for CNTs-Au NPs, it is $\sim 4 \times 10^5$. In our study, we have utilized isolated nanoparticles rather than bulk nanoparticles. So, in effect, the high enhancement obtained is just by some few isolated Au NPs (close to single particle enhancement) attached to the CNS matrices and it can be much higher if we increase the number of Au NPs. Fig. 8(b) show the normalized SERS plot to identify the peaks in a clearer manner.

4. Conclusions

In summary, we have developed different SERS substrate of isolated Au NPs embedded CNS. The whole class of different dimensional CNS based materials were used ranges from the 0D GQDs to 3D GHs. The as fabricated SERS substrate is advantageous owing to the electromagnetic enhancement from the Au NPs, while simultaneously connecting the surface plasmon of these noble metal nanoparticles by the underlying CNS matrix, which further provides chemical enhancement. For the underlying CNS matrix, i. e. 0D GQDs, 1D CNTs, 2D GO/RGO and 3D GHs along with isolated Au NPs have been fabricated, producing five CNS-Au NPs SERS substrates with enhancements enough to detect as low as 10^{-6} M concentration of Raman reporter molecule; 4-MBA. It is found that the all CNS-Au NPs based substrate showed distinguishable enhancement for the prominent bands of 4-MBA. Further the substrates showed the combined contribution at the peak centered at 1585 cm^{-1} and 1350 cm^{-1} raised both from 4-MBA as well as from the G and D band of the CNSs base materials confirming the presence of substrate materials as well as the Raman marker together. Among all substrate, the highest EF obtained for GQDs-Au NPs combination with an enhancement factor of 10^7. The other substrates also showed considerable and competing enhancement factor to prove themselves to be well promising. Interestingly, the hidden peaks (D and G band) of GQDs by the fluorescence becomes prominent when it works as a GQDs-Au NPs-4-MBA combination. So, the proposed CNS-Au NPs substrates are well promising candidate for the identification and monitoring of molecules relevant to biology, forensics, and chemistry through SERS as well as GERS (Graphene Enhanced Raman Spectroscopy), nevertheless its different dimensionalities.

Acknowledgements

SA, SKS and MK are thankful to Alexander von Humboldt for supporting this research work through AvH Research Group Linkage Program at Faculty of Chemistry, University of Duisburg, Essen, Germany. Authors are thankful to Christina Stefani of Max Planck Institute of Solid State Research, Stuttgart, Germany for XRD measurements. SA is thankful to Max Planck Institute of Solid State Research, Stuttgart for financial support and providing some of the characterization facilities.

Appendix A. Supplementary data

Supplementary material related to this article can be found, in the online version, at doi:https://doi.org/10.1016/j.snb.2018.06.066.

References

[1] A. Campion, P. Kambhampati, Surface-enhanced Raman scattering, Chem. Soc. Rev. 27 (1998) 241–250.
[2] R.L. McCreery, Raman Spectroscopy for Chemical Analysis, John Wiley & Sons, 2005.
[3] B. Pettinger, J. Lipkowski, P.N. Ross, Adsorption of Molecules at Metal Electrodes, VCH, New York, 1992, p. 285.
[4] M. Moskovits, Surface-enhanced Raman spectroscopy: a brief retrospective, J. Raman Spectrosc. 36 (2005) 485–496.
[5] T. Trindade, S. Fateixa, H. Nogueira, Hybrid nanostructures for SERS: materials development and chemical detection, Phys. Chem. Chem. Phys. (2015) 21046–21071.
[6] H. Dai, Y. Sun, P. Ni, W. Lu, S. Jiang, Y. Wang, Z. Li, Z. Li, Three-dimensional TiO_2 supported silver nanoparticles as sensitive and UV-cleanable substrate for surface enhanced Raman scattering, Sens. Actuators B Chem. 242 (2017) 260–268.
[7] J. Lin, Y. Shang, X. Li, J. Yu, X. Wang, L. Guo, Ultrasensitive SERS detection by defect engineering on single Cu_2O superstructure particle, Adv. Mater. 29 (2017) 1604797.
[8] M. Chen, Z. Zhang, M. Liu, C. Qiu, H. Yang, X. Chen, In situ fabrication of label-free optical sensing paper strips for the rapid surface-enhanced Raman scattering (SERS) detection of brassinosteroids in plant tissues, Talanta 165 (2017) 313–320.
[9] F. Tian, J. Conde, C. Bao, Y. Chen, J. Curtin, D. Cui, Gold nanostars for efficient in vitro and in vivo real-time SERS detection and drug delivery via plasmonic-tunable Raman/FTIR imaging, Biomaterials 106 (2016) 87–97.
[10] N. Zhou, G. Meng, C. Zhu, B. Chen, Q. Zhou, Y. Ke, D. Huo, A silver-grafted sponge as an effective surface-enhanced Raman scattering substrate, Sens. Actuators B Chem. 258 (2018) 56–63.
[11] E. Smith, G. Dent, Modern Raman Spectroscopy: A Practical Approach, John Wiley & Sons, 2005.
[12] S. Nie, S.R. Emory, Probing single molecules and single nanoparticles by surface-enhanced Raman scattering, Science (80-.) 275 (1997) 1102–1106.
[13] W. Yan, L. Yang, J. Chen, Y. Wu, P. Wang, Z. Li, In situ two-step photoreduced SERS materials for on-chip single-molecule spectroscopy with high reproducibility, Adv. Mater. 29 (2017) 1702893.
[14] N.J. Halas, S. Lal, W.-S. Chang, S. Link, P. Nordlander, Plasmons in strongly coupled metallic nanostructures, Chem. Rev. 111 (2011) 3913–3961.
[15] P. Kambhampati, C.M. Child, M.C. Foster, A. Campion, On the chemical mechanism of surface enhanced Raman scattering: experiment and theory, J. Chem. Phys. 108

(1998) 5013–5026.
[16] K. Sivashanmugan, H. Lee, C.-H. Syu, B.H.-C. Liu, J.-D. Liao, Nanoplasmonic Au/Ag/Au nanorod arrays as SERS-active substrate for the detection of pesticides residue, J. Taiwan. Inst. Chem. Eng. 75 (2017) 287–291.
[17] C. Han, Y. Yao, W. Wang, L. Qu, L. Bradley, S. Sun, Y. Zhao, Rapid and sensitive detection of sodium saccharin in soft drinks by silver nanorod array SERS substrates, Sens. Actuators B Chem. 251 (2017) 272–279.
[18] C.E. Talley, J.B. Jackson, C. Oubre, N.K. Grady, C.W. Hollars, S.M. Lane, T.R. Huser, P. Nordlander, N.J. Halas, Surface-enhanced Raman scattering from individual Au nanoparticles and nanoparticle dimer substrates, Nano Lett. 5 (2005) 1569–1574.
[19] W. Xie, S. Schlücker, Medical applications of surface-enhanced Raman scattering, Phys. Chem. Chem. Phys. 15 (2013) 5329–5344.
[20] W.L. Barnes, Light-emitting devices: turning the tables on surface plasmons, Nat. Mater. 3 (2004) 588–589.
[21] P. Zijlstra, J.W.M. Chon, M. Gu, Five-dimensional optical recording mediated by surface plasmons in gold nanorods, Nature 459 (2009) 410–413.
[22] K.A. Willets, R.P. Van Duyne, Localized surface plasmon resonance spectroscopy and sensing, Annu. Rev. Phys. Chem. 58 (2007) 267–297.
[23] M. Svedendahl, S. Chen, A. Dmitriev, M. Kall, Refractometric sensing using propagating versus localized surface plasmons: a direct comparison, Nano Lett. 9 (2009) 4428–4433.
[24] H. Tian, N. Zhang, L. Tong, J. Zhang, In situ quantitative graphene-based surface-enhanced Raman spectroscopy, Small Methods 1 (2017) 1700126 (1-6).
[25] X. Ling, J. Zhang, First-layer effect in graphene-enhanced Raman scattering, Small 6 (2010) 2020–2025.
[26] Y. Sun, K. Liu, J. Miao, Z. Wang, B. Tian, L. Zhang, Q. Li, S. Fan, K. Jiang, Highly sensitive surface-enhanced Raman scattering substrate made from superaligned carbon nanotubes, Nano Lett. 10 (2010) 1747–1753.
[27] S. Sun, P. Wu, Competitive surface-enhanced Raman scattering effects in noble metal nanoparticle-decorated graphene sheets, Phys. Chem. Chem. Phys. 13 (2011) 21116–21120.
[28] W. Xu, X. Ling, J. Xiao, M.S. Dresselhaus, J. Kong, H. Xu, Z. Liu, J. Zhang, Surface enhanced Raman spectroscopy on a flat graphene surface, Proc. Natl. Acad. Sci. 109 (2012) 9281–9286.
[29] F. Schedin, E. Lidorikis, A. Lombardo, V.G. Kravets, A.K. Geim, A.N. Grigorenko, K.S. Novoselov, A.C. Ferrari, Surface-enhanced Raman spectroscopy of graphene, ACS Nano 4 (2010) 5617–5626.
[30] L. Ouyang, Y. Hu, L. Zhu, G.J. Cheng, J. Irudayaraj, A reusable laser wrapped graphene-Ag array based SERS sensor for trace detection of genomic DNA methylation, Biosens. Bioelectron. 92 (2017) 755–762.
[31] X. Zhang, Z. Dai, S. Si, X. Zhang, W. Wu, H. Deng, F. Wang, X. Xiao, C. Jiang, Ultrasensitive SERS substrate integrated with uniform subnanometer scale “Hot spots” created by a graphene spacer for the detection of mercury ions, Small 13 (2017) 1603347 (1-8).
[32] C. Zhangt, C. Li, J. Yu, S. Jiang, S. Xu, C. Yang, Y.J. Liu, X. Gao, A. Liu, B. Man, SERS activated platform with three-dimensional hot spots and tunable nanometer gap, Sens. Actuators B Chem. (2017) 163–171.
[33] D. Brunazzo, E. Descrovi, O.J.F. Martin, Narrowband optical interactions in a plasmonic nanoparticle chain coupled to a metallic film, Opt. Lett. 34 (2009) 1405–1407.
[34] C. Ciracì, R.T. Hill, J.J. Mock, Y. Urzhumov, A.I. Fernández-Domínguez, S.A. Maier, J.B. Pendry, A. Chilkoti, D.R. Smith, Probing the ultimate limits of plasmonic enhancement, Science (80-.) 337 (2012) 1072–1074.
[35] D.C. Marcano, D.V. Kosynkin, J.M. Berlin, A. Sinitskii, Z. Sun, A. Slesarev, L.B. Alemany, W. Lu, J.M. Tour, Improved synthesis of graphene oxide, ACS Nano 4 (2010) 4806–4814.
[36] S. Park, J. An, J.R. Potts, A. Velamakanni, S. Murali, R.S. Ruoff, Hydrazine-reduction of graphite- and graphene oxide, Carbon N. Y. 49 (2011) 3019–3023.
[37] Y. Xu, K. Sheng, C. Li, G. Shi, Self-assembled graphene hydrogel via a one-step hydrothermal process, ACS Nano 4 (2010) 4324–4330.
[38] C.-W. Hsieh, P.-Y. Lin, S. Hsieh, Improved surface-enhanced Raman scattering of insulin fibril templated colloidal gold nanoparticles on silicon, J. Nanophoton. 6 (2012) 63501.
[39] Y. Li, J. Yang, Y. Zhou, N. Zhao, W. Zeng, W. Wang, Fabrication of gold nanoparticles/graphene oxide films with surface-enhanced Raman scattering activity by a simple electrostatic self-assembly method, Colloids Surf. A Physicochem. Eng. Asp. 512 (2017) 93–100.
[40] H. Cheng, Y. Zhao, Y. Fan, X. Xie, L. Qu, G. Shi, Graphene-quantum-dot assembled nanotubes: a new platform for efficient Raman enhancement, ACS Nano 6 (2012) 2237–2244.
[41] D. Liu, X. Chen, Y. Hu, T. Sun, Z. Song, Y. Zheng, Y. Cao, Z. Cai, M. Cao, L. Peng, Raman enhancement on ultra-clean graphene quantum dots produced by quasi-equilibrium plasma-enhanced chemical vapor deposition, Nat. Commun. 9 (2018) 193.

Shiju Abraham received his Ph.D. in Physics from Banaras Hindu University, Varanasi, India in 2016. He was working in the area of layered nanomaterials (graphene and its derivatives), emphasizing its application towards biosensing, photocatalysis and surface enhanced Raman spectroscopy. He is presently doing his Post-Doctoral Research in Zuckerberg Institute for Water Research since April, 2017. His main focus of research is on fabricating various patterned surfaces by lithographic techniques and study the self-assembly of lipid bilayers on this patterned surfaces using Atomic Force Microscopy.

Matthias König obtained his M.Sc degree in material science from University of Osnabrück in 2013. Since from the end of 2013 onwards, he is doing his Ph.D. at University of Duisburg-Essen. His research interest is about fabrication and characterisation of SERS substrates on single antenna level.

Sunil Kumar Srivastava obtained his M.Sc. degree in Physics from Banaras Hindu University in 2000 and Ph.D. from Banaras Hindu University in 2005 in the area of “Raman Spectroscopy”.Presently, employed as an Associate Professor at Department of Physics, Mahatma Gandhi Central University, Motihari, India. His current areas of research interests are “Protein-Peptide interaction using Resonance Raman Spectroscopy” and “Surface Enhanced Raman Spectroscopy of biologically important systems”.

Vinod Kumar is a postdoctoral fellow at Prof. Nurit Ashkenasy's group, Department of Materials Engineering, Ben Gurion University of the Negev, Israel. He received his Ph.D. degree in 2014 from Banaras Hindu University, India. His current research interests focus on functional nanopores and nanocontainers for controlled analytical purposes.

Bernd.Walkenfort is a technical Assistent at the working group of Prof. Schlücker in the field of Bio- and Nanophotonics at the University of Duisburg-Essen. Since 2009 his main researche interests is about the construction and operation of optical and electron optical setups for the characterisation of plasmonic nanostructures.

Dr. Anchal Srivastava received his PhD from Banaras Hindu University, India in 2002. He continued in the same department as a Post Doctoral Fellow and later joined as a lecturer in 2004. He is currently serving as a Professor at Department of Physics, BHU. He specializes in the area of synthesis, characterizations and applications of carbon nanomaterials. He has been awarded the Max Planck India fellowship and carried out his research at Max Planck Institute of Solid State Physics, Stuttgart, Germany in Professor Klaus Von Klitzing's group. He has also been awarded the BOYSCAST fellowship from government of India in 2008–2009 during which he carried out research on graphene and related materials at Professor P.M. Ajayan's group in Rice University. He has also been a Visiting Research Scholar at Rensselaer Polytechnic Institute, USA in 2006.

Sensors and Actuators B 218 (2015) 42–50

Contents lists available at ScienceDirect

Sensors and Actuators B: Chemical

journal homepage: www.elsevier.com/locate/snb

Colorimetric detection of cholesterol based on highly efficient peroxidase mimetic activity of graphene quantum dots

Narsingh R. Nirala[a], Shiju Abraham[b], Vinod Kumar[a,c], Anushka Bansal[d], Anchal Srivastava[b,*], Preeti S. Saxena[a,*]

[a] Department of Zoology, Banaras Hindu University, Varanasi 221005, India
[b] Department of Physics, Banaras Hindu University, Varanasi 221005, India
[c] Institute of Nanoscience & Technology, Mohali 160062, India
[d] Department of Metallurgical Engineering, IIT (BHU), Varanasi 221005, India

ARTICLE INFO

Article history:
Received 9 November 2014
Received in revised form 13 March 2015
Accepted 16 April 2015
Available online 2 May 2015

Keywords:
Graphene quantum dots (GQDs)
Horse radish peroxidase (HRP)
Cholesterol oxidase (ChOx)
Colorimetric
Peroxidase mimetic

ABSTRACT

In the present study, we report graphene quantum dots (GQDs), an enzyme mimetic of horse radish peroxidase (HRP), for unprecedented detection of free cholesterol. Synthesized directly from graphite using simple and quick one step wet chemical method, these GQDs in the presence of H_2O_2 exhibit highly efficient catalytic activity toward the oxidation of peroxidase substrate 3,3,5,5-tetramethylbenzidine (TMB) to produce a blue colored product. The proposed detection system based on GQDs allows wide range (0.02–0.6 mM) of cholesterol sensing with a detection limit as low as 0.006 mM. Further, higher V_{max} (7.3×10^{-6} M s^{-1}) along with lower K_m (0.01 mM) attest enhanced peroxidase like catalytic activity and better binding affinity of cholesterol oxidase (ChOx) to cholesterol resulting in good biosensor stability and resistance to environmental interferences. The proposed method without the use of sophisticated instruments perceives the cholesterol using naked eye with blue color compound formation. The potential of the method to be applied on field is shown by the proposed cholesterol measuring color wheel, where the shades of color are related to actual levels of cholesterol in the sample.

1. Introduction

Cholesterol is an important part of animal cell membranes, since it is required to maintain membrane structural integrity and fluidity over the range of physiological temperatures. Apart from its importance within cells, it also acts as a precursor for the biosynthesis of steroid hormones, bile acids, and vitamin D. Because of its essentiality for animals, all cells can synthesize cholesterol from simpler molecules. Desirable amount of cholesterol in healthy human serum is 200 mg/dL. Unregulated cholesterol production in human body can lead to serious diseases. When the summation of the amount of cholesterol synthesized and the cholesterol obtained via diet exceeds the amount required for the synthesis of membranes, bile salts, and steroids [1,2] pathological accumulations of cholesterol in blood vessels (atherosclerotic plaques) can develop, resulting in atherosclerosis, that is obstruction of blood vessels [3]. Linked to high levels of free cholesterol in the blood, particularly to high levels of low density lipoprotein (LDL) bound cholesterol, atherosclerosis results in arterial diseases with a possibility of culminating into a fatal heart attack [4]. Thus accurately detecting the levels of free cholesterol in blood serum and food are major parameters for diagnostic treatment. Initial analytical methods developed for cholesterol detection such as fluorescence based assay [5], electrochemical methods [6,7] and molecular imprinting [8] technology are all expensive and prone to denaturation, thus demanding alternative, highly sensitive, selective, simple and cost effective methods.

Horse radish peroxidase (HRP) are a large class of enzyme that catalyzes the oxidation-reduction reaction in analytical diagnosis [9–11]. However, expensive preparation/purification and storage processes along with extreme environmental sensitivity restrict HRP to be used in analytical diagnostics [12–14].

In order to overcome such challenges, recent research endeavors are committed to search or synthesize efficient HRP enzyme mimetic with strong catalytic activity and stability in both physical and physiological conditions for numerous biological applications. By way of examples for naturally occurring enzyme mimetics, hemin [15], porphyrin [16] and DNAzymes [17] have been reported, but being proteinaceouse in nature they are also susceptible to

* Corresponding authors. Tel.: +91 9450593210; fax: +91 0542 23681.
E-mail addresses: anchalbhu@gmail.com (A. Srivastava), pssaxena@rediffmail.com (P.S. Saxena).

http://dx.doi.org/10.1016/j.snb.2015.04.091
0925-4005/

environmental variations; specially pH and temperature. In contrary to natural enzymes, HRP enzyme mimetic synthesized using nanomaterials offers required high stability along with several advantages such as low cost, high surface area, tenability in catalytic activities and ease of preparation and purification [18]. For example, discovery of intrinsic peroxidase like activity in Fe_3O_4 nanoparticles opened a new area of research in nanomaterials based enzyme mimetics [19]. Similarly, peroxidase like activity of Co_3O_4 have been explored for sensing of H_2O_2 and glucose [20]. Down this line carbon nanomaterials have also been examined for their peroxidase like activity [21–23], among which single walled carbon nanotubes [24], graphene oxide [25], carbon dots [26], and graphene dots [27] have shown promising peroxidase like catalytic activity. Though used effectively for H_2O_2 and glucose detection, these carbons based nanomaterials demand complex and time consuming synthesis process. Moreover, the sensitivity of these methods is not satisfactory, particularly for GO, due to its low catalytic activity. To address these drawbacks, the development of low concentration, high diffusion rate and enhanced catalytic activity graphene-based nanomaterials is important.

Graphene quantum dots (GQDs), a class of carbon nanomaterials containing one or few layered sheets with lateral dimension less than 100 nm, have several unique properties over above discussed micrometer-sized SWCNTs, graphene and GO sheets [28]. GQDs have been recognized as better electron transporters and acceptors, rendering them as optimal candidates for electrochemical sensing materials [29]. Due to their quantum confinement [30] and edge effects [31] they possess high surface area, extraordinary optical, electrical and chemical properties [32–34] along with good solubility, robust chemical inertness, efficient stability against photo bleaching and excellent biocompatibility [35–37]. With such unique properties it is no wonder that GQDs have been explored for diverse applications in various sectors including biological imaging [38], electrochemical biosensors [39], organic photovoltaic devices [40], colorimetric detection [26] and catalysis [41]. GQDs with peroxidase like activity were first reported [42] in the year of 2013, but this work involved time consuming multistep synthesis process using special equipment's and expensive starting materials (such as carbon fibers and graphene oxide). Peroxidase like activity of GQDs have been only used for H_2O_2 detection [42].

To best of our knowledge the detection of free cholesterol in a complex system like human serum using peroxidase (HRP) like of GQDs has not been reported till date.

Hence, for the first time we report GQDs synthesized by a simple wet chemical method, as horse radish peroxidase (HRP) enzyme mimetic for enhanced free cholesterol detection. The synthesis route using simple instruments is not only cost effective due to the usage of graphite powder as the starting material, but is also fast and facile owing to one step synthesis of large scale graphene quantum dots (GQDs) with highly functionalized periphery carboxylic groups attached through acidic treatment of graphite powder. These as synthesized GQDs show efficient catalytic activity toward the oxidation of peroxidase substrate 3,3,5,5-tetramethylbenzidine (TMB) in the presence of H_2O_2 to produce a blue colored product used for the estimation of hydrogen peroxide and cholesterol (ChO). Higher V_{max} and lower K_m value suggest highly efficient peroxidase catalytic activity which supersedes the earlier reports of micrometer-sized GO sheets and many other nanomaterials. Finally to demonstrate the efficacy of our simple, economical yet sensitive system to work in complex systems, we have done successful free cholesterol detection in human serum sample, producing efficient results perceivable by naked eyes without the requirement of any specialized instruments by the blue colored compound formation when the system detects cholesterol. The potential of the method to be used effectively on field by simple observation lies in the direct relation the cholesterol level has with the obtained color shade. Hence, the current work proposes a cholesterol detection color wheel, which in future could be used to along with cost effective GQD based cholesterol detection strips for direct, effective and quick cholesterol measurement.

2. Materials and methods

2.1. Materials

Graphite powder (purity ≥99.99%), cholesterol oxidase and cholesterol were purchased from Sigma Aldrich, New Delhi, India. H_2SO_4 (98%) and HNO_3 (69–72%) were obtained from SD fine Chem. Ltd., Mumbai, India. 3,3′,5,5′-tetramethylbenzidine (TMB), hydrogen peroxide (H_2O_2), sodium carbonate (Na_2CO_3), disodium hydrogen phosphate (Na_2HPO_4) and monobasic sodium phosphate (NaH_2PO_4) were purchased from Fischer Scientific India Pvt. Ltd. All the chemical reagents used were of analytical grade. Dialysis bag was procured from Millipore Merck Ltd., Mumbai, India. Double distilled water was used throughout the experiment. All the reagents were used as received.

2.2. Instrumental details

The UV–vis absorption spectra were collected using a Perkin Elmer UV–Visible-Lambda 25 spectrophotometer. The morphological changes were observed employing using FEI Tecnai-G2 transmission electron microscopy (TEM). Fourier transform infrared (FT-IR) spectroscopy (Perkin Elmer Spectrum 65, FT-IR spectrometer) was employed for the identification of molecular structures. Atomic force microscope (AFM) images were acquired using Bruker Mutliomode 8 AFM. The specimen was prepared by casting the aqueous suspensions of GQDs on freshly cleaved mica surface and dried in air.

2.3. Methods

2.3.1. Synthesis of graphene quantum dots (GQDs)

GQDs were synthesized using graphite powder via wet chemical oxidation method. In brief, 0.20 g of graphite powder was added to a mixture of concentrated H_2SO_4 and HNO_3 (3:1, v/v). The solution was further sonicated for 2 h and 30 min at room temperature (RT) followed by stirring for 45 min at 90 °C. The resulting yellow colored solution was cooled to RT. The pH was adjusted to 7 with NaOH. The solution was further dialyzed through a dialysis bag (retained molecular weight: 2000 Da) for 3 days to get the final product as GQDs.

2.3.2. H_2O_2 detection using GQDs

Stock solution of TMB (5 mM) was prepared in anhydrous ethanol. Phosphate buffered saline (0.2 M) was prepared and pH was set to 3.5. For H_2O_2 detection, 10 μL of GQDs (0.5 μg/mL) were added to 150 μL of PBS solution having 20 μL of different concentrations of H_2O_2. 20 μL of TMB (5 mM) was added to the above reaction mixture followed by 5 min incubation. The maximum absorbance of the oxidized TMB was recorded at 652 nm. The final concentrations of H_2O_2 in the system varied from 0.02 mM to 0.1 mM.

2.3.3. Cholesterol detection using ChOx and GQDs

Cholesterol detection was done as follows: (a) 5 μL of ChOx (0.5 mg/mL) and 50 μL of different concentrations of cholesterol in PBS (0.5 mM, pH 7.0) were incubated at 37 °C for 30 min; (b) 10 μL of GQDs (0.5 μg/mL) and (c) 150 μL of PBS (0.2 M) (pH 3.5) were added into the above solution. The measurement was started by addition of 20 μL of TMB (5 mM). The product color was monitored

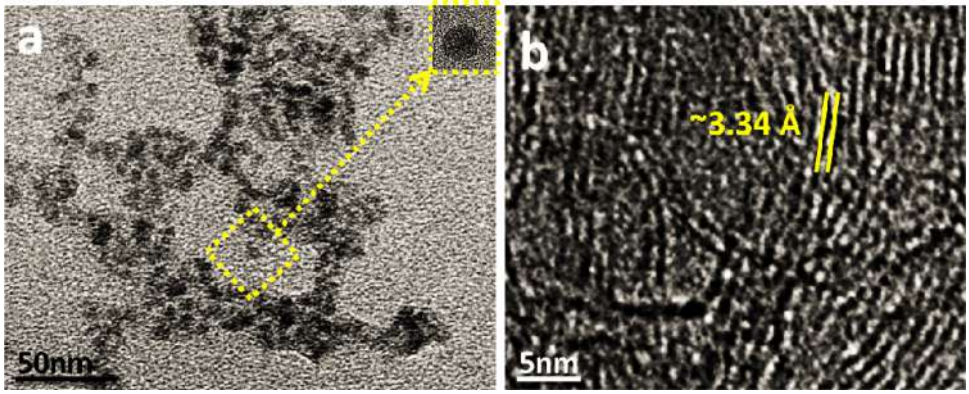

Fig. 1. (a) TEM and (b) HRTEM images of GQDs.

at 652 nm for 5 min. The final concentrations of cholesterol in the system varied from 0.02 mM to 0.6 mM.

3. Results and discussion

3.1. Characterization of GQDs

The optical properties of the source material i.e. graphite powder and synthesized GQDs were characterized using UV–vis absorption spectroscopy [(Fig. S1, Electronic Supplementary Information (ESI)]. The absorption peak of graphite powder as shown in Fig. S1(a) occurred at λ_{max} 270 nm which was blue shifted in case of GQDs as seen at λ_{max} 227 nm in Fig. S1(b) which pointed toward the fabrication of GQDs from graphite. Apart from absorption peak at λ_{max} 227 nm, one more shoulder peak at λ_{max} 303 nm was seen in GQDs. Both of these peaks developed due to transition of π–π^* C=C and n–$\pi^*$of C=O respectively.

The Fourier-transform infrared (FT-IR) spectra were used to identify the surface groups of the GQDs (Fig. S2, ESI). The presence of various several peaks confirmed the presence of various oxygen-containing groups, including carbonyl, carboxyl, hydroxyl, and epoxy groups that were introduced to the edges and onto the basal plane. In the FT-IR spectra of GQDs (Fig. S2), the peak at 1640 cm^{-1} was attributed to C=O stretching vibrations of carboxylic groups and 1390 cm^{-1} was assigned to (C—O) present in carboxylic group. The peak found at 1112 cm^{-1} was due to epoxide (C—O—C), peaks at 3436 cm^{-1} was imputable to —OH functional groups.

Transmission electron microscopy (TEM) and HRTEM (Fig. 1) images of (a) GQDs revealed narrow size distribution of monodispersed GQDs with an average diameter of 2 nm. Inset picture in Fig. 1(b) was high resolution TEM of GQDs which bespoke multilayered polycrystalline structure with interlayer spacing with ~3.3 Å.

Further, AFM study was also carried out to confirm the mostly average thickness of GQDs and was ascertained to be ~2 nm with a modest size distribution (Fig. 2).

3.2. Study of peroxidase mimetic catalytic activity of GQDs

The GQDs catalyzed peroxidase substrate (TMB) in the presence of H_2O_2 to rapidly produce a blue colored product from colorless used for cholesterol detection. Fig. S3 (ESI) shows the typical absorbance peak of oxidation used for estimation of hydrogen peroxide and products of TMB is at 652 nm. The absorbance of the

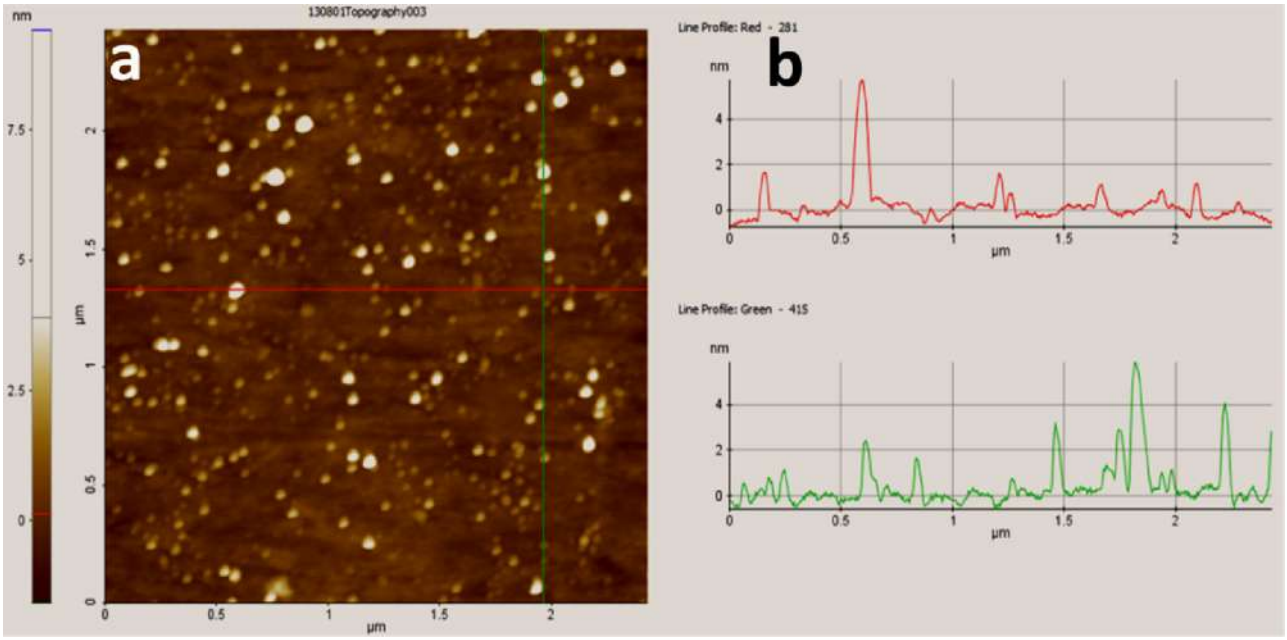

Fig. 2. (a) AFM image of the particle size distributions of GQDs and (b) a height profile along red and green line of the GQDs confirming average thickness of 2 nm. (For interpretation of the references to color in this figure legend, the reader is referred to the web version of the article.)

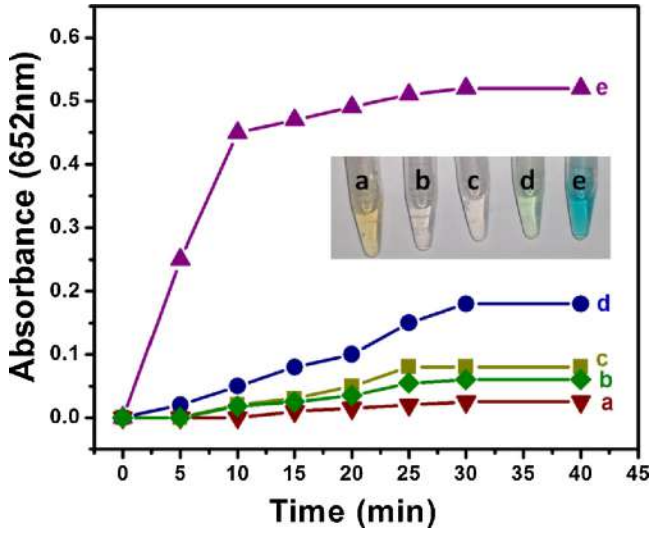

Fig. 3. Time-dependent absorbance changes at 652 nm of TMB in different reaction systems: (a) GQDs, (b) TMB, (c) GQDs + TMB, (d) TMB + H_2O_2 and (e) TMB + GQDs + H_2O_2. (For interpretation of the references to color in the text citation, the reader is referred to the web version of the article.)

GQDs–TMB–H_2O_2 system at 652 nm was much higher than that of the TMB–H_2O_2 and GQDs–TMB systems.

A small absorbance change of the system [Fig. 3 curve (d)] was observed due to the low reaction rate of TMB and H_2O_2. The absorbance intensity of the system was significantly enhanced with the addition of GQDs and was stable for a long duration [Fig. 3 curve (e)]. Fig. 3(inset) indicated optical image of oxidation color reaction of TMB with H_2O_2 catalyzed by GQDs.

GQDs were expected to be more stable than natural enzymes. It is known that the catalytic activity of HRP is largely inhibited after incubation at lower or higher pH and high temperatures (above 60 °C) [26]. To investigate the effect of pH on the GQDs-based catalytic reaction, the absorbance intensities of the system with or without H_2O_2 (50 mM) in 0.2 M acetate buffer of different pH were detected. As shown in [Fig. S4(a), ESI] the catalytic activity of GQDs was affected by pH. The catalytic oxidation of TMB with H_2O_2 using GQDs was much faster in acidic solutions, and the optimum pH was 3.5 according to the best signal-to-noise level. Also the effect of temperature was studied and it is observed that the catalytic activity of the GQDs was optimum at all temperature ranges [Fig. S4(b), ESI].

GQDs in contrast to HRP efficiently showed its catalytic activity even the concentration of H_2O_2 reached high levels [Fig. S4(c), ESI]. The catalytic activity of the GQDs was also studied by varying the concentration of GQDs [Fig. S4(d), ESI]. It was seen that the activity of GQDs was maximum when the concentration of GQDs reached to a level of 2–3 μg/ml. If the concentration was further increased, the activity decreased due to the other possible interactions of GQDs that may decrease the free GQDs available for the catalytic reaction.

To investigate the kinetic mechanism of the peroxidase-like activity of the GQDs, apparent steady-state kinetic parameters for the peroxidase-like color changing reaction were determined by changing the concentrations of TMB and H_2O_2 in this system, respectively. Initial reaction rate was calculated using the Beer–Lambert Law:

$$C = \frac{A}{\varepsilon b} \quad (1)$$

where, c is the substrate concentration, A is the absorbance, b is the thickness of the solution. The absorbance data were back-calculated to give concentrations using a molar absorption coefficient, ε, of 39,000 $M^{-1}\,cm^{-1}$ for the TMB derived oxidation products which is high concentration to other any nanomaterials [26]. Apparent steady-state reaction rates at different concentrations of the substrate were obtained by calculating the slopes of the absorbance changes with time [Table S1, ESI]. In this work, typical Michaelis–Menten curves were obtained for both TMB and H_2O_2. The Michaelis–Menten constant (K_m) and maximum initial velocity (V_{max}) were obtained from Michaelis–Menten equation (Fig. 5, Eq. (2)):

$$v_0 = \frac{V_{\max}[S]}{K_m + [S]} \quad (2)$$

where, v_0 is initial velocity, V_{max} is maximum initial velocity, $K_m = V_{max}/2$, [S] = substrate concentration. Smaller the value of K_m, stronger is the affinity between enzyme and substrate, resulting into more efficient catalyst. Higher V_{max}, suggested that higher catalytic toward TMB in presence of H_2O_2. The K_m value for GQDs was found to be higher in case of H_2O_2 (8 mM) than HRP as shown in Fig. 4(b), whereas in case of TMBs, it was found to be little smaller than HRP (0.01 mM) as shown in Fig. 4(a). These results can be attributed to the fact that in the first step, the concentration of TMB was kept fixed, therefore, the number of active sites that were present was fixed, constraining the catalytic activity and hence K_m value obtained was greater. Unlike, in the second step, the concentration of TMB was increased leading to enhanced number active number of sites and hence catalytic activity increased to a large extent resulting in lower K_m value. The observed high catalytic activity may be due to the small size of GQDs, which have a higher density of functional groups and unpaired electrons on its edge. Density functional theory study demonstrated that the functionalization of graphene surfaces with carboxylic groups was significant in the reduction reaction of H_2O_2 [27]. So, we presumed that similar effect existed for the edge functionalized carboxylic in the GQDs. Based on the above discussion, we can conclude that the catalytic mechanism probably originates from an increase in the electron density and mobility in the GQDs because of electron transfer from lone-pair electrons in TMB amino groups to the GQDs. This would result in acceleration of electron transfer from the GQDs to H_2O_2 [12], and the reaction rate of TMB oxidation by H_2O_2 would increase.

The comparison of the kinetic parameters of different nanomaterials and HRP using TMB as a substrate is shown in Table 1.

It was inferred from Fig. 5, the K_m value was found very low as compared to HRP and other nanomaterial and V_{max} was quite high because GQDs synthesized have larger surface area allowing more interaction with cholesterol oxidase and TMB molecules, highly functionalized, biocompatible and conductive. Thus it was established that GQDs shows promising behavior in cholesterol sensing applications.

3.3. H_2O_2 detection using GQDs as the catalyst

Apart from these advantages, GQDs can detect H_2O_2 even when its concentration is very low (2 μg/mL). As it can be seen from Fig. S4(a), ESI, a dramatic increase in the absorbance intensity was observed as the concentration of H_2O_2 was increased from 0.01 to 0.1 mM. This GQDs based method allows the detection of H_2O_2 at

Table 1
Comparison of the kinetic parameters of different nanomaterial and HRP using TMB.

Catalyst	K_m (mM)	V_{max} ($M\,s^{-1}$)
HRP [26]	0.434	10×10^{-8}
C-dots [43]	0.039	3.61×10^{-8}
Si-dots [43]	1.502	5.65×10^{-8}
GQDs	**0.01**	$\mathbf{7.3 \times 10^{-6}}$

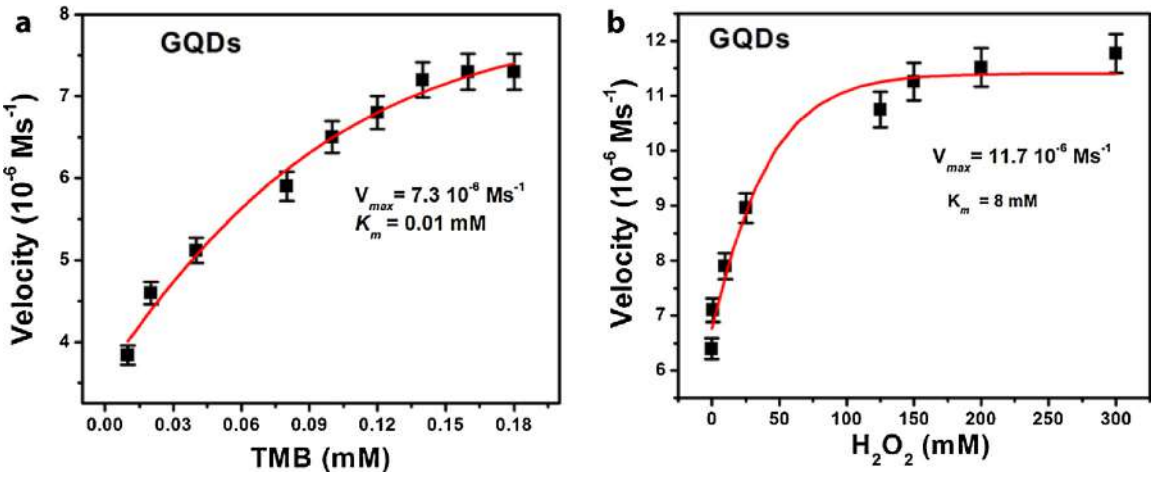

Fig. 4. Steady state kinetic assay and catalytic mechanism of graphene quantum dots (a, b). The velocity (v) of the reaction was measured using 2 μg/mL GQDs in 10 mL of 0.2 M NaAc buffer at pH 3.5 and 35 °C. The error bars represent the standard error derived from three repeated measurements. (a) The concentration of H_2O_2 was 50 mM for GQDs and the TMB concentration was varied (b) the concentration of TMB was 0.8 mM for GQDs and the H_2O_2 concentration was varied.

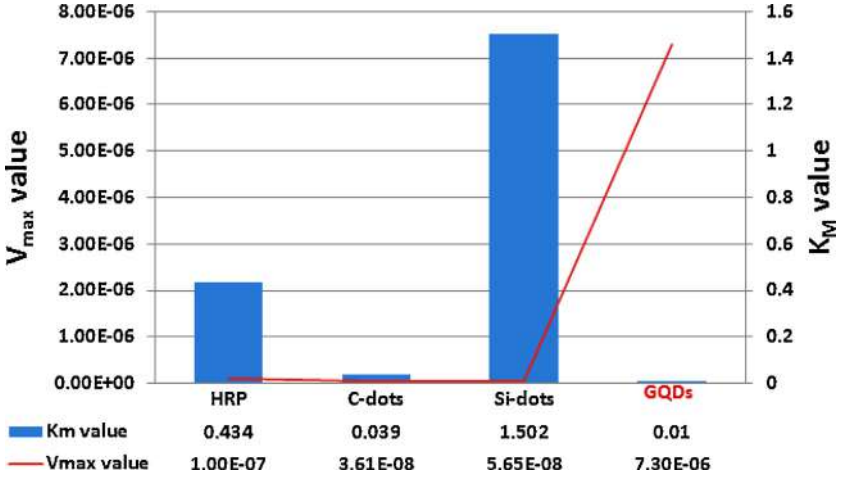

Fig. 5. Comparative study of discussed kinetic parameters (V_{max} and K_m) with the earlier reported biosensors.

concentration as low as 0.009 mM, which is lower than that of other nanomaterials catalyzed methods [Fig. S4(b), ESI].

3.4. Cholesterol detection using ChOx and GQDs

H_2O_2 is the main product of cholesterol oxidation by ChOx in the presence of oxygen. Thus, cholesterol detection could be realized by coupling GQDs based catalytic methods with the ChOx based cholesterol oxidation [Fig. 6].

To confirm the capability of the described cholesterol sensor, the absorbance of the system with different concentrations of cholesterol was analyzed. By considering the time efficiency and the signal to noise level, we chose 5 min as the optimum catalytic time of ChOx. To optimize the concentration, the absorbance intensity with the addition of cholesterol into the system for different concentrations was recorded, since just visualization was not enough to detect such small color variation shown in Fig. 7.

From the absorbance graph, we concluded that the as the concentration rose, the absorbance also increased indicating the increased rate of interaction between the reactants [Fig. 8(a)]. Also it can be observed that the minimum possible concentration of cholesterol that be detected through our proposed GQD system is 0.006 mM has been calculated by calibration curve [Fig. 8(b)]. Lower detection limits (LODs) have been calculated based on the standard deviation of the response (SD) and the slope (B) of the calibration curve (Fig. 8(b)) at levels approximating the LOD according to the formula: LOD = 3(SD/B). For doing so, the standard deviation of the response has been determined utilizing standard deviation of y-intercepts of regression lines.

3.5. Selectivity of the biosensor

The proposed GQDs based system also shows high selectivity for cholesterol detection. The selectivity described here was tested with cholesterol and other interference like uric acid, urea, ascorbic acid, cysteine and glucose which is generally present in blood, each at 1 mM).

The concentration was 0.6 mM for cholesterol, 2 mM for uric acid, urea, ascorbic acid, cysteine and glucose. This result clearly demonstrated that this GQDs based method showcased high selectivity toward cholesterol detection. Furthermore, the discrimination of cholesterol against others can be made by the naked eye [Fig. 9(a)]. From Fig. 8(a), the percentage interference (% interference) was calculated and a maximum of 21% for glucose, 16% for uric acids, 14% for urea, 13% for cysteine and 10% for ascorbic acids were found (Table 2).

Using this method, we detected cholesterol in complex systems (blood samples). Fig. 9(b), illustrates the response of cholesterol on

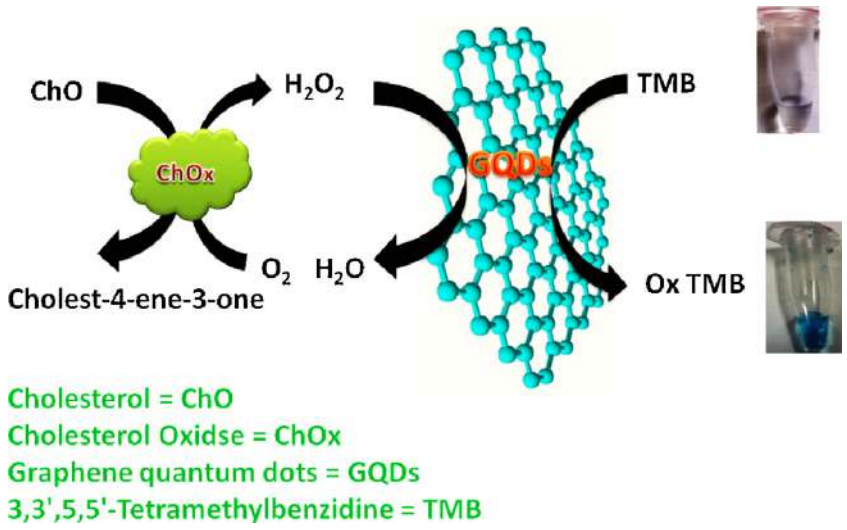

Fig. 6. Schematic illustration of oxidation color reaction of TMB by H_2O_2 catalyzed by GQDs.

Table 2
Sensing characteristics of the proposed methods (GQDs) along with those reported in literature.

Sensing element	Sensing method	Linear range	Detection limit	Reference
Molecularly imprinted polymer	Impedance	5–30 M	0.42 M	[44]
Ag nanoparticles	Amperometric	2.8×10^{-4}–3.3×10^{-2} M	2.8×10^{-4} M	[45]
ChOx/hemoglobin	Amperometric	10–600 M	9.5 M	[46]
ChOx/conducting polymer	Amperometric	10–130 M	0.3 ± 0.04	[47]
ChOx/peroxidase	Colorimetric	0–7 mM	–	[48]
ChOx/DNAzymes	Colorimetric	1–30 M	0.1 M	[49]
GQDs	Colorimetric	0.02–0.6 mM	0.006 mM	Present work

Fig. 7. Optical picture of GQDs + TMB + ChOx and interaction with different concentration of cholesterol (a) 0.02 mM/L (cholesterol), (b) 0.04, (c) 0.06, (d) 0.08, (e) 0.1, (f) 0.2, (g) 0.4, (h) 0.6)]. (For interpretation of the references to color in the text citation, the reader is referred to the web version of the article.)

application of this method to different serum samples and inset shows the images of production of colored product. These results indicated that the proposed method was largely free from the complicated sample matrix effect of the blood sample and the results agreed well with those obtained using the conventional Auto analyzer method (based on enzymatic reaction) method (Table S1).

Fig. 10(a) attests the consistent results of the proposed system when the experiment was repeated 8 times prepared in same set of conditions. Also, Fig. 10(b) shows consistent reproducibility of the results obtained when the experiment was performed using five samples prepared in same set of conditions.

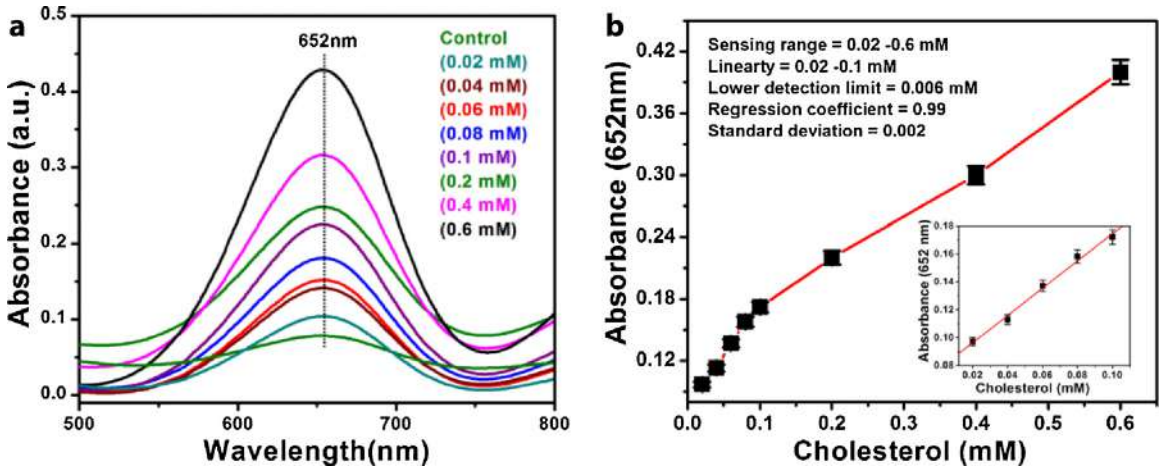

Fig. 8. (a) UV–vis spectra of GQDs + TMB + ChOx and interaction with different concentration of cholesterol (b) the calibration curves of cholesterol. Error bars represent the standard deviation for three measurements.

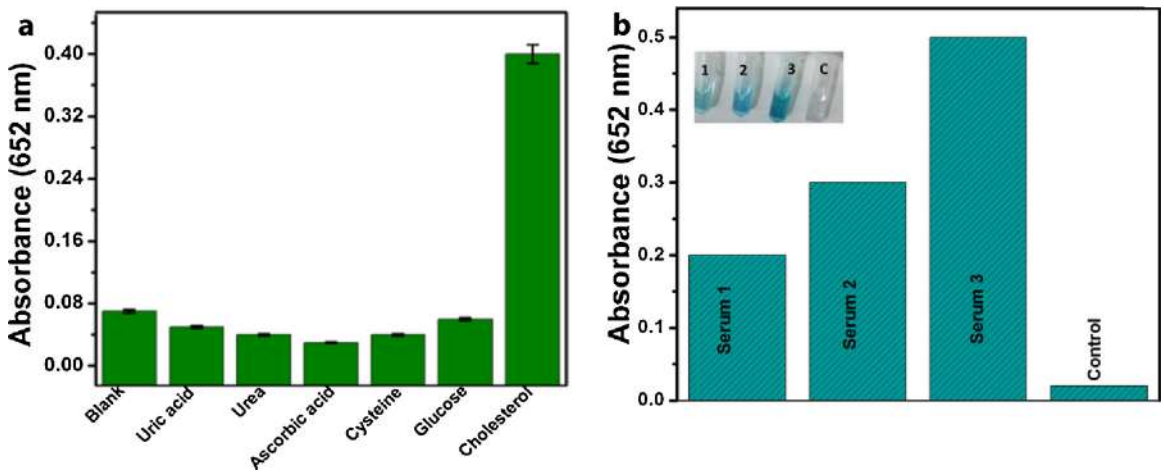

Fig. 9. (a) Selectivity of cholesterol detection. All measurements were performed in 0.5 mL of 0.15 M NaH_2PO_4 buffer solutions (pH 3.5) containing 1 mM TMB, 2 μg/mL GQDs and 1 mg/mL cholesterol oxidase. The error bars represent the standard deviation of three time measurements and (b) the absorbance at 652 nm for a 10 fold serial dilution of a serum sample. Inset: Images of production of colored product for serum samples. (For interpretation of the references to color in this figure legend, the reader is referred to the web version of the article.)

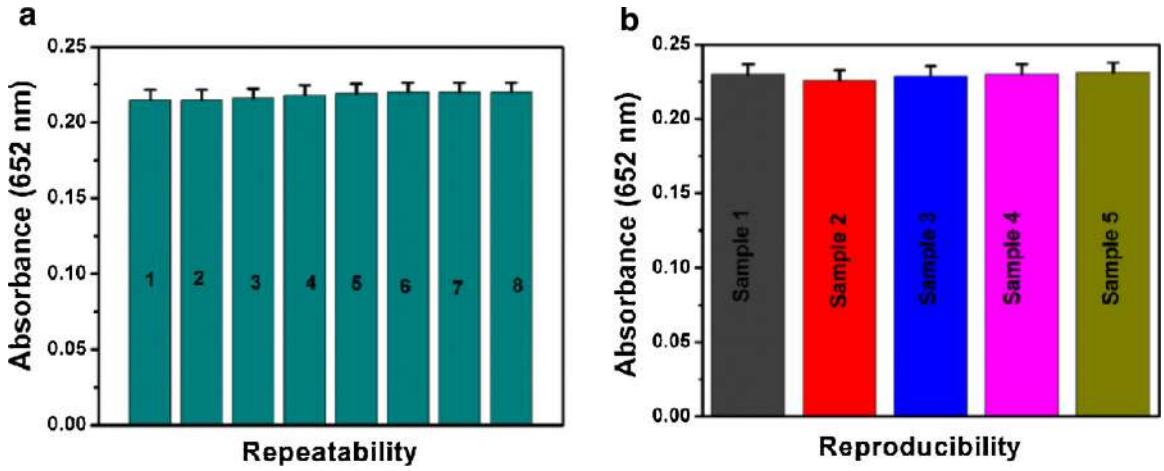

Fig. 10. (a) Repeated experiments for eight times using GQDs (2 μg/mL), (1 mM) TMB solution via the same set of procedure with ChOx (1 mg/mL) (0.1 mM) cholesterol conducted in 0.5 mL of 0.15 M NaH_2PO_4 buffer solutions and (b) the reproducibility for five samples using same set reaction.

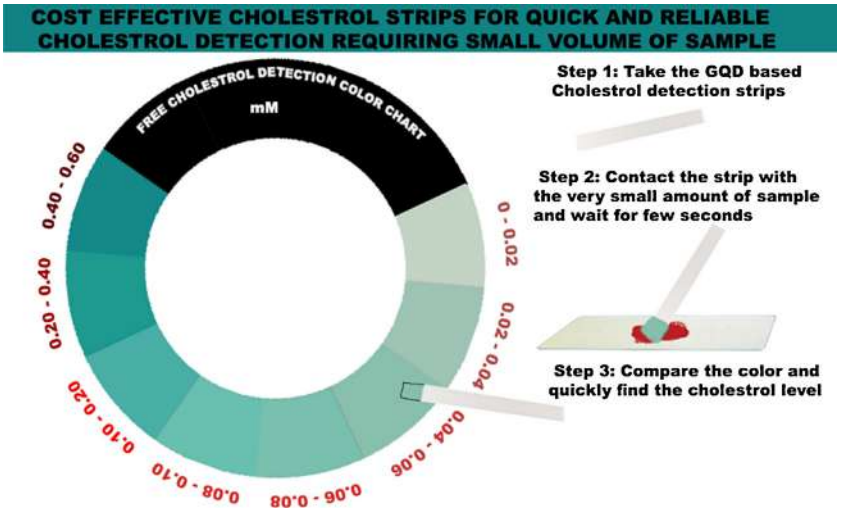

Fig. 11. The schematic representation of fabrication of cholesterol strip for cholesterol detection in sample.

Furthermore, because the color change from colorless to blue when the system meets cholesterol is observable by the naked eyes, it is easy to realize visual detection without any instrumentation or complicated design. Although the actual quantification of the cholesterol level requires the absorption study as discussed above, but the most acknowledgeable point here is that the shades of blue color obtained are in direct relation with the amount of cholesterol in the analyte. Hence in Fig. 11, we propose a cholesterol detection color wheel that can be used effectively with the combination with the system for immediate cholesterol detection. In future simple GQDs based cost effective cholesterol detection strips can be fabricated and used as illustrated in the figure for quick and reliable cholesterol measurement.

4. Conclusions

By the way of conclusion, we report cost effective, quick, facile single-step large scale synthesis of graphene quantum dots (GQDs) as an enzyme mimetic of horse radish peroxidases (HRP), for unprecedented application of free cholesterol detection. The results attest our system to be simple, inexpensive, highly sensitive and selective enough to work successfully when used to detect free cholesterol in a complex system of human serum. Typically, these GQDs show cholesterol detection limit as low as 0.006 mM along with high V_{max} and low K_m value. These values supersede most of the previously reported nanomaterials used in biosensing, suggesting highly efficient peroxidase like catalytic activity with better binding affinity of enzyme to substrate (cholesterol), which is desirable for good biosensor stability and resistance to environmental interferences. In addition, these ultra-small sized GQDs show high diffusion rate and excellent biocompatibility in aqueous solutions ensuring easy combination with biomolecules. Additionally the potential of the proposed system to be used on field lies in the direct relationship of the color shade with the amount of cholesterol in the analytes. Hence a cholesterol detection color wheel is presented here, which can be used in future along with cost effective cholesterol detection strip fabricated using the proposed system. Thus, this proposed GQDs system shows great potential for application in various fields, such as biosensing and medical diagnostics and has the potential of on field applications.

Acknowledgments

NRN acknowledges the financial assistance from UGC (RJNF-JRF-SC-252). Authors are thankful to Shobhit Pandey for editing the manuscript. P. S. Saxena acknowledges CAS program in Zoology Department, B.H.U., Varanasi, India, funded by UGC. A.S. acknowledges the DST, New Delhi, India, and CAS program in Department of Physics, B.H.U., India.

Appendix A. Supplementary data

Supplementary data associated with this article can be found, in the online version, at http://dx.doi.org/10.1016/j.snb.2015.04.091

References

[1] E. Ikonen, Cellular cholesterol trafficking and compartmentalization, Nat. Rev. Mol. Cell Biol. 9 (2008) 125–138.
[2] N.B. Myant, The Biology of Cholesterol and Related Steroids, Elsevier, 1981.
[3] S. Aravamudhan, A. Kumar, S. Mohapatra, S. Bhansali, Sensitive estimation of total cholesterol in blood using Au nanowires based micro-fluidic platform, Biosens. Bioelectron. 22 (2007) 2289–2294.
[4] S. Lan Hsia, R. Duncan, A.H. Schob, S.C. Chakko, R. Mulingtapang, J.L. He, et al., Serum levels of high-density lipoprotein phospholipids correlate inversely with severity of angiographically defined coronary artery disease, Atherosclerosis 152 (2000) 469–473.
[5] N. Zhang, Y. Liu, L. Tong, K. Xu, L. Zhuo, B. Tang, A novel assembly of Au NPs-beta-CDs-FL for the fluorescent probing of cholesterol and its application in blood serum, Analyst 133 (2008) 1176–1181.
[6] A. Devadoss, J.D. Burgess, Detection of cholesterol through electron transfer to cholesterol oxidase in electrode-supported lipid bilayer membranes, Langmuir 18 (2002) 9617–9621.
[7] R.S. Dey, C.R. Raj, Development of an amperometric cholesterol biosensor based on graphene–Pt nanoparticle hybrid material, J. Phys. Chem. C 114 (2010) 21427–21433.
[8] J. Li, Z. Zhang, S. Xu, L. Chen, N. Zhou, H. Xiong, et al., Label-free colorimetric detection of trace cholesterol based on molecularly imprinted photonic hydrogels, J. Mater. Chem. 21 (2011) 19267–19274.
[9] G. Wulff, Enzyme-like catalysis by molecularly imprinted polymers, Chem. Rev. 102 (2002) 1–28.
[10] P. Pang, Y. Zhang, S. Ge, Q. Cai, S. Yao, C.A. Grimes, Determination of glucose using bienzyme layered assembly magnetoelastic sensing device, Sens. Actuators B: Chem. 136 (2009) 310–314.
[11] Y.P. Chau, K.S. Lu, Investigation of the blood-ganglion barrier properties in rat sympathetic ganglia by using lanthanum ion and horseradish peroxidase as tracers, Acta Anat. (Basel) 153 (1995) 135–144.
[12] R. Breslow, Biomimetic chemistry and artificial enzymes catalysis by design, Acc. Chem. Res. 28 (1995) 146–153.
[13] E. Shoji, M.S. Freund, Potentiometric sensors based on the inductive effect on the pKa of poly(aniline): a nonenzymatic glucose sensor, J. Am. Chem. Soc. 123 (2001) 3383–3384.
[14] W.C. Ellis, C.T. Tran, M.A. Denardo, A. Fischer, A.D. Ryabov, T.J. Collins, Design of more powerful iron-TAML peroxidase enzyme mimics, J. Am. Chem. Soc. 131 (2009) 18052–18053.
[15] Q. Wang, Z. Yang, X. Zhang, X. Xiao, C.K. Chang, B. Xu, A supramolecular-hydrogel-encapsulated hemin as an artificial enzyme to mimic peroxidase, Angew. Chem. Int. Ed. Engl. 46 (2007) 4285–4289.
[16] M. Sono, M.P. Roach, E.D. Coulter, J.H. Dawson, Heme-containing oxygenases, Chem. Rev. 96 (1996) 2841–2888.
[17] G. Pelossof, R. Tel-Vered, J. Elbaz, I. Willner, Amplified biosensing using the horseradish peroxidase-mimicking DNAzyme as an electrocatalyst, Anal. Chem. 82 (2010) 4396–4402.
[18] C. Burda, X. Chen, R. Narayanan, M.A. El-Sayed, Chemistry and properties of nanocrystals of different shapes, Chem. Rev. 105 (2005) 1025–1102.
[19] L. Gao, J. Zhuang, L. Nie, J. Zhang, Y. Zhang, N. Gu, et al., Intrinsic peroxidase-like activity of ferromagnetic nanoparticles, Nat. Nanotechnol. 2 (2007) 577–583.
[20] J. Mu, Y. Wang, M. Zhao, L. Zhang, Intrinsic peroxidase-like activity and catalase-like activity of Co_3O_4 nanoparticles, Chem. Commun. (Camb.) 48 (2012) 2540–2542.
[21] X. Wang, K. Qu, B. Xu, J. Ren, X. Qu, Multicolor luminescent carbon nanoparticles: synthesis, supramolecular assembly with porphyrin, intrinsic peroxidase-like catalytic activity and applications, Nano Res. 4 (2011) 908–920.
[22] Y. Song, Y. Chen, L. Feng, J. Ren, X. Qu, Selective and quantitative cancer cell detection using target-directed functionalized graphene and its synergetic peroxidase-like activity, Chem. Commun. (Camb.) 47 (2011) 4436–4438.
[23] Y. Song, W. Wei, X. Qu, Colorimetric biosensing using smart materials, Adv. Mater. 23 (2011) 4215–4236.
[24] Y. Song, X. Wang, C. Zhao, K. Qu, J. Ren, X. Qu, Label-free colorimetric detection of single nucleotide polymorphism by using single-walled carbon nanotube intrinsic peroxidase-like activity, Chemistry 16 (2010) 3617–3621.
[25] Y. Song, K. Qu, C. Zhao, J. Ren, X. Qu, Graphene oxide: intrinsic peroxidase catalytic activity and its application to glucose detection, Adv. Mater. 22 (2010) 2206–2210.
[26] W. Shi, Q. Wang, Y. Long, Z. Cheng, S. Chen, H. Zheng, et al., Carbon nanodots as peroxidase mimetics and their applications to glucose detection, Chem. Commun. (Camb.) 47 (2011) 6695–6697.
[27] A.-X. Zheng, Z.-X. Cong, J.-R. Wang, J. Li, H.-H. Yang, G.-N. Chen, Highly-efficient peroxidase-like catalytic activity of graphene dots for biosensing, Biosens. Bioelectron. 49 (2013) 519–524.
[28] A.P. Alivisatos, Semiconductor clusters, nanocrystals, and quantum dots, Science 271 (1996) 933–937.
[29] Y. Wu, J. Zhou, N. Fishkin, B.E. Rittmann, J.R. Sparrow, Enzymatic degradation of A2E, a retinal pigment epithelial lipofuscin bisretinoid, J. Am. Chem. Soc. 133 (2011) 849–857.
[30] L.A. Ponomarenko, F. Schedin, M.I. Katsnelson, R. Yang, E.W. Hill, K.S. Novoselov, et al., Chaotic Dirac billiard in graphene quantum dots, Science 320 (2008) 356–358.
[31] S. Zhu, J. Zhang, C. Qiao, S. Tang, Y. Li, W. Yuan, et al., Strongly green-photoluminescent graphene quantum dots for bioimaging applications, Chem. Commun. (Camb.) 47 (2011) 6858–6860.
[32] Y. Zhu, S. Murali, W. Cai, X. Li, J.W. Suk, J.R. Potts, et al., Graphene and graphene oxide: synthesis, properties, and applications, Adv. Mater. 22 (2010) 3906–3924.
[33] M. Terrones, A.R. Botello-Méndez, J. Campos-Delgado, F. López-Urías, Y.I. Vega-Cantú, F.J. Rodríguez-Macías, et al., Graphene and graphite nanoribbons: morphology, properties, synthesis, defects and applications, Nano Today 5 (2010) 351–372.
[34] A.K. Geim, K.S. Novoselov, The rise of graphene, Nat. Mater. 6 (2007) 183–191.
[35] S. Chandra, P. Das, S. Bag, D. Laha, P. Pramanik, Synthesis, functionalization and bioimaging applications of highly fluorescent carbon nanoparticles, Nanoscale 3 (2011) 1533–1540.

[36] L. Cao, X. Wang, M.J. Meziani, F. Lu, H. Wang, P.G. Luo, et al., Carbon dots for multiphoton bioimaging, J. Am. Chem. Soc. 129 (2007) 11318–11319.
[37] S.C. Ray, A. Saha, N.R. Jana, R. Sarkar, Fluorescent carbon nanoparticles: synthesis, characterization, and bioimaging application, J. Phys. Chem. C 113 (2009) 18546–18551.
[38] X. Sun, Z. Liu, K. Welsher, J.T. Robinson, A. Goodwin, S. Zaric, et al., Nano-graphene oxide for cellular imaging and drug delivery, Nano Res. 1 (2008) 203–212.
[39] V. Gupta, N. Chaudhary, R. Srivastava, G.D. Sharma, R. Bhardwaj, S. Chand, Luminscent graphene quantum dots for organic photovoltaic devices, J. Am. Chem. Soc. 133 (2011) 9960–9963.
[40] K. Gong, F. Du, Z. Xia, M. Durstock, L. Dai, Nitrogen-doped carbon nanotube arrays with high electrocatalytic activity for oxygen reduction, Science 323 (2009) 760–764.
[41] Y. Zhang, C. Wu, X. Zhou, X. Wu, Y. Yang, H. Wu, et al., Graphene quantum dots/gold electrode and its application in living cell H_2O_2 detection, Nanoscale 5 (2013) 1816–1819.
[42] L. Su, J. Feng, X. Zhou, C. Ren, H. Li, X. Chen, Colorimetric detection of urine glucose based $ZnFe_2O_4$ magnetic nanoparticles, Anal. Chem. 84 (2012) 5753–5758.
[43] Q. Chen, M. Liu, J. Zhao, X. Peng, X. Chen, N. Mi, et al., Water-dispersible silicon dots as a peroxidase mimetic for the highly-sensitive colorimetric detection of glucose, Chem. Commun. (Camb.) 50 (2014) 6771–6774.
[44] A. Aghaei, M.R. Milani Hosseini, M. Najafi, A novel capacitive biosensor for cholesterol assay that uses an electropolymerized molecularly imprinted polymer, Electrochim. Acta 55 (2010) 1503–1508.
[45] Y. Li, H. Bai, Q. Liu, J. Bao, M. Han, Z. Dai, A nonenzymatic cholesterol sensor constructed by using porous tubular silver nanoparticles, Biosens. Bioelectron. 25 (2010) 2356–2360.
[46] C. Zhao, L. Wan, L. Jiang, Q. Wang, K. Jiao, Highly sensitive and selective cholesterol biosensor based on direct electron transfer of hemoglobin, Anal. Biochem. 383 (2008) 25–30.
[47] A.A. Abdelwahab, M.-S. Won, Y.-B. Shim, Direct electrochemistry of cholesterol oxidase immobilized on a conducting polymer: application for a cholesterol biosensor, Electroanalysis 22 (2010) 21–25.
[48] E. Viturro, M. Koenning, A. Kroemer, G. Schlamberger, S. Wiedemann, M. Kaske, et al., Cholesterol synthesis in the lactating cow: induced expression of candidate genes, J. Steroid Biochem. Mol. Biol. 115 (2009) 62–67.
[49] R. Li, C. Xiong, Z. Xiao, L. Ling, Colorimetric detection of cholesterol with G-quadruplex-based DNAzymes and ABTS2-, Anal. Chim. Acta 724 (2012) 80–85.

Biographies

Narsingh Raw Nirala, is a Ph.D. student in the Department of Zoology at Banaras Hindu University (BHU), India. He received his Master degree (M.Sc.) in Biotechnology from BHU, Varanasi, India. His current research interests focus on study of immobilization of biomolecules (enzyme and cancer biomarker) on different substrates (carbon materials and metal nanoparticles) for sensitive detection.

Shiju Abraham received his M.Sc. degree in Physics from Annamalai University, India in 2005. He is presently pursuing Ph.D. from Department of Physics at Banaras Hindu University. He has also been a visiting research scholar at Institute of Physical Chemistry, Jena and Solid State Nanophysics, Max Planck Institute for Solid State Research, Stuttgart, Germany. He is working in the area of graphene based biosensors and plasmonics.

Vinod Kumar is a postdoctoral fellow at the Institute of Nanoscience & Technology, Mohali, India. He received his Ph.D. degree in 2014 from Banaras Hindu University, India. His current research interests focus on biomedical application of carbon nanomaterials with a special attention in the field of tissue engineering and disease diagnosis.

Anushka Bansal is currently pursuing B.Tech. from Metallurgical Engineering, Indian Institute of Technology (BHU), Varanasi, India. Her research interest lies in applications of low dimensional nanomaterials and their composites in interdisciplinary fields.

Anchal Srivastava received his Ph.D. from Banaras Hindu University in 2002. He continued in the same department as a post-doctoral fellow and later joined as a lecturer in 2004. He is currently serving as an assistant professor at Department of Physics, BHU. He specializes in the area of synthesis, characterizations and applications of carbon nanomaterials. He has been awarded the Max Planck India fellowship and carried out his research at Max Planck Institute of Solid State Physics, Stuttgart, Germany in Professor Klaus Von Klitzing's group. He has also been awarded the prestigious BOYSCAST fellowship from government of India in 2008–09 during which he carried out research on graphene and related materials at Professor P.M. Ajayan's group in Rice University. He has also been a visiting research scholar at Rensselaer Polytechnic Institute, USA in 2006.

Preeti S. Saxena, received her Ph.D. from University of Rajasthan, Jaipur in 2003. At present, she is working as Assistant Professor at Department of Zoology, BHU. She is doing research in the area of nanobiology, nanotoxicology and biosensing. She has also been a visiting research scholar at Rensselaer Polytechnic Institute, USA in 2006.